ICF10

Honolulu (USA)

2001

Vol. D

POST-IMPACT FATIGUE BEHAVIOR OF HIGH TEMPERATURE POLYMER MATRIX COMPOSITES

Kazumi HIRANO

National Institute of Advanced Industrial Science and Technology (AIST), METI.
Namiki 1-2, Tsukuba-shi, Ibaraki-ken 305-8564, JAPAN

ABSTRACT

Recently, the feasibility studies have been done as a part of evaluating and predicting long-term durability performance of candidate composite and structures in Japan Supersonic Research Program for 2nd Generation Supersonic Civil Transport in order to achieve through long-term and short-term tests under conditions simulating SST flight, development of associated predictive and accelerated test methods, and assessment of durability performances for design. This paper discussed in details the long-term durability, especially post-impact fatigue performance of the interesting and candidate high temperature polymer matrix composites and summarized the effects of low-velocity impact damage on fatigue behavior in a comparison with the open-hole fatigue behavior.

KEYWORDS: Post-impact Fatigue, High Temperature Polymer Matrix Composites, Fully Reversed Tension-compression Fatigue, Low-velocity Impact Damage, Residual Compressive Strength

INTRODUCTION

Recently, the feasibility studies have been done as a part of evaluating and predicting long-term durability performance of candidate polymer matrix composite materials and structures in Japan Supersonic Research Program for 2nd Generation Supersonic Civil Transport [1] in order to achieve through long-term and short-term tests under conditions simulating SST flight, development of associated predictive and accelerated test methods, and assessment of durability performances for design.

It is very important for a wide practical use of polymer matrix composites how to ensure the impact damage tolerance for long-term structural integrity. Generally, static compressive strength of laminated composites can be significantly reduced by delamination. Delamination can develop at a free edge, particularly at a hole, where inter-laminar stresses are very high. Delamination can also develop from low-velocity impact. Impact damages have strong influences on not only static strength characteristics but also fatigue behavior. Relatively little information is available on the post-impact fatigue behavior of advanced high temperature thermosetting and thermoplastic polymer matrix composites as compared with conventional epoxy matrix composites.

The objective of this paper is to investigate the post-impact fatigue behavior between the interesting high temperature polymer matrix composites. The low-velocity impact damage was introduced into a narrow coupon type laminated specimen and then performed the fully reversed tension-compression fatigue tests. The effects of low-velocity impact damages on fatigue lives were summarized for both the screening of new

composite materials and the determination of a baseline fatigue design allowable for ensuring the long-term structural integrity of primary structural components.

MATERIALS AND EXPERIMENTAL PROCEDURE

Materials
The materials chosen in this study are carbon fiber reinforced, toughened bismaleimide (BMI), G40-800 /5260, thermoplastic polyimide, IM600/PIXA-M and thermosetting polyimide, MR50K/PETI-5. They are laid up into a 32-ply quasi-isotropic laminate with a $[+45°/0°/-45°/90°]_{4s}$ stacking sequence. Room temperature mechanical and chemical properties [2] are summarized in Table 1.

TABLE 1 Summary of mechanical and chemical properties

	G40-800/5260	IM600/PIXA-M	MR50K/PETI-5
OHT MPa	569	461	426
Tensile modulus GPa	NA	58.2	55.1
OHC MPa	385	309	317
Compressive modulus GPa	57.2	60	53.8
CAI (1500 in.·lb/in.)	358	383	298
Tg °C	274	235	250

Test Specimens
Post-impact fatigue specimens
A narrow coupon type specimen with same configuration and dimensions to open-hole (6.35 mm-dia.) fatigue specimen was used for the post-impact fatigue test. After machining from the as-fabricated panels, the impact damage was introduced at the center of specimen. Figure 1 shows the configuration and dimensions of the post-impact fatigue specimen. All specimens were nondestructively inspected before testing to document machining defects. There was no biasing of damage development due to initial defects.
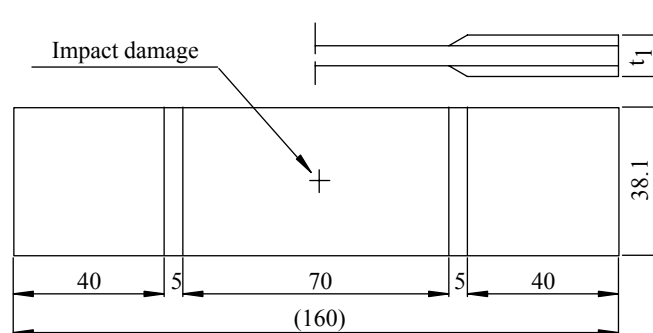

Figure 1: Post-impact fatigue test specimen dimensions

Test Equipment and Procedure
Impact test
Impact load was directly applied on a coupon type specimen by using an instrumented drop-weight impact tester. The test fixture used for the impact portion of this study contained a 30 mm-diameter opening. A free-falling mass impacted at the center of the specimen. The impactor set-up and test fixture are shown in Fig. 2. The total weight of the impactor with a 12.7 mm diameter steel spherical tup was approximately 1.9 kg. The impact acceleration and impact force were measured using a piezoelectric accelerometer and two strain gages mounted on the impactor. The impact acceleration and impact force were recorded with a digital data acquisition system.

The coupon-type specimens were mounted in the holder (see Fig. 2), and the bolts were torqued to 49 J. The instrumented impactor was centered above the coupon-type specimen at the required height to impact the desired impact energy per unit thickness. After the impactor struck the specimen, a piece of thick GFRP was quickly moved between the fixture and specimen to prevent the impactor from repeatedly hitting the

specimen. Three series of impact energy per unit thickness of 1668, 3336 and 6672 J/m (equal to 1500 in.·lb/in.), which are very low as compared with an industry standard for evaluating thick, quasi-isotropic laminates, were chosen.

Open-hole and post-impact fatigue tests
The open-hole fatigue and post-impact fatigue tests were performed with load controlled-mode, sinusoidal wave-form, at a constant cyclic frequency of 5 Hz using the personal computer-controlled MTS materials testing system with a environmental chamber kept temperature at $23 \pm 1°C$ and relative humidity at $50 \pm 2\%$. All specimens were loaded in fully reversed tension-compression fatigue with R= -1. Cyclic stress versus strain curves were continuously measured by using extensometer (gauge length 25.4 mm) mounted on the specimen side edge, and monitored stiffness changes as a means of evaluating damage accumulation during fatigue loading.

Laser optical microscope, SEM and soft X-ray radiograph examinations were also conducted at various fatigue cycles in order to examine fatigue damages initiated and propagated from both impact damaged area and a root of initial circular hole.
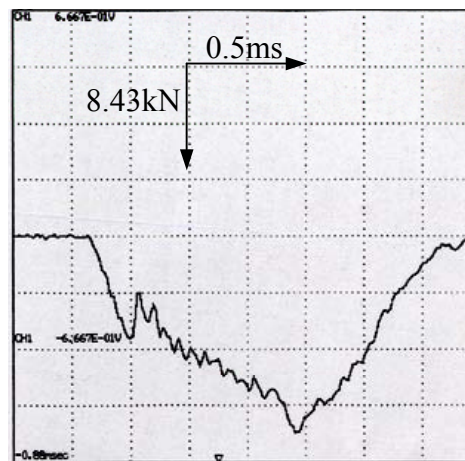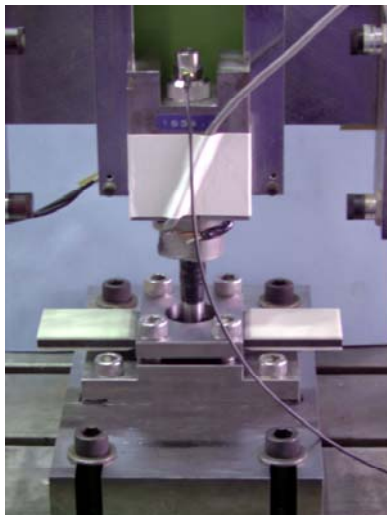
    (a) Impactor set-up and test fixture   (b) G40-800/5260 (3336 J/m)
Figure 2: An instrumented drop-weight impact tester and impact force versus time record

RESULTS AND DISCUSSION

Impact Damage
An example of typical impact force versus time record is shown for G40-800/5260 in Fig. 2(b). The peak impact force in a case of impact energy per unit thickness of 3336 J/m was approximately 14.75 kN. The force-time signals for all the impact tests were almost consistent for every material. The impactor rebounded on the first collision and was out of the way before the test specimen rebounded. The high-frequency oscillations throughout the load-time histories are mostly ringing of the impactor and vibrations of the specimens.

Before and after impact, each specimen was nondestructively evaluated to examine the extent of impact damage by laser optical microscope, soft X-ray and C-scanned ultrasonic examinations. The plastically deformed area at the impact surface was measured with the use of the laser optical microscope. The impact energy versus maximum depth of plastically deformed area relationships are shown in Fig. 3. At lower energy level, there is almost linear relationship regardless of materials. The G40-800/5260 composite had an even smaller plastically deformed area. The standard deviation was calculated for each of the impact area data sets. It showed a small variation especially within no fiber breakage damages for every material. This low standard deviation indicates that the impacts were consistent and repeatable.
Typical internal damage patterns observed by soft X-ray examinations are shown in Figs. 4(a), (b) and (c) for impact energy per unit thickness of 6672 J/m. The IM600/PIXA-M had a larger impact damaged area.

They had many transverse cracks in every 0°, ±45° and 90° laminate layers and delaminations especially at -45°/90° interlayer. There are much differences in extents of un-symmetric internal impact damages fundamentally depending on both toughness of matrix resin and inter-lamellar properties. Figure 4 also shows that these impact damaged area doesn't spread to whole specimen width within the limits of this experiment.
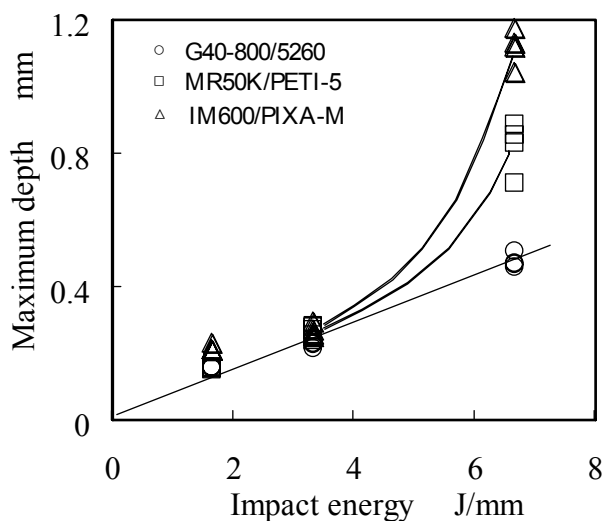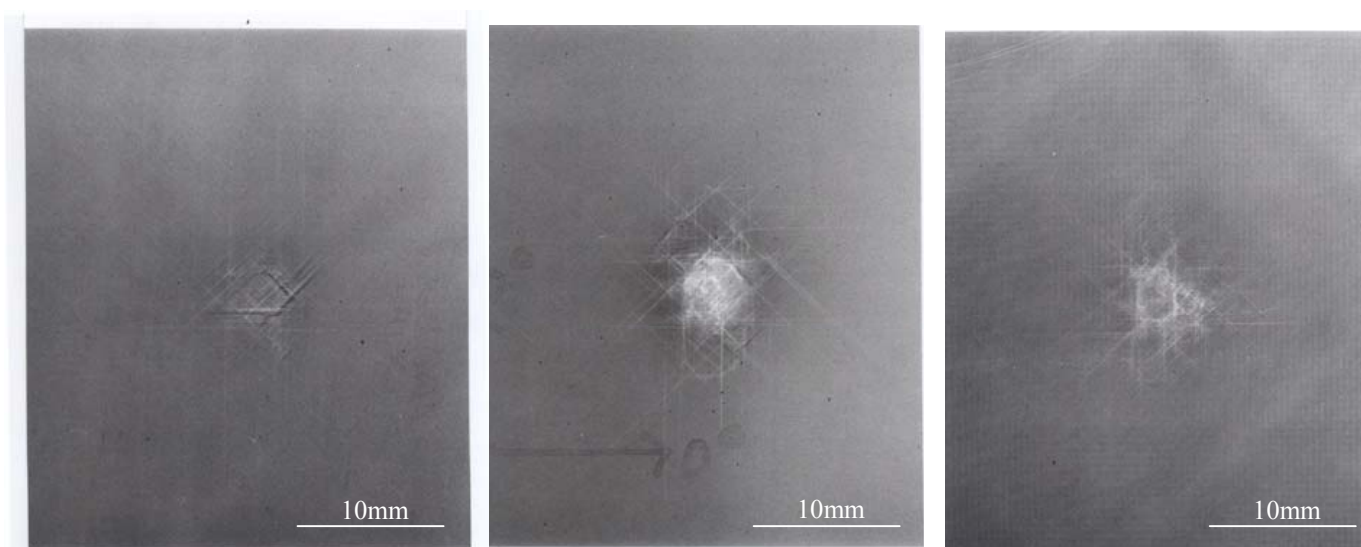

Figure 3: Relationships between impact energy and maximum depth of plastically deformed area

(a) G40-800/5260   (b) IM600/PIXA-M   (c) MR50K/PETI-5

Figure 4: Soft X-ray examinations of impact damages (Impact energy per unit thickness: 6672 J/m)

Post-impact Tension-compression Fatigue

To assess the effects of impact damage on fully reversed tension-compression fatigue behavior, the S-N curves were compared with the smooth and open-hole specimens. Minimum gross compressive stresses are plotted against cycles to failure (log scale) in Figs. 5 to 7. Linear least squares regression fits to the data are also drown. These figures show that there is a remarkable influence of low-velocity impact damage and fatigue lives rapidly decreases with increasing of impact energy. There is much influence for IM600/PIXA-M with a larger impact damaged area and a lower residual compressive static strength after impact.

On the other hand, the normalized S-N curves in terms of static strength are consistent with those of open-hole specimens regardless of materials. It is concluded here that the decreases of fatigue lives fundamentally resulted from the reduction of static strength after impact damage. It is successfully predicted the fatigue lives of impact damaged specimen from normalized S-N curve and residual compressive static strength. It is very interesting that there is also a distinguishable knee point in the S-N curves of impact

damaged specimen resulted from the transition in fatigue failure mode from compressive failure in the low cycles region to tensile failure in the high cycles region. There is no transition in fatigue failure mode in the whole cycles region for the MR50K/PETI-5.
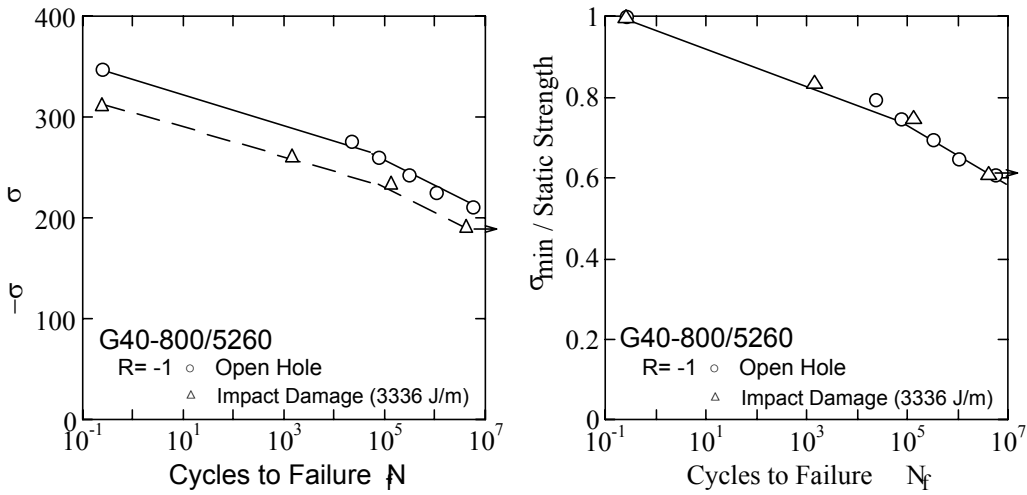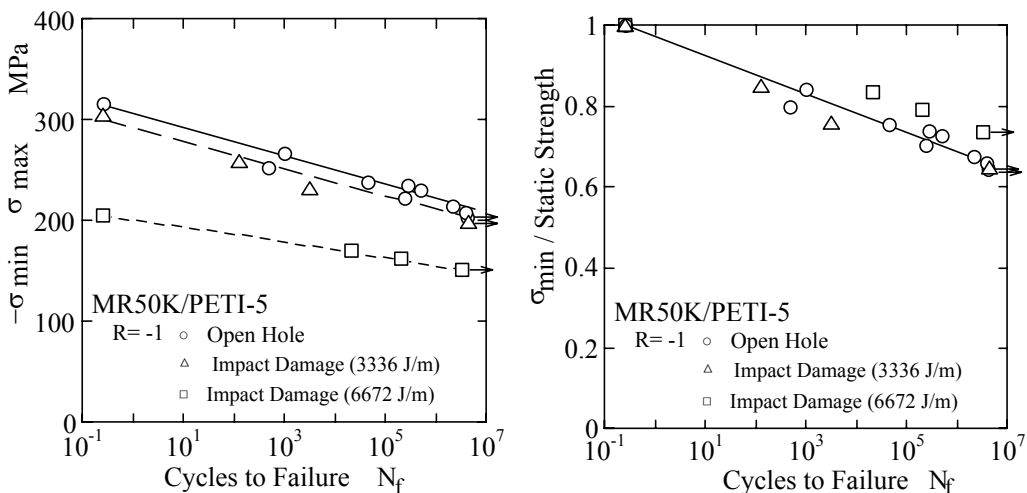

(a) S-N curves   (b) Normalized S-N curves

Figure 5: Comparisons of post-impact fatigue lives with open-hole specimens for G40-800/5260
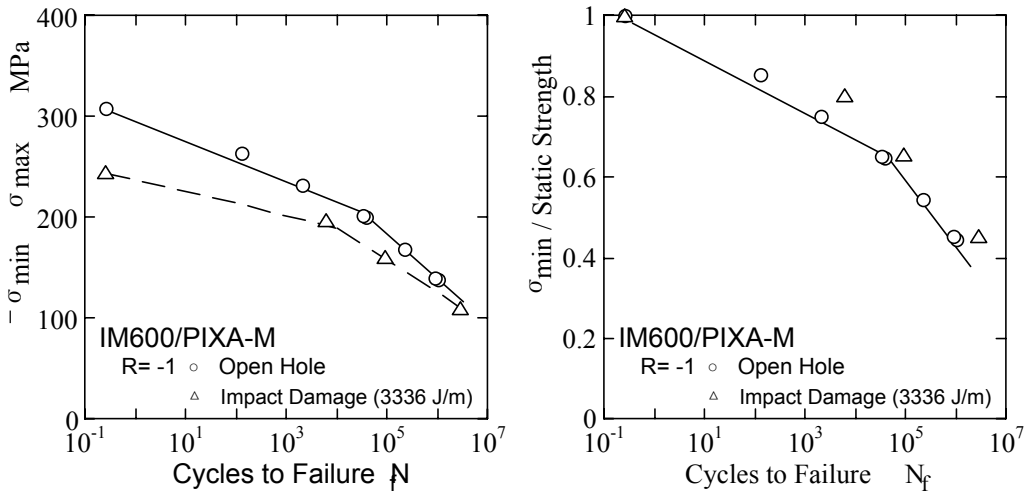
(a) S-N curves   (b) Normalized S-N curves

Figure 6: Comparisons of post-impact fatigue lives with open-hole specimens for IM600/PIXA-M

(a) S-N curves   (b) Normalized S-N curves

Figure 7: Comparisons of post-impact fatigue lives with open-hole specimens for MR50K/PETI-5

We have urgently done the following researches in order to achieve through long-term and short-term tests under conditions simulating SST flight, development of associated predictive and accelerated test methods,

and assessment of durability performances for design.
- Failure mode transition in open-hole fully reversed, tension-compression fatigue behavior [3]
- High temperature open-hole compressive fatigue behavior [4]
- Moisture absorption effects on open-hole fatigue behavior [5]
- Thermo-mechanical response under the simulated SST flight cycles [6] and long-term durability analysis and database [7]

CONCLUSIONS

(1) There is a quite difference in the extent of low-velocity impact damages among the high temperature polymer matrix composites. For low-impact damage, compared on equal impact energy level, the residual compressive static strengths of the G40-800/5260 were slightly greater than those of the IM600/PIXA-M and MR50K/PETI-5.

(2) There is a remarkable influence of low-velocity impact damage on fatigue lives. The IM600/PIXA-M with a larger impact damaged area and a lower residual compressive static strength after impact has lower fatigue lives than those of the G40-800/5260 and MR50K/PETI-5.The G40-800/5260 composite was more resistant to initial impact damage, but the MR50K/PETI-5 composite was more tolerant to fatigue damage after impact.

(3) The normalized S-N curves in terms of static strength are consistent with those of open-hole specimens regardless of materials. The decreases of fatigue lives fundamentally resulted from the reduction of static strength after impact damage. It is successfully predicted the fatigue lives of low-velocity impact damaged specimen from normalized S-N curve and residual compressive static strength.

ACKNOWLEDGEMENTS

REFERENCES

1. Hirano, K., Strategies for R&D on Construction and Preparation of Design Database for Advanced Composite Materials, *J. of the Japan Society for Composite Materials,* Vol.26, No.1 (2000), PP.3-8 (in Japanese)

2. NEDO Report, Studies on Establishment of Long-term Durability Testing and Methodologies for High Temperature Polymer Matrix Composites, March 31, 2000 (in Japanese)

3. Hirano, K., Long-term Durability Performance for Advanced High Temperature Polymer Matrix Composites, To be published in *ICCM-13*, June 25-29, 2001

4. Hirano, K., Miyake, S. and Yoshida, H., Moisture Absorption Effect on Open-hole Fatigue Behavior for High Temperature Polymer Matrix Composites, To be presented at *ICCE/8*, August 5-11, 2001

5. Hirano, K., Miyake, S. and Yoshida, H., Comparisons of Open-hole Fatigue Strength Characteristics for High Temperature Polymer Matrix Composites for the Next Generation Aircraft, To be published in Proc. of *APCFS&ATEM'01*, October 20-22, 2001

6. Hirano, K., Suzuki, T., Miyake, S., Noda, M. and Yamaguchi, Y., Thermo-mechanical Response under the Simulated SST Flight Profile and Residual Open-hole Tension/Compression Strength Characteristics for Advanced High Temperature Polymer Matrix Composites, To be presented at *5th International Conference on Durability Analysis of Composite Systems*, November 6-9, 2001

7. Hirano, K., Current Status and Future Prospects on Establishment of Design Database for Advanced Composites and Structures in Japan, To be presented at *7th Japan International SAMPE Symposium & Exhibition*, November 13-16, 2001

PREDICTING THE FATIGUE-LIFE OF STRUCTURAL ADHESIVE JOINTS

A.J. Kinloch, A.J. Curley[1], H. Hadavinia, and A.C. Taylor

Department of Mechanical Engineering, Imperial College of Science, Technology and Medicine, Exhibition Road, London SW7 2BX, UK.
[1]Present address: Kingston University, School of Computer Science and Electronic Systems, Kingston upon Thames, London, KT1 2EE, UK.

ABSTRACT

A fracture-mechanics approach has been used to predict the cyclic-fatigue performance of the adhesively-bonded single-lap joint and a typical bonded component, represented by an adhesively-bonded 'top-hat' box-beam joint. The joints were tested under cyclic-fatigue loading in either a 'wet' or 'dry' environment, respectively. Several steps were needed to predict the cyclic-fatigue lifetime of these joints. Firstly, fracture-mechanics tests were used to obtain the relationship between the rate of fatigue crack growth per cycle, da/dN, and the maximum strain-energy release-rate, G_{max}, applied during the fatigue cycle for the adhesive/substrate system under investigation, in both a 'dry' and a 'wet' test environment. Secondly, analytical and finite-element theoretical models were developed to describe the variation of the strain-energy release-rate, G, with crack length, a, as a function of the applied fatigue loads, for the single-lap joint and the 'top-hat' box-beam joint. Thirdly, the experimental results from the short-term fracture-mechanics tests, obtained under similar test conditions and in the same environment as were used for the single-lap or bonded box-beam joints, were combined with the modelling results from the theoretical studies. This enabled the cyclic-fatigue performance of the single-lap or bonded box-beam joints to be predicted over relatively long time-periods. The agreement between the theoretical predictions and the experimentally-measured cyclic-fatigue behaviour for the joints was found to be very good.

KEYWORDS

Adhesives, Fatigue, Finite-element analysis, Fracture mechanics, Lifetime predictions.

INTRODUCTION

The use of adhesive bonding in industry has greatly increased in recent years. However, its use in truly structural applications is still often limited. This is mainly due to a lack of confidence in the performance of adhesive joints, since the mechanical performance of the joints may deteriorate upon being subjected to cyclic-fatigue loading, especially if the joints are also exposed to a moist environment [1-4]. Thus, the ability to quantitatively describe this reduction in performance and to predict the lifetime of bonded joints would be a powerful tool, enabling manufacturers to make wider and more efficient use of adhesive bonding. In the present paper, mild-steel substrates have been employed which have been bonded using a rubber-toughened hot-curing epoxy adhesive.

Firstly, fracture-mechanics tests are undertaken to identify the relationship between the rate of fatigue crack growth per cycle, da/dN, as a function of the maximum strain-energy release-rate, G_{max}, applied during a fatigue cycle. These cyclic-fatigue tests are conducted in both a 'dry' environment of $23\pm1°C$ and 55% relative humidity, and a 'wet' environment of immersion in distilled water at $28\pm1°C$.

Secondly, the cyclic fatigue of bonded (uncracked) single-lap joints in the 'wet' environment is studied. Analytical and finite-element models are developed to describe the variation of the maximum strain-energy release-rate, G_{max}, with the length, a, of the growing fatigue crack in the adhesively-bonded single-lap joints. These models are then combined with the results from the above experimental fracture-mechanics data, which have also been conducted under cyclic-fatigue loading in the appropriate environment. These combined expressions are integrated between the initial (i.e. intrinsic or Griffith) flaw size, a_o, and the crack length at final failure. Hence, the predicted number of cycles to failure for the lap joints may be deduced as a function of the cyclically-applied load. These predictions are compared with the experimental results, and the accuracy of the two approaches (i.e. via the analytical and the finite-element modelling studies) assessed. The sensitivity of the predictions to the boundary conditions employed, for example to the initial flaw size, is also discussed. The fracture-mechanics approach to lifetime prediction described above assumes that the cyclic-fatigue life of the lap joints is dominated by the propagation of cracks, rather than the initiation of such cracks. Thus, it is of some importance to establish whether this assumption is indeed correct, and therefore a backface-strain technique [3,5,6] is used to investigate crack growth in the lap joints during the fatigue tests.

Thirdly, a finite-element model is used to predict the rate of crack growth in a typical adhesively-bonded component subjected to cyclic-fatigue loading, but in this case in a 'dry' environment. The component selected is a bonded 'top-hat' box-beam, loaded from one end of the bonded 'top-hat' section in a cantilever-bending mode. The predictions of the expected cyclic-fatigue life are again compared with the experimental results.

RESULTS AND DISCUSSION
Fracture-mechanics data
The fracture-mechanics data were obtained using tapered double-cantilever beam (TDCB) adhesive-joint specimens and the experimental results obtained relate the rate of cyclic-fatigue crack growth, da/dN, to the maximum strain-energy release-rate, G_{max}, applied during a fatigue cycle, see Figure 1 for example. Obviously, the fracture-mechanics tests need to be conducted under similar test conditions as the joints, or components, whose service-life is to be predicted. It is also important to ensure that the TDCB fatigue test specimens do indeed exhibit a similar locus of

failure as observed in the joints, or components, whose lifetime is to be predicted. The locus of failure of the different joints was therefore studied to ensure that this was indeed the case.

It was found that the threshold strain-energy release-rate, G_{th}, below which no cyclic-fatigue crack growth occurred, as measured in the 'dry' environment, was significantly lower than the value of the adhesive fracture energy, G_c, determined under monotonic loading. Further, the value of G_{th}, was often further reduced if the cyclic-fatigue tests were conducted in water, as opposed to the 'dry' environment. Since the time-scales of such 'wet' cyclic-fatigue tests are relatively short, they act as a very effective accelerated test technique and may readily be used to 'rank' the durability of adhesive joints. For example, 'wet' fatigue tests may be employed to compare, and develop, different and novel types of surface treatments for polymeric and metallic substrates - this is of particular importance since the surface treatment employed may have a major effect on the durability of the bonded joint.

Now, it is well established that the linear, central, region (labelled 'Region II' in Figure 1) of the plot of the relationship between logarithmic da/dN and G_{max} may be modelled by using an expression based upon the Paris Law [7]:

$$\frac{da}{dN} = DG_{max}^n \tag{1}$$

where D and n are obtained by fitting the above equation to the experimental data. However, as may be seen in Figure 1, the complete relationship between logarithmic da/dN and G_{max} is of a sigmoidal form. A lower-bound occurs at the fatigue threshold, G_{th}, where the crack growth rate is negligible ('Region I' in Figure 1) and an upper-bound occurs which is equivalent to the adhesive fracture energy, G_c, measured at a constant displacement-rate ('Region III' in Figure 1). Thus, the relationship between logarithmic da/dN and G_{max} may be better expressed by a modified form of the Paris Law, namely [8,9]:

$$\frac{da}{dN} = DG_{max}^n \left[\frac{1 - \left(\dfrac{G_{th}}{G_{max}} \right)^{n_1}}{1 - \left(\dfrac{G_{max}}{G_c} \right)^{n_2}} \right] \tag{2}$$

where G_{th} and G_c are the values of the cyclic-fatigue threshold and constant displacement-rate adhesive fracture energies respectively. The empirical constants n_1 and n_2 may again be obtained by fitting the above expression to the experimental data.

For example, the data obtained from the 'wet' cyclic-fatigue tests on steel TDCB specimens bonded with the epoxy adhesive give D and n values of $1.37 \times 10^{-13} m^2/N.cycle$ and 3.64 respectively. The relationship based upon Eqn. 1 is shown in Figure 1, together with the experimental data. The modified relationship, Eqn. 2, is also shown in Figure 1, and the values of n_1 and n_2 were found by fitting Eqn. 2 to the experimental data.

Modelling
The first step in modelling the cyclic-fatigue lifetime of the bonded joints and components is to obtain an expression to describe the experimentally-measured fracture-mechanics data, i.e. the relationships between the rate of crack growth per cycle, da/dN, and the maximum strain-energy

release-rate, G_{max}, in a fatigue cycle as given in Eqns. 1 or 2, see above. Secondly, the variation of G_{max} with crack length in the joint is theoretically modelled, using either an analytical or a finite-element approach. In the present work, both analytical and finite-element approaches were used for the single-lap joints, though only the finite-element approach was used for the bonded component. Finally, these data are combined and the resulting expression is integrated and, hence, the long-term cyclic-fatigue life of the joint may be predicted.

Predictions: Lap joints

The cyclic-fatigue lifetimes in the 'wet' environment for the single-lap joints predicted using the finite-element model are compared with the experimental results in Figure 2. The overall agreement between this numerical method, as well as via the analytical method, and the experimental results is relatively good, bearing in mind that the fatigue life has been predicted from first principles with no empirical 'fitting factors' being employed. For example, the finite-element modelling studies give a threshold value of the maximum load, T_{max}, per unit width in a fatigue cycle which could be applied to the lap joint of approximately 75 kN/m. This is equivalent to about 25% of the initial failure load, or fracture stress, of the lap joints. This predicted value of 75 kN/m may be compared with the measured value of 90 kN/m, which equivalent to 30% of the initial fracture strength of the lap joints.

However, as may be seen from Figure 2, whilst the agreement from the finite-element models around the threshold portion of the T_{max} versus N_f plots is good, the agreement is clearly poorer as one moves to higher values of T_{max}; i.e. to lower values of N_f. Nevertheless, it may be argued that predicting a lower limit, threshold, load (below which cyclic-fatigue crack growth will not be observed) is the appropriate design philosophy in the case of adhesively-bonded joints. The present models are clearly capable of achieving very good predictions in this respect. It should also be noted that, as discussed above, an upper- and a lower-bound value of the initial flaw size, a_o, may be calculated. However, as may be seen from Figure 2, the sensitivity of the predictions of the fatigue life upon the value of the initial flaw size via any of the above models and expressions is negligible.

Predictions: Bonded component

The adhesively-bonded 'top-hat' box-beam joint was tested under cyclic-fatigue loading in the 'dry' environment, and the predicted rate of crack growth per cycle, da/dN, for a given crack length, a, was calculated using Equation 1. For these predictions, the values of the strain-energy release-rate, G_{max}, as a function of the length, a, of the propagating cyclic-fatigue crack were calculated from the finite-element model of the bonded component. The values of D and n, that are also needed, were obtained from the experimental fracture-mechanics data (see above), from tests conducted of course in the 'dry' environment. The experimental results and the predictions are shown in Figure 3 and, as may be seen, the agreement between the predicted values and the experimental data is very good.

CONCLUSIONS

The main aim of the work described in the present paper has been to predict the service-life of bonded joints and components when they are exposed to cyclic-fatigue loading. The basic idea derives from the fact that the cyclic-fatigue fracture-mechanics data may be gathered in a relatively short time-period, but may be applied to other designs of bonded joints and components, whose service-life may then be predicted over a far longer time-span. Thus, cyclic-fatigue fracture mechanics test have been conducted, and the results then combined with analytical and finite-element models, to predict the fatigue performance of bonded single-lap joints and a bonded 'top-hat' box-beam joint. The theoretical predictions were compared with the experimental results and the agreement was found to be very good.

REFERENCES

1. Kinloch, A.J. (1987) *Adhesion and Adhesives: Science and Technology.* Chapman and Hall, London.
2. Mostovoy, S. and Ripling, E.J. (1966) *Journal of Applied Polymer Science,* 10, 1351.
3. Curley, A.J., Hadavinia, H., Kinloch, A.J. and Taylor, A.C. (2000) *Int. J. Fract.*, 103, 41.
4. Kinloch, A.J., Little, M.S.G. and Watts, J.F. (2000) *Acta Mater.,* 48, 4543.
5. Imanaka, M., Haraga, K. and Nishikawa, T. (1995) *Journal of Adhesion*, 49, 197.
6. Zhang, Z., Shang, J.K. and Lawrence, F.V., Jr. (1995) *Journal of Adhesion,* 49, 23.
7. Paris, P.C. and Erdogan, F. (1963) *Journal of Basic Engineering,* 85(4), 528.
8. Martin, R.H. and Murri, G.B. (1990) *ASTM STP,* 1057, 251.
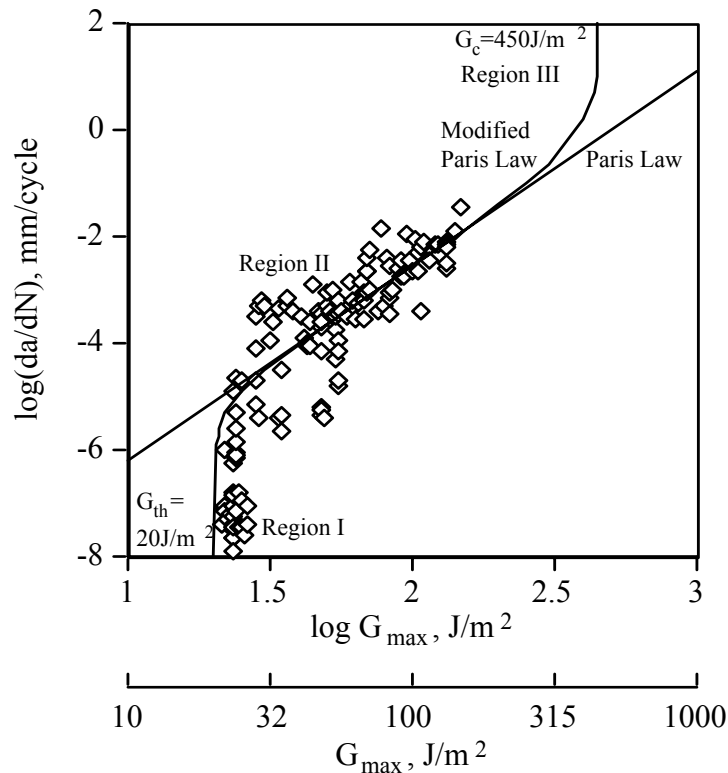9. Kinloch, A.J. and Osiyemi, S.O. (1993) *Journal of Adhesion,* 43, 79.

Figure 1: Logarithmic crack growth rate per cycle, *da/dN*, versus logarithmic, and linear, G_{max}, for the cyclic-fatigue fracture-mechanics tests performed in the 'wet' environment of 28°C and water immersion. The relationships for Eqns. 1 and 2 are shown by the solid lines.
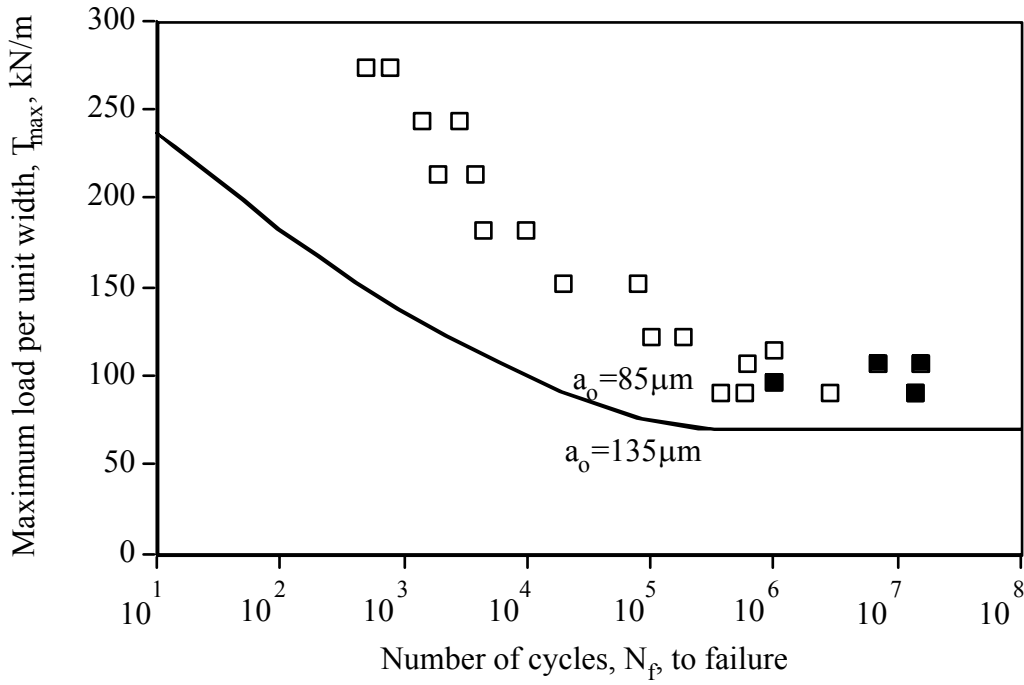
Figure 2: The number, N_f, of cycles to failure in a 'wet' environment for the single lap joints as a function of the maximum load, T_{max}, per unit width applied in a fatigue cycle. The points represent the experimental data whilst the lines are the predicted lifetimes using the finite-element model. Theoretical results are given for a_o values of 85 or 135μm by the solid and dashed lines, respectively.
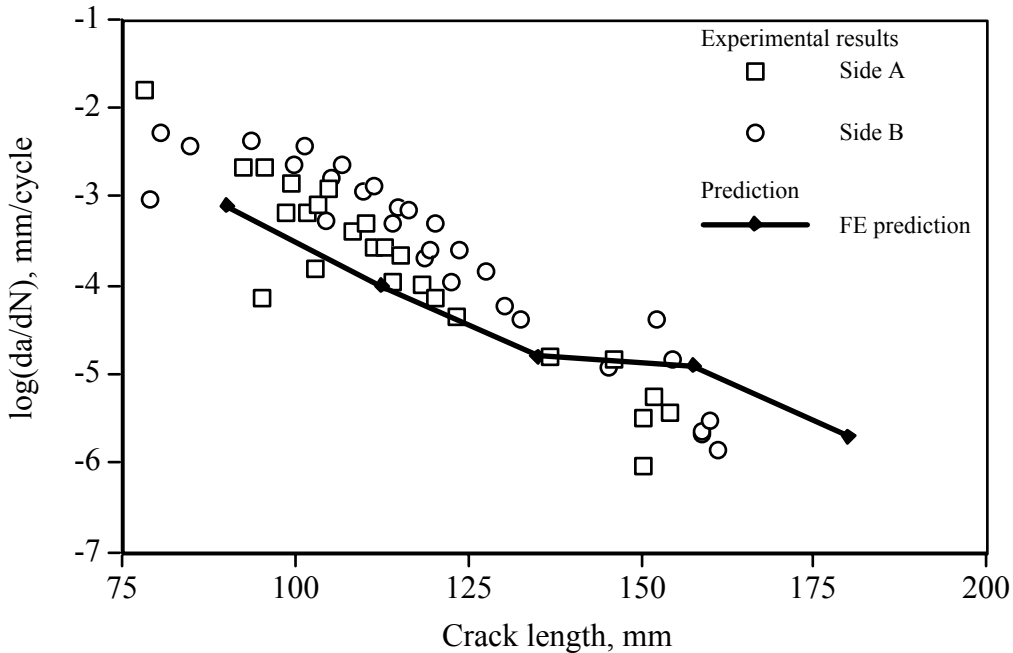

Figure 3: Logarithmic rate of crack growth per cycle, *da/dN*, versus the length, *a*, of the propagating cyclic-fatigue crack for the bonded 'top-hat' component tested in a 'dry' environment. The open points represent the experimental data, whilst the solid line is the predicted crack growth rate from using the finite-element model.

Prediction for Dry Sliding Wear in P/M Alloy:
A back-propagation ANN approach

Mohammed E. Haque [1] and K. V. Sudhakar [2]

[1] Department of Construction Science, Texas A&M University,
College Station, TX 77843-3137, USA
[2] Department of Industrial and Engineering Technology, Central Michigan University,
Mount Pleasant, MI 48859, USA

ABSTRACT

An artificial neural network (ANN) based model was developed, trained and evaluated for studying the dry sliding wear behavior of Fe-2%Ni based powder metallurgy (P/M) alloy as a function of heat treatment. The P/M alloy in the as-sintered (designated AS, hardness 7 HRC) as well as in the hardened and tempered at 813 K (designated HT1), and at 593 K (designated HT2) conditions having hardness 30 HRC and 40 HRC respectively were investigated for their wear behavior. Several different ANN back-propagation models with different layers/slabs connections, weights with various weight updating methods, and activation functions including logistic, symmetric logistic, linear, Gaussian, and Gaussian complement were trained. The presented ANN back-propagation model with logistic activation function exhibited the excellent statistical performance both in the training and evaluation phases. The wear rate was found to decrease initially and remain almost constant with increasing sliding distance in all the samples. This was consistent with the experimental observations. Based on the ANN trained model, wear rate predictions were made for higher hardness (60 HRC) for steel with varying percent of carbon contents (0.3%, 0.4% and 0.6%). Since, the ANN trained model exhibited excellent comparison with the experimental results, it will provide a useful predictor for dry sliding wear rates in powder metallurgy alloys.

KEYWORDS

Wear rate; artificial neural network (ANN); powder metallurgy (P/M) alloy; dry sliding wear; sliding distance

INTRODUCTION

Artificial Neural Networks (ANNs) are revolutionary computing paradigms that try to mimic the biological brain. These ANNs are modeling techniques that are especially useful to address problems where solutions are not clearly formulated [1] or where the relationships between inputs and outputs are not sufficiently known. ANNs have the ability to learn by example. Patterns in a series of input and output values of example cases are recognized. This acquired "knowledge" can then be used by the ANN to predict unknown output values for a given set of input values. Alternatively, ANNs can also be used for classification. In this case, the Artificial Neural Networks' output is a discrete category to which the item described by the input values belongs. ANNs are composed of simple interconnected elements called processing elements (PEs) or

artificial neurons that act as microprocessors. Each PE has an input and an output side. The connections are on the input side correspond to the dendrites of the biological original and provide the input from other PEs while the connections on the output side correspond to the axon and transmit the output. Synapses are mimicked by providing connection weights between the various PEs and transfer functions or thresholds within the PEs. Figure 1 illustrates a simple processing element of an ANN with three arbitrary numbers of inputs and outputs [2].
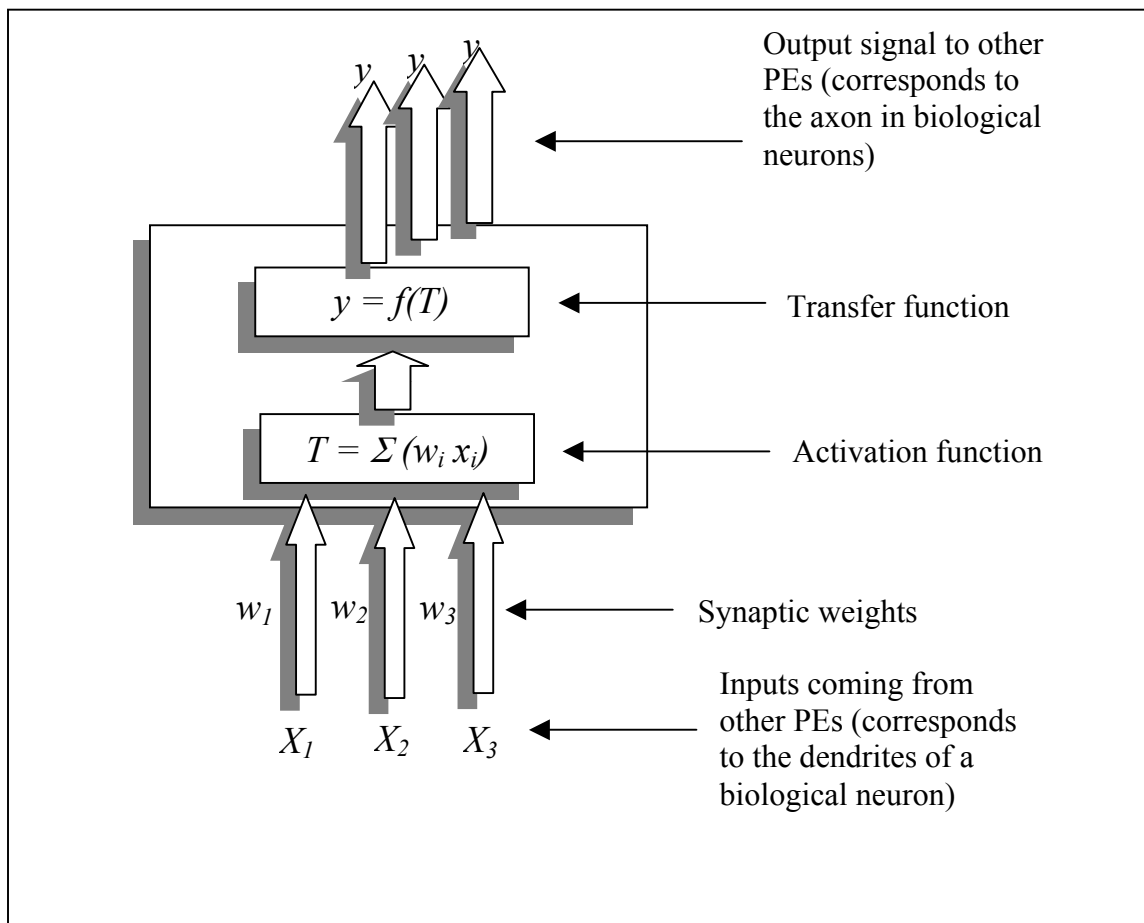

Figure 1 Processing element of an ANN model with three arbitrary numbers of inputs and outputs

The activation of the PE results from the sum of the weighted inputs and can be negative, zero, or positive. This is due to the synaptic weights, which represent excitatory synapses when positive ($w_i>0$) or inhibitory ones when negative ($w_i<0$). The PEs output is computed by applying the transfer function to the activation, which as a result of the synaptic weights, can be negative, zero, or positive. The type of transfer function to be used depends on the type of ANN to be designed. Currently, back-propagation is the most popular, effective and easy to learn model for complex networks [2,3]. To develop a back-propagation neural network, a developer inputs known information, assigns weight to the connections within the network architecture, and runs in the networks repeatedly until the output is satisfactorily accurate. The weighted matrix of interconnections allows the neural networks to learn and remember [4]. In essence, back propagation training adapts a gradient-descent approach of adjusting the ANN weights. During training, an ANN is presented with the data thousands of times (called cycles). After each cycle, the error between the ANN outputs and the actual outputs are propagated backward to adjust the weights in a manner that is mathematically guaranteed to converge [5].

The powder metallurgy processing has the advantage of forming near net shaped components. The advantages of producing complex shapes with close dimensional control at high density (porosity <2%) are

the distinct advantages of this process. There is no published research data in the area of artificial neural network for predicting the wear behavior for P/M alloys. Hence artificial intelligence approach has been used in the present study so that the recent investigation [6] on wear behavior of P/M alloys can be interpreted over a wide range of processing/design parameters.

ANN BACKPROPAGATION MODEL

The neural network used for the proposed model was developed with NeuroShell 2 software by Ward Systems Group, Inc., using a back-propagation architecture with multi- layers jump connections, where every layer (slab) is linked to every previous layer. The network was trained for wear rate. The inputs were sliding distance (500 through 6000 m), hardness (7 HRC, and 40 HRC), and carbon contents (0.3% and 0.4%), and outputs were the wear rate. The number of hidden neurons, for which the logistic activation function, $f(x)=1/\{1+exp(-x)\}$ was used, was determined according to the following formula [7]:

Number of hidden neurons = 0.5(Inputs + Outputs) + √(Number of training patterns)

Training data for the neural network training was obtained from the recent research work [6]. In the research dry sliding wear rate tests were carried out on a standard pin-on-disc machine. The data consisted of variation of wear rates with sliding distance as a function of heat treatments. Three different heat treatments were used which were: (1) AS, as-sintered, (2) HT1, hardened and tempered at 813 K, and (3) HT2, hardened and tempered at 593 K. Materials with two different carbon contents of 0.3% and 0.4% were tested. The training sets (total 100 experimental data points) included data corresponding to heat treatments 'AS' and 'HT2', and data corresponding to 'HT1' treatment (total 50 experimental data points) were used to evaluate the trained model.

Training ANN model

Network training is an act of continuously adjusting their connection weights until they reach unique values that allow the network to produce outputs that are close enough to the desired outputs. This can be compared with the human brain, which basically learns from experience. The strength of connection between the neurons is stored as a weight-value for the specific connection. The system learns new knowledge by adjusting these connection weights. The learning ability of a neural network is determined by its architecture and by the algorithmic method chosen for training. The training method usually consists of one of three schemes:
(1) Unsupervised learning where no sample outputs are provided to the network against which it can measure its predictive performance for a given set of inputs. The hidden neurons must find a way to organize themselves without help from the outside.
(2) Reinforcement learning where the connections among the neurons in the hidden layer are randomly arranged, then reshuffled as the network is told how close it is to solving the problem. Reinforcement learning is also called supervised learning, because it requires a teacher. The teacher may be a training set of data or an observer who grades the performance of the network results.
Both unsupervised and reinforcement suffers from relative slowness and inefficiency relying on a random shuffling to find the proper connection weights.
(3) Back propagation method is proven highly successful in training of multi-layered neural nets. The network is not just given reinforcement for how it is doing on a task. Information about errors is also filtered back through the system and is used to adjust the connection weights between the layers, thus improving performance.

The accuracy of the developed model, therefore, depends on these weights. Once optimum weights are reached, the weights and biased values encode the network's state of knowledge. Thereafter, using the network on new cases is merely a matter of simple mathematical manipulation of these values.

In the present research, several different ANN back-propagation trial models with different layers/slabs connections, weights and activation functions (including linear, Tanh, Tanh15, Sine, Symmetric Logistic, Gaussian, Gaussian Complement, etc.) were trained. In addition, pattern selections including "Rotation" and "Random" were used with weight updates using Vanilla, Momentum and TurboProp. The presented ANN back-propagation model with logistic activation function, "Rotation" for pattern selection, and "TurboProp" for weight updates was the best one among all other trials, which converges very rapidly to reach the excellent statistical performance (as illustrated in System Performance). Figure 2 demonstrates the graphical comparisons between the actual experimental data and the network predicted output during training and evaluation phases. They clearly demonstrate very good agreement between the actual and predicted performance.
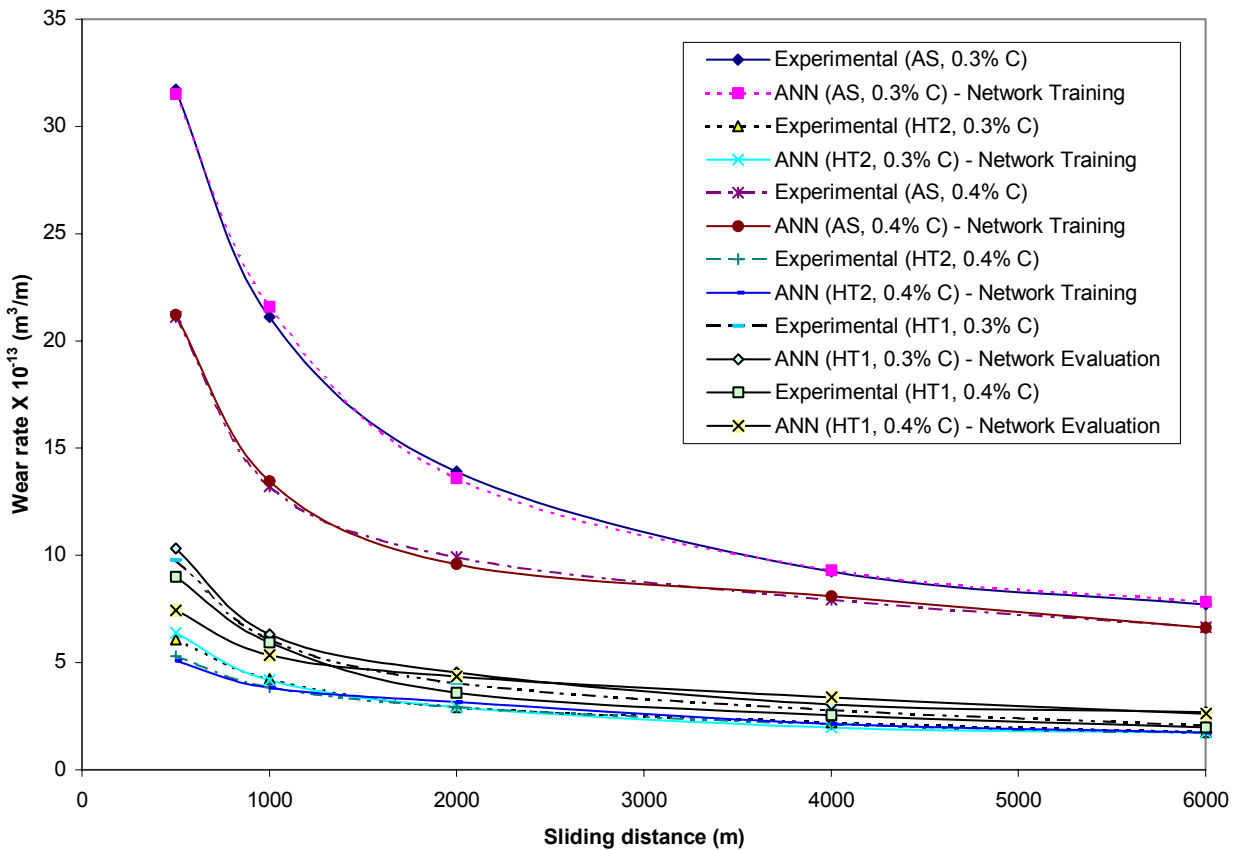

Figure 2 Wear rate vs. sliding distance - ANN training and evaluation performance

System Performance

The neural network used for the presented model demonstrated an excellent statistical performance as indicated by the R^2 and r values. During network training, R^2 was obtained as 0.9993 and 0.9237 during network evaluation, which were very close to 1.0 indicating a very good fit between the actual and the network prediction. R^2 is a statistical indicator usually applied to multiple regression analysis, and can be calculated using the following formulae [7]:

$$R^2 = 1 - (SSE/SS_{yy})$$

Where $SSE = \Sigma (y - \hat{y})^2$, $SS_{yy} = \Sigma (y - \bar{y})^2$, y is the actual value, $\hat{y}$ is the predicted value of y, and $\bar{y}$ is the mean of the y values.

4

The correlation coefficient, r is a statistical measure of the strength of the relationship between the actual vs. predicted outputs. The r coefficient can range from -1 to +1. It will show a stronger positive linear relationship when r is closer to +1, and a stronger negative linear relationship when r is closer to -1. During network training, *r* values were obtained as 0.9997, and 0.9699 during network evaluation, which were very close to +1.0 indicating a very good fit between the actual and the network prediction. The following formulae [7] were used to calculate r:

$$r = SS_{xy}/\sqrt{(SS_{xx}\,SS_{yy})}$$

Where

$$SS_{xy} = \Sigma xy - (1/n)\{(\Sigma x)(\Sigma y)\}$$

$$SS_{xx} = \Sigma x^2 - (1/n)(\Sigma x)^2$$

$$SS_{yy} = \Sigma y^2 - (1/n)(\Sigma y)^2$$

where *n* equals the number of patterns, *x* refers to the set of actual outputs, and *y* refers to the predicted outputs.

PREDICTION OF WEAR RATE

Based on the ANN trained model, wear rates were predicted as a function of sliding distance for P/M steel having hardness 60 HRC and carbon contents at 0.3%, 0.4%, and 0.6% as shown in Figure 3. It may be observed that the wear rate is sensitive and decreasing with the increase in carbon content up to about 4000 m sliding distance. Beyond a sliding distance of 4000 m, the wear rate remains constant and the same
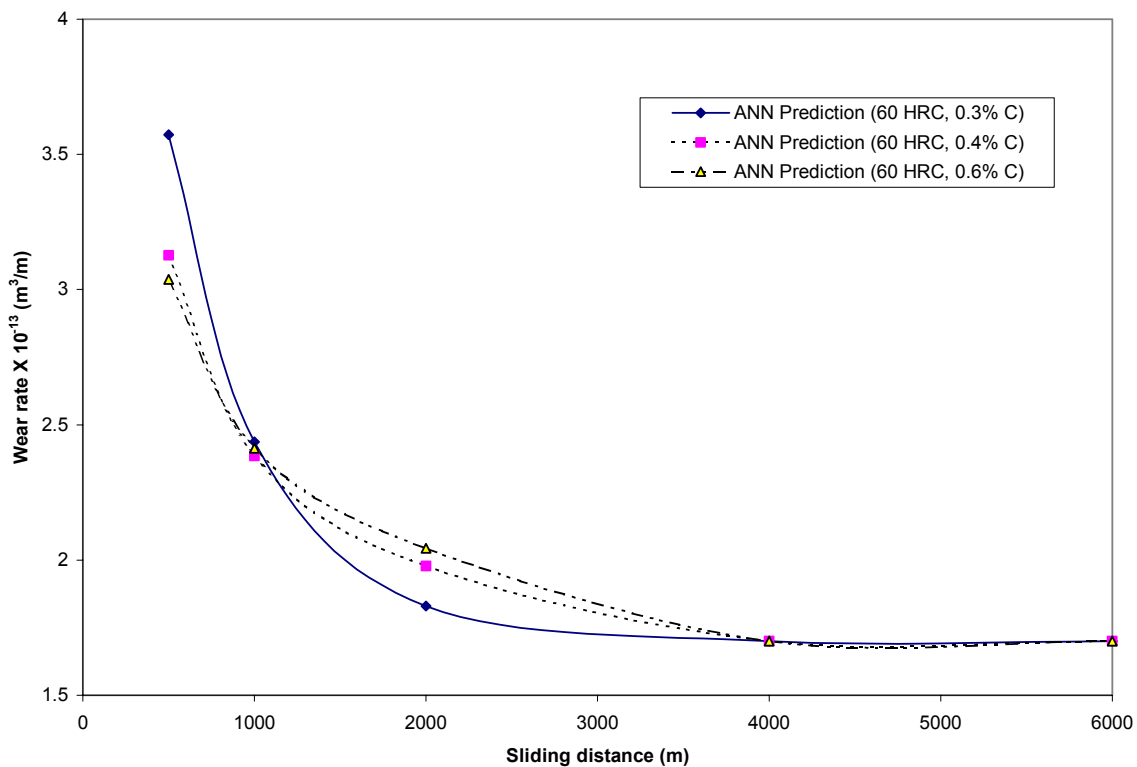

Figure 3 ANN network predicted wear rate vs. sliding distance

irrespective of the carbon contents. Figure 3 clearly predicts that the P/M alloy with 0.6% carbon content and 60 HRC hardness has the minimum wear rate (i.e. having maximum wear resistance) as compared to the other cases having lower carbon contents (0.4% & 0.3%). This is a valid observation since the addition of carbon usually contributes to improved hardness (by forming interstitial solid solution of carbon in iron lattice) in steel and thereby resulting in improved wear resistance property.

CONCLUSIONS

ANN Back-propagation model developed for studying the dry sliding wear behavior of powder metallurgy (P/M) alloys exhibited results consistent with the experimental findings. The prediction of wear behavior for P/M steel at higher hardness and/or higher carbon content is accurate and reliable with the expected trend. Hence, the present ANN based model can be used successfully over a wide range/combination of wear properties in P/M steel.

REFERENCES

1. Chester, M. (1993) *Neural Networks* - A Tutorial, Prentice Hall: Englewood Cliffs, NJ, USA
2. Haque, M.E., Sudhakar, K.V. (2001) ANN based Prediction Model for Fatigue Crack Growth in DP Steel. *Fatigue & Fracture of Engineering Materials and Structures*. (IN PRESS)
3. Haque, M.E., Sudhakar, K.V. (2001) Prediction of Corrosion-Fatigue behavior of DP Steel through Artificial Neural Network. *International Journal of Fatigue,* Vol. 23, Issue 1, pp. 1-4
4. Obermeier, K., and Barron, J. (1989) Time to Get Fried Up, *BYTE*,14 (8) pp. 227-233
5. Rumelhart, D., Hinton, G., and Williams, R. (1986) "Parallel distributed processing," MIT Press, Cambridge, MA., USA
6. K. V. Sudhakar, P. Sampathkumaran, and E. S. Dwarakadasa (2000) Dry sliding wear in High Density Fe-2%Ni based P/M alloys, WEAR (242), pp. 207-212
7. *NeuroShell 2 User's Manual* (1996) Ward Systems Group, Inc., Frederick, MD, USA

ICF100412OR

PREDICTION OF DUCTILE CRACK GROWTH IN POLYETHYLENE USING MEASURED TRACTION – SEPARATION CURVES

K. C. Pandya[1], A. Ivankovic[2] and J. G. Williams[2]

[1]BP (Grangemouth), Applied Technology 7, Bo'ness Road, Grangemouth, Stirlingshire FK3 9XH, UK
[2]Department of Mechanical Engineering, Imperial College of Science, Technology and Medicine, Exhibition Road, London SW7 2BX, UK

ABSTRACT

An accurate prediction of ductile fracture employing a cohesive zone modelling approach depends critically on the choice of the cohesive law used to characterise the material in the crack tip damage zone. A successful new method for direct experimental measurement of this law in tough pipe grade polyethylene has been described recently. Results indicate significant and quantifiable effects of rate and geometrical constraint on the measured cohesive zone parameters: energy of separation and cohesive strength. Here we present a cohesive zone model within the finite volume method to predict crack initiation and propagation history in a tough PE80 type pipe grade polyethylene. A family of experimentally measured rate dependent traction curves is used as a means of establishing the local fracture process. Model predictions indicate that the cohesive zone parameters are not constant but change with both time and position along the crack path depending on the prevailing rate and degree of constraint. By accounting for rate and constraint effects in this manner it should be possible to maintain perceptible physical validity in the representation of the behaviour of the crack tip process region, something not always apparent in many existing cohesive zone models.

KEYWORDS

Crazing, Polyethylene, Cohesive zone model, Ductile crack growth

INTRODUCTION

Conventional fracture mechanics methods are unable to achieve meaningful predictions of ductile crack growth in present-day high strength steels or tough engineering polymers. This is because for these materials, the choice of a single characterising fracture parameter such as a unique stress intensity factor or energy release rate is often a wholly inadequate representation of the material behaviour. The introduction of a material specific process zone ahead of the crack tip appears to

provide a means of overcoming this limitation. Cohesive zone models utilise some form of traction – separation law to describe the material degradation and load carrying capacity due to local deformation within the zone. Using this approach it becomes possible to segregate the local work of fracture from general plasticity within the continuum and thus to predict the global fracture response from a description of the local microstructural behaviour.

Medium density polyethylene may exhibit different modes of fracture, such as rapid crack propagation or slow crack growth, depending upon the prevailing loading rates and temperature. Both rapid crack propagation and slow crack growth are believed to be associated with the formation of a craze ahead of the crack tip. During slow crack growth large scale deformation does not occur, but rather the damage is highly localised. It is this fact that allows the postulation of a thin layer of material, in the most simple case along a prescribed single crack path with an associated cohesive law, to be used for the prediction of crack growth under low rates of loading. General applications of the cohesive zone model include modelling of ductile fracture under quasi-static loading [1] and the analysis of dynamic fracture problems [2,3]. It is increasingly becoming clear, however, that for such models to retain physical reality the cohesive zone parameters must be updated with time, allowing for local mechanisms such as rate dependent hardening and softening or variations in constraint along the crack path to be taken into account in the quantification of the local work of fracture [4,5,6,7]. Pandya and Williams have reported a scheme to measure the cohesive zone law as a function of rate and constraint [8,9] in a range of polyethylenes. These measurements were used for the numerical prediction of crack growth in a rate independent analysis using the finite volume method, which showed reasonable comparison with the measured macroscopic load behaviour [10]. Here we include rate dependence in this numerical scheme by incorporating a family of measured traction – separation curves into the model.

MEASUREMENT OF COHESIVE LAW

The techniques used in the measurement of cohesive zone parameters in tough polyethylene have been described in detail elsewhere [8,9]. In summary, rectangular bars were cut from pressed sheet of dimensions of 16 x 16 x 100 mm and circumferential notches were introduced by rotating the specimen in a lathe so as to produce a highly constrained circular ligament within a square section bar. The specimens were then tested in tension on a screw driven Instron. As the damage is confined within this ligament it is possible to measure the localised traction – separation behaviour of a given material over a range of applied rates. Both notch depth, which affects the degree of constraint, and the applied displacement rate have an effect on the measured law as indicated in Figure 1.
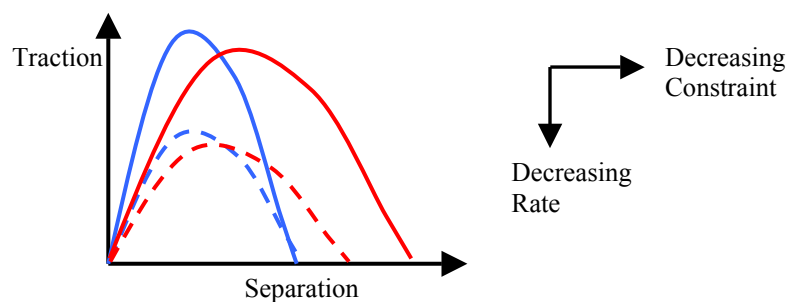

Figure 1: Schematic illustration of the effect of changes in constraint and rate on the measured cohesive law

METHODOLOGY

Results are presented for a pipe grade polyethylene, with a density of 940 kgm^{-3} and a Poisson's ratio of 0.3. A three point bend geometry was modelled within the finite volume method using a 2D plane strain analysis. A cohesive law was used to describe the local separation along a prescribed crack path while the surrounding bulk was treated as elastic-plastic using incremental J2 flow theory. Numerical simulations were performed at an applied displacement rate of 0.1 mm/min and the predicted load – time traces compared to experimental measurements. The boundary conditions for the model are shown in Figure 2. Boundaries 1, 2, 3 and 5 were traction free while the prescribed traction – separation law was applied to boundary 4 along a single layer of cells. The specimen was assumed to be supported on a friction free roller. Making use of geometrical symmetry only half the specimen was modelled.
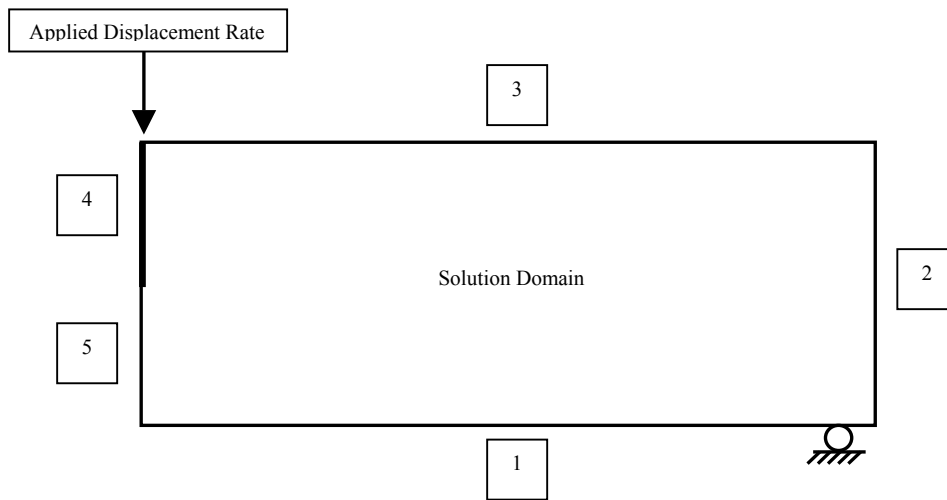

Figure 2: Boundary conditions for the three point bend geometry

Both a single rate and rate dependent analysis was performed. In the first case the initial crack tip opening rate in the three point bend geometry was estimated as 0.006 mm/min and a traction - separation curve measured at that rate in a deep notched, high constraint geometry was used as the cohesive law for all cells along the crack path. In the second case a family of traction - separation curves measured over a range of displacement rates was incorporated into the numerical method. A fully implicit updating procedure was employed to determine the holding traction for each cell by calculating the values of cell displacement and displacement rates via a two way iteration process within each time step. Mesh sensitivity studies were performed and indicated that convergence in the predicted load was achieved for a cell size of 0.1 x 0.1 mm corresponding to a total of 112 cells along the prescribed crack path.

RESULTS

Single Rate Analysis
Traction – separation curves at 0.006 mm/min and 0.004 mm/min were used to perform a single rate analysis and the load – time predictions were compared to the experimentally measured result as shown in Figure 3.
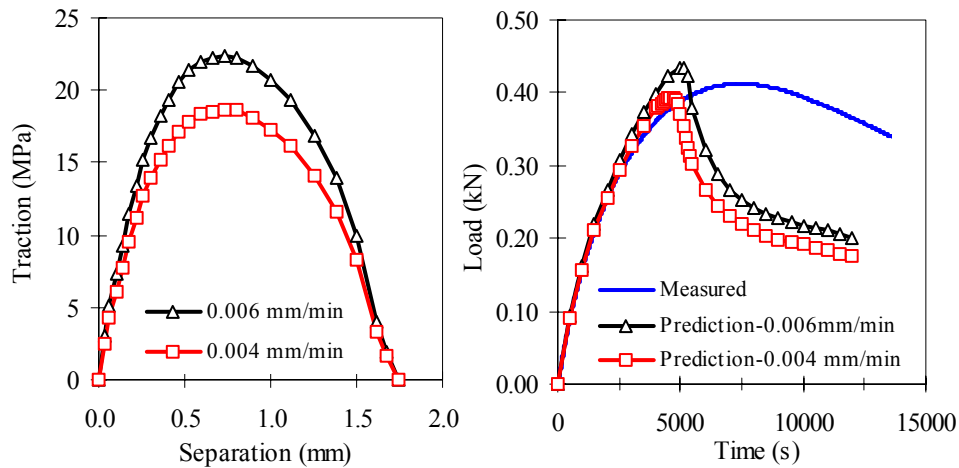
Figure 3: Load – time predictions using a fixed constraint, single rate cohesive law

Figure 3 shows that with a fixed constraint, single rate fracture criterion it is possible to accurately predict the initial part of the load – time curve and the onset of crack initiation. However, the load falling region of the experimental result is not adequately predicted by this method. It is also clear, comparing the two results, that the predicted peak load is directly dependent on the magnitude of the cohesive strength. Cell opening rates and holding tractions for the single rate analysis of 0.006 mm/min were computed at different positions along the prescribed crack path and are shown in Figure 4.
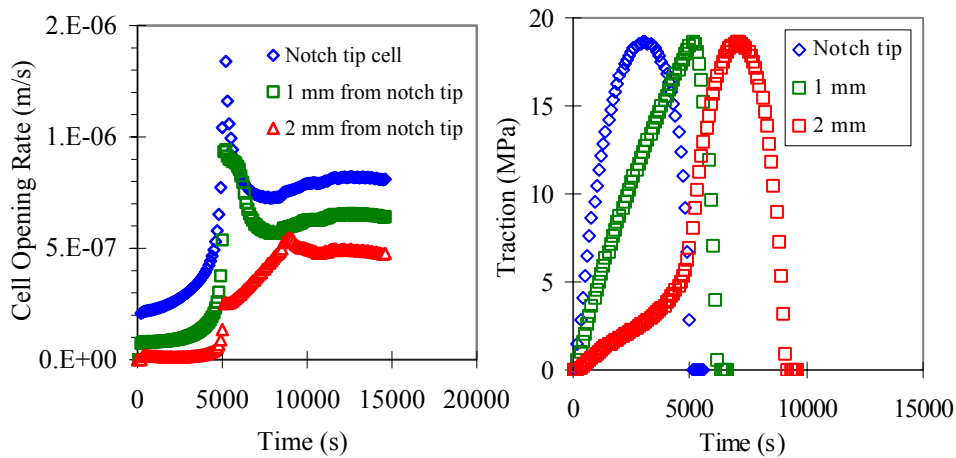

Figure 4: Cell opening rates and holding tractions as a function of time using a fixed constraint, single rate cohesive law

Figure 4 shows that cell opening rates change considerably with both time for a given cell and with position along the crack path, suggesting the need for rate dependence to be incorporated into the analysis.

Rate Dependent Analysis
A family of rate dependent curves was generated by measuring the traction – separation law in a high constraint geometry over a range of displacement rates. Indications from experimental studies on low constraint geometries had suggested that the main effect of a reduction in constraint was to increase the break separation values of the measured curve. On this basis a set of equivalent low constraint traction curves was postulated from the measured high constraint curves. Figure 5 shows a family of both high and low constraint curves along with the associated cohesive law for the notch

tip cell, which emerged as a prediction from the model in each case rather than having to be prescribed in advance. For both set of curves, the predicted notch tip holding traction for a given displacement and displacement rate was determined by interpolating between the curves using the method outlined earlier. The predicted rate dependent cohesive law is seen to deviate substantially from the single rate curve of 0.006 mm/min shown earlier in Figure 3, particularly in the decohesive region where cell opening rates changed rapidly.
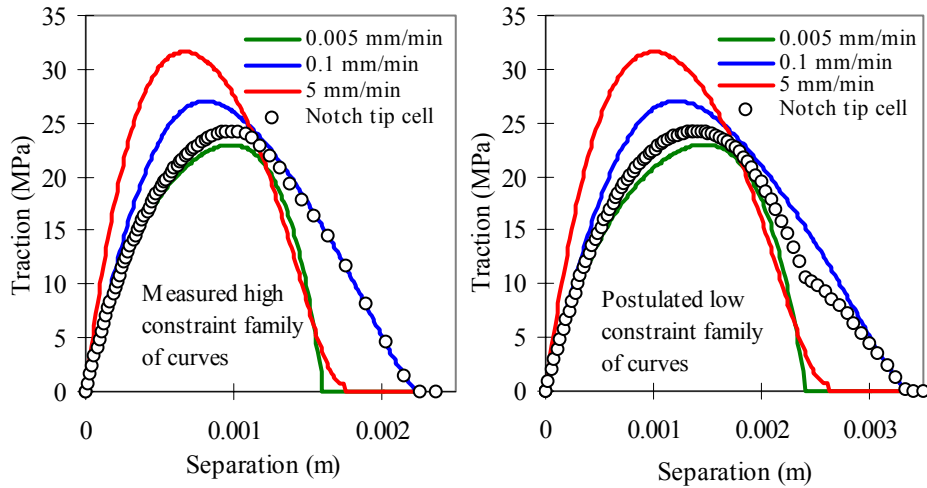

Figure 5: Prediction of the local work of fracture at the notch tip using a family of rate dependent high and low constraint traction curves

The predicted load – time response for the different models discussed above is shown in Figure 6.
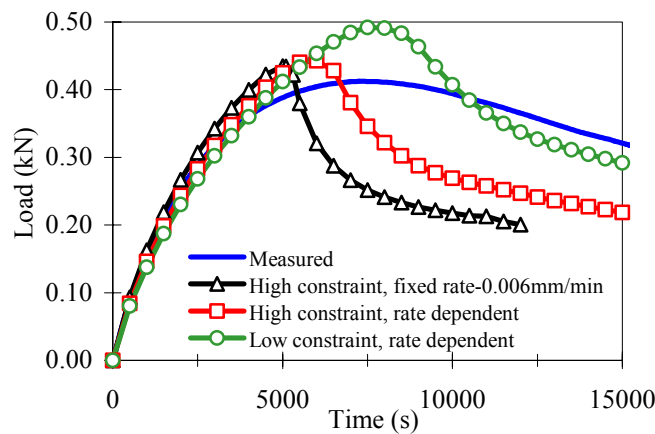

Figure 6: Load – time predictions for different local fracture criteria

Figure 6 indicates the need for constraint variations to be included in the choice of cohesive law, perhaps in a similar manner to the incorporation of rate dependence outlined above. While the high constraint, rate dependent analysis in Figure 6 improves the prediction of crack initiation, it cannot accurately predict global softening, where it is believed that the effect of different prevailing constraint factors along the crack path is not adequately modelled by a fixed constraint cohesive law. The prediction achieved using the family of low constraint curves matches the global softening behaviour more closely but over predicts the global energy dissipated prior to the initiation of crack growth. It seems, therefore, that neither rate or constraint dependence of the cohesive law can be prescribed in advance and that the time dependence of both must be incorporated into the analysis.

CONCLUSIONS

A physically based cohesive zone model was described using experimentally measured rate and constraint dependent traction – separation curves to establish a local cohesive law. Introduction of rate dependence in the choice of the cohesive law improved the prediction of crack initiation but was unable to adequately describe the global softening behaviour. It was suggested that it may be necessary to monitor and update the choice of holding traction at any point in time and position along the crack path in terms of variations in constraint as well as rate. This indicates that the cohesive law cannot be considered to remain constant with crack growth and that a single set of parameters are not sufficient to characterise rate dependent fracture in tough engineering polyethylenes.

REFERENCES

1.   Needleman, A. (1990) Int. J. Fract. 42, 21
2.   Ivankovic, A. (1999) Comput. Mod. Sim. Eng. 4, 227
3.   Murphy, N. and Ivankovic, A. (1999) Proc. 7th Conf. on Computational Mechanics, UK, ACME, pp. 99-102
4.   Knauss, W.G. (1993) Trans. ASME 115, 262
5.   Siegmund, T. and Brocks, W. (1999) Int. J. Fract. 99, 97
6.   Keller, K., Weihe, S., Siegmund, T. and Kroeplin, B. (1999) Comp. Mater. Sci. 16, 267
7.   Sha, Y., Hui, C.Y. and Kramer, E.J. (1999) J. Mater. Sci. 34, 3695
8.   Pandya, K.C. and Williams, J.G. (2000) Polym. Eng. Sci. 40, 1765
9.   Pandya, K.C. and Williams, J.G. (2000) Plast. Rubber Compos. 29, 439
10.   Pandya, K.C., Ivankovic, A. and Williams, J.G. (2000) Plast. Rubber Compos. 29, 447

PREDICTION OF FATIGUE CRACK GROWTH IN MARTENSITIC HIGH STRENGTH LOW ALLOY STEELS

P. Hübner and G. Pusch

University of Mining, Institute of Materials Engineering, D09596 Freiberg, Germany

ABSTRACT

The fatigue crack growth behaviour of ferritic pearlitic steels can be predicted by the model of Roven and Nes assuming that the damage in the cyclic plastic zone in front of the fatigue crack is the same like in an low cycle fatigue specimen. The low cycle fatigue data and the ferrite grain size as the primary dislocation barrier will be used for the prediction of the fatigue crack growth behaviour. The model shows deviations from experimental data in case of high strength low alloy steels with martensitic structure. Therefore the model was improved. The influence of the stress ratio on the fatigue crack growth curve and the threshold value were considered by using the damage parameter of Smith Watson and Topper instead of the Manson-Coffin curve. The primary dislocation barrier in martensitic structures is the size of packets which was used in the model. There is a well correspondence between the experimental data and the predicted fatigue crack growth. The influence of crack closure effects on the threshold was not considered. This results in an underestimation of the threshold.

KEYWORDS: fatigue crack growth, HSLA-steel, microstructure, LCF-damage model

INTRODUCTION

As suggested by Roven and Nes the fatigue crack growth of ferritic pearlitic steels can be predicted with the help of low cycle fatigue data [1]. For this prediction the ferrite grain size and the striations have to be known. Extensive experimental researches have shown, that the proceedings in the cyclic plastic zone before the fatigue crack tip are the same as the proceedings in the LCF-specimen. It also turned out, that the mean values of the striations are constant in a wide area of the fatigue growth. The striations increase with increasing da/dN-values over a critical value of cyclic stress intensity factor of $\Delta K'_{eff} > 20$ MPa$\sqrt{m}$. It follows that in an area $\Delta K_{eff} < \Delta K'_{eff}$ obviously several cycles are necessary to create a striation. Up to know most crack propagation models on the base of the LCF-concept require one cycle for the creation of a striation. There is a good correspondence between the data predicted by the model of Roven and Nes and the experimental data measured at ferritic steel. The applicability of this model to martensitic high strength low alloy steels has to be examined.

THE MODEL OF ROVEN AND NES

Roven and Nes assume that the cycles N_S for the creation of one striation can be calculated by the striation width s and the macroscopic fatigue growth velocity da/dN:

$$N_S = \frac{s}{da/dN} \tag{1}$$

N_S can be calculated by the part of Manson-Coffin curve with the plastic strain range at the crack tip $\Delta \varepsilon_{ap\ tip}$:

$$\Delta \varepsilon_{ap\ tip} = 2 \cdot \varepsilon'_f \cdot (2N_S)^c = 2 \cdot \varepsilon'_f \cdot \left(\frac{2s}{da/dN} \right)^c \tag{2}$$

There is a relation between $\Delta\varepsilon_{ap\,tip}$ and the cyclic crack tip opening displacement $\Delta\delta$:

$$\Delta\varepsilon_{ap\,tip} = \frac{\Delta\delta}{d} \qquad (3)$$

d is the primary dislocation barrier. If the linear fracture mechanics is valid, there exist an relation between $\Delta\delta$ and the cyclic stress intensity factor:

$$\Delta\delta = \frac{\Delta K_{eff}^2}{E \cdot R'_{p0,2}} \qquad (4)$$

ΔK_{eff} is the effective cyclic stress intensity factor corrected with the value of crack closure. Roven and Nes only took the amplitude of the cyclic yield $R'_{p0,2}$ into consideration instead of the range $2* R'_{p0,2}$.
From Eqn. (3) and (4) follows:

$$\Delta K_{eff} = \sqrt{2 \cdot \varepsilon'_f \cdot E \cdot R'_{p0,2} \cdot d \cdot (2N_s)^c} \qquad (5)$$

So that for the fatigue crack growth is valid:

$$\frac{da}{dN} = 2s \cdot \left(2 \cdot \varepsilon'_f \cdot d \cdot E \cdot R'_{p0,2}\right)^{1/c} \cdot \Delta K_{eff}^{-2/c} \qquad (6)$$

Roven and Nes showed, that the da/dN-curves of a low strength steel can be described by the model very well. Because of this the applicability of the model to martensitic steels will be examined. In table 1 the mean values for striation and packet width are given.

TABLE 1
STRIATION AND PACKET WIDTH OF HSLA S890 AND THE BUTT WELD [2]

	Striation width [μm]	Packet width [μm]	Prior austenit grain size [μm]
S890 base metal (BM)	0,32	9,4	17
S890 heat affected zone (HAZ)	0,38	27,1	55
S890 weld metal (WM)	0,28	20,9	64

Figure 1 shows the application of the model to martensitic high strength steel. There are deviations between the predicted and the experimental fatigue crack growth curve.
The limits of the model are that the threshold condition is not available automatically and the influence of the stress ratio on the fatigue crack growth curve is assumed to be caused only by crack closure effect. Crack growth measurements by Hück [3] on steel show a shifting of fatigue crack growth curve by the factor 1,3 if the stress ratio is changed from R = 0 to −1. This is an effect without crack closure because Hück has used the ΔK_{eff} - values for correction. This is in accordance with the fact, that crack closure effect arises at low stress intensity ratios.

IMPROVEMENT OF THE MODEL BY ROVEN AND NES

For improving the model following assumptions have been made:
The crack tip opening displacement has an elastic and a plastic part so the transition into the elastic region I of da/dN-curve can be described. The influence of the stress ratio on the da/dN-curve was considered by using the damage parameter of Smith, Watson and Topper [4] instead of using the Manson-Coffin curve. The yield stress $R'_{p0,2}$ in Eqn. (2) for describing the cyclic behaviour has to be doubled ($2*R'_{p0,2}$). The transition to the accelerated fatigue crack growth is considered with the term $\Delta K_{fc}/(\Delta K_{fc} - \Delta K/(1-R))$.
First we calculate the cycles N_s for a given da/dN-value and a constant striation width s. With the help of Eqn. (7) it is then possible to calculate the damage parameter P_{SWT}.

$$P_{SWT} = \sqrt{\left(\sigma'_f\right)^2 \cdot \left(2N_s\right)^{2b} + E \cdot \sigma'_f \cdot \varepsilon'_f \cdot \left(2N_s\right)^{b+c}} \qquad (7)$$

σ'_f, b, ε'_f and c are constants of Manson-Coffin-Curve $\varepsilon_a = \dfrac{\sigma'_f}{E} \cdot \left(2N\right)^b + \varepsilon'_f \cdot \left(2N\right)^c$.

P_{SWT} is defined as:

$$P_{SWT} = \sqrt{\sigma_o \cdot \varepsilon_{a\,tip} \cdot E} \qquad (8)$$

With the maximum stress $\sigma_o = \sigma_{a\,tip} *2/(1-R)$ follows:

$$P_{SWT} = \sqrt{\sigma_{a\,tip} \cdot \varepsilon_{a\,tip} \cdot E} \cdot \sqrt{2/(1-R)} \qquad (9)$$

and for the strain amplitude at the crack tip:

$$\varepsilon_{a\,tip} = \frac{\left(1-R\right) \cdot P^2_{SWT}}{2 \cdot E \cdot \sigma_{a\,tip}} \qquad (10)$$

For the calculation of ΔK_{eff} a separation from $\varepsilon_{a\,tip}$ and the cyclic yield stress $R'_{p\,0,2}$ in the region of the primary dislocation barrier d is necessary (Eqn. 3 and 4).

$$\Delta\delta = 2 \cdot \varepsilon_{a\,tip} \cdot d = \frac{\Delta K^2_{eff}}{E \cdot 2 \cdot R'_{p0,2}} \qquad (11)$$

That would mean a large-scale procedure by using the cyclic stress-strain-curve and the Neuber's rule. We consider, that $\sigma_{a\,tip}$ is in the order of the cyclic yield $R'_{p0,2}$ and can be used directly for the further calculations.

$$\frac{\Delta K^2_{eff}}{E \cdot 2 \cdot \sigma_{a\,tip}} = 2\varepsilon_{a\,tip} \cdot d \qquad (12)$$

$$\Delta K_{eff} = \sqrt{d \cdot 2 \cdot \varepsilon_{a\,tip} \cdot E \cdot 2 \cdot \sigma_{a\,tip}} \qquad (13)$$

This assumption would make the calculation easier, because $\sigma_{a\,tip}$ and $\varepsilon_{a\,tip}$ have not to be determined by the Neuber's rule. So Eqn. (13) is simplified:

$$\Delta K_{eff} = \sqrt{2 \cdot d \cdot \left(1-R\right)} \cdot P_{SWT} \qquad (14)$$

P_{SWT} has to be calculated with Eqn.(1) from the cycles N_S needed for the creation of one striation s. With the help of Eqn.(14) the ΔK_{eff} -value can be calculated with a given da/dN-value. This given da/dN-value

has to be corrected with the term Eqn. (15) because in the region III of the da/dN-curve an acceleration has to be taken into account.

$$\left(\frac{da}{dN}\right)_{korr} = \frac{da}{dN} \cdot \frac{\Delta K_{fc}}{\Delta K_{fc} - \dfrac{\Delta K}{1-R}} \quad (15)$$
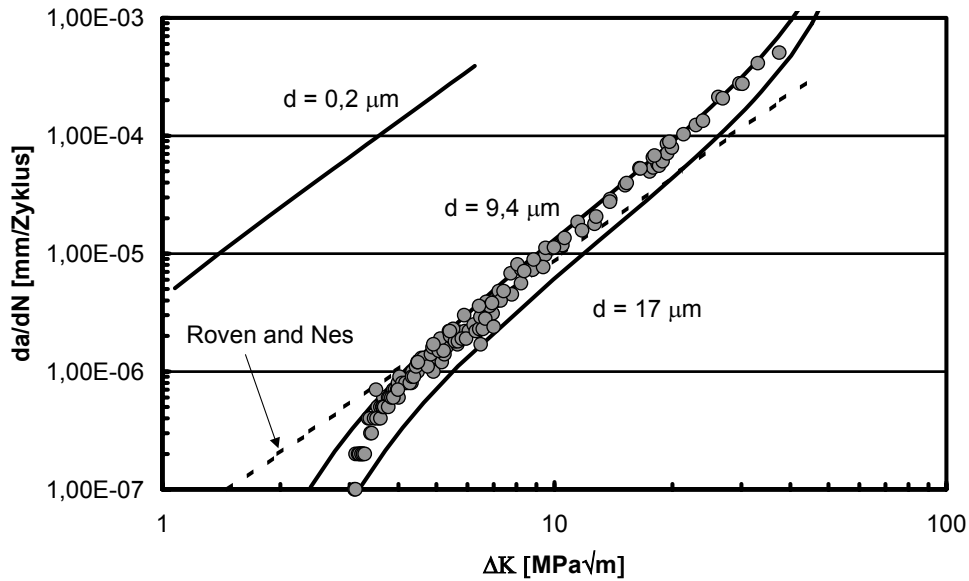

Figure 1: Influence of the primary dislocation barrier on the position of the fatigue crack growth curve (base metal S890 R=0,5)

The microstructure constant d introduced by Roven and Nes is in the case of ferritic steels similar to the grain size, because the high angle tilt boundaries have an influence as primary dislocation barriers. For martensitic and bainitic steels lattice width, packets and prior austenitic grain size are a possibility. Figure 1 illustrates, that for the base metal of S890 only the packets show an agreement between experiment and calculation. Normally lattices in the packets are not arranged exactly in the same parallel orientation. During the martensitic transformation the lattices in one packet get randomly orientated. Naylor [6] showed, that although this various orientation exists, the crack growth during a brittle fracture takes place without large angle deviations in the packets, because the several possible brittle fracture planes are located in a small angle region. Only at packet boundaries larger deviations occur. The neighbouring lattices in a packet have small angle deviations for plastic deformation, because the fracture planes are identical with the sliding planes. Lattice boundaries are a smaller barrier for plastic deformation than the packet boundaries. Because of this, packet boundaries should be defined as primary dislocation barrier. The packet boundaries correlates with the austenitic grains, but the packets are smaller then. In the case of heat affected zone, the prior austenitic grains are not verifiable anymore, so that only the using of packets is meaningful. With the values for striations s and the packets d (given in table 1) and the values of the Manson-Coffin-Curve (table 2) the fatigue crack growth curves for the high strength steel S890 and its welding joints were calculated (with Eqn.16 and 17) with different stress ratios.

TABLE 2
PARAMETER FOR THE CALCULATION [2]

	σ'_f [MPa]	b	ε'_f	c	ΔK_{fc} [MPa√m]
S890 BM	1605	-0,1	0,9924	-0,77	106
S890 HAZ	1254	-0,07	1,104	-0,8	98,5
S890 HAZ	1254	-0,07	1,104	-0,8	98,5

The figures 2 to 4 show a very good correspondence. The influence of the microstructure on the threshold region of da/dN-curve can be explained with the larger primary dislocation barrier d. When the packet width for the calculation of fatigue crack growth curve in the HAZ and in the WM is used, then the shifting of da/dN-curve to larger ΔK_{eff} -values can be understood. Also the influence of stress ratio on da/N-curve is reflected correctly. There are deviations from threshold value when the stress ratio R and the ΔK-values are small. These deviations can be explained by the crack closure effects, which were not considered.
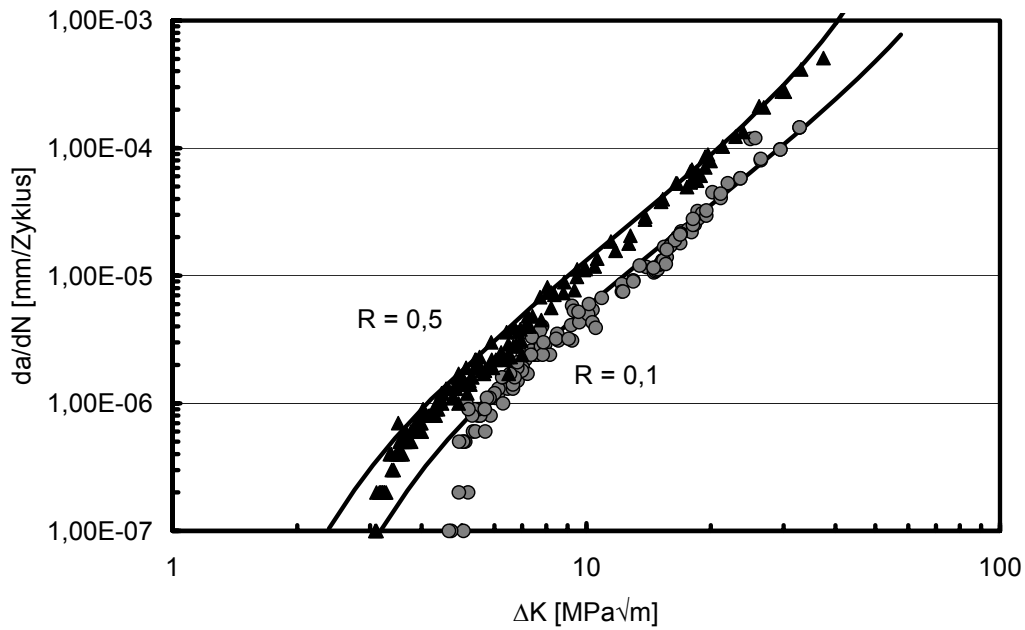

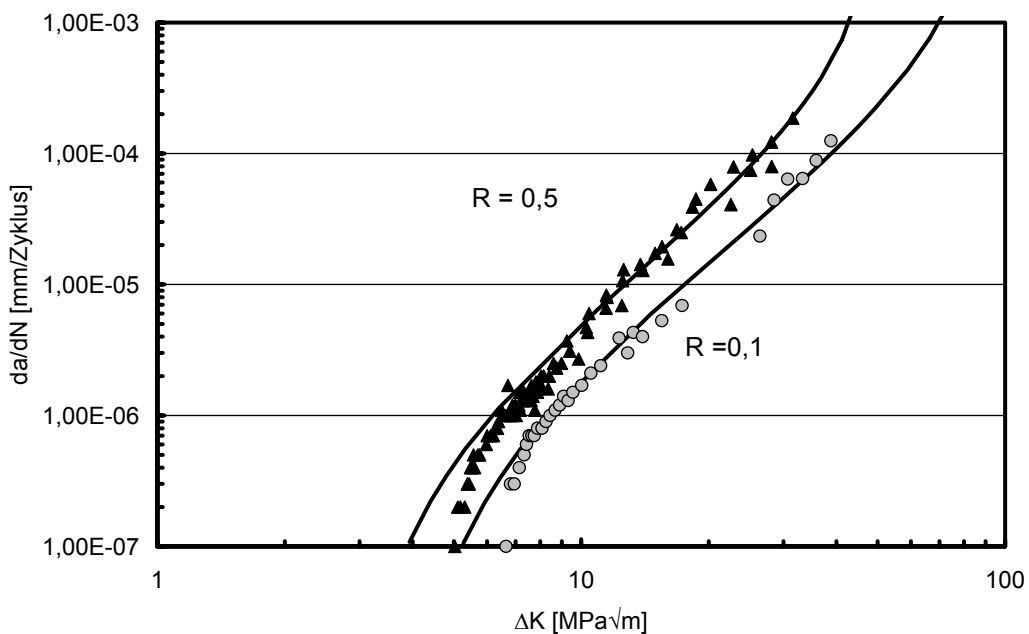**Figure 2:** Experiment and calculation for S890 base metal

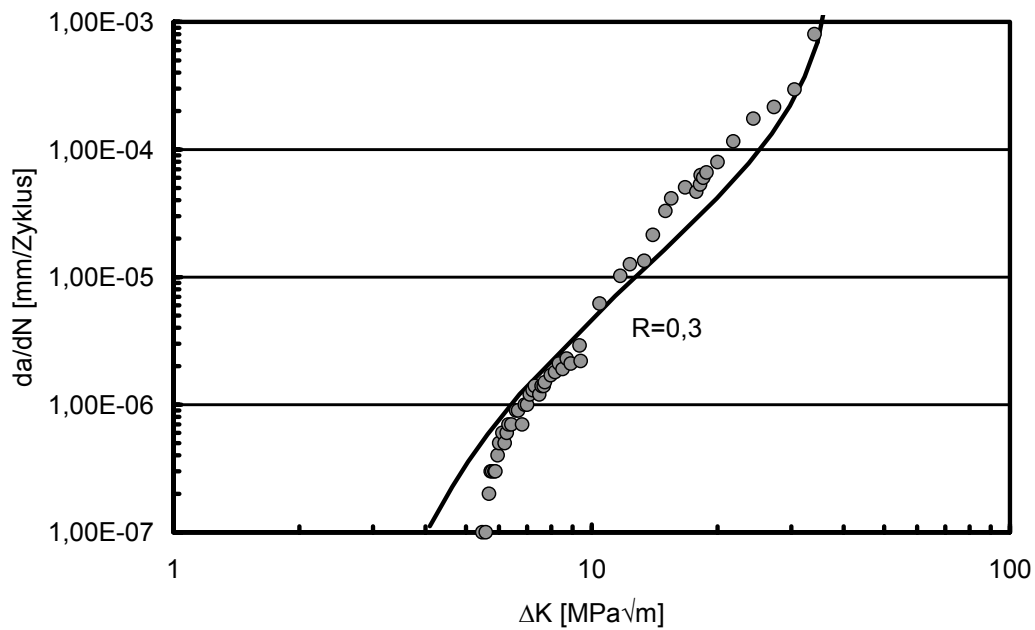**Figure 3:** Experiment and calculation for S890 heat affected zone

Figure 4: Experiment and calculation for S890 weld metal

REFERENCES

1.   Roven, H. J. and Nes, E. (1991)
     Overwiew No. 94 Acta metall. mater. Vol. 39, No. 8, pp. 1719-1754

2.   Hübner, P. (1996)
     Schwingfestigkeit der hochfesten schweißbaren Baustähle StE 885 und StE 960
     Dissertation TU Bergakademie Freiberg, Germany

3.   Hück, M. (1992)
     Mikrolegierte Stähle Vorhaben Nr. 122
     Bewertung der Schwingfestigkeit der mikrolegierten Stähle 27 Mn VS 6 und 38 Mn VS 5
     Forschungshefte des Forschungskuratorium Maschinenbau Heft 163

4.   Smith, K.N., Watson, P. and Topper, T.H. (1970)
     Journal of Materials, IMLSA, Vol. 5, No. 4, pp.767-778

5.   Naylor, J. P. (1979) Met. Trans. A Vol. 10 A 7 pp. 861-873

PREDICTION OF FRACTURE INITIATION AT THREE-DIMENSIONAL BIMATERIAL INTERFACE CORNERS: APPLICATION TO BUTT-JOINTS LOADED IN BENDING

Paul E. W. Labossiere[1] and Martin L. Dunn[2]

[1] Department of Mechanical Engineering, University of Washington, Seattle, WA
[2] Department of Mechanical Engineering, University of Colorado, Boulder, CO

ABSTRACT

Based on the universal nature of the asymptotic elastic fields at three-dimensional bimaterial interface corners, specifically that the stresses are singular with magnitude scaled solely by scalar stress intensities, we pursue the application of a fracture initiation criterion based on critical values of the stress intensities. To demonstrate this, we designed and fabricated a series of specimens consisting of two square aluminum prisms bonded together by a thin layer of epoxy. These butt-joint specimens were loaded in four-point flexure to failure. The orientation of the specimens was varied to encourage fracture to initiate at either the two-dimensional interface edge or the three-dimensional interface corner. We found that the failure stresses differ for each initiation mode, and depend significantly on the epoxy bond thickness. In order to apply the interface corner fracture initiation criterion, we carried out asymptotic calculations to determine the order of the stress singularity and the angular variation of the elastic fields at the interface corner. We determined the corresponding stress intensities, which depend on the far-field specimen geometry and loading, from full-field finite element calculations. From the measured failure stresses, we then determined the corresponding critical stress intensities. We found that although the failure stresses vary with epoxy thickness, the critical stress intensities do not, suggesting that they are a reasonable parameter to correlate fracture initiation.

KEYWORDS

Fracture Initiation, Bimaterial, Three-Dimensional, Interface Corner, Butt-Joint

INTRODUCTION

Consider the bimaterial interface corner geometry shown schematically in Figure 1. In general, the corner consists of intersecting faces (planes) and edges (lines) of arbitrary orientation. As shown, the edges may be *free* edges or *interface* edges. Each material, denoted by A and B, occupies a part of the solid and both materials may be anisotropic with principal material axes arbitrarily oriented with respect to the ($x\ y\ z$) axes. We consider the faces to be traction free, although other homogeneous boundary conditions can be easily handled and the solid is loaded at remote boundaries by tractions and displacements.
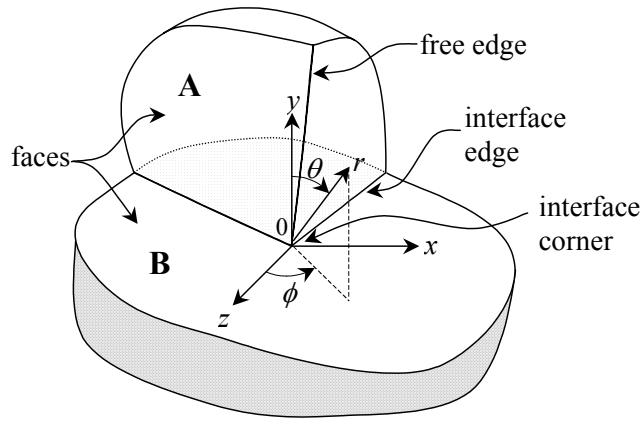
Figure 1: Three-dimensional bimaterial interface corner geometry showing coordinate axes. The faces (planes) and edges (lines) are arbitrarily oriented.

It is reasonably well known that a stress and a displacement field of the form [1-5]

$$
\sigma_{ij}^M = \sum_{m=-\infty}^{\infty} K_m^{3D} r^{\lambda_m - 1} f_{ij}^{Mm}(\theta, \phi)
$$

$$
u_i^M = \sum_{m=-\infty}^{\infty} K_m^{3D} r^{\lambda_m} g_i^{Mm}(\theta, \phi)
$$

(1)

exist in the region surrounding the tip of the three-dimensional bimaterial interface corner of Figure 1. In general, there are an infinite number of terms in the series, each corresponding to a specific deformation mode, m. Here $\lambda_m - 1$ are the orders of the stress singularities, $f_{ij}^m(\theta, \phi)$ and $g_i^m(\theta, \phi)$ describe the angular variation of the stress and displacement fields in each material ($M = A$, B) and K_m^{3D} are the corresponding stress intensities. $\lambda_m - 1$, $f_{ij}^m(\theta, \phi)$ and $g_i^m(\theta, \phi)$ depend on the elastic mismatch and asymptotic interface corner geometry, and K_m^{3D} depend on the far-field loading and geometry. This expansion of the stress state is a natural generalization of the classical mode I, II and III fields in homogeneous isotropic cracked solids; however, the deformation modes generally do not possess the simple symmetry of cracks in homogeneous media. The deformation modes strongly depend on the elastic mismatch and the nature of the asymptotic corner geometry. In Eqn. 1, λ_m, $f_{ij}^m(\theta, \phi)$ and $g_i^m(\theta, \phi)$ can be determined from an asymptotic analysis of the stress state near the three-dimensional interface corner [2-5]. Note that $f_{ij}^m(\theta, \phi)$ may be singular along reentrant free edges and interface edges (see Figure 1). Only the stress intensities K_m^{3D} cannot be determined from the asymptotic analysis. They depend on the far-field geometry and loading of the solid.

Terms that give rise to both singular and nonsingular stresses exist in the series. Finite strain-energy at the three-dimensional bimaterial interface corner requires $\mathrm{Re}\{\lambda\} > -1/2$ (for two-dimensional corners $\mathrm{Re}\{\lambda\} > 0$) and finite displacements require $\mathrm{Re}\{\lambda\} > 0$; however, as previously discussed [6,7] these are not completely satisfactory reasons for limiting the range of $\mathrm{Re}\{\lambda\}$ since they are based on assessment of the elastic solution in a region where it is not valid. Very close to the interface corner the actual solution is usually perturbed by material nonlinearity and/or geometric perturbations from the ideal interface corner, and far from the interface corner, it is perturbed by the far-field boundaries and loads. The terms with eigenvalues in the range $0 < \mathrm{Re}\{\lambda\} < 1$ may dominate the other terms in the series expansion of Eqn. 1 in an annular region surrounding the interface corner. In this annulus, these terms dominate higher-order singular terms because these have amplitudes that are small, and they dominate the nonsingular terms because the annulus is sufficiently close to the tip of the interface corner. Furthermore, in this elastic annulus the elastic fields for a particular loading mode exhibit a universal structure; their magnitude is simply scaled by a single parameter, the stress intensity K_m^{3D}. As such, this annulus is termed the K-annulus. The region where the higher-order singular terms are significant compared to the K_m^{3D}-term is embedded within

the K- annulus where material nonlinearities are likely to invalidate the elastic solution anyway. As in linear elastic fracture mechanics, K_m^{3D} is a measure of how the far-field load and geometry are communicated to the interface corner. Thus for a given material pair and three-dimensional bimaterial interface corner geometry, the asymptotic elastic fields are completely characterized by K_m^{3D}. For these reasons, we consider only values in the range $0 < \text{Re}\{\lambda\} < 1$; the results for the geometry and loads considered here show that for the analysis of fracture initiation, these terms are sufficient. We caution, however, that for other geometry and load cases, this may not be the case.

In practice, an interface corner can be the site of fracture initiation because of the existence of highly elevated stresses. Technological examples include microelectronics and microsensor packaging where interfaces arise due to various bonding and encapsulating processes that inevitably result not only in multimaterial interfaces, but also in multimaterial free edges and corners which are site of potential interface failure [8]. Given the universal nature of the stress field near the three-dimensional bimaterial interface corner, which is scaled by the three-dimensional stress intensities, a reasonable approach to correlate fracture initiation appears to be the use of critical values of the stress intensities. Specifically, in the spirit of Irwin for classical linear elastic fracture mechanics, we pursue a fracture initiation criterion of the form $f\left(K_m^{3D}\right) = f_{cr}$. This criterion says fracture will initiate at the three-dimensional interface corner when some combination of K_m^{3D} reaches a critical value. The criterion only addresses initiation; the subsequent crack propagation is a related, but different problem. In general, the functional form of $f\left(K_m^{3D}\right)$ and the critical value must be determined experimentally. The criterion can potentially be simplified to $K^{3D} = K_{cr}^{3D}$ if only one singular mode exists, as is the case for the interface corner geometry and material pair considered here or if one singularity dominates the effect of others (see for example Dunn et al., [9]). Further details regarding the approach presented here are given by Labossiere and Dunn [3]; they build heavily on similar ideas applied to two-dimensional situations. A comprehensive review of the use of critical stress intensities to correlate fracture initiation at two-dimensional bimaterial interface corners has recently been written by Reedy [10].

APPLICATION TO BUTT-JOINTS LOADED IN BENDING

We designed and fabricated a series of butt-joint test structures with three-dimensional bimaterial interface corners composed of 6061-T6 aluminum and cast West System 105-205 epoxy. Both materials are isotropic with $E = 70.0$ GPa and $v = 0.33$ for the aluminum and $E = 2.98$ GPa, $v = 0.38$, and $\sigma_y = 52$ MPa for the epoxy. A schematic of the test structures and the load configuration is shown in Figure 2. The structures are prisms with a square cross section and an overall length of 150 mm. The butt-joint of thickness a ranging from 0.05 to 1.1 mm is located in the center of the specimen, and the bimaterial interface is square with dimensions $w \times w$, where $w = 25.4$ mm. The specimens are loaded in four-point flexure in the -x-direction of Figure 3 with $L = 127$ mm and $l = 76.2$ mm. The load and supports are symmetrically located with respect to the butt-joint. A similar set of experiments was performed on two-dimensional specimens which were identical in geometry; however, the specimens were rotated 45 degrees about the z-axis in Figure 2, forcing fracture initiation to occur at the bottom interface *edge*, making the geometry and loading two-dimensional. This specimen geometry and load configuration was chosen for several reasons: four-point flexure loading is relatively simple to perform; fracture initiation occurs at one of the interface *corners* on the bottom of the specimen; by introducing only one finite length scale, a, the analysis is simplified, and; there is only one eigenvalue λ-1 giving rise to singular stresses at the three-dimensional bimaterial interface corner, which also simplifies the analysis and interpretation of the results.

The specimens were prepared as follows: The surfaces of the aluminum prisms to be bonded were machined flat and subsequently polished with 1500 grit paper and cleaned in 1-1-1 Trichloroethane, the aluminum prisms were placed in a mold coated with a wax release film and the epoxy was cast

within 20 minutes of the cleaning process. Once the epoxy cured at room temperature, the specimens were carefully removed and then wet polished to reveal well-defined interface corners and interface edges. The radius of curvature of the three-dimensional aluminum/epoxy interface corners was measured with optical microscopy and in all cases was less than 8 μm.
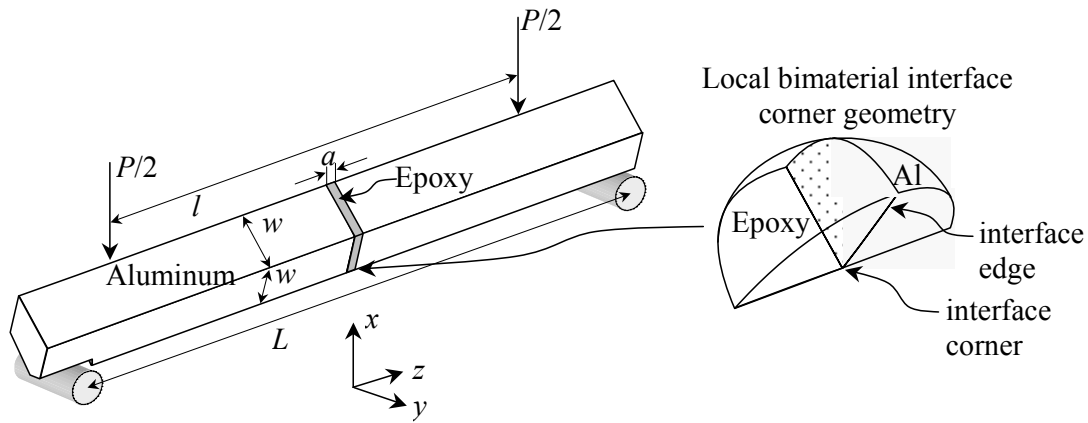

Figure 2: Four-point flexure test set-up showing butt-joint specimen dimensions and local three-dimensional bimaterial interface corner geometry.

The result of asymptotic calculations show that there is a stress singularity of order λ-1 = -0.351 at the three-dimensional aluminum/epoxy interface corner and a stress singularity of order λ-1 = -0.292 along the two-dimensional interface edges. The complete structure of the near tip fields for this geometry and material pair can be found in Labossiere and Dunn [3]. Dimensional considerations dictate that the stress intensity K^{3D} for the three-dimensional interface corner geometry considered here takes the form:

$$K^{3D} = \sigma_o^{3D} a^{1-\lambda}\ Y^{3D}(\frac{E_A}{E_B}, \nu_A, \nu_B). \tag{2}$$

Here a is the epoxy thickness, and σ_o^{3D} is the normal stress that would exist at the bottom tip of a homogeneous beam of dimension $w \times w$ under the four-point flexure loading of Figure 2:

$$\sigma_o^{3D} = \frac{3P(L-l)}{\sqrt{2}w^3}. \tag{3}$$

In general, Y^{3D} is a nondimensional function of both the elastic mismatch (E_A, E_B, ν_A, and ν_B are the Young's moduli and Poisson's ratios of the two materials) and the geometry, however, by designing our specimens with only one finite length scale a, the effect of geometry appears solely through $a^{1-\lambda}$, and Y^{3D} becomes a function of elastic mismatch only. Furthermore, since the elastic mismatch is fixed for the aluminum/epoxy material pair considered here, Y^{3D} is a constant. We determined Y^{3D} from detailed full-field finite element analyses of the three-dimensional aluminum/epoxy specimens loaded in four-point flexure using a commercially available finite element code. Typical finite element models contained ~100000 degrees of freedom with highly refined meshes near the interface corner to ensure accurate modeling of the asymptotic elastic fields. Y^{3D} was obtained from the finite element results by matching the finite element solution for the displacements near the interface corner with the asymptotic displacements of Eqn. 1 along certain rays emanating from the bimaterial interface corner using a least squares approach. Calculations for various epoxy thicknesses over the range being tested showed that Y^{3D} is indeed a constant and its value is $Y^{3D} = 0.431$. Although not presented here, similar analyses were performed for the two-dimensional specimen geometry.

MECHANICAL TESTING AND INTERPRETATION OF THE RESULTS IN TERMS OF CRITICAL STRESS INTENSITIES

Mechanical fracture testing was carried out using the four-point flexure configuration shown in Figure 2. A servo-hydraulic mechanical test system was used to load the specimens under load-point displacement control at a rate of 0.01 mm/sec. In all the tests, the load-displacement response was linear until brittle fracture occurred. The brittle fracture is characterized by a crack that initiated at one of the aluminum/epoxy interface corners on the tensile side of the specimen followed by unstable crack propagation along the interface. This is unlike *tougher* interfaces where the crack may kink away from the interface and run into one of the adherends (see for example Dunn et al., [9]).

Figure 3 shows the measured failure stresses calculated using Eqn. 3 plotted as a function of epoxy thickness a. Note that the measured failure stress depends strongly on the epoxy thickness invalidating its use as a failure criterion. The critical stress intensity criterion is applied by substituting into Eqn. 2, the measured specimen dimensions and failure stresses to calculate the corresponding critical values of the stress intensities. The critical stress intensities so obtained do not show a systematic variation with epoxy thickness suggesting they are universal parameters that can be used to correlate fracture initiation. The solid line of Figure 3 denotes the predicted failure stress based on the critical stress intensity fracture initiation criterion $K^{3D} = K_{cr}^{3D} = 6.6\,\mathrm{MPa\,mm}^{0.35}$. It accurately describes the variation of the measured failure stresses with epoxy thickness a. Although the results for the two-dimensional interface corner butt-joint specimens are not presented in detail here, the critical stress intensities also do not show a systematic variation with the geometry and the variation of the measured failure stresses with epoxy thickness is accurately described by the critical stress intensity fracture initiation criterion $K^{2D} = K_{cr}^{2D} = 4.4\,\mathrm{MPa\,mm}^{0.29}$. Note that the strength of the stress singularity is different in this case, thus the units of the corresponding stress intensity are also different as is the variation in the measured failure stress with epoxy thickness.
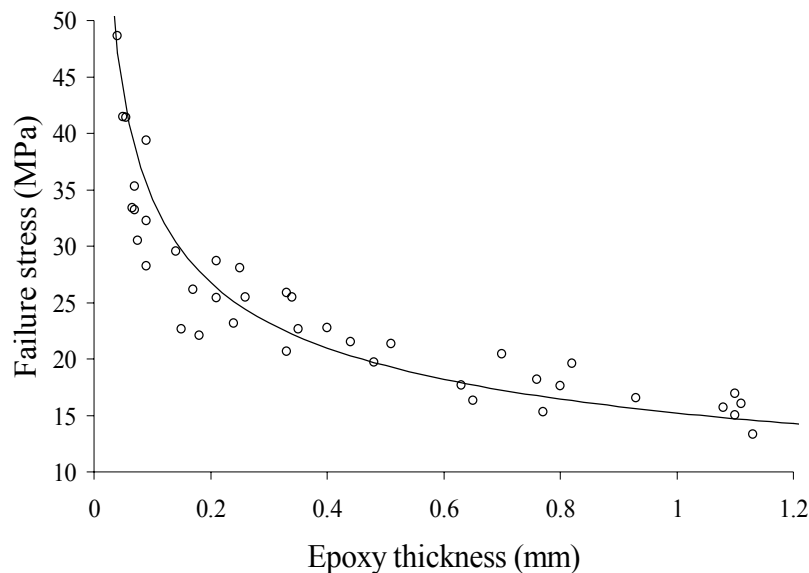

Figure 3: Measured failure stress versus epoxy thickness. The solid line is the prediction based on a constant critical stress intensity of $K_{cr}^{3D} = 6.6\,\mathrm{MPa\,mm}^{0.35}$.

The success of the critical stress intensity failure criterion requires that the elastic asymptotic solution of Eqn 1 accurately describes the actual solution in some region surrounding the interface corner where fracture initiation occurs. The size of the region in which the asymptotic solution accurately approximates the full-field solution obtained from finite element calculations (within ten percent error) as measured along the ray bisecting the aluminum/epoxy interface is roughly 0.014mm for the specimens with the thinnest epoxy layer ($a = 0.05$mm) and 0.3mm for the thickest epoxy layer ($a = 1.1$mm). We also examined the region of dominance along other rays emanating from the bimaterial

interface corner on the interface and in all cases, the region of dominance is larger along any other ray. Although this is relatively small compared to the specimen size, it is larger than the finite corner radius, which is less than 8 μm. It is also larger than any plastic zone size, which can be estimated using the von Mises yield criterion applied to the elastic asymptotic solution for the three-dimensional interface corner and is on the order of 2 μm [3]. Thus the correlation of fracture initiation based on a critical value of $K^{3D} = K^{3D}_{cr}$ seems reasonable.

CONCLUSIONS

We demonstrated an approach to characterize fracture initiation at three-dimensional bimaterial interface corners using critical values of the stress intensities that arise in a linear elastic analysis. We designed and fabricated a series of two-dimensional and three-dimensional aluminum/epoxy/aluminum butt-joint specimens with interface edges and corners, respectively. We mechanically loaded them to failure in four-point flexure. The measurements produced a critical nominal load (critical nominal stress), but these varied significantly with bond thickness and thus invalidated their use as critical values to correlate fracture initiation. From a rigorous analysis of the interface corner stress state, we determined the order of the stress singularity, the angular variations of the stress and displacement fields, and the corresponding stress intensity for the specified loading. The critical stress intensities obtained from the failure loads did not show a systematic variation with adhesive thickness, a feature suggestive of the universal nature of the criterion.

REFERENCES

1. Williams, M. L. (1952) *J. Appl. Mech.*, 19, 526-528.
2. Bazant, Z. P. (1974) *Int. J. Engng Sci.*, 12, 221-243.
3. Labossiere, P. E. W., and Dunn, M. L., (2001) *J. Mech. Phys. Solids*, Vol. 49, 609-634.
4. Ghahremani, F. (1991) *Int. J. Solids Structures*, Vol. 27, 1371-1386.
5. Picu, C. R. and Gupta, V. (1997) J. *Mech. Phys. Solids*, 45, 1495-1520.
6. Hui, C. Y., and Ruina, A. (1995) *Int. J. Fract.,* Vol. 72, 97-120.
7. Dunn, M. L., Hui, C. Y., Labossiere, P. E. W., and Lin, Y. Y., (2001) *Int. J. Fract.,* in press.
8. Chen, W. T., Read, D., Questad, D., and Sammakia, B. (1997) *Application of Fracture Mechanics in Electronic Packaging, ASME, AMD-Vol. 222/EEP*-Vol. 20, 183-192.
9. Dunn, M. L., Cunningham, S. J., and Labossiere, P. E. W. (2000) *Acta Materialia*, 48, 735-744.
10. Reedy, E. D., 2001, Strength of Butt and Sharp-Cornered Joints, *Comprehensive Adhesion Science*, in press.

PREDICTION OF PROBABILITY DISTRIBUTION OF NOTCH STRENGTH OF CERAMICS

J.H. Yan, X.L.Zeng, K.Zhao and H. Wang

College of Materials Science &Engineering, Northwestern Polytechnical University, Xi'an 710072, China

Abstract Based on the expression for notch strength of brittle material and the fundamental principle of probability theory, correlations between the statistical characteristic parameters of notch strength and those of flexural strength of ceramics are obtained and checked by test results. It's shown that for the normal distribution, the mean value and the standard deviation of the notch strength are, respectively, K_t times less than those of flexural strength, where K_t is the theoretical stress concentration factor. For the log-normal distribution, the mean value of logarithm of notch strength is equal to that of flexural strength minus the logarithm of K_t, and the standard deviation of the logarithm of notch strength keeps equal to that of flexural strength as K_t increases. For Weibull distribution, the product of characteristic value, i.e. the scale parameter of Weibull distribution of notch strength and K_t is equal to the scale parameter of Weibull distribution of flexural strength and the shape parameter of notch strength keeps constant as Kt increases. Based on the above results, procedures are developed to predict the probability distribution of notch strength of ceramics from that of the flexural strength. It is shown that the notch strength of ceramics follows the normal distribution, the log-normal distribution and Weibull distribution, and all of the above distributions can be predicted. The predicted results of three probability distributions of notch strength of ceramics mentioned above are in good agreement with test results. The possibility of predicting the probability distribution of notch strength of ceramics is of practical importance in the design and reliability assessment of ceramic structure elements.

Keywords: ceramics, notch strength, probability distribution, prediction

1. Introduction

Discontinuity of profile always exists in structural elements due to the need of joining and the structure design, and may be regarded as notch where the stress concentration occurs. So, it's necessary and important to investigate and predict the notch strength and its probability distribution in order to meet the requirement of the evaluation of strength and reliability assessment of ceramics elements[1-7].

Ref.[6] offered a method to predict the strength distribution of the notched specimen of ceramics from the crack length distribution, however, because the critical crack length and the effective surface in both notched and smooth (plane) specimens are difficult to be determined by experiment, the method is hard to be applied in engineering. In addition, the results obtained in ref.[6] are doubtful that the notch strength increases with the increasing of stress concentration factor of notch specimen of ceramics.

In the present study, different test results of notch strength of alumina ceramics given in ref.[7] are analyzed based on the formula for the notch strength of brittle materials given in ref.[8] and the general principle of probability theory. Furthermore, the correlations between the characteristic parameters of probability distribution of the notch strength and those of the flexural strength are obtained, which offers the possibility of predicting the probability distribution of notch strength of ceramics from test results of flexural

strength of smooth specimens. So it is of practical importance in the design and the reliability assessment of ceramics element, without the need to determine the notch strength of specific stress concentration factor, which are expensive and time consuming.

2. Expression for notch strength of ceramics

Based on the assumptions that the crack initiation at notch tip may occur due to the fracture of a hypothetical material element at notch root and the fracture of notched element occurs right after crack initiation without any sub-critical crack propagation because of the low values of K_{IC} and the critical crack length of brittle materials, a formula for notch strength of brittle materials was developed as follows[8]:

$$\sigma_{bN}=\sigma_f/K_t \tag{1}$$

where σ_f is the fracture strength of brittle material, K_t is the theoretical stress concentration factor, σ_{bN} is the fracture stress of notched element, i.e. notch strength.

Equ (1) has been checked by the test result of notch strength of brittle metal[8]. Wang, et al found that the test data of notch strength and fracture strength of ceramics under bending condition also followed the above-mentioned equation[3]. But under bending condition, σ_f in eqn.(1) should be replaced by the flexural strength of ceramics ,σ_{bb} ,as shown in eqn.(2) :

$$\sigma_{bN}=\sigma_{bb}/K_t \tag{2}$$

eqn.(2) shows the quantitative relationship between the flexural strength and the bending notch strength of ceramics. So, the quantitative relationship between the probability distribution of notch strength and that of flexural strength of ceramics can be achieved by using eqn.(2).
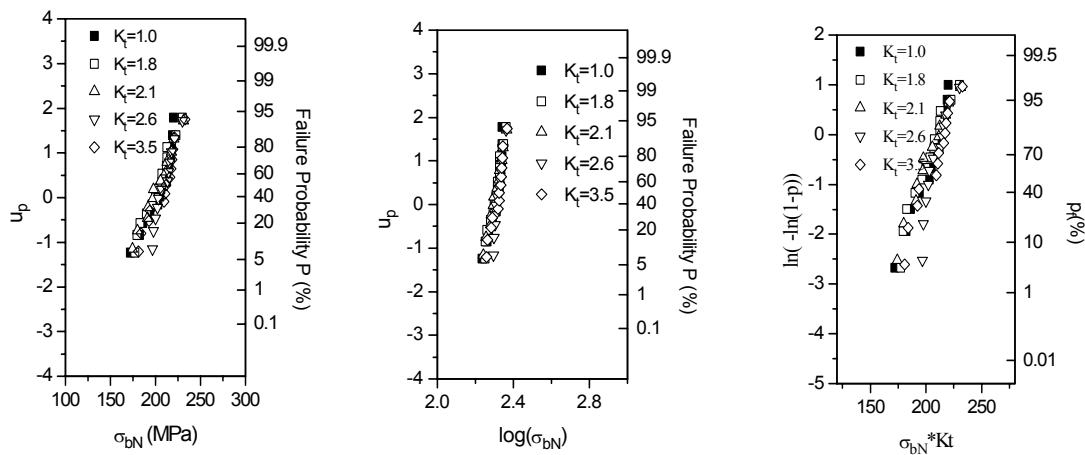
3. The probability distribution of flexural strength and notch strength of brittle ceramics

Eqn.(2) can be re-written as followings:

$$\sigma_{bN}*K_t=\sigma_{bb} \tag{3}$$

It can be seen that $\sigma_{bN}*K_t$ follows the same probability distribution as that of σ_{bb}.

Generally, it was thought that the fracture strength of brittle ceramics follows Weibull distribution[6,7,9]. In ref.[3] , it is found that the flexural strength of ceramics also follows the normal distribution on the basis of statistical analysis of the test results of strength of alumina ceramics when the number of sample is small. Actually, re-analysis on the test data contain 127 samples[9] shows that the test results of the flexural strength of ceramics can simultaneously follow the normal distribution, the log-normal distribution and Weibull distribution. So, $\sigma_{bN}*K_t$ also follows the normal distribution , the log-normal distribution and Weibull distribution respectively.

(a) normal distribution　　(b)log-normal distribution　　(c) Weibull distribution
Fig.1 The probability distribution of unified notch strength and flexural strength of alumina ceramics

In ref.[7], the test results of the fracture strength of smooth specimen and notch strength of notched specimen of alumina ceramics under bending loading condition are given. After unifying by using the notch

strength to times the stress concentration factor of the corresponding notch specimen, $\sigma_{bN}*K_t$ and σ_{bb} are simultaneously plotted in the same probability paper as shown in Fig.1. As may be seen from Fig.1, the unified notch strength and flexural strength of alumina ceramics almost form a straight line in the same probability paper, therefore, under the condition of normal distribution, log-normal distribution and Weibull distribution respectively, $\sigma_{bN}*K_t$ and σ_{bb} follows the same probability distribution as shown by eqn.(3). The above result is different from the results obtained in ref.[6] where the notch strength increases with the increasing of stress concentration factor of notch specimen of ceramics, so the unified notch strength.formed different lines from that of the flexural strength.

4. Prediction of probability distribution of notch strength from that of flexural strength

Since the dimension, direction and distribution of the defect in brittle ceramics are random, σ_{bb} and σ_{bN} in eqn.(3) are random variables. From ref.[10], it can be seen that the variations in the notch depth and notch root radius have little effect on the value of K_t. Thus, K_t can be taken as a constant .As a result, σ_{bN} can be regarded as a linear function of the random variable σ_{bb}, denoted as $\sigma_{bN}=\varphi(\sigma_{bb})$. The probability distribution density function of flexural strength such as $f(\sigma_{bb})$ can be relatively easy determined by the test result of smooth specimen. Then, on basis of eqn.(3) and the feature for distribution density function of linear function of random variable[11], the distribution density function of notch strength σ_{bN} can be determined as follows:

$$\phi(\sigma_{bN})=\left|g'(\sigma_{bN})\right|\bullet f(g(\sigma_{bN})) \tag{4}$$

where $g(\sigma_{bN})$ is the invert function of $\varphi(\sigma_{bb})$. As a result, the corresponding characteristic parameters of probability distribution of notch strength can be obtained.

When σ_{bb} follows the normal distribution, i.e. $\sigma_{bb}\sim N(\mu,\sigma^2)$,and its distribution density function is:

$$f(\sigma_{bb})=\frac{1}{\sigma\sqrt{2\pi}}\exp\left(-\frac{(\sigma_{bb}-\mu)^2}{2\sigma^2}\right) \tag{5}$$

where μ and σ are, respectively, the mean value and standard deviation of the population of variable σ_{bb}. Then the distribution density function of σ_{bN} can be obtained according to eqn.(4):

$$\phi(\sigma_{bN})=\frac{1}{\sqrt{2\pi}\left(\sigma/K_t\right)}\exp\left(-\frac{\left(\sigma_{bN}-\mu/K_t\right)^2}{2\left(\sigma/K_t\right)^2}\right) \tag{5}$$

Comparison of eqn.(5) with eqn.(6) tells that $\sigma_{bN}\sim N\left(\mu/K_t,\sigma^2/K_t^2\right)$ and the mean value and standard deviation of the population of variable, σ_{bN}, are, respectively, μ/K_t and σ/K_t, which are respectively, equal to $1/K_t$ times of those of σ_{bb}.

From eqn.(3) and the definition of the mean value and the standard deviation of the sample[21], the following equations should be satisfied:

$$\overline{\sigma}_{bN}=\overline{\sigma}_{bb}/K_t \tag{7}$$

$$s_{bN}=s_{bb}/K_t \tag{8}$$

where $\overline{\sigma}_{bN}$ and s_{bN} are, respectively, the mean value and the standard deviation of the sample of notch strength, $\overline{\sigma}_{bb}$ and s_{bb} are those for flexural strength, respectively. Since σ_{bb} and σ_{bN} both follow the normal distribution, and $\overline{\sigma}_{bb}$ (or $\overline{\sigma}_{bN}$) and s_{bb} (or s_{bN}) can be taken as the estimated values for μ (or μ/K_t) and σ (or σ/K_t) respectively. Thus, eqn.(7) and eqn.(8) are the expressions for characteristic parameters of probability distribution of notch strength of ceramics, which are both expressed by the corresponding characteristic parameters of flexural strength of smooth specimen divided by K_t.

After logarithmic transformation, eqn.(3) becomes:

$$\log\sigma_{bN}=\log\sigma_{bb}-\log K_t \tag{9}$$

It indicates that $log\,\sigma_{bN}$ is still a linear function of the random variable $log\,\sigma_{bb}$. Therefore, σ_{bN}, the notch

strength of ceramics should follow the log-normal distribution when σ_{bN}, the flexural strength of ceramics follows the log-normal distribution. Thus, it can be deduced from the similar analysis given in the above section that the characteristic parameters of log-normal distribution, such as the mean value and the standard deviation, of two random variables, i.e. σ_{bb} and σ_{bN}, should be correlated as follows:

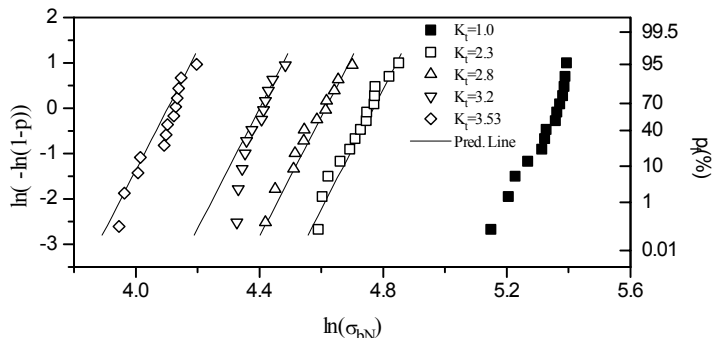$$\overline{\log \sigma}_{bN} = \overline{\log \sigma}_{bb} - \log K_t \qquad (10)$$

$$S_{\log \sigma_{bN}} = S_{\log \sigma_{bb}} \qquad (11)$$
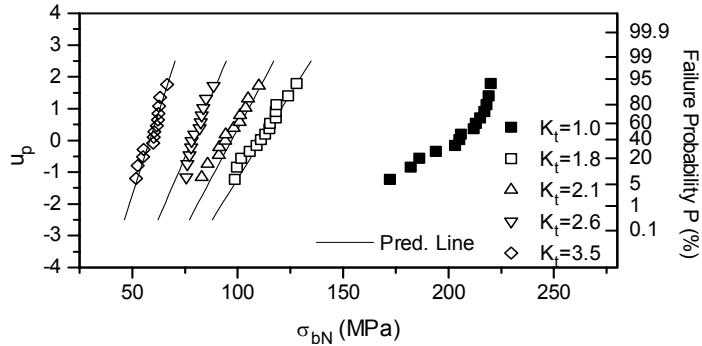
(a) normal distribution
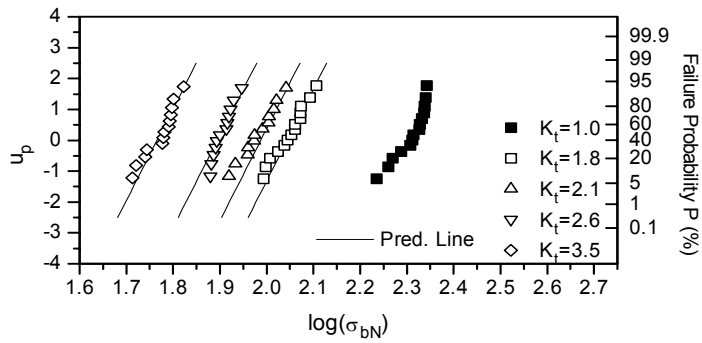
(b) log-normal distribution

(c) Weibull distribution

Figure 2 The predicted lines of normal distribution, log-normal distribution, Weibull distribution and test results[7] of notch strength of alumina ceramics at K_t=1.8, 2.1, 2.6, and 3.5

When σ_{bb} follows the 2-parameter Weibull distribution , its density function can be expressed as:

$$f(x) = \frac{m}{\sigma_0}\left(\frac{x}{\sigma_0}\right)^{m-1} \exp\left[-\left(\frac{x}{\sigma_0}\right)^m\right] \qquad (12)$$

where σ_0 is the scale parameter, i.e. the characteristic value of flexural strength when failure probability is 63%, and m is the Weibull modulus. According to eqn.(4), the density function of σ_{bN} is:

$$\varphi(\sigma_{bN}) = \frac{m}{\sigma_0/K_t}\left(\frac{\sigma_{bN}}{\sigma_0/K_t}\right)^{m-1} \exp\left[-\left(\frac{\sigma_{bN}}{\sigma_0/K_t}\right)^m\right] \qquad (13)$$

Comparison of eqn.(21) with eqn.(22) suggests that σ_{bN} follows Weibull distribution equally. Let σ_{0N} and m_N be the characteristic value and Weibull modulus of notch strength respectively, then we have:

4

$$\sigma_{0N} = \frac{\sigma_0}{K_t} \qquad (14)$$

$$m_N = m \qquad (15)$$

Based on the test results of the fracture strength of smooth specimen given in ref.[7] and its probablity distribution shown in Fig.1, the characteristical parameters of the flexural strength for normal distribution, log-normal distribution and Weibull distribution can be obtained respectively. Therefore the corresponding characteristical parameters of normal distribution, log-normal distribution and Weibull distribution of notch strength of notched specimen of alumina ceramics under bending loading condition can be determined according to the eqn.(7)-(8), eqn.(10)-(11) and eqn.(14)-(15) respectively, thereby, the probability distribution of notch strength of alumina ceramics can be predicted. Fig.2 show the test results of notch strength of alumina ceramics and the predicted probability distributions. As may be seen that the predicted probability distributions are in good agreement with the test results of notch strength of alumina ceramics. Therefore, the structure design and reliability assessment of notched elements made of ceramics can be simplified by using the conventional tests of fracture strength of smooth specimens instead of the costly and time consuming test of notched specimens of ceramics.

5. Conclusions

(1) The flexural strength of smooth specimens is K_t times of notch strength of ceramics, where K_t is the stress concentration factor of the notch specimen.

(2) Both notch strength and flexural strength under bending condition can simultaneously follow the normal distribution, the log-normal distribution and Weibull distribution.

(3) The characteristic parameters of the probability distribution function of notch strength can be determined from that of flexural strength and the stress concentration factor Kt.

(4) The normal distribution, the log-normal distribution and Weibull distribution of notch strength of ceramics can be predicted from that of flexural strength and the predicted results are in good agreement with test results.

(5) The possibility of predicting the probability distribution of notch strength of ceramics from test results of flexural strength of smooth specimens is of practical importance in the design and the reliability assessment of ceramics element, without the need to determine the notch strength of specific stress concentration factor, which are expensive and time consuming.

REFERENCES

[1] Quinn G. D, et al, Design Data for Engineering Ceramics: A Review of the flexure Tests, J. Am. Ceram. Soci. 74(9):2037(1991)

[2] J.Laman, Statistical Approaches To Failure For Ceramics Reliability Assessment, J. Am. Ceram. Soci. 71:106～112(1988)

[3] F. H. Wang, X. L. Zheng & M. X. Lu, Notch Strength of Ceramics and Statistical Analysis, Eng. Fract. Mech.,52(5):917～921(1995)

[4] Pei Gu, Notch Sensitivity of Filber-reinforced Ceramics, Int. J. Fract., 70(3):253～266(1994/1995)

[5] Charlis S. W. , et al, Notched Tensile Creep Testing of Ceramics, Mater.Sci.Eng., A203:217～221(1995)

[6]T. Fett, D. Hertel, D. Munz, Strength of notched ceramic bending bars, J. Materials Science Letters, 1999(18): 289-293

[7] Wen Chao, On Unnotched Strength and Notch Strength of Brittle Materials, Thesis for Master Degree, Northwestern Polytechnical University, Xi'an, China, 1996.3

[8] X. L. Zheng , On an Unified Model for Predicting Notch Strength and Fracture Toughness of Metals,Eng. Fract. Mech. 33(5):685～695(1989)

[9] Z. Jin, et al, Research of Weibull Statistics On the Strength Of Structural Ceramics, J. Chinese Cerm. Soci.18(2):130～136(1990)

[10] M. Nisida, Stress Concentration Factors, Mositoka Press, in Japanese(1971)

[11] P.Deng, Applications of Statistics in Measurements and Experiments, Press of Chemical Industry, Beijing (in Chinese)(1981)

PREDICTIVE FRACTURE MODEL FOR STEADY-STATE FAILURE OF ADHESIVELY-BONDED JOINTS WITH EXTENSIVE PLASTIC YIELDING

T. Ferracin[1], C.M. Landis[2], J.Y. Sener[3], F. Delannay[1] and T. Pardoen[1]

[1] Département des Sciences des Matériaux et des Procédés, Université catholique de Louvain, PCIM, Place Sainte Barbe 2, B-1348 Louvain-la-Neuve, Belgium
[2] MEMS, MS 321Rice University, P.O. Box 1892, Houston, TX 77251
[3] R & D Cockerill Sambre Groupe USINOR, Bd de Colonster B-52, Sart-Tilman, B-4000 Liège, Belgium

ABSTRACT

This work deals with the development of predictive models for the failure of adhesively bonded joints. Experimentally, the focus lies on industrial thin steel plates bonded by modified epoxy adhesives. Experimentally, a « plastic wedge-opened double-cantilever beam test » is used to measure the mode I steady-state adhesion of a sandwich structure made of two thin steel plates bonded with an epoxy adhesive. The assemblies fail with extensive plastic deformation of the adherents. Two parameters are measured: the radius of curvature of the deformed steel adherents and the current crack length. Classical linear elastic fracture mechanics relationships are not accurate for addressing cracking with extensive plastic deformation. Numerical simulations are thus required to allow quantitative data reduction. A cohesive zone model has been chosen to represent the behaviour of the adhesive bond material. The cohesive zone is characterised by two parameters: the strength of the epoxy layer and its intrinsic fracture toughness. In this first part of the study, the entire adhesive layer is represented by one row of cohesive elements. A steady state FE code accounting for finite rotation has been developed. This formulation appears much more efficient and faster than the standard formulation although it is limited to steady-state processes. Calibration of the cohesive zone parameters has been performed through comparison with the experimental results.

KEYWORDS

Wedge-opening peel test, adhesive, bonding, toughness, cohesive zone model, steady state

INTRODUCTION

For the last ten years, adhesive bonding of metal plates has become a very popular method in several industrial sectors. Simultaneously, an urgent need for the characterization and prediction of the failure of bonded structures has emerged. Due to the wide range of possible constraints imposed by the metal substrates, depending on the geometry and loading configuration, the toughness of the joints has to be measured using a test adapted for the foreseen application. The demand for new robust testing techniques, in particular when debonding involves plastic deformation of the substrates, is accompanied by the necessity of developing models for the transfer of laboratory results to real structures. Ultimately, these models will allow a reduction of the number of tests required for covering the variety of possible structural applications.

Fracture toughness of bonded joints has been measured using a wedge-peel test popularized by Thouless *et al*. [1]. In this test, two bonded metal plates are separated by means of a wedge inserted along the interface (Figure 1). The wedge induces a constant separation on the plates. If the plates are of sufficiently low thickness and yield stress, plastic bending of the substrates occurs during the failure of the adhesive bond. Fracture toughness can be derived from the measured value of the remaining radii of curvature R_f of the plastically deformed metallic plates and of the crack length a during debonding. This last value is taken as the distance between the crack tip and the point of contact of the wedge with the steel plates.
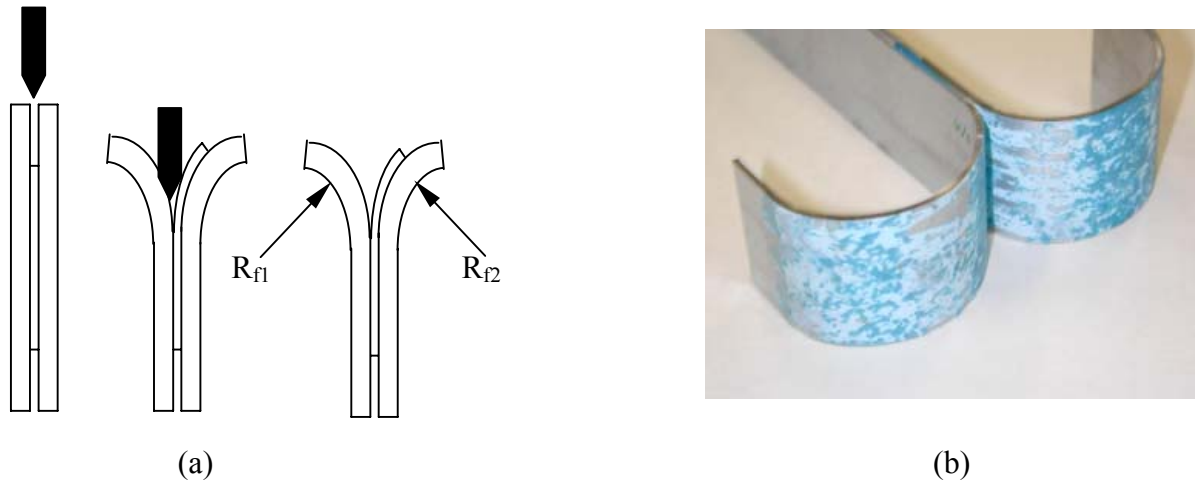

Figure 1: (a) Schematical presentation of the wedge-opening peel test, (b) Test specimen after fracture.

After a short transient following cracking initiation, the fracture process becomes steady state. The tests have been modeled using a steady-state finite element code. The deformation and fracture processes in the adhesive bond are represented by a traction-displacement or cohesive zone law, see [2,3,4]. The two key parameters of the cohesive zone model are the peak stress and the area under the traction-displacement curve, i.e. the work per unit area required for breaking the bond. A calibration procedure for these two parameters based on the wedge-peel test results is proposed and discussed.

EXPERIMENTAL PROCEDURE

Adhesively bonded joints were prepared using a commercial rubber modified epoxy-based adhesive for application in the automotive industry. This adhesive was deposited on steel plates between two Teflon tapes separated by 80 mm. The bond thickness was controlled by inserting uniform glass beads or metallic wires of diameter equal to the desired thickness of the adhesive layer between the plates. Specimen tests were made with different bond thickness. The adhesive between the plates was cured at 180°C for 45 minutes in order to obtain symmetrical specimens. The steel plates are produced by Cockerill Sambre Groupe Usinor. The plates are cut into coupons 200 mm long and 30 mm wide. Plate thicknesses of 0.78 mm and 1.16 mm were tested. The mechanical properties of the steel plates are given in Table 1.

The wedge-opening peel tests were performed using an Instron universal testing machine. A 1.8mm thick wedge was pushed down along the interface of the bonded joint of the specimen at a speed of 10 mm/min. After completion of the test, the radii of curvature of the two plastically deformed plates were measured using a profile projector. The bent substrates exhibited constant radii of curvature implying that the fracture operated in a steady-state manner. We also noticed failure to occur near one of the interfaces between the adhesive and the metal plate leading to a slightly asymmetrical mode of decohesion. The asymmetry sometimes induced significant differences between the two radii of curvature. Hence, an average of the two radii of curvature was used for subsequent data treatment.

TABLE 1

MECHANICAL PROPERTIES OF STEEL COUPONS FOR THE TWO DIFFERENT THICKNESSES

Thickness h (mm)	Yield stress σ_0 (Mpa)	Average hardening coefficient n
0.78	133	0.095
1.16	121	0.160

Figure 2 plots the variation of the average radius of curvature and crack length both normalized by the steel plate thickness (h=1.16 mm) as a function of the bond thickness. Each point on Figure 2 corresponds to the average of at least four different tests.
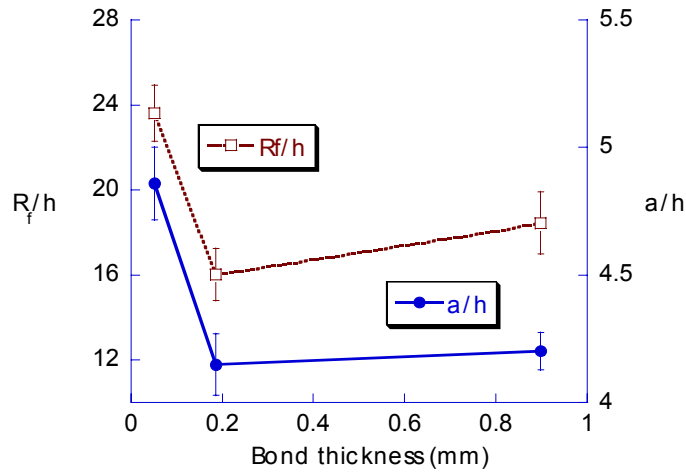

Figure 2: Average measured radii of curvature and crack lengths for the wedge-opening peel test with the adhesive bonded on a 1.16 mm thick steel plate which has n=0.16 and σ_0=121 MPa.

The reduction of the data consists of deriving the fracture toughness from the measured radius of curvature and crack length. Different methods have been investigated in other papers [5] relying on an analytical formula derived using beam theory and the energy release rate definition or based on the computational finite element model (FEM). Here, after a summary of analytical models, we propose a new method based on a steady-state finite element model.

ANALYTICAL BEAM MODEL

Considering steady state crack propagation, assuming that simple plastic beam theory applies, and that pure bending prevails, Yang *et al* [4] showed that:

$$\Gamma = \frac{Anh^{n+2}}{2^n(n+2)(n+1)R_f^{n+1}}$$

(1)

where n and A are material properties based on the Hollomon law, h is the metal beam thickness and R_f is the radius of curvature of the deformed beams.

This solution has aroused controversial discussion in Ref. [6,7,8]. Moreover, Sener [9] and Ferracin [5] have discussed the conditions when elastic-return of the metal adherent has a significant contribution to the toughness. Table 2 shows the toughnesses obtained with the complete model. The results presented in Table 2 show a decrease of the fracture toughness for thin adhesive layers due to the increasing confinement of the plastic zone. Quite surprisingly, the computed toughness decreases at very high adhesive thickness.

TABLE 2
CALCULATION OF TOUGHNESS USING AN ANALYTICAL EXPRESSION BASED ON PLASTIC BEAM THEORY

Joint thickness (mm)	Average radii of curvature (mm)	Toughness (kJ/m²)
0.050	27.38	0.87
0.185	18.57	1.33
0.898	21.39	1.07

COMPUTATIONAL STEADY-STATE FINITE ELEMENT MODEL

The fracture toughness can be estimated more accurately using a computational steady state FEM with a cohesive zone model (CZM) to simulate deformation and failure of the adhesive joint. The CZM consists of a traction-separation law whose general shape is given in Figure 3 as in Ref. [2,4]. The two relevant quantities characterizing the curve are the area under the curve Γ_0 which is the intrinsic toughness of the joint and the peak stress (which can be considered as the strength of the bond) σ_p. Notice that once the maximum separation δ_c, the peak stress σ_p and its shape parameters λ_1 and λ_2 are fixed, Γ_0 can be directly obtained from Eqn. 2.
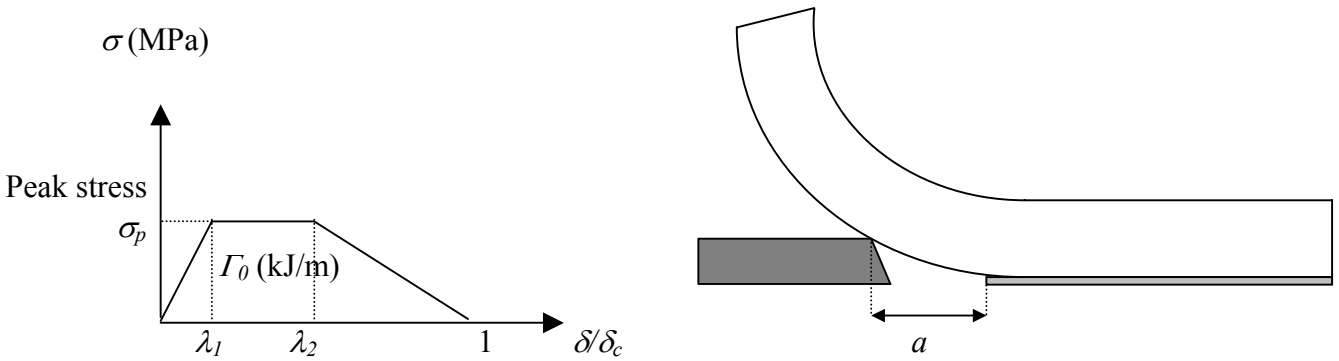

Figure 3: Traction separation law of the cohesive zone model and FEM model

$$\Gamma_0 = \frac{(1 - \lambda_1 - \lambda_2)}{2} \sigma_p \delta_c \tag{2}$$

The steady state formulation was first applied by [10] and recently extended to rate dependent fracture of epoxy by Landis *et al.* in [11]. The formulation consists of finding an equilibrium solution for the displacements based on a previous approximate distribution of plastic strains and then integrating the plasticity laws along streamlines to determine new approximations for stresses and plastic strains. This procedure is repeated until convergence is achieved.

Half of the specimen has been modeled using 8 node elements and the relevant boundary conditions have been imposed. Extensive mesh convergence analysis has been carried out. The mesh was particularly refined at the point of contact of the wedge and at the crack tip.

In a steady state formulation, most geometrical parameters like the crack length *a* can be fixed. The crack tip will effectively be located where it has been fixed if the crack tip opening displacement (CTOD) at this point is equal to the maximum separation of the cohezive zone δ_c. In order to determine the fracture parameters Γ_0 and σ_p the procedure was modified to update the value of σ_p by Eqn. 3 at each plasticity iteration so that when convergence is achieved, the value of the crack tip opening (CTO) equals δ_c.

$$\sigma_p = \sigma_p \frac{CTOD}{\delta_c} \qquad (3)$$

The solution obtained by this method is then used as a guess value in a standard steady-state formulation. Results are in agreement using the modified formulation or the standard formulation with the value of σ_p taken from the results of the modified procedure. We have compared the steady-state results with the one obtained from the standard, non-steady state FEM code ABAQUS used with a cohesive zone implemented as a user's subroutine element. The results are almost identical, however the calculation time is far greater with ABAQUS.

The fracture process is described by the couple (Γ_0, σ_p) and thus the calibration of the model requires two different experimental measurements. These measurements are the average radius of curvature and the crack length.

The following strategy is used for the calibration of the parameters of the CZM with our experimental results:
1. Steady-state FE simulations of the wedge-opening peel test geometry are carried out imposing a particular experimental crack length and using different values of δ_c. Each of these simulations gives rise to one steady-state radius of curvature and to a particular value of σ_p. For each simulation, the value of Γ_0 is calculated from (2). These results can be represented in a plot similar to Figure 4.
2. From the experimental value of the radius of curvature R_f, one can easily match the Γ_0 and the σ_p as shown by the arrows of Figure 4.
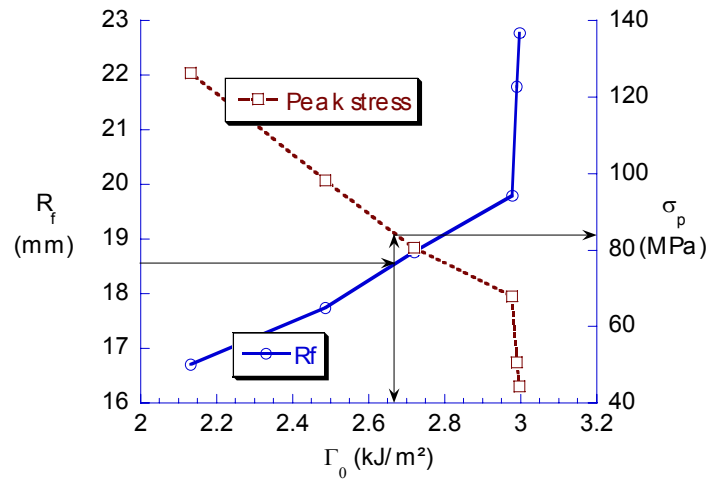

Figure 4: Calibration method used to calculate (Γ_0, σ_p) from (a, R_f).

Table 3 presents the calibration results obtained using this procedure. Although the peak stress in the adhesive layer has a maximum for an intermediate layer, the toughness of the joint keeps increasing with bond thickness. The value of the calibrated parameters are consistent with the one found by Yang *et al* [4] using another calibration method based on the evaluation of the stress in the adhesive layer.

TABLE 3
CALIBRATION RESULTS USING A STEADY-STATE FEM APPROACH

Joint thickness (mm)	Average radii of curvature (mm)	Crack length (mm)	Toughness (kJ/m²)	Peak stress (MPa)
0.050	27.38	5.638	1.43	32.9
0.185	18.57	4.813	2.69	83.2
0.898	21.39	4.874	2.88	56.6

The values calculated for a 0.185mm bond thickness were used to model the wedge-opening peel test with bonded assemblies made of 0.78mm thick steel plates. The results in terms of radii of curvature were predicted with an error less than 5%.

DISCUSSION AND CONCLUSION

The analytical beam model yields a toughness between 0.87 and 1.33 kJ/m² for the different bond thicknesses fractured at a wedge speed equal to 10 mm/min. These values are about a factor of 2 smaller than the ones obtained using the more accurate numerical approach. The analytical form is based on the assumption of pure bending, neglecting the contribution due to the opening force of the wedge, the contribution of shear forces and the deformation in the adhesive ahead of the crack tip. The FEM approach also showed a continuous increase of toughness with bond thickness.

In this paper, we have demonstrated how a computational FEM model with a cohesive zone law can be calibrated using two experimental measurements. This model offers a means to accurately evaluate the toughness of the joint and to assess the analytical formula. When properly calibrated the cohesive zone model can also be used in a standard FEM code for assessing the integrity of real structures. The robustness of the model has to be assessed with other experimental results with different plate thicknesses and plate properties. In principle, the model parameters have to be modified when the bond thickness is modified. Accounting for the bond thickness in a more fundamental way will require enriching the model such that the contribution of the overall deformation inside the bond and of the failure process are decoupled. This can be done by explicitly modeling the bulk adhesive. Furthermore, addressing the loading rate effect will require the introduction of some dependence of the peak stress on the opening rate in order to mimic the strain rate sensitivity of the polymeric bond (see [11]).

REFERENCES

1.   Thouless, M.D., Adams, J. L., Kafkalidis, M. S., Ward, S. M., Dickie, R. A. and Weterbeek, G. L. (1998) *J. Mater. Sc.* 33, 187.
2.   Needleman, A. (1987) *J. Appl. Mech.* 54, 525.
3.   Tvergaard, V. and Hutchinson, J.W. (1992) *J. Mech. Phys. Solids* 40, 1377.
4.   Yang, Q. D., Thouless, M. D. and Ward, S. M. (1999) *J. Mech. Phys. Solids* 47, 1337.
5.   Kinloch, A. J. and Williams, J. G. (1998) *J. Mater. Sc. Letters* 17, 81.
6.   Yang, Q. D. and Thouless, M. D. (1999) *J. Mater. Sc. Letters* 18, 2051.
7.   Kinloch, A. J. and Williams, J. G. (1999) *J. Mater. Sc. Letters* 18, 2049.
8.   Sener, J.Y. (1999). PhD Thesis, Université catholique de Louvain, Belgium.
9.   Ferracin, T. Pardoen T. Sener, J.Y. and Delannay, F. (2000). *Advances in mechanical behavior, plasticity and damage*. Elsevier, Oxford.
10. Dean, R.H. Hutchinson, J.W. (1980). *Fracture mechanics: 12th conference, ASTM STP 700*, American Society For Testing and Materials, 383
11. Landis, C. Pardoen, T. and Hutchinson, J.W. (2000) *Mech. of Mat*. 32, 663.

PRESTRAINING EFFECT ON CREEP BEHAVIOUR
OF Ni-BASE C263 SUPERALLOY

Yan-Hui Zhang and David M. Knowles

Department of Materials Science and Metallurgy
University of Cambridge, England CB2 3QZ

ABSTRACT

The effect of room temperature plastic deformation on the subsequent creep behaviour of C263 alloy has been studied. Creep tests were carried out at 800ºC and prestraining was conducted in tension up to 5.1%. Prestraining has increased primary and tertiary creep rates, but did not produce a discernible difference in the steady-state creep rate. Progressive loss of creep life and fracture ductility was found with increasing amount of prestrain. Concomitantly, the density of grain boundary cavities increased significantly, although intergranular fracture was predominant in all specimens. Cavities were found to nucleate at grain boundary carbides due to stress concentration produced by slip bands. Prolonged high temperature exposure resulted in plate-like η phase precipitation at grain boundaries. Its precipitation has been found to weaken grain boundary strength, creating cavity formation and producing microcracking.

KEYWORDS

Creep, Prestrain, Slip bands, Cavity, C263 superalloy

INTRODUCTION

It has been reported that creep performance of metals and alloys can be significantly influenced by prior plastic deformation [1-4]. Although creep strain is reduced by increased cavitation at grain boundaries, the effect of prestraining on creep strength and life is not resolved and depends on materials and testing conditions. These findings have clear technological implications since many engineering components may be strained plastically during fabrication. Another example of importance is that turbine components invariably suffer from cyclic thermal and mechanical stresses during the start-up, steady-state and shut-down operations. Plastic deformation at lower temperature can significantly influence high temperature deformation. This is especially prominent for a combustor since it suffers severe creep deformation at high temperature and plastic deformation at low temperature. In recent years, there has been an increasing interest in combustor lifing, which presents challenges not seen for turbine aerofoil and disc materials.

As part of an ongoing programme addressing combustor lifing in turbine engines, prestraining effects on creep behaviour of superalloy C263 at 800ºC have been studied in this work. This alloy is widely used in non-rotating components such as combustion chambers, casing, liners, exhaust ducting and bearing housing in aeroengines.

EXPERIMENTS

The chemical composition of C263 alloy is given in Table 1. After a standard heat treatment involving solutioning at 1150ºC for 2 h and ageing at 800ºC for 8h, the microstructure of the material contains a mean-linear-intercept grain size of about 104 μm, an average γ′ precipitate size of ~22 nm, many annealing twins and almost continuous precipitation of $M_{23}C_6$ carbides at grain boundaries. The γ′ volume fraction was determined as ~10% using a Semper image processing program (Synoptics Ltd). $M_{23}C_6$ carbides are present along grain and twin boundaries with a finer size at the latter and are coherent with one of the neighbouring grains exhibiting the typical cube-cube relationship, i.e. $(100)_\gamma$ $//(100)_{carbide}$, $[001]_\gamma // [001]_{carbide}$.

Table 1. Nominal chemical composition (wt. %) of C263 alloy.

Ni	Co	Cr	Fe	Mo	Mn	Si	Ti	Al	C
Bal.	20	20	0.7	5.8	0.6	0.4	2.15	0.45	0.06

Creep tests of non-prestrained and prestrained specimens were carried out under constant load control at 800ºC at an initial stress of 160 MPa using cylindrical creep specimens with a gauge length of 28.0mm and a diameter of 5.64mm. Prestraining was carried out at room temperature at slow crosshead speed. The specimens were heated via a three-zone furnace and the temperature was controlled to $\pm$ 1.0ºC over the specimen gauge length using three thermocouples and a three-term temperature controller. Strain was measured using linear variable displacement transducers capable of detecting displacement of 5×10^{-4} mm.

For detailed analysis of deformation and damage mechanisms, thin foils for transmission electron microscopy (TEM) observation were prepared from specimens either crept to the steady-state strain rate and then cooled down to room temperature under load, or crept to failure. TEM foils were examined in a JEOL 2000 FX electron microscope with an operating voltage of 200 kV. JEOL 820 SEM was used to characterise the microstructure of crept specimens on cross sections and fracture surfaces.

RESULTS

The creep curves of specimens prestrained and non-prestrained are shown in Fig. 1. It clearly illustrates the detrimental effect of plastic deformation on the creep life and rupture strain. This degradation in life and ductility increases consistently with increasing amount of prestrains. Comparison of these creep curves also suggests that prestraining has increased both primary creep rate and the rate of transition into tertiary creep, but not the steady-state creep rate, $\dot{\varepsilon}_S$. The average value of $\dot{\varepsilon}_S$ from three creep tests of non-prestrained specimens was 1.1×10^{-5}, and the difference from prestrained specimens was less than

30%. It was also noticed that the proportion of life spent in steady-state creep to that in tertiary creep increased, from 0.75 for the non-prestrained specimen to 1.16 for the specimen prestrained at 5.1%.
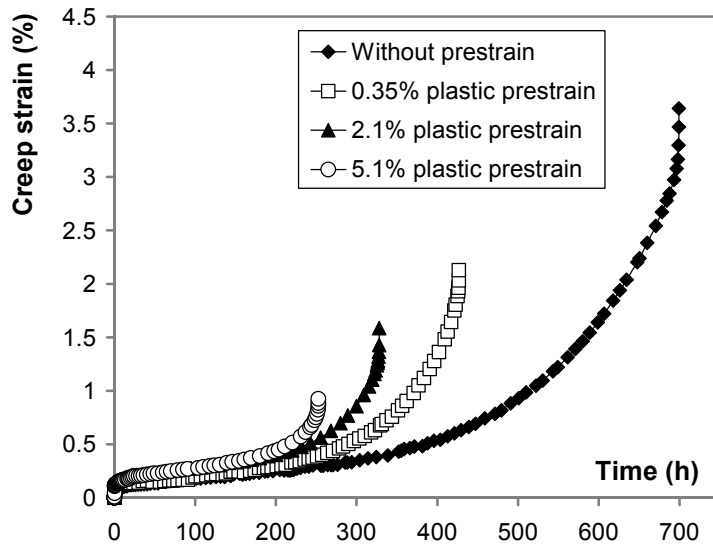

Fig. 1, Comparison of creep curves of specimens non-prestrained and prestrained, at 800°C.

Microstructure analysis using TEM and SEM revealed that the limited creep strain of the material was associated with the formation of creep cavities at grain boundaries. They nucleate at the interfaces with the grain boundary carbides, see Fig. 2. Cavities formed on grain boundaries predominately normal to the loading direction, Fig. 3, and their density increased with increasing prestrains. This was suggested by both examining the cross sections and fracture surfaces of failed specimens. Although all creep fractures exhibit predominantly intergranular characteristics, there was a difference in the failure mode. For the non-prestrained specimen, failure was caused by the initiation of cracks due to cavities nucleated on the preferential sites and followed by their propagation along grain boundaries. While for the specimens with large prestrain, failure resulted mainly from the formation of cavities with higher density and more uniform distribution at grain boundaries and their subsequent coalescence. The latter can be clearly seen in Fig. 4 where cavities have almost cover the whole fracture surface of the specimen prestrained to 5.1%.

During the process of creep testings, η phase began to precipitate from grain boundaries. It exhibits a plate-like structure. These precipitates have a specific orientation relation with the γ matrix: $[011]_\gamma$ // $[2\bar{1}\bar{1}0]_\eta$, and $(11\bar{1})_\gamma$ // (0001). Because of the grain boundary migration driven by the energy change associated with difference in the dislocation density and chemical compositions, η phase was often found to be present along grain boundaries in the form of plates. Its nucleation was often accompanied by γ phase precipitation, forming a laminar structure, Fig. 5. Cavities were also found at such boundaries with the matrix as can be seen in this figure.

DISCUSSION

For polycrystal materials loaded under creep conditions, it has been realised that vacancies can cluster at grain boundary stress concentration sites to form cavities. These cavities accumulate to form cracks and the growth of these cracks will lead to intergranular fracture with limited creep strain. But the origin of this stress concentration is still the subject of debate. Stress concentration has been suggested to come from grain boundary sliding [5,6], slip bands [7] or grain boundary dislocation pile-up [8].
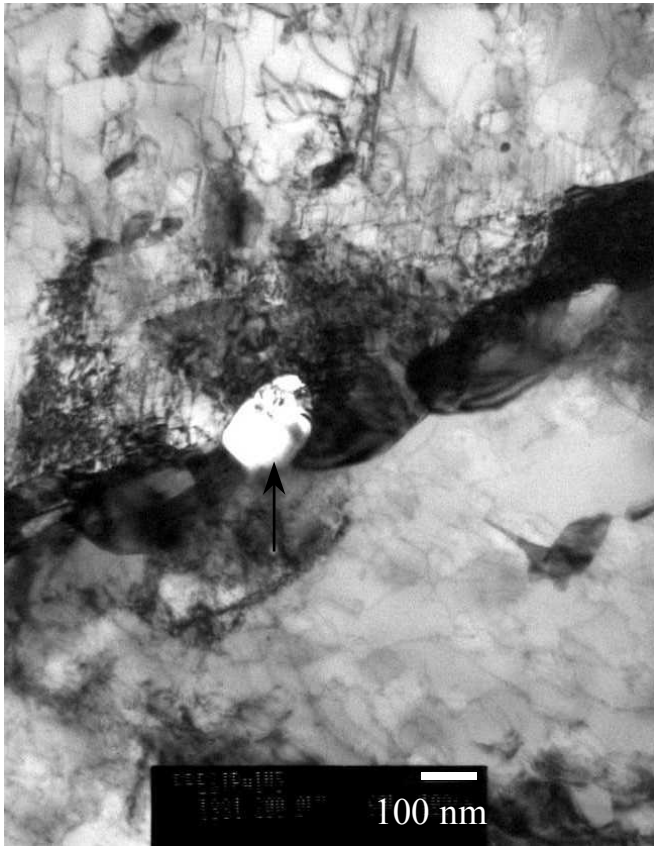
Fig. 2, TEM micrograph showing cavity nucleation (arrowed) near carbides at a grain boundary.
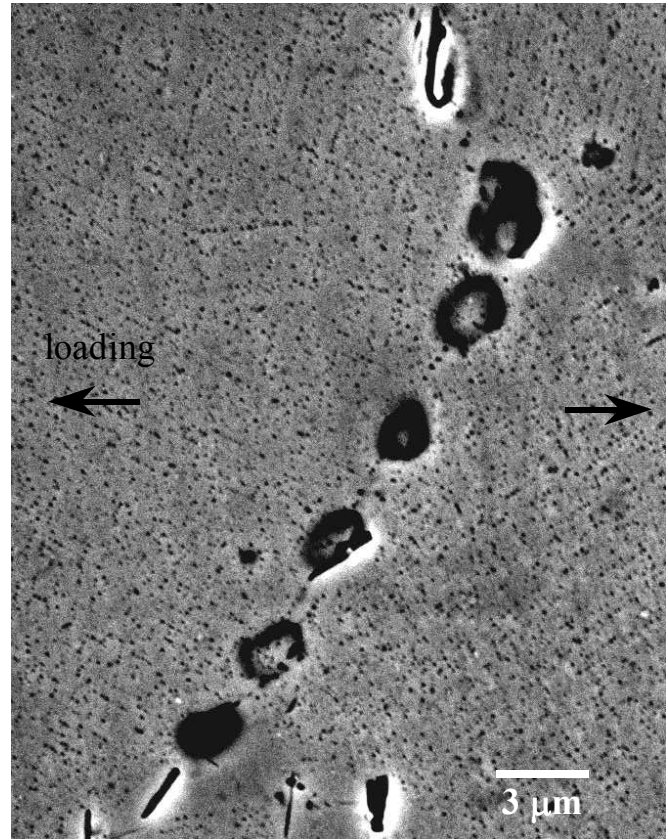

Fig. 3, Cavities nucleated extensively on grain boundary, predominantly normal to the loading direction, from the specimen prestrained to 5.1%.

A previous study on the deformation structure of the crept specimens of the alloy without prestraining has revealed that dislocation deformation was inhomogeneous and mainly located on a few slip bands during steady-state creep [9]. Stress concentration developed at the intersection of these bands with grain boundaries where carbides resides on. Cavities nucleate at the interface with the carbides due to stress concentration induced vacancy clustering. Failure was then caused by the propagation of cavity-induced cracks along grain boundaries, which resulted in a relatively extended tertiary creep stage. For the prestrained specimens, however, the current TEM observation has found that prestraining has markedly increased deformation homogeneity and produced more slip bands, see Fig. 6. This increases site density with high stress concentration at grain boundaries, resulting in a reduced incubation time for cavity formation and creating extensive cavitation on grain boundaries as can be seen in Fig. 4. Creep failure resulted from cavity linkage at grain boundaries, leading to a relatively steep tertiary creep curve.

Reports of prestraining effect on $\dot{\varepsilon}_s$ are not conclusive, as both increasing [2] and decreasing rate [3] have been observed. In this study, no discernible difference in $\dot{\varepsilon}_s$ among specimens with different amount of prestraining was detected. This might be because of the net outcome of the increased creep rate by the increased dislocation density through prestraining and the increased resistance to dislocation movement by slip band intersections. Further work will be required to identify the mechanism.

The precipitation of η phase has also been found to provide sites for cavity nucleation and microcracking [9]. Its precipitation was often accompanied by the creation of a γ′ depletion zone, which weakens the local strength of grain boundary. Furthermore, plates of this phase are regularly distributed along boundaries. Therefore, in order to improve the creep performance of the material, measures should be taken to avoid η phase precipitation at grain boundaries.
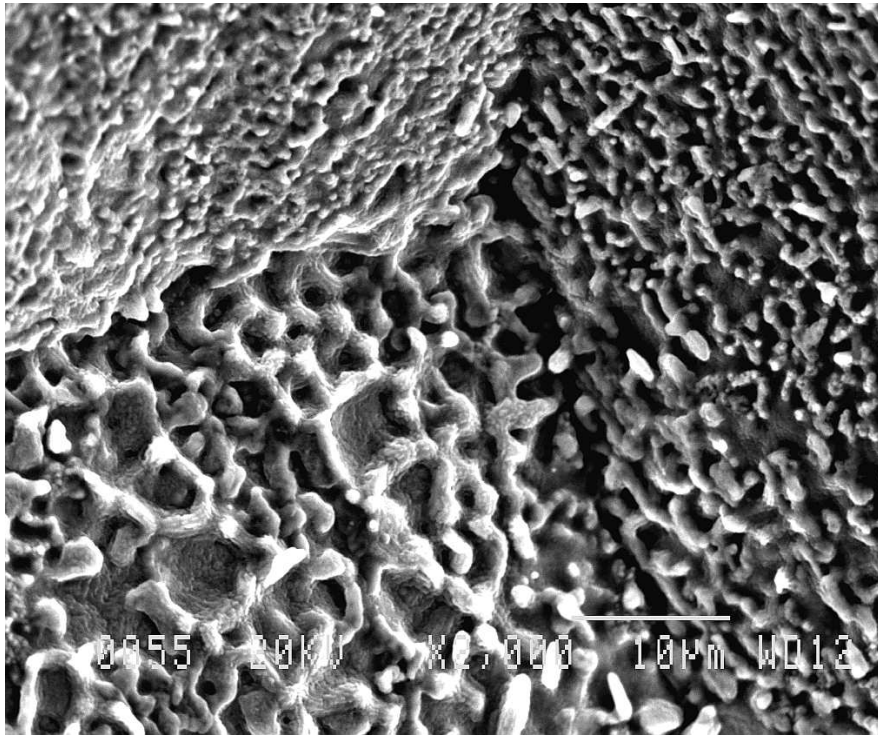
Fig. 4, SEM micrograph showing extensive cavitation on fracture surface of a crept specimen prestrained up to 5.1%.
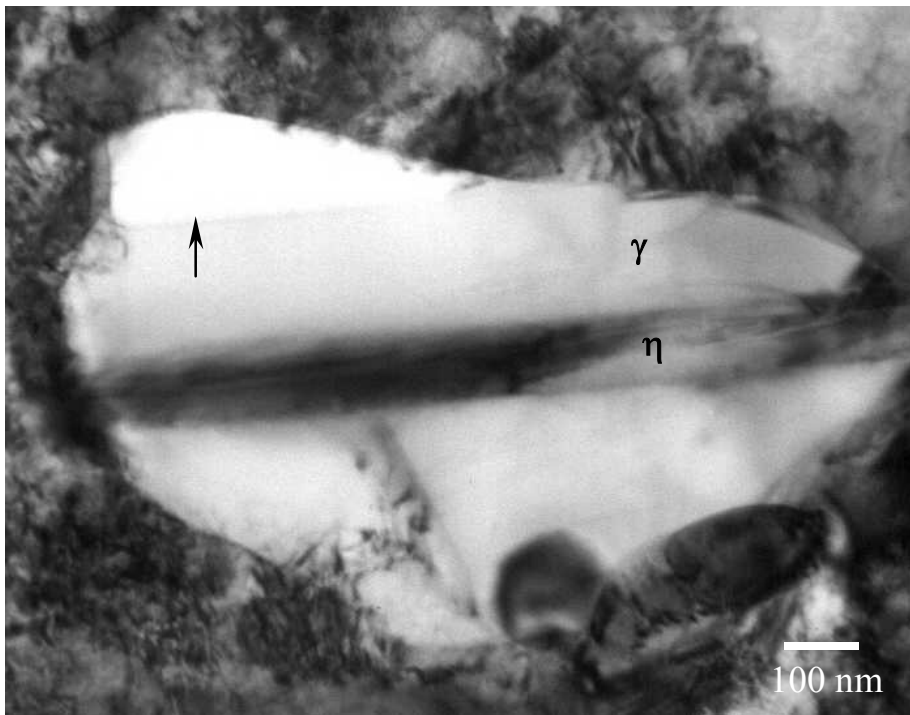

Fig. 5, Laminar structure composing of η and γ phases formed at grain boundaries. A cavity (arrowed) nucleated at the interface of γ/matrix.
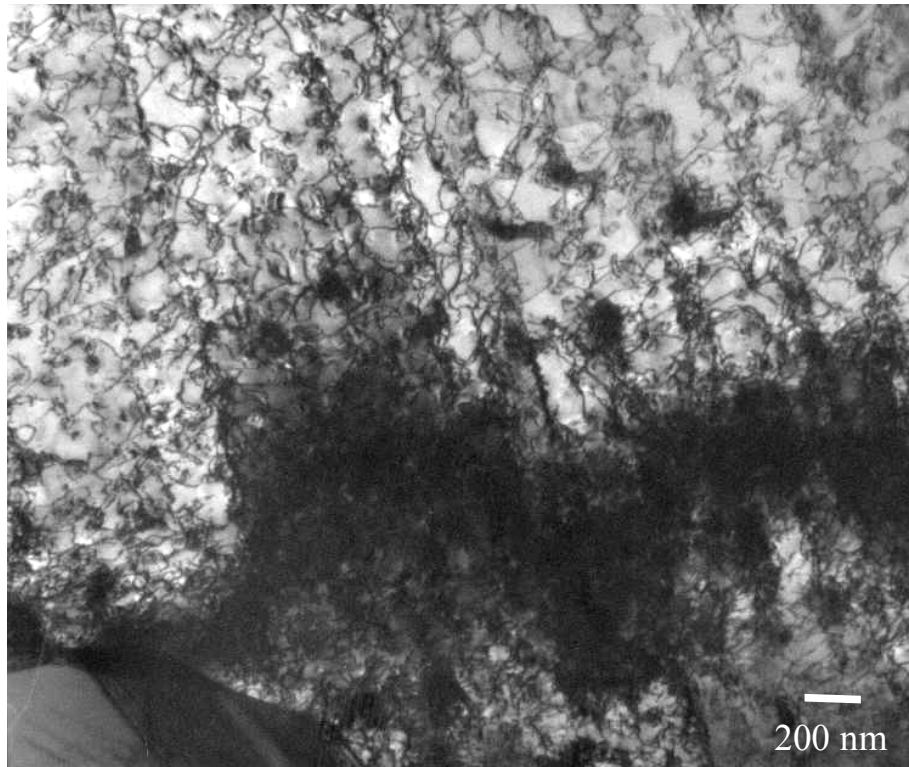
Fig. 6, TEM micrograph showing extensive slip bands structure observed in a specimen prestrained and then creep ruptured.

CONCLUSIONS

1. Creep life and rupture strain decreased with increasing prestraining.
2. Prestraining did not introduce a noticeable effect on steady-state creep rate.
3. Creep cavities nucleated near carbides at grain boundaries, which resulted in limited creep strain of the material.
4. It appears the increased cavity density with prestraining was caused by the increased stress concentration sites associated with plasticity-induced slip bands.

REFERENCES

1. Evans R.W. and Wilshire B. (1985). Creep of metals and alloys, The Institute of Metals, London.
2. Dyson B.F. and Rodgers M.J. (1974) *Metals Science*, **8**, 261.
3. Loveday M.S. and Dyson B.F. (1983) *Acta Metall.*, **31**, 397.
4. Burt H., Elliot I.C. and Wilshire B. (1981) *Metals Science*, **15**, 421.
5. Raj R. and Ashby M.F. (1975) *Acta Metall.*, **23**, 653.
6. Chen I.W. and Argon A.S. (1981) *Acta Metall.*, **29**, 1321.
7. Dyson B.F. (1983) *Scripta Met.*, **17**, 31.
8. Lim L.C. (1987) *Acta Metall.*, **35**, 1663.
9. Zhang Y.H. and Knowles D.M. (2001), Proc. 9th Int. Conf. on Creep and Fracture of Engineering Materials and Structures, edited by J.D. Parker, The Institute of Materials, U.K., pp.405.

REFERENCE: ICF1001003OR

Symposium on *Computation & Probabilistic Fracture Mechanics*
10th International Congress on Fracture, Honolulu, HI, Dec 2-7, 2001

PROBABILISTIC FAILURE ASSESSMENT OF A CARBON-CARBON SHELL FOR THE EARTH ENTRY VEHICLE CONCEPT

R. E. Kurth and F.W. Brust

Battelle Memorial Institute, 505 King Avenue, Columbus, OH 43201-2693

ABSTRACT

The goal of the first phase of this program is to demonstrate that it is feasible using currently accepted analyses procedures to estimate the probability of failure of the Earth Entry Vehicle (EEV) to be less than 1 in 1,000,000. Clearly, an experimental-only demonstration program is not feasible from either a cost or a time standpoint. Alternatively, an analyses-only effort is adequate only in the situation in which there is significant historical confidence in the methodologies. While titanium may have a sufficient history the Carbon-Carbon (C-C) composite material for the fore body and aft structure does not. Therefore, a two step process has been adopted. First, the combination of existing NASA Langley Research Center (NASA LaRC) mechanics analyses tools for composite structural analyses with probabilistic analyses tools is performed. This tool has been developed to demonstrate that a complete probability of failure calculation is feasible. Secondly, the probability of failure of the EEV C-C structure has been quantified with this tool. The important parameters for damage in the C-C aero-shell were determined and a statistical design for the development of a response surface fit to the finite element code was developed. Finite Element (FE) analyses of the EEV structure for the nominal entry condition with varying degrees of composite material damage were performed. These results were combined with the statistical design parameters to calculate a response surface fit to the FE code. The response surface was then analyzed using the fast probability integration method to obtain an estimate of the failure probability of the C-C.

KEYWORDS

Composite material, structural failure, risk assessment of structures

INTRODUCTION

The development of an estimate of the probability of failure of the C-C aero-shell proceeded in four steps. First, the existing data was reviewed. Second, a statistical design was developed for the fitting of a response surface[*] to the FE model. Next, the FE model was run as specified in the statistical design to obtain the response surface coefficients. These response surface coefficients

---

[*] A response surface is a polynomial fit to a complex model.

were then input to the fast probability integrator to determine the failure probability for the C-C composite structure.
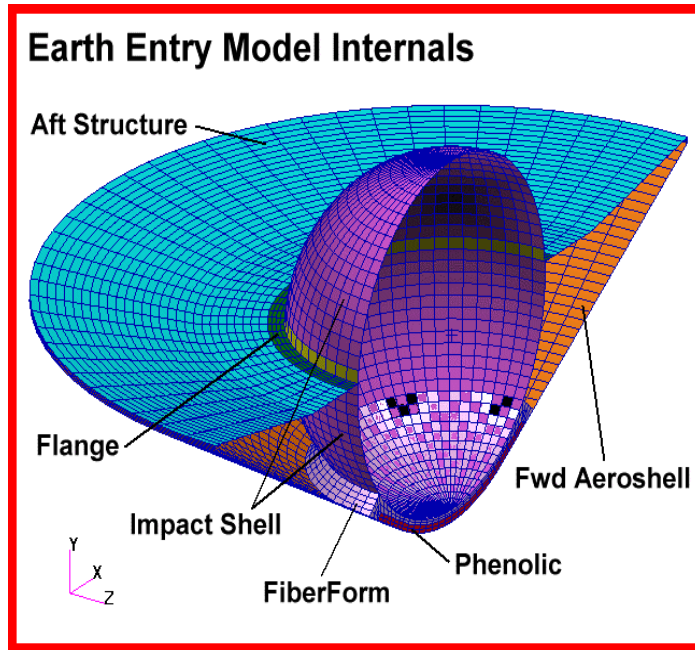

Figure 1. EEV Configuration Used In FE Analysis

FINITE ELEMENT (FE) MODELING

The finite element model was provided by NASA LaRC. The initial analyses were limited to the entry configuration for this phase. The reason is that the results of damage caused during the manufacturing process and the launch phase can be treated as inputs to the entry model. This will cut in half the number of FE analyses needed and allow the demonstration of the failure probability calculation. Provided that the damage that is assumed for the entry analysis is conservative (i.e. it bounds what the results of a launch analysis would provide) then the failure probability should only get lower as the more detailed launch analysis results are integrated into the final analyses.

RESPONSE SURFACE MODELING

The goal of the response surface modeling is to eliminate the need to perform FE analysis. By a response surface we mean a polynomial approximation to the FE code. Assuming that the maximum stress is the response of interest then:

$$\sigma_{max} = a_0 + \sum_{i=1}^{N} a_i x_i + \sum_{i<j} a_{ij} x_i x_j + \sum_{i<j<k} a_{ijk} x_i x_j x_k + \ldots + a_{123\ldots N} x_1 x_2 x_3 \cdots x_n$$

For the random variables represented by x_i we can calculate a distribution of σ_{max}. By comparing this distribution to the distribution of the ultimate strength we obtain the probability of C-C failure. How do we obtain this response surface? For the problem at hand we used a factorial experimental design.[*] The reason for this is two-fold. One this design will cover a large fraction of the input space. Secondly, it minimizes the number of runs needed for the response surface development.

FAILURE CRITERION DEVELOPMENT

The development of a failure criterion for the C-C composite does not actually involve a failure of the C-C material in the classical sense. Rather, the concern is that the strain in the C-C becomes high enough to cause the Thermal Protection System (TPS) material to crack the result of which is viewed as a failure of the EEV system. Because the failure data collected to date is in terms of stress we first need to establish a stress-strain relationship. This was done through classical statistical analysis, but is not reported in this paper. Rather, the results of these calculations are simply stated. For the C-C tensile strength data the mean is 21.18 ksi and the standard deviation is

---

[*] The "experiment" in this case is the FE analyses.

4.06 ksi. We obtain a value of β equal to 6.1 for the tensile strength data using a Weibull distribution to describe the strength.

We can now use these values for β and κ to calculate the probability that the load exceeds the strength. The algorithm for this calculation is taken from the TRACLIFE[1] program originally written for residual strength calculations in aircraft and first programmed by Wirsching and Wu.[2] On today's personal computers this algorithm gives almost instantaneous answers for very low probability events (on the order of 10^{-9}). Let us examine the current analyses.

In this analysis it is necessary to specify the *limit state equation*. This is simply a mathematical statement of the surface at which the system will fail. This is a very simple equation for this analysis since we are simply interested in the event that the strength, denoted S, is less than the stress, denoted L. Therefore, $S - L < 0$, is the limit state equation. For the shape parameter values, β, given such that the first two moments, i.e. the mean and variance, of the two-parameter Weibull distribution are matched to the "data" then the Rackwitz-Fiessler or Chen Lind algorithms can be used to calculate the probability that the limit state has been exceeded. The next section will produce preliminary P_F numbers. For now we move to the FE inputs needed to develop the response surface.

FINITE ELEMENT CODE ANALYSES FOR RESPONSE SURFACE DEVELOPMENT

The development of a response surface for the determination of the probability of failure for the C-C composite material is based on a fold-over factorial design. This design allows for future expansion of the response surface without losing the information contained in these original runs. A total of sixteen finite element analyses are performed to determine the peak strain values. Thus, five of these runs are used to determine the average value and the impact of the independent variables, also called "main effects" on the probability of failure, the remaining eleven runs are used to determine all of the interaction terms impacts on the failure probability. So what are the variables to be included in the analyses? Based on a review of nominal FE analyses the following four variables are recommended for inclusion:

Delamination of the C-C
Fiber cracking of the C-C
Matrix cracking of the C-C
Temperature

We recognize that there are other inputs to the analyses that can impact the failure probability but we believe they are of secondary importance to these variables. For example, there is a significant question about the entry angle because of the asymmetric loading that would be imposed. This is a variable that can be added at a later time by using the fold-over feature of the statistical design. It would require an additional 16 runs. All of the damage is recommended to be placed in the zone shown in Figure 1.

C-C FAILURE PROBABILITY CALCULATIONS

There were two types of failure probability assessments made during this study. First, a simple comparison of the predicted strains to the strength was studied. Secondly, the response surface analyses were performed.
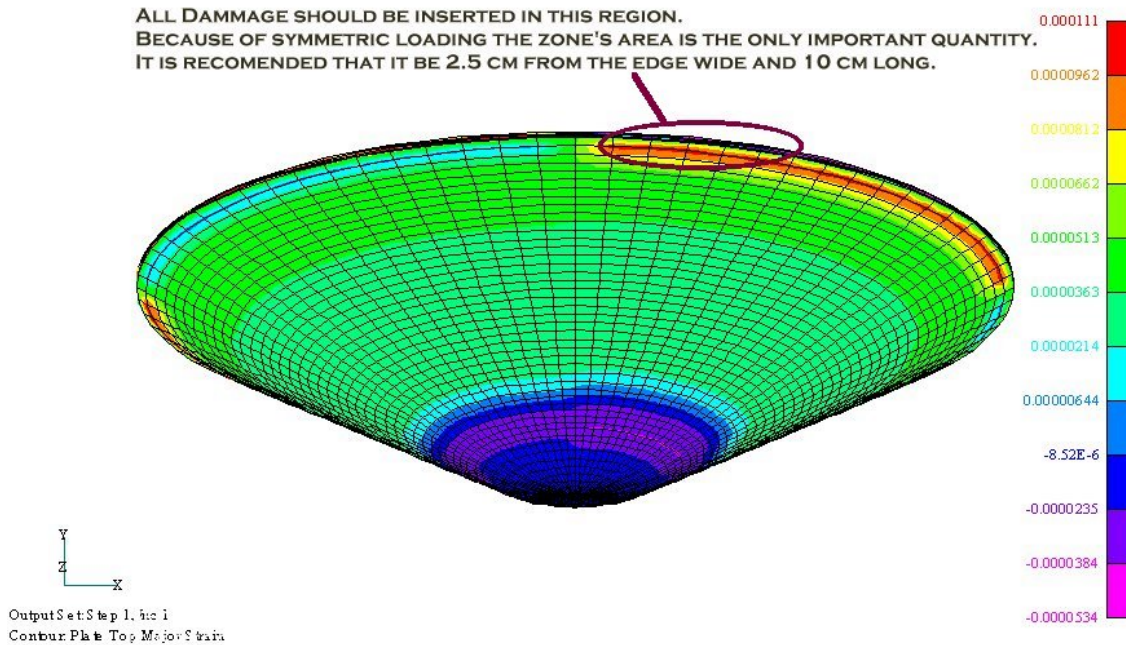
ALL DAMMAGE SHOULD BE INSERTED IN THIS REGION.
BECAUSE OF SYMMETRIC LOADING THE ZONE'S AREA IS THE ONLY IMPORTANT QUANTITY.
IT IS RECOMENDED THAT IT BE 2.5 CM FROM THE EDGE WIDE AND 10 CM LONG.

Figure 1. Recommended Damage Locations

The first step in the assessment of the structural strength was to examine the point estimate of the probability of failure. To do this we examine the calculated maximum principal strain calculated in the base case analysis and compare it to the (assumed) Weibull distribution for the strength. Thus, the maximum principal strain of 8.97 x 10^{-5} is compared to the TPS allowable strain distribution with a shape factor, β, equal to 2 and 4. When the value of 4 is used the maximum principal strain calculated by the FE code falls at a point in the strength distribution that states the strength would be less than this *point value* is equal to a probability of 4.5 x 10^{-7}. This is encouraging but we must recall that the Weibull distribution has very long.

We know look at the estimated failure probability for the C-C composite shell for all eight of the response surface calculations. These are shown in Table I. The estimated failure probabilities rang from 9 x 10^{-8} to 1.3 x 10^{-5}. However, we must remember that these probabilities are *conditional* probabilities, i.e. they are dependent on the inputs to the finite element model. Since these are *not* equally weighted we cannot simply take the arithmetic average of the numbers to determine the overall failure probability. Rather we must perform the FPI analysis of the fitted response surface to obtain our final result.

C-C RESPONSE SURFACE ANALYSES

The FE code analyses were performed using ABAQUS. The results of the FE analyses are reported as the maximum principal strain within the C-C shell structure. These results are given in Table I. Here we take these eight values and calculate the coefficients of the response surface equation.[*] A cursory examination of the values in Table I shows that the maximum principal strain changes by a factor of 2.2 from the highest to lowest value ratio. Table I indicates that the failure probability can

---

[*] Recall that since the temperature is no longer a variable all columns in Table VI involving the factor 4 must be removed from the analysis.

change by a factor of 144 or 2 and ½ orders of magnitude! This is the impact of the long tails in the assumed Weibull distribution.

An examination of the response surface coefficients shows that matrix cracking is the driver for the maximum principal strain with fiber cracking a factor of 3 lower. The impact of delamination on the maximum principal strain is an order of magnitude less than fiber cracking.

EEV Conceptual Design Assessment Battelle - NASA LaRC Strain Failure Criterion C-C Composite					
Load Condition	NASA Value	NASA Safety Factor	β=4.00		Strain Failure Safety Factor
50 g entry	Maximum principal stress	9.7	7.25E-06	1 in 137,894	6.2
CASE 1	8.970E-05 mm-mm	20.9	4.53E-07	1 in 2,206,302	13.4
CASE 2	7.700E-05 mm-mm	24.4	8.95E-08	1 in 11,169,403	15.6
CASE 3	1.000E-04 mm-mm	18.8	4.53E-07	1 in 2,206,302	12.0
CASE 4	1.040E-04 mm-mm	18.1	4.53E-07	1 in 2,206,302	11.5
CASE 5	1.530E-04 mm-mm	12.3	3.50E-06	1 in 285,937	7.8
CASE 6	1.690E-04 mm-mm	11.1	3.50E-06	1 in 285,937	7.1
CASE 7	1.940E-04 mm-mm	9.7	7.25E-06	1 in 137,894	6.2
CASE 8	2.000E-04 mm-mm	9.4	1.34E-05	1 in 74,432	6.0

Table I. Response Surface Results Point Estimates for Failure Probability of the C-C Aero-Shell

We can also examine how the variability in the individual effects impacts the overall response variability. To do so we note that the variance of the linear combination of two variable is given as:

$$Var(Z) = a_1^2 Var(x_1) + a_2^2 Var(x_2)$$

Repeatedly applying this equation to the response surface equation allows the variance in the maximum principal strain to be partition among the main effects (delamination, fiber cracking, and matrix cracking) and all of their interactions. The result of this partitioning demonstrates that over 90% of the variance in the maximum principal stress is derived from the variability in the assumed matrix cracking damage.

FPI ANALYSIS OF FE CODE RESULTS

The response surface coefficients derived in the previous section were input to the FPI analysis procedure. For the base case analysis we see the estimated failure probability is 3.4 x 10^{-6}.

These results are obtained by assuming a COV for the damage areas of 12.5%. If we increase this COV we will increase the probability of failure. As an example, if we increase the COV from 12.5% to 18.75% the probability of failure increases from 3.4 x 10^{-6} to 6.5 x 10^{-6}. We believe that the base case analysis is the most representative but that opinion is based on expertise not on data.

While the failure probability of 3.4 x 10^{-6} is exceptionally low, it is still too high for the PRA. Because this was a scoping PRA there are several conservative assumptions built into the analyses. These assumptions were reviewed via an expert panel. The failure probability number was then

revised, *based on expert opinion without further analyses*, to provide the input to the full PRA model.

CONCLUSIONS

When collecting all of these factors together it was the consensus that the C-C failure probability would be a factor of 4 to 6 lower in a best estimate analyses. Further, if it can be shown that the carbon phenolic material will be used for the TPS and that the bond line maintains integrity then there would be another factor of 4 to 10 reduction from the increased TPS allowable strain. However, without changes it was agreed that a factor of 5 reduction (the mid-range value) could be applied for the best estimate of the C-C failure probability or a value of 6.8×10^{-7}.

---

[1] Kurth, R.E. and Bigelow, C.A., *Transport Risk Assessment Containing Widespread Fatigue Damage: TRACWFD Analysis of Longitudinal and Circumferential Splice Joints to Determine the Onset of Widespread Fatigue Damage and Its Probability of Occurrence*, Second Annual Joint DoD/FAA/NASA Conference on Aging Aircraft, August, 1998, Williamsburg, VA

[2] Wirsching, P. and Wu, J.

PROPAGATION OF A FLUID-DRIVEN PENNY-SHAPED FRACTURE PARALLEL TO THE FREE-SURFACE OF AN ELASTIC SOLID

Xi Zhang[1]   Alexei Savitski[2]   Emmanuel Detournay[2]   Rob Jeffrey[1]

[1] CSIRO Petroleum, PO Box 3000, Glen Waverley, VIC, Australia

[2] Department of Civil Engineering, University of Minnesota, MN, USA

ABSTRACT

A computational procedure is developed for solving the problem of a penny-shaped fracture propagating parallel to the free-surface of an impermeable elastic solid. The fracture is driven by injection of an incompressible viscous fluid. The crack is modeled as a continuous distribution of dislocation disks associated to normal and shear displacement discontinuities along the fracture. The Green's functions for the elastic half-space are derived based on Eshelby's method for inclusions in infinite isotropic solids and a powerful "reflection" rule devised by Aderogba [1]. The resulting integro-differential equations are solved numerically for the viscosity-dominated regime of fluid-driven crack propagation. The strong non-linear coupling of elasticity and fluid flow is handled by a finite difference scheme, and the time step varies until the chosen increment of crack propagation is satisfied. Numerical results are presented for the crack radius, opening and net pressure as a function of radial distance and time, for the case of a given constant injection rate.

KEYWORDS

Hydraulic Fracture; Elasticity; Green's Functions; Half-Space; Viscosity-Dominated Regime

INTRODUCTION

Hydraulic fracturing is a stimulation technique of underground reservoirs of hydrocarbons, which relies on inducing a fracture in the reservoir rock by injecting a viscous fluid from a borehole. A hydraulic fracture can propagate from the borehole over large distance despite the presence of a confining (compressive) stress, due the internal pressurization by the fracturing fluid. Although most applications of this technique involve deep fractures, there are specific cases where the influence of a free-surface on fracture growth becomes significant or even dominant, as shown in Fig.1. Hydraulic fracture near a free surface has recently been applied to induce rock caving in mining [2]. In such cases, the hydraulic fracture is characterized by a ratio of the fracture radius over the distance from the free surface which can reach order 1 [3].

Knowledge of the Green's functions is crucial to establish the governing equations for the crack problems. In general, the penny-shaped cracks can be modelled by a continuous distribution of dislocations associated to normal and shear displacement discontinuites. By using Eshelby's method, closed-form Green's functions for many dislocation problems have been obtained, see Mura [4]. We present a brief summary of the solutions for a dislocatio loop in an elastic space by means of Eshelby's method. The solutions are then extended to a half-space using the "reflection" rule due to Aderogba [1].

Solutions for fluid-driven fractures are based on integral equations obtained by linear superposition of the Green's functions for dislocation disks along the fracture. The fracture process involves the coupled mechanisms of rock fracturing and flow of an incompressible viscous fluid. It is assumed that the energy dissipated in the creation of new fracture surface is small compared to that expended in viscous flow. This is the so-called viscosity-dominated regime. The corresponding self-similar asymptotic solution at the tip region was given by
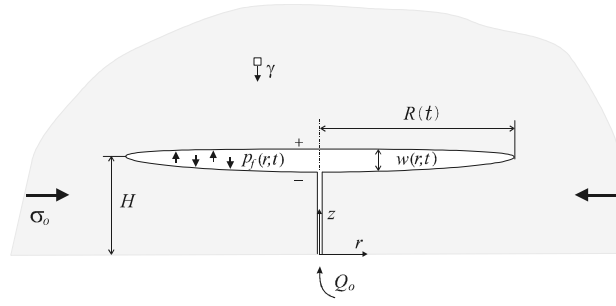
Figure 1: Penny-shaped hydraulic fracture propagating parallel to the free-surface of an elastic half-space

Desroches *et al.* [5]. A numerical algorithm is developed here for simulating the propagation of a hydraulic fracture at a fixed distance from the free surface.

GREEN'S FUNCTIONS FOR A HALF-SPACE

In linear elastic solids, the stresses and displacements can be expressed in terms of the Papkovich-Neuber(P-N) potentials $\{\Phi_i, \Psi\}$ $(i = 1, 3)$,

$$\sigma_{ij} = (\kappa - 1)(\Phi_{j,i} + \Phi_{i,j})/2 + (3 - \kappa)\Phi_{k,k}\delta_{ij}/2 - x_k\Phi_{k,ij} - \Psi_{,ij} \tag{1}$$

$$2\mu u_i = (\kappa + 1)\Phi_i - (x_j\Phi_j + \Psi)_{,i} \tag{2}$$

in which σ_{ij} is the Cauchy stress, ε_{ij} the strain tensor, u_i the displacement vector and μ and ν the material constants, $\kappa = 3 - 4\nu$. Consider a unit point force acting along the x_3-axis at $\mathbf{x}' = (x_1', x_2', x_3')$ in an infinite elastic solid. The P-N Potentials are given by

$$\Phi_1 = \Phi_2 = 0, \quad \Phi_3 = c/R, \quad \Psi = -cx_3'/R \tag{3}$$

in which $c = 1/(\kappa + 1)$. In the same way, we can obtain the Green's functions for unit point forces along the x_1 and x_2 directions. In the cylindrical coordinate system, a unit point force in the r (θ) direction can be decomposed into two parts: $f_1 = \cos\theta'(-\sin\theta')$ and $f_2 = \sin\theta'(\cos\theta')$ in the x_1 and x_2 directions. Then the displacements in the Cartesian coordinate system can be obtained by superposition. In a straightforward way, the Green's functions in the cylindrical system can be found by applying a coordinate transformation.

To model a crack, the concept of dislocation loops must be introduced. For an infinitesimal loop, the eigenstrain e_{ij}^T inside the loop can be taken as homogeneous and has the form

$$e_{ij}^T(\mathbf{x}) = -(b_i n_j + b_j n_i)\delta(\mathbf{S} - \mathbf{x})/2 \tag{4}$$

in which $\delta(\mathbf{S} - \mathbf{x})$ is the Dirac delta and b_i the Burgers vector.

When a uniform eigenstrain e_{ij}^T is prescribed within an infinitesimal closed subregion V, the eigenstress σ_{ij}^T can be obtained through Hooke's law

$$\sigma_{ij}^T = 2\mu\left[e_{ij}^T + \frac{\nu}{1 - 2\nu}e_{kk}^T\delta_{ij}\right] \tag{5}$$

From Eshelby's method, the displacement fields due to the disturbed eigenstresses can be expressed as

$$u_i(\mathbf{x}) = \int_V \sigma_{kl}^T(\mathbf{x}')\frac{\partial}{\partial x_l'}G_{ik}(\mathbf{x}, \mathbf{x}')d\mathbf{x}' \tag{6}$$

see details in [1,4]. Two specific cases are listed below:

1. Opening dislocations: The eigenstresses caused by the eigenstrain e_{zz}^T are

$$\sigma_{rr}^T = \nu P e_{zz}^T, \quad \sigma_{\theta\theta}^T = \nu P e_{zz}^T, \quad \sigma_{zz}^T = (1 - \nu)P e_{zz}^T \tag{7}$$

in which $P = 2\mu/(1 - 2\nu)$.

2. Shearing dislocations: The non-zero eigenstresses can be written as

$$\sigma_{rz}^T = 2\mu e_{rz}^T, \quad \sigma_{zr}^T = 2\mu e_{rz}^T \tag{8}$$

For a dislocation ring, displacements at any point in the space can be obtained by superposition of infinitesimal loops along the ring. It is found that all integrals can be expressed in terms of the Lifschitz-Hankel (L-H) integrals defined in [6]. Here, a modified form of L-H integrals are employed [7]

$$\bar{J}(m, n, p) = (\text{sgn}[\xi])^{m+n+p} J(m, n, p) \tag{9}$$

$$J(m, n, p) = \int_0^\infty J_m(t) J_n(\rho t) e^{-\varpi t} t^p dt \tag{10}$$

where $\rho = r/r'$, $\xi = z/r'$, $\xi' = z'/r'$, r' is the radius of the dislocation ring and $\varpi = \left|\xi - \xi'\right|$. Hence the displacements and the P-N potentials for the opening loop are given by

$$\bar{u}_r = d/r'[-(\kappa - 1)/2 \bar{J}(0, 1, 1) + (\xi - \xi')\bar{J}(0, 1, 2)] \tag{11}$$

$$\bar{u}_z = d/r'[(\kappa + 1)/2 \bar{J}(0, 0, 1) + (\xi - \xi')\bar{J}(0, 0, 2)] \tag{12}$$

with $d = 2\mu/(1 + \kappa)$. Substitution of displacements in (2) yields

$$\bar{\Phi}_z^t = d/r' \bar{J}(0, 0, 1) \tag{13}$$

$$\bar{\Psi}^t = -d[(\kappa - 1)/2 \bar{J}(0, 0, 0) + \xi' \bar{J}(0, 0, 1)] \tag{14}$$

and for shearing loops, we have

$$\bar{u}_r = d/r'[(\kappa + 1)\bar{J}(1, 1, 1) - 2(\xi - \xi')\bar{J}(1, 1, 2)] \tag{15}$$

$$\bar{u}_z = d/r'[-(\kappa - 1)\bar{J}(1, 0, 1) - 2(\xi - \xi')\bar{J}(1, 0, 2)] \tag{16}$$

This leads to

$$\bar{\Phi}_z^s = d/r' \bar{J}(1, 0, 1) \tag{17}$$

$$\bar{\Psi}^s = -d[(\kappa + 1)/2 \bar{J}(1, 0, 0) + \xi' \bar{J}(1, 0, 1)] \tag{18}$$

A very powerful tool developed by Aderogba [1] can be used to connect the solution for an infinite medium and the one for a bonded semi-infinite medium. A special case is considered here, i.e. Φ_r and Φ_θ vanish. Hence,

$$\Phi_z = \Phi_z^0(r, \theta, z) + \kappa \Phi_z^0(r, \theta, -z) + 2\frac{\partial}{\partial z}\Psi^0(r, \theta, -z) \tag{19}$$

$$\Psi = \Psi^0(r, \theta, z) + \kappa \Psi^0(r, \theta, -z) + (\kappa^2 - 1)/2 \int \Phi_z^0(r, \theta, -z)dz \tag{20}$$

Substitution of (13,14) in the above equations leads to the P-N potentials for half-space problems

$$\hat{\Phi}_z^t = d/r'[\bar{J}^{(1)}(0, 0, 1) - \bar{J}^{(2)}(0, 0, 1) - 2\xi' \bar{J}^{(2)}(0, 0, 2)] \tag{21}$$

$$\hat{\Psi}^t = d[-\frac{\kappa - 1}{2}\bar{J}^{(1)}(0, 0, 0) - \xi' \bar{J}^{(1)}(0, 0, 1) + \frac{\kappa - 1}{2}\bar{J}^{(2)}(0, 0, 0) + \kappa\xi' \bar{J}^{(2)}(0, 0, 1)] \tag{22}$$

for opening dislocation rings. Also, we can obtained the P-N potentials for shearing dislocation rings

$$\hat{\Phi}_z^s = d/r'[\bar{J}^{(1)}(1, 0, 1) - \bar{J}^{(2)}(1, 0, 1) + 2\xi' \bar{J}^{(2)}(1, 0, 2)] \tag{23}$$

$$\hat{\Psi}^s = d[-\frac{\kappa + 1}{2}\bar{J}^{(1)}(1, 0, 0) - \xi' \bar{J}^{(1)}(1, 0, 1) + \frac{\kappa + 1}{2}\bar{J}^{(2)}(1, 0, 0) - \kappa\xi' \bar{J}^{(2)}(1, 0, 1)] \tag{24}$$

in which $\bar{J}^{(1)}(m, n, p)$ and $\bar{J}^{(2)}(m, n, p)$ represent the modified L-H integrals for the dislocation ring and its image.

Now let us consider a dislocation disk. For the opening dislocations, we assumed a uniform distribution of displacement discontinuity on the whole circular dislocation disk with a radius R. On the other hand, since there is no shear displacement at the centre, we assumed that the shear displacement discontinuity is proportional to the distance from the center; then the Burgers vector is defined as

$$\bar{b}_{rz} = r' b_{rz}/R \tag{25}$$

After integration from 0 to R, the normal stress and shear stresses for the opening case are given by

$$\tilde{\sigma}^t_{zz} = -\bar{J}^{(1)}(1,0,1) - (\xi - \xi')\bar{J}^{(1)}(1,0,2) + \bar{J}^{(2)}(1,0,1) + (\xi + \xi')\bar{J}^{(2)}(1,0,2) + 2\xi\xi'\bar{J}^{(2)}(1,0,3) \tag{26}$$

$$\tilde{\sigma}^t_{rz} = -(\xi - \xi')\bar{J}^{(1)}(1,1,2) + (\xi - \xi')\bar{J}^{(2)}(1,1,2) + 2\xi\xi'\bar{J}^{(2)}(1,1,3) \tag{27}$$

and for the shear case

$$\tilde{\sigma}^s_{zz} = -(\xi - \xi')\bar{J}^{(1)}(2,0,2) + (\xi - \xi')\bar{J}^{(2)}(2,0,2) - 2\xi\xi'\bar{J}^{(2)}(2,0,3) \tag{28}$$

$$\tilde{\sigma}^s_{rz} = \bar{J}^{(1)}(2,1,1) - (\xi - \xi')\bar{J}^{(1)}(2,1,2) - \bar{J}^{(2)}(2,1,1) + (\xi + \xi')\bar{J}^{(2)}(2,1,2) - 2\xi\xi'\bar{J}^{(2)}(2,1,3) \tag{29}$$

in which $\tilde{\sigma}^{t(s)}_{ij} = 4R\sigma^{t(s)}_{ij}/E'$, $E' = E/(1 - \nu^2)$.

GOVERNING EQUATIONS AND SCALING

Using the singular solutions for dislocation loops, two singular integral equations can be established

$$\int_0^R G_{nn}\left(\frac{r}{R}, \frac{s}{R}; \mathcal{R}\right) d_n(s,t)ds + \int_0^R G_{ns}\left(\frac{r}{R}, \frac{s}{R}; \mathcal{R}\right) d_s(s,t)ds = -\frac{R}{E'}p(r,t) \tag{30}$$

$$\int_0^R G_{sn}\left(\frac{r}{R}, \frac{s}{R}; \mathcal{R}\right) d_n(s,t)ds + \int_0^R G_{ss}\left(\frac{r}{R}, \frac{s}{R}; \mathcal{R}\right) d_s(s,t)ds = 0 \tag{31}$$

in which $\mathcal{R} = H/R$, H the crack depth; $G_{nn} = \tilde{\sigma}^t_{zz}/4$, $G_{ns} = \tilde{\sigma}^s_{zz}/4$, $G_{sn} = \tilde{\sigma}^t_{rz}/4$ and $G_{ss} = \tilde{\sigma}^s_{rz}/4$; d_n and d_s are dislocation densities. The above equations are rearranged in terms of the opening w and shear displacement discontinuity u as

$$\mathcal{H}\{w; \mathcal{R}\} = p(r,t)/E' \tag{32}$$

The equation governing the flow of viscous fluid in the fracture [8] is

$$\frac{\partial w}{\partial t} = \frac{1}{12\gamma r}\frac{\partial}{\partial r}\left(rw^3\frac{\partial p}{\partial r}\right) \tag{33}$$

in which γ is the fluid viscosity. The condition that the fracture is in mobile equilibrium at the tip $r = R(t)$, $K_I = K_{Ic}$, can be expressed as

$$w \simeq \frac{K'}{E'}(R - r)^{1/2} \qquad R - r \ll R \tag{34}$$

Besides the condition $w(R,t) = 0$, the boundary conditions at the fracture inlet $r = 0$ are

$$q(R,t) = 0 \quad \text{and} \quad 2\pi \lim_{r \to 0} rq = Q_o \tag{35}$$

It follows from the above equation that $q \sim O(1/r)$ near the source and $p \sim -\ln r$. Alternatively, the source can be taken into account by the global continuity equation

$$2\pi \int_0^R r\, w\mathrm{d}r = Q_o t \tag{36}$$

Introduce an arbitrary time scale T. Given an injection rate Q_o, a fixed reference length $\bar{L}_\mu$ is defined as

$$\bar{L}_\mu = \left(\frac{E'Q^3T^4}{\gamma'}\right)^{1/9} \tag{37}$$

4

in which $\gamma' = 12\gamma$. After defining the dimensionless time $\tau = t/T$ and radial coordinate $\xi = r/\bar{L}_\mu$, the dimensionless fracture radius $\chi(\tau)$ ($0 \leq \xi \leq \bar{\chi}$), openings $\bar{\Omega}(\xi, \tau)$ and $\bar{\Xi}(\xi, \tau)$, and pressure $\bar{\Pi}(\xi, \tau)$ are introduced as follows [9]

$$\chi = R/\bar{L}_\mu \qquad \bar{\Omega} = w/\bar{\varepsilon}_\mu \bar{L}_\mu \qquad \bar{\Xi} = u/\bar{\varepsilon}_\mu \bar{L}_\mu \qquad \bar{\Pi} = p/\bar{\varepsilon}_\mu E' \qquad (38)$$

where the small number $\bar{\varepsilon}_\mu = \varepsilon_\mu(T)$ is defined as

$$\bar{\varepsilon}_\mu = (\gamma'/E'T)^{1/3} \qquad (39)$$

We can now formulate the set of equations to be solved for $\bar{\Omega}(\xi, \tau)$ and $\chi(\tau)$. By expressing $\bar{\Pi}$ in (33) in terms of $\bar{\Omega}$ using (32), a single integro-differential equation for $\bar{\Omega}$ can be formulated

$$\frac{\partial \bar{\Omega}}{\partial \tau} = \frac{1}{\xi} \frac{\partial}{\partial \xi} \left(\xi \bar{\Omega}^3 \frac{\partial}{\partial \xi} \mathcal{H}\{\bar{\Omega}; \mathcal{R}\} \right) \qquad (40)$$

The inlet boundary condition is translated in terms of the opening

$$\xi \bar{\Omega}^3 \frac{\partial}{\partial \xi} \mathcal{H}\{\bar{\Omega}; \mathcal{R}\} \bigg|_{\xi=0} = \frac{1}{2\pi} \qquad (41)$$

Finally, the tip behavior of the opening is given by the zero-toughness asymptote [4]

$$\bar{\Omega} = 2^{1/3} 3^{5/6} \dot{\chi}^{1/3} (\chi - \xi)^{2/3} \qquad 1 - \xi/\chi \ll 1 \qquad (42)$$

NUMERICAL ALGORITHM

We outline here the algorithm devised by Savitski [10] to construct the self-similar zero-toughness solution ($\mathcal{R} = 0$). Minor modifications were required here to solve the half-space crack problems. The numerical algorithm is based on a fixed grid with a constant element size $\Delta\xi$, and a variable time step $\Delta\tau$. At each step, the radius is increased by a fixed increment of size $\Delta\xi$ corresponding to an initially unknown time step $\Delta\tau$. After each radius increment $\Delta\xi$, the time step $\Delta\tau$ and the opening $\bar{\Omega}$ have to be calculated using a discretized form of (40-42). The calculations are started with an initial crack radius $\chi_{\min} = 5\Delta\xi$, and assuming the initial crack aperture to correspond to the solution for $\mathcal{R} = 0$. The computations are carried out until the fracture radius reaches a predetermined length $\chi_{\max} = N_{\max}\Delta\xi$.

A combination of a finite difference scheme and the displacement discontinuity method [11] is used to solve numerically (40-42). The following description relies on two indices: the subscript i to denote the nodes at the center of the spatial elements, and the superscript m for the time index. Also, the current number of active elements at time step m is denoted by N. Hence, $\bar{\Omega}_i^m = \bar{\Omega}(\xi_i, \tau_m)$ with $\xi_i = (i - 1/2)\Delta\xi$ and $i = 1, N$; also $\bar{\chi}(\tau_m) = N\Delta\xi$.

The discretized form of (40) can now be written as

$$\frac{\bar{\Omega}_i^m - \bar{\Omega}_i^{m-1}}{\Delta\tau} = \frac{1}{(\Delta\xi)^2} K_{ij} \left(\alpha_{\text{op}} \cdot \bar{\Omega}_j^m + (1 - \alpha_{\text{op}})\bar{\Omega}_j^{m-1} \right) + d_i, \qquad i = 1, N \qquad (43)$$

where the coefficient α_{op} takes values between 0 (explicit) and 1 (implicit). The source term $d_i = 0$ for all nodes, except for the first one at the well $d_1 = 1/2\pi\Delta\xi$. The matrix $\mathbf{K}$ is defined as

$$K_{ij} = a_i M_{i-1,j} - (a_i + b_i) M_{i,j} + b_i M_{i+1,j} \qquad (44)$$

where $\mathbf{M}$ is the elasticity matrix and $\mathbf{a}$, $\mathbf{b}$ the vectors of coefficients; see Savitski [10] for details.

The time step is the solution of the asymptotic equation (42) discretized as

$$\bar{\Omega}_{N+1-i} = 2^{1/3} 3^{5/6} \left(\frac{\Delta\xi}{\Delta\tau} \right)^{1/3} \left[\Delta\xi \left(i - \frac{1}{2} \right) \right]^{2/3} \qquad (45)$$

Therefore, the time step $\Delta\tau$ can be calculated as

$$\Delta\tau = \frac{1}{N_{\text{tip}}} 2 \cdot 3^{5/2} (\Delta\xi)^3 \sum_{i=1}^{N_{\text{tip}}} \frac{(i - 1/2)^2}{(\Omega_{N+1-i})^3} \qquad (46)$$

where N_{tip} is the number of nodes taken in the near tip region of the fracture dominated by the asymptotic behavior. Only one node near the tip can be used at the beginning of the simulation, when N is small. As the fracture propagates, more and more elements fall within that region and N_{tip} can be increased.
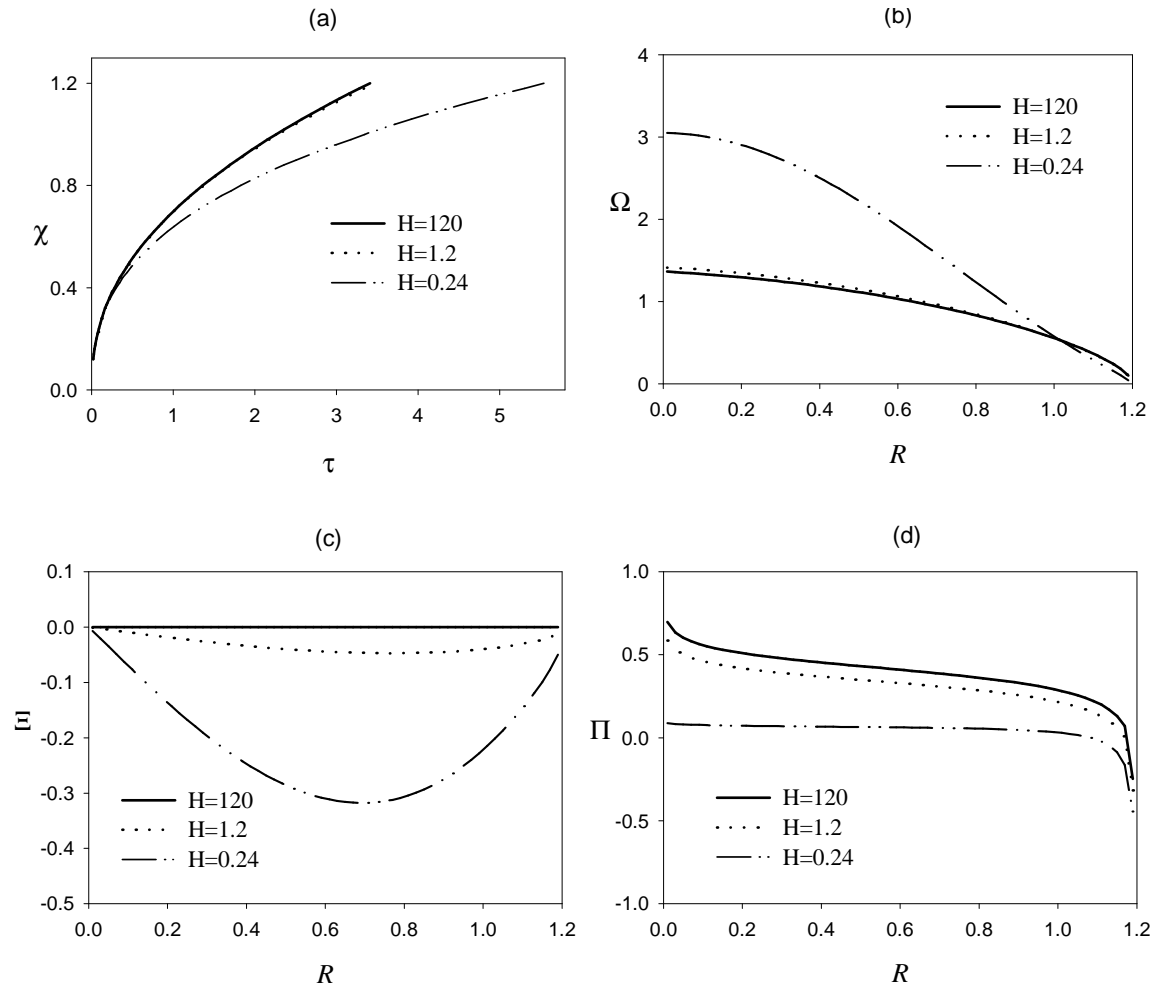
Figure 2: Dimensionless fracture properties at different crack depths, (a) Radius; (b) Opening; (c) Shearing and (d) Pressure.

RESULTS

Computations were performed using $\Delta \xi = 0.02$ and $N_{max} = 60$. Hence $\chi_{max} = 1.2$. Figure 2 provides the evolution of the fracture radius, the normal and shear discontinuity and the net pressure along the fracture for three difference crack depths $H = 120, 1.2, 0.6$. The evolution of the opening and pressure is given at the maximum crack radius χ_{max}. The expected singular distribution of the net pressure is evident in Fig. 2d. The effect of the free surface on the viscosity-dominated solution can also be observed in Fig. 2: the influence of the free surface is responsible for a larger opening, a smaller length of the fracture, and a smaller inlet pressure at a given time (corresponding to a given volume of fluid injected).

REFERENCES

1. Aderogba, K. (1977) *Phil. Mag.* 35,281
2. Jeffrey, R.G. and Mills, K. W. (2000) In: *Pacific Rocks 2000*, pp. 423-430, Balkema.
3. Pollard, D. and Hozhausen, G. (1979) *Tectonophysics*, 53, 27.
4. Mura, T. (1987) *Micromechanics of Defects in Solids*, 2nd ed. Martenus Nijhoff, Dordrecht.
5. Desroches, J. E., Detournay, E., Lenoach, B., Papanastasiou, P., Pearson, J. R. A., Thiercelin, M, and Cheng, A. H.-D. (1994) *Proc. Roy. Soc. London, Ser. A* A447, 39.
6. Eason, G., Noble, B. and Sneddon, I. (1955) *Phil. Mag. Roy. Soc. London, Ser A* 247, 529.
7. Korsunsky, A. M. (1995) *J. Mech. Phys. Solids* 43, 1221.
8. Batchelor, G. K. (1967) *An Introduction to Fluid Mechanics*, Cambridge University Press.
9. Detournay, E. (2001) In: *Computer Methods an d Advances in Geomechanics*, pp. 1277-1288, Balkema.
10. Savitski, A. (2000) Ph. D. Thesis, University of Minnesota.
11. Crouch, S. and Starfield, A. (1983) *Boundary Element Methods in Solid Mechanics*, George Allen & Unwin.

QUALIFICATION OF CLEAVAGE FRACTURE TOUGHNESS ON THE BASIS OF LOCAL FRACTURE CRITERION APPROACH

T. MIYATA* , T. TAGAWA* and C. E. CHAVES**

*Department of Materials Science & Engineering, Nagoya University,
464-8603 Nagoya, Japan
** CAE Applications Engineer, Embraer S/A, Av. Brigadeiro Faria Lima,
2170-CEP12227-901, S.J. dos Campos-SP, Brazil

ABSTRACT

Qualification of cleavage fracture toughness is discussed on the basis of the statistical local fracture criterion approach. The Weibull stress criterion is applied to the constraint loss field at the crack tip of the toughness specimen. The constraint effect has been described with the Toughness Scaling Model (TSM) proposed by Anderson and Dodds. New model in which the statistical nature of the cleavage fracture is explicitly taken into account has been proposed. Analytical prediction indicates that the specimen size requirements in toughness to obtain a valid value must be significantly depending on the value of strain hardening exponent and the Weibull shape parameter of the cleavage fracture stress. The 2-dimensional and 3-dimensional FE analysis were performed to confirm above analytical prediction. The 3-dimensional analysis also suggested that the thickness effect on toughness was mainly caused by the statistical volume effect.

The values of the strain hardening exponent, n and the Weibull shape parameter, m for various types of structural steels were experimentally investigated. The results coupled with the analytical prediction demonstrated that the specimen size requirements for a valid toughness shall be prescribed as ' $a, b > 100 J_c / \sigma_Y$' for the most of commercial steels, where a and b are crack size and ligament size of the specimen, respectively.

KEYWORDS

Cleavage fracture toughness, Statistical local fracture criterion, Weibull fracture stress, Constraint effect, Toughness qualification, Size requirement, FEM, Steels

INTRODUCTION

Loss of constraint due to a shallow notch or large scale yielding decreases the stress level at the crack tip and causes high toughness [1,2]. Dodds and Anderson [3] quantified the deviation in stress distribution caused by the loss of constraint and developed the toughness scaling model (TSM). Based on their works size requirements to achieve sufficient constraint that is equivalent with the small scale yielding condition is proposed approximately as in the ASTM E-1820-96:

$$B, b_0 > MJ_c / \sigma_Y, M = 200 \tag{1}$$

where B is the specimen thickness, b_0 is the ligament length of the specimen, J_c is the critical J-integral, and σ_Y is the effective yield strength of the material. The value of M, the constraint factor, was soon revised to be 50 according to 3-dimensional FE analysis [4]. Recently, the ASTM E-1820 (1999) was also revised to that M should be 100 except for given particular materials of M=50. The Weibull stress criterion [5,6] is applied to the toughness scaling model, and the effect of constraint loss is described as a function of the stress contour similarity ratio and the Weibull shape parameter, m of the cleavage fracture stress [7]. Analytical model predicts that the effect of constraint on the toughness strongly depends on the Weibull shape parameter of the material. The materials that have higher value of m, that implies small scatter in the cleavage fracture stress, are able to obtain a valid toughness in smaller specimens. In the present work, two- and three-dimensional FE analysis coupled with the Weibull stress criterion were performed to confirm the above theoretical prediction. Then, the value of the Weibull shape parameter in the commercial steels were investigated and the validity of the ASTM prescription on the size requirements has been discussed.

WEIBULL STRESS SCALING MODEL

Anderson and Dodds [1] quantified stress contour similarity at the crack tip between the large scale yielding (LSY) condition and the small scale yielding (SSY) condition. They successfully expressed the LSY stress field in terms of the constraint loss factor, ϕ and the SSY stress field. The variable, ϕ is defined as the similarity ratio in the area of a specified stress contour at the crack tip. The apparent J-integral for the LSY condition, J_{LSY} is converted to the J_{SSY} as,

$$J_{c\,SSY} = J_{c\,LSY}\phi^{1/2} \tag{2}$$

The Weibull stress σ_w is defined as [5],

$$\sigma_w = \left[\int_{V(\sigma_1 > \sigma_{th})} \sigma_1^m \frac{dV}{V_0} \right]^{1/m} \tag{3}$$

where V is the volume subjected to the maximum principal stress σ_1, and V_0 is a unit volume of the material. The exponent m is the Weibull shape parameter for the critical Weibull stress at cleavage fracture. When a stress singurarity can be assumed as a level of exponent β, the principal stress, σ_1 ahead of the crack tip can be described as

$$\left(\sigma_1 / \sigma_0\right)_{SSY} = g(\theta)\left(J_{SSY} / r\sigma_0\right)^{\beta} \tag{4}$$

The HRR stress field corresponds to $\beta = 1/(n+1)$, where n = the strain hardening exponent, and $g(\theta)$ is a geometrical function of the specimen. The stress field for the LSY can be written in analogy to the SSY as

$$\left(\sigma_1 / \sigma_0\right)_{\mathrm{LSY}} = g(\theta)\left(\phi^{1/2} J_{\mathrm{LSY}} / r\sigma_0\right)^{\beta} \tag{5}$$

Substituting Eq.(5) to Eq.(3), the following relation can be derived [7],

$$J_{c\,\mathrm{SSY}} = J_{c\,\mathrm{LSY}}\phi^{1/\beta m} \tag{6}$$

This formulation indicates that the TSM is the one particular case of the Weibull stress criterion dependent on the combinations of n and m. The values of ϕ are numerically given as a function of n by Anderson and Dodds [3] and the fitting equation of ϕ for a bend specimen with notch depth, $a/W=0.5$, as follows:

$$\frac{J_{\mathrm{LSY}}}{J_{\mathrm{SSY}}} = \frac{1}{\phi^{1/2}} = 1 + \Phi\left(\frac{J_{\mathrm{LSY}}}{b_0\sigma_0}\right)^{\gamma} \tag{7}$$

$$\Phi = 0.8425 n^{2.262}$$

$$\gamma = 1.126 + 0.01925n - 8.333 \times 10^{-5} n^2$$

Assuming that the SSY stress field can be described with the HRR solution, the exponent β is replaced with $1/(n+1)$. From Eq.(6) and Eq.(7), the ratio of J_{LSY} to J_{SSY} can be evaluated as:

$$\frac{J_{\mathrm{LSY}}}{J_{\mathrm{SSY}}} = \left(\frac{1}{\phi^{1/2}}\right)^{\frac{2n+2}{m}} = \left\{1 + \Phi\left(\frac{J_{\mathrm{LSY}}}{b_0\sigma_0}\right)^{\gamma}\right\}^{\frac{2n+2}{m}} \tag{8}$$

Figure 1 shows the results of Eq.(8), denoted as the WSSM, in comparison with the TSM. The specimen size requirement parameter, M ($=b_0\sigma_0/J_{\mathrm{LSY}}$) is solved for $J_{\mathrm{LSY}}/J_{\mathrm{SSY}} = 1.2$ as a function of n. The value of M indicates the limiting value to obtain the toughness within a deviation less than 20% from the SSY condition, and corresponds to the constraint factor, M in Eq.(1). Those results suggest that the SSY toughness of the materials with large value of m and smaller value of n can be obtained in smaller specimens.

2-D AND 3-D FEM ANALYSIS

In order to confirm above analytical prediction and to clarify the three dimensional size effect, 2- and 3-dimensional FE analysis were performed using the WARP 3D [8]. Finite element models for toughness specimens are shown in Fig.2. 2D-SSY analysis was performed using the semi-circular model with the boundary of the SSY singularity [4]. The Ramberg-Osgood type constitutive equation with yield strength, $\sigma_0 = E/500$, was adopted. The value of J-integral was calculated from both the path integral ($J_{\mathrm{d.i.}}$) and the load-displacement
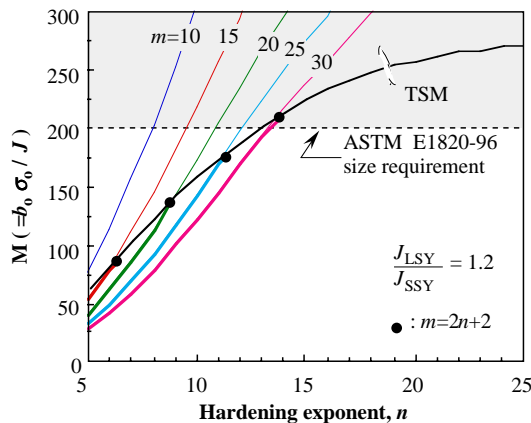

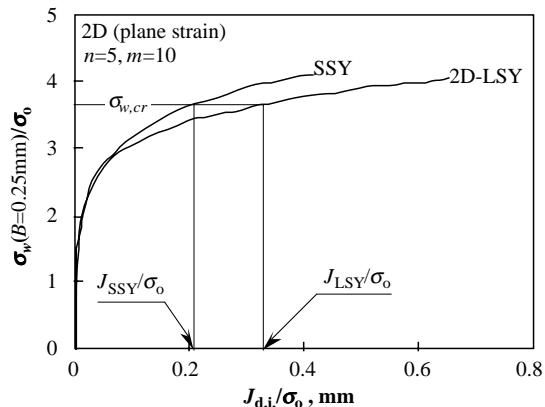**Fig.1** Comparison of WSSM with TSM on specimen size requirements.

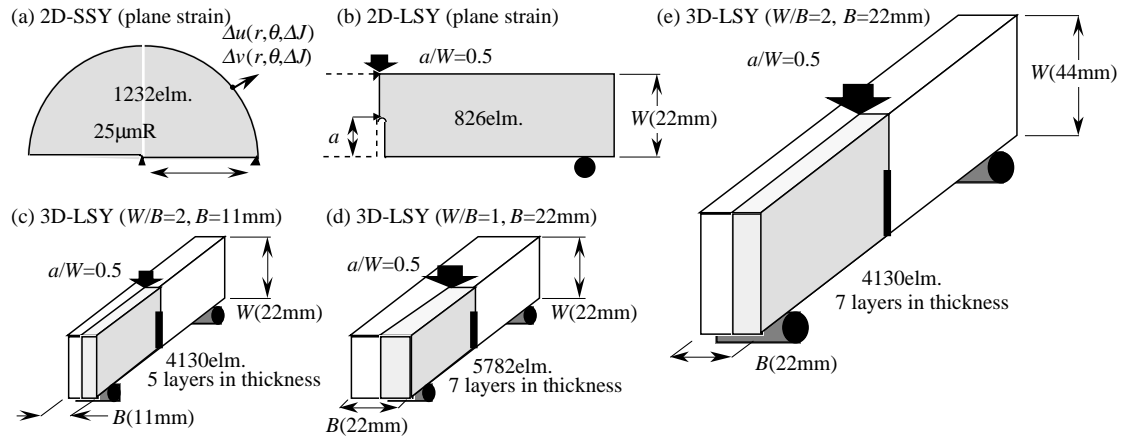**Fig.3** Relation between the Weibull stress, σ_w and J integral.

Fig.2 Finite element models for fracture toughness specimens.

curve ($J_{P-\delta}$). In the case of the 2-D plane strain analysis, both J integral values are consistent with others. The Weibull stress was calculated in the zone of $\sigma_1 > \sigma_{th} = 2\sigma_0$ and $\sigma_{th} = 3\sigma_0$.

Figure 3 shows an example of results on relation between the Weibull stress, σ_w and J-integral ($J_{d.i.}$). The ratio of J_{LSY} to J_{SSY} can be estimated with an assumption of the Weibull stress criterion according to the procedure shown in the figure. When the value of $\beta m = 2$, the TSM model must be coincide with the present WSSM model with the assumption of the HRR singularity. Figure 4 shows a comparison of the both model for the case of

Fig.4 Comparison between TSM and WSSM in the case of $\beta m = 2$.

Fig.5 Relations between the Weibull stress, σ_w and J integral for 3D models with the same in-plane specimen size.

$\beta m = 2$ in terms of relations between J_{LSY}/J_{SSY} and $b_0\sigma_0/J_{LSY}$. Bold lines indicate the results of Anderson and Dodds[1] and fine lines are the plane strain FEM results of the WSSM model. The results shown in Fig.4 support numerically the validity of the WSSM model.

The value of J integral in the 3-D FE analysis is varied with its definition. Path integral value in a given plane distributes along with the crack front in direction of the thickness. Average value through the thickness is different from $J_{P-\delta}$ especially in the large scale yielding. In the present work, $J_{P-\delta}$ is adopted for the discussion because $J_{P-\delta}$ is more significant in practical toughness testing. The estimated values of the Weibull stress of the specimens with different thickness but the same in-plane size are shown in Fig.5. Thicker specimen has larger value of the Weibull stress involving both the constraint effect and the statistical volume effect. Figure 6 shows an example on the ratio of J_{LSY} to J_{SSY} as a function of J_{LSY}. Bold line indicates the results on the plane strain 2-D FE analysis. The value of J_{SSY} in the 2-D analysis is modified to the equivalent value with the same thickness of the 3-D specimens. It implies that the effect of volume is eliminated in the value of the ratio. Although in the case of $m=10$, the constraint effect can be observed, the ratio of J_{LSY} to J_{SSY} is almost the same in the specimens of $B=11$mm and 22mm in the case of $m=20$ and 30. This result implies that the constraint effect due to the

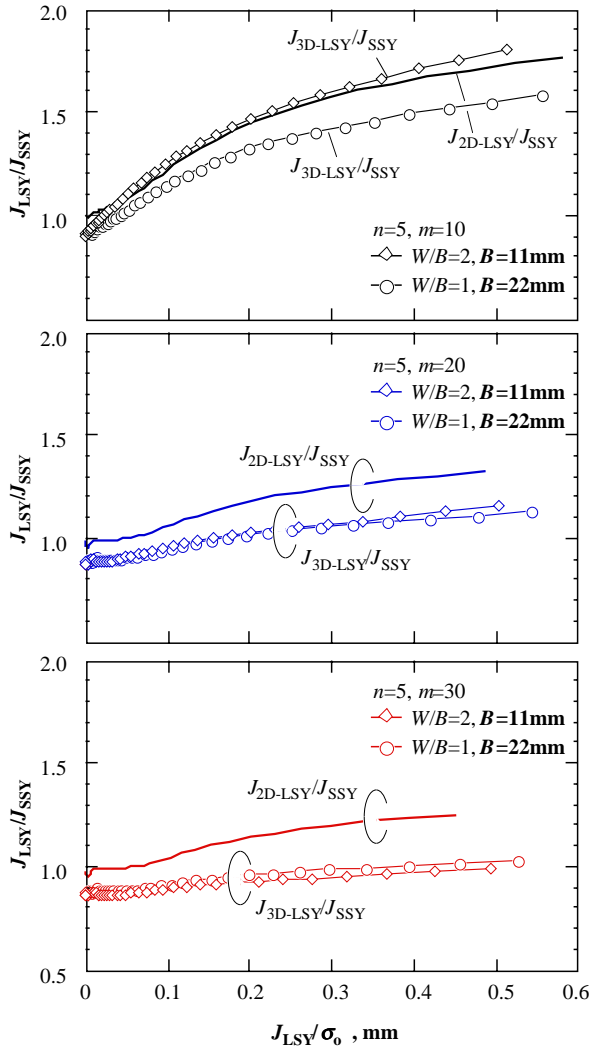**Fig.6** Comparison of constraint loss effect in the specimens of B=11mm and B=22mm.

Fig.7 Predicting flow for m from toughness transition data.

increase of the thickness is relatively small in the materials that have larger value of the Weibull shape parameter, m.

EXPERIMENTAL ANALYSIS ON THE WEIBULL SHAPE PARAMETER, m

Theoretical and numerical analysis suggest the significant role of the Weibull shape parameter, m in qualification of the cleavage fracture toughness. For several materials the value of m was investigated experimentally using notched round bar specimens. However, the data is insufficient to discuss general tendency in practical steels. The Beremin's model gives a description of the cleavage fracture toughness as [5]:

$$J_c = \frac{Const.}{B^{1/2}} \sigma_0{}^2 \left(\frac{\sigma_{w,cr}}{\sigma_0} \right)^{m/2} \tag{9}$$

The Weibull fracture stress and its shape parameter, m are assumed to be constant irrespective of the temperature. Equation (9) indicates that temperature dependence of the fracture toughness is mainly caused by the variation of the yield strength of the materials. From the experimental data on the toughness of various type of steels [9], the value of m was evaluated according to Eq. (9) and iteration procedure shown in Fig. 7. The evaluated values of m are shown in Fig. 8 as a function of the yield strength at room temperature together with the experimental values of m obtained in notched round bar specimens. The values of m vary in the range of 10
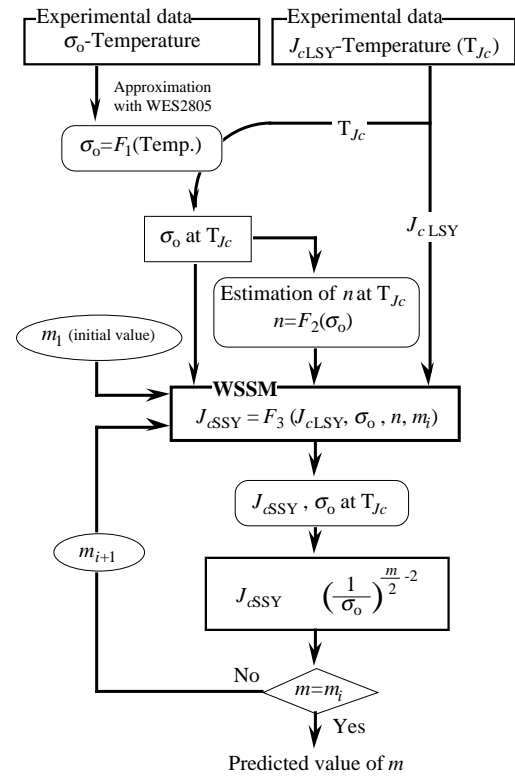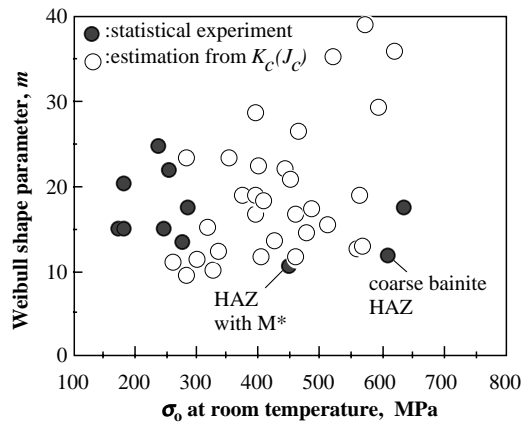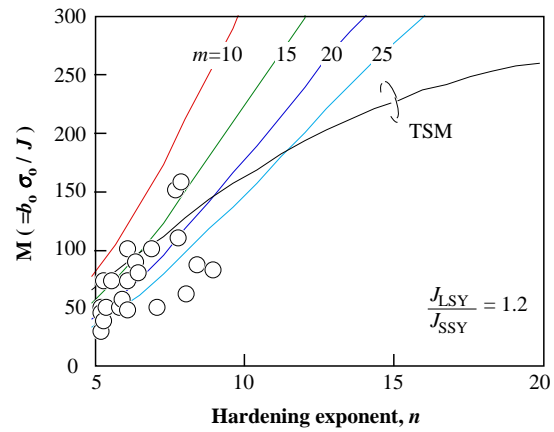
Fig.8 m values for low carbon steels.

Fig.9 Constraint factor, M for commercial steels.

to 40. The lower toughness material generally has a lower value of m. The values of the strain hardening exponent, n were simultaneously investigated. Based on these values of m and n, corresponding constraint factor, M that gives the ratio of J_{LSY} to J_{SSY} of 1.2 can be obtained from Eq. (8) as is shown in Fig.9. The results shown in Fig.9 indicate that the constraint factor, M in Eq. (1) for the most of the practical steels are in the range of 50 to 100 except for low toughness materials and the revision of the ASTM E1820 in 1999 is reasonable.

CONCLUSIONS

The Weibull stress criterion was applied to the toughness scaling model proposed by Anderson and Dodds [1]. The proposed new model suggests that the size requirements for specimen to obtain the sufficient constraint in toughness testing are strongly depending on the value of the Weibull shape parameter, m and the strain hardening exponent, n of the materials. This analytical prediction was confirmed by the FE analysis coupled with the Weibull stress criterion. Three dimensional FE analysis simultaneously indicates that the thickness effect in toughness is mainly caused by the statistical volume effect especially for the materials with the high value of m. The values of the shape parameter, m were estimated from the transition curve of the cleavage fracture toughness. The constraint factor, M to obtain the J_{SSY} is presumed as in the range of 50 to 100 for the most of commercial steels and it is consistent with the revision in the ASTM E 1820.

REFERENCES

[1]Anderson, T. L. and R. H. Jr. Dodds, (1991) J. Testing and Evaluation, 19, 123-134.

[2] O'Dowd, N. P. and C. F. Shih, (1992) J. Mechanics and Physics of Solids, 39, 898-1015.

[3]Dodds, R. H. Jr., T. L. Anderson and M. T. Kirk , (1991) Int. J. Fracture, 48, 1-22.

[4] Nevalainen, M. and R. H. Jr. Dodds, (1995) Int. J. Fracture, 74, 131-161.

[5] Beremin, F.M., (1983) Metallurgical Trans. A14, 2277.

[6] Mudry, F., (1986) Nuclear Eng. and Design 105, 65.

[7] Miyata, T. , T. Tagawa and Y. Hongkai, (2000) J. Testing and Evaluation, 28, 62-65.

[8] Koppenhoefer, K., A. Gullerud, C. Ruggieri, R. H. Jr. Dodds and B. Healy, (1997) WARP 3D 9.8 Dynamic Nonlinear Analysis of Solids Using a Preconjugate Gradient Software Archtecture, Structural Research Series 907, University of Illinois at Urbana-Champaign.

[9] Miyata, T., Tagawa, T. and Aihara, S., (1995) Tetsu to Hagane(J. the Iron and Steel Institute of Japan) 81, 583.

QUALIFICATION OF CLEAVAGE FRACTURE TOUGHNESS ON THE BASIS OF LOCAL FRACTURE CRITERION APPROACH

T. MIYATA* , T. TAGAWA* and C. E. CHAVES**

*Department of Materials Science & Engineering, Nagoya University,
464-8603 Nagoya, Japan
** CAE Applications Engineer, Embraer S/A, Av. Brigadeiro Faria Lima,
2170-CEP12227-901, S.J. dos Campos-SP, Brazil

ABSTRACT

Qualification of cleavage fracture toughness is discussed on the basis of the statistical local fracture criterion approach. The Weibull stress criterion is applied to the constraint loss field at the crack tip of the toughness specimen. The constraint effect has been described with the Toughness Scaling Model (TSM) proposed by Anderson and Dodds. New model in which the statistical nature of the cleavage fracture is explicitly taken into account has been proposed. Analytical prediction indicates that the specimen size requirements in toughness to obtain a valid value must be significantly depending on the value of strain hardening exponent and the Weibull shape parameter of the cleavage fracture stress. The 2-dimensional and 3-dimensional FE analysis were performed to confirm above analytical prediction. The 3-dimensional analysis also suggested that the thickness effect on toughness was mainly caused by the statistical volume effect.

The values of the strain hardening exponent, n and the Weibull shape parameter, m for various types of structural steels were experimentally investigated. The results coupled with the analytical prediction demonstrated that the specimen size requirements for a valid toughness shall be prescribed as ' $a, b > 100 J_c / \sigma_Y$ ' for the most of commercial steels, where a and b are crack size and ligament size of the specimen, respectively.

KEYWORDS
Cleavage fracture toughness, Statistical local fracture criterion, Weibull fracture stress, Constraint effect, Toughness qualification, Size requirement, FEM, Steels

INTRODUCTION

Loss of constraint due to a shallow notch or large scale yielding decreases the stress level at the crack tip and causes high toughness [1,2]. Dodds and Anderson [3] quantified the deviation in stress distribution caused by the loss of constraint and developed the toughness scaling model (TSM). Based on their works size requirements to achieve sufficient constraint that is equivalent with the small scale yielding condition is proposed approximately as in the ASTM E-1820-96:

$$B, b_0 > MJ_c / \sigma_Y, M = 200 \tag{1}$$

where B is the specimen thickness, b_0 is the ligament length of the specimen, J_c is the critical J-integral, and σ_Y is the effective yield strength of the material. The value of M, the constraint factor, was soon revised to be 50 according to 3-dimensional FE analysis [4]. Recently, the ASTM E-1820 (1999) was also revised to that M should be 100 except for given particular materials of M=50. The Weibull stress criterion [5,6] is applied to the toughness scaling model, and the effect of constraint loss is described as a function of the stress contour similarity ratio and the Weibull shape parameter, m of the cleavage fracture stress [7]. Analytical model predicts that the effect of constraint on the toughness strongly depends on the Weibull shape parameter of the material. The materials that have higher value of m, that implies small scatter in the cleavage fracture stress, are able to obtain a valid toughness in smaller specimens. In the present work, two- and three-dimensional FE analysis coupled with the Weibull stress criterion were performed to confirm the above theoretical prediction. Then, the value of the Weibull shape parameter in the commercial steels were investigated and the validity of the ASTM prescription on the size requirements has been discussed.

WEIBULL STRESS SCALING MODEL

Anderson and Dodds [1] quantified stress contour similarity at the crack tip between the large scale yielding (LSY) condition and the small scale yielding (SSY) condition. They successfully expressed the LSY stress field in terms of the constraint loss factor, ϕ and the SSY stress field. The variable, ϕ is defined as the similarity ratio in the area of a specified stress contour at the crack tip. The apparent J-integral for the LSY condition, J_{LSY} is converted to the J_{SSY} as,

$$J_{c\,SSY} = J_{c\,LSY}\phi^{1/2} \tag{2}$$

The Weibull stress σ_w is defined as [5],

$$\sigma_w = \left[\int_{V(\sigma_1 > \sigma_{th})} \sigma_1{}^m \frac{dV}{V_0} \right]^{1/m} \tag{3}$$

where V is the volume subjected to the maximum principal stress σ_1, and V_0 is a unit volume of the material. The exponent m is the Weibull shape parameter for the critical Weibull stress at cleavage fracture. When a stress singurarity can be assumed as a level of exponent β, the principal stress, σ_1 ahead of the crack tip can be described as

$$(\sigma_1 / \sigma_0)_{SSY} = g(\theta)(J_{SSY} / r\sigma_0)^{\beta} \tag{4}$$

The HRR stress field corresponds to $\beta = 1/(n+1)$, where n = the strain hardening exponent, and $g(\theta)$ is a geometrical function of the specimen. The stress field for the LSY can be written in analogy to the SSY as

$$\left(\sigma_1 / \sigma_0\right)_{\text{LSY}} = g(\theta)\left(\phi^{1/2} J_{\text{LSY}} / r\sigma_0\right)^{\beta} \tag{5}$$

Substituting Eq.(5) to Eq.(3), the following relation can be derived [7],

$$J_{c\,\text{SSY}} = J_{c\,\text{LSY}}\phi^{1/\beta m} \tag{6}$$

This formulation indicates that the TSM is the one particular case of the Weibull stress criterion dependent on the combinations of n and m. The values of ϕ are numerically given as a function of n by Anderson and Dodds [3] and the fitting equation of ϕ for a bend specimen with notch depth, $a/W=0.5$, as follows:

$$\frac{J_{\text{LSY}}}{J_{\text{SSY}}} = \frac{1}{\phi^{1/2}} = 1 + \Phi\left(\frac{J_{\text{LSY}}}{b_0\sigma_0}\right)^{\gamma} \tag{7}$$

$$\Phi = 0.8425 n^{2.262}$$

$$\gamma = 1.126 + 0.01925 n - 8.333 \times 10^{-5} n^2$$

Assuming that the SSY stress field can be described with the HRR solution, the exponent β is replaced with $1/(n+1)$. From Eq.(6) and Eq.(7), the ratio of J_{LSY} to J_{SSY} can be evaluated as:

$$\frac{J_{\text{LSY}}}{J_{\text{SSY}}} = \left(\frac{1}{\phi^{1/2}}\right)^{\frac{2n+2}{m}} = \left\{1 + \Phi\left(\frac{J_{\text{LSY}}}{b_0\sigma_0}\right)^{\gamma}\right\}^{\frac{2n+2}{m}} \tag{8}$$

Figure 1 shows the results of Eq.(8), denoted as the WSSM, in comparison with the TSM. The specimen size requirement parameter, M ($=b_0\sigma_0/J_{\text{LSY}}$) is solved for $J_{\text{LSY}}/J_{\text{SSY}} = 1.2$ as a function of n. The value of M indicates the limiting value to obtain the toughness within a deviation less than 20% from the SSY condition, and corresponds to the constraint factor, M in Eq.(1). Those results suggest that the SSY toughness of the materials with large value of m and smaller value of n can be obtained in smaller specimens.

2-D AND 3-D FEM ANALYSIS

In order to confirm above analytical prediction and to clarify the three dimensional size effect, 2- and 3-dimensional FE analysis were performed using the WARP 3D [8]. Finite element models for toughness specimens are shown in Fig.2. 2D-SSY analysis was performed using the semi-circular model with the boundary of the SSY singularity [4]. The Ramberg-Osgood type constitutive equation with yield strength, $\sigma_0 = E/500$, was adopted. The value of J-integral was calculated from both the path integral ($J_{\text{d.i.}}$) and the load-displacement
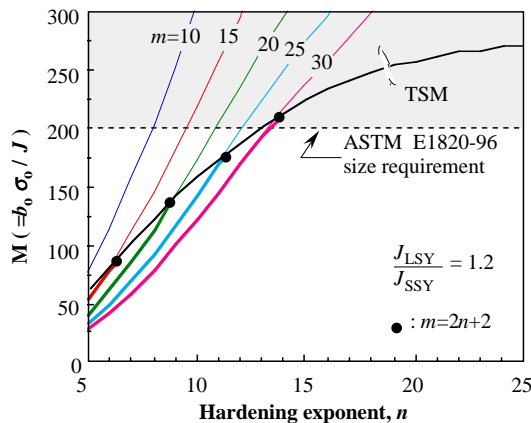

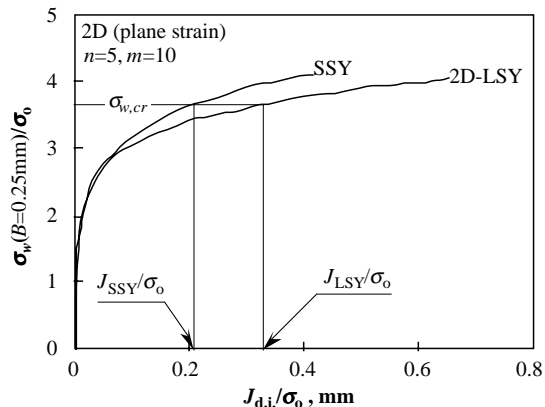**Fig.1** Comparison of WSSM with TSM on specimen size requirements.

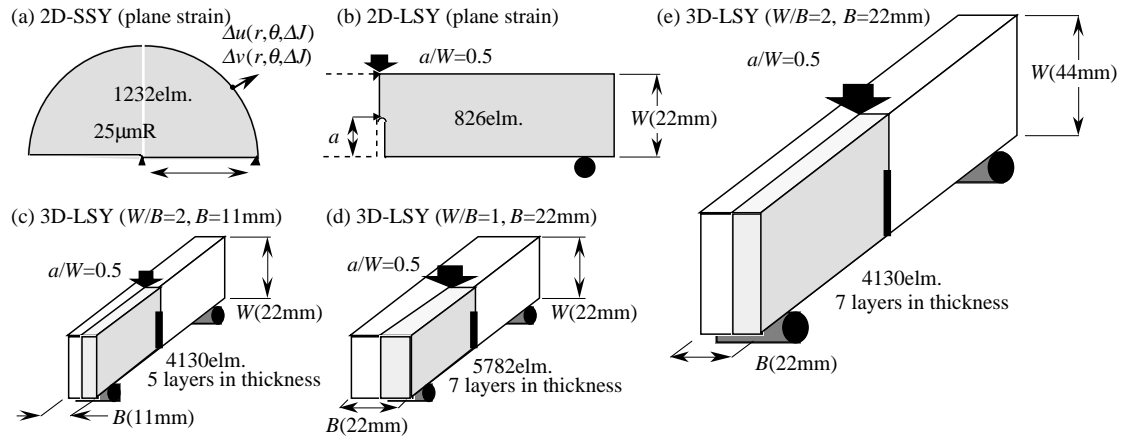**Fig.3** Relation between the Weibull stress, σ_w and J integral.

Fig.2 Finite element models for fracture toughness specimens.

curve ($J_{P-\delta}$). In the case of the 2-D plane strain analysis, both J integral values are consistent with others. The Weibull stress was calculated in the zone of $\sigma_1 > \sigma_{th} = 2\sigma_0$ and $\sigma_{th} = 3\sigma_0$.

Figure 3 shows an example of results on relation between the Weibull stress, σ_w and J-integral ($J_{d.i.}$). The ratio of J_{LSY} to J_{SSY} can be estimated with an assumption of the Weibull stress criterion according to the procedure shown in the figure. When the value of $\beta m = 2$, the TSM model must be coincide with the present WSSM model with the assumption of the HRR singularity. Figure 4 shows a comparison of the both model for the case of

Fig.4 Comparison between TSM and WSSM in the case of $\beta m = 2$.

Fig.5 Relations between the Weibull stress, σ_w and J integral for 3D models with the same in-plane specimen size.

$\beta m = 2$ in terms of relations between J_{LSY}/J_{SSY} and $b_0\sigma_0/J_{LSY}$. Bold lines indicate the results of Anderson and Dodds[1] and fine lines are the plane strain FEM results of the WSSM model. The results shown in Fig.4 support numerically the validity of the WSSM model.

The value of J integral in the 3-D FE analysis is varied with its definition. Path integral value in a given plane distributes along with the crack front in direction of the thickness. Average value through the thickness is different from $J_{P-\delta}$ especially in the large scale yielding. In the present work, $J_{P-\delta}$ is adopted for the discussion because $J_{P-\delta}$ is more significant in practical toughness testing. The estimated values of the Weibull stress of the specimens with different thickness but the same in-plane size are shown in Fig.5. Thicker specimen has larger value of the Weibull stress involving both the constraint effect and the statistical volume effect. Figure 6 shows an example on the ratio of J_{LSY} to J_{SSY} as a function of J_{LSY}. Bold line indicates the results on the plane strain 2-D FE analysis. The value of J_{SSY} in the 2-D analysis is modified to the equivalent value with the same thickness of the 3-D specimens. It implies that the effect of volume is eliminated in the value of the ratio. Although in the case of $m=10$, the constraint effect can be observed, the ratio of J_{LSY} to J_{SSY} is almost the same in the specimens of $B=11$mm and 22mm in the case of $m=20$ and 30. This result implies that the constraint effect due to the

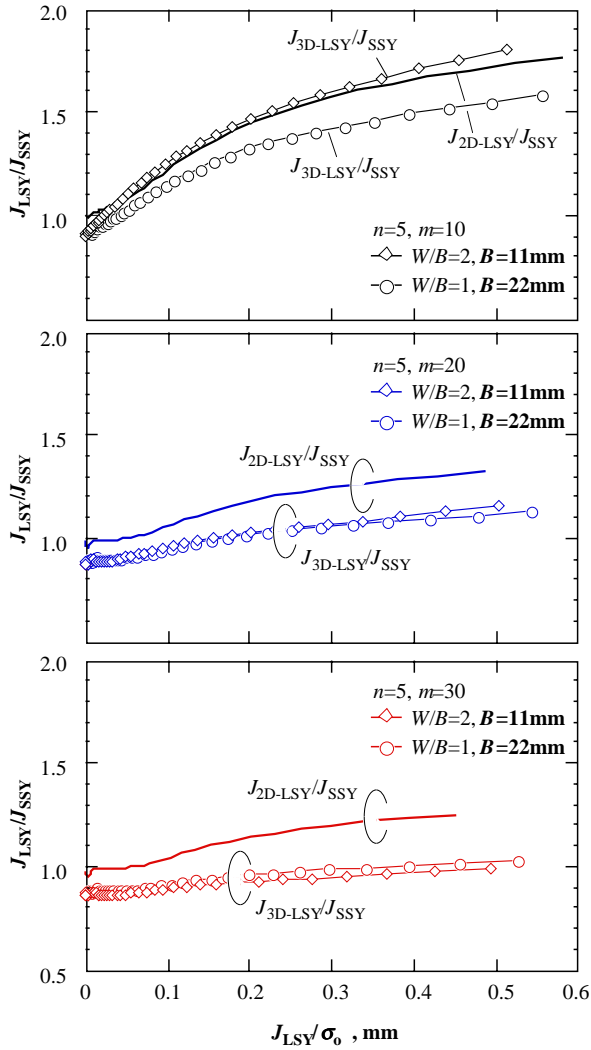**Fig.6** Comparison of constraint loss effect in the specimens of B=11mm and B=22mm.

Fig.7 Predicting flow for m from toughness transition data.

increase of the thickness is relatively small in the materials that have larger value of the Weibull shape parameter, m.

EXPERIMENTAL ANALYSIS ON THE WEIBULL SHAPE PARAMETER, m

Theoretical and numerical analysis suggest the significant role of the Weibull shape parameter, m in qualification of the cleavage fracture toughness. For several materials the value of m was investigated experimentally using notched round bar specimens. However, the data is insufficient to discuss general tendency in practical steels. The Beremin's model gives a description of the cleavage fracture toughness as [5]:

$$J_c = \frac{Const.}{B^{1/2}} \sigma_0^{\;2} \left(\frac{\sigma_{w,cr}}{\sigma_0} \right)^{m/2} \tag{9}$$

The Weibull fracture stress and its shape parameter, m are assumed to be constant irrespective of the temperature. Equation (9) indicates that temperature dependence of the fracture toughness is mainly caused by the variation of the yield strength of the materials. From the experimental data on the toughness of various type of steels [9], the value of m was evaluated according to Eq. (9) and iteration procedure shown in Fig. 7. The evaluated values of m are shown in Fig. 8 as a function of the yield strength at room temperature together with the experimental values of m obtained in notched round bar specimens. The values of m vary in the range of 10
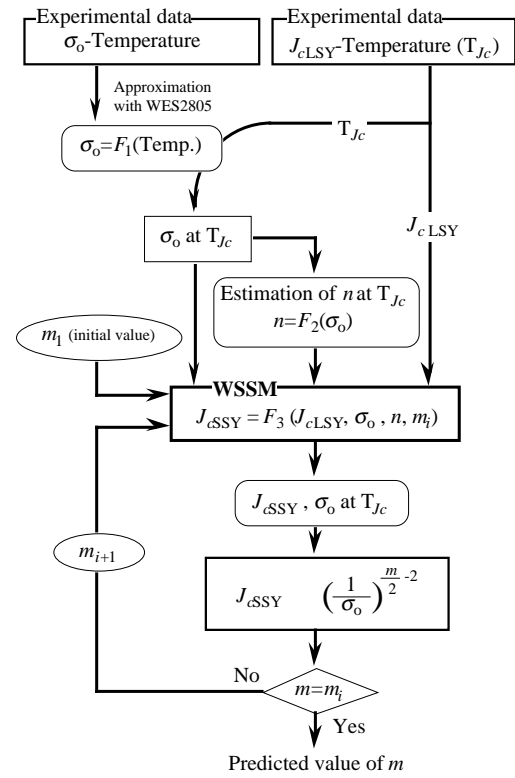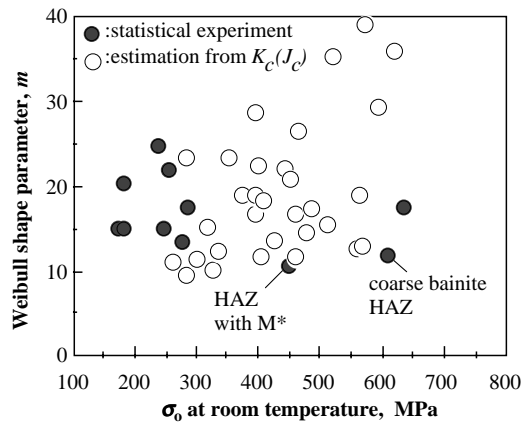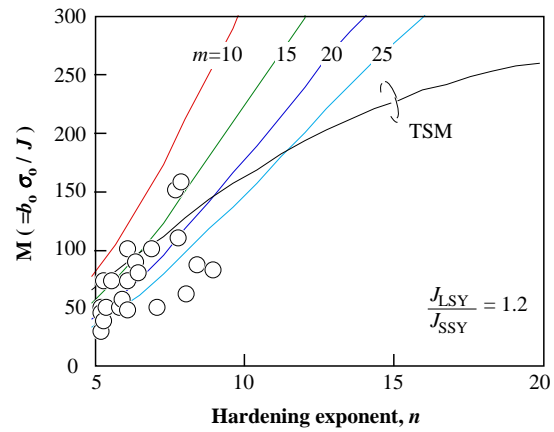
Fig.8 m values for low carbon steels.

Fig.9 Constraint factor, M for commercial steels.

to 40. The lower toughness material generally has a lower value of m. The values of the strain hardening exponent, n were simultaneously investigated. Based on these values of m and n, corresponding constraint factor, M that gives the ratio of J_{LSY} to J_{SSY} of 1.2 can be obtained from Eq. (8) as is shown in Fig.9. The results shown in Fig.9 indicate that the constraint factor, M in Eq. (1) for the most of the practical steels are in the range of 50 to 100 except for low toughness materials and the revision of the ASTM E1820 in 1999 is reasonable.

CONCLUSIONS

The Weibull stress criterion was applied to the toughness scaling model proposed by Anderson and Dodds [1]. The proposed new model suggests that the size requirements for specimen to obtain the sufficient constraint in toughness testing are strongly depending on the value of the Weibull shape parameter, m and the strain hardening exponent, n of the materials. This analytical prediction was confirmed by the FE analysis coupled with the Weibull stress criterion. Three dimensional FE analysis simultaneously indicates that the thickness effect in toughness is mainly caused by the statistical volume effect especially for the materials with the high value of m. The values of the shape parameter, m were estimated from the transition curve of the cleavage fracture toughness. The constraint factor, M to obtain the J_{SSY} is presumed as in the range of 50 to 100 for the most of commercial steels and it is consistent with the revision in the ASTM E 1820.

REFERENCES

[1]Anderson, T. L. and R. H. Jr. Dodds, (1991) J. Testing and Evaluation, 19, 123-134.

[2] O'Dowd, N. P. and C. F. Shih, (1992) J. Mechanics and Physics of Solids, 39, 898-1015.

[3]Dodds, R. H. Jr., T. L. Anderson and M. T. Kirk , (1991) Int. J. Fracture, 48, 1-22.

[4] Nevalainen, M. and R. H. Jr. Dodds, (1995) Int. J. Fracture, 74, 131-161.

[5] Beremin, F.M., (1983) Metallurgical Trans. A14, 2277.

[6] Mudry, F., (1986) Nuclear Eng. and Design 105, 65.

[7] Miyata, T. , T. Tagawa and Y. Hongkai, (2000) J. Testing and Evaluation, 28, 62-65.

[8] Koppenhoefer, K., A. Gullerud, C. Ruggieri, R. H. Jr. Dodds and B. Healy, (1997) WARP 3D 9.8 Dynamic Nonlinear Analysis of Solids Using a Preconjugate Gradient Software Archtecture, Structural Research Series 907, University of Illinois at Urbana-Champaign.

[9] Miyata, T., Tagawa, T. and Aihara, S., (1995) Tetsu to Hagane(J. the Iron and Steel Institute of Japan) 81, 583.

QUASI-MICROMECHANICAL MODELING OF EVOLUTIONARY DAMAGE IN QUASI-BRITTLE SOLIDS

Xi-Qiao Feng and Shou-Wen Yu

Department of Engineering Mechanics, Tsinghua University, Beijing 100084, China

ABSTRACT

Presented in this paper is a quasi-micromechanical model for simulating the constitutive response of microcrack-weakened materials subjected to complex loading. A novel effective medium scheme is first suggested to calculate the microcrack interaction effects on the effective elastic moduli in a convenient manner. The microcracking damage is characterized in terms of the orientation domain of microcrack growth (DMG) as well as a scalar microcrack density parameter. The DMG describes the complex damage and its evolution associated with microcrack growth, while the scalar microcrack density factor yields an easy estimation of the effects of microcrack interaction. Considering various micromechanisms of microcracking damage, the overall effective constitutive relation in different deformation stages including linear elasticity, pre-peak nonlinear hardening, stress drop and strain softening are expressed in a unified form.

KEY WORDS

Constitutive relation, quasi-micromechanical model, damage evolution, brittle material, microcracking, microcrack interaction

INTRODUCTION

In spite of significant development of damage mechanics during the past decades, some fundamental and important issues in this field have not yet been resolved. The description of evolutionary damage, the calculation of microcrack interaction, and the formulation of the effective constitutive relation of microcracked materials, among others, are still widely argued in the literature [1]. To establish a relatively comprehensive and applicable constitutive relation model, a promising approach is to combine the methods and strategies of both phenomenological and micromechanical damage mechanics. To this end, two alternatives seem worth considering. The first is to construct a model within the framework of continuum damage mechanics, while the definition of damage variable, the formulation of evolution law as well as the determination of key parameters are specified on the basis of micromechanical analysis. Such a damage model may be referred to as a micromechanics-based phenomenological model, or a quasi-phenomenological model [2]. The second is to build the basic framework of the model directly from micromechanical analysis, while some concepts and skills of continuum damage mechanics are incorporated to lead to a simple but more exact model with solid physical background. We refer to such a model as quasi-micromechanical. An attempt is made here to establish a quasi-micromechanical damage theory for calculating the overall constitutive relation of brittle materials with interacting and evolutionary microcracks.
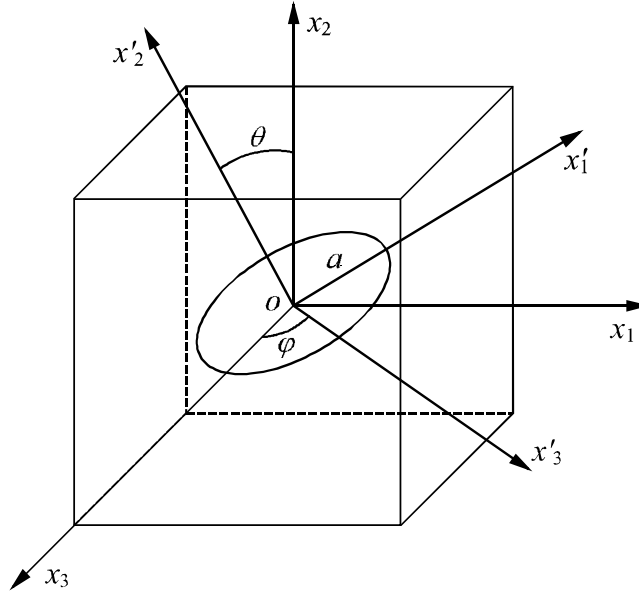
Figure 1: Global and local coordinate systems

ANALYSIS OF DAMAGE EVOLUTION

Domain of microcrack growth

Consider a quasi-brittle material weakened by randomly distributed microcracks of penny shape. Assume that the number density of microcracks is n_c, and that in the initial state all microcracks have the same statistically-averaged radius a_0. Choose a representative volume element (RVE), whose boundary is subjected to tractions in equilibrium with a uniform overall stress σ. First, consider a single microcrack, say the α-th, in it. Refer to a global Cartesian coordinate system $(o - x_1 x_2 x_3)$ and a local Cartesian coordinate system $(o - x_1' x_2' x_3')$, as shown in Fig. 1, in which the x_2'-axis is parallel to the normal **n** of the microcrack, and the x_3'-axis is coplanar with x_1 and x_3. Then the orientation of the microcrack is expressible in terms of the angles (θ, φ).

Adopt the mixed-mode fracture criterion for a penny-shaped microcrack in an isotropic medium as

$$\left(\frac{K_I'}{K_{IC}} \right)^2 + \left(\frac{K_{II}'}{K_{IIC}} \right)^2 = 1 , \tag{1}$$

where K_I' and K_{II}' represent the mode-I and II stress intensity factors (SIFs), K_{IC} and K_{IIC} their intrinsic critical values, respectively. K_I' and K_{II}' are defined by

$$K_I' = 2\sigma_{22}' \sqrt{\frac{a}{\pi}}, \qquad K_{II}' = \frac{4}{2 - \pi} \sqrt{\frac{a}{\pi} \left[(\sigma_{21}')^2 + (\sigma_{23}')^2 \right]} , \tag{2}$$

where $\sigma_{ij}' = g_{ik}' g_{jl}' \sigma_{kl}$ is the stress tensor in the local coordinate system, g_{ij}' is the transformation matrix between the two systems [3].

Once a microcrack satisfies the criterion (1), it will propagate in a stable fashion, increasing the radius from the initial value a_0 to a characteristic value a_u and being arrested by energy barriers (such as grain boundaries of different directions) with higher strength. The same assumption of high energy barriers that serve as a crack trapping mechanism was adopted by Krajcinovic [1], Ju and Lee [4] and some others.

Under loading, more and more microcracks may meet the criterion in (1) and then propagate. Thus, the microcracking damage state can be characterized in terms of the *orientation domain of microcrack growth* (DMG) [3], which is defined as the possible orientation scope in the orientation space (θ, φ) of all microcracks that have propagated in the aforementioned fashion. In other words, all microcracks whose orientations are within the orientation scope of DMG must have propagated and have the radius a_{u}. The concept of DMG is defined on the basis of solid physical consideration and has clear geometrical meaning in the orientation space. A DMG can also be considered as a set of all microcracks that have propagated.

The description of damage evolution in a brittle material under complex loading is generally a hard task for micromechanical damage models. Employing the concept of DMG, however, we can analyze easily the damage evolution using the calculation rules in set theory. As the applied stresses vary with time t, the evolution equation of DMG, $\Omega(t)$, is expressed by the summation of sets as [3]

$$\Omega(t + \Delta t) = \Omega(t) \bigcup \Omega(\sigma_{ij}(t + \Delta t)), \tag{3}$$

where $\Omega(\sigma_{ij})$ denotes the DMG corresponding to the stress tensor σ_{ij} under the condition of monotonically proportional loading. The detailed formulas for calculating $\Omega(\sigma_{ij})$ were given in [3].

Secondary growth of microcracks
With further increase in applied stresses, some microcracks normal or nearly normal to the maximum principal tensile stress may pass through the high-energy barriers and experience secondary growth. Similar to (1), the criterion of secondary growth of a circular microcrack may take the following form [5]

$$\left(\frac{K_{\mathrm{I}}'}{K_{\mathrm{ICC}}}\right)^2 + \left(\frac{K_{\mathrm{II}}'}{K_{\mathrm{IICC}}}\right)^2 = 1, \tag{4}$$

where K_{ICC} and K_{IICC} are respectively the critical values of mode I and II SIFs of energy barriers, often taken as the values of fracture toughness of the pristine matrix. When some microcracks have experienced secondary growth, the damage and deformation will be localized in the material causing the rapid stress drop and strain softening phenomena in the stress-strain curve [5].

AN ESTIMATION METHOD FOR EFFECTIVE MODULI

For an RVE as shown in Fig. 2(a), the overall average strain $\bar{\varepsilon}$ can be decomposed as

$$\bar{\boldsymbol{\varepsilon}} = \bar{\boldsymbol{\varepsilon}}^{\mathrm{m}} + \bar{\boldsymbol{\varepsilon}}^{\mathrm{c}}, \tag{5}$$

where $\bar{\boldsymbol{\varepsilon}}^{\mathrm{m}} = \mathbf{S}^{\mathrm{m}} : \boldsymbol{\sigma}$ denotes the matrix strain tensor averaged over the RVE, $\bar{\boldsymbol{\varepsilon}}^{\mathrm{c}}$ the microcrack-induced variation in the overall average strain, and $\mathbf{S}^{\mathrm{m}}$ the compliance of the matrix.

Assuming that all microcracks are planar, the variation of the volume-averaged strain can be calculated by

$$\bar{\boldsymbol{\varepsilon}}^{\mathrm{c}} = \frac{1}{2V} \sum_{\alpha=1}^{N} S^{(\alpha)} (\bar{\mathbf{b}}\mathbf{n} + \mathbf{n}\bar{\mathbf{b}})^{(\alpha)}, \tag{6}$$

where $N = n_{\mathrm{c}}V$ is the total number of microcracks in the RVE, the superscript (α) stands for a quantity of the α-th microcrack, $S^{(\alpha)}$, $\bar{\mathbf{b}}^{(\alpha)}$ and $\mathbf{n}^{(\alpha)}$ denote the surface area, the average opening displacement discontinuity vector and the unit vector normal to the crack faces, respectively.

Thus, the key problem becomes how to calculate the opening displacement of a microcrack embedded in a solid containing many disordered microcracks. For such a problem, some simplifications or approximations

are necessary [6]. On one hand, the medium surrounding a microcrack is weakened by the numerous microcracks, and then has a stiffness lower than the pristine matrix. On the other hand, the stress field to which the microcrack is exposed is perturbed due to the existence of other microcracks. As a straightforward approximate model, the microcrack is assumed to be surrounded by an effective medium, referred to also as the comparison or reference matrix, with compliance $\mathbf{S}^0$ and subjected to an effective stress $\boldsymbol{\sigma}^0$ in the far field, as shown in Fig. 2(b). This approximation is common to almost all the effective medium methods and the effective field methods, e.g. the DCM, SCM, DM and GSCM, although the definitions of $\mathbf{S}^0$ and $\boldsymbol{\sigma}^0$ in them are different [6].
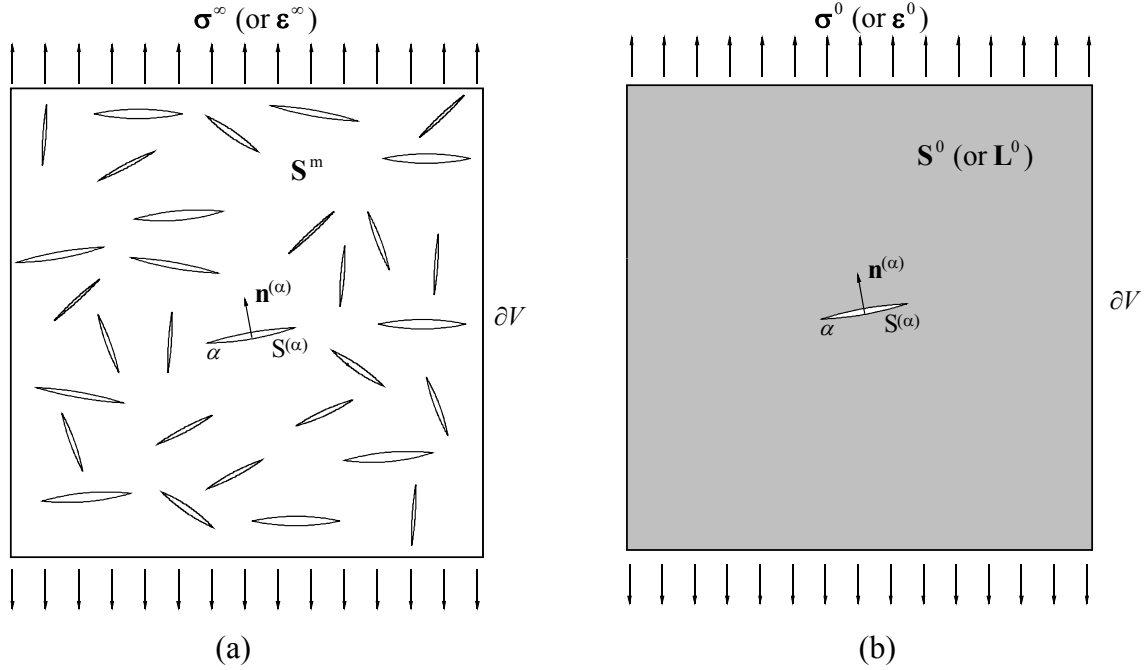
Figure 2: (a) RVE, and (b) approximate model for calculating microcrack opening displacements

In the approximate model in Fig. 2(b), the average opening displacement vector of a microcrack can be expressed as

$$\overline{\mathbf{b}} = \mathbf{B}(\mathbf{S}^0, G, \boldsymbol{\sigma}^0) \cdot \boldsymbol{\sigma}^0 \cdot \mathbf{n} , \tag{7}$$

where the second-rank symmetric tensor $\mathbf{B}$ is called the crack opening displacement tensor, and G signifies the geometry of the microcrack. Define a fourth-order tensor $\mathbf{H}$ by

$$\boldsymbol{\sigma}^0 = \mathbf{H} : \boldsymbol{\sigma} , \tag{8}$$

which relates the effective stress $\boldsymbol{\sigma}^0$ to $\boldsymbol{\sigma}$. Assume that the tensor $\mathbf{H}$ is same for all microcracks, as is consistent with the inherent assumptions of the effective medium methods.

Thus, the effective compliance increment due to the α-th single microcrack is obtained from (6)–(8) as

$$\overline{S}_{ijkl}^{c(\alpha)} = \frac{S^{(\alpha)}}{4V} H_{stkl} \left(n_i B_{js} n_t + n_j B_{is} n_t + n_i B_{jt} n_s + n_j B_{it} n_s \right)^{(\alpha)} . \tag{9}$$

Then, the overall compliance tensor $\mathbf{S}$, defined by $\overline{\boldsymbol{\varepsilon}} = \mathbf{S} : \boldsymbol{\sigma}$, is arrived at

$$S_{ijkl} = S_{ijkl}^m + \frac{1}{4V} H_{stkl} \sum_{\alpha=1}^{N} S^{(\alpha)} \left(n_i B_{js} n_t + n_j B_{is} n_t + n_i B_{jt} n_s + n_j B_{it} n_s \right)^{(\alpha)} . \tag{10}$$

Almost all the estimation techniques available in the literature, based on an effective medium or effective field, can be formulated in the form of (10), and, in other words, have a complete formal similarity. Apart from their heuristic foundations, the conventional methods for estimating the effective moduli are each developed from several possible choices of $\mathbf{S}^0$ and $\boldsymbol{\sigma}^0$, which are by no means better than others.

To define a simple and applicable estimation scheme, we specify here

$$\boldsymbol{\sigma}^0 = \boldsymbol{\sigma}, \ \mathbf{S}^0 = (1 - \xi f^\eta)^{-1} \mathbf{S}^m, \tag{11}$$

where ξ and η are two adjustable parameters, which can be determined by fitting experimental results or other theoretical results of good accuracy. By comparing the present method with the GSCM for the two extreme cases of isotropy and complete anisotropy, we suggest that $\xi = 4/9$ and $\eta = 1.0$.

Provided that the pristine matrix is isotropic, the suggested method calculates the opening displacement of a microcrack by assuming that it is embedded in an isotropic, infinite effective medium, analogously to Taylor's model. Their difference is that the effective medium in the presented method is, instead of the pristine matrix, an approximate reference medium with degraded effective elastic moduli depending upon the actual damage. The suggested scheme combines the advantages of both the DCM and first-order effective medium methods.

QUASI-MICROMECHANICAL DAMAGE MODEL

Description of damage
The problem of evolutionary damage in a brittle material subjected to complex loading is too complicated to be solved with such methods as SCM and DM. For this reason, little work has been done in the filed of micromechanics to consider the overall constitutive relation of brittle materials under complex loading. A promising approach to achieve this aim is to combine phenomenological and micromechanical damage mechanics. Such an attempt is made here to present a quasi-micromechanical damage model. Beside the concept of DMG, the scalar microcrack density parameter f [7] is adopted to describe the damage in a microcracked solid. The DMG describes exactly the anisotropic microcracking damage state, while f, which defines merely the magnitude of the isotropic part of the damage, is introduced to render the calculation of effective moduli much easier. In this way, the new estimation scheme proposed above can be implemented into the micromechanics-based DMG damage model. The parameter $f(t)$ is related to the DMG $\Omega(t)$ by

$$f(t) = n_c[\bar{a}(t)]^3 = n_c a_0^3 + n_c \iint\limits_{\Omega(t)} p(a,\theta,\varphi)(a_u^3 - a_0^3)\sin\theta \, \mathrm{d}\theta \mathrm{d}\varphi , \tag{12}$$

where $p(a,\theta,\varphi)$ denotes the probability density function describing the distribution of the orientations and sizes of microcracks in the material.

Then, the effective compliance tensor of the damaged solid can be estimated by embedding each microcrack into an effective medium with compliance $\mathbf{S}^0$ defined in (11) and subjected to the far-field stress $\boldsymbol{\sigma}$. In this case, the nonzero components of the crack opening displacement discontinuity vector $\mathbf{B}$ are

$$B'_{11} = B'_{33} = \frac{16(1-v^2)}{\pi E(2-v)(1-4f/9)}, \qquad B'_{22} = \frac{8(1-v^2)}{\pi E(1-4f/9)} . \tag{13}$$

Thus, the compliance tensor in (9) induced by the elastic deformation of a single microcrack is rewritten as

$$\bar{S}_{ijkl}^{c(\alpha)}(a) = \frac{\pi a^3}{6} B'_{mn}(g'_{2i}g'_{mj} + g'_{2j}g'_{mi})(g'_{2k}g'_{nl} + g'_{2l}g'_{nk}) . \tag{14}$$

Constitutive relation
In this paper, only open microcracks are considered. The overall effective constitutive relations for all the four

stages including linear elasticity, pre-peak nonlinear hardening, stress drop and strain softening [5,8] can be expressed in the following unified form:

$$\varepsilon_{ij} = \left[S_{ijkl}^{0} + S_{ijkl}^{c1} + S_{ijkl}^{c2} + S_{ijkl}^{c3} \right] \sigma_{kl} + \varepsilon_{ij}^{R} \tag{15}$$

where S_{ijkl}^{c1}, S_{ijkl}^{c2}, S_{ijkl}^{c3} denote the increment of the compliance tensor due to microcracks that have not propagated ($a = a_0$), that have experienced the first growth ($a = a_u$) and that have undergone the secondary growth ($a > a_u$), respectively, ε_{ij}^{R} denotes the strains due to the residual deformation of microcracks,

$$S_{ijkl}^{c1} = \int_0^{2\pi} \int_0^{\pi/2} n_c p(a,\theta,\varphi) \overline{S}_{ijkl}^{c}(a_0) \sin\theta \mathrm{d}\theta \mathrm{d}\varphi - \iint_\Omega n_c p(a,\theta,\varphi) \overline{S}_{ijkl}^{c}(a_0) \sin\theta \mathrm{d}\theta \mathrm{d}\varphi \tag{16}$$

$$S_{ijkl}^{c2} = \iint_\Omega n_c p(a,\theta,\varphi) \overline{S}_{ijkl}^{c}(a_u) \sin\theta \mathrm{d}\theta \mathrm{d}\varphi - \int_0^{2\pi} \int_0^{\theta_{cc}} n_c p(a,\theta,\varphi) \overline{S}_{ijkl}^{c}(a_u) \sin\theta \mathrm{d}\theta \mathrm{d}\varphi \tag{17}$$

$$S_{ijkl}^{c3} = \int_0^{2\pi} \int_0^{\theta_{cc}} n_c p(a,\theta,\varphi) \overline{S}_{ijkl}^{c}(a_s) \sin\theta \mathrm{d}\theta \mathrm{d}\varphi \tag{18}$$

$$\varepsilon_{ij}^{R} = \iint_\Omega n_c p(a,\theta,\varphi) \overline{\varepsilon}_{ij}^{R}(a_u) \sin\theta \mathrm{d}\theta \mathrm{d}\varphi + \int_0^{2\pi} \int_0^{\theta_{cc}} n_c p(a,\theta,\varphi) \left[\overline{\varepsilon}_{ij}^{R}(a_s) - \overline{\varepsilon}_{ij}^{R}(a_u) \right] \sin\theta \mathrm{d}\theta \mathrm{d}\varphi \tag{19}$$

where θ_{cc} is an angle parameter related to the number of microcracks that have experienced secondary growth [5], $\overline{\varepsilon}_{ij}^{R}(a)$ the residual strains induced by a microcrack of radius a [8], and a_s the radius of a microcrack during the secondary growth.

CONCLUSIONS

The quasi-micromechanical damage model developed here has the following main features. First, the microcracking damage is characterized in terms of both the DMG and the scalar microcrack density, which function as an exact representation of anisotropic damage and a key parameter in the proposed scheme for calculating the impacts of microcrack interaction, respectively. Second, the damage evolution under complex loading can easily be analyzed with the aid of set theory. Third, the constitutive relation formulated can be applied to the whole deformation process of quasi-brittle materials, including the stages of linear elasticity, nonlinear damage hardening, post-peak stress drop and strain softening. Fourth, the effects of microcrack interaction on effective moduli can be calculated as easily as the DCM. The present attention is focused on material behavior under tension, though the main idea can be extended to the case of compression.

ACKNOWLEDGEMENT

REFERENCES

1. Krajcinovic, D. (1997) *Damage Mechanics*, Elsevier, Amsterdam.
2. Krajcinovic, D., Basista, M. and Sumarac, D. (1991) *J. Appl. Mech.* 58, 305.
3. Yu, S.W. and Feng, X.Q. (1995) *Mech. Mater.* 20, 59.
4. Ju, J.W. and Lee, X. (1991) *J. Eng. Mech*, 117, 1495.
5. Feng, X.Q. and Yu, S.W. (1995) *Int. J. Solids Struct.* 32, 3359.
6. Feng, X.Q. (2000) *Key Eng. Mater.* 183–187, 667.
7. Bristow, J.R. (1960) *British J. Appl. Phys.* 11, 81.
8. Feng, X.Q. and Gross, D. (2000) *Int. J. Damage Mech.* 9, 79.

QUENCH CRACKING RESISTANCE OF
POWDER METALLURGY SUPERALLOYS

K.-M. Chang

Department of Mechanical and Aerospace Engineering, West Virginia University
P.O. Box 6106, Morgantown, WV 26506 USA

ABSTRACT

Quench cracking behavior of a high strength superalloy, Rene'95, has been investigated by a new approach based on fracture mechanics. A novel laboratory test was set up to identify the criterion for the occurrence of quench cracking. Pre-cracked specimens were loaded by thermal stress induced through the decrease of specimen temperature. When the specimen failed at a certain temperature, on-cooling fracture toughness was measured. Quench cracking toughness, K_Q, was found to be an order of magnitude lower than the room temperature fracture toughness. This brittle fracture at elevated temperature was found to be associated with the intergranular failure of quench cracking. Grain size played a secondary role on quench cracking toughness, and a fine grain structure offered a better resistance to quench cracking than a coarse grain structure.

KEYWORDS

P/M superalloy; quench cracking; intergranular failure; brittle-ductile transition; thermal stress; fracture mechanics; grain size; precipitate solvus.

INTRODUCTION

One of the major challenges in processing large components made of powder metallurgy (P/M) superalloys is to achieve the maximum cooling rate after the solution annealing through various quenching techniques [1-4]. Rapid cooling through the aging temperature range can retain the supersaturation of precipitation hardening elements without forming extensive cooling precipitates. Subsequent aging treatments would then develop a high density of homogeneous precipitates in the alloy matrix and attain a high strength. However, the aggressive cooling from an elevated temperature may result in problems such as severe distortions and excessive residual stresses in components with thick sections. In some cases, unexpected quench cracks may occur during quench process [5].

A fine grain structure of P/M superalloys provides advantages of high strength and low cycle fatigue (LCF) life at low temperatures, but suffers drawbacks of creep strength and fatigue crack propagation (FCP) at elevated temperatures. As the operation temperature of turbine engines increases, a moderate grain size is preferred. New generation P/M superalloys, which received solution anneal at temperatures above the solvus temperature of γ', were developed in early 1990's [6-8]. Quench process becomes essential to attain the desirable properties in new P/M superalloys. Alloy strength would be lower with annealing above γ'

solvus than that with annealing below γ′ solvus. A fast cooling rate from solution anneal is necessary for these P/M superalloys with a moderate grain structure.

In this work, the intrinsic alloy resistance to quench cracking has been investigated in a P/M superalloy, Rene'95, which is known as the strongest superalloy commercially available. Both coarse-grain and fine-grain structures were evaluated by a novel experimental setup that simulated the severest condition of quench process [9]. Quench cracking resistance for P/M superalloys was realized as one of fracture properties that resist high-temperature intergranular failure.

MATERIALS AND EXPERIMENTALS

Rene′95 is one of the earliest P/M superalloys being used commercially [10]. Its tensile strength at 650 °C can reach above 1,500 MPa, which is higher than that of any other superalloy. The nominal composition of P/M Rene′95 is Ni-13Cr-8Co-3.5Mo-3.5W-3.5Al-2.5Ti-3.5NB-.05Zr-.01B-.06C in weight percent. The alloy can develop about 50% volume fraction of γ′ precipitates through appropriate age treatments. The solvus temperature of γ′ precipitate is around 1155 °C.

Argon atomization and extrusion compaction of a 20 kg heat were carried out according to the standard procedures for commercial Rene′95 practice [11]. The measured mechanical properties of this laboratory heat met the specification of Rene 95 forging.

Thin sheet single-edge-notched (SEN) specimens were loaded on an Instron hydraulic close-loop machine; the gage section (25.4 mm) was heated by an induction heater. A thermal couple was spot-welded at the center of the specimen to monitor the specimen temperature. The cross section of the gage was 3.175 mm by 1.27 mm. The low thermal mass of this laboratory setup allows rapid heating as well as fast cooling of the gage section. The initial cooling rate from the solution temperature was estimated to be about 100 °C/s. Thermal stress was induced by fixing the displacement of gage length during cooling.

The catastrophical fracture usually occurred within 5 seconds after the quenching started if the quench cracking occurs. Fractography of quench cracks was examined under a scanning electron microscope (SEM) to determine the fracture mode. Metallographic samples were prepared using conventional mechanical grinding and polishing procedures according to the standard laboratory process. An etching solution consisting of 10 ml HCl, 10 ml HNO_3 , and 30 ml H_2O_2 was used to reveal grain structure.

RESULTS AND DISCUSSION

Occurrence of Quench Cracking
A metallographic sample of 12 mm × 12 mm × 12 mm cube was cut from P/M rene"95 forging and solution annealed at 1175 °C. After one hour of heat treatment, the sample was taken from the furnace and water quenched. Many quench cracks formed on the surface, and metallography in Figure 1 shows the intergranular nature of these cracks. The cracks initiated from the edge of the sample and propagated on the surface layer only. In many cases the crack branched as seen in Figure 1. The crack path was always along grain boundaries indicating the intergranular failure.

Examing the fracture surface of a typical SEN specimen showed two distinctive fracture modes: the intergranular fracture for quench crack and the transgranular fatigue failure for pre-crack. A clear beach mark is available for the measurement of pre-crack length, a. The intergranular fracture extends from the beach mark to the other end of the specimen. The observation of intergranular fracture mode confirms that the K_Q value measured by the designed test reflects alloy resistance to quench cracking.

The load curve attained from the thermal stress during cooling shows an abrupt failure without any sign of yielding. This catastrophic nature resembles the shop experience of quench cracking when processing P/M superalloy components. Quench cracks appear in a burst way when the cooling is too aggressive.
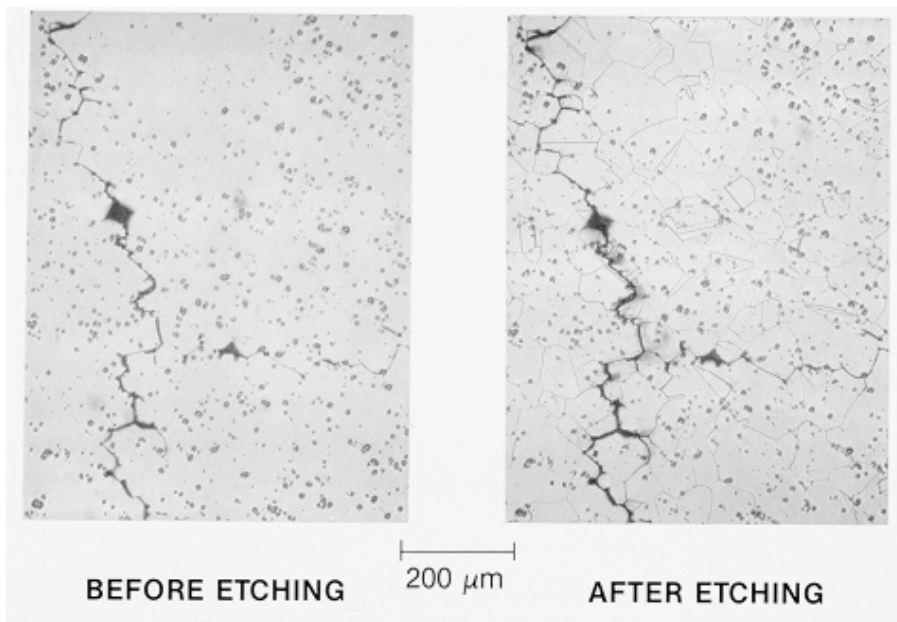
Figure 1
Metallography of quench cracked specimen revealing the nature of intergranular failure.

TABLE 1 lists all tests performed on the SEN specimens. Two solution annealing temperatures were selected in this study: 1175°C for supersolvus annealing, resulted in a coarse grain structure; and 1100°C for subsolvus annealing, resulted in a fine grain structure.

TABLE 1   Quench cracking resistance of powder metallurgy Rene'95 superalloy

Sample ID	Width mm	Thicknes mm	Precrack mm	Start Temp. °C	Fail Temp. °C	Max Load, N	K_Q, MPa√m
Coarse Grain Rene'95 – 1175 °C Annealed							
EX2A2	3.089	1.245	0.775	1180	1040	373.7	7.18
EX2A3	3.134	1.257	0.800	1181	1023	407.0	7.82
EX2A5	3.162	1.308	0.749	1178	1043	420.4	7.19
EX2A6	3.145	1.237	0.749	1123	924	611.2	11.14
EX2A9	3.147	1.267	0.610	1173	1000	560.5	8.32
EX2A10	3.142	1.265	0.267	1171	894	1063.1	9.13
EX2A11	3.165	1.283	1.537	1172	1095	177.9	8.22
EX2A12	3.145	1.295	0.762	1175	900	860.7	15.22
Fine Grain Rene'95 – 1100 °C Annealed							
EX2B1	3.228	1.273	1.461	1124	936	441.3	17.76
EX2B4	3.216	1.275	1.143	1121	N/A	524.9	14.43
EX2B6	3.226	1.273	1.524	1125	N/A	536.0	23.42

N/A: not available because of the failure of thermal couples.

Quench Cracking in Coarse Grains
Solution anneal at 1175°C, a temperature above γ', dissolves all γ' precipitates in P/M Rene'95. There are MC type carbides randomly dispersed in the matrix, and a coarse grain size of ASTM 7 is observed. Though the forging conditions may affect somewhat the final grain size, P/M superalloys after supersolvus

anneal (above γ′ solvus) usually develop grain size of ASTM 6 to 8. The grain size, which is significantly smaller than that of their C&W versions, does not keep increasing with annealing temperature and time.

In total, eight SEN specimens of coarse grain P/M Rene 95 were tested (Table 1). Specimens were heated up to 1175 °C and then cooled under constrain of constant displacement. The maximum thermal stress was reached at the temperature where the catastrophic fracture occurred in each specimen. Figure 2 shows a typical SEM fractography of a broken specimen. A complete intergranular failure occurs during quench cracking; grain boundaries on the fracture surface show very little features except for some carbide particles. No indication of any plastic deformation on the fracture process suggests a brittle nature of cracking.

The failure load was converted to quench cracking toughness, K_Q, for every specimen after the crack length was measured. The measured K_Q values were remarkably low, reflecting the fact of brittle intergranular failure. Typical fracture toughness for P/M Rene 95 is about 70 – 80 MPa√m at room temperature.

The dependence of quench cracking fracture on the fracture temperature seems relatively weak, though there is a tendency that the K_Q value increases slightly with the decrease of failure temperature. The thermal stress was primarily determined by the difference of the starting and failure temperatures. To reach a similar K_Q value, the specimen with a short pre-crack length required a high thermal stress. Consequently it would fail at a low temperature, at where the temperature difference is large enough to induce thermal stress required for fracture.
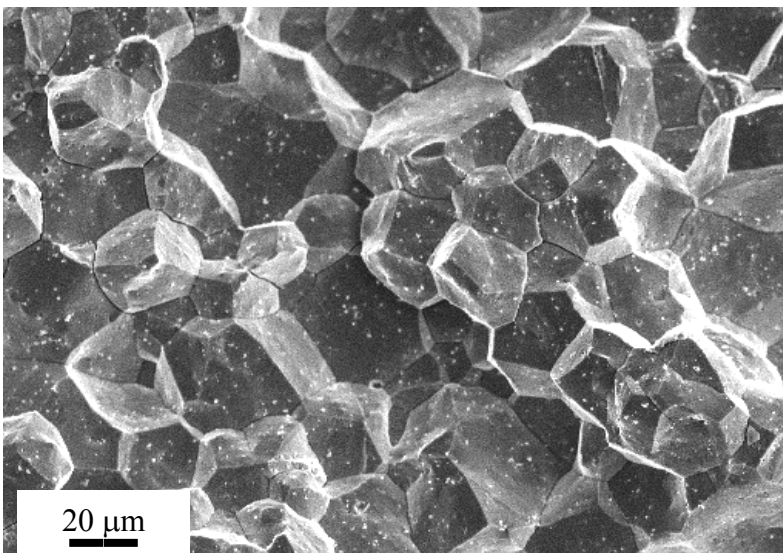
Figure 2
Scanning electron microscopy of intergranular quenching fracture in coarse grain P/M Rene'95.

Quench Cracking in Fine Grains

In the commercial applications, P/M Rene'95 usually receives a solution anneal at some temperature below the γ′ solvus. Such a sub-solvus annealing results in a fine grain structure of ASTM 12, which is the typical grain size for most of commercial P/M superalloys. Extensive primary γ′ particles with a diameter in micron level are observed. These γ′ precipitates formed during the forging process and pin the grain boundaries from coarsening. Such a dual-phase structure exhibits an excellent tensile ductility at high temperatures and is ready for superplastic deformation under the appropriate strain rate [11]. Super-plastic forming through isothermal forging has been employed as a commercial practice to P/M superalloy components. It is of great interest to measure quench cracking toughness of fine grain P/M superalloys.

SEN specimens were prepared from subsolvus annealed P/M Rene 95. After pre-cracking at room temperature, specimens were heated to 1125 °C for quench cracking toughness test. Because of low creep resistance of a fine grain structure at high temperature, there was some difficulty encountered in the setup. Several specimens failed by creep rather than by thermal quench.

In all successful quench cracking tests, specimens failed in the same catastrophic manner as those of coarse grains. The load curve increased linearly until an abrupt drop occurred at some failure temperatures. The results are also listed in Table 1. Two specimens lost their thermocouple during cooling so that no failure temperature was reported. It was expected that the failure occurred at a low temperature for a short pre-crack, and vise versa.

Fracture surfaces of broken specimens were examined under SEM. Intergranular fracture mode occurs through the entire quench crack area as shown in Figure 3. Many micron size primary γ' particles are also observed. This fracture feature is not usually observed since a fine grain structure is always ready to be plastically deformed at elevated temperatures. Grain boundary cleavage indicates a minimum amount of deformation before the failure occurs.
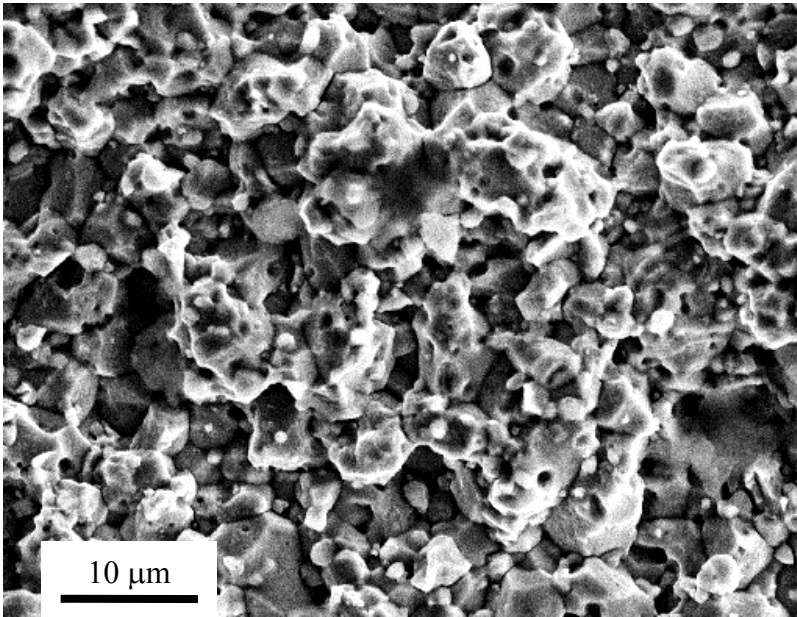
Figure 3
Scanning electron microscopy of intergranular quenching fracture in fine grain P/M Rene'95.

As seen in Table 1, fine grain P/M Rene 95 definitely exhibits a higher K_Q than that of coarse grains. However, these values are far below the room temperature fracture toughness. The brittle nature of intergranular fracture suggested that both fine grains and coarse grains of P/M Rene'95 had a low cohesive energy at elevated temperatures under thermal stress loading. The difference of K_Q values for different grain size is likely attributable to the topographic factor of the crack path. The intergranular cracking would change the direction of crack growth when the crack front encountered the intersection of grain boundaries. A fine grain structure deflected the cracking direction more frequently than the coarse grain structure. Those primary γ' particles on the grain boundaries might also have some beneficial effects.

CONCLUSIONS

A fracture mechanics approach adapted in this study offers a clear understanding on quench cracking behavior of P/M superalloys. Occurrence of quench cracking in the model alloy, P/M Rene'95, is directly related with the resistance to the intergranular fracture at elevated temperatures. Quench cracking, in both fine grain and coarse grain structures, occurs in an intergranular failure.

On-cooling fracture toughness test developed in this work provide a useful method to evaluate the quench cracking resistance. The measured quench cracking toughness, K_Q, in P/M Rene'95 indicated a brittle fracture mode at elevated temperatures, in consistence with the observation of intergranular failure on the fracture surface.

Grain size is not the key factor for the occurrence of brittle fracture at elevated temperatures. In comparison to the coarse grain structure, the final grain structure has a higher quench cracking resistance. However, the K_Q value measured at elevated temperatures is far less than the fracture toughness at low temperature.

ACKNOWLEDGMENTS

REFERENCES

1. R.I. Ramakrishnan and T.E. Houson (1992) *JOM*, Vol 44, No 6, p 29-32.
2. J.M. Franchet, F. Devy, P.E. Mosser, Y. Honnort and A. Benallal (1992) In: *Superalloys 1992*, p 73-82, S.D. Antolovich, et. al. (Eds), TMS-AIME.
3. D.R. Garwood, J.D. Lucas, R.A. Wallis and J.Ward (1992) *J. Mater. Eng. Perf.*, Vol 6, p 781-788.
4. R.A. Wallis and P.R. Bhowal (1988) In: *Superalloys 1988*, p 525-534, D.N. Duhl et. al. (Eds), TMS-AIME.
5. R.A. Wallis, N.M. Bhathena, P.R. Bhowal and E.L. Raymond (1988) *Industrial Heating,* Vol 30, January.
6. D.D. Krueger, R.D. Kissinger and R.G. Menzies (1992) In: *Superalloys 1992,* p 277-286, S.D. Antolovich et.al. (Eds), TMS-AIME.
7. K.-M. Chang, M.F. Henry, and M.G. Benz (1990) *JOM*, Vol 42, No 12, 1990, p 29-35.
8. K.-M. Chang (1989) *US Patent* No. 4,816,084,.
9. K.-M. Chang and Boqun Wu (1997) In: *1st International Conf. on Non-Ferrous Processing and Technology,* p 477-481, T. Bains and D. S. MacKenzie (Eds), ASM International.
10. D.R. Chang, D.D. Krueger and R.A. Sprague (1984) In: *Superalloys 1984*, p 245-273, M. Gell et. al. (Eds), TMS-AIME.
11. T.E. Howson, W.H. Couts, Jr. and J.E. Coyne (1984) In: *Superalloys 1984*, p 275-284, M. Gell et. al. (Eds), TMS-AIME.

RATE AND TEMPERATURE DEPENDENCE OF THE MECHANICAL PROPERTIES OF CHEDDAR CHEESE.

V. Imbeni[1], A.G. Atkins[2], J. Jeronimidis[2], J. Yeo[2]

[1]Lawrence Berkeley National Laboratory, University of California, Berkeley, USA
[2]Department of Engineering, University of Reading, Whiteknigths, Reading, UK

ABSTRACT

In this study, the mechanical properties of mature cheddar cheese (Young's modulus, E; yield strength, σ_y and "fracture toughness", R) were investigated at different rates and different temperatures. Most biological materials are viscoelastic and therefore their mechanical properties will depend on testing conditions. The ultimate aim is to incorporate the measured properties into a model for food cutting. The properties were obtained from uniaxial compression tests and three point bending tests over a range of strain rates and temperatures. Traditional fracture mechanics methods are not always applicable, given the viscoelasticity of cheese, but graphical methods are still appropriate. As expected, the resistance to cracking and yielding of cheddar cheese is both rate and temperature dependent.

KEYWORDS

Mechanical properties, toughness, cheese, viscoelasticity, cutting, rate-temperature dependence

INTRODUCTION

There is a crucial need to understand, model and explain the current 'rules-of-thumb' used for decision making in the food industry. Studies to date have related the mechanical properties of foods to sensory texture, ripening quality etc. but not to industrial processing operations. A thorough knowledge of the fracture behaviour of food materials is necessary to evaluate the relationship between their mechanical properties and industrial processing operations, such as cutting, slicing, flaking etc. 1. Cutting of brittle materials, polymers and biological materials has highlighted the need to consider crack resistance in addition to plastic shearing and friction. Reluctance to incorporate toughness in cutting models of ductile material arises, even now, because free-standing cracks running ahead of the tool are not seen. However it has been argued that the whole cut surface is, in fact, one side of a crack and that, during cutting, the crack moves precisely with the tool tip 8. In order to provide the basis for a more scientific approach to industrial cutting and food processing, data on mechanical properties will be collected. A model will then be constructed to predict the overall cutting force required under different conditions and identify the 'minimum' criteria (maximum rate of propagation with minimal applied force).

Characterisation of food materials is complex because of their heterogeneity and their viscoelastic nature: the mechanical properties are rate and temperature dependent. It is therefore clear that the properties collected for future modelling must be determined under conditions (such as strain rate, temperature) comparable with those found in commercial cutting machines.

Resistance to crack growth in a given material is defined by the fracture toughness, R, which is the amount of work required to propagate a crack by unit area.

The fracture toughness can be evaluated graphically from the area under a load-displacement diagram up to fracture. Most biological materials are viscoelastic i.e. highly extensible, non-linear and ductile, and plastic flow or other dissipative mechanisms might occur. In this case the strain (potential) energy change is not entirely absorbed by the fracture process and the total area under a load-displacement diagram will contain the combined contribution of flow and fracture work[1]. In this paper we are going to refer to **R** as the 'fracture toughness', however this value (area under the load-displacement curve divided by the area of fracture) may contain the sum of several energy dissipating mechanisms and is more correctly termed 'Work to Fracture'.

EXPERIMENTAL PROCEDURES

Mature cheddar cheese was chosen for the experiments, and it was always purchased from the same manufacturer and tested soon after to avoid ageing effects on the mechanical properties [2].

Different tests (uniaxial compression, three point bending) and different geometries were used. These tests were performed at equivalent strain rate rather than equal crosshead speeds: cylinders, beams and cracked beams have different strain rates at the same crosshead velocity. The specimens were loaded to failure at a given rate and temperature and the load-displacement diagram recorded. Mechanical properties obtained from different tests were therefore plotted as a function of strain rates and temperatures. Note that all tests were repeated: each point on the material properties graph represents an average of 4 results.

In a first set of tests the crosshead speeds and therefore the strain rates were varied; cheese was taken out of the fridge (-2°C) and then immediately tested.

As previously stated, tests should be performed at strain rates comparable to those currently used in industrial cutting. Such strain rates though cannot be obtained in the common testing machines. Cheese is a viscoelastic material and its behaviour is not expected to differ from some polymeric materials (i.e. PMMA): time-temperature superposition is believed to hold true for cheese also.

The second set of tests was therefore performed at decreasing temperatures ranging from -5 to –35 °C in a temperature controlled cabinet mounted on the Instron machine (fig.1). The temperature of the samples was also checked with a thermocouple during and after the tests.

Strain rates were also varied (~0.25, 1.00, 4.00 s^{-1}).

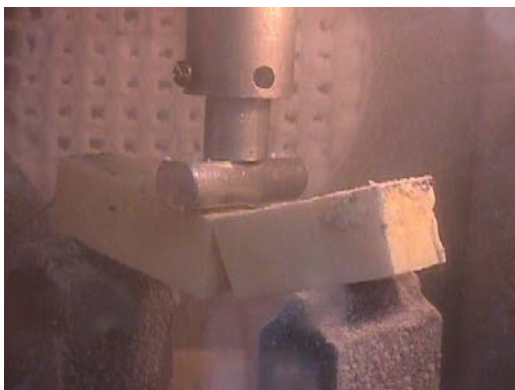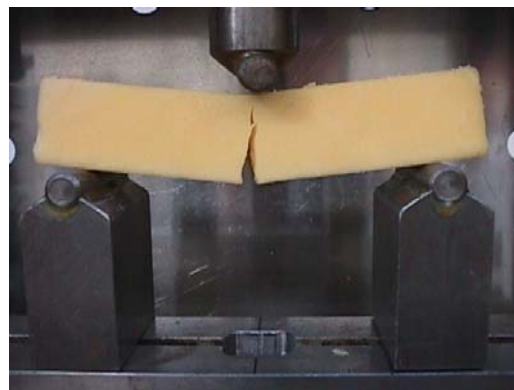**Figure 1: 3 point bending, low temperature test**

Figure 2: cheese beam loaded in 3 point bending

Compression tests (E, σ_y)
Uniaxial compression tests were performed on cylindrical samples (25x25mm): PTFE film was placed between the loading plates so that the deformation was homogeneous and no 'barrelling' due to friction occurred 345. The strain rate was given by crosshead velocity/H.

Three point bending tests (E, σ_y)
Un-notched cheese samples (25x25x130 mm) were loaded on an Instron testing machine with a 1000N load cell (fig xxx, loaded beam). The span, s is 100 mm.
The modulus for this geometry, according to beam theory, was given by E = load x span^3 / 48 x I x l$_y$ (deflection). The yield strength was given by σ_y = 6 load (from plot) x span /h. The strain rate is given by 6v (crosshead velocity) x h (width) / s^2.

Three point bending tests (R)
Single edge notched (by means of a razor blade, length of notch, a$_o$ was 8mm) cheese samples (25x25x130 mm) were loaded on an Instron testing machine with a 1000N load cell.
"Fracture toughness", R, was measured as the area under the force-displacement curve divided by the area of fracture (R= ηU/Bb$_o$, η=2 for beams, B is the thickness of the beam, b$_o$ is the difference between the height of the beam and the notch length). The strain rate was given by [ε_y(from compression)xcrosshead velocity]/l$_{crack}$(from plot).

RESULTS AND DISCUSSION

The mechanical properties of cheese vary with strain rate and with temperature.
Cheese also possesses directional properties (fig. 3). The long bars of rectangular section purchased for the testing are cut across the diameter of whole rounds of cheese. Pre-existing cracks run parallel to the round base of the cheese: this structure is due to the production process. Care was used so that specimens would always be tested in a given direction.

Figure 3: fractured surfaces showing directional properties

Constant T (2-3 ^{o}C), different strain rates (E, σ_y,R), compression and bending
E and σ_y increase with strain rate. Figure 4 shows R (fracture toughness or total work to fracture) plotted against strain rate. In three point bending on notched samples, although crack initiation was not always easily detected it was observed that it occurred in proximity of maximum load. R slightly increases with decreasing strain rates.
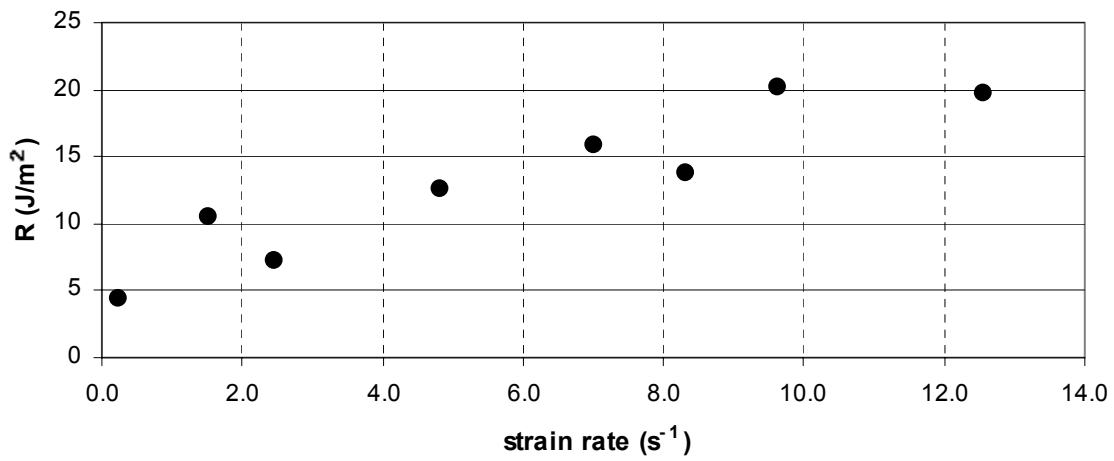
Figure 4: R (fracture toughness or total work to fracture) plotted against strain rate

Different T, different strain rates, compression (E, σ_y)

During the tests cracks at 45° (plane of maximum shear stress) appeared.

Both E and σ_y increase with increasing strain rate and decreasing temperature There seems to be a transition between $-15 \div 20°C$, confirmed by the change in shape of the load-displacement curves.
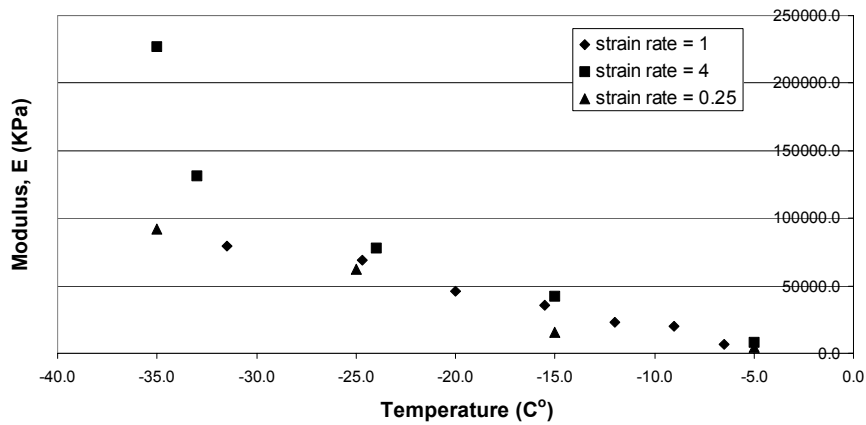

Figure 6: Mature cheddar cheese, Young's modulus (E), vs temperature (-5 to -35 oC) at different strain rates, compression test
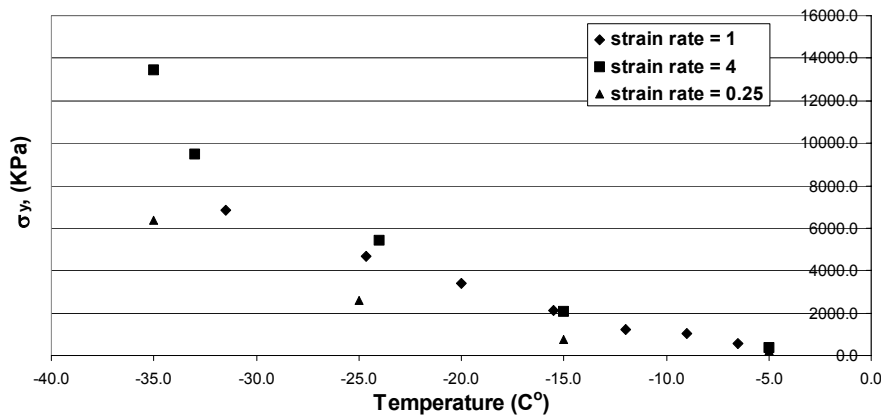
Figure 7: Mature cheddar cheese, yield strength, σy vs temperature (-5 to -35 oC) at different strain rates, compression test

Different T, different strain rates, bending (E, σ_y)
As in the compression test, both E and σ_y increase with increasing strain rate and decreasing temperature.

Different T, different strain rates, bending (R)
Figure 8 shows R against temperature at three different strain rates. Specimens tested at the two higher strain rates ($\sim$4, 1 s^{-1}) seem to display a similar behaviour, with two 'peaks' occurring between -10 and $-15°C$. A second, smaller peak seems to occur at around $-30°C$ (fig.10).
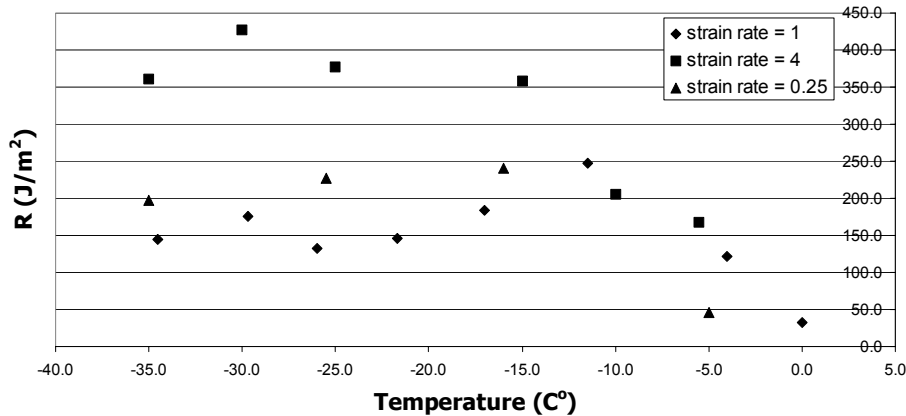
Figure 7: Mature cheddar cheese, work to fracture, R (J/m^2) vs temperature (-5 to -35 ^{o}C) at different strain rates, three point bending test (8 mm notch)

Compression and bending load-displacement curves at different temperature show the nature of deformation occurring in the material 1 (fig 9 showing different shapes of load-displacement curves at different T, similar to the one in 1). At -35 to $-30°C$ the area under the curve is small and the work to fracture is therefore low even though the peak load is high ('brittle' fracture). The area under a 'ductile' type curve (T=-10 to $-15°C$) is larger despite a lower failure load. It was observed that, after testing, the two halves of the specimen fitted together perfectly: the 'non linearity' was probably not due to permanent deformation but to viscoelasticity 2.
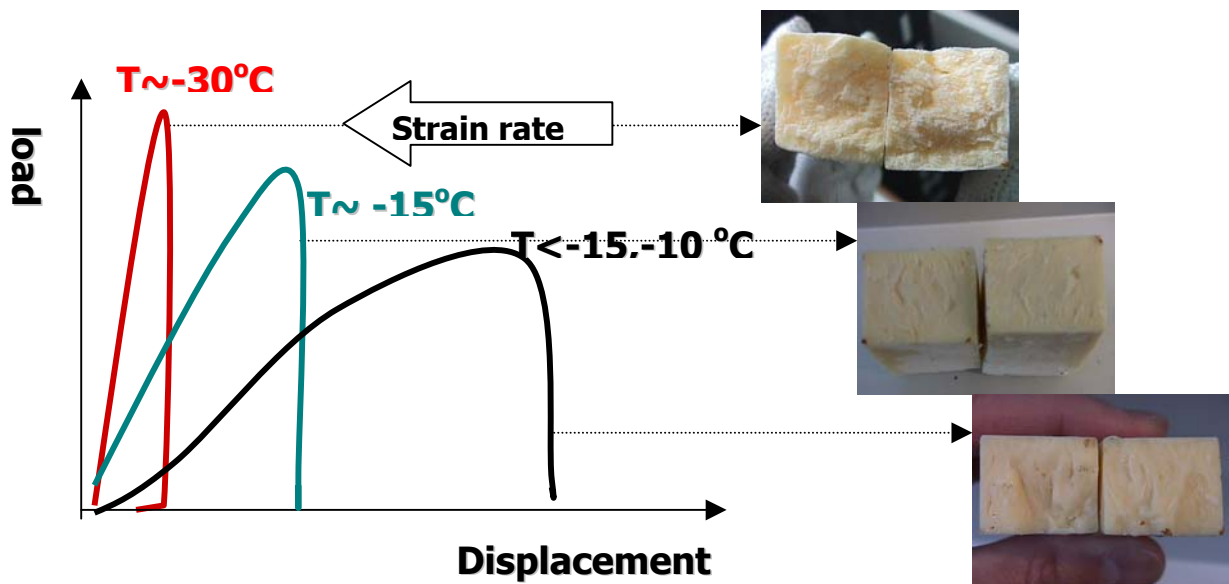

Figure 9: schematic diagram of different shapes of load-displacement curves at different T

CONCLUSIONS

The mechanical properties of mature cheddar cheese are strain rate and temperature dependent as expected. Cheese appears stiffer at increasing rates and decreasing temperature, due to its viscoelasticity. As in the case of polymers, such as PMMA 6 the resistance to cracking increases as the crack velocity (strain rate) increases and the temperature decreases.
The results can be interpreted in terms of a 'viscoelastic' type of behaviour at high temperatures and low strain rates, and a 'brittle fracture' type of behaviour at low temperatures and high strain rates7. Work is in progress to collect data on forces involved in the cutting process so that the model based on the mechanical properties can be applied.

REFERENCES

1. Dobraszczyk B.J., Atkins A.G., Jeronimidis G. (1987), "Fracture toughness of frozen meat", *Meat Science* 21, pp**.** 25-49
2. Charalambides M.N., Williams J.G., Chakrabarti S. (1995), *"A study of the influence of ageing on the mechanical properties of cheddar cheese"*, *Journal Of Material Science*, 30, pp. 3959-3967
3. Cooke M. and. Larke E.C (1945), *J. Inst. Metals* 71, 371
4. Culioli J. and Sherman P. (1976), *J. Texture Stud.* 7, 353
5. Casiraghi E.M., Bagley E.B. and Christianson D.D. (1985), *J. Texture Stud.* 29, 281
6. Atkins A.G., Lee C.S., Caddell R.M. (1975), "Time-temperature dependent fracture toughness of PMMA", *Journal of material science* 10, pp. 1381-1393
7. Munro P.A. (1983) *Meat Science*, 8, 43.
8. Atkins A.G(1974)., "Fracture toughness and cutting", *Int.J.Prod.Res* 12, pp. 263-274
9. Griffith, A.A. (1921), *Phil.Trans.Roy.Soc.Lond.* 299, 163
10. Anderson T.L. (1991) "Fracture Mechanics-fundamentals and applications", CRC press, Boston

ACKNOLEDGMENTS

RE-EXAMINATION OF OVER SPECIFIED CONDITION OF STRESS INTENSITY FACTOR FOR MULTI-MATERIAL WEDGES AND JUNCTIONS

Wei-Chung Wang[1] and Shin-Way Lin[2]

[1]Department of Power Mechanical Engineering, National Tsing Hua University,
Hsinchu, Taiwan 30013, Republic of China

[2]Industrial Technology Research Institute, Materials Research Laboratories,
Hsinchu, Taiwan 30040, Republic of China

ABSTRACT

Stress singularities often occur in wedges and junctions. Pageau and his colleagues [1] used the Airy's stress function to formulate the stress and displacement fields for the n-material wedges and junctions. In their analysis, it was found that "over specification" of two SIFs occurs while complex singularity appears. They proposed a standardized generalized stress intensity factor (GSIF) to characterize the stress field and avoid over specification. However, the proposed GSIF did not resolve over specification problem completely. Using complex variable technique, the over specified condition arisen from the traditional definition of complex SIF was disclosed in this paper.

A new definition of complex SIF was also introduced to additionally consider the conjugate part of the singularity and resolve the unconformity between the stress expansion and the traditional definition. By using the new definition, the mixed characteristics of SIFs for the multi-material wedges and junctions can be clarified while complex singularity can be degenerated into real singularity. Furthermore, the energy release rate for interfacial crack was re-analyzed to include the mixed mode effect. From the polar plots of $K_{\theta\theta}$ and $K_{r\theta}$, the modes corresponding to the singularities can be distinguished for the bi-material junction problems, in which Chen and Nisitani [2] solved. Due to geometrical symmetry, the singularities were decoupled for the tensile and shear modes. It was concluded that the patterns of the new defined SIFs can be used to characterize the stress fields and loading modes and be also applied to general multi-material structures without geometrical symmetry.

KEYWORDS
stress intensity factor, multi-material, wedge, junction

INTRODUCTION

Stress singularities are very commonly occurred in multi-material structures. Due to the infinite magnitude of stress near the tip of junction, the concept of stress intensity factor (SIF) based on the fracture mechanics is

often used to characterize the singular stress fields. In general, three methods are mostly used to analyze the stress singularity. They are (i) Airy's stress function proposed by Williams [3]; (ii) Mellin transform used by Bogy [4] and Dunders [5] as well as applied by Hein and Erdogan [6] on the analysis for various wedge angles; (iii) Kolosov-Muskhelishvili [7] stress function proposed by Theocaris [8]. It is well known that stress oscillation, which is caused by complex stress singularities, arises in some multi-material structures and annoys researchers very much.

Only few reports have devoted to the expansion of stress field because of algebraic difficulties. There is no widely accepted SIF for the general stress singular field. Rice [9] discussed several possible definitions of SIF for interfacial cracks. He pointed out that tensile and shear effects near the crack tip are intrinsically inseparable into analogues of classical mode I and mode II conditions. This problem also exists in junction structures [8]. Yang and Munz [10] determined eigenfunctions for both real and complex singularities. Chen and Nisitani [2] showed that the mode I and mode II solutions are decoupled due to geometrical symmetry for real singularities in a particular case of bi-material junction. Pageau et al. [1] noticed that the definition of the generalized SIF (GSIF) defined by Chen and Nisitani [2] for bi-material junctions differs from that of Yang and Munz [10] for bi-material wedges. In the work of Pageau et al. [1], some traditional definitions were reviewed. They proposed a standardization scheme for the definition of SIF by the Airy's stress function approach of Williams [3]. Two real constants M_I and M_{II} were introduced in terms of GSIF. They found that only normal stress and shear stress can be respectively used to define mode I and mode II SIFs, i.e. K_I and K_{II}, because of the behavior of the eigenfunctions at $\theta=0$, and θ is the polar angle. Herein, over specification of two SIFs corresponding to M_I and M_{II} was depicted. Although their scheme defines the GSIF to avoid over specification, whether the definition can be adopted on failure assessment due to the over specified condition is questionable and furthermore the definition depends on normal or shear stress conditionally. Specifically speaking, the GSIF proposed by Pageau et al. [1] cannot resolve the over specification completely.

In order to overcome the over specified condition and find a unified definition of GSIF, complex variable technique was applied to analyze the wedge and junction problems in this paper. A similar expression to that used by Pageau et al. [1] was derived. Obviously, the over specified condition is arisen from the traditional definition of the complex SIF. Hence, a new definition of SIF was proposed in this paper while conjugate singularity was taken account in the SIF expression. In the new definition, the mixed part of SIF was identified. The new definition of the SIF conforms to the stress field expansion; therefore, over specified condition no more occurs. The complex singularity can also be degenerated to the case of real singularity. Since the newly defined SIF overcomes the over specified condition and identifies the mixed part of modes, it can be properly used for failure assessments. On the other hand, the energy release rate for interfacial crack was re-analyzed to include the effect of mixed mode. It is found that the energy release rate can be composed by mode I, mode II and corresponding mixed parts.

ANALYSIS OF THE OVER SPECIFIED CONDITION

According to authors' previous work [11], stresses are expressed as

$$
\begin{aligned}
\sigma_{\theta\theta} &+ i\sigma_{r\theta} \\
&= (2\pi r)^\eta \{[Q_1 E_{\theta\theta}(\theta) - Q_2 F_{\theta\theta}(\theta)]\cos(\varepsilon \ln r) - [Q_1 F_{\theta\theta}(\theta) + Q_2 E_{\theta\theta}(\theta)]\sin(\varepsilon \ln r)\} \\
&+ i(2\pi r)^\eta \{[Q_1 E_{r\theta}(\theta) + Q_2 F_{r\theta}(\theta)]\cos(\varepsilon \ln r) + [Q_1 F_{r\theta}(\theta) - Q_2 E_{r\theta}(\theta)]\sin(\varepsilon \ln r)\}
\end{aligned}
\tag{1}
$$

where Q_1 and Q_2 are undetermined real constants, η is the real part of (λ-1), and ε is the so-called oscillation index and constant 2π is included in the expression. $E_{\theta\theta}$, $F_{\theta\theta}$, $E_{r\theta}$ and $F_{r\theta}$ are functions of θ. When ε becomes zero, the oscillation of trigonometric function disappears. It is seen that eqn (1), which is obtained through complex variables technique, is the same as that derived by Pageau et al. [1]. Based on this expression, the definition of SIF can be further discussed.

By following the definition of SIF for bi-material interfacial crack [12-14], the SIF is expressed as

$$\sigma_{\theta\theta} + i\sigma_{r\theta}\,|_{\theta=0} = (2\pi)^{-\frac{1}{2}} K r^{-\frac{1}{2}+i\varepsilon} = \frac{Kr^{i\varepsilon}}{(2\pi r)^{1/2}} = \frac{K_I + iK_{II}}{(2\pi r)^{1/2}} r^{i\varepsilon} \tag{2}$$

The over-specified problem can also be easily disclosed by expanding eqn (2).

$$
\begin{aligned}
&\frac{K_I + iK_{II}}{(2\pi r)^{1/2}} r^{i\varepsilon} \\
&= \frac{1}{(2\pi r)^{1/2}} \{ [K_I \cos(\varepsilon \ln r) - K_{II} \sin(\varepsilon \ln r)] \\
&\quad + i[K_{II} \cos(\varepsilon \ln r) + K_I \sin(\varepsilon \ln r)] \}
\end{aligned}
\tag{3}
$$

By comparing the expressions of K_I and K_{II} between eqns (1) and (3), it can be seen that the expressions of either K_I or K_{II} of the real part are different from those of the imaginary part. Therefore, if both the real and imaginary parts of eqns (3) are adopted to obtain the SIFs, they over specify the SIFs. In other words, K_I and K_{II} in eqns (3) represent SIFs of mode I and mode II, respectively, only when ε equals zero. They no longer mean pure mode I and mode II when ε is not zero, i.e., mode mixing occurs.

NEW DEFINITION OF STRESS INTENSITY FACTOR

As discussed in [11], the new SIFs are shown as follows:

$$
\begin{aligned}
&\sigma_{\theta\theta} + i\sigma_{r\theta} \\
&= (2\pi r)^{\eta} \{ [K_{I\theta} \cos(\varepsilon \ln r) - K_{I\varepsilon\theta} \sin(\varepsilon \ln r)] \\
&\quad + i[K_{II\theta} \cos(\varepsilon \ln r) + K_{II\varepsilon\theta} \sin(\varepsilon \ln r)] \}
\end{aligned}
\tag{4}
$$

where

$$
\begin{aligned}
K_{I\theta} &= Q_1 E_{\theta\theta}(\theta) - Q_2 F_{\theta\theta}(\theta) \\
K_{I\varepsilon\theta} &= Q_1 F_{\theta\theta}(\theta) + Q_2 E_{\theta\theta}(\theta) \\
K_{II\theta} &= Q_1 E_{r\theta}(\theta) + Q_2 F_{r\theta}(\theta) \\
K_{II\varepsilon\theta} &= Q_1 F_{r\theta}(\theta) - Q_2 E_{r\theta}(\theta)
\end{aligned}
\tag{5}
$$

Note that the notation θ is additionally added into the subscript of SIFs and that $K_{I\theta}$, $K_{II\theta}$, $K_{I\varepsilon\theta}$ and $K_{II\varepsilon\theta}$ are functions of θ only. In the homogeneous case, both K_I and K_{II} are clearly defined along $\theta = 0^\circ$. In the general multi-material wedge and junction problems, however, it is not straightforward to define the SIFs. In other words, $\theta = 0^\circ$ can be chosen arbitrarily. Furthermore, the SIFs defined in eqns (4) and (5) reflect the mixing characteristics inherent in the multi-material system. Alternatively speaking, fracture modes become rather complicated everywhere a simple loading is applied on a multi-material system.

REPRESENTATIONS FOR THE SHEAR AND TENSILE MODES

Since the mixed parts of GSIF for multi-material system are clarified, the role of mixed characteristics is examined for the widely used traditional criteria. Stress oscillation always causes a difficult situation in the

definition of SIF. From the previous sections, the newly defined SIF was proposed to be compatible with stress field and well applied on the case of stress oscillation.

The singular stress comes from the exponent η. In mixed state of stress, oscillation index ε annoys the engineers very much. It seems not easy to find a strength index not including the characteristic length r. Oscillation index ε causes variation of stresses with varying frequencies. As r is near zero, the spatial frequency becomes higher. While the spatial frequency is high and "wave length" is smaller than material microstructure characteristic length, the amplitude of the "wave" is a proper expression for the SIF. Eqn (4) can therefore be rewritten as

$$\sigma_{\theta\theta} = (2\pi r)^{\eta} \{ K_{\theta\theta} \cos(\varepsilon \ln r + \phi_{\theta\theta}) \}$$
$$\sigma_{r\theta} = (2\pi r)^{\eta} \{ K_{r\theta} \cos(\varepsilon \ln r + \phi_{r\theta}) \}$$

(6)

The factor $K_{\theta\theta}$ and $K_{r\theta}$ is a function of θ and is defined as

$$K_{\theta\theta} = \sqrt{K_{I\theta}^{2} + K_{I\varepsilon\theta}^{2}}$$
$$K_{r\theta} = \sqrt{K_{II\theta}^{2} + K_{II\varepsilon\theta}^{2}}$$

(7)

$K_{\theta\theta}$ becomes $K_{I\theta}$ and $K_{r\theta}$ becomes $K_{II\theta}$ when real singularity is used.

On the other hand, energy release rate is often used to measure the fracture resistance of materials. Considering the case of a bi-material interfacial crack, energy release rate should be changed to include the conjugate part of the singularity. The traction, $\sigma_{yy}+i\sigma_{yx}$, and the displacement jumps, $\delta_y+i\delta_x$, across the crack face are expressed as follows:

$$\sigma_{yy} + i\sigma_{yx}\Big|_{\theta=0} = \frac{K_1 r^{i\varepsilon}}{\sqrt{2\pi r}} + \frac{K_2 r^{-i\varepsilon}}{\sqrt{2\pi r}}$$

(8a)

$$\delta_y + i\delta_x = \frac{1}{(1+2i\varepsilon)\cosh(\pi\varepsilon)} \frac{4K_1 r^{i\varepsilon}}{E^*} \sqrt{\frac{2r}{\pi}} + \frac{1}{(1-2i\varepsilon)\cosh(\pi\varepsilon)} \frac{4K_2 r^{-i\varepsilon}}{E^*} \sqrt{\frac{2r}{\pi}}$$

(8b)

where $\dfrac{2}{E^*} = \dfrac{1}{E_1'} + \dfrac{1}{E_2'}$ and $E'=E$ for plane stress, $E'=E/(1-v^2)$ for plane strain. E_1 as E_2 are Young's moduli of materials 1 and 2, respectively.

The second terms of eqn (8) are the conjugated parts of the first terms, which are the traditional expressions [9]. Then the energy release rate G is derived by following Hutchinson's derivation [15]:

$$G = \frac{|K_1|^2}{\cosh^2(\pi\varepsilon)E^*} + \frac{|K_2|^2}{\cosh^2(\pi\varepsilon)E^*} = \frac{K_I^2 + K_{II}^2 + K_{I\varepsilon}^2 + K_{II\varepsilon}^2}{2\cosh^2(\pi\varepsilon)E^*}$$

(10)

It is seen that the mixed parts appear in the energy release rate clearly. In a homogeneous crack, both K_I and $K_{I\varepsilon}$ contribute to mode I.

NUMERICAL DEMONSTRATION

Consider a model of bi-material junction. There exist two singularities, 0.623716 and 0.755233. By arbitrarily

3

applying loads, $K_{\theta\theta}$ and $K_{r\theta}$ can be obtained for both singularities. Fig. 2 is the SIF distribution for λ=0.623716. It is found that $K_{\theta\theta}$ is not zero along line of symmetry, but $K_{r\theta}$ is. Obviously, this singularity 0.623716 corresponds to tensile mode. On the other hand, the SIF distribution for λ=0.755233 is shown in Fig. 3. $K_{\theta\theta}$ is zero along line of symmetry, but $K_{r\theta}$ is not. This singularity 0.755233 corresponds to tensile mode.   Hence, it is possible to distinguish modes by SIF distribution rather than mathematical formulation as done in [2]. Similar cases are also found in multi-material structures.
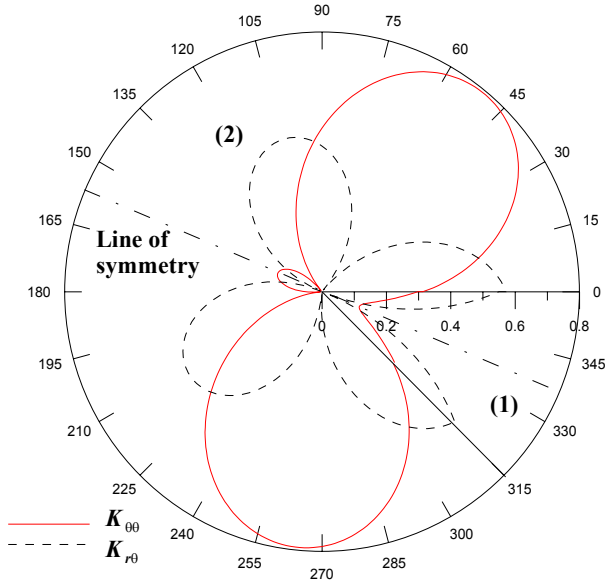
Figure 1.   Distributions of $K_{\theta\theta}$ and $K_{r\theta}$
for an open wedge and λ=0.623716
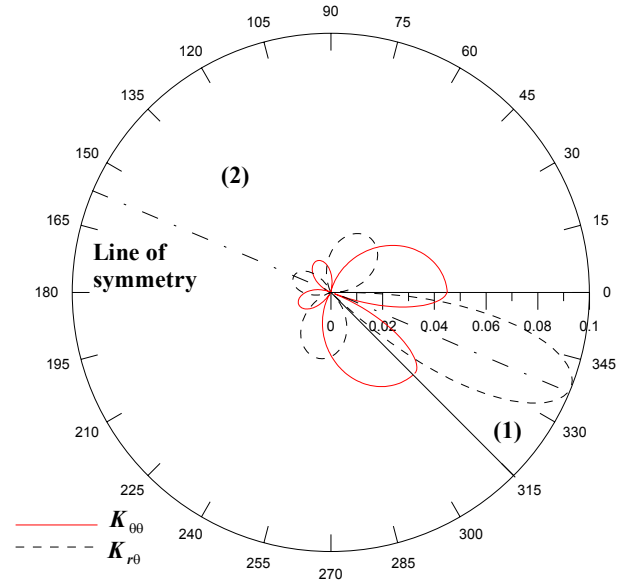
Figure 2. Distributions of $K_{\theta\theta}$ and $K_{r\theta}$
for an open wedge and λ=0.755233

DISCUSSIONS AND CONCLUSIONS

In this paper, a new definition of SIF was proposed by employing the complex variable method. The traditional expression of complex SIF is not complete due to the lack of inclusion of additional conjugate term and is over specified as pointed out in the paper by Pageau et al. [1]. An additional conjugate term was added and a new form of stress expression was derived in this paper. In the new form, the mixed parts of SIF were clarified. Consequently, the new form can be applied well on both real and complex singularities. Typically, the traditional energy release rate G was re-examined for the interface crack. And the mixing part $K_{I\varepsilon}$ and $K_{II\varepsilon}$ appears in the expression of G.

Here, the angular distrbution of $K_{\theta\theta}$ and $K_{r\theta}$ can be used to represent the loading mode. They are actually two different aspects for modes. It is doubtful if $K_{\theta\theta}$ and $K_{r\theta}$ are tensors as the stresses $\sigma_{\theta\theta}$ and $\sigma_{r\theta}$. They are indeed not tensors, since they are defined asymtotically near the singular point, that is r=0, but not at it. That is, it characterizes the behavior near the singular point.

It was shown that the loading modes could be examined from the patterns of the angular distribution of $K_{\theta\theta}$ and $K_{r\theta}$ rather than from the geometry. The patterns of $K_{\theta\theta}$ and $K_{r\theta}$ angular distribution are characteristic of stress fields for different geometries. The maximum $K_{\theta\theta}$ and $K_{r\theta}$ can be determined from the patterns. Therefore, the pattern of the $K_{\theta\theta}$ distribution represents the characteristics of the loading modes more properly. It is useless to distingush the tensile and shear modes when the reference coordinates cannot be set definitely.

Considering the spatial frequency of the stress oscillation, the new factors $K_{\theta\theta}$ and $K_{r\theta}$, which are functions of θ, are defined. And $K_{\theta\theta}$ and $K_{r\theta}$ can be degenerated into $K_{I\theta}$ and $K_{II\theta}$ when the singularity is real. The mode mixing can also be found clearly from the $K_{\theta\theta}$ and $K_{r\theta}$ angular distribution. Since the proper form of stress expression was obtained, the stress field can be derived and SIF can be extracted. It should be then noted that

the new form is more appropriately suitable for multi-material junction and wedge problems in which reference direction is not defined clearly.

ACKNOWLEDGEMENTS

REFERENCES

1. Pageau S. S., Gadi, K. S., Biggers, S. B. Jr. and Joseph, P. F., 1996, "Standardized Complex and Logarithmic Eigensolutions for N-material Wedges and Junctions," International Journal of Fracture, Vol.77, pp.51-76.
2. Chen, D. and Nisitani, H., 1993, "Singular Stress Field Near the Corner of Jointed Dissimilar Materials," ASME Journal of Applied Mechanics, Vol. 60, pp.607-613.
3. Williams M. L., 1952, "Stress Singularities Resulting from Various Boundary Conditions in Angular Corners of Plates in Extension," ASME Journal of Applied Mechanics vol.19 (1952) 526-528.
4. Bogy D. B., 1968, "Edge-bonded Dissimilar Orthogonal Elastic Wedge under Normal and Shear Loading," ASME Journal of Applied Mechanics, Vol.35, pp.460-466.
5. Dunders, J., 1969, 'discussion', ASME Journal of Applied Mechanics, Vol.36, pp. 650-652.
6. Hein, V. L. and Erdogan, F., 1971, "Stress Singularities in a Two-material Wedge," International Journal of Fracture Mechanics, Vol.7, pp. 317-330.
7. Muskhelishvili, N. I., 1953, "Some Basic Problems of Mathematical Theory of Elasticity," P. Noordhoff and Company, New York.
8. Theocaris, P. S., 1974, "The Order of Singularity at Multi-wedge Corner of a Composite Plate," International Journal of Engineering Science, Vol.12, pp.107-120.
9. Rice, J. R., 1988, "Elastic Fracture Mechanics Concepts for Interfacial Cracks", Journal of Applied Mechanics, Vol. 55, pp. 98-103.
10. Yang, Y. Y. and Munz, D., 1995, "The Stress Distribution in Dissimilar Materials Joint for Complex Singular Eigenvalues under Thermal Loading," Journal of Thermal Stresses, Vol.18, pp.407-419.
11. Lin, S. W. and Wang, W. C., 1999, " New Concept from the Standardization of Complex Eigensolutions for Wedges and Junctions," Advances in Electronic Packaging, EEP-Vol. 26-2, pp.2053-2059.
12. England, A. H., 1965, "A Crack between Dissimilar Media," ASME Journal of Applied Mechanics, vol. 32, pp. 400-402.
13. Erdogan, F., 1965, "Stress Distribution in Bonded Dissimilar Materials with Cracks," ASME Journal of Applied Mechanics, Vol. 32, pp. 403-410.
14. Rice, J. R., and Sih, G. C., 1965, "Plane Problems of Cracks in Dissimilar Media", ASME Journal of Applied Mechanics, Vol. 32, pp. 418-423.
15. Hutchinson, J. W., Mear, M. E., Rice, J. R., 1987, "Crack Paralleling an Interface Between Dissimilar Materials", ASME Journal of Applied Mechanics, Vol. 54, pp. 828-832.
16. Lin, S. W. and Wang, W. C., 1999, "General Transfer Method for the Multi-material Junction and Wedge Problems," Computational Mechanics, Vol. 23, pp. 502-509.

REAL-TIME HEALTH MONITORING SYSTEM AVAILABLE FOR ANY ANISOTROPIC CONDITION OF CFRP

J.-H. Koo[1], N. Toyama[1], B.-K. Jang[1], T. Junji[1],Y. Akimune[1] and T. Kishi[2]

[1] Smart Structure Research Center, National Institute of Advanced Industrial
Science and Technology, 1-1-1Umezono, Tsukuba, Ibaraki 305-8568, Japan
[2] National Institute for Materials Science,
1-2-1 Sengen, Tsukuba, Ibaraki 305-0047, Japan

ABSTRACT

In this work, we manufactured the piezoelectric ceramics transducers embedded CFRP and its more exact source location method on microcracking was investigated. Especially, we studied the way to determine the arrival time when high level noise is included and to use wavelet transformation when the amplitude of symmetric mode is so small that searching the arrival time is difficult. The transducers were able to detect the signals without any amplifier well. Control of oscilloscope by personal computer made real-time health monitoring possible. When a signal included a large noise in front of the real response, backward searching method (BSM) was useful to eliminate it. Wavelet transformation (WT) method was useful to determine the arrival time of the symmetric mode Lamb wave as well as that of anti-symmetric mode.

Keywords

Smart structure, Acoustic emission, Health monitoring, Piezoelectric ceramics, Source location, Lamb wave

INTRODUCTION

A large portion of the recent studies on smart materials and structures are concentrated on CFRP [1-5]. CFRP has so high specific strength and rigidity that it is used at important parts in aeronautic and astronautic field. Therefore, if it fails the loss is also so large. In order to prevent such failure, real-time health monitoring on microcracking like matrix cracking, debonding, delamination, transverse cracking and fiber breakage is required.

If the microcracking takes place, the released energy propagates as elastic wave. The elastic wave consists of symmetric mode Lamb wave and anti-symmetric mode Lamb wave. In the case of the study to identify the source of external shock similar to vertical shock, to deal with anti-symmetric mode is useful because out-of-plane component is dominant. Contrarily in the case of identifying a microcrack, symmetric mode is available as it has in-plane component.

So, in this work, we manufactured the piezoelectric ceramics transducers embedded CFRP and its more exact source location method on microcracking was investigated. Especially, we studied the way to determine the arrival time when high level noise is included and to use wavelet transformation when the amplitude of symmetric mode is so small that searching the arrival time is difficult.

WAVE VELOCITY IN CROSS PLY LAMINATES

In orthotropic plates, the Hook's law can be written by Equation (1) [6]. The Q_{ij} are the reduced stiffness components and x-axis is defined as in the fiber direction, y-axis transverse to the fiber, and s denotes shear component.

$$\begin{bmatrix} \sigma_{xx} \\ \sigma_{yy} \\ \sigma_{xy} \end{bmatrix} = \begin{bmatrix} Q_{xx} & Q_{xy} & 0 \\ Q_{xy} & Q_{yy} & 0 \\ 0 & 0 & Q_{ss} \end{bmatrix} \begin{bmatrix} \varepsilon_{xx} \\ \varepsilon_{yy} \\ \gamma_{xy} \end{bmatrix} \tag{1}$$

The reduced stiffness components can be expressed with some engineering constants as follows:

$$\begin{aligned} Q_{xx} &= E_x/(1-v_x v_y) \\ Q_{yy} &= E_y/(1-v_x v_y) \\ Q_{xy} &= v_x Q_{yy} = v_y Q_{xx} \\ Q_{ss} &= E_s \end{aligned} \tag{2}$$

where E_x is Young's modulus in the longitudinal direction, E_y means Young's modulus in the transverse direction, E_s indicates shear modulus, and v_x and v_y are major and minor Poisson's ratios individually.

On the other hand, the reduced stiffness components in the rotated coordinate-system can be transformed as follows:

$$\begin{aligned} Q_{11} &= m^4 Q_{xx} + n^4 Q_{yy} + 2m^2 n^2 Q_{xy} + 4m^2 n^2 Q_{ss} \\ Q_{22} &= n^4 Q_{xx} + m^4 Q_{yy} + 2m^2 n^2 Q_{xy} + 4m^2 n^2 Q_{ss} \\ Q_{12} &= m^2 n^2 Q_{xx} + m^2 n^2 Q_{yy} + (m^4 + n^4) Q_{xy} - 4m^2 n^2 Q_{ss} \\ Q_{66} &= m^2 n^2 Q_{xx} + m^2 n^2 Q_{yy} - 2m^2 n^2 Q_{xy} + (m^2 - n^2)^2 Q_{ss} \\ Q_{16} &= -m^3 n Q_{xx} + mn^3 Q_{yy} + (m^3 n - mn^3) Q_{xy} + 2(m^3 n - mn^3) Q_{ss} \\ Q_{26} &= -mn^3 Q_{xx} + m^3 n Q_{yy} + (mn^3 - m^3 n) Q_{xy} + 2(mn^3 - m^3 n) Q_{ss} \end{aligned} \tag{3}$$

where, $m = \cos(\theta)$ and $n = \sin(\theta)$. θ is the rotated angle.

Generally in-plane stiffness for the entire plate that consists of k layers can be calculated by integration of the reduced stiffness components in the range of thickness and the phase velocity of symmetric Lamb mode in 1-axis can be determined with A_{11}, density(ρ), and thickness(h).

$$A_{ij} = \int_{-h/2}^{h/2} Q_{ij}^{(k)} dz \qquad v_1 = \sqrt{\frac{A_{11}}{\rho h}} \tag{4}$$

In the case of cross ply laminates, however, the calculation of velocity is simplified. We can calculate the Q_{xx} and Q_{yy} by measuring the velocity in 0 degree direction. If we assume that $(Q_{xy}+2Q_{ss}) = c$ (constant), the value of c can be obtained by measuring a velocity (v_α) in another direction. Then, the velocity in a direction can be expressed by Equation (7).

$$Q_{11} = Q_{xx} = Q_{yy} = \rho v_0^2 \tag{5}$$

$$Q_{11} = (m^4 + n^4)Q_{xx} + 2m^2 n^2 c = \rho v_\alpha^2 \tag{6}$$

$$v_\theta = \sqrt{\frac{A_{11}}{\rho}} = \sqrt{\frac{hQ_{11}}{\rho h}} = \sqrt{\frac{(m^4 + n^4)Q_{xx} + 2m^2 n^2 c}{\rho}} \qquad (7)$$

$$c = \frac{\rho v_\alpha^2 - (m^4 + n^4)Q_{xx}}{2m^2 n^2} \qquad (8)$$

WAVE VELOCITY IN ARBITRARILY LAMINATED PLATES

In the case of arbitrarily laminated plates, for example [0/10/20/30/.../90], we should first calculate $Q_{ij}^{(1)}$, $Q_{ij}^{(2)}$, $Q_{ij}^{(3)}$, ..., $Q_{ij}^{(10)}$. Of course, for the calculation we needs E_x, E_y, E_s, ν, ρ and h in each layer. Then, all velocities can be calculated by Equation (4).

ARRIVAL TIME DETERMINATION

Backward Searching Method
Because the detected AE signals include some noise in front of main signal, the conventional threshold method sometimes makes mistake on determination of arrival time. Therefore we use Backward Searching Method (BSM) which is not influenced by the front noise. In BSM, as shown in Figure 1, when some points group that proceeds backward from maximum peak enters into a limited range, the last point of the group becomes the first arrived point.
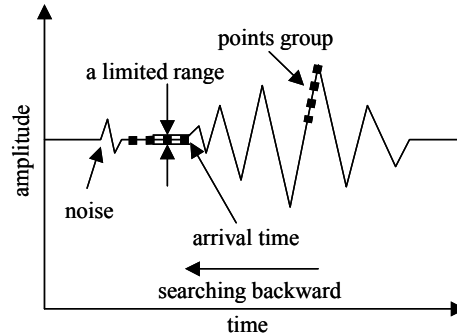
Figure 1: Backward Searching method

Wavelet Transformation Method
The definition of the continuous wavelet transformation (WT) of a function f(t) is as follows [7]:

$$(Wf)(b,a) = \frac{1}{\sqrt{a}} \int_{-\infty}^{\infty} f(t) \overline{\Psi\left(\frac{t-b}{a}\right)} dt \qquad (9)$$

where $a > 0$ and the overbar means the complex conjugate. From WT we can get the information of behavior of a particular frequency component in time domain. The calculation can be carried out at high speed by FFT. The mother wavelet used in this work is Gabor function (Equation (10)). Its Fourier transform is expressed as Equation (11). Here, ω_0 is the center frequency and γ is positive constant.

$$\Psi_g(t) = \frac{1}{\sqrt[4]{\pi}} \sqrt{\frac{\omega_0}{\gamma}} \exp\left(-\frac{(\omega_0/\gamma)^2}{2}t^2\right) \exp(i\omega_0 t) \qquad (10)$$

$$\hat{\Psi}_g(\omega) = \frac{\sqrt{2\pi}}{\sqrt[4]{\pi}} \sqrt{\frac{\gamma}{\omega_0}} \exp\left(-\frac{(\gamma/\omega_0)^2}{2}(\omega - \omega_0)^2\right) \qquad (11)$$

Generally WT method has been applied to anti-symmetric mode Lamb wave for calculation of velocity or determination of arrival time. It is not, however, impossible to apply to symmetric mode Lamb wave. Especially when the amplitude of symmetric mode is similar to that of noise, WT is very useful.

SOURCE LOCATION

Suppose that T_i and t_i are the true and measured arrival times of i-th transducer respectively. The true arrival time is expressed as follows:

$$T_i = \frac{\sqrt{(x-x_i)^2 + (y-y_i)^2} - r_i}{v_i} \qquad (12)$$

where (x, y) is a source position, (x_i, y_i) is a transducer position, r_i is a radius of transducer, and v_i is the velocity in the direction. If f_i is defined as Equation (13), we can find the (x,y) that satisfies Equation (14) by nonlinear least-square method.

$$f_i = (T_i - T_j) - (t_i - t_j) \qquad (13)$$

$$\sum f_i^2 < \varepsilon \qquad (14)$$

Here ε is convergence limit.

EXPERIMENTAL SETUP

When we manufactured $[0/90]_{2s}$ CFRP, a polyimide sheet with four embedded piezoelectric ceramics (Figure 2) was inserted between two center layers. The dimension of the composite is 145x200x1.8mm. The thickness and diameter of the piezoelectric ceramics is 200μm and 5mm. For source location test of out-of-plane AE source, pencil lead break test was carried out at the point of x=40, y=90mm. The pencil lead is 0.5mm 2H type. Two velocities (in 0 degree and 45 degree) were measured with pencil lead break for calculation of a velocity in an arbitrary direction. Any amplifier was not used. The block diagram is shown in Figure 3.
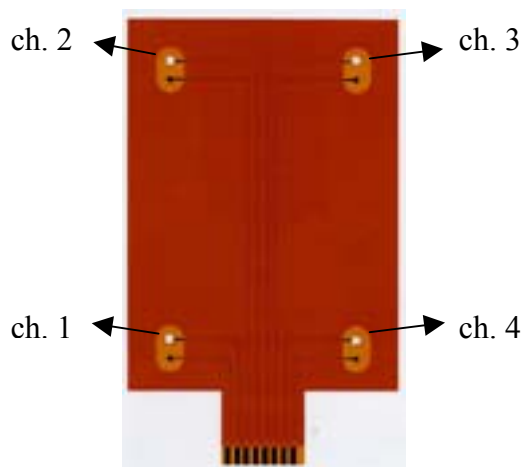
Figure 2: Photograph of the polyimide sheet with piezoelectric ceramics and circuit
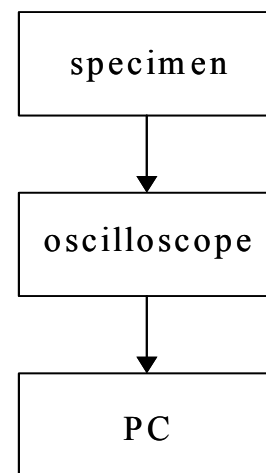
Figure 3: Block diagram of experimental setup

RESULTS AND DISCUSSION

The measured velocities of 0 and 45 degree are 6700 and 5150 m/s, respectively. There are four signals detected at each channel in Figure 4(a). The signals were modified with 0-point correction and noise filtering Figure 4(b). In order to avoid the influence of the residual large noise, arrival times were searched with BSM Figure 4(c). In this case, the source location error is very small, 0.8 mm.

On the other hand, we also tried to test the WT method on the same signals. As shown in Figure 5(a), the center frequency of the symmetric mode of the detected signal (eg., 1 ch.) is 474 kHz. Figure 5(b) shows the WT coefficients of 474 kHz component in time domain. We let the first peak arrival time. The source location error is also very small, 1.1 mm.
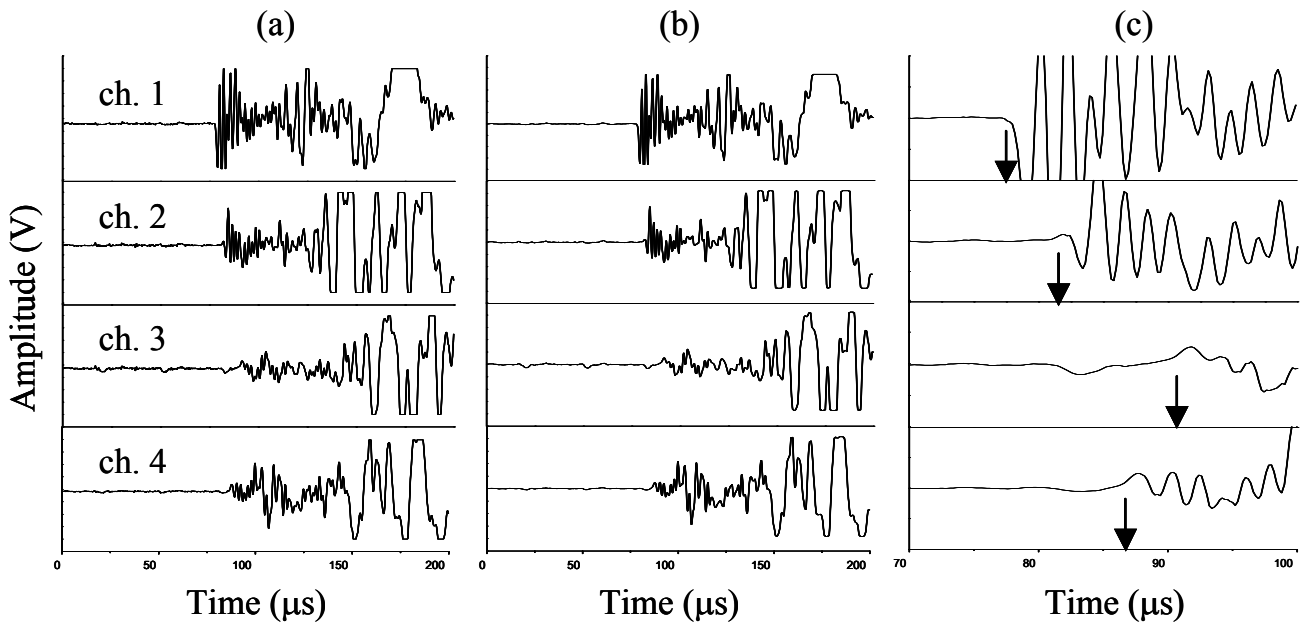
Figure 4: (a) detected signal, (b) filtered signals and (c) arrival times by BSM
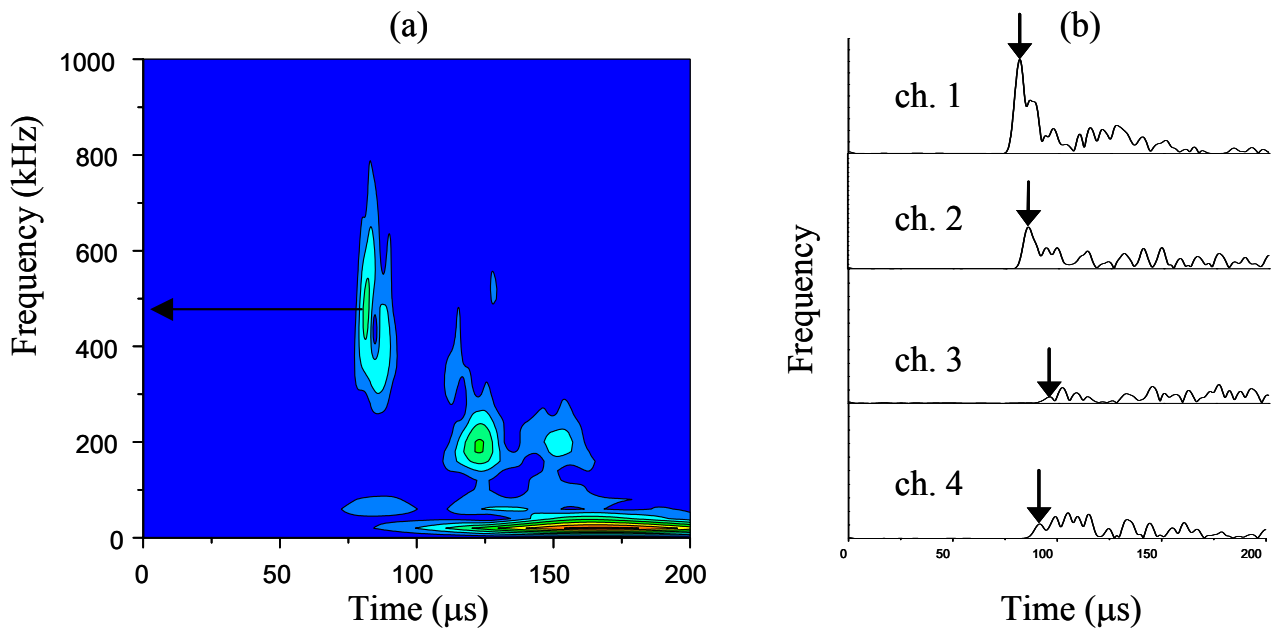
Figure 5: (a) WT of channel 1 and (b) WT at 474 kHz

CONCLUSION

Some piezoelectric ceramics were embedded into CFRP thin plate for sensing the simulated AE signal in this work. The transducers were able to detect the signals without any amplifier well. Control of oscilloscope by personal computer made real-time health monitoring possible. When a signal included a large noise in front of the real response, backward searching method was useful to eliminate it. Wavelet transformation method was useful to determine the arrival time of the symmetric mode Lamb wave as well as that of anti-symmetric mode. We think that the experimental results obtained in this work is in the case of cross ply thin plate but the analysis method can be adopted to any arbitrarily plied laminates.

REFERENCES

1. Tang, B., Henneke II, E. G. and Stiffler, R. C. (1988). In: *Acoustio-Ultrasonics: Theory and Application*, pp. 45-65, John, C. and Duke, Jr. (Eds). Plenum, New York.
2. Prosser, W. H., Gorman, M. R. and Humes, D. H. (1999) *Journal of Acoustic Emission* 7, 29.
3. Prosser, W. H., Seale, M. D. and Smith, B. T. (1999) *J. Acout. Soc. Am.* 105, 2669.
4. Seale, M. D. and Madaras, E. I. (2000) *J. Composite Mater.* 34, 27.
5. Seydel, R. and Chang, F. K. (2001) *Smart Mater. Struc.* 10, 354.
6. Daniel, I. M. and Ishai, O. (1994) *Engineering Mechanics of Composites.* Oxford University, New York.
7. Kishimoto K., Inoue, H., Hamada, M. and Shibuya, T. (1995) *J. Appl. Mech.* 62, 841.

REAL-TIME SPECKLE INTERFEROGRAM ANALYSIS AND ITS APPLICATION TO SUB-SURFACE DELAMINATION CRACK DETECTION IN CARBON FIBRE COMPOSITES

J. M. Huntley, C. R. Coggrave and Y. Shen

Department of Mechanical Engineering, Loughborough University,
Loughborough LE11 3TU, UK

ABSTRACT

A real-time system for analysing data from speckle interferometers, and speckle shearing interferometers, has been developed. Interferograms are continuously recorded by a CCD camera at a rate of 60 frames s^{-1} with temporal phase shifting carried out at the same rate. The images are analysed using a pipeline image processor. With a standard 4-frame phase-shifting algorithm (phase steps of $\pi/2$), wrapped phase maps are calculated and displayed at 15 frames s^{-1}. These are unwrapped using a temporal phase unwrapping algorithm to provide a real-time display of the relevant displacement component. The main advantage of temporal over spatial unwrapping methods is that unwrapping errors due to noise, specimen boundaries, and cracks do not propagate spatially. Each camera pixel (or cluster of pixels) behaves in effect as an independent displacement sensor. The reference speckle interferogram is updated automatically at regular user-defined intervals, allowing arbitrarily large deformations to be measured and errors due to speckle decorrelation to be minimized. The system has been applied to the problem of detecting sub-surface delamination cracks in carbon fibre composite panels.

KEYWORDS

Speckle interferometry, delamination cracks, defect detection, carbon fibre composites.

INTRODUCTION

The detection of delamination defects within composite structures is an important quality control step in the aerospace manufacturing industry. The traditional technique (ultrasound C-scan) is effective, but since it is a pointwise method, assessment of an entire aircraft is a time consuming and expensive process. The use of wholefield optical techniques, such as speckle interferometry and speckle shearing interferometry (shearography), is therefore potentially attractive. Electronic speckle pattern interferometry (ESPI) refers to the technique of generating fringe patterns on a TV monitor, by the real-time analysis of laser speckle interference patterns from objects with rough surfaces [1]. Traditional ESPI systems subtract a stored reference speckle pattern from the live camera image and display the modulus of the difference pattern. Systems have been constructed more recently in which further real-time data analysis is carried out using specialised pipeline image processors. By introducing phase-shifting devices, fringes with improved signal-to-noise ratio can be produced [2], or else wrapped phase maps (i.e., phase values lying in the range $-\pi$ to π) can be calculated in real time [3].

The drawback with such systems is that the calculated data are still not in the form of displacement or strain fields that can be readily understood by likely end users of the equipment. The normal method of obtaining such images is to post-process discrete "snapshots" of the wrapped phase change distribution, using the process known as phase unwrapping. The traditional method, which can be termed spatial unwrapping, involves comparing the phase at neighbouring pixels and adding suitable integral multiples of 2π so as to remove the 2π phase jumps. When the object contains real discontinuities, however, due for example to specimen edges or growing cracks, spatial unwrapping is risky because of the possibility of unwrapping across a boundary which can cause the spatial propagation of a large phase error. A wide variety of algorithms has been proposed over the years [4], but many of these are also computationally intensive, and have variable run times.

One solution to these problems is to analyse a sequence of interferograms measured throughout the entire deformation history. If the temporal sampling rate is sufficiently high, temporal phase shifting can be used to extract high quality phase maps, and temporal phase unwrapping allows absolute displacement fields to be obtained [5]. Absolute in this context means the total displacement since the start of the deformation process, as opposed to the displacement relative to some other point in the field of view, which is all that can be achieved with spatial unwrapping. The combination of temporal phase shifting and temporal phase unwrapping means that each pixel in the camera behaves as an independent displacement sensor. Several practical systems based on this approach have now been developed [6-8]. However, all of these involve storing the interferograms in memory and require subsequent post-processing.

The purpose of this paper is to describe a novel analysis system, suitable for use with either a speckle interferometer or shearography head, in which both the temporal phase shifting and temporal unwrapping calculations are carried out in real time. The result is a continuous colour-coded display of the displacement (or displacement-gradient) field which is updated at 15 Hz. The paper is illustrated with typical results from vacuum-loading experiments on a carbon fibre panel containing a simulated delamination crack.

DATA ANALYSIS

In this section we present a summary of the main numerical procedures described in References [5] and [8]. The measured intensity $I(t)$ at a given camera pixel follows the usual phase-shifting interferometry equation

$$I_n(t) = I_r + I_o + 2\sqrt{I_r I_o}\, \cos\left[\Phi(t) + \phi_n\right], \qquad \left[\phi_n = (n-1)\pi/2, \;\; n = 1,2,3,4\right], \tag{1}$$

where I_r and I_o are the reference and object beam intensities, t is the time index for the phase calculation ($t = 0, 1, 2,\ldots, s$), and $\Phi(t)$ is the speckle phase. ϕ_n is the phase shift which is introduced by means of a Pockels cell in the reference beam. Application of the standard 4-frame phase-shifting algorithm allows the change in phase Φ between times t_1 and t_2 to be calculated as

$$\Delta\Phi_w(t_2, t_1) = \tan^{-1}\left[\frac{N(t_2)D(t_1) - N(t_1)D(t_2)}{N(t_1)N(t_2) + D(t_1)D(t_2)}\right], \tag{2}$$

where the numerator $N(t)$ and denominator $D(t)$, respectively proportional to $\sin[\Phi(t)]$ and $\cos[\Phi(t)]$, are given by

$$N(t) = I_4(t) - I_2(t), \quad D(t) = I_1(t) - I_3(t). \tag{3}$$

Subscript w indicates that $\Delta\Phi_w(t_2, t_1)$ is wrapped onto the range $(-\pi, \pi)$.

In Eqn. (2), the numerator and denominator are proportional to the sine and cosine of the phase change between times t_1 and t_2, weighted by the square of the intensity modulation. Spatial smoothing can therefore be carried out by convolving the numerator and denominator with a kernel of equal constant values over data from neighbouring pixels, and it can be shown that the implicit weighting results in a phase-difference map with optimal signal-to-noise ratio [9]. Such an approach has been implemented on the pipeline image processor using a 3 by 3 kernel.

Eqn. (2) allows $\Delta\Phi_w(t,0)$, the total wrapped phase change since the start of the recording process, to be calculated. Temporal phase unwrapping is then carried out to restore the unknown integral multiple of 2π for each value of t. The unwrapped phase change distribution will be denoted $\Delta\Phi_u(t,0)$. The number of 2π phase jumps between two successive measurements of the phase change is calculated as follows:

$$d(t) = \mathrm{NINT}\left\{\left[\Delta\Phi_w(t,0) - \Delta\Phi_w(t-1,0)\right]/2\pi\right\}, \quad t = 2, 3,..., s, \tag{4}$$

where NINT denotes rounding to the nearest integer.

The total number of phase jumps by the time of the tth phase measurement, $v(t)$, is calculated by

$$v(t) = \sum_{t'=2}^{t} d(t'). \tag{5}$$

and the unwrapped phase difference map is obtained as

$$\Delta\Phi_u(t,0) = \Delta\Phi_w(t,0) - 2\pi v(t) \quad t = 2, 3,..., s. \tag{6}$$

If the deformation becomes too large, significant speckle decorrelation will occur causing an increase in the noise level of the measured displacement fields. Under such circumstances a new reference state should be chosen at times $t = t_1$, t_2, t_3, etc. in place of the state $t = 0$. The total unwrapped phase change after re-referencing κ times will then be

$$\Delta\Phi_u(t,0) = \Delta\Phi_u(t,t_\kappa) + \sum_{k=2}^{\kappa} \Delta\Phi_u(t_k,t_{k-1}) + \Delta\Phi_u(t_1,0). \tag{7}$$

IMPLEMENTATION USING PIPELINE PROCESSOR

Pipeline processing essentially converts a two-dimensional image consisting of a 2-D array of pixel values into a one-dimensional stream of individual pixels. The pixel stream can be processed one pixel at a time by a series of specialised processing elements, and then transformed back into a 2-D image. At the beginning and end of each 1-D pipeline is a 2-D surface that is stored on a virtual surface image memory (VSIM). Pipeline processing has an important performance advantage over fixed-data-path, general-purpose image processing architectures, which process whole images as discrete frames. This advantage is derived from placing the specialised processing hardware at the particular point in the 1-D stream where it can perform its individual processing task on each pixel, without waiting for the entire frame to be processed. The processing hardware can be assembled in a variety of configurations, each optimised for a particular application, thereby creating an image pipeline.

The hardware used to implement the algorithm described in the previous section is a Datacube VME system, consisting of two 20MHz MV250 pipeline processor boards. The boards host a total of twelve dual ported 4Mb image memories (VSIM), an AP advanced processor module, and a mmNMAC2 convolver module. A Motorola 33MHz MVME167 single board computer configures the pipeline processing boards and schedules the data transfers. The LynxOs real-time Unix operating system was selected to enable processes to be prioritised, thus allowing deterministic algorithm run-times to be achieved.

A 60Hz EEV CAM17 synchronous camera with a 512×512 pixel CCD array is used to acquire the speckle interferograms. The lens used was a Nikon 50 mm camera lens. The camera has an 8-bit digital output that feeds directly into the AD digital input port of one of the pipeline boards. The CCD camera provides the master pixel clock and framing pulses; the pipeline processor is then configured as a slave to this external clock. 8-bit resolutions are used to represent most images, with 16 bit representations for $\nu(t)$, and 24 bits for $\Delta\Phi_u(t,0)$. Pipeline altering threads are used to construct pipes as required, thereby ensuring efficient use of the computing resources. Full details of the pipeline architecture are given in Ref. [10].

EXPERIMENTAL

The experiment described in this paper used a standard out-of-plane speckle interferometer with illumination and observation directions almost normal to the specimen surface, and with the reference wave introduced by means of a beamsplitter so as to emerge from the centre of the objective lens aperture [1] (see Figure 1 below). The light source was a 5 W frequency doubled YAG Verdi laser manufactured by Coherent, running at a power output of 0.6 W. Phase-shifting was carried out by means of a Pockels cell in the reference beam. A speckle shearing interferometer has also been constructed using a standard Michelson arrangement in which phase shifting is carried out by moving one of the two mirrors by means of a high voltage PZT (Burleigh PZ-81). The image processing steps implemented on the pipeline processor are, however, identical for both types of interferometer.

The sample consisted of a plate $150 \times 100 \times 1.5$ mm^3, manufactured with the stacking sequence [0/90/0/0/90/0]. A double-layer of Teflon film (with dimensions 50×50 mm^2) was included between the first and second plies to simulate the presence of a delamination crack. After curing, the sample was coated with titanium dioxide developer powder to increase the surface reflectivity and reduce speckle decorrelation. The plate was placed in a vacuum chamber with optical access provided by means of a polymethyl methacrylate window. The surface displacement field was measured as the pressure was reduced by 150 mbar over a period of 64 s. Re-referencing was carried out every 6.7 s.
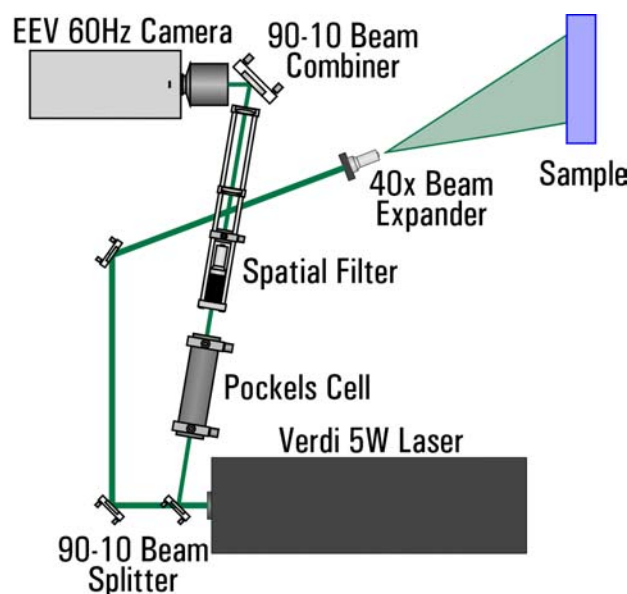

Figure 1: Optical arrangement for out-of-plane speckle interferometer.

Figure 2 shows the wrapped phase change map calculated by the pipeline processor over the course of the experiment. The grayscale colour map is such that $-\pi$ is represented by black, and $+\pi$ by white. The unwrapped phase map is represented on the monitor as a real-time colour coded image. In view of the difficulties of representing such images in a monochrome publication, we display the final unwrapped phase map as a surface mesh plot (Figure 3). This unwrapped phase map can be converted to the out-of-plane displacement component, $u_z(x, y)$, by multiplying by the constant $\lambda/4\pi = 42.3$ nm rad^{-1}, where λ is the wavelength of the light used (532 nm) [1].
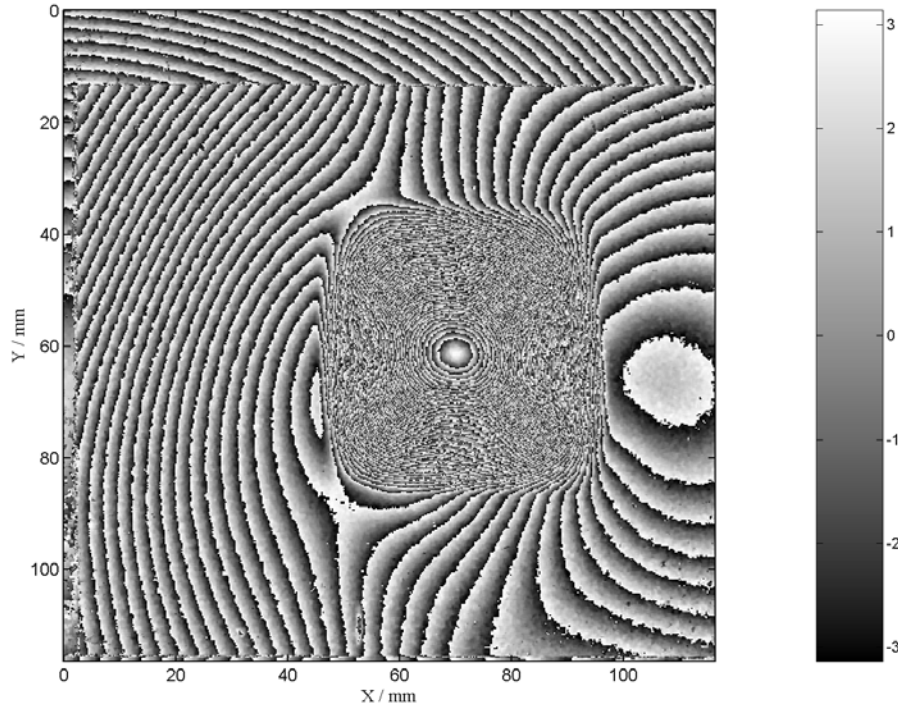
Figure 2: Wrapped phase map at end of test showing final deformation state of the carbon fibre sample.

CONCLUSIONS

This paper describes the first speckle interferometry analysis system which is capable of calculating and displaying maps of the displacement field in real time, i.e. at 15 frames s^{-1}. Data from 250,000 pixels are processed using a combination of temporal phase shifting and temporal phase unwrapping. Unwrapping errors due to low modulation pixels are effectively removed by convolution of the data with a 3×3 kernel, which therefore restricts spatial cross-talk to immediately adjacent pixels; each pixel cluster therefore behaves as an independent displacement sensor. In the case of spatial unwrapping, by contrast, each pixel is potentially influenced by every other pixel in the field of view. Increases in noise level in the measured displacement field due to speckle decorrelation are reduced by periodically re-referencing the phase map. In combination with a 24-bit representation of the speckle phase change, this allows specimen motion to be measured over an extended range (from −6.5 mm to +6.5 mm with respect to the initial position).

The performance of the system was demonstrated by high quality data calculated from a vacuum-loading test on a carbon-fibre composite panel containing a sub-surface delamination crack. The maximum measured displacement was ~20 μm, with an rms noise level of a few tens of nm, giving a signal-to-noise ratio of ~1000:1. This is significantly higher than values traditionally associated with the technique of speckle interferometry. Further research will involve the development of software to detect such defects automatically, and the use of inverse analysis techniques to quantify the flaw geometry [11].
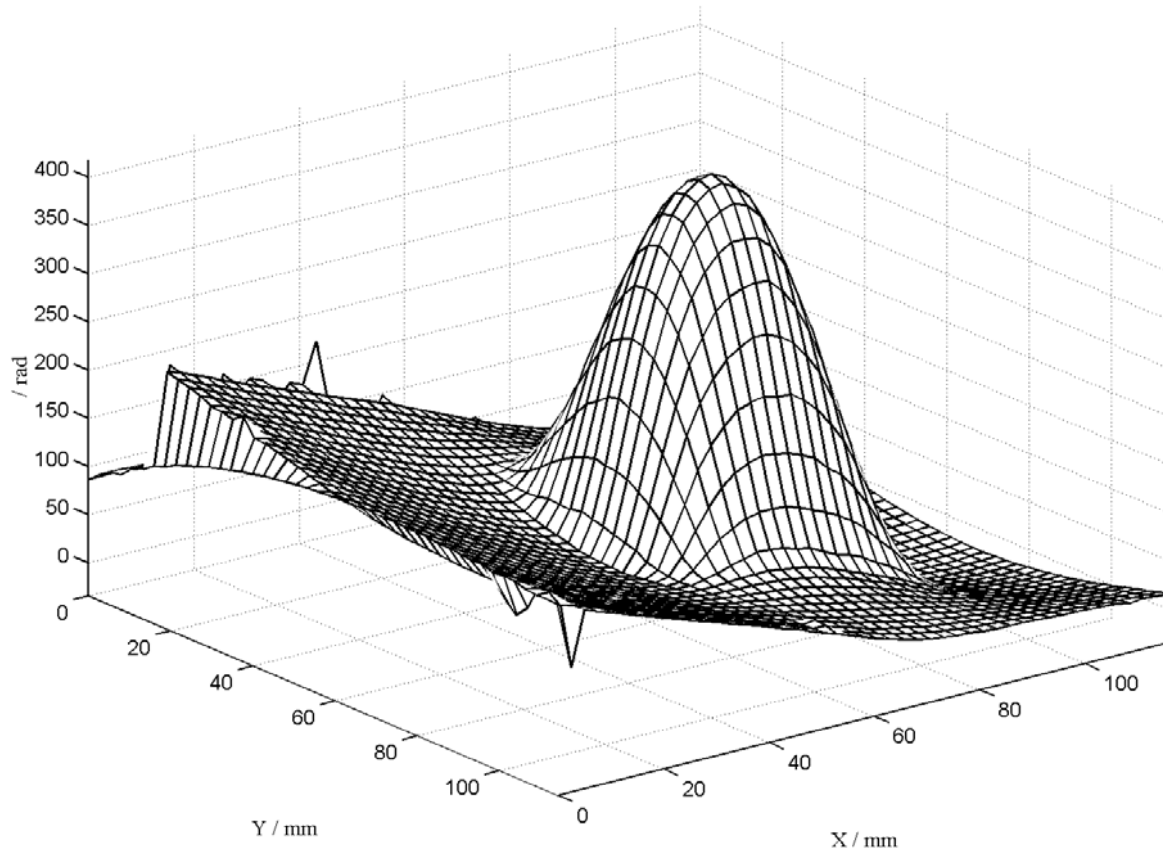
Figure 3: Result of temporal unwrapping of the phase map from Figure 2.

REFERENCES

[1]   Jones, R and Wykes, C. (1983). *Holographic and Speckle Interferometry*. Cambridge University Press, Cambridge.
[2]   Bushman, T. (1989) *Proc. SPIE* 1162, 66.
[3]   van Haasteren, A. J. P. and Frankena, H. J. (1993). In: *Proc 2nd Intl. Workshop on Automatic Processing of Fringe Patterns*, pp. 417-422, Jüptner, W. and Osten., W. (Eds). Akademie Verlag, Berlin.
[4]   Ghiglia, D. C. and Pritt, M. D. (1998). *Two-dimensional phase unwrapping*. J. Wiley & Sons, New York.
[5]   Huntley, J. M. and Saldner, H. (1993) *Appl. Opt.* 32, 3047.
[6]   Colonna de Lega, X. (1997). *Processing of non-stationary interference patterns: adapted phase-shifting algorithms and wavelet analysis*. PhD thesis, EPFL Lausanne.
[7]   Joenathan, C. Franze, B. Haible, P. and Tiziani, H. J. (1998) *Appl. Opt.* 37, 2608.
[8]   Huntley, J. M., Kaufmann, G. H. and Kerr, D. (1999) *Appl. Opt.* 38, 6556.
[9]   Huntley, J.M. (1997) *Opt. Lasers Eng.* 26, 131.
[10]   Coggrave, C. R. and Huntley, J. M. (1999) *Proc SPIE* 3744, 464.
[11]   Panni, D. C. and Nurse, A. D. (submitted 2001) *Computers and Structures*.

RECENT ADVANCES OF PHOTO-THERMAL SPECTROSCOPY

T. SAWADA and K. KATAYAMA

Graduate School of Frontier Sciences, The University of Tokyo
7-3-1 Hongo Bunkyo-ku, Tokyo 113-8656, Japan

ABSTRACT

Transient reflecting grating (TRG) measurements were applied to a silicon surface in the time range from femtoseconds to nanoseconds. Msurements with a time resolution of sub-nanoseconds provided a depth profiling of thermal and acoustic properties by changing the obserbed depth which is experimentally controllable. Two hundreds femtoseconds time-resoleved measurements offer an investigation on initial processes of heat generation, that is, an energy transfer from electrons to phonons. Further, an ultrafast temperature change at a slicon surface was selectivly and directly measured with a spectroscopic TRG method, so that the fundamental processes of heat generation can be investigated and also the signal can be used as a temperature indicator at a surface.

KEY WORDS

Transient grating, depth profiling, femtosecond, silicon

INTRODUCTION

In the latest device technology, device components get smaller and smaller to the size region of nanometers, and for example, thin films of several nanometers in thickness are practically used. As the size is reduced, the time of carrier transport between components also gets faster and faster to the time region of picoseconds. Ultrafast carrier transport generates heat in the nano-sized region, so that there are some local places with high temperature. To improve device performance, the fundamental physical processes of such heat generation at a surface or interface must be clarified and the temperature should be controlled. In order to clarify the origin of heat generation, the source processes, namely the photo-excited carrier dynamics should be studied. But comparatively there are not many such studies for silicon though it is one of the most fundamental device materials. For such studies, ultrafast photothermal methods can be used to observe carrier dynamics and the following heat generation. Transient reflecting grating (TRG) and Transient reflectivity (TR) are two of the ultrafast photothermal methods that have a detection region of several tens of nanometers.

We have developed TR and TRG methods for the last 10 years, and applied them to various solid surfaces [1,2,3], solid-liquid interfaces [4,5,6,7], multi-layered films [8] and liquid surfaces [9]. In the time region of several nanoseconds, thermal and acoustic properties can be observed by the TRG technique. In this paper, we applied the TRG method to a silicon surface. First, sub-nanosecond time-resolved TRG method was applied to a silicon surface, and the physical meanings were considered. Next, the time resolution of the TRG method was improved to have a time resolution of 200 fs. Using this equipment, ultrafast carrier dynamics was measured for a silicon in order to get information on heat origin. Further, we adapted a femtosecond white-light continuum as a probe light in the TRG technique, so that the signal gives time-resolved spectroscopic information [10]. The spectroscopic TRG spectrum was analyzed to clarify the detailed carrier dynamics and the following heat generation.

EXPERIMENTAL

Schematic illustration of the principle for the TRG method is shown in Fig.1. In the TRG technique, two crossed pump pulses are incident at a solid surface and, as a result, the focused spot is irradiated with a pulse of an interference pattern. The complex refractive index at the spot changes due to a physical property change, or grating-patterned surface deformation occurs mainly due to a surface acoustic wave. After the pump pulses irradiation, a probe pulse is also incident there, and the complex refractive index change and the grating-patterned surface deformation are detected through the diffracted light of the probe light. A refractive index change due to photoexcited carriers is observed until several picoseconds, and that due to temperature rise is observed from several picoseconds to nanoseconds. A surface deformation is detected in the time range of several nanoseconds.
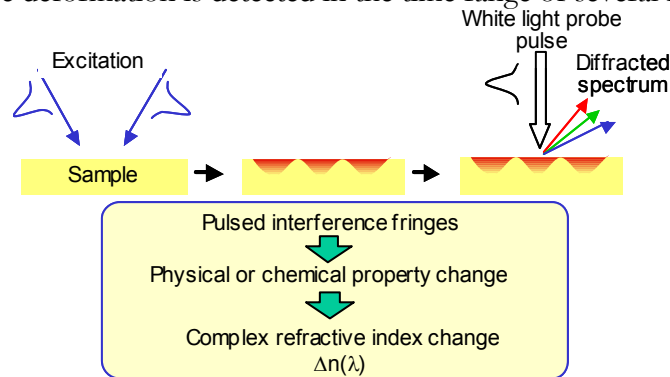

Fig.1 The principle of the transient reflecting grating method. The above figure corresponds in case of a white light pulses as probe pulses.

For measurement with a time resolution of sub-nanosecond, Nd-YAG laser (Pulse width :80 ps, Repetition frequency : 1 kHz, Wavelength : 1064 nm) was used as a light source. The wavelength was frequency-doubled to 532 nm. The pulse was separated into pump and probe pulses using a partial reflective mirror. The pump pulses were further divided into two pulses by a half mirror. The two pump pulses were crossed and irradiated onto the same spot of the sample surface, to coincide in time to form an interference pattern. The probe pulses were also incident at the spot after passing through a computer controlled optical delay line. The diffracted signal of the probe pulses were detected with a photomultiplier, and observed by a computer after averaging the signal with a box-car integrator.

In measurements with a time resolution of 200 fs, a regeneratively amplified titanium sapphire laser laser (CPA-1000; Clark-MXR Inc.) was used as a light source. The pulse train wavelength was 800 nm

with a repetition rate of 1 kHz and pulse width of 200 fs in full width at half maximum. Only the pump pulses were frequency doubled to a wavelength of 400 nm. The probe pulses remain 800 nm.

For spectroscopic measurements, the probe pulse was focused to a 10 mm thick cell filled with heavy water to generate a femtosecond white light continuum after passing through a computer controlled optical delay line. Used wavelengthes ranged from 470 nm to 800 nm. The reflected diffracted light with a rainbow of colors spread like a fan due to the diffraction conditions. It was directed to the entrance of the optical fiber end after being collected and focused by lens. The diffraction spectrum was detected using the PMA-11 (HAMAMATSU) with a built-in spectroscope and CCD camera. The used sample was a single crystalline Si (111) without any dopants after etched in 1% HF aqueous solution for 5 miniutes.

RESULTS AND DISCUSSION

TRG responses measured with the sub-nanosecond time resolution is shown in Fig.2. The signal had a small peak just after photo-excitation at the almost same time as incident pulse. The following signal shows an oscillating decay consisting of an exponential decay and an oscillating decay. The signal was separated to each component, which is shown in the right side of Fig.2.
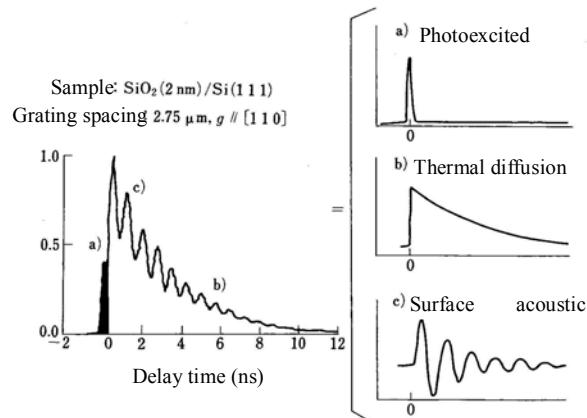
Fig.2 A response of transient reflecting grating for a silicon surface with a time resolution of 100ps. Three components comprising the response are also shown.

Considering the time range observed, the first peak corresponds to a refractive index change due to photo-excited carriers, and the exponential decay and the oscillating decay mean a thermal decay and a surface acoustic wave (SAW), respectively. It is very difficult to discuss the photo-excited carrier dynamic because the dynamics is considered to be faster processes than the used pulse width. About the thermal component, the decay occurs due to a thermal diffusion parallel to the interface, which disappears the temperature distribution like a grating pattern. Thus the decay time corresponds to the time during which heat diffuses for the length of the grating spacing. The grating spacing, Λ is expressed as $\Lambda = \lambda/2\sin(\theta/2)$, where λ is the wavelength of the pump pulses, and θ is the intersection angle of the two pump pulses. From the thermal decay time and the value of Λ, a thermal diffusion coefficient can be calculated, and this value is a property value in the depth region of Λ, which can be controlled by changing θ and has a typical length of $1 - 10$ μm. Then, this signal provides a depth profiling of the thermal diffusion coefficient. The acoustic oscillation of the SAW originates in thermal expansion due to heat generation with a grating pattern. The wavelength of SAW must agree with the

grating spacing, so that the SAW with a controllable wavelength can be generated and detected. Since a SAW have an elastic information in a surface region of the wavelength, this acoustic signal also offers a depth profiling of elastic properties.
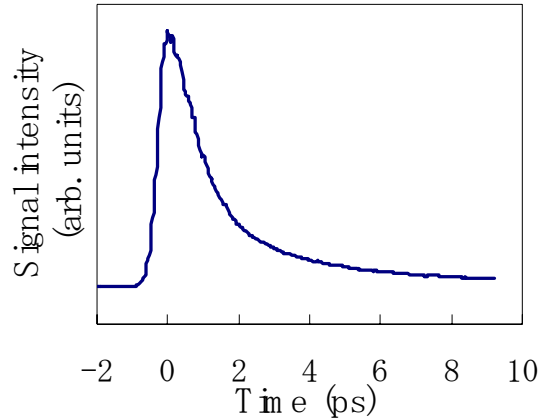

Fig.3 A response of transient reflecting grating for a silicon surface with a time resolution of 200fs. Three components
       comprising the response are also shown.

Next, the photoexcited carrier dynamic was focused on. The dynamics was observed in the first peak of the sub-nanosecond time-resolved TRG signal. To clarify the temporal response, the TRG measurement with the time resolution of 200 fs was applied to the same sample. The TRG response is shown in Fig.3. The signal rose just after photo-excitation and decayed in 2ps. The photo-excited carriers lose their energy due to scattering by phonons, that is, an energy transfer from photo-excited electrons to phonons. The process is the origin of a temperature rise. In the literature [11], it was reported that the scattering due to phonons occurs about a few picoseconds. Thus it was concluded that the TRG signal in the picoseconds time range includes information on the origin of heat generation, that is, an energy transfer from photo-excited electrons to phonons. But it makes difficult to analyze the signal that it has only a time-dependent response detected with a probe wavelength, though the signal consists of many time-dependent physical processes such as carrier-phonon (c-p) scattering, carrier diffusion, thermal diffusion, Auger recombination, trapping to surface states and so on.

In order to get more detailed information on the ultrafast dynamics, we adapted a femtosecond white-light continuum as a probe light in the TRG technique, so that the signal gives time-resolved spectroscopic information [12]. This improvement provided detailed information on the excited state of photo-excited carriers and thermal properties.

TRG spectrums for a silicon until 20 ps and 300 ps are shown in Figs.4 (a) and (b), respectively. Looking at the Fig.1(a), the intensity of the TRG spectrum rose in the observed whole spectral range just after irradiation of the pump pulses, and decreased in a few picoseconds. After the decay, the spectrum intensity increased again only below the probe wavelength of 550 nm, and remains almost constant until 20 ps. From the Fig.1(b), the component decayed about 300 ps.

The faster decay in a few picoseconds is considered to correspond to a relaxation of photoexcited carriers due to carrier-phonon (c-p) scattering and carrier diffusion. Here, the slower component observed below 550 nm was investigated in detail. As mentioned in the experimental section, a permittivity change at a solid surface is measured by a TRG technique. Investigating what physical

processes induced the wavelength-dependent dielectric function change ($\Delta\varepsilon(\lambda)$) in the time range of 300 ps. There is a possibility of carrier density change at a specific energy state in a bulk silicon. In case there is an interband transition in the probe wavelength range, a change in carrier density at the states related to the interband transition brings about a dielectric function change around the wavelength of the interband transition. But interband transitions for silicon lies at 3.4, 3.4 and 4.3 eV for L, Γ and X, respectively [13,14], that is, no interband transitions in the used probe wavelength range. Next possibility is carrier density change at a surface state. For silicon surfaces, various surface states are known and the energy positions were investigated mainly by the photoemission spectroscopy [15,16,17]. Carrier dynamics at several types of surface states were investigated in the literature [18,19,20], and the results indicate that trapped carriers at surface states show a different behavior about a decay time and energy states only by changing the structure of the first layer. But no difference of the TRG spectrums was observed for a hydrogen-terminated and oxidized silicon surface. Thus this possibility is also denied. The left possibility is a temperature rise. It is reported that a temperature rise induces a wavelength dependent dielectric function change. Considering the signal intensity increased in a few picoseconds, the rise time agrees well with that for a temperature rise for general semiconductors. Further, the profile of the observed TRG spectrum was compared with that of a dielectric function change spectrum for various temperatures. The profile of the observed TRG spectrum resembled that of the permittivity change spectrum. Thus, it was concluded that the observed TRG spectrum is induced by a temperature rise at the silicon surface. This observation is the first one that provides a direct and selective measurement of ultrafast temperature change at a solid surface by selecting a transient response at an appropriate wavelength. Analyzing the TRG spectrums until a few picoseconds, the origin of heat generation can be studied, for example, carrier-carrier, c-p, defect scattering and so on. Further, the signal decay can be used as an in-situ indicator of temperature at a solid surface.
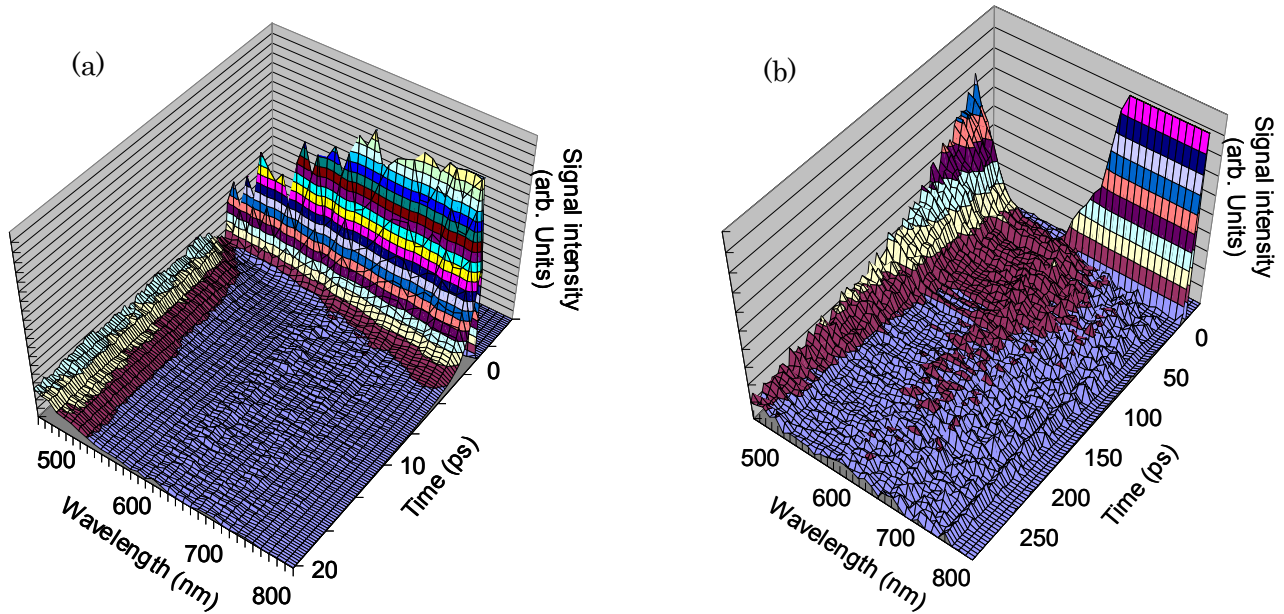

Fig.4 Three dimensional TRG spectrums for a silicon surface until 20 ps (a) and 300 ps (b). The probe wavelength ranges from 470 to 800 nm.

CONCLUSION

The TRG method was applied to a silicon surface in the time range from femtoseconds to nanoseconds. In a measurement with a time resolution of sub-nanoseconds, the signal gave

information on thermal diffusion and SAW. This method provides a depth profiling of thermal and acoustic properties by changing the experimentally controllable obserbed depth. Ultrafast time-measurement with 200fs time resolution offers an investigation of an initial heat generation, that is, an energy transfer from electrons to phonon. It was proved that the TRG spectrum below 550 nm shows a temperature rise and decay. This signal provides direct and selective temperature measurement at a solid surface, so that the fundamental processes of heat generation can be investigated and also the signal can be used as a temperature indicator at a surface.

REFERENCES

[1] K. Katayama, Q. Shen, A. Harata and T. Sawada, Appl. Phys. Lett. **69**, p. 2468 (1996).

[2] K. Katayama, Q. Shen, A. Harata and T. Sawada, Phys. Rev. B **58**, p. 8428 (1998).

[3] A. Harata, N. Adachi and T. Sawada, Phys. Rev. B **58**, p. 7319 (1998).

[4] A. Harata, T. Kawasaki, M. Ito and T. Sawada, Anal. Chim. Acta **299**, p. 349 (1995).

[5] A. Harata, T. Edo and T. Sawada, Chem. Phys. Lett. **249**, p. 112 (1996).

[6] A. Hibara, A. Harata and T. Sawada, Chem. Phys. Lett. **272**, p. 1 (1997).

[7] K. Katayama, T. Sawada, I. Tsuyumoto and A. Harata, Bull. Chem. Soc. Jpn. **72**, p. 2383 (1999).

[8] Q. Shen, A. Harata and T. Sawada, J. Appl. Phys. **77**, p. 1488 (1995).

[9] S. Ikeda, K. Katayama, I. Tsuyumoto, T. Tanaka, A. Harata and T. Sawada, J. Chem. Phys. **111**, p. 9393 (1999).

[10] K. Katayama, Y. Inagaki and T. Sawada, Phys. Rev. B **61**, p. 7332 (2000).

[11] A. Othonos, J. App. Phys. **83**, p. 1789 (1998).

[12] K. Katayama, Y. Inagaki and T. Sawada, Phys. Rev. B **61**, p. 7332 (2000).

[13] D. E. Aspnes and A. A. Studna, Phys. Rev. B **27**, p. 985 (1983).

[14] T. Miyazaki and S. Adachi, J. Appl. Phys. **77**, p. 1741 (1995).

[15] H. Neddermeyer, U. Misse and P. Rupieper, Surf. Sci. **117**, p. 405 (1982).

[16] F. J. Himpsel and Th. Fauster, J. Vac. Sci. Technol. A **2**, p. 815 (1984).

[17] M. Fujita, H. Nagayoshi and A. Yoshimori, Surf. Sci. **208**, p. 155 (1989).

[18] J. Bokor, R. Storz, R. R. Freeman and P. H. Bucksbaum, Phys. Rev. Lett. **57**, p. 881 (1986).

[19] N. J. Halas and J. Bokor, Phys. Rev. Lett. **62**, p. 1679 (1989).

[20] M. W. Rowe, H. Liu, G. P. Williams, Jr. and R. T. Williams, Phys. Rev. B **47**, p. 2048 (1993).

RECENT DEVELOPMENTS IN THE WEIBULL STRESS MODEL FOR PREDICTION OF CLEAVAGE FRACTURE IN FERRITIC STEELS

Xiaosheng Gao[1] and Robert H. Dodds, Jr.[2]

[1]Department of Mechanical Engineering, The University of Akron, Akron, OH 44325, USA
[2]Department of Civil & Environmental Engineering, University of Illinois, Urbana, IL 61801, USA

ABSTRACT

This paper reviews recent developments in the Weibull stress model for prediction of cleavage fracture in ferritic steels. The procedure to calibrate the Weibull stress parameters builds upon the toughness scaling model between two crack configurations having different constraint levels and eliminates the recently discovered non-uniqueness that arises in calibrations using only fracture toughness data obtained under small scale yielding (SSY) conditions. The introduction of a non-zero threshold value for Weibull stress in the expression for cumulative failure probability is consistent with the experimental observations that there exists a minimum toughness value for cleavage fracture in ferritic steels, and brings numerical predictions of the scatter in fracture toughness data into better agreement with experiments. The calibrated model predicts accurately the toughness distributions for a variety of crack configurations including surface crack specimens subject to different combinations of bending and tension.

Keywords: Cleavage fracture, Failure probability, Weibull stress, Calibration, Surface crack

1. INTRODUCTION—THE WEIBULL STRESS MODEL FOR CLEAVAGE FRACTURE

In the ductile-to-brittle transition (DBT) region of ferritic steels, transgranular cleavage initiated by slip-induced cracking of grain boundary carbides often triggers the brittle fracture event which results in catastrophic failure of structural components. Due to the highly localized character of the failure mechanism and microstructural inhomogeneity of the material, the cleavage fracture toughness often exhibits a large amount of scatter and a strong sensitivity to the local stress and deformation fields [1, 2]. This complicates greatly the interpretation of fracture toughness data to define meaningful values for application in fracture assessments of structural components, and has stimulated a rapidly increasing amount of research on micromechanical descriptions of the cleavage fracture process. The Weibull stress model originally proposed by the Beremin group [3] based on weakest link statistics provides a framework to quantify the relationship between macro and microscale driving forces for cleavage fracture. They introduced the scalar Weibull stress (σ_w) as a probabilistic fracture parameter, computed by integrating a weighted value of the maximum principal (tensile) stress over the process zone of cleavage fracture (i.e., the crack front plastic zone). The Beremin model adopts a two-parameter description for the cumulative failure probability

$$P_f(\sigma_w) = 1 - \exp\left[-\left(\frac{\sigma_w}{\sigma_u}\right)^m \right] , \qquad (1)$$

with

$$\sigma_w = \left[\frac{1}{V_0} \int_{\overline{V}} \sigma_1^m dV \right]^{1/m} . \qquad (2)$$

Here parameters m and σ_u denote the Weibull modulus and the scale parameter of the Weibull distribution. Moreover, m defines the shape of the probability density function for microcrack size [3]. In Eq. (2), $\overline{V}$ represents the volume of the cleavage fracture process zone, V_0 defines a reference volume to normalize the integral units and σ_1 is the maximum principal stress acting on material points inside the fracture process zone.

The Weibull stress thus defines a local, crack front parameter to couple remote loading with a micromechanical model that incorporates the microcracks in a weakest link philosophy. Under increased remote loading described by J (or K_J), differences in evolution of the Weibull stress, $\sigma_w = \sigma_w(J)$, reflect the potential strong variations in crack-front fields due to the effects of constraint loss and volume sampling. The inherently 3D formulation for σ_w defined by (2) readily accommodates variations in J (or K_J) along the crack front in a weighted sense.

The Weibull stress concept enables construction of a toughness scaling model between crack configurations exhibiting different constraint levels. Based on equal probabilities of fracture, the scaling model requires the attainment of the same Weibull stress value to trigger cleavage in different specimens, even though the J values may differ widely [4, 5, 6]. The quantitative relationships enable the simple transfer (or scaling) of critical J values from one geometry and loading condition to another to accommodate constraint and volume sampling differences.

2. CALIBRATION OF THE WEIBULL STRESS MODEL

The applicability of the Weibull stress model to predict failure probability and/or to scale fracture toughness values between different crack configurations relies on the calibrated values of Weibull parameters, m and σ_u. Initial efforts to calibrate Weibull parameters used notched (round) bars tested at lower-shelf temperatures (e.g., [3]) and assumed identical values apply for defect assessments in the DBT region. Anticipating that m and σ_u may very well depend on temperature, stress-strain gradient and plastic strain levels present in cracked components operating in the DBT region, many researchers (e.g., [7]) proposed to calibrate m and σ_u using fracture toughness data measured at a temperature comparable to the application.

Previous studies have shown that fracture toughness values in the DBT region follow a Weibull distribution, $P_f(J_c) = 1 - \exp[-(J_c/\beta)^\alpha]$, where β defines the toughness value at 63.2% failure probability and α quantifies the scatter. Reliable estimates of the Weibull slope α require a large number of measured toughness values (J_c) in the data set while as few as 6-10 J_c-values suffice to establish the characteristic toughness value β with high confidence levels [8]. The conventional calibration method employs an iterative procedure to determine m and σ_u such that the micromechanics model (1) predicts the measured toughness distribution. Because the calibrated values of m and σ_u depend on the measured toughness distribution (i.e., both α and β), the experimental data set must contain a large number of J_c-values. However, most experimental data sets do not satisfy this requirement. Experimental sets of J_c-values often have limited number of specimens (6-10) and therefore, large uncertainties must be expected in m and σ_u determined in this manner. Moreover, experimental programs usually employ deep-notch SE(B) specimens or C(T) specimens which fail under small scale yielding (SSY) conditions. Both theoretical studies and experimental results suggest that $\alpha = 2$ for SSY. Gao *et al.* [5] have shown that the conventional calibration method leads to non-unique values of m and σ_u under SSY conditions, i.e., many (m, σ_u) pairs can be found such that the microscopic model (1) predicts the same failure probability as the macroscopic model.

Recognizing these problems of the conventional calibration method, we propose a new approach to calibrate m and σ_u [5]. This approach requires testing of two sets of specimens giving rise to different constraint levels at fracture (e.g., SE(B) specimens with different a/W ratios). By using the toughness scaling model based on σ_w, the calibration process seeks

the m-value which corrects the two sets of fracture toughness data to have the same statistical properties under SSY conditions, i.e., the two constraint-corrected SSY toughness distributions have the same β-value. A maximum likelihood estimate of β for the constraint-corrected SSY toughness distribution uses the theoretical value for α ($= 2$), and 6-10 J_c-values in each set are sufficient to obtain β with high confidence. Once m is determined, σ_u is just the computed Weibull stress value at $J = \beta$ in the SSY configuration with the specified reference thickness.

In contrast to the conventional calibration method which attempts to find the values for m and σ_u by curve fitting the predicted P_f vs. J distribution to the experimental data, the new procedure adopts a fracture mechanics basis rather than a purely numerical fitting process. This approach has been successfully applied to calibrate m and σ_u for several ferritic steels [5, 9, 10].

3. THE THRESHOLD σ_w FOR CLEAVAGE FRACTURE

The Weibull stress model defined by Eqs (1-2) represents a pure weakest link description of the fracture event. This two-parameter model describes the unconditional cleavage probability that assumes no microcracks arrest (macroscopic cleavage fracture occurs once the critical microcrack experiences propagation). However, the unconditional probability has significant shortcomings to predict cleavage fracture [5, 11]. First, it implies that a very small K_I (stress intensity factor due to applied load) leads to a finite failure probability, which is not true in reality. Cracks cannot propagate in polycrystalline metals unless sufficient energy exists to break bonds, to drive the crack across grain boundaries and to perform plastic work. Consequently, there must exist a minimum toughness value ($K_{\min}$) below which cracks arrest. $K_{\min}$ has an experimentally estimated value of 20 MPa$\sqrt{m}$ for common ferritic steels under SSY conditions, independent of the crack front length. The value of $K_{\min} = 20$ MPa$\sqrt{m}$ has been adopted by ASTM E-1921 [8]. Second, the unconditional probability often over-estimates the measured scatter of fracture toughness (see Anderson *et al.* [11] and Gao *et al.* [5] for examples).

Some researchers (e.g., Bakker and Koers [12], Xia and Shih [13], and others) introduce a threshold stress (σ_{th}) into computation of the Weibull stress to reflect the observed macroscopic threshold toughness. One such proposal for the integrand to compute the Weibull stress has the form $(\sigma_1 - \sigma_{th})^m$. But rational calibration procedures for σ_{th} remain an open issue. Moreover, introduction of σ_{th} into the Weibull stress expression does not imply the existence of $K_{\min} > 0$. A finite value of σ_w (and thus a finite value of failure probability) exists at a very small K-value even though $\sigma_{th} > 0$ is introduced in the Weibull stress formulation.

To introduce an explicit threshold toughness into the Weibull stress model, we propose a modified form for Eq. (1) given by

$$P_f(\sigma_w) = 1 - \exp\left[-\left(\frac{\sigma_w - \sigma_{w\text{-}\min}}{\sigma_u - \sigma_{w\text{-}\min}} \right)^m \right] , \qquad (3)$$

where $\sigma_{w\text{-}\min}$ represents the minimum σ_w-value at which macroscopic cleavage fracture becomes possible. Consistent with the definition of $K_{\min}$, we define $\sigma_{w\text{-}\min}$ as the value of σ_w calculated at $K = K_{\min}$ in the (plane strain) SSY model, where the SSY model has a thickness equal to the configuration of interest for which (3) is applied. Therefore, calibration of $\sigma_{w\text{-}\min}$ is straightforward and does not require any additional experimental data. According to this three-parameter Weibull stress model (3), the toughness scaling model between specimens having different geometries and loading conditions should be constructed at identical $\bar{\sigma}_w$-values, where $\bar{\sigma}_w = \sigma_w - \sigma_{w\text{-}\min}$. Gao *et al.* [5] and Gao and Dodds [6] provide detailed discussions about the three-parameter Weibull stress model and the toughness scaling method based on Weibull stress with $\sigma_{w\text{-}\min} > 0$.

4. PREDICTION OF CLEAVAGE FRACTURE IN A PRESSURE VESSEL STEEL

This section describes an application of these recent developments in modeling cleavage fracture to predict the behavior for various crack configurations of an A515-70 pressure vessel steel, including surface crack specimens loaded by different combinations of tension and bending. Joyce and Link [14] and Tregoning (see Gao *et al.* [9]) recently performed extensive fracture tests on this material in the DBT region. The material has a Young's modulus of 200 GPa, Poisson's ratio of 0.3 and yield stress of 280 MPa at -7^oC and 300 MPa at -28^oC. Twelve plane-sided 1T C(T) specimens ($a/W = 0.6$) were tested at -28^oC and twelve plane-sided 1T SE(B) specimens ($a/W = 0.2$, $B \times 2B$ cross-section) were tested at -7^oC. In addition, seven bolt-loaded and seven pin-loaded surface crack specimens were tested at -7^oC. The pin-loaded specimen experiences a higher bending moment whereas the bolt-loaded specimen experiences predominantly tensile loading. All specimens failed by cleavage without prior macroscopic ductile tearing.

Fracture toughness data for the deep-notch C(T) specimens and the shallow-notch SE(B) specimens are used to calibrate the Weibull stress parameters. Because the C(T) specimens and the SE(B) specimens have different test temperatures, toughness values for the C(T) specimens are needed at -7^oC. Here, we employ the "master curve" approach of ASTM E-1921 [8] to adjust the C(T) toughness values for the temperature change. The "master curve" for ferritic steels makes possible the prediction of median fracture toughness (for 1T thickness) at any temperature in the transition region, provided the reference temperature (T_0) for the material has been determined from SSY fracture toughness data at a single temperature. The calibration for m is as follows: 1) Assume an m-value and compute the σ_w vs. K_J history for C(T) and SSY (plane strain) configurations respectively using the material flow properties at -28^oC. Scale the measured toughness values for C(T) specimens to the SSY configuration. Determine T_0 using the constraint corrected toughness values and estimate K_0 (K_J at 63.2% failure probability) at -7^oC (denote as K_0^A) according to ASTM E-1921; 2) Compute the σ_w vs. K_J history for SE(B) and SSY (plane strain) configurations respectively at -7^oC. Scale the measured toughness values for SE(B) specimens to the SSY configuration. Estimate K_0 for the constraint corrected toughness distribution and denote it as K_0^B; 3) Define an error function as $R(m) = (K_0^B - K_0^A)/K_0^A$. If $R(m) \neq 0$, repeat the above steps for additional m-values. The calibrated Weibull modulus, $m = 11.2$, makes $R(m) = 0$ for the A515-70 steel tested at the current conditions. After m is calibrated, σ_{w-min} and σ_u can be easily determined. At -28^oC, the values of σ_{w-min} and σ_u corresponding to the thickness of the C(T) specimen are 790 MPa and 1378 MPa. At -7^oC, the values of σ_{w-min} and σ_u corresponding to the thickness of the SE(B) specimen are 741 MPa and 1435 MPa.

Figure 1 compares the predicted failure probabilities for the C(T) and SE(B) specimens using the calibrated Weibull stress model (3) with the median rank probabilities for the measured J_c values. The dashed lines indicate the 90% confidence limits for the estimates of the experimental rank probabilities. To compute these confidence limits, we assume that the (continuous) P_f values from Eq. (3) provide the expected median rank probabilities for an experimental data set containing the number of measured J_c-values. The calibrated Weibull stress model predicts accurately the shape of the toughness distribution and captures the strong constraint effect on fracture toughness.

Finally, we apply the calibrated three-parameter Weibull stress model to predict the cumulative failure probability for cleavage fracture of the tested surface crack specimens. Because the crack front length of the surface crack specimen equals to $1.67 \times$ the crack front length of the SE(B) specimen, the values of σ_{w-min} and σ_u for surface crack specimens are slightly different from those for SE(B) specimens. Here, $\sigma_{w-min} = 776$ MPa and $\sigma_u = 1470$ MPa. The model predictions capture the measured toughness distributions for both bolt-loaded and pin-loaded specimens, see Fig. 2, where the J-values for plotting are computed at the center-plane (the deepest point on the crack front). The pin-loaded specimen has a greater bending load and thus exhibits a higher failure probability at the same J-level
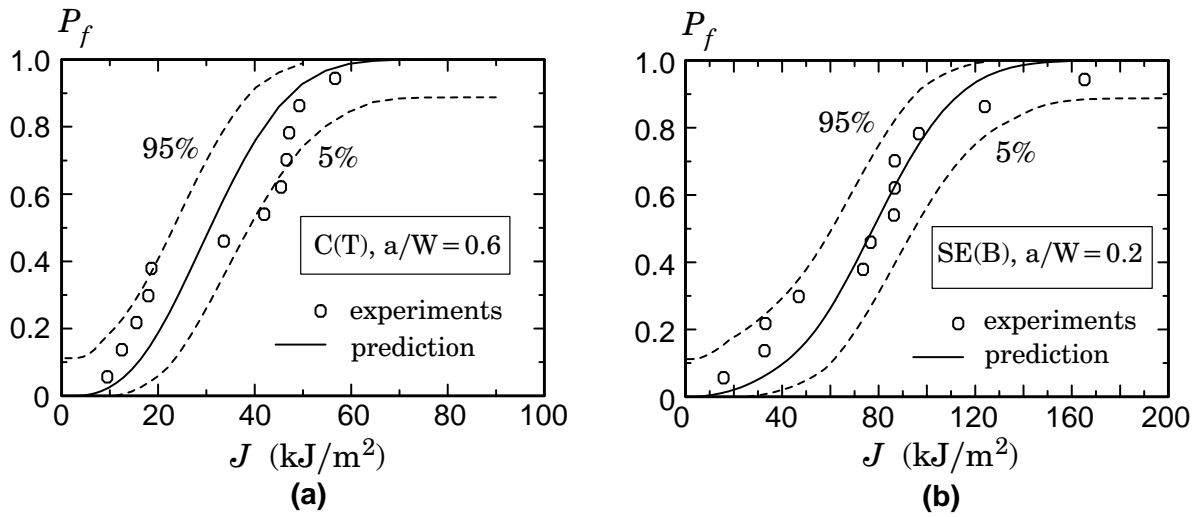
Fig. 1. Comparison of predicted cleavage probabilities (solid lines) with rank probabilities for measured J_c-values (symbols). The dashed lines represent the 90% confidence limits for the median rank probabilities. (a) deep-notch C(T) specimens; (b) shallow-notch SE(B) specimens.

compared to the bolt-loaded specimen. Fig. 2 shows two curves for the predicted failure probabilities of the bolt-loaded specimens. In Eq. (2), the principal stress (σ_1) value appearing in the Weibull stress integral can be assigned the current value at the loading level (J) or the maximum value experienced by the material point during the loading history. Of the four crack configurations examined in this work, the choice of σ_1 definition makes a difference only for the bolt-loaded surface crack specimen as shown. Consequently, the calibrated values of m, σ_u and $\sigma_{w\text{-}min}$ do not depend on the choice of σ_1 definition. Constraint loss in the bolt-loaded configuration leads to a slight decrease in near-front stresses under large scale yielding, and thus use of the maximum σ_1 values raises the failure probability. Stresses have smaller values under large scale yielding but the process zone volume for cleavage continues to grow with crack front blunting which leads to monotonically increasing failure probabilities. The prediction that includes the history effect provides a slightly better agreement with the experimental data for this very low constraint configuration.
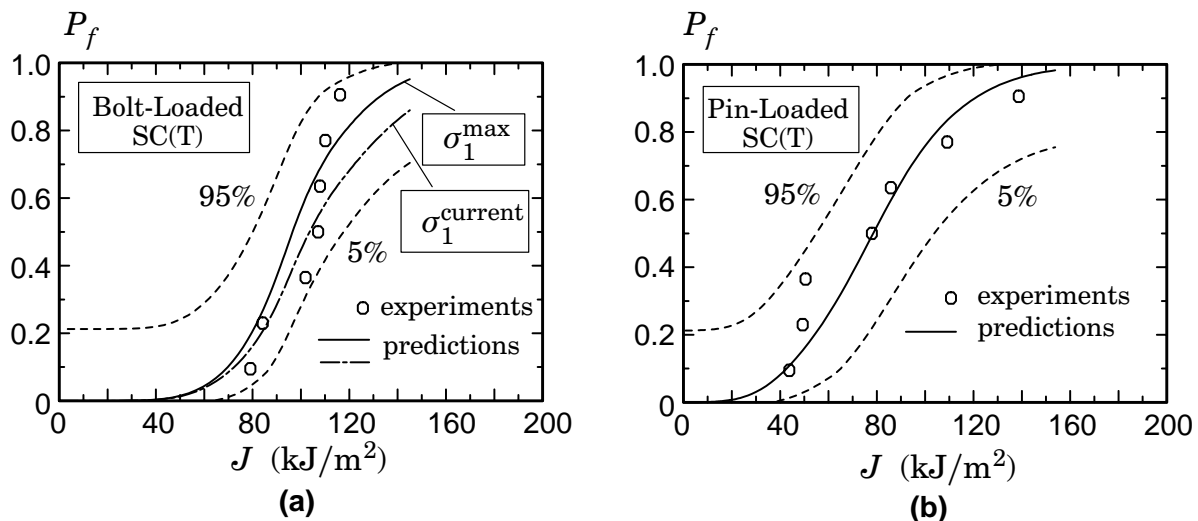
Fig. 2. Comparison of predicted toughness distributions (solid lines) for both bolt-loaded and pin-loaded SC(T) specimens with experimental data. The symbols represent rank probabilities for the measured J_c-values and the dashed lines represent the 90% confidence limits for the rank probabilities. (a) bolt-loaded specimens; (b) pin-loaded specimens.

5. CONCLUDING REMARKS

This work applies recent developments in the Weibull stress model to predict cleavage fracture in an A515-70 pressure vessel steel. The procedure to calibrate the Weibull stress parameters builds

upon the toughness scaling model between two crack configurations having different constraint levels and exhibits very strong sensitivity to m. It eliminates the recently discovered non-uniqueness that arises in calibrations which use only deep-notch SE(B) or C(T) data. The calibrated Weibull modulus for the A515-70 steel at -7°C is $m = 11.2$. The introduction of a non-zero threshold value for Weibull stress ($\sigma_{w-\min}$) in the expression for cumulative failure probability reflects an approximate treatment of the conditional probability of propagation in the DBT region and is consistent with the experimental observations that there exists a minimum toughness value for cleavage fracture in ferritic steels. It brings numerical predictions of the scatter in fracture toughness data into better agreement with experiments. Calibration of the threshold Weibull stress makes use of the generally accepted, minimum toughness value for ferritic steels and requires no additional experimental effort. The calibrated three parameter Weibull stress model accurately predicts the toughness distributions for all specimen configurations and captures the strong constraint effect on cleavage fracture due to differences in crack geometry and loading mode (bending *vs*. tension).

REFERENCES

1. Wallin, K. (1984). The scatter in K_{Ic} results. *Engineering Fracture Mechanics*, **19**, 1085–1093.

2. Sorem, W.A., Dodds, R.H. and Rolfe, S.T. (1991). Effects of crack depth on elastic-plastic fracture toughness. *International Journal of Fracture*, **47**, 105–126.

3. Beremin, F.M. (1983). A local criterion for cleavage fracture of a nuclear pressure vessel steel. *Metallurgical Transactions*, **14A**, 2277–2287.

4. Ruggieri, C. and Dodds, R.H. (1996). A transferability model for brittle fracture including constraint and ductile tearing effects: a probabilistic approach. *International Journal of Fracture*, **79**, 309–340.

5. Gao, X., Ruggieri, C. and Dodds, R.H. (1998). Calibration of Weibull stress parameters using fracture toughness data. *International Journal of Fracture*, **92**, 175–200.

6. Gao, X. and Dodds, R.H. (2000). Constraint effects on the ductile-to-brittle transition temperature of ferritic steels: a Weibull stress model. *International Journal of Fracture*, **102**, 43–69.

7. Minami, F., Bruckner-Foit, A., Munz, D. and Trolldenier, B. (1992). Estimation procedure for the Weibull parameters used in the local approach. *International Journal of Fracture*, **54**, 197–210.

8. American Society for Testing and Materials, Philadelphia (1998). Test Method for the Determination of Reference Temperature, T_0, for Ferritic Steels in the Transition Range (ASTM E-1921).

9. Gao, X., Dodds, R.H., Tregoning, R.L., Joyce, J.A. and Link, R.E. (1999). A Weibull stress model to predict cleavage fracture in plates containing surface cracks. *Fatigue and Fracture of Engineering Materials and Structures*, **22**, 481–493.

10. Ruggieri, C., Gao, X. and Dodds, R.H. (2000). Transferability of elastic-plastic fracture toughness using the Weibull stress approach: significance of parameter calibration. *Engineering Fracture Mechanics*, **67**, 101–117.

11. Anderson, T.L., Stienstra, D. and Dodds, R.H. (1994). A theoretical framework for addressing fracture in the ductile-to-brittle transition region. In *Fracture Mechanics: 24th Volume, ASTM STP 1207* (Edited by J.D. Landes, D.E. McCabe and J.A. Boulet). American Society for Testing and Materials, Philadelphia, 186–214.

12. Bakker, A. and Koers, R. W. J. (1991). Prediction of cleavage fracture events in the brittle-ductile transition region of a ferritic steel. In *Defect Assessment in Components – Fundamentals and Applications, ESIS/EG9* (Edited by Blauel and Schwalbe), Mech. Engng Publications, London, 613-632.

13. Xia, L. and Shih, C. F. (1996). Ductile crack growth – III. Transition to cleavage fracture incorporating statistics. *J. Mech. Phys. Solids* **44**, 603–639.

14. Joyce, J.A. and Link, R.E. (1996). Ductile-to-brittle transition characterization using surface crack specimens loaded in combined tension and bending. In *Fracture Mechanics: 28th Volume, ASTM STP 1321* (Edited by J.H. Underwood, B.D. Macdonald and M.R. Mitchell). American Society for Testing and Materials, Philadelphia, 243–262.

RECONSTRUCTION OF FRACTURE PROCESS OF SPHEROIDAL GRAPHITE CAST IRON BY ANALYZING THE CONFOCAL SCANNING LASER MICROSCOPE IMAGES

Yasuhiko Mori[1], Yoshihiko Obata[1], Shuichiro Nose[1]
P. Kriengsak[2] and Takateru Umeda[2]

[1]College of Industrial Technology, Nihon University, Chiba 275-8575, Japan
[2]Faculty of Engineering, The University of Tokyo, Tokyo 113-8656, Japan

ABSTRACT

In order to investigate the reason of low notch sensitivity in the strength of cast iron, tensile tests and acoustic emission measurements were conducted on the notched bar specimens of pearlitic spheroidal graphite cast iron. The fracture process occurred inside the material was reconstructed by the computer aided image processing for the topography of conjugate areas of the fracture surfaces observed by a confocal-optics-based scanning laser microscope. Reconstructed fracture process revealed that crack initiation and growth started in the middle of the specimen. Initial microcrack was created in the matrix around a graphite nodule. Acoustic emission onset load level, i.e., microfracture onset load level was approximately 90 % of the failure strength of the specimen, and the generation of acoustic emission was continuously observed until specimen rapture. As the load was increased, debonding occurred at the graphite/matrix interface, and coalesced with an initial microcrack to form a crack. Increasing load further caused slight growth of the crack in the matrix, and microcracks formation around the graphite nodules located near or ahead of the crack front. Thus, the crack growth in the specimen resulted from the repeated process of microcrack formation around the graphite nodule, growth, and coalescence to form a main crack. This study visually demonstrates that the graphite nodule acts as internal crack under the tri-axial stress state.

KEYWORD

fracture process, cast iron, notch effect, graphite, internal crack, scanning laser microscope

INTRODUCTION

It is known that the cast iron shows the low notch sensitivity in the strength [1]. The strength of the cast irons, however, depends on the sample shape or ductility of the materials. For instance, in the case of the bar specimen, it has been reported that the existence of notch had little influence on the strength [2] or on the contrary, increased the strength [3, 4]. Several models have been proposed for the explanation of this low notch sensitivity, such as the effect of the ununiformity of stress distribution around the notch root [3, 5, 6], or the internal notch effect of graphite nodule distributed in the matrix [7]. However, the detail of the fracture behavior occurred in the material has not been clarified. Therefore, the observation and analysis of the fracture process occurred inside the material is desired to give an answer for the reason of low notch sensitivity.

Kobayashi, et al. [8] has developed a fracture surface topography analysis technique, FRASTA, which combines a confocal-optics-based scanning laser microscope (SLM) and computer software to match three-dimensional features of conjugate fracture surfaces and reconstruct detailed fracture processes that occurred inside the material. Authors also have developed a technique, which can reconstruct the fracture process in microscopic detail, by using the computer aided image processing for the topography of conjugate fracture surfaces obtained by a SLM.

In the present paper, tensile tests and acoustic emission measurements were conducted on the bar specimens of pearlitic spheroidal graphite cast iron. SLM technique was applied for the broken sample to examine how the graphite nodules in the matrix contributed to the fracture process in the material. Actual dynamic fracture events occurred in the sample were estimated by the acoustic emission signals. This paper describes an attempt to seek an explanation for the reason of low notch sensitivity in the strength of the material tested and proposes a fracture model around the graphite nodule.

EXPERIMENTAL

The material used was a pearlitic spheroidal graphite cast iron, having retained pearlite of 98.9 %, nodularity of graphite of 81 %, graphite area of 9.5 %, graphite nodule per area of $244/mm^2$, and mean graphite nodule of 22 micron.

Smooth bar with diameter of 6 mm and circumferentially notched bars with outer diameter of 10 mm were stressed and fractured in tensile. Shape of notches were U- and V-type, and these elastic stress concentration factor of notches, α, were evaluated to be 2.0 and 3.8, respectively.

Tensile test results showed that every type of specimens ruptured in rectangular fracture. Fracture strength (= tensile strength) of the smooth bar specimen was 940 MPa, showing the elongation of 6.6 %. Fracture strength of V-notched (α=3.8) specimen was 880 MPa. On the other hand, the sample failure of the U-notched specimen (α=2.0) occurred at a stress of 980 MPa, which exceeded the tensile strength of the smooth specimen by approximately 4 %.

Figure 1 shows the applied stress, σ, and the cumulative counts of AE events, N, as a function of elapsed time of tensile test, t, for the U-notched specimen. Stress applied increases continuously until the specimen rupture took place. Acoustic emissions start at stress level about 90 % of the fracture strength of the specimen and increase continuously until the specimen rupture.

Fracture surface analysis by using a scanning electron microscope (SEM) showed that in the case of the V-notched specimen, fracture initiated at the notch root. This resulted in the decrease in its strength from the strength of smooth specimen. In the case of U-notched specimen, however, the traces of crack initiation site were not clearly left on the fracture surface. So the fracture process occurred inside the U-notched specimen was reconstructed and analyzed by using SLM technique.
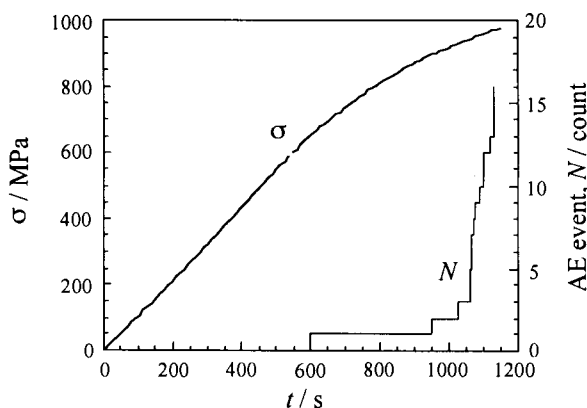
Figure 1: Applied stress, σ, and AE event counts, N, as a function of the testing time, t. U-notched specimen.

RECONSTRUCTION OF FRACTURE PROCESS

Figure 2 shows the macroscopic features of conjugate fracture surfaces of the U-notched sample. SLM observations were performed on the five locations on the conjugate surfaces, which are labeled I to V in Figure 2, because of the limitation of SLM field of view.

Figure 3 shows scanning-laser micrographs and corresponding gray-scale image topographs of conjugate fracture surfaces of the area location III in figure 2. Scanning-laser micrographs show that the graphite nodules are individually distributed in the matrix. Gray-scale images of the fracture topography of the conjugate fracture surfaces in the bottom of Figure 3 show that lighter areas are higher in elevation than darker areas.
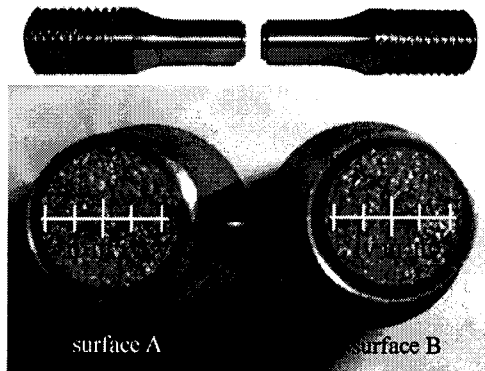
Figure 2: Macroscopic fracture surfaces of U-notched specimen broken in tensile.

surface A   surface B   50 μm
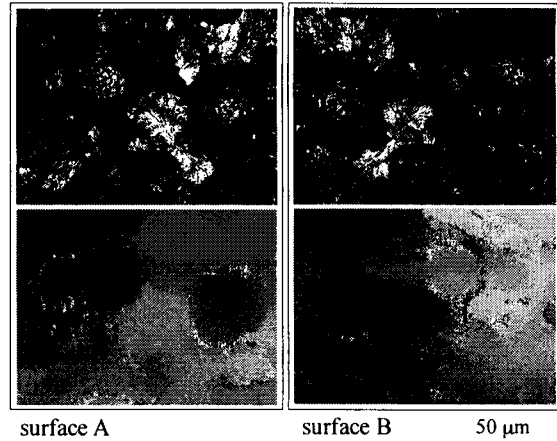
Figure 3: Scanning-laser micrographs, top, and corresponding topographs, bottom, of conjugate fracture surfaces of the location III in Figure 2.

The fracture process of this area was reconstructed using topographic information from Figure 3 (bottom) in digitized form. Maximum elevation resolution is 0.03 μm which is determined by dividing a specified range, i.e., the difference in elevation between the highest and lowest point within the observation field, by 256. Reconstruction of fracture process is accomplished by the following procedure. (1) Matching the three-dimensional features of conjugate fracture surfaces in a direction vertical to the specimen axis with the aid of a computer (Figure 4a through 4d). This makes a reference state (Figure 4d) for the successive procedure. If the surface irregularity, i.e., an elevation profile on the fracture surface is caused only by interaction of the crack tip with the microstructure and without inelastic deformation, the conjugate surface profiles should match precisely. Any mismatch appearing as overlap between the conjugate surface profiles indicates inelastic deformation (Figure 4d). (2) Separating the two surface irregularities from a

(a) conjugate surface irregularities

(b)

(c)
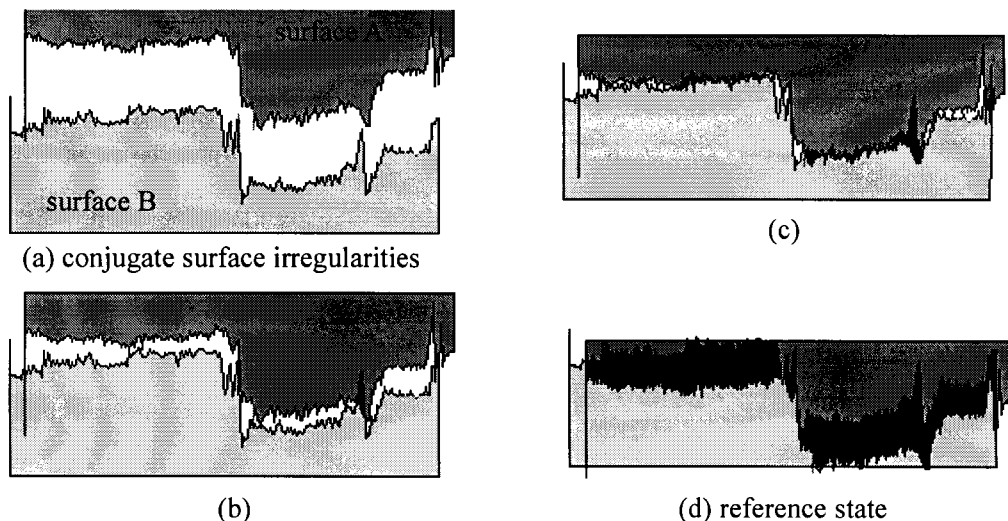
(d) reference state

Figure 4: Procedure of fracture process reconstruction, showing conjugate surface irregularities in two-dimension. Matching process, (a) through (d); reconstruction of fracture process, (d) through (a).

matching reference state in a direction vertical to the specimen axis using computer software (Figure 4d through 4a). Displacement of the separation (ds) is increased step-by-step at a certain increment. Gaps, which appeared between the two surface irregularities in this sequential process, are projected on display equipment.

Figure 5 is a result of fracture process reconstructed for the location III shown in Figure 2, showing the step-by-step development of the fracture. Black areas, where the conjugate surface profiles overlap, denote intact material. White areas, where the surface profiles do not overlap, are considered locations where the fracture surfaces are separated, i.e., cracked. Projection diagrams of fractured areas show that cracking initiated in the matrix around graphite nodules (Figure 5a). As the applied stress is increased (see Figure 1), i.e., as the conjugate fracture surfaces are displaced relative to one another, as denoted as "ds" in Figures 5, microcracks grow slightly, debonding starts at the graphite/matrix interface (Figures 5b and 5c). Increasing the stress further causes coalescence of microcracks (Figure 5d) and development in the matrix forming a crack (Figure 5e).

SLM image   (a) ds=20 μm   (b) ds=40 μm

(c) ds=60 μm   (d) ds=80 μm   (e) ds=100 μm
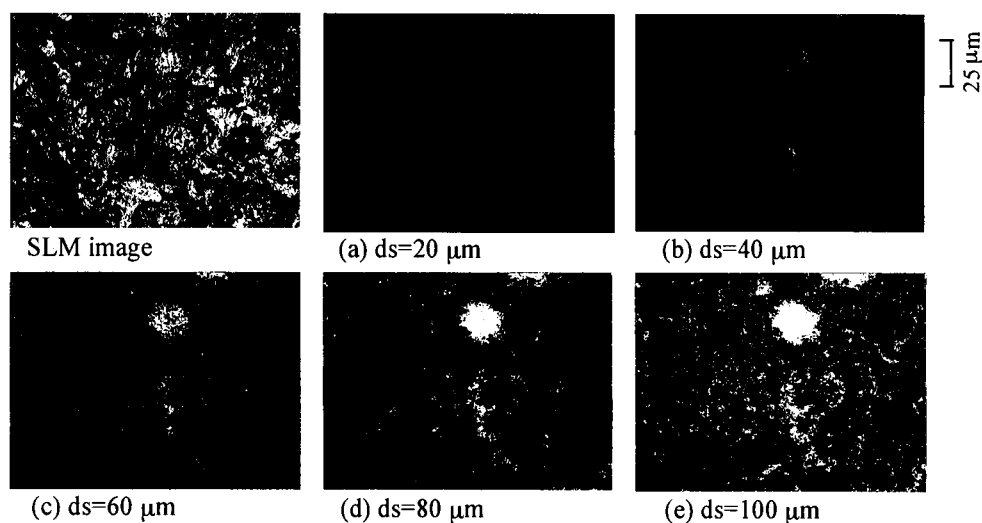
Figure 5: Scanning-laser micrograph, left top, and a series of projection diagrams of fractured areas, (a) to (e), of the location III shown in Figure 2.

In order to estimate the entire fracture process occurred in the specimen, fracture process for the locations I to V shown in Figure 2 were reconstructed with a same reference state. The reference state, that is, the state of the specimen before loading, was found in the location III, at which the matching of the conjugate surface profiles was completed. A series of fractured area projection diagrams in Figure 6 show the step-by-step development of the fracture. The reference state is the top of location III (center of the specimen) in the diagram. This result clearly demonstrates that as the stress is applied, microcrack initiates at around the graphite nodules distributed in the middle of the specimen (location III), as seen in Figure 5 in detail. With increasing the stress further, the microcracks are also created successively at the graphite nodules in the locations of II, I, IV and V. Then crack is formed by the coalescence of these microcracks and grows outward (toward the notch root of locations I or V), and specimen rupture takes place.

The displacement, ds, associates with the applied stress level, since the stress continuously increased until the specimen failure, as seen in Figure 1. In addition, acoustic emissions started at stress level about 90 % of the fracture strength of the specimen and increased continuously until the specimen rupture. Therefore, the fracture process shown in Figure 6 suggests for certain that crack initiation and growth started in the interior of the specimen. From the acoustic emission measurement, the nominal stress level of crack initiation was estimated to be approximately 850 MPa (Figure 1).

In this fracture process, the graphite nodule in the matrix behaves as void or pore in the typical ductile materials stressed in tensile. A model shown in Figure 7 could be proposed to explain the fracture process around the spheroidal graphite nodule. As the material (Figure 7a) is stressed in tensile and the stress reaches at a critical level, microcrack initiates in the part of matrix around graphite nodule (Figure 7b). Such Saturn's rings shape crack perpendicular to the stress axis could be created in the case, where the bonding between the graphite/matrix interface is not so rigid under the tri-axial stress state. As the stress
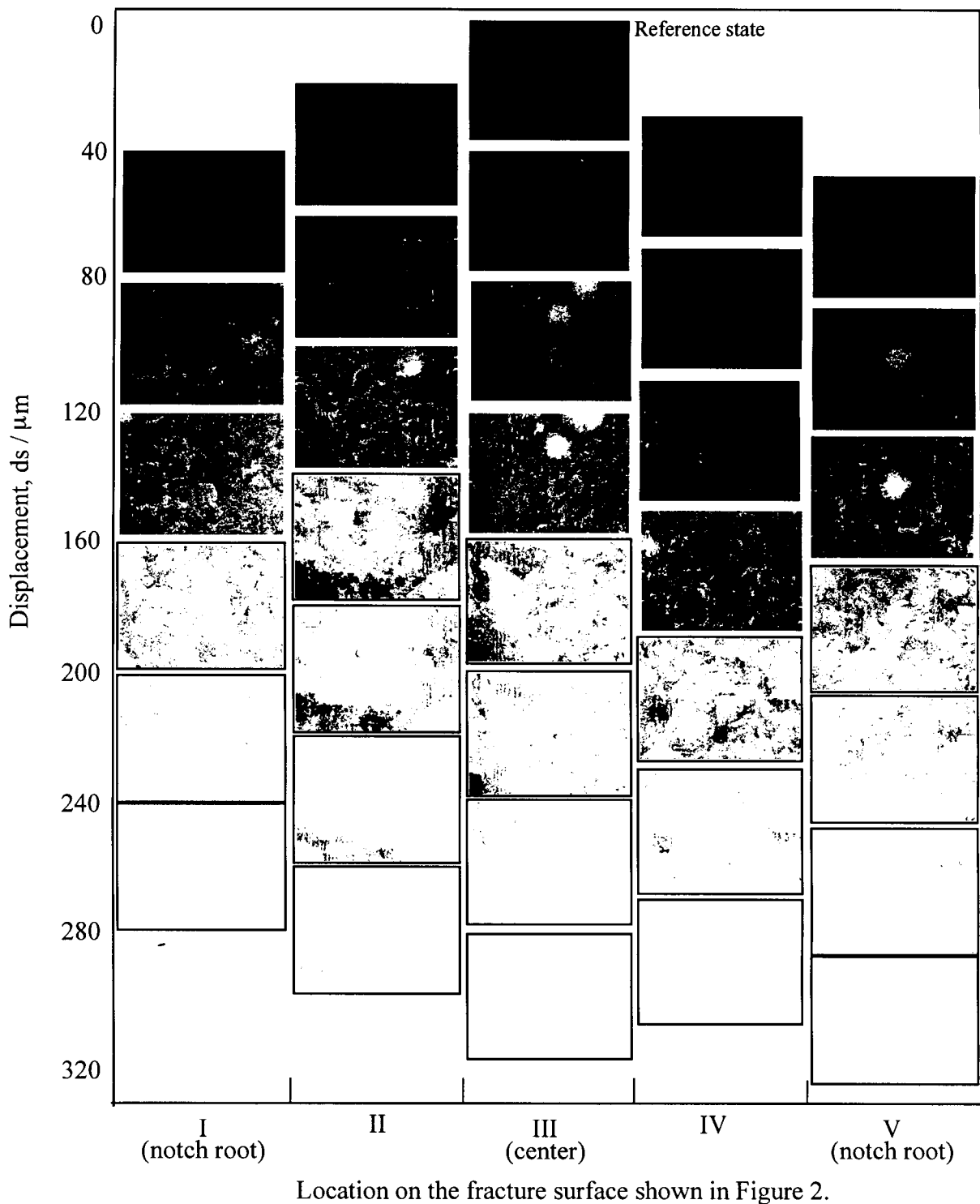
Figure 6: Fractured area projection diagrams for the locations I to V shown in Figure 2. Reconstructions of fracture process were performed with a same reference state.
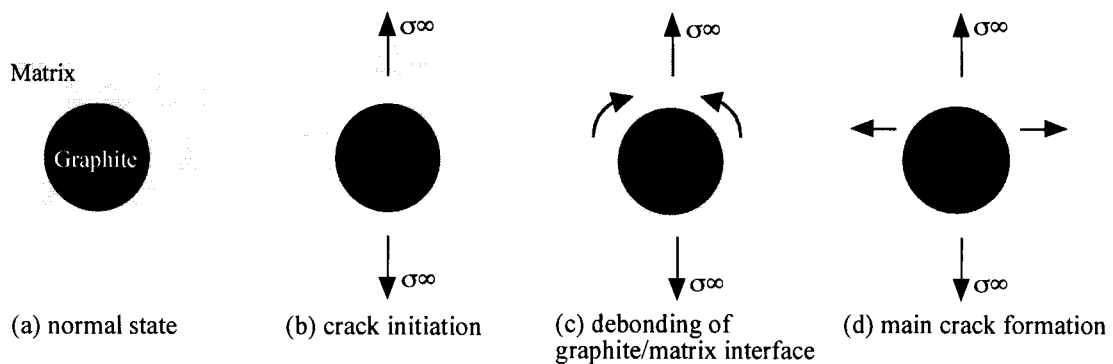

(a) normal state   (b) crack initiation   (c) debonding of graphite/matrix interface   (d) main crack formation

Figure 7: Model of fracture process occurred around the spheroidal graphite nodule.

is increased further, the debonding starts at the graphite/matrix interface, so that the ring shape crack merges into a crack (Figures 7c), then the crack grows into the matrix, forming a main crack (Figure 7d).

Cross sectional views of the fractured specimen observed by a scanning electron microscope are shown in Figure 8. Trace of the main crack shown in Figure 8a shows that the crack path twists around the surfaces of graphite nodules. Internal crack initiated from a graphite nodule, as shown in Figure 8b, is also found near the main crack path. These observations support the validity of the model proposed in Figure 7.

| (a) surface of main crack | (b) crack observed near the main crack |
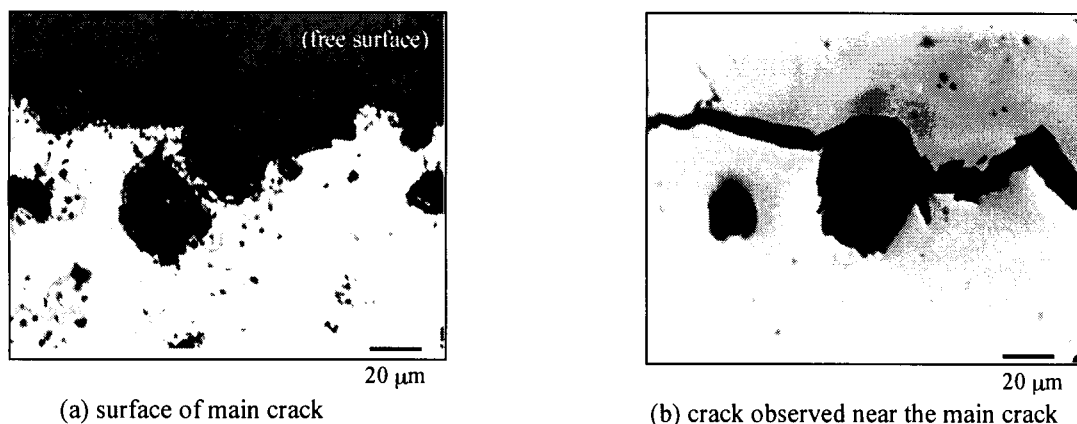
Figure 8: Cross sectional views of the fractured sample.

SUMMARY

Regarding the reason of low notch sensitivity in the strength of cast iron, tensile tests and acoustic emission measurements were conducted on the notched bar specimens of pearlitic spheroidal graphite cast iron, and the fracture process occurred inside the material was reconstructed by the computer aided image processing for the topography of conjugate areas of the fracture surfaces observed by a confocal-optics-based scanning laser microscope.

Reconstructed fracture process revealed that crack initiation and growth started in the middle of the specimen. Initial microcrack was created in the matrix around a graphite nodule at a stress level of approximately 90 % of the specimen failure strength, which was estimated by the acoustic emission.

A model, which explains the fracture process occurred around the spheroidal graphite nodule under the tri-axial stress state, was proposed.

This study visually demonstrates that the graphite nodule acts as internal crack under the tri-axial stress state, and the strain energy release or redistribution of the internal stress due to this internal crack effect contributes to the elevation of the strength of notched specimen.

REFERENCES

1. A. F. S. (1957). *Cast Metal Handbook*. Des Plaines, Illinois, p. 92.
2. Nakanishi, F. and Okamoto, S. (1951). *Transaction of the Japan Society of Mechanical Engineering*, 17, 103.
3. Noguch, T. (1980). *J. The Society of Materials Science, Japan*, 29, 387.
4. Kriengsak, K., Satoh, K., Mori, Y., Paritud, B. and Umeda, T. (1995). *Proc. of the 3rd. Asian Foundry Congress*, pp. 296-303, The Korean Foundrymen's Society.
5. Noguchi, T. (1988). *Transaction of the Japan Society of Mechanical Engineering*, A, 54-507, 1962.
6. Takao and Nisitani. (1987). *J. The Society of Materials Science, Japan*, 36, 1060.
7. Ishibasi, T. (1952). *Transaction of the Japan Society of Mechanical Engineering*, 18, 87.
8. Kobayashi, T. and Shockey, D. A. (1987). *Metallurgical Transactions A*, 18A, 1941.

Relationship Between Rockwell C Hardness and Inelastic Material Constants

Akihiko Hirano[1], Masao Sakane[2] and Naomi Hamada[3]

[1] Department of Automotive Engineering Faculty of Junior College of Automotive Industry,
Osaka Sangyo University, Junior College
3-1-1, Nakagaito, Daito-shi, Osaka, 574-8530, Japan
[2] Department of Mechanical Engineering, Faculty of Science and Engineering,
Ritsumeikan University
1-1-1, Nojihigashi, Kusatsu-shi, Shiga, 525-8577, Japan
[3] Department of Mechanical Engineering, Hiroshima Kokusai Gakuin University
16-21, Nakano, Aki-ku, Hiroshima-shi, Hiroshima, 739-0321, Japan

ABSTRACT

This paper describes the relationship between Rockwell C hardness and elastic-plastic material constants by using finite element analyses.   Finite element Rockwell C hardness analyses were carried out to examine the effects of friction coefficient and elastic-plastic material constants on the hardness.   The friction coefficient and Young's modulus have no influence on the hardness but the inelastic materials constants, yield stress and strain hardening coefficient and exponent, have a significant influence on the hardness.   A new equation for predicting the hardness was proposed as a function of yield stress and strain hardening coefficient and exponent.   The equation evaluated the hardness within a $\pm 5\%$ difference for all the finite element and experimental results.

KEYWORDS

FEM analisis, Rockwell C hardness, Inelastic constitutive relationship, Strain hardening coefficient, Strain hardening exponent

INTRODUCTION

Hardness testing is one of the most frequent to material testings and is understood as a testing to measure the resistance to compressive permanent deformation.   However, the physical meaning of hardness has been an open question.   Especially, inelastic material contains are supposed to have some connection but a quantitative   relationship has not been well defined.   Experimental studies tried to obtain the quantitative relationship between the materials constants and hardness using many different materials that have different tensile properties, but they did not succeed because every material constant changes when using a different material [1].   To develop a quantitative relationship, an analytical method of changing only a specific material constant is needed keeping the other constants unchanged.   Recent development finite element (FE) contact analysis enables this .   The authors applied this approach to Brinell hardness and proposed a quantitative relationship [3].   Rockwell C hardness (HRC), however, is a representative hardness testing and a quantitative equation has been also needed. This paper studies the relationship between Rockwell C

hardness and the elastic-plastic material constants using finite element analyses. Finite element contact analyses were made by varying yield stress and strain hardening coefficient and exponent. Based on the quantitative relationship between HRC and those material constants, an equation predicting the hardness from the material constants well be proposed. The accuracy of the equation well be discussed by comparing the hardness between the prediction, FE analysis and experiments.

RESULTS AND DISCUTION
Finite Element Model
Figure 1 shows the FE meshes used for the analysis. An axi-symmetric 2D isoparametric 4-nodes element was used to obtain the relationship between HRC and the inelastic material constants, Figure 1 (a).
The same mesh was used for analyzing the critical thickness for the hardness testing. An isoparametric 3D 8-nodes element was used for the analysis of the critical distance from specimen edge, Figure 2 (b). A quarter part of a whole model was meshed in 3D analysis from the symmetry of the model. The circular

| (a) 2D mesh | (b) 3D mesh |
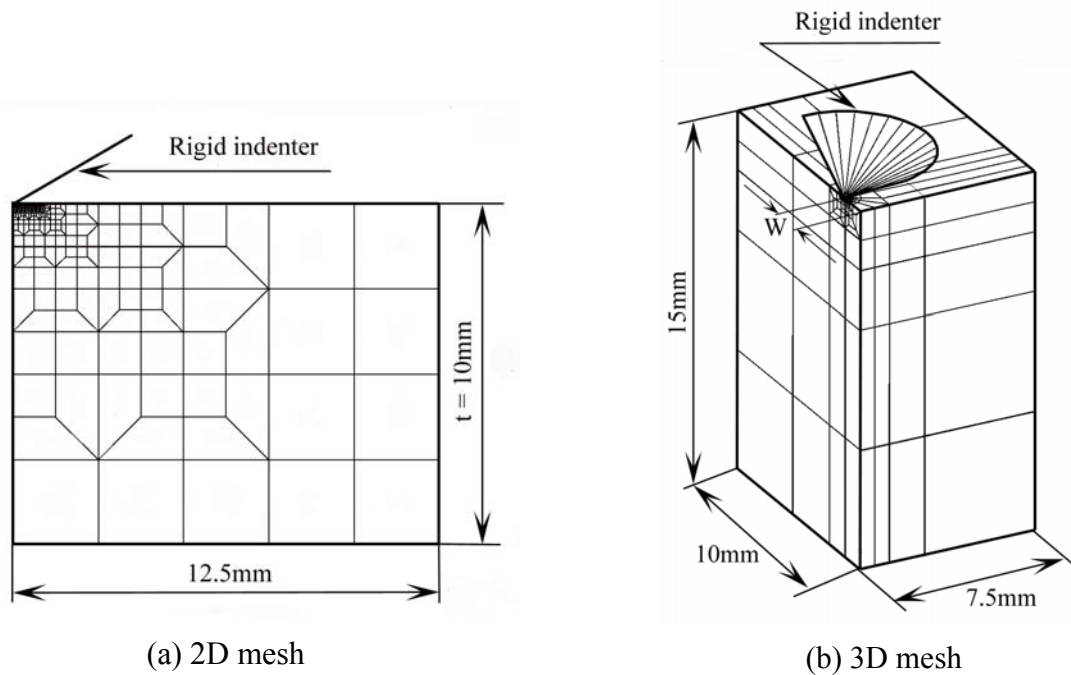
Fig.1 FEM meshes used for analyses.

conical indenter with a flank angle of 120 degrees and 0.2 mm tip radius was modeled to a rigid body in both meshes based on the previous result that the elastic deformation of the indenter has no effect on Brinell hardness [3]. The numbers of nodes and elements are 773 and 727 in the 2D mesh, and those of nodes and elements are 3785 and 2136 in the 3D mesh, respectively. Thickness, t, in Figure 1 (a) was changed from 0.156 mm to 5.00 mm and the edge distance, w, in Figure 1 (b) from 0.45 mm to 5.00 mm.

In FE analysis, load of 98 N was initially applied, increased to the maximum value of 1471 N and decreased to 98 N to simulate HRC testing. The relative indenter displacement (δ^*) between 98 N in loading stage and 98 N in unloading stage was analyzed to obtain HRC values. HRC values were calculated by $HRC = 100 - (\delta^* / 100)$.

MARC K6 was used as a FE code and MENTAT II as pre and post processors. True stress - logarithmic strain relationships were used in the FE calculation with large deformation, update and finite strain options [4]. Contact was judged when the indenter approached to the specimen in a distance less than 1.0×10^{-5} mm. The Coulomb friction below was employed to express a friction force in the analysis.

$$F = \mu \cdot W \qquad (1)$$

where F is the friction force, μ the friction coefficient and W the normal force at a contact point.

Effect of inelastic material constants on HRC

Effects of the friction coefficient and Young's modulus on HRC

Figure 2 shows an example of force – indenter displacement curve. The curve is approximated with a quadratic function as $P = a\delta^2 + b\delta + c$, where P is the load applied to the indenter and δ is the indenter displacement. In the Brinell analysis with a ball indenter, the curve was not quadratic but a linear relationship was found in the initial loading stage [2]. These results suggest that the type of indenter influences the shape of load – indenter curve.
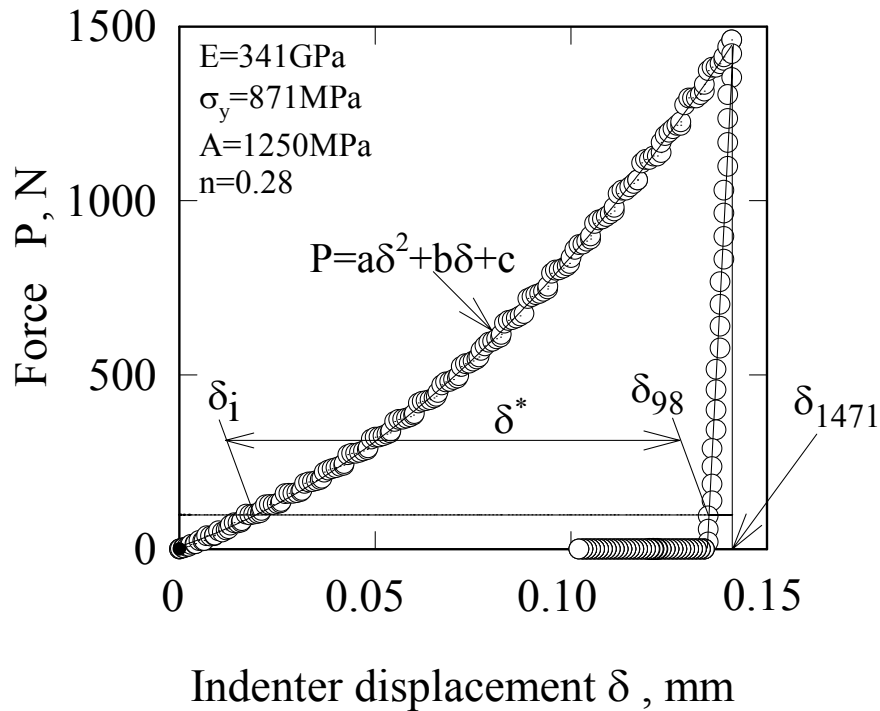
Fig.2 Relationship between penetration force and indenter displacement.

This study assumes the power law inelastic constitutive equation expressed below

$$\varepsilon_p = \left(\frac{\sigma - \sigma_y}{A}\right)^{\frac{1}{n}} \tag{2}$$

where ε_p, σ, σ_y, A and n are plastic strain, flow stress, yield stress and work hardening coefficient and exponent, respectively. These material constants of TAB6400 titanium alloy, INCONEL 718 nickel base superalloy and SCM 430 ferritic alloy are tabulated in Table 1 together with the hardness of those materials in FE analysis and experiments. The hardness in FE analysis is 7-8 % smaller than that in experiments for TAB6400 and INCONEL 718 that have relatively large yield stresses. However, the difference is only 2 % for SCM4320 where FE analysis gives a slightly smaller value than the experimental result. The satisfactory agreement shown in the table ensures the applicability of FE analysis to the simulation.

Table 1 Material constants and HRC in FE analysis and experiment.

	E, GPa	σ_y, MPa	A, MPa	n	HRC (Exp.)	HRC (FEM)	$\dfrac{\text{HRC(Exp.)}}{\text{HRC(FEM)}}$
TAB6400	105	870	694	0.411	33.3	31.0	1.07
INCONEL718	341	871	1250	0.280	44.2	41.0	1.08
SCM430	164	390	1053	0.217	25.6	25.0	1.02
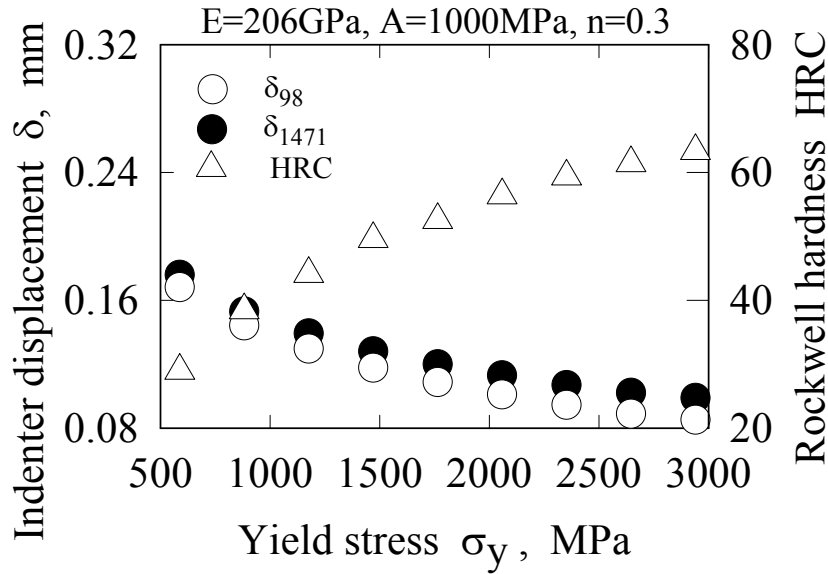
Fig.3 Variations of indenter displacement and hardness with yield stress.
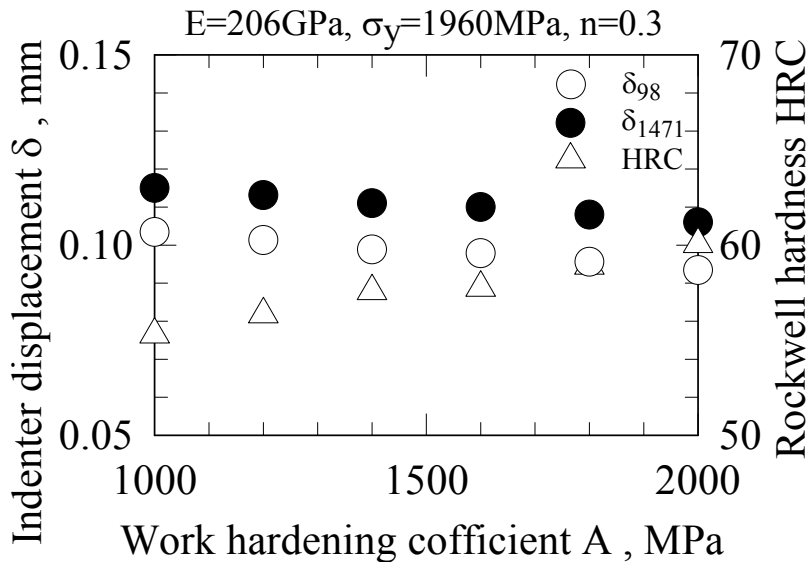
Fig.4 Variations of indenter displacement with strain hardening coefficient.

The variation of the hardness with yield stress is plotted in Figure 3 for E=206 GPa, A=1000MPa and n=0.3. The indenter displacements decrease with increasing yield stress and HRC increases accordingly.   Yield stress has a significant effect on the hardness.   Figure 4 depicts the effect of the strain hardening coefficient on HRC for E=206GPa, $\sigma_y = 1960\,\text{MPa}$ and n=0.3.   The indenter displacements linearly decrease with increasing A and HRC increases with increasing A.

Figure 5 plots the effect of strain hardening exponent on the relative indenter displacement δ^* for respective σ_y and A denoted in the figure.   The relative displacement linearly increases with increasing the exponent for all the cases shown in the figure.   The displacement takes smaller values at smaller σ_y and smaller A.   Since HRC inversely related with the relative displacement, HRC takes smaller values at smaller σ_y, smaller A and smaller n.

Quantitative formulation of HRC with inelastic material constants
As shown in Figure 5, the relative displacement δ^* can be equated as a linear logarithmic function of n, so the relationship is expressed as

$$\delta^* = 10^{\beta} n^{\alpha} \tag{3}$$

A \ σ_y	588	1764	3727
800	○	●	⊕
1000	△	▲	▲
1200	▽	▼	▼
1400	□	■	⊞
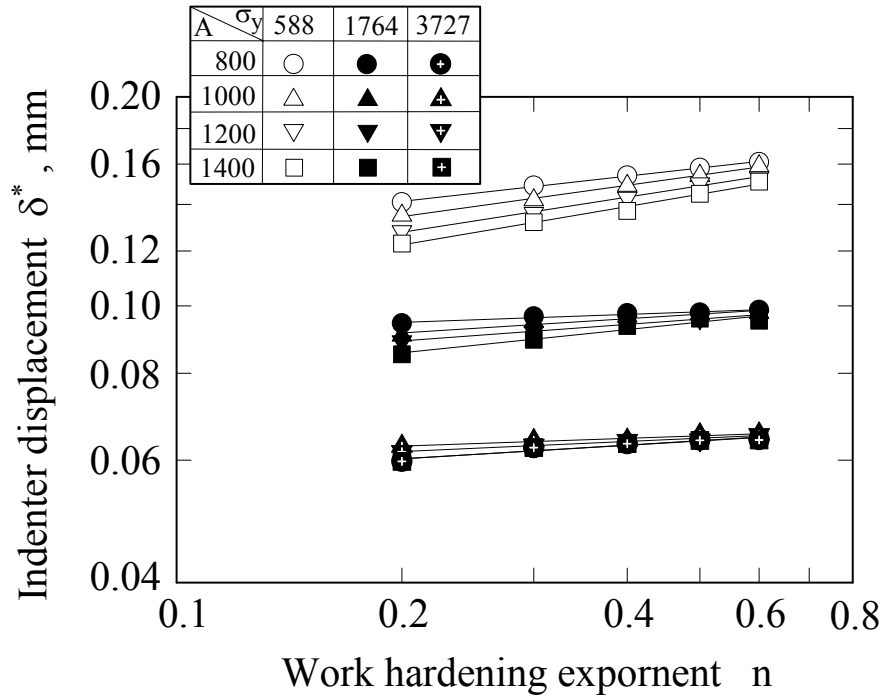
Fig.5 Variation of indenter displacement with strain hardening exponent.

α and β are a function of σ_y and A.

The constants α and β are equated as

$$\alpha = 1.55\times10^{-8}\sigma_y^2 - 8.178\times10^{-5}\sigma_y + (1.09\times10^{-4}A + 0.646) \tag{4}$$

$$A : \text{MPa}, \quad \sigma_. : \text{MPa}$$

The exponent in equation(3) is only a function of and is expressed with a quadratic equation.

$$\beta = 2.270\times10^{-8}\sigma_y^2 - 2.246\times\sigma_y - 0.6642 \tag{5}$$

$$\sigma_. : \text{MPa}$$

Substituting Eq. (4) and (5) into Eq. (3) gives the relationship between the relative displacement δ^* and the inelastic material constants as,

$$\delta^* = 10^{2.270\sigma_y^2 - 2.246\times10\sigma_y - 0.6642} \cdot n^{1.155\times10^{-8}\sigma_y^2 - 8.178\times10^{-5}\sigma_y + (1.09\times10^{-4}A + 0.646)} \tag{6}$$

Figure 6 compares the predicted HRC by Eq.(6) with the FE results.   In the figure, the hardness of the three materials is superimposed of which the predicted values are calculated using Eq. (6) from the inelastic material constants listed in Table 1.   All the hardnesses including the experimental results are correlated within a narrow scatter band of a factor of 1.05.   In the correlation in Figure 6, the inelastic material constants are ranged from 588 to 3727 MPa for σ_y, from 800 to 1440 MPa for A and 0.2 to 0.6 for n. These ranges mostly cover the actually existing materials suitable for HRC testing.   Thus, Eq.(6) is an appropriate equation for predicting HRC from the inelastic material constants for a wide range of matrials. Eq.(6) also indicates that how the inelastic material constants, yield stress and strain hardening coefficient and exponent, influence HRC value quantitatively.

CONCLUSIONS
1.   Friction coefficient has no influence on Rockwell C hardness.
2.   The maximum indenter displacement at 1471 N decreases with increasing Young's modulus.   However,
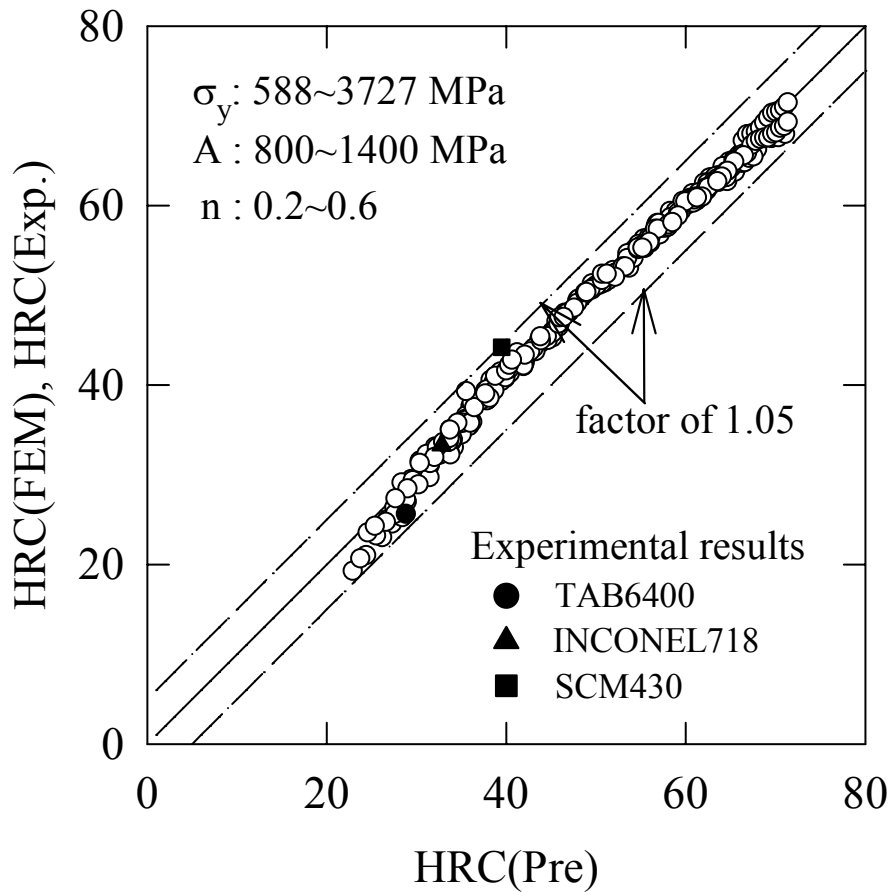
Fig.6 Comparison of HRC between FEM and experiment.

  Young's modulus has no influence on Rockwell C hardness.

3. Rockwell C hardness increases with increasing yield stress and strain hardening coefficient. The hardness increases with decreasing strain hardening exponent.

4. Relative indenter displacement δ^* at 98N between loading and unloading stages is equated with strain hardening exponent, n, as $\delta^* = 10^\beta n^\alpha$, where α and β are functions of yield stress and strain hardening coefficient A expressed below.

$$\alpha = 1.55 \times 10^{-8} \sigma_y^2 - 8.178 \times 10^{-5} \sigma_y + (1.09 \times 10^{-4} A + 0.646)$$

$$\beta = 2.270 \times 10^{-8} \sigma_y^2 - 2.246 \times \sigma_y - 0.6642$$

The equations predicted the FE and the experimental results within a factor of 1.05 in the hardness range between 20 and 70.

References

1.Yoshizawa, T.(1967), "*Hardness Testing and Its Applications*", Shokado Pub., Tokyo.
2. Japan Industrial Standards, JIS Z 2245 (1997) , " *Rockwell Hardness Test* ".
3.Hamada, N., and Sakane, M.(1999), *Trans. Japan Society of Mechanical Eng.*, A63, 254.
4.Marc (1995), "*Mark User Information K-6*", C3-177.

RESIDUAL STRENGTH ANALYSES OF SINGLE- AND MULTIPLE-STIFFENED PANELS

B. R. Seshadri [1] and J.C. Newman, Jr. [2]

[1] Research Associate Professor, Old Dominion University, Norfolk, Virginia, 23508, USA
[2] Senior Scientist, NASA Langley Research Center, Hampton, Virginia, 23681, USA

ABSTRACT

This paper presents a residual-strength methodology to predict the failure of single- and multiple-stiffened panels with single- and multiple-through cracks using the critical crack-tip-opening angle (CTOA, Ψ_c) fracture criterion. The critical CTOA value was obtained from tests and analyses of middle-crack tension specimens. To account for high constraint conditions around the crack tip, a "plane-strain" core option was used in the STAGS finite-element shell code analyses. Comparison of measured and predicted load-crack extension and local strain variation for the stiffened panels with either cut or intact stiffeners agreed well. Comparisons made at both the global and local levels indicate that by using two parameters: (1) critical CTOA to control crack extension and (2) a plane-strain core height to define the high-constraint region at the crack front, the residual strength of built-up structures could be accurately predicted (within 5%).

KEYWORDS

Fracture, CTOA, cracks, aluminum alloy, finite element method, plasticity, buckling

INTRODUCTION

Widespread fatigue damage is of concern to the aging commercial transport fleets because the residual strength of a fuselage with a large crack may be significantly reduced by the existence of smaller cracks at adjacent rivet holes, as postulated by Swift [1]. Tests on panels with long lead cracks and multiple-site damage (MSD) have shown that the presence of an array of small adjacent cracks strongly degrades residual strengths [2]. One of the objectives in the NASA Airframe Structural Integrity Program [3] was to develop the methodology to predict failure in damaged fuselage structures in the presence of widespread fatigue damage. The approach was to use a finite-element shell code with global-local, adaptive mesh capabilities and appropriate local fracture criteria to predict progressive failure in complex structures.

Stable crack extension in metallic materials has been studied extensively using elastic-plastic finite-element methods. These analyses were performed to study various fracture criteria. Of these, the crack-tip-opening angle (CTOA) or displacement (CTOD) criterion was shown to be the best suited for modeling stable crack extension and instability during the fracture process. By using high-resolution photographic camera with a video system, Dawicke et al. [4], have shown that the critical angles during stable crack extension in thin-sheet aluminum alloys were nearly constant after a small amount of tearing. Seshadri and Newman [5,6] have also used the finite-element method and the CTOA criterion to predict stable tearing in the presence of severe out-of-plane buckling for several aluminum alloys and a steel. In an effort to develop the methodologies required to predict the residual strength of complex fuselage structures with MSD, a series of tests and analyses have been performed from the coupon level to subscale fuselage simulation tests [6,7]. These series of tests were used to verify the residual-strength methodology based on the critical crack-tip-opening angle (CTOA) failure criterion.

EXPERIMENTS

NASA Langley and the FAA Hughes Technical Center jointly sponsored a series of fracture tests from laboratory specimens to wide stiffened panels with a lead crack and multiple-site damage (MSD) at many adjacent rivet holes [6]. The laboratory specimens and some of the wide panels were tested with anti-buckling guides. Various width compact tension, C(T), and middle-crack tension, M(T), specimens were tested (see Fig. 1). Fracture tests with a single crack, with or without MSD, were conducted with or without anti-buckling guides. A typical MSD crack configuration is shown in Figure 2. MSD crack sizes ranged from 0.25 to 1.3 mm. A series of 305-mm wide M(T) specimens with a central stiffener (intact or cut) was also tested without anti-buckling guides (Fig. 3). Wide panel tests were also conducted on 1016-mm wide panels with five riveted stiffeners (see Fig. 4). The stiffened panels were made of 2024-T3 sheet material (1.6-mm thick) with 7075-T6 stiffeners (2.3-mm thick). The wide panels were allowed to deform out-of-plane and buckle. Measurements were made of load, crack extension, applied end displacement, strain field in the crack-tip region, strains in the intact and broken stiffeners, and displacement fields (local and global).

Large M(T) panels (restrained against buckling) were tested to measure the critical CTOA on the 1.6-mm thick sheet 2024-T3 material during stable tearing and fracture. Two methods were used to measure CTOA: (1) the optical method (OM) [4] and the digital-imaging-correlation (DIC) method [8]. Critical CTOA values are plotted against crack extension in Figure 5. The open and solid symbols show measurements made on opposite sides of the large panels using the OM and DIC method, respectively. After a small amount of crack extension, the critical CTOA values were nearly constant. The average angle was 5.25 degrees (solid line). For small amounts of crack extension, large CTOA values are generally measured on the surface of the specimen, possibly due to severe crack tunneling. The determination of CTOA (5.4 deg., dashed line) that will be used with the STAGS code to predict stable crack extension and fracture will be discussed later.

ANALYSES

The fracture analysis of all laboratory specimens and the wide stiffened panels was made using the STAGS (STructural Analysis of General Shells) code [9] with the critical CTOA fracture criterion. The STAGS code, with the "plane-strain" core option [10], was used in all analyses. Previous analyses of wide, flat panels have shown that the high-constraint conditions around a crack front, like plane strain, have to be modeled in order for the critical CTOA fracture criterion to predict wide panel failures from small laboratory tests [6,7]. The through the thickness deformations around the crack-front region, even in thin-sheet materials, produce a high through the thickness stress, σ_z, which couples with the in-plane stresses, σ_x and σ_y, to greatly elevate the flow stress of the material (increase constraint).

Modeling of Sheet material, MSD, Stiffeners, and Rivets
The critical CTOA (Ψ_c) and the plane-strain core height (h_c) for the thin-sheet 2024 alloy were determined from failure loads on middle-crack tension specimens (no buckling). The fracture constants were then used with STAGS to predict the fracture behavior of C(T) specimens, M(T) specimens that were allowed to buckle, and flat stiffened panels. From previous parametric and convergence studies, it was found that a minimum crack-tip element size of 1-mm (linear-strain element) was sufficient to model stable tearing under elastic-plastic conditions. Crack extension was governed by monitoring the critical CTOA (Ψ_c) at 1-mm behind the crack tip. Rivet connectivity, rivet yielding, stiffener yielding, out-of-plane buckling, and stiffener-sheet contact behavior were modeled during the stable tearing process.

Determination of Critical CTOA and Plane-Strain Core Height
Load-crack-extension results from M(T) specimens (restrained from buckling) were used to determine the critical CTOA and plane-strain core height. Figure 6 shows the failure stress S_f against specimen width. The symbols show test results on specimens with crack-length-to-width ratios of 1/3. Using a critical angle of 5.4 degrees, the failure stresses predicted under plane-stress or plane-strain conditions are shown as the dashed or dash-dot curves, respectively. Neither plane-stress nor plane-strain analyses could capture the experimental trend. To account for high constraint in two-dimensional analyses, a plane-strain core region was defined around the crack tip [10]. The solid curve with the same critical angle and a plane-strain core height of 2 mm, captured the experimental trends very well. There is a small discrepancy between the average value

(5.25 deg.) and CTOA values used in the analyses (5.4 deg.), see Figure 5. There could be numerous reasons for this discrepancy. However, measurements and analyses tend to indicate that the critical CTOA is nearly constant for large amounts of stable tearing and for conditions of extreme plastic deformations.

Comparison of Out-of-plane Displacements

A series of wide panels were tested to demonstrate that the critical CTOA value obtained from laboratory specimens could be used to predict the residual strength of wide panels. A 1016-mm wide panel with a 338-mm crack was tested without anti-buckling guides. Crack extension was monitored at one crack tip and out-of-plane (w) displacements were measured on the other side of the panel using the digital-image correlation system. With increasing applied load, the material along the crack plane, which is under compressive stresses, tend to buckle outwards. A typical comparison between the measurements and the STAGS analyses is shown in Figure 7. The analysis results compare fairly well with the test data all along the crack plane.

FRACTURE ANALYSES OF STIFFENED PANELS

Results from the analyses of the 305- and 1016-mm wide stiffened panels are presented here. The specimens were strain gauged to measure sheet and stiffener strains (and load transfer) as a function of remote load and crack extension. Comparison between the tests and the analyses were made at both global and local levels.

Single Stiffener Specimens

The specimen with a single crack and intact stiffener is shown in Figure 3. Load-crack-extension values measured on a specimen with intact or cut stiffener are shown in Figure 8, as symbols. Because the configuration and loading were symmetric, only a quarter of the sheet and stiffener was analyzed. Results from the STAGS fracture analyses, using the critical CTOA and plane-strain core height, are shown as curves. The predicted results agreed well with the test data. In the analyses, the intact stiffener carried almost 50% of the total load, allowing the specimen with the intact stiffener to carry about 200 kN, and also preventing severe out-of-plane buckling. When the stiffener was cut, the specimen tended to buckle and the load carried by the cut stiffener was dumped near the crack region, causing a severe reduction in failure load.

The load carried by the intact stiffener against the applied load is plotted in Figure 9. The load carried by the stiffener was calculated from the strain-gauge reading. The predicted results (solid curve) agreed well with the measured results until the end of the test. Here the stiffener failed in the test, whereas in the analysis, failure of stiffener was not simulated.

Multiple Stiffened Panel with Single Crack

The specimen configuration and finite-element model for the stiffened panel are shown in Figures 4 and 10, respectively. Because the configuration and loading were symmetric, only a quarter of the sheet and stiffeners was modeled. This model had 13,145 elements, 17,287 nodes, 97,254 degree-of-freedoms (DOF). Figure 11 shows the load-crack extension measurements (circular symbols). The insert shows the relative location of the stiffener. Crack extension was measured until the crack went underneath the stiffener. Once the crack emerged from under the stiffener, the panel failed (open symbols). Whether failure of the panel was due to sheet failure or stiffener failure could not be determined. Failure of either would immediately result in panel failure because the stiffeners were carrying about one-half of the applied load. Two predictions were made using STAGS. First, the panel was restrained against buckling and the predicted results are shown by the dashed curve. The restrained analysis tended to over predict the test data and the predicted failure load was much higher than the test load. However, the unrestrained analysis (buckling allowed) under predicted the early stages of stable tearing but agreed well after about 30 mm of crack extension. The predicted failure load from the fracture of the sheet was 4% higher than the test failure load. The calculated stiffener failure load (x symbol) was extremely close to the actual test failure load. (Stiffener failure load was based on fracture tests conducted on the 305-mm wide specimens with a single intact stiffener at x = 0.)

Wide Stiffened Panels with Lead Crack and Multiple-Site Damage

A comparison of the measured and predicted load-against-crack extension for the wide stiffened panel with a lead crack and the 1.3-mm MSD is shown in Figure 12. The insert shows the relative location of the lead crack, open holes, MSD, and the intact stiffener. Open symbols show the test data. The measured load-crack

extension values for the data underneath the stiffener were inferred from the load-time trace recorded on this specimen. The solid curve shows the predicted results using the STAGS fracture analysis with the critical CTOA value. Again, the solid symbol denotes the maximum failure load on the panel. After the lead crack linked with the MSD cracks and grew pass the stiffener, the sheet failed when all 24 MSD cracks linked. These results show that MSD at open holes reduce the residual strength by about 30% from that of a panel with only a single crack. The predicted load-crack extension behavior matched the test results very well.

Strain Gauge Measurements and Analyses
In this section, the local strain gauge readings are compared with the analysis results. Each of the wide panel tested had strain gauges mounted on the sheet near the crack-tip region and on either side (front and back) of the stiffeners. On the sheet, strain gauges were placed at three distinct locations as shown in Figure13 around the crack-tip region. The strain gauge readings corresponding to the gauge just above the initial crack tip is shown by square symbols. With an increase in applied load, the strain level builds up monotonically upto a certain point after which it decreases gradually with crack extension. Only the permanent deformation remains in the plastic wake. The strain gauge readings at a location 203-mm ahead of the initial crack tip is shown by circular symbols. At this location, there is a build up of strain with increase in applied load till the crack tip reaches this material point. With further increase in applied load and subsequent crack extension, elastic unloading takes place at this location and only the permanent deformation is left in the wake. Triangular symbols indicate the strain gauge reading corresponding to a location, which is far from the initial crack tip. At this location, the strain value increases with applied load and continues to build with crack extension. Analysis results, represented by the three curves, compared well with the test measurements. Similarly, the strain gauge readings for the first and second intact stiffener compared well with the analyses.

CONCLUDING REMARKS

The STAGS finite-element code and the CTOA fracture criterion were used to predict stable tearing and residual strength of C(T) and M(T) specimens, unstiffened and stiffened wide panels. The measured critical crack-tip-opening angle (CTOA) was nearly constant after a small amount of crack extension for the thin-sheet 2024-T3 aluminum alloy. The STAGS finite element code predicted the out-of-plane deformations quite well. Comparison of measured and predicted loads carried by the intact stiffeners also agreed well. Using the critical CTOA fracture criterion with the plane-strain core option, the STAGS analyses were able to predict stable tearing behavior and residual strength of wide stiffened panels with single cracks and multiple-site damage (MSD) under severe buckling within about 5% of the test loads. Comparisons of local strain variation around the crack-tip region from STAGS analyses compared very well the test data.

REFERENCES

1. Swift, T. (1987) In: *New Materials and Fatigue Resistant Aircraft Design*, pp. 1-77, D. L. Simpson (Ed) EMAS Ltd.
2. McGuire, J. F. and Goranson, U. G. (1992) In: *NASA CP-3160*, pp. 33-48, C. E. Harris (Ed). Washington, D.C.
3. Harris, C. E.; Newman, J. C., Jr.; Piascik, R. and Starnes, J. H., Jr. (1998) *J. Aircraft.* 35 (2), 307-317.
4. Dawicke, D. S.; Sutton, M. A.; Newman, J. C., Jr. and Bigelow, C. A. (1995) In: *ASTM STP 1220*, pp. 358-379, F. Erdogan (Ed). American Society for Testing and Materials, PA.
5. Seshadri, B. R. and Newman, J. C., Jr. (1998) In: *ASTM STP 1332*, pp. 114-134, T. L. Panontin and S. D. Sheppard (Eds). American Society for Testing and Materials, PA.
6. Seshadri, B. R., Newman, J. C., Jr., Dawicke, D. S. and Young, R. D. (1999) In: *NASA/CP-1999-208982, Part 2*, pp. 513-524, C. E. Harris (Ed). Washington, D.C.
7. Young, R. D.; Rouse, M.; Ambur, D. R. and Starnes, J. H., Jr. (1999) In: *NASA/CP-1999-208982, Part 2*, pp. 408-426, C. E. Harris (Ed). Washington, D.C.
8. Dawicke, D. S. and Sutton, M. A. (1994) Exper. Mech. 34 (4), pp. 357-368.
9. Rankin, C. C.; Brogan, F. A.; Loden, W. A. and Cabiness, H. D. (1997) "STAGS User Manual - Version 2.4," Lockheed Martin Advanced Technology Center, Report LMSC P032594.
10. Newman, J. C., Jr.; Booth, B. C. and Shivakumar, K. N. (1988) In: *ASTM STP 945*, pp. 665-685, D. T. Read and R. P. Reed (Eds). American Society for Testing and Materials, PA.

RESIDUAL STRESS EFFECTS ON FATIGUE CRACK PROPAGATION IN FRICTION STIR WELDS

Claudio Dalle Donne and Gilles Raimbeaux

German Aerospace Center, Institute of Materials Research, D-51170 Cologne, Germany

ABSTRACT

Fatigue crack propagation (FCP) tests of 4mm thick friction stir welded (FSW) joints of the aluminum alloys 6013-T6 and 2024-T3 were carried out with compact tension specimens at different mean stress levels (R-ratios) and crack orientations. The da/dN-K curves of the welded specimens are correctly predicted using a simple approach based on the parent material da/dN-K_{eff} data and the residual stress intensity factor distribution obtained from the cut compliance technique. It is concluded that the differences in the FCP behavior were almost completely caused by residual stresses and not by the different resistance of parent and weld material to FCP.

KEYWORDS

Friction stir welding, fatigue crack propagation, residual stresses, cut compliance technique, effective stress intensity factor

INTRODUCTION

Friction stir welding (FSW) is a relatively new process patented by TWI (Cambridge, UK) in 1992 [1]. A friction stir butt weld is produced by plunging a rotating tool into the facing surfaces of the two plates, Figure 1. The tool consists of a shoulder and a profiled pin emerging from it. As the rotating pin moves along the weld line, the material is heated up by the friction generated by the shoulder and stirred by the rotating pin in a process similar to an extrusion. Since the temperatures are well below the melting point, problems associated with the liquid/solid phase transformation are avoided. This allows high quality joining of materials that have been traditionally troublesome to weld conventionally without distortion, cracks or voids such as high strength aerospace aluminum alloys like 2024 or 7475.

Currently, a very limited amount of data on fatigue crack propagation (FCP) in friction stir welded joints exists [2-4], even though the FCP behavior of long cracks under defined environment is one of the key issues during the material selections for light weight aerospace structures. Most of the work on fatigue of aluminum friction stir welds has been restricted to the generation of S-N data [4-7].

Preliminary FCP experiments with welded specimens of the aluminum alloys 2024-T3 [3] and 6013-T6 [4] displayed lower crack growth rates in the weld than in the base material, especially in the range of low crack propagation rates and stress ratios. It has been suggested that increased resistance against FCP is connected to the fine grained material in the weld [2] or to compressive welding stresses in the compact tension

specimens used in the FCP investigations [3, 4]. The objective of this paper is to examine the influence of residual stresses on the fatigue crack propagation curves of friction stir welded joints in 2024-T3 and 6013-T6 aluminum alloys.
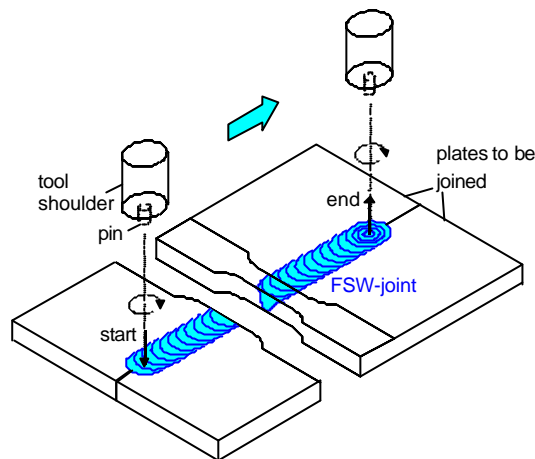
Figure 1: Schematic of friction stir butt welding

EXPERIMENTAL PROCEDURE

Materials and Friction Stir Welding

Two types of 4 mm thick aluminum alloy sheets, 2024-T3 and 6013-T6, were welded on conventional milling machines at DLR and EADS Corporate Research Center on the basis of the TWI patent. The welding direction was always in rolling direction. The ultimate tensile strength values of the joints were in the range of 90 % (2024-T3) and 80 % (6013-T6) of the parent material's ultimate strength. Further details such as process parameters, microstructures, hardness distributions and strength values are found in [4, 5, 8].

FCP tests

The test were carried out with 50 mm wide compact tension specimens at different mean stress levels (R-ratios) and crack orientations, Figure 2. The negative load ratio curves of the 6013-T6 base material were obtained from 80 mm wide middle cracked tension specimens (M(T)). All tests with FSW specimens were performed in the "as-welded" condition.

The "longitudinal weld" LW specimens had cracks in the center of the weld propagating parallel to the welding direction. On these specimens constant amplitude da/dN-K tests were carried out at room tem-perature and in laboratory air on a computer controlled servo-hydraulic testing machine following ASTM E 647 [9]. In the "transverse weld" TW specimens the crack approached the weld perpendicularly. These tests were carried out only with 6013-T6 FSW joints at constant K-values. In parent material specimens this procedure would have led to constant crack propagation rates. Therefore differences and changes in da/dN of the TW-specimens can be directly attributed to residual stresses or changes in microstructure. Crack propagation was always monitored through the potential drop technique.
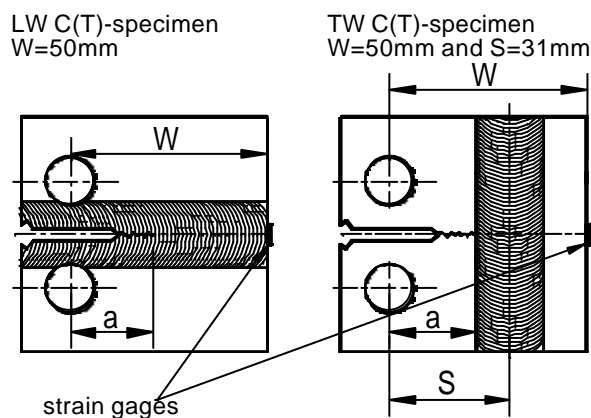
Figure 2: Welded specimen configurations.

Residual stress intensity factor measurement

The stress intensity factor due to residual stresses K_{rs} was determined directly with the so called "cut compliance method" [10, 11]. The method is based on the crack compliance method: a narrow saw cut is introduced progressively in the potential crack plane of the considered specimen or component and the resulting strain change is measured by a strain gauge. The desired stress intensity factor is proportional to the slope of the measured strain plotted as a function of the depth of the cut (i. e. crack length a):

$$ K_{rs} = \frac{E'}{Z(a)}\frac{d\varepsilon}{da} \qquad\qquad Z(a) = -\frac{2.532}{(W-a)^{1.5}}\left(1 - e^{-6.694\frac{a}{W}}\right) \qquad (1) $$

The proportionality factor or influence function $Z(a)$ is a unique function, that depends only on the cut depth, the geometry of the specimen or component and the strain measurement location. In this investigation a strain gage was glued on the C(T) specimen at the location indicated in Figure 2. The influence function for the set-up was obtained by a fit of the finite element results of Schindler [12] also given in eqn. (1).

Besides its simplicity, the great advantage of this method is that it delivers the information about residual stresses in a suitable form for direct use in fracture mechanics. Moreover the elastic re-distribution of residual stresses with increasing crack or slit length is already included in the K_{rs} versus a/W solution.

Figure 3 shows the distribution of K_{rs} measured by introducing an 0.3 mm wide fret saw cut in the ligament of the welded C(T) specimens. Mean values of at least 2 cutting test were used for one curve. The measured strain versus cut depth (a) data of the LW specimens were fitted by third to fifth degree polynomials, whereas a 12 degree polynomial was employed for the -a-relationship of the TW specimen.

The negative stress intensity factors of Figure 3 are related to compressive residual stresses ahead of the crack. In the longitudinal weld specimens, the residual stresses re-arrange after a crack growth increment in such way that compressive stresses are maintained at the crack tip. With increasing crack length the magnitude of the compressive residual stresses decreases and finally only small amounts of tensile stresses are active at the tips of long cracks. Such a behavior was also observed in C(T) specimens cut out from gas metal arc welded steel plates [13].

Cutting of TW-specimens out of the 6013-T6 plates resulted also in compressive residual stresses ahead of the crack, Figure 3 right side. The residual stresses are however higher in magnitude than in the longitudinal weld case and two peaks are reached in the heat affected zones of the weld.
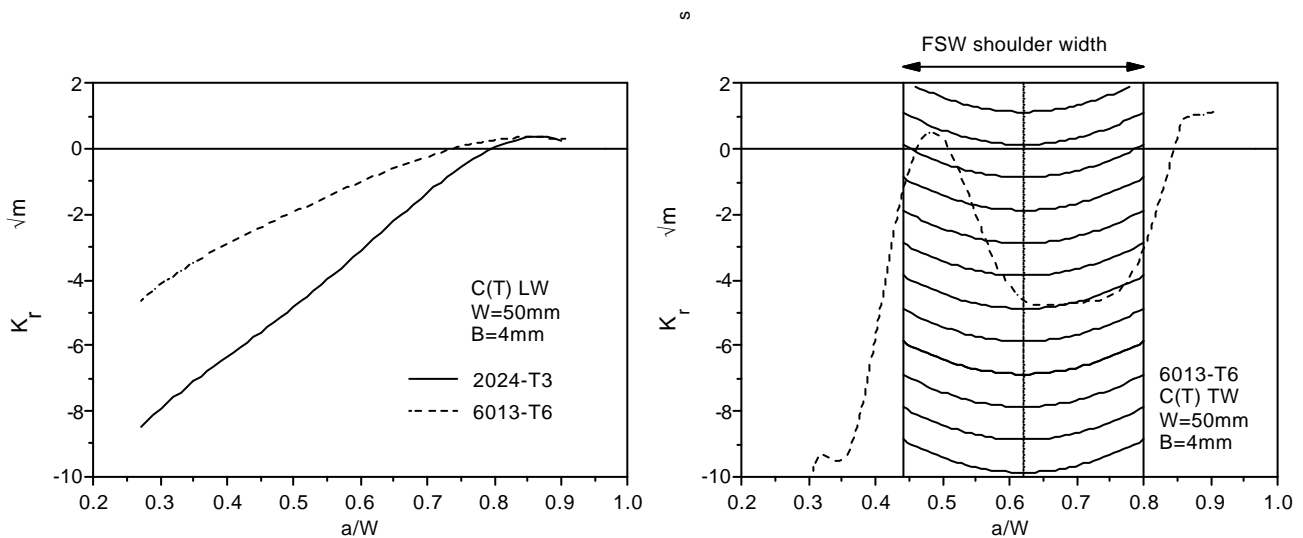
Figure 3: Distribution of the stress intensity factor due to residual stresses in the ligament of the C(T) specimens (left: longitudinal weld specimen, right: transverse weld specimen).

FCP IN LONGITUDINAL WELD SPECIMENS

In Figure 4 the da/dN-K curves of longitudinal weld specimens (closed symbols) are compared to the base material curves (open symbols). At high mean stress levels or R-ratios there is no difference in the FCP behavior of parent material and welded joint. At low R-ratios and loads (R = 0.1, K < 15 MPa√m) there is however an apparent improvement of the welded material properties in both alloys. It is now demonstrated, that this effect is entirely caused by the residual stresses, which were not considered in the evaluation of the welded specimen data.

When a fatigue crack is propagating in a residual stress field, for example in a welded plate, the stress intensity at the crack front is influenced by the combined effect of residual stresses and the stress resulting from the externally applied (nominal) load. Within the validity limit of linear elasticity the total stress intensity factor acting at the crack tip is given by the sum of the residual stress and external loading contributions (superposition principle) [14]. The K value (= $K_{max} - K_{min}$) remains unaffected by K_{rs}, since the residual stress K_{rs} has to be added to the whole nominal or applied loading stress intensity range K. On the other hand the true load ratio $R_t = (K_{min}+K_{rs})/(K_{max}+K_{rs})$ differs from the applied load ratio R. In other words, residual stresses rise (tensile stresses) or lower (compressive stresses) the mean stress or load ratio R of the applied loading.

Compared to steel, da/dN-K curves of aluminum alloys are much more sensitive to load ratio effects, especially at low load levels and in the range of R < 0.5 [15]. For a given load K crack growth rates increase with increasing R. The reason for this behavior is that particularly at low or negative R-ratios only a part of the applied K, designated as the "effective stress intensity factor range K_{eff}", acts as driving force at the crack tip [16]. The underlying physical mechanisms of this effect are still being debated [17]. So far it is important to know, that K_{eff} is usually calculated from empirical relationships which depend on K and R [18].

Assuming that the real resistance against FCP of the welded specimens is equal to the parent material resistance, it is now possible to predict the constant amplitude da/dN-K curves of the welded specimens. For a given crack length and nominal load ratio the true load ratio R_t is calculated using the K_{rs} distribution of Figure 3. The effective stress intensity factor range K_{eff} of the welded specimens is obtained by inserting
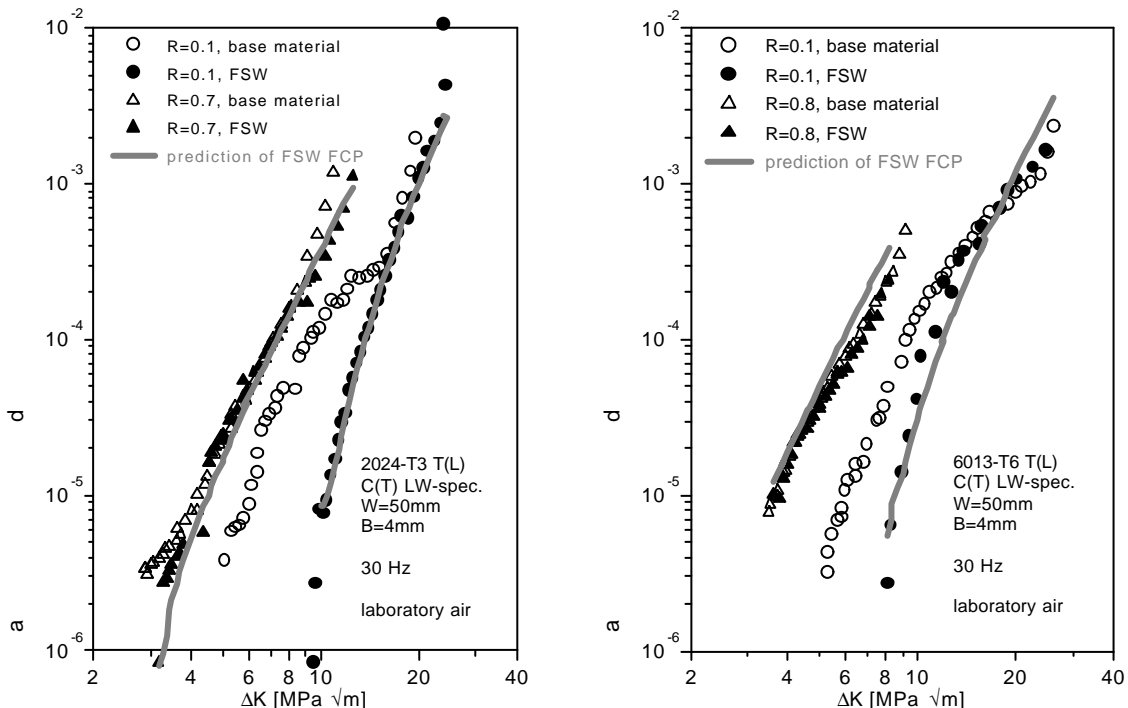
Figure 4: Fatigue crack propagation curves of longitudinal weld specimens compared to the base material data and the prediction.
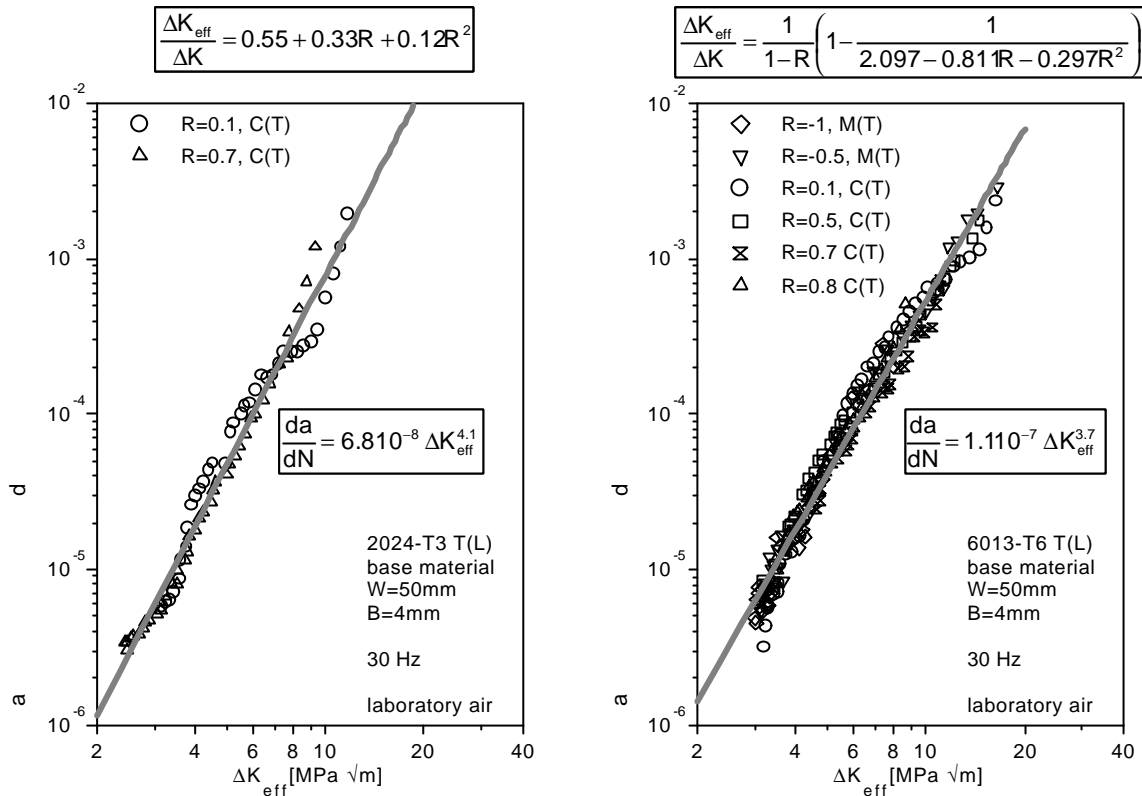
Figure 5: Effective parent material FCP curves fitted by power laws. K_{eff} was calculated by the empirical formulas on top of the figures taken from [18] (2024-T3) and [8] (6013-T6).

R_t in the K_{eff}-K-relationships given on top of Figure 5. The fatigue crack growth rate da/dN is then estimated by the simple power laws shown in Figure 5. The predicted FCP curves are very close to the data measured with the welded specimens, Figure 4. This means that our assumption was right and that the apparent improvement of FGP properties at low loads and load ratios displayed in Figure 4 is solely caused by compressive residual stresses present in the crack tip region of the C(T) specimens.

FCP IN TRANSVERSE WELD SPECIMENS

To get pronounced residual stress effects on da/dN it was essential to keep K and R constant at relatively low values (K < 15 MPa√m, R = 0.1) during the tests of the transverse weld (TW) C(T)-specimens. Because of the very low loads at the end of the tests (< 1 % of machine capacity), R and K deviated slightly from the constant values at a/W > 0.75. In Figure 6 the FSW fatigue crack propagation results of two TW specimens were therefore normalized with the respective fatigue crack propagation values of the parent material at the same nominal loading. The da/dN-prediction was calculated as described in the previous section. Also for this specimen geometry there is a favorable agreement between experimental and predicted values. This indicates that acceleration, deceleration and final acceleration of the crack crossing the weld is mainly caused by residual stresses and not by varying resistance to FCP of the different weld microstructures.

CONCLUSIONS

On the basis of the effective stress intensity factor range K_{eff}-approach and a simple residual stress intensity factor estimation it was shown that the differences in FCP behavior of welded specimens and parent material (2024-T3 and 6013-T6) are almost completely caused by residual stresses and not by the different resistance to FCP of the various weld microstructures.

ACKNOWLEDGEMENTS
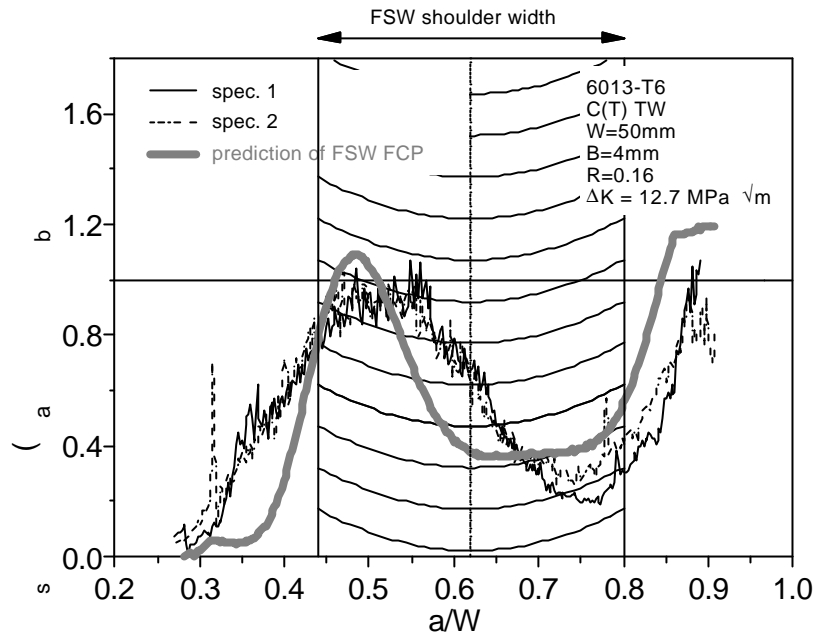
Figure 6: Fatigue crack propagation rates of TW specimens under constant K and R loading compared to the prediction using base material K_{eff} data and the K_{rs} distribution in the specimens.

REFERENCES

[1] Thomas, W.M. et al. (1992). *European Patent*, EP 0 615 480 B1.

[2] Haagensen, P.J., Midling, O.T. and Ranes, M. (1995). In: *2nd International Conference on Surface Treatment 95*, Vol. II, pp. 225-237.

[3] Dalle Donne, C. and Biallas, G. (1999). In: *European Conference on Spacecraft Structures, Materials and Mechanical Testing*, Stavrinidis, C., Rolfo, A. and Breitbach, E. (Eds.), ESA SP-428, pp. 309-314.

[4] Braun, R., Biallas, G., Dalle Donne, C. and Staniek, G. (1999). In: *Materials for Transportation Technology EUROMAT '99 - Vol. 1*, Winkler, P.J. (Ed.), Wiley-VCH, pp. 150-155.

[5] Biallas, G., Braun, G., Dalle Donne, C., Staniek, G. and Kaysser, W. (1999). In: *1st International Symposium on Friction Stir Welding*, TWI, UK, cd-rom.

[6] Bussu, G. and Irving, P. E. (1999). ibid.

[7] Hori, H., Makita, S. and Hino, H. (1999). ibid.

[8] Dalle Donne, C., Biallas, G., Ghidini, T. and Raimbeaux, G. (2000). In: *Second International Conference on Friction Stir Welding*, TWI, UK, cd-rom.

[9] Bachmann, V., Marci, G. and Sengebusch, P. (1994). In: *Automation in Fatigue and Fracture: Testing and Analysis, ASTM STP 1231*, Amzallag, G. (Ed.), ASTM, Philadelphia, 1994, pp. 146-163.

[10] Schindler, H.-J., Cheng, W. and Finnie, I. (1997) *Experimental Mechanics*, 37, pp. 272-277.

[11] Prime, M.B. (1999) *Fatigue Fract. Engn. Mater. Struct.*, 22, pp. 195-204.

[12] Schindler, H.-J. and Landolt, R. (1996). In: *Proc. of the 4th European Conference on Residual Stresses*, pp. 509-517.

[13] Ohta, A., Sasaki, E., Nihei, M., Kosuge, M. and Inagaki, M. (1982) *Int. J. Fatigue*, 4, pp. 233-237.

[14] Beghini, M. and Bertini, L. (1994) *Engng. Fracture Mech.*, 36, pp. 379-387.

[15] Bucci, R.J. (1996). In: *ASM Handbook Vol. 19, Fatigue and Fracture*, Lampman, S.R. (Ed.), ASM International, 1996, pp. 771-812.

[16] Elber, W. (1970) *Engng. Fracture Mech.*, 2, pp. 37-45.

[17] Lang, M. and Marci, G. (1999). In: *Fatigue and Fracture Mechanics: 29th Volume, ASTM STP 1332*, Panontin, L. and Sheppard, D.S. (Eds.), ASTM, 1999, pp. 474-495.

[18] Schijve, J. (1988). In: *Mechanics of Fatigue Crack Closure, ASTM STP 982*, Newman, J.C and Elber, W (Eds.), ASTM, Philadelphia, 1988, pp. 5-34.

RESIDUAL STRESS ESTIMATED BY NEW EMPIRICAL METHOD AND ITS CORRELATION WITH STRENGTH IN CERAMICS

T. Hoshide and J. Abe

Department of Energy Conversion Science, Graduate School of Energy Science,
Kyoto University,
Sakyo-ku, Kyoto 606-8501

ABSTRACT

An easier method for the residual stress estimation in ground ceramics was investigated as the alternative to the X-ray diffraction method. A new empirical procedure to evaluate grinding-induced residual stresses was described based on the indentation fracture (IF) method. The formulation to calculate the peak residual stress on the ground surface was derived from the critical equilibrium growth of the indentation-induced crack. Alumina and two kinds of silicon nitride ceramics, which were ground under different grinding conditions, were prepared for experiments. The comparison of the residual stress estimated by the present procedure with the residual stress measured by the X-ray diffraction method showed a quantitative correspondence between them. The relation between the bending strength and the grinding-induced residual stress estimated by the present procedure was also investigated. In all materials, a larger compressive residual stress was found to result in a higher strength. It was clarified that the strength normalized by using material constants, the fracture toughness and the mean grain size, was almost uniquely correlated with the estimated residual stress independently to the examined materials.

KEYWORDS

Ceramics, Residual stress, Estimation, Indentation fracture method, Bending strength, Grinding

INTRODUCTION

Residual stresses in ceramic components are generated in their grinding processes, which are inevitable to improve the accuracy of dimension in engineering applications. It should be noted that strength properties of ceramics are remarkably influenced by the grinding-induced residual stress as well as surface defects [1-7]. Although the X-ray stress measurement method has a wide applicability to the residual stress estimation in various materials, alternative simpler methods for the residual stress estimation are required considering practical needs. For ceramics, especially, a possible candidate procedure to estimate the residual stress is suggested to be the indentation fracture (IF) method [5, 8-12], which has been developed as a convenient procedure to evaluate the fracture toughness of ceramics. In the IF method, the length of an indentation-induced crack is one of dominant parameters in the fracture toughness evaluation, and the crack length may be affected by a pre-existing residual stress field. This implies that the information on residual stress can be included in the toughness value evaluated by the IF method.

In this work, an empirical procedure to evaluate the grinding-induced residual stress is introduced on the basis

of the IF method. Residual stresses in alumina and silicon nitride ceramics, which are machined under different grinding conditions, are estimated by using the proposed method. The estimated results are also verified by comparison with residual stresses measured by the X-ray method. Finally, the bending strength is correlated with the estimated residual stress, and the discussion is made on the obtained relation between them.

ESTIMATION PROCEDURE OF RESIDUAL STRESS

Estimation Principle by IF Method

At a critical level for equilibrium crack growth in an indented ceramic material with a residual stress, the net stress intensity factor K_{net} remains constant as follows [9].

$$K_{net} = K_{CA} + K_R = K_{IC} , \qquad (1)$$

where K_{IC} is the fracture toughness and K_R is a residual stress intensity factor associated with the residual stress field. In Eqn. 1, K_{CA} is a fracture toughness evaluated by using an IF method. It is noted that K_{CA} is an apparent fracture toughness affected by the residual stress. The evaluation procedures for K_{CA} and K_R are described in the following.

Several formulae to evaluate the fracture toughness K_C of ceramics by using the IF method have been proposed [ex. 13], though the following equation recommended in the Japanese Industrial Standard (JIS) R 1607 [14] is adopted in this work.

$$K_C = \frac{\alpha [E\ P]^{1/2} (d/2)}{a^{3/2}} , \qquad (2)$$

where α, E and P are an empirical coefficient, the Young's modulus of an indented material and the indentation peak load set in a Vickers hardness tester, respectively. The coefficient α in Eqn. 2 is given as 0.026 in JIS R 1607. Other dimensions d and a are the diagonal length of a Vickers impression and the half surface-length of a crack well-developed after indentation, respectively. The measured crack length a is affected by a residual stress field as illustrated in Fig. 1. In this case, the toughness K_C calculated by Eqn. 2 should be interpreted as an apparent fracture toughness K_{CA}. Since the growth of an indentation-induced crack is restrained under a compressive stress field, the crack length a_{com} under a compressive stress is expected to be shorter than the length a_o in no residual stress field. On the contrary, it is anticipated that the crack length a_{ten} observed under a tensile stress is longer than the length a_o.
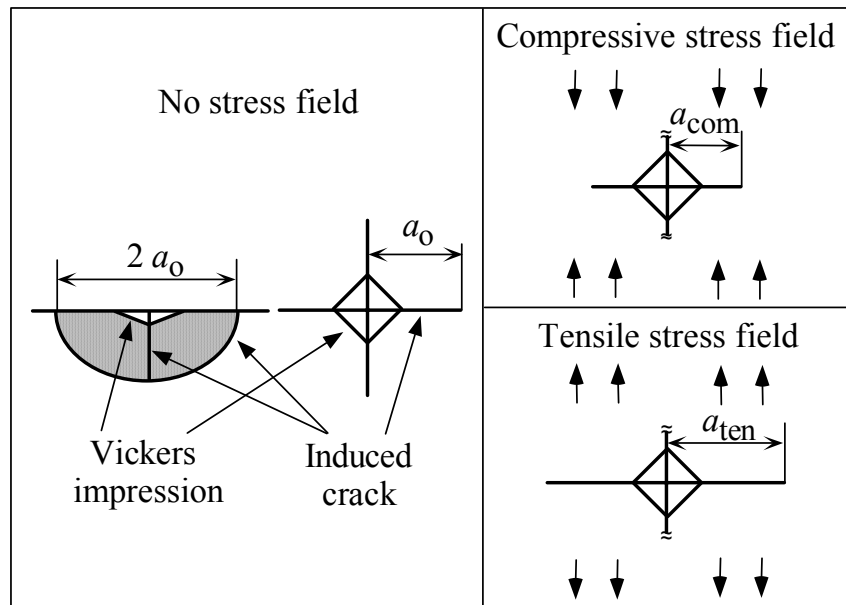
Figure 1: Illustration of indentation-induced crack

A grinding-induced residual stress σ_R is generally known to be compressive. In experimental studies [4-6, 15],

it is also reported that the compressive residual stress σ_R has its peak σ_{RO} on or near the ground surface of a ceramic specimen and vanishes toward the specimen-depth direction. Since the well-developed crack induced by an indentation is usually approximated as a semi-elliptical crack, K_R for the crack in a residual stress filed can be expressed by the typical form as

$$K_R = \frac{\sigma_{RO}(\pi \lambda a)^{1/2}}{\Phi(\lambda)} M_R .$$ (3)

In Eqn. 3, λ is the aspect ratio defined as the ratio b/a of the crack depth b to the surface half length a, and $\Phi(\lambda)$ is the complete elliptic integral of the second type depending on λ. The parameter M_R in Eqn. 3 is a magnification factor determined by a given residual stress distribution, λ and b/t, where t is the specimen thickness.

Residual Stress Estimate by IF Method
By substituting Eqn. 2 with $\alpha = 0.026$ and Eqn. 3 into Eqn. 1, we have the following equation to estimate the peak residual stress σ_{RO}.

$$\sigma_{RO} = \frac{K_{IC}(\pi a)^{-1/2} - 0.026(E P / \pi)^{1/2}(d/2)\, a^{-2}}{\lambda^{1/2} M_R} \Phi(\lambda) .$$ (4)

Recently, using the IF method, the standard JSMS-SD-4-01 for the evaluation of grinding-induced residual stresses in ceramics has been established by the Society of Materials Science, Japan (JSMS). In this standard, the peak residual stress is evaluated by using the formulation:

$$\sigma_{RO} = \frac{K_{IC}(\pi a)^{-1/2} - 0.026(E P / \pi)^{1/2}(d/2)(a)^{-2}}{M} .$$ (5)

The coefficient M in Eqn. 5 is found to be equivalent to $\lambda^{1/2} M_R / \Phi(\lambda)$ by comparison with Eqn. 4. This means that M may be calculated if the parameters λ and M_R are known. Usually, however, it is difficult to get the information about λ and M_R. In the standard, therefore, $M = 1.4$ is empirically determined on the basis of the result obtained in the round robin test which was conducted by the working group organized by JSMS Committee on Fatigue of Materials.

EXPERIMENTAL PROCEDURES

Materials and Specimen Preparations
Materials to be used in experiments have been investigated in other works; i.e. two lots of a pressureless sintered alumina produced by Japan Fine Ceramics Center (AL-PL1 [16] and AL-PL2), a gas pressure sintered silicon nitride produced by NGK Spark Plug Co. Ltd. (SN-GP [16]), and two kinds of pressureless sintered silicon nitrides (SN-PL1 [5] and SN-PL2) by TOTO Ltd. and Japan Fine Ceramics Center, respectively. The bulk density ρ, the Young's modulus E and the fracture toughness K_{IC} of the materials are as follows; $\rho = 3.93$ Mg/m^3, $E = 380$ GPa and $K_{IC} = 4.4$ MPa·m$^{1/2}$ for AL-PL1 and AL-PL2, $\rho = 3.23$ Mg/m^3, $E = 320$ GPa and $K_{IC} = 6.0$ MPa·m$^{1/2}$ for SN-GP, $\rho = 3.23$ Mg/m^3, $E = 310$ GPa and $K_{IC} = 5.7$ MPa·m$^{1/2}$ for SN-PL1 by TOTO, and $\rho = 3.23$ Mg/m^3, $E = 259$ GPa and $K_{IC} = 7.1$ MPa·m$^{1/2}$ for SN-PL2 by Japan Fine Ceramics Center. The fracture toughness of each material was obtained by the standard method specified in JIS R 1607 or its equivalent procedure.

Geometry of specimen machined in this work was of a square rod type with a dimension of $4 \times 3 \times 36$ mm^3 which is specified for the bending specimen in JIS R 1601 [17]. In all cases, the grinding direction was set in the longitudinal direction of specimen. For AL-PL1 and SN-GP, two types of specimens were finally prepared by grinding with wheels of #400 and #800 grit sizes. The cutting depth per one pass was set to be 4 μm for #400 grinding and 2 μm for #800 grinding, respectively. Another series of AL-PL2 and SN-PL2 specimens were also

prepared by using grinding wheels of #80, #200 and #800 grit sizes. In this series, the cutting depths per pass in the conditions using #80, #200 and #800 grinding wheels were respectively 20 µm, 8 µm and 2 µm, while surfaces of specimens ground by using #80 wheel were slightly polished so that the indentation-induced crack could be more easily observed. On the other hand, specimens of SN-PL1 were machined under six different conditions as follows. Three distinct grit sizes of grinding wheel, #170, #270 and #600, were adopted. Two values of the cutting depth were selected for each grit size; i.e. 5 µm and 40 µm for #170 and also for #270, and 1 µm and 25 µm for #600.

Testing Procedures
In the present study, specimens were indented by using an ordinary Vickers hardness tester, and the indentation force was set to be in the range from 196 to 490 N. The surface length $2a$ of the crack was measured through an optical microscope, while the crack tip was sometimes identified by using a laser scanning microscope with a higher resolving power.

Bending strength has been obtained for AL-PL1 [16], SN-GP [16] and SN-PL1 [5], respectively. Smooth specimens of AL-PL1 and SN-GP were loaded by four-point bending with an outer span of 30 mm and an inner span of 10 mm, while bending tests for smooth specimens of SN-PL1 were conducted under three-point mode with a span length of 20 mm. In each case, tests were carried out under load-controlled condition, and the loading rate was controlled so that the rate of the maximum tensile stress in a specimen might be about 100 MPa/s.
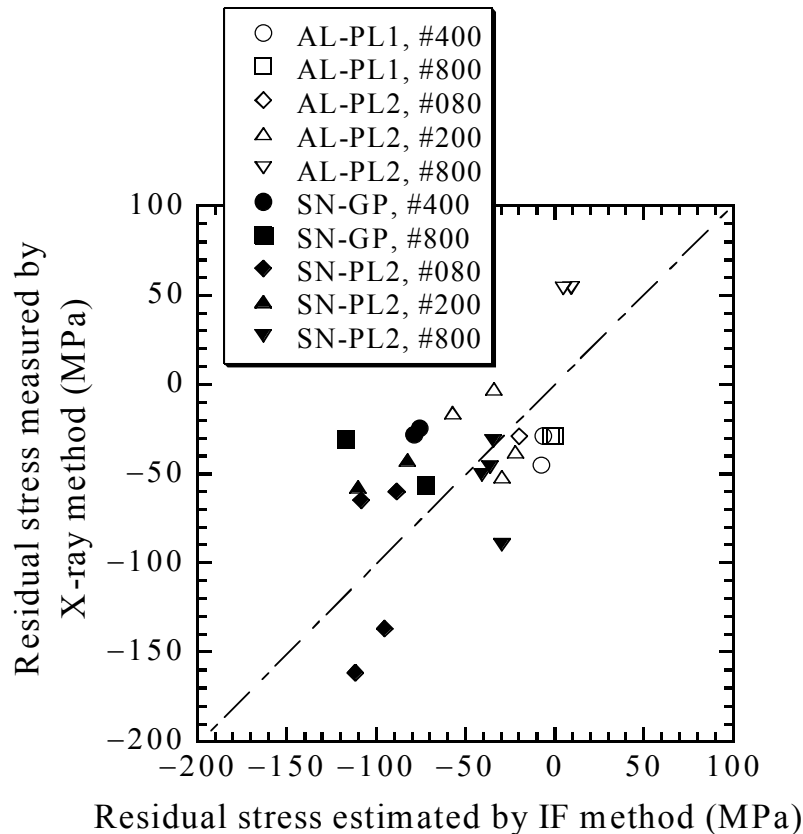
Figure 2: Comparison between residual stresses evaluated by X-ray and IF methods

EXPERIMENTS AND DISCUSSIONS

Comparison between Residual Stresses Measured by Proposed and X-Ray Procedures
Grinding-induced residual stresses in AL-PL1, AL-PL2, SN-GP and SN-PL2 specimens were also measured by using an X-ray diffraction method. For the materials, the residual stress measured by the X-ray diffraction method is compared with that estimated by the present procedure in Fig. 2. Although a little bit large scatter is seen in the figure, a good coincidence is found between the residual stresses by the X-ray and the IF methods. Consequently, it may be concluded that the proposed procedure gives a quantitative correspondence to the

X-ray measurement. This implies that the proposed procedure is applied as a simpler estimation of grinding-induced residual stress in ceramic materials.
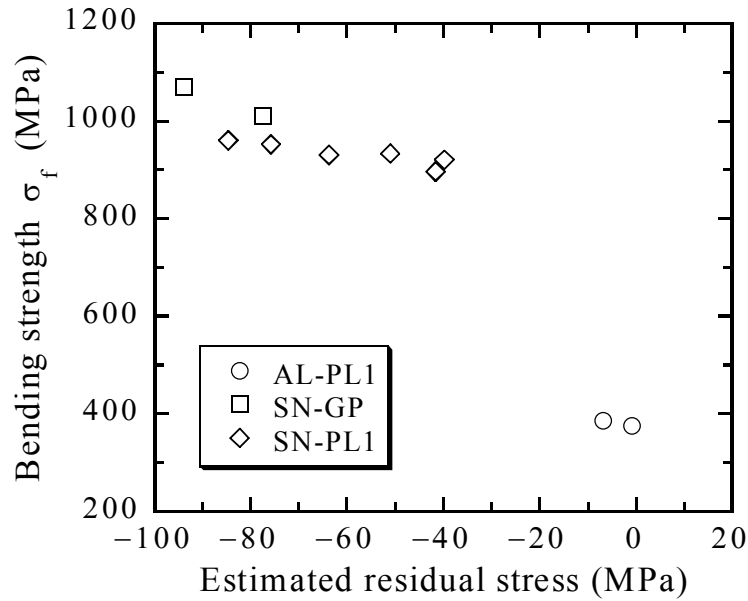
Figure 3: Relation between estimated residual stress and bending strength
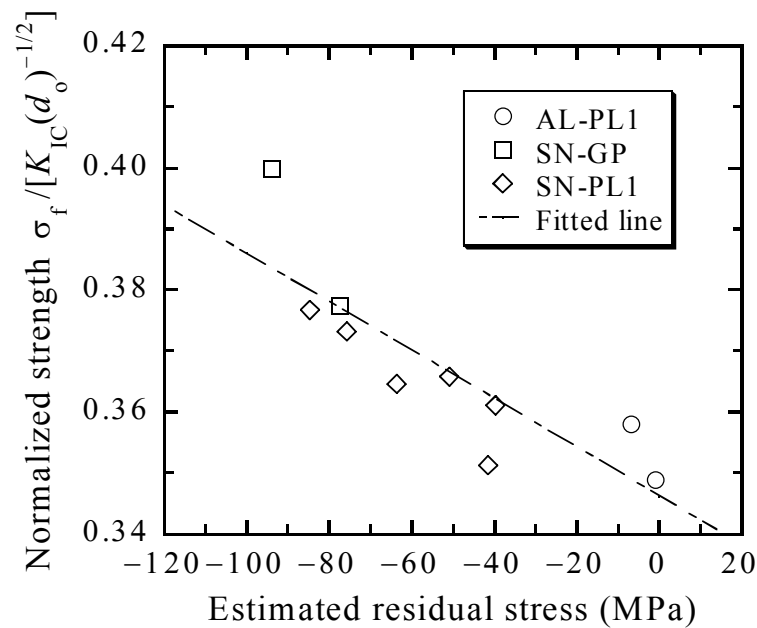
Figure 4: Relation between estimated residual stress and bending strength normalized
by using material constants

Relation between Strength and Estimated Residual Stress

As mentioned in the introduction, the strength of ceramic materials is affected by the residual stress. In this section, the strength is correlated with the grinding-induced residual stress estimated by the proposed procedure. Figure 3 shows the relation of the mean strength σ_f depending on the grinding condition with respect to the estimated peak residual stress σ_{RO}. Using the fracture toughness K_{IC} and the mean grain size d_o, the strength is normalized by a stress parameter $K_{IC}(d_o)^{-1/2}$, and the normalized strength is also correlated with the estimated residual stress in Fig. 4. As seen in Fig. 4, the relation between the normalized strength and the estimated residual stress is well fitted by the linear relationship as depicted with the dot-dash line, and the relation is found to be independent of the examined materials.

As shown in Fig. 3 and Fig. 4, a larger compressive residual stress is found to result in a larger strength. This result is reasonable, because the compressive stress restrains the crack growth from inherent and

grinding-induced defects, and improves the material strength.

CONCLUDING REMARKS

In this work, a new empirical procedure to estimate grinding-induced residual stresses based on the indentation fracture method was described for ground ceramic materials. The peak residual stress appeared on the ground surface was formulated from the critical equilibrium growth of an indentation-induced crack. The proposed procedure was applied to a pressureless sintered alumina, a gas pressure sintered and pressureless sintered silicon nitrides, which were ground under different grinding conditions. The residual stress estimated by the present procedure was almost coincided with the residual stress measured by the X-ray diffraction method. It was revealed that estimated residual stresses were compressive in the investigated materials. A reasonable correlation was also seen between the estimated residual stress and the bending strength; i.e. a larger compressive residual stress increased the strength. It was also clarified that the strength normalized by using material constants, the fracture toughness and the mean grain size, was almost uniquely correlated with the estimated residual stress independently to the examined materials. Consequently, it was concluded that the proposed procedure was effective in the estimation of residual stresses generated in ground ceramic materials.

REFERENCES

1. Lewis, D., III, (1982) *Ceram. Bull.* 61, 1208.
2. Fessler, H., Fricker, D.C. and Godfrey, D.J. (1983) *Ceram.-Perform. Appl.* 3, 705.
3. Hawmann, M.W., Cohen, P.H., Conway, J.C. and Pangborn, R.N. (1985) *J. Mater. Sci.* 20, 482.
4. Suzuki, K., Tanaka, K., Yamamoto, Y. and Nakagawa, H. (1989) *J. Soc. Mater. Sci., Japan* 38, 582.
5. Hoshide, T., Okumura, K. and Inoue, T. (1991) *J. Soc. Mater. Sci., Japan* 40, 217.
6. Suzuki, K. and Tanaka, K. (1991) *J. Soc. Mater. Sci., Japan* 40, 818.
7. Richerson, D.W. (1992). *Modern Ceramic Engineering Properties, Processing, and Use in Design*, 2nd Ed. Marcel and Dekker, Inc., New York, Chap. 12.
8. Marshall, D.B. and Lawn, B.R. (1979) *J. Mater. Sci.* 14, 2001.
9. Marshall, D.B., Lawn, B.R. and Chantikul, P. (1979) *J. Mater. Sci.* 14, 2225.
10. Zeng, K. and Rowcliffe, D. (1993) *Paper No. SIX-23-93, 95th Ann. Meet. Am. Ceram. Soc.*
11. Salomonson, J. and Rowcliffe, D. (1995) *J. Am. Ceram. Soc.* 78, 173.
12. Hoshide, T. (1998) *Mater. Sci. Res. Int.* 4, 294.
13. Lawn, B.R. (1983). In: *Fracture Mechanics of Ceramics* Vol. 5, pp. 1-25, Bradt, R.C., Evans, A.G., Hasselman, D.P.H. and Lange, F.F. (Eds). Plenum Press, New York.
14. *Japanese Industrial Standard JIS R 1607* (1995) Japanese Standards Association.
15. Sakaida, Y., Harada, S. and Tanaka, K. (1993) *J. Soc. Mater. Sci., Japan* 42, 641.
16. Hoshide, T. and Masuda, M. (1995) *Mater. Sci. Res. Int.* 1, 108.
17. *Japanese Industrial Standard JIS R 1601* (1990) Japanese Standards Association.

RESIDUAL STRESS IN PIEZOELECTRIC THIN FILM PREPARED BY PULSE LASER BEAM ABLATION

Y.C.Zhou[1,2], Z.Y.Yang[1], X.J.Zheng[1], J.Y.Li[3]

[1]Institute of Fundamental mechanics and Material Engineering, Xiangtan University, Xiangtan, Hunan, 411105, China
[2]Fracture Research Institute, Tohoku University, Sendai, 980-8579, Japan
[3]Department of Mechanical Engineering, California Institute of Technology, Pasadena, CA91125, USA

ABSTRACT

In the investigation, the piezoelectric thin film $Pb(Zr_xTi_{1-x})O_3$(PZT) was prepared by a pulse laser deposition method. The residual stress in piezoelectric thin film was tested by x-ray diffractometer (XRD). The relation of properties such as microstructures, piezoelectric response with residual stress was investigated. A theoretical model for residual stress formed mechanism is proposed. The model is based on the combined effects of the difference of thermal mismatch between substrate and thin film, the phase transformation and the different of lattice constant between thin film and substrate.

KEYWORDS

Piezoelectric thin film, Pulse laser ablation method, Residual stress

INTRODUCTION

Piezoelectric thin films are currently attention due to the potential application in MEMS (micro-electro-mechanical systems), information storage, et al[1]. Many methods are used to prepare piezoelectric thin films. Pulsed laser deposition (PLD) is one of the considerable deposition methods. In the investigation, the prepared lead zirconate titanate $(Pb(Zr_{0.52}Ti_{0.48})O_3;PZT)$ piezoelectric ceramics were used as a target, Nd:YAG pulse laser as an evaporate source, Si(100) crystal slice as a substrate, oxygen as ambient gas. Residual stresses will be produced inevitably between thin film and substrate due to the structural misfit and thermal misfit of the thin films/substrate and the process from high temperature to low temperature during the preparation process of the thin films. The structure and properties of thin films have relation with residual stress in some degree. In the present paper, the residual stress in PZT thin film was tested by x-ray diffractometer (XRD) and a theoretical model was proposed to predict the residual stress. The effect of

residual stress on piezoelectric property is also discussed.

EXPERIMENTAL PROCEDURE

Samples Preparation
PZT thin films were deposited on single crystalline silicon (100) by pulsed laser deposition (PLD). The substrates were coated beforehand with an 0.2μm-thick platinum film as a sub-electrode. A pulsed KrF laser beam with a wavelength of 248nm was focused on a $Pb(Zr_{0.52}Ti_{0.48})O_3$ target with an angle of 45^0. The frequency and pulse duration of the laser beam were, respectively, 5Hz and 30ns. The target was rotated with 5r/min in order to prepare a uniform thickness film. The target-substrate spacing was 60mm, and the incident energy density of laser beam was $1.5J/cm^2$. The substrate temperature and oxygen pressure in the chamber were 650^0C and 30Pa, respectively. When the target material was deposited on the substrate, the substrate was slowly cooled to ambient temperature. After PZT thin film was deposited, an 0.2μm-thick platinum film as a super-electrode was coated on the surface of film by pulse laser deposition. The ferroelectric hysteresis was measured by normal pulse measure system RT66A.

X-ray Diffraction and c-axis Orientation Ratio
The structure and residual stress of the samples were investigated with X-ray diffraction D500 and texture goniometer. The x-ray radiation source was Cu K_α with wavelength of 1.5406nm. The scanning angle was in the region of 20^0-70^0, scanning velocity was 4 degree/min and degree increment was 0.02^0. The diffractometer was operated at 36kV and 30mA. The c-axis orientation ratio is an important parameter which is defined as,

$$\alpha = \frac{I(002)}{I(110) + I(002)} \tag{1}$$

where I(002) and I(110) are the x-ray diffraction intensities of (002) and (100) reflection, respectively. It is considered that the orientation represents the volume ratio of a and c domains in the film.

Test Principle
Residual stress determination by means of X-ray diffraction is based on measurements of changes in crystal lattice spacing, which manifest themselves as shifts in angular positions of respective diffraction peaks [2]. From a set of lattice spacing in different orientations and a stress-free lattice spacing, an elastic strain tensor is constructed, which is then converted to stress tensor using Hooke's law [2]. When a beam of X ray with the wavelength of λ and is impinged to the surface of the samples with an incident angle Ψ, the diffraction of the X ray will occur with Bragg's diffraction equation,

$$n\lambda = 2d \sin \theta \tag{2}$$

where n is an integral, d is the crystal plane distance, θ is Bragg's diffraction angle. When there is a residual stress in the samples, the crystal plane distance d is different from that of the samples without residual stress, thereby the diffraction angle is different. The strain in thin film is related with the difference of crystal plane distance d,

$$\varepsilon_\psi = \frac{\Delta d}{d} = \frac{d_\psi - d_0}{d_0} = -\cot(\theta_\psi - \theta_0) \tag{3}$$

where θ_0 is the Bragg's angle at diffraction peak in the samples without residual stress, θ_ψ is the Bragg's angle at diffraction peak in the samples with residual stress. Generally, thin film is so thin that the residual stress in the thin film can be regarded as in plane stress. In this case, the residual stress σ_ϕ in the thin film along ϕ direction can be given

$$\sigma_\phi = -\frac{E}{2(1+v)} \cot \theta_o \frac{\pi}{180} \frac{\partial(2\theta)}{\partial(\sin^2 \psi)} \tag{4}$$

where the unit of 2θ is degree, and E is Young's modulus，ν is Poisson's ratio of the thin film. Much research has shown that the relationship between 2θ and $\sin^2\psi$ is linear. In experiment, the slope of straight line on the plane of $2\theta_\psi$- $\sin^2\psi$can easily obtained by measuring different diffraction peak displacement under different ψ. Finally, the residual stress σ_ϕ in the thin films can be measured by using expression (4).

EXPERIMENTAL RESULTS

c-axis Orientation Ratio and Ferroelectric Properties
The structure of the ferroelectric thin films is sensitive to substrate temperature and oxygen pressure in the chamber during deposition. The dependence of micro-structure on substrate temperature and oxygen pressure was discussed by Luo, et al. [3]. $Pb(Zr_{0.52}Ti_{0.48})O_3$ thin film, having a perovskite structure, was successfully deposited on single crystalline silicon (100) by pulsed laser deposition (PLD) at substrate temperature of 650^0C and oxygen pressure in the chamber of 30Pa. Figure 1 shows the ferroelectric properties with hysteresis, remnant polarization and coercive field for different film thickness. One can see that remnant polarization P_r increases linearly with increasing film thickness when the electric field is at a constant. However, the coercive decreases with increasing film thickness when the electric field is at a constant. When the film is thinner than 0.5μm, the coercive field decreases fast with increasing film thickness. When the film is thicker than 0.5μm, the coercive field decreases slowly with increasing film thickness. Figure 2 shows the c-axis orientation ratio for different thickness film. It is shown that the c-axis orientation ratio increases with increasing film thickness.

| (a) | (b) | (c) |
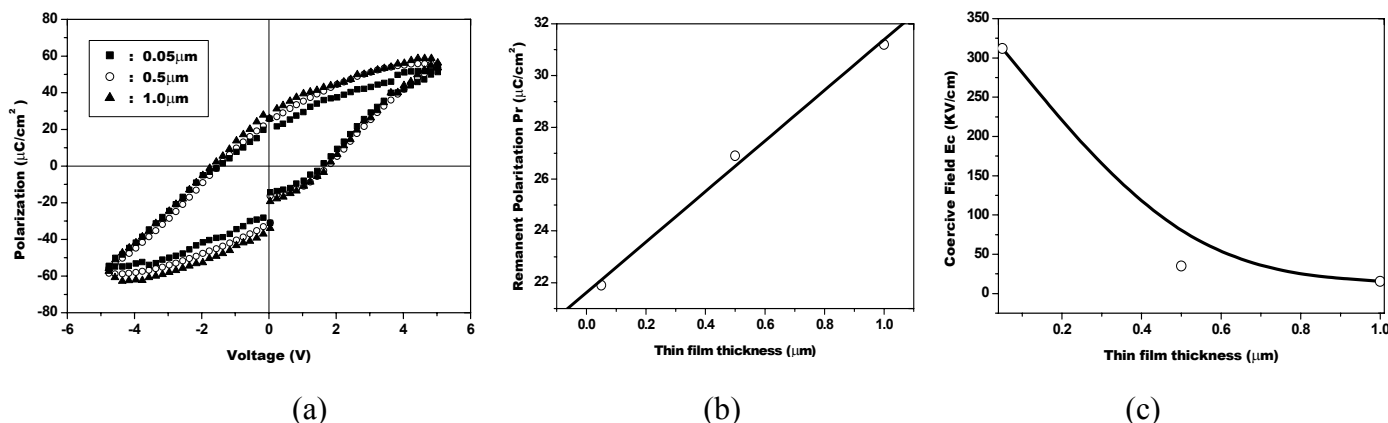
Figure 1: Ferroelectric properties: (a) hysteresis, (b) remnant polarization, (c) coercive field.
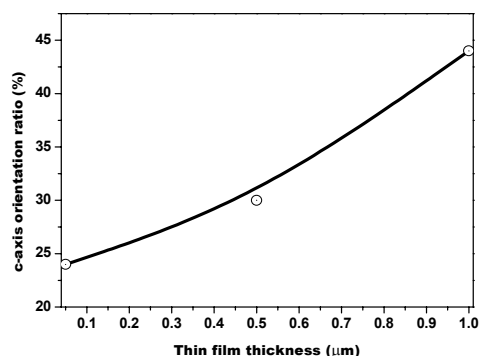
Figure 2: Relationship between film thickness and c-axis orientation ratio

Residual Stress
The incident angle ψ was adopted as three values which were $\psi=0^0$, 15^0, 30^0 and 45^0 in the residual stress test by X-ray diffraction. The diffraction peak displacement could easily be measured for different incident angle ψ. The results of $2\theta_\psi$ with $\sin^2\psi$ for different film thickness are listed in table 1 and shown in figure 3. One can easily obtained the slope of straight line from the figures. Based on formula (4) and the slope of $2\theta_\psi$ with $\sin^2\psi$,

the residual stress in PZT thin film can be obtained. In the experiment, the mechanical parameters E and ν for PZT thin film were taken as 85Gpa and 0.28, respectively, and 2θ was taken as 64.68^{o}. Figure 4 shows the relationship between residual stress and film thickness. One can see that the residual stress is compressive stress. It gradually decreases with increasing film thickness.
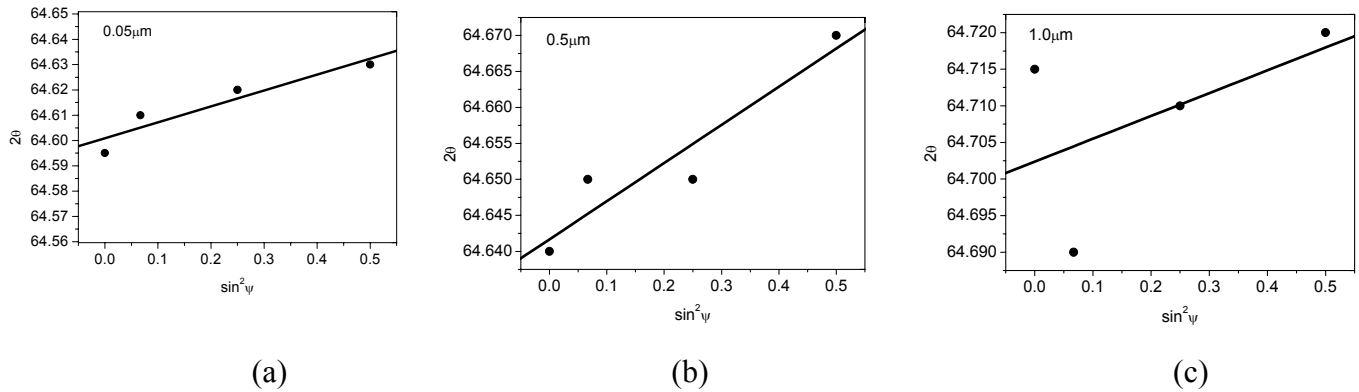
Figure 3: The linear relationship of $2\theta_{\psi}$ with $\sin^2\psi$ for different film thickness: (a) 0.05μm, (b) 0.5μm, (c) 1.0μm

DISCUSSIONS

In the PZT thin film preparation by laser beam ablation, the PZT target materials were melted and vaporized. The melting and vaporous materials were deposited on the substrate by reverse impulse. During the film deposition at elevated temperature, strain due to misfit between the film and substrate would be developed. During cooling from the deposition temperature, thermal and transformation strains are developed in the film. The combination of these strains, lattice misfit, thermal misfit, and transformational, together with the effects of any structural relaxation processes, such as interfacial dislocation formation, leads to a net stress condition whin the film which affects the configuration of 90^{0} domain structures in the film below the ferroelectric phase transition. Therefore, during the preparation of PZT thin film, there should have are four stress in the thin film which are epitaxial stress σ_{ep}, intrinsic stress σ_{in}, thermal stress σ_{th} and transformation stress σ_{t}[3]. The epitaxial stress is caused by the mismatch of the lattice parameter between thin films and substrate. The thermal stress is caused by the differences of the thermal expansion coefficients between thin film and substrate material. The intrinsic stress is generally caused by a collision of paraelectric particles which have kinetic energy to the deposited film. The phase transformation stress is the results from the change in lattice parameters of the PZT thin film during the process of ferroelectric phase transition at T_c. When the cubic PZT structure with a single lattice parameter a_o transforms to the tetragonal structure, there are two modes. One is the phase transition to a domains, and another is transition to c domains. Therefore, the phase transformation stress is caused by the mismatch between a or c and a_0. These four stresses all contribute to the change of the free energy during the forming process of PZT piezoelectric thin film.

$$F_{tot} = F_{ep} + F_{in} + F_{th} + F_{tr} + F_{sub} \tag{5}$$

where F_{tot} is total free energy of the film/substrate system, F_{ep}, F_{in}, F_{th}, F_{tr}, F_{sub} are , respectively, the

contribution of epitaxial stress σ_{ep}, intrinsic stress σ_{in}, thermal stress σ_{th}, transformation stress σ_{t} and substrate to the total free energy. During the PZT film deposition process, the total energy will have a potential of system at minimum free energy. The free energy was discussed in the literature. Therefore, the residual stress in thin film should be written as,

$$\sigma_{res} = \sigma_{ep} + \sigma_{in} + \sigma_{th} + \sigma_{tr} \tag{6}$$

Epitaxial stress results from the lattice mismatch at the growth temperature between the film a_0 and the

substrate a_s and can be written as,

$$\sigma_{ep} = \frac{E_f}{1-v_f} \frac{a_s - a_0}{a_s} \tag{7}$$

where a_0 is the lattice parameters of the PZT(0.58/0.42) thin film in the cubic phase before phase transition at the deposition temperature $T_s = 650^oC$. a_f and a_s are the lattice parameters of the film and the substrate in the cubic phase. E_f and v_f are, respectively, Young's modulus and Poisson's ratio of the thin film and they are, respectively, 85GPa and 0.28. Since the substrate thickness is much greater than that of the film, the resulting epitaxial stress during growth in the film is tensile for $a_s > a_0$ and compressive for $a_s < a_0$ if we assume the absence of structural relaxation. However, since epitaxial strain develops at the growth temperature, it is reasonable that structural relaxation mechanisms (i.e., the formation of misfit dislocations at film/substrate interfaces) should be active to relieve this stress. Therefore, epitaxial stress has not contribute to residual stress[4].

The intrinsic stress can be relaxed by the orientation change. The difference of the c-axis lattice parameter before and after the annealing process was used to calculate the stored intrinsic stress as follows,

$$\sigma_{in} = -\frac{E_f}{2v_f} \frac{[A(c)_f - B(c)_f]}{A(c)_f} \tag{8}$$

where $A(c)_f$ and $B(c)_f$ are c-axis lattice parameters of PZT thin film in tetragonal phase at room temperature before and after annealing, respectively. The lattice parameters were calculated with the (002) peak position in the XRD patterns. In the investigation the c-axis lattice parameters $A(c)_f$ are, respectively, 4.0958 A^0, 4.0861 A^0 and 4.0817 A^0 for the thickness of 0.05μm, 0.5μm and 1.0μm PZT thin film. The c-axis lattice parameters $B(c)_f$ are, respectively, 4.0958 A^0, 4.0861 A^0 and 4.0817 A^0 for the thickness of 0.05μm, 0.5μm and 1.0μm. The intrinsic stresses for different film thickness are shown in figure 4. One finds that the intrinsic stress has the same profile as the total stress. Therefore, it is obvious the intrinsic stress greatly contributes to the total stress.
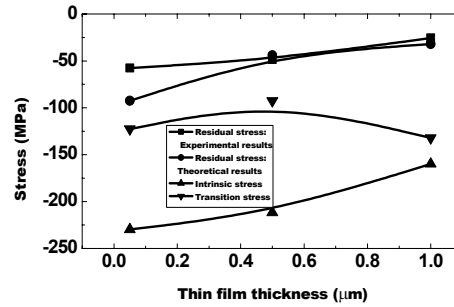
Figure 4: The contributions of intrinsic stress and transition stress to residual stress in PZT thin film

The thermal stress develops from thermal expansion mismatch between the film and substrate during cooling from the processing temperature to room temperature. The thermal stress can be written as,

$$\sigma_{th} = \frac{E_f}{(1-v_f)} \{[(\alpha(c)_f - \alpha_s)](T_s - T_{tr}) + [(\alpha(T)_f - \alpha_s)](T_{tr} - T_0)\} \tag{9}$$

where $\alpha(c)_f$ and $\alpha(T)_f$ are the thermal expansion coefficients of PZT (0.58/0.42) thin film in the basal plane for the cubic and tetragonal phases, respectively and they are assumed to be same and are taken as 7.0×10^{-6}/K. α_s is the thermal expansion coefficients of the substrate is taken as 3.5×10^{-6}/K. The thermal stress is about 0.26GPa and it is not dependent on film thickness. Since it is difficult for structural relaxation to occur at low temperature, thermal stresses are stored in the film. For many materials, the resultant residual stress often result in microcracking of the film.

During the cooling from the growth temperature, the PZT thin film undergoes a ferroelectric phase transition from a cubic phase to a tetragonal phase at 490^0C. Consequently, a high stress field is induced in the film. The stress in the film can be relieved by a domain formation. The phenomenon is similar to the formation of coherent alternating twins in martensites. The phase transition stress can be expressed as,

$$\sigma_{tr} = (1-P)\frac{E_f}{1-\nu_f}\frac{[a(T)-a_0]}{a_0} + \alpha\frac{E_f}{1-\nu_f}\frac{[c(T)-a_0]}{a_0} \qquad (10)$$

where $a(T)$ and $c(T)$ are a-axis and c-axis lattice parameters of tetragonal PZT at transition temperature and a_0 is the lattice parameter of cubic phase. the a-axis and c-axis lattice parameters of tetragonal structure (before annealing). The a-axis lattice parameters are, respectively, $4.030A^0$, $4.030A^0$ and 4.017 A^0 for the film thickness of 0.05μm,0.5μm and 1.0μm. The c-axis lattice parameters are, respectively, $4.0958A^0$, $4.0861A^0$ and $4.0817A^0$ for the film thickness of 0.05μm,0.5μm and 1.0μm. The contribution of phase transition stress to residual stress is shown in figure 4. It is obvious the phase transition stress has greatly contribution to the total residual stress. It is shown that the theoretical results and the experimental results for residual stress in PZT thin film are relatively consistent.

Observing the results for ferroelectric properties shown in figure 1, c-axis orientation ratio shown in figure 2 and residual stress shown in figure 4, one can see that there is a relationship of ferroelectric properties with residual stress. When the film is thin, the compressive residual stress is high and in this case, remnant polarization P_r and c-axis orientation ratio are both low. When the film is thick, the compressive residual stress is low and in this case, remnant polarization P_r and c-axis orientation ratio are both high. One can have the conclusion that the high compressive residual stress will result in the low values of remnant polarization P_r and c-axis orientation ratio. During the PZT thin film deposition, when the residual stress was gradually eliminated, crystal particles were ease to grow and the spontaneity polarization would be easy to progress.

CONCLUSIONS

In the investigation, the piezoelectric thin film $Pb(Zr_xTi_{1-x})O_3$(PZT) was prepared by a pulse laser deposition method. The residual stress in piezoelectric thin film was tested by x-ray diffractometer (XRD). The relation of properties such as microstructures, piezoelectric response with residual stress was investigated. A theoretical model for residual stress formed mechanism is proposed. The model is based on the combined effects of the difference of thermal mismatch between substrate and thin film, the phase transformation and the different of lattice constant between thin film and substrate. Remnant polarization P_r linearly increases with increasing film thickness and the coercive field gradually decreases with increasing film thickness at the same electric field. The residual stress has a great effect on ferroelectric properties of PZT thin films. Remnant polarization P_r decreases with increasing residual stress. The coercive field gradually increases with increasing residual stress.

ACKNOWLEDGMENTS

REFERENCES

1. Haertling, G. H. (1999) *J. Am. Ceram. Soc.*, 82, 797.
2. Noyan, I. C., Cohen, J. B., (1987) Residual Stress-Measurement by Diffraction and Interpretation, Springer-Verlag, New York.
3. Luo, H., Zheng, X. J. and Zhou, Y. C., (2000) *J.Chinese Laser*, (in press)
4. Foster, C. M., Li, Z., Buckett, M., et al.(1995) *J. Appl. Phys.*, 78, 2607.

RESONANCE AND CRACK PROPAGATION IN PRESTRESSED ORTHOTROPIC MATERIALS CONTAINING AN INCLINED CRACK

E.M. Craciun[1], E. Soos[2]

[1]Departament of Mathematics-Mechanics, "Ovidius" University Constanta, B[dul] Mamaia 124, 8700, Constanta , Romania
[2]Institute of Mathematics of the Romanian Academy, P.O. Box 1-174,RO-70700, Bucharest, Romania

ABSTRACT

In a previous paper [6] we have established for a prestressed orthotropic material containing a crack the direction of crack propagation and the critical incremental stresses, using Sih's generalised fracture criterion and considering all classical modes. Also, we concluded that in the case of prestressed isotropic materials acted by symmetrically distributed constant normal stresses the classical hypothesis used in Griffith-Irwin theory is justified according Sih's new fracture criterion. For all three-fracture modes we observed that Griffith-Irwin theory and Sih's new fracture criterion lead to the nearly same values of the critical incremental stresses producing crack propagation. In this paper we apply Sih's generalised fracture criterion to determine the critical incremental stresses producing crack propagation as well as the direction of the crack propagation in a prestressed orthotropic elastic material containing an inclined crack. Also, using numerical analysis we study the resonance phenomenon for two prestressed composite materials.

KEYWORDS

Inclined crack, prestressed composite materials, Sih's fracture criterion, resonance.

1. INTRODUCTION

We consider a prestressed material containing an inclined crack of a length $2a$ situated in $x_1 x_3$ plane. We supposed that the material is unbounded and the crack faces are acted by constant normal incremental stresses p. The initial applied stress σ_0 is in direction of the crack.

Our first aim is to determine the elastic state produced in the body using Guz's representation theorem.

Our second aim is to determine the critical values of the incremental stresses and the direction of crack propagation. To do this, we use Sih's generalised fracture criterion for an orthotropic and for transversally isotropic materials assuming that the body in not initially deformed. We assume that the stress free reference configuration of material is locally stable and initial deformation is infinitesimal.

In the last part we verify that the critical value of the initial applied stress σ_0 for which the phenomenon of resonance can appear σ_0^c obtained by Guz [1] and Soós [2] is also available in the case of right crack parallel to the initial applied stresses.

2.GUZ'S REPRESENTATION THEOREM FOR INCREMENTAL FIELDS

We consider a prestressed, orthotropic, linear elastic material. We take as co-ordinate planes the symmetric planes of the material. We assume that the material is unbounded and contains a right crack of length *2a*, situated in a plane making with $x_2 x_3$ an angle β. We supposed that the material is prestressed by an initial applied stress σ_0 acting in the direction of x_1 - axis see Figure 1. We assume that the magnitude of the initial applied stress σ_0 is sufficiently small and it produces only infinitesimal initial deformations. We suppose that the upper and lower faces o the crack are acted by distributed incremental stress having a constant value *p>0*, see Figure 1. Finally, we consider that the initial deformed equilibrium configuration of the body is locally stable.
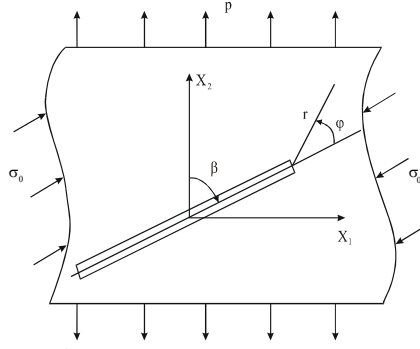
Figure 1: - Inclined crack in a prestressed orthtropic material

As it was shown by Guz [1,3,4] and independently by Soós [2] the incremental elastic state of the body can be expressed by two analytical complex potentials $\Psi_j(z_j)$ defined in two complex planes z_j, *j=1,2*. We denote by u_1, u_2 and respectively by θ_{11}, θ_{12}, θ_{21} and θ_{22} the involved components of incremental displacements, respectively incremental stresses.

According Guz's representation formulae we have:

$$u_1 = 2\,\mathrm{Re}\{b_1\Phi_1(z_1)+b_2\Phi_2(z_2)\} \quad ; \quad u_2 = 2\,\mathrm{Re}\{c_1\Phi_1(z_1)+c_2\Phi_2(z_2)\} \tag{2.1}$$

$$\theta_{11} = 2\,\mathrm{Re}\{a_1\mu_1^2\Psi_1(z_1)+a_2\mu_2^2\Psi_2(z_2)\} \quad ; \quad \theta_{12} = -2\,\mathrm{Re}\{\mu_1\Psi_1(z_1)+\mu_2\Psi_2(z_2)\} \tag{2.2}$$

$$\theta_{21} = -2\,\mathrm{Re}\{a_1\mu_1\Psi_1(z_1)+a_2\mu_2\Psi_2(z_2)\} \quad ; \quad \theta_{22} = 2\,\mathrm{Re}\{\Psi_1(z_1)+\Psi_2(z_2)\} \tag{2.3}$$

In this relations

$$\Psi_j(z_j) = \Phi_j'(z_j) = \frac{d\Phi_j(z_j)}{dz_j}, j = 1,2 \tag{2.4}$$

and

$$z_j = x_1 + \mu_j x_2, j = 1,2. \tag{2.5}$$

The parameters a_j, b_j, c_j, *j=1,2* have following expressions

$$a_j = (\varpi_{2112}\varpi_{1122}\mu_j^2 - \varpi_{1111}\varpi_{1212})/(B_j\mu_j^2); \; b_j = -(\varpi_{1122}+\varpi_{1212})/B_j; \; c_j = (\varpi_{2112}\mu_j^2 + \varpi_{1111})/(B_j\mu_j) \tag{2.6}$$

$$B_j = \varpi_{2222}\varpi_{2112}\mu_j^2 + \varpi_{1111}\varpi_{2222} - \varpi_{1122}(\varpi_{1122}+\varpi_{1212}). \tag{2.7}$$

The instantaneous elasticities ϖ_{klmn}, *k,l,m,n=1,2* can be expressed through the elastic coefficients C_{11}, C_{12}, C_{22} and C_{66} of the material and through the initial applied stress σ_0 by the following relations.

$$\varpi_{1111} = C_{11} + \sigma_0 \; \varpi_{1212} = C_{66} \; ; \; \varpi_{2222} = C_{22} \; \varpi_{1221} = C_{66} + \sigma_0 \; ; \; \varpi_{1122} = C_{12} \; \varpi_{2112} = C_{66}. \tag{2.8}$$

In their turn the elastic coefficients can be expressed using the engineering constants of the material and we have:

$$C_{11} = \frac{1-\nu_{23}\nu_{32}}{E_2 E_3 H} \qquad C_{22} = \frac{1-\nu_{13}\nu_{31}}{E_1 E_2 H} \qquad C_{12} = \frac{\nu_{12}+\nu_{32}\nu_{13}}{E_1 E_2 H} \qquad C_{66} = G_{12} \tag{2.9}$$

with

$$H = (1 - \nu_{12}\nu_{21} - \nu_{23}\nu_{32} - \nu_{31}\nu_{13} - \nu_{21}\nu_{32}\nu_{13} - \nu_{12}\nu_{23}\nu_{31})/(E_1 E_2 E_3) \tag{2.10}$$

In this relations E_1, E_2, E_3 are Young's moduli in the corresponding symmetry directions of the material ν_{12}, ..., ν_{32} are Poisson's ratios and G_{12}, G_{23}, G_{31} are the shear moduli in the corresponding symmetry planes. We recall that by σ_0 we have designed the initial applied stress acting in x_1 direction. The parameter μ_j can be obtained determining the roots ν_j, $j=1,2$ of algebraic equation :

$$\nu^2 + 2A\nu + B = 0 \qquad (2.11)$$

with

$$A = [\varpi_{1111}\varpi_{2222} + \varpi_{1221}\varpi_{2112} - (\varpi_{1122} + \varpi_{1212})^2]/(\varpi_{2222}\varpi_{2112}) \quad B = (\varpi_{1111}\varpi_{1221})/(\varpi_{2112}\varpi_{2222}). \qquad (2.12)$$

As was shown by Guz [1,3,4] the above equation (2.11) can not have real roots if the initial deformed equilibrium configuration of the body is locally stable. The complex parameters μ_j can be calculated through the roots ν_j, $j=1,2$ using equations (see Guz [1, 3, 4] and Soós [2])

$$\mu_1 = \sqrt{\nu_1}, \mu_2 = -\sqrt{\nu_2} \ \text{ if } \text{Im}\,\nu_j \neq 0, j = 1,2 \qquad (2.13)$$

and

$$\mu_1 = \sqrt{\nu_1}, \mu_2 = -\sqrt{\nu_2} \ \text{ if } \text{Im}\,\nu_j = 0 \ \text{ and } \text{Re}\,\nu_j < 0, j = 1,2. \qquad (2.14)$$

It can be shown that the parameters μ_j, $j=1,2$ satisfy the relations

$$\text{Im}(\mu_1\mu_2) = 0 \quad \text{ and } \quad \text{Re}(\mu_1 + \mu_2) = 0. \qquad (2.15)$$

In what follows we assume that parameters μ_1 and μ_2 are not equal i.e.

$$\mu_1 \neq \mu_2. \qquad (2.16)$$

The above condition is satisfied for orthotropic materials as well as for prestressed isotropic materials.

The expressions of the complex potentials $\Psi_j(z_j)$, $j=1,2$ corresponding to our incremental boundary value problem were determined by Guz [1,3,4] and later independently by Soós [2] and have the following equations

$$\Psi_j(z_j) = \frac{(-1)^{j-1}}{\chi_j(\varphi)} \cdot \frac{a_j\mu_j K_I + K_{II}}{2\Delta\sqrt{2\pi r}}, j = 1,2 \qquad (2.17)$$

where

$$\Delta = a_2\mu_2 - a_1\mu_1 \qquad (2.18)$$

$$\chi_j(\varphi) = (\cos\varphi + \mu_j \sin\varphi)^{1/2}, j = 1,2 \qquad (2.19)$$

and

$$K_I = p\sin^2 \beta\sqrt{\pi a}, \ K_{II} = p\sin \beta\cos \beta\sqrt{\pi a} \qquad (2.20)$$

are the stress intensity factors corresponding to the first respectively second mode of fracture for an applied incremental stress $p>0$.

3. SIH'S ENERGETICAL CRITERION IN A MIXED FRACTURE MODE

We denote by W *the incremental strain energy density* i.e.

$$W = \frac{1}{2}\theta_{kl}u_{l,k}, \quad k,l = 1,2 \qquad (3.1)$$

where

$$u_{l,k} = \frac{\partial u_l}{\partial x_k}$$

The expressions (2.17) of the complex potentials $\Psi_j(z_j)$, $j = 1,2$ show that near a crack tip the incremental strain energy density W has a singular part as well a regular part. We design by r and φ the radial distance from considered crack tip and the angle between radial direction and the line ahead the crack, see Figure 1.

Using the expressions (2.17) of complex potentials and Guz's formulae (2.1) – (2.3) after long but elementary calculus we obtain that near, the considered crack tip the strain energy density have the following structure

$$W(r,\varphi) = \frac{S(\varphi)}{r} + a \ regular \ part \tag{3.2}$$

Here $S(\varphi)$ is *Sih's incremental strain energy density factor* and is given by the following equation

$$S(\varphi) = \frac{(a_1\mu_1 K_1 + K_{11})(a_2\mu_2 K_1 + K_{11})}{4\pi} s_m(\varphi) \tag{3.3}$$

where the function $s_m(\varphi)$ depends on the elastic constants of the material and on the initial applied stress having the following expression :

$$s_m(\varphi) = \mathrm{Re}\left[\frac{a_1 a_2 \mu_1 \mu_2}{\Delta}\left(\frac{\mu_1}{\chi_1(\varphi)} - \frac{\mu_2}{\chi_2(\varphi)}\right)\right]\mathrm{Re}\left[\frac{1}{\Delta}\left(\frac{a_2\mu_2 b_1}{\chi_1(\varphi)} - \frac{a_1\mu_1 b_2}{\chi_2(\varphi)}\right)\right] + ... \tag{3.4}$$

In above equation

$$\chi_j(\varphi) = \sqrt{\cos\varphi + \mu_j \sin\varphi}, j = 1,2. \tag{3.5}$$

We extend the validity of Sih's fracture criterion, (see [5]) for orthotropic or isotropic prestressed elastic materials assuming that:

H1: Crack propagation will start in a radial direction φ_c along with the incremental strain energy density factor $S(\varphi)$ is a minimum, *i.e.*

$$\frac{dS}{d\varphi}(\varphi_c) = 0, \qquad\qquad \frac{d^2 S}{d\varphi^2}(\varphi_c) > 0. \tag{3.6}$$

H2: The critical intensity

$$S_c = S_{\min} = S(\varphi_c) \tag{3.7}$$

governs the onset of the crack propagation and it represents a material constant independent of the crack geometry, loading and initial applied stress. The assumed Sih's type fracture criterion is based on local density of the incremental strain energy near the crack tip and requires no apriori assumptions concerning the direction in which energy is released by separating crack surfaces. Using the equations (2.19), (3.3) and (3.7) we obtain the incremental stress p_c for which crack propagation starts at critical direction φ_c

$$ap_c^2 = 4S_c / s_m(\varphi_c). \tag{3.8}$$

In above relation S_c is Sih's new material parameter, which takes the place of Griffith's specific surface energy γ in the new theory of brittle fracture. Once S_c is known, the relation (3.8) can be used to get p_c.

4. CRACK PROPAGATION FOR UNPRESTRESSED ORTHOTROPIC MATERIALS

In this section we suppose that our material is not initially deformed *i.e.*:

$$\sigma_0 = 0. \tag{4.1}$$

Long, but elementary calculus shows that in this case we have

$$a_1 = a_2 = 1. \tag{4.2}$$

Hence, according to equation (2.18) we get

$$\Delta = \mu_2 - \mu_1. \tag{4.3}$$

Obviously, the relation (3.3) giving Sih's strain energy factor $S(\varphi)$ rest valuable, but now the function $s_m(\varphi)$ will have a simplified form. In the following we present the results of our numerical analysis concerning the possible values of critical angle φ_c versus angle β for two anisotropyc materials. For simplicity we have assumed transversally isotropic materials, $x_2 x_3$ being isotropy plane. In this case we have

$$E_2 = E_3, v_{12} = v_{13}, v_{23} = v_{32}, G_{12} = G_{31}, v_{21} = v_{31} \tag{4.4}$$

and

$$\frac{v_{12}}{E_1} = \frac{v_{21}}{E_2}, \quad G_{23} = \frac{E_2}{2(1 + v_{23})}. \tag{4.5}$$

We consider two transversally isotropic materials characterised by the following values

(i) $E_2 = 5.56 GPa\,, v_{23} = 0.2\,, G_{23} = 2.3 GPa\;\; E_1 = 75 GPa\,, v_{12} = 0.22\,, G_{12} = 2GB$ (4.6)

and

(ii) $E_2 = 10.3 GPa\,, v_{23} = 0.28\,, G_{23} = 4.02 GPa\,, E_1 = 181 GPa\,, v_{12} = 0.46\,,\;\; G_{12} = 2 GPa$ (4.7)

The set (i) corresponds to a fibber reinforced aramid / epoxy composite and the set (ii) corresponds to a fibber reinforced graphite / epoxy composite. The dependence of the crack propagation angle φ_c versus angle β for the
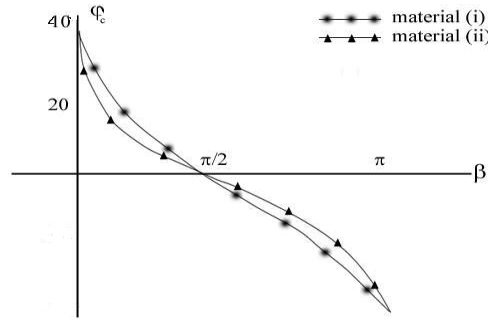
Figure 2 - Angle φ_c versus angle β

two materials (i) and (ii) is presented see in Figure 2. We observe that critical angle φ_c decrease when crack's angle β increases. Also, a remarkable result is obtained in the case when, $\beta = \dfrac{\pi}{2}$ which corresponds to the first classical fracture mode. In this case we obtain a well-known result that the crack will propagate along its line (see [6]).

5.RESONANCE PHENOMENON FOR AN INCLINED CRACK

As Guz [3] shows the phenomenon of internal stability or resonance has a well-defined physical meaning and can be elucidated taking into account the fact that all materials have an internal structure. The phenomenon concerns the loss of stability of the structure and depends on the geometrical and mechanical characteristics of the body as a whole . A rigorous study of this phenomenon has to take into account explicitly the parameters describing the internal structure of the body. Takings into account that such phenomenon can take place arise the following question: May exist a critical value σ_0^c of the initial applied stress σ_0 such that when σ_0 starting from zero converges to σ_0^c, the incremental stress p_c converges to zero?. For a fibber reinforced composite the answer to this question was given by Guz and it is positive (see [1], Chap. 2). How for a fibber reinforced composite material Young's modulus E_1 is greater than E_2 and than shear modulus G_{12}, Guz was able to show that the critical value σ_0^c is given by the following relation:

$$\sigma_0^c \approx -G_{12}\left\{1 - \frac{G_{12}^2}{E_1 E_2}\left(1 - v_{13}v_{31}\right)\left(1 - v_{23}v_{31}\right)\right\} < 0. \tag{5.1}$$

Since $E_2 \ll E_1$ and $G_{12} \ll E_1$ the critical compression stress σ_0^c produces only infinitesimal strains in the prestressed material. In what follows we verify in the case β is constant, for our reinforced materials (*i*) and (*ii*) characterised by the values given by eqs (4.6) respectively (4.7) that phenomenon of resonance can appear when σ_0^c converges to $\sigma_{0(i)}^c$ for material (*i*) and to $\sigma_{0(ii)}^c$ for material (*ii*). Here we denoted by $\sigma_{0(i)}^c$ and respectively $\sigma_{0(ii)}^c$ the critical value for materials (*i*) and respectively (*ii*) from expression (5.1) and we obtained the following values :

$$\sigma^c_{0(i)} = -1.9805 GPa \quad \text{and} \quad \sigma^c_{0(ii)} = -1.9957 GPa \,. \tag{5.2}$$

Using equation (3.8) we obtain for the critical incremental stress following expression:

$$p_c = 2\sqrt{\frac{S_c}{a s_m(\varphi_c)}} \,. \tag{5.3}$$

Table 1 presents the dependence of the incremental stress φ_c and of critical fracture angle φ_c for materials (*i*) and (*ii*). How Sih's parameter S_c and the fracture's length are constant we shall study the variation of the new stress function $\pi_c = \pi_c(\sigma_0)$ given by :

$$\pi_c = \frac{p_c}{2}\sqrt{\frac{a}{S_c}} \,. \tag{5.4}$$

TABLE 1

THE VALUES OF π_c AND φ_c VERSUS σ_0 FOR MATERIALS (*i*) AND (*ii*)

Material	σ_0	-1.99	-1.98	-1.96	-1.94	-1.92	-1.90	-1.75	-1.50	-1.25	-1.00	-0.50	-0.25	-0.10	0
(*i*)	π_c (GPa)		0.03	0.22	0.28	0.34	0.38	0.56	0.72	0.82	0.91	1.03	1.09	1.12	1.14
	φ_c (°)		44.4	43.8	43.6	43.5	43.4	42.5	41.8	41.4	41.1	40.9	40.5	40.4	40.3
(*ii*)	π_c (GPa)	0.05	0.26	0.33	0.39	0.43	0.47	0.62	0.77	0.87	0.94	1.05	1.10	1.14	1.15
	φ_c (°)	44.5	44.3	44.1	43.9	43.8	43.7	43.0	42.4	42.1	41.8	41.2	41.1	41.0	40.9

6. FINAL REMARKS

From our numerical analysis we conclude that:

- critical fracture angle φ_c decreases when crack's angle β increases;
- when crack's angle β is equal with $\pi/2$ case corresponding to the first classical fracture mode we obtain a well-known result, that $\varphi_c = 0$, *i.e.* the crack propagates along its line;
- when σ_0 decreases to the critical value σ^c_0 also the incremental stress p_c decrease. When σ_0 converges to σ^c_0 we observe that p_c converges to zero, *i.e* the crack will start to propagate even that p_c is approximately zero. In this case resonance phenomenon occurs.
- critical fracture angle φ_c decreases when incremental stress σ_0 decreases. In the case $\beta = \pi/2$, which corresponds to the first classical fracture mode, for $\sigma_0 = 0$ we obtain that critical fracture angle φ_c is in a vicinity of 40°, (see [6]).

REFERENCES

1. A. N. Guz (2000), *Fracture mechanics of composite materials acted by compression*, Naukova Dumka, Kiev, (1989), (in russian).
2. E. Soós, (1996) *Resonance and stress concentration in a prestressed elastic material containg a crack. An apparent paradox.* Int J. Engn. Sci., **34**, pp. 363-374.
3. A.N.Guz (1991), *Brittle fracture of material with initial stress,* Naukova Dumka, Kiev, (in russian).
4. A.N.Guz(1986), *The foundation of the three dimensional theory of stability of deformable bodies,* Visha Schola, Kiev.
5. G. C. Sih and H. Leibowitz (1968), *Mathematical theory of brittle fracture – An advanced treatise, vol. II, Mathematical fundaments*, pp 68-591, Academic Press, New York.
6. E. M. Crǎciun and E Soós, *Sih's fracture criterion for anisotropic and prestressed materials,* Rev. Roum. Sci. Tech. – Mec. Appl., tome **44** (in press).

RESPONSE AND FAILURE OF COMPOSITE STRUCTURES EXPOSED TO FIRE

J.A. Burdette[1] and K.L. Reifsnider[1]

[1] Department of Engineering Science and Mechanics, Virginia Tech
Blacksburg, VA 24061, USA

ABSTRACT

A methodology for evaluating the performance of composite structures subjected to simultaneous mechanical loading and fire exposure is presented in this paper. The experimental procedure (along with the newly-developed equipment required for these tests) is described. A series of computer models used to simulate the entire fire exposure, material degradation, and structural failure processes is discussed. Experimental results for composite structures under various degrees of mechanical loading and subjected to fires of various intensities are then presented and discussed. The results indicate that the durability of composite structures in a fire is strongly influenced by the interaction between the fire characteristics, the initial mechanical load level, and the material degradation mechanisms thereby making it unwise to apply conclusions drawn from specific experiments to the general problem of structural response to fire.

KEYWORDS

fire, composites, durability, material simulation

INTRODUCTION

The work presented in this paper focuses on evaluating the response of composite structures to simultaneous mechanical loading and fire exposure. The work represents several "firsts" for the fire research community. It is the first attempt to experimentally evaluate the thermo-mechanical response of loaded structures exposed to a real fire source (as opposed to radiant heat sources that don't accurately represent the time and space-varying nature of heat fluxes from fires). Also, it is the first attempt to integrate a series of computer models, each of which simulates a specific phenomenon relating to fire exposure, in order to simulate the entire exposure process (from fire evolution, through material degradation and the associated stress re-distribution within the structure, and ending with structural failure). The experimental procedures and equipment, along with the simulation methodologies and computer models should not only serve to expand the base of knowledge on the behavior of composites in fire, but should also prove valuable to the fire research community in general by providing meaningful ways to assess the response of any structure to any fire.

In this paper, the experimental equipment and procedures that have been developed, as well as the computer models used for the analysis, are discussed. Some results are then presented and interpreted to illustrate some complications that arise when predicting the response of a loaded structure to fire exposure that don't arise in more typical engineering analyses.

BACKGROUND

As composite materials continue to gain popularity and more serious consideration for use in applications that have long been served by metals, new design issues and constraints are inevitably encountered. This fact is clearly illustrated by efforts within the military, infrastructure, and transportation communities to replace traditional metallic structures and components with lighter and more corrosion-resistant polymer-matrix composite (PMC) parts. While this will likely lead to savings in cost and weight, there is legitimate concern about the durability of polymeric materials in the presence of fire (an issue of little concern when designing with metals). Concerns stem not only from the fact that many polymers release toxic fumes upon burning, but also that polymers (and PMCs) are known to lose structural integrity at much lower temperatures than metals.

Despite these major concerns, the potential advantages are great enough that the Navy has devoted a large amount of time and money to studying the behavior of composites exposed to fire [1]. Most of the fire studies have focused on the flammability and burning characteristics of composites. There has been only limited work aimed at evaluating the mechanical response of composite structures exposed to fire [2,3,4]. Much of this work focused on the degradation of mechanical properties by comparing measurements taken *before* and *after* fire exposure (providing no information about the performance of the material *during* fire exposure). Some work in which simultaneous exposure to "fire" and mechanical loading was considered is deficient in that the "fire" conditions to which the loaded structures were exposed involved steady-state and uniform heating (which is not at all representative of the conditions encountered in a real fire).

The aim of the work presented here is to expand the limits of past fire research and perform as complete an analysis as possible of the fire exposure and subsequent material degradation and failure processes associated with composites in a fire. On the experimental side, unique equipment and procedures were developed to enable simultaneous mechanical loading and real fire exposure while also allowing for observation and measurement of the structure's response. On the theoretical side, a complete set of computer models was developed to describe the entire fire exposure and thermo-mechanical response process. The set of models assembled for this work is more complete than any developed previously to simulate the response of a loaded structure to fire. The final result of this research will be the capability to predict the service-life of a loaded composite structure in the presence of fire and the experimental procedures and equipment needed to validate the predictions. In this paper, some preliminary experimental results, along with descriptions of the models used for the analyses are presented.

EXPERIMENTAL

Clearly, one of the reasons simultaneous exposure to fire and mechanical loading has never previously been considered is the danger and difficulty associated with testing with real fire. Typical experimental procedures, equipment, and instrumentation are inadequate when the intense heat fluxes and temperatures resulting from real flames are introduced. A novel experimental technique, along with the required equipment, was thus developed as part of this research.

To apply a mechanical load to the composite specimens for this work, thin layers of composite material (with total length L = 200 mm) are bent out-of-plane and constrained between 2 stationary supports (subjecting them to large deflections and a non-uniform state of stress along the length of the sample). This method of testing was adopted by Mahieux et. al. [5] and provides a very simple way to load the samples without the use of expensive instrumentation or equipment that could be damaged by the intense heat. The loaded specimens are placed above a diffusion burner (fed at controlled flow-rates by a liquid propane fuel supply). The sample and burner are both housed within a specially-designed fire chamber to contain the heat from the fire and subject the specimen to fire conditions representative of those it could experience in service. Figure 1. shows a schematic of the experimental set-up.
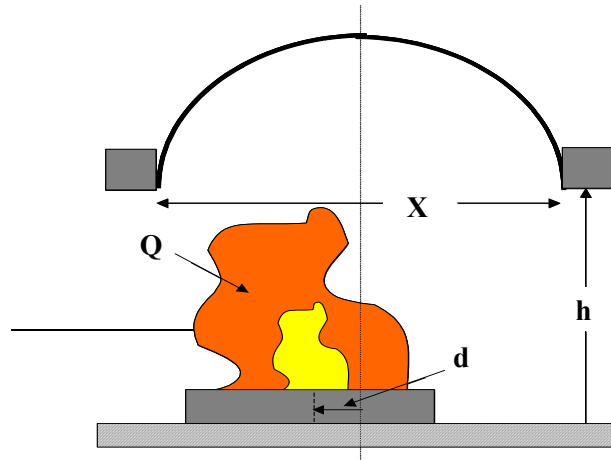
Figure 1: Schematic of experimental set-up

For the work reported here, 3 experimental parameters were varied. Experiments were performed for 2 initial load levels (X/L = 7/8 and X/L = 6/8), 2 fire sizes (Q = 0.176 kW and Q = 0.247 kW), and 2 distances between the sample and the burner (h = 127 mm and h = 178 mm). At least 3 replicates were performed at each of the 8 conditions. For each case, both the time-to-failure and the temperature distribution along the length of the sample were measured.

THEORETICAL

In order to accurately predict the thermo-mechanical structural response observed during the experiments, it is necessary to simulate the entire fire exposure and degradation process – a feat never previously accomplished for structures exposed to real fires in a confined chamber. To accomplish this, a set of 5 distinct models has been assembled, each of which addresses a specific process and feeds information to the next model in the series. The 5 models are briefly described in the sub-sections below.

Model 1 – fire model to predict conditions in chamber

A sophisticated computational fluid dynamics model developed by the National Institute of Standards and Technology has been adopted for this simulation. This model, known as the Fire Dynamics Simulator (FDS), accepts information about the chamber geometry and contents of the chamber (such as the loaded sample) as well as the fire size and location and outputs the ambient temperatures and heat fluxes (both radiative and conductive) to the specimen.

Model 2 – thermal response model

A heat transfer model was developed to accept the time-dependent heat flux and ambient temperature distributions over the length of the sample and compute the evolution of the material temperature distribution over time.

Model 3 – temperature-property model

A scheme to represent the temperature-dependent property distribution within the composite specimen is applied. This model accepts the non-uniform temperature profiles over time and computes the non-uniform stiffness profiles over time in a manner introduced by Mahieux [6].

Model 4 – mechanical response model

This model accepts the non-uniform stiffness distributions computed by Model 3 as well as the initial load level and sample geometry (input by the user to match the experimental conditions). The model utilizes a numerical scheme (shooting method employing a 4th order Runga-Kutta integration scheme) to solve the

exact, non-linear differential equation for bending of the beam with non-uniform stiffness. The model outputs the shape profile and the stress and strain distributions along the length of the sample over time.

Model 5 – material failure model

Several material failure models deemed appropriate for the experiments and materials of interest here are used to define the deteriorating strength of the thermally and mechanically-loaded specimens. The predicted strengths from this model are compared with the evolving stress profiles (from Model 4). The time at which the increasing local stress in a critical material element exceeds the decreasing material strength in that element is defined as the time-to-failure. These time-to-failure predictions can be compared with the time-to-failure measurements for a range of fire sizes, fire locations, and initial load levels.

RESULTS & DISCUSSION

As the deformed composite specimens are exposed to fire over time, the material begins to degrade and stresses are re-distributed within the samples. This induces changes in the deformed shape of the loaded specimens. Eventually, the local state of stress or strain in the deforming sample is significant enough to exceed the strength of the degrading material. The time at which this occurs is defined as the time-to-failure. Time-to-failure measurements for the range of conditions investigated during these experiments are shown in Figure 2.
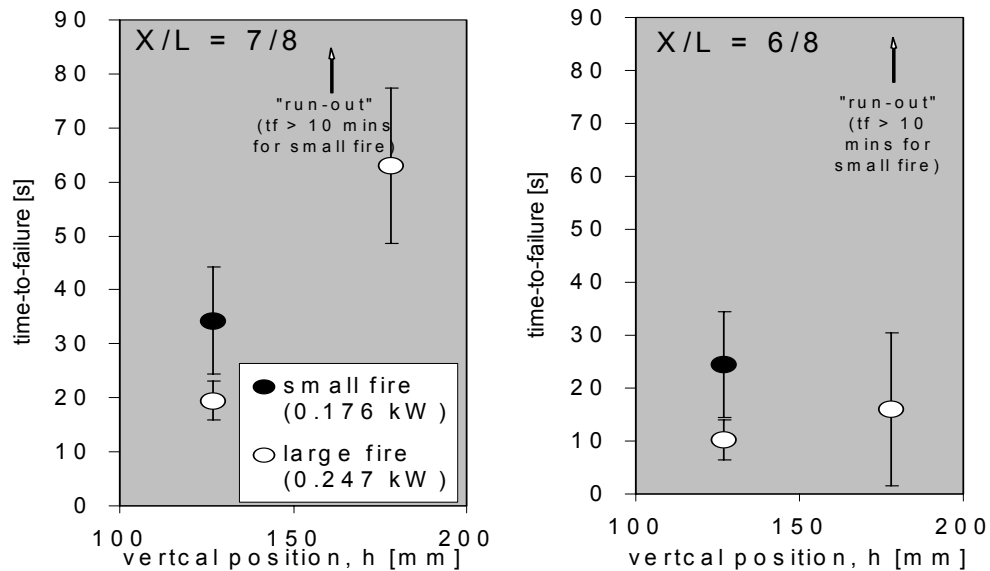
Figure 2: Time-to-failure measurements

First considering the low initial load level (X/L = 7/8), it is shown that increasing the fire size decreases the time-to-failure from an average of 29 s to an average of 19 s when the samples are positioned 127 mm from the surface of the burner. When the samples are moved 178 mm from the surface of the burner and exposed to a large fire, the time-to-failure dramatically increased to an average of 68 s. Samples positioned 178 mm from the burner and subjected to small fires, however, survived longer than 10 min (defined as "run-outs") without failing.

Similar behavior was observed for the samples loaded to a greater initial load level (X/L = 6/8). Loading the samples more severely in the presence of both large and small fires (with the samples positioned 127 mm from the burner) slightly reduced the measured times-to-failure. Moving the samples exposed to large fires a distance of 178 mm from the burner only slightly increased the times-to-failure for the case of severe initial loading (as opposed to the strong effect observed for more moderate mechanical loading). Again, when the samples were placed 178 mm from the burner and subjected to the smaller fire, they survived more than 10 mins without failing.

Consideration of the measured temperature distributions at the time-of-failure for these samples reveals additional information about the nature of the failures. Consider, for example the 4 conditions (2 fire sizes and 2 sample heights) for the case of low initial loading. The measures temperature distributions at the time-of-failure (or at run-out) for samples subjected to each condition are shown in Figure 3.
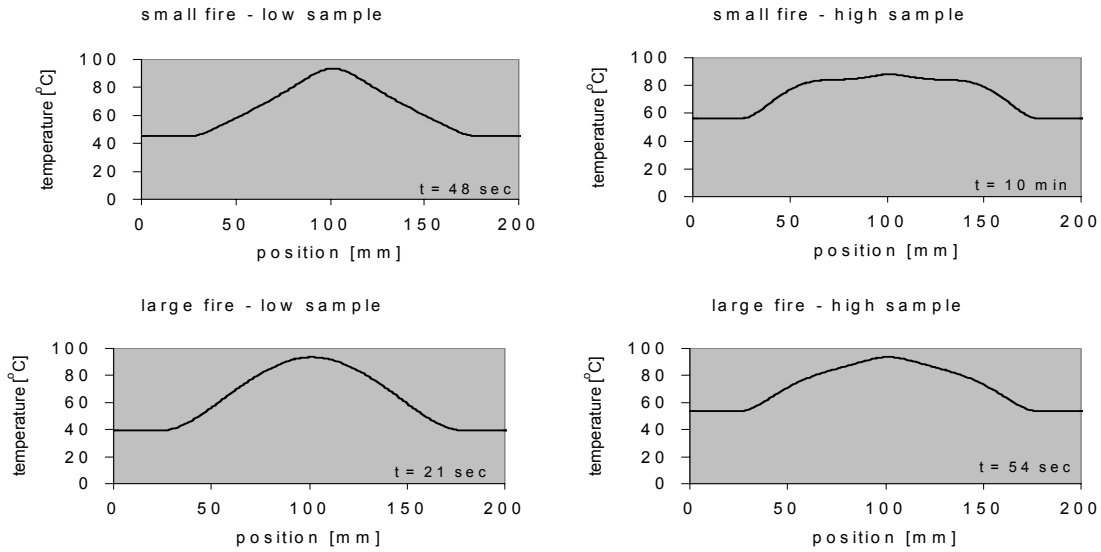
Figure 3: Measured temperature and computed stiffness distributions at time-of-failure (or at run-out)

It is shown that the maximum temperature achieved for the samples positioned closer to the fire (for both large and small fires) is approximately 95°C (~ T_g of the composite). Also, the peaks in the temperature distribution near the center of these samples (where the flame is centered) are quite sharp. Moving the samples farther from the burner serves to flatten out these sharp temperature peaks. It is interesting that sample positioned close to the burner and exposed to the large fire to induce failure also failed with a maximum temperature of 95°C, although the temperature distribution was much different than those positioned close to the fire. The sample positioned far from the fire but exposed to a smaller fire achieved a slightly lower maximum temperature ($T_{max} = 90$°C) than those that failed. It is interesting that this maximum temperature should still have weakened the material significantly, though the sample ran-out without failing.

An effort is made to explain this phenomenon by considering not only the temperatures, but also the strains at failure. The measured temperature profiles and computed stiffness profiles (from Figure 3) were input to Model 4 in order to obtain the strain distributions for each specimen at the time-of-failure (or run-out). The results are shown in Figure 4.
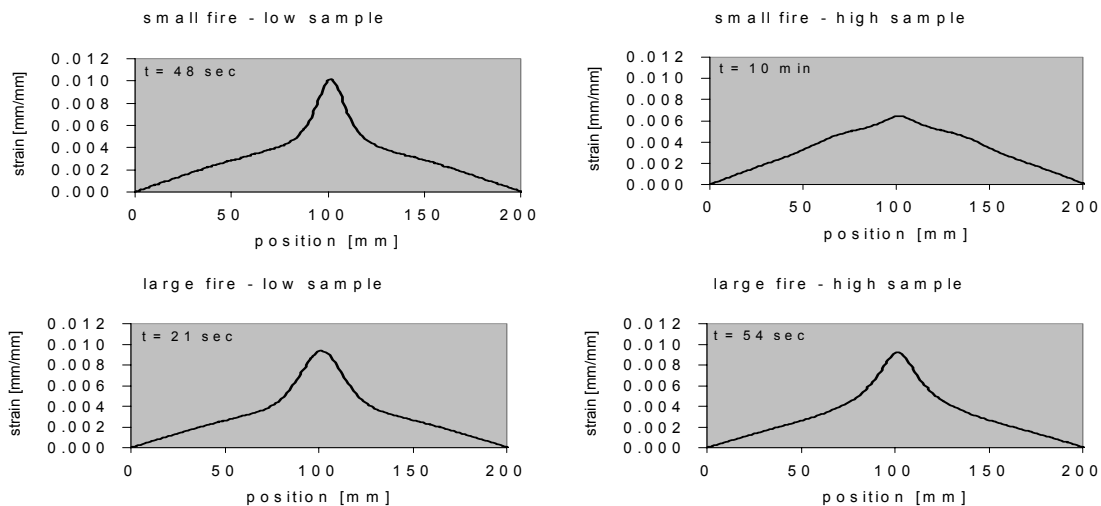
Figure 4: Computed strain profiles at time-of-failure (or at run-out) based on measured temperatures

It is shown that the 3 samples that failed (all with $T_{max} = 95^{o}C$) also exhibited approximately the same maximum strain at the time-of-failure ($\varepsilon_{max} \sim 1.0\%$). The run-out sample (with T_{max} only slightly lower than $95^{o}C$) only achieved $\varepsilon_{max} = 0.62\%$. It appears (based on this limited data) that there is some critical strain that cannot be exceeded in order for the loaded sample to survive, regardless of fire size or fire location.

It is interesting that although the maximum temperature of the run-out sample considered here was nearly as high as the samples that failed, the fact that the temperature distribution was more uniform for this case actually prevented a sharp strain concentration from forming. Interpretation of this result leads to a somewhat surprising conclusion. The sample that absorbed a large amount of thermal energy actually survived much longer than a sample that absorbed a much smaller amount of thermal energy under identical initial mechanical loading conditions. It is this type of interaction between fire size, fire location, and mechanical loading that complicates studies of structural response to fire.

SUMMARY

The work described in this paper represents several "firsts" in the field of fire research. The experiments performed here are the first in which structures have been subjected to simultaneous mechanical loading and real fire exposure. Also, the models developed and assembled for this work provide the very first complete simulation of the entire fire exposure and structural response and failure processes. The experimental data reported here indicates that the durability of a loaded composite structure in the presence of fire depends very strongly on the interactions among initial mechanical loading, the characteristics of the fire, and the way in which the material from which the structure is made deteriorates as a result of the heat from the fire (leading to re-distribution of the stresses within the structure and degradation of the structure's strength). It is clear that applying conclusions drawn from a specific set of experiments to more general conditions can be quite dangerous. This fact highlights the importance of the simulation scheme being developed from the 5 models discussed in this paper. This will ultimately enable predictions of the service life of any loaded composite structure to any fire, hopefully reducing the need to rely on expensive and inconvenient experiments.

REFERENCES

1. Sorathia, U., R. Lyon, T. Ohlemiller, A. Grenier, SAMPE Journal, <u>33</u>, 4, 22, (1997).

2. Sorathia, U. C. Beck, and T. Dapp, Journal of Fire Sciences, <u>11</u>, May/June, (1993).

3. Griffis, C.A., J.A. Nemes, F.R. Stonesifer, C.I. Chang, Journal of Composite Materials, <u>20</u>, May, 216, (1986).

4. Petrie, G.L., U. Sorathia, L.W. Warren, SAMPE: Evolving and Revolutionary Technologies for the New Millenium, <u>44</u>, book 1, 1165 (1999).

5. Mahieux, C.A., B.E. Russell, and K.L. Reifsnider, Journal of Composite Materials, <u>32</u>, 14, (1998).

6. Mahieux, C.A., PhD Dissertation, Virginia Tech, Blacksburg, (1999).

Reverse Bending Fatigue Failure of an Emergency Power Turbine Shaft

N.S. Xi, P.D. Zhong and C.H. Tao

Failure Analysis Center, Institute of Aeronautical Materials, Beijing 100095, China

ABSTRACT

A premature failed turbine shaft in an emergency power unit was investigated. Damage and fracture features of the shaft and relative self-lock screw cap and turbine disk were observed with low-powered microscope and Scanning Electronic Microscope. The shaft, including two symmetric fatigue areas and a central instantaneous fracture area, showed typical features of reverse bending fatigue failure. In correspond positions fretting wears were found on both the shaft and the screw cap. This suggests that fretting wear occur before the fracturing of the shaft. Operation principle of the emergency power unit was studied and metallurgical qualities of the shaft and the screw cap were inspected. Grain growth and drop, which implies overlarge electric current in spark-erosion machining, were found near the thread surface in the screw cap. It is reasonable that the grain growth and drop led to crack initiation in screw thread and then fretting in the shaft. Material change and cool forming instead of hot-forming and other preventative measures were provided.

KEYWORD

Turbine shaft, fatigue fracture, failure analysis, reverse bending

INTRODUTION

Turbine shafts are the key components in power units. Their fracture failures often imply disastrous accidents. According to their attributes and stress conditions, shafts fails mainly in (bending, tensile-tensile or torsion) fatigue fracturing, tough fracturing, and brittle fracturing [1]. Therefore, based on the analysis of failure modes of the shafts, we can judge the service conditions whether are normal or abnormal, find further failure causes, and propose effective preventive measures.

An emergency power unit was discovered flamed on the exhaust pipe in operation testing. After the emergency stop and disintegration, it was found that the turbine shaft was fractured, the turbine disk thrown [2].

The damage features of the turbine shaft and the shelf-lock screw cap were observed and analyzed, then the failure modes were determined. For finding the failure causes, metallurgical qualities of the shaft and the screw cap were inspected and the mechanical and technological factors resulted in this failure mode were investigated. At last, the preventive measures were provided.

DAMAGE CHARACTERISTICS OF TURBINE SHAFT AND SHELF-LOCK SCREW CAP

Turbine Shaft

The shaft fractured in the transitional corner of the screw thread near the behind end of the turbine disc, as shown in Figure 1. The are two symmetric fatigue regions and one central tough fracture region on the fracture surfaces, as can be seen from Figure 2. From the roughness, sizes and colors of the two fatigue regions, it can be referred that A region is the main fatigue region and B region is the second fatigue region. The two fatigue regions were originated from the screw thread and appeared multi-origins, where no metallurgical defects were found. The instantaneous fractured region, which has a large area (approximately 50% of the fractured area), shows typical equi-axial dimples. The above fracture features indicate that the shaft was failed by reversal bending fatigue load.

Different damages of the screw thread in the disc hole were found: A side has the most serious damage, showing even wearing plane and high temperature oxidized blue-yellow color (Figure 3). On the surface of the shaft and near the fracture surface 26mm (point C in Figure 1), a wear pit with diameter of approximately 3.0mm was discovered. The bottom of the pit shows typical fretting wear features, which were resulted from the point contact between the disc hole and the shaft. This pit slightly opposites to the main fatigue region. The above features demonstrate that the contact points (A and C) between the disk hole and the shaft surface had a little range of relative movement.

Figure 1: Outward and fracture site of the turbine shaft. C is a fretting wear pit.

Figure 2: Fracture surface of the turbine shaft. A and B are the chief and secondary fatigue regions.

Shelf-lock Screw Cap

The wear marks on the side surface of the shelf-lock screw cap which contact with the disk appeared uneven distribution. More serious wear marks can be seen on the site corresponding to fatigue regions (A and B); very slight wear on the site corresponding to the instantaneous fractured region, where silver-plating layer was loomed as shown in Figure 4. This indicates that there were fretting on the contact surfaces of the disk and the screw cap with a boundary of D-D line.

Figure 3: Serious wears of the thread near A side.

Figure 4: Wear of the screw cap side. A and B sides heavy.

The first thread in the screw cap near the disk side fractured a half at the B side. The origin, propagation and instantaneous areas are obvious. The propagation region has small size whereas the tough region has large size

about 70% of the fractured area. Figure 5 gives a zoomed appearance of the origin and the growth region, where arrow shows the crack propagation direction (i.e. axial direction). Fracturing initiated at the transitional corner of the thread bottom. Although the fracture surface underwent axial secondary damage, local fatigue features can be seen in the growth region and shear dimples in the tough region. Therefore, the thread failure is low-cycle shear fatigue fracture.

METALLRUGICAL ANALYSIS

Turbine Shaft

The turbine shaft is made from GH4169 superalloy, its heat treatment is 960°C×10h solution (air cooling), 720°C×8h aging, 50°C/h furnace cooling to 620°C×8h, and then air cooling to room temperature. Microstructure shows fine grains and hardness check indicates HV401~446 (equivalent to HRC42~45). The two test results agree with technical standard requirements.

Self-lock Screw Cap

Made from GH2132 superalloy, the cap underwent 990°C solution, latheing thread, spark-erosion machining for the shape, 710°C×12h aging and then air cooling. The hardness is HV311~349 (equivalent to HRC31~34.5) and agrees with the standard requirement.

Metallurgical inspection reveals that in the female thread of the screw cap the surface grains grew obviously, some grains fallen and grain boundary became wide, as shown in Figure 6. These suggest there was overlarge electric current in spark-erosion machining, then high temperature in the surface layer and finally surface coarse grain and wide grain boundary.

Figure 5: Origin and propagation of the screw thread fracture surface

Figure 6: Grain growth and drop of the self-lock screw cap

FAILURE CAUSES AND PREVENTIVE MEASURES

Operation Principle Of The Emergency Power Unit

Figure 7 shows the diagram of the emergency power unit. High-pressure admission flows to the blades on the disk, chiefly generates torsional and axial load, which transfer to turbine shaft. The shaft then drives the gears. From Figure 7 we can see that, in normal condition, the turbine shaft mainly undergoes torsional and axial load, and the bending load due to the air flow turbulent and dynamic unbalance of turbine disk are negligible. In another word, if there were no changes of work conditions, the fracture failure of the shaft due to metallurgical or machining quality was only the tensile-tensile or torsion fatigue fracture; if there were other types of fatigue fracture failure, then work conditions of the shaft changed.

Figure 7: Dramatic diagram of the emergency power unit (AB is the fracture site)
1 Turbine shaft; 2 Drive gear shaft; 3 Bearing (2); 4 Turbine disk; 5 Self-lock screw cap.

Failure Causes

According to the macro and micro features of the failed turbine shaft, it is determinable that the shaft failure was a reverse bending fatigue-fracturing [3]. This indicates the shaft underwent cyclic bending stresses at the fracture site. Moreover, because the fracture site is just situated at the transitional corner of the thread bottom, in which high stress concentration existed, the fracture surface embodied the features of reverse bending low-cycle fatigue fracturing.

From the fracture features of the turbine shaft and damage marks of the relative components, it can be referred that the reverse cyclic bending stresses at the fracture site were generated neither from the shaft deformation nor from the peg-top eddy motion. An agreeable situation is that, owing to the axis deviation of the turbine disk, under the impact effects of the high rotation and air flow changes, the disk swung in the axial direction whereas rested to the shaft in rotational direction, then the shaft bore reverse cyclic bending stresses. Because the bending load was supported by A and C points, fretting began at A and C points first. Furthermore, A point is at the thread bottom and had smaller section area than C point, so crack initiated at A point. With the crack propagation, the disk swung more and more violently, then another fatigue crack initiated at B point first, finally the shaft failed in reverse bending fatigue fracturing.

The disk and the shaft assembled in transitional match and fixed by the screw cap. A torsion moment of 35N•m (equivalent to 24kN of axial prestressed force) was applied to the screw cap for preventing relative rotation between the shaft and disk and for ensuring coincidence of the disk axis and the shaft axis. Therefore, the prestressed force is a key factor for normal rotation of the turbine.

The above analysis shows there was low-cycle fatigue fracturing in the first thread of the screw cap. Because the first thread undertook the maximum load (about 30% of the sum load), its fracturing would lead lease of the prestressed force at B side and deviation of the disk axis. Thus the fatigue fracturing of the screw cap is the direct cause of the shaft.

Besides the axial prestressed force, the screw cap carried cyclic axial load coming from the disk. These axial loads act as shear load on the thread, which is the mechanical factor for low-cycle fatigue fracturing of the thread. Made from GH2132 superalloy, the screw cap has lower mechanical properties than GH4169 [4]. In the test to the failed components, the HRC of the screw cap is 10 lower than that of the turbine shaft. More important is that, in the spark-erosion machining, overlarge electric current lead to surface grain growth and drop in the screw cap, which greatly reduced the resistant of the thread. So that the spark-erosion machining is

the direct cause of cracking of the first thread in the screw cap, and is also the further cause of the reverse bending fatigue fracturing of the shaft.

Preventive Measures

In order to ensure the operation reliability of the power unit and in accordance with this failure causes, preventive measures should be concentrated on improvement of the self-lock screw cap.

(i) Manufacturing the screw cap with GH4169 alloy instead of GH2132 alloy. This will not only promote the strength and fatigue properties but also eliminate the clearance between the cap and the shaft resulted from the difference of the thermal expansion coefficient, which will augment the clearance and release the prestressed force.

(ii) Using cool forming to machine the shape of the screw cap. This will avoid the surface grain growth and drop in the thread, increase the fatigue resistance, and be beneficial to ensuring the 45° prick plane and rigidity.

(iii) Substituting the slight convexity in the center with slight concave for increasing the contact area and rigidity.

At the same time, other preventive measures will be also effective such as: surveying the side pulsation of the disk, eliminating the combined error in assemble, monitoring the vibration of the power unit, cold extruding the shaft thread for enhance the fatigue strength.

CONCLUSIONS

(i) The failure of the turbine shaft was a reverse bending fatigue fracturing, and its failure cause is resulted from the deviation of the turbine shaft axis.

(ii) The low-cycle fatigue fracturing of the first thread in the self-lock screw cap, which leads to the releasing of the prestressed force, is responsible for the deviation of the disk axis. The surface grain growth and drop in self-lock screw cap is the direct cause of the low-cycle fatigue fracturing of the thread and the further cause of the reverse bending fatigue fracturing of the shaft.

(iii) Substituting the material of the screw cap with same material of the turbine shaft, using cool forming to manufacture the screw cap, and changing the convex plane in the center into concave, will avoid similar failures.

REFERNCES

1. Tao C.H., Zhong P.D., Wang R.Z. and Nie J.X. (2000). *Failure Analysis and Prevention for Rotor in Aero-engine* (in Chinese), Defense Industries Press, Beijing.
2. Zhong P.D., Xi N.S. (1997) *Failure Analysis Report* (in Chinese), Failure Analysis Center of Aviation Industries, China.
3. Zhang D., Zhong P.D. and Tao C.H. (1997). *Practical Analysis for Mechanical Failure*, (in Chinese), Defensive Industries Press, Beijing.
4. Yan M.G. (1989). *Handbook of Chinese Aeronautical Materials* (in Chinese), Chinese Standards Press, Beijing, China.

REVERSE BULGING AND PLUGGING IN METAL FOIL INDUCED BY HIGH POWER LASER

Y. C. Zhou[1,2], Z. P. Duan[2]

[1]Institute of Fundamental Mechanics and Material Engineering, Xiangtan University, Xiangtan, Hunan, 411105, China
[2]Institute of Mechanics, CAS, Beijing, 100080, P. R. China

ABSTRACT

A new failure mode is observed in circular brass foils induced by laser beam. The new failure is based on the following experimental facts: (1) the peripheries of the circular brass foils are fixed and the surfaces of the foils are radiated by a laser beam; (2) the laser beam used is considered to be non-Gaussian spatially, actually an approximately uniform distribution limited in a certain size spot; (3) the pulse duration of the laser beam is $250 \mu s$, i.e. so called long duration pulse laser. The failure process consists of three stages; i.e., thermal bulging, localized shear deformation and perforation by plugging. The word 'reverse' in 'reverse bulging and plugging mode' means that bulging and plugging occur in the reverse direction of laser beam incidence. The new failure mode is analyzed with the thermal-elastic plate theory, parabolic shear deformation theory as well as one-dimensional buckling theory. The theoretical study can explain the new phenomenon and predict the critical laser intensity. The calculated results for temperature fields, deflection as well as shear deformation distribution show that the newly discovered failure mode is attributed to the spatial structure effect of laser beam indeed.

KEYWORDS

High power laser beam, Circular brass foil, Reverse bulging and plugging

INTRODUCTION

In the last two decades, a great deal of attention had been paid to the interaction of high power laser with material in the fields of materials and/or structural damage and laser processing [1-2]. The damage modes which may be spallation, melting and/or vaporization depend on laser parameters, for example laser power, laser beam diameter and pulse duration. There is the potential of failure by thermal stress for the intensity of CW (continuous wave) laser in the order of $10^3 \, W/cm^2$. The damage may occur by melting and/or vaporization for the laser intensity in the order of $10^5 - 10^8 \, W/cm^2$ and the pulse duration in the order of milliseconds. In this case, the thermal stress concentrated around the crater plays an important role in material and/or structure damage. The formation of plasma may generate shock waves propagating into the materials for the laser intensity in the order of $10^8 - 10^{10} \, W/cm^2$ and the pulse duration in the order of nanoseconds. When the wave reflection takes place between two surfaces, there is the potential of failure by spallation.

However, people ignored more or less the fact that the spatial shapes of the laser beam could also play an

important role in controlling the failure mode. Those situations prevail where the size and intensity of the laser beam are such that the spatial structure effect will contribute to the mode of failure such as bulging followed by plugging. Such are the cases considered in this investigation.

EXPERIMENTAL PROCEDURE AND OBSERVATION

Experimental Procedure

A new kind of failure mode was observed in circular brass foils in which their peripheries were fixed and their front surface was subjected to a long pulsed laser over a central region, as shown in Fig.1(a). In the figure, z- and r-direction are aligned normal and parallel to the specimen, respectively, 2a is the diameter of the laser spot with size 2-6mm. The foil has a diameter of 30mm and thickness of 0.1mm and is composed of 65% copper, 33.6%zinc, 0.03% iron, 0.06% antimony and other microelements that are negligibly small in percentage by weight.

The laser beam used is a single pulse Nd: glass with a wavelength of 1.06μm, intensity order of 10^5-10^6W/cm^2 and energy from 25-40J. The diagnostics of the laser parameters provide a traditional monitoring of the laser beam characteristics, such as energy, temporal and spatial shapes. In the experiment, temperature rise on the rear surface of samples during laser irradiation is measured by a focused, imaging system of infrared (IR) detectors. The particular system consists of eight 0.1×0.1mm indium antimonide (INSb) Infrared detectors mounted on a liquid nitrogen Dewar bottle.
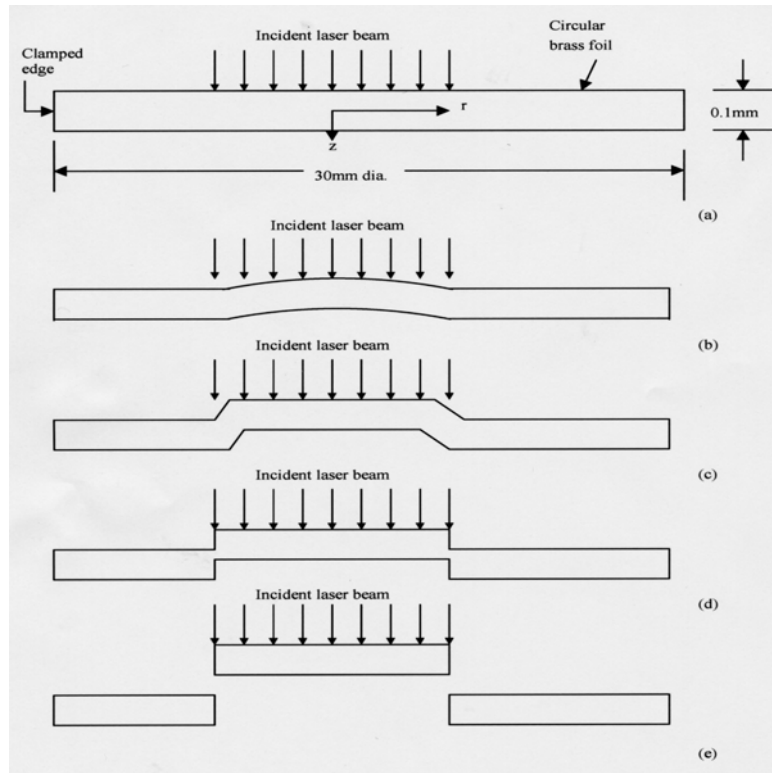
Figure 1: Schematics of the sample and failure mode: (a) schematic diagram of a normal incident laser beam impinging on a circular brass foil specimen; (b) bulging; (c) localized shear deformation; (d) plugging initiation; (e) perforation

The normalized laser intensity I/I$_{max}$ vs time and space coordinates r/a is shown in figure 2, where r and a are the radial distance and the radius of the laser spot, respectively. The full time width at half maximum of the laser is approximately 250μs. The laser intensity distribution of laser intensity is non-Gaussian and roughly uniform within the laser irradiated region and declines very sharply towards the edge where the laser spot terminates. For the convenience of numerical analysis, the laser intensity I is approximated by,

$$I = I_{max}e^{-\alpha t}(1 - e^{-\beta t})f(r) = I_{max}g(t)f(r) \tag{1}$$

where α and β are determined experimentally test, and equal to 1.5×10^4/s and 8.0×10^4/s, respectively. Therefore, laser energy $E_J = \beta \pi a^2 I_{max} / \alpha(\alpha + \beta)$ and we have

$$f(r) = \begin{cases} 1 & , & 0 \le r \le a \\ 0 & , & a \le r \le \infty \end{cases} \qquad (2)$$

and $f(r) = e^{-(r/a)^2}$ which are characterized by the non-Gaussian and Gaussian nature of the laser beam, respectively.

(a)   (b)
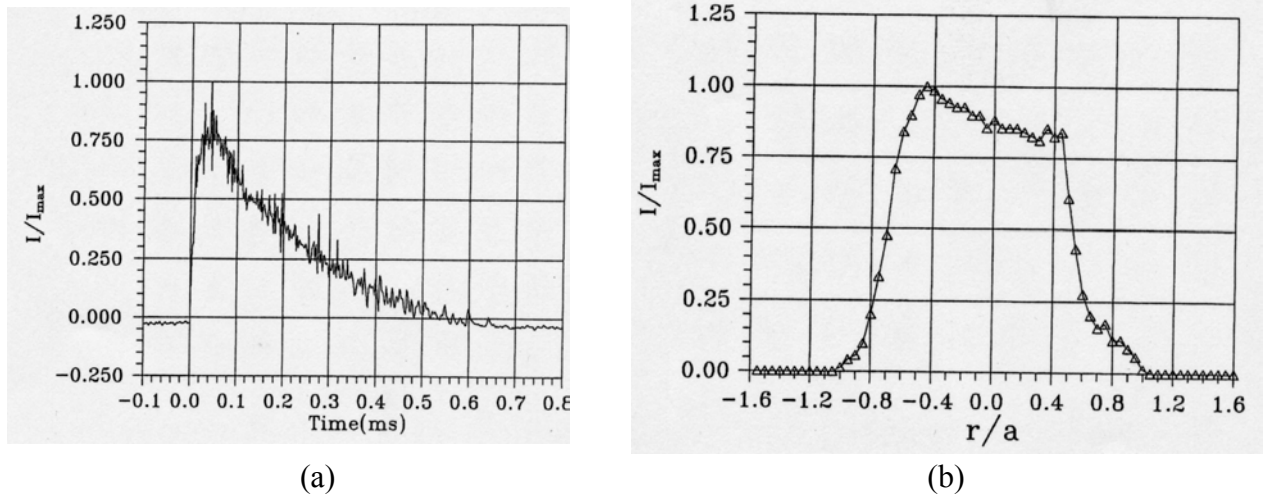
Figure 2: Temporal and spatial shape of Nd:glass pulsed laser intensity, (a) temporal shape, (b) spatial shape

Experimental Results

Description of failure mode

The evolution of specimen failure is illustrated schematically in Fig.1. Fig.1(b) shows bulging of the brass foil at the earlier stage of laser irradiation. Note that this occurs towards the side of the incident laser beam where the temperature would be higher. Significant shear deformation occurs around a rim near the outer edge of the laser beam which is shown in Fig.1(c). This leads to the softening of the material due to intense heating.

Further intensification of the energy around the periphery of the laser beam leads to the initiation of plugging and final perforation which are shown in Fig.1(d)-(e), respectively. The plugging mode of failure is customarily known to be associated with metal projectiles penetrating through mode of failure is customarily known to be associated with metal projectiles penetrating through metal targets in plate form. A plug of the target material is normally ejected in the direction of the energy source that is the moving projectile. While in the present case of laser induced the new failure mode, the plug is normally ejected in the direction opposite to the incident laser beam. The initial bulging occurs on the side with higher temperature that determines the direction of plugging.
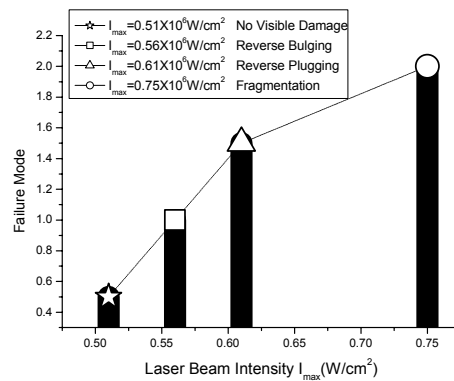
Figure 3: Failure mode in brass foil

Threshold intensity

According to the test data in this study, the failure modes and their related threshold are shown in figure 3. When the laser energy density was lower than 151J/cm^2, or equivalently, the laser intensity was less than

0.51×10^6W/cm^2, no visible macroscopic damage was observed on the front or rear surface of the brass specimen. When the laser intensity was increased to 0.56×10^6W/cm^2, the bulging of the brass specimen was observed. A slight melting was observed on the front surface at the periphery of the laser spot. The laser intensity threshold value I_{cr} for plugging to occur was about 0.61×10^6W/cm^2. As I exceeds I_{cr}, local melting of the material begins to take place. When the laser intensity was increased to 0.75×10^6W/cm^2, the brass foil was totally fractured and fragmented. A study on laser-induced spallation in 0.1mm thickness copper foil has been made by Eliezer and coworkers[2]. The intensity for spallation was of the order of 5.3×10^{10}W/cm^2 which was five orders of magnitude larger than that for that for failure by plugging which was about 0.71×10^6W/cm^2. The thresholds of the laser energy for the two different failure modes are almost not distinguishable and they are both approximately equal to 210J/cm^2.

Damage evolution

Scanning electron microscopy (SEM) showed that increased laser intensity led to the initiation of microcracks in the peripheral region with r~a. The macrocracks appeared on the rear surface and then spread into the material. They would grow and coalesce into macrocracks that rapidly in the circumferential direction as well as in the thickness direction. The macroscopic damage evolutions are shown in figures 4(a), (b) and (c) which, respectively, correspond to the schematic illustration of damage evolutions as shown in Fig.1(b), (d) and (e). The photograph of a polished section of brass specimen is shown in figure 4(a). Bulging in the direction opposite to the incident laser beam was observed with a maximum center deflection of 0.03mm which corresponded to a laser energy of 8.2J; an intensity greater than 0.61×10^6W/cm^2, and a spot diameter of 2.3mm. Softening of the material began around the outer edge of the laser spot.

When the laser intensity was increased to 0.61×10^6W/cm^2, the plugging began to take place in the brass foil. Figure 4(b) shows the circular brass foil failed by plugging opposite to the direction of the incident laser beam. This photograph of brass foil failure by plugging is viewed from the rear surface with a laser energy of 29J over region 4.5mm in diameter and the failure process corresponds to that described in Fig.1 (d).

When the intensity was increased to 0.75×10^6W/cm^2 the brass foil is totally fractured and fragmented. Figure 4(c) shows a sectioned photograph of fractured and fragmented brass foil subjected to a laser energy of 9.2J over a region 2.3mm in diameter and the failure process corresponds to that described in Fig.1(e).

| (a) | (b) | (c) |
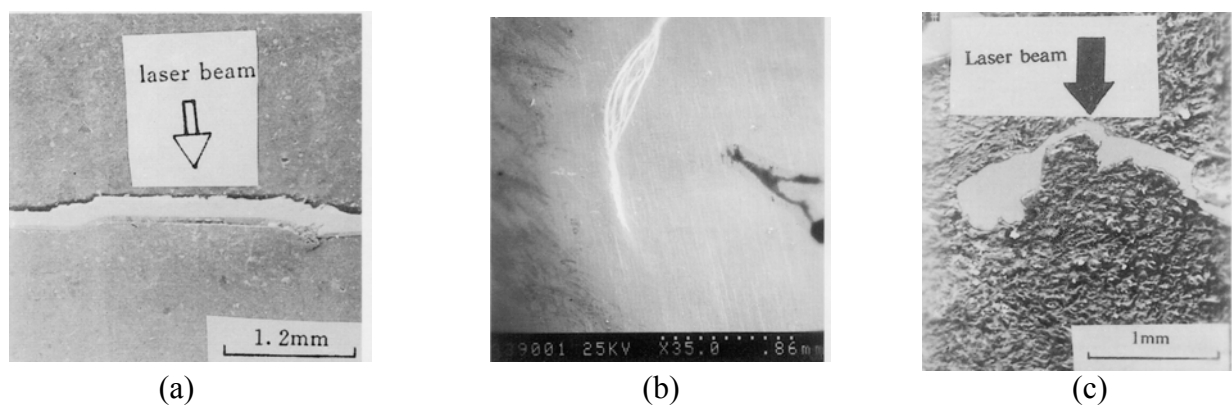
Figure 4: Photograph of failure mode: (a) sectioned photograph at the bulging state with a laser energy of 8.2J over an area of 2.3mm in diameter; (b) photograph of failure by plugging viewed from the rear surface with laser energy of 29J over a region 4.5mm in diameter; (c) photograph of fractured and fragmented foil subjected to a laser energy of 2.9J over a region 2.3mm.

DISCUSSIONS

A Thermal-elastic Analysis

As shown in section 2, at the earlier stage of laser irradiation, the brass foil bulged towards the side of the incident laser beam. The classical Kirchhoff plate theory can be used to determine the reverse bulging. In the analysis, the temperature distributions are obtained in terms of Hankel transformation and series expansion techniques. Using this temperature solution and classical Kirchhoff plate theory, deflection curve, i.e.,

reverse bulging w can be determined analytically under the assumption of thermal-mechanical decoupling. Fig.8 shows the three-dimensional profile of deflection curve for the brass foil. The thermal-elastic analysis reveal that: (a) thermal reverse bulging is mainly due to highly non-uniform spatial distribution of temperature in normal direction of target material, i.e., the temperature gradient in z-direction; (b) a steep temperature gradient across the periphery of the laser spot causes the shear strain at the periphery of the laser spot to be much larger than that in other regions. It is the temperature rise and subsequent shear deformation localization which control the whole process of the new failure mode. (c) The spatial structure of the laser beam plays an important role in controlling the damage.
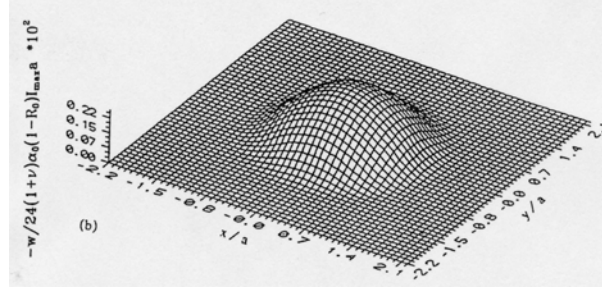
Figure 5: Three-dimensional profile of deflection curve for the brass foil.

Shear Deformation Analysis

We obtained new coupled governing equations of shear deformation and large deflections of a heated, non-homogeneous circular plate. The governing equations are obtained based on the large deflections of Berger [1] and the parabolic shear deformation theory of Bhimaraddi and Stevens [1]. We use the new coupled governing equations to analyze the failure mode induced by laser. The new non-linear coupled equations were solved by employing the Galerkin and iterative methods. Numerical results of the average shear strain at different time are shown in Fig.6. It is observed that only the shear strain γ is not zero within the laser spot edge region. This important result confirms the experimental observation, i.e. the existence of large shear strain γ within the laser spot edge. From the comparison of the shear strain distribution induced by a non-Gaussian laser beam and by a Gaussian laser beam, one can conclude that the former offers a formidable potential for the new type of failure by plugging, however, the latter has a little potential for the new type of failure by plugging. This reveals that the spatial shapes of a laser beam, indeed, play an important role in controlling the damage types.
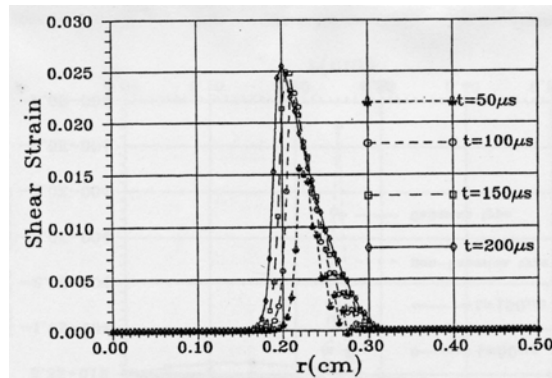
Figure 6: Transient average shear strain distributions vs the radial coordinate for the non-Gaussian type of laser beam with E_J=10J at different times.

Prediction of Reverse Plugging

The theory of one-dimensional Euler column can be used to predict the critical laser intensity at which the reverse plugging may take place. In the laser- irradiated region, the compressive stress can be obtained as,

$$\sigma_{rr} = -\frac{1}{2}\alpha_0 E \frac{I_{max}(1-R_0)}{\rho C_p h}[\frac{1}{\alpha}(1-e^{-\alpha t}) - \frac{1}{\alpha+\beta}(1-e^{-(\alpha+\beta)})] \tag{3}$$

where α_0, E, ρ, C_p and R_0 are, respectively, thermal expansion, Young's modulus, mass density, specific heat.

It is well known that the critical classical buckling stress σ_c of a clamped-clamped wide plate is,

$$\sigma_c = \frac{\pi^2}{12} \frac{E}{1-\nu^2} (\frac{h}{a})^2 \tag{4}$$

The thermal stress $\sigma_{ther} = -\sigma_{rr}$ must exceed σ_c if the foil in the laser-irradiated region is to buckle away from the remained region. The nondimensional "loading parameter" is σ_{ther}/σ_c and it is shown in figure 7 for different laser intensities. It is very interesting that the loading parameter is larger than one with $I_{max} \geq 0.61 W/cm^2$. It is the critical laser intensity at which the reverse plugging takes place.
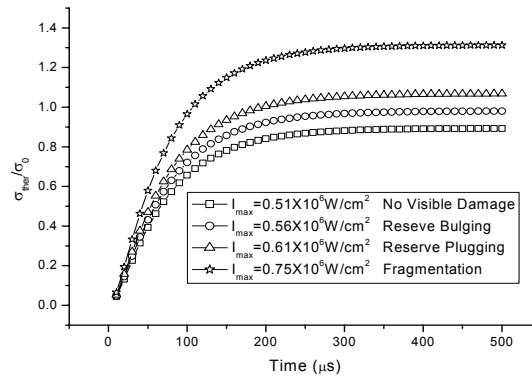
Figure 7: Histories of "loading parameter"

CONCLUSIONS

A new failure mode is observed in circular brass foils induced by laser beam. The failure process consists of three stages; i.e., thermal bulging, localized shear deformation and perforation by plugging. The word 'reverse' in 'reverse bulging and plugging mode' means that bulging and plugging occur in the reverse direction of laser beam incidence. The new failure mode is analyzed with the thermal-elastic plate theory, parabolic shear deformation theory as well as one-dimensional buckling theory. The theoretical study can explain the new phenomenon and predict the critical laser intensity. The calculated results for temperature fields, deflection as well as shear deformation distribution show that the newly discovered failure mode is attributed to the spatial structure effect of laser beam.

ACKNOWLEDGEMENTS

REFERENCES

1. Zhou, Y. C. and Duan, Z. P. (1998) *Int. J. Non-Linear Mech.* 33, 433.
2. Eliezer, S., Gilath, I. and Bar-Noy, T. (1990) *J. Appl. Phys.* 67, 715.

REVISITED ENERGY CRITERIA FOR INTERFACE CRACK DEFLECTION

D. Leguillon[1], C. Lacroix[1] and E. Martin[2]

[1] Laboratoire de Modélisation en Mécanique, CNRS - Université P. et M. Curie, 8 rue du Capitaine Scott, 75015 PARIS - France.
[2] Laboratoire de Génie Mécanique, IUT A, Université de Bordeaux 1, 33405 TALENCE Cedex – France.

ABSTRACT

Crack deflections by interfaces increase the apparent toughness of composites. Predictions are based on the comparison between the energy released during the crack growth along the interface or within the inclusions. We propose a review of our recent works in the topic. In a first step, using matched asymptotics and singularity theory, we exhibit a slightly modified form of the He and Hutchinson criterion. Next, an analysis of the residual thermal stresses leads to conclude that they have a little influence on the deflection criterion (but of course not on the further growth of the extensions). In a second step, we establish a revisited criterion, which deals with the excess of energy produced in some cases during the crack advance. Finally another mechanism is investigated: the interface is assumed to fail prematurely leaving initially an unbroken ligament between the primary crack tip and the debonded interface. Deflection results of the linking of the primary and the interface cracks.

KEYWORDS

Composites, interfaces, crack deflection, residual stresses.

INTRODUCTION

Fibers or other inclusions are inserted in brittle materials to promote toughening processes [2]. Cracks growing within the matrix are expected to kink along the interfaces and either to blunt the primary crack tip or to develop dissipative processes by friction. In ceramic matrix materials it is an essential mechanism which limits matrix cracks path and delays the final ruin of the structure. An efficient criterion able to predict such crack deflection is of course essential to tailor these composites. An approach, proposed by He and Hutchinson [3] (HH), is based on the analysis of energy release rates at the tip of virtual crack extensions either deflecting along the interface or penetrating into the fiber.

In a first step, using matched asymptotics and singularity theory, we propose a slightly modified form of the HH criterion involving the amount of energy that the primary crack requires to extend [11]. It emphasizes on the awkward role of the arbitrary extension lengths introduced in both models.

Next, an analysis of the residual thermal stresses leads to slightly different conclusions than that of He et al. [4]. At the leading order, it is drawn that they have few influence on the deflection criterion (but of course not on the possible further growth of the extensions) [10].

Prior to these extensions, the primary crack is assumed to impinge on the interface. In some cases this is questionable because of the non-classical character of the singularity, it makes the primary crack growth easier and easier as it approaches the interface. Thus, in a second step, we propose a revisited criterion that deals with the excess of energy (with respect to the Griffith criterion) produced during the crack advance. Surprisingly, arbitrary extension lengths definitions are no longer necessary; it is obviously a noticeable improvement of the HH criterion although its formulation remains very simple [8].

Finally another mechanism, first suggested by Cook and Gordon [1], is investigated: the interface is assumed to fail prematurely leaving initially an unbroken ligament between the primary crack tip and the debonded interface, as observed by Lee et al. [6]. Deflection results finally of the linking of the primary and the interface crack. Necessary conditions to such a mechanism are derived. In particular, in case of a stiff matrix, interface debonding ahead of the primary crack is shown to be almost inhibited [9].

MATCHED ASYMPTOTICS AND THE GRIFFITH CRITERION
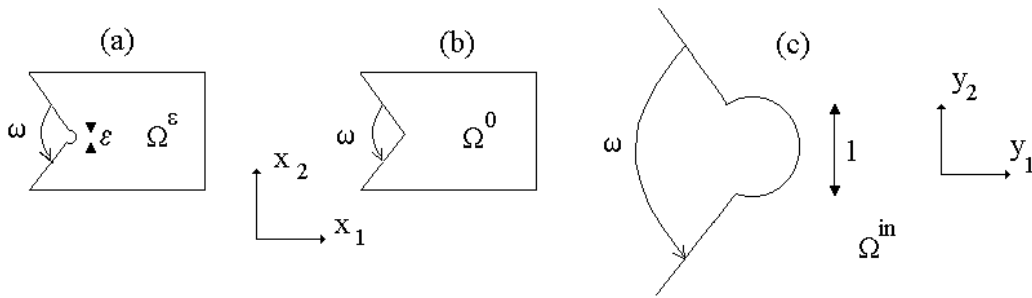
Figure 1: The perturbed (a), unperturbed (b) and stretched domains (c).

Matched asymptotics procedure is briefly recalled here. We consider a domain Ω^ε in which a corner is slightly perturbed by a flaw (a short crack, a small void,) with dimensionless diameter ε (figure 1(a)). The solution $\vec{U}(\varepsilon, x_1, x_2)$ to a plane elasticity problem in this domain can be expressed as

$$\vec{U}(\varepsilon, x_1, x_2) = \vec{U}(0, x_1, x_2) + \text{smaller terms}, \tag{1}$$

where $\vec{U}(0, x_1, x_2)$ is solution to a similar problem but in the unperturbed domain Ω^0 (figure 1(b)). This term is singular in the corner and expands as

$$\vec{U}(0, x_1, x_2) = kr^\lambda \vec{u}(\varphi) + \vec{U}^R(x_1, x_2). \tag{2}$$

r and φ are the polar co-ordinates; $0 < \lambda < 1$ is the singularity exponent, it is solution to an eigenvalue problem and $\vec{u}(\varphi)$ is the associated eigenvector, k is the generalized intensity factor. The remaining part $\vec{U}^R(x_1, x_2)$ is a smooth complement. For simplicity, we do not take into account multiple, complex or defective eigenvalues. Of course, the far field in eqn. (2), is valid out of a vicinity of the perturbation. To have information on the near field, one has to stretch the initial domain by $1/\varepsilon$ and then consider the limit domain Ω^{in} as $\varepsilon \to 0$ (figure 1(c)). The solution now writes

$$\vec{U}(\varepsilon, x_1, x_2) = \vec{U}(\varepsilon, \varepsilon y_1, \varepsilon y_2) = k\varepsilon^\lambda [\rho^\lambda \vec{u}(\varphi) + \vec{V}(y_1, y_2)] + \text{smaller terms}, \tag{3}$$

where $y_i = x_i / \varepsilon$ and $\rho = r / \varepsilon$. The particular form of the first term of the expansion is due to the matching conditions; it behaves at infinity like the first term of eqn. (2) near 0. There is an intermediate area in which both outer (eqn. (1)) and inner (eqn. (3)) expansions hold.

The Betti's theorem allows expressing the change in potential energy between an initial (unperturbed) state and a next (perturbed) one

$$\delta W_p = \frac{1}{2}\int_{\Gamma}[\sigma(\vec{U}(\varepsilon,x_1,x_2))\vec{n}\,\vec{U}(0,x_1,x_2) - \sigma(\vec{U}(0,x_1,x_2))\vec{n}\,\vec{U}(\varepsilon,x_1,x_2)]dx,\tag{4}$$

where generically $\sigma(\vec{U})$ denotes the stress field associated to $\vec{U}$. Γ is any contour surrounding the corner and $\vec{n}$ its normal pointing toward the corner, it can be taken either in Ω^0 or Ω^{in}. Replacing the above expansions in eqn. (4) leads to the following relation

$$\delta W_p = k^2 K \varepsilon^{2\lambda} + \ldots, \quad \text{with} \quad K = \frac{1}{2}\int_{\Gamma}[\sigma(\vec{V}(y_1,y_2))\vec{n}\,\rho^\lambda\vec{u}(\varphi) - \sigma(\rho^\lambda\vec{u}(\varphi))\vec{n}\,\vec{V}(y_1,y_2)]dy.\tag{5}$$

Clearly, K depends on the shape of the perturbation but not on its actual size. Moreover it is independent of the applied loads, which appear in eqn. (3) only through the multiplicative coefficient k.
This procedure will be used in the following with a new short crack or a short crack increment as a perturbation. From eqn. (5), the incremental expression of the Griffith criterion takes the Irwin-like form

$$\delta W_p = k^2 K \varepsilon^{2\lambda} \geq G_c \varepsilon \implies G = k^2 K \varepsilon^{2\lambda-1} \geq G_c.\tag{6}$$

CRACK DEFLECTION AT AN INTERFACE – THE HE AND HUTCHINSON CRITERION
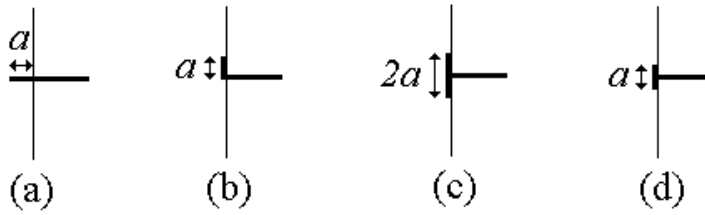
Figure 2: Penetration (a), single deflection (b), double deflection (c and d) of a crack at an interface.

A crack lies in material 1 and impinges on the interface with another component denoted material 2 and the problem is to determine the crack path. As a consequence of eqn. (6) the difficulty is the following, if material 2 is stiffer than material 1 then $\lambda > 1/2$ and $G = 0$, and in the opposite situation $\lambda < 1/2$ and $G \to \infty$. The usual differential form of the Griffith criterion is inappropriate. To avoid this obstacle, He and Hutchinson [3], using integral equations, compare the energy release rates G_p and G_d (the differential form) respectively at the tip of a penetrated (figure 2(a)) and a deflected (figures 2(b), 2(c)) crack at a short distance a of the impinging point. From their analysis, deflection is promoted if

$$\frac{G_d}{G_p} \geq \frac{G_{ic}}{G_{2c}},\tag{7}$$

where the right hand side is the ratio of the interface and material 2 toughness G_{ic} and G_{2c}. The left hand side arises to be independent of the applied loads and of the increment length a.
Similarly G_p and G_d (the incremental form) can be computed from eqn. (6). They correspond now to the energy released during the crack growth and the equivalent to eqn. (7) leads to [11] (LS)

$$\frac{K_d}{K_p} \geq \frac{G_{ic}}{G_{2c}},\tag{8}$$

where K_p and K_d are defined by eqn. (5) and correspond respectively to the penetrated and deflected geometries. Although they look similar, the two criteria are different. HH assume the penetration and deflection increment lengths and study the local fields at the tip of the new extensions. It is thus consistent to carry out the analysis at a same distance a of the primary crack tip (figures 2(a), 2(b), 2(c)). On the contrary, in the present approach, the question is to determine the energy balance that allows creation of crack extensions. In this context, it is consistent to examine equal crack extensions. It makes an important difference in case of symmetrical double deflection along the interface. In the HH case the total interface debonding length is $2a$ (figure 2(c)) whereas it must be a in present one (figure 2(d)). A comparison shows a good agreement between HH and LS criteria provided extension lengths are consistent. Nevertheless, there is no reason to take equal increments in both directions. But, otherwise the two criteria (eqns. (7) and (8)) become dependent on the ratio of the increment lengths that is unknown, making them questionable. It is discussed in a next paper by He et al. [4].

THE ROLE OF RESIDUAL THERMAL STRESSES
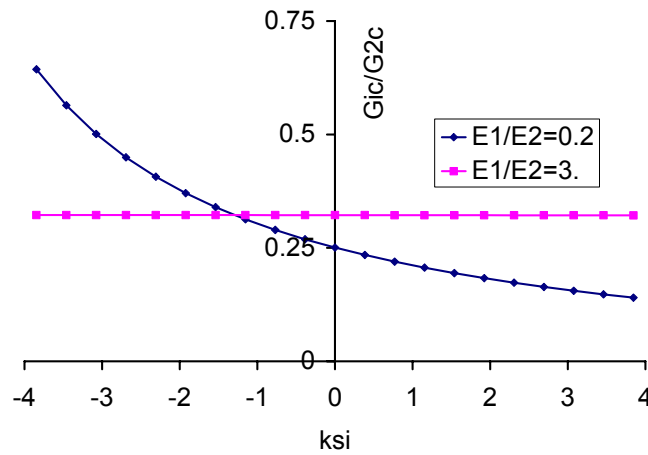
Figure 3: The influence of residual thermal stresses on the deflection/penetration criterion. The vertical axis corresponds to the absence of residual stresses.

In addition to the above discussion, He et al. [4] analyze the role of residual thermal stresses resulting of a cooling process. The problem can also be examined through the matched asymptotics procedure. As a first consequence, the generalized intensity factor in eqn. (2) splits in two parts

$$k=k_m+k_\theta , \tag{9}$$

which are respectively the contributions of the mechanical k_m and thermal k_θ loadings. Then the main role of residual thermal stresses is to modify the intensity factors, whereas the criterion (eqn. (8)) remains unchanged at the leading order from mechanical to thermal and to combined mechanical and thermal loadings. Residual stresses influence the load level at which the mechanism starts but not the mechanism itself. If secondary effects are accounted for, there is an additional term in the criterion [10] deriving from the generalization of the non-singular "T-stress"

$$\frac{K_d+H_d\,T/k\,a^{1-\lambda}}{K_p+H_p\,T/k\,a^{1-\lambda}} \geq \frac{G_{ic}}{G_{2c}} , \tag{10}$$

where T is a non-singular traction depending on the applied mechanical and thermal loadings and where H_p and H_d are coefficients similar to K_p and K_d. This criterion involves explicitly the increment length a. Moreover, it is non-local since it contains k and T which depend on the applied loads, on the processing temperature and on the geometry of the whole structure. T itself splits in two parts

$$T = T_m + T_\theta \, , \tag{11}$$

The mechanical contribution T_m is omitted in the He et al. [6] analysis. Figure 3 shows the trend of residual stress effects for two elastic contrasts between the materials. The dimensionless parameter ξ is proportional to the thermal expansion coefficients mismatch, $\xi = c(\alpha_1 - \alpha_2)$. When fiber is stiffer than the matrix, deflection is promoted if $\xi < 0$ (i.e. if $\alpha_2 > \alpha_1$). On the contrary, if $\alpha_2 < \alpha_1$ the deflection trend is lowered by the residual stresses. Moreover, the influence is almost negligible in the opposite situation of a stiff matrix and a soft fiber. It must be pointed out that these conclusions concern the prediction of the crack branching, i.e. the very beginning of the process, they do not inform on the possible further growth of the extensions.

THE PARTICULAR CASE $\lambda < 1/2$

In the above sections, it has been assumed that prior to any penetration or deflection, the crack impinges on the interface. This is questionable, especially when $\lambda < 1/2$, i.e. when material 1 is stiffer than material 2 as it is observed in reinforced ceramic matrix materials. Fibers are softer than the matrix and inserted only to promote toughening processes. Indeed, the energy release rate increases to infinity as the matrix crack approaches the interface (the Griffith criterion is more and more violated) and then decreases after penetration or deflection and finally drops below the critical toughness G_{2c} or G_{ic} (at a distance a_p or a_d known from eqn. (6)). Thus, the above assumption is not realistic. The kinetic energy δW_{kp} or δW_{kd} produced by the fracture process before the energy release rate drops below the critical toughness can be estimated in the two cases [6]

$$\delta W_{kp} = \delta W_{k1} + G_{2c} a_p \frac{1-2\lambda}{2\lambda} \quad \text{or} \quad \delta W_{kd} = \delta W_{k1} + G_{2c} a_d \frac{1-2\lambda}{2\lambda} \, , \tag{13}$$

where δW_{k1} is the kinetic energy produced before the crack reaches the interface. Thus we assume that deflection is promoted if $\delta W_{kd} \geq \delta W_{kp}$ which corresponds to a principle of maximum decrease in total energy as suggested by Lawn [5]. It leads to a slightly different form of eqn. (8)

$$\left(\frac{K_d}{K_p} \right)^{1/2\lambda} \geq \frac{G_{ic}}{G_{2c}} \, , \tag{14}$$

Which does not require the introduction of any arbitrary increment length. It is obviously a noticeable improvement of the HH criterion although the formulation remains very simple.

INTERFACE DEBONDING AHEAD OF THE PRIMARY CRACK

The premature failure of the interface can be invoked as another mechanism for crack deflection by an interface. It has been suggested by Cook and Gordon [1] and observed in many other situations [6]. The matched asymptotics procedure is particularly suited to study this situation.

The interface debonds on a length a while the primary crack tip is at a distance b of the interface (figure 4). The ligament is considered as the perturbation and is associated to the small parameter $\varepsilon = b/L \ll 1$ of the expansions (L is any characteristic length of the structure). The coefficient K in (5) depends on the local geometry, then if we set $\mu = a/b$, two coefficients $K(0)$ and $K(\mu)$ arise respectively from figure 4(a) and 4(b) and the change in potential energy between the two states (prior and after debonding) writes

$$\delta W_p = k^2 (K(\mu) - K(0)) \varepsilon^{2\lambda} + ... \tag{15}$$
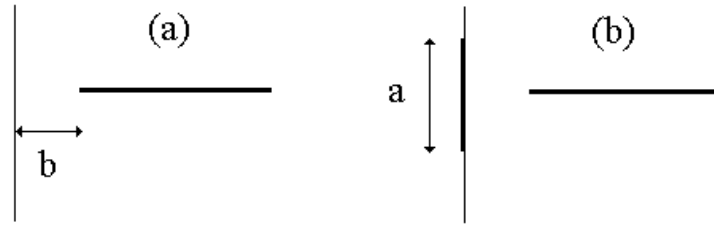
Figure 4: Interface debonding ahead of the primary crack.

The competition between the debonding and the primary crack growth within material 1 (without debonding) can be analyzed. It involves of course the material 1 toughness G_{1c}. It is shown in [9] that early interface debonding is promoted if

$$g(\mu)=\frac{K(0)-K(\mu)}{2\lambda K(0)\mu}\geq\frac{G_{ic}}{G_{1c}}.$$ (16)

$g(\mu)$ is plotted in figure 5 for different contrasts between the components. When there is no contrast (figure 5(b)) or when material 1 is stiffer than material 2 (figure 5(c)), $g(\mu)$ has a maximum g_{max} such that if $G_{ic}/G_{1c}>g_{max}$, then the interface cannot debond prematurely. For high contrasts $E_1 >>E_2$, this maximum is very low and the early debonding process is almost inhibited except for very weak interfaces. On the contrary, when material 2 is stiffer than material 1 (figure 5(a)), the knowledge of the ratio G_{ic}/G_{1c} provides a lower bound μ_{min} for the interface debonding length. However, the early failure cannot be predicted, eqn. (16) is a necessary condition but is not sufficient. A much thorough investigation shows that, in this latter case, it is necessary to invoke in addition a stress criterion to have a complete prediction of the mechanism [7]. The stress criterion gives an upper bound for the admissible debonding lengths and it must be checked that it is consistent with the lower bound μ_{min}.
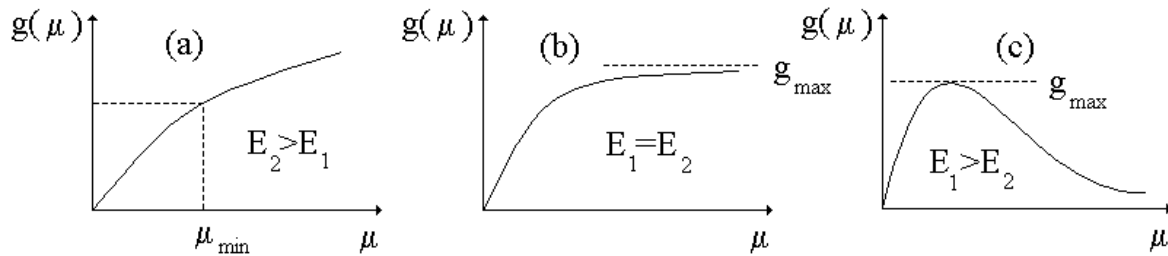
Figure 5: The function $g(\mu)$ for different contrasts between the components.

REFERENCES

1.   Cook J., Gordon J.E. (1964) *Proc. Roy. Soc*. 282A, 508-520.
2.   Evans A.G. (1997) *Acta. Mater.* 45, 23-40.
3.   He M.Y., Hutchinson J.W. (1989) *Int. J. Solids Structures* 25, 1053-1067.
4.   He M.Y., Evans A.G., Hutchinson J.W. (1994) *Int. J. Solids Structures* 31, 3443-3455.
5.   Lawn B. (1993) *Fracture of brittle solids*, Cambridge University Press, Cambridge.
6.   Lee W., Howard S.J., Clegg W.J. (1996) *Acta Mater*. 44, 3905-3922.
7.   Leguillon D. (2001) to appear in *C. R. Acad. Sci. Paris*.
8.   Leguillon D., Lacroix C., Martin E. (2000) *C. R. Acad. Sci. Paris* 328(IIb), 19-24.
9.   Leguillon D., Lacroix C., Martin E. (2000) *J. Mech. Phys. Solids* 48, 2137-2161.
10.   Leguillon D., Lacroix C., Martin E. (2001) To appear in *Int. J. Solids Structures*.
11.   Leguillon, Sanchez-Palencia E. (1992), *Studies in Applied Math.*, 32, Elsevier, Amsterdam, 423-434.

ROLE OF NONDESTRUCTIVE EVALUATION FOR THE PURPOSE OF THE UNDERSTANDING FRACTURE MECHANISM

Y. J. Park [1][*], M. Enoki [1], T. Suga [2] and T. Kishi [3]

[1] Department of Materials Science, School of Engineering, The University of Tokyo
7-3-1 Hongo, Bunkyo-ku, Tokyo 113-8656, Japan
[2] Research Center for Advanced Science and Technology, The University of Tokyo
4-6-1 Komaba, Meguro-ku, Tokyo 153-8904, Japan
[3] National Institute for Material s Science, 1-2-1 Sengen, Tsukuba, Ibaraki 305-0047, Japan

ABSTRACT
The bonded area is largely affected by the surface morphology and mechanical properties of materials by surface activated bonding (SAB) process, because the room temperature bonding process is carried out under a low temperature and low pressure for short time. Accordingly, interfacial defects cause fatally harmful problems in many cases. For an application of this technique, it is important to know the effect of interfacial defects on fracture behavior. The fracture mechanism and its criterion for the growth of interfacial defects were investigated using the Al/Sapphire joint. It became clear that the growth of interfacial defects is the dominant factor for crack propagation. An estimation of stress intensity factor for the growth of interfacial defects was tried in two ways, stress criterion and energy criterion. A critical stress intensity factor for the growth of interfacial defects was estimated as $0.3-0.5 \text{MPam}^{1/2}$ by the analysis of FEM calculation and experimental observation.

KEYWORD room temperature bonding, interfacial fracture, fracture criterion, FEM

INTRODUCTION

With the traditional method of joining the metals, semiconductors and ceramics, diffusion and reaction driven by heat at high temperature provided bonding with the joint [1-3]. Some harmful effects due to the process involving heating, such as the generation of residual thermal stress [2,4] and the formation of brittle reaction products [3,5] at the interface region, on mechanical and functional property have been noticed as the barrier for the application.

In recent years, a novel method of Surface Activated Bonding (SAB) was invented [6-8] and its engineering importance is now being emphasized. The basic concept underlying this technique is that two atomically clean solid surfaces under contact show a strong adhesive force [9]. The surface exposed to ambient atmosphere is covered with oxides and adsorbed layers. By means of sputtering or radical beam treatment in an ultra high vacuum, impurity layers are removed so that a clean surface emerges. Therefore, direct bonding at atomic level is acquired between high-energy state pure surfaces. Because work of adherence between dissimilar solid materials is positive except in extremely rare cases, it is regarded that bonding is achieved only if they are in intimate contact of atomic bonding distance.

The SAB process brought about innovative benefits because all the processes are carried out under low temperature and pressure. That is, this technology is free from the interfacial problems pointed out at high temperature and also enables to bond electronic devices that are not allowed to be heated.

Until now, research activities have been concentrated on the study of the bonding mechanism and on the investigation into the factors affecting mechanical properties. On the theoretical side, calculations of atomic and electronic structures of interfaces indicating the bonding type have been fruitful [10,11]. There have been the rigorous attempts to understand the phenomena of frictional adherence under high vacuums, like space [6,9,12]. On the other hand, the report was restricted to the results of joint strength as a function of bonding conditions [7,8]. Consequently the situation is that the knowledge on fracture mechanism and its criterion are almost unknown. From the comparison between measured bonded area and finite element method (FEM) simulated one for Al/Sapphire system, authors have already made clear the process of contact deformation in a quantitative manner [13]. Bonded area is largely affected by the surface morphology and mechanical properties of materials, because the SAB process is carried out under a low temperature and pressure for a short time. Accordingly, it can be generally stated that the existence of interfacial defects (unbonded parts) is an unavoidable problem. And moreover, it is already known that the mechanical properties of bonded materials, such as fracture behavior and fracture energy, depend on the bonded area to a great extent [14].

It is commonly agreed that elucidation of the effect of interfacial defects on fracture behavior is the most necessary task for an application of this technology. In this research, fracture mechanism and its criterion of Al/sapphire joint were investigated by a fracture mechanical approach.

FABRICATION OF SPECIMEN AND TEARING-OFF TEST

Polycrystalline aluminum of 99.5% (2nine) and 99.999% (5nine) purity and c-plane cut sapphire are selected as a model system. Aluminum is known by all-purpose material for SAB joint owing to good bonding for both metal and ceramic. And through the transparent sapphire, bond interface can be observed by CSLM (confocal scanning laser microscope, model 1LM21H, Lasertech Co.). An aluminum foil of 1μm thickness was inserted to provide a precrack, and pressures of 20 MPa and 40MPa were applied to get joint. All the processes were conducted under ultra high vacuum of 10^{-7}Pa or more. Bonded interface is square rectangle of 5x5 mm^2. Shape of specimen and confirmation of precrack is shown in Fig. 1. Details of fabrication process and instruments are available in another paper [13].
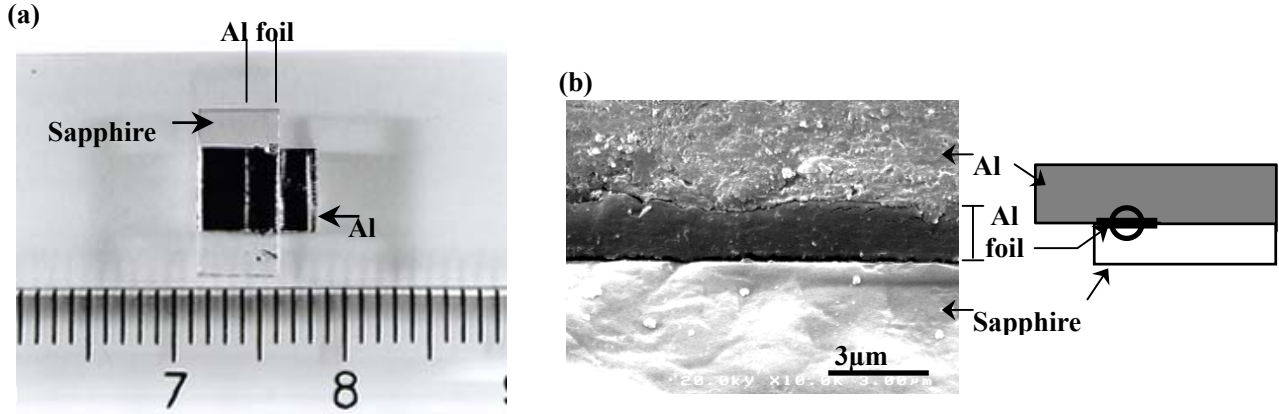
Figure 1 Shape of Tearing-Off Test Specimen Fabricated by SAB Process
(a) top view of specimen (b) cross section view of precrack

The tearing-off test was conducted in the following way. After fixing the sapphire part, the protruded part of aluminum was pulled up at constant speed of 0.1mm/min for propagation of precrack. During the crack propagation, real time observation was made using a video-microscope. Both load and length within which interfacial defect grows are given from this monitoring. Crack front of unloaded specimen and fracture surface were observed by CSLM and SEM, respectively.

ESTIMATION OF STRESS INTENSITY FACTOR FOR THE INTERFACIAL DEFECT
The criterion for the growth of interfacial defects was derived by the combination of characteristic values of experimental and FEM calculation. Because pure aluminum indicates an elastic-plastic behavior with low yield stress, the stress field at the interface region was calculated by FEM. An estimation of stress intensity factor for the growth of interfacial defect was tried in two ways, one is by stress criterion and the other by energy criterion. The validity of these two approaches is discussed.
For the stress criterion, the stress field at the interface region (σ_t and τ_t) developed by main crack and external load was acquired from the finite element mesh without containing defect element, at first. Calculated values are used as a boundary condition for interfacial defects. Stress intensity factor at interfacial defect is derived from $K=(K_1^2+K_2^2)^{1/2}$ using Eqn. (1)[15].

$$K_1 = \frac{\sqrt{a}}{\cosh \pi\varepsilon}\{\sigma_i\left[\cos(\varepsilon\log 2a)+2\varepsilon\sin(\varepsilon\log 2a)\right]$$
$$+ \tau_i\left[\sin(\varepsilon\log 2a)-2\varepsilon\cos(\varepsilon\log 2a)\right]\}$$

$$\tag{1}$$

$$K_2 = \frac{\sqrt{a}}{\cosh \pi\varepsilon}\{\tau_i\left[\cos(\varepsilon\log 2a)+2\varepsilon\sin(\varepsilon\log 2a)\right]$$
$$- \sigma_i\left[\sin(\varepsilon\log 2a)-2\varepsilon\cos(\varepsilon\log 2a)\right]\}$$

where a is for radius of penetrated interfacial defect, ε for materials constant which characterizes the compatibility of bimaterial joint and β for Dunders' parameter.
With the energy criterion, J-integral for the growth of interfacial defects was done by VCEM (Virtual Crack Extension Method)[16]. Defect element having radius a is located at the critical distance of d_c from the main crack. According to the SSV (Z.Suo, C.F.Shih and A.G.Varias) model [17,18], an elastic layer of thickness h was introduced to aluminum side (shown in Fig.2). For the comparison, J-integral values are converted into stress intensity factor adopting the following Eqn. (2)[19].

$$G = \frac{1}{16\cosh^2(\varepsilon\pi)}(\frac{\chi_1+1}{\mu_1} + \frac{\chi_2+1}{\mu_2})(K_1^2+K_2^2) \tag{2}$$

where $\chi=3-4\nu$ and μ is shear modulus.

The finite element mesh was constructed by 4-node rectangle of two dimensional plane strain element. The total number of elements was 5400 at maximum. The elements near the interfacial defect were small enough to achieve accurate calculations. The shortest was 1000 times shorter than interfacial defect. To verify the convergence, iterative calculation was conducted from coarse mesh to fine mesh by increasing the number of element. Material size and mechanical properties used as input data for calculation are given in Table 1.
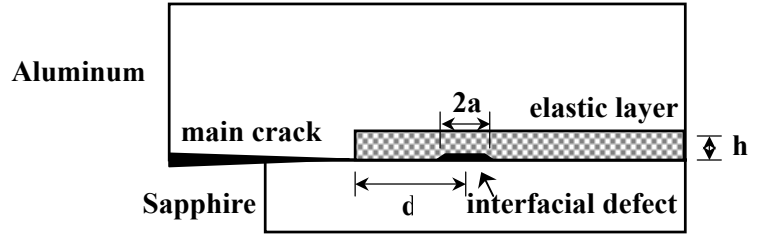
Figure 2 Schematic Illustration for the Concept of SSV Model

Table 1 Conditions for FAB (fast atom beam) Irradiation and Surface Analysis by XPS

FAB conditions		XPS conditions	
FAB source		Stage tilt angle	45 º
acceleration voltage	1.5kV	Analysis area	0.8 mm dia.
beam current	15mA	Vacuum level	3.6-4.5×10⁻⁸ Pa
Vacuum level		Step size	1eV
FAB chamber	2.0~3.3×10⁻⁷ Pa	Time/step	20ms
(during operation ~2.0×10⁻¹ Pa)		Repeats	5
transfer chamber	1.1~4.9×10⁻⁷ Pa		
joining chamber	4.0×10⁻⁷~9.3×10⁻⁸ Pa		

RESULTS AND DISCUSSION

The interfacial structure of as-bonded joint was observed through transparent sapphire (shown in Fig.3) and the distribution of defect size was obtained (shown in Fig.4). With aluminum 2nine, interfacial defects are originated from the etch-pit of the second phase, which existed originally. The maximum defect size is about 30μm. Distribution of defect size is characterized as small sized high frequency compared with that of aluminum 5nine joint. In the case of Al 5nine-bonded at 20MPa, which is lower than yield strength of used aluminum, bonded and unbonded region alternate periodically. Defect size ranged from 10μm to 100μm. On the other hand, the specimen bonded at high pressure of 40MPa showed a bonded area of 95% or more and the strength of the joint was strong enough to cause a fracture not in the interface but in the sapphire side. Crack propagation occurred in Al 2nine-bonded at 40MPa and Al 5nine-bonded at 20MPa. Thus, results are reported about
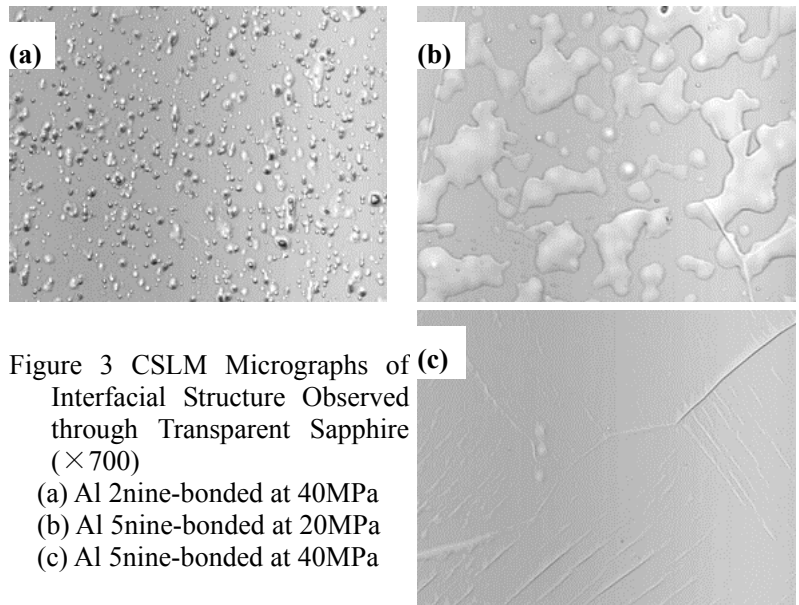
Figure 3 CSLM Micrographs of Interfacial Structure Observed through Transparent Sapphire (×700)
(a) Al 2nine-bonded at 40MPa
(b) Al 5nine-bonded at 20MPa
(c) Al 5nine-bonded at 40MPa
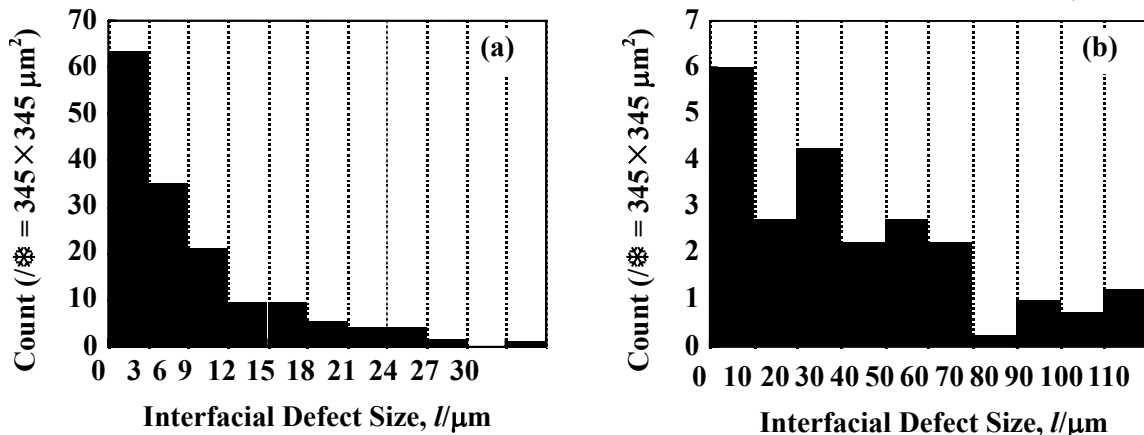
Figure 4 Distribution of Interfacial Defect Size
(a) Al 2nine-bonded at 40MPa (b) Al 5nine-bonded at 20MPa

these two cases below.

In order to investigate defect growth behavior more precisely, CSLM observation of crack front in unloaded specimen was made (shown in Fig.5). The main crack and propagating direction are marked in the figure. The growth of interfacial defects is clearly seen in the front region of the main crack in both joints. In case of Al 5nine-bonded at 20MPa, round circled island like parts surrounded by grown interfacial defects are still bonded. Blunting of interfacial defect after growth is recognized by a ripple pattern contrast on CSLM and fracture surface morphology on SEM. At these parts, not interfacial fracture but ductile fracture of bonded aluminum is expected at the next step. Figure 6 is a low magnified in-situ observation of loaded specimen and the area of white contrast represents the growing interfacial defects. Reaching maximum load, the main crack begins to propagate. Therefore, we could distinguish the crack propagation from the defect growth. In this paper, the length of this zone is defined as a critical length d_c. They were measured as 200μm and 330μm for Al 2nine-bonded at 40MPa and Al 5nine-bonded at 20MPa, respectively.

From the SEM micrographs of fracture surfaces, crack path can be inferred (shown in Fig.7). Fig.7 (a) is for aluminum-side of Al 2nine-bonded at 40MPa. On the matching surface of sapphire, any traces of aluminum attached were not recognized, so that crack propagated along the interface. Here it is noticeable that defects smaller than 10μm (arrowed) did not grow and defined as a critical defect size. Fig.7 (b) is for aluminum-side of Al 5nine-bonded at 20MPa and aluminum was attached on the matching surface of sapphire, as shown in Fig.7(c). Furthermore, the area of aluminum attached is smaller than that of as-bonded joint, that means the growth of interfacial defects. For Al 5nine-bonded at 20MPa, determination of critical defect size on the fracture surface was not so easy.

Figure 5 In-Situ Observation of Crack Propagation through Transparent Sapphire (CSLM x700)
(a) Al 2nine-bonded at 40MPa (b) Al 5nine-bonded at 20MPa
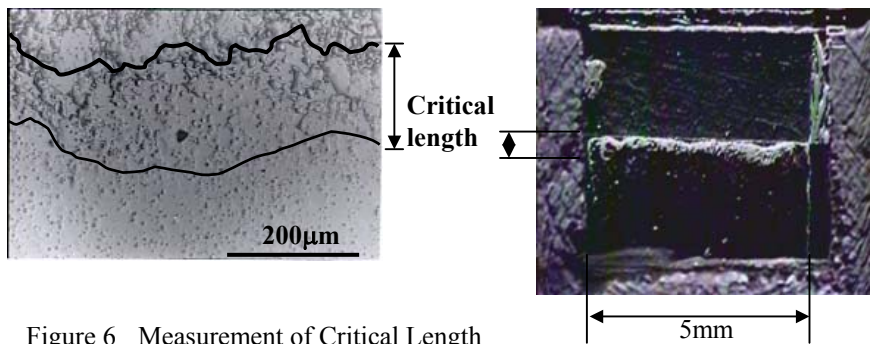
Figure 6 Measurement of Critical Length
(a) Al 2nine-bonded at 40MPa (b) Al 5nine-bonded at 20MP**a**
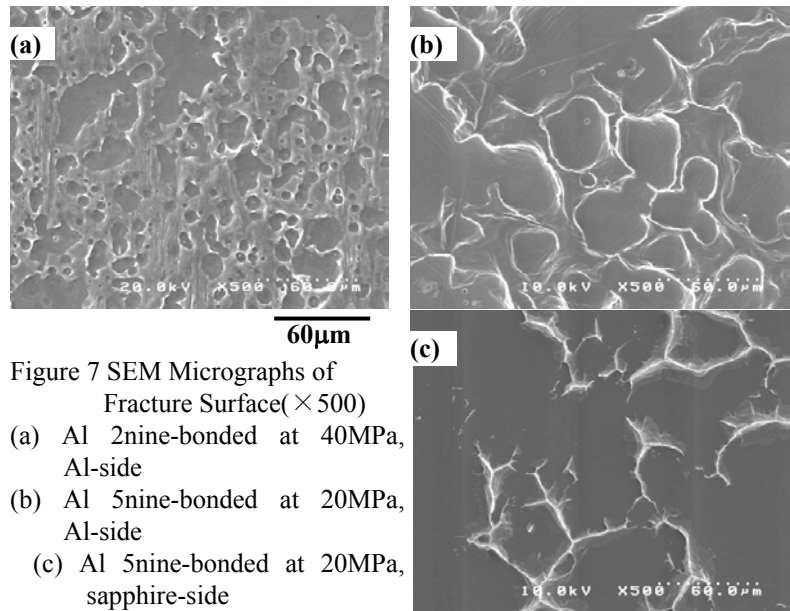
Figure 7 SEM Micrographs of Fracture Surface($\times$500)
(a) Al 2nine-bonded at 40MPa, Al-side
(b) Al 5nine-bonded at 20MPa, Al-side
(c) Al 5nine-bonded at 20MPa, sapphire-side

As is already known with the ductile metal-ceramic joint without brittle interphase, the propagation of the main crack itself is impossible owing to the blunting [20]. However, interfacial defects were allowed to grow in this research, which resulted in the apparent crack propagation. This fracture mechanism was also ascertained by nondestructive evaluation method using AE source characterization [21].

It became clear that the growth of interfacial defects is a dominant factor in joint fractures. With or without loading mixity, a crack located at the bimaterial interface undergoes mixed mode fracture due to the difference in an elastic modulus [22]. The fracture mechanical approach to the growth of interfacial defects is discussed in the remaining parts of this paper.

The stress intensity factor for the penetrated defect (see Eqn. (1)) and penny shaped defect (see Eqn. (3)[23]) were plotted in Fig. 8.

$$K_1 + i\,K_2 = 2\sigma_i \sqrt{a}\ \Gamma(2 + i\varepsilon)\ /\ \Gamma(1/2 + i\varepsilon) \qquad (3)$$

Defects were located at the critical length of 200μm for Al 2nine-bonded at 40MPa and the stress field used as boundary condition was calculated at the load of crack propagation. For the defects of smaller than 30μm, maximum defect size, stress intensity factor showed almost the same dependency on the defect size. According to these results and for the convenience of constructing the mesh, two-dimensional analysis was carried out with the assumption of interfacial penny shaped defect as penetrated defect.

Table 2 Properties and Size of Materials

Al (HT2)	Sapphire
Polycrystal (99.999%)	Single crystal (c-plane)
Specimen size $5 \times 7 \times 3$ mm^3	Specimen size $5 \times 10 \times 1$ mm^3
Yieldstress 30Mpa	Treated as rigid
Work-hardening ($\sigma = k\varepsilon^n$)	
k=179 MPa	
n=0.4	

For the stress criterion, stress intensity factor on interfacial defects was calculated on the basis of characteristic values of experimental and stress field at crack propagation load. The characteristic values and measurement conditions are summarized in Table 2. The stress intensity factor for several sizes of interfacial defects was plotted as a function of a distance from the main crack. For Al 2nine-bonded at 40MPa (Fig.9 (a)), critical stress intensity factor was estimated as 0.3MPam$^{1/2}$ from the critical defect size (a=5μm). A predicted critical length of 200μm, by the critical stress intensity factor and maximum defect size (a=15μm), shows good agreement

Figure 8   Stress Intensity Factor for the Interfacial Defects of Al 2nine Located at the Critical Length of 200μm

with the experimentally measured one. A similar result was acquired in the case of Al 5nine-bonded at 20MPa (Fig.9 (b)). Growth of interfacial defects by debonding was restricted to a certain amount and ductile fracture of still bonded aluminum followed. The reason for a change in the crack path is ascribed to the decreased stress intensity factor caused by the blunting of grown defect as mentioned before. The height of interfacial defects in as-bonded state was about 1μm, while that of growth stopped was measured about 5μm or more.

Because the Eqn. (1) used here is an analytic solution of elastic mechanics, its application to the Al/Sapphire system

Figure 9 Determination of Critical Stress Intensity Factor for the Growth of Interfacial Defect by Stress Criterion
(a) Al 2nine-bonded at 40MPa (b) Al 5nine-bonded at 20MPa

exhibiting elastic-plastic behavior should be doubted. However, the appropriateness of this equation was verified from the calculated results that the dimension of von Mises yield region is smaller than the critical length of this research (shown in Fig.10). Consequently, it is rational to apply Eqn. (1) for interfacial defect located at critical length.

In the course of J-integral adopting the SSV model, an elastic layer at aluminum side along the interface has the same elastic modulus and Poisson ratio. This layer came from the knowledge of a mean distance among the dislocations of material [17]. That is, the area within distance h from the interfacial defect can be treated as elastic, because there are no dislocations. Thickness h is known as 0.1-1μm. Another hypothesis to explain the existence of this layer is the phenomena of crack propagation along the bimaterial interface of ductile metal and ceramic, which is possible only if there is sufficient stress concentration built by not blunt interfacial defect [18]. This is true with this paper. While the main crack became blunt to be stationary, interfacial defects showed a certain amount of growth before they were stopped.

Preliminary calculation of stress field revealed little difference between 1μm and 10μm thick elastic layer. For convenience in constructing the mesh and concerning the previous results, thickness of elastic layer was assumed as 10μm.

Figure 11 represents the results of J-integral performed near the interfacial defects. Amount of released energy, J value, increases as applied external load increases. On the other hand, J value shows the maximum at an intermediate size of interfacial defect for constant external load. Results having same tendency were reported in the simulation of tensile loading for metal/rigid joint [18]. Critical energy release rate, J_c, is obtained at the maximum defect size and fracture load. That value ranged 1.3-2.3J/mm^2 and is smaller than the fracture energy of sapphire, 12J/mm^2. It is consistent with our previous finding that the process of defect growth is nothing but an interfacial debonding. Stress intensity factor converted from energy release rate is given in Fig. 12.
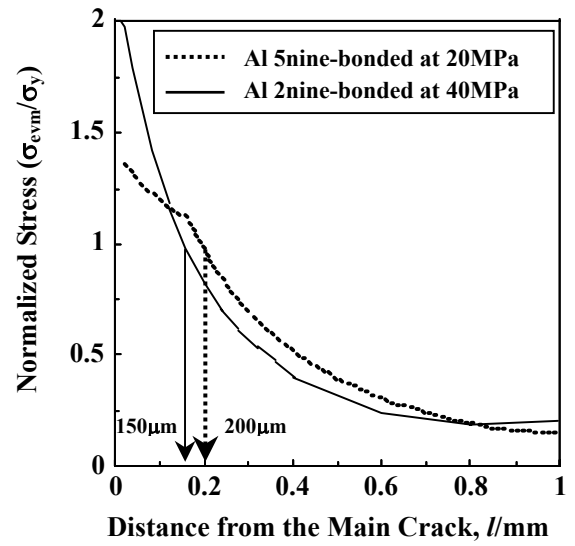
Figure 10 Calculated Length of Small Scale Yielding Zone by Equivalent von Mises Stress at the Interfacial Region
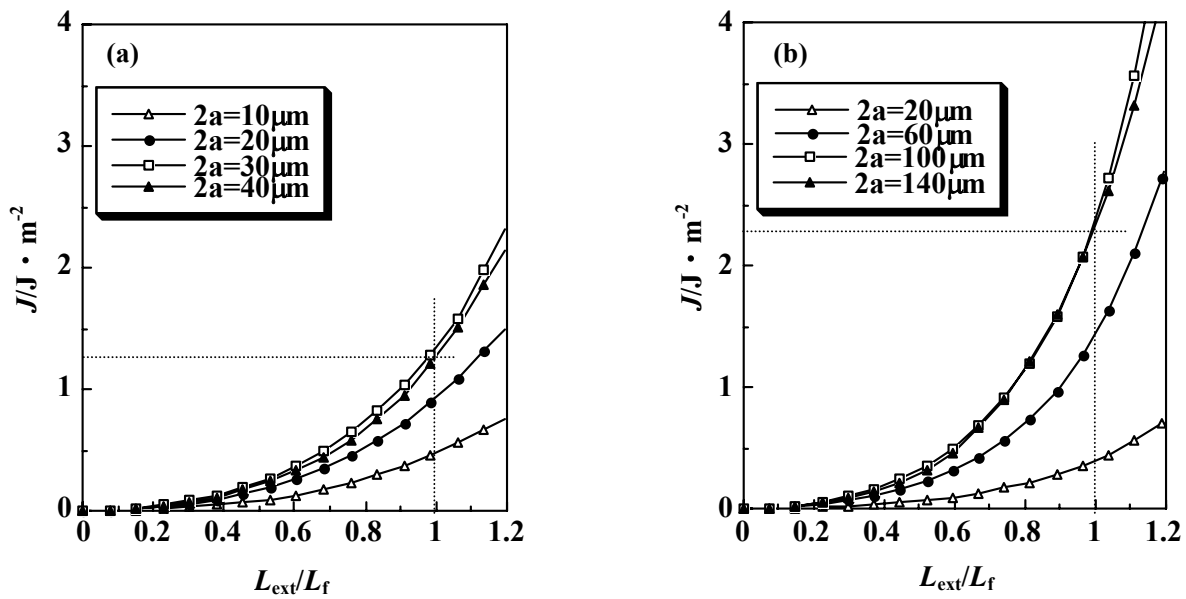
Figure 11 Calculation of J-Integral by VCEM for Interfacial Defects Located at the Critical Length
(a) Al 2nine-bonded at 40MPa (b) Al 5nine-bonded at 20MPa
(where, L_{ext}:external load, L_f:fracture load)
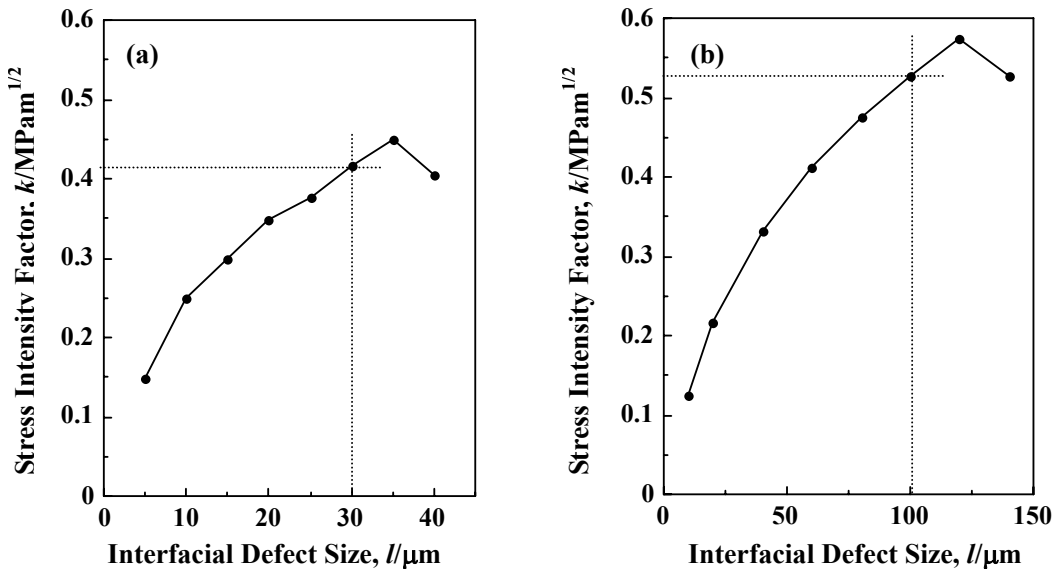
Figure 12 Conversion of Calculated J-Integral Values into Stress Intensity Factor
(a) Al 2nine-bonded at 40MPa (b) Al 5nine-bonded at 20MPa

Critical value is estimated as 0.4MPam$^{1/2}$ for Al 2nine-bonded at 40MPa and 0.5MPam$^{1/2}$ for Al 5nine-bonded at 20MPa,

respectively. They are a little larger than the values obtained by stress criterion. This resulted from the difference in the dealing method of the interaction between the main crack and interfacial defects. That is, energy criterion including that mechanism is thought to be more effective.

CONCLUSIONS
The findings of this research are summarized as following.
1. It became clear that the growth of interfacial defects is a dominant mechanism for the crack propagation. The crack propagated by means of the growth of interfacial defects.
2. The criterion for interfacial defects growth was estimated by the combination of experimental results and FEM calculation.
3. Fracture criterion was approached from two methods, stress intensity criterion and energy criterion. Energy criterion, which takes into account of an interaction between the main crack and interfacial defects, is considered more accurate.

REFERENCES
1. Gibbesch, B and Elssner, G. (1992) *Acta Metall. Mater.* 40, pp. S59-S66.
2. Kirchner, H. P., Conway, J. C. and Segall, A. E. (1987) *J. Am. Ceram. Soc.* 70, pp. 104-109.
3. Elssner, G. and Petzow, G. (1990) *ISIJ Int.* 30, pp. 1011-1032.
4. Yuuki, R. and Xu, J. Q. (1994) *Trans. Jpn. Soc. Mech. Eng.* 60, pp. 2544-2552.
5. Bartlett, A. and Evans, A. G. (1993) *Acta Metall. Mater.* 41, pp. 497-504.
6. Pepper, S. V. (1976) *J. Appl. Phys.* 47, pp. 801-808.
7. Funakubo, H. and Akaike, M. (1982) *J. Japan Inst. Metals* 46, pp.935-943.
8. Suga, T., Takahashi, Y., Takagi, H., Gibbesch, B. and Elssner, G. (1992) *Acta Metall. Mater.* 40, pp. S133-S137.
9. Keller, D. V. (1963) *Wear* 6, pp. 353-365.
10. Kruse, C., Finnis, M. W., Milman, V. Y., Payne, M. C., Vita, A. D. and Gillan, M. J. (1994) *J. Am. Ceram. Soc.* 77, pp. 431-436.
11. Kohyama, M. (1996) *Modeling Simul. Mater. Sci. Eng.* 4, 397-408.
12. Buckley, D. H. (1967) *ASTM Spe. Tech. Pub.* 431, p .248.
13. Park, Y. J., Enoki, M., Suga, T. and Kishi, T. (1999) *J. Japan Inst. Metals* 63, pp.1485-1489.
14. Ohashi, O. and Hashimoto, T. (1976) *J. of JWS* 45, pp. 485-491.
15. Sih, G. C. (1973) *Handbook Stress Intensity Factors, Institute of Fracture and Solid Mechanics*, Lehigh University, Bethlehem, PA, p. 1.8.1.
16. Parks, D. M. (1974) *Int. J. Fract.* 10, pp. 487-502.
17. Suo, Z., Shih, C. F. and Varias, A. G. (1993) *Acta Metall. Mater.* 41, pp. 1551-1557.
18. He, M. Y., Evans, A. G. and Hutchinson, J. W. (1996) *Acta Mater.* 44, pp. 2963-2971.
19. Malyshev, B. and Salganik, R. (1965) *Int. J. Fract. Mech.* pp. 1114-119.
20. Turner, M. R. and Evans, A. G (1996) *Acta Mater.* 44, pp. 863-871.
21. Park, Y. J., Enoki, M., Suga, T. and Kishi, T. (1999) Proc. 9th NDC, Sydney, Australia, pp. 21.
22. Erdogan, F. (1965) *J. Appl. Mech.* 32, pp. 403-411.
23. Kassir, M. K. and Bregman, A. M. (1972) *Trans. ASME, Ser. E, J. Appl. Mech.* 39, pp. 308-310.

ROLE OF TWINNING IN BRITTLE FRACTURE: INTERMETALLIC COMPOUNDS

M. H. Yoo

Metals and Ceramics Division, Oak Ridge National Laboratory,
Oak Ridge, TN 37831-6115, USA

ABSTRACT

Our current understanding of the role twinning plays in microcrack initiation, polycrystalline ductility, and crack-tip microplasticity in intermetallic compounds is critically reviewed. Microtwinning in γ' phase of Ni-base superalloys under creep conditions and {111} cleavage fracture in Ni_3Al at room temperature are interpreted in terms of the competition between slip/twin transfer and microcrack initiation. Domain and grain boundaries are effective sites for twin nucleation and lead to a measurable ductility of two-phase lamellar Ti-Al alloys. Formation of superlattice intrinsic stacking faults (SISFs) at a crack-tip in Ni_3Al and $(Co,Ni)_3Ti$ makes a contribution of "stacking fault toughening". Twin toughening in Mn-doped Ti-54at.%Al gives more than a seven-fold increase over the critical Griffiths stress intensity factor. Mode-mixity effects of coplanar twinning and/or slip at the tip of a {111} mode-I crack causes unstable crack propagation, leading to "quasi-brittle" or "semi-brittle" shear fracture in many $L1_2$ and $L1_0$ compounds. Unresolved critical issues are discussed, and future research directions are suggested.

KEYWORDS:

Twinning, intermetallic compounds, dislocations, stacking faults, microcrack, quasi-brittle, toughness

INTRODUCTION

The role of twinning in fracture of metals and alloys was reviewed in 1981 by focusing on three crystal-classes of b.c.c., f.c.c., and h.c.p. structure types. In b.c.c. and f.c.c. metals and alloys, the available experimental data show a dichotomy in that deformation twinning can effectively strengthen a material under some circumstances and weaken it under others [1,2]. In h.c.p. metals and alloys, on the other hand, those that deform by both "tension twins" and "compression twins" (with respect to the c-axis) are more ductile than those that deform by only one twin system [3]. Since then, it has been increasingly recognized that twinning plays an important role in brittle fracture of some intermetallic compounds of non-cubic crystal structures [4,5]. In polysynthetically twinned (PST) two-phase TiAl alloys, both heterophase (α_2/γ) lamellar interfaces and lamellar boundaries in γ-phase play crucial roles in propensity of twin nucleation and increase of fracture toughness [6-9]. Possible intrinsic effects of stacking faults, nano-twins, and pseudo-twins (martensites) on toughening by crack-tip microplasticity have been the subjects of many research works dealing with single-phase intermetallic compounds, e.g., Ni_3Al [10], $(Co,Ni)_3Ti$ [11], and TiAl [12]. The purpose of this paper is to review the role of twinning in microcrack initiation, polycrystalline ductility, and crack-tip plasticity and to assess unresolved critical issues regarding the effects of temperature, strain-rate, alloy composition, microstructure, test environment, and neutron irradiation on twinning and fracture.

TWIN NUCLEATION AND CRACK INITIATION

Both twin nucleation and crack initiation require an internal stress concentration and, therefore, share common heterogenous nucleation sites in the microstructure of a given material. Schematic illustrations of Fig. 1 depict a variety of possible cases of slip, twin, and crack initiation at γ_1/γ_2 grain or domain boundaries which act as effective barriers against a dislocation pile-up. In Fig. 1, (a) and (b) indicate that an interface can be a source and a sink of slip/twin dislocations, (c) a site for slip/twin transfer, (d or e) for crack initiation within the grain (or domain) or into the next grain (or domain), and finally (f, g, and h) for microcracking along the interface. When the dislocation initiation, absorption, and transfer at interfaces, (a-c), are prevalent,

this localized microplasticity may lead to a relatively large elongation at failure. On the other hand, when the

conditions for crack nucleation of any one of the latter five cases, (d-h), are satisfied before the localized microplasticity sets in, microcracking will occur, resulting in a relatively low ductility.
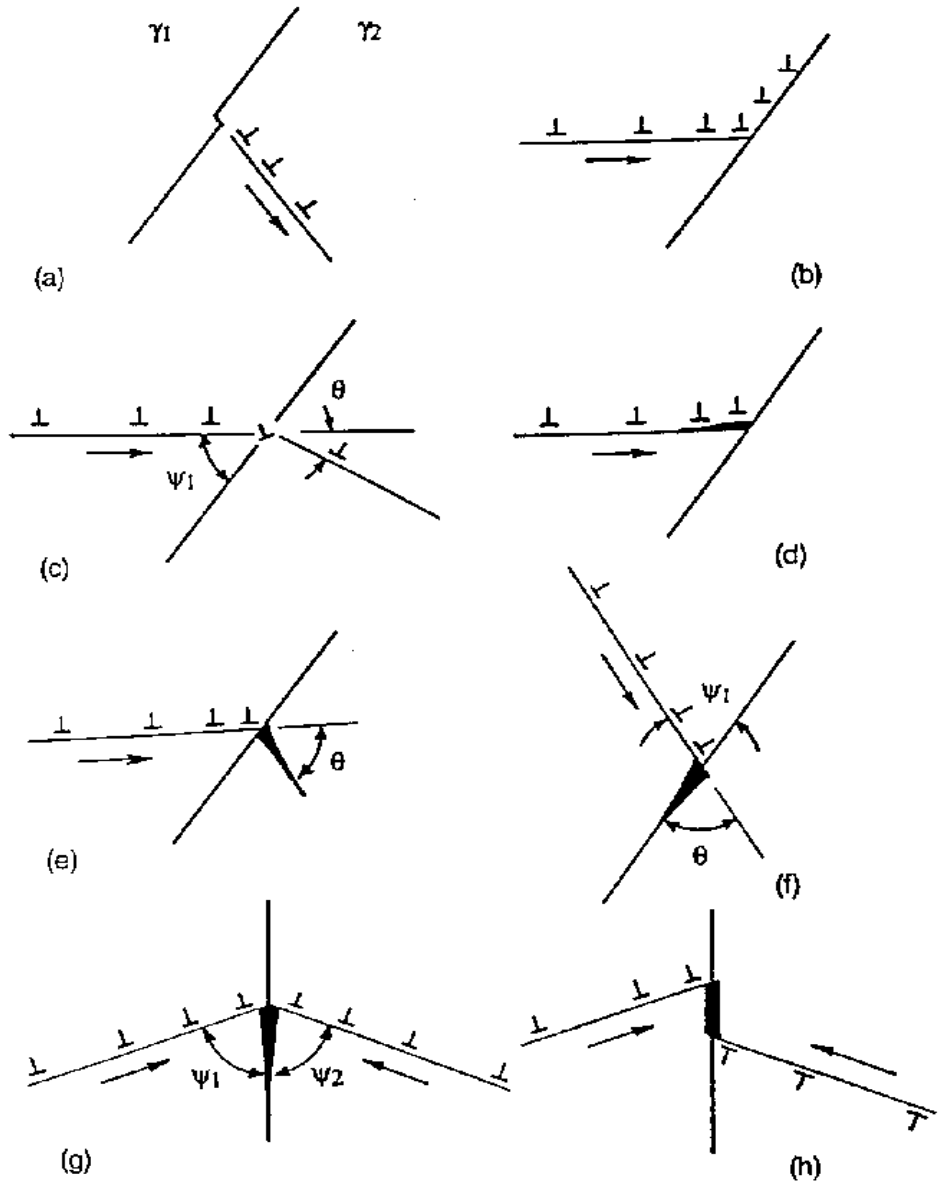
Fig. 1: Various pile-up configurations of slip/twin dislocations against γ_1/γ_2 interfaces

Some special cases of [110] symmetric tilt boundaries in the $L1_2$ structure were investigated earlier using the anisotropic elasticity theory of dislocations and fracture [13,14] and available surface and grain-boundary cohesive energies [15]. The results show that, in the case of Fig. 1(c), the transmission of the

primary slip dislocations across the boundary into the conjugate slip system occurs with a certain degree of difficulty, which is eased by localized disordering. The difficulty of true-twinning in fully-ordered $L1_2$ alloys may also be alleviated by the locally-disordered boundary, especially at elevated temperatures. Microtwinning in γ' phase of Ni-base superalloys under creep deformation condition at elevated temperatures [16] and resulting tension/compression asymmetry [17] may be interpreted with the aid of Fig. 1(c) with γ on the left and γ' on the right where $\psi_1 = 54.7°$ and $\theta = 0°$. Deformation twinning within the localized slip regions resulted in formation of cavities in the twin boundaries [16]. As for Fig. 1 (e) versus (f), cleavage fracture on the (111) plane is predicted, rather than intergranular fracture [13,14]. The available transmission electron microscopy (TEM) data on Ni_3Al are in good agreement with the prediction [10,18].

In PST TiAl alloys, in addition to α_2-γ interfaces, the three different types of intervariant γ_1/γ_2 lamellar interfaces are (1) true-twin boundaries, (2) pseudo-twin boundaries, and (3) 120° rotation boundaries [8]. All of these boundaries, especially when they are in a semicoherent form, can act as effective sites for slip and/or twin initiation [7,8]. The role of these lamellar boundaries as dislocation sources, Fig. 1 (a) and (c), may be partly responsible for the measurable ductility reported in two-phase lamellar Ti-Al alloys as compared to single-phase γ-TiAl alloys [19]. The case of slip/twin transfer, Fig. 1 (c), and the four cases of crack initiation, Fig. 1 (e-h), can be discussed in terms of a Hall-Petch type relationship and Stroh mechanism, respectively. Hazzledine and Kad [20] interpreted the anisotropy of yield and fracture stresses reported in PST TiAl crystals [8]. In view of the fact that all the deformation modes in γ-TiAl occur on {111} planes and the ideal cleavage (Griffiths) energy is the lowest on these planes, Yoo et al. [21] pointed out the importance of mode-mixity (I-II or I-III) not only in crack-tip plasticity, but also in microcrack nucleation by stress concentration due to a dislocation pile-up at interfaces.

Additional heterogeneous nucleation sites are extended lattice defects, viz., dislocations and stacking faults. Faulted Frank loops of vacancy and interstitial types in the $L1_0$ structure have {111} habit planes. The so-called radiation-induced ductility (RID) of nearly two-fold increase in tensile elongation at 600°C reported in two-phase TiAl alloys [22] is attributed to a mechanism that involves additional deformation twins, nucleating during neutron irradiation and growing during tensile deformation after irradiation [23]. Extending the pole mechanism for the $L1_0$ structure [24], we [23] explained the experimental data [22] quantitatively on the basis of (a) the stability of large faulted interstitial-type Frank loops, (b) the pole mechanism facilitated by the interaction of ordinary dislocations and a Frank loop, and (c) the formation of effective twin embryos and the kinetics of twin formation. The recorded data that no appreciable changes in yield strength and work hardening were observed in this experiment [22] can be explained also by the model [23], which requires a moderate stress concentration by a pile-up of about six ordinary dislocations only.

CRACK-TIP TWINNING AND TWIN TOUGHENING

Twinning plays two different roles in crack-tip microplasticity, which may be discussed with the aid of Fig. 2 for fcc-derivative superlattice structures (e.g., $L1_2$ and $L1_0$ types). When a (001)[1-10] mode-I crack is subjected to an uniaxial tension along the [001] direction, shown schematically in Fig. 2(a), crack-tip-blunting type of microplasticity is possible by the formation of two symmetric group of superlattice intrinsic stacking faults (SISF) or nano-twins. Even though crack blunting was not effected, extensive symmetric distribution of SISFs on both sides of a mode-I crack was observed by *post mortem* TEM in $(Co,Ni)_3Ti$ [11]. Extended SISFs trailed by super-Shockley partial dislocations, emitting from a discontinuously propagating crack-tip, were directly observed in stoichiometric Ni_3Al by *in situ* straining TEM [10]. Since the SISF energy of Ni_3Al is 40 mJ/m^2 and the extent of SISF strip is on the order of 1 μm [10], toughening of a (001)[1-10] mode-I crack is energetically feasible in Ni_3Al by stacking fault generation, viz., "stacking fault toughening". In case of $(Co,Ni)_3Ti$, however, extensive faulting at the crack was attributed in part to hydrogen in the test environment [11].

In the case of the $L1_0$ structure, the two symmetric twins in Fig. 2(a) are "tension twins" of the complementary (anti-twinning) type [5,10]. This was experimentally confirmed in Mn-doped Ti-54at.%Al single crystals by Phan-Courson [12]. Using the twin boundary energy of 60 mJ/m^2 and the (001) cleavage energy of 5.6 J/m^2 [6,8], the calculated values for stoichiometric TiAl at 0 K, one can estimate the length of the tension twins to be $l \geq 10\,\Delta a$, where Δa is the width of an incremental crack extension.

Figure 2 (b) or 2(c) shows the case when the mode-II or mode-III component of an external loading is mixed with a (111)[1-10] mode-I crack. According to the compilation of cleavage energies calculated for transition-metal aluminides and silicides [25], the cleavage energy of {111} habit planes is lower than that of the (001)

plane in both Ni_3Al and Ni_3Si [10], and it is the lowest (4.4 mJ/m^2) among the four low index planes in TiAl [21]. Since the (111) plane is also twinning plane or slip plane, coplanar deformation twinning or ordinary slip can occur, as indicated in Fig. 2 (b) or (c), so as to shield the crack-tip shear stress field. Because the stress field corresponding to the Mode-I component is not relaxed by the crack-tip twinning or slip, this type of coplanar microplasticity concentrated on the (111) habit plane may induce an unstable crack propagation, leading to {111} translamellar fracture as observed in Ti-rich TiAl alloys [7,8]. This may explain quasi-brittle, or semi-brittle, shear fracture as observed in Ni_3Al and Ni_3Si [10].
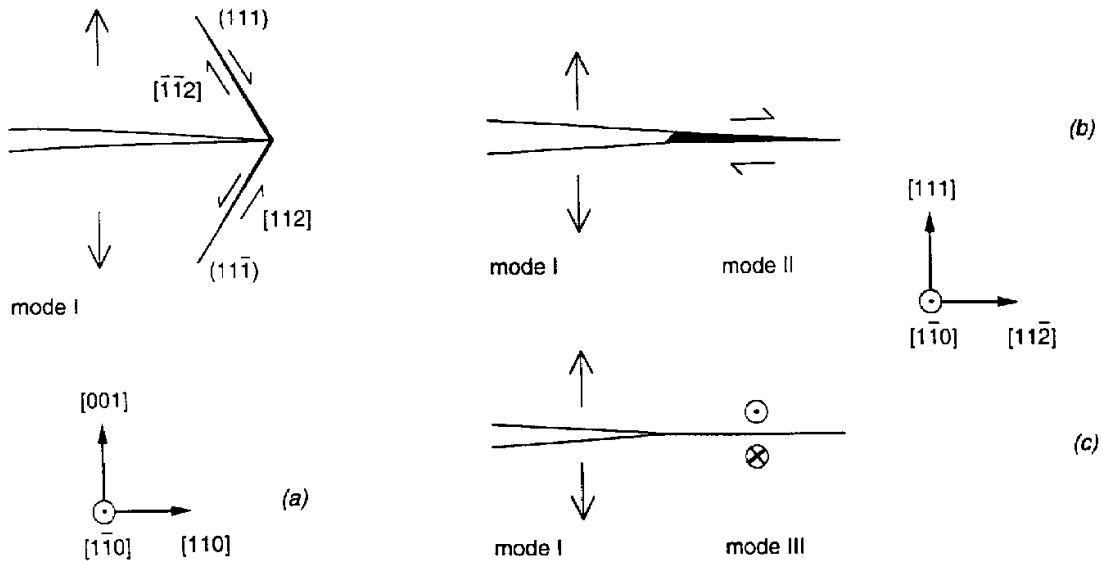
Fig 2: Crack-tip microplasticity by twinning and slip: (a) two symmetric twins, (b) coplanar twinning (edge character), and (c) coplanar slip (screw character)

Fracture toughness of binary Ti-54at.%Al single crystals at room temperature is $K_{IC} \approx 1$ MPa-√m [26], essentially equal to theoretical stress intensity factors of k_{IG}, Griffith values [21]. Increases in provisional K_{IC} value to $K_Q > 7$ MPa-√m in Mn-doped single crystals [12] and $K_Q = 10$ MPa-√m in polycrystals [27] are attributed to crack-tip twinning and intergranular microcracking, respectively. According to the description of a plastic zone by Cherpanov [28], the former occurs in the "superfine structure" at the atomically sharp tip of a slit crack, and the latter in the "fine structure" beyond the transition region.

In two-phase multicomponent TiAl alloys, fracture toughnesses are reported to be reasonably good, e.g., K_Q = 10-32 MPa-√m with duplex microstructures [27], $K_Q = 25$-43 MPa-√m with lamellar microstructures [29], and $K_Q > 50$ MPa-√m with fine lamellar microstructures [30]. The presence of various lamellar interfaces and grain boundaries strongly influences the crack-tip plasticity, because of its orientation dependence, and therefore affects translamellar and interfacial microcracking in the crack-tip process zone in a complex manner. From a broad perspective viewpoint of two-phase microstructure, fracture toughness may result from various mechanisms such as, ductile-phase blunting, ductile-phase bridging, ligament toughening, and twin toughening [29]. One area yet to be explored is whether synergistic toughening effects can be obtained by combining some of these mechanisms.

The recent study of crack-initiation and "small-crack" growth during the ambient-temperature fatigue of a multicomponent γ-TiAl based alloy [31] showed that crack initiation resistance in the duplex microstructure was observed to be superior to that in the lamellar microstructure. Such a small crack effect is typically seen when its size is comparable to the characteristic dimensions of the microstructure [32]. This result is contrary to that of their earlier work on large cracks in the same alloy. In view of the discussion of twin

nucleation and crack initiation (Fig. 1), it appears that microcrack initiation by means of the possible mechanisms of Figs. 1 (d-h) might have been as effective as twin nucleation mechanism by either Fig. 1(a) or 1(c) in the lamellar microstructure of this particular alloy. A quantitative assessment of the specific contribution of twinning and microcracking in the fracture toughness of two-phase alloys is yet to be made.

DISCUSSION

In the main, our mechanistic understanding of the competition between slip/twinning and microcracking at various interfaces has been attained based on energetic aspects of a dislocation pile-up model under a static equilibrium condition. This model cannot be applied to treat dynamic aspects of a stress concentration, which may strongly influence the effect of temperature and strain rate on yield stress and fracture strain of polycrystals or multilayered materials. A preliminary analysis indicated that the kinetics of dislocation reactions at an interface resulting from the leading dislocation of a pile-up are far more important than any energetic factors involved [33]. In other words, how effectively the reaction products move away from the site of intersection, Fig. 1 (b) and (c), seems to be crucial to whether or not the following dislocations can be incorporated into the interface. Pestman et al. [34] investigated atomic processes of slip interactions with a tilt boundary in f.c.c. and $L1_2$ crystals using a computer simulation method and found that the interaction in ordered compounds showed similarities to that in f.c.c. metals.

A few atomistic simulation results showing nano-twinning at the tip of a mode-I crack have been reported, viz., the two cases of {11-2}<111> twinning, equivalent to Figs. 2(a), and 2(b) in bcc crystals [35,36], and transonic twin formation in the forward direction [37]. No computer simulation result of crack-tip twinning in intermetallic compounds has been reported. The only experimental evidence of twin toughening in single-phase intermetallic compound was given in Mn-doped γ-TiAl by Phan-Courson [12]. By using PST TiAl crystals, the anisotropy of fracture toughness was measured in the three principal orientations [38,39], but the specific contribution of twinning was not determined. The paper entitled "twin toughening in titanium aluminides" by Deve and Evans [40] reported that twinning occurred within a process zone and crack bridging ligaments, with about equal contributions arising from the process and bridging zones.

Most of the creep strength and ductility data of titanium aluminides published in the past decade are on multicomponent alloy systems having many different microstructures. It is, therefore, difficult to understand the mechanistic role of twinning in creep flow and fracture behavior in these alloys at elevated temperatures. To list a few outstanding problems in two-phase TiAl alloys: the intrinsic effect of aluminum content on deformation twinning and fracture, effects of interfacial sliding and true-twinning parallel to the lamellar boundaries on creep strength and ductility, mechanistic role of enhanced twin nucleation in the radiation-induced ductility (RID), solute effects (e.g., Nb, V, Mn, etc.) on twinning propensity and enhanced cleavage strength, and environmental effects (O, H) on twinning and fracture remain unresolved issues.

As we seek tougher and stronger intermetallic alloys with ultra-high melting temperatures for structural applications, which have mostly non-cubic crystal structures, twinning as a deformation mode would play an important role in maintaining their integrity throughout processing, handling, and deforming. In the past two decades, there has been a significant advance in our mechanistic understanding of the role twinning plays in brittle fracture of intermetallics, e.g., Ni-base $L1_2$ alloys and TiAl-base alloys. More effort in experimental and theoretical interdisciplinary research at multi-levels of length and time scales is needed, particularly in the evolution of internal stress concentration and kinetics of twin nucleation and/or microcrack initiation.

SUMMARY

A critical review is given on the role twinning plays in brittle fracture of intermetallic compounds, and the highlights are:
1. Tension/compression asymmetry of creep strength in Ni-base superalloys was attributed to deformation twinning in γ' phase, and cavity formation was observed to occur at twin boundaries.
2. {111} cleavage fracture at <110> tilt boundaries in the $L1_2$ structure was predicted based on the available surface and interfacial energies, and was confirmed by TEM observations in Ni_3Al.
3. Formation of extensive SISFs at an advancing crack-tip, reported to occur in Ni_3Al and $(Co,Ni)_3Ti$, may give rise to the so-called "stacking fault toughening."
4. Grain and domain (including true-twin) boundaries are effective sites for twin nucleation, and also for microcrack initiation, in two-phase γ-TiAl-based alloys.

5. Twin toughening in Mn-doped Ti-54at.%Al single crystals was reported to be $K_Q > 7$ MPa$\sqrt{m}$, a factor of about 7 larger than Griffith stress intensity factor.
6. Mode-mixity of coplanar twinning and/or slip is a cause for unstable crack propagation which leads to quasi-brittle shear fracture, observed in many $L1_2$ and $L1_0$ compounds.

ACKNOWLEDGMENT

REFERENCES

1. Reid, C. N. (1981) *Met. Trans A.* 12, 371.
2. Remy, L. (1981) *Met. Trans.A* 12, 387.
3. Yoo, M. H. (1981) *Met. Trans.A* 12, 409.
4. Yoo, M. H., Fu, C. L. and Lee, J. K. (1991). In: *High-Temperature Ordered Intermetallic Alloys IV,* pp. 545-554, Johnson, L. A., Pope, D. P. and Stiegler, J. O. (Eds). MRS Vol. 213, Pittsburgh, PA.
5. Yoo, M. H., Fu, C. L. and Lee, J. K. (1991) *J. Phys. III,* 1, 1065.
6. Yoo, M. H. and Fu, C. L. (1998) *Metall. Mater. Trans. A* 29, 49.
7. Appel, F. and Wagner, R. (1998) *Mater. Sci. Eng. R* 22, 187.
8. Yoo, M. H. and Yamaguchi, M. (2000). In: *Microstructure and Properties of Materials,* Vol. 2, pp. 79-138, Li, J.C.M. (Ed). World Science, Singapore.
9. Yoo, M. H. (2001). In: *Intermetallic Compounds - Principles and Practice,* Vol. 3, *Progress,* Westbrook, J. H. and Fleischer, R. L. (Eds). John Wiley & Sons, New York. (in press)
10. Yoo, M. H., Fu, C. L. and Horton, J. A. (1994) *Mater. Sci. Eng. A* 176, 431.
11. Liu, Y, Takasugi, T., Izumi, O. and Takahashi, T. (1988) *Acta Metall.* 36, 2959.
12. Phan-Courson, I. (1993). Doctoral Thesis, Univ. of Paris VI, France.
13. Yoo, M. H. and King, A. H. (1988) *J. Mater, Res.* 3, 848.
14. Yoo, M. H. and King, A. H. (1990) *Met. Trans.* 21A, 2431.
15. Foiles, S. M. and Daw, M. S. (1987) *J. Mater. Res.* 2, 5.
16. Ardakani, M. G., McLean, M. and Shollock, B. A. (1999) *Acta Mater.* 47, 2593.
17. Kakehi, K. (1999) *Scr. Mater.* 41, 461.
18. Baker, I., Schulson, E. M. and Horton, J. A. (1987) *Acta Metall.* 35, 1533.
19. Kim, Y.-W. and Dimiduk, D. M. (1991) *J. of Metals* 43, 40.
20. Hazzledine, P. M. and Kad, B. K. (1995) *Mater. Sci. Eng A* 192/193, 340..
21. Yoo, M. H., Zou, J. and Fu, C. L. (1995) *Mater. Sci. Eng. A* 192/193, 14.
22. Hishinuma, A., Fukai, K., Sawai, T. and Nakata, N. (1996) *Intermetallics* 4, 179.
23. Yoo, M. H. and Hishinuma, A. (1999). In: *Advances in Twinning,* pp. 225-238, Ankem, S. and Pande, C. S. (Eds). TMS, Warrendale, PA.
24. Yoo, M. H. (1997) *Phil. Mag. Lett.* 76, 259.
25. Yoo, M. H. and Yoshimi, K. (2000) *Intermetallics* 8, 1215.
26. Booth, A. S. and Roberts, S. G. (1997) *Acta Mater.* 45, 1045.
27. Mitao, S., Tsuyama, S. and Minakawa, K. (1991) *Mater. Sci. Eng. A* 143, 51.
28. Cherpanov, G. P. (1977) In: *Mechanics of Brittle Fracture*, p. 270, McGraw Hill, New York, NY.
29. Chan, K. S. and Kim, Y.-W. (1994) *Metall. Trans. A* 25, 1217.
30. Liu, C. T., Schneibel, J. H., Maziasz, P. J., Wright, J. L. and Easton, D. S. (1996) *Intermet.* 4, 429.
31. Kruzic, J. J., Campbell, J. P. and Ritchie, R. O. (1999) *Acta Mater.* 47, 801.
32. Ritchie, R. O. and Lankford, J. (1986) *Mater. Sci. Eng. A* 84, 11.
33. Yoo, M. H. (1995). In: Int. Symp. on *Gamma Titanium Aluminides*, pp. 259-266, Kim, Y.-W., Wagner, R. and Yamaguchi, M. (Eds). TMS, Warrendale, PA.
34. Pestman B. J., De Hosson, J. Th. M., Vitek, V. and Schapink, F. W. (1991) *Phil. Mag. A* 64, 951.
35. Kohlhoff, S., Gumbsch, P. and Fischmeister, H. F. (1991*) Phil. Mag. A* 64, 851.
36. Tang, Q. H. and Wang, T. C. (1998) *Acta Mater.* 46, 5313.
37. Cerv, J., Landa, M. and Machova, A. (2000) *Scr. Mater.* 43, 423.
38. Nakano, T., Kawanaka, H., Yasuda, H. Y. and Umakoshi, Y. (1995) *Mater. Sci. Eng. A* 194, 43.
39. Yokoshima, S. and Yamaguchi, M. (1996) *Acta Mater.* 44, 873.
40. Deve, H. E. and Evans, A. G. (1991) *Acta Metall. Mater.* 39, 1171.

ROUGHNESS WAVES AS DETECTED ON GLASSY MATERIALS BY DCDC EXPERIMENTS IN THE LOW SPEED REGIME: THE ROLE OF MICROSTRUCTURE.

C. Marlière, F. Despetis and J. Phalippou

Laboratoire des Verres, Université Montpellier 2, UMR CNRS 5587, CC69,
F-34095 Montpellier cedex 5, France

ABSTRACT

We studied the low speed fracturation regime (10^{-4} – 10^{-9} m.s^{-1}) in different glassy materials (soda-lime glass, glass-ceramics) with variable but controlled length scale of heterogeneity. The chosen mechanical system enabled us to work in pure mode I (tensile) and at a fixed load on DCDC (double cleavage drilled compression) specimen. The internal residual stresses of studied samples were carefully relaxed by appropriate thermal treatment. By means of optical and atomic force (AFM) microscopy techniques fracture surfaces were examined. We evidenced for the first time that the crack front line underwent an oscillating behavior - with a wavelength in the micrometer range - as a result of a reproducible sequence of instabilities. This new phenomenon was observed for different glassy materials providing that their typical length scale was lower than a threshold limit estimated to few nanometers.

KEYWORDS

Fracture, double cleavage drilled compression, surface, crack front waves, AFM.

INTRODUCTION

Quasistatic brittle fracture is a subject of importance for both practical and fundamental reasons. Mainly two classes of experimental set-up have been developed in order to propagate cracks in a stable and controllable manner. The first one is based on a thermally induced stress field [1,2]. According to values of thermal gradient and width of the glass plate three types of crack propagation regime can develop from the small initial notch made to ensure the nucleation of a single propagating crack : no propagation, straight propagation and wavy propagation. Such propagating cracks were observed for velocities between 10^{-2}m.s^{-1} and 10^{-5} m.s^{-1}. An attempt of explanation was done [1] by using the Cotterell and Rice criterion [3] but partially failed when the real experimental temperature profile was measured [2].

An other classical way to propagate slow cracks is to use double cleavage drilled compression DCDC specimen. This method initially developed by Janssen [4] has numerous advantages : compression

loading, mid plane crack stability and auto precracking. Though the associated stress intensity factor (in mode I) K_I and the average crack speed are at the same order of magnitude as for the "thermal" set-up, to our knowledge no evidence of crack instability has been reported till now.

By working at a fixed load on DCDC specimen, the internal residual stresses of which were carefully relaxed by appropriate thermal treatment, we evidenced - for the first time- that the crack front line underwent an oscillating behavior as a result of a reproducible sequence of instabilities. The wavelength was in the micrometer range.

EXPERIMENTAL

DCDC samples were parallelepipedic ($4 \times 4 \times 40 mm^3$) with a central hole of 1mm in diameter (nominal) drilled perpendicularly to two of large parallel faces. Details of experiments have been reported in a previous paper [5]. The sample was then placed in equilibrium on the horizontal basis of our experimental set-up with its large faces vertical. By means of a freely moving piston the upper face of the specimen was then loaded by a variable weight at a rate of about $25 N.s^{-1}$ till the crack was initiated. Then the sample was loaded at a constant weight of typically 1500N. These experiments were done at a constant temperature of $22 \pm 1°C$ and at a relative humidity of $50 \pm 5\%$.

The crack front position was measured in the middle of the specimen (at equal distances of the lateral surfaces) by i) a standard video-recorder system for crack speed between 10^{-4} m.s^{-1} and 10^{-6} m.s^{-1} and ii) an optical system with a magnification of x40 for lower crack speeds (10^{-6} m.s^{-1} - 10^{-9} m.s^{-1}). In that last case the position of crack front relatively to the center of the specimen was measured with an accuracy of 0.01mm. The stress intensity factor, K_I, was deduced from the measured crack length, using the equation of reference [6]. The $v = f(K_I)$ was then plotted. When the crack speed reached a value of 10^{-9} m.s^{-1} the samples were reloaded in order to gently fracture the sample all over its length. Special care was taken in order to preserve the two halves of the specimen from eventual damages.

Then the fracture surfaces were analyzed by an experimental system (Veeco, D3100®) combining optical microscopy and atomic force microscopy (AFM). Both methods could be simultaneously performed. The samples were glued on the sample holder. This one was moveable under the fixed AFM-optical system thanks to a step-by-step motor. The position of the center of the studied portion of surface relatively to the center of the specimen was measured with an accuracy of less than 10μm. As a matter of fact it was thus possible to virtually know for every point of the AFM or optical images the value of K_I and the speed the crack had when it ran through this point.

AFM experiments were done in a high amplitude resonant mode (« tapping » mode). Experiments were performed in ambient conditions at a relative humidity of $35 \pm 5\%$ and a temperature of $22.0 \pm 0.5°C$. More details are given in reference [7].

Experiments were performed on two kinds of materials. The first one was a soda-lime silicate glass. A thermal treatment (530°C) was done before fracture experiment in order to remove residual stresses. The second set of samples was made from a lithium alumino-silicate glass-ceramics. By modifying thermal treatments three types of structure were observed : the first one (sample A) corresponds to a pure glassy state as controlled by X-ray diffraction (660°C). The second one (sample B) is related to a slightly unglassy state where small crystals of β-quartz phase were nucleated. This structure was got after a two-steps thermal treatment at plateau temperatures of $T_1 = 750°C$ and $T_2 = 900°C$. Samples C are related to a more unglassy state (increased number of crystallites of larger size) due to a higher temperature (950°C) for the second step of thermal treatment.

RESULTS

In the Figure 1 are plotted typical $v = f(K_I)$ curves as obtained with the different types of samples we studied. A noticeable feature is that for the glass ceramics (open symbols) the curves are shifted towards higher K_I values when the thermal treatment is enforced. The reproducibility of these experiments is revealed by the very good superimposition of the two $v = f(K_I)$ curves performed on two different samples (B1 and B2: up and down triangles) which underwent the same thermal treatment.
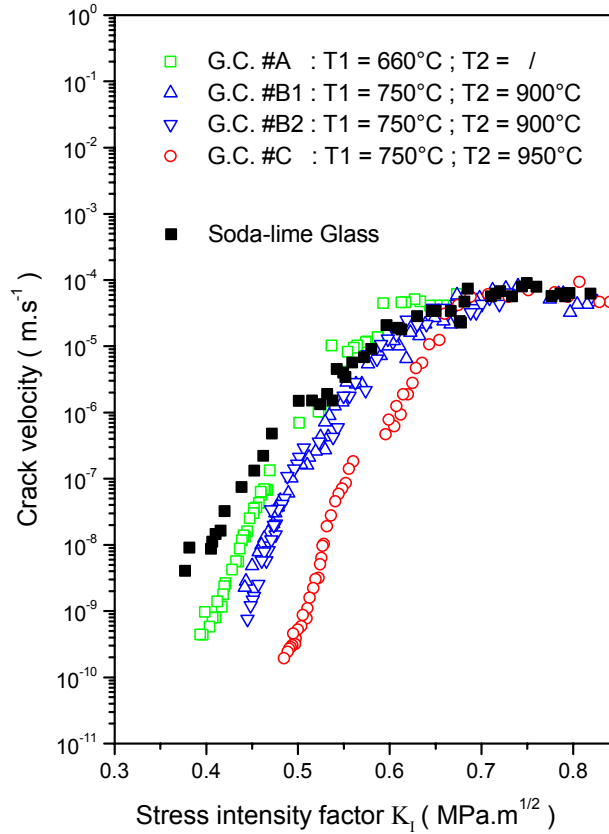
Figure 1: Crack speed versus K_I plots for different materials (G.C. : Glass-ceramics).

The fracture surfaces were then systematically characterized by our optical-AFM system. We put a special attention to the part of the surface fracture corresponding to crack speed reachable (10^{-4}m.s^{-1} – 10^{-9}m.s^{-1}) with our experimental mechanical set-up. We firstly concentrated on the lowest speed regime. The RMS roughness values were characterized by AFM on 10μmx10μm surfaces where crack speed was in the range of 10^{-8} m.s^{-1}. The results are reported on Table 1.

TABLE 1

RMS ROUGHNESS ON 10μmx10μm SURFACES FOR DIFFERENT SUBSTRATES

Soda-lime glass	1 nm
Glass ceramics : sample A	1 nm
Glass ceramics : sample B	5 nm
Glass ceramics : sample C	10 nm

These RMS roughness values for pure glassy materials are very similar whatever the chemical composition of glasses. But for the glass ceramics with an increasing number of larger β-quartz nanocrystals an important enhancement of the RMS roughness is observed.

For higher crack speeds (except for glass-ceramics sample C; see below) an original phenomenon was observed. The study of the fracture surface revealed the presence of periodical variations of its height (in the direction normal to the mean crack plane) along the crack propagation direction. These roughness waves were observed all along the virtual line followed by the crack front of the specimen on both fracture surfaces and for the two symmetrical parts of each of them in relation to the axis of the 1mm diameter hole. An example (soda-lime glass, average crack speed $\approx 2.10^{-5}$ m.s^{-1} and $K_I \approx 0.6$MPa.m$^{1/2}$) is shown on Figure 2. The 70µmx70µm AFM scan of Figure 2.a shows alternate black (deep) and white (high) bands parallel to the crack front. The sine-like shape of these roughness oscillations is better evidenced in Figure 2.b where all the lines parallel to the crack propagation direction (i.e. perpendicular to the black and white bands) of an independent 10µmx10µm AFM scan (not shown) are averaged.

(a)   (b)
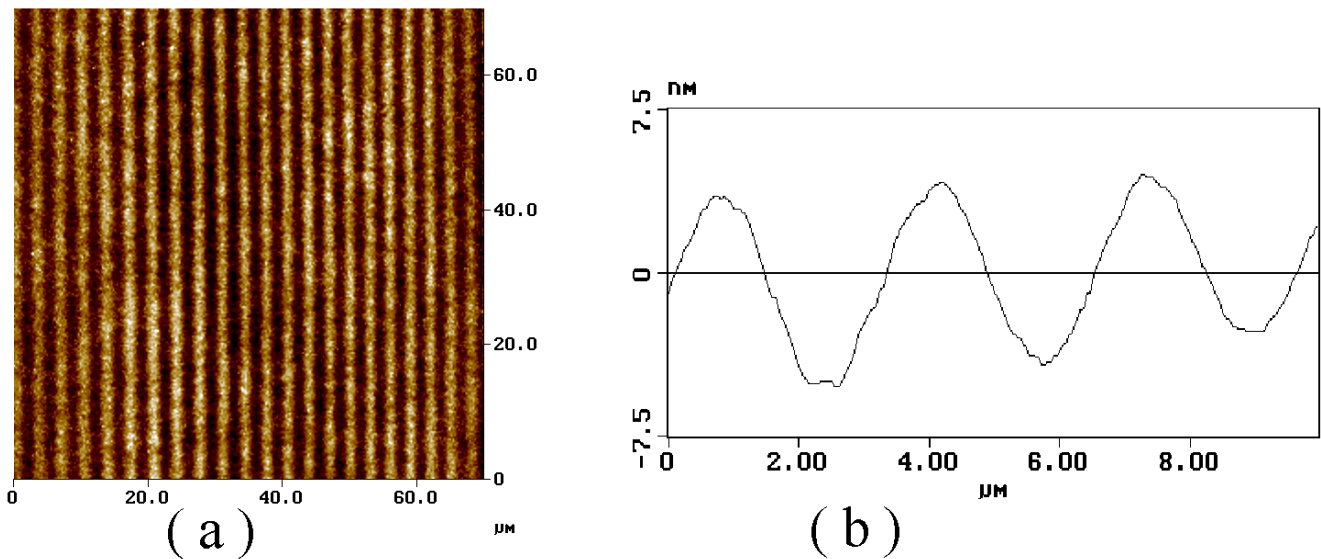
Figure 2: AFM data of fracture surface of soda-lime glass; the vertical scale corresponds to 15 nm.
a) 70µmx70µm scan; b) averaged profile of roughness oscillations as obtained on an independent 10µmx10µm scan (not shown)

The occurrence (or not) of such a phenomenon was followed for all the previously described samples. The following common features have been found:

a) Samples of materials in pure glassy state (soda-lime and glass ceramics) revealed this wavy behavior for a large domain of K_I values. For instance, in the case of soda-lime glass, that K_I domain was delimited by following values: $K_I = 0.8$ MPa.m$^{1/2}$ and $K_I = 0.5$ MPa.m$^{1/2}$ respectively corresponding to crack front speeds of 10^{-4} m.s^{-1} and $1.5 \cdot 10^{-6}$ m.s^{-1}. Between these two limiting values the crack ran over a distance of 9mm in approximately 9 minutes. However for samples of glass ceramics –in the pure glassy state- the oscillating domain is slightly narrower $\Delta K_I = 0.17$ MPa.m$^{1/2}$.

b) One striking feature is that the K_I-width of occurrence of the roughness waves is strongly reduced for samples in intermediate unglassy state (sample B): $\Delta K_I = 0.08$ MPa.m$^{1/2}$. No such oscillations were observed on highly unglassy samples (sample C);

c) The scaling of the wavelength of roughness waves with K_I values was systematically studied. Figure 3 shows the typical variation as observed in the case of soda-lime samples. It evidences a large decrease of the wavelength with decreasing values of K_I. Similar variations – in the same range of wavelength - were observed for glassy or slightly unglassy samples.
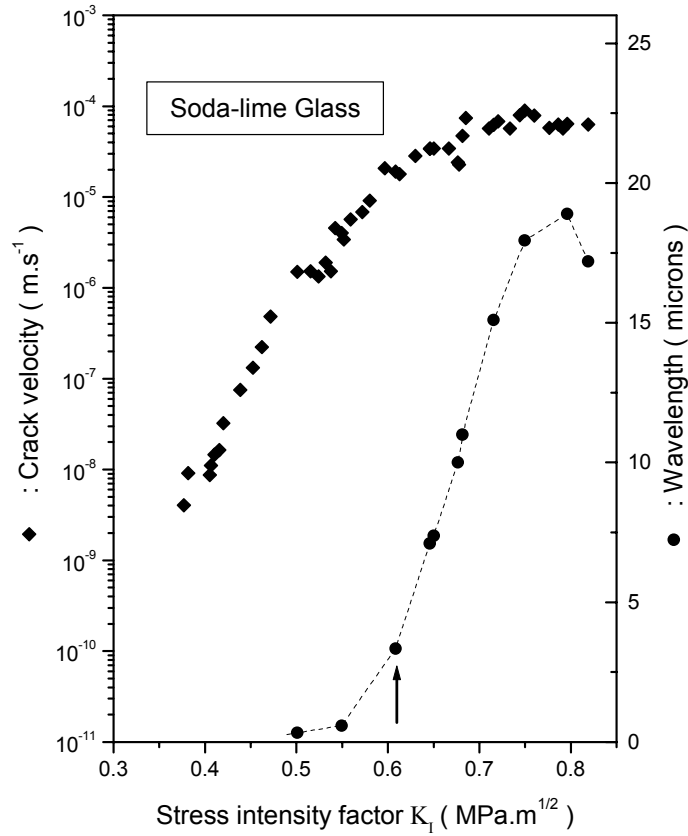
Figure 3: Crack speed (diamonds) and roughness oscillations wavelength (circles) versus K_I for soda-lime glass. The arrow indicates the case corresponding of AFM data of Figure 2.

DISCUSSION

The experimental study presented in this paper revealed that fracture surfaces of various glassy materials are modulated by roughness waves the wave vector of which is parallel to the crack propagation direction. These roughness waves were observed for various heterogeneous materials providing that length scale of the heterogeneities - which can be very roughly estimated by the RMS roughness of surface created by crack propagating at low speed (lower than 10^{-8} m.s^{-1}), see table I – is lower than 10 nm. It means that this phenomenon is directly correlated to the length scale of microstructural heterogeneities inside the broken materials. The wavelength of these ripples is in the micrometer range.

It must be emphasized that, even if the aspect of these roughness ripples presents similarities with patterns observed in stress wave fractography, such an explanation is not relevant for the observations reported in this paper. Indeed no external transverse stress wave generator [8] was used. Furthermore the experimental set-up was working in a very quiet acoustical environment. Moreover the role of hypothetical residual external mechanical vibrations of the DCDC apparatus may be excluded. The resonance frequency and the quality factor of the equivalent mechanical system was indeed estimated to be higher than 70Hz and 6.10^4 respectively. Consequently the hypothetical residual vibrations would have a negligible amplitude at the frequency range (between 0.1Hz to 1Hz) related to the observed roughness waves and calculated by the ratio between the crack front speed and the related wavelength.

Similar results were previously reported by Yuse *et al.* [1] and Ronsin *et al.* [2]. These authors studied the steady propagation of a crack localized within a thermal gradient and observed an oscillatory behavior for given values of crack speed and glass plate width, *W*. Furthermore, Yuse's experiments [1] showed that the related wavelength scaled linearly with *W*. This last result can be presented in an

equivalent manner by plotting (curve not shown) the roughness wavelength versus the stress intensity factor K_I related to this mechanical system using thermal stress according to calculation of Marder [9]. We found that i) this plot reveals similar variations as those deduced from our own experiments and ii) K_I values for wavy behavior are at the same order of magnitude for the two types of experiments (thermal and DCDC). As the wavelength of oscillatory behavior induced by thermal stress was in the millimeter range such as the width of the region of rapid temperature change, it was assumed [1,2] that the related instability mechanisms were only due to 'external' parameters such as stresses induced by the thermal field, independently with the microstructure of broken materials.

Then a very likely explanation to the occurrence of such oscillations in our DCDC experiments is that the crack front similarly undergoes a reproducible sequence of instabilities. As the wavelength is in the micrometer range, the destabilizing factor –in the sense of Cotterell and Rice criterion [3] - from a straight propagation of the crack is likely due to the microstructure of broken materials. When the length scale of heterogeneity is low enough such wavy propagating behavior is observed. On the opposite, materials with larger heterogeneities the fracture surface only presents an incoherent structure (with a much higher roughness). The origin of this instability is perhaps to find in the recently predicted crack front waves [10] which can be generated when fracture occurs in mode I. As experimentally observed [11] the *local* crack speed may exceed the mean crack speed by several order of magnitudes. Therefore it can be forecast that even in the low (mean) speed regime crack front waves may be generated.

CONCLUSION

Experiments were done on a DCDC mechanical set-up working at a fixed load. The internal residual stresses of specimen were carefully relaxed by appropriate thermal treatment. We evidenced for the first time that the crack front line underwent an oscillating behavior along the direction of crack propagation. The wavelength was in the micrometer range and the peak-to-peak amplitude in the nanometer's one. This phenomenon was observed for different glassy materials providing that their typical length scale was lower than a threshold limit estimated to few nanometers. Studies are now performed at sub-micrometer scale in order to understand how this reproducible sequence of instabilities is developing.

REFERENCES

1.   Yuse, A. and Sano, M. (1993) *Nature* 362, 329.
2.   Ronsin, O., Heslot, F. and Perrin, B. (1995) *Phys. Rev. Letters* 75, 2352.
3.   Cotterell, B. and Rice, J.R. (1980) *Int. J. Fract.* 16, 155
4.   Janssen, C. (1974) In: *Proc. 10th Int. Cong. On Glass*, pp.10.23-10.30
5.   Despetis, F., Etienne, P. and Phalippou, J. (2000) *Phys. Chem. Glasses* 41, 104
6.   He, M.Y., Turner, M.R., Evans, A.G. (1995) *Acta Metall. Mater.* 43, 3453.
7.   Marlière, C. *et al.* (2001) *J. Non-Cryst. Solids*, in press
8.   Richter, H.G. and F. Kerkhof (1994) *Fractography of Glass*, Plenum Press, New York.
9.   Marder, M. (1994) *Phys. Rev.* E49, R51.
10.   Morrissey, W. and Rice, J.R. (2000) *J. Mech. Phys. Solids* 48, 1229
11.   Delaplace, A., Schmittbuhl, J. and Maloy, K. (1999) *Phys. Rev.* E60, 1337.

RUBBER-PARTICLE-SIZE DEPENDENT STRAIN RATE EFFECTS ON MECHANICAL PROPERTIES AND DEFORMATION BEHAVIOUR OF HIGH-IMPACT POLYSTYRENE

Takashi Kuboki[1], Kiyoshi Takahashi[1], Pean-Yue Ben Jar[2], Tetsuya Shinmura[3]

[1] Research Institute for Applied Mechanics, Kyushu University, 6-1 Kasuga-koen, Kasuga-city, Fukuoka 816-8580, Japan
[2] Department of Mechanical Engineering, University of Alberta, Edmonton, Alberta, T6G2G8, Canada
[3] Research & Development Department, Chiba Plant, Denki Kagaku Kogyo Co., Ltd., 6 Goiminamikaigan, Ichihara, Chiba, 290-0045, Japan

ABSTRACT

Mechanical properties and deformation behaviour of two high-impact polystyrenes, named 0.45S and 0.84S that have salami-structured rubber particles of 0.45 m and 0.84 m in diameter, respectively, were studied as a function of strain rate ranging from 2.8×10^{-3} s^{-1} to 1.8×10 s^{-1}. Comparison of fracture energies obtained from force-displacement curves suggested that values for 0.84S were slightly higher than those for 0.45S under strain rates up to 1.6×10^{-1} s^{-1}. However, the difference was significantly increased at the highest strain rate, mainly because the values for 0.84S remarkably increased while those for 0.45S decreased. Transmission electron microscopic observation showed that at the highest strain rate, crazes were generated only from a few rubber particles in 0.45S while many crazes were generated from rubber particles in 0.84S. It is concluded that the fracture energy difference at the highest strain rate was caused by the difference in the number of crazes generated from each of the rubber particles.

KEYWORDS

HIPS, rubber particle size, strain rate, deformation behaviour, craze

INTRODUCTION

Mechanical properties of polymers strongly depend on time and temperature due to their viscoelastic nature of deformation behaviour. In general, brittleness of polymers is known to increase with the increase of the strain rate. However, for high-impact polystyrene (HIPS) Vu-Khanh [1], based on results from three-point bending tests on notched specimens, reported the increase of fracture energy for crack initiation at a loading speed above 1 m/s. We also reported a similar fracture energy increase for un-notched HIPS specimens under a high strain rate [2].

It is yet to be certain if the above toughness increase at the high strain rate is universal for HIPS of different

compositions, as many parameters, such as molecular weight of the matrix, rubber content, rubber particle size, rubber particle structure, and rubber cross-link density, affect the mechanical properties. The most significant factor for HIPS fracture resistance is believed to be the size of the rubber particles, as only HIPS with a certain range of particle size shows the optimum mechanical properties [3-7].

In this paper, effects of the strain rate on mechanical properties for two HIPSs that have different rubber particle size are studied.

EXPERIMENTAL

Materials
Two HIPS materials were used in the study (named 0.45S and 0.84S). Composition of styrene (St) and butadiene (Bd), weight average molecular weight of polystyrene (PS), average size of rubber particles and morphology of rubber particles are given in Table 1. The main difference between the two materials is rubber particle size, 0.45 m and 0.84 m for 0.45S and 0.84S, respectively. TEM micrographs showed that particles of salami structure with polystyrene occlusions were well dispersed in the polystyrene matrix for each material.

Mechanical Tests
Mechanical tests were carried out on un-notched tensile specimens using a servo-hydraulic tensile machine for lower strain rates and a falling weight type impact tensile test machine [8] for higher strain rates. Strain was measured using an optical-fibre extensometer [9] constructed in our laboratory [8].

Examination of Deformation Behaviour
Fractured specimens were studied by transmission optical microscopy and transmission electron microscopy (TEM). Regions near the fracture surface were selected for the TEM study. The TEM specimens were firstly stained in the vapour of an OsO_4 solution of 2 weight percent before being sliced by an ultramicrotome equipped with a diamond knife. Hitachi H7100 TEM, operated at 75 kV, was used for the observation.

RESULTS AND DISCUSSION

Mechanical Tests
Fig. 1 shows typical stress-strain curves at different strain rates. At the highest strain rate of 1.8 10 s^{-1}, oscillation was observed in the curves for both 0.45S (Fig.1 (a)) and 0.84S (Fig. 1 (b)). The oscillation is an indication of the dynamic loading effect, due to vibration and stress wave propagation. When the oscillation occurred, the maximum stress was determined based on the "oscillation-centre", defined as the mean value of the adjacent maximum oscillating stress values. The curves also provide mechanical properties such as Young's modulus and strain at fracture.

TABLE 1   Characteristics of the HIPSs.

Material	Composition (wt%)		Weight average molecular weight of PS	Average size of rubber particles (m)	Morphology of a rubber particle
	St	Bd			
0.45S	92	8	239,500	0.45	Salami
0.84S	92	8	225,300	0.84	Salami
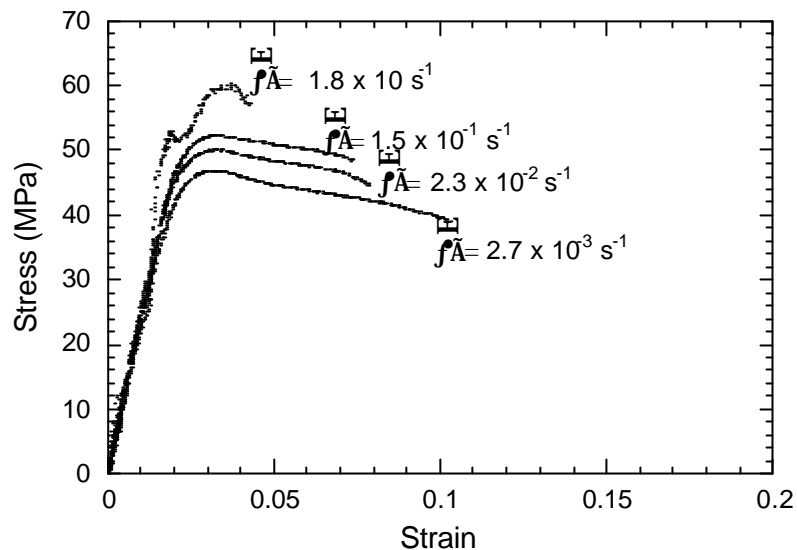
(a) 0.45S
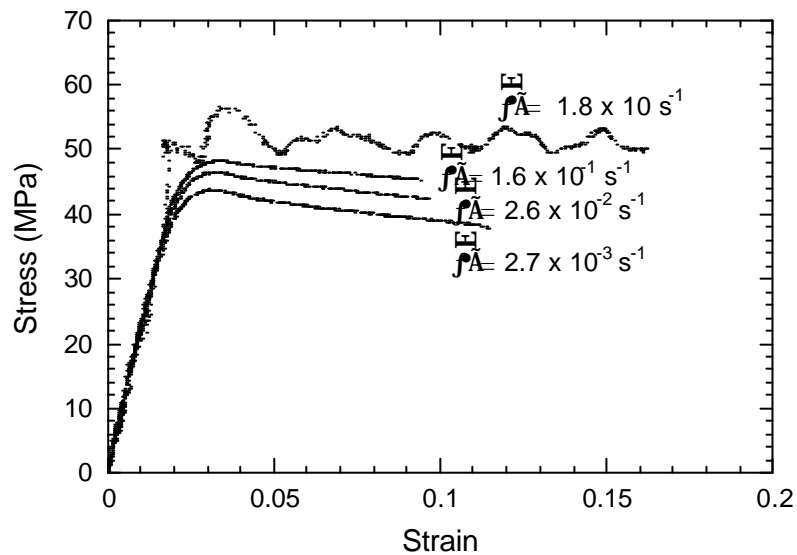
(b) 0.84S

Figure 1: Typical stress-strain curves under various strain rates.

Both materials showed that the maximum stress increased with the increase of strain rate. The maximum stress values of 0.45S were always higher than those of 0.84S at all strain rates. Young's modulus of the former was also slightly higher than that of the latter at all strain rates. However, the modulus values showed little change with the increase of the strain rate. For the strain at fracture, 0.45S showed a continuous decrease with the increase of the strain rate; but 0.84S firstly showed the decrease with the increase of the strain rate up to 1.6×10^{-1} s^{-1}, and then a remarkably increase by ca. 61 % with a further increase of the strain rate to 1.8×10 s^{-1}. It should be noted that the fracture strain of 0.84S at the highest strain rate of 1.8×10 s^{-1} is even higher than that at the lowest strain rate of 2.8×10^{-3} s^{-1}. Comparing the fracture strains at the same strain rate, 0.84S was always higher than 0.45S.

Fig. 2 shows fracture energy as a function of strain rate. Fracture energy was calculated based on the total area under the force-displacement curve. The values of 0.45S continuously decreased with the increase of the strain rate. On the other hand, the values of 0.84S firstly showed a decrease with the increase of the strain rate from 2.8×10^{-3} s^{-1} to 2.5×10^{-2} s^{-1}; a slight increase with a further increase of the strain rate to 1.6×10^{-1} s^{-1}, and a significant increase by ca. 83 % for a further increase of the strain rate to 1.8×10 s^{-1}. The fracture energy of 0.84S was always higher than that of 0.45S at the same strain rates. The value of 0.84S
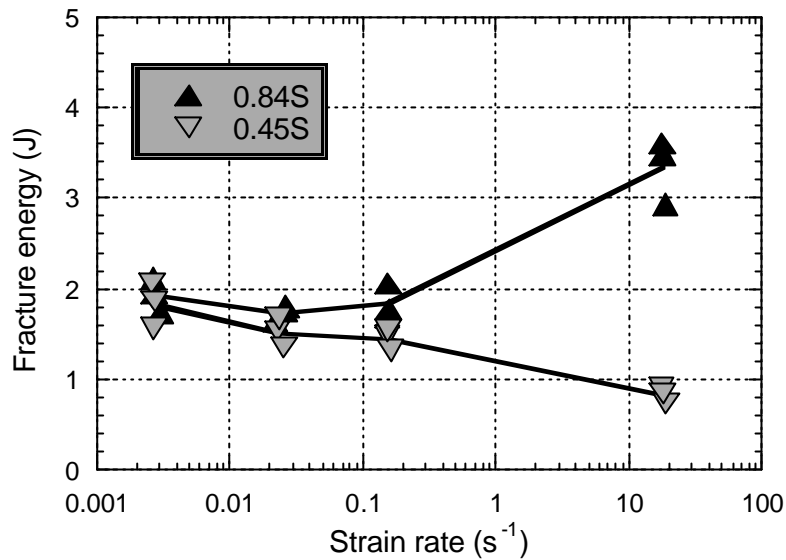
Figure 2: Fracture energy as a function of strain rate.

at the highest strain rate of 1.8 × 10 s⁻¹ was the highest obtained from the study. We also noticed that the difference of fracture energy between the two materials increases with the increase of the strain rate, and the difference is remarkable at the highest strain rate of 1.8 × 10 s⁻¹.

As the fracture energy variation is dominated by the energy absorption after the point of the maximum stress, as shown in Fig. 1, the fracture energy variation follows very closely the variation of the fracture strain. Therefore, the fracture energy variation is mainly dominated by the strain energy for plastic deformation after the maximum stress point.

Deformation Behaviour
The deformation mechanisms in the post-fracture specimens were examined in order to facilitate the understanding of the significant difference in the fracture energy between 0.45S and 0.84S at the highest strain rate.

Results of the transmission optical microscopy showed that the size of the stress-whitening zone in 0.84S increased with the increase of the strain rate from 1.6 × 10⁻¹ s⁻¹ to 1.8 × 10 s⁻¹, while that in 0.45S decreased. This is consistent with the variation of the fracture energy between the two materials.

Fig. 3 shows TEM micrographs for specimens fractured at the lowest strain rate of 2.8 × 10⁻³ s⁻¹. Figs. 3 (a) and 3 (b) represent the micrographs of 0.45S and 0.84S, respectively. The micrographs were taken in regions just beneath the fracture surface. An arrow on the micrographs indicates where the fracture surface is. The arrow is also oriented to be parallel to the direction of the tensile loading. Many highly deformed, widely open crazes are shown in both micrographs, in which some of the craze fibrils have already broken down. Such deformation behaviour suggests that crazes have been well developed in the specimens and that fracture was initiated by coalescence of the crazes. Little difference was found in width and number of the crazes in these two micrographs.

Fig. 4 shows TEM micrographs for specimens fractured at the highest strain rate of 1.8 × 10 s⁻¹. The micrograph of 0.45S (Fig. 4 (a)) shows that crazes are generated only from some of the rubber particles. On the other hand, the micrograph of 0.84S (Fig. 4 (b)) shows many crazes being generated from each rubber particle. There is a remarkable difference between 0.45S and 0.84S in the number of crazes. Compared to the micrographs from specimens tested at the lowest strain rate, Fig. 3, the number of crazes in Fig. 4 (a) has largely decreased with the increase of the strain rate, while that in Fig. 4 (b) has significantly increased.
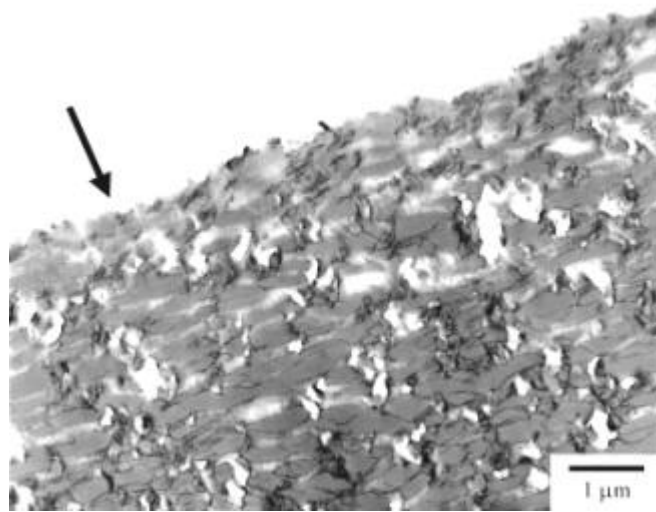
(a) 0.45S
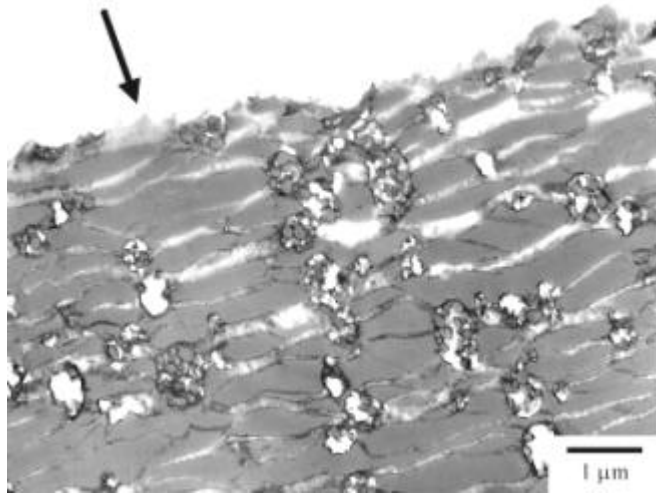
(b) 0.84S

Figure 3: TEM micrographs for specimens fractured at the lowest strain rate of 2.8 $\times$ 10^{-3} s^{-1}.

TEM observation showed that crazing was the dominant deformation mechanism in all specimens. At the lowest strain rate, there was no significant difference in the width and number of crazes between the two HIPSs. However, at the highest strain rate, a small number of crazes occurred in the 0.45S and were generated only from a few rubber particles; while many more crazes were generated in the 0.84S and were found from every rubber particle in the micrograph. Therefore, the difference in number of crazes has caused the significant difference in the fracture energy at the highest strain rate.

CONCLUSIONS

It is concluded that the particle size has strongly affected the fracture energy of the HIPS, especially at the highest strain rate. This is mainly because at the highest strain rate, the rubber particle size has affected the number of crazes generated from each rubber particle.

ACKNOWLEDGEMENT
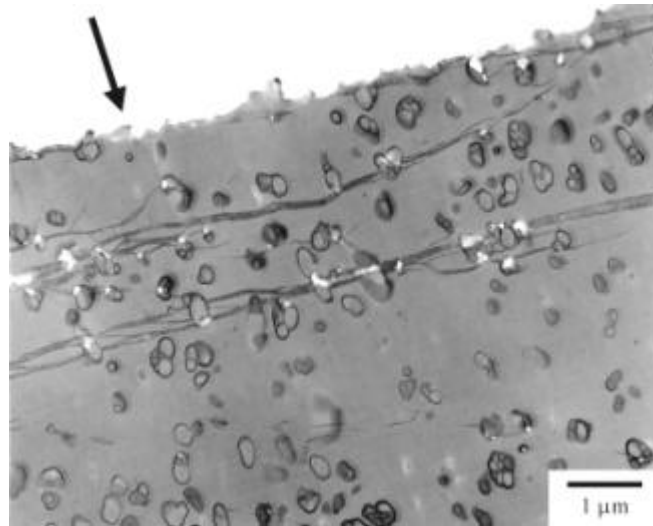
(a) 0.45S
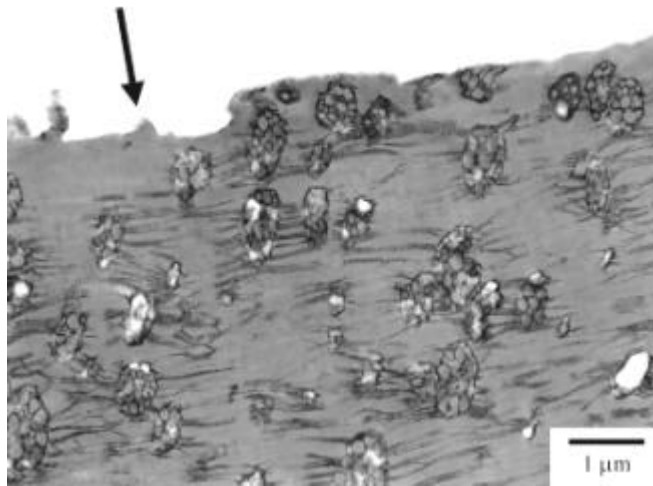
(b) 0.84S

Figure 4: TEM micrographs for specimens fractured at the highest strain rate of $1.8 \quad 10$ s^{-1}.

REFERENCES

1. Vu-Khanh, T. (1998) *Theoret. Appl. Fract. Mech.* 29, 75.
2. Kuboki, T., Jar, P.-Y. B., Takahashi, K. and Shinmura, T. (2000). *11th International Conference on Deformation and Fracture of Polymers*, Cambridge, 429.
3. Moore, J.D. (1971) *Polymer* 12, 478.
4. Silberberg, J. and Han, C.D. (1978) *J. Appl. Polym. Sci.* 22, 599.
5. Bucknall, C.B., Davies, P and Partridge, I.K. (1987) *J. Mater. Sci.* 22, 1341.
6. Cook, D.G., Rudin, A. and Plumtree, A. (1993) *J. Appl. Polym. Sci.* 48, 75.
7. Daðli, G., Argon, A.S. and Cohen, R.E. (1995) *Polymer* 36, 2173.
8. Takahashi, K., Mada, T. and Beguelin, Ph. (1998) *Trans. Jpn. Soc. Mech. Eng.* A64, 2975 (in Japanese).
9. Beguelin, Ph., Barbezat, M. and Kausch, H. H. (1991) *J. Physique* III 1, 1867.

SCALING OF QUASI-BRITTLE FRACTURE :
MORPHOLOGY OF CRACK SURFACES AND ASYMPTOTIC ANALYSIS.

S. Morel [1], E. Bouchaud [2] and G. Valentin [1]

[1] Lab. de Rhéologie du Bois de Bordeaux, UMR 5103,
Domaine de l'Hermitage, B.P.10, 33610 Cestas Gazinet, France
[2] C.E.A. Saclay, (D.S.M./D.R.E.C.A.M./S.P.C.S.I.),
91191 Gif-Sur-Yvette Cedex, France

ABSTRACT

Recently, the *anomalous* scaling properties, observed on crack surfaces of quasi-brittle materials, was proposed to be related to the experimental *R*-curve behavior and size effect on the critical energy release rates [1]. On this basis, an energy-based asymptotic analysis allows to extend the link between anomalous roughening of crack surfaces to the nominal strength of structures. The established relation represents a smooth transition from the case of no size effect, for small structure sizes, to a power law size effect which appears as a decrease of the linear elastic fracture mechanics theoretical one, in the case of large sizes. This predicted size effect is confirmed by fracture experiments on wood.

KEYWORDS

Scaling, Quasi-brittle materials, Roughening, Asymptotic analysis, Energy release, Size effect.

INTRODUCTION

Fracture of quasibrittle materials such as concrete, wood, tough ceramics or various rocks and composites, is characterized by the effect of structure size on its nominal strength [2]. In these materials, a large fracture process zone (FPZ) with microcracking damage develops inducing stress redistributions which greatly increases the effective fracture energy. This particular behavior, known as the resistance curve (*R*-curve), leads to the release of the stored energy by the stable macrocrack growth, before the maximum load is reached, and is at the origin of the size effect.

A recent study has shown that the *R*-curve behavior of quasi-brittle materials could be linked to the morphology of crack surfaces [1]. This link between macroscopic fracture properties and the fractal nature of cracks at the microscale is based on the analysis of the complete scaling behavior of the local fluctuations of crack surfaces obtained in two quasi-brittle materials : granite [3] and wood [4]. The scaling law (called *anomalous* scaling [5,6]) needed to describe accurately the crack developments in the perpendicular and parallel directions of crack propagation involves three scaling exponents, one is the universal local roughness exponent $\zeta_{loc} = 0.8 - 0.9$ (*i.e.* independent of the fracture mode and of the material [7]) and two other exponents which are material dependent, the global roughness exponent ζ and the dynamic exponent z. The measured values of the global roughness exponent are $\zeta = 1.2$ in granite [3] and respectively 1.35 and 1.60 in the case of two species of wood (pine and spruce [4]). Moreover, it has been shown in [3,4], that fracture surfaces starting from a straight notch, exhibit anomalous roughness development for crack length increments $\Delta_a \ll \Delta a_{sat}$. This is followed by a stationnary regime where the magnitude of the roughness saturates and appears to be dependent on the specimen size for crack length increments $\Delta_a \gg \Delta a_{sat}$. On this basis, the revisited Griffith criterion [1] which takes into account the energy required to create a rough surface at the microscale, leads to a *R*-curve

behavior (1) linked to the anomalous roughness development of fracture surfaces. In (1), G_R is the resistance to crack growth and 2γ the specific surface energy (considered as an average value taking into account the heterogeneous character of the material). The terms A and B are prefactors and l_o is the lower cutoff of the fractal range of the fracture surface (*i.e.* the characteristic size of the smaller microstructural element relevant for the fracture process). Note that the term under square root is dimensionless.

$$G_R(\Delta a \ll \Delta a_{sat}) \simeq 2\gamma \sqrt{1 + \left(\frac{AB^{\zeta-\zeta_{loc}}}{l_o^{1-\zeta_{loc}}}\right)^2 \Delta a^{2(\zeta-\zeta_{loc})/z}} \tag{1}$$

$$G_{RC}(\Delta a \gg \Delta a_{sat}) \simeq 2\gamma \sqrt{1 + \left(\frac{A}{l_o^{1-\zeta_{loc}}}\right)^2 (C\,L)^{2(\zeta-\zeta_{loc})}} \tag{2}$$

On the other hand, on the zone where the roughness saturates (*i.e.* for crack length increments $\Delta_a \gg \Delta_{sat}$), the link [1] leads to a *critical* resistance to crack growth G_{RC} (2) where L is the characteristic size of the structure (homothetic structure) and C a proportionality coefficient. Note that in (1) and (2) the crack length increment Δa has to be understood as an elastically equivalent crack length increment in the sense of linear elastic fracture mechanics (LEFM).

The main consequence of the link between fracture mechanics and anomalous roughening of fracture surfaces [1] is the size effect on the critical resistance to crack growth (2) which is induced by the the dependence of the maximum magnitude of the roughness as a function of the structure size L. As shown in Fig. 1 for arbitrary values of the scaling exponents, the size effect on the critical resistance G_{RC} (2) exhibits two asymptotic behaviors. The transition happens for the the crossover length $L_C = 1/C\,(l_o^{1-\zeta_{loc}}/A)^{1/(\zeta-\zeta_{loc})}$. For small structure sizes (*i.e.* $L \ll L_C$) where the roughness of fracture surfaces is weak, there is no size effect : $G_{RC} \simeq 2\gamma$, while for large structure sizes (*i.e.* $L \gg L_C$), which correspond to important fracture roughness, the critical resistance evolves as a power law : $G_{RC} \sim L^{\zeta-\zeta_{loc}}$.

Figure 1: Size effect on the critical resistance to crack growth obtained for: $\zeta = 1.3$, $\zeta_{loc} = 0.8$, $A = 0.1$ and $l_o = 1$.

Figure 2: Geometrically similar TDCB fracture specimens of different sizes $L = 7.5, 11.3, 15.0, 22.5, 30.0$ and 60.0 mm.

The purpose of the present paper is to revisit the size effect relation on nominal strength of structures proposed by Bažant [8] by introducing the modifications induced by the link [1] between anomalous roughening of fracture surfaces and material fracture properties of quasi-brittle materials previously mentioned.

ANOMALOUS ROUGHENING AND SIZE EFFECT ON NOMINAL STRENGTH

In the frame work of reference [8], the size effect (for two-dimensional problem) in geometrically similar structures can be described by using the nominal stress :

$$\sigma_N = \frac{P}{d\,L} \tag{3}$$

where P is the external load applied on the structure (considered to be a load independent of displacement), L is the characteristic size of the structure and d is the ligament length (Fig. 2). When $P = P_u$, i.e. the ultimate load, σ_N is called the nominal strength of the structure.

In the case of a quasi-brittle material, the nominal strength σ_N depends on the crack length a corresponding to the ultimate load P_u such as : $a = a_o + \Delta a_{sat}$ where a_o is the length of the initial crack and Δa_{sat} id defined as the critical effective length of the fracture process zone (under P_u). In order to obtain dimensionless energy release expression, we introduce the relative crack length : $\alpha = \alpha_o + \theta$, where $\alpha_o = a_o/d$ and $\theta = \Delta a_{sat}/d$ are dimensionless variables. The main problem to establish any size effect relation on nominal strength is to determine the effective length of the process zone Δa_{sat}. Indeed, the dependence between Δa_{sat} (or in other terms the crack length increment below which the *R*-curve (2) applies) and the specimen size does not appear clearly in the roughness analysis [3,4]. A possible way to resolve this problem consists in considering that the material failure of a quasi-brittle material is not only characterized by the specific surface energy 2γ [1] per unit surface of the actual crack (Eq. 1 and 2), but also by a critical damage energy release rate G_d per unit volume of *damaged* material (*i.e.*, per unit volume of FPZ). Thus, one can assume that failure at maximum load is obtained for the energy balance :

$$G_d \, V_{FPZ} = \; 2\gamma \, A_r(\Delta a_{sat}) \tag{4}$$

where $A_r(\Delta a_{sat})$ is the real crack surface corresponding to the effective crack length increment Δa_{sat}. The volume of the fracture process zone can be estimated as $V_{FPZ} = L \, \Delta a_{sat}{}^2/n$ where $L \Delta a_{sat}$ corresponds to the projected crack surface and $\Delta a_{sat}/n$ is the *height* of the FPZ (n is a constant, *i.e.* independent of the size L). On the other hand, at the maximum load, the crack corresponding to the crack length increment Δa_{sat} propagates if its energy release rate G (obtained at constant load P or σ_N) becomes equal to the critical resistance to crack growth G_{RC} defined in (2) :

$$G = \frac{1}{L} \left[\frac{\partial W^*}{\partial a} \right]_{\sigma_N} = \; G_{RC} \tag{5}$$

where the complementary energy W^* characterizes the energy stored in the structure. This energy can be expressed as a function of the relative crack length α : $W^* = \sigma_N{}^2 L \, d^2 f(\alpha)/E$ where f is a dimensionless function characterizing the geometry of the structure. Thus, knowing the relative crack length for which the maximum load is reached, the nominal strength of the structure can be written as :

$$\sigma_N = \sqrt{\frac{E \, G_{RC}}{d \, g(\alpha)}} \tag{6}$$

in which $g(\alpha) = \partial f(\alpha)/\partial \alpha$ corresponds to the dimensionless energy release rate function.

On the other hand, in structures said to be of positive geometry (*i.e.* $\partial g(\alpha)/\partial \alpha > 0$) which is the restricted case of this study, the crack length increment Δa_{sat} at maximum load represents the limit of stability of the crack growth if the structure is under load control rather than displacement control.

Large-size asymptotic expansion of the size effect

As previously mentioned, the crack length increment Δa_{sat} corresponding to the maximum load P_u can be determined by Eq.(4). Moreover, for large structure sizes (*i.e.* $L \gg L_C$), the corresponding real crack surface A_r can be easily estimated from [1] as : $A_r \simeq \beta \, L \, \Delta a_{sat} \, (L/L_C)^{\zeta - \zeta_{loc}}$ where β is a constant (function of the scaling exponents). Substituting A_r in (4) yields the expression of the crack length increment :

$$\Delta a_{sat} = c^* \beta \left(\frac{L}{L_C} \right)^{\zeta - \zeta_{loc}} \tag{7}$$

where $c^* = n2\gamma/G_d$ can be consider as a material length. Thus, for large structure sizes, the relative crack length of the FPZ (*i.e.* $\theta = \Delta a_{sat}/d$) is expected to evolve as a power law $\theta \sim L^{\zeta - \zeta_{loc} - 1}$ and $lim \, \theta = 0$ for $L \to +\infty$. In other terms, in large structures, the fracture process zone is expected to lie within only an infinitesimal volume fraction of the body and so $lim \, \alpha = \alpha_o$ for $L \to +\infty$. Note that this result is in agreement with the assumption made in [8]. Hence, $g(\alpha)$ being a smooth function, we may expand it into Taylor series around $\alpha = \alpha_o$ and Eq.(6) thus yields :

$$\sigma_N \; = \; \sqrt{\frac{E \, G_{RC}}{d}} \left[g(\alpha_o) + g_1(\alpha_o) \, \theta + g_2(\alpha_o) \, \frac{\theta^2}{2!} + g_3(\alpha_o) \, \frac{\theta^3}{3!} + ... \right]^{-1/2} \tag{8}$$

$$= \sigma_M \sqrt{\frac{\left(1 + \left(\frac{L}{L_C}\right)^{2(\zeta-\zeta_{loc})}\right)^{1/2}}{\frac{L}{L_1} + \left(\frac{L}{L_C}\right)^{\zeta-\zeta_{loc}} + b_2 \frac{L_1}{L}\left(\frac{L}{L_C}\right)^{2(\zeta-\zeta_{loc})} + b_3\left(\frac{L_1}{L}\right)^2\left(\frac{L}{L_C}\right)^{3(\zeta-\zeta_{loc})} + ...}} \qquad (9)$$

where $g_1(\alpha_o) = \partial g(\alpha_o)/\partial\alpha$, $g_2(\alpha_o) = \partial^2 g(\alpha_o)/\partial\alpha^2$, ..., and $b_2 = g(\alpha_o)g_2(\alpha_o)/(2g_1(\alpha_o)^2)$, $b_3 = g(\alpha_o)^2 g_3(\alpha_o)/(6g_1(\alpha_o)^3)$, ..., and,

$$\sigma_M = \sqrt{\frac{2\gamma E}{mg(\alpha_o)L_1}} \qquad (10)$$

$$L_1 = c^* \frac{\beta}{m} \frac{g_1(\alpha_o)}{g(\alpha_o)} \qquad (11)$$

are all constants. The terms m in (10) is a proportionality coefficient between the ligament length d and the characteristic size L of the specimens ($d = mL$). Expression (9) provides a large-size asymptotic series expansion of the size effect but is expected to diverge for structure sizes $L \to 0$ as shown in Fig. 3.
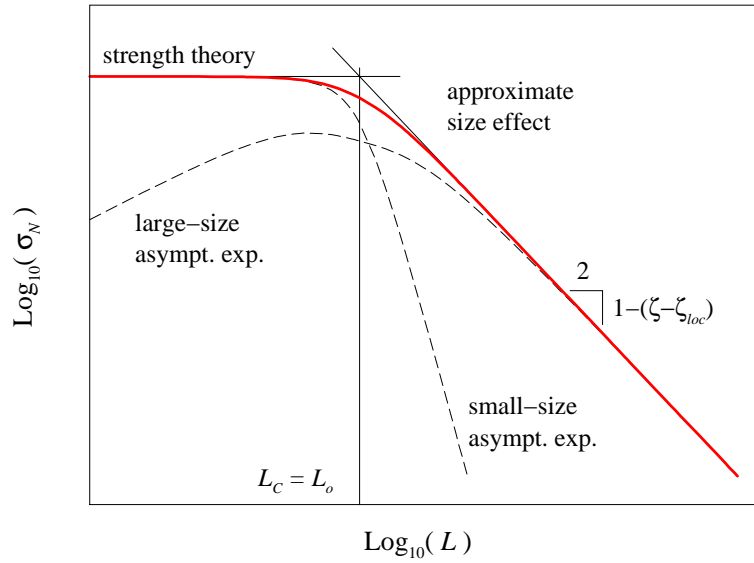
Figure 3: Approximate size effect on the nominal strength (solid curve) and asymptotic series expansions (dashed curves).

Moreover, in (9) the terms of non zero powers in denominator vanish for $L \to \infty$ and so, the large-size first-order asymptotic approximation can be obtained by truncating the series after the linear term :

$$\sigma_N = \sigma_M \sqrt{\frac{\left(1 + \left(\frac{L}{L_C}\right)^{2(\zeta-\zeta_{loc})}\right)^{1/2}}{\frac{L}{L_1} + \left(\frac{L}{L_C}\right)^{\zeta-\zeta_{loc}}}} \qquad (12)$$

Thus, the main consequence of the anomalous roughening for the size effect in the case of large sizes is that the nominal strength is expected to decrease as $\sigma_N \sim L^{-1/2+(\zeta-\zeta_{loc})/2}$ (as shown in Fig. 3) instead of the theoretical result of LEFM $\sigma_N \sim L^{-1/2}$ [8]. This difference originates in the fact that, in the case of an anomalous roughening, the critical resistance to crack growth G_{RC} (2) is expected to evolve as a power law $G_{RC} \sim L^{\zeta-\zeta_{loc}}$ for large structure sizes (as shown in Fig. 1) while in the theoretical case of LEFM, the critical resistance G_{RC} is assumed constant. Nevertheless, in the case where there is no anomalous roughening, *i.e.* $\zeta = \zeta_{loc}$ [1], the theoretical size effect of LEFM is recovered.

Small-size asymptotic expansion of the size effect
In Bažant's theory [8], no size effect is expected for small structure sizes ($L \to 0$); this is the domain of the strength theory. A possible justification is that, in small structures, the fracture process zone occupies the entire volume of the structure and hence, there is no stress concentration and so no distinct fracture at maximum load.

Such an argument can be also obtained by substituting the real crack surface A_r created in small structures into the the fracture criterion (4). Indeed, in small structure sizes (*i.e.* $L \ll L_C$), the roughness being negligible, actual crack surfaces are not so different from the projected one : $A_r \simeq L\Delta a_{sat}$. Hence, from (4), the crack length increment Δa_{sat} (or in other terms the effective fracture process zone size) tends to the material length : $\Delta a_{sat} = n2\gamma/G_d = c^*$ for $L \ll L_C$. Thus, when the material length $c^* = d - a_o$ (Fig. 2), the fracture process zone occupies the entire ligament of the structure.

On the basis of Bažant's theory [8] and in order to obtain a small-size asymptotic expansion of the size effect, let us now introduce a new variable and a new function :

$$\eta = \frac{1}{\theta} = \frac{d}{\Delta a_{sat}} \ , \qquad \psi(\alpha_o, \eta) = \frac{g(\alpha_o + \theta)}{\theta} = \eta \, g(\alpha_o + 1/\eta) \tag{13}$$

The function $\psi(\alpha_o, \eta)$ corresponds to the dimensionless energy release rate function of the inverse relative size of the fracture process zone. Substituting (13) into (6) and expanding $\psi(\alpha_o, \eta)$ into Taylor series about the point $(\alpha_o, 0)$ since $\lim \eta = 0$ when d or $L \to 0$, leads to the nominal strength :

$$\sigma_N = \sqrt{\frac{E \, G_{RC}}{c^*}} \left[\psi(\alpha_o, 0) + \psi_1(\alpha_o, 0) \, \eta + \psi_2(\alpha_o, 0) \, \frac{\eta^2}{2!} + \psi_3(\alpha_o, 0) \, \frac{\eta^3}{3!} + ... \right]^{-1/2} \tag{14}$$

$$= \sigma_{M'} \sqrt{\frac{\left(1 + (\frac{L}{L_C})^{2(\zeta - \zeta_{loc})}\right)^{1/2}}{1 + \frac{L}{L_2} + c_2(\frac{L}{L_2})^2 + c_3(\frac{L}{L_2})^3 + ...}} \tag{15}$$

where $\psi_1(\alpha_o, 0) = \partial\psi(\alpha_o, 0)/\partial\eta$, $\psi_2(\alpha_o, 0) = \partial^2\psi(\alpha_o, 0)/\partial\eta^2$, ..., and $c_2 = \psi_2(\alpha_o, 0)\psi(\alpha_o, 0)^2/(2\psi_1(\alpha_o, 0)^2)$, $c_3 = \psi_3(\alpha_o, 0)\psi(\alpha_o, 0)^3/(6\psi_1(\alpha_o, 0)^3)$, ..., and,

$$\sigma_{M'} = \sqrt{\frac{2\gamma E}{\psi(\alpha_o, 0)c^*}} \ , \qquad L_2 = c^* \frac{\psi(\alpha_o, 0)}{m \, \psi_1(\alpha_o, 0)} \tag{16}$$

are all constants. The small-size asymptotic series expansion of the size effect on the nominal strength (15) is plotted in Fig. 3. As shown in Fig. 3, the nominal strength tends to a constant when $L \to 0$ (*i.e.* $\sigma_{M'}$ as expected in the case of a strength theory) but diverges from the large-size asymptotic behavior of the size effect (9) for $L \to \infty$ (which coincides to the straight line of slope $-1/2 + (\zeta - \zeta_{loc})/2$).

Approximate size effect

Now, the main problem consists in interpolating between the large-size (9) and the small size (15) asymptotic series expansion in order to obtain an approximate size effect valid everywhere. In our case the intermediate behavior seems very difficult to determine because the the first two terms at the numerators of the two asymptotic expansions are different. Nevertheless, it is interesting to observe in Fig. 3 that a satisfactory approximate size effect can be obtained by truncating the small-size asymptotic series expansion after the linear term :

$$\sigma_N = \sigma_{max} \sqrt{\frac{\left(1 + (\frac{L}{L_C})^{2(\zeta - \zeta_{loc})}\right)^{1/2}}{1 + \frac{L}{L_o}}} \tag{17}$$

where the contants σ_{max} and L_o will be discussed in the following. Indeed, this size effect curve is seen to represent the transition between a horizontal asymptote, characterizing the strength theory for which there is no size effect, and a decreasing asymptote, corresponding to a power law of exponent $-1/2 + (\zeta - \zeta_{loc})/2$ characterizing the decrease of the LEFM size effect caused by the growth of the critical energy release rate for large structure sizes. A possible justification is that, in the large-size first order expansion (12), the second term in numerator has no influence on the large size asymptotic behavior of the size effect but induces a divergence at small sizes.

However, one limitation of the approximate size effect (17) is that the values of σ_M and $\sigma_{M'}$ (characterized by σ_{max}), and the values of L_1 and L_2 (characterized by L_o) would be surely different if these values were to be determined from large size data or from small size data. The approximate size effect (17) only gives the shape

of the size effect relation on the nominal strength but does not allow for a determination of the parameter values σ_{max} and L_o. Only the crossover length L_C and the scaling exponents ζ_{loc} and ζ are univoquely determined from the roughness analysis.
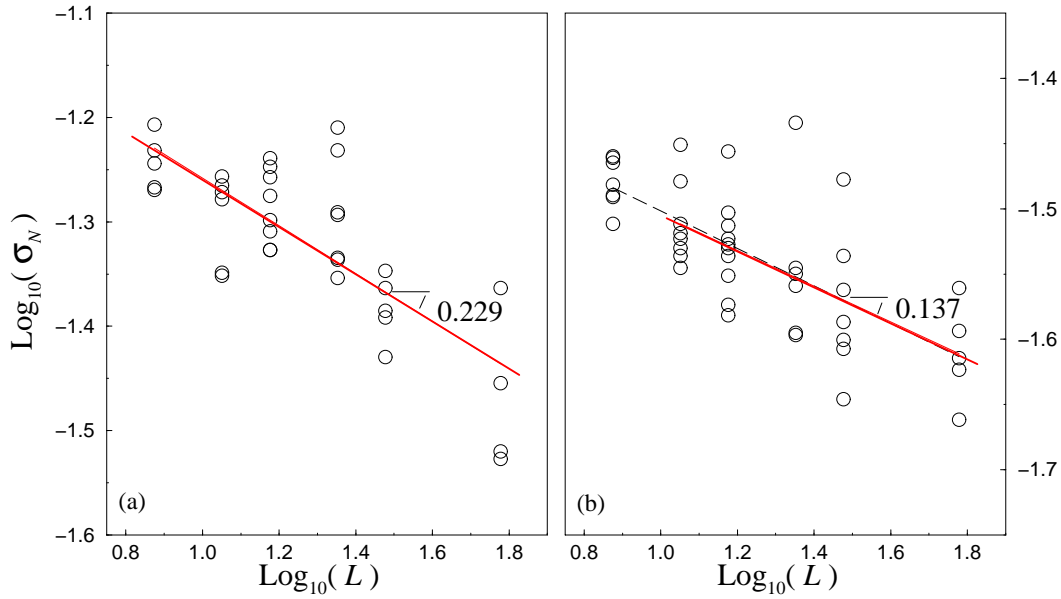
Figure 4: Size effect on nominal strength respectively for pine (a) and spruce (b). The expected slope from the roughness analysis [1] are $-\frac{1}{2} + \frac{\zeta - \zeta_{loc}}{2} = -0.265 \pm 0.085$ for pine (a) and -0.135 ± 0.085 for spruce (b).

On the other hand, it seems difficult to compare the crossover lengths L_1 and L_2, or in other terms L_o in Eq.17, to the crossover length L_C by means of their analytical expressions : the first one being deduced from a mechanical approach and the second one from a roughness analysis. However, from a physical point of view, both have the same meaning. For small structure sizes , *i.e.* $L \ll L_C$ or L_o, the energy release from the structure is negligible, while for large sizes, *i.e.* $L \gg L_C$ or L_o, the energy release is dominant. Hence, it seems reasonnable to assume that both crossover lengths are of the same order of magnitude (it is the case in Fig. 3 where it is assumed that $L_o = L_C$).

In Fig. 4, the nominal strength σ_N obtained from geometrically similar mode I fracture TDCB specimens is plotted versus the characteristic size L. With the assumption that $L_o = L_C$, it has been shown in [1] that the crossover length L_C was smaller than the sizes L of tested specimens. Hence, the size effect on nominal strengths is expected to evolve (see Eq. 17), as a power law $\sigma_N \sim L^{-1/2+(\zeta-\zeta_{loc})/2}$. The latter power law behavior is in good agreement with the observed experimental size effect in wood as shown in Fig. 4.

In conclusion, a modification of the Bažant's size effect law [8] has been proposed on the basis of the size effect on the energy release observed in the case of an anomalous roughening of fracture surfaces. It has been found that the approximate size effect relation (17) is slightly different from the *classical* size effect law [8] for large structure sizes, and predicts an asymptotic behavior $\sigma_N \sim L^{-1/2+(\zeta-\zeta_{loc})/2}$ instead of the size effect of LEFM, $\sigma_N \sim L^{-1/2}$. However, if the roughening of fracture surfaces is only slightly anomalous (*i.e.* $\zeta \to \zeta_{loc}$ [1]), the theoretical size effect of LEFM is recovered, which corresponds to the fracture behavior of a purely elastic brittle material.

REFERENCES

1. Morel, S., Bouchaud, E., Schmittbuhl, J. and Valentin, G. (2000). *Phys. Rev. Lett.* **85** (8), 1678.
2. Bažant, Z.P., Kazemi, M.T. (1990). *J. Am. Ceram. Soc.* **73** (7), 1841.
3. López J.M. and Schmittbuhl, J. (1998). *Phys. Rev. E* **57**, 6405.
4. Morel, S., Schmittbuhl, J., López, J.M. and Valentin, G. (1998). *Phys. Rev. E* **58** (6), 6999.
5. Das Sarma, S., Ghaisas, S.V. and Kim, J.M. (1994). *Phys. Rev. E* **49** (1), 122.
6. López, J.M. and Rodríguez, M.A. (1996). *Phys. Rev. E* **54** (3), R2189.
7. Bouchaud, E., Lapasset, G. and Planés, J. (1990). *Europhys. Lett.* **13**, 73.
8. Bažant, Z.P. (1997). *Int. J. Fract.* **83**, 19, and references therein.

Scientific Support for the Investigation of a Helicopter Collision

G. Clark[1] and K P Roberts[2]

[1] Defence Science and Technology Organisation, PO Box 4331,
Melbourne, 3001, Australia

[2] WGCDR, Royal Australian Air Force, RAAF Base Richmond, NSW.

ABSTRACT

This paper discusses some aspects of scientific support provided during the investigation of an accident in which two Black Hawk helicopters collided during an exercise; both helicopters were destroyed in the collision, with substantial loss of life. One aircraft was reconstructed at DSTO, with extensive analysis of parts, to allow determination of the collision mechanics. The investigation succeeded in its main aims of determining the location of the collision point, and the likely track of each aircraft, as well as the details of the collision. Extensive support was also provided on many other aspects of the accident. The investigation required development of several innovative approaches, including a way of analysing the wreckage distribution to establish the collision location, as well as producing some challenges in component failure analysis. This paper provides a brief discussion of the reconstruction and the wreckage analysis.

KEYWORDS

Aircraft, accident investigation, failure analysis, wreckage analysis.

INTRODUCTION

Six Black Hawk helicopters were involved in a practice assault on a hill top near Townsville; the critical part of the formation comprised a row of three aircraft flying abreast, with the lead aircraft (referred to as BLACK 1) located on the left. It was dark, and the aircrew relied on night vision goggles (NVGs) for visual clues; these significantly impair vision by reducing the field of view to approximately 40 degrees, less than half normal vision, and reduce the contrast of the terrain. During the final stages of approach to the target area, the lead aircraft and the aircraft to its immediate right (referred to as BLACK 2) collided in-flight. Both aircraft fell to the ground where they were consumed by fire. In all, 18 men lost their lives.

After initial investigation which did not identify a single most likely description of the accident, and was complicated by a multitude of witness statements, many apparently contradictory, the Board of Inquiry (BOI) ordered a supplementary technical investigation by RAAF and DSTO staff. The team was given one month to complete the investigations and report to the BOI. The Terms of Reference, in brief, were to establish
 (a) the serviceability status of the aircraft before, during and after the accident,
 (b) the flight paths of the aircraft before, during and after the collision,
 (c) the crash sequence, and
 (d) the point in space of the initial contact, with estimates of confidence

This was a major challenge given the extent of the destruction caused by the post accident fires, however, the deadline was met and a most probable scenario deduced.

ICF1001035OR

This paper presents a brief summary of the wreckage which was recovered, and gives a few examples of techniques used to deduce information from the wreckage distribution.

WRECKAGE EXAMINATION

The wreckage was consolidated at the AMRL facility at Fishermans Bend, Melbourne. It included substantial sections of main rotor blades (MRBs) and tail rotor blades (TRBs) from both aircraft, and a range of components from BLACK 2 which had been flung away from the burning wreckage during the accident. Significant items included the severed tail assembly, the APU, DME antenna, aft sections of the engines, the right engine exhaust system and engine cover door, left cargo door, right side drive train access door and a pneumatic 'Buddy Start' fitting, all of which had blade impact witness marks. A three dimensional mock-up, as shown in Figure 1, was constructed in order to re-build what was left of BLACK 2. Because BLACK 1 was essentially complete when it impacted the ground, with the exception of its MRBs, very little physical evidence was available from it because of the intense fire which engulfed the wreckage and melted the aluminium components.

Figure 1   View of the recovered tail section along with other major components.

Figure 2   The reconstructed tail section of BLACK 2 looking in-plane with the upper cut through the tail section and the lower cut through the tail boom.

Assessment of BLACK 2 damage
Using the mock-up of BLACK 2 it became clear that a number of the cuts caused by the passage of MRBs began to line up. Reconstruction of the tail section of BLACK 2 as shown in Figure 2,

2

revealed the alignment of rotor blade strikes in the fin and stabilator, and the tail boom and stabilator. The tail section had evidence of four MRB strikes. The first two were clearly identified from two cuts through the horizontal stabilator, one of which severed the tail rotor drive shaft, and a third from a blade tip penetration near the 45 degree gearbox. However, a fourth strike was not evident until a small fragment of the fin leading edge was replaced in its position on the fin. This strike was barely a glancing blow, and its discovery emphasises the need for thoroughness in parts recovery and airframe reconstruction. The horizontal stabilator actuator was recovered and, because it lost all inputs from the flight control system during the first MRB strike (severed hydraulic line), its configuration was able to determine the stabilator angle, which was then used to estimate the speed of BLACK 2.

Figure 3   Reconstructed left side cargo door from Black 2 showing three cuts.

Cargo Door

The left cargo door (Figure 3) had three distinct cuts/impact marks while the right cargo door had one impact mark.   (The evidence for this section includes the cargo doors because they were open (slide to the rear) during the collision.   In their closed position, they are part of the cargo area).

Cargo Area/Centre Fuselage.
Numerous fittings (including the pneumatic 'Buddy Start' fitting) and small access doors from the left side, the APU exhaust duct (located on the left side), GPS receiver, TACAN adapter Receiver/transmitter, the avionic bay air cleaner top and various smaller pieces of structure had MRB impact witness marks. Blade witness marks were also observed on or through upper panels, the APU, left and right engine exhaust system, the right engine cowl, seating framework, hydraulic lines and the GPS antenna.

Blade Strikes
After extensive examination, only **four** distinct MRB strikes could be identified - significantly fewer than initially thought. Because large sections of the four MRBs from BLACK 1 were found well clear of the wreckage, each blade passed through the fuselage of BLACK 2 only once before breaking away and being projected into the distance.

3

Hence it can be estimated that the collision took approximately 0.25 seconds to complete, ie four blade passes at 17.2 passes per second. This conclusion supported the views of several witnesses who described the impact as an explosion. The tracks of the four strikes are illustrated in Figure 4.

Figure 4   The port side of a Black Hawk showing the deduced positions of the mrb cuts/strikes on BLACK 2

The following key deductions could then be made:

Angle of Collision.
The MRB tracks through the airframe of BLACK 2 indicated that during the collision, BLACK 1 was inclined at 25 to 35°, left side low, relative to BLACK 2. This can be most clearly seen from the cuts through the horizontal stabilator.

MRB Condition.
Almost all sections of the MRBs from BLACK 1 were recovered from the accident site. The blades bore a range of impact marks and embedded components which confirmed that they had cut through the fuselage of BLACK 2. Critical evidence included:
   (a) a significant crushing indentation in an MRB titanium spar cap which matched the deformation to the rear of the APU,
   (b) an impact mark which matched the pneumatic 'Buddy Start' fitting,and
   (c) a piece of fuselage structure from the transition area which was recovered from the leading edge of one MRB.

MRB Impact Sequence.
Matching witness marks were then used to identify key points of intersection. At least two points on each MRB could be related to specific points the BLACK 2 airframe which enabled simple triangulation to be used to identify actual blade tracks through the structure. The value of this analysis lies in being able to identify the rotor disc movement during the collision, and hence the track of the closing aircraft relative to BLACK 2.

Approach Velocity.
By using the aircraft centres of gravity (CoG) obtained from triangulating back from the known points of impact, a relative movement of BLACK 1 to BLACK 2 could be estimated (Figure 5). Given the normal blade pass frequency was known (17.2 blade passes per second) and the relative movement of the CoGs, the approach velocity could be estimated. Over the four MRB strikes, the centre moved longitudinally along the fuselage of BLACK 2 by approximately 4.6 metres.
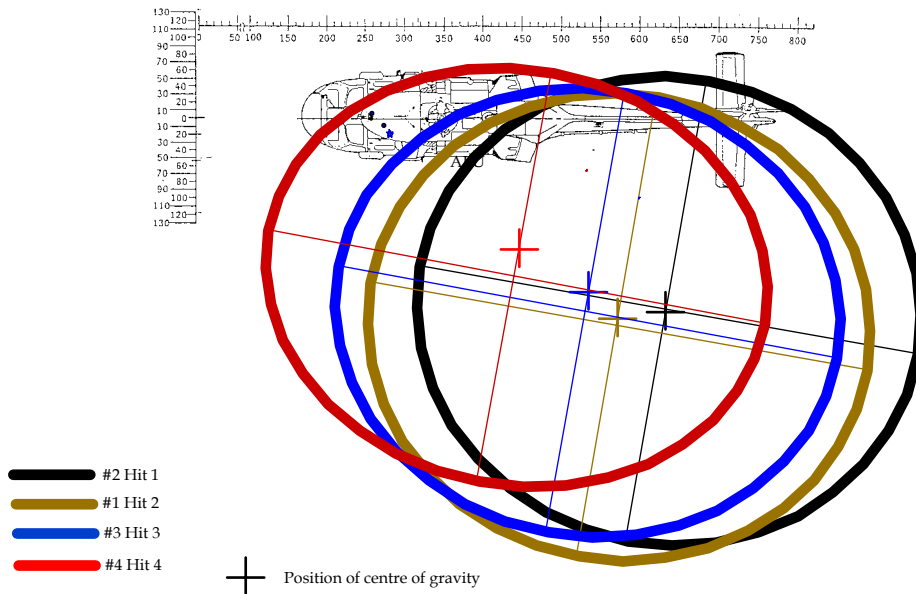
Figure 5 The estimated rotor disc sizes and locations, and the progression of the BLACK 1 centre of gravity through the collision. Note that the angle of bank has been increased from 25 to 35 as the collision progressed, corresponding to the physical evidence from the cuts.

Given that the horizontal stabilator actuator setting indicated that BLACK 2 was travelling at between 50 and 70 kt, BLACK 1 appeared to travelling at a speed of between 70 and 114 kt.   The resultant approach angle when viewed from the ground was approximately 14°.

In an effort to understand the dynamics of the rotor disc during manoeuvres, the AMRL Black Hawk simulator was used to explore ways in which a 25° to 35° angle of bank could be generated by BLACK 1 on its approach to BLACK 2.   A range of simulations of BLACK 1 was conducted which sought to combine the deduced approach speed towards BLACK 2 and expected evasive manoeuvres by BLACK 1.   The first simulation modeled a 65 kt speed and full left cyclic input. This demonstrated that the energy of the manoeuvre during the first approximately 10 blade passes is consumed in rotating the aircraft.   By this point, the blades have achieved a bank angle of approximately 20° assuming a rigid rotor (Figure 6). Thereafter, the aircraft commences to move to the left.   When an 8 m/sec side speed is introduced to the simulation and the blade tracks are superimposed on an adjacent aircraft, ie BLACK 2, a clear correlation with the MRB witness marks through BLACK 2 was clear.
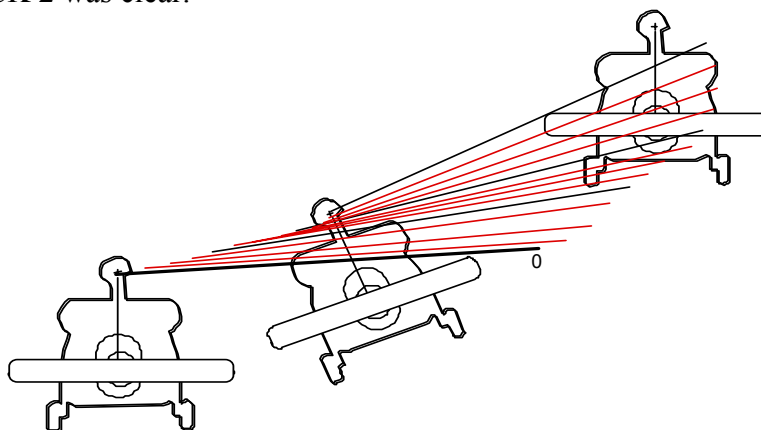
Figure 6   Full left cyclic applied at blade pass 0, moving 8m/s to right, 2m/s climb, relative to other aircraft.

Wreckage Plot

The wreckage plot developed by the initial AIT revealed that parts were widely scattered around the site, many travelling for several hundred metres. Conventionally, analysis of wreckage distributions supports a trajectory analysis which itself will identify the point in the sky where separation occurs; many tools are available for assessing the effect of prevailing weather on the distribution of parts.   In this case, however, the collision occurred at low level, and weather was not a major factor. Unfortunately, the complexity of the distribution made it difficult to identify any overall pattern with any certainty, and this prevented any direct approach to determining the impact location. Accordingly, an alternative approach was required. The method developed proposed that the areas of probable impact could be estimated by analysing groups of wreckage types, and that repetition of this process would

    (a) lead to identification of the impact site, and to

    (b) preparation of a contour plot representing overlapping areas of probability that the contour enclosed the impact location.

Five main groups of wreckage were identified, from each of which some estimate of the collision region could be obtained; two such groups consisted of fuel-impregnated foam pieces (and areas of spot fires), and light perspex pieces from the LH cargo door of BLACK 2. These parts were considered likely to have been ejected to the left of BLACK 2 at collision.

Based on the height of trees at the accident site, the assumption was made that the minimum height of the collision was 11 metres, which equates to a 1.5 second fall time in a vacuum ie the minimum time for an object in free fall.   From the evidence of the horizontal stabilator actuator, the forward velocity of BLACK 2 at the time of the collision was approximately 50 to 70 kt.   Using computer modeling of a small piece of perspex (representative of a window fragment from BLACK 2) and the assumed ground speed range of 45 to 75 knots for BLACK 2 (a greater range than indicated by the stabilator), the minimum and maximum throws were estimated to be 20 metres and 45 metres respectively.   Therefore, 20 metres was identified as the threshold distance from the light debris field on the ground back to the point of the collision.
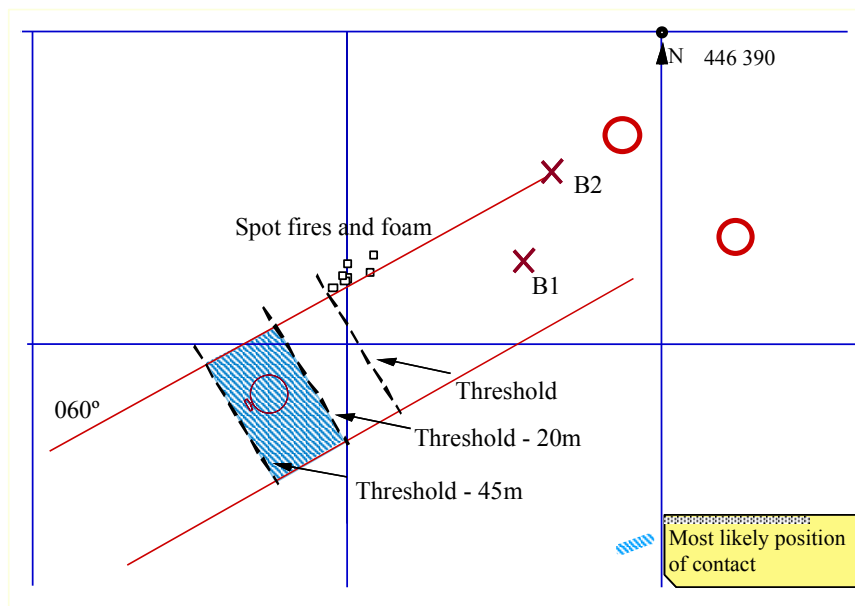
Figure 7   Location of spot fires, light foam material, and likely location of collision.

Spot Fires and Fuel Cell Foam from BLACK 2.
Given the extremely light weight of the fuel cell foam and the relatively tight grouping of the foam and spot fires, a probable area of collision could be estimated using the 20 metre and 45 metre limits identified by trajectory analysis. The width of the area was estimated as 45 metres for the same reason. Figure 7 shows the overall area, with the airframe ground locations B1 and B2, as well as some target revetments shown as circles. The shaded area represents an estimate of the likely position of BLACK 2 at the time of collision.

Probable Area of Collision.
The crucial feature of this approach is to increase confidence in the estimate of collision position by superimposing several estimates. Figure 8 shows the superposition of five separate estimates of the location in this accident; a most likely area of probable impact was defined based on the area common to all five estimates. A lower probability was given to areas which were contained in only four of the five estimates, and so on. In this way, a contour map of probable likely location was generated. The result was a high level of confidence that the location had been identified to within one rotor diameter. Furthermore, placing the two aircraft at this location then effectively identified the tracks of the two aircraft, and met the requirements of the Board of Inquiry.
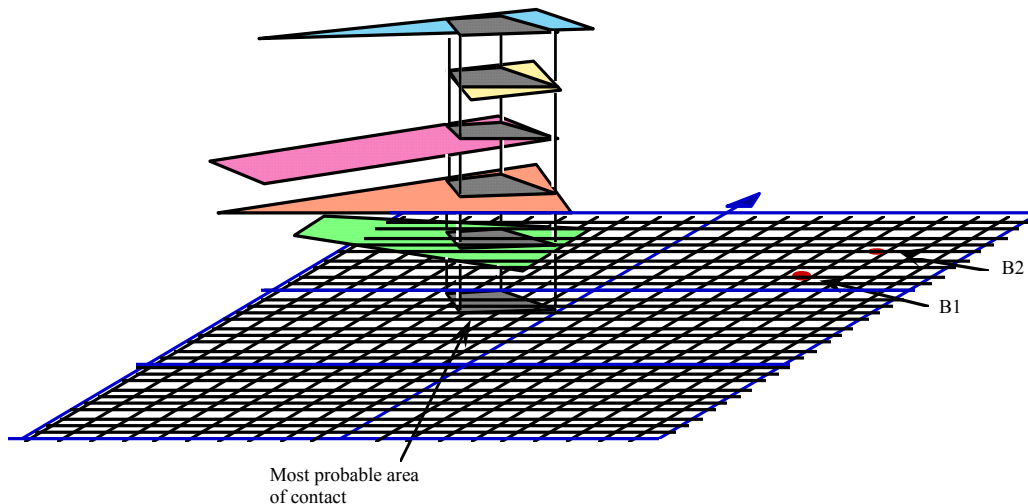
Figure 8 Identification of the most probable area of contact by superimposing best estimates of contact regions.

CONCLUSIONS
The development of innovative ways of assessing wreckage distributions allowed the team to identify the location of the collision point. The use of aircraft reconstruction, extensive parts examination, coupled with simulation, provided a high level of confidence in the identification of the collision sequence, collision mechanics, post-collision behaviour, and the tracks of the two aircraft at the time of collision. The investigation also used damage assessment and modelling to conclude that just before impact with BLACK 2, BLACK 1 banked sharply to the left during which time its main rotor blades passed through the aft section of BLACK 2.

This paper has sought to summarise the investigation of the Black Hawk accident and, as such, has sought only to summarise the key points. More detailed reports were tabled to the Military Board of Inquiry and later released by AMRL under DSTO-DDP-0190 dated 21 May 97.

The authors wish to acknowledge the many individuals who took part in the investigation, particularly Simon Barter, SQNLDR Mark French, Nick Athiniotis and Ashley Arney.

SCRATCH TESTING AND ACOUSTIC EMISSION OF NANOSTRUCTURED PARTIALLY STABILIZED ZIRCONIA COATINGS

M. R. Gold, R. S. Lima, A. Kucuk and C. C. Berndt

State University of New York at Stony Brook
Stony Brook, NY 11794-2275, USA

ABSTRACT

The crack propagation and fracture surface of nanostructured and conventional partially stabilized zirconia (PSZ) coatings were evaluated via scratch test, acoustic emission (AE), Vickers indentation at high loads, and scanning electron microscopy (SEM). Under the same experimental scratch test conditions, the nanostructured coatings exhibit lower AE activity than that of the conventional ones. This effect is attributed to the localized zones of plasticity exhibited by non-molten nanostructured particles in the coating microstructure.

KEYWORDS

Nanostructure, thermal spray, partially stabilized zirconia, scratch test, crack propagation.

INTRODUCTION

The mechanical performance of thermal spray coatings may improve with the use of nanostructured materials. This class of materials is characterized by microstructure sizes of 2 to 100 nm [1]. Different views are considered concerning the performance of nanostructured metals and ceramics. In metals, nanostructured materials increase their yield strength according to the Hall Petch relationship [2]. It is suggested that the benefits of these materials lie in the increased ductility and yield strength. This ductility has been speculated to be due to the increase in the grain boundary area and, thus, an increase in the grain boundary sliding [1]. Strain energy is absorbed and the potential for cracking is reduced because the material can deform.

Recently Lima et al. [3, 4] have observed that plasma sprayed nanostructured partially stabilized zirconia (PSZ) coatings demonstrate a bimodal distribution with respect to the coating mechanical properties. This bimodal distribution originates from the two-phase composite like structure of the coatings; i.e., the molten and non-molten nanostructured PSZ particles contained in the coating microstructure. Nanostructured PSZ feedstock particles are formed by a successive agglomeration of individual nanosized particles. These nanosized particles (~100 nm diameter) are agglomerated into clusters (1 – 5 μm diameter), which are then post agglomerated into spherical microscopic particles (10 – 160 μm diameter) [3, 4]. These spherical microscopic particles are porous and the clusters are poorly bound among each other. As a consequence, mechanical properties, such as microhardness, will exhibit values due to the weak binding of the clusters. The bimodal distribution will be given by (i) the molten particles (dense phase) and (ii) the non-molten particles (soft phase) encountered in the coating microstructure [3, 4].

The presence of non-molten particles in the coating microstructure was one of the objectives of this work. If the nanostructured feedstock particles were totally molten, then any important property that the nanostructured PSZ may demonstrate would be destroyed during plasma spraying. The present paper is a continuation of previous work [3, 4]. Therefore, it is hypothesized that the presence of non-molten nanostructured PSZ particles in the coating microstructure creates zones or sources of localized plasticity. This localized plasticity would be caused by cluster yielding and rearrangement upon the application of a load. Due to this characteristic, nanostructured coatings may present a higher resistance to crack propagation and enhanced toughness when compared to conventional coatings.

A key tool that can be employed to study the fracture of TBCs is acoustic emission (AE). The physics of acoustic emission can be characterized as a stress or pressure wave that travels through a dense medium because of dynamic processes occurring in the material [5] The dynamic process under consideration in this paper is the production of cracks initiated within the thermal spray coating produced by the scratch indenter during the scratch test. Once AE is emitted from a crack, the pressure wave propagates through the material and is then received by the transducer and recorded for post-processing and detailed analysis.

In this study, nanostructured PSZ was plasma sprayed with parameters that produced a varying degree of nanostructured phase within the coating. Scratch testing and acoustic emission were performed on the coating top surface to investigate the fracture properties of the material. Conventional PSZ was also plasma sprayed to compare the crack propagation behavior of nanostructured and conventional coatings.

EXPERIMENTAL PROCEDURE

Sample Preparation
The nanostructured PSZ feedstock (ZrO_2-7wt.%Y_2O_3) Nanox S4007 (Inframat Corp., North Haven, CT, USA) was sprayed using a Metco 3MB plasma torch (Sulzer-Metco Inc., Westbury, NY, USA) with the following configuration: GH nozzle and powder port #2. The conventional PSZ feedstock (ZrO_2-8wt. %Y_2O_3) Metco 204 NS (hot oven spherical particle – "HOSP") was

sprayed using the identical plasma torch, configuration and spray parameters employed for spraying the nanostructured material. Low carbon steel substrates were used for all coatings.

Acoustic Emission

Acoustic emission was recorded during the scratch testing of conventional and nanostructured coatings. A 5 mm diameter ultrasound transducer (Physical Acoustics Corp., Princeton Junction, NJ, USA) was placed on the back of the steel substrate beneath the scratched area. The placement of the transducer was selected to increase the reception of the acoustic signal. The system was calibrated prior to scratching the sample to affirm that background noises did not contribute to the data set. A 40-dB pre-amplifier (Model 2/4/6-AST, Physical Acoustics Corp, Princeton Junction, NJ, USA) was used to process the signal prior to input by the data acquisition board in the personal computer. The system threshold was fixed at 35 dB to filter the background noise associated with nearby mechanical and electrical equipment. Data was collected using a conventional software program (Mistras 2001, Physical Acoustics Corp., Princeton Junction, NJ, USA).

Scratch Testing

Scratch testing was performed using an in-house built machine. The scratch tip was a Vickers diamond indenter. The direction of the indenter was oriented with the corner of the diamond at the leading edge. The scratch speed and distance was controlled using a personal computer and stepper motor controller card. The scratching speed was set as 0.03mm/sec. This speed was chosen to permit a significant amount of AE and force data to be gathered during a test. The length of the scratch was set to 2 mm to ensure that a large number of particles/splats would be traversed and provide sufficient data for statistical analysis of the AE. A normal load of 1000 g was applied for each sample. The total time of each test was 60 seconds. All samples were polished with 0.01 μm alumina suspension prior to scratch testing.

RESULTS AND DISCUSSION

Coating Microstructure

Two types of nanostructured coatings were chosen [4]. Each coating has a different amount of non-molten nanostructured particles embedded in its microstructure, 38% and 23% in area; respectively. It is expected that the two distinct microstructures produce different responses to the mechanical stresses generated during the scratch tests. When comparing a coating sprayed with an agglomerated nanostructured feedstock (Fig. 1a) to a coating sprayed with a conventional feedstock (Fig. 1b); the nanostructured coatings (Fig. 1a) exhibit two distinctive regions or phases. A dense region consisted of fully molten particles, equivalent to the overall conventional coating microstructure (Fig. 1b), and another region consisted of low density areas represented by non-molten agglomerated nanostructured particles. The fully molten particles retain the non-molten particles in the coating microstructure [3, 4, 6].
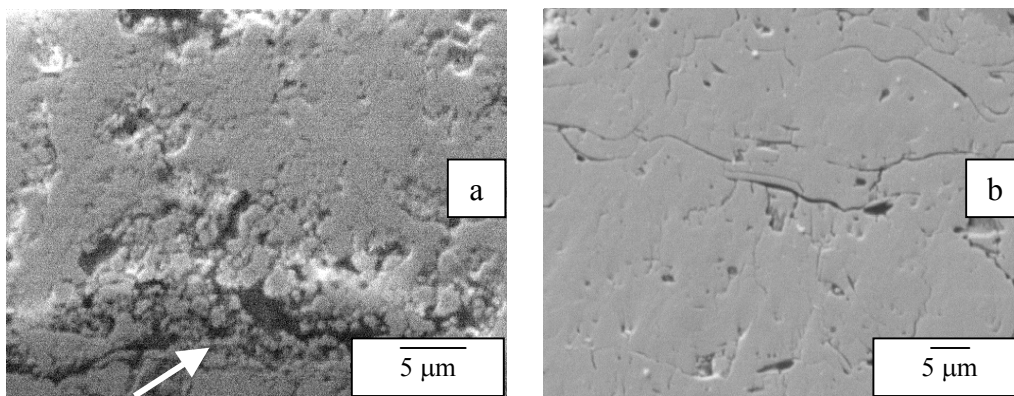
Figure 1: (a) Typical microstructure of a nanostructured coating. The white arrow indicates a region where non-molten agglomerated nanostructured particles are observed. (b) Typical microstructure of a conventional coating. The majority of the particles are fully molten.

The non-molten region of the nanostructured coatings, due to its low density zone should provide cluster mobility, rearrangement and yielding. Such mechanical behavior is the mechanism by which localized plasticity is speculated to operate, as previously discussed. The ability to deform by cluster yielding provides a mechanism through which strain energy is dissipated and crack propagation is resisted [3, 4]. Due to the reduction in the strain energy, any AE energy emitted during deformation is low and, thus, a low number of AE signals may be detected. Furthermore, a coating that exhibits a predominant dense phase (fully melted particles) in its microstructure, may result in release of energy via transgranular cracking. This might account for the greater count of AE events in the coatings than coatings where particles were fully melted.

Scratch Scars and Crack Activity
The collection of the AE emitted from the samples was used to characterize the degree of energy absorbed by the coating system during the scratch process. The AE information that is found to be characteristic of the cracking event is the maximum amplitude of the impulse related to the crack energy release and the number of events occurring during the scratch process [7]. Based on these characteristics, the maximum amplitude and number of events (cracks) for nanostructured and conventional coatings will be analyzed.

Figure 2 shows the number of AE events, representative of the number of cracks, for the nanostructured and conventional coatings. It is evident that there is a difference in the number of cracks for the nanostructured and conventional coatings. The conventional coatings demonstrate on average of ~9 times more cracks than the nanostructured ones. Explanations for this behavior are; (i) that the AE in the nanostructured coatings would be reduced due to localized plastic deformation rather than cracking, (ii) the energy associated with major cracking mechanisms in conventional coatings would be considerably high because the crack path may exhibit not only intergranular but also a transgranular crack mode, and (iii) the energy associated with fracture and removal of the nanostructure material is low due to the presence of non-molten particles in the coating microstructure.
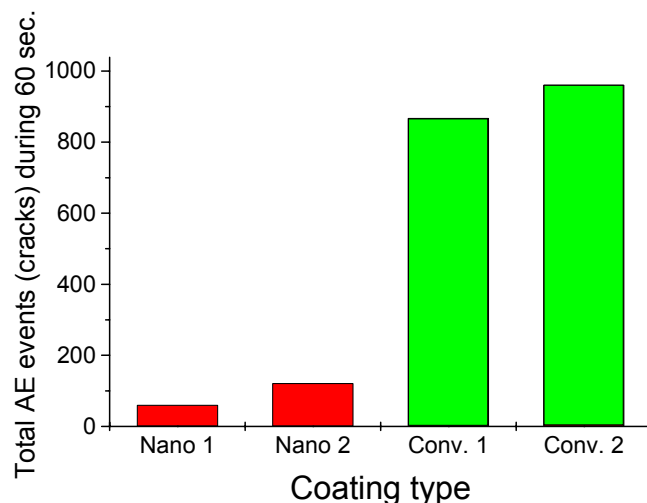
Figure 2: Total AE events (cracks) for each type of nanostructured and conventional coatings.

The SEM micrographs of the nanostructured and conventional coatings (Fig. 3) indicate that the scratch scar appears to be smooth or polished and suggests a cutting process with the diamond tip for the conventional material (Fig. 3c). These features have similar characteristics with those of Fig. 3b, which represents the sample with the lowest amount of nanostructured material. Further analysis of the conventional coating shows that there are cracks parallel to major scratch scar. Apparently the top surface of the conventional coating (Fig. 3b) was locally depressed as the indenter went through it. Since conventional coatings exhibit predominantly fully molten particles, their ability to comply to an applied stress is limited and the regions immediately surrounding the indenter stylus collapse in a catastrophic mode during the scratch. This phenomenon could explain the high AE activity observed for the conventional coatings.
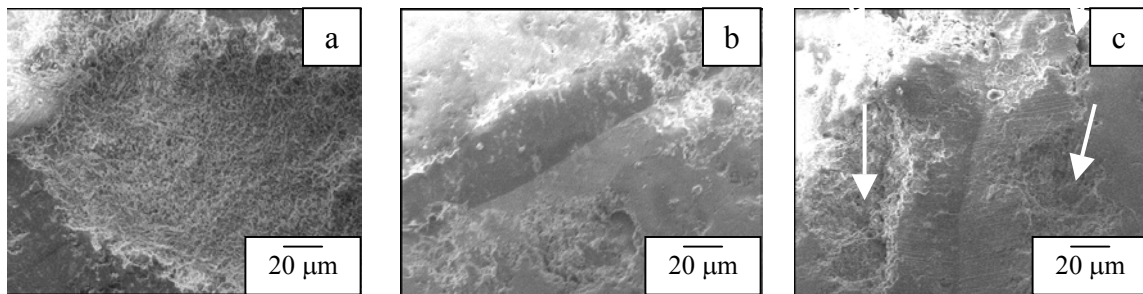
Figure 3: SEM pictures of the scar scratch made on nanostructured and conventional coatings. (a) Coating containing 38% of non-molten nanoparticles. (b) Coating containing 23% of non-molten nanoparticles. (C) Conventional coating. The white arrows represent parallel cracks following the scratch scar.

This effect was not observed for nanostructured coatings because they demonstrate localized plasticity.

Crack Propagation via Indentation
In the present work, the indentation tests (Vickers – 20 kgf load) were used to investigate further the fracture response of the materials under load. The conventional coating exhibits a higher degree of cracking, Fig. 4a. For the nanostructured coating (Fig. 4b), just one distinctive crack is observed from the corner of the indenter.
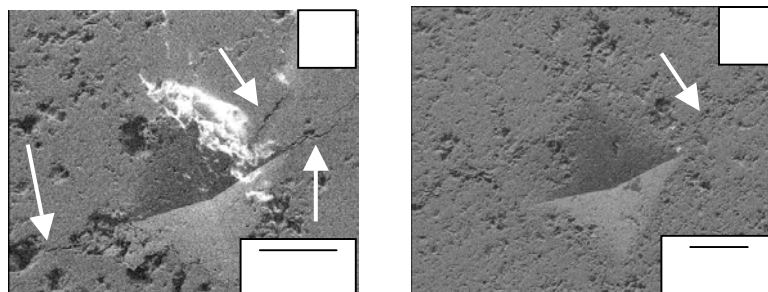
Figure 4: Vickers indentation on (a) conventional coating and (b) nanostructured coating. The white arrows are pointing towards cracks.

CONCLUSIONS

The nanostructured PSZ coatings resist crack propagation more than conventional PSZ coatings. It is thought that the non-molten agglomerated nanostructured particles embedded in the coating microstructure yield under stress, creating localized plastic deformation zones in the coating structure. The conventional coatings, due to a lack of plasticity, tend to release strain energy via crack propagation.

REFERENCES

[1] Weertman, J. R., Farkas, D., Hemker, K., Kung, H., Mayo, M., Mitra, M. R. and Van Swygenhoven, H. (1999) MRS Bulletin, February 1999, 44.
[2] Gleiter, H. (1999) Acta Materialia, 48, 1.
[3] Lima, R. S., Kucuk, A., Berndt, C. C. Journal of Materials Processing Technology (accepted for publication).
[4] Lima, R. S., Kucuk, A., Berndt, C. C. Materials Science & Engineering A (accepted for publication).
[5] Liptai, R. G., Harris, D. O., Tatro, C. A. (1972) Acoustic Emission, Special Technical Publication 505, Ed. American Society for Testing and Materials, Philadelphia, PA, USA, 1972.
[6] Lima, R. S., Kucuk, A., Berndt, C. C. (2001) Materials Science & Engineering A, 313, 75.
[7] Stebut, J. V., Lapostolle, F., Bucsa, M., Vallen, H. (1999) Surface and Coatings Technology, 116-119, 160.

SELF-CONSISTENT CONSTITUTIVE MODELING OF PARTICLE DISPERSED COMPOSITE MATERIALS WITH MICRO-CRACK TYPE DAMAGES

Michihiko NAKAGAKI, Huajian CHANG and Yadong WU

Department of Mechanical Systems Engineering, Kyushu Institute of Technology
680-4 Kawazu Iizuka-City, Fukuoka-Ken, Japan 820-8502

ABSTRACT

The treatment of perfectly bonded interface between the particles and matrix of composite is sometimes considered to be inappropriate in describing the physical nature. The effect of imperfect interface on the overall behavior of particle-reinforced composites is studied. In order to investigate the detrimental effects of the slightly weakened interface on the overall material properties, a rigorous constitutive model was schemed, which uses a self-consistency scheme based on the Eshebly's equivalent inclusion method, and is capable to reflect the meso-local damage effects even in the range where the volume fraction of particles is high. Both the tangential and normal discontinuities at the interface are independently modeled, and these relative displacements are directly proportional to the corresponding components of tractions at the interface. The numerical results are also shown. It is found that the imperfect interface conditions of debonding and/or sliding give detrimental effects on the overall properties of composites. Thus, the establishment of the most appropriate model describing properly the meso-local phenomena.

KEYWORDS

Composites, Imperfect Interface, Sliding and Debonding, Constitutive Model

INTRODUCTION

The inhomogeneity problem has received considerable attention since Eshelby[1] published his well-known paper on the treatment of ellipsoidal inclusion. Based on the Eshelby's equivalent inclusion model, quite a few works have been performed, which assume perfect bonding at the interface between the inhomogeneity and the matrix. However, the solutions of perfect bonding condition have not been considered to be sufficient in describing the mechanical properties of the meso-local inhomogeneity problem of situations involving debonding and sliding. It is obvious that the interface conditions dramatically affect the mechanical behavior of the composites. Therefore, there have been considerable interests in imperfect interface problems as may be appropriate in the case of either pre-existing defects or interface damage due to, for example, the cyclic loading. The most popular model for quantifying this imperfection is the linear spring-layer model, in which a relationship at the interface between the traction vector and the displacement jump is assumed. This model of the linear interface has been employed by Hashin[2,3], Qu[4,5], Zhong[6,7], and Gao[8] among others in the development of the relevant problems. One of the interesting works in this area is by Gao[8], who has modeled the circular inclusion in the matrix imperfect interface under a uniform tension to find the equivalent eigen strain values. In meso-mechanics of solids, elastic solutions to the inhomogeneity problem are often used to relate the overall deformation and the corresponding stress field in the composites. In this paper, an Eshelby tensor, is derived accounting for the mechanics of the imperfect interface. The Eshelby tensor is averaged over the entire area of an inclusion to obtain the average effect that is concerned for evaluating the overall properties of composites. On the local study inside and around an inclusion, a constitutive law that accounts for the meso-local imperfection,

based on a self-consistent scheme is developed, which applies the Eshebly's equivalent inclusion method to the particle-matrix domain, thus an averaged compliance was determined rigorously. The present constitutive modeling was carefully devised to be capable of reflecting the effect of slightly-weakened interface on the overall properties of the composites, even in the range where the volume fraction of particles is high.

MODELING IMPERFECT INTERFACE

As pointed out by some researchers, the conditions of initially perfect bonding at the interface between the inhomogeneities and the matrix sometimes may deteriorate. Boundary-sliding as well as debonding are normal phenomena seen after a period of service for some composites. Especially under cyclic loadings, defect and damage may occur on the particle-matrix interface. They would incur the imperfections of the interface. Consider a circular inclusion Ω embedded in an infinitely extended elastic domain (matrix) D-Ω. $\partial\Omega$ represents the imperfect surface area, as depicted in Fig. 1. The defected interface is modeled by a spring layer with its vanishing thickness. It is assumed that the tractions on the interface remain continuous (may not be equal to that of the perfect bonding case), but the displacements are not. Furthermore, the normal and tangential displacement-discontinuities on the interface are assumed directly proportional to the corresponding traction components. Then, the interfacial conditions can be expressed as

$$\left(\sigma_{ij}\big|_{\partial\Omega^+} - \sigma_{ij}\big|_{\partial\Omega^-}\right)l_j = 0 \tag{1}$$

$$u_i\big|_{\partial\Omega^+} - u_i\big|_{\partial\Omega^-} = \eta_{ij}\sigma_{jk}l_k \tag{2}$$

where, l_i denotes the unit outward normal vector of the interface $\partial\Omega$, the second order tensor η_{ij} indicates the compliance of the hybrid spring layer at the interface, which is usually expressed as

$$\eta_{ij} = \delta_{ij}/t + (1/n - 1/t)l_i l_j. \tag{3}$$

In the above, δ_{ij} is the Kronecker delta, the two scalars t and n represent the tangential and the normal stiffness of the spring, respectively.

Gao[8] derived a solution to this problem by assuming an Airy stress functions for both the matrix and the inclusion. After the stress field inside of the inclusion was found, the total strain in the inclusion were derived using Hooke's law. Then the Eshelby tensor is determined from the eigen strain so that the strain would be equivalently generated due to the corresponding part of the eigen strain. Since for evaluating the overall properties of the composite with the imperfect interface, only the average effect is concerned, thus the Eshelby tensor is defined such that

$$\overline{S}_{ijkl} = \frac{1}{\Omega}\int_\Omega S_{ijkl}(r,\theta)d\Omega \tag{4}$$

The expressions of S^M for circular inclusions are given in Appendix in detail.
The effects of the imperfect interface on overall properties of composite have been taken into account by the use of the obtained average Eshelby tensor. Thus, the effective properties of the composite with imperfect interfaces can be obtained by further averaging the effect to multi-particle dispersed domain problem.
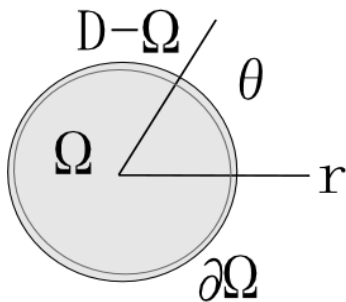
Fig.1 Schematic of particle with imperfect interface
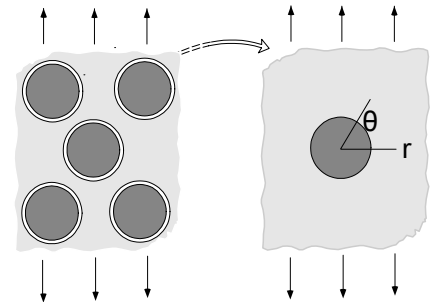
Fig.2 Composite with imperfect interface and equivalent domain

AVERAGING METHOD

The macro-local average properties of a composite with the imperfect interface can be obtained more reasonably by employing the self-consistent compliance (SCC) method. Based on Eshelby's equivalent inclusion theory, the stress and strain state of a virtual inclusion in the medium can be made equal to that of the real inclusion by imposing some proper amount of eigen strain to be solved. Mori and Tanaka[9] took the medium to be the matrix material, while later Mura[10] as well as Wu and Nakagaki[11] assumed it to be the averaged material of the composite. The latter is called the SCC model in the present report. It is assumed that a macro-local property of the composite with the inclusions with imperfect interface can also be treated by the same manner. Thus, the meso-local average stress and strain state as well as the properties of the macro-composite materials(Fig. 2). Following the approach used by Wu and Nakagaki (1999), and considering the present condition of the imperfect of interface, the equivalent relationship of stress can be expressed as in the following:

$$\mathbf{E}_2(\hat{\boldsymbol{\varepsilon}} + \boldsymbol{\varepsilon}^c) = \hat{\mathbf{E}}(\hat{\boldsymbol{\varepsilon}} + \boldsymbol{\varepsilon}^c - \boldsymbol{\varepsilon}^{*a}) \tag{5}$$

The **Bold** type characters stand for a second or fourth order tensor. The subscript 2 indicates the variable is of the inclusion, and the superscript (^) indicates that the quantity is of an averaged value. $\mathbf{E}_2$ represents the material tensor for the inclusion material, $\hat{\mathbf{E}}$ is the average material tensor for the composite material, $\hat{\boldsymbol{\varepsilon}}$ stands for the average strain of the composite, $\boldsymbol{\varepsilon}^c$ indicates the strain mismatch between the inclusion and the composite, and $\boldsymbol{\varepsilon}^{*a}$ is the total eigen strain that is the sum of the eigen strain($\boldsymbol{\varepsilon}^*$) for the material inhomogeneity and the eigen strain($\boldsymbol{\varepsilon}^{*i}$) due to the effect of the imperfection at the interface between particles and the matrix. According to the Eshelby theory and by considering the conditions of imperfect interface, we have,

$$\boldsymbol{\varepsilon}^c = \overline{\mathbf{S}}\,\boldsymbol{\varepsilon}^{*a}. \tag{6}$$

The role of the Eshelby tensor in imperfectly bonded inclusion problems now assumes the effects of the material inhomogeneity and the imperfection, and the treatment of the rest is similar to the case of the perfectly bonded-inclusion composite problems. Substituting Eq. (6) into Eq. (5), the following will be found,

$$\boldsymbol{\varepsilon}^* = \mathbf{A}_0\,\hat{\mathbf{E}}\,\hat{\boldsymbol{\varepsilon}} \tag{7}$$

where,

$$\mathbf{A}_0 = [\mathbf{E}_2(\hat{\mathbf{E}} - \mathbf{E}_2)^{-1}\hat{\mathbf{E}} - \hat{\mathbf{E}}(\overline{\mathbf{S}} - \mathbf{I})]^{-1} \tag{8}$$

Here, $\mathbf{I}$ stands for the identity tensor of the fourth order.

The stress $\boldsymbol{\sigma}_2$ in the inclusion can also be obtained as in the following,

$$\boldsymbol{\sigma}_2 = \mathbf{B}\,\boldsymbol{\sigma}_0 \tag{9}$$

$$\mathbf{B} = \mathbf{I} + \hat{\mathbf{E}}(\overline{\mathbf{S}} - \mathbf{I})\mathbf{A}_0 \tag{10}$$

where, $\boldsymbol{\sigma}_0$ is the average stress of the composite.

Once determining the stresses in the inclusion phase, it is easy to establish the constitutive law of the composite as follows.

$$\boldsymbol{\varepsilon}_0 = \hat{\mathbf{L}}\,\boldsymbol{\sigma}_0 \tag{11}$$

$$\hat{\mathbf{L}} = \mathbf{L}_1[\mathbf{I} - f\mathbf{B})] + f\mathbf{L}_2\,\mathbf{B} \tag{12}$$

where $\mathbf{L}_1$ and $\mathbf{L}_2$ are the elastic compliances for the matrix and the inclusions, respectively, $\hat{\mathbf{L}}$ is the global average compliance of the composite material, which is equal to the inverse of the global average property tensor $\hat{\mathbf{E}}$. Because the right hand of Eq. (12) contains the yet-unknown tensor $\hat{\mathbf{E}}$, the present scheme is of the self-consistent compliance(SCC) method. To solve those averaged values, an iterative algorithm is undertaken.

NUMERICAL RESULTS AND DISCUSSIONS

In order to investigate the effect of imperfect interfaces on the overall properties of composites, and to verify the performances of the spring-layer model with the averaging theory, numerical analyses were conducted. The used values for the Young's modulus and the Poisson's ratio of the matrix material and the particles are such that:

Matrix E_1=2.0Gpa, ν_1=0.35
Particles E_2=40Gpa, ν_2=0.18

Both the matrix and particles are assumed to be isotropic. The particles are spherical in shape. Two typical cases of plane problems, i.e. the plane strain and the plane stress were studied.

Variation for volume fractions of particles
Fig. 3 shows the computed equivalent Young's modulus of the composite with the use of Eq. (12) under three conditions with imperfect interfaces: i.e. pure sliding, pure debonding, and combined sliding and debonding, under the plane strain condition. Normalized Young's modulus defined by the following is shown for the variation of the particle volume fraction.

$$E_{nd} = \frac{\hat{E} - E_1}{E_2 - E_1} \qquad (13)$$

The considered interface conditions are regulated the tangential and the normal stiffness of the spring, t and n. In the present, either 0, 1, or ∞ is considered for these factors and denoted so hereafter, whereas the unit value of the sliding/debonding parameter is equal to the spring stiffness of the matrix material evaluated per unit area. The solid line indicates the case of the perfect interface. It is quite clear that all of the imperfect interface conditions give a detrimental effect to the composite stiffness, as expected. Furthermore, the perfect debonding(short-dashed line) is more detrimental than the sliding with no friction, where other parameters are unchanged. The totally debonding case, that is when both the tangential and the normal stiffness of these springs tend to zero, the rigidity of the composite will become lowest. But it should be noted that the stiffness of the totally debonnded case is still much higher than that of the void inclusion case. When the sliding and debonding parameters have certain finite values(e.g. $t=n=1$ in Fig. 3), the line will drop somewhere in between the two ultimate conditions of the interface. Another interesting result is that the detriment effect of the imperfect interface becomes greater as the volume fraction of particles gets larger. For instance, when $f = 0.3$, the equivalent Young's modulus of the composite with the imperfect interface(totally debonding) is 79.2% of that of the corresponding perfect interface. While, this value will be approximately 76.1% when $f = 0.7$. Fig. 4 shows the similar results of Young's modulus in case of the plane stress.
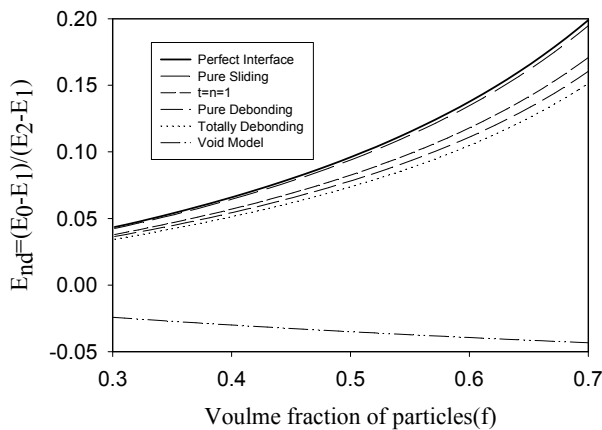
Fig.3 Young's modulus of composite with various interface conditions(Plain Strain)
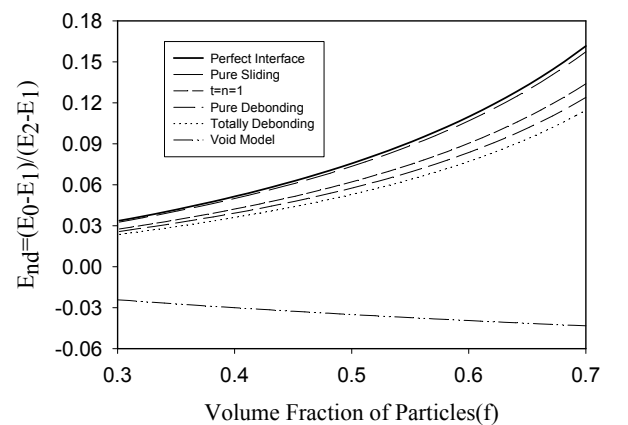
Fig.4 Young's modulus of composites with various interface conditions(Plain Stress)

Effect of sliding and debonding parameters
In order to investigate the effect of the two imperfect parameters in detail, i.e. sliding and debonding, on the overall properties of composite, two typical cases of only sliding and only debonding were studied. Fig. 5

and 6 show the results obtained for the plane strain case, with f =0.5. It is learned from these results that there is a range of transition in these imperfection springs for both the sliding and the debonding from the completely defective to the perfect interface. It is noteworthy that the range of the transition is spanned on approximately 0.1 to 10 for both the cases.
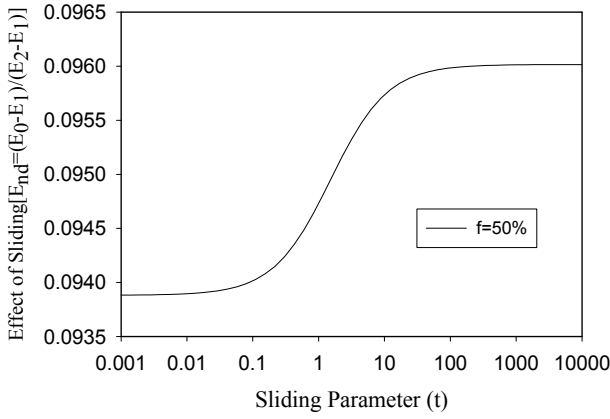
Fig.5 Effect of sliding parameter on overall properties
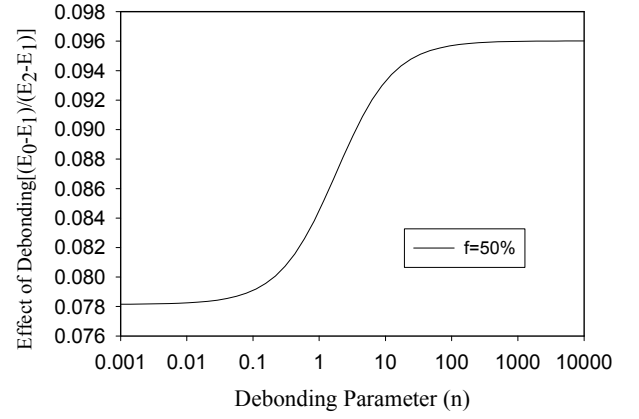
Fig.6 Effect of spring parameter on overall properties

Effect of sliding or debonding for particle volume fractions

For investingating the effect of the sliding and the debonding parameters on the overall Young's modulus with various particle volume fractions, the average Young's modulus of the composite is normalized by that with perfect interface of the same volume friction of particles that,

$$E_{nor} = \frac{E_{imperfect}}{E_{perfect}} \qquad (14)$$

Fig. 7 shows the results for the case of debonding for f = 0.3, 0.5, and 0.7. It is obvious that the relative detrimental-effect of debonding is more serious at higher volume fraction of particles. However, it is interesting to know that this is not the case for the sliding. Fig. 8 shows the results of sliding for the same selected particle volume fractions as in the previous problem. Unlike the debonding case, the sliding around the particle does not give marked effects to the macroscopic characteristics of the composite. The effect is small, but the sliding effect for the low volume fraction of the inclusion stands over that of the higher fractions.
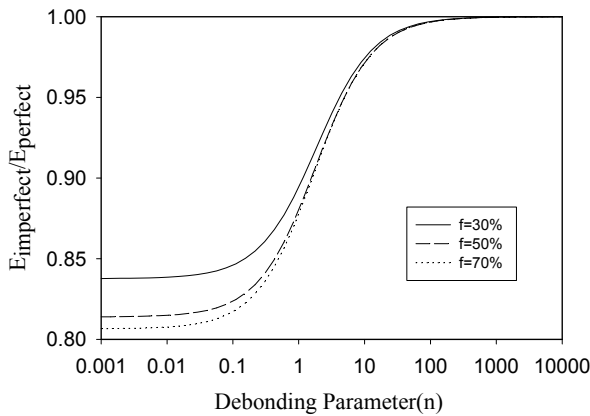
Fig.7 Comparison of effect of interface debonding for various volume fractions
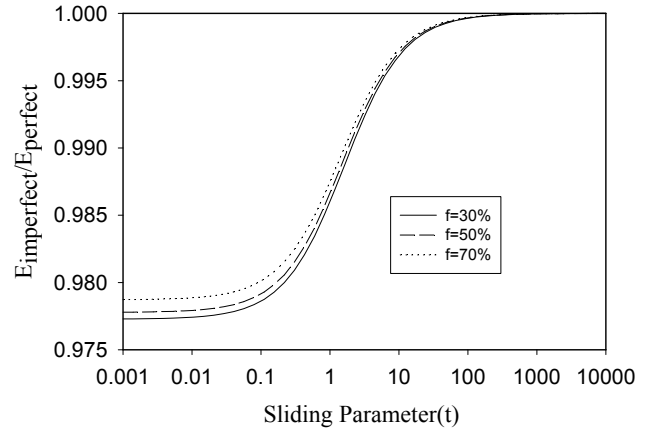
Fig.8 Comparison of effect of interface sliding for various fractions

5

CONCLUSIONS

The effect of imperfect interface on the overall behavior of particle-reinforced composites is studied. The interface is modeled as a spring layer with vanishing thickness. By assuming that, (a) the tractions on the interface remain continuous, but (b) the displacements are discontinuous, and (c) the normal and tangential displacement-discontinuities on the interface are directly proportional to the corresponding traction components, an averaged solution of Eshelby's S-tensor were obtained. This Eshelby tensor was applied to the carefully schemed Self-consistent Compliance model in order to develop the constitutive model for the composite incurring particle-matrix damages in the meso-mechanics level. The present model is used to investigate the effect of a slightly weakened interface. The following conclusions could be made by the numerical analysis. (1) The imperfect interface conditions give a detrimental effect on the overall properties of composites, where debonding is more detrimental than sliding. (2) The detrimental effect of the debonding interface is getting higher as the volume fraction of particles becomes larger. (3) Although the effect is small, the sliding effect in the composite is rather marked for the low volume fraction case of the inclusion than the higher fractions.

REFERENCES

J.D. Eshelby, The determination of the elastic field of an ellipsoidal inclusion and related problems, Proc. Roy. Soc., Vol. A241, pp.376-396.

Z. Hashin, Thermoelastic properties of particulate composites with imperfect interface, J. Mech. Phys. Solids, Vol. 39, No. 6, pp. 745-762, 1991.

Z. Hashin, The spherical inclusion with imperfect interface, Journal of Applied Mechanics, Transactions of ASME, Vol. 58, pp.444-449, 1991.

J. Qu, Eshelby tensor for an elastic inclusion with slightly weakened interface, Journal of Applied Mechanics, Transactions of ASME, Vol. 60, pp.1048-1050, 1993.

J. Qu, The effect of slightly weakened interface on the overall elastic properties of composite materials, Mechanics of Materials, Vol. 14, pp.269-281, 1993.

Z. Zhong, S. A. Meguid, On the imperfectly bonded spherical inclusion problem, Journal of Applied Mechanics, Transactions of ASME, Vol. 66, pp.839-846, 1999.

Z. Zhong, S. A. Meguid, On the eigenstrain problem of a spherical inclusion with an imperfectly bonded interface, Journal of Applied Mechanics, Transactions of ASME, Vol. 63, pp.877-883, 1996.

Z. Gao, A circular inclusion with imperfect interface: Eshelby's tensor and related problems, Journal of Applied Mechanics, Transactions of ASME, Vol. 62, pp.860-866, 1995.

T. Mori and K. Tanaka, Average stress in matrix and average energy of materials with misfitting inclusions, Acta, Metallurgica, Vol. 21, pp.571-574, 1973.

T. Mura, Micromechanics of Defects in Solids, Martinus Nijhoff, Boston, 1987.

Y. Wu, M. Nakagaki, Constitutive model for fiber dispersed composite, Transactions of the Japan Society of Mechanical Endineers, Vol. 65, No. 633, pp.1003-1009, 1999.

APPENDIX: THE MODIFIED ESHEBLY'S S-TENSOR

$S_{1111}=S_{2222}=Q_1-Q_2-Q_3+1,$ $S_{1122}=S_{2211}=Q_1+Q_2+Q_3,$ $S_{1212}=-Q_2-Q_3$

Other $S_{ijkl}=0$.

where $Q_1 = \dfrac{nr(1-k_2)}{2(nrk_2 - nr + 4 + 2n)}$, $Q_2 = \dfrac{rn(rtk_2 + t + 6)}{2P}$, $Q_3 = \dfrac{6r(t-n)}{4P}$

and $P = 3p_1 p_2 + ntp_2 p_3 + p_3 p_1 + 12$, $p_1 = n+t$, $p_2 = r+k_1$, $p_3 = rk_2 +1$

$r = \mu_1/\mu_2$ k_i=3-4ν_i for plain strain,   and k=(3-ν_i)/(1+ν_i) for plain stress, i=1,2.

SELF-HEALING POLYMER COMPOSITES

S. R. White[1], N. R. Sottos[2], J. S. Moore[3], P. H. Geubelle[1],
M. R. Kessler[2], S. R. Sriram[3], E. N. Brown[2]

[1]Department of Aeronautical and Astronautical Engineering
[2]Department of Theoretical and Applied Mechanics
[3]Department of Chemistry
University of Illinois, Urbana, IL 61801

ABSTRACT

Thermosetting polymers, used in a wide variety of applications ranging from microelectronics to composite airplane wings, are susceptible to damage in the form of cracking. Often these cracks form deep within the structure where detection is difficult and repair is virtually impossible. In fiber reinforced polymer composites, cracking in the form of fiber-matrix interfacial debonding, ply delamination, and simple matrix cracking leads to degradation. In microelectronics, polymer encapsulates and polymer matrix composite printed circuit boards suffer from similar forms of damage, but in addition to mechanical failure, cracks cause electrical failure of the component. Microcracking induced by thermal and mechanical fatigue is a longstanding problem in polymer adhesives. Regardless of the application, once cracks have formed within polymeric materials, the integrity of the structure is significantly compromised. The concept of self-repair has been discussed previously, but the only successful crack healing methods that have been reported require some form of manual intervention. Inspired by biological systems in which damage triggers a healing response, here we demonstrate the development of a new structural polymeric material with the ability to *autonomically* heal cracks. Experiments on fracture specimens have yielded as much as 75% recovery of virgin toughness. This work will lead to safer and more reliable materials in a wide range of applications and represents the first step in developing materials systems that possess greatly extended lifetimes

KEYWORDS

healing, repair, polymers, fracture, microcracking, failure, composites

INTRODUCTION

The natural process of fatigue in brittle polymers and composite leads to microcracking and other forms of micro-damage [1-5]. Eventually these microcracks coalesce to form large-scale cracks that propagate and lead to ultimate failure. The traditional approach to these problems has been to increase the inherent toughness of brittle polymers through addition of reinforcement phases or elastomers, or to repair the article once the cracks are large and of a critical size.

A new *self-healing* materials system was recently developed [6] and offers an alternative to these traditional approaches. Whenever damage occurs in a self-healing polymer, the repair process is triggered and after sufficient healing time, the inherent strength and toughness of the material is recovered. Self-healing polymers are designed to heal the microcracks that occur naturally during

fatigue, thereby preventing large-scale cracks from forming. As a result, the fatigue life and the useful mechanical function of these materials are expected to be significantly extended.

SELF-HEALING CONCEPT

The self-healing concept is shown in Figure 1. A microencapsulated healing agent is embedded along with a catalyst into a polymer matrix. When damage occurs in the polymer a crack propagates through the matrix rupturing the microcapsules in the crack path. The ruptured microcapsules release the healing agent which is then drawn into the crack through capillary action. Once the healing agent within the crack plane comes into contact with the embedded catalyst, a chemical reaction is triggered and polymerization of the healing agent occurs. Afterwards, the crack faces are bonded and the strong singularity at the crack tip is relieved.
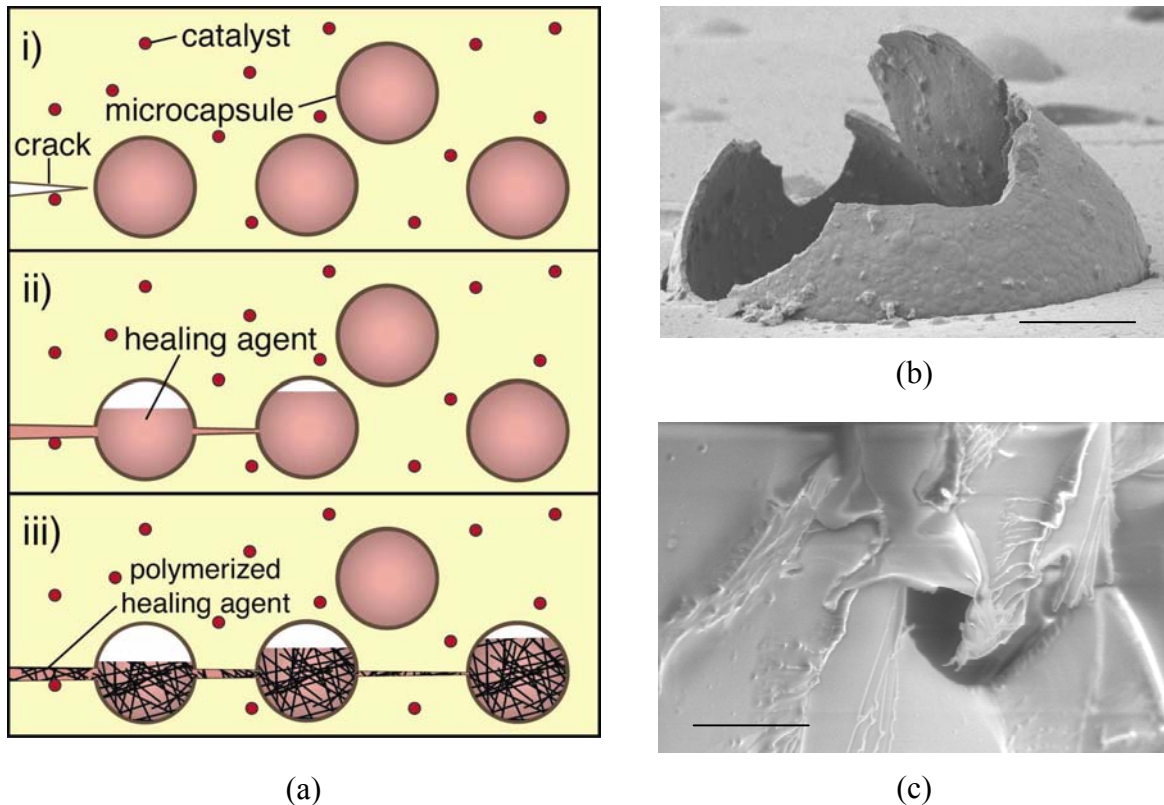
Figure 1. *The Self-Healing Concept.* (a) Schematic representation of self-healing material where i) a microencapsulated healing agent and catalyst is dispersed in a polymer matrix, ii) an advancing crack intersects the embedded microcapsules which rupture and release the healing agent into the crack through capillary action, iii) the healing agent contacts the catalyst and polymerization occurs. [scale bar = 10 µm] (b) SEM image of the fracture plane of a self-healing material showing a ruptured microcapsule. (c) SEM image of the healed fracture plane showing the polymerized healing agent covering the fracture plane. [scale bar = 100 µm].

MANUFACTURING PROCEDURE

Self-healing polymers are created in a two-step process beginning with the microencapsulation of the healing agent. Figure 2 shows a schematic of the microencapsulation procedure. An emulsion of the healing agent (dicyclopentadience, DCPD) is created with an aqueous solution of urea and formaldehyde. In situ polymerization occurs at the DCPD surface at controlled temperature and pH. The emulsion is agitated throughout the process and the size of the capsules can be controlled by the agitation rate. Typically, we obtain 100-200 µm microcapsules at 450 rpm at 50°C and 3.5 pH.

In Situ Polymerization

CORE — UREA + FORMALDEHYDE + WATER (PREPOLYMER MIX)

PREPARE EMULSON | ADJUST pH TO 3.5 FOR POLYMERIZATION | HEAT TO COMPLETE POLYMERIZATION

X+Y

$-(X-Y)_n-$
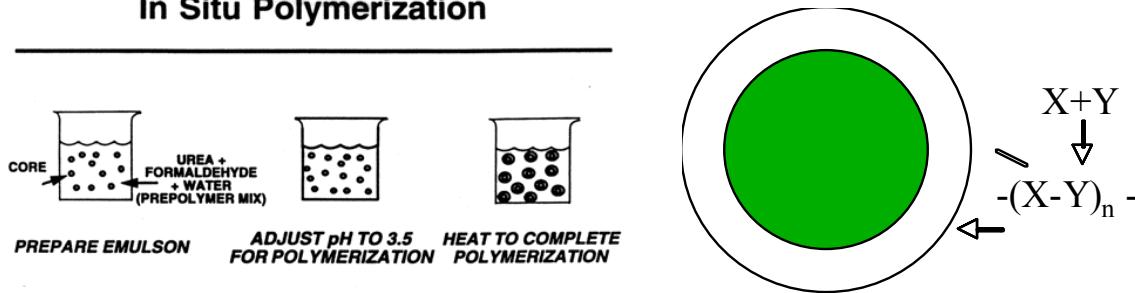
Figure 2. *Microencapsulation Procedure.* An emulsion of dicyclopentadiene (core) is created with urea and formaldehyde and water. In-situ polymerization of urea-formaldehyde occurs at the surface of the DCPD cores and continues under controlled temperature and pH.

Once the microcapsules are prepared they are mixed with the polymer matrix. For the examples which follow, a bisphenol-A based epoxide (EPON 828) was used along with a tetra-functional amine curing agent (DETA). The microcapsules are mixed with the epoxide prepolymer at 10 wt.% (total). The catalyst (Grubbs' catalyst)[1] [7] is then added at a typical concentration of 2.5 wt.% (total). The mixture is then degassed and the curing agent is then added. The resin mixture is next poured into a mold and cured at room temperature for 24 h followed by a postcure of 40°C for 24 h. Figure 3 shows an example self-healing fracture toughness specimen after manufacture.

HEALING EFFICIENCY

Based on the work of Jud and Kausch [8] and Wool and O'Connor [9] we define the *healing efficiency* as,
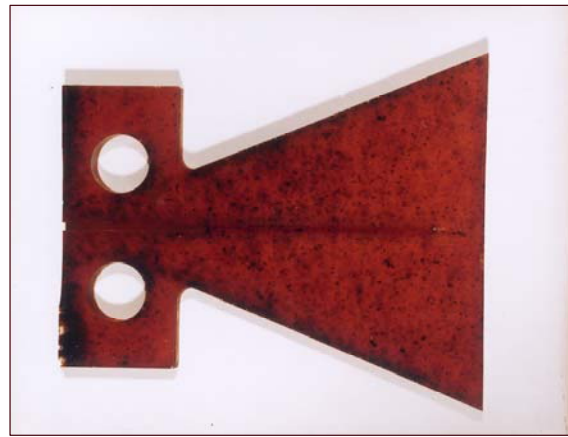
Figure 3. *Self-Healing Polymer Specimen.* NOTE: The geometry of the fracture toughness sample is designed for controlled crack propagation along the centerline of the sample and constant compliance with increasing crack length.

$$\eta = K_{IC}^{healed} \Big/ K_{IC}^{virgin} \qquad (1)$$

where K_{IC} is the critical mode-I stress intensity factor. A ratio of unity indicates complete recovery after healing. The healing efficiency depends on a number of factors including the concentration of catalyst and healing agent, the healing kinetics, the diffusion rate of the healing agent in the polymer matrix, the capillary pressure in the crack plane, the adhesive bond strength between the healing agent and polymer matrix, etc. An example result from a fracture toughness test is included in Figure 4. A fracture toughness sample similar to the one shown in Figure 3 was loaded in mode-I and a starter crack was propagated along the centerline of the specimen. The curve labeled "virgin" corresponds to the load-deflection data obtained for this test. Subsequently, the specimen was unloaded and allowed to heal for a total of 48 hours. The specimen was then reloaded to failure and the load-deflection data labeled "self-healed" was obtained. Analysis of the fracture data reveals that the healing efficiency for this specimen is approximately 75%.

---

[1] Grubbs' catalyst is a Ruthenium transition metal catalyst that initiates a ring-opening metathesis polymerization of the DCPD healing agent.
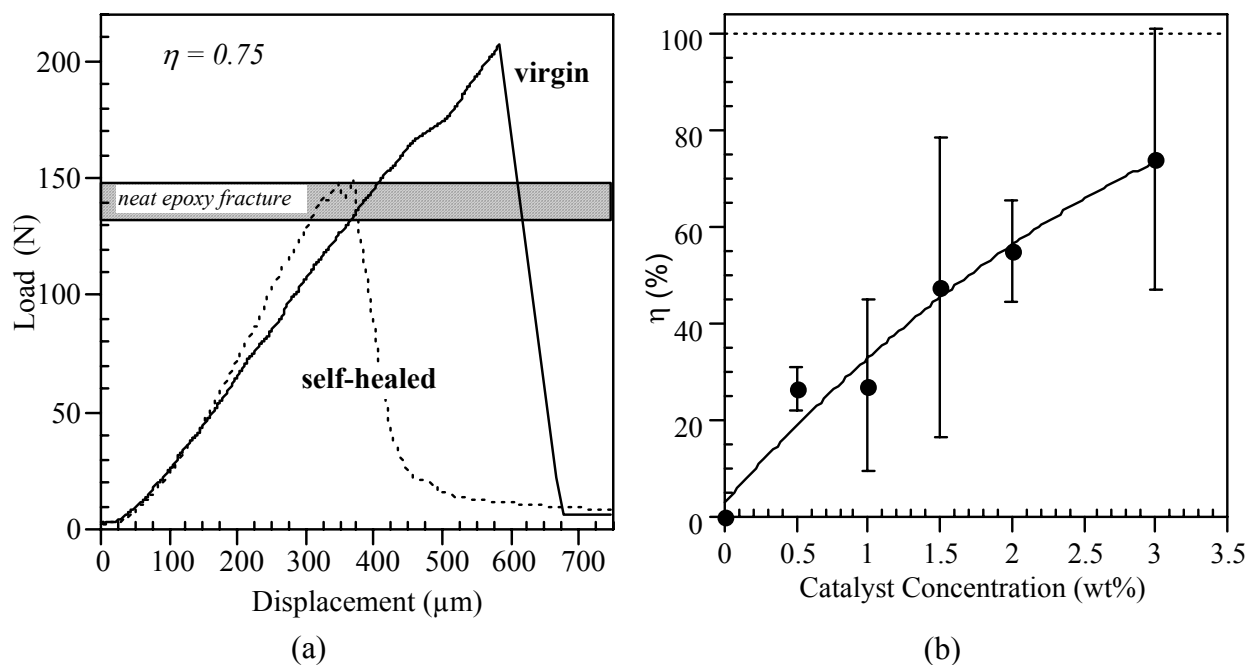
Figure 4. *Self-Healing Fracture Toughness Results.* (a) A virgin specimen similar to that shown in Figure 3 is loaded to failure. The specimen is then unloaded and allowed to heal for 48 hours. The healed specimen is then loaded to failure again. The healing efficiency for this specimen is approximately 75%. (b) Effect of catalyst concentration on healing efficiency.

Optimization of the materials system for maximum healing efficiency is an on-going research goal. Healing efficiency is a complex material property that not only depends on the factors listed above, but on their interplay *in situ*. For example, the healing kinetics must be sufficient rapid so that the healing agent does not have time to diffuse into the surrounding polymer matrix. Yet, the rate of healing is controlled primarily by the concentration of the catalyst on the crack plane as well as the temperature at which healing occurs. Figure 4b shows the dependence of healing efficiency on catalyst concentration. With increasing concentration the healing efficiency increases monotonically. Yet, the concentration of catalyst on the crack plane itself can be quite different from that which is added to the resin mixture during manufacturing and this *in situ* concentration will depend on the uniformity of dispersion, the size of the catalyst particles, and any clustering of particles that occurs during manufacturing.

FUTURE DIRECTIONS

Optimization of healing efficiency will require a more thorough understanding of the complex interplay between factors that influence healing kinetics. Research is on going to measure the in situ healing kinetics and the influence of catalyst concentration. Subsequent generations of self-healing polymers will incorporate more robust and active catalyst-healing agent materials systems with increased tolerance to thermal and environmental extremes. The future goals in this emerging field of research will include microcirculatory systems to replenish the supply of healing agents and catalysts to the host material.

ACKNOWLEDGEMENTS

REFERENCES

1. Talrega, R. (1989). *J. Strain Anal. Eng. Des.* **24**, 215.

2. Talrega, R. (Ed) (1994). *Damage Mechanics of Composite Materials*. Elsevier, New York.

3. Gamstedt, E. K. and Talrega, R. (1999). *J. Mat. Sci*. **34**, 2535.

4. Pecht, M. G., Nguyen, L. T., and Hackim, E. B. (1995). *Plastic-Encapsulated Microelectronics*. John Wiley & Sons, New York.

5. Lee, L. H. (1991). *Adhesive Bonding*. Plenum Press, New York.

6. White, S.R., Sottos, N.R., Geubelle, P.H., Moore, J.S., Kessler, M.R., Sriram, S.R., Brown, E.N., and Viswanathan, S. (2001). *Nature*. **409**, 794.

7. Schwab, P., Grubbs, R. H., and Ziller, J. W. (1996). *J. Am. Chem. Soc.* **118**, 100.

8. Jud, K. and Kausch, H.H. (1979) *Polymer Bulletin*. **1**, 697.

9. Wool, R.P. and O'Conner, K.M. (1982). *Journal of Applied Physics*. **52**, 5953.

SEMI-WEIGHT FUNCTION METHOD OF THREE-DIMENSIONAL PROBLEM IN FRACTURE MECHANICS

Liu Chuntu   Ma Kaiping

(Institute of Mechanics, Chinese Academic Sciences, Beijing, 100080, China)

ABSTRACT

In two-dimensional fracture analysis, Bueckner proposed a weight function method to solve several problems efficiently. However, there are many difficulties and complexities because the analytical expression of the weight function can not be obtained easily. Liu put forward a concept of semi-weight function and got analytical expression of stress intensity factors and semi-weight functions and satisfactory results in plane problems. Because of the complexity of three-dimensional fracture problems, finite element method and other numerical methods are commonly used, the weight function method can not be used directly and often be used in analysis and calculation after some engineering simplification. The semi-weight function method is used and developed in this paper to solve three dimensional fracture problems, as an extension from plane problems. This paper has contributions as below:

1. From principle of virtual work(reciprocal work theorem), analytical expression of the relationship between semi-weight functions and fracture parameters is obtained through strict theoretical derivation;
2. Analytical expression of semi-weight functions is obtained. A few conditions are satisfied on average;
3. SIF for mode I in three-dimensional problems of plates is analyzed and calculated with use of this method. The stress intensity factors and the distribution across thickness are solved. Relatively exact results are got from calculation example.

The calculation results show that among high precision calculation methods, compared with the weight function method, this method provides applicable analytical expressions of semi-weight functions and in less restrict condition. Compared with finite element method, it needs less amount of calculation.

KEYWORDS

semi-weight function method, stress intensity factors, three-dimensional problems, reciprocal work theorem

INTRODUCTION

The stress intensity factor(SIF) is an important parameter in fracture mechanics. In a three-dimensional finite

body, the variation of SIF along the crack front needs to be computed. In most cases, two methods are used to solve typical problems.

One is the finite element method(FEM). With a three-dimensional finite element elastic stress analysis, Raju and Newman[1] calculated the SIF for some commonly used fracture specimens that have a through-the-thickness crack. However, FEM requires great amounts of computation time, especially when large numbers of elements are concentrated near the crack tip. Singular elements, where shape functions have the same stress singularity as the stress field near the crack tip, were developed. The problems are how to construct a singular element and determine the size of singular element.

Another one is the weight function method. Bueckner proposed the weight functions concept in 1970[2]. The weight functions possess many interesting characteristics which make it possible to obtain the SIF by simply calculating an integral along any of the paths around the crack tip. However, in many cases it is more difficult to find the weight functions than the SIF directly.

Liu [3] put forward the semi-weight function method for two dimensional problems in 1991. The semi-functions are independent of boundary conditions and it is only necessary to calculate displacements and tractions along any of the paths around the crack tip. If one uses FEM to calculate displacements and tractions along one of the paths, one need not use many elements near the crack tip and a lot of complex work is saved. This paper considers about how to use this method in calculating Mode-I SIF along the through-the-thickness crack front of finite-thickness fracture specimens.

ANALYSIS

Conclude SIF Expression from Semi-weight Functions

Consider a plate with through-the-thickness crack(figure 1). The thickness of the plate is 2h. In an elastic body, we consider an arbitrary region Ω, including free surfaces and crack face. The boundary of this region is $\partial V = C_s + \Gamma$, where C_S is the crack face and Γ is the other boundary. If we cut out a cylinder with radius
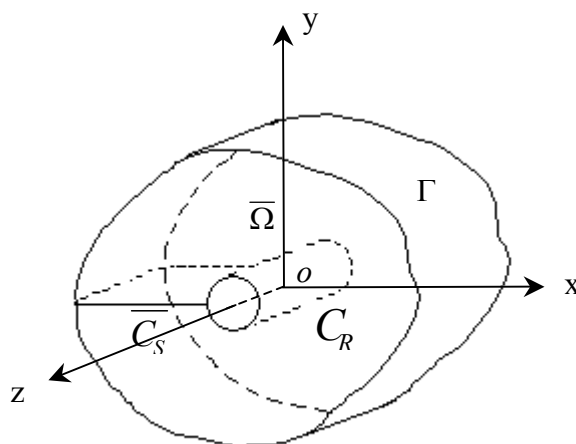
Fig.1: Three-dimensional crack and integration region

R from the crack tip, and the boundary of the cylinder is C_R. The region after cutting out is $\overline{\Omega}$, the crack face is $\overline{C}_S$ and outer boundary is Γ. Then we get

$$\begin{cases} \lim_{R \to 0} \overline{\Omega} = \Omega \\ \lim_{R \to 0} \overline{C}_S = C_S \end{cases}$$

From the principle of virtual work(reciprocal work theorem), we get

$$\int_{\Omega} f_i^{(s)} u_i d\Omega + \int_{\Gamma + \overline{C}_s + C_R} p_i^{(s)} u_i ds = \int_{\Omega} f_i u_i^{(s)} d\Omega + \int_{\Gamma + \overline{C}_s + C_R} p_i u_i^{(s)} ds \qquad (1)$$

where (u_i, p_i, f_i) and $(u_i^{(s)}, p_i^{(s)}, f_i^{(s)})$ are two sets of displacements, tractions and volume forces respectively. Expand and transform the above expression along integral path and ignore volume force we get

$$\int_{C_R} (p_i^{(s)} u_i - p_i u_i^{(s)}) ds + \int_{\overline{C}_s} (p_i^{(s)} u_i - p_i u_i^{(s)}) ds = \int_{\Gamma} (p_i u_i^{(s)} - p_i^{(s)} u_i) ds \qquad (2)$$

Assume that (u_i, p_i) the real displacements and tractions there must be $p_i = 0$. We set $(u_i^{(s)}, p_i^{(s)})$ as the virtual displacements and tractions which satisfy the conditions of equilibrium equation, stress and strain relationship, $\lim_{r \to 0} u_i = O(r^{-1/2})$ near the crack tip and the traction free on the crack face $p_i^{(s)} = 0$. We name these virtual displacements and tractions semi-weight functions. The above expression can be changed to

$$\int_{C_R} (p_i^{(s)} u_i - p_i u_i^{(s)}) ds = \int_{\Gamma} (p_i u_i^{(s)} - p_i^{(s)} u_i) ds \qquad (3)$$

Consider about the singularity near to crack tip, we set

$$u_i^{(s)} = r^{-\frac{1}{2}} f_i^{(s)}(\theta) g_i^{(s)}(z), \qquad (4)$$

$$\begin{cases} u = \dfrac{K_I(z)}{8G} \sqrt{\dfrac{2}{\pi}} r^{1/2} ((5 - 8\nu) \cos \dfrac{\theta}{2} - \cos \dfrac{3\theta}{2}) \\ v = \dfrac{K_I(z)}{8G} \sqrt{\dfrac{2}{\pi}} r^{1/2} ((7 - 8\nu) \sin \dfrac{\theta}{2} - \sin \dfrac{3\theta}{2}) \end{cases}, \qquad (5)$$

where $f_i^{(s)}$ are functions and not volume forces any more. Take the SIF expression form in plane strain, and change the original K_I to $K_I(z)$. We know, for the through-the-thickness crack problem, physical characteristics in the region at crack tip always behave as in plane strain. Substitute these two expression to left side of equation (3).
We get

$$\lim_{r \to 0} \int_{C_R} (p_i^{(s)} u_i - p_i u_i^{(s)}) ds = \int_{-h}^{h} K_I(z) \Phi(z) dz \qquad (6)$$

where $\Phi(z) = \dfrac{1}{4\sqrt{2\pi}(-1 + 2\nu)} (g_1(z)(\int_{-\pi}^{\pi} (f_1(\theta) h_1(\theta) d\theta + A) + g_2(z) \int_{-\pi}^{\pi} (f_2(\theta) h_2(\theta) d\theta)$

and $h_1(\theta) = \cos \dfrac{\theta}{2} ((3 - 4\nu)^2 + (-5 + 4\nu) \cos \theta + 2 \cos 2\theta)$

$h_2(\theta) = \sin \dfrac{\theta}{2} ((3 - 4\nu)^2 + (-1 + 4\nu) \cos \theta + 2 \cos 2\theta)$

$A = -8(-1 + \nu)(-1 + 2\nu)(f_1(-\pi) + f_1(\pi))$

thus expression (1) can be changed to

$$\int_{-h}^{h} K_I(z)\Phi(z)dz = \int_{\Gamma}(p_i u_i^{(s)} - p_i^{(s)} u_i)ds. \qquad (7)$$

That is the expression of SIF from semi-weight functions.

Three-dimensional Semi-weight Functions

From the process of obtaining SIF, we see that $(u_i^{(s)}, p_i^{(s)})$ satisfy three conditions, that is the conditions of equilibrium equation, stress and strain relationship, $\lim_{r \to 0} u_i = O(r^{-1/2})$ near the crack tip and the traction free on the crack face, $p_i^{(s)} = 0$. Any functions that satisfy these conditions can be regarded as semi-weight functions.

We set displacement functions in semi-weight functions as

$$\begin{cases} u^{(s)} = r^{-\frac{1}{2}} f_1(\theta) g_1(z) \\ v^{(s)} = r^{-\frac{1}{2}} f_2(\theta) g_2(z) \ , \\ w^{(s)} = r^{-\frac{1}{2}} f_3(\theta) g_3(z) \end{cases} \qquad (8)$$

and find that the condition of equilibrium equation can not be strictly satisfied. It means that equilibrium equation, no matter what expressions these functions are, can not be zero. We relax this condition and let the integration of equation along thickness of plate be zero. For the two-dimensional problem, these conditions can be all strictly satisfied[2].

If we select proper functions, other conditions can be satisfied. Finally we get semi-weight functions for three-dimensional problems

$$\begin{cases} u^{(s)} = \dfrac{1}{G} r^{-\frac{1}{2}} \cos\theta \cos\dfrac{m\pi z}{h} \\ v^{(s)} = \dfrac{\nu}{2G(1-\nu)} r^{-\frac{1}{2}} \sin\theta \cos\dfrac{m\pi z}{h} \ , \\ w^{(s)} = 0 \end{cases} \qquad (9)$$

where G is shear modulus and *m* is any natural number.

APPLICATION

As an application, we calculate SIF along the crack front of center-crack tension, which is a classical example in three-dimensional problems, and compare the result of Newman[1]. In our application, we expand $K_I(z)$ in an power series as $K_I(z) = \sum_{i=0}^{m} k_i(\dfrac{z^2}{h^2})^i$. In this place, the selection of number m is the same as in semi-weight functions. With the selection of different m, equations can be introduced. Solving the equations, we get every k_i and finally $K_I(z)$. When we calculate the integration in the right side of (3),

we calculate the actual displacements and stresses with FEM. In our FEM model, no singularity elements were used.

Compare with [1], we select $\dfrac{b}{a}=0.875$, $\dfrac{c}{a}=0.5$, $\dfrac{h}{c}=1.5$, $v=\dfrac{1}{3}$. In our model, we set $a=10m$,
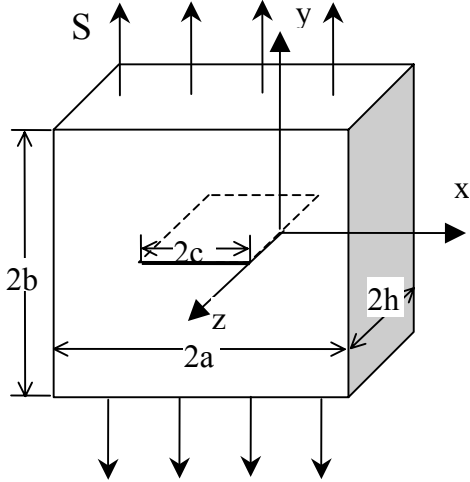
Fig.2: Model of center-crack tension
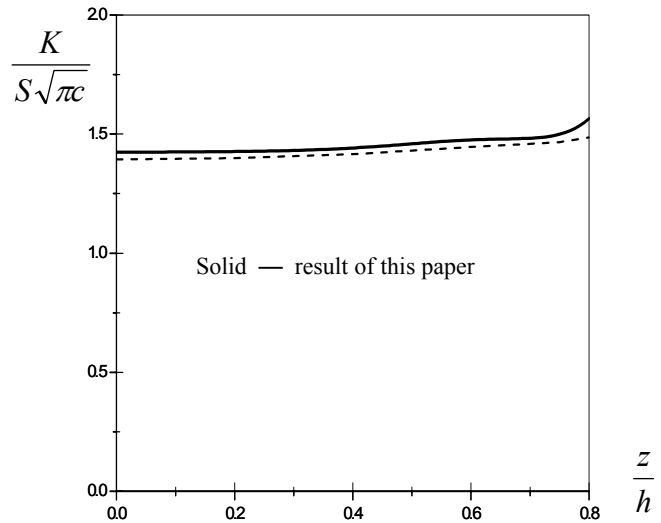
Fig.3: Comparison of SIF between this paper and ref.[1]

$b=8.75m$, $c=5m$, $h=7.5m$, Youngs modulus $E=2.110^{11}pa$, $S=1000pa$, and get the result expression

$$F(\xi)=1.424+0.0709501\xi^{2}-0.292252\xi^{4}+5.83877\xi^{6}-18.2836\xi^{8}+16.3159\xi^{10}, \qquad (10)$$

where $\xi=\dfrac{z}{h}$, $F=\dfrac{K_{I}}{S\sqrt{\pi c}}$

Change the thickness ratio h/c and compare with result of reference[1]

Table 1: Comparison of SIF of various thickness specimens between this paper and refer.[1]

	0.5	1	1.5	2
This paper	1.4781	1.4458	1.4247	1.3910
Newman[1]	1.4833	1.4333	1.401	1.3833
Difference %	-0.35	0.87	1.69	0.56

We can see the result of this paper and ref.[1] are very close. The maximum difference does not exceed 5%

CONCLUSION

This paper extends the semi-weight function method to three-dimensional fracture problems. It deduced three-dimensional SIF expression in a form of integration from semi-weight functions. Analytic expression of three-dimensional semi-weight functions are also introduced. Comparison of application results between this method and classical the FEM results shows that they are very close, the difference is less than 5%. The semi-weight function method is a convenient method for calculating the SIF in various problems. It is only

necessary to know the tractions and displacements along any paths around the crack tip. By using this method the complex analysis near the crack tip can be avoided. Even when the approximation of far field is not very accuracy, the semi-weight function method can also get some satisfactory result in engineering application.

REFERENCES

1. I. S. Raju and J. C. Newman (1977) *NASA*, TN D-8414.
2. H. F. Bueckner(1970), ZAMM 50, 9, 529
3. Liu Chun-Tu and Zhang Duanzhong(1991), Int. J, Fract. 48,R3

SHAPE SENSITIVITY AND RELIABILITY ANALYSES IN NONLINEAR FRACTURE MECHANICS

G. Chen and S. Rahman

Department of Mechanical Engineering, The University of Iowa,
Iowa City, IA 52242

ABSTRACT

This paper presents a new method for shape sensitivity analysis of a crack in a homogeneous, isotropic, and nonlinearly elastic body subject to mode-I loading conditions. The method involves the material derivative concept of continuum mechanics, domain integral representation of the *J*-integral, and direct differentiation. Unlike virtual crack extension techniques, no mesh perturbation is required in the proposed method. Based on the continuum sensitivities, the first-order reliability method was employed to perform probabilistic analysis. Numerical examples are presented to illustrate both the sensitivity and reliability analyses. The maximum difference between the sensitivity of stress-intensity factors calculated using the proposed method and the finite-difference method is less than four percent. Since all gradients are calculated analytically, the reliability analysis of cracks can be performed efficiently.

KEYWORDS

Shape sensitivity analysis, velocity field, *J*-integral, probabilistic fracture mechanics, reliability.

INTRODUCTION

In probabilistic fracture mechanics (PFM), the derivatives of the *J*-integral or stress-intensity factors (SIFs) are often required to predict the probability of fracture initiation and/or instability in cracked structures. The calculation of these derivatives with respect to load or material parameters, which constitutes size-sensitivity analysis, is not unduly difficult. However, the evaluation of derivatives with respect to crack size is a challenging task, since it requires shape sensitivity analysis. Using a brute-force type finite-difference method to calculate the shape sensitivities is often computationally expensive, because numerous deterministic finite element analyses may be required for a complete reliability analysis. Hence, some analytical methods have appeared to predict the sensitivities of SIFs under mode-I loading condition. For example, finite element methods (FEMs) based on virtual crack extension techniques have been developed to calculate the first- and second-order derivatives of SIFs [1]. However, these methods require mesh perturbation – a fundamental requirement of all virtual crack-extension techniques. For second-order derivatives, the number of elements affected by mesh perturbation surrounding the crack tip has a significant effect on solution accuracy [1]. Recently, alternative methods based on continuum sensitivity theory have emerged to obtain derivatives of SIFs for linear-elastic cracked structures [2,3]. No mesh perturbation is necessary in the latter formulation involving continuum shape sensitivity analysis.

However, these methods are valid only for linear-elastic structures. Hence, there is a need to develop similar sensitivity equations for nonlinear cracked structures.

This paper presents a new method for predicting the first-order sensitivity of the J-integral for a crack in a nonlinearly elastic structure under mode-I loading conditions. The method involves the material derivative concept of continuum mechanics, domain integral representation of the J-integral, and direct differentiation. Based on the proposed sensitivities, the first-order reliability method is employed for predicting stochastic response and reliability of cracked structures. Several numerical examples are presented for calculating both the sensitivity of the J-integral and reliability of cracked structures.

SHAPE SENSITIVITY ANALYSIS

The governing variational equation for a nonlinearly elastic structural component with the domain Ω can also be written as [4]

$$a_\Omega(z,\overline{z}) = \ell_\Omega(\overline{z}), \quad \text{for all } \overline{z} \in \mathbf{Z} \tag{1}$$

where z and $\overline{z}$ are the actual displacement and virtual displacement fields of the structure, respectively, $\mathbf{Z}$ is the space of kinematically admissible virtual displacements, $a_\Omega(z,\overline{z})$ and $\ell_\Omega(\overline{z})$ are energy and load linear forms, respectively. In Equations 1, $a_\Omega(z,\overline{z})$ is nonlinear and must be linearized by a_Ω^* (say) for iterative solution of z. Taking the material derivative of the linearized form of Equation 1 yields,

$$a_\Omega^*(z;\dot{z},\overline{z}) = \ell_V'(\overline{z}) - a_V'(z,\overline{z}), \quad \forall \, \overline{z} \in \mathbf{Z}, \tag{2}$$

where the subscript V is used to indicate the dependency of the terms on the velocity field [4], and

$$a_\Omega^*(z;\dot{z},\overline{z}) = \int_\Omega \frac{\partial \sigma_{ij}}{\partial \varepsilon_{kl}} \varepsilon_{kl}(\dot{z}) \varepsilon_{ij}(\overline{z}) d\Omega \tag{3}$$

$$\ell_V'(\overline{z}) = \int_\Gamma \left\{ -T_i\left(z_{i,j}V_j\right) + \left[\left(T_i\overline{z}_i\right)_{,j} n_j + \kappa_\Gamma\left(T_i\overline{z}_i\right)\right]\left(V_i n_i\right) \right\} d\Gamma \tag{4}$$

$$a_V'(z,\overline{z}) = -\int_\Omega \left[\frac{\partial \sigma_{ij}}{\partial \varepsilon_{kl}}\left(z_{k,m}V_{m,l}\right)\varepsilon_{ij}(\overline{z}) + \sigma_{ij}(z)\left(\overline{z}_{i,m}V_{m,j}\right) - \sigma_{ij}(z)\varepsilon_{ij}(\overline{z})\operatorname{div}V \right] d\Omega . \tag{5}$$

where T_i is the ith component of the surface traction, V_i is the ith component of V, n_i is the ith component of unit normal vector n, and κ_Γ is the curvature of the boundary, and $z_{i,j} = \partial z_i/\partial x_j$, $\overline{z}_{i,j} = \partial \overline{z}_i/\partial x_j$, and $V_{i,j} = \partial V_i/\partial x_j$. For a performance measure ψ with a functional form

$$\psi = \int_{\Omega_\tau} g\left(z_\tau, \nabla z_\tau\right) d\Omega_\tau , \tag{6}$$

the material derivative of ψ at Ω is [4]

$$\dot{\psi} = \int_\Omega \left[g_{,z_i}\dot{z}_i - g_{,z_i}\left(z_{i,j}V_j\right) + g_{,z_{i,j}}\dot{z}_{i,j} - g_{,z_{i,j}}\left(z_{i,j}V_j\right)_{,j} + \operatorname{div}(gV) \right] d\Omega \tag{7}$$

where $z_{i,j} = \partial z_i/\partial x_j$, $\dot{z}_{i,j} = \partial \dot{z}_i/\partial x_j$, $g_{,z_i} = \partial g/\partial z_i$, $g_{,z_{i,j}} = \partial g/\partial z_{i,j}$ and V_j is the jth component of V. To evaluate the sensitivity expression of Equation 7, a numerical method is needed to solve Equation 1. In this study, standard nonlinear FEM was used to solve Equation 1. However, the solution of $\dot{z}$ can be obtained efficiently from Equation 2, since it is actually a linear system. Since the sensitivity equation is always linear even for nonlinear systems, the continuum shape sensitivity method is more efficient than the finite-difference method that requires solving at least two nonlinear systems of equations. In this study, the ABAQUS finite element code [5] was used for all numerical calculations.

THE J-INTEGRAL AND ITS SENSITIVITY

A widely used constitutive equation for J_2-deformation theory of plasticity, usually under small-displacement conditions, is based on the well-known Ramberg-Osgood relation [6], given by

$$\varepsilon_{ij} = \frac{1+\nu}{E} s_{ij} + \frac{1-2\nu}{3E} \sigma_{kk}\delta_{ij} + \frac{3}{2}\alpha\varepsilon_0 \left(\frac{\sigma_e}{\sigma_0}\right)^{n-1} \frac{s_{ij}}{\sigma_0} \tag{8}$$

where σ_{ij} and ε_{ij} are stress and strain components, respectively, E is the Young's modulus, ν is Poisson's ratio, σ_0 is a reference stress, α is a dimensionless material constant, n is the strain hardening exponent, δ_{ij} is the Kronecker delta, $s_{ij} = \sigma_{ij} - \frac{1}{3}\sigma_{kk}\delta_{ij}$ is the deviatoric stress, and $\sigma_e = \sqrt{\frac{3}{2} s_{ij}s_{ij}}$ is the *von Mises* equivalent stress. The deformation theory assumes that the state of stress determines the state of strain uniquely as long as the plastic deformation continues. This is identical to the nonlinearly elastic stress-strain relation as long as unloading does not occur. This paper is concerned with the development of sensitivity equations for the *J*-integral using only the deformation theory of plasticity.

Under quasi-static condition, in the absence of body forces, thermal strains, and crack-face traction, the domain integration form of the *J*-integral for a two-dimensional problem is [6]

$$J = \int_A \left[\left(\sigma_{11}\frac{\partial z_1}{\partial x_1} + \sigma_{12}\frac{\partial z_2}{\partial x_1}\right)\frac{\partial q}{\partial x_1} + \left(\sigma_{21}\frac{\partial z_1}{\partial x_1} + \sigma_{22}\frac{\partial z_2}{\partial x_1}\right)\frac{\partial q}{\partial x_2} - W\frac{\partial q}{\partial x_1}\right] dA, \tag{9}$$

where W is the strain energy density, A is the area inside an arbitrary contour, q is a weight function which is unity at the outer boundary of A and zero at the crack tip. For a mode-I problem, the velocity field $V = \{V_1, 0\}^T$. By applying the shape sensitivity concept described earlier, the sensitivity of J is

$$\dot{J} = \int_A \left(H_1 + H_2 + H_3 + H_4 - H_5\right) dA \tag{10}$$

where

$$H_1 = \frac{\partial z_1}{\partial x_1}\frac{\partial q}{\partial x_1}\left[\frac{\partial \sigma_{11}}{\partial \varepsilon_{11}}\left(\frac{\partial \dot{z}_1}{\partial x_1} - \frac{\partial z_1}{\partial x_1}\frac{\partial V_1}{\partial x_1}\right) + \frac{\partial \sigma_{11}}{\partial \varepsilon_{12}}\left(\frac{\partial \dot{z}_1}{\partial x_2} + \frac{\partial \dot{z}_2}{\partial x_1} - \frac{\partial z_1}{\partial x_1}\frac{\partial V_1}{\partial x_2} - \frac{\partial z_2}{\partial x_1}\frac{\partial V_1}{\partial x_1}\right)\right]$$

$$+\frac{\partial z_1}{\partial x_1}\frac{\partial q}{\partial x_1}\frac{\partial \sigma_{11}}{\partial \varepsilon_{22}}\left(\frac{\partial \dot{z}_2}{\partial x_2} - \frac{\partial z_2}{\partial x_1}\frac{\partial V_1}{\partial x_2}\right) + \sigma_{11}\frac{\partial q}{\partial x_1}\left(\frac{\partial \dot{z}_1}{\partial x_1} - \frac{\partial z_1}{\partial x_1}\frac{\partial V_1}{\partial x_1}\right) \tag{11}$$

$$H_2 = \frac{\partial z_2}{\partial x_1}\frac{\partial q}{\partial x_1}\left[\frac{\partial \sigma_{12}}{\partial \varepsilon_{11}}\left(\frac{\partial \dot{z}_1}{\partial x_1} - \frac{\partial z_1}{\partial x_1}\frac{\partial V_1}{\partial x_1}\right) + \frac{\partial \sigma_{12}}{\partial \varepsilon_{12}}\left(\frac{\partial \dot{z}_2}{\partial x_1} + \frac{\partial \dot{z}_1}{\partial x_2} - \frac{\partial z_2}{\partial x_1}\frac{\partial V_1}{\partial x_1} - \frac{\partial z_1}{\partial x_1}\frac{\partial V_1}{\partial x_2}\right)\right]$$

$$+\frac{\partial z_2}{\partial x_1}\frac{\partial q}{\partial x_1}\frac{\partial \sigma_{12}}{\partial \varepsilon_{22}}\left(\frac{\partial \dot{z}_2}{\partial x_2} - \frac{\partial z_2}{\partial x_1}\frac{\partial V_1}{\partial x_2}\right) + \sigma_{12}\frac{\partial q}{\partial x_1}\left(\frac{\partial \dot{z}_2}{\partial x_1} - \frac{\partial z_2}{\partial x_1}\frac{\partial V_1}{\partial x_1}\right) \tag{12}$$

$$H_3 = \frac{\partial z_1}{\partial x_1}\frac{\partial q}{\partial x_2}\left[\frac{\partial \sigma_{12}}{\partial \varepsilon_{11}}\left(\frac{\partial \dot{z}_1}{\partial x_1} - \frac{\partial z_1}{\partial x_1}\frac{\partial V_1}{\partial x_1}\right) + \frac{\partial \sigma_{12}}{\partial \varepsilon_{12}}\left(\frac{\partial \dot{z}_2}{\partial x_1} + \frac{\partial \dot{z}_1}{\partial x_2} - \frac{\partial z_2}{\partial x_1}\frac{\partial V_1}{\partial x_1} - \frac{\partial z_1}{\partial x_1}\frac{\partial V_1}{\partial x_2}\right)\right]$$

$$+\frac{\partial z_1}{\partial x_1}\frac{\partial q}{\partial x_2}\frac{\partial \sigma_{12}}{\partial \varepsilon_{22}}\left(\frac{\partial \dot{z}_2}{\partial x_2} - \frac{\partial z_2}{\partial x_1}\frac{\partial V_1}{\partial x_2}\right) + \sigma_{12}\frac{\partial q}{\partial x_2}\frac{\partial \dot{z}_1}{\partial x_1} - \sigma_{12}\frac{\partial q}{\partial x_1}\frac{\partial z_1}{\partial x_1}\frac{\partial V_1}{\partial x_2} \tag{13}$$

$$H_4 = \frac{\partial z_2}{\partial x_1}\frac{\partial q}{\partial x_2}\left[\frac{\partial \sigma_{22}}{\partial \varepsilon_{11}}\left(\frac{\partial \dot{z}_1}{\partial x_1} - \frac{\partial z_1}{\partial x_1}\frac{\partial V_1}{\partial x_1}\right) + \frac{\partial \sigma_{22}}{\partial \varepsilon_{12}}\left(\frac{\partial \dot{z}_2}{\partial x_1} + \frac{\partial \dot{z}_1}{\partial x_2} - \frac{\partial z_2}{\partial x_1}\frac{\partial V_1}{\partial x_1} - \frac{\partial z_1}{\partial x_1}\frac{\partial V_1}{\partial x_2}\right)\right]$$

$$+\frac{\partial z_2}{\partial x_1}\frac{\partial q}{\partial x_2}\frac{\partial \sigma_{22}}{\partial \varepsilon_{22}}\left(\frac{\partial \dot{z}_2}{\partial x_2} - \frac{\partial z_2}{\partial x_1}\frac{\partial V_1}{\partial x_2}\right) + \sigma_{22}\frac{\partial q}{\partial x_2}\frac{\partial \dot{z}_2}{\partial x_1} - \sigma_{22}\frac{\partial q}{\partial x_1}\frac{\partial z_2}{\partial x_1}\frac{\partial V_1}{\partial x_2} \tag{14}$$

$$H_5 = \frac{\partial q}{\partial x_1}\frac{\partial W}{\partial \sigma_{ij}}\left[\frac{\partial \sigma_{ij}}{\partial \varepsilon_{11}}\left(\frac{\partial \dot{z}_1}{\partial x_1}-\frac{\partial z_1}{\partial x_1}\frac{\partial V_1}{\partial x_1}\right)+\frac{\partial \sigma_{ij}}{\partial \varepsilon_{22}}\left(\frac{\partial \dot{z}_2}{\partial x_2}-\frac{\partial z_2}{\partial x_1}\frac{\partial V_1}{\partial x_2}\right)\right]$$
$$+\frac{\partial q}{\partial x_1}\frac{\partial W}{\partial \sigma_{ij}}\frac{\partial \sigma_{ij}}{\partial \varepsilon_{12}}\left(\frac{\partial \dot{z}_2}{\partial x_1}+\frac{\partial \dot{z}_1}{\partial x_2}-\frac{\partial z_1}{\partial x_1}\frac{\partial V_1}{\partial x_2}-\frac{\partial z_2}{\partial x_1}\frac{\partial V_1}{\partial x_1}\right) \tag{15}$$

Equations 11-15 are valid for both plane stress and plane strain conditions and can be inserted in Equation 10 to yield the first-order sensitivity of J with respect to crack size. The integral in Equation 10 is independent of the domain size and can be calculated numerically using the standard Gaussian quadrature. A 2×2 or higher integration rule is recommended for calculating $\dot{J}$.

FRACTURE RELIABILITY ANALYSIS

Consider a cracked structure with uncertain mechanical and geometric characteristics that is subject to random loads. Denote by X an N-dimensional random vector with components X_1, $X_2,\cdots$, X_N characterizing all uncertainty in load, geometry, and material parameters. Let J be a relevant crack-driving force that can be calculated from FEM. Suppose, the structure fails when $J > J_{Ic}$, where J_{Ic} is the mode-I plane strain fracture toughness of the material. This requirement cannot be satisfied with certainty, because J depends on input X which is random and J_{Ic} itself is a random variable. Hence, the performance of the cracked structure should be evaluated by the probability of failure P_F, defined as

$$P_F \overset{\text{def}}{=} \Pr\left[g(X) < 0\right] \overset{\text{def}}{=} \int_{g(x)<0} f_X(x)dx \tag{16}$$

where $f_X(x)$ is the joint probability density function of X, and $g(X) = J_{Ic}(X) - J(X)$ is the performance function. The failure probability in Equation 16 involves multi-fold probability integration for its evaluation. In this study, the first-order reliability method (FORM) [7] was used to compute this probability. The calculation of failure probability in the context of FORM can be viewed as a constrained nonlinear optimization problem, which in turn requires first-order sensitivities of J with respect to all random parameters. The proposed shape sensitivity method can be effectively applied to FORM when the crack size is modeled as a random parameter.

NUMERICAL EXAMPLES

Example 1: Sensitivity Analysis of M(T) and SE(T) Specimens
Consider a middle-tension [M(T)] and a single-edged-tension [SE(T)] specimens with width, $2W = 1.016$ m, length, $2L = 5.08$ m and a crack length, $2a$, that are subjected to far-field remote tensile stress, $\sigma^\infty = 172.4$ MPa. Two distinct crack sizes with normalized crack lengths, $a/W = 0.25$ and 0.5 were considered for both specimens. For material properties: reference stress, $\sigma_0 = 154.8$ MPa; elastic modulus, $E = 207$ GPa; Poisson's ration, $v = 0.3$; and Ramberg-Osgood parameters, $\alpha = 8.073$ and $n = 3.8$. Figures 1 and 2 show the geometry and loads of the M(T) and SE(T) specimens, respectively. A finite element mesh for 1/2 model of the SE(T) specimen and 1/4 model of the M(T) specimen is shown in Figure 3. A plane stress condition was assumed. Second-order, eight-noded quadrilateral elements from ABAQUS [5] library were used. The number of elements and nodes were 208 and 691, respectively. Focused elements with collapsed nodes were employed in the vicinity of crack tip. A 2×2 Gaussian integration was used.

Tables 1 and 2 show the results of J and $\partial J/\partial a$ for M(T) and SE(T) problems, respectively. For $\partial J/\partial a$, two sets of results are shown. One is based on the proposed sensitivity method described in this thesis. The other is based on the finite-difference method using a one-percent perturbation of crack length. The results of Tables 1 and 2 show that the continuum sensitivity method provides very accurate results of

$\partial J/\partial a$ when compared with the corresponding results of the finite-difference method. Unlike the virtual crack extension techniques, no mesh perturbation is needed in the proposed method. The difference between the results of the proposed method and the finite-difference method is less than four percent.

Example 2: Reliability Analysis of DE(T) Specimen

Consider a double-edged-tension [DE(T)] specimen with width, $2W = 1.016$ m, length, $2L = 5.08$ m, and random crack length, a. It is subject to a far-field tensile stress, σ^∞, as shown in Figure 4. The load (σ^∞), crack size (a/W), and material properties (E, α, and J_{Ic}) were treated as statistically independent random variables with their properties listed in Table 3. The Poisson's ratio, $\nu = 0.3$ and the Ramberg-Osgood exponent, $n = 3.8$ were assumed to be deterministic. The same finite element mesh of Figure 3 was used for this DE(T) specimen (at mean crack length) for 1/4 model. A plane stress condition was assumed.

Using continuum sensitivity of J and FORM, reliability analyses were conducted to calculate the probability of failure P_F, as a function of mean far-field tensile stress $E[\sigma^\infty]$. Figure 5 shows the plots of P_F vs. $E[\sigma^\infty]$ for both deterministic ($v_{a/W} = 0$) and random ($v_{a/W} = 10$, 20 percent) crack sizes, where $v_{a/W}$ denotes the coefficient of variation (COV) of a/W. The results indicate that the failure probability increases with the COV (uncertainty) of a/W as expected and can be much larger than the probabilities calculated for a deterministic crack size, particularly when the uncertainty of a/W is large. For $v_{a/W} = 10$ percent, failure probability was also calculated by Monte Carlo simulation with the sample size at least 10 times the inverse of failure probability being estimated. According to Figure 5, the probability of failure by FORM is in good agreement with the simulation results.
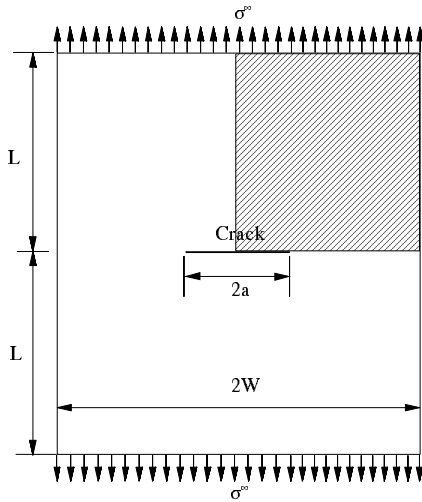
Figure 1: M(T) specimen
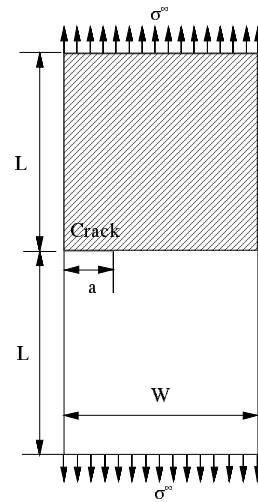
Figure 2: SE(T) specimen
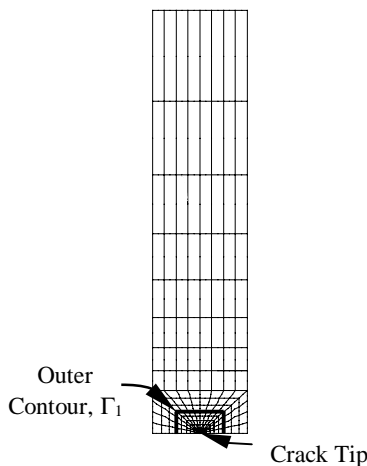
Figure 3: Finite element mesh
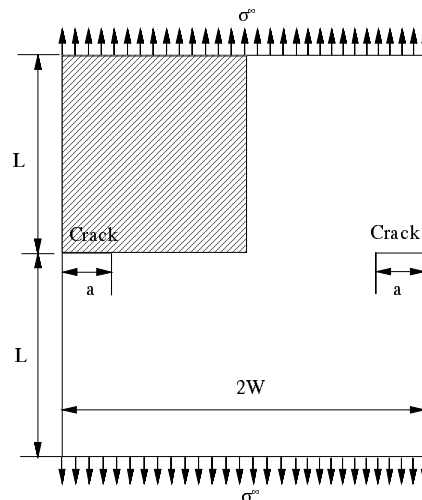
Figure 4: DE(T) specimen

TABLE 1
SENSITIVITY OF J FOR M(T) SPECIMEN

		Sensitivity of J ($\partial J/\partial a$) kJ/m^3		
a/W	J kJ/m^2	Prop. Method	Finite Diff.	Diff. %
0.25	2.00×10^3	27.6×10^3	26.8×10^3	2.87
0.5	11.2×10^3	17.2×10^4	17.6×10^4	-2.73

TABLE 2
SENSITIVITY OF J FOR SE(T) SPECIMEN

		Sensitivity of J ($\partial J/\partial a$) kJ/m^3		
a/W	J kJ/m^2	Prop. Method	Finite Diff.	Diff. %
0.25	6.20×10^3	14.7×10^4	14.4×10^4	1.82
0.5	3.70×10^5	17.1×10^6	16.6×10^6	3.29

TABLE 3
STATISTICAL PROPERTIES OF INPUT

Random Variable	Mean	COV	Probability Distribution
a/W	0.5	0-0.2	Uniform
E	207 GPa	0.05	Gaussian
α	8.073	0.1439	Lognormal
σ^∞	40-110 MPa	0.1	Gaussian
J_{Ic}	1243 kJ/m^2	0.47	Lognormal
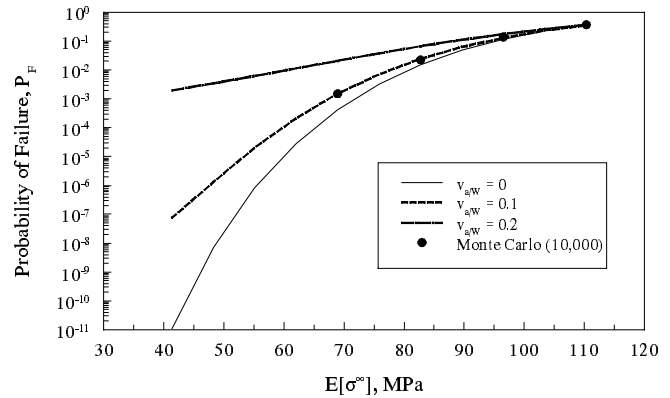
Figure 5: Failure probability of DE(T)

CONCLUSIONS

A new method was developed for continuum shape sensitivity analysis of a crack in a homogeneous, isotropic, nonlinearly elastic body subject to mode-I loading conditions. The method involves the material derivative concept of continuum mechanics, domain integral representation of the J-integral, and direct differentiation. Unlike virtual crack extension techniques, no mesh perturbation is required in the proposed method. Numerical examples have been presented to illustrate the proposed method. The results show that the maximum difference between the sensitivity of stress-intensity factors calculated using the proposed method and reference solutions obtained by the finite-difference method is less than four percent. Based on the continuum sensitivities, the first-order reliability method was formulated to perform probabilistic fracture-mechanics analysis. A numerical example is presented to illustrate the usefulness of the proposed sensitivity equations for probabilistic analysis. Since all gradients are calculated analytically, the reliability analysis of cracks can be performed efficiently.

REFERENCES

1. Hwang, C., Wawrzynek, P., Tayebi, A., and Ingraffea, A. (1998), *Engng. Frac. Mech.*, 59, 521.
2. Chen, G., Rahman, S., and Park, Y. H. (2001), accepted in *Comp. Mech.*
3. Taroco, E. (2000), *Comp. Meth. Appl. Mech. Engng.,* 188 (4), 697.
4. Haug, E., Choi, K., and Komkov, V. (1986), *Design Sensitivity Analysis of Structural Systems*, Academic Press, New York.
5. ABAQUS (2000), *User's Guide and Theoretical Manual*, Version 5.8, Hibbitt, Karlsson, and Sorenson, Inc., Pawtucket, Rhode Island.
6. Anderson, T. L. (1995), *Fracture Mechanics - Fundamentals and Applications*, CRC Press.
7. Madsen, H., Krenk, S., and Lind, N. (1986), *Methods of Structural Safety*, Prentice-Hall, Inc., Englewood Cliffs, New Jersey.

SHEAR LAG MODELLING OF THERMAL STRESSES IN UNIDIRECTIONAL COMPOSITES

Chad M. Landis

Department of Mechanical Engineering and Materials Science, MS 321,
Rice University, P.O. Box 1892, Houston, TX, 77025
landis@rice.edu, ph: 713-348-3609, fax: 713-348-5423

ABSTRACT

A two-dimensional shear lag model is presented to analyze the steady state distributions of stress and temperature in unidirectionally reinforced composites. Equations allowing for variations in axial displacement and temperature along any given fiber or matrix region are developed. The derivation of the governing equations is greatly simplified by the assumptions that displacements perpendicular to the fiber direction can be ignored, the axial displacement and temperature are uniform over the cross section of any fiber and the distributions of temperature and axial displacement are bilinear within the matrix regions. These equations are then solved for a configuration with uniformly spaced matrix cracks and used to determine the effective Young's modulus and thermal conductivity of the cracked material.

KEYWORDS

Composites, thermal stresses, shear lag

1. INTRODUCTION

The analysis of stress and strain in multi-fiber composites has been facilitated by the development of shear lag models. These shear lag models treat fibers as one-dimensional load carrying structures that transfer loads to one another through shear stresses within the matrix material. The original multi-fiber shear lag model was formulated by Hedgepeth[1] in 1961. Since then a number of researchers have enhanced this model by including effects like sliding at the fiber matrix interface or the load carrying capability of the matrix, see Landis and McMeeking[2]. A direct two-dimensional extension of the Hedgepeth[1] model was proposed by Beyerlein and Landis[3] to include the effects of matrix stiffness that reduces to the Hedgepeth[1] model in the appropriate limit. The work presented in this paper will build on the model of Beyerlein and Landis[3] to include the effects of steady state temperature distributions. These shear lag

models are most useful in large scale composite failure simulations like those carried out by Ibnabdeljalil and Curtin[4] and Landis *et al.*[5] where more detailed stress calculations would be untenable.

2. GOVERNING EQUATIONS

The model system considered is depicted in Figure 1 with the fibers separated by the matrix in a periodic fashion.
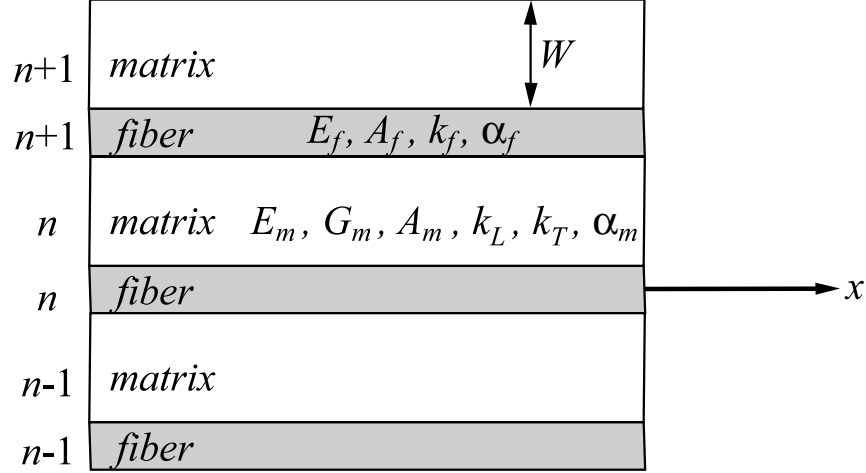
Figure 1: Two dimensional fiber/matrix configuration.

The Young's modulus, area, thermal conductivity and thermal expansion coefficient of the fibers are E_f, A_f, k_f and α_f. The Young's modulus, shear modulus, area, longitudinal thermal conductivity, transverse thermal conductivity, thermal expansion coefficient and width of the matrix regions are E_m, G_m, A_m, k_L, k_T, α_m and W. The thickness of the system is t, hence $A_m = Wt$. Following the procedure outlined by Landis and co-workers [2-3] the equations governing the axial displacement and temperature along the nth fiber, u_n^f and T_n^f, and the center of the nth matrix region, u_n^m and T_n^m, are

$$\left(1+\frac{\eta}{3}\right)\frac{d^2T_n^f}{dx^2} + \frac{\eta}{12}\frac{d^2T_n^m}{dx^2} + \frac{\eta}{12}\frac{d^2T_{n-1}^m}{dx^2} + 2\bar{k}\left(T_n^m + T_{n-1}^m - 2T_n^f\right) = 0 \tag{1}$$

$$\frac{\eta}{3}\frac{d^2T_n^m}{dx^2} + \frac{\eta}{12}\frac{d^2T_{n+1}^f}{dx^2} + \frac{\eta}{12}\frac{d^2T_n^f}{dx^2} + 2\bar{k}\left(T_{n+1}^f + T_n^f - 2T_n^m\right) = 0 \tag{2}$$

$$\left(1+\frac{\rho}{3}\right)\frac{d^2u_n^f}{dx^2} + \frac{\rho}{12}\frac{d^2u_n^m}{dx^2} + \frac{\rho}{12}\frac{d^2u_{n-1}^m}{dx^2} + 2\bar{G}\left(u_n^m + u_{n-1}^m - 2u_n^f\right) = \left(\alpha_f + \frac{\rho}{3}\alpha_m\right)\frac{dT_n^f}{dx} + \frac{\rho}{12}\alpha_m\left(\frac{dT_n^m}{dx} + \frac{dT_{n-1}^m}{dx}\right) \tag{3}$$

$$\frac{\rho}{3}\frac{d^2u_n^m}{dx^2} + \frac{\rho}{12}\frac{d^2u_{n+1}^f}{dx^2} + \frac{\rho}{12}\frac{d^2u_n^f}{dx^2} + 2\bar{G}\left(u_n^f + u_{n+1}^f - 2u_n^m\right) = \frac{\rho}{3}\alpha_m\frac{dT_n^m}{dx} + \frac{\rho}{12}\alpha_m\left(\frac{dT_{n+1}^f}{dx} + \frac{dT_n^m}{dx}\right) \tag{4}$$

$$\rho = \frac{E_f A_f}{E_m A_m} \quad , \quad \eta = \frac{k_f A_f}{k_L A_m} \quad , \quad \bar{G} = \frac{G_m t}{E_f A_f W} \quad , \quad \bar{k} = \frac{k_T t}{k_f A_f W} \tag{5}$$

The essential assumptions required to obtain these equation are that the material is constrained to displace in the x direction only, shear deformation and transverse temperature gradients in the fibers are neglected and the displacement or temperature profile along the transverse direction in the matrix is bilinear.

3. N-INDEPENDENT SOLUTIONS

In general Eqns. (1-4) represent a large set of coupled ordinary differential equations for the displacement and temperature in each fiber and matrix region. However, if the locations of imperfections, i.e. fiber or matrix cracks, are distributed uniformly over all fiber or matrix regions then Eqns. (1-4) reduce to four governing ordinary differential equations. In other words if the distributions of displacement and temperature are independent of the fiber or matrix region number n then the following equations govern the system:

$$\left(1+\frac{\eta}{3}\right)T_f'' + \frac{\eta}{6}T_m'' + 4\bar{k}\left(T_m - T_f\right) = 0 \tag{6}$$

$$\frac{\eta}{3}T_m'' + \frac{\eta}{6}T_f'' + 4\bar{k}\left(T_f - T_m\right) = 0 \tag{7}$$

$$\left(1+\frac{\rho}{3}\right)u_f'' + \frac{\rho}{6}u_m'' + 4\bar{G}\left(u_m - u_f\right) = \left(\alpha_f + \frac{\rho}{3}\alpha_m\right)T_f' + \frac{\rho}{6}\alpha_m T_m' \tag{8}$$

$$\frac{\rho}{3}u_m'' + \frac{\rho}{6}u_f'' + 4\bar{G}\left(u_f - u_m\right) = \frac{\rho}{3}\alpha_m T_m' + \frac{\rho}{6}\alpha_m T_f' \tag{9}$$

where T_f, T_m, u_f and u_m are the temperature and displacement distributions in all fibers and all matrix regions. The ' and the " denote first and second derivatives with respect to x. The general solutions to Eqns. (6-9) are

$$T_m = T_0 + q_0 x + C_{T1}e^{\beta_T x} + C_{T2}e^{-\beta_T x} \tag{10}$$

$$T_f = T_0 + q_0 x - \frac{\eta}{\eta+2}C_{T1}e^{\beta_T x} - \frac{\eta}{\eta+2}C_{T2}e^{-\beta_T x} \tag{11}$$

$$\begin{aligned} u_m = u_0 &+ \frac{\alpha_f + \rho\alpha_m}{\rho+1}T_0 x + \varepsilon_0 x + \frac{\alpha_f + \rho\alpha_m}{2(\rho+1)}q_0 x^2 \\ &+ C_{m1}e^{\beta_T x} - C_{m2}e^{-\beta_T x} + C_{u1}e^{\beta_u x} + C_{u2}e^{-\beta_u x} \end{aligned} \tag{12}$$

$$\begin{aligned} u_f = u_0 &- \frac{\left(\alpha_f - \alpha_m\right)\rho}{8\bar{G}(\rho+1)}q_0 + \frac{\alpha_f + \rho\alpha_m}{\rho+1}T_0 x + \varepsilon_0 x + \frac{\alpha_f + \rho\alpha_m}{2(\rho+1)}q_0 x^2 \\ &+ C_{f1}e^{\beta_T x} - C_{f2}e^{-\beta_T x} - \frac{\rho}{\rho+2}C_{u1}e^{\beta_u x} - \frac{\rho}{\rho+2}C_{u2}e^{-\beta_u x} \end{aligned} \tag{13}$$

$$C_{f1,2} = C_{T1,2}\frac{\eta\alpha_f - \rho\alpha_m - \dfrac{\beta_T^2 \eta\rho}{48\bar{G}}\left(4\alpha_f + \rho\alpha_m\right)}{\beta_T(\eta+2)\left[\dfrac{\beta_T^2 \rho}{48\bar{G}}(\rho+4)-(\rho+1)\right]} \tag{14}$$

$$C_{m1,2} = C_{T1,2} \frac{\eta\alpha_f - \rho\alpha_m + \dfrac{\beta_T^2\eta\rho}{48\overline{G}}\left[2\eta\alpha_f + \alpha_m\eta(\rho+2) + 2\alpha_m(\rho+4)\right]}{\beta_T(\eta+2)\left[\dfrac{\beta_T^2\rho}{48\overline{G}}(\rho+4) - (\rho+1)\right]} \tag{15}$$

$$\beta_T = \left(\frac{48k_T(\eta+1)}{k_L W^2(\eta+4)}\right)^{1/2}, \quad \beta_u = \left(\frac{48G_m(\rho+1)}{E_m W^2(\rho+4)}\right)^{1/2} \tag{16}$$

where T_0, q_0, u_0, ε_0, C_{T1}, C_{T2}, C_{u1} and C_{u2} must be determined from boundary conditions.

The general solution listed in Eqns. (10-16) can be used to determine the effective Young's modulus and effective longitudinal thermal conductivity of a composite with a uniform matrix crack spacing. Consider the crack geometry illustrated in Figure 2.
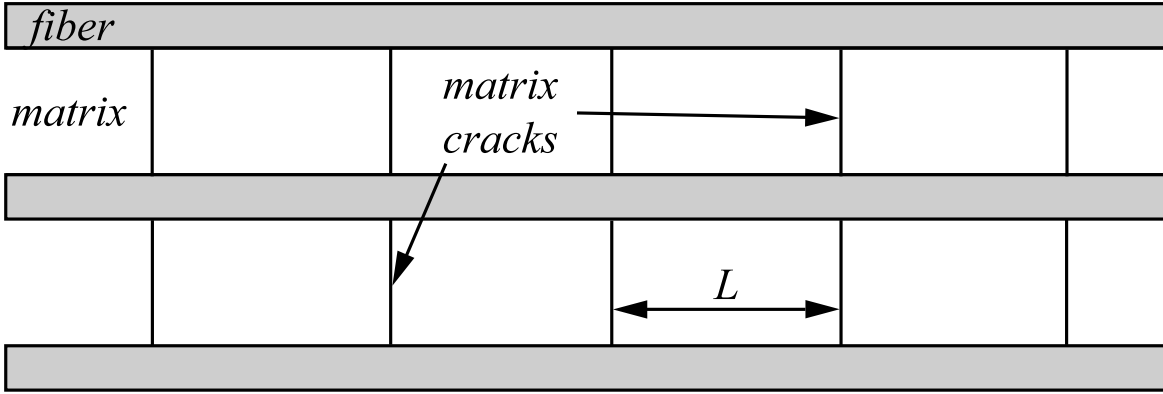
Figure 2: Uniform matrix crack spacing configuration. The matrix cracks are assumed to be traction-free and perfectly insulating.

To analyze the effective thermal conductivity of the cracked composite only the temperature solution needs to be considered and to determine the effective modulus only the displacement solution needs to be considered. Since the distribution of temperature or displacement is bilinear across a matrix region only the *average* heat flux or stress at a matrix crack can be specified to be zero. So for the thermal conductivity calculation the average temperature gradient is set to zero at $x=0$ and at $x=L$. The solution for the temperature distribution in a given segment of material between two matrix cracks is

$$T_f = T_0 + q_0\left[x + \frac{\eta}{\beta_T}\frac{\cosh\beta_T x - \cosh\beta_T(x-L)}{\sinh\beta_T L}\right] \tag{17}$$

$$\overline{T}_m = T_0 + q_0\left[x + \frac{1}{\beta_T}\frac{\cosh\beta_T(x-L) - \cosh\beta_T x}{\sinh\beta_T L}\right] \tag{18}$$

where $\overline{T}_m = (T_f + T_m)/2$ is the average temperature across the matrix at a given x location. The effective thermal conductivity of the composite is then just the average heat flux through the composite divided by the average temperature gradient across the same region. Note that care must be taken to include temperature jumps across the matrix cracks in these averages. The effective thermal conductivity of the cracked composite is

$$k_c = \left(\frac{k_f A_f + k_L A_m}{A_f + A_m} \right) \bigg/ \left(1 + \frac{2\eta}{\beta_T L} \frac{\cosh\beta_T L - 1}{\sinh\beta_T L} \right) \qquad (19)$$

Eqn. (19) is identical to the result obtained by Lu and Hutchinson [6]. From a solution similar to Eqns. (17-18) for the displacements the effective Young's modulus is

$$E_c = \left(\frac{E_f A_f + E_m A_m}{A_f + A_m} \right) \bigg/ \left(1 + \frac{2\rho}{\beta_u L} \frac{\cosh\beta_u L - 1}{\sinh\beta_u L} \right) \qquad (20)$$

Notice that when the crack spacing, L, goes to infinity then the composite conductivity or modulus is the area fraction weighted average of the fibers and matrix. When L goes to zero then the conductivity and modulus of the composite are $k_c = k_f A_f / (A_f + A_m)$ and $E_c = E_f A_f / (A_f + A_m)$.

Another simple solution for the uniform matrix crack configuration is the distribution of stress in the fibers and matrix when the temperature of the composite, T, is uniform. The fiber stress, σ_f, and the average matrix stress, $\bar{\sigma}_m$, are

$$\sigma_f = E_f (\alpha_m - \alpha_f) T \frac{\rho}{\rho+1} \left[1 + \frac{\sinh\beta_u(x-L) - \sinh\beta_u x}{\sinh\beta_u L} \right] \qquad (21)$$

$$\bar{\sigma}_m = E_m (\alpha_f - \alpha_m) T \frac{1}{\rho+1} \left[1 + \frac{\sinh\beta_u(x-L) - \sinh\beta_u x}{\sinh\beta_u L} \right] \qquad (22)$$

Notice since there is no applied load, only temperature, that $\sigma_f A_f + \bar{\sigma}_m A_m = 0$.

4. DISCUSSION

The simple solutions presented in Eqns. (10-16) do not exploit the true value of the shear lag model. Generally, solutions to the equations of thermoelasticity could be obtained with series solutions for the simple geometry considered in Figure 2 leading to more accurate estimates of the composite conductivity and modulus. However, it is difficult to obtain exact solutions for the distributions of stress and temperature around even a single fiber break. Contrarily, simple superposition techniques exists that can solve Eqns. (1-5) for any finite number of arbitrarily located fiber or matrix cracks. Hence, the simplified shear lag model is most useful in large failure simulations like those carried out in [4] and [5] where rapid solutions for the interactions of cracks with one another and the loading are important.

REFERENCES

1. Hedgepeth, J.M. (1961) NASA TN D-822.
2. Landis, C.M. and McMeeking, R.M. (1998) *Int. J. Solids Structures*, 36, 4333-4361.
3. Beyerlein, I.J. and Landis, C.M. (1999) *Mechanics of Materials*, 31, 331-350.
4. Ibnabdeljalil, M. and Curtin, W.A. (1997) *Int. J. Solids Structures*, 34, 2649-2668.
5. Landis, C.M., Beyerlein, I.J. and McMeeking, R.M. (2000) *J. Mech. Phys. Solids*, 48, 621-648.
6. Lu, T.J. and Hutchinson, J.W. (1995) *Philos. Trans. R. Soc. London Ser. A*, 351, 595-610.

SHORT FATIGUE CRACK GROWTH UNDER MULTIAXIAL NONPROPORTIONAL LOADING

J. HOFFMEYER [1], R. DÖRING [2], T. SEEGER [1] AND M. VORMWALD [2]

[1] Fachgebiet Werkstoffmechanik, TU Darmstadt, 64287 Darmstadt, Germany
[2] Institut für Strukturmechanik, Bauhaus-Universität Weimar, 99421 Weimar, Germany

ABSTRACT

Initiation and growth of short fatigue cracks under nonproportional cyclic push-pull and torsion loading have been investigated. The final aim is the improvement of the accuracy of lifetime prediction. The crack growth has been studied experimentally using the plastic replica technique in the length range from 5µm to 500µm. More than 95% of the fatigue life is governed by short fatigue crack growth. A critical plane approach based on elastic-plastic fracture mechanics is used to model the fatigue process. A Paris-type crack growth law, using the effective cyclic J-integral ΔJ_{eff} and a mixed mode criterion, is integrated to give crack growth curves. The J-integral and crack opening stresses and strains are calculated with approximation equations. Stress-strain paths are predicted using the plasticity model of Jiang [1]. The agreement between model and real damage evolution is shown comparing experimentally determined crack growth curves, cracking directions and life curves for the materials S460N and Al 5083.

KEYWORDS

fatigue, short cracks, multiaxial nonproportional loading, lifetime prediction, mixed mode, cyclic plasticity

INTRODUCTION

For metallic materials the number of cycles to initiate a fatigue crack of technical size of about 0.5mm is determined by the growth of short cracks [2]. Therefore, the fatigue process can be successfully modelled based on fracture mechanics. A significant improvement of lifetime predictions for uniaxial [3, 4] and proportional multiaxial [5, 6] variable amplitude loading has been achieved applying such concepts. Based on this the crack nucleation and the stage of short fatigue crack growth under nonproportional multiaxial loading is investigated and modelled here. The model is described and its accuracy is examined.

Fatigue cracks often nucleate in areas close to the surface where the crystalline microstructure exhibits minor microscopic defects. In metallic alloys these are usually inclusions or surface defects from the manufacturing process. In pure or smoothly finished materials crack nucleation may arise from intrusions and extrusions resulting from micro-plastic deformations. An overview is given for example by Suresh [2] or McDowell [7], with special reference to multiaxial loading by Socie and Marquis [8]. For the microcrack growth, following the microcrack nucleation, the stages I and II are distinguished. During stage I the growth is determined by the maximum shear stress amplitudes. Dependent on the microstructure and the amplitudes a change of the crack growth plane occurs into the direction perpendicular to the maximum normal stress amplitude (stage II). The phase of crack nucleation, the stage I and II short crack growth is illustrated in damage maps by Socie and Marquis [8]. Nucleation, stage I and early stage II crack growth is influenced by

the microstructure. Models describing such effects are published for uniaxial or proportional multiaxial loading. An extension to nonproportional cases has been recently proposed by Suhartono [9]. It is based on a concept proposed by Socie und Furman [10]. Beyond this, more than 100 hypotheses for lifetime prediction under multiaxial cyclic loading have been published during the last decade. A survey of the current state of the art can be found in [8]. The hypotheses can be divided into stress, strain, energy and fracture mechanics based models. The concept proposed in this paper belongs to the latter.

MATERIAL DATA AND EXPERIMENTAL PROCEDURE

The materials investigated are the fine grained steel S460N (E = 208500 MPa, $R_{p0.2}$ = 500 MPa, R_m = 643MPa) and the aluminium alloy Al 5083 (E = 68000 MPa, $R_{p0.2}$ = 169 MPa, R_m = 340 MPa). The steel shows a cyclic hardening for high and softening for low strain amplitudes. Al 5083 exhibits cyclic hardening and behaves linearly-elastically except for very high strains. The material properties are described in detail by Savaidis [6]. The multiaxial tests have been performed on unnotched thin-walled tube specimens. The internal diameter is 36 mm, the wall thickness 2.5 mm. Standard hourglass shaped specimens (diameter 6 mm) have been used for uniaxial tests and for the identification of the material parameters of the plasticity model. The tests have been conducted on a hydraulic tension-torsion machine at room temperature under strain control. For further details see [5, 11]. Damage mechanisms and the lives have been investigated under in-phase and 45º and 90º out-of-phase constant amplitude loading. Life to technical crack size, cyclic deformation behaviour, short crack growth and crack closure have been determined. During some of the tests replicas have been taken to examine the nucleation and growth of short cracks. Crack growth could thus be traced back to 2-10µm surface crack length. For the examination of crack closure replicas have been taken at different positions of one hysteresis loop in 90º out-of-phase tests [11].

MODELLING OF FATIGUE CRACK GROWTH

A reliable model for the calculation of stress-strain paths is a prerequisite for an accurate lifetime prediction. Therefore, Jiang`s plasticity model [1] is used here. Details of its application may be found elsewhere [Hof00]. The model proposed in the following is used to calculate the crack growth of short fatigue cracks applying fracture mechanics. Simplifying assumptions had to be made for such a model as outlined below:
1. The directions of the principal axes are not constant under nonproportional multiaxial loading. The critical plane is determined iteratively by carrying out the calculations for each potential direction. The plane with the highest crack growth rate is regarded as the critical one.
2. As there are no closed hysteresis loops the usual rainflow cycle counting has to be substituted. It is modified in the way that the stresses and strains perpendicular to the plane under consideration are treated as primary damage variable as described in [12].
3. A semi-circular surface crack of the initial length a_0 is assumed that keeps its direction and remains in its plane. The quantity a_0 is determined from the strain life curve of uniaxial experiments by resolving the crack growth law in terms of a_0. The growth of a single crack is modelled. The influence of crack coalescence and changes from stage I to II are – in case of occurrence – only included in an averaging way by the initial crack length a_0 .
Because the requirements for applying linear-elastic fracture mechanics are not fulfilled for short cracks elastic-plastic parameters have to be applied. The crack growth rate is described by a Paris-type law using an effective, that means crack closure adjusted cyclic crack tip parameter, eqn. (1). The approximation equation for the cyclic J-integral ΔJ according to Dowling [13] is used. For nonproportional multiaxial loading the equation has to be modified to consider the mixed mode situation, i.e. the combination of crack opening mode I and plane shear mode II, eqn. (2) and (3). Life (to cracks of technical size) is defined as the number of cycles calculated from the fictitious initial crack length a_0 to a = 250µm.

$$\frac{\mathrm{d}a}{\mathrm{d}n} = C\left(\Delta J_{\mathrm{eff}}\right)^m \qquad (1) \quad ; \quad \Delta J_{\mathrm{eff}} = \Delta J_{\mathrm{I,eff}} + \Delta J_{\mathrm{II,eff}} \qquad (2)$$

$$\Delta J_{I,eff} = \left(1.24 \cdot \frac{\left(\Delta\sigma_{eff}\right)^2}{E} + 1.02 \cdot \frac{\Delta\sigma_{eff} \cdot \Delta\varepsilon_{p,eff}}{\sqrt{n'}}\right) \cdot a \quad , \quad \Delta J_{II,eff} = \left(1.24 \cdot \frac{\left(\Delta\tau_{eff}\right)^2}{G} + 1.02 \cdot \frac{\Delta\tau_{eff} \cdot \Delta\gamma_{p,eff}}{\sqrt{n'}}\right) \cdot a \tag{3}$$

The index „p" indicates plastic deformation, E, G and n' are Young's and shear modulus and the cyclic hardening exponent. As a mixed mode state occurs at the crack tip an equivalent quantity has to be derived from the mode-separated parameters. For static and proportional cyclic loading a number of mixed mode fracture criteria have been derived (for long cracks). However no comparable criteria are known to the authors for nonproportional cyclic loading, particularly in the realm of elastic-plastic fracture mechanics. Therefore, the J-integrals are simply added in the model, eqn. (2), yielding capabilities to improvements by results of further research on this topic.

Crack closure is considered as an essential aspect because it explains sequence effects for service loads [3]. In the model it is supposed to be responsible for sequence effects, the description of the mean stress dependency, and the ratio of multiaxiality $\lambda = \sigma_2/\sigma_1$. Crack opening stresses are estimated using an equation originally proposed by Newman [14], eqn. (4), for long cracks, which is modified and extended here by certain terms to improve and include the effects mentioned above.

$$\sigma_{op} = \begin{cases} \sigma_O \cdot \left(A_0(\lambda) + A_1(\lambda) \cdot R + A_2(\lambda) \cdot R^2 + A_3(\lambda) \cdot R^3 + c_\lambda(\lambda)\right) & \text{for } \sigma_{min}/\sigma_{max} > 0 \\ \sigma_O \cdot \left(A_0(\lambda) + A_1(\lambda) \cdot R + c_\lambda(\lambda)\right) & \text{for } \sigma_{min}/\sigma_{max} \leq 0 \end{cases} \tag{4}$$

$$A_0(\lambda) = 0{,}535 \cdot \cos\left(\frac{\pi}{2} \cdot \frac{\sigma_O}{\sigma_F(\lambda)}\right) + a_{mitt}(\lambda) \qquad ; \qquad A_1(\lambda) = 0{,}344 \cdot \frac{\sigma_O}{\sigma_F(\lambda)} + a_{mitt}(\lambda) ;$$

$$A_3 = 2 \cdot A_0 + A_1 - 1; \quad A_2 = 1 - A_0 - A_1 - A_3; \quad c_\lambda(\lambda) = 0{,}535 \cdot \cos\left(\frac{\pi}{2} \frac{\sigma_w(\lambda)}{\sigma_F(\lambda)}\right) - 0{,}344 \cdot \frac{\sigma_w(\lambda)}{\sigma_F(\lambda)} + \frac{\Delta\sigma_o}{\sigma_w(\lambda)} - 1$$

$$\sigma_F(\lambda) = \frac{\sigma_F}{\sqrt{1 - \lambda + \lambda^2}}, \qquad \sigma_w(\lambda) = \frac{\sigma_w}{\sqrt{(1+\lambda)^2 - \left(\frac{\sigma_w}{\tau_w}\right)^2 \cdot \lambda}}, \qquad \sigma_{sch}(\lambda) = \frac{\sigma_{sch}}{\sqrt{(1+\lambda)^2 - \left(\frac{\sigma_{sch}}{\tau_{sch}}\right)^2 \cdot \lambda}}$$

$$a_{mitt}(\lambda) = 1 - 0.535 \cos\left(\frac{\pi}{2} \frac{\sigma_{sch}(\lambda)}{\sigma_F(\lambda)}\right) - \frac{\sigma_w(\lambda)}{\sigma_{sch}(\lambda)}\left[1 + 0.344 \frac{\sigma_w(\lambda)}{\sigma_F(\lambda)} - 0.535 \cos\left(\frac{\pi}{2} \frac{\sigma_w(\lambda)}{\sigma_F(\lambda)}\right) + c_\lambda(\lambda)\right]$$

$\sigma_F(\lambda)$ is a fictitious yield stress in terms of λ, $\sigma_w(\lambda)$ is the endurance limit (for $R = \sigma_{min}/\sigma_{max} = -1$) under uniaxial loading, $\sigma_{sch}(\lambda)$ is the corresponding endurance limit for $R = 0$. Thus, the mean stress dependency is taken into account via σ_w and σ_{sch}, the effect of the ratio of multiaxiality enters the equation via the shear endurance limits for $R = -1$ and $R = 0$, respectively.

For shear stress dominated cycles the roughness of the crack flanks is the most important quantity. This is not yet described by the model. It is assumed that shear stresses can only act at the crack tip when the crack is opened by mode I loading. When the crack is closed the tip is protected by friction and surface contact. Experimental investigations on crack opening behaviour support this idea, but there is a continuous transition between completely closed and completely opened crack.

RESULTS: CRACK GROWTH CURVES, CRACK ANGLES AND STRAIN LIFE CURVES

Replicas taken during some of the tests have been examined by scanning electron microscopy yielding series of crack pictures, fig. 1, and crack growth curves, fig. 2. Microcracks could be found already after 2-5% of lifetime. This means that nucleation of critical cracks is completed in a very early stage of fatigue. This justifies its neglecting in the model. As mentioned this portion of fatigue life is implicitly considered by the starting crack length a_0.

Cracks were traced back to ranges under 10 µm. For all investigated loading cases and crack modes the characteristic growth of short cracks, e.g. [7], was observed. Microcracks grow fast under accelerations and decelerations, followed by a stage of slower growth and finally the crack length increases dramatically. The data of table 1 together with the load sequences form the input data for the calculations. For S460N the plasticity model was applied. For Al 5083 linear-elastic deformation was assumed.

For both materials the crack growth curves for 90º and 45º out-of-phase loading can be described well by the model, fig. 2. For torsion with a superimposed static normal stress the calculation is slightly conservative for S460N. There are noticeable effects of deceleration of crack growth for S460N, especially under torsion loading indicating roughness induced closure. Generally only between 3 and 5 cracks could be detected. Their distance was too large to cause any interaction.

n = 1512   n = 3500   n = 8507   n = 17011
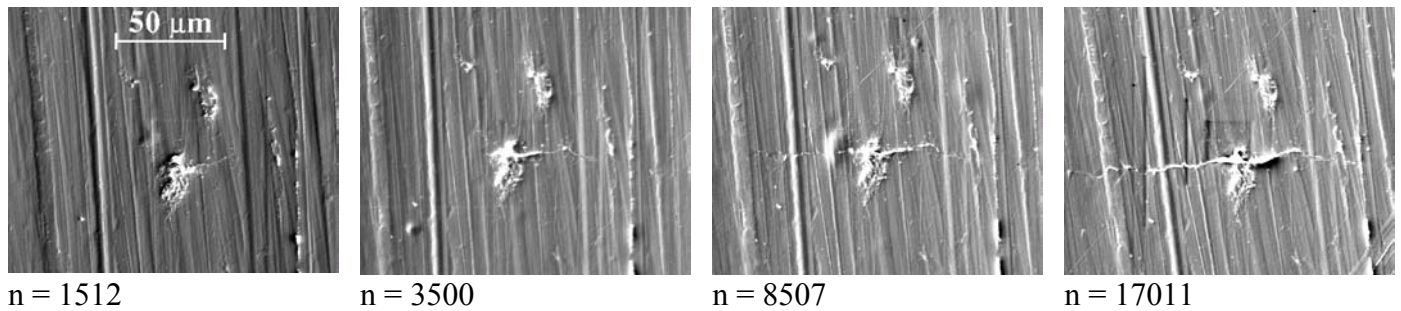
Figure 1: Short crack; Al 5083; ε_a=0.231%; γ_a=0.4%; 90° out-of-phase loading; life to failure: 26000 cycles

Table 1. Input data for the short crack growth model

Material	C [mm/cyc. $(N/mm)^{-m}$]	m [-]	$\Delta K_{th,\ eff}$ [MPa·mm$^{1/2}$]	σ_w [MPa]	τ_w [MPa]	$\Delta\sigma_{sch}/2$ [MPa]	σ_F [MPa]	a_0 [µm]
Al 5083	$2\cdot10^{-4}$	1.55	28	180	105	130	352	25
S460N	$3.9\cdot10^{-5}$	1.575	110	340	200	245	432	33
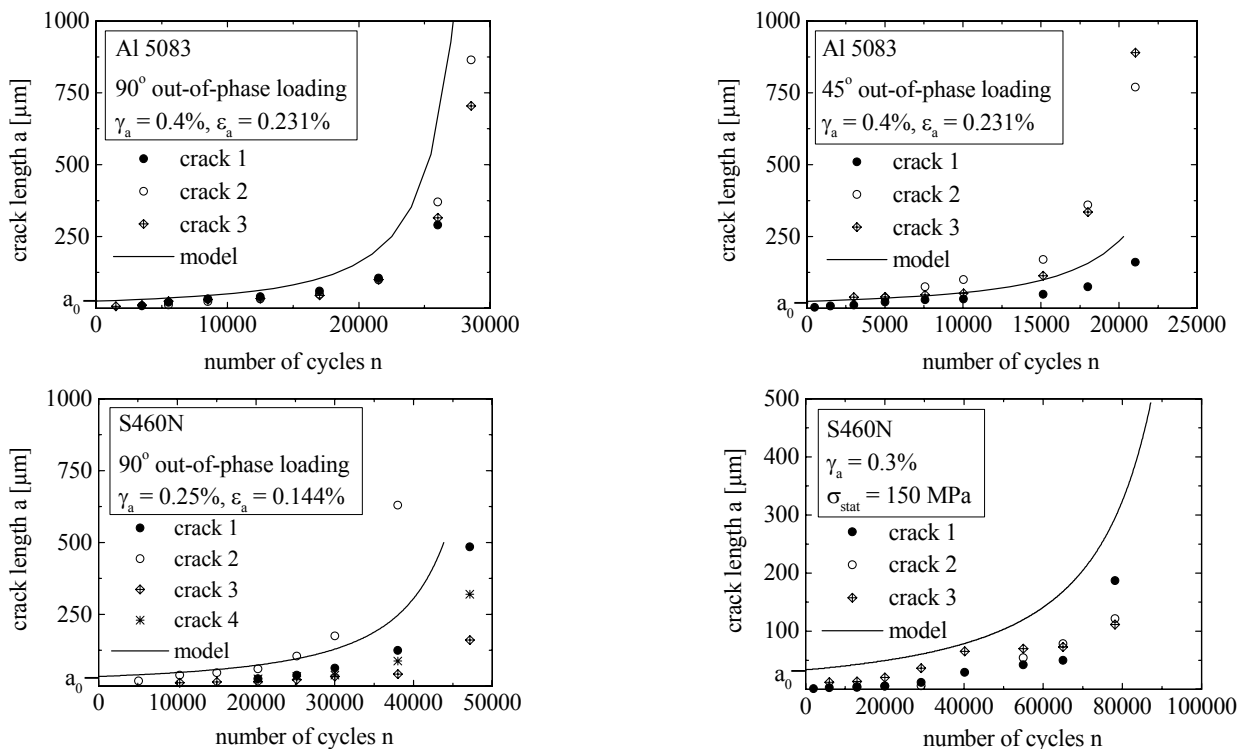
Figure 2: Comparison of short crack growth curves, calculated and determined by replicas

As the critical plane is determined by iteration, angles of surface cracks are obtained by the simulations. The orientations give information about the crack mode and are basis for the choice of crack driving force pa-

rameters. Under push-pull and proportional loading short cracks grew as mode I cracks perpendicular to the maximum principal stress amplitude, under torsion in the directions of the maximum shear stress amplitude [Sav97]. Experimental results for out-of-phase loading show clearly the good correlation between simulation, where mode I driven growth is assumed, and experiment, fig. 3 and 4. For S460N cracks angles of 5° to 25° were measured in the very early stage of crack growth. For longer cracks a value of 20° was found, fig. 3. The calculation yields a constant value of 19°. For out-of-phase loading the model describes no dependency of the angles on the crack length but on plastic deformations. For elastic material behaviour, as assumed for the Al 5083, an angle of 0° is calculated for 90° out-of-phase loading. At higher (plastic) amplitudes the angle is supposed to increase similar as for the steel. For Al 5083 crack angles of 4° were found in the very early stage in this experiment. The orientation changes with the growing crack to 15°, fig. 4. Reason for deviations could be plastic deformations. Under 45° out-of-phase loading values from 30° to 50° have been measured, the simulation yields 25°. For proportional loading angles of 30° to 50° have been determined in the experiment and 26° in the calculation.

The microcracks and short cracks usually did not change their orientation. If however this change occurred, it happened continuously. No distinct kinks as a consequence of a transition from mode II to mode I have been observed. This justifies the model assumption that cracks remain plane. The results are accurate if mode I controlled crack growth occurs. For shear mode crack growth, as observed under pure cyclic torsion, deviations arise because its accurate consideration would require an extended crack growth criterion.

a) n=30000 (microcrack) b) n=47100 (short crack) c) comparison with calculation

20° experiment
19° calculation
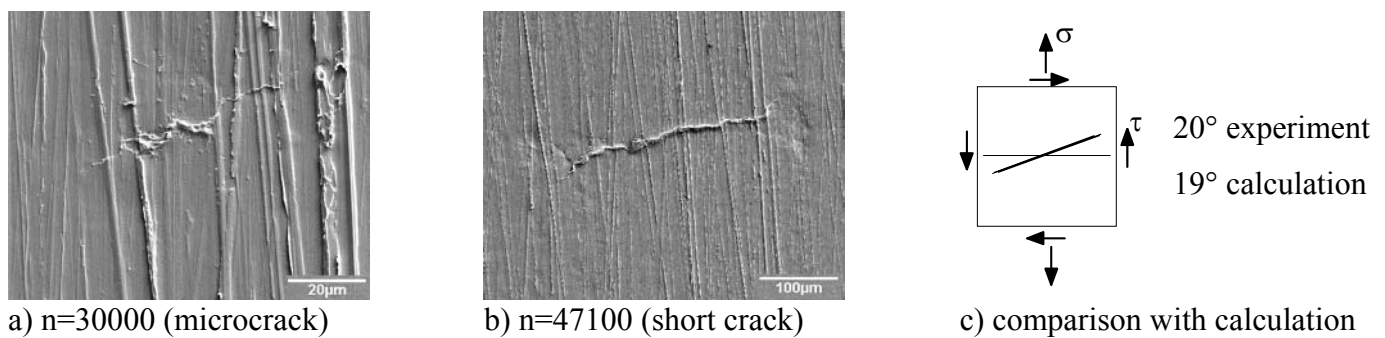
Figure 3: Crack angles: a) microcrack and b) short crack (S460N; 90° out-of-phase loading; $\varepsilon_a = 0.144\%$, $\gamma_a = 0.25\%$; polishing marks in direction of specimen axis)

a) n=12500 (microcrack) b) n=28500 (crack of technical size)

15° experiment
0° calculation
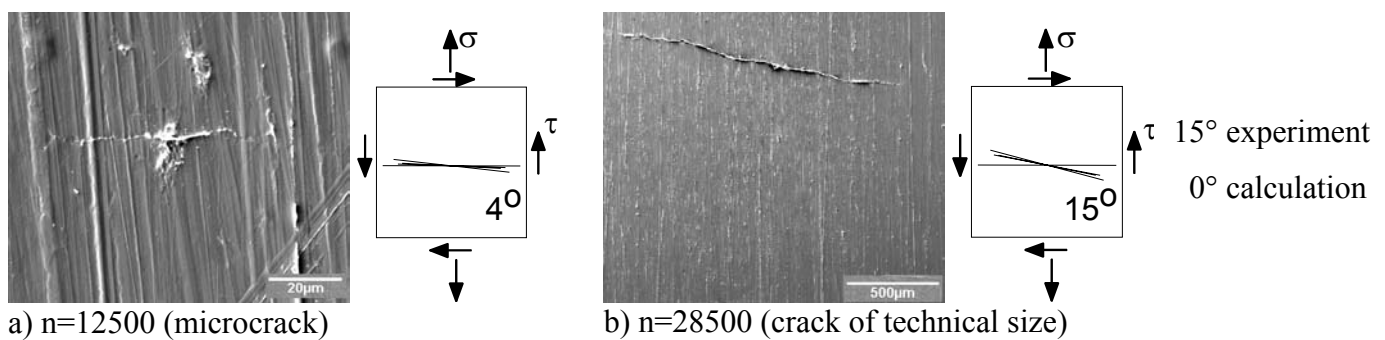
Figure 4: Crack angles: a) microcrack and b) crack of technical size (Al 5083, 90° out-of-phase loading, $\varepsilon_a = 0.231\%$, $\gamma_a = 0.4\%$)

Under 45° and 90° out-of-phase loading for both materials the fatigue life is slightly shorter compared to proportional loading, fig. 5. For all phase-shifts the simulated lives agree well with the experimentally determined lives for S460N. The lifetime prediction results tend to slightly underestimate lives except for severe plastic deformations under 90° out-of-phase loading. In the simulations and experiments the strain life curves for 45° and 90° phase-shifts are close together. The conspicuous convolution of the strain life curve for 90° out-of-phase loading results from the determination of the critical plane that changes with higher amplitudes. Cross-hardening is not considered in the plasticity model. This might lead to deviations in the lifetime prediction. Also for Al 5083 the calculations give accurate results for all phase-shifts. Under 90° out-of-phase loading calculated lives agree with the experimentally determined lives as shown for S460N. At the highest strain plastic deformations ought to be considered. Also for Al 5083 the strain life curves for

45° and 90° phase-shifts are close together in the simulation and experiment. By using a mixed mode criterion and plasticity including cross-hardening further improvements could be achieved.
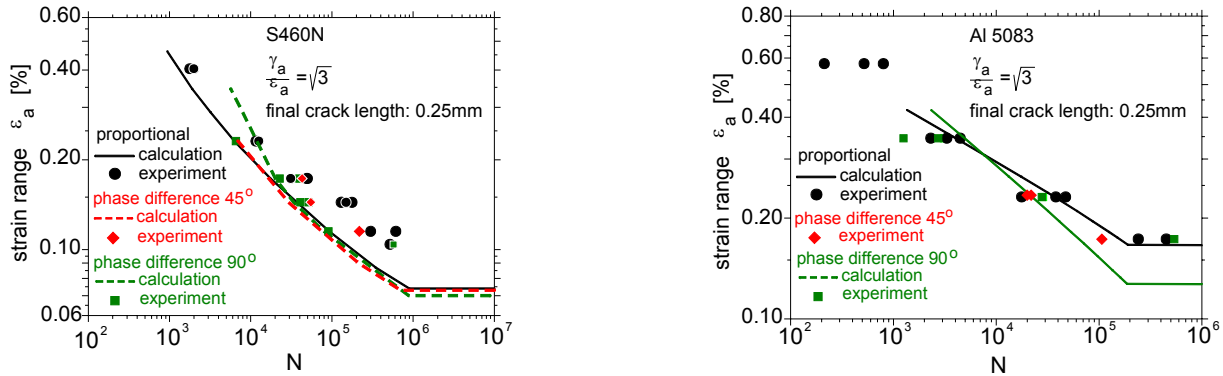
Figure 5: Strain life curves: Influence of out-of-phase loading on fatigue life and comparison of calculated and experimentally determined lives for S460N (a) and Al 5083 (b)

SUMMARY

The proposed concept can be used to calculate the growth of short fatigue cracks to technical size under nonproportional multiaxial loading with good to acceptable accuracy. The agreement of the theoretical perceptions as stated in the model with the real damage behaviour was shown by comparisons of calculated and experimentally determined crack growth curves, crack directions and life curves. Jiang's plasticity model is employed to describe the plastic deformation behaviour. Crack growth in a critical plane is computed from a Paris-like crack growth law using the cyclic J-integral for mixed-mode loading including crack closure. The essential damage mechanisms and quantities that influence the fatigue life are considered. Further investigations regarding mode II crack growth, mixed mode criteria and crack closure will be necessary for improving the lifetime prediction. For the moment the model is not intended to explicitly describe influences of the microstructure, coalescence, microcrack initiation and stage I crack growth, and crack growth at notched components.

ACKNOWLEDGEMENT

REFERENCES

1. Jiang, Y. (1993). PhD. Thesis, University of Illinois at Urbana-Champaign.
2. Suresh, S. (1993). *Material Science and Technology*, 6, 509.
3. Vormwald, M. (1989). PhD. Thesis, TH Darmstadt.
4. Vormwald, M.; Heuler, P. and Krae, C. (1994). In: *ASTM STP 1231*, pp. 221-240, West Conshohocken.
5. Savaidis, G. (1995). PhD. Thesis, TH Darmstadt.
6. Savaidis, G. and Seeger T. (1997). In: *Proceed. of the 5th Int. Conf. On Biaxial/Multiaxial Fatigue and Fracture*, Volume I, pp.81-98, Cracow.
7. McDowell, D.L. (1996). *Int. Journ. Fracture*, 80, 103.
8. Socie, D. F. and Marquis, G.B. (2000). *Multiaxial Fatigue*. SAE Warrendale, ISBN 0-7680-0453-5.
9. Suhartono, H.A. (2000). PhD. Thesis, TU Clausthal.
10. Socie, D. F. and Furman, S. (1996). In: *Fatigue 96, Proc. 6th Int. Fat. Congress*, pp. 967, Lütjering, G., Nowack, H. (Eds.), Elsevier, Oxford.
11. Hoffmeyer, Döring, Schliebner, Vormwald, Seeger. (2000). *Report FD-04/2000*, TU Darmstadt.
12. Bannantine, J.A. and Socie, D.F. (1989). In: *3rd Int. Conf. biaxial/multiaxial fatigue*, pp. 12ff, Stuttgart.
13. Dowling, N.E. and Begley, J.A (1976). In*: Mechanics of crack growth, ASTM STP 590*, pp. 82-103.
14. Newman, J.C. Jr. (1984). *Int. Journ. Fracture*, 24, R131.

Simulation of Adiabatic Shear Band Propagations

Shaofan Li[1] Wing Kam Liu[†][2], and Ares J. Rosakis[‡][3]

Department of Civil and Environmental Engineering,
University of California, Berkeley, CA 94720 U.S.A.
†Department of Mechanical Engineering, Northwestern University,
2145 Sheridan Road, Evanston, IL 60208 U.S.A.
‡Graduate Aeronautical Laboratories, California Institute of Technology,
Pasadena, CA 91125 U.S.A.

Abstract

Constitutive modeling and numerical simulation of dynamic shear band propagation in an impact-loaded pre-notched plate has been carried out in both two and three dimensions.

It has been found that (1) There is strain rate concentration region in front of an adiabatic shear band tip with multiple dimensional character, which is believed to be induced by wave trapping mechanism (Wu and Freund (1984)). It implies that a possible singular strain rate field exists in front of the shear band tip, which is in contrast with the notion that adiabatic shear band tip is diffused in nature (Gioia and Ortiz (1996)). (2) There is a thermal-mechanical instability occurring inside fully grown adiabatic shear band in the post-bifurcation regime, which supports the recent experimental observation by Guduru et al Guduru et al. (2001b). The authors believed that this newly discovered thermal-mechanical instability suggests a second instability that might be used as the criterion for the onset condition of adiabatic strain localization.

1 Strain rate concentration

It has been found in the numerical simulation that there is high strain rate region ahead of the adiabatic shear band tip. This region appears to be locally

---

[1] corresponding author, li@ce.berkeley.edu
[2] w-liu@northwestern.edu
[3] rosakis@aero.caltech.edu

self-similar in shape, and has extremely high strain rate concentration. In Fig. 1, the spatial distribution of effective strain rate observed in numerical computation is juxtaposed with temperature signature of the adiabatic shear band. It indicates that there exists an asymptotic strain rate tensor field moving with the adiabatic shear band tip. We postulated that this high concentrated strain rate field is induced by a pointwise "wave trapping" mechanism (see one-dimensional (1D) model by Wu and Freund (1984)). Based on Wu-Freund 1D linear (or logarithmic) rate sensitivity model, one may expect that the strain rate will become unbound at the shear band tip. To the authors' knowledge, the simulations shown here is the first numerical realization reported of wave trapping induced strain rate concentration in front of an adiabatic shear band tip in multiple dimensions. Most of previous studies on shear band tip processing zone failed to take into account the wave-trapping mechanism.

It is natural to draw a comparison between asymptotic strain rate tensor field in front of an adiabatic shear band with the asymptotic stress tensor field in front of a brittle crack. It is possible that there is a local, autonomous, self-similar, high strain rate concentration field at the adiabatic shear band tip, playing a similar role as the autonomous singular stress field at a propagating crack tip in moving crack tip (See Fig. 1).

Based on this analogy, an adiabatic shear band toughness may be obtained from the intensity factors of the strain rate field, just as stress intensity factors used as the measure of fracture toughness. It is speculated that adiabatic shear localization may be controlled by the intensity of strain rate tensor field ahead of the adiabatic shear band tip. After effective strain rate reaches a certain level, it causes damage as well as stress collapse in the newly formed material instability zone, i.e. shear band tip front. It then significantly reduces the flow stress carrying capacity at the tip, which leads to shear stress concentration in the undamaged region and drastic narrowing of the band width, i.e. strain localization and advance of the strain localization zone.

Since in the adiabatic shear localization, there is a gap between softening-instability and strain localization. Stress collapse inside instability zone signals the onset of the localization Wright and Walter (1987); Wright (1990). An invariant criterion to measure the onset of adiabatic strain localization is still missing.

2 Thermal-mechanical instability inside shear band

In most previous studies of adiabatic shear bands, the field variables, such as temperature, shear strain, or effective stress distributions are found smoothly varying along the shear band width Oilellio and Olmstead (1997a,b); Wright

2
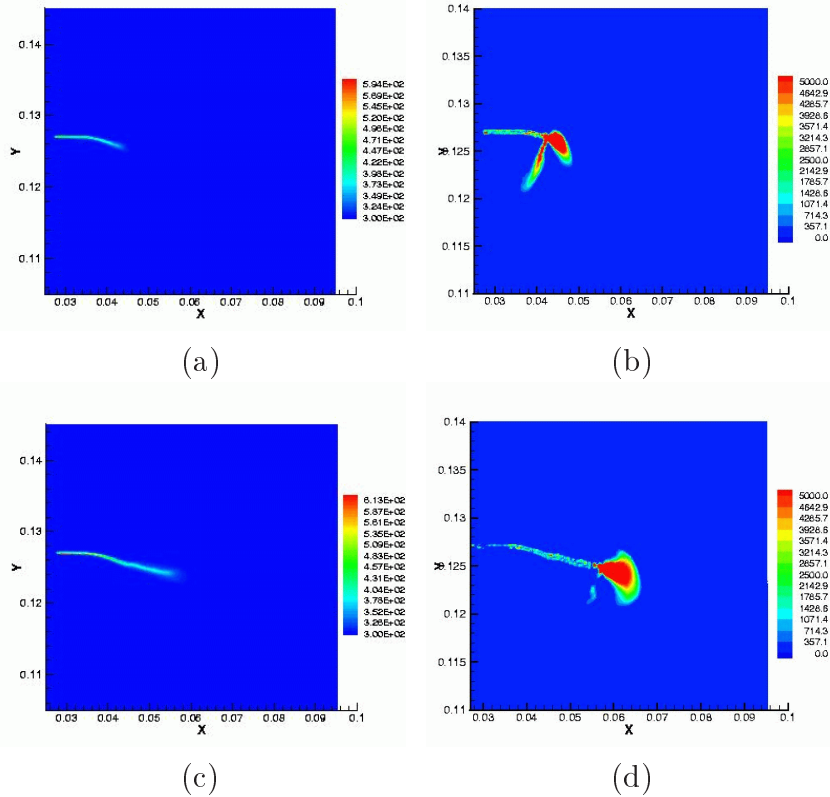
Fig. 1. Temperature contours (a,c) and strain rate contours ($V = 37m/s$) (b,d) ahead at the tip of the shear band : (a), (b) $t = 12\mu s$; (c), (d) $t = 24\mu s$;

and Ockendon (1992); Wright and Ravichandran (1997); Dinzart and Molinari (1998), i.e. there is basically no "life" within the narrow region inside the shear band.

The numerical simulations reveals that there is periodic oscillation in the temperature distribution within the adiabatic shear band both in space and time (Fig. 2). The numerical results support the recent experimental measurement done by Guduru et al. (2001a), in which it was found that the temperature inside the adiabatic shear band is not uniform, nor quiescent, but has a periodic fluctuation and oscillatory pattern. We compare the optical measurement with numerical computations. The experimental results (Fig. 2a,b,c) are juxtaposed with numerical results (Fig. 2d,e,f). As shown in Fig. (2), there is a strong qualitative agreement between experimental data and numerical results.

In the experiment conducted by Guduru et al. (2001b,a), the adiabatic shear band has an initial width about 100 μm (Fig. 2 a). As the localized high temperature starts to diffuse (yellow or green background in Fig. 2 a, b, c), the shear band width gradually increase to about 300 μm or more. Because of the absence of heat conduction in numerical simulation, the shear band width remain the same throughout the course of simulation, at approximately
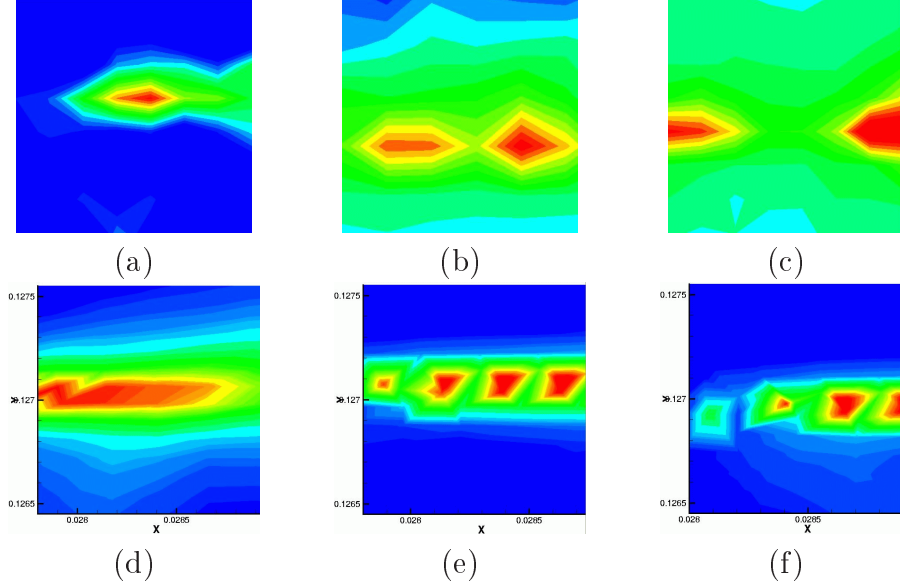
Fig. 2. Qualitative comparisons between experimental data and numerical computation on temperature distribution within the shear band ($V = 37m/s$): (a),(d) $t = 12\mu s$; (b),(e) $t = 36\mu s$; (c), (f) $t = 72\mu s$; (Experimental results : (a,b,c); Numerical results :(d,e,f)).

$200\mu m$ to $300\mu m$. The width actually depends somewhat on the discretization, or particle density in the Y-direction. In the computation shown in Fig. 2, there are about 10 particles distributed in the Y-direction.

A global picture of "hot spot" temperature pattern is displayed in Fig. 3 in a three level zooming process. From Fig. 3, one can observe how such thermal-mechanical instability, i.e. periodic "hot spots", move towards downstream, and interact with each other. In fact, a similar oscillation pattern in stress components as well as strain components have also been observed in numerical simulations. The preliminary results have been reported in Li et al. (2001b,a). A further study of such thermal-mechanical instability inside the adiabatic shear band in the post-bifurcation phase is under way.

The cause of this thermal-mechanical instability may be viewed as a thermal plastic flow under either viscous heating, or hydrostatic pressure driven temperature convection, which is characterized by the following constitutive equation in the damaged stress collapsing zone,

$$\frac{\partial v_i}{\partial t} + v_j \frac{\partial v_i}{\partial x_j} = \frac{\alpha K^*}{\rho(T)} \frac{\partial (T - T_0)}{\partial x_i} + \frac{\mu^*(T)}{\rho(T)} \nabla^2 v_i \tag{1}$$

$$v_{i,i} = 0 \tag{2}$$

$$\frac{\partial T}{\partial t} + v_j \frac{\partial T}{\partial x_j} = \frac{\chi}{2\rho(T)C_p} \sigma_{ij} \Big(\frac{\partial v_i}{\partial x_j} + \frac{\partial v_j}{\partial x_i} \Big) \tag{3}$$
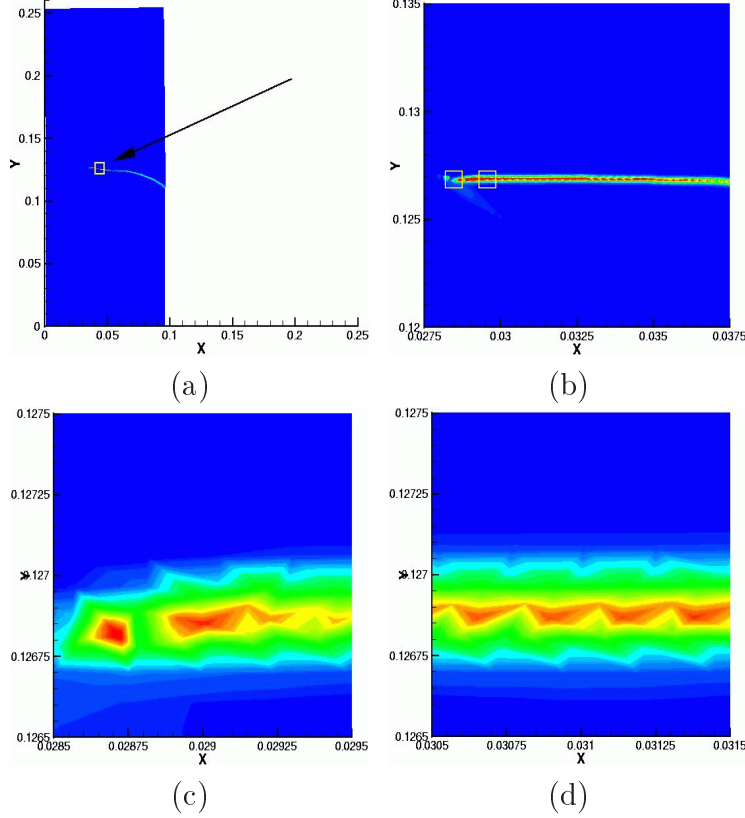
Fig. 3. The micro-structure (temperature profile) of adiabatic shear band: (a) level one; (b) level two; (c) level three (1); (d) level three (2)

where T is the temperature, v_i is the velocity field, density $\rho = \rho_0(1 - \alpha(T - T_0))$, α is the linear thermal expansion coefficient, and K^* is the damaged bulk modulus. The viscosity dependence on temperature is described by the Arrhenius law, i.e.

$$\mu^*(T) = \mu_0 \exp\left(-\beta\frac{T - T_0}{T_0}\right) \tag{4}$$

Based on the simulation results, we postulated that the onset localization of adiabatic shear deformation may be marked by the onset condition of a second thermal-mechanical instability of a shear band in the intermediate stage. This second instability is different from the initial material instability caused by thermal-softening. The second thermal-mechanical instability occurs in the post-bifurcation regime as observed in this simulation as well as the experiment by Guduru et al. (2001a). The critical condition of the second instability marks the onset of strain localization. This definition may lead an invariant basis for the susceptibility of a material to the adiabatic shear band. The rationale for this speculation is that if the damage due to microvoids or microcracks do occur in a shear band, it will provide a further softening mechanism which will accelerates the localization process. The subsequent softening may leads to a self-sustained instability path, which should be able to quantified by a

second instability.

References

Dinzart, F., Molinari, A., 1998. Structure of adiabatic shear bands in thermoviscoplastic materials. European Journal of Mecahnics, A/Solids 17, 923–938.

Gioia, G., Ortiz, M., 1996. The two-dimensional structure of dynamic boundary layers and shear bands in thermoviscoplastic solids. Journal of Mechanics and Physics of Solids 44, 251–291.

Guduru, P., Ravichandran, G., Rosakis, A. J., 2001a. Observations of transient high temperature vortical microstructure in solids during adiabatic shear banding. Aceepted for publication in "Mechanics of Materials" .

Guduru, P., Rosakis, A. J., Ravichandran, G., 2001b. Dynamic shear bands: An investigation using high speed optical and infrared diagnostics. Mechanics of Materials 23, 371–402.

Li, S., Liu, W. K., Qian, D., Guduru, R., Rosakis, A. J., 2001a. Dynamic shear band propagation and micro-structure of adiabatic shear band. Accepted for publication in: Computer Methods in Applied Mechanics and Engineering .

Li, S., Liu, W. K., Rosakis, A. J., Belytschko, T., Hao, W., 2001b. Meshfree galerkin simulations of dynamic shear band propagation. Accepted for publication in: International Journal of Solids and Structures .

Oilellio, J. A., Olmstead, W. E., 1997a. Shear band formation due to a thermal fliux inhomogeneity. SIAM Journal of Applied Mathematics 57, 959–971.

Oilellio, J. A., Olmstead, W. E., 1997b. Temporal evolution of shear band thickness. Journal of Mechanics and Physics of Solids 45, 345–359.

Wright, T. W., 1990. Approximate analysis for the formation of adiabatic shear bands. Journal of Mechanics and Physics of Solids 38, 515–530.

Wright, T. W., Ockendon, H., 1992. A model for fully formed shear bands. Journal of Mechanics and Physics of Solids 40, 1217–1226.

Wright, T. W., Ravichandran, G., 1997. Canonical aspects of adiabatic shear bands. International Journal of Plasticity 13, 309–325.

Wright, T. W., Walter, J. W., 1987. On stress collapes in adiabatic shear band. Journal of Mechanics and Physics of Solids 35, 701–720.

Wu, F. H., Freund, L. B., 1984. Deformation trapping due to thermoplastic instability in one-dimensional wave propagation. Journal of the Mechanics and Physics of Solids 32, 119–130.

SIMULATION OF CRACK PROPAGATION IN HETEROGENEOUS BRITTLE SOLIDS: SCALING PARAMETERS

V. V. Silberschmidt

Wolfson School of Mechanical and Manufacturing Engineering, Loughborough University, Loughborough, Leicestershire, LE11 3TU, UK

ABSTRACT

Crack propagation in real (quasi)brittle materials possesses signs of stochasticity; a tortuous character of fracture surfaces, multiple cracking and crack branching observed in experiments are a vivid confirmation of it. Traditional approaches of fracture mechanics represent cracks as geometrically smooth objects with straight (or curved) crack fronts, thus usually neglecting morphology of real cracks. An introduction of a direct account for stochastic features of the failure process can lead to a more adequate description of real fracture processes. Numerical schemes accounting for a spatial scatter in material properties are proposed for a description of crack propagation. These schemes unify approaches of fracture mechanics with ideas of continuum damage mechanics (CDM). CDM describes a macroscopic manifestation of various failure processes developing at lower length scales. Such unification being one of the possibilities for a micro-macro transition in a study of failure processes allows an analysis of non-uniform crack propagation and of multiple cracking. A necessity to describe a crack with its length changing along its front presupposes an utilisation of local stress-intensity factors. A description of complicated morphology of cracks or of a random set of cracks in a case of multiple cracking necessitates an introduction of additional quantitative parameters characterising fracture processes in heterogeneous brittle materials. This is implemented by means of scaling analyses of the crack front roughness, of the stress distribution character and of the free-energy release. It is shown that spatial scaling parameters can be linked to the type of material's randomness (thus being material parameters), while temporal scaling parameters are independent of it and characterise the fracture process.

KEYWORDS

Crack propagation, brittle fracture, randomness, numerical simulations, scaling

INTRODUCTION

Real brittle materials usually exhibit – to a different extent – a spatial randomness in their properties. This can result from processes of genesis for natural materials (rocks) or of manufacturing for artificial ones (ceramics, composites, etc.). The most common reason for such randomness is non-uniformity in distributions either of phases/components or of defects. A macroscopic manifestation of this randomness is the vivid difference in a crack trajectory and/or in a fragmentation type (number and shape of fragments) of identical specimens of the same material under identical loading conditions. Another sign of it is a well-known scatter in mechanical parameters at the moment of fracture observed for twin specimens of brittle materials. Studies of their microstructure usually show considerable variations in distributions of phases or defects, which result in different scenarios of generation and evolution of failure. Utilisation of micro- or nanoindentation also traditionally demonstrates a high sensitivity to the indenter's position; indentation

measurements performed in neighbouring microscopic regions belonging to a weak matrix and to a rigid inclusion/precipitate will show considerably different results.

There is a distinct difference in types of mechanical analysis of brittle random materials. Their deformational properties can be obtained with the use of various homogenisation schemes provided the specimen size is considerably larger than the characteristic dimension of microstructure elements. These methods are mostly effective for dilute concentration of such (non-interacting) elements but modifications of these methods can also deal with systems with high degrees of randomness or even with spatially changing properties (functionally graded materials). The fracture analysis of these materials, in contrast, cannot be reduced to a study of their effective properties, since the critical and post-critical behaviour is unique for each specimen of brittle materials because of its microstructure. So, one possibility is a statistical (Weibull-like) analysis of large sets, or, a direct introduction of randomness into simulations. This paper deals with the latter approach.

MODEL OF STOCHASTIC BRITTLE SOLID WITH MODE-I CRACK

Modelling Stochastic Materials

An introduction of spatial randomness of material properties into the model can be implemented by various methods but they all exploit any type of the distribution of material's properties over different parts of the analysed area. These parts should normally fulfil requirements for a representative volume element (unit cell). It means that, on the one hand, they should be sufficiently large to contain a large number of microscopic elements and, on the other hand, their dimensions should be sufficiently small compared to dimensions of the whole specimen/structure. The character of spatial distributions should reflect the scatter of respective properties, experimentally obtained either on twin specimens or from different parts of the same specimen. Obviously, different materials have different reasons for spatial randomness, which should be respectively accounted for in a model.

In this paper a spatial non-uniformity in the stiffness level is considered to be the main stochastic property of the modelled brittle material. This can be true for rocks [1, 2] and composites [3]; another approach is used, for instance, in modelling of sintered ceramics where stochasticity in a distribution of pores can be treated as a main source of randomness [4, 5]. The studied area of such material is divided into M elements with varying stiffness, the level of which for the jth element is determined by the following relation:

$$ G_j = G_r \left(1 + \left(\sin \frac{\pi k}{M} \right)^r \right) K_{\text{ren}}, \quad \left(j, k = \overline{1, M} \right). \tag{1} $$

Here, G_r is the minimal local stiffness, k is a random number. Parameter r determines the material's extent of randomness: its higher magnitude corresponds to higher non-uniformity. This parameter is linked with the effective coefficient of the distribution's half-width $K_{0.5}$:

$$ K_{0.5}(r) = \frac{1}{\pi} \operatorname{arcsec} \sqrt[r]{2} . \tag{2} $$

It is obvious that the ratio of maximal stiffness to minimal one is equal 2 for any r. The last multiplier in Eqn. 1 is introduced in order to exclude the influence of the total stiffness of the area $G^* = \sum_{j=1}^{M} G_j$ on results of simulations and it is determined from the requirement $G^* = const$. Three various distributions of stiffness for different levels of $K_{0.5}$ are shown in Figure 1.

Mode-I Crack and Local Stress-Concentration Factors

A specimen with a V-shaped notch (with its edge EF and its symmetry plane xOy containing this edge laying in the middle cross-section ABCD of the specimen) is shown in Figure 2. It can be used for the mode-I fracture analysis. Let us note that a standard analysis within the framework of fracture mechanics is usually

carried out for another plane, namely, a plane orthogonal to the edge EF of the notch (yOz). This reduction of the crack front to its trace – a single point in yOz – cannot be applied here since material properties change along the front.
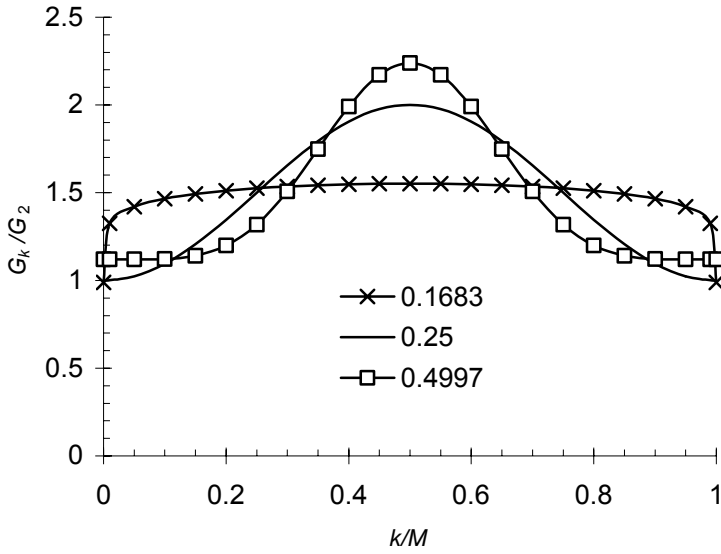
Figure 1: Stiffness distributions for various levels of $K_{0.5}$
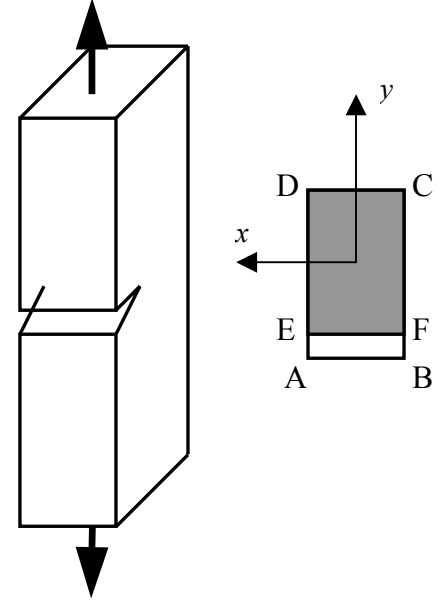
Figure 2: Mode-I crack and specimen's middle cross section

Cross-section ABCD is discretised into an orthogonal network of M rectangular elements with a pair of indices p and q denoting the element belonging to the pth row and qth column of elements (rows being parallel to EF and columns orthogonal to it). Then the level of stresses in elements can be calculated by integrating the well-known relation for a mode-I crack [6, 7] $\sigma_{zz} = \sqrt{2\pi y}$ over elements in rows and accounting for their different stiffness in the form

$$\sigma^{pq} = \frac{MG^{pq}}{G*}\frac{\overline{G}^q}{\widetilde{G}^q} K_{\mathrm{I}}^q \sqrt{\pi\, l_y}\left(\sqrt{p+1-n^q} - \sqrt{p-n^q}\right)\sigma_{zz}^{\infty}, \quad p \geq n^q. \tag{3}$$

Here $\overline{G}^q$ and $\widetilde{G}^q$ are initial and current levels of stiffness of the qth column; the local stress-intensity factor K_{I}^q can be approximated for a given geometry/loading by known relations from handbooks on stress-intensity factors (e.g., [8]); l_y is an elements' dimension along the y axis; n^q is a number of elements occupied by crack in the qth column; σ_{zz}^{∞} is the uniformly-distributed stress acting far from cross section ABCD.

Damage Accumulation and Crack-Damage Interaction
A deterioration of material under loading is described in terms of continuum damage mechanics by means of introduction of additional variables into the model. They describe macroscopic effects of microscopic evolution in an ensemble of defects. The choice of these additional macroscopic parameters should be related to respective mechanisms responsible for failure evolution. Some damage parameters for different deformation/fracture modes with respective damage accumulation laws are discussed in [9, 10]. Another approach utilizing a different damage parameter was used in [4, 5]. The damage level is also treated as a field function distributed over the network of elements described before.

The presence of crack naturally influences evolution of failure processes at lower length scales and should be reflected in respective model schemes. It is implemented in terms of stress concentration in the vicinity of the crack front: higher stress levels correspond to higher local damage accumulation rates [9].

An additional element in modelling crack-damage interaction is a local failure criterion: an element is considered to fail (with its stiffness diminishing from the initial level to the near-zero residual one) if its damage level exceeds a threshold value. If a locally failed element adjoins the crack front then the crack is considered to increase its length in this column of elements by l_y. The local crack growth in the qth column causes stress redistribution linked with two factors – a local stiffness decrease under the unchanged level of the external load and an increasing level of K_1^q. Both factors are accounted by Eqn. 3.

Spatial non-uniformity in material properties obviously results in different response of various regions to external loading. Both initial non-uniformity in internal stresses even under uniform external loading and difference in distribution of microscopic defects result in spatially varying rates of failure process development. Thus, crack propagation and stress redistribution lead to the stress growth in elements, accelerating, in its turn, the damage accumulation process and the consequent failure of these elements in front of the crack. In the case of a totally isotropic material this trend would result in a shift of crack front as a straight line parallel to its initial position (EP)– the standard case for fracture mechanics. But material's spatial non-uniformity and random processes of stress redistributions and elements' failures cause the difference in local levels of the crack propagation rate, which results in a complicated morphology of crack fronts (Figure 3).
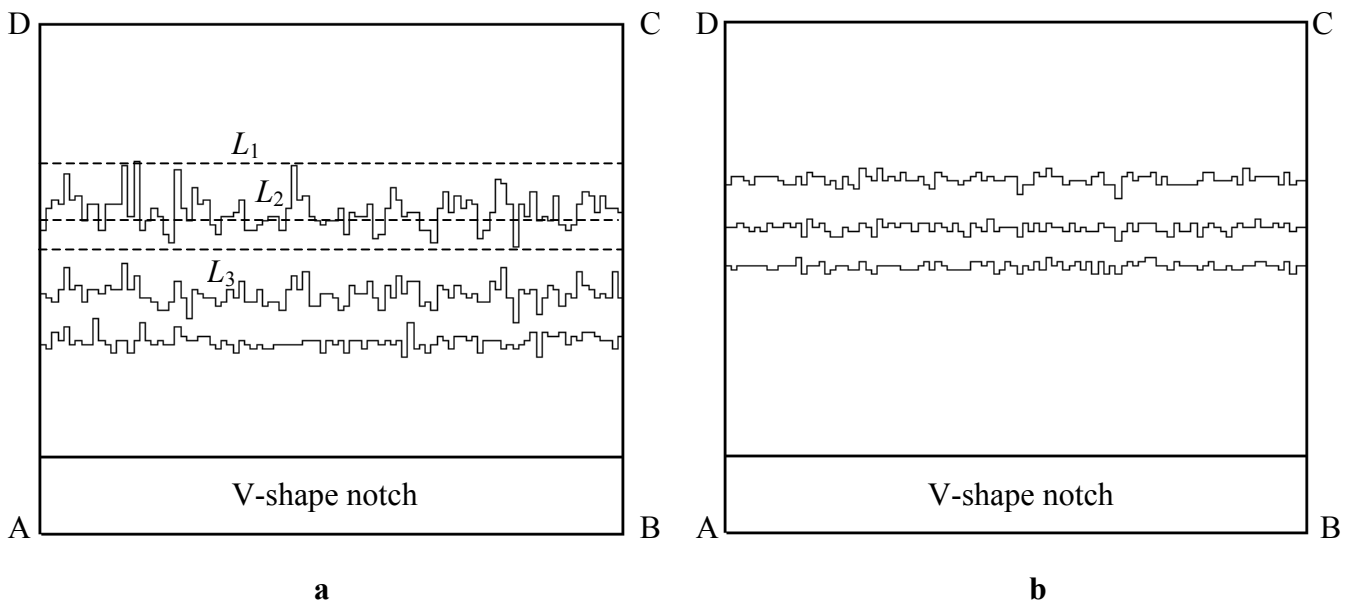
Figure 3: Position of crack fronts at different stages of crack propagation in specimens with different extents of material's randomness: (a) $K_{0.5} = 0.1683$; (b) $K_{0.5} = 0.4997$

SCALING CHARACTERISTICS OF CRACK PROPAGATION

Each statistical realisation of the spatial distribution of material's properties should result in the unique scenario of crack propagation and the unique crack-front morphology. This presupposes both a modification of traditional characteristics of fracture and introduction of new ones. To characterise a position of the crack front three different parameters are introduced instead of the traditional crack length. They characterise positions of the farthest – with respect to the initial notch – rows containing (a) at least one element belonging to the crack (shown as L_1 in Figure 3a), (b) half elements occupied by the crack (L_2) and (c) only failed elements (L_3). So, different moments of fracture (linked with respective time-to-fracture parameters) of a specimen can be considered: between the first exit of the crack front on its opposite – to the V-shape notch – edge (the crack "touches" it) and the final rupture of the specimen when all the elements of the cross-section fail.

Two types of scaling are used to describe the crack's tortuosity and randomness in crack propagation

dynamics: spatial parameters and temporal ones.

Spatial scaling parameters

The theory of fractals [11] can be effectively used in scaling analysis. The *fractal dimension* of cracks calculated by the box-counting method shows that the fractal dimension D increases with the growth of material's homogeneity (growing $K_{0.5}$) with a natural limit $D \to 2$ for the uniform stiffness distribution and crack propagation as a straight line parallel to its initial position.

Another scaling parameter characterising tortuousity of crack fronts can be obtained by means of the in-plane roughness analysis [12, 13], based on the general scheme for characterization of self-affine profiles [11]. The *roughness index* (also known as the *Hurst exponent*) ζ is determined from the scaling relation $y_{max} \propto r^{\zeta}$, where

$$y_{max}(r) = l_y \left\langle \max n^q(r') \Big|_{x<r'<x+r} - \min n^q(r') \Big|_{x<r'<x+r} \right\rangle \Big|_x . \tag{4}$$

Here $y_{max}(r)$ is a distance along the y-axis between the farthest – with respect to the initial V-notch – locally failed element, belonging to a propagating crack, and the nearest one within the given window of size r along the crack front. The level of ζ obtained from microscopic observations was found to be equal 0.60±0.04 for 8090 Al-Li alloy and 0.54±0.03 for a Superα_2 Ti$_3$Al-based alloy on the length scale from 1 μm to 1.5 mm [19]; the detailed analysis of universality of ζ is given in [13]. The roughness of fracture surfaces (*out-of-plane roughness*) measured, for instance, by mechanical profilometry is a material-sensitive parameter: for sandstone the roughness exponent ζ was found to be close to 0.5 (0.47±0.03) and for basalt it was higher (0.80±0.04) for scale length from 25 μm up to several cm [14]. Results of numerical simulations based on the introduced description of spatially random brittle media show the effect of the extent of non-uniformity in material properties on the in-plane roughness: $\zeta = 0.56\pm0.03$ for $K_{0.5} = 0.1683$ and $\zeta = 0.62\pm0.01$ for $K_{0.5} = 0.4997$.

The multifractal analysis [15] can be used to quantify the load distribution character in the vicinity of tortuous crack fronts. It was shown [16] that the material's stochasticity type influences the *multifractal properties* of the load distribution: an increase in spatial uniformity causes the decrease of the width of multifractal spectra. The same formalism was applied to multiple matrix cracking of fibre-reinforced laminate composites under tensile fatigue [17-19]. It was shown that spatial distributions of both matrix cracks and of their length possess multifractal properties. Both the loading conditions (level of matrix stresses and number of cycles) and the structure of laminates (their stacking order) affect scaling characteristics of these distributions [17].

Temporal scaling parameters

The most important temporal features of the fracture process is time to fracture t_{fr} and its change with loading conditions (stress level σ and initial length of the V-shape notch). Detailed numerical modelling shows that *time-to-fracture scaling*, determined by the relation $t_{fr} \propto \sigma^{-n}$ is independent of material's spatial randomness. All types of non-uniformity in material properties (characterised by $K_{0.5}$) have the same level of the temporal scaling exponent n for all introduced parameters of the crack front position (see above) [20]. The same is true for the time-to-fracture dependence on the initial crack length.

Free-energy release is one of the standard parameters of fracture mechanics [6, 7]. The proposed model allows an estimation of energy release linked with local failures of elements at crack propagation. This process is characterised by rather non-trivial dynamics [21]. Multifractal formalism discussed in the previous subsection can also be applied to the study of this dynamics. It is shown that multifractal spectra for energy release at crack propagation in brittle materials are considerably more sensitive to the type of material randomness than respective scaling characteristics used in analysis of random events.

CONCLUSIONS

Crack propagation in brittle heterogeneous materials is a considerably more complicated case of fracture development than that of isotropic materials treated within the framework of standard fracture mechanics. Non-uniformity both of the spatial distribution of mechanical properties and of the evolution of ensembles of defects can result in multiple cracking, tortuosity of crack fronts and roughness of fracture surface. All these features are well known from fractography and should be adequately reflected in modelling schemes. One of the variants of such a scheme unifying ideas of fracture mechanics and continuous damage mechanics and utilising the spatial discretisation of the analysed region into elements with different properties is suggested. The fracture development obtained in numerical simulations within the framework of this model resembles real fracture processes. Complicated morphology of these processes needs an introduction of additional parameters. Various scaling parameters are shown to be useful in quantification of both spatial and temporal features of crack propagation. They also allow an effective comparison between experimental data obtained by precise measurements of crack roughness and results of numerical simulations.

REFERENCES

1. Silberschmidt, V.V. and Silberschmidt, V.G. (1990) *Terra Nova* 2, 483.
2. Silberschmidt, V.V. (1994). In: *Fractals and Dynamic Systems in Geoscience*, pp. 65-76, Kruhl, J.H. (Ed.). Springer-Verlag, Berlin e. a.
3. Silberschmidt, V.V. (1993). In: *Composites Behaviour*, Vol. 5, pp. 771-778. Miravete, A. (Ed.). Woodhead Publishing Ltd., Cambridge.
4. Najar, J. and Silberschmidt, V.V. (1998) *Arch. Mech.* 50, 21.
5. Silberschmidt, V.V. and Najar, J. (1998) *Comp. Mat. Sci.* 13, 160.
6. Liebowitz, H. (Ed.) (1968). *Fracture*, Vol. I-VII. Academic Press, New York.
7. Knott, J.F. (1973). *Fundamentals in Fracture Mechanics.* Butterworth, London.
8. Murakami, Y. (Ed.) (1987). *Stress Intensity Factors Handbook*. Elsevier Science B.V. North Holland, Amsterdam e. a.
9. Silberschmidt, V.V., and Chaboche, J.-L. (1994) *Int. J. Damage Mech.* 3, 57.
10. Silberschmidt, V.V. (1998) *Int. J. Damage Mech.* 7, 84.
11. Feder, J. (1988). *Fractals.* Plenum Press, New York.
12. Daguier, P., Bouchaud, E. and Lapasset G. (1996) *Europhys. Lett.* 31, 367.
13. Bouchaud, E. (1997). *J. Phys.: Condens. Matter* 9, 4319.
14. Boffa, J.M., Allain, C. and Hulin, J.P. (2000) *Physica A* 278, 65.
15. Halsey, T.C., Jensen, M.H., Kadanoff, L.P., Procaccia, I. and Shraiman, B.I. (1986) *Phys. Rev. A* 33 1141.
16. Silberschmidt, V.V. (1993) *Europhys. Lett.* 23, 593.
17. Silberschmidt, V.V. (1995) *Mech. Comp. Mater. Structures* 2, 243.
18. Silberschmidt, V.V., and Hénaff-Gardin, C. (1996). In: *ECF 11. Mechanisms and Mechanics of Damage and Failure*, Vol. 3, pp. 1609-1614. Petit, J. (Ed.). EMAS Ltd, London.
19. Silberschmidt, V.V. (1998) *Comp. Mat. Sci.* 13, 154.
20. Silberschmidt, V.V. and Yakubovich, Yu.M. (1993) *Int. J. Fracture* 61, R35.
21. Silberschmidt, V.V. (1996) *Geol. Rundsch.* 85, 116.

Simulation of damage mechanisms in high-speed grinding of structural ceramics

Philippe H. Geubelle and Spandan Maiti

Department of Aeronautical and Astronautical Engineering,
University of Illinois at Urbana-Champaign,
Urbana, IL 61801, USA

ABSTRACT

Due to the brittleness of ceramics, the machining of this class of materials is quite challenging. Assessing the surface and sub-surface damage associated with the machining process is of considerable interest nowadays. Most of the work in this area refers to the static indentation and/or scratch test. In this paper, we discuss an explicit grain-based cohesive-volumetric finite element scheme which can capture the complex dynamic initiation and propagation of intergranular cracks, near surface plasticity, and subsequent fragmentation of the material during dynamic scratch tests.

KEYWORDS

Ceramics, Dynamic fracture, Intergranular crack, Cohesive volumetric finite element, Grain-based meshing, Dynamic scratch test

INTRODUCTION

Many applications of advanced structural ceramics require high dimensional accuracy and surface finish, and, despite recent advances in the development of new surface finishing techniques such as electric discharge, laser beam and ultrasonic machining, conventional methods such as grinding, lapping and polishing [1] are still the common methods used in the industry. However, the brittleness of ceramics greatly increases the complexity of the grinding process, as the material removal process is often accompanied by surface and sub-surface damage in the form of cracks that sometimes penetrate deeply into the machined component. This residual damage can lead to substantial degradation of the mechanical strength, and hence the performance of the component [2,3]. Due to this added complexity, grinding alone accounts for 20 to 85% of the total cost of the machining process.

High-speed grinding, involving wheel rotation speed in excess of $20,000$ rpm and contact times in the $10...100$ μs range, is increasingly being considered not only to improve the productivity of machining process, but also as a way to reduce the amount of residual damage in the machined part [4]. However, the strain rates (in excess of $1000/s$) involved with such high speed of the machine tool render most of the existing analytical tools inadequate. Additional effects such as inertia, rate dependence, frictional heating and thermomechanical coupling must be taken into

account. Moreover, the existing analytical methods, mostly based on static continuum-level indentation solutions, are often oversimplified in their description of the complex interactions between various damage mechanisms taking place in the vicinity of the tool/specimen interface, and always involve a single grit system. Also, most of these analyses are performed at a macroscopic continuum level, disregarding the heterogeneous granular microstructure inherent to ceramic materials, and the complex propagation and branching paths of the cracks.

The objective of the research project described in this paper is the development and implementation of a numerical scheme aimed at the simulation of the complex damage process taking place during the high-speed machining of brittle materials that have a granular microstructure. In addition to the discrete microstructure of the material, emphasis is placed in this work on the capture of the inertial effects associated with high-strain rate loading, the spontaneous motion and interaction of cracks, and the complex interaction between the tool and the machined component. The numerical approach is based on an explicit, cohesive-based finite element scheme specially developed for the meso-scale level simulation of dynamic fracture in granular materials. The basic components of the numerical scheme are summarized in the next section.

Special emphasis is placed in this work on the simulation of the dynamic version of a common machinability test, the so-called *scratch test*, in which a single abrasive particle representing a
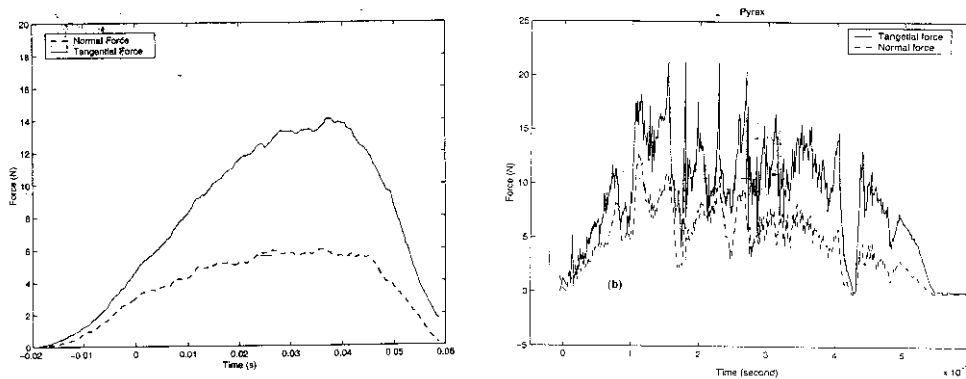
Figure 1: Experimental reaction trace at the base, a) for pyrex glass showing the brittle removal of material and a) for ASTM 1018 steel with much smoother curve signifying plastic flow of the material around the tool and b) for pyrex glass showing brittle removal of material [5].

single grit of the grinding wheel is scratched through the surface of the specimen for a prescribed length, allowing for the controlled study of the effect on the damage process of various parameters such as the depth of cut, the tool shape, the grit velocity and the material microstructure. The reaction trace at the base of the specimen obtained experimentally for the scratch test (Figure 1) shows the characteristic features for the brittle or plastic failure, with a smooth curve for the plastic case, and a curve with lots of spikes for the brittle one. A discussion of the simulation of these two tests is presented in the last section.

NUMERICAL SCHEME

The material removal process appearing in the grinding of ceramic materials has been shown to be associated with three distinct mechanisms: microfracture and chipping of individual grains, removal of large chunks of material by propagation of cracks parallel to the surface (referred to as lateral cracks), and intergranular microfracture and grain dislodgement. A small plastic
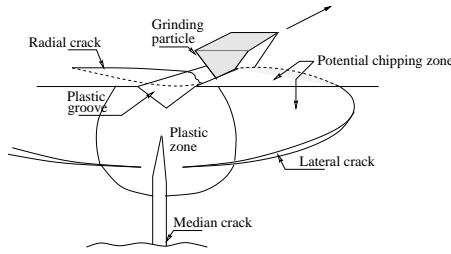
Figure 2: Scratch test of ceramic materials, showing the appearance of radial and lateral cracks and the formation of a plastic zone in the vicinity of grinding particle. (Adapted from [6]).

zone also develops in the vicinity of the surface. Special emphasis is placed in this work on the simulation of intergranular crack propagation and grain dislodgement, which have been shown to be dominant, especially at higher temperatures. In addition to assuming the intergranular nature of the process-induced cracks, we rely on two other important assumptions in the work described hereafter: the analysis is conducted in plane strain, and no thermomechanical coupling is so far considered. While these assumptions clearly limit the scope of the analysis, preventing for example, the study of the interaction between two parallel grits, we believe that the simplified model described hereafter captures the essential features of the physical problem.

Cohesive-based finite element scheme

To capture the spontaneous initiation, propagation, arrest and possible interaction of cracks in the specimen, we rely on a special form of the the cohesive-based finite element scheme, which has shown great success over the past few years in the capture of a variety of dynamic fracture problems [7,8,9]. The method relies on the combination of conventional (volumetric) elements used to capture the bulk response of the material, and interfacial (cohesive) elements used to simulate the spontaneous dynamic motion of intergranular cracks. The traction-separation law for the cohesive elements is taken to be bilinear [9]. According to this law, the relation between the normal (T_n) and tangential (T_t) cohesive tractions and the corresponding normalized displacement jumps ($\tilde{\Delta}_n$ and $\tilde{\Delta}_t$) takes the form

$$T_n = \frac{\mathcal{S}}{1-\mathcal{S}}\tilde{\Delta}_n \sigma_{max}, \qquad T_t = \frac{\mathcal{S}}{1-\mathcal{S}}\tilde{\Delta}_t \tau_{max}. \tag{1}$$

The normalized displacement jumps are defined as

$$\left\{ \begin{array}{c} \tilde{\Delta}_n \\ \tilde{\Delta}_t \end{array} \right\} = \left\{ \begin{array}{c} \Delta_n/\Delta_{nc} \\ \Delta_t/\Delta_{tc} \end{array} \right\}, \tag{2}$$

where

$$\tilde{\Delta}_{nc} = \frac{2G_{Ic}}{\sigma_{max}\mathcal{S}_{initial}}, \qquad \tilde{\Delta}_{nt} = \frac{2G_{IIc}}{\tau_{max}\mathcal{S}_{initial}}, \tag{3}$$

in which G_{Ic} and G_{IIc} are the critical energy release rates for mode I and mode II failures respectively, and $\mathcal{S}$ is the coupling factor between normal and tangential displacements and is a function of the norm of the displacement jump vector. Note that, the expression for T_n is only valid for the tension case. In compression, we always use the initial value of $\mathcal{S}$, which is close to unity, to generate a large compressive traction to ensure no overlapping between crack faces. This approach works well as long as the separation is small, and cohesive nodes maintain their initial connectivity. But after a large separation between initially adjacent nodes, this simple method cannot be used calling for more sophisticated contact detection and enforcement algorithms to prevent overlapping of newly created crack surfaces.

3

Grain-based mesh generation

Another critical aspect of this research is to capture the microstructure of the ceramic materials. Ceramic materials are essentially granular in nature. The cracks generally pass through grain boundaries generating a highly tortuous path. To capture the granular microstructure mentioned above, we use the Voronoi tessellation, a geometric structure with similar space-filling properties as the actual microstructure of the ceramics. The interior of Voronoi cells are further tessellated in Delaunay triangles, which act as volumetric elements in the finite element scheme. The nodes on the grain boundaries are doubled to generate the cohesive elements.

Explicit Elastic-Viscoplastic scheme

During grinding, grains can be subjected to large rotations and deformations, requiring the use of finite kinematics. Also, they can exhibit considerable plasticity. We assume the total deformation gradient admits a multiplicative decomposition into an elastic part $\boldsymbol{F}^e$ and a plastic part $\boldsymbol{F}^p$ [10] according to

$$\boldsymbol{F} = \boldsymbol{F}^e \boldsymbol{F}^p. \tag{4}$$

We compute $\boldsymbol{F}^{p-1}$ iteratively through the relation

$$\left(\boldsymbol{F}^{p-1}_{n+1}\right)_{ij} = (\boldsymbol{F}^{p-1})_{ik}\left[\sum_A \frac{1}{\exp\left\{\frac{\Delta\gamma}{\sqrt{2}\bar{\sigma}}\sigma'^A\right\}}(\boldsymbol{N}^A)_k(\boldsymbol{N}^A)_j\right]. \tag{5}$$

The subscript n denotes the quantities in nth time step, whereas $n+1$ denotes the same for $(n+1)th$ time step. In this equation, $\Delta\gamma$ is the discretized plastic strain increment given by

$$\Delta\gamma = \Delta t\,\dot{\gamma}, \tag{6}$$

and the stress deviator $\boldsymbol{\sigma}'$ is defined as

$$\boldsymbol{\sigma}' = \sum_A (\boldsymbol{\sigma}^A - \frac{\boldsymbol{I}_1^\sigma}{3})\boldsymbol{n}^A \otimes \boldsymbol{n}^A. \tag{7}$$

The Lagrangian strain tensor $\boldsymbol{E}$ is related to second Piola-Kirchoff stress tensor $\boldsymbol{S}$ by the constitutive relation

$$\boldsymbol{S} = \boldsymbol{\mathcal{L}}\boldsymbol{E}, \tag{8}$$

where $\boldsymbol{\mathcal{L}}$ contains the elastic moduli of the material.

The finite element formulation used in the CVFE scheme is derived using principle of virtual work. An explicit central-difference time-stepping scheme [11] is used to calculate displacement $\boldsymbol{u}$, velocity $\dot{\boldsymbol{u}}$ and acceleration $\ddot{\boldsymbol{u}}$ at each time step.

Contact algorithm

The contact algorithm is necessary to enforce tool/grain and grain/grain contact. The algorithm has two major components: contact search and contact enforcement. The contact search is the most expensive part of the whole numerical scheme. To optimize it, we resort to a two-step search. The first step called the preliminary search quickly establishes the potential contact pairs. We take only the grains with at least one side broken as potential contact candidates. An axis-aligned rectangular bounding box is established around the grains/tool. The grains/tool with intersecting bounding boxes form the potential contact pair. In the next step, called the detailed search, only potential contact pairs are searched. An exhaustive search based on point-in-polygon principle is performed. For the contact enforcement, we resort to an explicit master/slave technique [12]. This technique is not particularly successful for closely packed grains with angular corners, as in our case. We are currently investigating other contact algorithms based on non-smooth contact dynamics. Coulomb friction is also taken into account.

RESULTS AND DISCUSSION

In the following example, the ceramic material is chosen as alumina (Young's modulus $E = 400\ GPa$, Poisson's ratio $\nu = 0.27$, and density $\rho = 3800\ kg/m^3$), whereas the tool is made of synthetic diamond (Young's modulus $E = 863\ GPa$, Poisson's ratio $\nu = 0.20$, and density $\rho = 3360\ kg/m^3$). The fracture toughness of the alumina in Mode I (K_{I_c}) as well as in Mode II are taken as $5.3\ MPa\sqrt{m}$, and maximum cohesive stress is chosen as 1/100th of the Young's modulus. The coefficient of friction is taken as 0.5.
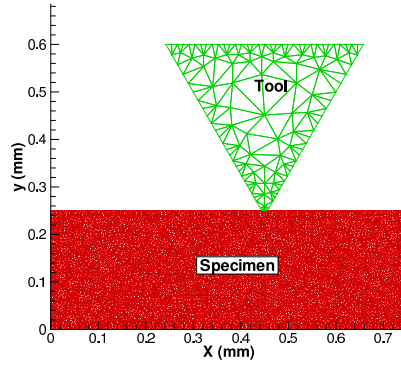
Figure 3: Finite element mesh for the scratch test simulation.

Figure 3 shows the typical meshing used for the problem with average grain size of 30 μm. The
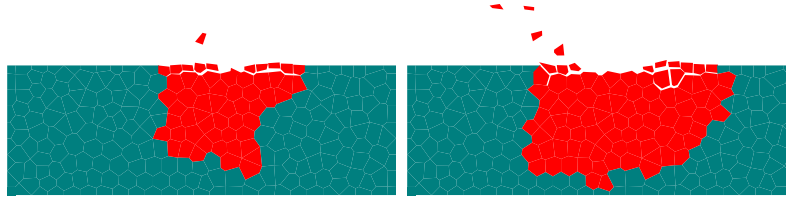
Figure 4: The deformed specimen at different time points for the brittle case : a) at time $= 300 \times 10^{-8}$ s, b)at time $= 700 \times 10^{-8}$ s. The darker region shows the damage zone.

horizontal velocity of the indenter is 66.66 m/s, whereas the vertical velocity varies linearly from 66.66 m/s to $-66.66\ m/s$. The ratio of yield stress to maximum cohesive stress, σ_y/σ_{max} is taken to be 1. Figure 4 shows snapshots of the material removal process. As can be seen from these pictures, we are able to capture the spontaneous initiation and the propagation of the intergranular cracks and grain dislodgement of the ceramic specimen. The normal reaction at the base (Figure 5a) shows the brittle nature of the damage process characterized by sharply discontinuous peaks and oscillations in the reaction trace. The same system is studied for a more ductile system with $\sigma_y/\sigma_{max} = 5$. Figure 5b depicts the normal bottom reaction for this problem. It can be seen that, at the beginning, the failure process is ductile, and reaction curve is smooth. But, as the strain rate increases, the yield stress increases also, ultimately transforming the failure process to a brittle one.

5
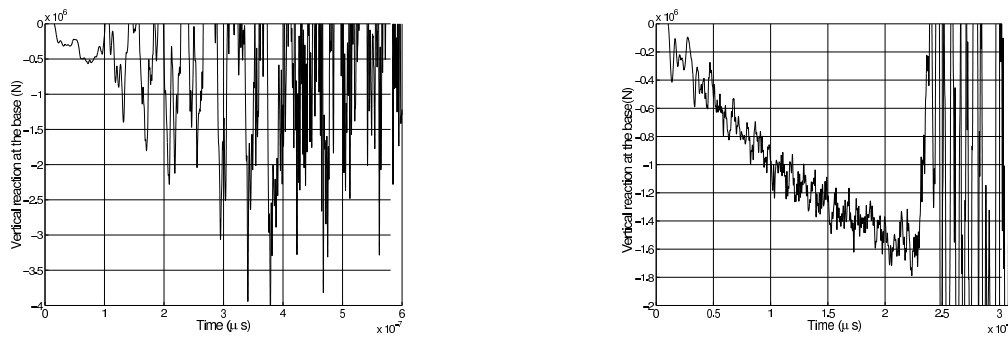
Figure 5: The vertical reactions at the base of the specimen for the scratch test : a) for the brittle case, $\sigma_y/\sigma_{max} = 1$, b) for the ductile case, $\sigma_y/\sigma_{max} = 5$.

Conclusions

In this paper, we have shown the capability of our model to capture the dynamic crack growth with an emphasis on the granular microstructure of the ceramic material. The model can capture the brittle and ductile failure process associated with high strain rate. Detailed analyses are underway to characterize the effects of tool velocity and trajectory on the damage process.

Acknowledgements

References

1. Klocke, F. (1996) *J. Eur. Ceram. Soc.* 17, 457.
2. Liu, D. M., Fu, C. T. and Lin, L. J. (1996) *Ceramic Int.* 22, 267.
3. Esposito, L., Tucci, A. and Andalo, G. (1997) *J. Eur. Ceram. Soc.* 17, 479.
4. Malkin, S. and Ritter, J. E. (1989) *J. Eng. Ind.* 111, 167.
5. Subhash, G., Loukus J. E. and Pandit, S. M. (2001). In preparation.
6. Li, K. and Liao, T. W. (1996) *J. Mat. Proc. Techn.* 57, 207.
7. Camacho, C. and Ortiz, M. (1996) *Int. J. Solids Struct.* 33, 2899.
8. Xu, X.-P. and Needleman, A. (1994) *J. Mech. Phys. Solids* 42, 1397.
9. Geubelle, P. H. and Baylor, J. (1998) *Comp. B* 29, 589.
10. Simo, J. C. (1988) *Comp. Meth. Appl. Mech. Engr.* 66, 199.
11. Belytschko, T., Chiapetta, R. L. and Bartel H. D. (1976) *Int. J. Numer. Meth. Eng.* 10, 579.
12. Taylor, L. and Flanagan, D. (1987). Report SAND86-0584, Sandia National Laboratories, Albuquerque.

SIMULATION OF DOMAIN SWITCH–TOUGHENING IN FERROELECTRIC CERAMICS

M. Kuna and A. Ricoeur

Freiberg University of Mining and Technology, Institute of Mechanics and Machine Components
09596 Freiberg, Germany

ABSTRACT

The influence of an electric field upon the fracture toughness of ferroelectric ceramics has been observed by many researchers. Our investigations deal with the calculation of ferroelectric/ferroelastic domain switching events near the tip of an electromechanically loaded crack. The calculations are based on a semi–analytical solution of the piezoelectric field problem yielding electric and mechanical fields around a crack tip. By means of a switching criterion, the specific work is related to a treshold value, deciding upon location and species of switching events. The thus determined extension of the fracture process zone is the basis for calculating changes in the fracture toughness due to domain processes. On this basis the influence of electric loads is investigated and results for two different orientations of material poling are presented. If the crack faces are aligned perpendicularly with the poling direction a positive electric field enhances the Mode–I fracture toughness. In the case of crack faces beeing orientated along the material poling axis the Mode–I fracture toughness is scarcely influenced by an external electric field, whereas the Mode–II toughness is strongly affected.

KEYWORDS

ferroelectrics, piezoelectrics, switch–toughening, smart ceramics

INTRODUCTION

Piezoelectric and ferroelectric ceramics find an application as actuators, sensors or ultrasonic transducers in many fields of technology. Because of their brittleness, problems of strength and reliability have to be major subjects of investigation. For the fracture analysis of smart ceramic structures a fracture criterion is needed, which relates relevant fracture quantities to the material toughness values, deciding on whether a given crack grows or not. In fracture mechanics of piezo– and ferroelectric solids, such a fracture criterion is not known yet. Within the scope of the K–concept, the loading of the crack tip can be described by the three classical stress intensity factors K_I, K_{II} and K_{III} and an additional electric intensity factor K_{IV} representing the singular behaviour of the electric displacement D_i in front of the crack tip [1]:

$$\sigma_{ij}(r,\theta) = \frac{1}{\sqrt{2\pi r}} \left[K_I f_{ij}^I(\theta) + K_{II} f_{ij}^{II}(\theta) + K_{III} f_{ij}^{III}(\theta) + K_{IV} f_{ij}^{IV}(\theta) \right]$$

$$D_i(r,\theta) = \frac{1}{\sqrt{2\pi r}} \left[K_I\, g_i^I(\theta) + K_{II}\, g_i^{II}(\theta) + K_{III}\, g_i^{III}(\theta) + K_{IV}\, g_i^{IV}(\theta) \right]$$

$$(1)$$

A fracture criterion on the basis of the K–concept should be formulated by one single quantity K_A, being a function of the K–factors including K_{IV}. This quantity, representing the applied loading of

a fracture criterion equation, has to be compared to a material inherent critical value, the fracture resistance K_C. However, there is experimental evidence [2], that the critical value on the right hand side of the equation is a function of the electric field E_i and the poling direction P_i. It is assumed to be sufficient if only mechanical stress intensity factors are considered on the left hand side of the fracture criterion. The effect of an electric field is included in the material function on the right hand side and in the mechanical stress intensity factors by piezoelectric coupling. The fracture criterion is supposed to be

$$K_A(E_i) = K_C\left(E_i, P_i\right) \tag{2}$$

The micromechanical model, presented in this paper, has been developed as a tool to investigate the material function $K_C(E_i, P_i)$. Calculations also based on a micromechanical model recently have been published by Zhu and Yang [3,4]. In their work, piezoelectric field coupling is not considered, though.

CLOSED FORM SOLUTION FOR A CRACK IN AN INFINITE PIEZOELECTRIC

To find the eigensolutions of a piezoelectric material, the displacements u_i and electric potentials ϕ are represented by the function [5]

$$u_n = \left(\begin{array}{c} u_i \\ \phi \end{array} \right) = \left(\begin{array}{c} A_i \\ A_4 \end{array} \right) f(z) = A_n\, f(z) \; ; \quad z = x_1 + p x_2 \tag{3}$$

which assumes the two field variables to depend on the coordinates x_1 and x_2. Since derivations with respect to x_3 vanish, the strain tensor component ϵ_{33} and the component of the electric field vector $E_3 = \phi_{,3}$ are zero. The problem to be solved is governed by the following system of equations, which is derived from the field equations of linear elasticity and electrostatics as well as the constitutive equations of piezoelectricity:

$$\begin{aligned} C_{ijkl}\, u_{k,jl} + e_{ijl}\, \phi_{,jl} &= 0 \\ e_{ikl}\, u_{k,il} - \kappa_{il}\, \phi_{,il} &= 0 \end{aligned} \tag{4}$$

The elastic, piezoelectric and dielectric material constants are represented by the tensors C_{ijkl}, e_{ijl} and κ_{il}. In Eqn. 4 volumetric forces and charges are neglected. Inserting Eqn. 3 into Eqn. 4 yields a generalized eigenvalue problem revealing A_n and p as eigenvectors and eigenvalues, respectively. With the exception of x_3 beeing the material poling axis, which means that the $x_1 - x_2$ plane is the plane of isotropy, all four eigenvectors are linear independent. Thus, in Eqn. 3 the summation over all linear independent eigenvectors and –values can be introduced to be inserted subsequently into the constitutive law of piezoelectricity. Furthermore, introducing a stress function χ_i ($\chi_{i,1} = \sigma_{i2}$, $\chi_{i,2} = -\sigma_{i1}$) and an electric displacement function θ ($\theta_{,1} = D_2$, $\theta_{,2} = -D_1$) and integrating with respect to z finally yields

$$\Phi_m = \left[\begin{array}{c} \chi_i \\ \theta \end{array} \right] = M_{m\alpha}\, f_\alpha(z_\alpha) + \bar{M}_{m\alpha}\, \bar{f}_\alpha(\bar{z}_\alpha) \tag{5}$$

with the matrix

$$M_{m\alpha} = \left[\begin{array}{c} (C_{i2k1} + C_{i2k2}\, p_\alpha)\, A_{k\alpha} + (e_{1i2} + e_{2i2}\, p_\alpha)\, A_{4\alpha} \\ (e_{2k1} + e_{2k2}\, p_\alpha)\, A_{k\alpha} - (\kappa_{21} + \kappa_{22}\, p_\alpha)\, A_{4\alpha} \end{array} \right] \tag{6}$$

Bars denote conjugate complex quantities. Eqn. 5 represents the general solution of the piezoelectric field problem. The solution of the crack problem is found adapting the function $f_\alpha(z_\alpha)$ to the boundary conditions of a Griffith crack with electrically impermeable and mechanically traction free crack faces. Furthermore, the crack faces, oriented parallel to the x_1–axis of the crack coordinate system, are assumed to be free of electric charges. The external loads are accounted for by $T_m = [\sigma_{12}^\infty, \sigma_{22}^\infty, \sigma_{32}^\infty, D_2^\infty]$ comprising the stresses σ_{i2}^∞ and electric displacements D_2^∞ at infinity.

The function $f_\alpha(z_\alpha)$ can be determined applying a Fourier transformation. Finally, two sets of dual integral equations are obtained which are solved following Pohanka and Smith [6]. After resubstituting the stress and electric displacement functions χ_i and θ, the results for stresses and electric displacements

are [7]

$$\begin{bmatrix} \sigma_{k1} \\ D_1 \end{bmatrix} = -\Re \left\{ M_{k\alpha} \; N_{\alpha m} \; p_\alpha \left[(z_\alpha^2 - 1)^{-\frac{1}{2}} z_\alpha - 1 \right] \right\} \; T_m$$

$$\begin{bmatrix} \sigma_{k2} \\ D_2 \end{bmatrix} = \Re \left\{ M_{k\alpha} \; N_{\alpha m} \left[(z_\alpha^2 - 1)^{-\frac{1}{2}} z_\alpha - 1 \right] \right\} \; T_m \tag{7}$$

$\Re\{..\}$ denotes the real part of a complex quantity, $N_{\alpha m}$ is the inverse of $M_{k\alpha}$. In Eqn. 7 the coordinates x_i (involved in the function z_α) are normalized with respect to the half crack length a.

CALCULATION OF FERROELECTRIC/FERROELASTIC SWITCHING ZONES

In the x_1–x_2 plane it has to be distinguished between three different kinds of switching events. A tetragonal unit cell can switch 90 degrees clock– or anti–clockwise ($\pm 90°$) or it can switch 180 degrees ($180°$). Switching events with a resulting orientation of the c-axis in the x_3–direction i.e. parallel to the crack front are not under consideration. If ϕ is the angle between the c–axis of a unit cell and the crack faces, the change in polarization going along with a switching event can be described by the vector

$$\Delta \vec{P} = b \, P^0 \begin{pmatrix} \sin(\phi + \varphi) \\ -\cos(\phi + \varphi) \end{pmatrix} \tag{8}$$

$$b = \begin{cases} -\sqrt{2} & \text{for} \;\; +90° \\ \sqrt{2} & \text{for} \;\; -90° \\ -2 & \text{for} \;\; \pm 180° \end{cases} \quad , \quad \varphi = \begin{cases} +\pi/4 & \text{for} \;\; +90° \\ -\pi/4 & \text{for} \;\; -90° \\ +\pi/2 & \text{for} \;\; \pm 180° \end{cases}$$

with the amount of the spontaneous polarization of a unit cell P^0. The specific electric work, which has to be supplied for the switching is calculated from

$$W_e = \int E_i \, dD_i \approx E_i \, \Delta P_i \tag{9}$$

The approximate solution of the integral is based on the assumption, that the electric field E_i remains unchanged in the course of the switching process. This implies, that the material constants are not influenced by the switching. Therefore the calculations have to be seen as a first order approximation. Furthermore in Eqn. 9 it is assumed, that the change in the electric displacement is dominated by the ferroelectric/–elastic switching, linear piezoelectric contributions are neglected.

Corresponding to the polarization switch vector of Eqn. 8, the change in strain due to the switching can be described by the tensor

$$\Delta \epsilon_{ij} = -\epsilon_D \begin{pmatrix} \cos 2\phi & \sin 2\phi \\ \sin 2\phi & -\cos 2\phi \end{pmatrix} \; ; \qquad \epsilon_D = \frac{c - a}{a_0} \tag{10}$$

The parameter ϵ_D contains the constants of the tetragonal and the cubic lattice a, c and a_0. In the case of a $180°$ switching event ϵ_D is zero, since this species doesn't go along with a change in strain. The specific mechanical work, which has to be supplied for the switching is calculated from

$$W_m = \int \sigma_{ij} \, d\epsilon_{ij} \approx \sigma_{ij} \, \Delta \epsilon_{ij} \tag{11}$$

accounting for the same assumptions as in Eqn. 9. A simple switching criterion can be derived from Eqns. (9) and (11) relating the sum of specific mechanical and electric works to a treshold value, that approximately represents half of the area of a polarization hysteresis

$$\sigma_{ij} \, \Delta \epsilon_{ij} + E_i \, \Delta P_i \geq 2 \, E_C P^0 \tag{12}$$

The coercitive field is denoted by E_C. Eqn. 12 was first used by Hwang et al. [8]. It neglects contributions of grain boundary and domain wall energies [9]. The switching criterion has to be applied seperately
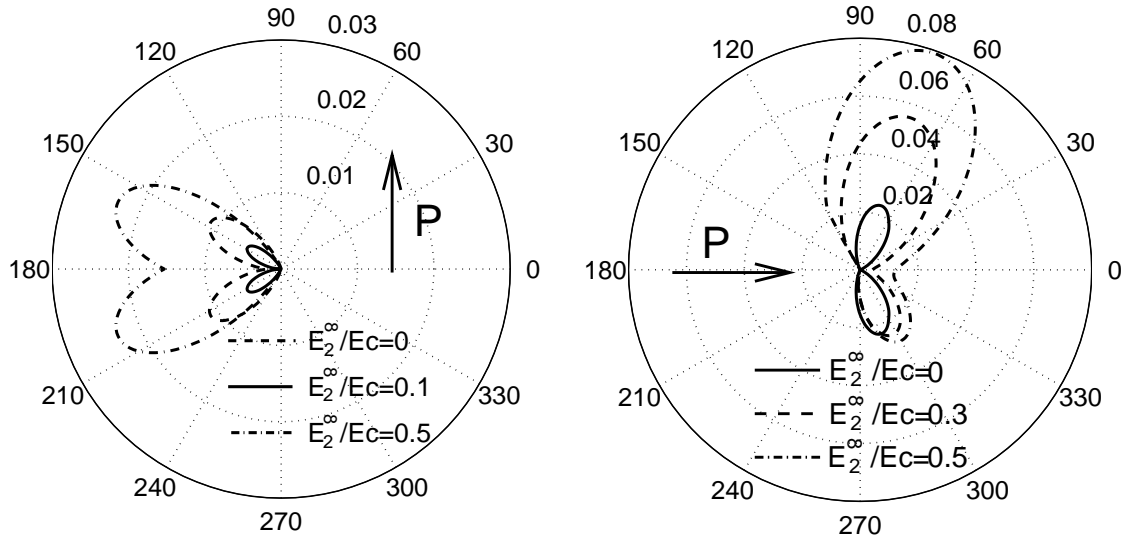
Fig. 1: Process zones for poling perpendicular (left) and parallel (right) to the crack faces

to the possible switching events, i.e. $\pm 90°$ and $180°$. For $180°$ events the first term in Eqn. 12 vanishes. Consequently, $180°$ switchings cannot be caused by mechanical fields. By means of the switching criterion it is decided, which one of the three events could occur at an arbitrary point in the $x_1 - x_2$-plane. If there are several possibilities, the one variant will be chosen, which goes along with the highest amount of switching work. Stress tensor and electric field vector are inserted from the analytical solution for a crack, Eqn. 7, taking into account the constitutive law of piezoelectricity. Thus, a nonlinear algebraic equation for the determination of the switching zone boundaries is obtained. The union of the $+90°$ and $-90°$ zones is considered as the ferroelectric/-elastic fracture process zone, since it influences the fracture process by producing additional strain. There may be $180°$ switching events which dominate over possible $\pm 90°$ events. Boundaries of the process zone being caused by an intersection of $180°$ and $\pm 90°$ regions are calculated equating the switching energy densities of $\pm 90°$ and $180°$ events:

$$\sigma_{ij}\,\Delta\epsilon_{ij}^{\pm 90} + E_i\,\Delta P_i^{\pm 90} = \sigma_{ij}\,\Delta\epsilon_{ij}^{180} + E_i\,\Delta P_i^{180} \tag{13}$$

Fig. 1 shows process zones for two different poling directions. The origin of the polar coordinate system coincides with the crack tip, the radius r is normalized with respect to the half crack length. The crack is coming from the left side with the crack faces lying at $\theta = 180°$. In both diagrams three different electric loads are superimposed with a mechanical Mode–I loading. All calculations have been performed with the material constants of bariumtitanate. The electric loading is controlled by D_2^∞, only. D_1^∞, like e.g. σ_{11}^∞ results in a nonsingular, homogeneous electric displacement field and therefore is not relevant for fracture mechanics. E_2^∞ is approximately proportional to D_2^∞ and can be converted by the corresponding dielectric constant. Therefore, in Fig. 1 the electric loads are measured in multiples of the coercitive field intensity ($E_C = 200$ V/mm). Fig. 1 shows, that the process zones for a poling perpendicular to the crack faces are smaller than for a parallel poling. Furthermore, it should be noticed that the process zones become asymmetrical if the directions of poling and electric loading are different as in the case of a parallel poling.

INFLUENCE OF SWITCHING EVENTS ON THE FRACTURE TOUGHNESS

The inelastic strain, caused by the $\pm 90°$ switching events, can be interpreted as a residual strain thus leading to an additional loading or unloading of the crack. Its influence can be described by an additional stress intensity factor ΔK, which is defined as

$$\Delta K = \oint_S t_i\,h_i\,ds \tag{14}$$

The integration is performed over the boundary S of the process zone where the stresses t_i act due to a restraint of the residual strain. Eqn. 14 has been applied by McMeeking and Evans [10] to the investigation of transformation toughening. The function h_i describes the influence of a unit force in the crack tip near field on the stress intensity factors. Applying the method of complex stress functions for isotropic, elastic materials the effect of a force $F_i = [Q, P]^T$ is found [11]

$$K = K_I - i\,K_{II} = \frac{1}{\sqrt{2\,\pi}}\,\frac{1}{\kappa+1}\left\{(Q+i\,P)\left(\frac{1}{\sqrt{z_0}} - \kappa\frac{1}{\sqrt{\bar{z}_0}}\right) + \frac{(Q-i\,P)\,(\bar{z}_0-z_0)}{2\,\bar{z}_0\,\sqrt{\bar{z}_0}}\right\} \qquad (15)$$

acting at the location $z_0 = x_{10} + i\,x_{20}$ (conjugate complex $\bar{z}_0$). For plane strain conditions it is $\kappa = 3 - 4\,\nu$ with Poisson's Ratio ν. Separating real and imaginary parts and taking into account the relations $K_I = F_i\,h_i^I$ and $K_{II} = F_i\,h_i^{II}$, we find in polar coordinates (r, θ):

$$h_i^I = \frac{1}{2\sqrt{2\pi\,r}(1-\nu)}\left(\begin{array}{c} \cos\left(\dfrac{\theta}{2}\right)\left(2\nu - 1 + \sin\left(\dfrac{\theta}{2}\right)\sin\left(\dfrac{3\theta}{2}\right)\right) \\ \sin\left(\dfrac{\theta}{2}\right)\left(2 - 2\nu - \cos\left(\dfrac{\theta}{2}\right)\cos\left(\dfrac{3\theta}{2}\right)\right) \end{array}\right) \qquad (16)$$

Here, $r = |z_0|$ denotes the distance of the applied force from the crack tip. Bückner [12] interpreted Eqn. 16 as weight function, that's why h_i is often referred to as Bückner's weight function. For the Mode–II weight function it is found from Eqn. 15:

$$h_i^{II} = \frac{1}{2\sqrt{2\pi\,r}(1-\nu)}\left(\begin{array}{c} \sin\left(\dfrac{\theta}{2}\right)\left(2 - 2\nu + \cos\left(\dfrac{\theta}{2}\right)\cos\left(\dfrac{3\theta}{2}\right)\right) \\ \cos\left(\dfrac{\theta}{2}\right)\left(1 - 2\nu - \sin\left(\dfrac{\theta}{2}\right)\sin\left(\dfrac{3\theta}{2}\right)\right) \end{array}\right) \qquad (17)$$

In Eqn. (14) the stress vector can be replaced by the stress tensor using Cauchy's Theorem $t_i = \sigma_{ij}\,n_j$. Applying Hooke's Law, the stress tensor is expressed by the strain tensor, whereby the condition of isochoric deformations was taken into account($\epsilon_{ll} = 0$):

$$\sigma_{ij} = \frac{E}{1+\nu}\left(\epsilon_{ij} + \frac{\nu}{1-2\nu}\,\epsilon_{ll}\,\delta_{ij}\right) = \frac{E}{1+\nu}\,\epsilon_{ij} \qquad (18)$$

The strain tensor represents the additional strain, therefore being replaced by $\Delta\epsilon_{ij}$ from Eqn. (10). Eqn. (14) thus yields

$$\Delta K = \frac{E}{1+\nu}\oint_S \Delta\epsilon_{ij}\,h_i\,n_j\,ds = \frac{E}{1+\nu}\int_A \Delta\epsilon_{ij}\,h_{i,j}\,dA \qquad (19)$$

The domain integral, which has been used for all calculations, is introduced using Gauß's Integral Theorem. E and ν are effective constants of an isotropic model material, which have to be calculated from the anisotropic elastic material tensor. Using polar coordinates, the integration with respect to r can be carried out analytically.

To take into account a statistical distribution of local unit cell orientations ϕ around the macroscopic poling angle ϕ_0, a probability density function $w(\phi)$ is introduced. Inserting Eqns. 10 and 16 (17) into Eqn. 19 supplies an equation for the calculation of ΔK_I (ΔK_{II}). For ΔK_I it is for example

$$\Delta K_I = -\frac{3\,\epsilon_D\,E}{4\,\sqrt{2\pi}\,(1-\nu^2)}\int_{-\pi}^{\pi}\int_{-\pi}^{\pi}\sqrt{R(\theta)}\left[\cos\left(2\phi - \frac{7\theta}{2}\right) - \cos\left(2\phi - \frac{3\theta}{2}\right)\right]d\theta\,w(\phi)\,d\phi \qquad (20)$$

$R(\theta)$ denotes the radius of the process zone boundary. If the crack grows by an amount Δa, the switching zone is also extended along the crack faces. If we assume, that no back switches occur in the course of the crack growth, there will be a homogeneous switching zone with the height of the original process zone ($\Delta a = 0$) enclosing the crack. In front of this background, R–curves can be calculated. Then the effective fracture toughness K_C^∞ is of interest:

$$K_{IC}^\infty = K_{IC}^{tip} - \Delta K_I \;; \quad K_{IIC}^\infty = K_{IIC}^{tip} - \Delta K_{II} \qquad (21)$$
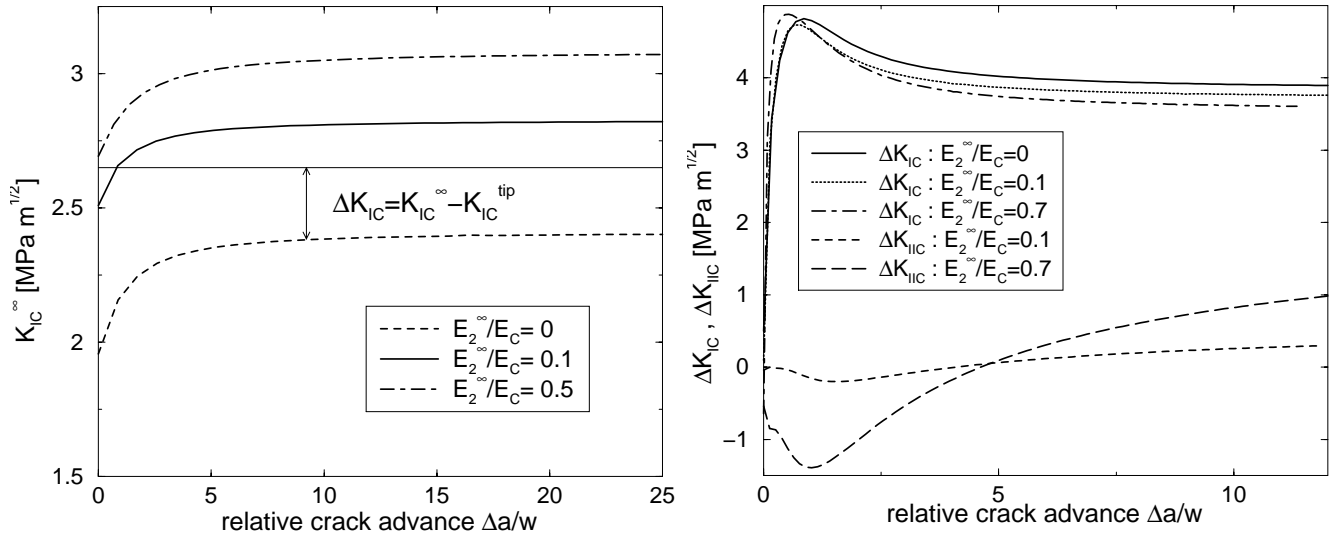
Fig. 2: Fracture toughness for poling perpendicular (left) and parallel (right) to the crack faces

It is the difference between a hypothetical (pure mechanical) fracture toughness at the crack tip K_{IC}^{tip}, K_{IIC}^{tip} neglecting switching effects, and the additional loading ($\Delta K > 0$) or unloading ($\Delta K < 0$) of the crack due to switching events, which is calculated from Eqn. 19.

Fig. 2 shows R–curves for the two poling directions depicted in Fig. 1. The crack length is normalized with respect to the largest extension w of the process zone perpendicular to the crack faces. Material constants and loading conditions are the same as in Fig. 1. In the left plot, the shape of the R–curves looks like expected. The calculations are based on a statistical distribution of the polarization angle with a maximum deviation from ϕ_0 of 30° and a Heaviside function as probability density function. K_I^{tip} was assumed as 2.65 MPa m$^{1/2}$. The screening effect $\Delta K_I = -\Delta K_{IC}$ obviously can be positive and negative. The Mode–I fracture toughness increases with increasing electric loading, ΔK_{II} is zero. The influence of electric fields shown in the diagram could be confirmed performing experiments on DCB specimens [2]. In the case of a parallel poling (right plot), little influence of the electric field can be observed for ΔK_{IC}, although the sizes of the process zones differ much. The reason lies in the fact, that around the crack tip within the section between 70° and 140° (Fig.1) the contribution of switching events to ΔK_{IC} changes its sign. So, a growing process zone produces both positive and negative contributions. The reason for the maximum in the R–curves is similar. When the crack starts growing it first passes the region of a positive contribution leading to a marked rise of ΔK_{IC}. During the crack growth negative contributions are produced leading to the maximum. In contrast with the case of perpendicular poling, there is a finite ΔK_{IIC} for parallel poling in connection with electric loads due to the asymmetry of the process zones. However, the amount of ΔK_{IIC} is smaller than the amount of ΔK_{IC}.

REFERENCES

1. Suo, Z., Kuo, C.M., Barnett, D.M. and Willis, J.R. (1992). *J. Mech. Phys. Solids* 40, 739.
2. Kuna, M. and Ricoeur, A. (2000). In: *Proc. of the SPIE Vol. 3992*, p. 185, Lynch, C.S. (Ed.).
3. Yang, W. and Zhu, T. (1998). *J. Mech. Phys. Solids* 46(2), 291.
4. Zhu, T. and Yang, W. (1997). *Acta mater.* 45(11), 4695.
5. Park, S.B. and Sun, C.T. (1995). *Int. J. of Fracture* 70, 203.
6. Pohanka, R.C. and Smith, P.L. (1988). *Electronic Ceramics.* Marcel Dekker, New York.
7. Ricoeur, A. and Kuna, M. (2001). *J. Mech. Phys. Solids* – submitted.
8. Hwang, S.C., Lynch, C.S. and McMeeking, R.M. (1995). *Acta Metall. Mater.* 43, 2073.
9. Arlt, G. (1990). *Journal of Materials Science* 25, 2655.
10. McMeeking, R.M. and Evans, A.G. (1982). *J. Am. Ceram. Soc.* 65(5), 242.
11. Erdogan, F. (1962). In: *Proc. of the 4th U.S. Nat. Congress of Appl. Mech.*, p. 547.
12. Bückner, H.F. (1970). *Z. Angew. Math. Mech.* 50, 529.

Simulation of fatigue crack propagation processes in arbitrary three-dimensional structures with the program system ADAPCRACK3D

M. Fulland, M. Schöllmann, H.A. Richard

Institute of Applied Mechanics, University of Paderborn
D – 33098 Paderborn, Germany

ABSTRACT

The following paper provides both an overview on the abilities and general functionality of the three-dimensional crack simulation program ADAPCRACK3D and introduces a new three dimensional concept for the prediction of crack growth processes, that also takes the effects of Mode-III into consideration. ADAPCRACK3D, which has been developed at the Institute of Applied Mechanics at the University of Paderborn, is a finite element based code, that is able to perform crack propagation simulations in arbitrary structures under arbitrary loading conditions. Therefore, on the one hand an adaption of the existing FE-mesh to the change of geometry due to crack growth is needed in every single step of the simulation. As generally the manipulation of a FE-mesh causes a deterioration of the mesh quality, many algorithms especially adjusted to a crack growth simulation have been implemented to improve the quality of the FE-mesh. On the other hand an automatic fracture mechanical evaluation of the crack front is performed, that results in the computation of crack propagation. This procedure also includes the new concept, that – different from the rare existing three-dimensional simulation tools – also calculates the effect of the stress intensity factor K_{III} on crack growth direction and rate. This new concept is described in detail. The outcome of the simulation shows good agreement with experimental results.

KEYWORDS
crack simulation, Mixed-Mode, ADAPCRACK3D, mesh-adaption, crack growth concept, 3D fracture criterion

INTRODUCTION
In the last years lightweight construction has become more and more important in all fields of mechanical engineering. This development can be seen as a consequence both of ecological (resource conserving) and economical (saving of material) considerations. However, lightweight construction generally shows a greater liability to the initiation of cracks during its proposed lifetime. So the damage tolerant design is of increasing importance in relation to safe life design. Nevertheless failure especially of critical structures such as power plants, aircraft, ships etc. must not be tolerated, so the urgent need for simulation tools for the prediction of three-dimensional crack growth processes is obvious. These simulations then can be used to determine the appropriate point of time to substitute a crack damaged component and to find suitable inspection intervals for them. ADAPCRACK3D is a new program, that can be used to perform this necessary simulations in arbitrary three-dimensional components. In conjunction with the implemented new three dimensional crack

propagation concept it is a powerful tool for damage tolerant design of components in all fields of engineering practice.

THE CRACK SIMULATION PROGRAM ADAPCRACK3D

ADAPCRACK3D consists of three independent modules, the mesh-adaption NETADAPT3D, that provides all necessary manipulations of the FE-mesh, the well known commercial FE-solver ABAQUS and the module NETCRACK3D performing the fracture mechanical evaluation. Figure 1 shows the simplified functionality scheme of ADAPCRACK3D with its three modules. As major input objects a description of the uncracked object in terms of a three-dimensional FE-mesh consisting of tetrahedrons and a description of the crack (2D triangular elements) are requested.
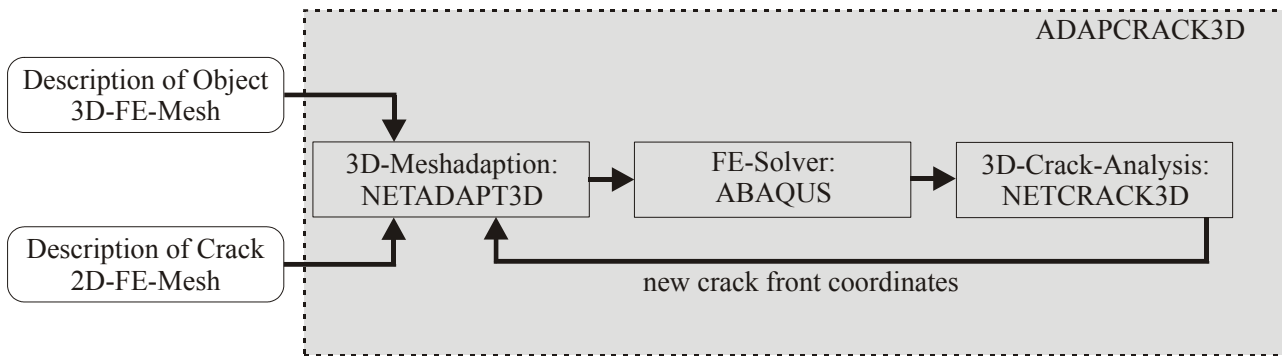
Figure 1: Simplified functionality scheme of ADAPCRACK3D

In the first simulation step both input files are composed to a description of the cracked object. The resulting FE-model is solved by the finite element code ABAQUS. Afterwards NETCRACK3D uses the results of the FE-calculation to compute new crack front coordinates. These new coordinates are sent back to the module NETADAPT3D and define the necessary geometry modification for the next simulation step. In the following some important aspects of the modules of ADAPCRACK3D will be discussed including the presentation of the new crack propagation concept already implemented in NETCRACK3D.

The module NETADAPT3D
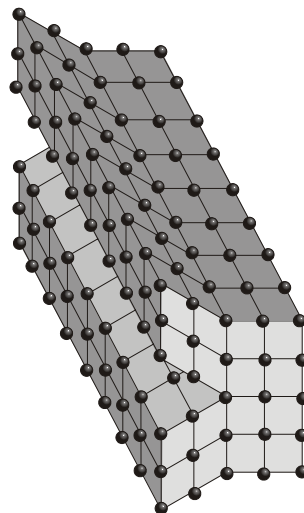
Figure 2: Submodel for straight crack front

The module NETADAPT3D has two major tasks within ADAPCRACK3D. First of all it has to realize the geometry changes due to crack growth in the describing FE-model. Beyond this it has to assure a sufficiently good mesh quality during the whole simulation procedure especially in regions near the crack front. The good mesh quality can be obtained by the use of ABAQUS submodeling technique [1] by defining a hexahedral submodel along the crack front as can be seen in Figure 2. Besides the obviously good mesh

quality the main advantage of this submodel can be found in its regular structure, which allows an easy automatic evaluation of the fracture mechanical parameters at the crack front. Moreover, this technique simplifies the manipulation of the (global) FE-model, that is necessary to adjust it to the changing geometry, as it is no longer essential to guarantee an extra high mesh quality at the crack front of the global model. All model-manipulation work regarding the realization of the initial crack (first simulation step) and the crack propagation (all further steps) is performed by inserting additional nodes into the existing model. By choosing appropriate locations for these nodes a global FE-model can be created, that contains all necessary crack describing objects (nodes, edges, faces) [2]. If this is done, the correct crack description consisting of two crack surfaces lying directly at one another can then easily be obtained by doubling those nodes, edges and faces and unstitching the FE-Model along the crack face. The node insertion itself can – by user's choice – either be performed with a Delaunay-algorithm [4] or a more direct approach minimizing the influenced region of the node insertion within the model [3]. The main advantage of the direct method in comparison to the Delaunay technique is the fact, that this algorithms never destroys already existing edges and faces, which simplifies the algorithmic implementation, as only one iteration for the insertion procedure in each simulation step is necessary. Its greatest disadvantage can be found in the generally worse mesh quality obtained by this method. Nevertheless both methods generate a mesh quality that needs to be improved in order to obtain reliable results. Therefore improvement algorithms especially adapted to the requirements of a crack simulation of different classes (Table 1) have been implemented.

TABLE 1
CLASSES OF IMPROVEMENT ALGORITHMS IMPLEMENTED IN ADAPCRACK3D

	Number of nodes changed	**Number of nodes unchanged**
during insertion process	Bisection algorithm	Flip algorithm
after insertion process is finished	Melting of nodes Local domain decomposition	Laplacian algorithm Controlled displacement

The Bisection algorithm originally presented by Rivara [5] is used as a rule to subdivide elements without quality deterioration. The Flip algorithm changes the connectivity of 5 nodes at a time and is applied within ADAPCRACK3D for the Delaunay Method of node insertion. After the insertion process is finished, the mesh quality can – depending on the local situation – be improved either by adding nodes (Local domain decomposition) or removing nodes by melting them. Another also implemented improvement strategy, in which the number of nodes remains unchanged, is to reposition the existing nodes for the purpose of a better node distribution in the model. Therefore both the well known and very easy Laplacian algorithm and another algorithm controlling the displacement by calculating the reposition effect on the quality are implemented [2,3].

The module NETCRACK3D
The module NETCRACK3D provides all fracture mechanical evaluations within ADAPCRACK3D. At first the energy release rates are calculated for all nodes of the crack front. This is performed under utilization of the special structure of the submodel (Figure 2) with use of the modified virtual crack closure integral (MVCCI) method [7,8]. The energy release rates are converted afterwards into cyclic stress intensity factors ΔK_I, ΔK_{II} and ΔK_{III} for all three crack opening modes. By user's choice this can be done either under plane strain or plain stress conditions. The calculated stress intensity factors are then used by the new three-dimensional concept discussed in the next chapter to compute the cyclic comparative stress intensity factor ΔK_V as well as the direction of crack growth for each node of the crack front. The cyclic stress intensity factor ΔK_V can be compared to the limiting values ΔK_{th} and ΔK_c for stable crack growth. Moreover it is the determining factor for the computation of the crack growth rate according to the law of Erdogan and Ratwani [6]. With the knowledge of crack growth direction and rate the new coordinate for each crack front node is uniquely defined.

THE NEW CRACK PROPAGATION CONCEPT
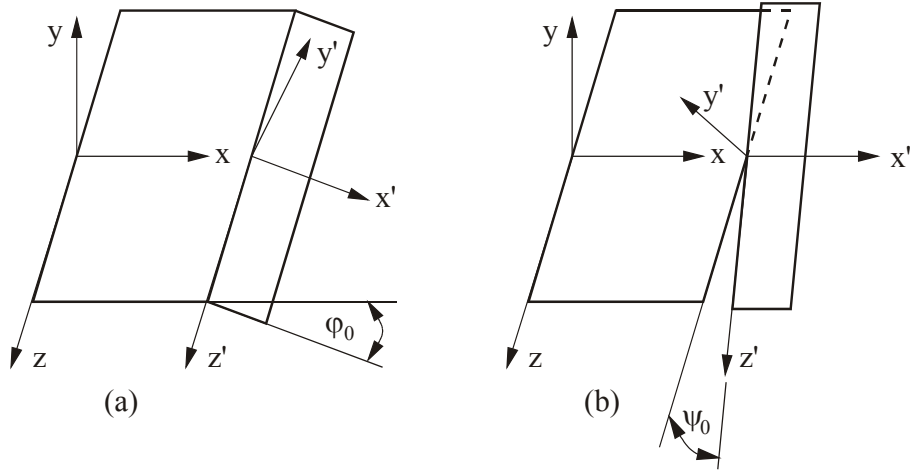
Figure 3: The definition of the angles φ_0 and ψ_0

For the simulation of superimposed Mode-I/ Mode-II loading it is sufficient to compute one angle φ_0 for the description of crack growth. As soon as Mode-III is also under consideration, it is essential to define a second angle ψ_0 describing the rotation around the x-axis (see Figure 3). The new criterion is based on the assumption, that crack propagation occurs perpendicular to the direction of the biggest principal normal stress $\sigma_{1'}$ which can be found on a cylindrical sphere around the crack front (Figure 4). For planar mixed-mode situations this definition is equivalent to the MTS-criterion of Erdogan and Sih [9], where $\sigma_{\varphi\,max}$ also is the maximum normal stress on the same cylindrical sphere. In three-dimensional loading cases the crack propagation is no more perpendicular to the maximum tangential stress σ_φ, but perpendicular to $\sigma_{1'}$ which is given by

$$\sigma_{1'} = \frac{\sigma_\varphi + \sigma_z}{2} + \frac{1}{2}\sqrt{(\sigma_\varphi - \sigma_z)^2 + 4\tau_{\varphi z}^2} , \tag{1}$$

with
$$\sigma_\varphi = \frac{K_I}{4\sqrt{2\pi r}}\left\{3\cos\left(\frac{\varphi}{2}\right)+\cos\left(\frac{3\varphi}{2}\right)\right\} - \frac{K_{II}}{4\sqrt{2\pi r}}\left\{3\sin\left(\frac{\varphi}{2}\right)+3\sin\left(\frac{3\varphi}{2}\right)\right\}$$

$$\sigma_z = \nu(\sigma_r + \sigma_\varphi) = \frac{8\nu}{4\sqrt{2\pi r}}\left\{K_I\cos\left(\frac{\varphi}{2}\right)-K_{II}\sin\left(\frac{\varphi}{2}\right)\right\} \tag{2}$$

$$\tau_{\varphi z} = \frac{K_{III}}{\sqrt{2\pi r}}\cos\left(\frac{\varphi}{2}\right)$$
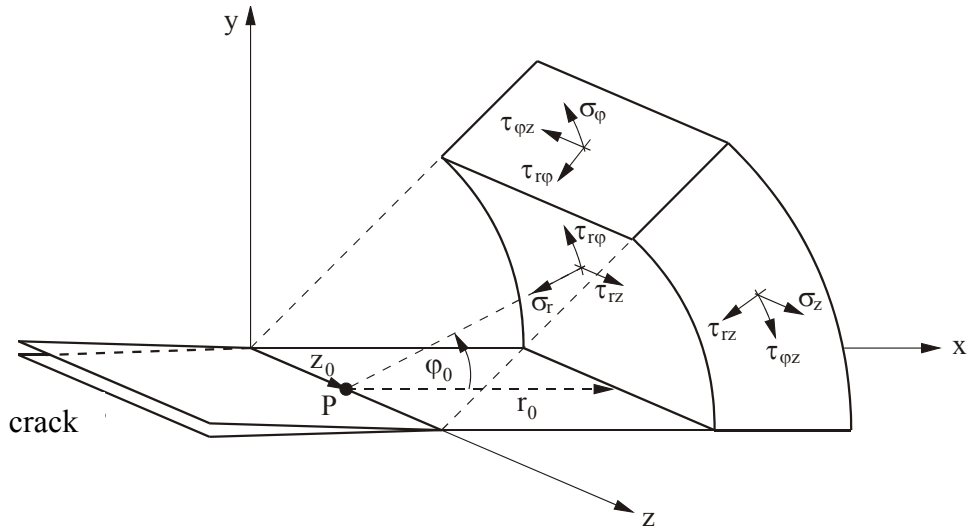
Figure 4 : Cylindrical coordinate system at a three-dimensional crack front

So the kinking angle φ_0 can be calculated by the partial derivatives

$$\frac{\partial \sigma_{1'}}{\partial \varphi} = 0 \quad \text{and} \quad \frac{\partial^2 \sigma_{1'}}{\partial \varphi^2} < 0. \tag{3}$$

The second angle ψ_0 can then easily be found by the calculation of the angle of the principal normal stress given by

$$\tan(2\psi_0) = \frac{2\tau_{\varphi z}(\varphi_0)}{\sigma_\varphi(\varphi_0) - \sigma_z(\varphi_0)}. \tag{4}$$

Equations 3 and 4 obviously present a formulation for the determination of the two kinking angles for three dimensional crack growth, that take all stress intensity factors K_I, K_{II} and K_{III} into consideration, which makes them suitable for arbitrary mixed-mode-combinations. The solution of Eqn. 3 can be found in [10]. It can not be solved in a close form, but Figure 5 shows the visualization of the numerical results for a grid of different K_I-K_{II}-K_{III}-ratios.
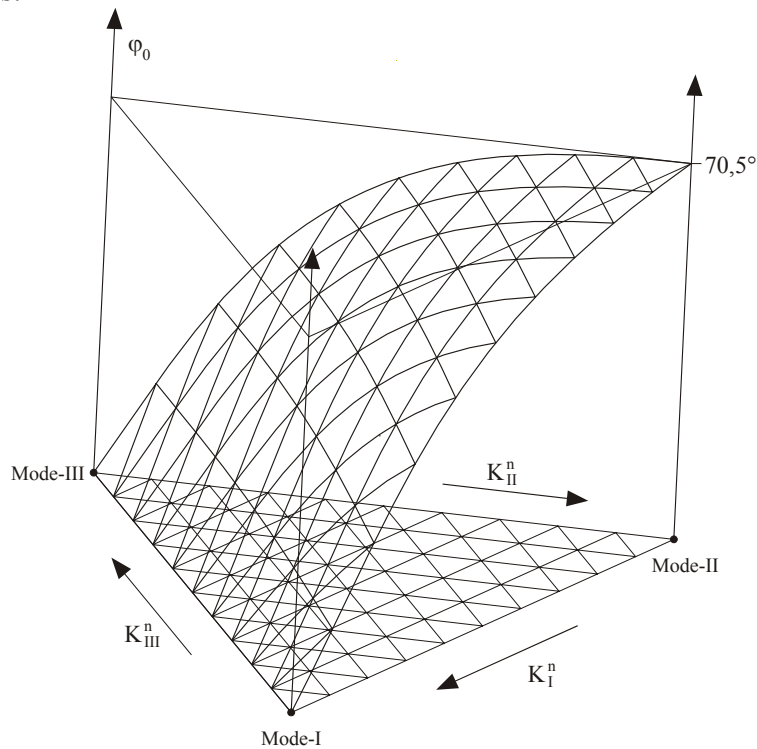
Figure 5 : The angle φ_0 depending on the mixed-mode ratio
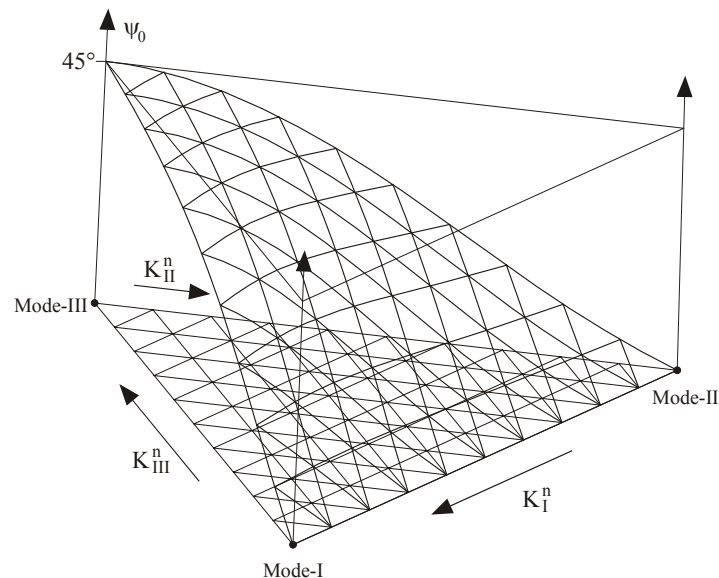
Figure 6 : The angle ψ_0 depending on the mixed-mode ratio

Figure 6 presents the angle ψ_0 according to Eqn. 4. In both figures the stress intensity factors are normalized by

$$K_I^n = \frac{K_I}{K_I + |K_{II}| + |K_{III}|}, \; K_{II}^n = \frac{K_{II}}{K_I + |K_{II}| + |K_{III}|} \; \text{and} \; K_{III}^n = \frac{K_{III}}{K_I + |K_{II}| + |K_{III}|}, \tag{5}$$

which results in a barycentric coordinate system. The front line of Figure 5 (between Mode-I and Mode-II) redelivers the MTS criterion for planar loading situations. With the use of the calculated φ_0 the comparative stress intensity factor can be obtained by $K_v = \sigma_{I'}\sqrt{2\pi r}$ as

$$K_v = \frac{1}{2}\cos\left(\frac{\varphi_0}{2}\right)\left\{ K_I\cos^2\left(\frac{\varphi_0}{2}\right) - \frac{3}{2}K_{II}\sin(\varphi_0) + \sqrt{\left[K_I\cos^2\left(\frac{\varphi_0}{2}\right) - \frac{3}{2}K_{II}\sin(\varphi_0)\right]^2 + 4K_{III}^2} \right\}. \tag{6}$$

CONCLUSIONS

The presented program ADAPCRACK3D is a powerful tool for the simulation of three-dimensional crack propagation processes. Due to its modular structure the three general simulation functions *Meshadaption*, *FE-solving* and *Crack Analysis* can be modified and adapted to new investigations independent of each other. The module 3D-Meshadaption provides the insertion of a crack into a former uncracked FE-model and asserts the necessary good mesh quality The crack analysis module performs all fracture mechanical evaluations. Its special purpose is the computation of new crack front coordinates for the next simulation step in order to run a fully automatic crack growth analysis. The new three-dimensional criterion introduced above is implemented in this module and used for both the calculation of the kinking angles and the determination of ΔK_v. First numerical simulations are extraordinarily encouraging in comparison to experimental and analytical results known so far. Examples can be found in [2, 10]. Nevertheless a lot of experimental review is still to be done in order to verify this new theoretically found criterion.

REFERENCES

1. Hibbitt, Karlsson and Sorensen (1998). ABAQUS / Standard User's Manual. Version 5.8.

2. Schöllmann, M., Fulland, M. and Richard, H.A. (2000). In: *Fracture Mechanics: Applications and Challenges, CD-Rom Proceedings ECF13*, section 9, paper 5, pp. 1-8, Fuentes, M., Martín-Meizoso, A. and Martínez-Esnaola J.-M. (Eds). Elsevier, Oxford.

3. Fulland, M., Schöllmann, M. and Richard, H.A. (2000). In: *Advances in Computational Engineering & Sciences*, Vol. 1, pp. 948-953, Atluri, S.N. and Brust, F. (Eds). Tech Science Press, Palmdale.

4. Joe, B. (1992). In: *Artificial Intelligence, Expert Systems and Symbolic Computing,* pp.215-222, Houstics, E.N. and Rice, J.R. (Eds.). Elsevier Science Publishers.

5. Rivara, M.C. (1996). In: *Proceedings 5th International Meshing Roundtable,* pp. 77-86.

6. Erdogan, F. and Ratwani, M. (1970). *International Journal of Fracture Mechanics*, 6, 379.

7. Rybicki, E.F. and Kanninen, M.F. (1977). *Engineering Fracture Mechanics*, 9, 931.

8. Buchholz, F.-G. (1984). In: *Accuracy, Reliability and Training in FEM Technology*, pp. 650-659, Robinson, J. (Ed). Robinson and Associates, Dorset.

9. Erdogan, F. and Sih, G.C.(1963). *Journal of Basic Engineering*, 85, 519.

10. Schöllmann, M., Fulland, M., Kullmer, G. and Richard, H.A. (2001) *DVM-Bericht 233 Bruchvorgänge,* pp. 199-213.

SIMULATION OF FATIGUE CRACK PROPAGATION RATES IN SMOOTH BENDING SPECIMENS, FROM THE ONSET OF LOADING, USING THE TWO-TERM MODEL

H. Saguy[1], M.P. Weiss[2] and D. Rittel[2]

[1] Rafael Inc., P.O.Box 2250, Haifa 31021, Israel
[2] Faculty of Mechanical Engineering, Technion
Haifa 32000, Israel

ABSTRACT

The fatigue growth of cracks emanating from smooth specimens with stress concentration was investigated. A two-term model of fatigue for step-by-step evaluation of crack propagation from very short cracks to fracture was used to predict the crack growth. Base metal of T1 steel (ASTM 514F) was tested. Growth rates were monitored using the Direct Current Potential Drop method. System calibration was made using an accurate model of the specimen and a numerical solution of the Laplace equation for the electric potential. The two-term model is presented and discussed, and life predictions are compared with experimental results.

KEYWORDS

fatigue modeling, short crack propagation, notches, fatigue diagram

INTRODUCTION

The growth of fatigue cracks based on fracture mechanics, primarily relies on laboratory fatigue tests on specimens containing "long" flaws, which are typically tens of millimeters in length. The continuum approaches, which have been adopted for the characterization of small fatigue flaws, show that the growth rates of small flaws can be significantly greater than the corresponding rates of long flaws when characterized in term of the same nominal driving force [1]. Current design methodology based on linear elastic fracture mechanics (LEFM) provides accurate estimates of fatigue life when the initial size of fatigue flaw is long enough (about half of millimeter). When the material contains defects that are smaller, life predictions nominally based on LEFM may give a non-conservative value (even if small-scale yielding condition prevail). The actual growth characteristics, crack path tortuosity or closure processes for small flaws can be different from those of longer flaws. The problem is further exacerbated by the flaw size detection limit of the non-destructive inspection method. Pearson [2] found that short surface flaws, 0.006 to 0.5 mm deep, grew up to 100 times faster than longer flaws, tens of millimeters in size, which were subjected to the same nominal stress intensity factor range (ΔK). Figure 1 shows a schematic behavior of short crack growth. This figure shows a marked reduction in the rate of growth of the micro-structural short
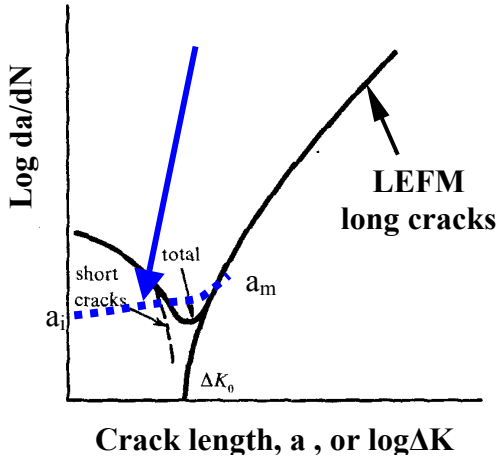
Figure 1: A Schematic of sub-threshold growth of a micro-structurally small fatigue

crack with increasing crack length and when the growth reached the LEFM regime, it starts to increase again as a function of the crack length a.

The growth rate of the retarded short crack subsequently increases with crack length until it merges with the long crack growth data characterized by LEFM. A two-term fatigue life prediction model, from the onset of loading in a smooth specimen until separation by fracture or by gross yielding, has been introduced by one of the authors [3]. The model, based on two terms for crack propagation calculation, has been shown to yield very close fatigue life predictions, compared to experimental results, for AISI 4340 low alloy steel specimens with zero mean stress (i.e. with R=-1) and for block loading with Low-High, and High-Low sequences [4]. In the model a fictitious "equivalent crack" was defined [5] so that the initial micro-crack size - a_i, the intermediate crack size - a_m,

and the number of propagating cycles between the two are the same as for the real crack. The fictitious crack rate is monotonic rising. Due to the fact that the size of the intermediate crack a_m, just at the start of the LEFM long crack size is only a few tenths of a mm, one can use the "equivalent crack" for all engineering purposes, and its propagation can be easily simulated with the two term model. Test results from various sources were successfully simulated. The model is based on the assumption that various fatigue mechanisms that have often been observed in fractured fatigue specimens, have been caused by different fatigue regimes. In certain cases, the different regimes exist concurrently in the same fatigue zone and each one causes the crack to propagate independently. In the current study, life predictions are compared with experimental results.

EXPERIMENTAL PROCEDURE

The material used for this study was T1 steel (ASTM 514F) in the form of rolled sheets. T1 steel composition and mechanical properties are presented in tables 1,2. The specimens were machined so as to be parallel to the rolling. The specimens were not machined on the outer surface.

TABLE 1
BASE METAL CHEMICAL COMPOSITION

C	Si	Mn	P	S	Cr	Ni	Mo	V	Ti
0.17	0.22	1.39	0.009	0.001	0.24	0.07	0.48	0.019	0.005

TABLE 2
THE MECHANICAL PROPERTIES OF T1 STEEL

S_y (MPa)	S_{UTS}	Elongation (%)	VHN
780	850	22.4	270

A Keyhole specimen was chosen due to the large amount of experimental data available. This specimen permits studies of both crack initiation and propagation. The crack growth of the specimens was monitored using the Direct Current Potential Drop (DCPD) method. Determination the crack size relies on the principle

that the electrical field in a cracked specimen with a current flowing through it, as a function of the specimen geometry and the crack size. For a constant current flow, the voltage drop across the crack will increase with increasing crack size due to the modification of the electric field. The change in the voltage was translated to crack size using a numeric model and experimental calibration relationship. The numeric model was written using the PDE (Partial Differential Equation) toolbox from Matlab. After drawing the specimen geometry, and defining the boundary condition, the model calculates the Laplace equation. A schematic of the direct current electrical potential crack monitoring system is presented in figure 2.
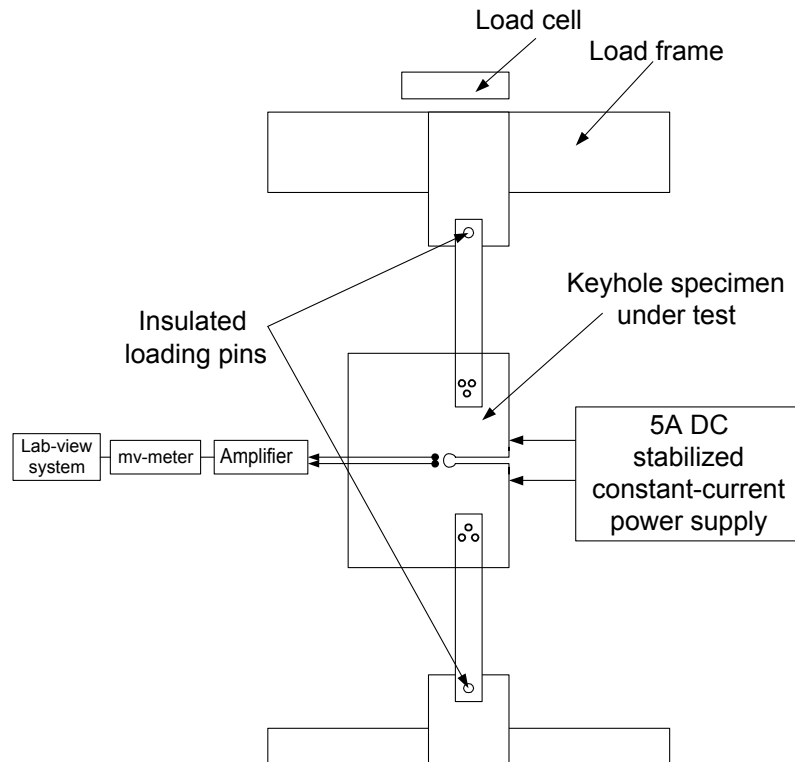
Figure 2: Schematic of the direct current electrical potential crack monitoring system

The specimens were tested under constant amplitude sinusoidal loading at a frequency of 10 Hz. The minimum-maximum load ratio was fixed at R=0.1. The stress intensity factor was calculated separately for short and long cracks and the results were compared with finite element analysis for different crack length.

THE FATIGUE DIAGRAM

The fatigue diagram introduced by Weiss [3,4,] is depicted in Fig 3 and a short description of the zones and regimes follows. The diagram is shown for particular specimen geometry and loading function. For other cases, a different but conceptually similar diagram can be constructed. The diagram covers the whole fatigue domain, starting with the smallest practical micro-cracks (1 micrometers or even less) until the largest and from zero stress amplitude until the ultimate tensile strength. The whole fatigue and fracture domain has been classified, and divided into discrete zones and fatigue regimes, on one comprehensive diagram. Fatigue damage from the onset of loading, is expressed in terms of accumulated crack length, in the whole range of very short, short and long crack ranges. The fatigue domain is divided into six zones by three constant stress amplitudes lines: the endurance limit S_e, the yield strength line S_y, and the ultimate tensile strength S_u, and by two constant stress intensity factor (SIF) lines: the plane strain fracture toughness K_{1c} and the effective threshold SIF range ΔK_{theff}. The use of the diagram helps to explain different fatigue behavior in the same specimen, under different loading regimes, results that in the past were often explained as fatigue scatter. The model that was built based on the diagram, enables to predict the crack propagation quantitatively, cycle by cycle, from the onset of loading, till final fracture. In the very short cracks regime the "equivalent crack" is used instead of the real crack, but for all engineering purposes it is fully adequate.
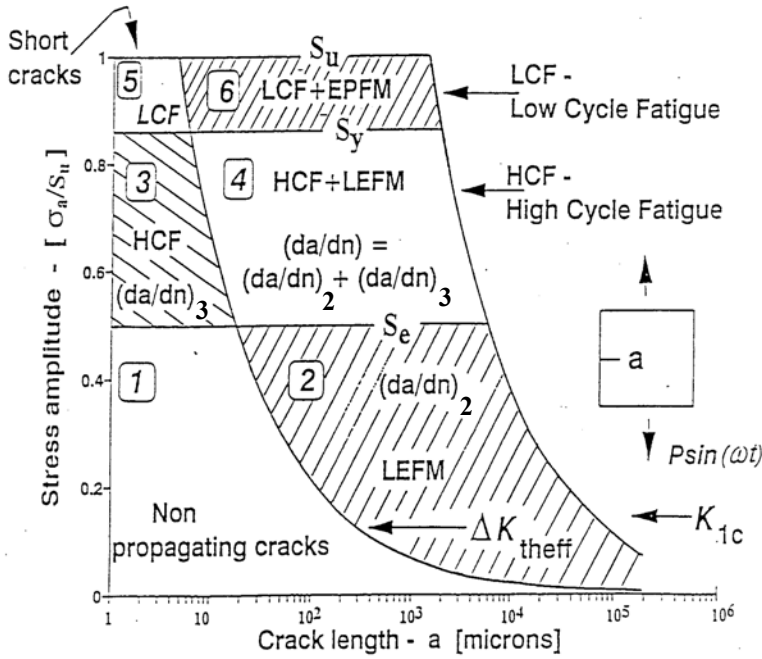
Figure 3: The fatigue domain divided into fatigue and fracture regimes and six zones

The zones differ by the fatigue regimes, as follows:

1. The safe zone. It may contain non-propagating cracks. It lies below both the endurance limit and the effective threshold stress intensity range (below the Kitagawa line).
2. Linear Elastic Fracture (LEFM) regime. Here mostly striation law is a good predictor of experimental results.
3. High cycle fatigue (HCF) regime with very short and short propagating cracks. The classical smooth specimens fatigue tests start here. This is the formerly called crack initiation zone.
4. Both HCF and LEFM regimes are active here concurrently. Crack propagation is formed by a combination of mechanisms and predicted by the superposition, of separately calculated propagation values, for each regime. In this regime most of the industrial failures take place. Here the stress amplitude is higher than the endurance limit and the Stress Intensity Factor range is above the threshold.
5. Low Cycle Fatigue (LCF) regime, very short and short propagating cracks. Parallel to zone 3, but in the plastic range. Industrial structures are not designed here, but pressure vessels are.
6. Both LCF and Elasto Plastic Fracture Mechanics (EPFM) regimes are active here. Crack propagation is formed and can be predicted by a combination of mechanisms. Fatigue understanding in this (and the previous) zones need additional research.

The fatigue diagram makes it possible to designate any cycle of a fatigue test or result, to a certain zone on the diagram, and therefore helps to classify the fatigue experimental domains and compare only test results, when they come from the same zone only. In the past, fatigue results from different zones were used for model evaluation without distinction, and erroneously referred to as fatigue scatter. Real fatigue scatter will thus become much smaller than before, if in the future, valid results will be compared for the same fatigue zone.

SIMULATION

The simulation program calculates the crack increment Δa in each loading cycle. The momentary crack length is calculated as the integration of the crack propagation rate- da/dN, according to the regime on the fatigue diagram where the test takes place. For each stress amplitude and crack length, the program resolves the zone in which crack propagation takes place for that specific loading cycle, and calculates the crack extension for that cycle. The extension is added to the previous depth and so the new crack length is created. The crack growth rate is composed of two separate terms, which depicts the crack growth rate of large cracks above the threshold stress intensity range and cracks at a nominal stress, that are above the endurance limit. A microcrack of 5 μm is assumed to exist. The form of the first crack propagation rate, in the LEFM zone 2, is calculated by the following relation:

$$\left(\frac{da}{dN}\right)_2 = C_1 \cdot \Delta K_{eff}^m \cdot \left(\frac{1-\left(\Delta K_{th}/\Delta K\right)^p}{1-\left(\Delta K/K_{1c}\right)^q}\right) \tag{1}$$

This relation is valid for zone 2 -the LEFM regime only.

The material parameters are C_1 and m (as in the Paris' law). The other term deals with crack propagation due to stress amplitude above the endurance limit. The term $(da/dN)_3$ is defined as:

$$\left(\frac{da}{dN}\right)_3 = C_2 \cdot a^\alpha \cdot \left(\frac{\sigma_a - S_e}{S_u}\right)^n \cdot \left(\frac{1}{1-(\sigma_a/S_u)^q}\right) \quad (2)$$

Where C_2, α and q are materials parameters. The parameter N_i has been eliminated and the stress amplitude σ_a introduced. The form of the equation already includes the entire above mentioned boundary effects. The crack rate reaches zero for $\sigma_a = S_e$, and reaches infinity for $\sigma_a = S_u$

The combined relation for crack propagation in specimen or part, under loading conditions for all four zones below the yield strength, is the superposition of eq. (1) and (2), as follows:

$$\left(\frac{da}{dN}\right) = C_1 \cdot \Delta K_{eff}^m \cdot \left(\frac{1-(\Delta K_{th}/\Delta K)^p}{1-(\Delta K/K_{1c})^q}\right) + C_2 \cdot a^\alpha \cdot \left(\frac{\sigma_a - S_e}{S_u}\right)^n \cdot \left(\frac{1}{1-(\sigma_a/S_u)^q}\right) \quad (3)$$

RESULTS AND DISCUSSION

Experimental fatigue crack growth curve was compared with the simulation prediction. The fatigue crack growh is shown in figure 4.
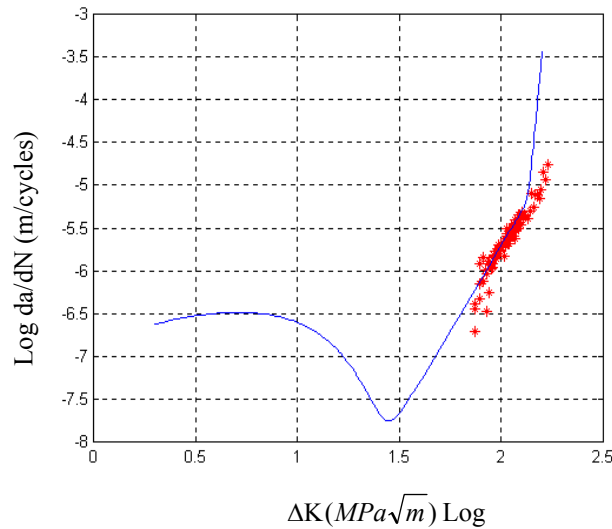
Figure 4: Experimental (stars) and simulated crack (line) propagation rates in a keyhole steel specimen.

The experimental data coincides with the simulation output results at the higher crack sizes. It was not possible to detect cracks below 0.8 mm in the method used. The total fatigue crack growth rate is a sum of the two-fatigue crack growth rates, which suit different zones in the fatigue diagram. The high cycle fatigue crack growth rate $(da/dN)_3$ exhibits crack growth rate beneath the conventional threshold stress intensity range ΔK_{th} and merges with the LEFM crack growth rate $(da/dN)_2$ at the threshold stress intensity range. The experimental results depicted on the fatigue diagram are presented in figure 5. The crack propagates out from the stress concentration, and therefore the line drops down from zone 3 to 4 and then to zone 2. Only after exiting the stress concentration totally, the crack climbs again up to zone 2 and zone 6, where it breaks
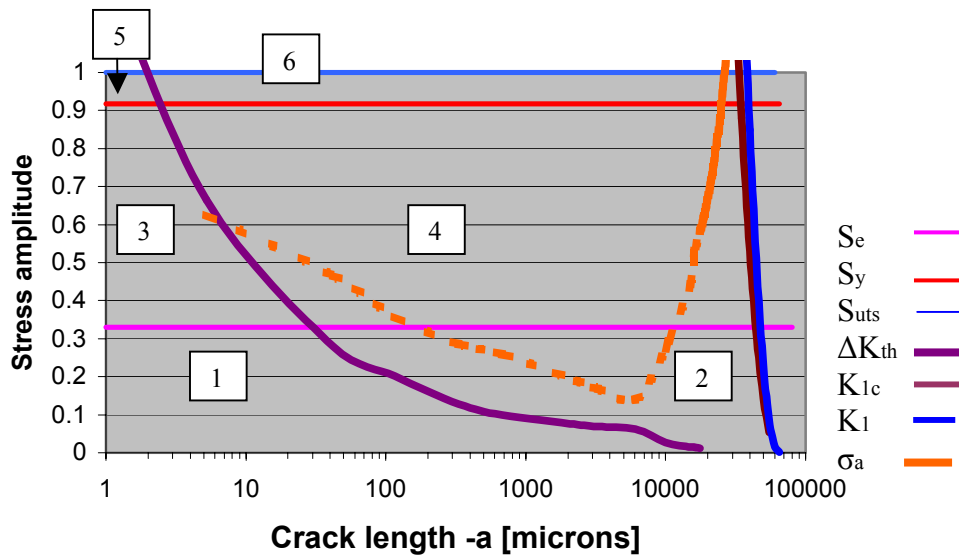
Figure 5 : The Fatigue diagram with the experimental crack
propagation line depicted on it

by gross yielding, when reaching the ultimate tensile strength. The line here is unique, because of the large bending stresses in the keyhole type specimen, and it being in plane stress regime

As to the crack propagation rate: as the crack length increased the growth rate decelerated to below the long crack value. After passing through a minimum, the growth rates increased and tended towards the experimental long crack scatter band. As the notch crack extended, the effect of the notch stress field diminished, and led to a reduction on the stress level. On the other hand, as the crack grows the stressed area decreases, and contributes to stress increase. The finite elements analysis for different cracks length also showed a reduction of stress until the crack length reaches 6 mm and then the stress increases. This phenomenon very similar to fatigue cracks behavior, presented in figure 1.

CONCLUSIONS

This study is an additional step in demonstrating the general validity of the fatigue diagram and model, as a practical tool to indicate in which fatigue zone a certain loading cycle takes place and which fatigue regime prevails. It has been shown that a two-term crack propagation equation is a good predictor of fatigue crack propagation.

In our study, the initial detected crack length was of 0.8mm. Measurement of short cracks in the future by visual means is needed in order to compare the results predicted by the model with experimental data.

REFERENCES

1. Suresh S. (1998) : Fatigue of Materials, pp 541-564, Cambridge
2. Pearson, S (1975) "Initiation of fatigue cracks in commercial aluminum alloys and the subsequent propagation of very short cracks". Eng. Fracture Mechanics 7, pp 235-247.
3. Weiss, M.P. (1992) "Estimating fatigue cracks, from the onset of loading, in smooth AISI 4340 specimens, under cyclic stresses", Int J Fatigue **2**, pp 91-96.
4. Weiss M.P. and Hirshberg Z., (1996) "Crack extension under variable loading, in the short and the long crack regime, using a general fatigue diagram", Fatigue Fract. Engng. Mater. Struct. Vol. 19. No 2/3 pp. 241-249. (1996).
5. Weiss M.P. & Peles S.: "Extension of the fatigue two-term model for mean stresses and the crack closure effect", submitted to Engineering Fracture Mechanics.

SIMULATION OF PROBABILITY DISTRIBUTION OF FATIGUE LIFE OF NOTCHED FRICTION WELDED JOINTS UNDER VARIABLE-AMPLITUDE LOADING

J.H. Yan, X.L.Zeng, K.Zhao and H. Wang

College of Materials Science &Engineering, Northwestern Polytechnical University, Xi'an 710072, China

Abstract Experimental investigation is first carried out on the fatigue property of notched friction welded (FW) joints of mild-carbon steel under constant amplitude loading. The fatigue life of notched specimen of FW joints can be expressed as the function of equivalent stress amplitude $\Delta\sigma_{eqv}$ i.e. $N_i = C[\Delta\sigma_{eqv}^{2/(1+n)} - (\Delta\sigma_{eqv})_{th}^{2/(1+n)}]^{-2}$, where C and $(\Delta\sigma_{eqv})_{th}$ are respectively the fatigue resistant coefficient and the threshold expressed by equivalent stress amplitude below which no crack initiates at the notch root and $N_i \rightarrow \infty$, and n is the strain-hardening exponent. C and $(\Delta\sigma_{eqv})_{th}$ are found to follow the log-normal distribution. According to the physical meaning and their probability distribution of fatigue resistant coefficient C and threshold $(\Delta\sigma_{eqv})_{th}$ in the fatigue life expression, a new method is proposed to simulate the fatigue test and the probability distribution of fatigue life of notched FW joints of mild-carbon steel under variable amplitude loading and checked by test results on notched FW joints under a programmed block loading spectrum. It is shown that both the simulated fatigue life and the test result of fatigue life of 45 steel notched friction welded joints under variable amplitude loading follow the log-normal distribution, and the two distributions agree well with each other, which is important and essential for the life estimation and the reliability assessment of FW joints under variable-amplitude loading.

Keywords: probability distribution, simulation, fatigue life, variable amplitude loading, friction welding，Monte Carlo approach

1. Introduction

Since considerable amount of mechanical elements including the friction welded (FW) structures work under cyclic loading of variable amplitude, it's of practical importance in the design and reliability assessment of mechanical elements to investigate experimentally the probability distribution of fatigue life under variable amplitude loading(VAL). Some work has been devoted to the cyclic fatigue of FW joints[1], nevertheless, the fatigue test under VAL is often very difficult, expensive and time consuming, and the probability distribution under VAL is then determined based on the fatigue test under VAL with relatively small sample size. Obviously there exist some limitations in the experimental investigation. In order to guarantee the safety and reliability of mechanical elements in service, it is imperative to develop the simulation model and method for fatigue life under VAL with big sample size.

In the present study, the fatigue tests under constant-amplitude loading (CAL) and analyses on the results are carried out on the notched friction welded joints of 45 carbon steel, which is similar to the AISI 1045 steel and used for half-shaft and cam shaft of car. Then, according to the physical meaning and their probability distribution of fatigue resistant coefficient and threshold in the fatigue life expression[2,3],

attempts are made to find an approach for simulating the fatigue life and its probability distribution of 45 steel notched FW joints under VAL, the simulated results are compared with the test results under VAL.

2. Experimental Procedure

Hot rolled bars of 16 mm diameter of 45 carbon steel in normalized condition were taken as the test material. The composition (wt. %) of 45 steel is as follows: 0.51C, 0.22Si, 0.65Mn and balance Fe. The experimentally measured tensile properties of this steel are: ultimate strength σ_b = 703 MPa, yield strength σ_s = 441MPa, elongation δ_{10} = 15.3%, reduction in area ψ=50.7%, and strain-hardening exponent n=0.134.

The friction welding process was performed on C25 type continuous driving friction welding machine. The welding parameters used are: heating pressure 130 MPa, heating time 1.4 sec, forge pressure 270 MPa and forge holding time 4 sec. The fracture of the joint in tension was found at the base metal and the tensile properties are found almost the same as those of the base metal. The as-welded joints were then turned and optically ground into standard fatigue specimen with notch at the welding interface. Consequently, before ground the specimen were corroded to display the welding interface. The stress concentration factor of the notched specimen is determined from ref.[4] to be K_t=2.0 as shown in Figure 1.

The fatigue tests were carried out on the rotating bending fatigue machine. The loading frequency was 50 Hz and the stress ratio was -1. The fatigue life was defined as the number of cycles to failure of the notched FW joints. The fatigue tests under constant-amplitude loading were performed at five cyclic stress levels with 10 specimens for each stress level to obtain five groups of fatigue test data. The fatigue tests under variable-amplitude loading were performed according to the programmed block loading shown in Figure 2.

Figure 1 Sketch of the notched fatigue test specimen of FW joints.
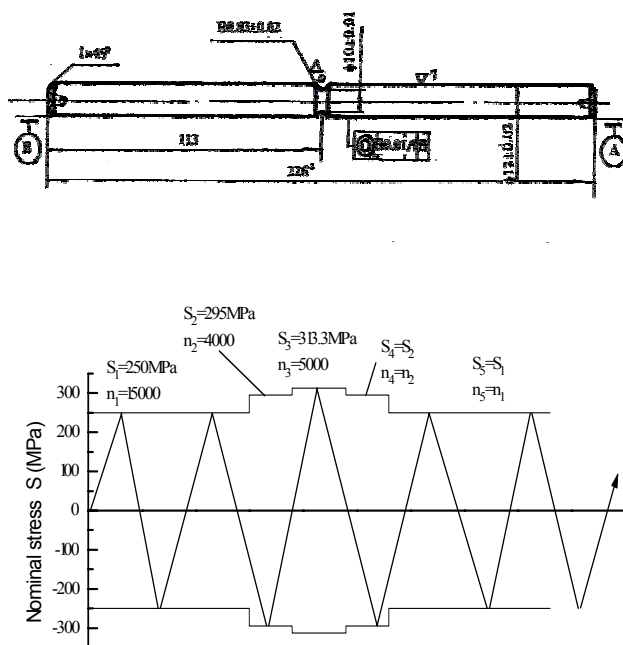
Figure 2 Sketch of the block loading

3. Fatigue Test Results under CAL and Analysis

Expression for Fatigue Life

Theoretical analysis[2] and experimental results[3,5-7] indicate that the fatigue crack initiation (FCI) life of notched specimen of metals and welds can be expressed as the function of equivalent stress amplitude $\Delta\sigma_{eqv}$,

$$N_i = C[\Delta\sigma_{eqv}^{2/(1+n)} - (\Delta\sigma_{eqv})_{th}^{2/(1+n)}]^{-2} \tag{1}$$

where

$$\Delta\sigma_{eqv} = \sqrt{\frac{1}{2(1-R)}}K_t \cdot \Delta S \tag{2}$$

In eqn(2) ΔS, R are the nominal stress range based on the net section and the stress ratio, respectively; K_t is the stress concentration factor. In eqn (1) C and $(\Delta\sigma_{eqv})_{th}$ are, respectively, the FCI resistant coefficient and the threshold expressed by equivalent stress amplitude, and n is the strain-hardening exponent.
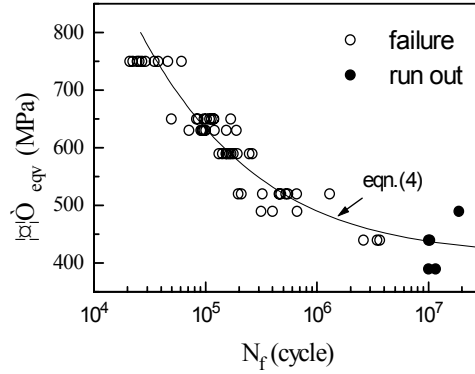
Figure 3 Test and fitting results of fatigue life

The fatigue test results of 45 steel notched FW joints under CAL are shown in Figure 3. As it may be seen from Figure 3, most data for fatigue life are beyond 10^5 cycles. Moreover, multiple cracks initiate surrounding the notch root and coalesce to form a large crack, which was observed on the fracture surface. Therefore, it may be thought that the FCI life occupied the dominant part of the fatigue life. In this case, eqn(1) can be approximately used to fit the test data of fatigue life N_f. Replacing N_i in eqn(1) with N_f and making the logarithmic transformation, eqn(1) becomes

$$\log N_f = \log C - 2\log[\Delta\sigma_{eqv}^{2/(1+n)} - (\Delta\sigma_{eqv})_{th}^{2/(1+n)}] \tag{3}$$

Eqn(3) represents a straight line with a slope of -2 on a logarithmic scale, i.e., $\log N_f$ vs. $\log[\Delta\sigma_{eqv}^{2/(1+n)} - (\Delta\sigma_{eqv})_{th}^{2/(1+n)}]$ scale. By using a trial and error approach to write a computer program for linear regression analysis, whose flow chart is shown in ref.[2], the values of C and $(\Delta\sigma_{eqv})_{th}$ can be obtained with the condition that the slope is within the range of -2±0.002.

By substituting the values of C and $(\Delta\sigma_{eqv})_{th}$ so-obtained back into eqn(1), the expression for fatigue life of 45 steel notched FW joints can be reached :

$$N_f = 2.179 \times 10^{14}[\Delta\sigma_{eqv}^{1.764} - 411.7^{1.764}]^{-2} \tag{4}$$

where n= 0.134 for the base material is taken as that for FW joint. Regression analysis gives the value of linear correlation coefficient r=0.9213 much higher than 0.28, the critical value for all data. This means that eqn(1) can be applied to successfully fit the test data of the fatigue life of 45 steel notched FW joints. Figure 3 shows the fatigue life curve drawn according to eqn(4).

Probability distribution of fatigue life, the constants C and $(\Delta\sigma_{eqv})_{th}$

The test data for the fatigue life at each cyclic stress in Figure 3 are respectively plotted on the normal probability paper as shown in Figure 4(a), where the mean rank is taken as the estimated value of the failure probability, P_f of the population[8]. Transforming the failure probability into the standard normal deviate, U_p, a straight line between $\log N_f$ and U_p can be obtained. The values of linear correlation coefficient between $\log N_f$ and U_p at each given equivalent stress amplitude given by regression analysis is much higher than the critical value of linear correlation coefficient given in ref.[8]. It shows that the fatigue life of 45 steel notched FW joints follows the usual log-normal distribution. Further examination by using Sharpiro-Wilk approach[8] leads to the same conclusion.

According to the approach in ref.[3,5], taking each one from the rearranged five groups of test data at five different stress levels in sequence can form 10 sets of fatigue test data. Using eqn(3) to fit so obtained 10 sets of fatigue test data respectively, 10 pairs of C and $(\Delta\sigma_{eqv})_{th}$ values can be obtained, where the values of correlation coefficient are higher than the critical value of the correlation coefficient[8]. It suggest that eqn(1) can be successfully applied to fit the test data of each set of fatigue life of 45 steel FW joints.

The so-obtained values of C and $(\Delta\sigma_{eqv})_{th}$ are rearranged according to the increasing order and plotted on the normal probability paper as shown in Figure 4(b) and (c). The values of the correlation coefficient given by the above-mentioned regression analysis are much higher than the critical value. Further examination by Shapiro-Wilk method shows that C and $(\Delta\sigma_{eqv})_{th}$ of 45 steel notched FW joints follow the log-normal distribution. The logarithmic mean value and standard deviation of C are 14.3405 and 0.0982, and those of $(\Delta\sigma_{eqv})_{th}$ are 2.6120 and 0.0222. It is also found that $(\Delta\sigma_{eqv})_{th}$ follows the normal distribution as well.

(a)   (b)   (c)   (d)
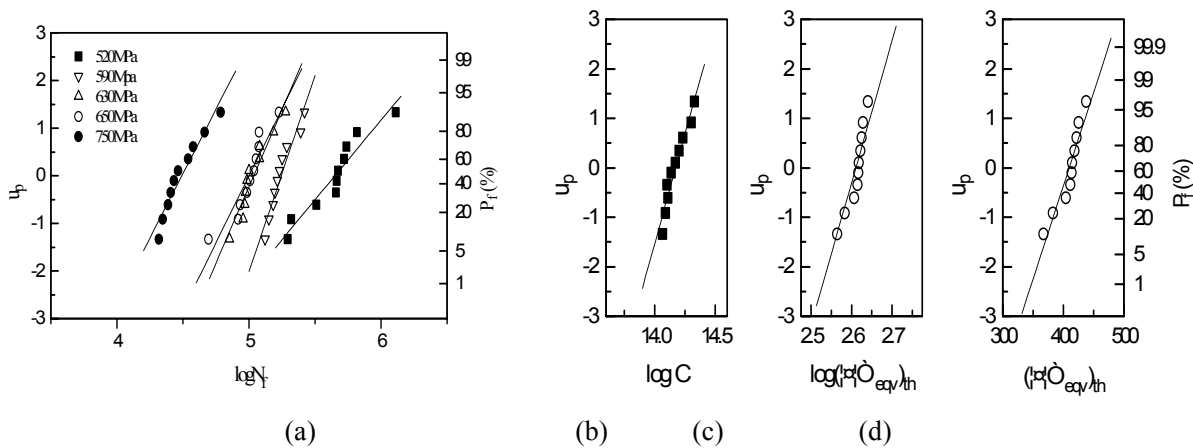
Figure 4 Probability distribution of (a) fatigue life N_f, (b)log C, (c) log $(\Delta\sigma_{eqv})_{th}$ and (d) $(\Delta\sigma_{eqv})_{th}$ of 45 steel notched FW joints on normal probability paper

4. The principle and method for simulating fatigue life test under VAL

Investigations[2,6] show that C and $(\Delta\sigma_{eqv})_{th}$ are material constants determined by the crack forming mechanism and tensile properties and follow certain probability distribution. Analyses on many fatigue test results indicate that C and $(\Delta\sigma_{eqv})_{th}$ follow the log-normal distribution. Therefore, the probability distribution of C and $(\Delta\sigma_{eqv})_{th}$ can be used to represent the probability distribution characteristics of fatigue properties of the material, if only the probability distribution of C and $(\Delta\sigma_{eqv})_{th}$ is known, the corresponding fatigue properties of the material can be settled consequently.

Based on the above consideration and results, and regarding the famous hypothesis of Weibull on the S-N curve of individual [9], the following model for fatigue test procedure can be developed:
1) The distribution of C and $(\Delta\sigma_{eqv})_{th}$ can be used to represent the distribution characteristics of fatigue properties of the material, i.e., for a definite material, its fatigue curves with different survivabilities (P-S-N curves) are determined.
2) Each individual specimen has a corresponding S-N curve, which is one member of the P-S-N curves family, i.e., different fatigue specimen is assumed to be distinguished by different combination of C and $(\Delta\sigma_{eqv})_{th}$.
3) The scatter of the fatigue life results from the difference between the fatigue specimens, i.e., from the random sampling of individual specimen from the population of specimens, or from the random selection of P-S-N curve from the family of P-S-N curves of the material.

It is pointed out that for the notch elements of metals with non-continuous hardening characteristic such as 45 steel and its welds, the so-called overloading effect factor, z.=0, in this case, Miner's rule and the expression for the fatigue life can be directly applied to predict the fatigue life and cumulative fatigue damage of notched elements of metals with non-continuous strain-hardening characteristic under VAL. According to the above model and the research result, the simulation for the fatigue test result under VAL can be carried out following the below procedures to write a computer program:

1) According to the approach in ref.[5,6], determine the probability distribution and its characteristic parameters such as logarithmic mean value and standard deviation of C and $(\Delta\sigma_{eqv})_{th}$ from the results of group fatigue life test under different constant amplitude loading.
2) Adopt Monte Carlo approach to produce 10000 simulating values of C according to the logarithmic mean value and standard deviation of C, then rearrange the so-obtained 10000 C according to the order of increasing value.
3) Adopt Monte Carlo approach to produce 10000 simulating values of $(\Delta\sigma_{eqv})_{th}$ according to the logarithmic mean value and standard deviation of $(\Delta\sigma_{eqv})_{th}$, then rearrange the so-obtained 10000 $(\Delta\sigma_{eqv})_{th}$ according to the order of increasing value.
4) Take each one from the rearranged C and $(\Delta\sigma_{eqv})_{th}$ in sequence to get 10000 pairs of C and $(\Delta\sigma_{eqv})_{th}$ values and constitute the family of 10000 P-S-N curves, which forms the parent specimens.
5) Randomly sample n pairs of C and $(\Delta\sigma_{eqv})_{th}$ from the above obtained 10000 pairs to represent n specimens, then substitute the n pairs of C and $(\Delta\sigma_{eqv})_{th}$ into equation (1) to yield n expressions of S-N curves.
6) Transform the nominal stress spectrum into the equivalent stress amplitude spectrum by substituting the values of K_t, ΔS and R (see Figure 2) into eqn(2).
7) Calculate the fatigue life $N_{f,j}$ (j=1,2,...,5) at each level of $\Delta\sigma_{eqv}$ in the equivalent stress amplitude spectrum by substituting the equivalent stress amplitude into one of the so obtained expressions of S-N curves, which corresponds to a fatigue test specimen.
8) Calculate the cumulative fatigue damage of one load block according to Miner's rule, $D_0=\Sigma n_j/N_{f,j}$, where n_j is the number of cycles at stress level j in load spectrum.
9) Obtain the fatigue life expressed by load blocks N_b when the total fatigue damage accumulation reaches 1.0, i.e., $N_b=1.0/D_0$.
10) Repeat step 7) to step 9) to obtain the fatigue life N_b under VAL corresponding to the sampled n specimens.
11) Make statistical analysis on the n fatigue life N_b under VAL to determine the probability distribution and its corresponding characteristics of fatigue life under VAL.
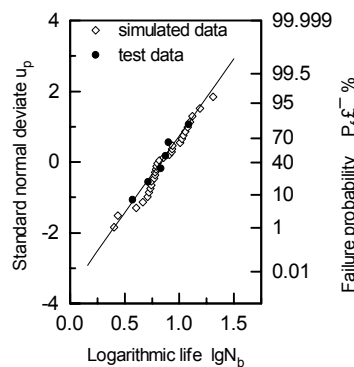
Figure 5 Probability distribution of the simulated and test fatigue life of 45 steel notched FW joints

5. Simulation results of probability distribution of fatigue life under VAL and substantiation

By following the above procedures and considering the logarithmic mean value and standard deviation of C and $(\Delta\sigma_{eqv})_{th}$ obtained in section 3, the simulation of fatigue life of notched 45 steel FW joints under VAL shown in Figure 2 can be carried out. The so-obtained 30 values of N_b are rearranged according to the increasing order and plotted on the normal probability paper as shown in Figure 5. The value of linear correlation coefficient between $logN_b$ and U_p by regression analysis is 0.9847, much higher than the critical value of linear correlation coefficient [8]. It shows that the fatigue life N_b of 45 steel notched FW joints under VAL follows the usual log-normal distribution[5,6]. Further examination by using Sharpiro-Wilk approach[8] leads to the same conclusion. The logarithmic mean value and standard deviation of N_b are 0.8588 and 0.2061.

The fatigue test results with 6 specimens of 45 steel notched FW joints obtained under the programmed

block loads shown in Fig. 2 are also plotted in Figure 5. It can be seen that the fatigue test results under VAL follow the log-normal distribution. The logarithmic mean value and standard deviation of the test N_b are 0.85284 and 0.1745. Further examination by using Shapiro-Wilk method shows that the test results of fatigue life under VAL mentioned above still follow a log-normal distribution.

Further test on the significant difference between the simulated and test lgN_b in Figure 6 by following the approach in ref.[8] suggest that there is no significant difference between the two logarithmic mean fatigue lives, and between the two logarithmic standard deviations under the significance level of 5%. Therefore, the fatigue test results of the notched FW joints under VAL of figure 2 simulated according to the procedures in section 4 come from the same population of the test results, thereby the simulated probability distribution of fatigue life is in good agreement with that of test results of notched 45 carbon steel friction welded joints. Therefore, the probability distribution of fatigue life under VAL can be simulated by the model developed in the paper, which offer the base for fatigue design and reliability assessment of notched elements under VAL.

6. Conclusions

(1) The test results and analysis show that the fatigue life of 45 steel notched FW joints can be expressed as a function of the equivalent stress amplitude as shown by eqn(1), which contains only two fatigue constants C and $(\Delta\sigma_{eqv})_{th}$.

(2) The test results of fatigue life of 45 steel notched FW joints of small size follow the log-normal distribution as usual. In this case, the fatigue resistant coefficient and threshold of 45 steel notched FW joints follow the log-normal distribution, respectively, and the fatigue threshold follows the normal distribution as well.

(3) According to the physical meaning and their probability distribution of fatigue resistant coefficient C and threshold $(\Delta\sigma_{eqv})_{th}$ in the fatigue life expression (1), a new method is proposed to simulate the fatigue test and the probability distribution of fatigue life of notched elements under variable amplitude loading.

(4) The simulated fatigue life of 45 steel notched friction welded joints under variable amplitude loading of figure 2 follow the log-normal distribution, and agree well with the test result of fatigue life.

REFERENCES

[1] Hasegawa, M., Ieda, T. and Taki, N.. Fatigue strength of friction-welded joints with flash in various carbon steels[J]. Welding Int., 1997, 11(12): 950~957.

[2] Zheng Xiulin. A further study on fatigue crack initiation life--Mechanical mode for fatigue crack initiation[J], Int. J. Fatigue, 1986, 8(1):17~21.

[3] Zheng, X. L., Quantitative Fatigue Theory for Metals, Press House of Northwestern Polytechnical University, Xi'an, China, 1994.1

[4] M. Nisida, Stress Concentration Factors, Mositoka Press, in Japanese(1971)

[5] Zheng X.L., Li Z. and Lu B.T.. Prediction of probability distribution of fatigue life of 15MnVN steel notched elements under variable amplitude loading[J]. Int. J.Fatigue, 1996, 18(2):.81~86.

[6] Wei, J. F., On Models For Prediction Probability Distribution of fatigue Life under Variable Amplitude Loading, A Dr. Dissertation , Northwestern Polytechnical University, Xi'an China, 1996.11

[7] Lin C, Zheng XL. Overload Effects on Fatigue Life Prediction of 16Mn butt welds Steels. Transaction of China welding Institue, 1991, 12(4):247~251.

[8] P.Deng, Applications of Statistics in Measurements and Experiments, Press of Chemical Industry, Beijing (in Chinese)(1981)

[9] Weibull W.. Fatigue testing and analysis of results[M]. New York: The Macmillan Company, 1961.

SIMULATION OF PROPAGATION OF SMALL FATIGUE CRACKS INTERACTING WITH GRAIN BOUNDARY

Y. Akiniwa [1], K. Tanaka [1] and H. Kimura [2]

[1] Department of Mechanical Engineering, Nagoya University,
Furo-cho, Chikusa-ku, Nagoya 464-8603, Japan
[2] Graduate School, Nagoya University,
Furo-cho, Chikusa-ku, Nagoya 464-8603, Japan

ABSTRACT

The propagation behavior of microstructurally small fatigue cracks was numerically simulated on the basis of the plasticity-induced crack closure model. The effects of the frictional stress of dislocation motion and the strength of the grain boundary blocking on the crack closure behavior were analyzed. Then the simulation of the propagation of a crack nucleated in the weakest grain was conducted by assuming that the crack growth rate was controlled by the crack-tip opening displacement, $\Delta CTOD$. The grain size, the critical value of microscopic stress intensity factor at grain boundary and the frictional stress were given as random variables following two-parameter Weibull distributions. When the crack approached adjacent grains with higher frictional stresses, $\Delta CTOD$ decreased and the crack opening stress increased. The grain boundary and the higher frictional stress act as a resistance to crack propagation. When compared at the same stress intensity range, $\Delta CTOD$ increased with increasing stress ratio. The effect of the stress ratio on the fatigue limit was analyzed on the basis of the results of the simulation. The relation between the fatigue limit and the value of the applied mean stress is nearly identical to the modified Goodman relation.

KEYWORDS

Fatigue, Crack closure, Crack opening displacement, Fatigue limit, Mean stress, Simulation, Microstructure, Grain boundary

INTRODUCTION

The propagation behavior of long fatigue cracks is uniquely determined by the stress intensity range, ΔK. On the other hand, small fatigue cracks show anomalously high irregular propagation rates when compared with long cracks at the same ΔK [1-6]. This fast propagation rate has been ascribed to microstructural effects, premature crack closure and macroplasticity [3,5]. The irregular propagation behavior is caused by the microstructural inhomogeneity. In our previous study [7,8], a model for crack-tip slip band blocked by a grain boundary based on the continuously distributed dislocation theory was proposed. The statistical nature of propagation behavior of small cracks could be successfully derived by the Monte Calro simulation. However, the effect of the crack closure was not taken into account.

In this study, the propagation behavior of microstructurally small fatigue cracks was numerically simulated. The effects of the frictional stress of the adjacent grain and the strength of the neighboring grain boundary on the crack closure behavior were analyzed. Then the simulation of the propagation of a crack nucleated in the weakest grain was conducted. The effects of the microstructural parameters and the value of the applied mean stress on the propagation behavior and on the fatigue limit were investigated.

CRACK CLOSURE ANALYSIS

Analytical Model

The interaction model between grain boundary and slip band ahead of a crack-tip is shown in Fig. 1. The isolated crack is located at the center of a grain and the slip band is assumed to spread in the same plane. In the figure, L_{q-1} is the distance between the $(q$-1)th grain boundary and the center of the crack. σ^f_q is the frictional stress of the qth grain. When the slip band is blocked by the grain boundary, the stress field near the tip of the slip band has a singularity with the following intensity [7]:

$$K^m = \beta\sigma\sqrt{\pi c}$$
$$\beta = 1 - \frac{2\sigma^f_1}{\pi\sigma}\cos^{-1}\left(\frac{a}{c}\right) \tag{1}$$

The microscopic stress intensity factor, K^m, increases with crack length. When K^m becomes larger than the critical value of the strength of the grain boundary, K^m_c, the slip band propagates into the adjacent grain as shown in Fig. 1 (c). When the crack becomes large, the slip bands spread into several grains (Fig. 1 (d)). When the crack-tip and the tip of the slip band are in the jth and the qth grain, respectively, the plastic zone size, $\omega (= c\text{-}a)$, can be calculated by [7]

$$\frac{\pi}{2}\sigma_{max} - \sigma^f_j\cos^{-1}\left(\frac{a}{c}\right) - \sum_{k=j+1}^{q}\left(\sigma^f_k - \sigma^f_{k-1}\right)\cos^{-1}\left(\frac{L_{k-1}}{c}\right) = 0 \tag{2}$$

where σ_{max} is the maximum applied stress.
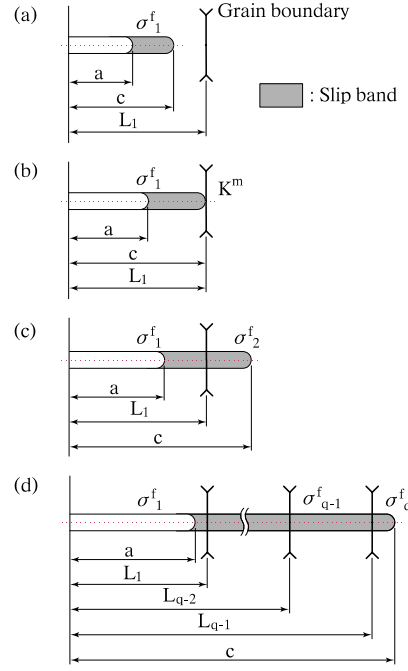
Figure 1. Slip band model.

Microstructural Parameters

Microstructural parameters used in this study are the grain size, d, the critical microscopic stress intensity factor, K^m_c, and the frictional stress, σ^f. Those parameters were given as random variables following two-parameter Weibull distributions. The random variables were generated by using their mean value (denoted by suffix μ) and a variance (denoted by suffix v). A fatigue crack is assumed to initiate from the weakest grain having the largest value of the following strength parameter Γ [9]:

$$\Gamma_k = d_k \, (\, \Delta\sigma - 2\sigma^f_k)$$

(3)

where $\Delta\sigma \, (=\sigma_{max}-\sigma_{min})$ is the applied stress range, d_k is the grain size. The mean frictional stress, σ^f_μ, and Young's modulus, E, are assumed to 400 MPa and 206 GPa, respectively.

Crack Propagation

In our previous study [7,8], we simulated the propagation behavior of microstructurally small fatigue cracks without taking into account of crack closure. The results correspond to the propagation of Stage I cracks. In this study, cracks are assumed to propagate in a Stage II manner under the influence of crack closure. Fatigue crack propagation behavior was simulated to evaluate the development of the plasticity-induced crack closure with crack growth by using an analytical closure model proposed by Newman [10]. The initial crack, a_i, and the plastic zone, ω_{max}, at the maximum applied stress were divided into 20 and 40 elements, respectively. The amount of crack extension was prescribed to be $\Delta a = 0.002\omega_{max}$.

Budiansky et al. [11] analyzed the plasticity induced crack closure of semi-infinite cracks and showed that $\Delta CTOD$ was related to the effective stress intensity range, ΔK_{eff}, as

$$\frac{\Delta CTOD}{CTOD_{max}} = 0.73 \cdot \left(\frac{\Delta K_{eff}}{K_{max}} \right)^2$$

(4)

The threshold value of $\Delta CTOD$ is evaluated by Eq. (4). By assuming the threshold value of ΔK_{effth} as 1, 2 and 3 MPam$^{1/2}$, the threshold value of $\Delta CTOD$ is calculated to 8.86×10^{-6}, 3.54×10^{-5} and 7.97×10^{-5} mm.

RESULTS AND DISCUSSION

Effect of Friction Stress

Fatigue crack propagation behavior was simulated to investigate the effect of the frictional stress of an adjacent grain on crack closure. Both the length of an initial Stage I crack and the distance between the crack-tip and the grain boundary were assumed to be 50 μm. Figure 2(a) shows the change of $\sigma_{\text{op}}/\sigma_{\text{max}}$ with crack length. The maximum applied stress is 180 MPa. The frictional stress of the first grain, σ^f_1, is 400 MPa, and $\sigma^f_2/\sigma^f_1 = 0.8$, 1.0, 1.2 and 2.0 in the second grain. There is no barrier at the grain boundary ($K^m_c = 0$ MPam$^{1/2}$). The value of $\sigma_{\text{op}}/\sigma_{\text{max}}$ for $\sigma^f_2/\sigma^f_1 > 1.0$ becomes larger than that for $\sigma_2/\sigma^f_1 = 1.0$. When the extension of the plastic zone is constrained by the adjacent grain with a higher frictional stress, the crack opening stress increases with crack length. Namely, the effective component of the stress range decreases as a consequence of the constraint. The crack opening stress takes a local maximal value in the first grain before the crack tip reaches the grain boundary. When the crack propagates into the adjacent grain, the crack opening stress increases sharply, and takes the maximum value in the second grain. On the other hand, for the case of $\sigma^f_2/\sigma^f_1 < 1.0$, the behavior is in contrast with the result obtained for $\sigma^f_2/\sigma^f_1 > 1.0$. The change of $\Delta CTOD$ with crack growth is shown in Fig. 2(b). $\Delta CTOD$ first decreases due to the development of the residual stretch, then increases until the tip of the plastic zone reaches the grain boundary. For the case of $\sigma^f_2/\sigma^f_1 > 1.0$, $\Delta CTOD$ begins to decrease, as the plastic zone crosses the grain boundary. When the driving force of crack propagation is given by $\Delta CTOD$, the higher frictional stress of the neighboring grain act as a resistance of crack propagation. If the threshold value of $\Delta CTOD$ is assumed to be 3.54×10^{-5} mm, the crack becomes non-propagating at the crack length of 0.097 mm for the case of $\sigma^f_2/\sigma^f_1 = 2.0$. It is interesting to note that $\Delta CTOD$ takes a minimum value at the crack length of 0.103 mm in the second grain.
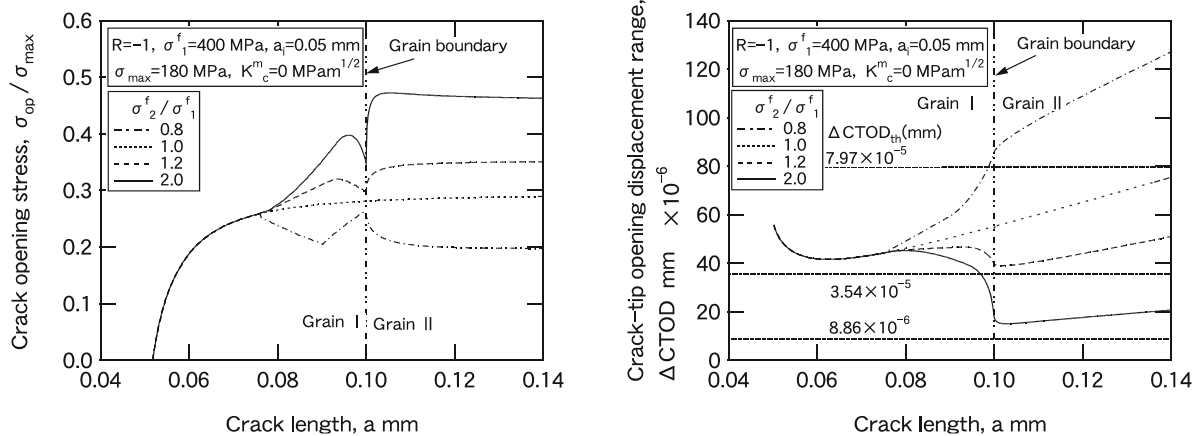
(a). Change of σ_{op} with crack length.   (b) Change of $\Delta CTOD$ with crack length.

Figure 2. Effect of frictional stress of adjacent grain.

Statistical Analysis of Crack Propagation

The same simulation was conducted to investigate the effects of the grain-boundary blocking and the applied mean stress on the threshold condition of small cracks. The frictional stress and the grain size were given

as random variables. The initial crack length is a_i=5 μm. The mean frictional stress and grain size are 400 MPa and 50 μm, respectively. The variances of those values are $(\sigma^f/\sigma^f_\mu)_v$=0.2 and d_v=50 (μm)^2. The mean value and the variance of the critical value of the microscopic stress intensity factor are $(K^m_c/\sigma^f_\mu (\pi d_\mu)^{1/2})_\mu$=0.4 and $(K^m_c/\sigma^f_\mu (\pi d_\mu)^{1/2})_v$=0.04, respectively. The relation between $\Delta CTOD$ and ΔK is shown in Fig. 3(a). The applied stress is σ_a/σ^f_μ=0.5. In the figure, the broken line indicates the relation obtained for the constant mean frictional stress and K^m_c =0, and has a slope of two in the log-log diagram. The results obtained from 30 kinds of random number sequence are plotted. The scatter diminishes as the crack propagates and converges to the broken line. This corresponds to the experimental results of propagation behavior of small fatigue cracks [6]. When the threshold value of ΔK_{effth} is assumed to be 1 MPam$^{1/2}$, the threshold value of $\Delta CTOD$ becomes 8.86×10^{-6} mm. In this case, 24 cracks out of thirty are arrested at the first grain boundary. The abscissa was subdivided into 20, and the arithmetical averages of $\Delta CTOD$ and ΔK were calculated within each subdivision. Figure 3(b) shows the relation between the arithmetical average of $\Delta CTOD$ and ΔK. In the figure, the results obtained for the stress ratio of -1.5 and -0.5 were also plotted. The dotted lines in the figure are the results obtained for $\sigma^f_\kappa=\sigma^f_\mu$ and K^m_c =0 under each stress ratio. When compared at the same ΔK, $\Delta CTOD$ increases with increasing stress ratio. Two and twenty eight cracks out of thirty are arrested under the stress ratio of -0.5 and -1.5, respectively. The number of arrested cracks decreases with stress ratio.

Figure 4 shows the Haigh diagram which is the relation between the stress amplitude and the mean stress at the fatigue limit. The fatigue limits are calculated as the fracture probability of 50%. The threshold value are given as $\Delta CTOD_{th}$= 8.86×10^{-6}, 3.54×10^{-5} and 7.97×10^{-5} mm. The fatigue limit decreases linearly with the mean stress irrespective of the threshold value. The dot-dash line is the modified Goodman relation obtained by assuming σ_B/σ^f_μ=1.15 [12]. The slope is close to the simulated results.

(a) 30 cracks (b) Mean value
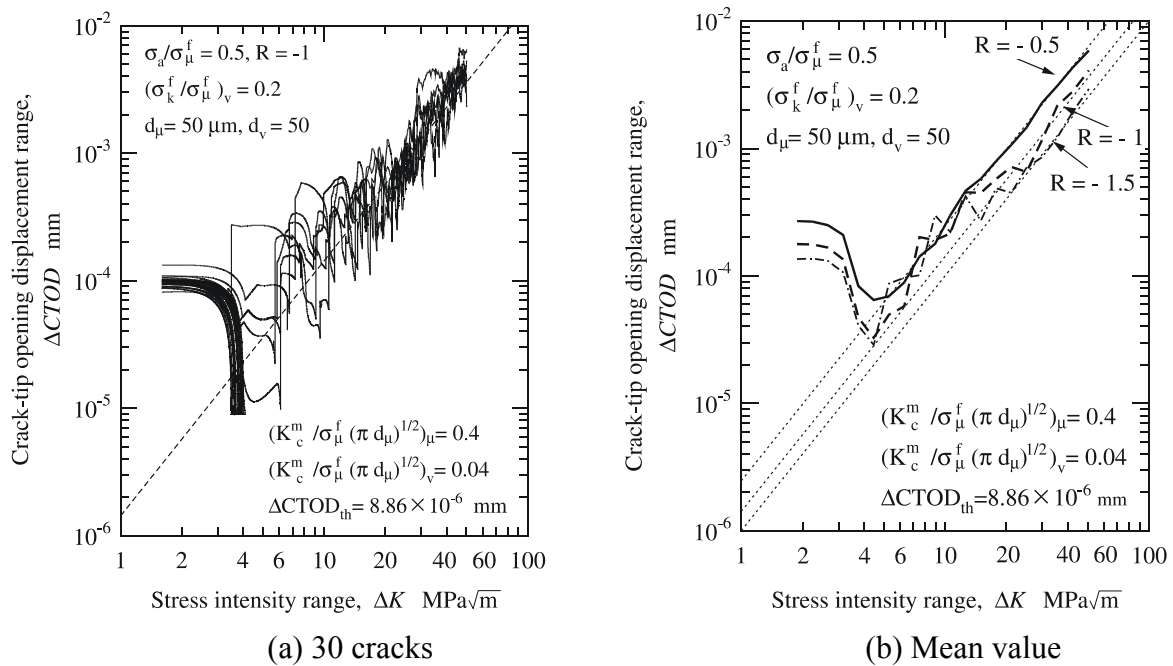
Figure 3. Relation between $\Delta CTOD$ and ΔK.
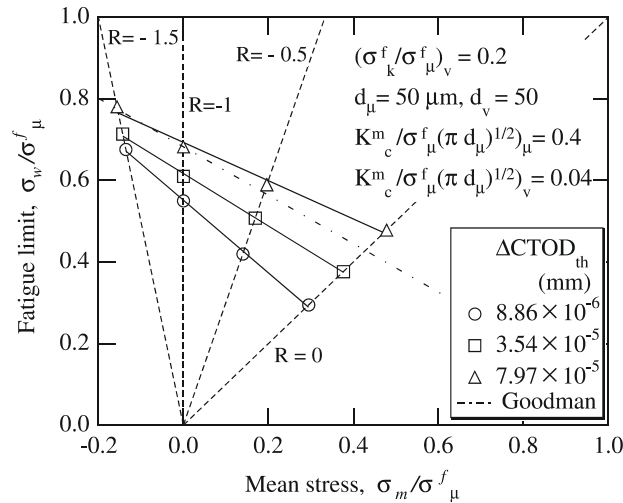
Figure 4. Haigh diagram.

CONCLUSION

The propagation behavior of microstructurally small fatigue cracks was numerically simulated on the basis of the plasticity-induced crack closure model.

(1) When the crack approached grains with higher frictional stresses, $\Delta CTOD$ decreased and the crack opening stress increased. The grain boundary blocking and higher frictional stress act as a resistance to crack propagation.

(2) The scatters of $\Delta CTOD$ diminished as the crack length becomes longer. When compared at the same stress intensity range, $\Delta CTOD$ increased with stress ratio.

(3) The relation between the fatigue limit and the applied mean stress is nearly identical to the modified Goodman relation.

REFERENCES

1. S. Pearson, Eng, Fract. Mech., **7** (1975) 235.
2. K. Tanaka, M. Hojo and Y. Nakai, ASTM STP 811 (983) 207.
3. S. Suresh and R. O. Ritchie, Int. Metall. Rev., **29** (1984).
4. K. Tokaji, T. Ogawa and Y. Harada, J. Soc. Mater. Sci. Japan, **35** (1986) 394.
5. K. Tanaka, Trans. JSME, 35 (1987) 1.
6. Y. Akiniwa and K. Tanaka, Mater. Sci. Eng., **A104** (1988) 105.
7. K. Tanaka, Y. Akiniwa, Y. Nakai and R. P. Wei, Eng. Fract. Mech., **24** (1986) 803.
8. Y. Akiniwa and K. Tanaka, J. Soc. Mater. Sci. Japan, **38** (1989) 1169.
9. K.Tanaka and T. Mura, J. Appl. Mech., **48** (1981) 97.
10. J. C. Newman, Jr., ASTM STP 748, (1981) 53.
11. B. Budiansky and J. W. Hutchinson, Trans. ASME, J. Applied Mech., **45** (1978) 267.
12. Y. Akiniwa , L. M. Zhang and K. Tanaka, Trans. Japan Soc. Mech. Enges, **A-64** (1998) 1229.

SIMULATING TRANSVERSE FRACTURING
OF THIN PLASTIC SHEET

B.J. Carter,[1] A.R. Ingraffea,[1] and Yeh-Hung Lai[2]

[1]Cornell University, Ithaca NY USA
[2]Eastman Kodak Company, Rochester, NY 14652-4333 USA

ABSTRACT

Slitting or transverse fracturing of thin plastic sheet products is common practice in industry, but the process is based mostly upon empirical evidence and experience. The slitting process involves large plastic deformation and fracturing or tearing under the shearing action of the rolling knife blades. Coupling the capabilities of two finite element programs, ABAQUS and FRANC2D allows the process to be simulated numerically. ABAQUS provides capabilities for modeling elasto-plastic material behavior, geometric nonlinearity, and contact between the knives and the plastic sheet -as well as self-contact of the plastic sheet. FRANC2D provides capabilities for inserting and growing multiple arbitrary cracks using element delete and fill routines to remesh the modified geometry and topology. FRANC2D was modified to communicate with ABAQUS to perform the slitting simulations based on an updated Lagrangian formulation with remeshing algorithms to prevent element distortion. Numerical simulations of the slitting process match experiments reasonably well.

KEYWORDS

FRAC2D, ABAQUS, slitting, cutting, plastic sheet, transverse fracture, crack propagation

INTRODUCTION

Slitting or transverse fracturing during manufacturing and processing of thin sheet products is common practice in industry. Automated slitting and cutting machinery is used to cut wide sheets or rolls of material into a number of narrower strips and for trimming the edges of rolled sheets. For example, photographic film is manufactured in wide sheets and then slit into various smaller widths for different camera types. Other products that are slit include paper, plastic film, aluminum foil, adhesive tape, and even food products. Slitting is differentiated from other cutting processes based upon the use of circular knives. Other cutting and related manufacturing processes include: (1) single-point turning, such as a lathe, (2) boring, drilling, reaming or tapping, (3) planing, (4) milling or sawing, (5) threading, (6) blanking, and (7) cropping or guillotining, Dodd and Bai [1].

Although slitting and cutting processes are widely used, they have not been well studied; the industry processes are based mostly upon empirical evidence from experiments and field studies. In metal processing, there are guidelines for cutting that are based on experiments and experience, Chang and Swift [2]. Experiments can be time consuming and expensive as cutting behavior is affected by many factors, some of which include cutting force and speed, sheet tension, material properties, and knife geometry. As new products are developed, a large number of experiments are needed to determine the best value or range of values for these factors to produce the best cut-surface. Alternatively, if experiments are not conducted, a large amount of waste material might be generated if the parameters are not optimal.

Numerical studies of cutting processes have concentrated mostly on single tool cutting related to operations like milling or drilling and are aimed at analyzing the deformation and plasticity that occurs during chip and burr formation, Hashimura et al. [3], Ehmann et al. [4]. Analytical studies to determine cutting forces have also been completed, e.g., Zhou and Wirzbickia [5], but these have limited applicability because of the complex shearing and large-scale plasticity that usually accompanies the cutting process. A recent study by Wisselink [6] examines guillotining and slitting processes in metal cutting using a special purpose finite element program, DiekA, Huetink [7]. Fractures are simulated in addition to modeling the plastic deformation and contact. Only three papers describing slitting of photographic film were found in the open literature, Bollen et al. [8], Arcona and Dow [9], and Meehan and Burns [10], but none of these include numerical simulations.

The reason for studying the slitting process is to produce higher quality cut surfaces while reducing waste material. A single, clean, cut-surface that is orthogonal to the sheet surface is desired with no extra debris generated. This is not possible in most materials, so the best that can be done is to vary the cutting parameters to produce the best cut possible. Cutting occurs in three stages: (1) initial elastic deformation, (2) significant knife penetration and plastic deformation, and finally, (3) fracture or tearing. An effective method of studying the complete cutting process is to use finite elements. Finite element analysis allows for material and geometric nonlinearity as well as contact mechanics and fracture. It allows one to study variations in knife geometry, cutting speed, and other factors without performing numerous experiments.

The cutting process is modeled herein by coupling two computer programs, ABAQUS (www.abaqus.com) and FRANC2D ([11] and www.cfg.cornell.edu). ABAQUS provides a finite element base for simulating material and geometric nonlinearity as well as contact and fracture. FRANC2D provides a finite element base for simulating multiple arbitrary crack initiation and propagation with automatic meshing. The combination of these two programs provides a unique and suitable system for simulating cutting of thin plastic sheet material.

MECHANICS AND DEFORMATION OF SLITTING THIN PLASTIC SHEETS

Bollen et al. [8] and Meehan and Burns [10] describe the knife cutting velocities associated with slitting thin plastic sheets. Figure 1 shows the relative velocity vectors of the knives as depicted by Meehan and Burns; the components of the relative velocity vector correspond to the three fractures modes - opening, sliding and shearing. They continue by analyzing the cutting force and the stress field at the crack tip. However, this analysis has limited applicability as it ignores the material and geometric nonlinearity as well as the contact conditions. Arcona and Dow [9] use the force model (Figure 2) presented by Ford [12] to determine the cutting force based on the knife geometry, cutting speed, and material properties, specifically the material yield stress. This model was designed for ductile materials and provides an initial estimate for the force required for knife penetration based on the shear yield locus of the material. These analytical models have limited applicability, as the shearing and fracturing processes are too complex. Figure 3 shows a simplified sketch of the slit surface. The actual surface in photographic film is much more complex, Bollen et al. [8], Arcona and Dow [9].

Bollen et al. describe an additional damaging phase where the cut surfaces rub on the knives and suffer additional deformation. The amount of plastic deformation is very dependent upon the material properties of

the thin plastic sheet. Two types of material are used for the base material of photographic film, a relatively brittle cellulose acetate and a tough, ductile polyethylene terephthalate (PET). The PET is visco- plastic and is, therefore, dependent upon cutting speed. Polymer fracture is complex, Kausch [13]; thus, the simulations below are based on simplified models.
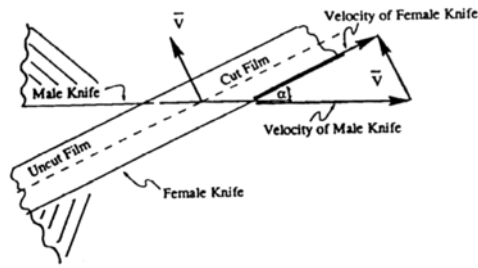
Figure 1. Relative knife velocity vector (from Meehan and Burns [10]).
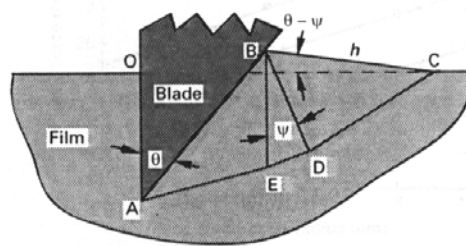
Figure 2. Cutting force model (from Arcona and Dow [9]).
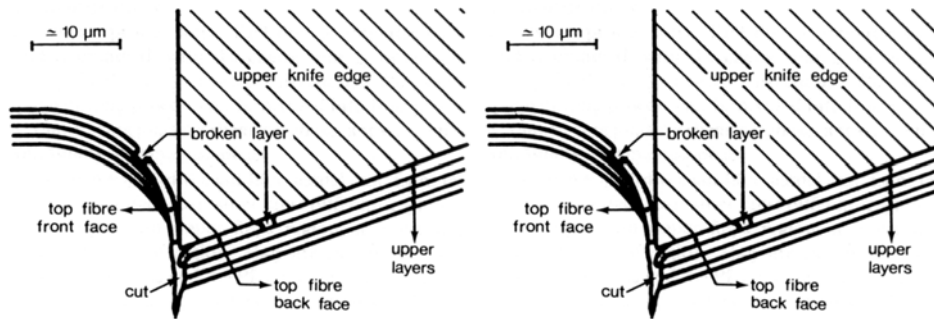
Figure 3. Sketch of deformed cut surfaces (from Bollen et al. [8]).

SLITTING SIMULATION SOFTWARE

Although no numerical simulations of slitting of plastic sheets were found in the open literature, there have been simulations of slitting of metal sheets. There have also been a number of numerical simulations of other cutting or blanking processes; Wisselink [6] provides a summary of the relevant studies. Only a few finite element simulations of the complete slitting process have been completed, and these have quite restrictive algorithms for crack growth, usually based on element extinction methods.

There are two basic finite element formulations, Lagrangian and Eulerian. In the Lagrangian formulation, the frame of reference is fixed with respect to the geometry. An updated Lagrangian formulation has a frame of reference that is fixed with respect to the geometry at the beginning of the time step, but the frame of reference moves when the geometry is updated, usually based on the deformed state at the end of the

previous step. In the Eulerian formulation, the frame of reference is fixed in space and the material flows through the frame.

The Lagrangian formulation can lead to element distortion as the material deforms. Therefore, it must be augmented with remeshing algorithms. The Eulerian formulation does not suffer from element distortion, but special procedures are required to follow free surfaces and cracks as the material boundaries are not coincident with the element edges in general. An alternative formulation is that used by Wisselink [6], the arbitrary Lagrangian-Eulerian (ALE) formulation. This is a combination of the two formulations where the frame of reference can be chosen based on the material deformation. The drawback to the ALE formulation is that the mesh topology must remain constant during the entire simulation, so it is not possible to follow the complete crack growth process.

FRANC2D has been used for over a dozen years to analyze arbitrary multiple crack growth. FRANC2D has routines for modifying the topology and geometry of the model to grow the crack. During the process of growing the crack, the mesh is locally modified near the crack tip through a delete and fill algorithm. However, FRANC2D does not have geometric nonlinear analysis or contact capabilities.

The combination of the two codes, ABAQUS and FRANC2D, provides a unique and much more powerful model for simulating the complete slitting process. An updated Lagrangian formulation is employed where the model geometry is updated based on the deformed state of the current step of analysis. FRANC2D was modified to communicate with ABAQUS, along with the additional capabilities to update the state and to remesh if the element distortion becomes excessive. This system is used to produce the slitting simulations discussed in the next section.

PRELIMINARY SLITTING SIMULATIONS

The first set of analyses was conducted entirely within FRANC2D using linear elastic material properties, small strain assumptions, and linear elastic fracture mechanics. Eastman Kodak Company provided the model geometry and material properties. The FRANC2D model after 40 crack growth steps is shown in Figure 4. The knife 'load' was modelled as a point force and cracks were initiated at the top and bottom at the same time. Note that the crack trajectory does not agree with those observed from the experiment. This model was primarily used to evaluate the required boundary conditions and crack growth behaviour (specifically crack face contact).
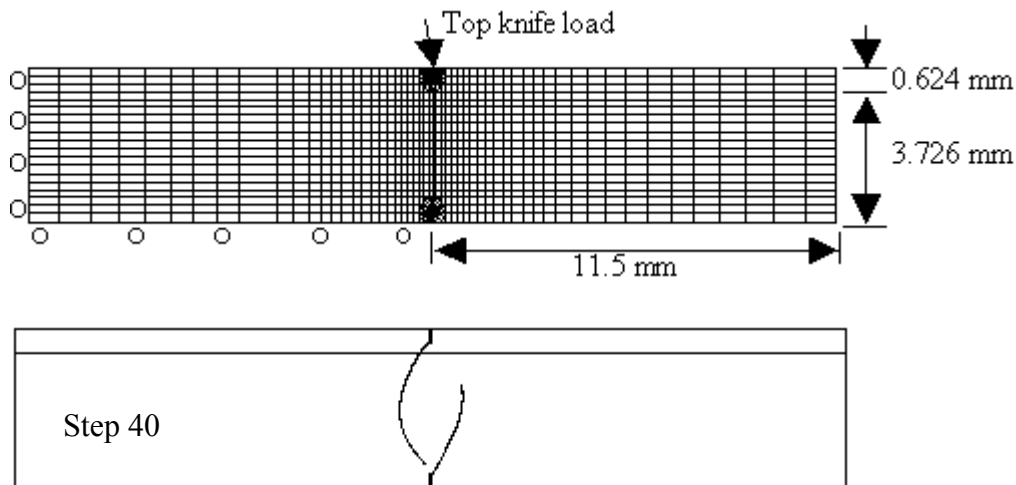
Figure 4. FRANC2D initial mesh model for slitting and model boundary after 40 crack growth steps.

The following cutting simulations used the coupled ABAQUS-FRANC2D approach. An initial ABAQUS model, with rigid surfaces for the blades and elasto-plastic strain hardening material data, was created and an

initial analysis was done in ABAQUS; contact was made between the knife and plastic sheet. The model and results were sent to FRANC2D where a crack was nucleated at the top surface of the plastic sheet at the knife contact 'point'. The results from the original analysis were mapped forward to the new mesh and the model was sent back to ABAQUS for subsequent analysis. Upon convergence in ABAQUS, the model and results were sent back to FRANC2D; the crack was propagated and the model was sent back to ABAQUS. This process continued until ABAQUS no longer converged or until it was deemed that the crack growth was sufficient such that the material effectively had been cut.

An initial cutting simulation where the stress and strain were not mapped forward is shown first. The model consists of a gelatine coating layer on top of a PET base layer. The material suffers plastic deformation at each increment and the deformation is recorded by updating the model based on the deformed state, but the plastic strain is not accumulated. A crack was initiated on the upper surface first and this crack was propagated for several steps before the second crack was initiated on the lower surface. The upper crack grew downwards while the lower crack grew very little, probably because the lower crack was located off the knife tip. The final configuration is shown in Figure 5 after 12 steps of crack growth.
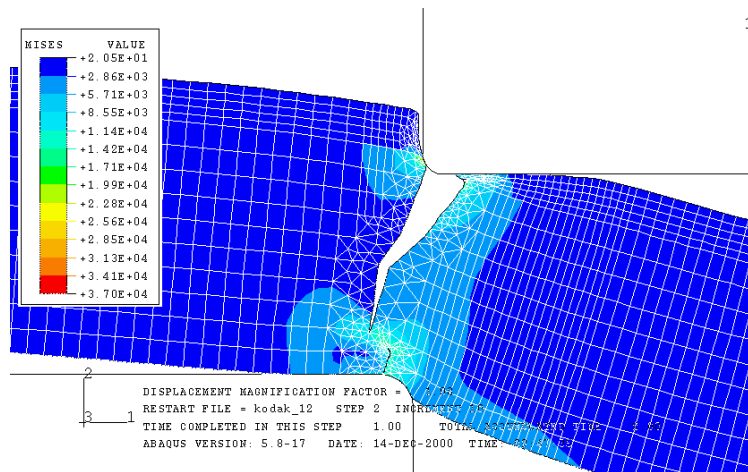
Figure 5. von Mises stress after 12 increments of crack growth (1X magnification).

The next cutting simulation was based on a simplified model consisting of a layer of acetate material only. The stress and strain were mapped forward. The material suffered plastic deformation at each increment and the deformation was recorded by updating the model based on the deformed state. The plastic strain was accumulated. A crack was initiated on the upper and lower surfaces during the same increment. Two simulations were performed. The first used the maximum hoop stress criterion to determine crack growth direction. For the second, the crack was forced to grow approximately in the direction of maximum shear. The final configurations are shown in Figures 6 and 7 after 10 and 13 steps of crack growth, respectively. ABAQUS does not converge for the subsequent steps in either series.

CONCLUSIONS

The combination of ABAQUS and FRANC2D provides a unique and powerful system for simulating the complete slitting process of thin plastic sheets. The simulations match observed slitting phenomena reasonably well. Additional effort is required to increase convergence rates and numerical stability. A more thorough study on the fracture criterion for various plastic sheet materials will also be investigated.
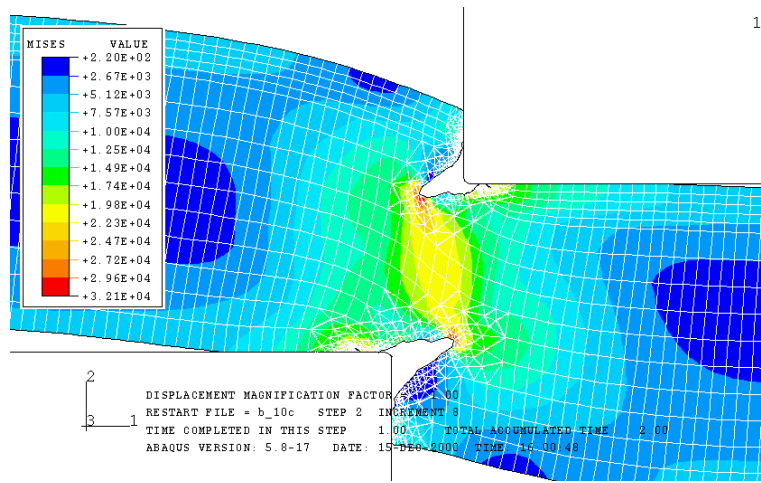
Figure 6. von Mises stress after 10 crack growth increments; LEFM fracture criterion (1X).
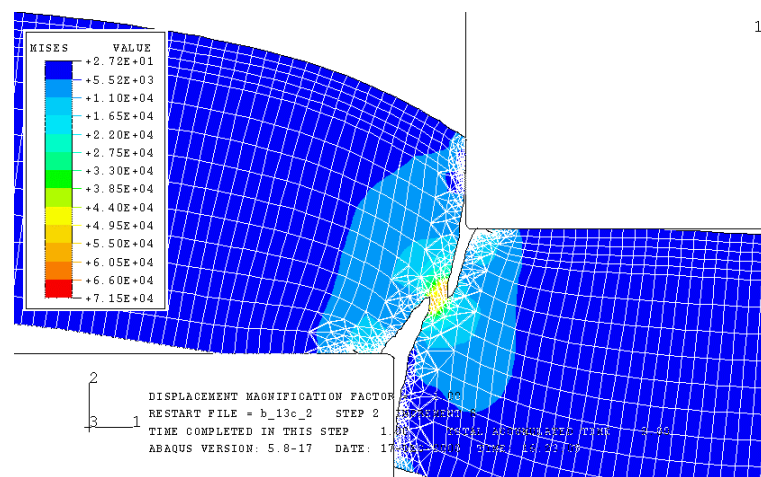
Figure 7. von Mises stress after 14 crack growth increments; fracture trajectory controlled manually based on shear stress and plastic equivalent strain (1X magnification).

REFERENCES

1. Dodd, B. and Bai, Y. (1987) *Ductile Fracture and Ductility, Applications to Metalworking*, Academic Press, London.
2. Chang, T.M. and Swift, H.W. (1950) *J. Inst. Metals*, 78, 119
3. Hashimura, M., Chang, Y.P. and Dornfeld, D. (1999) *J. Manufacturing Science and Engrg*, 121, 1.
4. Ehmann, K.F., Kapoor, S.G., DeVor, R.E. and Lazoglu, I. (1997) *J. Manufacturing Science and Engineering*, 119, 655.
5. Zhou, Q. and Wiezbickia, T. (1996), *Int. J. Mechanical Sciences*, 38, 303.
6. Wisselink, H. (2000). Ph.D. Thesis, University of Twente, The Netherlands.
7. Huetink J. (1986). Ph.D. Thesis, University of Twente, The Netherlands
8. Bollen, D., Deneir, J., Aernoudt, E. and Muylle, W. (1989) *J Materials Science*, 24, 2957.
9. Arcona, C. and Dow, T.A. (1996) *J Materials Science*, 31, 1327.
10. Meehan, R.R. and Burns, S.J. (1998) *Experimental Mechanics*, 38, 2, 103.
11. Wawrzynek, P., Ingraffea, A. R., "Interactive Finite Element Analysis of Fracture Processes: An Integrated Approach", Theoretical and Applied Fracture Mechanics, 8, 1987, pp.137 - 150.
12. Ford, H. (1963). *Advanced Mechanics of Materials*, Wiley, New York.
13. Kausch, H.-H. (1987). *Polymer Fracture*. Springer-Verlag Berlin Heidelberg.

SIZE EFFECT OF CORROSION FATIGUE PROPERTIES IN MICRO-SIZED 304 AUSTENITIC STAINLESS STEEL SPECIMENS

Y. Mizutani, M. Shimojo, K. Takashima and Y. Higo

Precision and Intelligence Laboratory, Tokyo Institute of Technology,
4259 Nagatsuta-cho, Midori-ku, Yokohama, 226-8503, Japan

ABSTRACT

Corrosion fatigue properties of micro-sized materials are extremely important to design MEMS devices and micro-machines used in corrosive environments. However, there have been few studies that investigate corrosion fatigue properties of micro-sized materials. Thus, it is necessary to develop a corrosion fatigue test method for micro-sized materials. However, there are several difficulties in corrosion fatigue tests on micro-sized specimens. It is also necessary to clarify the problems for the method and to find their solutions. Corrosion fatigue tests for micro-sized 304 austenitic stainless steel specimens have been carried out in air and a 0.9% NaCl solution and the size effects on corrosion fatigue properties have been discussed. Specimens of cantilever-beam-type with dimensions of 10 x 10 x 50 μm^3 were prepared from a 304 austenitic stainless steel thin sheet by focused ion beam machining. The fatigue life of the specimen tested in air was more than 270000 cycles, while that tested in the corrosive environment was 9900 cycles. Distinct environmental effects on fatigue properties were observed. Several problems and solutions for the testing method were also described.

KEYWORDS

Micro-sized specimens, 304 austenitic stainless steel, Corrosion fatigue, Fatigue life, NaCl solution

INTRODUCTION

MEMS(Micro electromechanical systems) devices are expected to be used in human body as Bio-MEMS (diagnosis and treatment devices) and in corrosive environments as inspection devices. The size of components used in such MEMS devices are considered to be in the order of microns. This size is smaller than the grain diameter in conventional metals and alloys. Mechanical properties of such micro-sized materials are considered to be different from those of bulk materials. In addition, the effect of corrosion is considered to be more prominent, because the specific surface area of micro-sized specimens is larger compared with that of bulk specimens. Crevices, the size of which is also in the order of microns, may exist in MEMS devices and thus crevice corrosion is also important. Therefore, corrosion fatigue properties of micro-sized materials are extremely important to design such devices. However, there have been few studies to investigate corrosion fatigue properties of micro-sized materials. This may be due to difficulties

in corrosion fatigue tests on micro-sized specimens. In our previous study [1], we have developed a corrosion fatigue testing machine for micro-sized specimens and have succeeded to carry out corrosion fatigue tests.

In this investigation, corrosion fatigue tests for micro-sized austenitic stainless steel specimens have been carried out in a 0.9% NaCl solution and the size effect on corrosion fatigue properties has been discussed.

EXPERIMENTAL PROCEDURE

The material used in this study was a 304-type austenitic stainless steel thin sheet. At present, austenitic stainless steels and titanium alloys are widely used for medical applications. The 304 austenitic stainless steel thin film is commercially available, and has a fine grain (about 7.6 μm in diameter) structure.

The thickness of the as-received sheet of 304 austenitic stainless steel was 10 μm. A disc with a diameter of 3mm was cut by a punch press. Then, a cantilever beam type specimen was prepared by focused ion beam machining as shown in Figure 1. The thickness and the width of the specimen were 10 μm. Two grooves with a radius of 1 μm were introduced at the both sides of the specimen as stress concentration sites as shown in Figure 1. The stress concentration sites were 10 μm away from the fixed end of the specimen. Thus, the distance from the loading point to the stress concentration sites, L, was 30 μm.
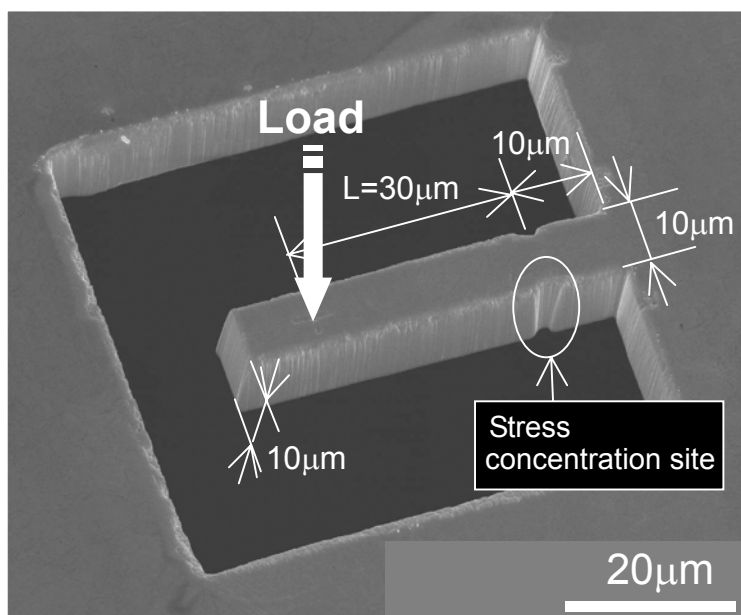
Figure 1: Micro-cantilever beam specimen of the 304 austenitic stainless steel

(a)   (b) acrylic resin stand

Φ0.8mm penetrated hole

6mm
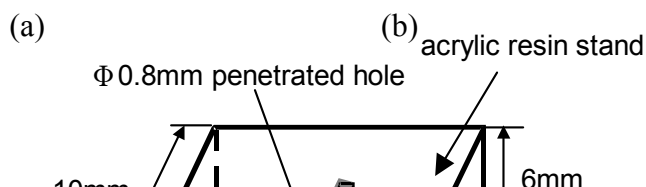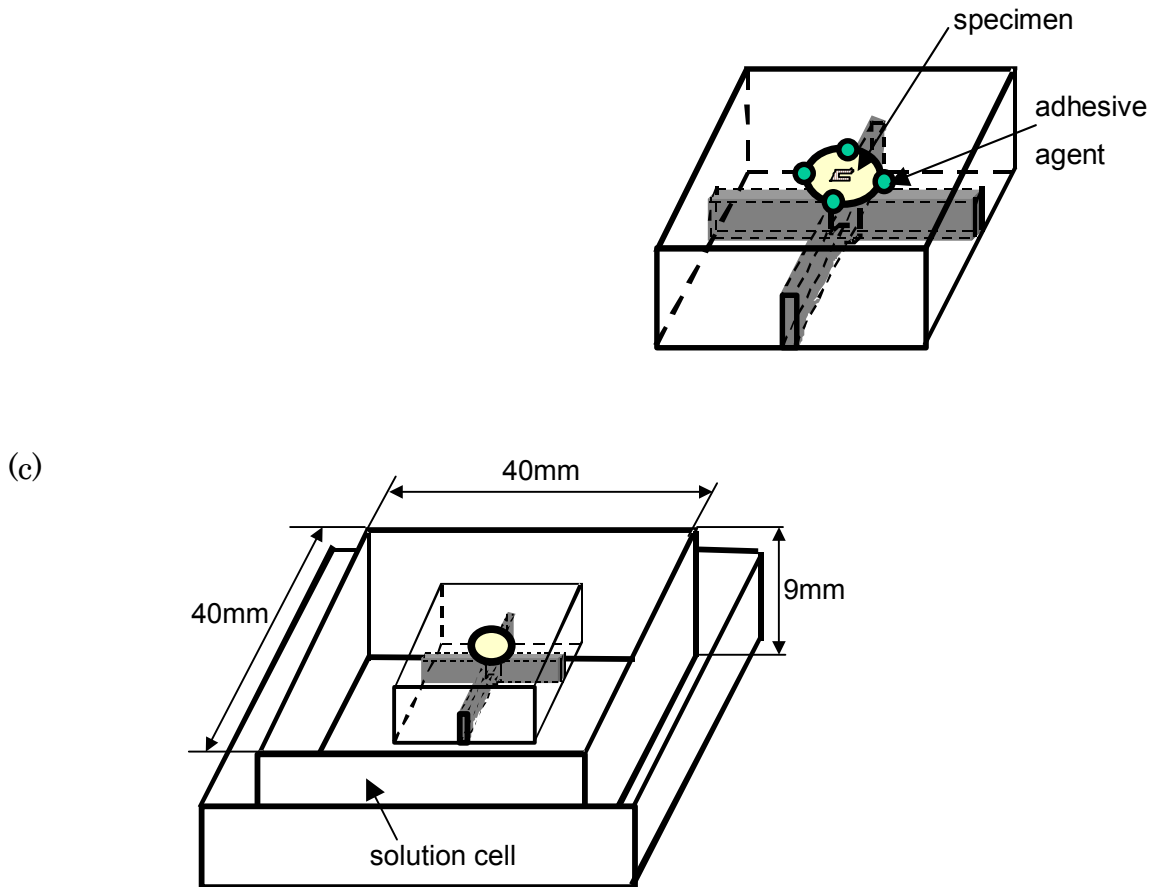
Figure 2: (a) Specimen holder made of acrylic resin. A specimen is mounted on the holder using an adhesive as shown in (b) and the specimen with the holder is immersed in solution as shown in (c).

As shown in Figure 2, a specimen was mounted using an adhesive at the 0.8 mm hole penetrated at the intersection of two 1x3 mm^2 ditches in a stage made of acrylic resin. The specimen with the stage was immersed in the solution cell with dimensions of 40 mm square and 9 mm depth. 0.9% NaCl solution, which simulates human body fluid, was poured into the solution cell. The cell can be positioned with an accuracy of 0.1μm using a precise X-Y stage of the mechanical testing machine for micro-sized materials. A diamond tip (5 μm in radius) was attached to a pushrod. A load cell was connected between the pushrod and the actuator. The load resolution of the load cell used was 10 μN, and the displacement resolution of this testing machine was 0.005 μm. The details of this testing machine, which has been developed in our previous investigation, are described in our previous papers [2-6].

Static bending tests were performed prior to the fatigue tests. The position of the diamond tip connected to the actuator was placed at the loading point, which was 40 μm from the fixed end of the specimen. The specimen was then gradually deflected by descending the diamond tip with displacement steps of 0.3 μm/s. The load applied to the specimen was recorded with the corresponding displacement.

Fatigue life tests were performed at a frequency of 10Hz in air and of 1Hz in the NaCl solution and at a stress ratio (the ratio of minimum to maximum load applied over fatigue cycle) of 0.5. The maximum load (P_{max}) over the fatigue cycle was controlled to 0.7 P_B, where P_B is the bending strength measured in the static bending tests. Specimens were observed after the tests using a field emission gun scanning electron microscope (FE-SEM). This testing machine is set up in a clean room with constant temperature and humidity to eliminate dust and the effect of temperature change during the measurement. The testing machine is also placed in a wind screen box to shield from the slight wind stream in the room.

RESULTS AND DISCUSSION

In order to develop a corrosion fatigue test method for micro-sized materials, three problems had to be solved. The first problem was how to hold the specimen in the aqueous solution. The specimen holder should not elute into the aqueous solution to avoid any contamination and should not be made of metals to avoid galvanic corrosion. Thus, a specimen stage was made of acrylic resin and a specimen was fixed with an adhesive.

The second problem was how to cover the specimen with aqueous solution. Aqueous solution does not enter thin holes or ditches due to water repellency and surface tension. Thus, we poured the aqueous solution into the cell in a vacuum chamber and the coverage of the specimen was confirmed using a CCD (charge coupled device) camera.

The third problem was how to eliminate error in load measurements. In micro-sized testing, the measuring load would be so small that the buoyancy of the pushrod might not be negligible. In addition to this, the viscosity and surface tension of the aqueous solution would cause error in load measurements. For example, surface tension would be added to and reduced from the actual load applied to the specimen due to the fluctuation of the meniscus during corrosion fatigue tests, as shown in Figure 3. During this situation, the buoyancy of the pushrod also fluctuates because the deflection of the specimen results in a change in the depth of the pushrod immersed under the aqueous solution. The evaporation of the aqueous solution also causes a change in the buoyancy during the tests. Thus, it is quite difficult to correct the error completely. However, no detectable difference in phase was observed between applied displacement and detected load signals, when the loading frequency was reduced to 1Hz. Thus, the error caused by the viscosity of the aqueous solution was negligible at this loading frequency. (Note that the inclusion of the force caused by viscosity leads to a change in phase because the viscosity resistance of Newtonian fluid is in proportion to the velocity.)

(a)   (b)   (c)
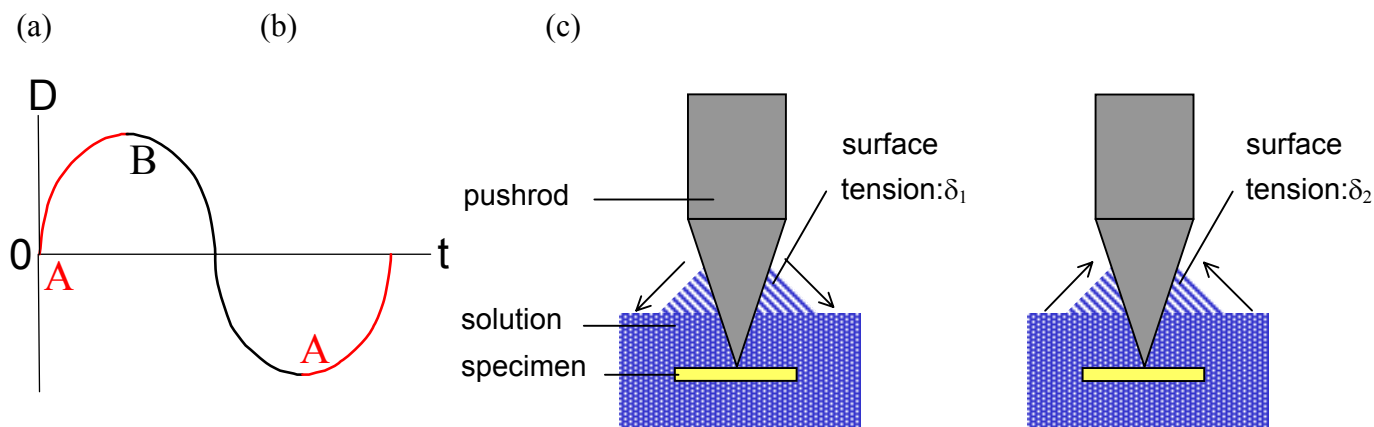
Figure 3: (a) Schematic diagram of displacement as a function of time, and schematic illustrations around the pushrod showing that surface tension (b) added at A and (c) subtracted at B from the actual loads.

(a)   (b)
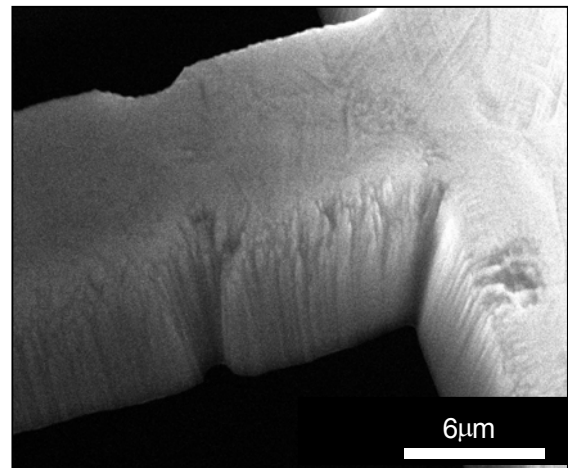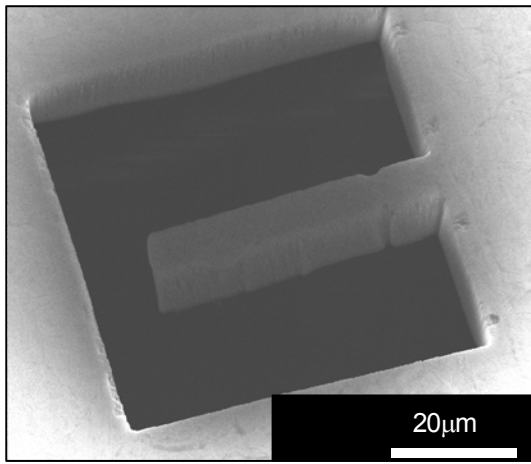
Figure 4 : Stainless steel specimen after a fatigue test in air, showing that (a) the specimen did not fail, and (b) no crack was found at the stress concentration sites.
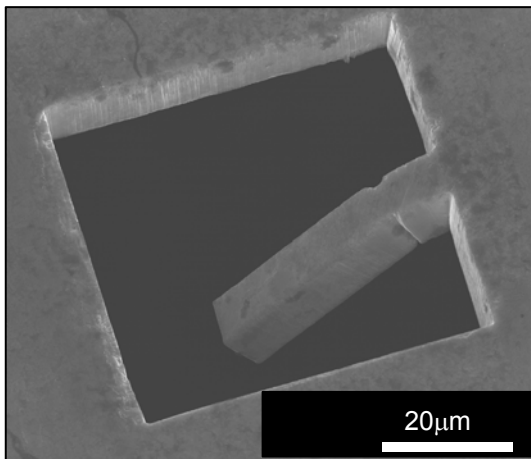
(a)   (b)
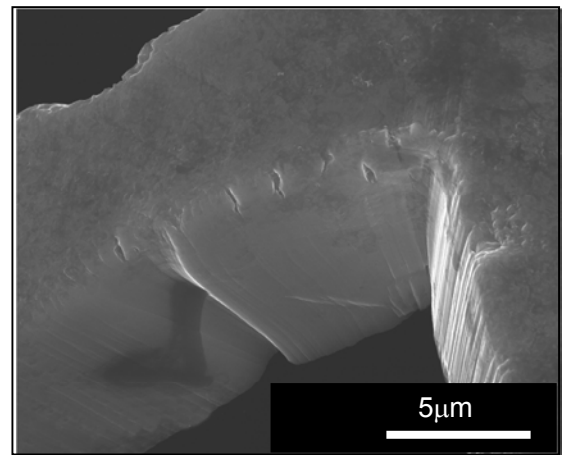
Figure 5: Stainless steel specimen after a corroison fatigue test, showing that (a) the specimen failed, and (b) cracks were found at the stress concentration sites and also the root.

The stainless steel specimens did not fail after 2.7×10^5 cycles in air, on the other hand, failed after only 9.9×10^3 cycles in the NaCl solution. Figure 4 shows SEM-images of the stainless steel specimen after fatigue test in air. No crack was found on the stainless steel specimen fatigue tested in air. Figure 5 shows SEM-images of the stainless steel specimen after fatigue test in the corrosive environment. Some cracks were found at the fixed end of the specimen and at the stress concentration sites of the specimen tested in the corrosive environment. The fatigue life of the micro-sized specimen tested in the corrosive environment was one order of magnitude lower than that tested in air, which corresponded with data of ordinary-sized specimens.

The fatigue life in the corrosive environment was much lower than that in air. No crack was found on the specimen fatigue tested in air, but some cracks were found at the fixed end and at the stress concentration sites on the specimen fatigue tested in the corrosive environment. Therefore, environmental effects on fatigue properties of micro-sized specimens were clearly observed.

CONCLUSIONS

The fatigue life of the specimen tested in air was more than 270000 cycles, while that tested in the corrosive environment was 9900 cycles. In other words, the fatigue life of the micro-sized specimen tested in the corrosive environment was one order of magnitude lower than that tested in air, which corresponded with data of ordinary-sized specimen. Distinct environmental effects on fatigue properties were observed. Several problems and solutions for the testing method were also clarified

REFERENCES

1. Mizutani, Y., Higo, Y., Ichikawa, Y., Morita, A. and Takashima, K. (2000). In: *Materials Science of Microelectromechanical Systems (MEMS) Devices Ⅲ*, in press, deBoer, M., Judy, M., Kahn, H. and Spearing, S.M. (Eds). The Materials Reserch Society, Pennsylvania.
2. Maekawa, S., Takashima, K., Shimojo, M.., Higo, Y., Sugiura, S., Pfister, B. and Swain, M. V. (1999). *Microprocesses and Nanotechnology Conf.*, pp.132-133, Horiike, Y. (Eds). The Japan Society of Applied Physics, Tokyo.
3. Ichikawa, Y., Maekawa, S., Takashima, K., Shimojo, M., Higo, Y. and Swain, M. V. (2000). In: *Materials Science of Microelectromechanical Systems (MEMS) Devices Ⅱ*, pp.273-278, deBoer, M., P., Heuer, A.H., Jacobs, S.J. and Peeters, E.(Eds). The Materials Reserch Society, Pennsylvania.
4. Maekawa, S., Takashima, K., Shimojo, M., Higo, Y. and Swain, M. V. (2000). In: *Materials Science of Microelectromechanical Systems (MEMS) Devices Ⅱ*, pp.247-252, deBoer, M., P., Heuer, A.H., Jacobs, S.J. and Peeters, E.(Eds). The Materials Reserch Society, Pennsylvania.
5. Takashima, K., Ichikawa, Y., Shimojo, M., Higo, Y. and Swain, M. V. (2000). *Proc. 3rd Int. Conf. and Poster Exhibition on MicroMaterials*, pp.526-529.
6. Maekawa, S., Takashima, K., Shimojo, M.., Higo, Y., Sugiura, S., Pfister, B. and Swain, M. V. (1999). *Jpn. J. Appl. Phys.*, 38, 7194.
7. Maekawa, S., Takashima, K., Shimojo, M.., Higo, Y., Sugiura, S., Pfister, B. and Swain, M. V. (1999). In: *Fatigue '99(Proc. 7th Int. Fatigue Cong.)*, pp. 1871-1876, Wu, X-R. and Wang, Z-G.,(Eds). Higher Education Press, Beijing
8. Takashima, K., Higo, Y., Sugiura, S. and Shimojo, M. (2001). *Mat. Trans.*, 42, 68.

SLOW BRITTLE FRACTURE

C. J. McMahon, Jr.

Department of Materials Science and Engineering
University of Pennsylvania, Philadelphia, PA 19104

ABSTRACT

In contrast to the catastrophic types of brittle fracture in which cracks propagate unstably at hundreds of meters per second, brittle fracture can occur in a stable fashion at speeds that are many orders of magnitude slower. This occurs as a result of surface contamination by a mobile embrittling element that is induced to diffuse into a solid, usually along grain boundaries, under the influence of an applied stress. Examples are common in various engineering structures, but it is not widely recognized that they all belong to the same generic form of brittle fracture.

KEY WORDS: dynamic embrittlement, brittle fracture, intergranular fracture

INTRODUCTION

The term "brittle" is used here to denote fracture by decohesion that occurs apart from any plastic process. That is, plasticity may occur concomitantly, but it is not an essential part of the decohesion process. In the familiar fast brittle fracture in metals by transcrystalline cleavage or intergranular decohesion, plasticity is usually essential to crack nucleation, but is only incidental to crack propagation. The same applies here to slow brittle fracture.

Slow brittle fracture involves the propagation of a crack in a solid the surface of which is contaminated by an element that, when concentrated in the solid, would reduce the local cohesive strength. The application of a tensile stress to a solid in which a crack has nucleated both stretches bonds and causes the embrittling element to diffuse inward at the tip of the crack. This allows the crack to spread at a rate dependent upon the rate of diffusion of the embrittling element from the surface into the region ahead of the crack tip. This process has been termed "dynamic embrittlement" [1,2].

The phenomenon of dynamic embrittlement can be categorized according to the available concentration of embrittling element at the crack tip. The three categories being studied systematically in alloys are the following:

(i) Low concentration. The embrittling element comes by way of surface segregation from the alloy itself.

(ii) Moderate concentration. The element comes from the vapor phase around the alloy.

(iii) High concentration. The embrittling species is in a liquid phase.

EMBRITTLEMENT FROM SURFACE SEGREGATION

The phenomenon was first recognized in the context of stress-relief cracking of alloy steels [3]. This is sometimes found in the coarse-grained heat-affected zone of welds, usually in thick sections. During the welding process, the HAZ reaches temperatures high enough to allow some dissolution of sulfides in the steel. During cooling, the dissolved sulfur segregates to austenite grain boundaries and then re-precipitates as very fine (probably metastable) sulfides in these boundaries. When the structure is later heated to allow relief of the residual stresses by creep, cavities can nucleate around large intergranular particles, like oxides or sulfides. If the stress is high enough, brittle cracks can grow from these cavities. This is caused by the presence of elemental sulfur that is segregated on the surfaces of the cavity and the subsequent crack and is then induced to diffuse into the grain boundary ahead of the crack by the tensile stress normal to the grain boundary, as illustrated schematically in Fig. 1. Sulfur is a very potent embrittling element in iron, and the concentration needed for decohesion at the stresses involved is probably less than one atom in ten [21].
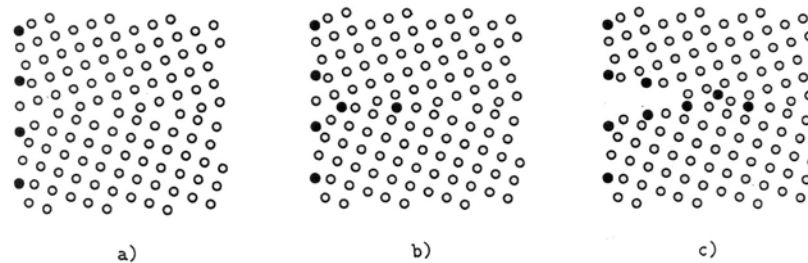
Fig. 1 Schematic representation of (a) surface adsorption of an embrittling element, (b) inward diffusion driven by a tensile stress, (c) decohesion in the diffusion zone.

The process depicted in Fig. 1 is analogous to the classical Hull-Rimmer mechanism of diffusive growth of creep cavities [4], which is the reverse of the sintering process. The stress across the grain boundary provides a gradient in chemical potential of atoms on the surface *vs*. in the bulk solid. That is, the stress does work when surface atoms diffuse into the bulk in exchange for lattice vacancies. Unlike in creep-cavity growth where the diffusing atoms are the same as in the bulk, in dynamic embrittlement the surface atoms are a mobile (i.e., low-melting) element that is adsorbed on the cavity/crack surface.

In a detailed study of stress-relief cracking using a simulated HAZ in a NiCrMnMo steel cooled rapidly from a high temperature [1], the following characteristics were found:

(i) The initial crack growth is macroscopically discontinuous, occurring in bursts, as indicated by the results from a compact-tension specimen under a constant load at

550˚C in vacuum, as shown in Fig. 2. Fractography by SEM showed that each burst represented cracking of a number of grain boundaries.

(ii) The local rate of crack advance is highly variable, depending on the grain-boundary structure, which determines the rate of diffusion of the surface element into the boundary. This results in a highly irregular crack front and in slow-cracking ligaments left behind the main crack front.

(iii) The tip of the growing crack is so sharp that no appearance of blunting could be found by examination of the fracture surface at the highest available resolution in the scanning electron microscope.

To test the hypothesis that this is a generic form of brittle fracture, similar experiments were carried out on a Cu-8%Sn alloy (without the prior high-temperature treatment). Compact-tension specimens loaded at 265˚C in vacuum exhibited behavior essentially similar to the steel [5], including intergranular decohesion and cracking in bursts. In this model material the tin played the role of sulfur in the steel. It is surface active [6], and it is a low-melting embrittling element in steel [7]. The conclusion is that the low creep ductility [8] and the hot shortness [9] exhibited by Cu-Sn alloys are both analogous to stress-relief cracking in steels.
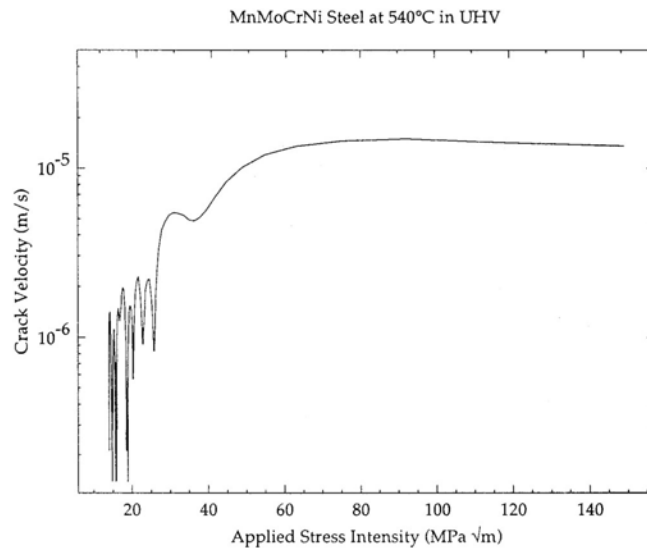
Fig. 2 Example of crack growth in bursts in the early stages of sulfur-induced dynamic embrittlement (stress-relief cracking) [1].

To test the idea that dynamic embrittlement requires diffusive penetration of the solid, which depends on the grain-boundary diffusion rate and thus grain-boundary structure, experiments were done on Cu-Sn bicrystals [10]. In specimens with Σ=5 (031)[100] symmetrical tilt boundaries made by diffusion bonding and loaded in vacuum at 265˚C, it was found that a crack could be grown easily along the tilt axis, but not transverse to the tilt axis. This corresponds to cracking along the fast-diffusion direction but not the slow-diffusion direction.

In the initial set of experiments, the boundaries had a residue of sub-micron-size alumina particles from metallographic polishing. Later, specimens were prepared without this residue [10], and still later by growth from the melt, also without particles [11]. The boundaries in this set of specimens were found to be difficult to crack, even along the fast-diffusion direction. Two conclusions were drawn from this. The first is that dynamic embrittlement may well follow the pattern of other types of grain-boundary failure [12-14] in which boundaries with Σ-value less than about 29 are particularly resistant to failure. The second conclusion is that the presence of particles probably enhanced the surface concentration of tin by decohering ahead of the crack and allowing tin to segregate to the new surfaces thereby created. They would thus have served a role analogous to that of the small sulfides in the steel. The influence of grain-boundary particles is an area that deserves further study.

EMBRITTLEMENT FROM THE ENVIRONMENT

Motivated by reports of oxygen-induced intergranular cracking in Cu-0.25%Be [15] and in nickel-base alloys, particularly alloy 718 [16], experiments were carried out to see if these types of cracking were analogous to the phenomena described above. When the steel and the Cu-Sn alloy were loaded at fixed displacement as notched bars in vacuum at elevated temperatures and the Cu-Be and alloy 718 were loaded similarly in oxygen, essentially the same behavior was found in all cases. The crack velocity could be calculated from the load-relaxation curve and the relation between specimen compliance and crack length. An example of the effect of oxygen pressure is given in Fig. 3.
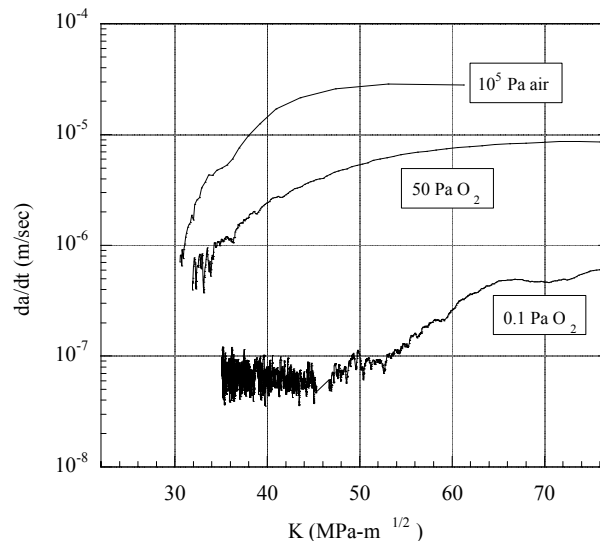
Fig. 3 Crack velocity *vs*. stress intensity curves derived from the load-relaxation curves and the compliance-calibration curve for alloy 718 at 650˚C in various pressures of oxygen [17].

Examination [17] of the fracture surfaces of the alloy 718 showed the typical decohesion appearance when the oxygen pressure was high enough. However, at very low pressures the growth rate dropped by several orders of magnitude, and the fracture appearance changed to a series of striations marked by strings of oxide, indicating that the cracking occurred in jumps at time intervals long enough for significant oxidation at the crack tip. The cracking at

higher oxygen pressures was also discontinuous (on the sub-micron scale), but the time intervals were much shorter, and the crack remained essentially sharp. Similar crack-arrest marks have been seen in all cases of dynamic embrittlement in polycrystalline specimens, but the cracking of the Cu-Sn bicrystals was continuous [10].

Our interpretation [17] of the fracture-surface observations was as follows: Cracking in polycrystals at sufficiently high surface concentration of the embrittling element occurs by the advance of sharp intergranular cracks caused by oxygen-induced decohesion, but at different rates along the crack front, depending on the local grain-boundary diffusivity. At any instant the main crack is advancing in some places, but not in others, and the load is therefore carried by the non-cracking regions. This shields the cracking regions from stress and allows the existence of sharp crack fronts. However, at any region of cracking the local stress relaxes as the crack moves forward, and the crack then has to stop and wait for creep of the non-cracking regions to raise the stress again. Thus, the cracking of a polycrystal is discontinuous because of the constraint imposed by non-cracking regions at any moment in time. The result is that large stress intensities are borne by the specimen (Fig. 3), but this does not reflect the stress intensity at the points of sharp-crack advance. In addition, the temperature dependence of cracking is found [17] to be consistent with that of self-diffusion in the alloy, rather than with the intergranular diffusion of the embrittling element in from the surface, because the cracking is constrained by the rate of power-law creep in the non-cracking regions.

Continuing this interpretation, in the case of cracking at very low oxygen pressures, oxygen atoms arrive at the crack tip so slowly that they have time to diffuse away along the grain boundary, down the gradient of chemical potential provided by the local stress. The crack then has time to blunt, and the oxygen collects in the region of maximum stress ahead of the blunt crack. When the concentration becomes high enough, cracking occurs back to the crack tip, and the process is repeated.

Oxygen-induced cracking in nickel-base alloys has been studied mainly in the context of cyclic loading and the effects of hold-time and loading rate on intergranular fatigue-crack growth [16,18]. The results obtained under fixed displacement conditions [17] indicate that the cyclic nature of the loading in the previous studies is incidental to the crack-growth process.

Experiments to study cracking in liquid metals using the same fixed-displacement, load-relaxation approach as outlined above have been only partly successful. It has been found with mercury and several copper-base alloys that the cracking is either too rapid to control or is so slow that it has to be driven with a moving cross head on the testing machine [19,20]. Much more work is needed in this area.

SUMMARY

It is now evident that dynamic embrittlement is a generic form of brittle fracture that involves decohesion caused by the inward diffusion of surface-adsorbed embrittling

elements, driven by an applied tensile stress. The source of the embrittling element can be the alloy itself (e.g., sulfur in steel and tin in Cu-Sn alloys) or the surrounding environment (e.g., oxygen in Cu-Be or in nickel-base alloys). Liquid-metal-induced cracking is thought to be a form of dynamic embrittlement, but this has not yet been demonstrated satisfactorily.

ACKNOWLEDGEMENTS

References

1. Bika, D. and McMahon, C. J. Jr. (1995). *Acta Metall.* 43**,** 1909.
2. Liu, C. T.and White, C. L. (1987) *.Acta Metall.* 35**,** 643.
3. Shin, J. and McMahon, C. J. Jr. (1984) *Acta Metall.,* 32, 1535.
4. Hull, D. and Rimmer, D. E. (1959) *Philos. Mag.,* 4, 673.
5. Barrera, E. V., Menyhard, M., Bika, D., Rothman, B. and McMahon, C. J. Jr., (1992) *Scripta Metall.*, 27**,** 205.
6. Hofmann, S. and Erlewien, J. (1976) *Scripta Metall.* 10, 857.
7. Steven, W. and Balajiva, K. (1959) *J. Iron Steel Inst*. 193, 141.
8. Kanno, M. and Shimodaira, N. (1987) *Trans. Japan Inst. of Metals*,28, 742.
9. Metals Handbook, American Society for Metals, (1948) p. 860.
10. Muthiah, R. C., Pfaendtner, J. A., Ishikawa, S. and McMahon, C. J. Jr., Acta Mater. 47 (1999) 2797.
11. Woods, Seamus S. and McMahon, C. J. Jr., (2001) submitted for publication.
12. Palumbo, G., Lehockey, E. M. and Lin, P. *JOM* **50(2)** 40 (1998).
13. Was, G. S. Thaveeprungsriporn, V. and Crawford, D. C. *JOM* **50(2**) 44 (1998).
14. Kumar, M., King, W. E. and Schwartz, A. J. *Acta Materialia*, **48** 2081 (2000).
15. Guha, A. Brush-Wellman Inc., private communication 1993
16. Chang, K-M, Henry, M. F. and Benz, M. G. (1990), *JOM*, 42, 29.
17. Pfaendtner,. J. A. and McMahon, C. J. Jr, (2001) *Acta Mater.* in press.
18. Molins, R. Hochstetter, G. Chassaigne, J.C. and Andrieu, E. (1997) *Acta Metall.* 45 663.
19. Lerner, Jeffrey, Woods, Seamus S., Peng, Edward and McMahon, C. J. Jr. (2001) submitted for publication.
20. Lerner, Jeffrey and McMahon, C. J. Jr. (2001) submitted for publication.
21. Shin, K. S. and Meshii, M. (1983) *Scripta Metall.* 17, 1121.

SMALL FATIGUE CRACK INITIATION AND GROWTH BEHAVIOR OF Fe-0.5Ni-1Mo SINTERED STEEL

A. Sugeta, M. Jono and Y. Uematsu

Department of Mechanical Engineering and Systems, Osaka University,
Yamada-oka, Suita, Osaka, 565-0871, Japan

ABSTRACT

The effects of porosity and worked layer on small fatigue crack initiation and growth behavior were investigated on Fe-0.5Ni-1Mo sintered steels and recompressed ones with high density. Reversed plane bending fatigue tests were carried out using an electro-magnetic type bending machine and small fatigue cracks were observed by means of plastic replica technique. A shallow notch was machined by using a milling machine (type-m) or an electric discharge machine (type-e) in the center of the specimen surface so as to localize the crack initiation site within a small area. The milling process resulted in the worked layer near the specimen surface and induced the compressive residual stress. Fatigue crack initiation lives of type-e specimens were found to be shorter than these of type-m specimens on both materials. Although fatigue cracks initiated from pores irrespective of materials, crack initiation site changed from the surface to the interior of the specimen by introducing the worked layer, resulting in the increase of fatigue crack initiation life. It was found that the recompression of porosity had small effect on crack initiation. Because the recompress process collapsed the pores but could not reweld the interfaces, the fatigue crack easily initiated from them. The crack growth resistance was found to be improved by the recompress process irrespective of machining method.

KEYWORDS

Powder metallurgy sintered alloy, Fatigue crack initiation, Small fatigue crack growth, Recompress process, Machining process, Pore, Worked layer

INTRODUCTION

It is well known that powder metallurgy (P/M) process leads to the development of alloy systems with high performance. The P/M process is efficient because it produces near-net shapes, with almost no raw material loss. During the last few decades, the demand for the reduction of weight resulted in the use of P/M steel for highly stressed fatigue-loaded components such as a non-lubricant bearing or a transmission gear of car. Although it was widely reported that the mechanical properties was affected by the porosity, and shapes and distribution of pores[1-4], there are few study on the effect of porosity on fatigue crack initiation and small crack growth behavior. In this study, reversed plane bending fatigue tests under constant amplitude loading were carried out on Fe-0.5Ni-1Mo sintered steels and a recompressed ones with high density using an electro-magnetic type bending machine. And the effects of porosity and machining on fatigue properties were investigated.

MATERIALS AND EXPERIMENTAL PROCEDURE

Two kinds of sintered P/M alloys were investigated. Fe-0.5Ni-1Mo alloy powder was produced by atomization process. The alloy powders were then compacted at room temperature under high pressure of 600 MPa followed by sintering at 1573 K for 1 hour in nitrogen gas environment. After that, the sintered alloy was hold at 1123 K for 1 hour, oil quenched and then tempered for 1.5 hours at the temperature of 473 K. For convenience, the alloy manufactured by this process will be referred to as material A hereinafter. In order to investigate the effect of porosity on fatigue behavior, the alloy with high density was manufactured by recompressing the material A. This Alloy will be referred to as material B. The chemical composition of these alloys in percentage mass is shown in Table 1. Table 2 shows the mechanical properties of the material A and B. Density and tensile strength of the recompressed material B is higher than that of material A. A fatigue test specimen is shown in Fig.1. A shallow notch, the stress concentration factor of which was 1.26, was machined by using a milling machine (type-m) or an electric discharge machine (type-e) in the center of the specimen surface so as to localize the crack initiation within a small area. Fully reversed plane bending fatigue tests under constant amplitude loading were carried out using an electro-magnetic type bending machine at a frequency of 30 Hz. The measurement of crack length and number of cracks were made by means of plastic replicas taken from the shallow notch area at the proper intervals during fatigue tests. Optical microphotographs of specimen surface at the notch root are shown in Fig.2. Pores are observed on the surface of notch root machined by the electric discharged machine irrespective of the materials. On the other hand, the surface machined by the milling is found to be smooth. Pores near the specimen surface were crushed under the milling process, resulting in the worked layer at the surface.

TABLE 1 CHEMICAL COMPOSITION OF MATERIAL USED. (mass%)

C	O	Si	Mn	P	S	Ni	Mo	Fe
0.001	0.08	0.01	0.19	0.014	0.017	0.56	1.07	bal.

TABLE 2 MECHANICAL PROPERTIES OF MATERIALS.

Material	Tensile strength σ_B (MPa)	0.2% proof stress $\sigma_{0.2}$ (MPa)	Elongation δ (%)	Young's modulus E (GPa)	Poisson's ratio	Density ρ (Mg/m^3)	Porosity (%)
A	1461.2	1374.0	0.6	162	0.27	7.20	8.16
B	1558	-	0	172	0.26	7.41	5.48
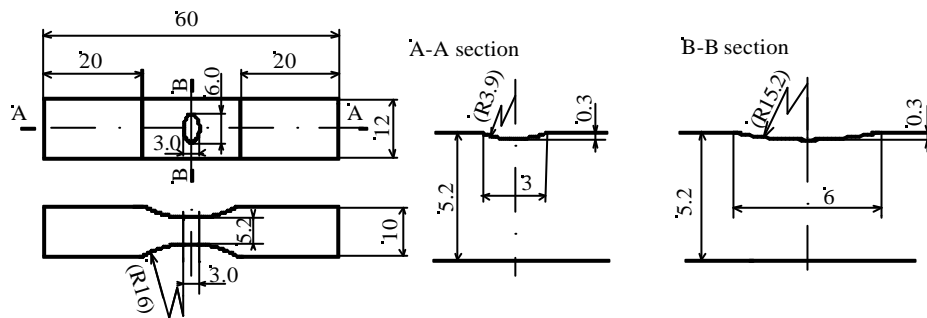
Figure 1: Test specimen configuration
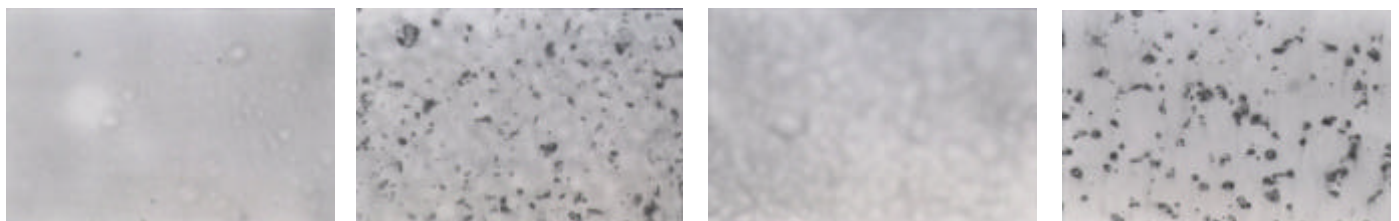
(a)A-m specimen　　(b)A-e specimen　　(c)B-m specimen　　(d)B-e specimen

Figure 2: Optical micrographs of specimen surface at notch root.

EXPERIMENTAL RESULTS AND DISCUSSION

Figure 3 shows relationships between the stress amplitude at the notch root and the number of cycles to

crack initiation, N_i, and that to failure, N_f. The stress amplitude indicated in the left hand ordinate means the local one at the shallow notch root, which is calculated by multiplying the stress concentration factor to the nominal stress. The crack initiation life, N_i, and the fracture life, N_f, are defined as the number of stress cycles at crack length of 0.2 mm and 2 mm, respectively. Fatigue crack initiation lives of type-e specimens were found to be shorter than these of type-m specimens on both materials. The effect of the machining on the crack initiation was observed. On the other hand, there found no effect of the recompress process on fatigue crack initiation and the endurance limit. In the case of type-e specimens, fatigue crack growth lives of the material B is longer than that of the material A, indicating that the recompress process resulted in the improvement of fatigue crack growth resistance.

Figure 4 shows SEM photographs of fracture surface near crack initiation site of type-m and -e specimens on the materials A and the arrows in these photographs indicate the fatigue crack origins. In the type-e specimen, the fatigue crack initiated at the surface pore and grew to the interior. On the other hand, the worked layer, depth of which is about 50 μm, is observed at the specimen surface in the type-m specimen and the fatigue crack initiated at the internal pore of specimen. Introduce of the worked layer by the milling resulted in the change of the crack initiation site from the surface to the interior of specimen, although fatigue crack initiated from pores irrespective of the machining methods. The increase of crack initiation life was thought to be resulted from the compressive residual stress at the surface, which was about –200 MPa, and the decrease of the stress at the internal pore, at which crack initiated, due to the stress gradient.

Figures 5 and 6 show optical photographs of fatigue crack initiation and growth behavior in the type-e and the type-m specimens of the material A. In the type-e specimen, many pores were observed on the specimen surface and five fatigue cracks initiated at the surface pores (Fig.5(a)). The fatigue cracks coalesced and/or overlapped into the main crack and grew in the direction perpendicular to the loading axis.
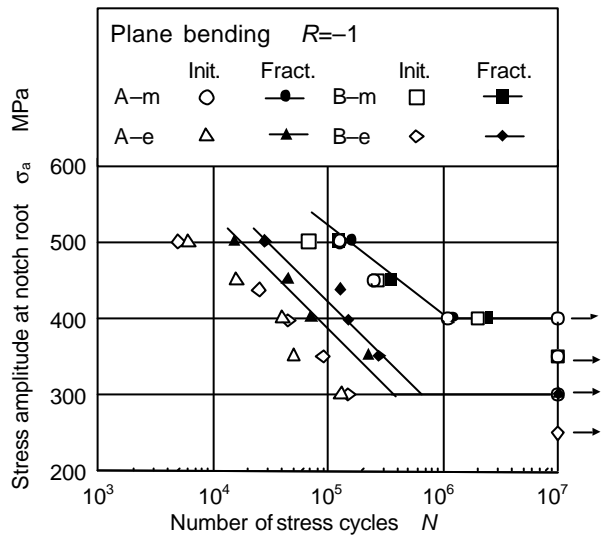
Figure 3: *S-N* curves.
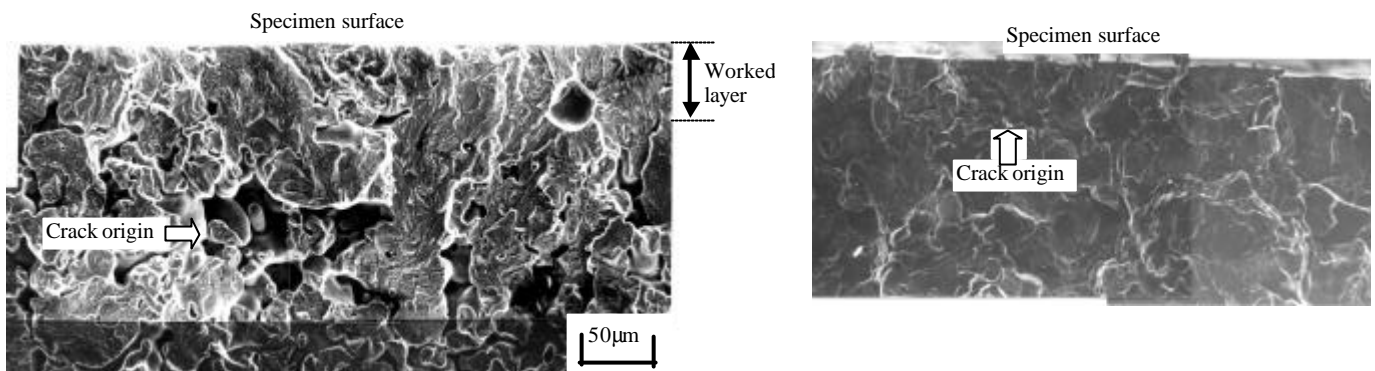
(a)A-m specimen, σ_a=500 MPa   (b)A-e specimen, σ_a=500 MPa

Figure 4 : Fracture surface near crack origin
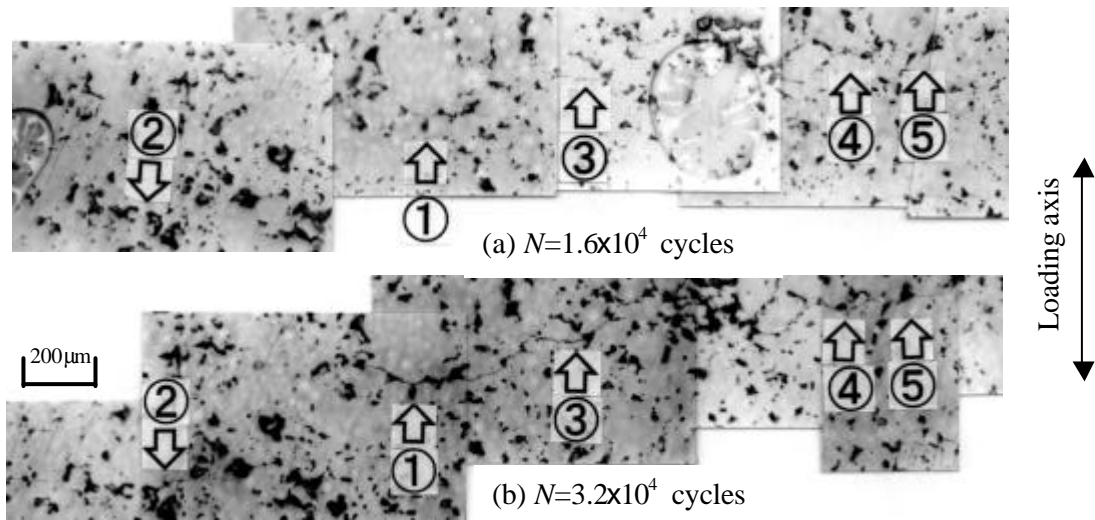
Figure 5 : Observation of fatigue crack behavior in A-e specimen at σ_a=450 MPa.

(a) N=1.6x10^4 cycles

(b) N=3.2x10^4 cycles
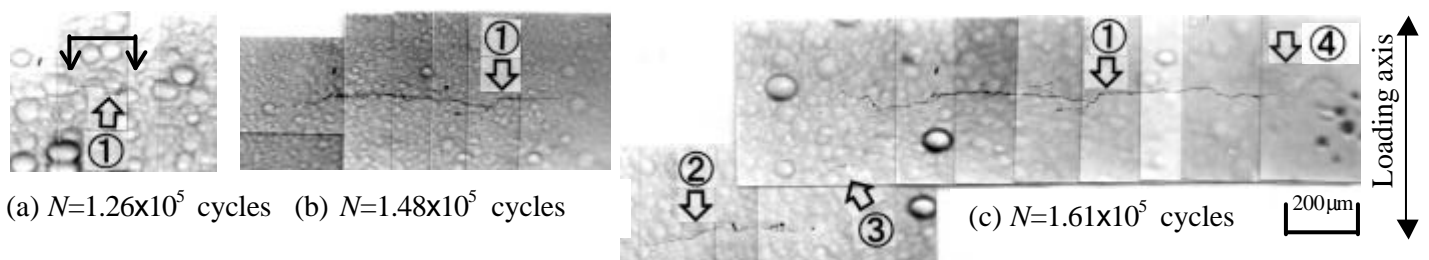
Figure 6 : Observation of fatigue crack behavior in A-m specimen at σ_a=500 MPa.

(a) N=1.26x10^5 cycles (b) N=1.48x10^5 cycles (c) N=1.61x10^5 cycles

(a) Material A, σ_a=500 MPa

(b) Material B, σ_a=500 MPa.
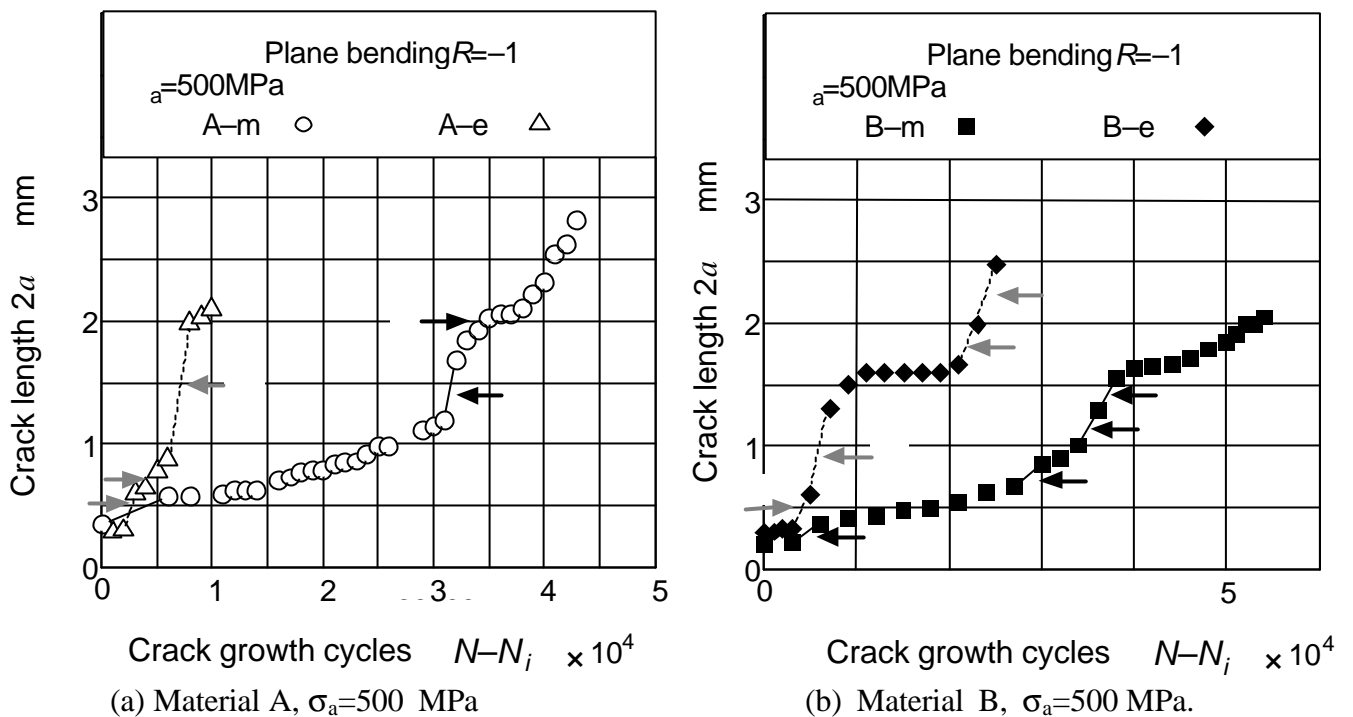
Figure 7 :Crack propagation curves.

In the type-m specimen, surface was very smooth and there was no pore on the specimen surface. The photograph shown in Fig.6(a) was taken when the crack was initially observed in the surface. In this photograph, the black arrows indicate the crack tips. Only one fatigue crack initiated and the crack length was about 200 μm at this stage, indicating that the fatigue crack initiated at an interior pore and grew until it breached the specimen surface, and it was longer than the initial crack length observed in the type-m specimen. In this case, the main crack, No.1, grew solely in the early stage and then overlapped with the

relatively short subcracks, No.2 and No.3. Similar fatigue crack initiation and growth behavior was observed on the material B, and there found no effect of the recompress process on fatigue crack initiation behavior. It was considered that the fatigue crack easily initiated at the collapsed pores because the pores were collapsed by the recompress process but the interface was not adhered sufficiently.

Figure 7 shows crack growth curves of the materials A and B at σ_a=500 MPa. In these figures, the abscissa is the number of stress cycles after crack initiation, N– N_i. On both materials, fatigue crack growth life, defined as N_f– N_i at the crack length of 2 mm, is found to be longer in the type-m specimen comparing with the type-e specimen. The arrows in these figures denote the crack coalescence or overlapping site and it was observed that fatigue cracks often coalesced or overlapped irrespective of the materials and the

(a) Material A (b) Material B
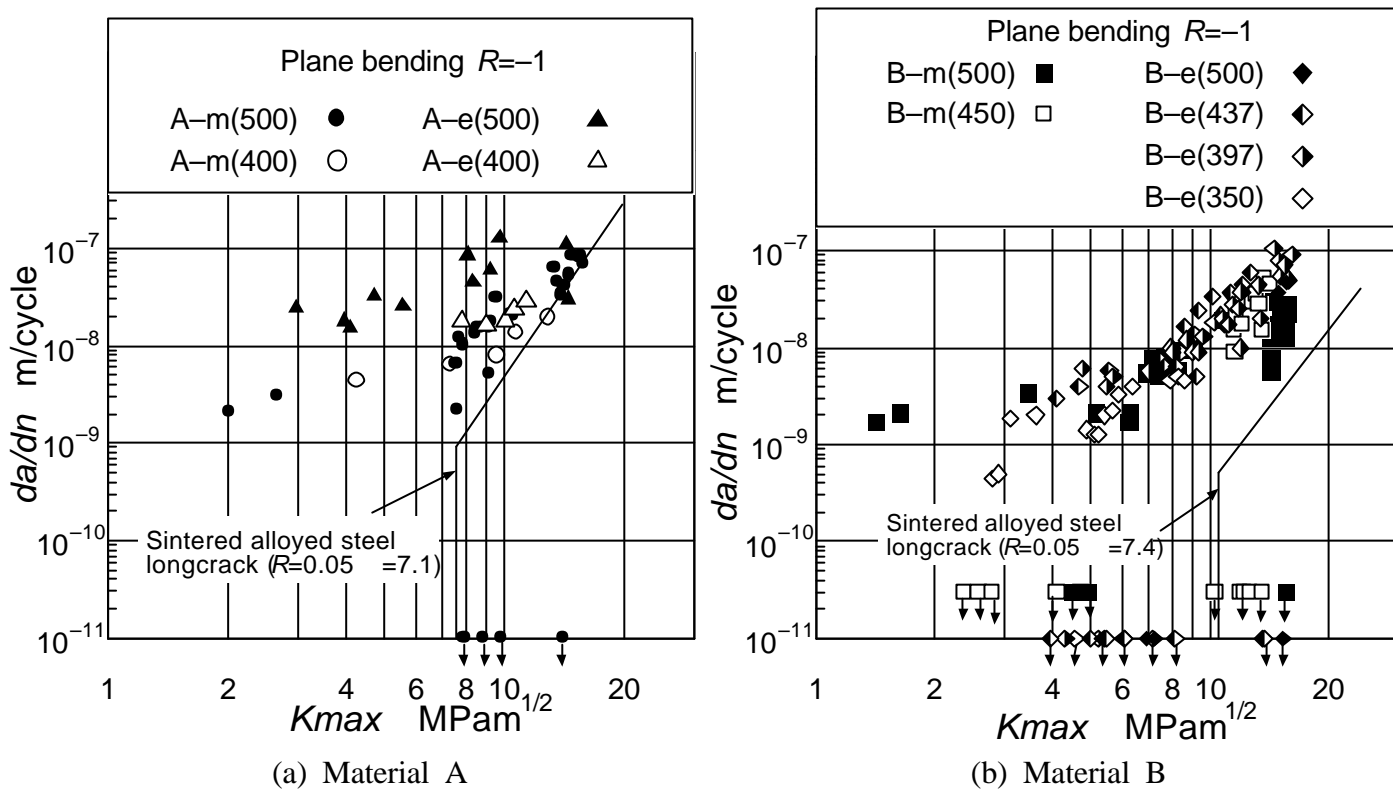
Figure 8 : da/dn-K_{max} relationships.
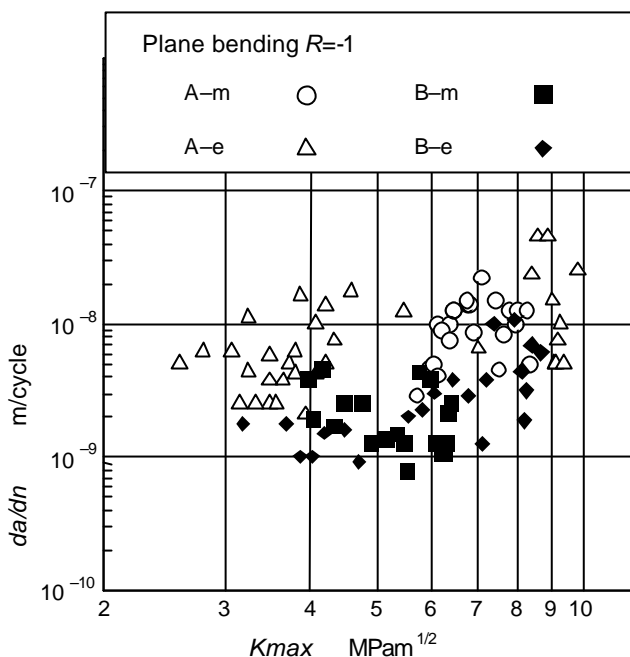
Figure 9 : da/dn – K_{max} relationship.

machining types. The crack growth increment caused by the crack coalescence or overlap in the type-m specimens is larger than that in the type-e specimens. The four cracks overlapped at point 3 in the A-e specimen and the five cracks coalesced at the point 2 in the B-e one. Such large number of coalesced cracks is thought to result in the short crack growth life in the type-e specimen. Comparing crack growth curves during crack extension from 0.5 to 1 mm, the slope of the type-m specimen is found to be gentle. It was thought that residual compressive stress in the worked layer induced by the milling process resulted in the relatively slow crack growth in the type-m specimen.

Figure 8 shows da/dn-K_{max} relationships of both materials. The stress intensity factor was calculated by the Newman-Raju[5] equation using the aspect ratio of the bounding rectangle that fully contained the area of a semi-circular crack or coalesced cracks. Data on crack growth acceleration caused by the crack coalescence were omitted in these figures. The solid lines in these figures indicate the da/dn-K_{max} relationships of long fatigue crack on Fe-4Ni-1.5Cu sintered alloy. Growth rates of small fatigue crack were found to be higher than that of long crack in the low K region irrespective of the materials, and also it could grow at the maximum stress intensity level even below the crack growth threshold. It was found that crack growth rates in the type-m specimens is slightly lower that that in the type-e ones irrespective of the materials. This low growth rates was thought to be resulted from the residual compressive stress in the worked layer. Figure 9 shows the comparison crack growth rates of the material A with these of the recompressed material B. Crack growth rate of the material B was found to be lower than that of the material A, indicating that the recompress process improved the fatigue crack growth resistance. The low growth rate on the material A was thought to be resulted from that the fatigue crack frequently coalesced with internal pores ahead of the fatigue crack.

CONCLUSIONS

The effects of porosity and worked layer on small fatigue crack initiation and growth behavior were investigated on Fe-0.5Ni-1Mo sintered steels and recompressed ones with high density. Reversed plane bending fatigue tests were carried out using an electro-magnetic type bending machine and small cracks were observed by means of plastic replica technique. The results obtained can be summarized as follows;

(1)In the materials without the worked layer (type-e specimen, shallow notch of which was machined by the electric discharge machine), there observed a large number of pores at the specimen surface and many fatigue cracks easily initiated at pores, resulting in the short fatigue crack initiation life. When the shallow notch was machined by milling machine, test specimen had worked layer and pore was hardly observed at the specimen surface (type-m specimen). In these specimens, fatigue crack initiated at the internal pore and crack initiation life was increased.

(2)There was no effect of the recompress process on the fatigue crack initiation behavior. It was considered that the fatigue crack easily initiated at the collapsed pores because the recompress process collapsed the pores but could not reweld the interfaces.

(3)In the type-e specimen, a large number of fatigue cracks initiated and frequently coalesced, resulting in the crack growth acceleration and the decrease of fatigue crack growth life.

(4)It was found that the recompressing process resulted in the increase of crack growth resistance since it reduced the porosity and decrease the frequency of crack coalescence.

REFERENCES
1 . Salak A. (1995). Ferrous Powder Metallurgy. Cambridge International Science Publishing.
2. Danninger H., Spoljaric D. and Weiss B. (1997). Int. J. Powder Metallurgy, 33, 43.
3. Drar H. and Bergmark A. (1997). Fatigue & Fract. Eng. Mat. & Strruct., 29, 1319.
4. Sudhakar K.V. (2000). Int. J. Fatigue 22, 729.
5. Newman, Jr. J.C. and Raju I.S. (1983). ASTM STP 791, 238.

SOFTENING BEHAVIOUR OF PLAIN CONCRETE BEAMS

A. P. Fantilli and P. Vallini

Department of Structural and Geotechnical Engineering, Politecnico di Torino
Corso Duca degli Abruzzi 24, 10129 Torino, Italy

ABSTRACT

In this paper, a one-dimensional discrete cohesive model is put forward to study the softening behaviour of plain concrete beams. In particular, a block of beam bounded by two cracks is analysed, namely the "open crack" (with variable crack width) and the "closed crack" (i. e.with virtual crack width). By means of this model, both the bearing capacity and the post-peak response of concrete beams can be evaluated, taking into account the effects produced on the softening branch by fictitious crack models and by fracture energy as well. A good agreement between numerical and experimental results is obtained, with a fracture energy value higher than the conventional ones.

KEYWORDS

Plain concrete, fictitious crack model, bending beams, fracture energy.

INTRODUCTION

In many papers plain concrete beams have been the object of direct experimental researches. Oladapo [1], for example, inquired into the effects produced by different concrete mixtures on the mechanical behaviour of bending beams with the same dimension. Moreover, the author [1] describes the two stages of the gradual process of cracking in these beams (Fig. 1) as follows:
- The "Critical Stage" develops when the concrete tensile stress exceeds the strength f_{ct} (which is obtained by means of direct tensile tests), in the portion of the beam where the bending moment M is greater than the cracking moment M_{cr}. In this portion, a diffuse micro-cracking is present (Fig. 1a).
- The "Failure Stage" starts when the bending moment reaches the maximum value M_u (Fig. 1b) (where $M_{cr} / M_u = 0.7 \div 0.9$). In this stage, a single wide crack usually appears.

Bosco et al. [2], have investigated on the so-called "size effect" of three point bending elements, by changing the beam dimensions for the same concrete. The bending moment M-deflection η curves (Fig.1b) show an increase in beam brittleness for the greater dimension of the beams. The softening branch of the "Failure Stage" can be measured, even when a snap-back is present, if the loading process is controlled by a monotonically increasing function of the time, like the crack mouth opening displacement (CMOD) [2]. For this reason, Giuriani and Rosati [3] built a testing machine able to set the maximum value of crack width w in a concrete block in bending. In the literature, many theoretical nonlinear approaches for plain concrete beams have been proposed. As is well-known, for quasi-brittle materials like concrete, the dimension of fracture process zone is not small with respect to the beam's dimension. Therefore, nonlinear fracture mechanics (NFLM) models are needed for concrete elements in bending [4,5].
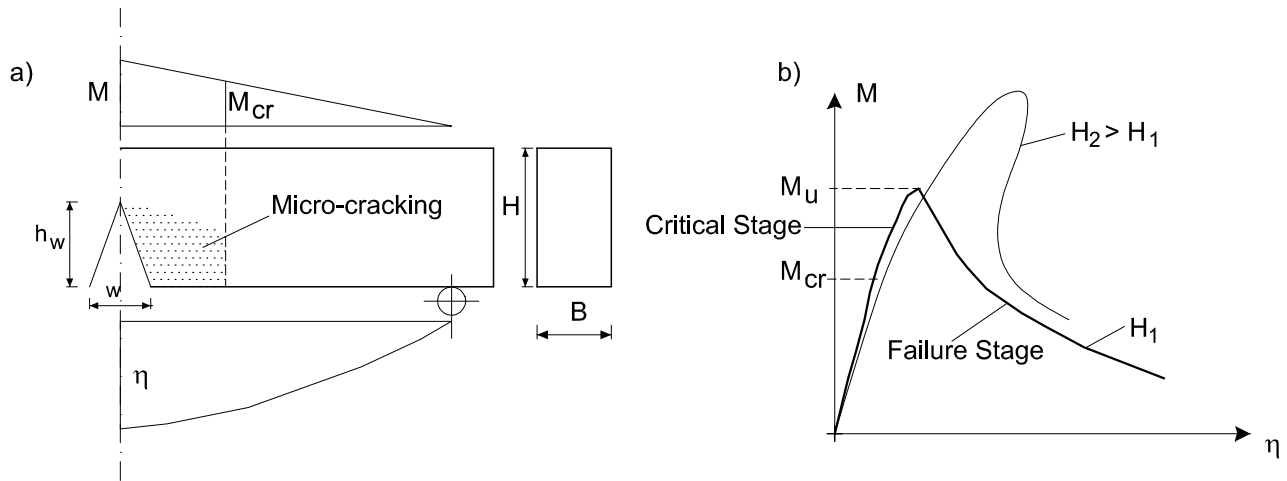
Figure 1: Plain concrete beam: a) three point bending test; b) possible M-η curves.

In particular, the Mode I cracking phenomenon can be reproduced by means of two nonlinear models: the fictitious crack model (or cohesive model) and the crack band model. With the fictitious crack model, introduced by Hillerborg et al. [6], the fracture process zone is represented through a crack line where the stress σ - crack width w relationship is applied. The simplest application of cohesive model for plain concrete beams, is made possible by means of the bidimensional Boundary Element Methods (BEM), i.e. the multidomain BEM [7] or dual BEM [8, 9]. In this case, all the body volume remains linear elastic and the nonlinearity is included in the crack line by the cohesive model. An alternative approach, is that of using bidimensional Finite Element Methods (FEM). With these methods, the cracking phenomenon is analysed in a "discrete" manner [6], changing the initial mesh (remeshing).

With the crack band model, the inelastic strains of the fracture process zone are smeared on a band of appropriate length, located around the crack. Several crack band models were developed to study the cracking phenomenon in concrete, not only for beams in bending. The so-called "smeared FEM", for example, are able to reproduce the mechanical behaviour of bidimensional structures, by considering concrete like a continuous body by means of suitable stresses-strains σ-ε law [4,5]. In other models, the authors exploited some simplifications to study plain concrete beams in a one-dimensional way, in particular they analysed a restricted portion of beam close to the main crack [10, 11]. It is also possible to reduce the observations to only cracked section [12], where the application of limit strain analysis can be useful to define the analytical formulation of the maximum bending moment M_u of the concrete beam [13].

PROPOSED MODEL

The bidimensional FEM approaches, discrete or smeared, are able to represent both stresses and strains also in the uncracked parts of a plain concrete beam far from the cracked section. Structural response of bending beams is usually calculated by a one-dimensional or sectional approach, thus the introduction of new one-dimensional models to study unreinforced concrete beams during the cracking phenomenon is justified. In the previous sectional [12, 13] or block [10, 11] models, hypothesis and simplifications were introduced about stress and strain distributions, so that is not possible to evaluate them in all the sections of the beam.

The proposed cohesive block model is able to define the structural response of cracked plain concrete beams, through the computation of stress and strain distributions in a wide portion of beam delimited by a crack. It can be considered an intermediate approach between the cohesive bidimensional FEM and the sectional models. The problem can be solved by means of a one-dimensional model, by introducing a suitable simplified strain profile for every cross-section of the beam. Cracking in plain concrete bending elements is characterized by one main crack [1, 2, 3], called "open crack", whose stress and strain profiles are depicted in Fig. 2a. The structural response of this section, with a plane crack, is evaluated with a trial and error procedure. In particular, for a given value of crack width w and depth h_w (Fig. 2a), the position of the neutral axis x can be computed by the static cross-sectional equilibrium condition. In this way, it is also possible to define the bending moment M, the slope of linear strain profile and the corresponding stresses.
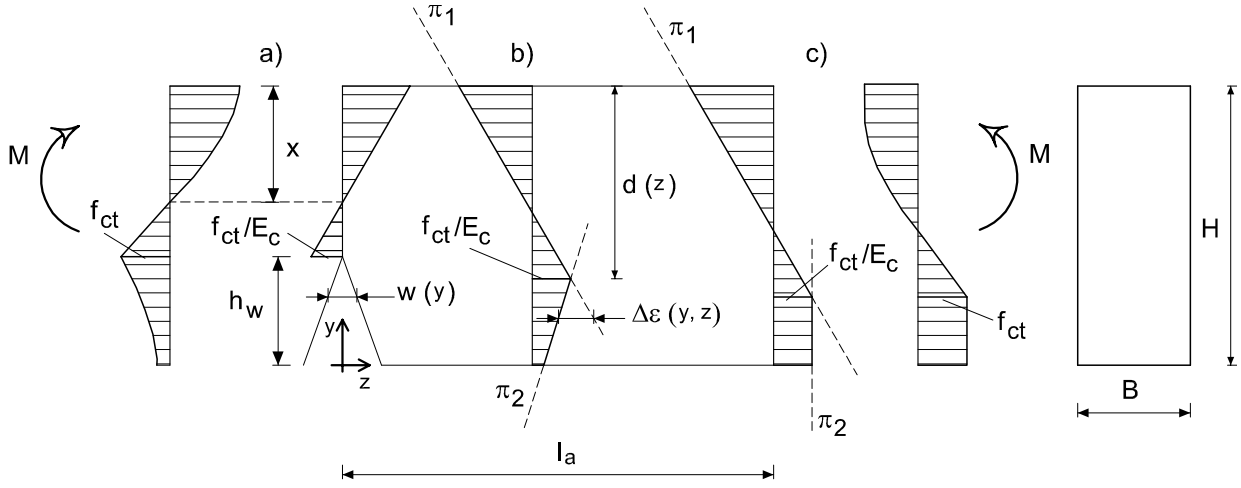
Figure 2: Observed concrete block: a) stresses and strains in the "open crack"; b) strain profile within l_a; c) strains and stresses in the "closed crack".

In the "Critical Stage", when then bending moment is higher than the cracking one M_{cr} [1], in the concrete block there is a diffuse micro-cracking, which can be reproduced, according to cohesive model, as "virtual" cracks. In other words, besides the main crack, there are many cracked sections where the stresses could be computed by means of "closed crack" model. As shown in Fig. 2c, the concrete stress is constant and equal to the tensile strength f_{ct} within the crack length h_2. Stress and strain in a closed crack section could be computed like in a continuous body, if the strain profile develops on two different planes π_1 and π_2 (Fig. 2c). The stress and strain analysis for a block delimited by the open cracked section and by the closed one (Fig. 2), allows to calculate the distance l_a between the two sections, which is an unknown of the problem. In a generic section within l_a, the strain profile lies on the planes π_1 and π_2 (Fig. 2b). In particular, both the slope of π_2 and the depth $d(z)$ of π_1 increase when shifting from the main crack (Fig. 2a) to the closed crack, where π_2 is vertical and $d(z)$ is maximum. At distance y from the bottom of the beam, the crack width $w(y)$ due to the strain difference $\Delta\varepsilon(y, z)$ measured on the two planes along l_a, can be computed through the following integration:

$$w(y) = \int_0^{l_a} \Delta\varepsilon(y, z)dz \qquad (1)$$

Based on this strain hypothesis, also supported by the experimental analysis [1, 3], it is possible to found an horizontal tangent in the function $d(z)$ near the tip of the main crack. In the case of constant bending moment M, $d(z)$ shows an horizontal tangent also near the tip of the virtual crack (Fig. 3a).

Broms [14] supposed that the maximum concrete tensile strain, in reinforced concrete elements in bending and tension, is localized inside a circle whose radius corresponds to the crack length and whose centre is on the reinforcement axis. Outside this circle, compressive or small tensile strains are present. By means of an analogy with this strain diffusion hypothesis, $d(z)$ could be considered as the zone where compressive or small
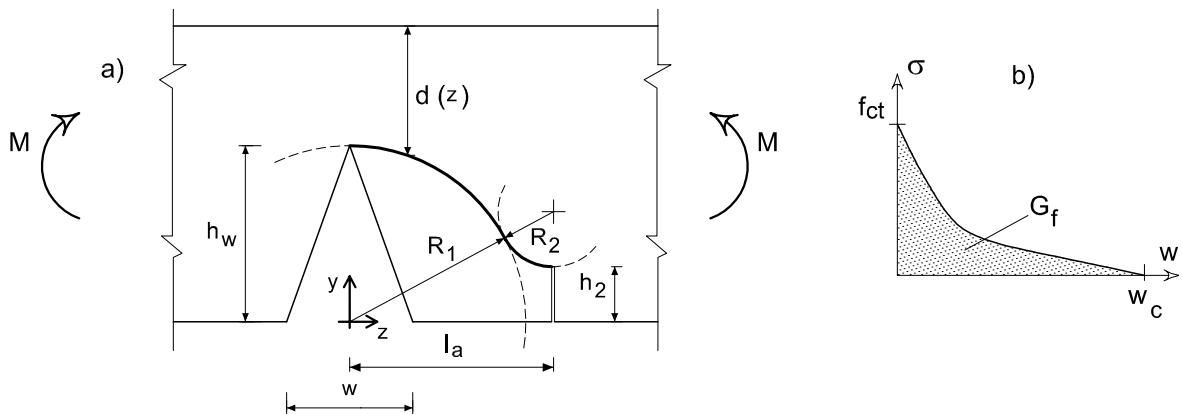
Figure 3: Observed concrete block: a) function $d(z)$ along the block; b) a cohesive model.

tensile strains are located, as shown in Fig. 3a by the thick line tangency at the tips of the open and closed cracks. Indeed, $d(z)$ is a function drawn on two tangency circles: the first circle has the centre on the bottom of the cracked section and its radius R_1 is the crack length h_w; the radius R_2 of the second circle is the length of the virtual crack h_2 and the centre of this circle is distant $R_2 + h_2$ from the bottom of closed crack section. In the "Failure Stage", when $M < M_{cr}$, the virtual crack vanishes ($h_2 = 0$ in Fig. 3a) and it possible to observe only the presence of the main crack, with one circle in the open crack section [14]. Moreover, the distance between the open crack section and the closed one can be computed through the following equation:

$$l_a = \sqrt{(h_2 + h_w)^2 + 4(h_2)^2} \qquad (2)$$

For the plain concrete beam of Fig. 1, whose constitutive laws for the uncracked concrete and the cohesive model (Fig. 3b) are known, the relationship M-η can now be obtained as the maximum width w of the open crack section increases, by means of the following trial and error procedure (Fig. 3a):

1. select a crack width w;
2. assume a value of crack length h_w;
3. compute, in the open crack section, the bending moment M;
4. compute, in the closed crack section, the crack length h_2;
5. compute l_a according to equation (2);
6. compute $\Delta\varepsilon(y, z)$ within l_a;
7. if the equation (1) is not verified, with a new trial value of h_w, go back to step 3.

For an imposed value of w in the main crack, this procedure yields the stresses and strains in a concrete block of length l_a, as in a bidimensional finite elements analysis. According to Bosco et al. [2], the loading process is controlled by w (a monotonically increase function), so that the possible positive slopes of the softening branch (in M - η curves), during the "Failure Stage", can be computed. Moreover, in this way, both the distance l_a between the cracks and the length h_w of the main crack increase monotonically, and in particular, at the end of "Failure Stage", they are both equal to the height H of the beam.

COMPARISON BETWEEN NUMERICAL AND EXPERIMENTAL RESULTS

Before testing the validity of the proposed model, it is necessary to define the two constitutive laws of the concrete. According to [4, 7, 12], a linear elastic stress strain relationship for the uncracked concrete is assumed (Fig. 4a). In this relationship, E_c represents the modulus of elasticity, f_c and f_{ct} are respectively the compressive and the tensile concrete strength. As is well-known, a cohesive crack model valid for all the concretes does not exist [4]. In fact, many σ-w curves were obtained for particular concrete with a limited number of experimental data. For the plain concrete beam in Fig. 1, the M-η response is strongly depending on the cohesive model adopted. As shown in [15], where a bilinear σ-w is used, the maximum bending moment M_u depends on the slope of the first part of the cohesive law, while the last part of σ-w influences the softening branch of the "Failure Stage". Moreover, if the fracture energy G_f, i. e. the area under the σ-w curve (Fig. 3b), were kept constant, both the "Critical Stage" and the "Failure Stage" of M-η should be different.
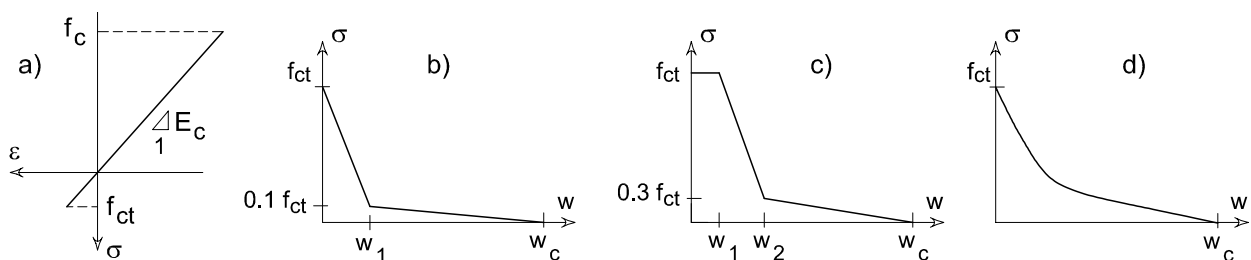
Figure 4: Constitutive laws: a) linear elastic law for uncracked concrete; b) cohesive bilinear model [16]; c) cohesive trilinear model [17]; d) cohesive exponential model [18].

Cohesive models adopted

In order to define the structural response of a plain concrete beam, in this paper the results obtained with three different fictitious models are compared. The bilinear model [16] (Fig. 4b), the trilinear model [17] (Fig. 4c) and the exponential model [18] (Fig. 4d) have been used. Usually, the practitioners do not know the σ-w relationship: they simply set the compressive strength f_c and the maximum aggregate size Φ_{max}. For these reasons, the adopted cohesive models, with the exception of the exponential model [18], depend on f_c and Φ_{max}.

Numerical analysis of the Giuriani's and Rosati's beam [3]

As a first approach, our numerical results and the experimental ones, obtained by Giuriani and Rosati [3], are compared. The Authors, concentrated in the cracked section of a concrete block (Fig. 5), where they imposed the maximum crack width w and measured both the crack depth h_w and the bending moment M. In particular, the crack growth were measured by means of geometric moiré. By introducing the cohesive laws reported in Fig. 4, the proposed model is able to evaluate, for the cracked section in Fig. 5, both the bending moment M - crack width w and the bending moment M -crack depth h_w curves. In Fig. 6, the numerical and experimental M-w and M-h_w diagrams are compared. In Fig. 6c, the proposed model calculated with the trilinear σ-w law,

H=250 mm
B=50 mm
L=500 mm
E_c=32300 N/mm^2
f_c=40.86 N/mm^2
f_{ct}=3.14 N/mm^2 (estimated in [10])
Φ_{max}=15 mm
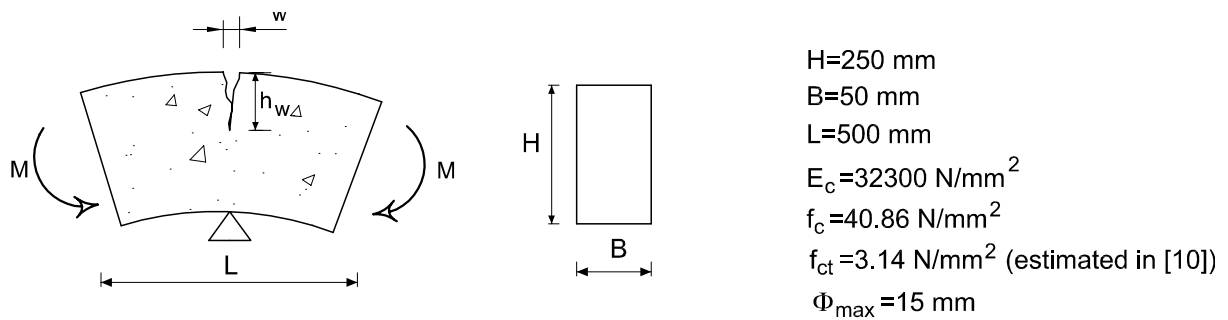
Figure 5: Giuriani's and Rosati's beam [3].
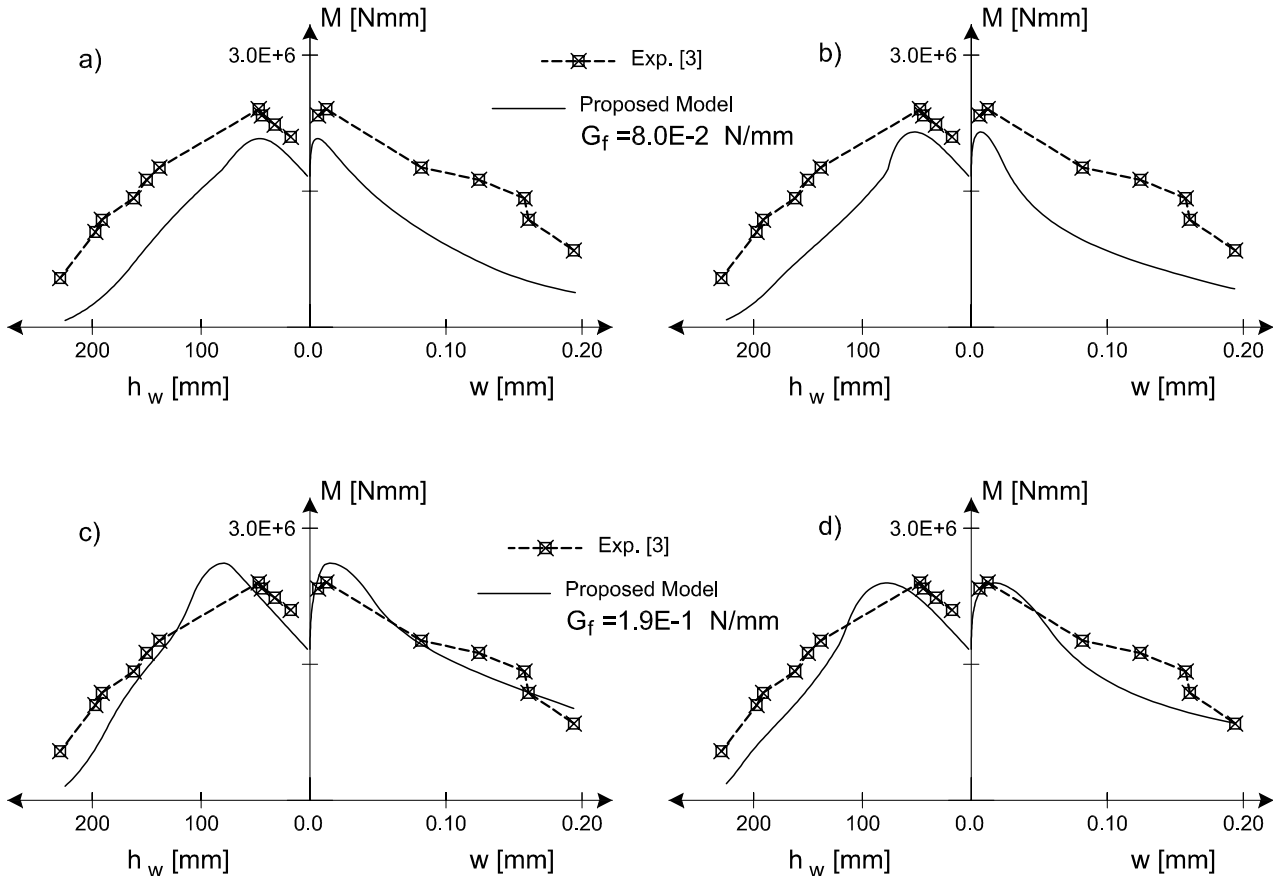
Figure 6: Comparison between experimental and numerical results: a) cohesive bilinear model [16] G_f= 8.0E-2 N/mm; b) cohesive exponential model [18] G_f= 8.0E-2 N/mm; c) cohesive trilinear model [17] G_f= 1.9E-1 N/mm; d) cohesive bilinear model [16] G_f= 1.9E-1 N/mm.

provides the best fitting of the experimental measurements. In this case, the fracture energy G_f = 1.9E-1 N/mm (which is function of f_c) is far greater than the value adopted for the bilinear and the exponential fictitious crack model (Fig. 6a and Fig. 6b, respectively), where G_f=8.0E-2 N/mm was estimated according to CEB Model Code [16]. As pointed out in [8] for the experimental results [2], if in the bidimensional BEM analysis G_f were higher than the conventional measured value, numerical results should be closer to the experimental ones. To confirm this observation, Fig. 6d shows a good agreement between the numerical and experimental results also for the bilinear model [16] with the higher G_f.

CONCLUSIONS

Due to limited number of comparisons with the experimental data, it is not possible, at the moment, to give general rules about plain concrete beams behaviour. Results obtained with the proposed model show a good agreement with the experimental ones [3], only when the fracture energy is higher than the conventional measured or computed values. In these cases, the proposed model represents an effective alternative to the classical bidimensional BEM and FEM analyses. Moreover, this model is able to define the better σ-*w* relationship to model the reinforced concrete beams, whose structural response depends both on the fracture mechanics of tensile concrete and on the bond between steel and concrete [19].

REFERENCES

1. Oladapo, I.O. (1964) *Magaz. Concr. Res.* 16, 103.
2. Bosco, C., Carpinteri, A. and Debernardi, P.G. (1990) *Eng. Fract. Mech.* 35, 665.
3. Giuriani, E. and Rosati, G. (1984) *Studi e Ricerche* 6, 151 (in Italian).
4. Bazant, Z.P. and Planas, J. (1998). *Fracture and Size Effect in Concrete and Other Quasibrittle Materials.* CRC Press, Boca Ranton.
5. Shah, S.P., Swartz, S.E. and Ouyang, C. (1995). *Fracture Mechanics of Concrete: Applications of Fracture Mechanics to Concrete, Rock and Other Quasibrittle Materials.* John Wiley & Sons, New York.
6. Hillerborg, A., Modeer, M. and Petersson, P.E. (1976), *Cem. Concr. Res.* 6, 773.
7. Maier, G., Cen, Z., Novati, G. and Tagliaferri, R. (1991). In: *Fracture Processes in Concrete, Rock and Ceramics*, pp. 561-570, van Mier, J.G.M., Rots, J.G. and Bakker, A. (Eds). E & FN Spon, London.
8. Aliabadi, M.H. and Saleh, A.L. (1999). In: *Computational Fracture Mechanics in Concrete Technology*, pp. 163-192, Carpinteri, A. and Aliabadi, M. (Eds). Wit Press, Boston.
9. Saleh, A.L. and Aliabadi, M.H. (1995) *Eng. Fract. Mech.* 51, 533.
10. Giuriani, E. and Rosati, G. (1987) *Studi e Ricerche* 9, 107.
11. Ulfkjaer, J.P., Krenk S. and Brinker, R. (1995) *ASCE Jour. Engng. Mech.* 121, 7.
12. Ananthan, H., Raghuprasad, B.K. and Sundara Raja Iyengar, K.T. (1990) *Eng. Fract. Mech.* 45, 195.
13. Aagren, P. and Harrison, N.L. (1986) *ACI Jour.* 83, 156.
14. Broms, B.B. (1965) *ACI Jour.* 62, 1237.
15. Alvaredo, A. M. and Torrent, R.J. (1987) *Mat. and Struct.* 20, 448.
16. Comité Euro-International du Beton (1993). *CEB-FIP Model Code 1990: Design Code.* Thomas Telford, London.
17. Liaw, B.M., Jeang, F.L., Du, J.J., Hawkins, N.M. and Kobayashi, A.S. (1990) *ASCE Jour. Engng. Mech.* 116, 429.
18. Hordijk, D.A. (1991). Doctoral Thesis, TU-Delft, Netherlands.
19. Fantilli, A.P., Ferretti, D., Iori, I. and Vallini P. (1998). In: *Minimum Reinforcement in Concrete members,* pp. 99-125, Carpinteri, A. (ed.). Elsevier, Amsterdam.

SOFTWARE METHODOLOGIES FOR MULTISCALE DESCRIPTIONS OF DEFECTS, DEFORMATION AND FRACTURE

C. R. Myers[1], T. Cretegny[2], N.P. Bailey[2], C.-S. Chen[1], A.J. Dolgert[2], L.O. Eastgate[2], E. Iesulauro[3], A. R. Ingraffea[3], M. Rauscher[2], and J.P. Sethna[2]

1 Cornell Theory Center, Cornell University, Ithaca, NY 14853 USA
2 Laboratory of Atomic and Solid State Physics, Cornell University, Ithaca, NY 14853 USA
3 School of Civil and Environmental Engineering, Cornell University, Ithaca, NY 14853 USA

ABSTRACT

We examine some of the software implications of multiscale modeling of material deformation and fracture. Research in this field is aided through the development of flexible software frameworks for managing disparate degrees-of-freedom, constructing complex models, and interrogating simulation data at various scales. We describe some of the highlights of our Digital Material system for multiscale materials modeling, and discuss its use in the study of intergranular fracture in polycrystals.

KEYWORDS

Multiscale modeling, fracture, software engineering, Digital Material, grain boundary decohesion, molecular dynamics

INTRODUCTION

Computational mechanics, in general, and computational fracture mechanics, in particular, are becoming increasingly multidisciplinary. This trend is driven to a large extent by a desire to model material structures at many length and time scales, in order to more faithfully capture processes of relevance to material deformation and failure. Modeling across scales, however, introduces a new set of challenges, such as the need to develop frameworks for composing software components and material descriptions, manage disparate computational degrees-of-freedom in a consistent fashion, and construct algorithms that can exploit multiscale representations.

In this paper, we highlight some of the software challenges posed by multiscale modeling of materials deformation and failure, and discuss some of the approaches we have taken to build useful computational problem-solving environments for the study of such problems. We will discuss an application example using some of these tools, namely the modeling of decohesion of grain boundaries in polycrystalline materials.

MULTISCALE MODELING OF MATERIAL DEFORMATION AND FAILURE

Multiscale modeling is in many ways a problem of optimization, balancing the desire for greater fidelity (gleaned from explicit inclusion of smaller-scale degrees-of-freedom) with the need for compact and efficient modeling forms (typically embodied in more coarse-grained descriptions). One is striving, in some sense, for the smallest possible set of modeling degrees-of-freedom that are capable of describing the phenomena of interest. Conventional single-scale models, such as descriptions of continuum fields evolving according to constitutive laws, are able to offer compact representations, but often at the expense of having ad hoc constitutive models characterized by a large and unsystematic set of adjustable parameters. One of the benefits of multiscale modeling is that the space of material behaviors being approximated by these ad hoc constitutive models can be factored into a geometric piece and a functional piece. Collections of smaller-scale structures, described in turn by their own constitutive laws (which one hopes are more fundamental and less ad hoc than the more coarse-grained constitutive laws), are allowed to organize themselves so as to produce an emergent constitutive description at larger scales. The recently developed quasicontinuum method [1], for example, can be thought of as an extension of the finite-element method for solving continuum models of material response, where atoms are introduced and allowed to organize under their own mutual self-interaction in order to provide better constitutive descriptions of materials containing lattice defects. In many situations, however, it is far preferable to perform multiscale modeling implicitly, by finding a reduced-order description of smaller-scale processes for inclusion at larger scales. One approach of ours has been to focus on the development of appropriate *functional forms* that are capable of capturing the smaller-scale behavior [2]. In many cases, these functional forms have nonanalytic behavior (e.g., near bifurcations, or near configurations with high symmetry) that will dictate what small-scale information is most crucial for accurate modeling. It is important to study coarse-grained theories to determine what information from smaller scales is needed, and to determine how to construct dialogues across scales, rather than simply throwing information "over the wall" from small scales for use elsewhere.

Modeling of the behavior of materials across scales, however, differs from standard multiscale techniques in that the relevant material degrees-of-freedom vary widely from scale to scale. (Conventional numerical methods designed to address problems with structure on many scales benefit from the self-similarity of those methods across scales. Techniques such as multigrid [3] and multiresolution wavelet analyses [4] introduce bases or other discrete representations of continuum fields which represent equivalent types of information at each scale.) Fracture mechanics, for example, has been studied computationally at many scales, involving a whole menagerie of material structures, including electrons, atoms, vacancies, dislocations, voids, dislocation structures, grains, grain boundaries, and various continuum fields (see Figure 1).

(a)   **(b)**   **(c)**
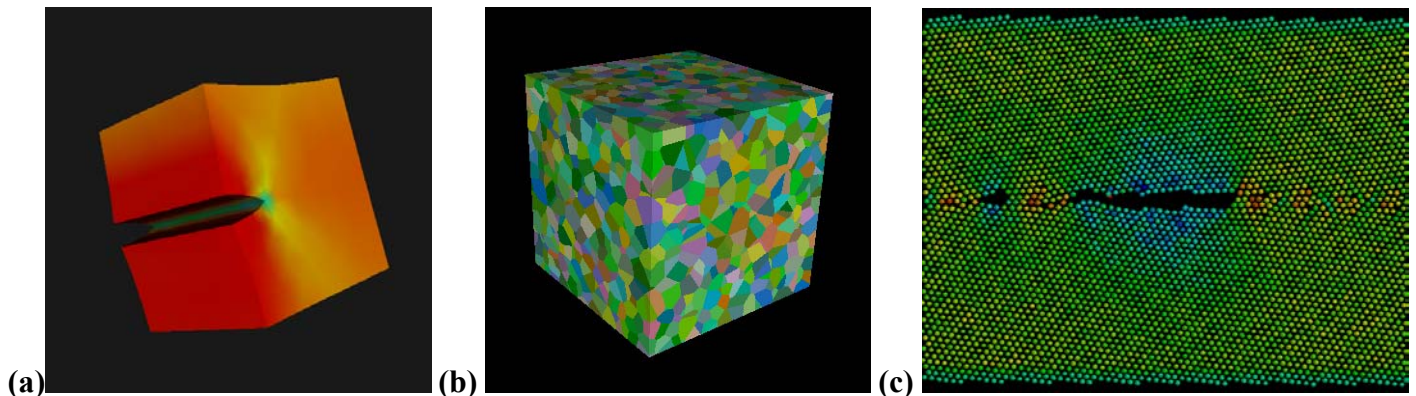
Figure 1. Models of materials at various scales. (a) Continuum fields at the macroscale; (b) Polycrystalline grain assemblies at the mesoscale; (c) Atoms near a grain boundary at the nanoscale.

Because of such diversity and heterogeneity, management of these degrees-of-freedom is significantly more complex than in methods such as multigrid. Furthermore, the fundamental algorithms required to efficiently

pass information across scales are not well-understood. Therefore, it is imperative that one construct software environments that provide flexible and expressive mechanisms for composing material descriptions and numerical kernels in order to experiment with different classes of models, algorithms, descriptions, etc.

This problem of *component composition* therefore becomes paramount. In order to explore a variety of material structures in a variety of different contexts, it is important to develop appropriate computational abstractions so that components may be reused. We would like to be able to synthesize, for example, the relevant pieces of code for molecular dynamics (MD) modeling with those for finite-element modeling in order to implement the quasicontinuum (QC) method, without having to maintain two separate bases of code for MD and QC. In addition, we would like to be able to compose high-level geometric descriptions (say, parameterizing a polycrystalline collection of grains with different lattice orientations) with underlying numerical models in order to build complex applications out of constituent pieces.

SOFTWARE ENGINEERING FOR MULTISCALE MODELING: DIGITAL MATERIAL

We have been addressing some of these issues through the development of *Digital Material,* an amalgam of software frameworks designed to support multiscale investigations of material structure and response [5]. This effort has many facets. Considerable activity has gone into developing a framework for atomistic simulations (e.g., MD, QC, etc.), which we will describe in more detail below. One application of the atomic-scale modeling framework is to provide quantitative input to mesoscale finite-element models of grain boundary fracture in polycrystals [6]. A different set of problems revolves around the use of phase-field models to study problems of interfacial evolution, including the formation and propagation of cracks [7]. Yet another area of investigation centers around the characterization of texture (orientation and misorientation distribution functions) in polycrystals [8], with one goal of relating texture to microcrack initiation and growth. Finally, we continue to work to build software bridges between these tools and more conventional finite-element software systems for investigating crack growth in continuum models [9].

The Digital Material system is built upon a set of broad software design philosophies. First, we have sought to develop abstractions that separate material structures from algorithms or numerical models that act on those structures. This is important because a central feature of multiscale modeling is that a given material structure can play different roles in different contexts, depending on how it fits into a larger material model. Second, in order to support the sort of flexible and expressive software composition described above, we make use of extensions to object-oriented design techniques such as *design patterns* [10] to encapsulate aspects of our programs that need to change. Design patterns deal with the collaboration between sets of computational objects. In our system, design patterns are used, for example, to enforce the separation between material structures and the

```
from MD3D import *
from BiCrystalInitializer import *

potential       = EMTPotential('Cu')
latticeConstant = potential.GetLengthScale() * sqrt(2)
lattice         = FCCLattice(latticeConstant)
atoms           = PrimitiveListOfAtoms()
cutoff          = potential.GetCutoffDistance()
neighborLocator = CellNeighborList(cutoff, .05*cutoff)

atoms.SetNeighborLocator(neighborLocator)
atoms.SetMass(63.54)

pbc = SimplePeriodicBoundaryConditions()
atoms.SetBoundaryConditions(pbc)

initializer = SymmetricalTiltGBInitializer(lattice,
            [lengthX, gbLength, minWidthZ],
            interfacePlane = [2, 2, 1],
            normalPlane = [1, -1, 0], bc)
initializer.Create(atoms)
print 'The number of atoms is :', atoms.GetNumber()
```

Figure 2. Sample Python script showing the initialization of some of the components used in an atomistic simulation of grain boundary decohesion.

algorithmic tools that act to modify or interrogate those structures. While some of the standard design patterns (e.g., observers) are appropriate for large-scale scientific computing, other patterns need to be developed in recognition of the constraints imposed by numerical modeling. In particular, the need for high computational performance has led us to phrase many of our basic abstractions in terms of aggregates of material objects (e.g., collections of atoms), so that those aggregates can be acted on efficiently without incurring a large computational overhead. Finally, we recognize the value of having high-level, interpreted control of our simulations, in order to support rapid prototyping, component composition, and interactive interrogation of simulation data. To achieve this, we use Python [11], an interpreted, object-oriented programming language, to drive many of our computational kernels and to "glue" together sets of computational objects. SWIG [12] is another system that assists in this process: SWIG generates the necessary glue/wrapper code for Python to talk to underlying C++ objects and functions, based on C++ interface declarations (e.g., class definitions and function prototypes). An example Python script for setting up an atomistic simulation of grain boundary fracture is shown in Figure 2. From within Python, users are able to manipulate references to compiled C++ objects as if they were native Python objects.

APPLICATION EXAMPLE: GRAIN-BOUNDARY FRACTURE

As mentioned, one of our goals is to provide quantitative input to mesoscale finite-element models of grain boundary fracture in polycrystals [6]. At the mesoscopic scale, the polycrystal is modeled via finite elements where the geometrical and physical properties of the grains are individually taken into account. At that scale, grain boundaries are modeled with interface elements, whose behavior is governed by a *cohesive zone model* (CZM), which relates the traction on the interface to its opening. We are conducting atomistic simulations of grain boundary decohesion, in part to provide appropriate CZMs for the mesoscale modeling. This work aims to develop not only cohesive models for a single grain boundary, but functional forms describing entire families of grain boundaries as parameterized by the orientations of the adjacent grains.

The main quantities we are interested in are the energy release rate, the peak stress and the range of the cohesive zone model. The energy release rate is the integral of the traction-separation curve, and represents the amount of energy per unit length that is dissipated in the crystal while the crack tip propagates. For a grain boundary in 3 dimensions, the CZM parameters will be functions of 5 independent degrees of freedom (DOFs): 3x2 rotational DOFs describing the orientation of the two adjacent grains, minus 1 DOF associated with invariance due to rotation of both grains about the normal to the interface. (We may choose to add other parameters, such as temperature, which play a role in the nature of the decohesion). Often one considers only 3 parameters, describing the interface misorientation. In doing so one assumes that the orientation of the interface does not play a significant role. This is a great simplification, but is hard to justify. For example, the limit of zero misorientation corresponds to the single crystal, for which lattice effects make crack propagation properties very anisotropic. On the other hand, special grain boundaries with reduced numbers of DOFs, such as symmetrical tilt grain boundaries (STGBs), can be usefully studied.

We have performed some preliminary simulations of STGBs, such as that depicted in Figure 3(a). These boundaries allow the use of periodic boundary conditions in the plane of the interface (typically around 10 atomic layers thick). In the orthogonal direction, we enforce prescribed displacement boundary conditions through the imposition of constraints on the outer two layers of atoms at either boundary. (Fixed displacement conditions on the outer layer results in a pinning of emitted dislocations at the outer boundary. Alternatively, constraining the center-of-mass motion of the outer layers allows such dislocations to exit the system. Switching between different types of constraints is straightforward in our system since constraints are specified in separate objects that are attached to the group of atoms being simulated.) We have performed dynamical simulations with a Verlet algorithm that periodically rescales the velocities of the atoms such that a fixed temperature can be prescribed.

We want to relate the interfacial opening to the traction in the surrounding bulk. Defining the opening of the grain boundary is delicate because from the atomistic point of view, there is no distinction between those atoms in the bulk and those on the grain boundary. We assume that the stress on the external boundaries of the grains is uniform, which requires a grain size large compared to the emergent inhomogeneities in the grain boundary. We also assume that the displacement of the atoms far from the interface can be written as $\vec{u_n} = (\mathbf{1} + \boldsymbol{\varepsilon}) \cdot \vec{u_{n,0}} + \vec{\delta}$, where n is the index of the atom with position $\vec{u_{n,0}}$ in the unstrained grain boundary, $\boldsymbol{\varepsilon}$ is the strain tensor, and $\vec{\delta}$ is defined as the grain boundary opening. (More precisely, we can sum up the contribution to $\vec{\delta}$ from each grain). We must check the validity of the decomposition on a case-by-case basis. The actual determination of $\vec{\delta}$ and $\boldsymbol{\varepsilon}$ is done by linear regression. The relevant points should be located as far as possible from the interface but not too close to the external constrained surface. We expect some inhomogeneities in the directions orthogonal to the GB, so we compute an average of $\vec{\delta}$ over the entire simulation box. A typical traction-separation curve for our decohesion simulations is shown in Figure 3(b).

(a)   (b)
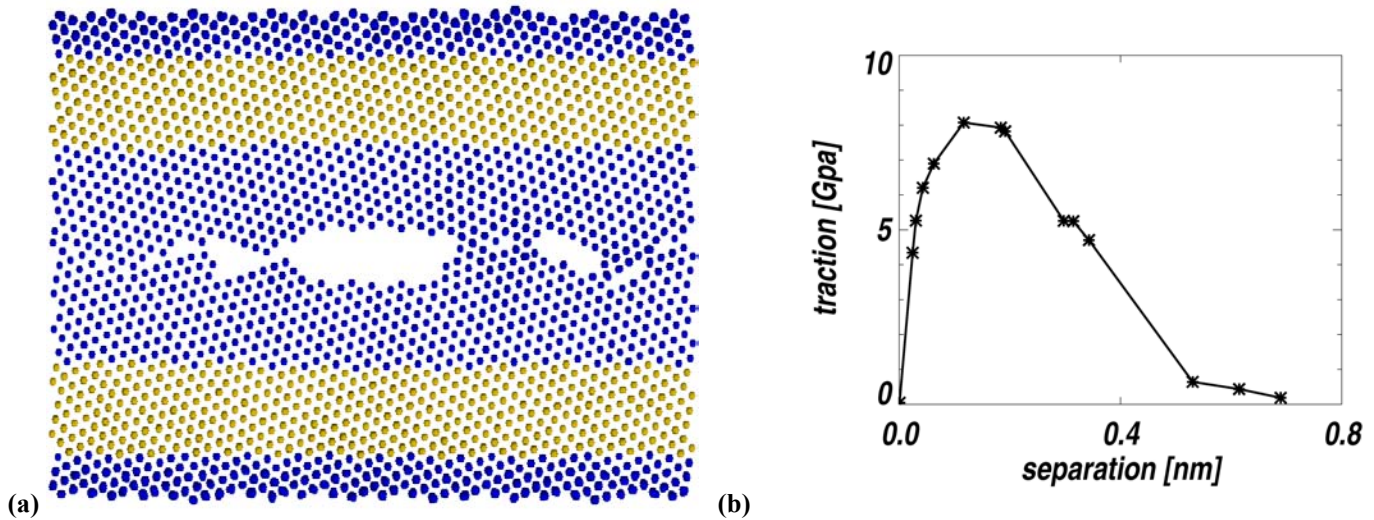
Figure 3. Decohesion of a [441] symmetric tilt grain boundary (i.e., the plane of the boundary is a [441] plane for each grain). (a) Snapshot from an MD simulation (highlighting those atoms used in the linear regression to determine the traction-separation relation). (b) Traction-separation curve derived from MD simulation.

A lingering difficulty is that the CZMs they provide are not, in and of themselves, so useful for the mesoscale finite element models. Typically the energy release rate and the range of the cohesive zone model are too small and the peak stress is too high. We are currently exploring reasons for these discrepancies. For example, the size of the atomistic system is very small compared to the typical size of the mesoscale interface elements: in an MD box the GB length is about 10 nm, while the width and thickness of the grains is of the order of 3 nm. With these dimensions the allowed ductility is quite small: the maximal opening will typically be on the order of a nanometer. One of our goals is to understand how the size of the damage zone scales with the dimensions of the atomistic simulation. Additionally, the properties of polycrystals crystals are often dominated by defects. Real materials will be substantially more heterogeneous than our simulation samples, and the large peak stress we measure in MD might naturally be explained by the lack of inelastic behavior driven by defects in the sample (e.g., acting as sites for the nucleation of dislocations or microvoids).

FUTURE DIRECTIONS

There are several directions in which this work ought to be extended. One important goal revolves around the notion of *adaptivity*. Our current system is built to allow researchers to experiment with different sorts of multiscale representations and algorithms, so that more formal and general multiscale methods can be identified. Our system encourages the development of heuristic approaches, which one would eventually like

to automate, so that the system itself could adaptively select the appropriate level of resolution to address a certain problem. Adaptivity needs to be broadly planned for at multiple levels: at the *application* level (where one might switch between models being solved based on the nature of the solution), at the *algorithm* level (where one might switch between different methods used to solve the problem at hand), and at the *system* level (where one might need to balance computational loads in response to changing resource requirements, or migrate to different platforms in response to changing resource availability).

Even with advanced software engineering techniques, the barriers to composing complex and adaptive applications are still substantial, and we must consider what other sorts of software generation technologies are available to assist in that construction process. One such framework that we are beginning to explore is *Loci* [13], a system for synthesizing the control flow of large and complex applications by deducing that flow from dependency information among the computational components being assembled. While this technology is still under development and being extended to handle larger classes of numerical models, there is promise that a system such as Loci might automate the construction of complex, distributed, multiscale applications from high-level problem specifications.

ACKNOWLEDGEMENTS

REFERENCES

1. Shenoy, V.B. Miller, R. Tadmor, E.B., Rodney, D., Phillips, R., and Ortiz, M. (1999). *Journal of Mech. Phys. Solids*. 47, 611.
2. Bailey, N.P., Sethna, J.P., and Myers, C.R. (2000). *Mat. Res. Soc. Symp. Proc.* 578, 249.
3. Brandt, A. (1977). *Mathematics of Computation* 31, 333.
4. Arias, T.A. (1999). *Reviews of Modern Physics* 71, 267.
5. Digital Material, http://www.tc.cornell.edu/Research/Multiscale/DigitalMaterial
6. Iesulauro, E., Dodhia, K., Cretegny, T., Chen, C.-S., Myers, C.R., and Ingraffea, A.R. (2001). "Continuum-atomistic modeling for crack initiation and propagation in polycrystals", to appear in Proceedings of the 10th International Conference on Fracture.
7. Eastgate, L.O., Sethna, J.P., Rauscher, M., Myers, C.R. and Chen, C.-S. (2001). "Modeling Crack Propagation: A Phase-Field Approach", to appear in Proceedings of the 10th International Conference on Fracture.
8. Myers, C.R., Loge, R.E., Arwade, S.R., Chen, C.-S., Miller, M.P., and Dawson, P.R., in preparation.
9. Carter, B., Chen, C.-S., Chew, L.P., Chrisochoides, N., Gao, G.R., Heber, G., Ingraffea, A.R, Krause, R., Myers, C.R., Nave, D., Pingali, K., Stodghill, P., Vavasis, S., and Wawrzynek, P.A., (2000). In: *Lecture Notes in Computer Science*, pp. 443-449, Vol. 1800, J. Rolim (Ed.), Springer-Verlag, Heidelberg.
10. Gamma, E., Helm, R., Johnson, R., and Vlissides, J. (1995). *Design Patterns: Elements of Reusable Object-Oriented Software*. Addison-Wesley, Reading, MA.
11. Python, http://www.python.org
12. SWIG, http://www.swig.org
13. Luke, E. (1999). In: *Proceedings of ISCOPE'99*, pp. 142-153, Matsuoka, S., Oldehoeft, R.R., Tholburn, M. (Eds.), Springer-Verlag, Heidelberg.

SOME ASPECTS OF FATIGUE CRACK PROPAGATION AFTER OVERLOADING CYCLES

M. S. Ramos [1], M. V. Pereira [2], F. A. Darwish [2] and S. H. Motta [3]

[1] Petrobrás / SEGEN, Rio de Janeiro, RJ, Brazil
[2] Department of Materials Science and Metallurgy / PUC-Rio, Rio de Janeiro, RJ, Brazil
[3] Companhia Brasileira de Amarras / BRASILAMARRAS, Niterói, RJ, Brazil

ABSTRACT

This research was carried out to determine the influence of overload cycles on the fatigue crack growth resistance of a structural steel. Single tensile overload cycles were applied to evaluate the influence of the overloading ratio on the fatigue crack retardation and residual stresses were measured in the region near crack tip. The results indicated that the extended fatigue life increases with increasing the magnitude of overloading and in the presence of higher compressive residual stress fields. The effect of two equal and consecutive overloads, with the second one applied at different intervals of crack propagation from the first, was also considered. The residual life after overloading was found to increase after some crack propagation between the two overloads. Larger intervals of crack propagation lead to higher fatigue resistance.

KEYWORDS

Residual life, fatigue resistance, overloading, residual stresses, structural steel.

INTRODUCTION

Fatigue crack propagation prediction is considered essential for structural integrity assessment based on damage-tolerance considerations. The determination of the resistance of a mechanical or structural component to fatigue crack propagation and calculation of defect tolerance are two aspects intimately related to the dependence of crack growth rate on the variation of the stress intensity factor. Frequently, complex loading conditions exist with different amounts of static and dynamic loads or mixed loading modes, depending on the stress distribution near the crack. However, load interactions complicate life prediction and structural components when in service under cyclic loading may be subjected to either variable amplitude loading or occasional overloading cycles. It is well known that overloading cycles can cause some beneficial effects on the fatigue resistance and lead to crack retardation [1]. Although much effort has been given to the overloading effect since 1961, when presented by Schijve and co-authors [2], the phenomenon is still not fully understood. Plasticity induced closure [3-6], "micro-roughness" model [7-8], crack blunting [9], strain hardening at the crack tip [10,11] and residual compressive stress fields ahead of the crack tip [1,12-13] are often cited as the mechanism responsible for crack growth retardation.

EXPERIMENTAL

The work was carried out on a low carbon structural steel (0.26 C, 1.75 Mn, 0.20 Cr and 0.35 Ni) with offshore applications. Concerning the mechanical properties, the material presented a yield and ultimate tensile strength of 600 and 690 MPa, respectively. The typical microstructure consisted of tempered martensite. Compact tension specimens were machined in the L-T orientation, according to the ASTM E647-99 recommendation [14]. The specimen width (W) and specimen thickness (B) were adopted equivalent to 32mm and 8mm, respectively, and a starter notch was machined to a depth of 7.0mm. After machining, the surfaces of the specimens were polished and fine lines were drawn parallel to the specimen axis in order to facilitate monitoring the crack propagation. The specimens were stress relieved at 600°C for 2h in a vacuum furnace to remove any residual machining stresses. Finally, the specimens were precracked up to a crack length of 2.5 mm, i.e. to a crack-length to specimen width ratio, a/W, equal to 0.30.

Fatigue crack propagation study was carried out to characterize the typical da/dN versus ΔK curve of the material under constant amplitude as well as to determine the overloading effect on the material's fatigue resistance. The tests were performed at room temperature making use of a servo-hydraulic machine, which operated at a frequency of 20 Hz. All specimens were tested in a tension-tension mode I loading, with a load ratio R (R = K_{min} / K_{max}) equivalent to 0.3. The crack length was monitored using a travelling microscope.

Overloading cycles were applied manually under load control by increasing the load to the designated overload value, decreasing to the minimum value of 3kN and returning to loading scheme prior to overloading. Regarding the first overload series, the specimens were subjected to single overloading cycles applied at a/W = 0.34. The overload ratio (R_{OL}) was defined as R_{OL} = K_{OL} / K_{max} where K_{OL} and K_{max} represent the overload stress intensity factor and the maximum value of the stress intensity factor prior to overloading, respectively. Two different values of R_{OL} equal to 2 and 3 were selected. During the second overload series, some specimens were subjected to two consecutive overloads, with the second overloading applied immediately after the first one or at different intervals of crack propagation. The overload ratio was selected equal to 2. Table 1 summarizes the test parameters for single and consecutive peak overloads.

Transverse residual stresses, acting in a direction perpendicular to the crack plane, have been measured near crack tip region by means of X-ray diffraction techniques, according to the multiple exposure $\sin^2\psi$-method [15].

TABLE 1
TEST PARAMETERS FOR OVERLOADING CYCLES

R_{OL}	K_{min} (MPa.m$^{1/2}$)	K_{max} (MPa.m$^{1/2}$)	K_{OL} (MPa.m$^{1/2}$)
2	10.5	31.5	63.0
3	10.5	31.5	94.5

RESULTS AND DISCUSSION

The fatigue life of the material under constant amplitude (N_f) concerning the first overloading series was determined as 91,350 cycles. This value was adopted to calculate normalized extended life in overload tests. The influence of single overloading cycles on the material's fatigue resistance is given in Table 2 where R_{OL} and K_{OL} are related to the overload monotonic plastic zone ($2r_{OL}^m$), overload cyclic plastic zone ($2r_{OL}^c$), delay cycles number (N_d) and delay cycles ratio (D_r). The values of $2r_{OL}^m$, $2r_{OL}^c$ and D_r were calculated using equations (1), (2) and (3) respectively.

$$2r_{OL}{}^m = \alpha \ (\ K_{OL} / \sigma_y \ )^2 \qquad\qquad (1)$$

$$2r_{OL}{}^c = \alpha \ (\ (\ K_{OL} - K_{min} \ ) / 2\sigma_y \ )^2 \qquad\qquad (2)$$

$$D_r = N_d / N_f \qquad\qquad (3)$$

where α and σ_y represent the Irwin's coefficient ($1/\pi$) and the yield strength, respectively.

TABLE 2
OVERLOAD PARAMETERS AND CRACK GROWTH RETARDATION DUE TO SINGLE OVERLOADING

R_{OL}	K_{OL} (MPa.m$^{\frac{1}{2}}$)	$2r_{OL}{}^m$ (mm)	$2r_{OL}{}^c$ (mm)	N_d	D_r
2	63.0	3.51	0.62	15,030	0.16
3	94.5	7.90	1.58	259,220	2.84

It is well known that single or multiple peaks of tensile overloading decreases the fatigue crack growth rate and different theories have been proposed to explain such retardation. The oldest one was postulated by Schijve [16], attributing the crack growth retardation to the generation of compressive residual stresses in the crack tip region. One can observe in Figure 1 the presence of compressive residual stresses in that region for both overloading ratios. As mentioned earlier, the residual stresses were measured by means of X-ray diffraction technique and therefore the stress distribution shown in Figure 1 refers to points on the surface of the specimen. At points removed from the surface, the residual stress levels are expected to be higher, consistent with the fact that the strain gradient ahead of the crack tip in the central region of the specimen (plane strain) is higher than that developed under essentially plane stress conditions on the specimen surface. This is borne out by the observation that residual stress levels calculated using a J integral approach were found to be consistently higher than those measured on the specimen surface [17]. After applying overloading cycles, the crack propagation was retarded in both conditions. However, for the higher overloading ratio, larger area with higher compressive stress levels is induced. For this reason, the overloading of 3 gives a better lifetime benefit concerning crack retardation when compared with that obtained with a ratio of 2.

Another important evidence of overload effect is shown in Figure 1, where maximum compressive residual stresses are found at the crack tip and changing over to tensile stresses at points removed from the tip. In both overloading conditions presented, the stress fields have their maximum values shifted in front of the crack tip and compressive residual stresses on the crack flanks are completely reduced.

One explanation for the influence of the overloading ratio on residual stress fields is that increasing R_{OL} causes an enhancement in K_{OL} and, consequently, an increase in the overload monotonic plastic zone size. In the post-overloading condition, the crack grows under the influence of a large compressive residual stress field created by the overload plastic zone. For this reason, the fatigue crack growth rate is significantly low during the overload affected crack growth.

In addition to the overload monotonic plastic zone, overload cyclic plastic zone is considered to be of significant importance. Matsuoka and Tanaka [18] demonstrated that the size of the compressive residual stress field at the crack tip is about 2.5 times the overload cyclic plastic zone and, therefore, postulated that the crack closure effect is most pronounced in this region. Considering the values of $2r_{OL}{}^c$ given in Table 2 and taking into account the correlation proposed by Matsuoka and Tanaka, one can calculate the size of the compressive residual stress fields presented in Figure 1. It should be about 1.6 and 4.0 mm for overloading ratios of 2 and 3, respectively. The experimental results seem to be in a good agreement with these calculated values.
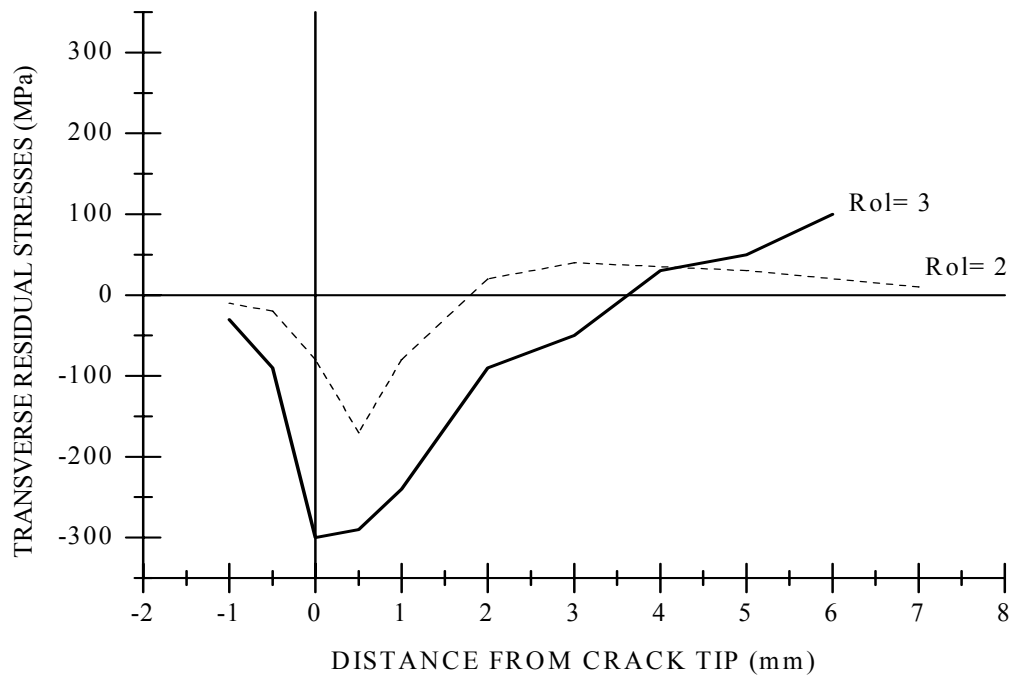
Figure 1: Residual stress distribution on the specimens' surfaces after single overload cycles.

The increase in fatigue life of the material due to consecutive overloads is presented in Figure 2. This figure reveals that the improvement of the delay cycles number is related to the interval that separates the two consecutive overloads. The larger the interval of crack propagation between the two consecutive overloads, the lower the fatigue crack growth rate, i.e. the higher the residual life of the material. Table 3 reinforces the affirmation that the second overloading affected the fatigue resistance of the material significantly. In this table d means the intervals of crack propagation between the consecutive overload cycles, while N_{d2} and D_{r2} represent the delay cycles number and delay cycles ratio, respectively. The fatigue life of the material under constant amplitude (N_f) concerning the second overloading series was determined as 61,950 cycles.

If one compares the delay cycles ratios related to R_{OL} (equal to 2 in Table 2) with those presented in Table 3, it is clearly observed that the second overloading cycle applied after crack propagation has improved the fatigue life of the material. The second overloading cycle increases the crack growth retardation brought about by the first overloading as a result of a significant influence on the rate of the fatigue crack propagation. Simões obtained similar results with an aluminium alloy for the aeronautic industry [19-20].

Regarding the effects of a second overloading applied after some crack growth, it is believed that the role played by such an overloading is largely influenced by the amount of crack growth as compared to the monotonic plastic zone size created by the first overloading [21-22]. According to this assumption, the higher efficiency of the second overloading associated with a larger crack growth interval may be attributed to a more effective interaction between the monotonic plastic zones resulting from the consecutive overloads. In this respect, one may mention that a larger amount of crack growth before applying the second overload means a larger extension of the compressive residual stress field under which the crack will propagate. Further, a higher K level and hence a larger monotonic plastic zone size are associated with the presence of a longer crack at the moment of applying the second overload. A more effective interaction between the monotonic plastic zones may also signify higher compressive residual stress levels, more influential crack closure and more effective strain hardening of the material ahead of the crack tip. No attempt, though, was made in this work to measure hardness levels or to map compressive residual stresses ahead of the crack tip in terms of the interval of crack propagation. However, in a previous work [21], it was observed that a larger compressive residual stress field was created by the second overloading cycle applied after some crack propagation from the first one.
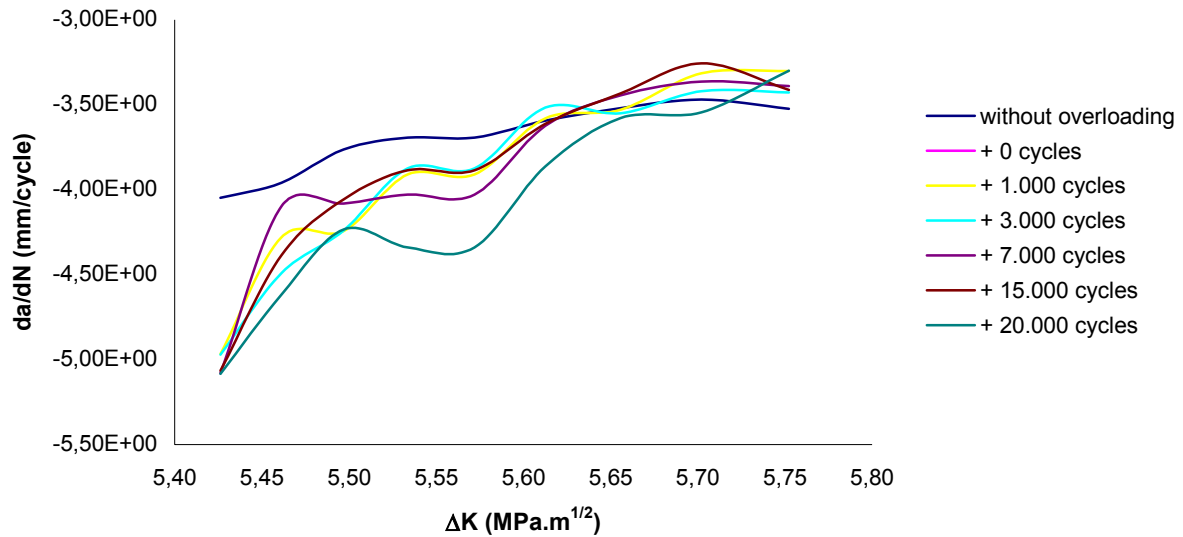
Figure 2: Crack growth rate (da/dN) versus the variation in the stress intensity factor (ΔK) for the material after the second overload series.

TABLE 3
OVERLOAD PARAMETERS AND CRACK GROWTH RETARDATION DUE TO
CONSECUTIVE OVERLOADING CYCLES

D (cycles)	d (mm)	N_{d2}	D_{r2}
0	0.00	143,150	2.3
1000	0.01	162,190	2.6
3000	0,03	175,560	2.8
7000	0,06	184,340	3.0
15000	0,13	185,430	3.0
20000	0,17	235,200	3.8

CONCLUDING REMARKS

The purpose of this work was to determine the improvement in fatigue residual life of a structural steel due to overloading. Overload cycles resulted in an increase in the fatigue resistance of the material and the extended life is related to the presence of compressive residual stress fields acting in the region near the crack tip. The higher the overload ratio, the higher the delay cycles number. An increase in the overload ratio is more efficient for fatigue residual life in virtue of an increase in the mentioned stress fields.

Further, some tests were carried out aiming to study the influence of the overloading interaction on the fatigue crack growth. In this sense, the effect of two equal and consecutive overloads, with the second one applied at different intervals of crack propagation from the first, was also considered. The application of two overloads of the same magnitude increased in a more effective way the fatigue residual life of the material. The larger the interval of crack propagation between the two consecutive overloads, the higher the fatigue crack growth retardation.

REFERENCES

1. Lang, M. and Marci, G. (1999). *Fatigue Fract. Engng. Mater. Struct.* 22, 257.
2. Schijve, J., Broek, D. and Rijk, P. de (1961). NRL–TN M 2094.
3. Elber, M. (1971). *ASTM STP* 486, pp. 230-242.
4. Shin, C.S. and Fleck, N.A. (1987). *Fatigue Fract. Engng. Mater. Struct.* 9, 379.
5. Ward-Close, C.M., Blom, A.F. and Ritchie, R.O. (1989). *Engng. Fract. Mech.* 32, 613.
6. Damri, D. and Knott, J.F. (1991). *Fatigue Fract. Engng. Mater. Struct.* 14, 709.
7. Ritchie, R.O. and Suresh, S. (1982). *Met. Trans.* 13A, 937.
8. Suresh, S. (1983). *Engng. Fract. Mech.* 18, 577.
9. Hammouda, M.M.I., Ahmad, S.S.E., Sherbini, A.S. and Sallam, H.E.M. (1999). *Fatigue Fract. Engng. Mater. Struct*. 22, 145.
10. Jones, R.E. (1973). *Engng. Fract. Mech.* 5, 585.
11. Knott, J.F. and Pickard, A.C. (1977). *Metal Sci.* 11, 399.
12. Wheeler, O.E. (1972). *J. Basic Engng. Trans. ASME* 4, 181.
13. Matsuoka, S. and Tanaka, K. (1978). *J. Mater. Sci.* 13, 1335.
14. ASTM (1999). ASTM E647-99, U.S.A.
15. Pereira, M. (1993). PhD Thesis, Kassel University, Germany.
16. Schijve, J. (1960). NRL-MP 195.
17. Pereira, M.V., Wohlfahrt, H. and Darwish, F. (1997). In: Advances in Fracture Research, pp. 2087-2094, Karihaloo, B.L, Mai, Y.-W., Ripley, M.I. and Ritchie, R.O. (Eds). Pergamon, Amsterdam.
18. Matsuoka, S. and Tanaka, K. (1978). *Engng. Fract. Mech*. 10, 515.
19. Simões, A.F. (1997). MSc Thesis, PUC-Rio, Brazil.
20. Simões, A.F., Pereira, M. and Godefroid, L. (1999). In: *Fatigue'99*, pp. 1069-1074, Wu, X.R. and Wang, Z.R. (Eds). EMAS, West Midlands.
21. Ramos, M.S., Pereira, M. and Motta, S.H. (2000). In: Fracture Mechanics: Applications and Challenges (ECF-13), CD-Rom, Fuentes, M., Elices, M., Martín-Meizoso, A. and Martínez-Esnaola, J.M. Elsevier Science, Amsterdam.
22. Ramos, M.S. (2001). MSc Thesis, CEFET-RJ, Brazil.

SPALLING OF RAILWAY TUNNEL CONCRETE AND ITS CAUSES

T. Asakura[1], Y. Kojima[2], K. Mizuno[2], K. Yashiro[2], T. Muguruma[2] and Y. Matsuda[3]

[1]Department of Earth Resources Engineering, Kyoto University,
Yosidahonmachi, Sakyo-ku, Kyoto-shi, Kyoto, Japan
[2]Railway Technical Research Institute
8-38 Hikari-cho 2 chome, Kokubunji-shi, Tokyo, Japan
[3]West Japan Railway Company
4-24 Shibata 2 chome, Kita-ku, Osaka-shi, Osaka, Japan

ABSTRACT

A number of accidents of concrete block spalling from tunnel linings occurred recently in Japan.   Although there were no personal injuries, trust of people in the safety and durability of tunnel was lost, because some accidents took place in Shinkansen (high speed railroad) tunnels.   Investigations, model tests and numerical analyses were performed on the largest three accidents in particular to study the mechanisms and causes of spalling of concrete.   This paper outlines the accident at the Fukuoka Tunnel out of these accidents and reports the causes of spalling through investigations, model tests and numerical analyses.

KEYWORDS

Tunnel, Concrete, Spalling, Model test, Measurement, Fatigue, Failure

1. INTRODUCTION

It is said that tunnels have longer lives than structures constructed on the ground because they are constructed underground in the stable environment.   There are over 4,700 railway tunnels in service In Japan with a total length of about 3,000km. (Figure 1)   Half of these tunnels were constructed before World War II.   While the tunnel linings are normally made of plain concrete in which cracks easily occur, they remain stable even with a number of cracks because they are arch-shaped and surrounded by the ground.
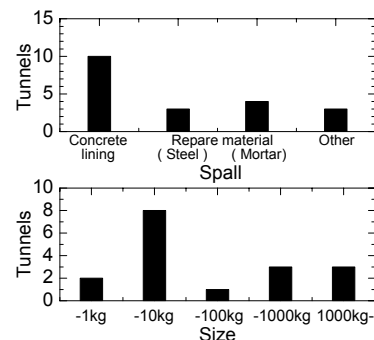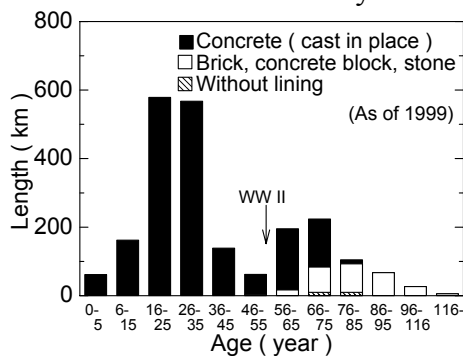
Figure 1: Length of railway tunnels by age and material

Figure 2: Accidents of tunnel concrete spalling

This is a fact that has already been proved by experience, model tests and numerical analyses. However, a number of accidents of concrete block spalling from tunnel linings occurred recently in Japan. Figure 2 summarizes the accidents of tunnel occurred from January 1998 to January 2000. Among these accidents, there was a case where about two tons of concrete block fell from a concrete lining. Although there were no personal injuries, trust of people in the safety and durability of tunnel was lost, because some accidents took place in Shinkansen (high speed railroad) tunnels. For this reason, the Ministry of Transport held a study meeting to discuss the causes of spalling and how to maintain tunnels from now on. Investigations, model tests and numerical analyses were performed on the largest three accidents in particular to study the mechanisms and causes of spalling of concrete. [1,2,3] They were the accidents occurred at the Fukuoka Tunnel and the Kita - Kyushu Tunnel on a Shinkansen line and the Rebunhama Tunnel on the Muroran Main Line. This paper outlines the accident at the Fukuoka Tunnel out of these three accidents and reports the causes of spalling through investigations, model tests and numerical analyses.

2. ACCIDENT AT THE FUKUOKA TUNNEL

2.1 *Outline*
On June 27, 1999, a block of concrete fell from the arch of the tunnel lining at the Fukuoka tunnel, and hit the roof of a Shinkansen train which was passing by. (Photo 1, Figure 3) This tunnel was constructed in 1975 to a length of 8,488 m, with the lining made of cast-in-place plain concrete. The geology of the ground around the tunnel at the accident point is greenschist and the earth covering is about 100m.
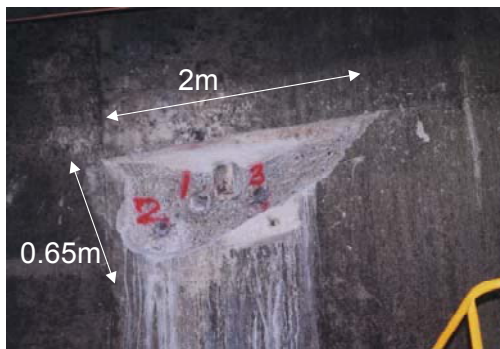
Photo 1: Lining from which a block of concrete fell   **Figure 3**: Outline of spalling (illustration)
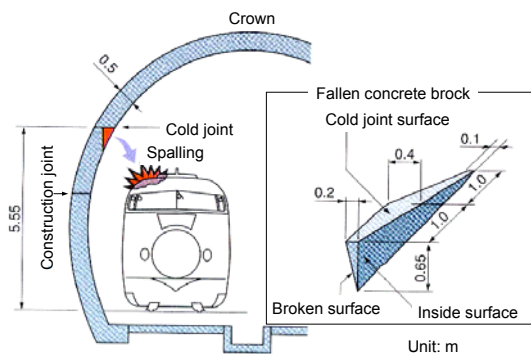
2.2 *Supposed causes of spalling*
There was a cold joint (discontinuity resulting from a delay in concrete placement to preclude union of the material in two successive lifts) right above the separation area. Because the upper side of the block was the cold joint surface and separated, the lining below the cold joint had been easy to fall. Therefore, the cold joint was obviously one of the main causes of spalling. The maximum depth of carbonation at the broken surface was 5mm. It was found that this crack had occurred behind the surface years before. It was also found that the ground around the tunnel was not such a geology that would cause earth pressure or water pressure. There was no construction work near the tunnel. It was found that concrete of the lining had sufficient strength. (compression strength: about 27.5 MPa) There was a very small quantity of typical gel of the alkali-aggregate reaction on the surface of coarse aggregates, but from the results of accelerated tests of the alkali-aggregate reaction, we found that the ratio of volume swell of specimen from the lining of the Fukuoka tunnel was about 0.005% and it was not so much as it was able to cause a problem usually. Therefore we concluded that the alkali-aggregate reaction was not the cause of spalling. Furthermore, the lining of this tunnel was made of plain concrete, and cast-in chlorides had nothing to do with spalling. After the above mentioned consideration, the following factors in addition to the cold joint were picked out as suspected causes of spalling.
    1) Vibration by trains
    2) Change of air pressure by trains
    3) Decrease of concrete strength due to fatigue
    4) Decrease of concrete strength due to change of temperature, water leakage and repetition of wet and dry conditions, etc.
    5) Improper construction of tunnel lining which might cause initial discontinuity inside the lining

We were not able to choose only one factor among these factors as the cause of spalling because they influenced each other. In regard to the factor in 4), long-term research is necessary to study a chemical change of concrete. In regard to the factor in 5), there is a problem that the Fukuoka Tunnel was constructed about 30 years ago and lacks the information on its construction work. Because of these reasons, we focus on the factors in 1), 2) and 3) among these suspected factors and discuss the causes of spalling.

3. VIBRATIONS AND CHANGE OF AIR PRESSURE OF THE TUNNEL

As there were few detailed reports on vibration and strain of the lining and change of air pressure in the tunnel caused by trains, at first, we measured them at the accident point. Figure 4 shows the results of the measurement. The results can be summarized as follows.

    1. Vibration velocity: Max. 0.3 cm/s (z: vertical direction)

                                              Max. 0.1 cm/s (x: radius direction)

    2. Change of air pressure: Max. - 5 kPa (at the passage of train tail)

    3. Tensile strain: Max. $10*10^{-6}$ (z: vertical direction)

It is generally said that the vibration velocity and tensile strain that cause cracks in linings is 20 - 30 cm/s and $200*10^{-6}$, respectively. [4] Then, from these results, we were able to confirm that the vibration and change of air pressure by trains were not the primary causes of spalling of the lining without cracks. On the other hand, we were not able to clarify the relation between the growth of cracks and repeated load caused by vibration or change of air pressure caused by trains. Therefore, we performed bend fatigue tests of plain concrete beams.
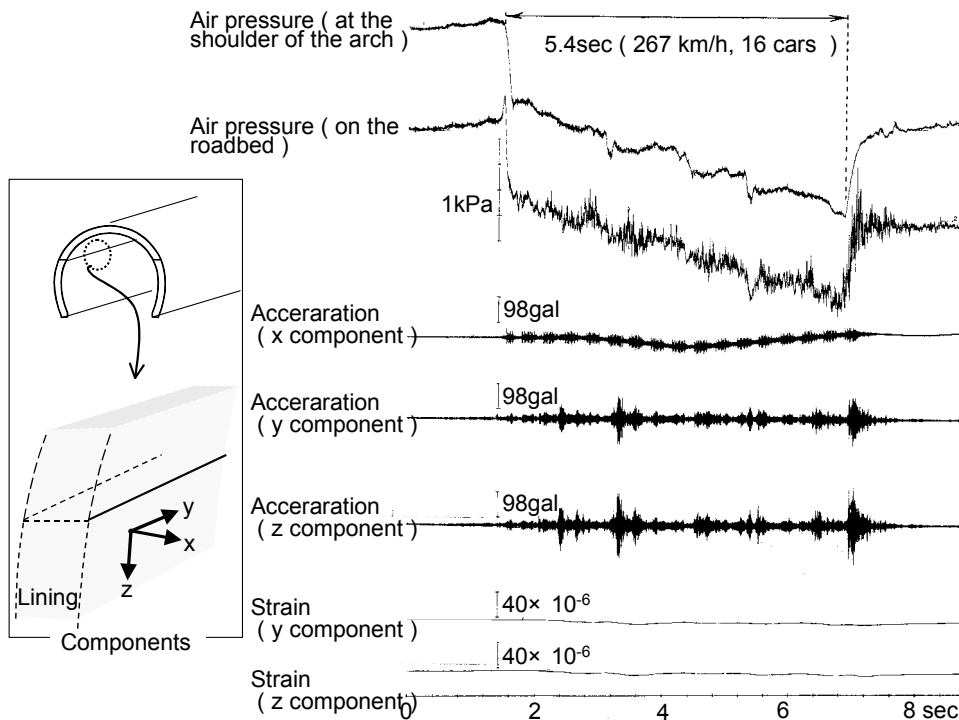
Figure 4: Results of the measurement

4. BEND FATIGUE TEST OF CONCRTE

4.1 *Testing procedure*

Based on the results of measurement shown in Chapter 3, a negative air pressure of 5kPa was repeatedly caused on linings by trains. Therefore, we performed bend fatigue tests of plain concrete to study the effect of repeated load on linings. We performed static bend tests and bend fatigue tests. Photo 2 shows the experimental equipment, and Figure 5 the dimension of specimens. The specimen was a concrete beam made of plain concrete with a width of 200mm, height of 200mm and length of 700mm. The compressive strength of concrete was about 18 N/mm^2. On some specimens, we made a notch with a width of 0.2mm on their bottom side to study the effect of the presence and depth of initial cracks. The depth of the notch was 10 mm or 50 mm. In the tests, we measured the load and displacement at the loading point and strain

at the bottom and side surface of the specimen. At first, we performed static bend tests to grasp the behavior of plain concrete at failure, and decide the input condition of loads for bend fatigue tests. TABLE 1 shows the test cases.
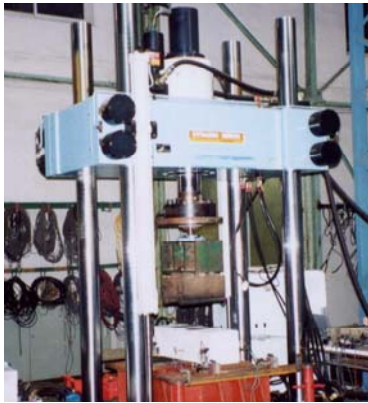
Photo 2: Experimental equipment
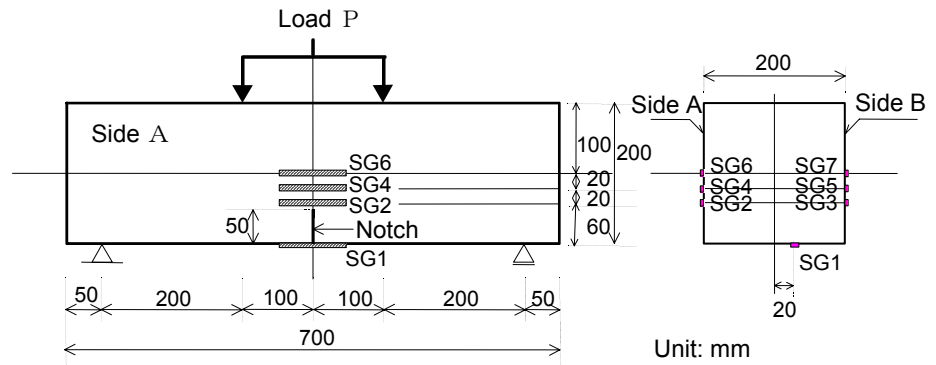
Figure 5: Dimension of specimens

TABLE 1: Test cases

Case No.		Notch	Method of loading
Static bend test	1	None	Monotonic
	2	Depth: 10 mm	
	3	Depth: 50 mm	
Bend fatigue test	4	None	Cyclic
	5	Depth: 10 mm	
	6	Depth: 50 mm	

4.2 *Results of static bend tests*

Figure 6 shows the results of static bend tests, and Photo 3 a specimen after failure. The results of static bend tests can be summarized as follows.

1) A crack occurred at the maximum load on the constant bending section, and grew immediately to lead a beam failure.
2) The bending strength is the largest at the model without notch and becomes smaller with the depth of the notch.
3) The deflection at the failure is the smallest at the model without notch and becomes larger with the depth of the notch
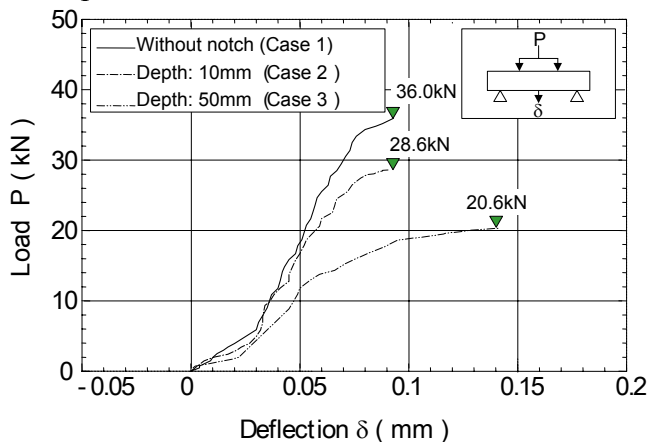
Figure 6: Relation between load and deflection
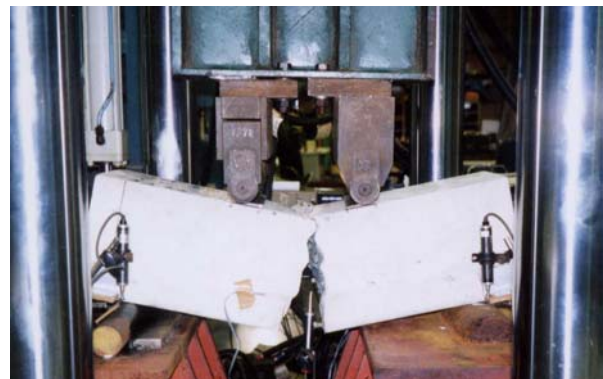
Photo 3: Specimen after failure (static bend test)

4.3 *Results of bend fatigue tests*

Then, we performed bend fatigue tests by applying a repeated load. Figure 7 shows the input condition of the load. The load was input as a sine wave. The upper limit of the load was varied between 50% and

90% of the maximum load of the static bend test, and the lower limit was fixed at 3.2kN because of the restriction of the test unit.　Figure 8(a)-(c) show the relation between the strain at the beam surface and the number of load cycles obtained from the tests. Figure 8(a)-(c) indicate that the strain increases with the number of load cycles at every strain gauge.　Figure 9 shows the relation between the normalized strain and the number of load cycles, where the strain is normalized by that when the number of load cycles is 80.　We can realize that the strain near the bottom surface of the beam increased first and then that near the upper surface.　From this Figure, we can also realize that the crack grows upward with the repeated load.　We performed a number of bend fatigue tests by changing the depth of the notch and the upper limit of the load. Figure 10 shows the relation between the upper limit load at the failure and the number of load cycles to cause failure.　From this Figure we can conclude that the load is larger and the initial cracks is deeper, in other words, the stress at the edge of the notch is larger, a small number of load cycles is enough to break the beam.　Therefore, we can confirm that plain concrete is influenced by fatigue.
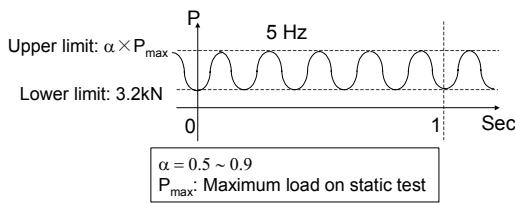
Figure 7: Input condition of load
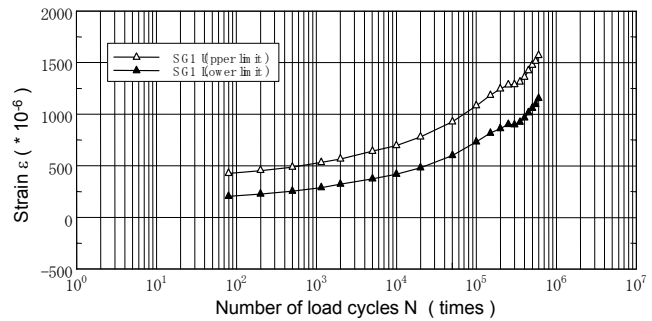
Figure 8(a): Relation between the strain at the beam surface and the number of load cycles
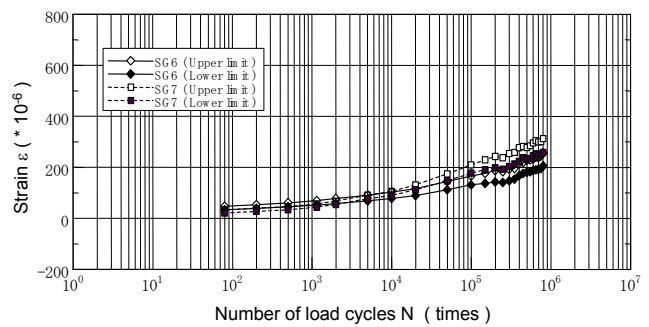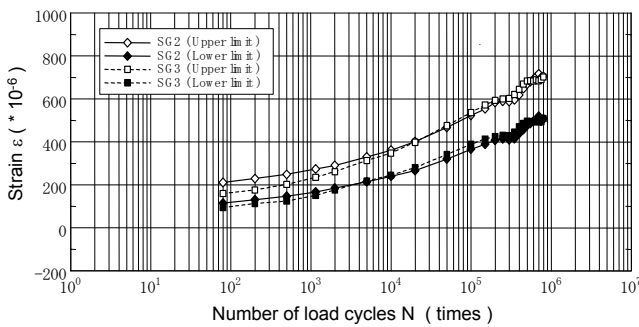
Figure 8(b), (c): Relation between the strain at the beam surface and the number of load cycles
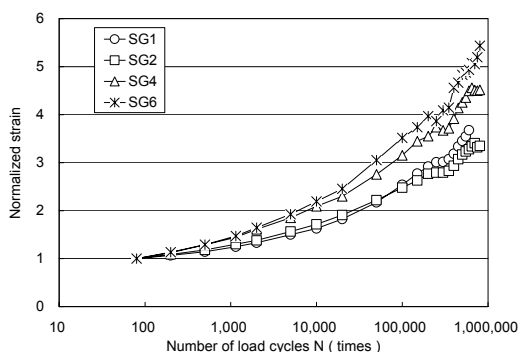
Figure 9: Relation between normalized strain and the number of load cycles
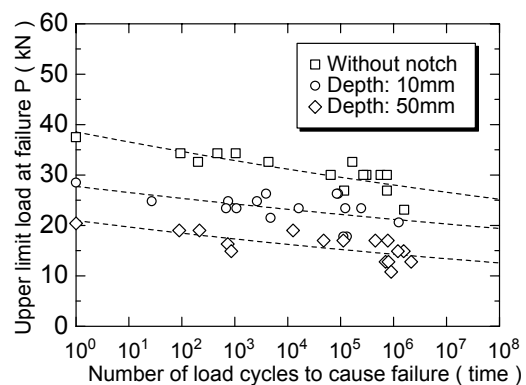
Figure 10: Relation between upper limit load at failure and the number of load cycles to cause failure

4.4 *Comparison of stress state between a real tunnel and the model*

We calculated the estimated stress at the edge of the initial crack at the separation area of the Fukuoka Tunnel by FEM analysis and compared it with the stress at the bend fatigue test.　It was supposed that there had already been considerable deep cracks in the tunnel at the separation area of the Fukuoka Tunnel, but we

were not able to know the exact depth of the cracks.   So, we assumed that the depth of the crack had been 700mm from the surface of the lining as shown in Figure 11.   The shape of the real lining was three-dimensional, but we modeled it by a two-dimensional model for simplification.   The cracks were modeled by duplicated nodes and we applied the negative air pressure (- 5 kPa) by trains on the surface of the lining.   From the analysis, we found that the stress at the edge of the crack was about 1.2 N/mm^2. Figure 12 shows the relation between the stress at the edge of the notch and the number of the load cycles to cause failure, where we calculated the stress at the edge of the notch by Equation 1.   The stress at the edge of the crack of the real tunnel acquired from the FEM analysis was visualized by a spotted line. Shinkansen trains pass the Fukuoka Tunnel about 40,000 times per year and total passage of the trains after opening of the Shinkansen is about a million times.   Therefore, we can conclude that the fatigue failure might occur at the assumed crack depth of 700mm and exsistence of the initial crack. (such as the cold joint)   We can expect that the possibility of fatigue failure becomes higher with deeper cracks and severer stress concentration.

$$\sigma_e = \frac{M}{Z} = \frac{Pl/2}{bd^2/6} \quad (1)$$
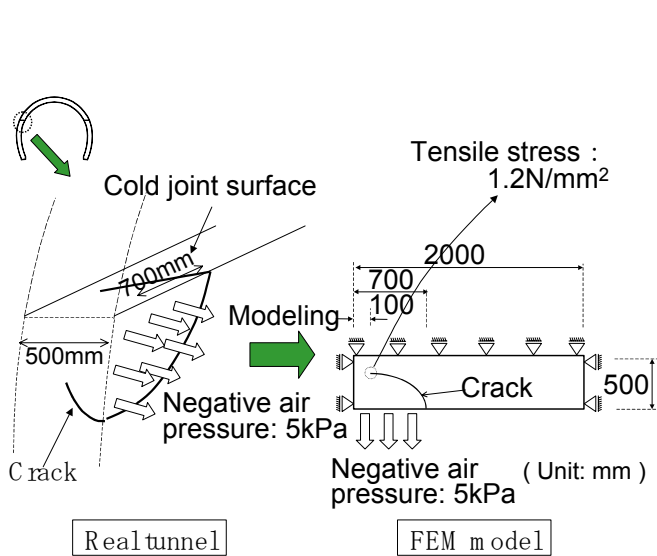
Figure 11: Analysis model of the lining of the separation area of the Fukuoka Tunnel
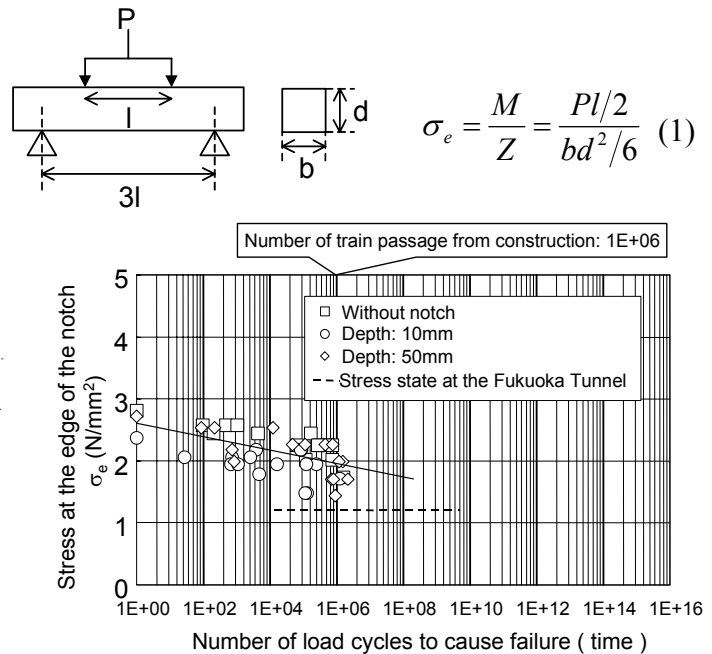
Figure 12: Relation between the stress at the edge of the notch and the number of load cycles to cause failure

5. CONCLUSIONS

We can conclude that plain concrete is influenced by fatigue and its strength decreases with repeated loads from results of bend fatigue tests.   We can also conclude that if there are initial deep crack in the lining and the stress is concentrated at the edge of the crack, the fatigue failure or spalling of concrete can occur by the vibration and change of air pressure by trains.   We were not able to consider other factors sufficiently such as change of temperature, water leakage, repetition of wet and dry conditions, and cracks due to improper construction works, which affect the durability of the lining.   We will study the effect of these factors from now on.   At the close of the report, we express special thanks to Mr. Murata and Mr. Kondo (West Japan Railway Co.) and Mr. Sasaki and Mr. Saito, (Railway Technical Research Institute) who gave us quire a lot of advice on this study.

REFERENCES

1. The Tunnel Safety Meeting (2000). *Report of the Tunnel Safety Meeting* (in Japanese), Japan
2. Kojima, Y. et al. (2000). *Lined Concrete Separation from Railway Tunnel and Its Assumed Causes: Tunnels and Underground,* (in Japanese) pp.815-822, Japan Tunnel Association, Japan
3. Kojima, Y. et al. (2000). *New Maintenance Guide for Railway Tunnels,* (in Japanese) pp.937-944, Japan Tunnel Association, Japan

4. Langefors, U. (1978). *Rock Blasting,* John Wiley & Sons.

SPATIAL STATISTICS OF PARTICLE CLUSTERS
AND MODELING OF PITTING CORROSION

D.G. Harlow and R.P. Wei

Mechanical Engineering and Mechanics, Lehigh University,
19 Memorial Drive West, Bethlehem, PA 18015-3085, USA

ABSTRACT

Localized (pitting) corrosion is recognized as a primary degradation mechanism that affects the durability and integrity of structures made of aluminum alloys, and it is a concern for commercial transport and military aircraft. Corrosion pits have been shown to commence at constituent particles, and to evolve into severe pits by growth through clusters of these particles in the alloys. These severe pits serve as nucleation sites for subsequent corrosion fatigue cracking. Thus, the role of clusters of constituent particles is critical to the quality of aluminum alloys subjected to deleterious environments. To formulate a stochastic model of corrosion, as a part of the methodology for structural reliability analysis, it is essential to have quantitative descriptions of the spatial statistics of the particles and particle clusters, including their location, size, density and chemical composition. A simple probability model incorporating the role of clustered particles on the growth of corrosion pits is presented and discussed. The proposed model includes the effect of randomness in the number and sizes of the clusters. The applicability of the model is considered in terms of experimental data from 2024-T3 aluminum alloy specimens that had been exposed to a 0.5 M NaCl solution.

KEYWORDS

Particle statistics, Cluster statistics, Aluminum alloys, Corrosion, Pitting corrosion, Probability modeling

INTRODUCTION

Pitting corrosion in aluminum alloys has been recognized as a significant degradation mechanism, specifically as a precursor to corrosion fatigue crack initiation and growth, that impacts the reliability, durability, and integrity of both military and commercial aircraft [1-4]. It has been shown that pitting results from the galvanic coupling of constituent particles with the alloy matrix [5-9]. Pit growth is a stochastic process that depends upon material properties and environmental conditions. In fact, severe pits with depths greater than 20 μm have been observed as nuclei for the early onset of fatigue crack growth and subsequent reductions in fatigue live.

The scanning electron microscopy (SEM) micrograph in Fig. 1(a) shows a typical pit that resulted from the galvanic coupling between a surface particle and the matrix. The complex geometrical structure of a severe corrosion pit is illustrated by the SEM micrographs in Fig. 1(b) and (c) of an epoxy replica of a typical severe pit. The rounded features on the surface correspond to individual constituent particles, and indicate that the
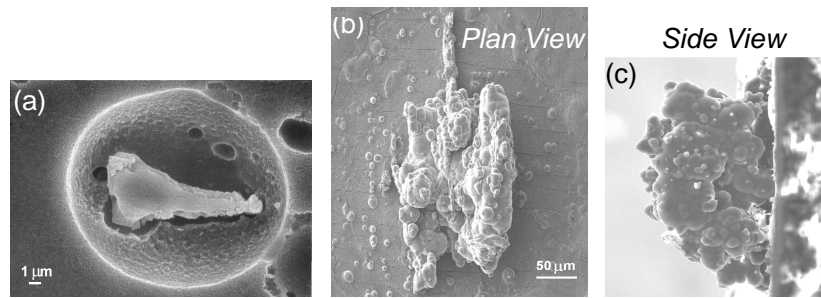
Figure 1: SEM micrographs – (a) particle induced corrosion pit; and epoxy replica of a severe corrosion pit: (b) plan (bottom) and (c) side (elevation) views relative to the original pit in a 2024-T3 aluminum alloy sheet [1,6,8].

pit evolved by progressive particle-induced dissolution through a cluster of particles. Thus, the size and location of particle clusters is an essential component in the stochastic evolution of pitting. The purpose here is to incorporate spatial statistics of constituent particles and clusters of particles into a simple mechanistically based probability model for corrosion pit growth.

Polished sections of 2024-T3 aluminum alloy, the area of which was approximately 340 μm × 1030 μm, were observed using SEM. In order to estimate accurately the particle geometry and clustering for the alloy, observations were made on the LS, TS, and LT surfaces. One area was considered on each of the LS and TS surfaces, but two different areas were observed of the LT surface. Subsequently, the same two areas about 20 μm deeper were analyzed on the LT surface. The average numbers of particles per mm^2, with an area of at least 0.5 $μm^2$, were found to be 3850, 3820, and 3180 for the LS, TS, and LT surfaces, respectively. Detailed properties for this alloy may be found in [1].

PARTICLE STATISTICS

Figure 2 is an SEM micrograph of an LT surface that is typical of polished specimens of 2024-T3 aluminum alloy, and it illustrates the inherent randomness in the number, size, and location of the constituent particles. It is impossible to describe adequately this complex spatial pattern from observations alone. Certainly, there is no apparent spatial structure, and the need for modeling is manifest. Many different models have been suggested for irregularly shaped and randomly distributed particles [10]. The primary concern herein is the statistical description of particle clustering that reflects not only geometrical, but also electrochemical considerations induced by deleterious environments. It has been shown, using spatial statistics, that the constituent particles in 2024-T3 are statistically clustered [11], and that was confirmed for the material used herein. Furthermore, it has been demonstrated that corrosion pits are statistically, regularly spaced because pitting encompasses several clustered particles [11].
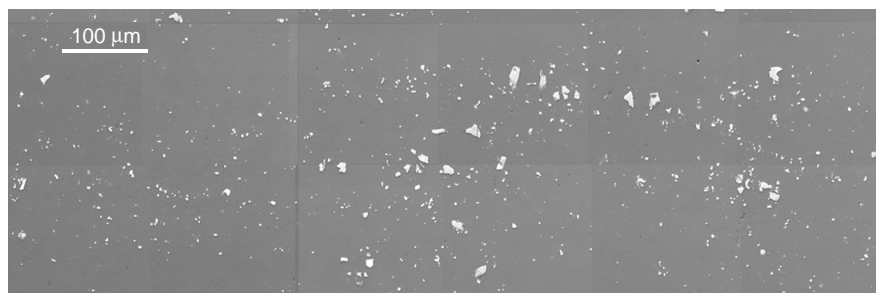
Figure 2: Typical SEM micrograph of a polished section of the LT surface of 2024-T3 aluminum alloy.

One of the key random variables (rvs) for the ensuing probability computations is the particle area A_p. The cumulative distribution function (cdf) for A_p was estimated from the observation of over 7,000 particles. The truncated two-parameter Frechet cdf, given by

$$F(x) = \exp\{-[(x/\beta)^{-\alpha} - (\delta/\beta)^{-\alpha}]\}, \quad x \geq 0, \quad \alpha > 0, \quad \beta > 0, \quad \delta > 0, \tag{1}$$

where α is the shape parameter, β is the scale parameter and δ is the maximum value, was fit using maximum likelihood estimation (MLE) [12]. This Frechet cdf was selected because it characterizes the maxima of rvs. Since the largest particles induce the most severe damage, it is preferred. Furthermore, the geometrical features of the material necessarily have an upper bound. The Frechet MLE estimates are acceptable for the data with a confidence level of 99%, based on the Kolmogorov-Smirnov (K-S) goodness-of-fit test [12]. Using the likelihood ratio test [12] with a confidence over 97.5%, the six data sets may be merged, which is evidence that A_p for each surface is statistically similar. The estimates for the merged data for A_p are as follows: $\hat{\alpha} = 2.0$, $\hat{\beta} = 5.1 \ \mu m^2$, $\hat{\delta} = 285.7 \ \mu m^2$, $\hat{\mu} = 5.8 \ \mu m^2$, and $\hat{cv} = 52\%$, where μ is the mean and cv is the coefficient of variation. Note that the scatter is large, which indicates extensive variability in particle sizes.

MODELING THE CLUSTER SIZE FOR CONSTITUENT PARTICLES

It has been demonstrated that the galvanic current induced from a particle subjected to a deleterious environment has a "throwing power" radius that can be approximated by ma_p, where m is an appropriate multiple ranging from 2 to 4 [13] and a_p is the particle radius. If additional particles are within that distance, galvanic dissolution will continue, thus propagating pitting corrosion. Herein, two particles are considered to be in the same cluster if the distance between their centroids is less than ma_p. Consequently, the cluster size is estimated by counting the total number of particles n_{pc} that satisfy this pair-wise criterion. In order for a severe corrosion pit to form, n_{pc} must be sufficiently large to sustain the galvanic dissolution needed for pit growth. It is assumed that $n_{pc} \geq 4$ is reasonable, and empirically such an assumption matches statistical observation quite well. Figure 3 shows the centroid for each particle in Fig. 2. The polygons shown on the figure are schematic approximations for the effective area of each cluster according to this criterion for which $m = 3$ and $n_{pc} \geq 4$. The cluster areas exhibit considerable scatter. Since each point is sized equally, the figure is somewhat deceiving. Also, the polygons are rough approximations for the cluster area. Refer to Fig. 1 for a typical cluster. Again, the cdf of Eqn. 1 is a very good characterization for the particle cluster radius a_{pco}, which is another critical rv for the probability analysis. All six sets of cluster radii are very tight, and they may be merged according to the likelihood ratio test for any confidence greater than 70%. Thus, a_{pco} for the LT, LS, and TS planes may be considered to be statistically identical with parameters of $\hat{\alpha} = 1.8$, $\hat{\beta} = 14.3 \ \mu m$, $\hat{\delta} = 42.2 \ \mu m$, $\hat{\mu} = 14.4 \ \mu m$, and $\hat{cv} = 50\%$. Based on the K-S goodness-of-fit test, any confidence greater than 70% is appropriate for the fit. The large $\hat{cv}$ for the clusters is confirmed graphically on Fig. 3.

Given the clustering criterion, the number of particles per cluster n_{pc} is well characterized by the discrete
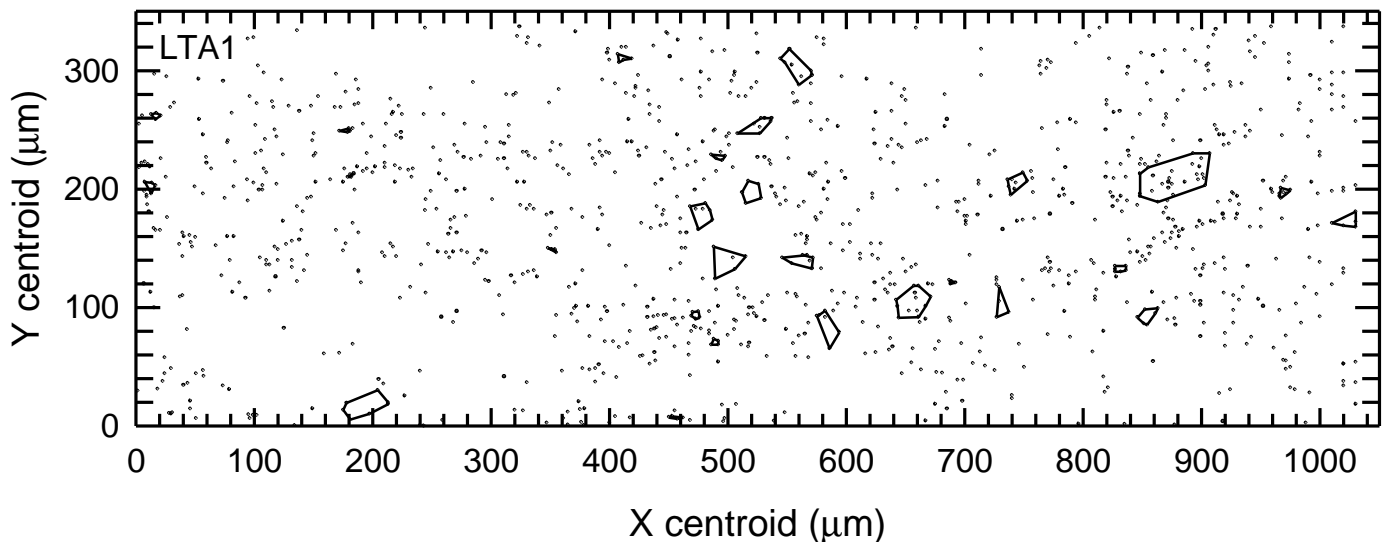
Figure 3: Schematic representation of the particle centroids and clusters for the LT surface in Figure 2.

Pareto distribution [14] given by

$$p_k = \Pr\{n_{pc} = k\} = ck^{-(\rho+1)}; \quad k \geq 1, \tag{2}$$

with any confidence greater than 70% using the K-S test. The estimated parameters are $\hat{c} = 2.8$ and $\hat{\rho} = 1.7$. Since the cluster area is small, it is assumed that in its related volume the particle distribution is uniformly distributed. Thus, the local volume particle density is assumed to be equal to the area particle density.

SIMPLIFIED MODELING OF CORROSION PITTING

Plausible models for particle induced pitting have been explored [14]. A simplified model for pit growth was adopted and used, with success, in exploring the implications of pitting corrosion on the evolution of corrosion and fatigue damage in high-strength aluminum alloys and in aircraft that had been in long-term commercial service [4,15]. Although there is ample experimental support for this model for characterizing pitting corrosion around an isolated particle, or a small cluster of particles at the surface, its extension to describe the development and growth of a severe corrosion pit is problematic. The pitting current cannot be constant, as assumed above; it must reflect the galvanic dissolution of the alloy matrix through its coupling with the entire cluster of constituent particles that are progressively exposed by pitting [13]. The model envisions pit growth to be sustained by galvanic current from a small group of constituent particles that are exposed at the surface to initiate pit growth.

For simplicity, the model assumed the pit to be hemispherical in shape, with radius a, and its growth would be at a constant volumetric rate, obeying Faraday's law. Specifically, the pit volume is $V = (2/3)\pi a^3$. The rate of pit growth is given in terms of Faraday's law, and the time evolution of pit size and the time required to reach a given pit size are determine from direct integration of the rate equation, and are as follows:

$$\frac{da}{dt} = \frac{da}{dV}\frac{dV}{dt} = \frac{1}{2\pi a^2}\frac{dV}{dt} = \frac{MI_{pit}}{2\pi n\rho F}\frac{1}{a^2}, \tag{3}$$

where M is the molecular weight; I_{pit} is the pitting current; n is the valence; ρ is the density; F is Faraday's constant (9.65×10^7 C/kg-mol). For aluminum, $M = 27$ kg/kg-mol; $n = 3$; and $\rho = 2.7 \times 10^3$ kg/m^3. For particle induced pitting, I_{pit} is defined by the cathodic current density that can be supported by the cluster of particles and their effective surface area.

Explicitly, I_{pit} is assumed to be given by the following:

$$I_{pit} = \sum_{i=1}^{n_{pc}} (i_{co})_i (2\pi a_p^2)_i, \tag{4}$$

where $(i_{co})_i$ is the limiting cathodic current density for particle i, $(2\pi a_p^2)_i = (2A_p)_i$ is the surface area of particle i that is exposed to the electrolyte within a growing pit at time t, and n_{pc} is a rv for the number of particles that are exposed on the surface of a hemispherical pit of radius a at time t. The exposed portion of a cluster includes all of the constituent particles at the pit surface. Pit growth is sustained by the galvanic coupling current between the matrix constituting the pit surface and the exposed particles. Even though the particle composition and electrochemical conditions evolve for each particle in a pit, $(i_{co})_i$ for $i \geq 1$ are assumed herein to be identically distributed and are taken to be constant for simplicity.

Integrating Eqn. 3 leads to the following for the time evolution of cluster induced corrosion pitting:

$$a = \left[\frac{3MI_{pit}}{2\pi n \rho F} t + a^3_{pco} \right]^{1/3} \quad \text{and} \quad t = \frac{2\pi n \rho F}{3MI_{pit}} (a^3 - a^3_{pco}) ,\tag{5}$$

where a_{pco} is a rv for the initial pit size, *i.e.*, the size of the initiating cluster of particles.

COMPUTATIONS, COMPARISONS, AND DISCUSSION

The rvs that play a key role in the following mechanistically based probability computations are $(i_{co})_i$, a_{pco}, n_{pc}, and $(A_p)_i$. The limiting values of $(i_{co})_i$ depend on the composition of the particles and the electrochemical conditions within the pit, and it can range between 40 and 600 $\mu A/cm^2$. To estimate the influences of particle composition, solution acidification, dealloying and copper deposition, $\hat{\mu} = 200 \ \mu A/cm^2$ and $c\hat{v} = 52\%$ were assumed for $(i_{co})_i$ throughout; see [7,8]. The statistical properties of the other rvs were given above. In order to validate the model, computations were made and compared to experimentally measured pit depths that were formed in 2024-T3 aluminum alloy sheet specimens after immersion in 0.5M NaCl solution for 16 to 384 h [13]. The measured pit depths are shown as a function of exposure time on Fig. 4. The lines are probability percentile lines computed from the model given in Eqn. 5. The solid line is the median (50th percentile), whereas the lines with symbols are the percentiles appropriate for the 80%, 90%, and 95% confidence bands. The dashed line is the linear least squares regression through the data. The regression and median predicted from the mechanistically based probability model are very close over the range of the data, which is reassuring that the model has merit. The predicted lower confidence bounds agree well with the data. The deviation between the lower bounds is small because the data for the rvs in Eqn. 5 are skewed toward the lower tails of the cdfs. The 80% and 90% predicted upper bounds are also quite good; however, the 95% upper bound is quite broad. The divergence in these upper bounds is attributable to the large scatter in upper tails of the data for the rvs in Eqn. 5. In other words, in the upper percentiles of the data are very disperse and are considerably larger in magnitude than the preponderance of the data. Furthermore, longer exposures to deleterious environments may yield more variability than indicated by this data. Thus, additional investigations, both modeling and experimental, are warranted.
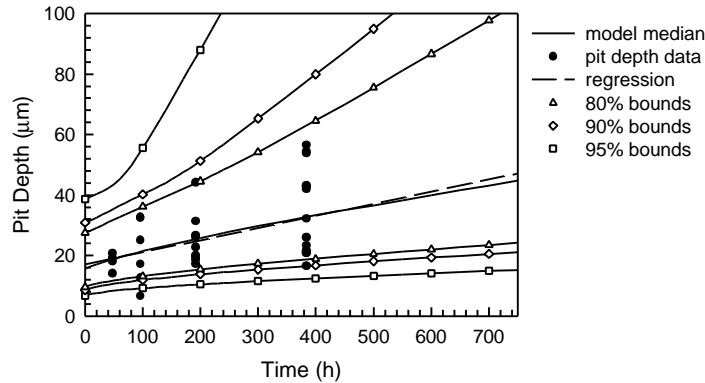
Figure 4: Pit depth data with the linear regression and 95% statistical confidence bounds and the median and 95% confidence bounds computed from the simplified pitting corrosion model.

The cdf for a given t also can be computed from Eqn. 3, and Fig. 5 shows selected cdfs plotted on Frechet probability paper as t varies. For $t = 0$, the graph is the cdf for a_{pco}, which is truncated at the maximum 42.2 μm. The large variability in each cdf is evident, increasing with increasing t, which corroborates the broad confidence bounds in Fig. 4. Also as t increases, the cdfs become nearly linear, indicating that a two-parameter Frechet cdf, *i.e.* $\delta = 0$, would be an excellent approximation for these cdfs.
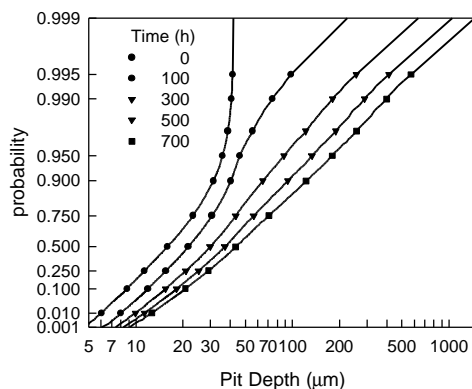
Figure 5: Evolution of the cdf for pit depth *a*.

CONCLUSIONS

A simplified probabilistic model incorporating the role of clustered particles on the growth of corrosion pits has been presented and discussed. The proposed pit growth model includes the galvanic dissolution of the alloy matrix through its coupling with clusters of constituent particles that are progressively exposed by the pitting process. The merit of the model was considered by comparing model predictions to experimental data from 2024-T3 aluminum alloy specimens that had been exposed to a 0.5 M NaCl solution. The model predictions included estimations for the random variables that were obtained from independent measurements. The predicted median evolution and 90% confidence bounds agree well with the data. The effect of randomness in the number and sizes of the constituent particles and clusters of particles on pitting is quite pronounced. Thus, the role of clusters of constituent particles is critical to the quality of aluminum alloys subjected to deleterious environments. This effort provides a basis for a mechanistically based probability model for reliability analysis in life-cycle design and management of engineered systems when corrosion is the operative damage mechanism. Even so, additional pitting corrosion experiments and better modeling to account for material anisotropy and volume effects are planned for the future.

ACKNOWLEDGMENTS

REFERENCES

1. Chen, G.S., Gao M., and Wei R.P. (1996) *Corrosion* **52**, 8.
2. Chen, G.S., Wan, K.-C., Gao, M., Wei, R.P., and Flournoy, T.H. (1996) *Matls Sci. and Engr.* **A219** 126.
3. Harlow, D.G. and Wei, R.P. (1999) *Fatigue Fract. Engng Mater. Struct.* **22** 427.
4. Harlow, D.G. and Wei, R.P. (2001) *Fatigue Fract. Engng Mater. Struct.* (to appear).
5. Wei, R.P., Liao, C.-M., and Gao, M. (1998) *Metall. Mater. Trans.* **29A** 1153.
6. Liao, C.-M., Olive, J.M., Gao, M., and Wei, R.P. (1998) *Corrosion* **54** 451.
7. Gao, M., Feng, C.R., and Wei, R.P. (1998) *Metall. Mater. Trans.* **29A** 1145.
8. Liao, C.-M., Chen, G.S., and Wei, R.P. (1996) *Scripta Mater.* **35** 1341.
9. Liao, C.-M. and Wei, R.P. (1999) *Electrochimica Acta* **45** 881.
10. Cressie, N.A.C. (1991) *Statistics for Spatial Data.* Wiley, New York.
11. Cawley, N. and Harlow, D.G. (1996) *J. Mat. Sci.* **31** 5127.
12. Lawless, J. (1982) *Statistical Models and Methods for Lifetime Data.* Wiley, New York.
13. Wei, R.P. (2001) *Scripta Mater.* (to appear).
14. Harlow, D.G. and Wei, R.P. (1998) *Engr. Frac. Mech.* **59** 305.
15. Harlow, D.G. and Wei, R.P. (1994) *J. A.I.A.A.* **32** 2073.

SQUID DAMAGE MONITORING
FOR AUSTENITIC STAINLESS STEEL

T. Suzuki[1], K.Hirano[1] and T.Teramoto[2]

[1] Advanced Materials& Structural Integrity Group,
Institute of Mechanical Systems Engineering,
National Institute of Advanced Industrial Science and Technology
AIST Tsukuba East 2-1 Namiki 1-Chome, Tsukuba-shi, Ibaraki-ken, 305-8564, Japan
[2] Institute of Engineering Mechanics and Systems, University of Tsukuba
1-1-1   Tennodai, Tsukuba-shi, Ibaraki-ken, 305-8573, Japan

ABSTRACT

In-situ SQUID output monitoring tests for smooth and cracked specimens of austenitc stainless steel under monotonic and cyclic loading were performed. Under monotonic loading for smooth specimens SQUID output changed with increase of load, and it was divided into two stages. The changes in SQUID output in the first stage were reversible, and they recovered after unloading. While the changes in SQUID output in the second stage were irreversible, and there existed residual magnetization after unloading. The changes in SQUID output in the first stage were caused by the magneto-elastic effect, and the changes in SQUID output in the second stage were caused by martensitic transformation. Then it was found that the changes in SQUID output were correspondent with deformation behavior of austenitic stainless steel under monotonic loading. During fatigue crack growth, the changes in SQUID output amplitude were related to stress intensity factor range, and it increased with increase of stress intensity factor range. Then it was found that there was a possibility that fatigue crack growth rate was predicted by the changes in SQUID output amplitude during fatigue crack growth.

KEYWORDS

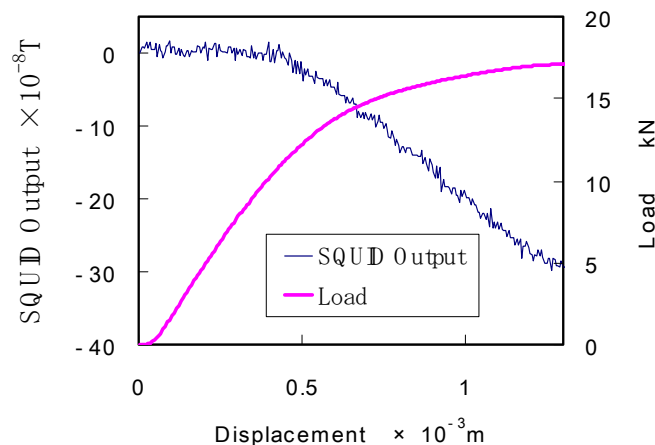SQUID, Austenitic Stainless Steel, In-situ Damage Monitoring, Monotonic Loading, Cyclic Loading, Fatigue Crack Growth, Magneto-elastic Effect, Martensitic Transformation

INTRODUCTION

In order to ensure the integrity of structures, it is necessary to perform in-situ damage monitoring. However, there have been few researches[1-3] to perform in-situ damage monitoring by magnetic characterization. In addition, in these researches only ferromagnetic materials were investigated because of the limitation of sensitivity for their magnetic sensors. SQUID(Superconducting Quantum Interference Device) is an ultrahigh sensitive magnetic sensor and has become useful for non-destructive damage evaluation[4-6]. Then if SQUID is used as a magnetic sensor for in-situ damage monitoring, there is a possibility that in-situ damage monitoring for various kinds of materials including non-magnetic materials can be performed.

In this study in-situ damage monitoring tests were performed using a developed in-situ SQUID damage

monitoring system[5]. The effects of monotonic and cyclic loading for austenitic stainless steel on magnetic characteristics were investigated with smooth and cracked specimens. The changes in SQUID output in magnetic characteristics were discussed related to the development of monotonic and cyclic deformation.

MATERIALS AND EXPERIMENTAL PROCEDURE

The material investigated in this study was austenitic stainless steel SUS304(C0.04, Si0.46, Mn0.86, P0.028, S0.003, Ni8.17, Cr18.17 wt%). Smooth specimens, which dimensions were $140 \times 20 \times 2mm$, were used for tensile tests. And center notched plate tension specimens, which dimensions were $140 \times 20 \times 2mm$ and which initial notch dimensions were $7.5 \times 0.3mm$, were used for fatigue crack growth tests. In the case of fatigue crack growth tests fatigue pre-cracks were introduced with the final maximum stress intensity factor of $63.5MPam^{1/2}$.

The changes in magnetization under monotonic and cyclic loading were examined by a developed in-situ SQUID damage monitoring system[5]. The system consisted of a SQUID sensor, a SQUID controller, a cryostat, and an electrohydraulic nonmagnetic materials testing machine. The DC·SQUID sensor, which operated at liquid helium temperature, was used with a 1-dimensional axial differential pickup coil to remove environmental magnetic noise around the system. In the electrohydraulic nonmagnetic materials testing machine only non-magnetic structural materials were used within 1m around the SQUID sensor. The distance between the bottom of the cryostat and the specimen was 1mm.

Tensile tests were performed at a crosshead speed of 0.5mm/min. Fatigue crack growth tests were performed at a stress ratio R=0.1 at a frequency of 10Hz. The crack length was measured by a traveling microscope and a scanning laser microscope on the specimen surface. All the tests were performed at room temperature and no magnetic field was imposed during in-situ SQUID output monitoring.

EXPERIMENTAL RESULTS AND DISCUSSION

Changes in SQUID Output under Monotonic Loading for Smooth Specimens
Typical relationships between SQUID output, load and displacement for smooth specimen of austenitic stainless steel under monotonic loading are shown in Figure 1(a). Although austenitic stainless steel was originally non-magnetic, SQUID output clearly changed with increase of displacement. It was found that a knee point appeared in the relationship between SQUID output and displacement and the changes in SQUID output were divided into two stages. In the first stage before the knee point SQUID output decreased with increase of displacement. In the second stage after the knee point SQUID output changed to increase with increase of displacement. And the inclination between SQUID output and displacement at the second stage was larger than that at the first stage.

Another relationships between SQUID output, load and displacement for smooth specimen of austenitic stainless steel under monotonic loading are shown in Figure 1(b). SQUID output changed with increase of displacement and the changes in SQUID output are also divided into two stages. However, the polarity of SQUID output was not the same as is shown in Figure 1(a), in the second stage after the knee point SQUID output decreased again with increase of displacement.

Because specimens were not magnetized before the tests, and no magnetic field imposed during in-situ damage monitoring, the polarity of SQUID output depended on the initial magnetization in each specimen. Then by using the absolute value of SQUID output the changes in SQUID output under monotonic loading are essentially expressed as shown in Figure 2.

Changes in SQUID Output under Monotonic Loading and Unloading for Smooth Specimens
In order to clarify the magnetic characteristics under monotonic loading, the changes in SQUID output under monotonic loading and unloading in each stage of the tensile tests were measured. Relationships between SQUID output, load and displacement for smooth specimen of austenitic stainless steel under
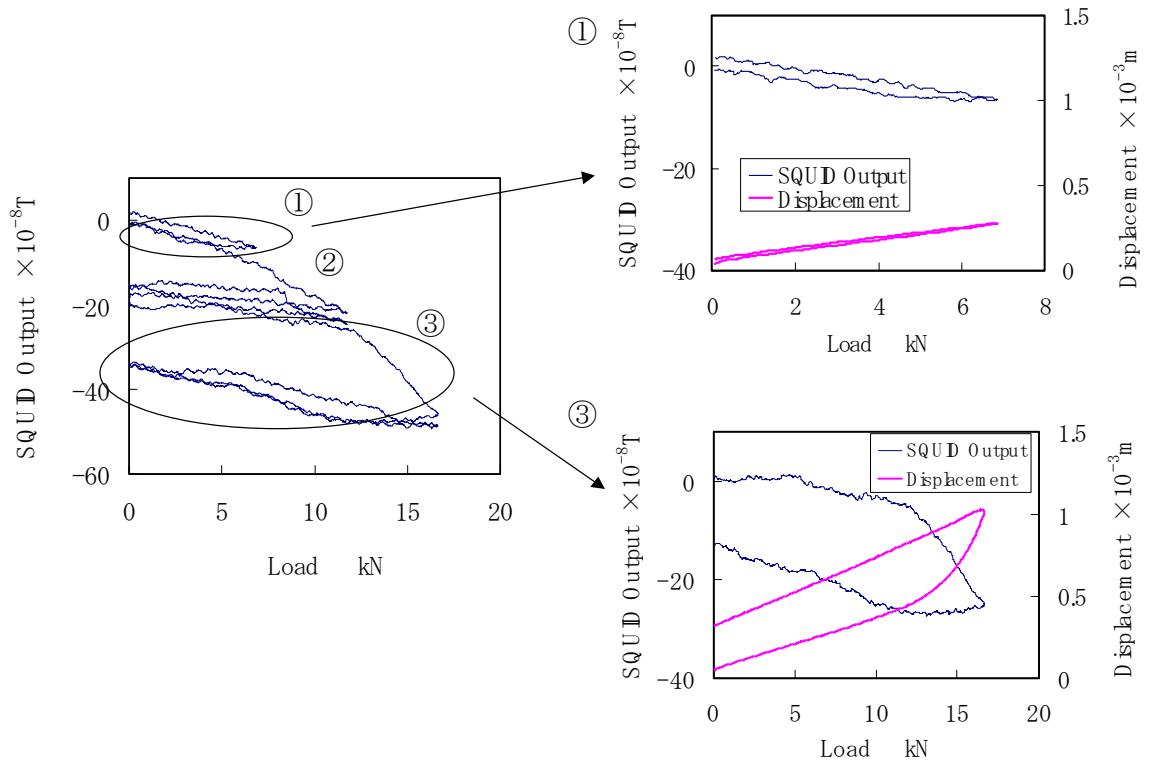
monotonic loading and unloading in each stage of tensile test are shown in Figure 3. As shown in Figure 3①, in the first stage the relationship between load and displacement was linear and there existed almost no hysteresis in the load-displacement curve. In this case SQUID output increased again during unloading and there existed almost no hysteresis in the SQUID output-displacement curve. Then the changes in SQUID output in the first stage were found to be reversible. It was previously reported by Atherton et al.[1-3] that in ferromagnetic steels magnetization changed under stress conditions and it increased or decreased under monotonic loading, and by unloading magnetization completely recovers because of magneto-elastic effect in low magnetic field. Austenitic stainless steel is classified as a non-magnetic material. However, by using an ultrahigh sensitive magnetic sensor of SQUID, it was found that the effect of stress on magnetization was able to be measured.

While as shown in Figure 3③, where the relationship between load and displacement became nonlinear, there existed hysteresis in the load-displacement curve. And in this case there existed residual magnetization after unloading and hysteresis in the SQUID output-displacement curve was clearly observed . Then the changes in SQUID output in the second stage were found to be irreversible. It is well-known that SUS304 has a meta-stable austenitic phase and it easily changes to α'-martensite, which is a ferromagnetic phase, with increase of strain because of strain induced martensitic transformation. Then it was found that the hysteresis in the SQUID output –displacement curve was resulted from strain induced martensitic transformation of α'-martensite.

Changes in SQUID Output during Fatigue Crack Growth
Fatigue crack growth resistance for austenitic stainless steel is shown in Figure 4. It was found that fatigue crack growth rate was expressed by the power law. Relationships between SQUID output, load and displacement for austenitic stainless steel during a cyclic loading at a stress intensity factor range ΔK of 21.5MPam$^{1/2}$ are shown in Figure 5. During a cyclic loading there existed almost no hysteresis in the load-displacement curve. And in the SQUID output-load curve there also existed almost no hysteresis. Then it was found that fatigue crack growth behavior could not related to the hysteresis of SQUID output-load curve.

Changes in SQUID output amplitude between maximum and minimum loading for austenitic stainless steel during fatigue crack growth is shown in Figure 6. It was found that changes in SQUID output amplitude were related to the stress intensity factor range uniquely and it increased during fatigue crack growth. This was because the sizes of martensitic transformation region increased with increase of stress intensity factor range. Then there was a possibility that the fatigue crack growth rate could be predicted by the changes in SQUID output amplitude.

CONCLUSIONS

1. In the measurement of in-situ SQUID output monitoring for smooth specimens of austenitc stainless steel under monotonic loading, it was found that SQUID output changed with increase of displacement, and the changes in SQUID output were divided into two stages.
2. By the measurement of in-situ SQUID output monitoring under monotonic loading and unloading, it was found that the changes in SQUID output in the first stage were caused by the magneto-elastic effect. While the changes in SQUID output in the second stage were caused by martensitic transformation of α'-maretensite.
3. In the measurement of in-situ SQUID output monitoring during fatigue crack growth, the changes in SQUID output amplitude were related to the stress intensity factor range and they increased with increase of stress intensity factor range. Then it was found that there was a possibility that the fatigue crack growth rate was predicted by the changes in SQUID output amplitude during fatigue crack growth.

ASKNOWLEDGEMENT

REFERENCES

1. Atherton, D.L. and Jiles, D. C. (1986) *NDT International*, 19-1,15.
2. Atherton, D.L., Sudersena Rao, T. and Shonbachler, M.(1988) *IEEE Transactions on Magnetics*, 24-3, 2033.
3. Krause, T. W., Donaldson, R. M., Barnes R., and Atherton D.L., (1996) *NDT&E International*, 29-2, 79.
4. Suzuki, T. and Hirano, K. (1999)In: *Progress in Experimental and Computational Mechanics in Engineering and Material Behavior*, pp.432-437, Zhu D. and Kikuchi M.(Eds). Northwestern Polytechnical University Press, China.
5. Suzuki, T., Hirano, K. and Lee, K.W. (2000) In: *Nondestructive Characterization of Materials X*, pp.349-355, Green Jr, R.E.(Eds).Elsevier, Oxford.
6. Kasai, N., J. Applied Physics(1998) 67-4, 417.
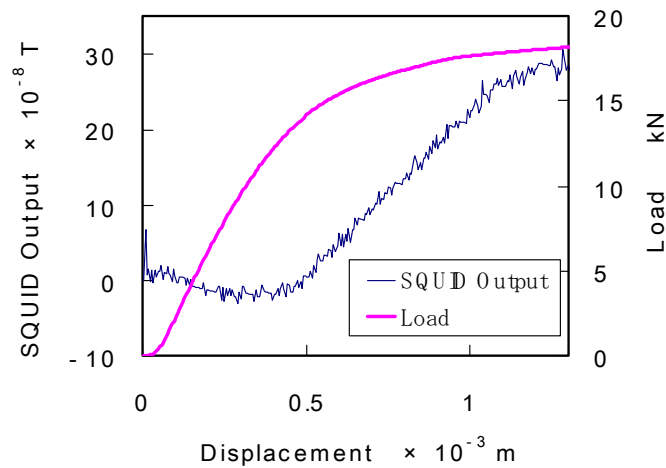
(a)

(b)

Figure 1: Relationships between SQUID output, load and displacement
for smooth specimen of austenitic stainless steel
under monotonic loading
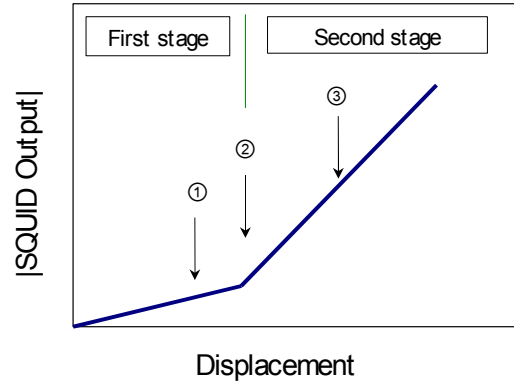
Figure 2: Schematic representation of changes in SQUID output
under monotonic loading

Figure.3: Relationships between SQUID output, load and displacement
for smooth specimen of austenitic stainless steel under monotonic
loading and unloading in each stage of tensile test
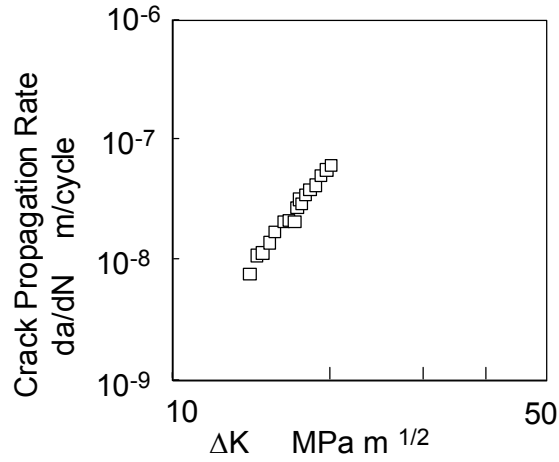
Figure 4: Fatigue crack growth resistance for austenitic stainless steel
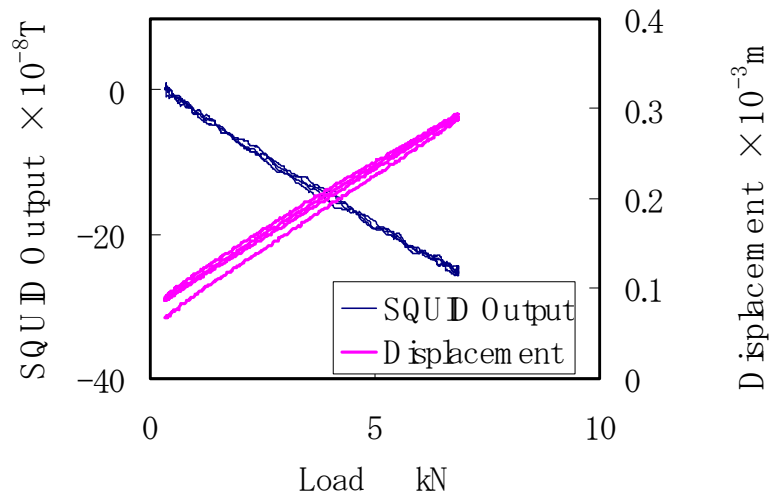
Figure 5: Relationships between SQUID output, displacement and load for austenitic stainless steel during a cyclic loading at a stress intensity factor range of 21.5MPam$^{1/2}$
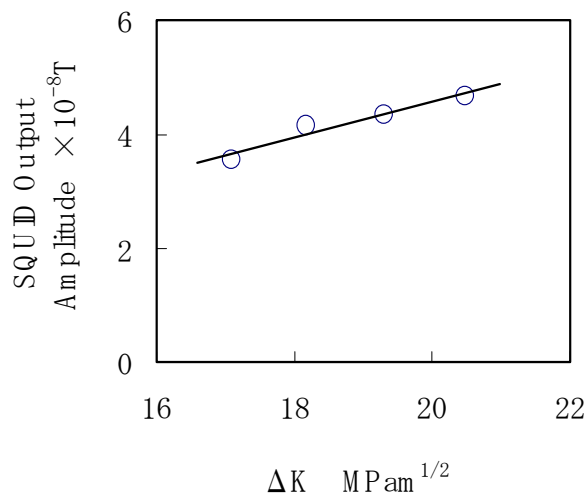
Figure 6:Changes in SQUID output amplitude for austenitic stainless steel during fatigue crack growth

STANDARDISATION OF CREEP/FATIGUE CRACK GROWTH TESTING IN COMPONENTS

K M Nikbin
Mechanical Engineering Department
Imperial College
London SW7 2BX
UK

ABSTRACT

In both power generation plants and the chemical industries there is a need to assess the significance of defects which may exist in high temperature equipment operating in the creep and creep/fatigue range. The defect assessment codes [1-4] need verifiable materials data for use in their analysis. The fracture committee in Versailles Agreement for Materials and Standards (VAMAS) has been active in developing and disseminating testing and analysis methodology in this field since 1987. This paper reviews the methods of analysis used in short term small laboratory creep crack growth data and their relevance to long term crack initiation and growth in components. It is clear [4] that industry needs additional justifications in order to accept further the present defect assessment codes. The review of industrial needs indicates that feature component testing which best simulates the stress state of the actual component should be used to validate the failure predictions and increase confidence in defect assessment codes. It is therefore concluded that a standardisation programme for testing and analysis would be relevant. The programme objectives for VAMAS TWA25 committee on 'Creep/fatigue crack growth of components' are reviewed and conclusions are presented as to the future developments.

KEYWORDS

Fracture, creep, fatigue, crack growth, VAMAS, test standards

INTRODUCTION

VAMAS has been active in the field of standardisation of testing and analysis of elevated temperatures fracture mechanics specimens since 1987. Between 1987-1992 a new working group, TWA 11, was setup to develop and formulate a standard for a high temperature test method. This involved making recommendations for measuring the creep crack growth properties of materials and using the creep fracture mechanics parameter C^* in the analysis of the data. The method was restricted to creep ductile situations. The findings were incorporated into ASTM test procedure E1457-92 [5] that was the first standard to deal with crack growth testing at elevated temperatures.

This methodology was extended under TWA 19 (1993-1998) to conditions where only limited creep deformation or otherwise creep brittle conditions were observed. As a consequence of a Round Robin testing and analysis programme on four relatively creep brittle alloys, namely two aluminium a titanium and a carbon-manganese alloy, recommendations were made to change the original procedure, to incorporate the

methodology for a more creep brittle circumstances. Subsequently a revised version of the ASTM testing standards E1457-98 [6] was produced. Furthermore E1457-98 is about to be replaced with a new version in the year 2001 which will take into account most of VAMAS TWA 19 recommendations [7]. It will cover the wider range of creep ductile to creep brittle testing conditions observed in engineering alloys.

It is clear [4] that industry needs additional justifications in order to accept further the present defect assessment codes. As a result of experience gained from TWA 11 and TWA 19 the present TWA 25 was established in June 1999 with the broad aim of recommending testing, analysis and life prediction methods for assessing elevated temperature creep and creep/fatigue crack growth in metallic components containing defects. The overall objectives of TWA 25 are defined as follows

- Recommend accurate and reliable procedures for test methods in creep and creep/fatigue crack growth of non-standard geometries at elevated temperatures.
- Determine best procedures for analysing the test data using fracture mechanics concepts.
- Provide validation of results against measurements on standard laboratory specimens using the ASTM E1457-98.
- Propose relevant models for life assessment methods for cracked components.

BACKGROUND TO CRACK GROWTH RATE ANALYSIS

Crack growth in creep and fatigue can be described in various way using different correlating parameters [7-8]. However three parameters such as stress intensity factor, K [9], reference stress, σ_{ref} [10] and C^* [11] have been widely used, both in test data and the codes [1-6] to correlate creep crack growth rate data at elevated temperatures. The correlations of steady state crack growth rate with K, reference stress and C^* can be represented by straight lines of different slopes on log/log plots and expressed by power laws of the form

$$\dot{a} = AK^m \tag{1}$$

$$\dot{a} = H(\sigma_{ref})^p \tag{2}$$

$$\dot{a} = D_o C^{*\varphi} \tag{3}$$

where A, H, D_o, m, p and φ and are material constants. A steady state relationship between crack growth rate and the parameters in eqns. 2 and 3, physically imply a progressively accelerating creep crack growth rate. The elastic stress intensity factor K and the C^* parameter have generally been proposed for creep-brittle and creep-ductile materials, respectively. However it is necessary to verify the suitability of any of these parameters with respect to crack growth prediction in different materials.

For fatigue it is assumed that the mechanism is time and temperature independent. At room temperature under cyclic loading conditions, crack propagation usually occurs by a fatigue mechanism where the Paris Law can describe crack growth/cycle $(da/dN)_F$ in terms of stress intensity factor range ΔK by

$$(da/dN)_F = C\Delta K^m \tag{4}$$

Where da/dN is fatigue crack growth rate per cycle, C and m are material dependent parameters, which may be sensitive to the minimum to maximum load ratio R of the cycle. At elevated temperatures combined creep and fatigue crack growth may take place.

In most cases the crack growth rate at elevated temperature is described in terms of eqn. (3). The cracking per cycle due to fatigue is calculated from the equation (4). The predictions made using these equations may be over conservative where the stresses at one end of the cycle are compressive. If the margins against failure are insufficient, the fatigue crack growth calculations can be refined using the method given in the British Energy's R5 Procedure. The corrections for compressive stress given in BS7910 should not be used, as these are inapplicable when creep occurs. Total crack growth per cycle, (da/dN), is given by

$$(da/dN) = (da/dN)_C + (da/dN)_f \qquad (5)$$

Where this linear summation combines creep and creep/fatigue components. Previous studies [1-3] have shown that a simple cumulative damage law can be applied to describe creep/fatigue interactions.

The choice of the most appropriate crack growth rate relating parameter depends on whether the material exhibits creep-ductile or creep-brittle behaviour. Validity Criteria are employed [4-5] for choosing the appropriate crack growth rate relating parameter. For steady-state creep crack growth Ct or $C^*(t)$ [5-6] correlate rates in creep-ductile materials. C_t is used for data in the small-scale creep region to the extensive creep region and $C^*(t)$ for data in the extensive creep region. Using Eqn. 7 the steady-state creep crack growth rate in creep-brittle materials [6] is correlated by K.

Estimates of C^* can be obtained by experimental, numerical and limit analysis methods [1,11-13]. The experimental procedure is applicable to laboratory specimens as specified in ASTM E1457 [5-6] and the other two methods are needed when C^* is calculated for components. Experimentally C^* is calculated from the general relationship,

$$C^* = (P\dot{\Delta}_c / WB_n)F \qquad (6)$$

where $\dot{\Delta}_c$ is the load-line creep displacement rate, F is a non-dimensional factor which can be obtained from limit analysis techniques [13-14], B_n is the net thickness of the specimen with side-grooves and W is the width. In general, eqn. (6) is used to estimate the values of C^* for tests in the laboratory.

The method, which has been widely adopted in life assessment codes [1-3], is one based on reference stress concepts [1-3]. Reference stress procedures are employed to evaluate C^* for feature and actual component tests where the load-line deformation rate is not available. By determining;

$$C^* = \sigma_{ref} . \dot{\varepsilon}_{ref} \left(\frac{K}{\sigma_{ref}} \right)^2 \qquad (7)$$

Where $\dot{\varepsilon}_{ref}$ is the creep strain rate at the reference stress, σ_{ref} and K is the stress intensity factor. Usually it is most convenient to employ limit analysis to obtain $\sigma_{ref} = \sigma_y(P/P_{lc})$, where P_{lc} is the collapse load of a cracked body and σ_y is the yield stress. The value of P_{lc} will depend on the collapse mechanism assumed and whether plane stress or plane strain conditions apply. σ_{ref} can be derived from either limit load solutions [14] or directly from numerical calculations using elastic/plastic finite element analysis.

INDUSTRIAL BACKGROUND

Manufacturer's recommendations and their past experience have usually been the basis for the design of vital engine components such as turbine blades, vanes and discs and in critical engineering components such as gas steam pipes, pressure vessels and in weldments which might contain pre-existing defects. In recent times however crack growth initiation and failure analyses have become more acceptable as an independent design and remaining life assessment methodology. The development of high temperature fracture mechanics concepts, through which the time dependent effects of creep could be modelled, uses experimental uniaxial and crack growth data from simple laboratory tests specimens in order to predict failure times under operating conditions. Furthermore the improvement in non-destructive inspections and testing methods (NDT) has allowed smaller and smaller defects to be detected and the need for more reliable methods for predicting crack initiation/incubation periods and steady crack growth rates.

The final objective of developing testing procedures is to improve the reliability of life assessment codes, which use test information. In developing a testing standard methodology for laboratory specimens [5,6] a

first step was taken to improve life prediction procedures of components. However life extension calculations of components requires a validated fracture mechanics model for crack initiation and growth as well as detailed knowledge of component non-linear time dependent stress analysis, past service records and postulated future operations together with 'appropriate' mechanical properties. It therefore seems appropriate to develop a testing method for components and integrate it with life assessment codes for creep and creep/fatigue of components.

BACKGROUND TO LIFE ASSESSMENT CODES

Components in the power generation and petro-chemical industry operating at high temperatures are almost invariably submitted to static and/or combined cycle loading. They may fail by net section rupture, crack growth or a combination of both. The development of codes in different countries has moved in similar direction and in many cases the methodology has been borrowed from a previously available code in another country. The early approaches to high temperature life assessment show methodologies that were based on defect-free assessment codes. For example ASME Code Case N-47 [15] and the French RCC-MR [16], which have many similarities, are based on lifetime assessment of un-cracked structures. More recent methods make life assessments based on the presence of defects in the component. The more advanced codes dealing with defects over the range of creep and creep/fatigue interaction in initiation and growth of defects are the British R5, BS 7910 and French A16 [1-3] which have clear similarities in terms of methodology.

Generally defect assessment can be divided into two regions. Firstly the initiation region whose limit can be determined either from micro-mechanical models or from NDT limits and secondly the steady crack growth region which can be described using the fracture mechanics parameters such as K, reference stress σ_{ref} and C^*. The more recent defect assessment procedures mentioned above are based on experimental and analytical models to assess crack initiation and growth and to determine the remaining useful life of such components. These codes base their analysis on tests taken from laboratory specimens, which are invariably derived from small specimens at short test times. Therefore there is no direct verification of the predicted results with component testing [17]. This is an important point since size and geometry differences impose various degrees of constraint, which affects crack growth and initiation. Furthermore the development of residual stresses [18] during fabrication and loading history which may be non-existent in small laboratory testing will need to be considered for components.

In addition it is clear from these assessment methods that the correct evaluation of the relevant fracture mechanics parameters, for which the lifetime prediction times are dependent upon, are extremely important. It is also evident that the detailed calculation steps, which are proposed in these documents, do not in themselves improve the accuracy of the life prediction results. In any event as these procedures have been validated for limited sets of geometries and material data their use in other operating conditions will need careful judgment.

The codes [1-3] attempt to deal comprehensively with assessment and remaining life estimation procedures that can be used at the design stage and for in service situations. They stress upon a life assessment approach allowing the expert to decide upon the applicability of the predictions in relation to the operating circumstances. The concept implies that the codes need to show they are both reliable and understandable over a range of material and loading conditions that may not been have previously examined or validated by the code developer. This is particularly important as new higher strength steels, which have little or no long-term material properties database, are developed or used by the power industry.

Therefore the trend in the development of the codes is suggesting that, in addition to verification of data between laboratory tests and component tests, increased flexibility in dealing with the information and the analysis is an important factor. This acknowledges the fact that calculations however detailed and sophisticated will not necessarily come up with the correct predictions due to various unknowns in assessment procedure. These can be attributed to a number of factors many of which are beyond the control of the engineer using the code. They are as follows

- The available material property data for the analysis is invariably insufficient or crude and since they are usually taken from either historical data, results from different batches of material or tested in different laboratories with insufficient number of tests specimens they are likely to contain a large scatter.
- The scatter and sensitivity in creep properties inherently produce a large variation in the calculations. Upper and lower bounds are therefore introduced which give widely different life prediction results.
- The evaluation of the relevant parameters such as K, limit load concepts, reference stress σ_{ref} and C^* are different according to the method of derivation.
- The uses of short-term small laboratory data for use in long-term component life predictions further increases the possibilities of a wrong prediction.
- Difficulty in ascertaining the level of crack tip constraint and multi-axiality effects in the component will reduce the accuracy of crack growth predictions by about a factor of 30.
- Unknowns in modelling the actual loading history, component system stresses and additional unknowns such as little or no knowledge of past service history, residual stresses also act as sources of error in predictions.
- Non-destructive (NDT) methods of measuring defects in components, during operation and/or shutdown and insufficient crack measurement data during operation, is likely to add to errors involved in life-time assessment.

All these factors suggest that however detailed sophisticated and accurate a particular calculation is, the result will still need to be treated with caution. In addition the similarity of the approaches in the various codes do not necessarily imply that calculations by the different methods will give the same predictions. It may be possible that under certain controlled and validated circumstance the predictions can be optimised. It is clear that a critical comparison is only possible when the same method is used on another material and condition or the same test cases are examined by the different codes.

TWA 25 will attempt to fill this gap in order that modelling methods and test data from standard laboratory and feature component tests can be used with increased confidence in life estimation codes. Early indications are that relevant ASTM and ASME, API (American Petroleum Institute) and PVRC (Pressure Vessels Research Council (USA)) bodies have shown interest in the progress of this project. Clearly the recommendations resulting from this project will be useful for increasing confidence in defect assessment codes.

OBJECTIVES FOR TWA 25

On the basis of the established background of creep and creep/fatigue crack growth test methods and also life assessment methodology that has been discussed a programme of work has been setup in TWA 25. This is presented in this section.

The main objective is to establish accurate and reliable procedures for assessing creep crack growth at elevated temperatures in components, which contain defects, determine procedures for analysing the test data using fracture mechanics concepts and validation of results against measurements on standard laboratory specimens using ASTM E1457-98. Finally, in the light of established results, to propose recommendations to both testing methods for components and changes to life assessment codes.

It has been clear that there is substantial interest shown by the power generation industry in developing this field. A number of participants from Europe, Japan and USA are involved. The core group contains over 25 institutions that have registered interest and participate at the meetings. The overall programme for **TWA 25** is spread over 4 years. The plan for implementing the objectives are described below;

a) Gather together experts from industry and research institutes in order to identify their specific needs with respect to feature component testing.
b) Produce a data-base of available feature component test data

c) A survey of experts in relation to their preferred testing and analysis methods at high temperatures
d) A round robin analysis exercise using data from actual feature tests
e) Identify acceptable feature components and best practice for test methods.
f) Establish reliable methods for the analysis and interpretation of the data.
g) Develop methods of calibrating the results in terms of material crack growth properties data of standard fracture mechanics specimens.
h) Dissemination and recommendation of results via a special publication produced by experts in the field.

CONCLUSIONS

The background to the present TWA 25 has been presented and it has been established that there is a need in industry to improve life assessment methods in terms of creep and creep/fatigue crack initiation and growth in components, which operate at elevated temperatures. Therefore a programme of works has been set up where the emphasis has been initially placed on collecting information and experience from participating partners. The collection and the development of this knowledge database will dictate, to a great extent, the decisions regarding next round of this collaborative project. Indications are that there is firm industrial support for TWA 25 and it is hoped that over the next three years positive collaboration from members will make this a successful TWA.

REFERENCES

1. Ainsworth, R. A, (1999), editor R5: *Assessment procedure for the high temperature response of structures*, British Energy Generation Ltd. Procedure R5 Issue 2,.
2. British Standards- 7910: (1999), *Guide to methods of assessing the acceptability of flaws in fusion welded structures*, BSI, London.
3. AFCEN (1995), *RCC-MR, Appendix A16*, AFCEN, Paris.
4. K. Nikbin, *A unified European approach to high temperature defect assessment code and its incorporation in a Knowledge Base System*, In Proc. High Temperature Defect Assessment Conference, HIDA2', Stuttgart, Oct 2000.
5. ASTM E 1457-92, (1992), *Standard Test Method for Measurement of Creep Crack Growth Rates in Metals*, ASTM Standards 03.01.
6. ASTM E 1457-98, (1998), *Standard Test Method for Measurement of Creep Crack Growth Rates in Metals*, ASTM Standards 03.01.
7. Schwalbe, K.H., Ainsworth, R.H., Saxena, A. and Yokobori, T., (1999), *Recommendations for Modifications of ASTM E1457 to Include Creep-Brittle Materials*, Engineering Fracture Mechanics, Vol. 62, pp123-142.
8. A.Fuji ,M.Tabuchi, A.T.Yokobori,Jr., and T.Yokobori, (1999), *Engineering Fract. Mechanics vol*. 62, pp. 23-32.
9. Siverns, M. and Price, A.T., (1973), *Int. J. of Fracture, 9*, 199-207.
10. Williams, J.A. and Price, A.T., (1976), *Trans ASME* , 2114-222.
11. Nikbin, K. M., Smith, D. J. and Webster, G. A., *J Eng. Mat. and Tech*.,(1986), *ASME,* 108, 186-191.
12. Saxena, A., "Evaluation of Crack Tip Parameters for Characterizing Crack Growth: Results of the ASTM Round-Robin Program*", Materials at High Temperatures*, (1992), Vol.10, pp 79-91.
13. Webster, G. A., And Ainsworth, R. A., H*igh temperature component life assessment*, Chapman & Hall, 1994.
14. Miller A. G., *Int. J. of Press Vess.* And Piping(19880), 32, p 197-327.,.
15. ASME Boiler and Pressure Vessel Code (1991), *Case N-47 (29), Class 1 components in elevated temperature service, Section III, Division I,* ASME, New York.
16. RCC-MR (1985) Technical Appendix A3, Section 1, *Subsection Z, Materials design and construction rules for mechanical components of FBR nuclear test islands,* AFCEN, Paris.
17. Nikbin, K., *Comparison between crack growth in fracture mechanics specimens and feature component tests carried out in a low alloy steel*, (Feb. 2000), ASME Pressure Vessels and Piping Journal,.
18. Webster, G. A., *Role of residual stress in engineering application*, Mat. Science Forum, (2000), Vols, 347-349-pp1-9.

STATIC AND DYNAMIC FRACTURE PROPERTIES OF HIGH STRENGTH STEEL CHAIN MATERIALS

J. T. Dutton, D. M. Shuter and W. Geary

Health and Safety Laboratory, Broad Lane, Sheffield S3 7HQ, UK.

ABSTRACT

The development of future standards for high strength lifting chain will be based on performance, thus it is likely that toughness specifications will be included in these standards. Fracture mechanics makes it possible to define a minimum fracture toughness level for a component such that, in the presence of a defect, failure will not occur at the safe working load. The intention of this programme of research was to determine the fracture behaviour of conventional and boron-containing high strength steel chains over a range of operating temperatures and develop performance criteria for chain material to replace existing material specific requirements.

Charpy impact, quasi-static and dynamic fracture toughness tests were carried out on a conventional alloy chain material and two boron-containing chain materials, over the full operational temperature range of lifting chains. The differences between the materials were quantified in terms of ductile-brittle transition curve behaviour. The results clearly illustrated the superior behaviour of the alloy chain material with respect to the two boron-containing chain steels.

Engineering critical assessment methods were utilised to develop performance criteria for these lifting chain materials, allowing fracture stress data to be investigated as a function of defect size. Critical defect sizes, therefore, for a given applied loading regime, could be obtained for each of the materials.

Keywords: Lifting Chains, Quasi-Static Fracture Toughness, Dynamic Fracture Toughness, Engineering Critical Assessment (ECA).

INTRODUCTION

Current ISO and CEN product standards for high strength lifting chain are material specific rather than performance based. There are no toughness requirements contained within the current BS EN standard for 'short link chain for lifting purposes - safety'[1]. The main test criteria are based on the application of a manufacturing proof force, MPF (of at least 2.5 times the safe working load limit (WLL)) and subsequent examination by competent persons.

The development of future standards may be based on performance, thus there is a possibility that toughness specifications, in terms of Charpy energy requirements, may be included in ISO chain standards. In the past, such values have been based on "engineering judgement" rather than fracture mechanics considerations. Using the latter, it is possible to define a minimum fracture toughness level for a particular component such that, in the presence of a typical defect, failure will not occur at the safe working load. Conversion to an appropriate Charpy value, which can then be written into standards, can be achieved using a suitable

correlation, if available. This approach is used in many industries to define appropriate levels of toughness as there is general recognition that fracture toughness tests are too complicated and/or too expensive to be included in standards.

Boron steel is used in the manufacture of lifting chain in a number of countries, however, the performance of boron steels has not been fully documented. Boron steels are known to exhibit good levels of hardenability and adequate mechanical properties. The fracture toughness properties of these materials, however, has not been fully explored. This paper deals with the :

(i)   determination of fracture properties of grade 8 low alloy and boron steel chain material; and
(ii)   development of performance criteria for grade 8 chain material to replace existing material specific requirements.

MATERIALS

Three materials were selected for investigation. The materials chosen were: (i) an alloy chain steel containing 0.31% chromium, 0.57% nickel and 0.30% molybdenum, designated material A; (ii) a low alloy 1.5% manganese Japanese boron steel designated material J; and (iii) an EU manufactured low alloy boron steel, material B. The material was provided in the form of 13mm bar, heat treated by a chain manufacturer to achieve the relevant material properties. The chemical analysis of these materials is shown in Table 1. Only material A met the requirements outlined in BS EN 818-2,1996, i.e. contains at least 0.4% Nickel. Materials B and J contained very low levels of both molybdenum and nickel compared to the alloy steel. Materials B and J also contained relatively high levels of sulphur and phosphorus, respectively. It should also be noted that materials B and J contained similar levels of Boron. In the case of the alloy steel the very low Boron level is likely to be a tramp element rather than a deliberate addition. All three materials exhibited similar tempered martensitic structures, however, the structure of material J was somewhat coarser than the other two materials.

TABLE 1
CHEMICAL COMPOSITION OF CHAIN MATERIALS

Material	C	S	P	Si	Mn	Cr	Ni	Mo	Cu	Ti	B
A	0.251	0.003	0.005	0.301	1.57	0.317	0.590	0.307	0.03	0.004	0.0009
J	0.249	0.003	0.016	0.272	1.47	0.135	0.017	0.017	0.02	0.011	0.0035
B	0.22	0.013	0.005	0.204	1.04	0.246	0.036	0.036	0.08	0.046	0.003

EXPERIMENTAL AND RESULTS

Charpy Impact Energy

Sub-standard (9x9mm) specimens were tested in accordance with the Charpy 'V' notch testing standard [2]. The tests were performed over a range of temperatures between -40°C and +20°C (likely to cover the operational range of high strength chain materials). The Charpy impact transition temperature data is shown in Fig 1.

For many weldable structural and wrought steels, a minimum Charpy impact toughness requirement of 27J (0.34 J/mm^2) (~ 21J when corrected for the effect of using 9 x 9mm Charpy specimens) is specified. Materials A and B exhibit good levels of toughness over a wide range of temperatures - approximately 25J at -40°C and 50J at 20°C. Even at temperatures as low as -20°C these materials exhibited lower bound
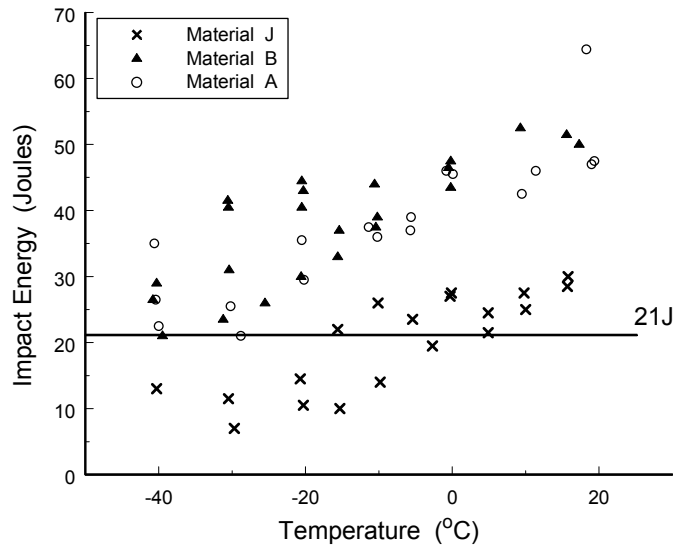
Figure 1 : Charpy Impact Data for all Three Chain Steels

toughness values well in excess of the 21J level. In contrast to the other materials it is evident from the Charpy impact data, that the J material exhibited much lower toughness levels over the whole test temperature range, i.e.10J was obtained at -40°C and 28J at +20°C, with the lower bound toughness data only exceeding the 21J level at ~5°C. In this case, the brittle fracture surfaces exhibited significant areas of low energy intergranular fracture, as shown in Fig 2. It should be noted that both cleavage and intergranular fracture were apparent even at the highest test temperatures (approaching room temperature).
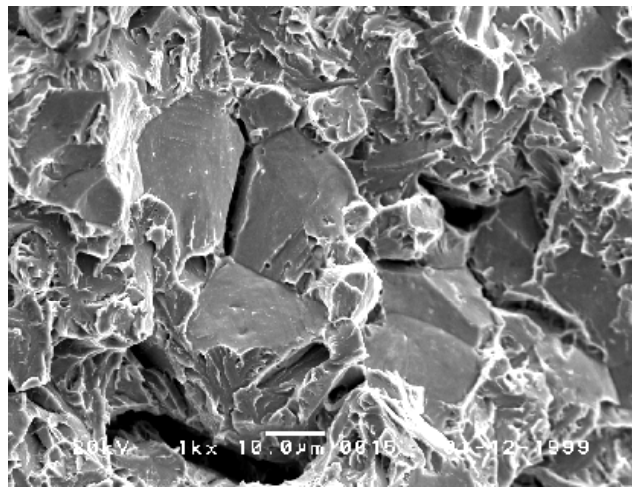
Figure 2 : Example of Intergranular Fracture Observed in Chain Material J

Fracture Toughness

A number of single edge notched bend (SENB) specimens, 9x9mm in section, were machined from each of the materials. It should be noted that a 60° notch was used rather the normal 45° (used in Charpy impact testing) to aid in the initiation of a fatigue pre-crack. The specimens were pre-cracked under fatigue conditions to create a sharp ~4.5mm long crack, suitable for fracture toughness testing.

Quasi-Static Fracture Toughness

All quasi-static tests were carried out on a servo-hydraulic test machine over a temperature range expected to produce both upper and lower shelf behaviour in these materials. Displacement during the tests was monitored using (i) a transducer connected to the actuator; and (ii) a calibrated clip gauge which was attached to the mouth of the test specimen. During each test, the applied load together with both displacement data outputs were captured for further analysis. These tests were performed in accordance with

the British Standard BS 7448 for conducting fracture toughness tests [3]. In order to derive full ductile-brittle transition temperature (DBTT) curves for the three materials, the amount of ductile crack growth prior to cleavage (measured using a scanning electron microscope) was plotted against temperature, as shown in Figure 3. (It should be noted that this approach was utilised, as excessive data scatter was obtained when plotting fracture energy as a function of temperature).
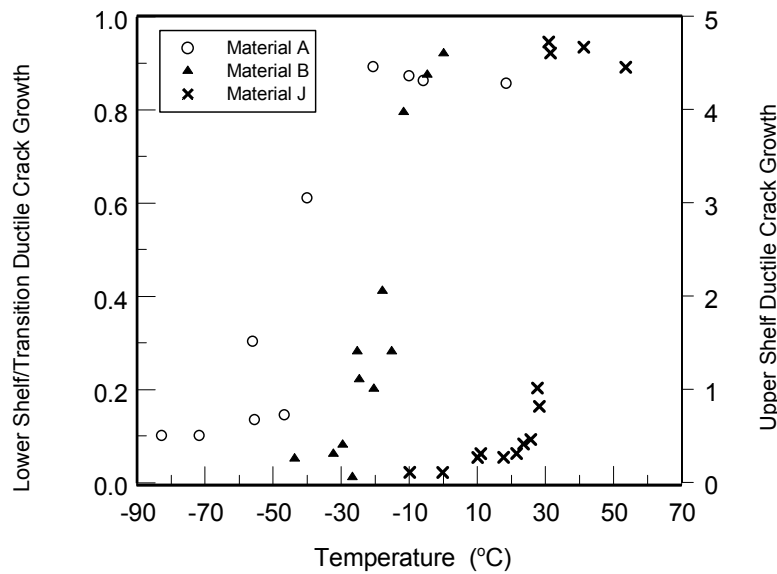
Figure 3 : Quasi-Static DBTT Curves Obtained for Materials A, B and J

The transition temperature range for material A appears to be from -50 to -35°C and for material B from -30 to -15°C. The DBTT curve obtained for material J indicates that even at ambient temperatures, lower transition behaviour will be exhibited.

Dynamic Fracture Toughness

All dynamic tests were conducted on an instrumented falling weight impact machine. Impact forces (F) were measured using a piezoelectric force transducer mounted just behind the striker mass. From the force (F) and the striker mass (m), the acceleration was calculated and by double integration of the acceleration, the displacement during the impact test was obtained. The specimens were loaded in three point bending using a mass of 12.9kg with an impact velocity of 2m/s. Dynamic fracture toughness, J, was calculated from the energy under the load-displacement curve using the methods outlined in BS 7448 [3]. Figure 4 shows the dynamic fracture toughness results, plotted as a function of temperature. The lower shelf dynamic toughness of materials A, B and J are broadly similar, however, the upper shelf toughness of material A is some 60% higher than that of materials B and J.

DISCUSSION

Fracture Properties

The Charpy DBTT curves (see Fig 1) obtained for materials A and B are very similar, which is in direct contrast to the results obtained from the dynamic fracture toughness tests, where materials B and J exhibit significantly different behaviour to that shown by material A (shown in Figure 4). The dynamic tests had been carried out on pre-cracked specimens and the differences in behaviour could be attributable to the fact that the boron chain steels (materials B and J) are particularly sensitive to defects.

Intergranular crack growth was observed on the fracture surfaces of the boron chain steels. This is a low energy mechanism and will reduce the toughness of a material and thus explains the reduction in toughness observed for materials B and J, when subjected to both quasi-static and dynamic loading conditions.
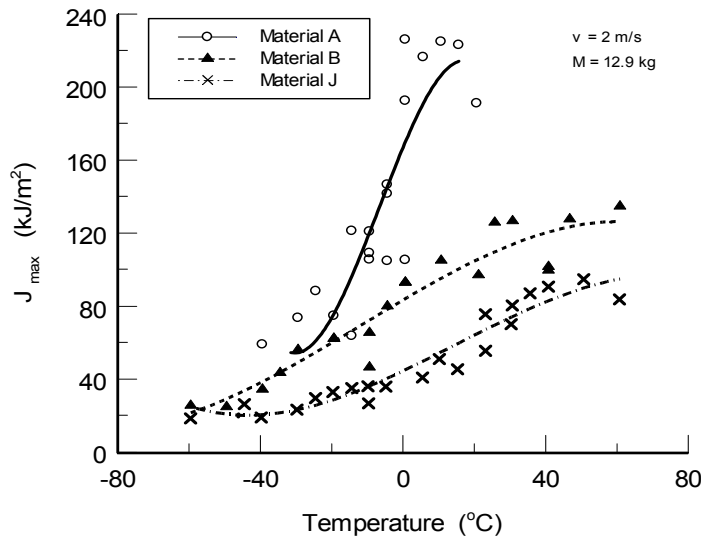
Figure 4 : Dynamic DBTT Curves Obtained for Chain Materials A, B and J

Material J contains high concentrations of phosphorus and B contains relatively high concentrations sulphur. The intergranular mode of failure, observed in materials B and J could be associated with either an accumulation of impurity elements or the formation of a film of a brittle phase on the grain boundaries and suggests that the heat treatment or the metallurgical balance of the material was not optimised.

As may be expected, under dynamic loading conditions, the effect of increasing the strain rate is to substantially increase transition temperatures obtained for the three materials. For example, for the alloy steel chain, the mid-toughness transition temperature increases from -45°C, for quasi-static loading, to -10°C obtained under dynamic loading conditions. This effect is not as pronounced for the two boron steels and, in the case of the J series material, upper shelf behaviour was not obtained, even at the highest test temperature (~60°C). It is also evident that the upper shelf fracture toughness values obtained under dynamic test conditions for all three materials appear to be greater than those obtained from quasi-static tests conducted on similar specimens. This may be accounted for by the increase in the material yield strength associated with an increased strain rate.

Performance Criteria

The most conservative toughness (K_{mat}) values (even when compared with those obtained under quasi-static and dynamic loading conditions) were obtained using the relevant Charpy energy-K_{IC} correlations contained within Appendix J of the British Standard Guide on Methods for assessing the acceptability of flaws, BS 7910 [4]. (It should be noted, however, that the correlations contained within BS 7910 are based on Charpy impact data obtained from 10x10mm specimens). Engineering critical assessments (ECA) were performed using these conservative K_{mat} values and the methods contained in BS 7910 [4], in order to develop performance criteria for the three chain materials (allowing fracture stress to be investigated as a function of defect size).

Results suggest that at a nominal stress of 300MPa (i.e. equivalent to a WLL of 5.3 tonnes for a 13mm chain diameter [1]), materials A and B could tolerate defects in excess of 5mm in depth, even on the lower shelf, which is in agreement with results obtained elsewhere [5]. Even the worst case material (lower shelf J material), at the working load limit, was determined to be capable of withstanding a defect of ~2.8mm in depth prior to brittle fracture. It is suggested, therefore, that Charpy impact toughness values of 21J (or 0.34 J/mm^2), obtained from 9 x 9 mm sub-size specimens, and above will lead to critical defect depths in excess of 5mm for these chain materials operating at safe working load levels.

It should be noted that the safety factors [1] used in the determination of the safe working load limits for chains allow relatively large defects to exist in the chain (over the whole range of operating temperatures) prior to brittle fracture. By using non-destructive test (NDT) techniques, such as dye penetrant, therefore, such cracks should be detected before they can reach a critical size. Other NDT methods such as magnetic

particle inspection (MPI) may be difficult to implement. Based on a true mean stress at the manufacturing proof force (MPF) of ~750 MPa [1], however, recalculating the critical defect sizes for material J yields values between 0.53mm (at -40°C) and 2.7mm (at +20°C). For materials A and B, the recalculated critical defect sizes ranged from ~3.0mm (at -40°C) to ~4.2mm (at +20°C). It is clear that defects, in the case of material J for example, of 0.53mm in depth could survive the MPF and would be stable at the WLL. Consideration would need to be given, therefore, to the propagation of sub-critical defects by a corrosion or fatigue mechanism, for example, and this would inform decision making on NDT or proof test intervals

CONCLUSIONS

Materials A and B exhibit good levels of Charpy impact toughness over a wide range of temperatures. Even at temperatures as low as -20°C, both materials exhibit lower bound notch toughness values well in excess of 21J. The J material exhibits much lower toughness levels, with the lower bound Charpy impact toughness data only exceeding 21J at ~5°C. In this case the brittle fracture surfaces exhibited significant areas of low energy intergranular fracture.

In general, boron chain steels (materials B and J) are particularly sensitive to crack like defects. This may be attributed to intergranular cracking along grain boundaries which occurs in these materials even during pre-cracking. It is evident therefore that the toughness and thus the defect tolerance of these boron chain steels will be low compared with that of the alloy steel chain.

K_{mat} values derived from Charpy impact data, yielded lower bound toughness values. The critical defect sizes calculated, based on these K_{mat} values (as opposed to K values based on the results from fracture toughness tests), were thus conservative.

It is recommended that chain steels should exhibit a minimum Charpy impact energy of 27J (0.34 J/mm^{2}) (equivalent to 21J for a 9 x 9mm sub-size specimen) over the full range of operating temperatures. This level of toughness in the parent material ensures that critical defect sizes, based on either the WLL or MPF will be large enough to be detected by current NDT techniques. Below this level, particularly for load levels approaching the MPF, critical defect sizes become relatively small and could prove difficult to detect.

ACKNOWLEDGEMENT

REFERENCES

1. BS EN 818-2 (1997). Short link chain for lifting purposes - Safety. Part 2 : Medium tolerance chain for chain slings – Grade 8, BS EN 818-2, 1997.
2. BS 10045-1 (1990). British Standard for Charpy Impact Test on Metallic Materials. Test Method ('U' and 'V' Notches). BS EN 10045-1. 1990.
3. BS 7448 (1991).British Standard for Fracture Mechanics Toughness Tests : Part 1. Method for Determination of K_{IC}, Critical CTOD and Critical J Values of Metallic Materials. BS 7448 : Part 1: 1991.
4. BS 7910 (1999).British Standard guide on methods for assessing the acceptability of flaws in fusion welded structures. BS 7910, 1999.
5. Cadman, A. J. and Bann, P. J. (1985).'Assessment of the material properties of a high strength low alloy chain steel containing a boron addition' RLSD Section Report No. IR/L/MM/85/2. Health & Safety Executive, Research and Laboratory Services Division. Sheffield. 1985.

STATISTICAL STUDY OF FRACTURE IN CONCRETE

Tai K. Wang[1], J.G.M. van Mier[2] and T. N. Bittencourt[1]

[1]Department of Structural Engineering and Foundation
Polytechnic School of University of Sao Paulo, Sao Paulo, Brazil
[2]Faculty of Civil Engineering and Geosciences
Delft University of Technology, Delft, the Netherlands

ABSTRACT: This paper describes the use of statistical distributions (Gaussian and Weibull distributions) for simulating the material heterogeneity of concrete in order to overcome the computational problems which limit the application of lattice-type fracture models in large-scale structures. Uniaxial tensile tests are simulated using a regular triangular lattice to compare with the numerical results obtained earlier by Van Vliet [3]. The numerical results obtained by this method proved to be useful to predict the structural behaviour of concrete. Since the statistical distributions omit the influence of real microstructure of concrete, the method appears to be less suitable for simulating correct crack patterns.

KEYWORDS: statistical distribution, numerical simulation, lattice model, concrete

INTRODUCTION

In the "Delft lattice model" concrete is schematised as a network of two noded Bernoulli beams [2,5,9]. Concrete is a heterogeneous material, and the most straightforward way to include effects from heterogeneity is through direct implementation of disorder. Several methods can be distinguished [1,5]. The most common way to include the material heterogeneity is to superimpose the mesh (lattice) on top of a computer generated or digital image of a real concrete structure [1,5]. For concrete three material phases are distinguished, namely aggregate, matrix and interfacial transition zone (bond). Different stiffness and strength are assigned to the beams that fall in each phase. By removing in each loading step the beam element with the highest stress over strength ratio, fracture is simulated. A simple fracture criterion is used as described in [2,5], which is based on the effective stress.

Note that lattice analyses are size dependent, although this deficiency is overcome to a large extent by including the condition that the individual beam length should be smaller than (at least) 1/3 of the minimum aggregate of the specimen. Then, it is necessary to use rather small beam lengths, which require considerable computational power. One of the solutions is to employ statistical distributions to introduce the material heterogeneity on coarser meshes without discretized aggregate structures. The strength of the beam elements is the most obvious choice as parameter in a statistical distribution. Several examples of the use of statistical distributions can be found in [5,6,7]. However, a systematic survey of the effect of a certain statistical distribution on fracture processes in concrete has never been carried out. In this paper Gaussian and Weibull distributions are employed to evaluate the effect of different scales of heterogeneity.

NUMERICAL SIMULATIONS

In order to allow for a comparison with the results obtained by Van Vliet [3], all the elastic computations were performed on a regular triangular lattice of 80×80 mm^2. Figure 1 shows the geometry, boundary and load conditions used by Van Vliet [3]. Firstly, five examples were run with the beam length l =1 mm and different aggregate structures were generated by computer with $2 \leq d \leq 16$ mm and P_k = 0.75 for these five examples respectively, where d is particle diameter and P_k the volume ratio of aggregates. The particles were assumed to be distributed according to a Fuller curve. The input parameters are: $E_m=E_b=25$ GPa, $E_a=70$ GPa (Young's modulus of matrix, bond and aggregate, respectively) and $f_m=5$MPa, $f_b=1.25$MPa, $f_a=10$MPa (tensile strength of matrix, bond and aggregate phases, respectively) where the beam height was given from the relation h/l with the global Poisson ratio $\nu = 0.2$ [10].
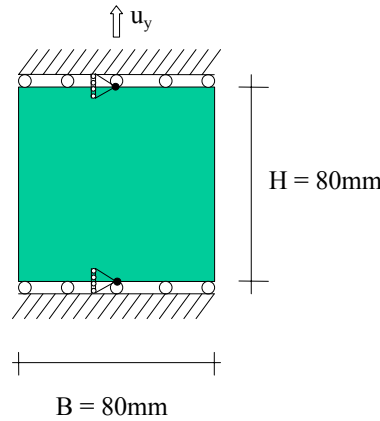
Figure 1. Geometry, boundary and load conditions used for numerical simulations.

Secondly, the same numerical simulations were performed using random number generators according to the Gaussian and the Weibull distribution, to assign different tensile strengths to the beams in a regular triangular lattice. Four different scales were investigated (i.e. beam lengths of 1, 2, 4 and 10 mm),which are compared with the five aggregate structures mentioned above with lattice length l = 1mm. A minimum and a maximum tensile strength was defined for the beam elements (f_{min} = 1.25 MPa and f_{max} = 10 MPa), which correspond to the tensile strength of the bond and the aggregate elements of the particle structures. When the generated strength is smaller than f_{min} or greater than f_{max} , a new value will be generated. For the Gaussian distribution, two input parameters were employed, namely the mean value (μ) and standard deviation (λ). The mean strength was taken equal to 6 MPa, whereas the standard deviations varied from 2 to 4 MPa. For the Weibull distribution, two parameters were employed, namely the scale parameter (δ) and the shape parameter (β). In this paper the scale parameter is assumed to be equal to 4 MPa and the shape parameter is varied from 1 to 3 MPa. The strength distribution of interface, matrix and aggregate elements in two different particle distributions was shown in figure 2 to compare with the strength distributions generated by Gaussian and Weibull distributions. More details about these two distributions can be found in Montgomery et al. [4].
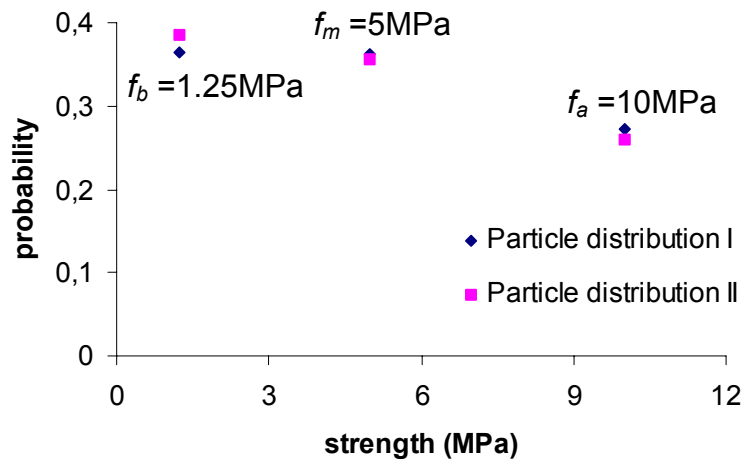
Figure 2a. Strength distribution of bond, matrix and aggregate phases in two particle distributions

(b)

(c)
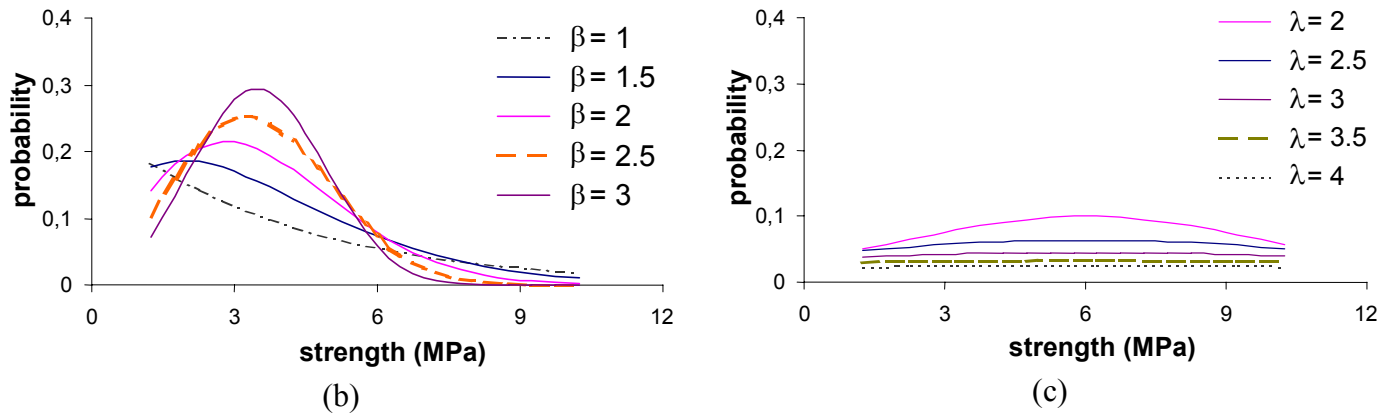
Figure 2b-c. Comparison of strength distribution: b) following different Gaussian distributions and c) following different Weibull distributions.

Figure 3 shows a comparison of crack patterns of an aggregate structure, of the Gaussian distribution structures with λ=2 MPa, l=2 and 4 mm and of the Weibull distribution with β=1 MPa, l=2 and 4 mm. The two crack stages in each analysis correspond to the situation at peak load and at the end of the analysis.

404 beams removed

1146 beams removed

a) crack propagation in a lattice with a computer generated particle distribution

63 beams removed   211 beams removed

b1) Gaussian distribution (l=2mm)

50 beams removed   400 beams removed

c1) Weibull distribution (l=2mm)

23 beams removed   75 beams removed

b2) Gaussian distribution (l=4mm)

30 beams removed   145 beams removed

c2) Weibull distribution (l=4mm)

Figure 3. Comparison of crack evolution of (a) a computer generated particle distribution structure (b) Gaussian distribution structures and (c) Weibull distribution structures

The results of the numerical simulations with aggregate structures are shown in figure 4a1. In order to compare with the results obtained by statistical distributions, normalised load-displacement curves of aggregate structures and statistical distributions are presented in figure 4b and 4c.
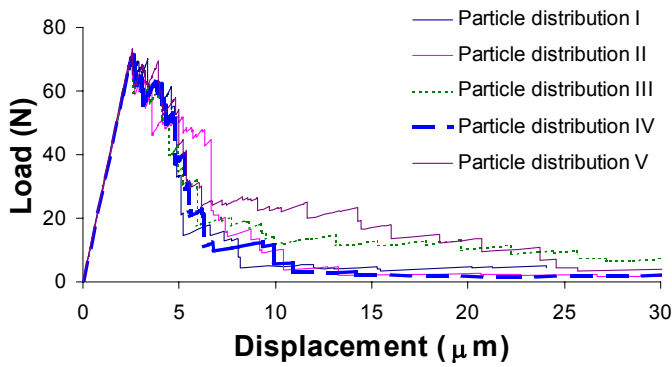
a1) load-displacement curves
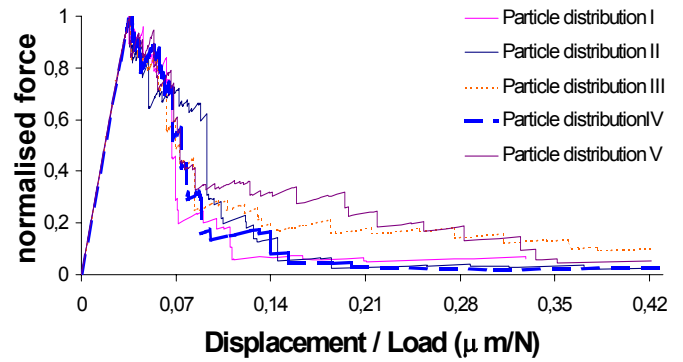
a2) normalised load-displacement curves

Figure 4a. Smoothened results of five different aggregate structures (l = 1mm)

b) Gaussian Distribution

c)Weibull distribution
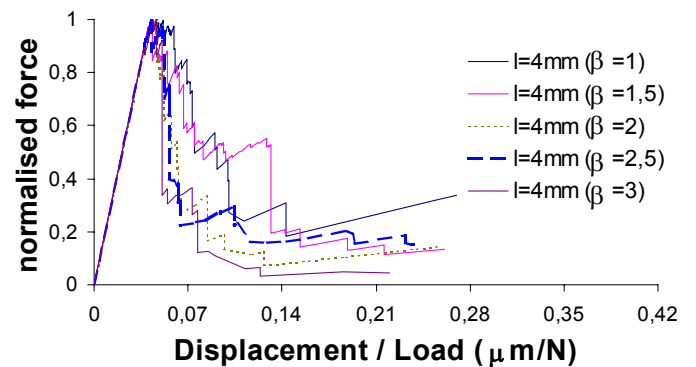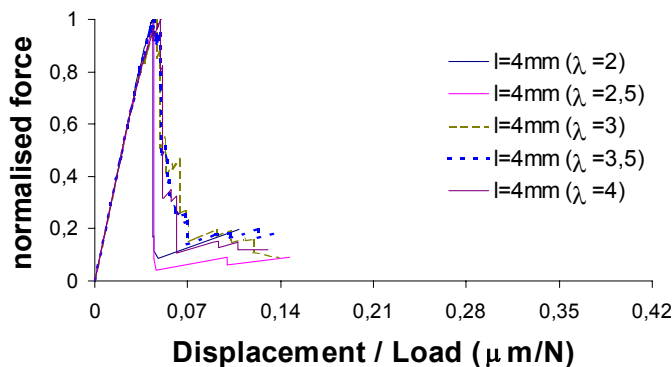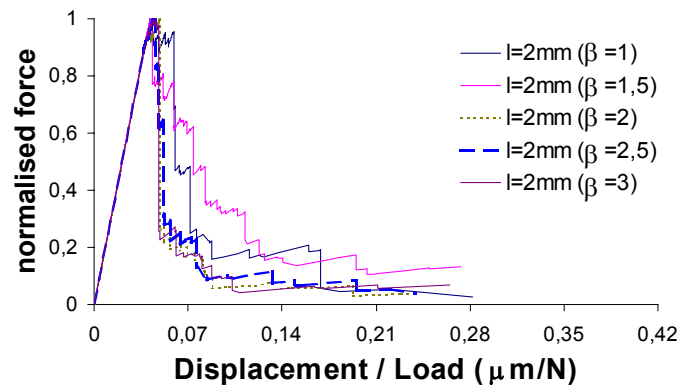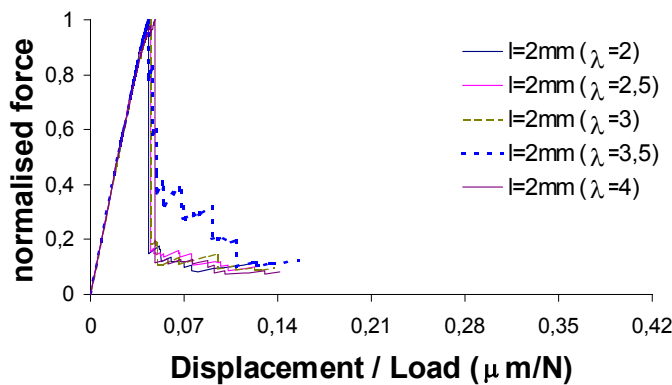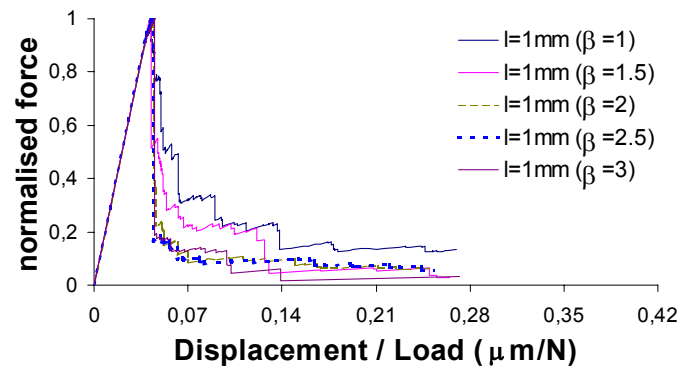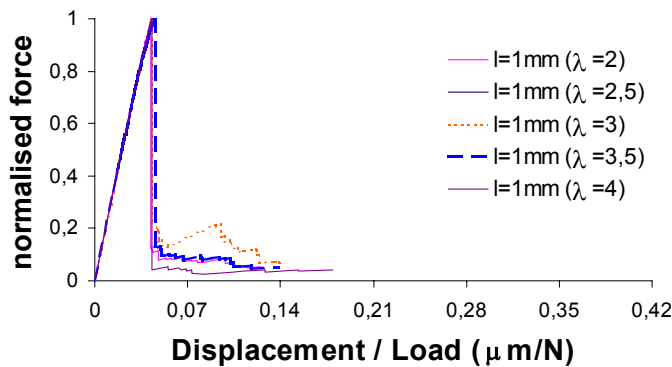
b) Gaussian Distribution   c)Weibull distribution
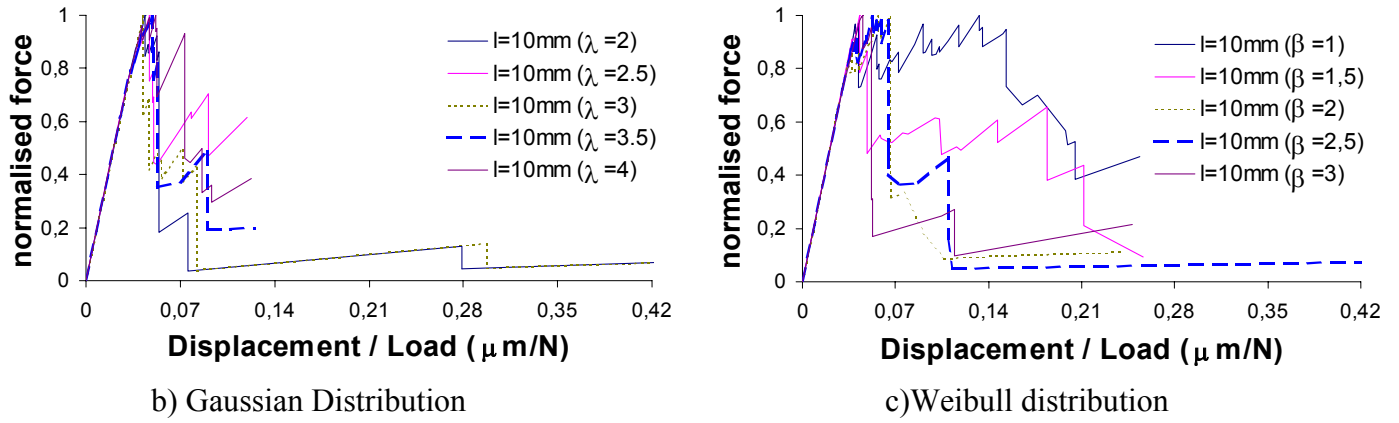
Figure 4b-c. Comparison of normalised force–displacement: b) Gaussian distribution with λ varying from 2 to 4 and c) Weibull distribution with β varying from 1 to 3. Note that both the x-axis and y-axis have been normalised with respect to the maximum load in each analysis.

DISCUSSION

For the two statistical distributions, we can observe that, in a certain range of lattice beam sizes, the structural behaviour corresponds to the results obtained from the analyses with aggregate overlay. But when the mesh size increases, in particular to $l = 10$ mm, there is a clear discrepancy. It means that, to some extent, a rather coarse mesh ($l = 2$-4 mm) can be used with statistically distributed beam properties to analyse the behaviour of a large-scale structure instead of using a much more refined mesh with an underlying aggregate structure. With the increase of the beam length, the computational time per beam removal decreases significantly, whereas also less beams need to be removed until the end of the analysis in the coarser meshes. In this way the computational problems encountered in lattice-type fracture models for the analysis of large-scale structures can be dismissed. From figure 4a it can be observed that the different particle distributions affect mostly the softening parts of the load-displacement diagrams. Even for absolute force-displacement curves, quite small difference in maximum admissive tensile forces for different particle distributions exist (a maximum of 3.1% of difference was observed by numerical simulations). From the force-displacement curves of figure 4 it can be observed that the Weibull distribution corresponds better to the results obtained from aggregate structures. As shown in figure 2, the distribution of tensile strength in an aggregate structure in the lattice beams is more similar to a Weibull distribution than to a Gaussian distribution.

Comparing the crack patterns between regular lattices with and without underlying aggregate structures (see figure 3), it can be seen that cracking is initially more distributed when a statistical distribution of beam strength is used rather than a particle overlay. In the latter case, the positions of the particles have a big influence on the crack patterns. For the analyses with a particle distribution the weak elements are grouped in the interface zones around the aggregates. The variation of beam lengths also has a significant effect on the crack evolution: with increasing length much detail in the fracture patterns is lost. Fracture in a regular triangular lattice with the same strength assigned to all beam elements results in a subsequent removal of all the elements along a single row, see for example in Van Vliet [3]. The phenomenon does not occur when a particle distribution is imposed on the lattice, see figure 3a. Also from figure 3, it can be seen that subsequent removal of elements in the same row does not occur when a statistical distribution of beam strength due to the random distribution of weak elements is applied, which is especially true for the Weibull distribution. In the case of a Gaussian distribution the final fracture plane almost seems to follow a single row of elements (figure 3b1 and 3b2), but this should be expected in view of the relatively 'flat' strength distribution of Figure 2c.

Van Vliet [3] showed that the amount and location of weak elements decides how crack propagation proceeds, which explains why the use of statistical distribution without considering the microstructure of concrete leads to consequent incorrect crack patterns. This shows the limitation of this method where statistical information is used rather than a correct representation of material structure.

Experimental observations show that cracks in concrete are not continuous but show a lot of overlaps, mainly around the aggregate particles. Pieces of material bridge the two crack faces and as a consequence transfer of stress remains possible, see Van Mier [8]. Small overlaps (bridges) observed in experiments can not be captured in the simulations where the beam length is much larger than the size of the bridges. Thus, in order to obtain both correct crack patterns (and crack mechanisms) and load-displacement behaviour, the disorder implemented in the model has to be related to the real heterogeneity in the material. Unfortunately, however, this leads to an enormous increase of computational effort.

REFERENCES

1. Schlangen, E. and Garboczi, E. J. (1997) Fracture simulations of concrete using lattice models: computational aspects. *Engineering Fracture Mechanics*, Vol. 57, No. 2/3, pp. 319-332.
2. Vervuurt, A. (1997) *Interface fracture in concrete*. Ph.D. thesis, Delft University of Technology.
3. Van Vliet, M.R.A. (2000) *Size Effect in Tensile Fracture of Concrete and Rock*. PhD thesis, Delft University of Technology.
4. Montgomery, D.C. and Runger, G.C. (1999) Applied statistics and probability for engineers. 2nd. Edition, John Wiley & Sons, Inc.
5. Schlangen, E. (1993) Experimental and numerical analysis of fracture processes in concrete. PhD thesis, Delft University of Technology.
6. Hermann, H. J., Hansen, H. and Roux, S. (1989) Fracture of disordered, elastic lattices in two dimensions, Physical Review B, 39(1), pp. 637-648.
7. Chiaia, B., Vervuurt, A. and van Mier, J. G. M. (1997) lattice model evaluation of progressive failure in disordered particle composites. *Engineering Fracture Mechanics*, Vol. 57, No. 2/3, pp. 301-318.
8. Van Mier, J. G. M. (1991) Mode I fracture of concrete: discontinuous crack growth and crack interface grain bridging. Cement and Concrete Research, 21(1), pp. 1-15.
9. Schlangen, E. and Van Mier, J.G.M. (1992) Experimental and Numerical Analysis of the Micro-mechanisms of Fracture of Cement-Based Composites, *Cem. Conc. Comp.*, 14(2), pp. 105-118.
10. Schlangen, E. and Van Mier, J.G.M. (1994) Fracture Simulations in Concrete and Rock using a Random Lattice, in *Computer Methods and Advances in Geomechanics* (Siriwardane, H. and Zaman, M.M., eds.), Balkema, Rotterdam, pp. 1641-1646.

STATISTICS OF ACOUSTIC EMISSION IN PAPER FRACTURE

L.I. Salminen[1], A.I. Tolvanen[1], M.J. Alava[1], and K.J. Niskanen[2]

[1]Laboratory of Physics, Helsinki University of Technology, P.O. Box 1100, FIN-02015 HUT, Finland
[2]KCL Science and Consulting, P.O. Box 70, FIN-02151 Espoo, Finland

ABSTRACT

Experiments on acoustic emission during the tensile failure of paper are reported. These support the idea that the AE activity is correlated with a decrease in the elastic modulus which reduces the stored elastic energy. Tests with different strain rates indicate that in general the AE statistics depend quite weakly on the rate. This is demonstrated for the intervals between individual events. They follow for large intervals a power-law probability distribution independent of the strain rate, with the exponent close to unity. The event energy distributions have power-law tails, too.

KEYWORDS

acoustic emission, fracture, paper, power law, energy release, time interval, crack propagation

INTRODUCTION

Acoustic emission (AE) is a phenomenon whereby transient elastic waves are generated by the rapid release of energy from a localized source within a material. Therefore it is a experimental technique that can be applied to following damage and fracture development in disordered materials. In such systems the acoustic emission should follow the formation of microcracks. There are intriguing observations of power-law -like scaling laws in the AE statistics from various experimental situations [1, 2, 3]. It seems that e.g. the distribution of the released energy can follow such a power-law -like probability distribution. Understanding such scaling behavior in terms of the statistical mechanics of fracture is still an open question [4, 5, 6, 7, 8].

The structure of paper is strongly heterogeneous on two lengthscales. The characteristic dimensions of the building blocks, fibers vary between 1 μm and 1 mm. The fibers form flocs, which in the manufacturing process are organized in a random manner to assemble a paper sheet. The local areal mass density has a typical coefficient of variation of the order of 10 %. Likewise, the local fracture properties (strain, stress, ductility) vary even more. Unlike in most composite materials, the properties of fibers have a large quantitative effect on the structure they constitute. Both the properties of the furnish (fiber raw-material) and the network are difficult to connect to fracture.

The microscopic origins of AE release in paper are not known in detail. Whatever the actual source, AE can be considered as an indication of elementary rupture events. As an analogy, in fiber composites four methods of energy dissipation exist: 1) plastic elongation of fibers, 2) breaking of fibers, 3) breaking of bonds, and 4) fiber-to-fiber friction when fibers pull-out. Bond breakages are considered as the primary microscopic breaking
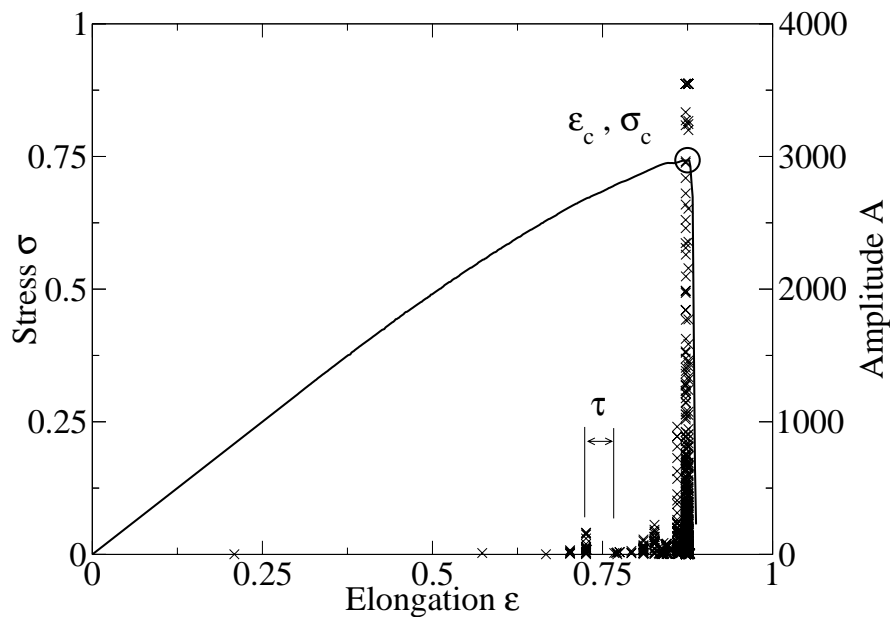
Figure 1: Example of a tensile test and acoustic emission in paper fracture. The crosses are the amplitudes A of acoustic emission, the solid line is the stress-strain curve, ϵ_c, σ_c denote the position of maximum load. τ is the silent interval between two events. (MD dry, rate of elongation 10 %/mm).

process in paper though fiber failures may also contribute. Plastic elongation produces probably no AE. The relative orders of magnitude of AE originating from these mechanisms are in any case unknown. Work by Yamauchi et al. implies that fiber and bond breakages could be distinguished by the amplitude spectrum[9].

EXPERIMENTS

The aim of the experiments was to use AE to resolve the dynamics of damage in mode I tensile tests on paper [10]. The main tool is statistical analysis which also allows a comparison to other statistical fracture results. We measured only one sample material, newsprint, a paper consisting of wide range of size of mechanically pulped fiber fragments. Basis weight (surface-mass) of paper was 44 g/m^2. Mode I tests were done in two principal sample orientations, the machine direction "MD" and the cross direction "CD". The fiber orientation is strongly biased to MD. In MD we analyzed two moisture contents 8 %, (dry), and 16 %, (wet). The properties of wet MD are presumably in between dry MD and dry CD. The span length l_0 was 100 mm, the width w of strips 100 mm and a single edge notch of 15 mm was cut. Each measurement was repeated 20 times. We had 7 elongation rates in the range 0.1 mm/min - 100 min/min, ie. the rate was varied over three orders of magnitude.

The stress-strain behavior of paper has a few general features. If the stress is parallel to MD, the response is relatively brittle. The strain at break is always close to 1 per cent. The material obeys Hooke's law i.e. the tangential modulus remains almost the same through the rising part. After the load maximum σ_c the load decreases and a crack propagates rapidly (Figure 1). In CD the functional behavior is much more ductile, the strain at break is 2 - 4 per cent and the elongation includes a plastic component from the very beginning. The tangential modulus may decrease by 50 per cent. The final crack propagates much slower and may even stop a few times.

The experimental apparatus consists of an AE transducer, an amplifier, and data acquisition and signal conditioning software. The transducer is a rubber faced piezoelectric transducer from Etalon Inc. The rest of the apparatus has been developed in the Laboratory of Physics at HUT. The time resolution by which individual AE events can be observed is 10 μs. In our geometry the source-to-transducer transmission time of AE is about
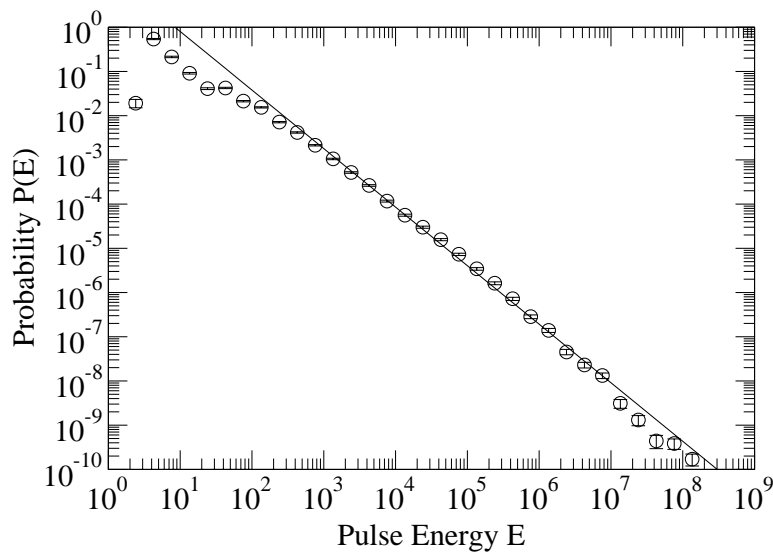
Figure 2: A power law fit for AE pulse energy $P(E) \sim E^{\gamma}$, with $\gamma = -1.3 \pm 0.2$. The circles are the experimental data. The error in E is equal to the bin-width, and only the errors in P are shown. (MD wet, 100 %/mm, a fast rate of elongation.)

10 μs. During the test we do not threshold the signal in any way. The analysis is done completely off-line. The acoustic coupling between the transducer and the paper is lost at the end of test, so the final events are sometimes missing. Further details of the apparatus are described elsewhere. In our experiments the velocity of the crack is always slow so that the stress-field is close to static except during individual AE events, perhaps.

RESULTS

The occurrence of AE in paper is relatively rare so statistical analysis is needed. Here correlation analysis is not justifiable since the tensile test is not stationary in time. Logarithmically scaled histograms are capable of presenting the frequent and infrequent events in same figure, and eventual power laws $y \sim x^{-\alpha}$ are seen as straight lines on a log-log scale. One of the advantages of scaling analysis is its robustness concerning the experimental details like signal thresholding and pulse detection procedures. To benefit from power law analysis, large data sets are essential.

Tensile test and the crack propagation vs. AE
The experiments indicate that the properties of acoustic emission are not directly related to the critical strength or strain or the sample elastic modulus. The mean number of AE events before the rupture is about constant and has no correlation with $\dot{\epsilon}$, the rate of elongation. The number of events after the maximum load σ_c decreases roughly in an exponential manner as $\dot{\epsilon}$ increases. For elongation rates less than 10 mm/min most events happen during the crack propagation phase. It is possible that the same holds for higher elongation rates. The correlation of the number of events in the crack propagation phase and the strain rate implies that the fracture process zone (FPZ) may be reduced in size with $\dot{\epsilon}$. The newsprint is rather brittle, thus it is not surprising that the tensile index is found to be almost independent of $\dot{\epsilon}$. As $\dot{\epsilon}$ is varied the behavior of the average magnitude of the elastic modulus has a nice correlation with the average amplitude of AE. However for individual samples any direct correlation is absent. This reflects the statistical nature of AE.

Statistical laws
The energy probability distribution is found to follow a power-law behavior, in analogy with the Gutenberg-Richter scaling of earthquakes. The energy of an AE pulse E is defined as the integral of the squared amplitude of a pulse. We have used four alternative methods for pulse discrimination with no qualitative differences, to
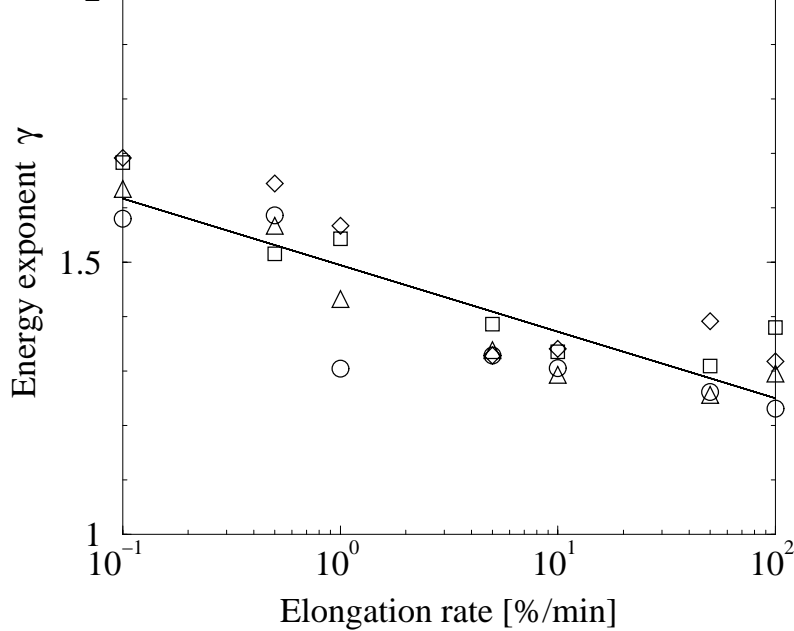
Figure 3: The energy exponent γ as a function of the rate of elongation $\dot{\epsilon}$. The four different symbols represent the energy scaling exponents γ of dry MD samples determined with four interchangeable methods. The power-law scaling regime extends always at least 2 decades in E. The line shows a least square fit ($\gamma \sim 1.5 + 0.05\% \times \log(\dot{\epsilon})$) to all the datapoints.

account for the possible lack of temporal resolution which would result in several AE events being joined together. The pulse energy probability scales as $P(E) \sim E^{-\gamma}$, where γ defines the energy exponent (Figure 2 shows an example of a fit). For amplitudes the same scaling law reads $P(A) \sim A^{-\beta}$, with $\frac{1+\beta}{2} = \delta$.

In our experiments the exponent γ varies slightly with the rate of elongation (shown Figure 3) and also with the test direction. The rate-dependence seems to be a logarithmic function of $\dot{\epsilon}$, irrespective of the discrimination method. High elongation rates give lower values of the exponent γ. With wet MD the scaling region is shorter and the exponents are higher than for dry MD. Experiments in CD give the highest and least reliable values of γ. In practice these results imply that the microcrack tolerance of paper increases in the order MD dry - MD wet - CD dry. To compare, for infinitely slow elongation rates i.e. in a creep test in cellular glass the measured exponent γ is found to be 1.5[1]. For high pressure tanks the energy exponent is 2.0[12]. For AE experiments in volcanic rocks the exponent $\gamma = 1.5 \pm 0.1$[11]. As a function of reduced stress $\frac{\sigma_c - \sigma}{\sigma_c}$ we found no power-law for the cumulated energy $\int E$. In wood and fiberglass Guarino et al. reported a proportionality of $\int E \sim \left(\frac{\sigma_c - \sigma}{\sigma_c}\right)^{-\eta}$, with $\eta \approx 0.26$[2].

The inter-pulse times τ ('dead time') between AE events obey an an Omori-type power law for large τ, similarly to earthquake data. This means that the probability $P(\tau)$ is proportional to $\tau^{-\kappa}$. Within the statistical errors the exponent κ is uncorrelated with the rate of elongation $\dot{\epsilon}$ and the value is close to 1.0 (Figure 4). For creep experiments on cellular glass κ has been reported to be 1.3 [1] and in volcanic rocks $\kappa = 1.2 - 1.3$[11]. The apparent stochasticity in the time delays between AE events before critical crack growth can be interpreted as a lack of correlation between consecutive events. Slight caution should be applied since the temporal resolution of the system may not be sufficient during the most active time span. This does not however affect the large-τ tail of P and the conclusions drawn from it.

CONCLUSIONS

In paper, a disordered two-dimensional material, relatively few AE events occure before the crack initialization, in agreement with the fact that the elastic modulus should decrease only modestly. After the crack starts to propagate we observe strong simultaneous AE activity. In contradiction to creep tests in perhaps more
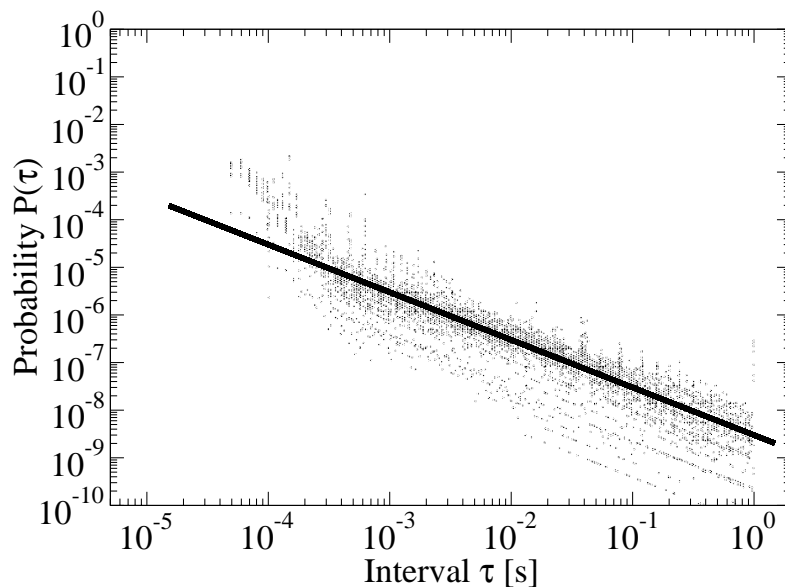
Figure 4: The distribution of time intervals τ obeys an Omori's law -like scaling $P(\tau) \sim \tau^{-1}$. The gray dots are experimental data, the thick line with slope -1 is a guide to the eye. For very short intervals ($\tau < 10^{-4}$s) the data can be skewed due to the accuracy of the experimental setup.

homogeneous materials we are unable to observe any reliable precursors of the critical crack (compare with the claims in ref. [12]). So even in ideal circumstances AE cannot be applied as predictive indicator of the web break. However, the results imply, that AE can be applied as an indirected way to measure drops in E_{mod}. Thus the technique should be of interest in comparing the microscopic damage processes in different papers and the roles of fiber and bond failure in the energy dissipation, while their relative importance can as such be analyzed with other methods than AE.

The experiments imply that the number of events decreases as the rate of elongation increases. Meanwhile, the mean amplitude of AE events remains the same. In our opinion this originates from a reduction of the size of the FPZ. As fracture becomes faster the fractureline may become less branched and fluctuate less. A concomitant decrease in microscopic damage would be expected. The behavior of the number of AE events implies that the way the energy dissipated in fracture process depends on the elongation rate.

We have also presented a brief analysis of AE energy and time-interval statistics [10]. One practical conclusion is, due to the large dynamic range of the apparatus which allows the detection of very small amplitude events, one can not discern between the two main failure processes, fiber and bond rupture, directly from the statistics, in contrast to some claims. The scaling laws indicate that in the failure of paper the viscoelastic relaxation processes do have an effect on the energy statistics, which nevertheless seem to follow rough power-law scalings. For large strain rates, ie. in the brittle limit, the energy exponent γ approaches unity which case should allow for the easiest comparison with theoretical models. On the other hand, the interval distributions show evidence of being invariant of the strain rate. Since the time between two acoustic events should only depend on the strain rate, the very fast relaxation of the stress field, and the internal processes typical of the material, we therefore conclude that the last ones determine the typical timescales.

REFERENCES

[1] C. Maes, A. Van Moffaert, H. Frederix, H. Strauven, (1998), Phys. Rev. B, 57, 4987.

[2] A. Guarino, A. Garcimartín, S. Ciliberto, (1998), Eur. Phys. Jour. B., 6, 13. A. Garcimartín, A. Guarino, L. Bellon, S. Ciliberto, (1997), Phys. Rev. Lett., 79, 3202.

[4] S. Zapperi, P. Ray, H.E. Stanley, A. Vespignani, (1997), Phys. Rev. Lett., 78, 1408.

[5] V.I. Räisänen, M.J. Alava, R.M. Nieminen, (1998), Phys. Rev. B, 58, 14288.

[6] S. Roux, (2000), Phys. Rev. E, 62, 6164.

[7] G. Caldarelli, F. D. Di Tolla, A. Petri, (1996), Phys. Rev. Lett., 77, 2503.

[8] M. Kloster, A. Hansen, P. C. Hemmer, (1997), Phys. Rev. E, 56, 2615.

[9] T. Yamauchi, S. Okumura, N. Noguchi, (1990), J. Pulp and Paper Science, 16, 45.

[10] A detailed analysis of the statistical aspects is reported elsewhere (L.I. Salminen et al., submitted for publication).

[11] P. Diodati, F. Marchesoni, S. Piazza, (1991), Phys. Rev. Lett., 67, 2239 .

[12] J.-C. Anifrani, C. Le Floc'h, D. Sornette, B. Souillard, (1995), J. Phys. I. France, 5, 631.

Statistics of chemical and mechanical fractures of corroded solids

A. Baldassarri[1], A. Gabrielli[2], and B. Sapoval[3]

[1] INFM - Dip. di Matematica e Fisica, Univ. di Camerino, Via Madonna delle Carceri, I-62032 Camerino, Italy

[2] INFM - Dipartimento di Fisica, Univ. di Roma "La Sapienza", P.le A. Moro, 2, ls I-00185 Roma, Italy

[3] Laboratoire de Physique de la Matière Condensée, Ecole Polytechnique, 91128 Palaiseau, France

ABSTRACT

The maximal penetration depth reached by a finite corrosion solution during the etching of a random solid is studied in a two-dimensional model. It is found that the statistical distribution of the maximal depth values follows a Gumbel law both through theoretical arguments and numerical simulation . When the maximal penetration of the corrosion front reaches the size of the sample, a chemical fracture occurs. It is shown that the probability of this chemical fracture obeys a law which is practically indistinguishable from the empirical Weibull law used to describe the statistics of mechanical fractures of brittle material. It is also shown that the statistics of the mechanical failure of a previously corroded sample follows a similar law.

KEYWORDS

INTRODUCTION

Chemical etching of disordered solids is an issue in several technological problems and in the theory of random systems. Etching can lead to the rupture of a sample if the etching
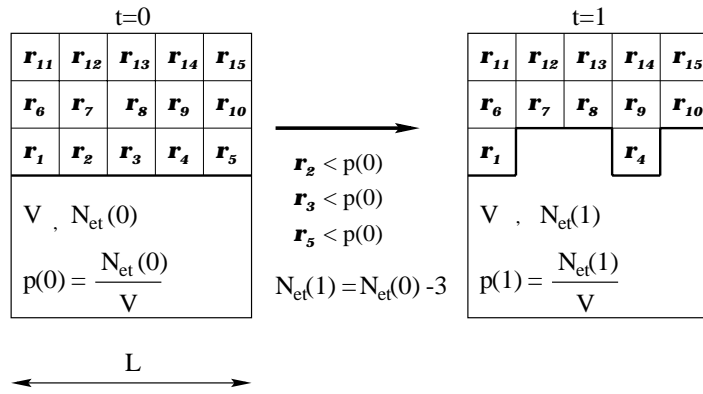
Figure 1: Sketch of the etching dynamics in a square lattice: the sites $2, 3, 5$ are etched at the first time-step as their resistances are lower than $p(0)$. At the same time the number of etchant particles in the solution decreases by 3 units, and a new part of the solid is uncovered.

solution is strong enough, or the solid thin enough. This is defined as a "chemical fracture". Its statistical behavior is studied here in a two-dimensional model. It is found numerically [1] as well as theoretically that the *chemical* fracture probability obeys Gumbel statistics [2] which is typical of an extremal variable. This law has been previously proposed by (e.g. [3, 4]) as a possible law fitting the statistics of *mechanical* fractures of samples under identical conditions of stress. The distribution found is hardly distinguishable from the Weibull distribution, which is the empirical law generally used to fit mechanical fracture statistics [5]. Furthermore, we show that the same statistics applies to the *mechanical* failure of a sample which has been *previously corroded* to some extent.

The Gumbel law is found through a study of the extremal properties of the etching front in a simple two-dimensional corrosion model previously introduced [6]. This model describes the chemical etching of a random solid by a finite volume of corrosive solution. It was inspired by an experimental study of pit corrosion of aluminum films [7] and reproduces the phenomenology of the experiment. It predicts that the etching stops spontaneously on a fractal liquid-solid interface as observed experimentally. The model dynamics are characterized by a progressive weakening of the corrosive power of the solution and a simultaneous progressive "hardening" of the solid-liquid interface. When this surface is too hard to be etched by the weakened solution, the corrosion stops. However, if the solid is too thin, it will have been fractured before the end of the process. In order to obtain the fracture statistics, one examines the probability that the maximal depth reached by the solution during the corrosion process is larger than the sample depth.

The etching model is recalled in Fig. 1 and is described as follows[8]:

1. The solid is represented by a lattice of sites exhibiting random "resistances to corrosion" $r_i \in [0, 1]$ uniformly distributed. It has a width L and a given fixed depth Y. At any time t the "etching power" of the solution is proportional to the etchant concentration

2
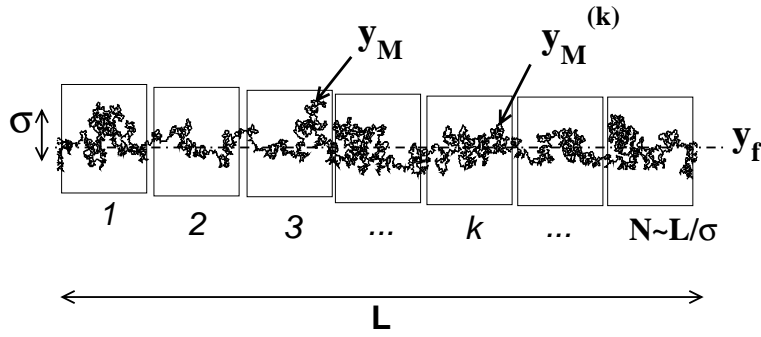
Figure 2: Final corrosion front: It is composed of $N \sim L/\sigma$ independent regions of size σ (σ can be considered as the correlation length of the system). The extremal front position y_M is indicated. It is the max between the N independent values of $y_M^{(k)}$ of each region.

$p(t)$. The etching solution has a finite volume V and contains an initial number $N_{et}(0)$ of etchant molecules. The initial etching strength is then $p(0) = N_{et}(0)/V$. Hereafter we choose $p(0) > p_c$, where p_c is the percolation threshold of the lattice.

2. The solution is initially in contact with the solid through the bottom boundary $y = 0$. At each time-step t, all surface sites with $r_i < p(t)$ are dissolved and a particle of etchant is consumed for each corroded site. Hence, at each time-step the concentration of the solution decreases.

At the beginning, the corrosion front stays quite smooth and advances layer by layer up to approximatively the time t_c when $p(t) = p_c$. In this regime one can show [8] that $p(t) = p_0 \exp(-t/\tau)$ with $\tau = V/L$. Therefore, this smooth part of the dynamics lasts for a period on the order of V/L reaching a depth $y_{lin.} \sim V/L$. After this regime the corrosion front becomes very irregular and finally stops at $t = t_f$. At t_f the etching power $p_f = p(t_f)$ is slightly smaller than p_c and the final corrosion front is fractal with dimension $D_f = 7/4$ up to a characteristic width $\Delta y = \sigma$ (see Fig. 2). As shown in [8], the model presents the scaling laws of Gradient Percolation [9] where the role of the gradient is played by the ratio L/V. This implies that σ can be seen as a percolation correlation length and $\sigma \sim (L/V)^{-1/D_f}$. The total front shown in Fig. 2 can then be considered as a juxtaposition of nearly independent fractal zones of lateral width σ. The total number of independent regions (hereafter σ-boxes) is $N \sim L/\sigma$. The maximal depth y_M reached by the front can be written as $y_M = \max_{k=1}^N y_M^{(k)}$, where $y_M^{(k)}$ is the maximal final depth reached by the corrosion in the kth σ-box. The set of $y_M^{(k)}$ is then a collection of L/σ nearly independent and identically distributed random variables. Since σ is a percolation correlation length, we can say that the distribution of $y_M^{(k)}$ has an exponential tail with a characteristic scale y_0 of order σ. We have then to search y_M as the maximal value among a large set of independent and exponentially distributed identical random variables. Therefore, in the limit of large N, y_M has the following standard Gumbel distribution [2]:

3
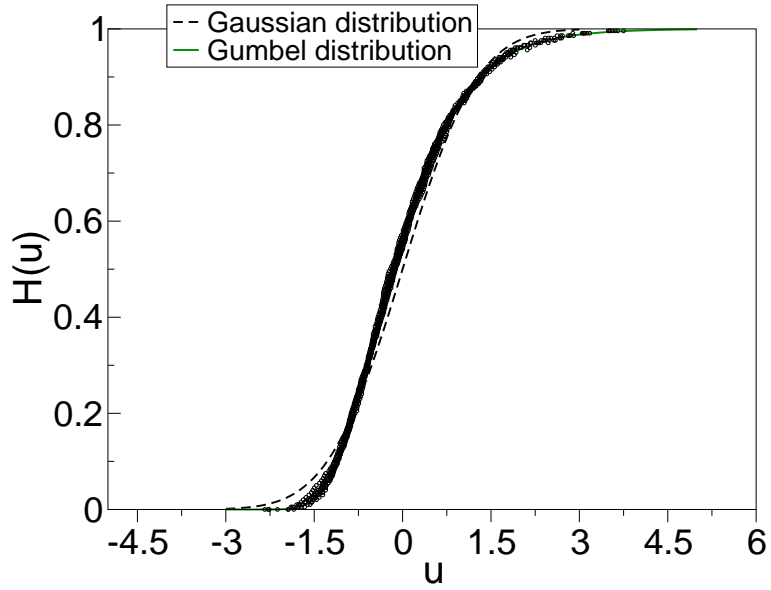
Figure 3: Integrated probability distribution for reduced y_M (zero mean and unitary variance) are compared with standard Gaussian and Gumbel distributions. The simulation results collapse on the Gumbel distribution given by Eq. (1) (continuous line, hidden by data points).

$$H(u) \equiv Prob\left(\frac{y_M - \langle y_M \rangle}{\Sigma} < u\right) = e^{-e^{-(bu+a)}} \, , \tag{1}$$

where Σ is the standard deviation of y_M, and $a \simeq -0.5772$ and $b \simeq \sqrt{1.64493}$.

The quantities $\langle y_M \rangle$ and Σ can be written[2]:

$$\langle y_M \rangle \quad \simeq \quad \left\langle y_M^{(k)} \right\rangle + 2y_0 \log N \tag{2}$$

$$\Sigma \simeq \ 2\, y_0 \, , \tag{3}$$

From the previous discussion, one can show also that:

$$y_f \quad \simeq \quad c_1 V/L + c_2 (V/L)^{4/7}$$

$$\left(\left\langle y_M^{(k)} \right\rangle \ - \ y_f\right) \sim \sigma \sim (V/L)^{4/7} \tag{4}$$

where y_f is the average depth of the final corrosion front. In summary, (i) $[\langle y_M \rangle - y_f]$ scales as σ if L/σ is fixed, and (ii) $\langle y_M \rangle$ dependends linearly on $\log L$ for given σ. These theoretical results are confirmed by extensive numerical simulations. The direct numerical evidence for a Gumbel statistics is shown in Fig. 3, where the numerical probability distribution function of the reduced variable $[y_M - \langle y_M \rangle]/\Sigma$ is represented.

It is now possible to study the chemical fracture of a solid sample with finite depth Y. This fracture probability is then given by $Prob\,(y_M > Y)$:

4
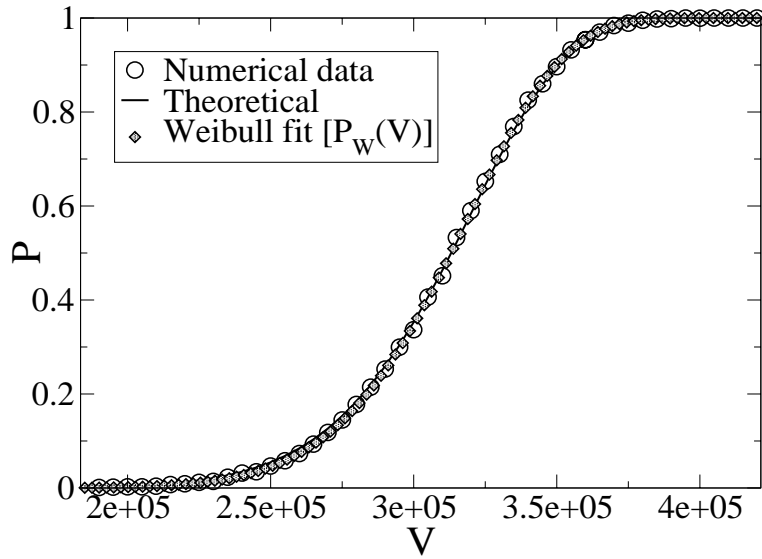
Figure 4: *Chemical fracture* probability $Prob\,(y_M > Y)$ as a function of the solution volume V which measures the "chemical force". Small circles are the numerical extimated probabilities. The line is the result of our theory. Diamond shaped points represent the fit of the fracture data with a Weibull law.

$$Prob\,(y_M > Y) = 1 - \exp\left\{ -A \left(\frac{L}{\Sigma}\right)^b \exp\left[\frac{b(y_f - Y)}{\Sigma}\right] \right\} \,, \tag{5}$$

where Eqs. (1), (2) and (3) have been used, and A is a positive constant.

By substituting y_M as a function of V/L, one obtains the chemical fracture probability distribution $P(V)$, as a function of the *chemical force* V for a given p_0 (i.e. the initial etchant concentration) and L. This distribution is determined but the value of A, which has to be fitted to the numerical fracture statistics (i.e. the fraction of simulation runs that break the sample as a function of V). The result is shown in Fig. 4. Also shown in the figure is a direct comparison of the best fit of a Weibull law [5] with the direct chemical fracture statistics. Here again the agreement is good. The Weibull law, introduced to describe the statistics of brittle materials failure, has the following form:

$$P_W(V) = 1 - e^{-\left(\frac{V - V_0}{V_1}\right)^m} \,, \tag{6}$$

where V represents an applied stress, V_0 is the minimal stress to have finite fracture probability, V_1 and m are suitable parameters. The extreme similarity between the Gumbel and Weibull behaviors observed in our model suggests that the underlying probabilistic structure controlling chemical and mechanical fracture could be the same. This would be a case of universality.

We now extend the analysis to the case of the *mechanical* failure of a partially corroded solid. Here this means that an uniaxial mechanical force F is applied to the lateral sides of a

5

sample which has been previously corroded up to $y_M < Y$. The most reasonable hypothesis is that the force produces the maximal stress at the point where the solid is the thinnest. The solids fails if this stress, equal to $F/(Y - y_M)$, is larger than a critical value s_c characteristic of the material. The failure probability is then equal to $P[y_M > (Y - F/s_c)]$. Therefore, in this model, even the *mechanical failure* of a corroded solid presents statistics related to the extremal Gumbel law. It is worth to note that this case of failure can be seen as the effect of a *stress under corrosion*, while it is *corrosion under stress* that is typically studied experimentally. The relationship between these two mechanisms requires further study.

ACKNOWLEDGEMENTS

REFERENCES

[1] A. Baldassarri, *Statistics of Extreme Persistent Events*, Ph.D.Thesis, University of Paris XI, 1999.

[2] E.J. Gumbel, *Statistics of Extremes*, Columbia University Press, New York, 1958; J. Galambos, *The Asymptotic Theory of Extreme Order Statistics* (R. E. Krieger Publishing Co., Malabar, Florida, 1987).

[3] P. M. Duxbury, P. L. Leathand P. D. Beale, Phys. Rev. B **36**, 367 (1987).

[4] H. Herrmann and S. Roux, *Statistical models for the fracture of disordered media* (North-Holland ed., Amsterdam, Netherlands, 1990).

[5] W. Weibull, J. Appl. Phys. **18**, 293 (1951).

[6] B. Sapoval, S. B. Santra and Ph. Barboux, Europhys. Lett., **41**, 297 (1998). S. B. Santra and B. Sapoval, Physica A., 266, 160-172 (1999).

[7] L. Balázs, Phys.Rev. E **54**, 1183 (1996)

[8] A. Gabrielli, A. Baldassarri, and B. Sapoval, Phys. Rev. E, **62**, 3103 (2000).

[9] B. Sapoval, M. Rosso and J. F. Gouyet, J. Phys. Lett. (Paris), **46**, L149 (1985); B. Sapoval, M. Rosso and J. F. Gouyet, in *"The Fractal Approach to Heterogeneous Chemistry"*, edited by D. Avnir (John Wiley and Sons Ltd., New York, 1989).

STEREOSCOPIC FRACTURE ANALYSIS BY SEM USING STEREO MATCHING AND INTEGRATING SECONDARY ELECTRON SIGNALS

J. JIANG and S. SAKAI

Department of Mechanical Engineering, The University of Tokyo
7-3-1, Hongo, Bunkyo-ku, Tokyo 113-0033, Japan

ABSTRACT

Three-dimensional analysis of a fracture surface using a scanning electron microscope (SEM) is necessary to clarify the cause of the fracture. Stereo matching and the integration of the angles calculated based on the intensity of secondary electron signals are widely used methods because of their versatility and simplicity. The former method is advantageous because of its accuracy, and the latter method is advantageous because of its resolution; however, it is rather difficult to attain both accuracy and high resolution. In this paper, a new method is described to solve this problem, which is attained by the combination of these two methods. In this method, the profile heights of fracture surface calculated by stereo matching are revised with those correct inclinations measured by secondary electron signal intensity so as to lessen the error of stereo matching. The application of the developed method on several typical fracture surfaces of metals will be shown. In order to examine its precision, the accuracy of the proposed method was investigated and satisfactory results were obtained. A personal computer takes approximately only six minutes for 3 dimensional analysis of one picture, this results shows the developed method is practical. It also shows that the method will become a powerful tool to analyze fracture surface and understand fracture.

KEYWORDS

fractography, fracture surface, SEM, 3-dimensional measurement, fracture, stereo matching, secondary electron.

INTRODUCTION

In the field of fractography, three-dimensional analysis of a fracture surface is helpful when trying to clarify the cause of the fracture. At the nano-scale, it is valid to analyze the fracture surface with a scanning tunneling microscope (STM) or an atomic force microscope (AFM), but at the micro-meso scale region, especially at the scale of grain size and subgrain size, a scanning electron microscope (SEM) shows superior property to analyze the stereoscopic information of the fracture surface. As for the 3D analysis by SEM, the stereo matching and the integration of secondary electron signals are widely used [1]. Stereo matching is the process of taking a pair of stereo images at different inclination angles of a specimen and determining the height or depth by measuring deviations of corresponding points on the two images. This method is advantageous for measuring the height of edge points and has no accumulated error, but it is disadvantageous when measuring no characterized region, such as a smooth plane or a gentle curved surface. Because stereo matching can only calculate the height in every pixel unit, it is unavoidable to lead to the discretized error of the height, so the resolution of height is limited and a plane or a curved surface may appear as a jagged surface [2]. Another method for reconstructing a fracture surface profile is to use a pair of secondary electron detectors [3]. Using the system installed in a SEM, the surface profile is obtained by integrating secondary electron signals, whose intensity is in proportion to the inclination of the surface profile. This method is superior for measuring planes or gently curved surfaces, but the accuracy is not assured at the edge points or at the point where the inclination angle of the surface is more than 65 degree. Thus, the error accumulates along the integrating line and this problem is not solved yet.

In summary, neither stereo matching nor the integration of secondary electron signals satisfactorily can meet both accuracy and resolutions, which are requirements of micro-fractography for microscopic 3-dimensional measurements. Thus, in order to obtain real 3-dimensional fracture surface profiles, a new method is proposed, which is the combination of the two methods.

NEW METHOD OF MEASURING FRACTURE SURFACE PROFILES

In this method, the profile heights of fracture surface calculated by stereo matching are revised with those correct inclinations measured by secondary electron signal intensity so as to lessen the error of stereo matching. At first, using SEM stereo images (source image and oblique image) of fracture surface are taken. And in the meantime, the height data of surface profile for source image is also obtained by integrating secondary electron signals. It is necessary for stereo matching that the data interval of heights between neighboring points is not less than 8 pixels. Hereafter, the length between neighboring points is called as mesh and is shown in Figure 1. To ensure that the two methods can be combined, the position of point (i,j) reconstructed with stereo matching must correspond to the position determined by integrating secondary electron signals. Then, in order to lessen the error of stereo matching and obtain the real height H(i,j) of point (i,j), it is necessary to revise the height $H_m(i,j)$ of stereo matching with the inclination θ_s (namely clockwise $\theta_s(i,j-1)$, $\theta_s(i-1,j)$, $\theta_s(i,j+1)$, $\theta_s(i+1,j)$) which is

between point (i,j) and neighboring 4 points. And here θ_s is measured by secondary electron signal detectors. In cases where each inclination θ_m (clockwise $\theta_m(i, j-1)$, $\theta_m(i-1, j)$, $\theta_m(i, j+1)$, $\theta_m(i+1, j)$) calculated by stereo matching is less than 65 degree, the degree θ_s detected by secondary electron signals is much more correct than that of stereo matching. So the revised height is the average of $H_m(i,j)$ and $H'_m(i, j-1)$, $H'_m(i,j+1)$, $H'_m(i-1,j)$, $H'_m(i+1,j)$. Here, $H'_m(i, j-1)$, $H'_m(i,j+1)$, $H'_m(i-1,j)$, $H'_m(i+1,j)$ are the heights calculated from neighboring points and their inclinations detected by secondary electron signals. For example:

$$H'_m(i, j-1) = H_m(i, j-1) + mesh \times \tan(\theta_s(i,j-1))$$ (1)

However, it is not appropriate to revise the height at the point where one of the inclinations calculated by stereo matching is more than 65 degree because the degree detected by secondary electron signals cannot be assured. For example, if $\theta_m(i, j-1)$ is less than 65 degree, the revised height of (i,j) will be the average of $H_m(i, j)$, $H'_m(i,j+1)$, $H'_m(i-1,j)$, $H'_m(i+1,j)$
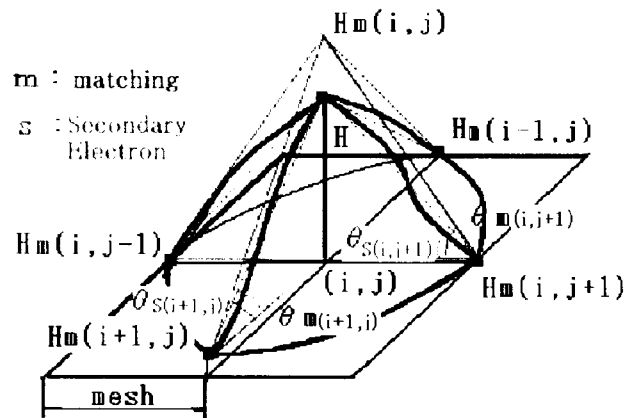
Fig. 1. Illustration of calculation for the height of point (i,j) revised with the heights and inclinations of neighboring points. The position of point (i,j) reconstructed with stereo matching is correspond to the position measured by integrating secondary electron. The interval (namely mesh) between the points is not less than 8 pixels. Hm(i,j) is the heights calculated by stereo matching.

According to this concept, the revised height is also calculated for all points. The height of every point is revised the two times to lessen the discretized error of stereo matching.

APPLICTION OF THE METHOD TO FRACTURE SURFACES

The proposed method is applied to several fracture surfaces. Figure 2 shows the image of a ductile fracture surface on a Charpy V-notch specimen. The material used is steel JIS G3106 SM400B whose chemical composition is C =0.2%, Si=0.35%, Mn=0.60%, 0.14%, P<0.035%. The left side of the figure is

a SEM photograph of the source image and the right side of the figure is the oblique image tilted by 5 degrees. These digital images are taken directly with a scanning electron microscope (ERA-8800, manufactured by Elionix Co. of Japan), with which the surface profile is also measured by integrating secondary electron signals. The area outlined by the white line of Fig. 2 (a) is reconstructed by the proposed method. In order to minimize the number of mismatching points, a modified template method of stereo matching is employed, in which the template size is varied from 51×51 to 7×7 pixels[4]. It takes about 5 minutes to process all the heights of 130×90 points in a workstation (SUNW, Axil-245) with a 245-MHz CPU, 64 M of memory, or about 6 minutes in a personal computer with a 233-MHz CPU and 64 M of memory. Thus, it is considered to be practical for the analysis.
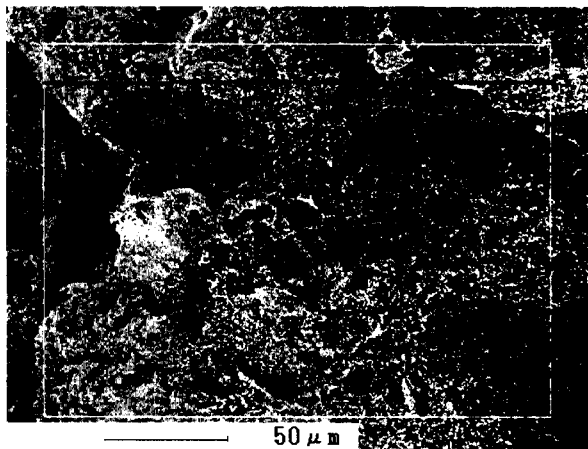
(a) Source image (0 degree)   (b) Oblique image (5 degree)
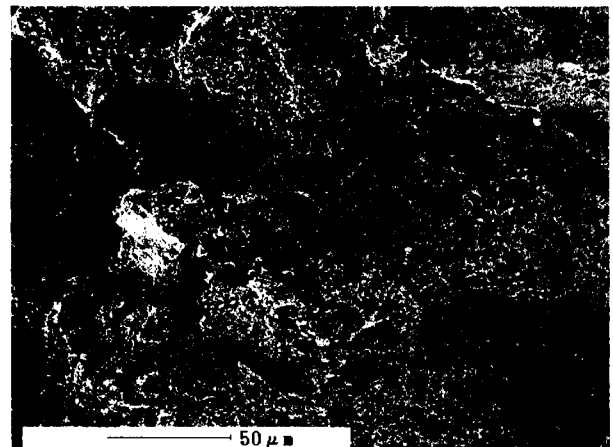
Fig. 2. SEM photographs of the ductile fracture surface on a Charpy
impact specimen of JIS SM400B   (Image size: 1200×900 pixels)
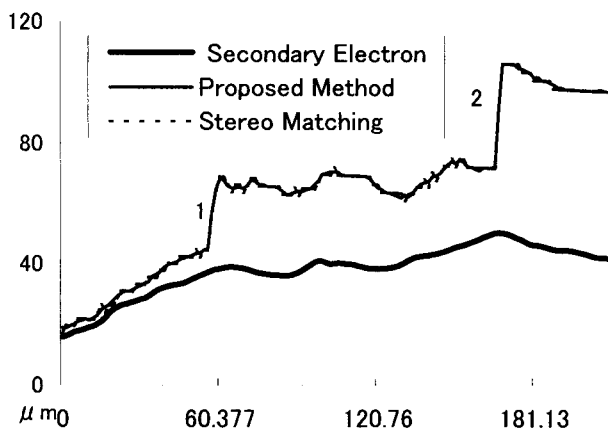
Fig. 3. Profile height of one line in the source image
of Fig.2 measured by proposed method. The results
calculated with stereo matching and integrating
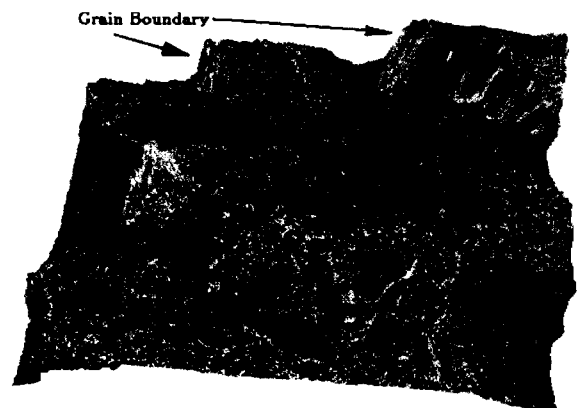
Fig. 4. Bird's-eye view of the fracture surface
of the object in Fig. 2

Figure 3 shows the profile heights along the black line in the source image of Figure 2. The profile is measured by three methods: the proposed method, stereo matching and integrating secondary electron signals. The lowest height of the measured area is set to 0 μ m. On the one hand, the grain boundary or edge points 1, 2 shown in the figure can be found from the result of stereo matching, stereo matching gives poor resolution and the results are jagged. Although, the result of integrating secondary electron signals gives good resolution and one can obtain a gentle curve, but the edge point where the inclination is more than 65 degree cannot be found from the curve. On the other hand, the proposed method doesn't have the disadvantages of these two methods. Namely, using the proposed method, not only the grain boundary can be easily judged but also the resolution is high. It's shown that the results of three methods are similar except the edge points and the edge points yield a huge accumulated error of integrating secondary electron signals. Figure 4 shows the reconstructed 3-dimensional bird's-eye view whose area is
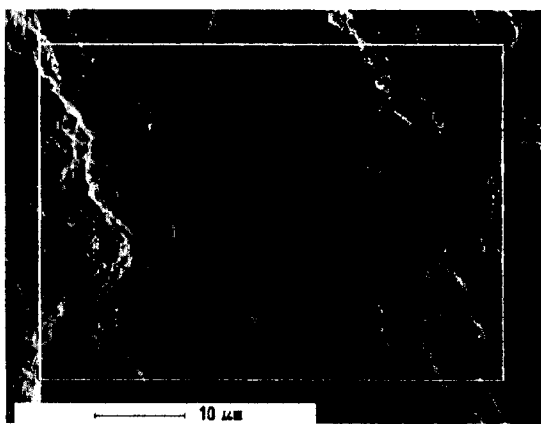
(a) SEM photograph of the fracture surface
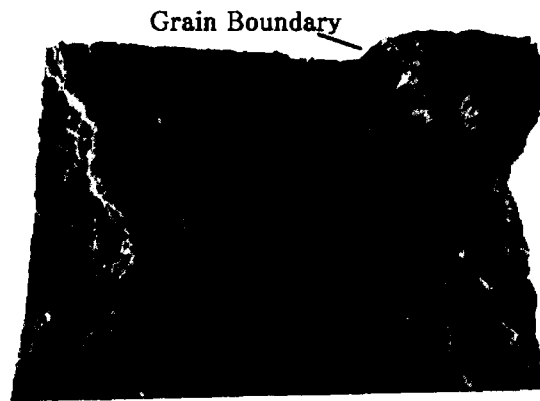
(b) Bird's-eye view of the fracture surface

Fig. 5. Creep-fatigue fracture surface on a specimen of 2 ¼ Cr-1Mo failed in vacuum
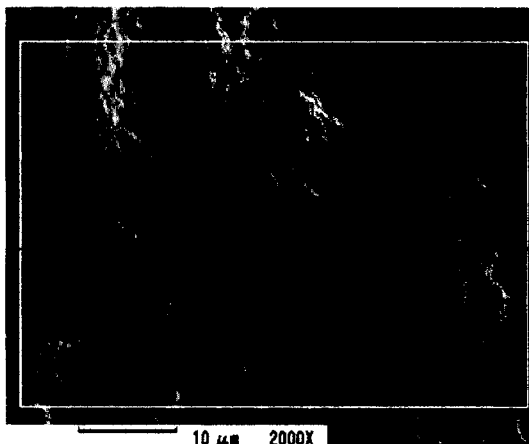
(a) SEM photograph of the fracture surface
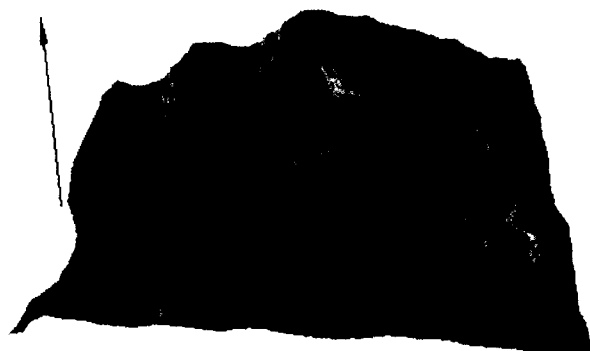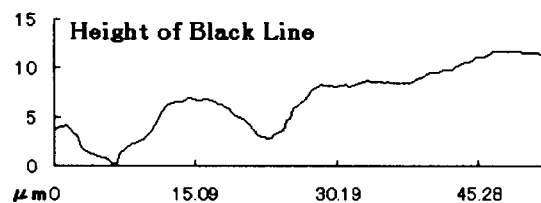
(b) Bird's-eye view of the fracture surface

Fig. 6. Creep-fatigue fracture surface on a specimen of 2 ¼ Cr-1Mo failed in vacuum

corresponding to the zone enclosed with white line in Figure 2, and the fracture surface is displayed in texture mapping of a VRML (Virtual Reality Modeling Language) file. The fracture surface is complicated, and it is difficult to find the grain boundary from just a 2-dimensional SEM image. From a 3-dimensional reconstructed image, however, the grain boundary can be easily found, where the surface is acute.

Figure 5 (a) shows an SEM photograph of the creep-fatigue fracture surface on a specimen of 2¼ Cr-1Mo failed in vacuum at 500 ℃. Figure 5 (b) is the 3-dimensional bird's-eye view of the area inside the white line of Figure 4 (a), which is reconstructed with the proposed method. Most of the fracture surface is shown to be gentle intragranular surface. The grain boundary in the fracture surface can be easily found. It can also be concluded that this fracture is a fracture surface of transgranular fracture.

Figure 6 shows the fracture surface on another area of the same specimen of 2¼ Cr-1Mo. Figure 6 (b) is the bird's-eye view of the area inside the white line of Figure 6 (a). Two cavities can be seen in the fracture surface. From the height of the black line, the average depth of the cavities is about 6 μm and the diameter is about 10 μm.

CONCLUSIONS

Conclusions would be summarized as follows:
1. Neither the stereo matching method nor the method of integrating the angles detected by the intensity of secondary electron signals is completely adequate for making a 3-dimensional measurement of a fracture surface.
2. A new method by combining stereo matching and integrating secondary electron signals has been developed.
3. The proposed method was applied to several typical fracture surfaces of metals. The accuracy of the proposed method is examined and satisfactory results are obtained.
4. The processing time for 3-dimensional analysis in personal computer was short enough to make the method practical. It shows that the method will become a powerful tool to analyze fracture surface and understand fracture.

REFERENCES

[1]. JSMS Committee on Fractography (2000), Fractgraphy (In Japanese).
[2]. S. Tadao (1985), "Measurement of Surface Topography Using SEM with Two Secondary Electron Detectors", Journal of Electron Microscope, Vol.34, No.4, 328.
[3]. T. Mikio, S. Haruhisa (1991), Handbook of Image Analysis,707.
[4]. Jiang Jun, S. Sakai (2000), 10th Fractography Symposium, Kyoto Japan. "Stereoscopic Fracture Analysis by SEM using advanced Stereo Matching". 7.

STOCHASTIC ANALYSIS OF FATIGUE CRACK GROWTH

C. Proppe[1] and G.I. Schuëller[1]

[1] Institute of Engineering Mechanics, Leopold-Franzens University, A-6020 Innsbruck, Austria, EU

ABSTRACT

Due to cost and time limitations, experiments for fatigue crack growth are only feasible below certain cycle numbers. In this paper, it is investigated whether or not fatigue crack growth laws allow for an extrapolation of the statistics of the cycle number to reach a certain crack length from limited experimental data, and hence reduce costs.

KEYWORDS

fatigue crack growth laws, probabilistic fracture mechanics

INTRODUCTION

From experimental investigations [1, 2] fatigue crack growth appears as a process with random properties. These random properties seem to vary not only from specimen to specimen but also during crack growth, cf. Figure 1. A great number of stochastic models that account for the random behavior have been proposed. They are based either on suitable "randomized" empirical crack growth laws or on data fitting.

In this paper, the practical use of already proposed models is assessed. In engineering practice, there is often insufficient financial means as well as time available to carry out fatigue tests with a greater number of load cycles. As a consequence, there is a need to extrapolate the fatigue crack growth prediction by means of stochastic models from data that were obtained from a limited number of load cycles.

This paper investigates the requirements in complexity for a stochastic model of fatigue crack growth in order to approximately extrapolate the statistical characteristics of fatigue crack growth. For this, results from experimental investigations are compared to model predictions, where from all specimen only a part of the measured crack lengths were used to calibrate the model.
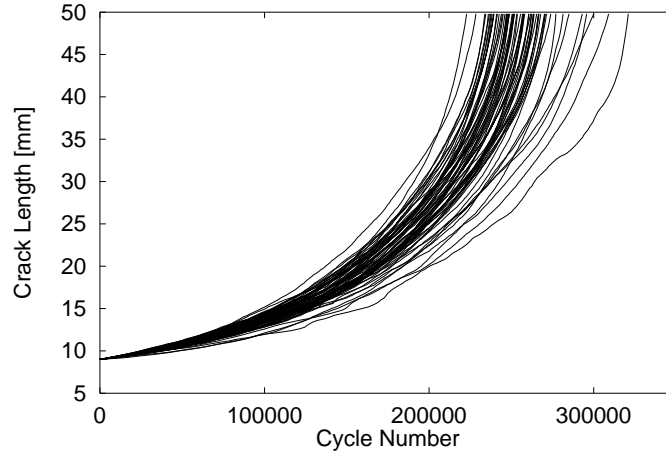
Figure 1: Fatigue crack growth for centre cracked specimen as measured by Virkler et al. [1].

FATIGUE CRACK GROWTH MODELS

Elementary fatigue crack growth laws assume a relationship between the stress state at the crack tip and the crack growth velocity. Several deterministic crack growth laws have been proposed for fitting the mean values of experimentally measured data. These laws have then been extended to account for the random phenomena inherent in crack growth. The main efforts are summarized in this section.

Deterministic Fatigue Crack Growth Laws

The extended crack growth law

$$\frac{\mathrm{d}\,a}{\mathrm{d}\,N} = C \frac{(1-R)^m \Delta K^n}{((1-R)K_c - \Delta K)^q},$$ (1)

where a is the crack length, N the number of load cycles, ΔK the increment of the stress intensity, K_c the critical stress intensity factor and $R = \sigma_{max}/\sigma_{min}$ the stress ratio summarizes Paris' law ($m = q = 0$), Forman's law ($m = 0, q = 1$) and Walker's law ($q = 0$). Paris' law is a straight line in the $\ln(\mathrm{d}\,a/\mathrm{d}\,N)$-$\ln(\Delta K)$ representation. This is a good approximation for stable crack growth, but does not account for the different behavior of small cracks and in the range of instable crack growth. The typically S-shaped crack growth curve can only be approximated by a nonlinear relationship between the logarithm of the crack growth velocity and the logarithm of the stress intensity factor, respectively. For example, a cubic polynomial approximation would lead to

$$\ln(\frac{\mathrm{d}\,a}{\mathrm{d}\,N}) = C_0 + C_1 \ln(\Delta K) + C_2(\ln(\Delta K))^2 + C_3(\ln(\Delta K))^3,$$ (2)

where dependence on R can be accounted for by substituting Elber's [3] effective stress intensity factor $\Delta K_{eff} = (A + BR)\Delta K$, where A and B are constants that have to be determined from experiments, for ΔK. A similar approximation can be obtained from the hyperbolic sine law

$$\frac{\mathrm{d}\,a}{\mathrm{d}\,N} = 10^{(C_1 \sinh(C_2(\ln \Delta K + C_3)) + C_4)}.$$ (3)

Stochastic Crack Growth Models

Relatively simple stochastic crack growth models assume that the uncertainties in one or several parameters of the deterministic crack growth laws are modeled as random variables. These models, however, can not explain the variability of the crack growth rate during the crack growth process.

Models based on stochastic differential equations, in fact, are suited to account for this type of variability. E.g. Tsurui et al. [4, 5] and Tang and Spencer [6] proposed crack growth equations with a time-correlated stochastic process. A model with a jump process has been introduced in [7].

If the random variations of the crack growth process of a single specimen are attributed to material inhomogeneity, the correlation of the stochastic process should rather be attributed to the spatial dimension. Therefore, Ortiz and Kiremidjian [8] proposed a model of the form

$$\frac{\mathrm{d}\,a}{\mathrm{d}\,N} = f(\delta K)Z(a), \tag{4}$$

where $\log Z(a)$ is a Gaussian process whose correlation depends on the crack length.

Markov chain models [9] reflect the fact that the load process is often discretized into independent events and that an absorbing state - failure -can be introduced. Markov chain models can be directly fitted to experimental data. However, this makes predictions for other load conditions or geometrical configurations a difficult task. This problem can be circumvented by using a suitable stochastic crack growth model for the determination of the transition probabilities [10].

PARAMETER IDENTIFICATION

As has been pointed out by several authors [11, 12], parameter estimation should be carried out with the crack length as independent variable in order to avoid a systematic bias. Defining the approximation error as the sum of the squared differences between the experimentally and theoretically predicted cycle numbers at each measured crack length, an optimal set of parameters can be determined for each specimen. Assuming a distribution (e.g. log-normal for C and normal for n) for the random variables in the model, the distribution parameters as well as the correlation can be estimated from these optimal sets of parameters.

The properties of the stochastic process are then obtained from an analysis of the residuum. Considering all samples, the standard deviation of the difference between the cycle numbers obtained from the experiments and from the deterministic model with optimal sample parameters respectively can be computed either for each measured crack length separately or cumulated for all measured crack lengths. By assuming a Gaussian distribution with this standard deviation and zero mean for the error in the cycle number at each crack length, one obtains a stochastic process model with an non stationary and a stationary Gaussian white noise process, respectively.

SENSITIVITY ANALYSIS
The following arguments demonstrate that the sensitivity of the predicted cycle numbers with respect to small

changes of the parameters in the crack growth law is very high. Thus, possible variations of these parameters have to be taken into consideration.
Consider the Paris law for an infinite plate under tension ($\Delta K = \Delta\sigma\sqrt{\pi a}$). The solution of the differential equation yields

$$N(a) = \frac{1}{C\pi^{n/2}(\Delta\sigma)^n}\left(\frac{a^{(1-\frac{n}{2})} - a_0^{(1-\frac{n}{2})}}{1 - \frac{n}{2}}\right), \tag{5}$$

where a_0 is the initial crack length at $N = 0$. The derivatives of the number of load cycles with respect to the parameters C and n read:

$$\frac{\mathrm{d}\,N}{\mathrm{d}\,C} = -\frac{N(a)}{C} \tag{6}$$

and

$$\frac{\mathrm{d}\,N}{\mathrm{d}\,n} = -\frac{1}{2}N(a)\ln(\pi) - N(a)\ln(\Delta\sigma) + \frac{aN(a)}{2-n} - \frac{1}{2}\frac{\ln(a)a^{(1-\frac{n}{2})} - \ln(a_0)a_0^{(1-\frac{n}{2})}}{(1-\frac{n}{2})C\pi^{n/2}(\Delta\sigma)^n}. \tag{7}$$

From this, one can see that the number of cycles to reach a certain crack length is very sensitive to changes of the parameter C. Similar observations can be made for Forman's and Walker's law.
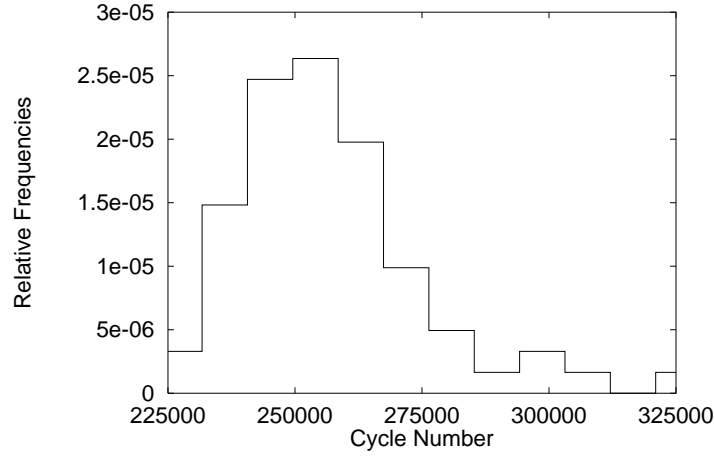
Figure 2: Histogram for the cycle numbers to reach a crack length of 49.8 mm obtained from the experiments carried out by Virkler et al. [1].

CYCLE NUMBER PREDICTION

The experimental results of Virkler et al. [1] have been used to study the prediction capabilities of Paris´ and Forman´s law with random parameters andwith an additional Gaussian white noise process which represents the randomness during crack growth. The target was the prediction of the cycle number to reach a crack length of 49.8 mm – the ultimate crack length measured by Virkler et al. From the experimental results, the mean cycle number to reach this crack length is 257164, with a standard deviation of 18310 (see Figure 1). This leads to a coefficient of variation of 7.12 %, which is relatively low, as the experiments have been carried out under well controlled conditions. The distribution is nearly log-normal with a skewness of 1.15. The histogram is given in Figure 2.

In the fatigue crack growth laws of Paris and Forman, the parameter C was assumed to be lognormally distributed and the correlation between $\ln(C)$ and m was determined by linear regression. The parameters were estimated from the full data set and from the first part of the cycle numbers, respectively. The relative errors, defined by

$$\frac{X_{theory} - X_{experiment}}{X_{experiment}}, \tag{8}$$

where X_{theory}, $X_{experiment}$ are the mean value, standard deviation, coefficient of variation (c.o.v.) or the skewness coefficient obtained from computations and experiments, resp., are summarized in Table 1 and 2. The theoretical results were estimated from 10000 generated sample curves.

One can see that at least 50% of the cycle numbers need to be considered in order to accurately predict the mean cycle number to reach the final crack length of 49.8 mm. However, the other statistical characteristics are not well represented, even by when all experimental data are being considered. Thus, the random variable model seems to be only suitable for mean value predictions.

Table 3 and 4 list the corresponding results for a stochastic process model with random variables and additional stationary Gaussian white noise. It can be seen that the error in the standard deviation is reduced by approximately 30%, but remains still relatively large. Results obtained with a non stationary process were nor much better. Also in this case, a limited amount of data (at least 50 % in order to accurately predict the mean value) is sufficient for the calibration of the model, i.e. its parameters.

TABLE 1:

PERCENTAGE RELATIVE ERROR FOR THE PREDICTION OF CYCLE NUMBERS TO REACH A CRACK
LENGTH OF $a = 49.8$mm. PARIS´ LAW WITH RANDOM VARIABLES.

percentage of cycle numbers retained	mean	std. deviation	c.o.v.	skewness
100	-2	-88	-87	-63
50	-9	-62	-58	13
25	-15	12	32	18
10	-29	93	171	58

TABLE 2:

PERCENTAGE RELATIVE ERROR FOR THE PREDICTION OF CYCLE NUMBERS TO REACH A CRACK
LENGTH OF $a = 49.8$mm. FORMAN´S LAW WITH RANDOM VARIABLES.

percentage of cycle numbers retained	mean	std. deviation	c.o.v.	skewness
100	-5	-84	-83	-60
50	-13	-74	-71	32
25	-19	-11	10	13
10	-32	62	137	40

TABLE 3:

PERCENTAGE RELATIVE ERROR FOR THE PREDICTION OF CYCLE NUMBERS TO REACH A CRACK LENGTH
OF $a = 49.8$mm. PARIS´ LAW WITH RANDOM VARIABLES AND ADDITIONAL GAUSSIAN WHITE NOISE.

percentage of cycle numbers retained	mean	std. deviation	c.o.v.	skewness
100	-2	-66	-65	-94
50	-9	-45	-40	69
25	-15	22	45	-15
10	-29	97	177	38

TABLE 4:

PERCENTAGE RELATIVE ERROR FOR THE PREDICTION OF CYCLE NUMBERS TO REACH A CRACK
LENGTH OF $a = 49.8$mm. FORMAN´S LAW WITH RANDOM VARIABLES AND ADDITIONAL GAUSSIAN
WHITE NOISE.

percentage of cycle numbers retained	mean	std. deviation	c.o.v.	skewness
100	-5	-61	-59	-89
50	-13	-50	-43	81
25	-19	2	26	-32
10	-32	68	146	16

CONCLUSIONS

In this paper, the practical use of probabilistic fatigue crack growth models is assessed. By comparison with experimental data, the possibility to extrapolate the crack growth behavior is investigated for various models with different complexity.

It has been shown that random variable models may be used to extrapolate the mean cycle number to reach a certain crack length. However, these methods will fail to predict other statistical characteristics. Especially, they underestimate the variance. Hence, in order to account for these characteristics, more complex models have to be established.

Stochastic process models, where the residuum is explained by a Gaussian white noise process, lead to a better approximation of the second moments. However, the relative errors are still quite large.

Both random variable and stochastic process models respectively do not reproduce the crossing of measured crack growth curves from different specimen well. For the random variable models under consideration, crossing of crack growth curves is impossible, while for stochastic process models, the model predicts more crossings than are experimentally observed. This fact has been also noticed by other investigators, (see e.g. Bolotin [13], p. 213).

For reliability predictions with usually small probabilities, random variable models are much more efficient than stochastic process models, as variance reducing Monte Carlo simulation schemes can be easily applied.

REFERENCES

1. Virkler, D.A., Hillberry, B.M. and Goel, P.K. (1979). *J. Eng. Mat. Tech.* 101, pp. 148.
2. Ghonem, H. and Dore, S. (1987). *Eng. Fract. Mech.* 27, pp. 1.
3. Elber, W. (1971). *Damage Tolerance in Aircraft Structures*, pp. 230-242, ASTM STP 486.
4. Tsurui, A., Tanaka, H. and Tanaka, T. (1989). *Prob. Eng. Mech.* 4, pp. 120.
5. Tsurui, A., Nienstedt, J., Schuëller, G.I. and Tanaka, H. (1989). *Eng. Fract. Mech.* 34, pp. 153.
6. Tang, J. and Spencer Jr., B.F. (1989). *Eng. Fract. Mech.* 34, pp. 419.
7. Lin, Y.K., Wu, W.F. and Yang J.N. (1985). In: *Probabilistic Methods in Mechanics of Solids and Structures*, pp. 103-110, Eggwertz, S. and Lind, N.C. (Eds.), Springer, Berlin.
8. Ortiz, K. and Kiremidjian, A.S. (1986). *Eng. Fract. Mech.* 24, pp. 657.
9. Bogdanoff, J.L. and Kozin, F. (1985). *Probabilistic Models of Cumulative Damage*, Wiley, New York.
10. Oswald, G. F. and Schuëller, G.I. (1984). *Eng. Fract. Mech.*, 20, pp. 479.
11. Kozin, F. and Bogdanoff J.L. (1981). *Eng. Fract. Mech.* 14, 59.
12. Ostergaard, D.F. and Hillberry, B. M. (1983). In: *Probabilistic Methods for Design and Maintenance of Structures*, ASTM STP 798.
13. Bolotin, V.V. (1999). *Mechanics of Fatigue*, CRC Press, Boca Raton.

STRAIN ENERGY DENSITY AS THE LINK BETWEEN GLOBAL AND LOCAL APPROACH TO FRACTURE

Hans-Jakob Schindler

Mat-Tec Ltd., Winterthur, Switzerland
(formerly EMPA, Duebendorf, Switzerland)

ABSTRACT

Fracture toughness is a material property only under certain restrictions concerning size, thickness, crack-length, loading mode, notch root radius, etc. To quantify such effects on the crack resistance the "local approach" is usually applied, which is very demanding in terms of numerical modelling and computational power. For practical engineering application as well as for teaching purposes, simpler analytical considerations are needed, which allow these effects to be predicted at least qualitatively. In the present paper simplistic mechanical models in conjunction with a suitable fracture criterion are outlined. A key element in the analysis is the local fracture criterion, which is required to link the global and local fracture behaviour. A suitable and promising parameter is the critical strain energy density. As pointed out in this paper, this parameter enables one to obtain relatively simple but surprisingly accurate formulas to predict effects of crack-tip constraints, finite notch root radius, and mixed mode loading on the fracture behaviour. Even problems of repeated loading like low-cycle fatigue of notched or cracked components can be dealt with.

KEY WORDS

Strain energy density, specific fracture energy, constraints, tearing, cleavage, notch, toughness.

INTRODUCTION

The concept of engineering fracture mechanics is essentially based on the hypothesis of autonomy of the fracture process zone, and a few parameters that are able to characterise the loading state of this zone, like the stress intensity factor in linear-elastic fracture mechanics or the J-integral in elastic-plastic fracture mechanics. The critical values of these parameters, called fracture toughness, characterise the resistance of the material against crack extension. Engineering fracture mechanics enables one to predict the behaviour of a crack without requiring a detailed analysis of the complex local fracture mechanisms. However, the autonomy of the fracture process zone is not guaranteed absolutely, since the fracture behaviour depends on the local constraints, which are affected by several system parameters, like component size, crack-length, geometry and loading case of the system. This means that fracture toughness is not a pure material property, but dependent on these parameters.

To quantify the effects of the above-mentioned parameters on the constraint conditions and the local fracture mechanisms, a detailed analysis of the crack-tip region is required, known as the "local approach". However, the corresponding non-linear 3D-FEM-analysis to compute the basic local parameters is quite

demanding in terms of modelling, computational effort, hard- and software capacity, thus not well suited for engineering application. For such practical purposes as well as in teaching much simpler, rather analytical approaches are needed.

In this paper, semi-analytical ways to deal with the above mentioned local effects are pointed out, including constraints, notch root radius, mixed mode loading, and cyclic loading. A key element in such an analysis is a suitable failure criterion. It is shown how the critical strain energy density as suggested by Gillemot [1] can serve for this purpose. This material property seems to represent a linking parameter between local fracture and the global behaviour, and to control most aspects of ductile fracture. Therefore the first part of the paper deals with the definition and determination of this interesting physical quantity. Then simplistic local models to predict the behaviour of fracture toughness by simple closed-form formulas are outlined. Due to a lack of space the author restricts himself to discussing the key ideas and presenting the main results, rather than giving strict mathematical derivations. The objective of this paper is just to give an overview on the possibilities of these types of semi-analytical and semi-local approaches.

CRITICAL STRAIN ENERGY DENSITY

According to Gillemot's general failure criterion [1] an elastic-plastic material will fail in a ductile manner if the strain energy density U reaches a critical, material-dependent value U_f, i.e. if

$$U = \int_0^{\varepsilon_{ij}} \sigma_{ij} \cdot d\varepsilon_{ij} = U_f \tag{1}$$

U_f is a material property. Since (1) holds for any loading case, the simplest way to determine U_f is by a uniaxial tensile test, where it represents the area under the true-stress-true strain-curve up to fracture. (right hand side of Fig. 1). The average true strain during the entire test, including the necking phase, is obtained as $\varepsilon_t = \ln(A_0/A)$, where A_0 and A denote the initial cross section and the actual one, respectively. In the range of uniform strain (i.e. $0 < \varepsilon_t < \ln(1+A_g)$) the true stress-strain-curve can be approximated as

$$\sigma_t = C \cdot \varepsilon^n \qquad \text{with} \qquad C = \frac{R_m \cdot (1+A_g)}{n^n}; \qquad n = \ln(1+A_g) \tag{2}$$

where A_g denotes the engineering strain at maximum load (i.e. standard uniform fracture strain). In the subsequent necking phase, the true stress-strain-diagram is often more or less straight, as shown in Fig. 1. With these assumptions, U_f is determined by

$$U_f = U_m + U_{nf} \quad \text{with:} \qquad U_m = \frac{R_m \cdot (1+A_g) \cdot n}{n+1} \qquad U_{nf} = \left[\frac{R_m \cdot (1-Z) + R_f}{2 \cdot (1-Z)} \right] \cdot \left[\ln \frac{1}{1-Z} - \ln(1+A_g) \right] \tag{3}$$
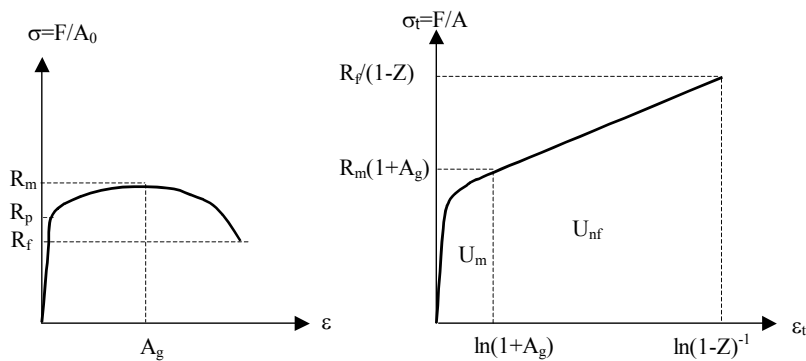
Fig. 1: Determination of the true stress-strain-curve (right) from the engineering one (left) and definition of the portions U_m and U_{nf} of the specific fracture energy $U_f = U_m + U_{nf}$

$Z=(A_0-A_f)/A_0$ denotes the standard reduction of area of a tensile test specimen. If R_f is not known, which often the case if the full stress-strain-curve is not available, the following approximate relation is useful:

$$U_{nf} = \frac{R_m}{2}\left[\frac{1+(1+A_g)\cdot(\ln(1-Z)-n)}{\ln(1-Z)-n}\right] \tag{4}$$

Eq. (4) follows analytically from the assumptions underlying (2) and (3) and the condition of continuity at the transition at $\varepsilon_t=\ln(1+A_g)$. If not even A_g is known, then we suggest the rough estimation

$$U_f \cong \frac{\sigma_f \cdot Z}{1-Z} \tag{5}$$

according to [3], where $\sigma_f=(R_p+R_m)/2$ denotes the commonly used flow stress.

LOCAL STRESSES AND STRAINS

It is well known from non-linear finite element calculations that the so-called HRR-field [3] breaks down in the vicinity of the crack tip. Fig. 2 shows schematically the actual distribution of the stress in y-direction. The peak stress, σ_{ymax}, can be expressed as

$$\sigma_{ymax}=\gamma\cdot R_p \tag{6}$$

where the factor γ depends primarily on the crack-tip constraints and the hardening behaviour of the material. It is about 3 for non-hardening elastic-plastic materials and standard constraint conditions, which means plane strain and saturated in-plane constraints. Actually, to determine γ accurately a 3D-FEM-analysis is required. However, according to previous findings of the author [4, 5], a rough estimation sufficient for practical purposes is possible by

$$\gamma \cong \left(2m + \frac{\upsilon\cdot T_{max}}{(1-2\upsilon)\cdot R_p}\right)\cdot\frac{\sigma_f}{R_p} \tag{7}$$

where υ is Poisson's ratio and m is the factor appearing in the basic relation

$$J=m\cdot R_p\cdot\delta \tag{8}$$

T_{max} is the "T-stress" (second term of Williams' expansion [6]) at maximum load of the system.
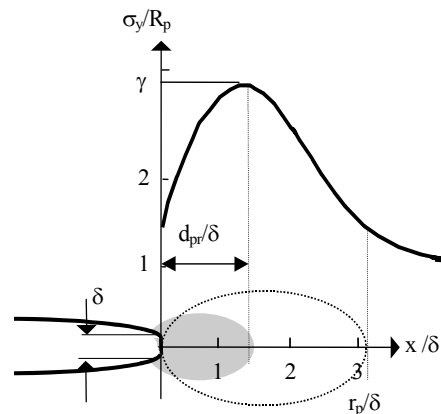
Fig. 2: Non-dimensional representation of the stress distribution in the vicinity of a crack-tip

The ductile fracture process by void growth and coalescence takes place in a relatively small area of width d_{pr} next to the crack-tip (shaded area in Fig. 2). The plastic strain in this "fracture process zone" in y-direction, ε_{yp}, can be assumed to be proportional to the crack-tip opening displacement δ, because the initial volume taking part in this process will not change much during the loading process. Thus,

$$\delta \propto \varepsilon_{yp} \tag{9}$$

Assuming that a certain portion of strain energy density, corresponding about to U_m, is already consumed in the preceding phase of general plastic straining according to the HRR-strain-field, Gillemot's criterion (1) applied to the process zone can be written as

$$\gamma \cdot R_p \cdot \ln(1 + \varepsilon_{yp}) = U_{nf} \tag{10}$$

By (8) – (10) the local strain is related to the global crack load J.

EFFECT OF CRACK-TIP CONSTRAINTS ON FRACTURE TOUGHNESS

Ductile Tearing
The value of J near initiation of ductile tearing is size independent only if the corresponding standard size and geometry requirements [7] are met. The effect of reduced constraints on the J-value at crack-initiation, is experimentally well known [8], but difficult to model and predict analytically. However, from (8) – (10) a relation between the constraint-characterising parameters m and γ and the apparent fracture toughness J_{it} follows readily:

$$\frac{J_{it}}{m \cdot \left\{ \exp\left[\dfrac{U_{nf}}{R_p \cdot \gamma} \right] - 1 \right\}} = \text{const} \tag{11}$$

J_{it} represents a near initiation value of the J-R-curve, corresponding to the standard $J_{0.2/Bl}$ in the case of standard constraint conditions [7]. For a non-hardening material the latter correspond to about $m \approx 1.5$ and $\gamma \approx 3$, so $J_{it}(m \approx 1.5, \gamma \approx 3)$ equals $J_{0.2/Bl}$. By (11) the effect of reduced constraints (reflected by lower values of m and γ) on the fracture toughness can be determined. Predictions from (11) compare well with experimental results [4].

Cleavage Fracture
In some elastic-plastic materials an unstable cleavage fracture may be triggered at a certain value of J, J_c, which can be lower than the above considered J_{it}. J_c is known to be significantly constraint-dependent. In the following, this dependence is estimated. As discussed in [4] unstable cleavage require the following two criteria to be met:

i) The maximum stress in the vicinity of the crack tip must exceed the cleavage stress σ_c^*, i.e.

$$\sigma_{ymax} = \gamma \cdot R_p > \sigma_c^* \tag{12}$$

ii) The elastic energy $W_{el}^* = \int U_{el}\, dV$ stored in a critical Volume V^* in the vicinity of the process zone must be sufficient to produce a cleavage fracture in the range $0 < x < d_{pr}$.

Criterion ii) means that the ratio W_{el}^*/d_{pr} has to exceed a certain critical value. Using the proportionalities $U_{el} \propto (\gamma \cdot R_p)^2$ and $V^* \propto \delta^2$ leads to $W_{el}^* \propto (\gamma \cdot R_p)^2 \cdot \delta^2$. With $d_{pr} \propto \delta$ one readily finds the proportionality

$$J_c \cdot \frac{\gamma^2}{m} = const \qquad for\ \gamma > \sigma_c^*/R_p \qquad\qquad (13)$$

As discussed above, $J_c(m=1.5, \gamma=3)$ corresponds to the standard J_{uc} according to [7]. By (13) the effect of reduced constraints on J_{uc} can be determined. For $\gamma < \sigma_c^*/R_p$ no cleavage occurs. Predictions from (13) compare well with experimental results shown in [8].

NOTCH TOUGHNESS

Consider a sharp notch with a finite root radius ρ. If the end-points of the integration-path to calculate J are located on the parallel surfaces, J is path-independent and, thus, able to characterise the loading state of the notch. It can be calculated either on a remote path Γ_r (dashed line in Fig. 3) or a local path surrounding the notch root (dotted path-sections Γ_1 and Γ_4). In order to estimate the effect of the root radius on the critical J-integral, J_{inotch}, we calculate J for a notch that is assumed to be in its critical loading state, which means just before initiation of crack extension occurs. Under this condition, the local path to calculate J must not simply follow the notch surface (sections Γ_1 and Γ_4), because near y=0 there already are voids which act as discontinuities in the strain field, disturbing the path-independence of J. Therefore the integration path is chosen to surround the process zone by a "detour" denoted by Γ_2 and Γ_3 in Fig. 3. In case of sharp notches (i.e. $\rho \ll$ plastic zone width r_p) the stress-strain-fields in the vicinity of the x-axis is expected to be about the same as in the case of a crack, so the corresponding integration is expected to give about the value of the critical J of a crack, J_{icrack}. The parts Γ_1 and Γ_4 of the integration path deliver the contribution ΔJ_ρ resulting from the notch radius, which has the form $U_F \rho$ for dimensional reasons. Thus:

$$J_{inotch} = J_{icrack} + \Delta J_\rho = J_{icrack} + c \cdot U_f \cdot \rho \qquad\qquad (14)$$

The adjustable factor c turned out to be about 0.7, for mild steel [2], high strength steel [9] and even brittle materials like ceramics.
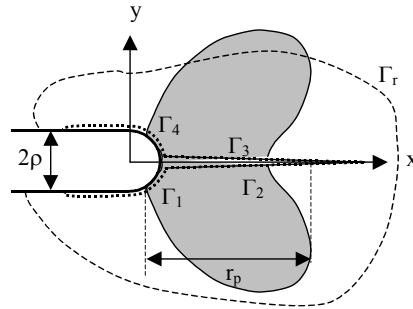
Fig. 3: Schematic representation of the root region of a sharp notch and the corresponding plastic zone

FRACTURE TOUGHNESS IN MIXED MODE

The maximum hoop-stress criterion as commonly used in LEFM for mixed-mode-loading is known to be not valid in the case of ductile fracture. Various experimental studies reveal that the critical stress-intensity factor in Mode II, K_{IIC}, is about $2 - 3$ times higher than K_{Ic}. This behaviour can be explained, as shown below, by postulating for physical reasons an analogy between mode I and mode II and extending the relation (11) to mode II. In mode II there is essentially no constraint, so one can assume $\gamma = \gamma_{II} = 1$ and $m = m_{II} = 1$ (values of m for mode II are hard to find in the literature, eventually it lies in the range $0.6 < m_{II} < 1$). This leads to

$$\frac{J_{IIit}}{J_{it}} = \frac{m_{II} \cdot \exp\left(\dfrac{U_{nf}}{R_p}\right) - 1}{1.5 \cdot \left[\exp\left(\dfrac{U_{nf}}{3R_p}\right) - 1\right]} \tag{15}$$

where J_{IIit} denotes the critical J for pure antisymmetric loading (i.e. pure mode II). In case of mixed-mode loading, a physically plausible mode-interaction is a linear damage accumulation in terms of δ or J, thus

$$\frac{K_I^2}{K_{Ic}^2} + \frac{K_{II}^2}{K_{IIc}^2} < 1 \tag{16}$$

with

$$K_{IIc} = \sqrt{\frac{J_{IIit} \cdot (1 - \upsilon^2)}{E}} \tag{17}$$

This relation represents at least a qualitative explanation of experimental data [9].

DISCUSSION AND CONCLUSIONS

The purpose of the present paper was to show that even complex phenomena associated with local fracture, like constraint effects, influences of a mode-II-loading components, or a finite notch-tip radius, can be successfully and efficiently treated by simple analytical models. Unlike detailed numerical models, they result in easy to handle closed form formulas, which allow these effects to be discussed qualitatively, which is advantageous in practical applications as well as in teaching.

It shall be emphasised that the critical strain energy density can serve well for various purposes concerning fracture. Especially it is well suited to link global to local behaviour. It is the author's believe that the role and the possibilities of this parameter in engineering fracture mechanics is still not yet fully recognised. Another big field of its application, which was not discussed here due to the lack of space, is the behaviour of notched and cracked components under repeated elastic-plastic-straining, like low-cycle fatigue. As shown in [10], even high-cycle fatigue crack growth can be analytically treated based on a corresponding local fracture criterion.

REFERENCES

1. Gillemot, L.F., Engineering Fracture Mechanics, Vol. 8, 1976, 239-253
2. Hutchinson, J.W., J. Mechanics and Physics of Solids, 16, 1968, p.13
3. Schindler, H.J, Proc. of 6th, Int. Conf. Mech. Behaviour of Materials, Kyoto, 1991, p. 159 - 164
4. Schindler, H.J., Proc. of 8th Int. Conf. on the Mechanical Behaviour of Materials, Victoria, CA, 1999, pp. 25 – 30
5. Schindler, H.J.,Proc. of 33. Tagung des DVM-AK Bruchvorgänge, Deutscher Verband für Materialforschung, DVM-Report No. 233, 105-114 (in german)
6. Williams, M.L., "On the Stress distribution at the base of a stationary crack", J. Appl. Mechanics, 24, 1957, 109-114
7. International Standardisation Organisation, ISO-Standard ISO 12135, Metallic Materials – Unified method of test for the determination of quasistatic fracture toughness. 2000
8. Sumpter, J.D.G., Forbes, A.T., Shallow Crack Fracture Mechanics, Paper No. 7, Cambridge, UK, 1992
9. Veidt, M., Schindler, H.J., Eng. Fracture Mechanics, Vol. 58, 1997, 223-231
10. H.J. Schindler, , Berichtband der 31. Tagung des DVM AK Bruchvorgänge, DVM-Report 231, Darmstadt, 1999, 121-131, (in german)

STRENGTH EVALUATION OF THE ECCS-GDH PIPING CONNECTION AND DETERMINATION OF THE CRITICAL CRACK UNDER WATERHAMMER EVENT

G. Dundulis, L. Nedzinskas

Lithuanian Energy Institute
3 Breslaujos str., 3035 Kaunas, Lithuania

ABSTRACT

Strength evaluation of the piping connection between the Emergency Core Cooling System (ECCS) and the Group Distribution Header (GDH) under waterhammer event is presented. This includes the determination of critical crack configuration. Strength calculations of the piping connection were performed according to ASME III Subsection NC using the PIPEPLUS computer code. Strength analysis of the ECCS-GDH piping connection showed that the structural integrity would be maintained under waterhammer event. The determination of critical crack configurations was then analyzed by the R6 method using the SACC 4.0 computer program. For comparison sake semi-elliptical critical size surface crack was calculated by ASME XI Appendix C methodology. The 3-D finite element model of ECCS-GDH piping connection was created using ALGOR finite element computer code to analyze stress distribution through the wall in the piping connection. Calculated stress distribution was used in postulated cracks analysis. The most dangerous crack type, size and location, regarding crack propagation, were determined.

KEYWORDS

Waterhammer, strength, crack, piping connection.

INTRODUCTION

The Ignalina Nuclear Power Plant (NPP) is a twin-unit of RBMK-1500, graphite moderated, boiling water, channeled reactors. The circulation circuit of the RBMK-1500 reactor has a series of check valves in the Group Distribution Headers (GDH) that serve for the coolant distribution to the fuel channels. Following a pipeline or header rupture, protection of the RBMK-1500 reactor core is provided by the emergency core cooling system (ECCS). This supplies water to the core via the GDH. However, to prevent the emergency coolant water leaking through the break, check valves in the GDH have to be closed. In the case of the hypothetical guillotine break of pipelines upstream of GDH, the check valves and adjusted pipeline integrity is a key issue for the reactor safety during rapid closure. A demonstration is needed that the valves and associated pipelines remain intact following such accidents. This includes a structural integrity analysis of the effect of waterhammer, i.e. the pressure pulse generated by the valves slamming closed.

The strength analysis was conducted in the present study using the PIPEPLUS code, the dynamic loads of which were calculated by computer code RELAP5 in thermal-hydraulic analysis. Also, the postulated crack

size analysis for determination of the critical crack was conducted by R6 method using the SACC 4.0 computer program. For comparison sake, semi-elliptical critical size surface crack was calculated using ASME XI Appendix C methodology. For crack analysis by R6 method stress distribution in the wall was calculated using 3-D finite element ECCS-GDH pipe connection model constructed by the ALGOR computer program.

STRENGTH ANALYSIS OF THE ECCS-GDH PIPING CONNECTION

In the case of guillotine rupture of pressure header or guillotine break upstream of GDH, the pressure in the GDH from the side of main circulation pump (MCP) pressure header drops rapidly down to atmospheric pressure, while the pressure in the circulation circuit decreases slowly following the reactor power decrease. A GDH check valve is closed practically instantaneously after initial rupture because of backflow. The closure of GDH check valves prevents the loss of flow from the main circulation circuit (MCC). Rapid closure of these valves leads to coolant flow and pressure pulses.

The strength analysis of the ECCS-GDH piping under waterhammer event was performed using the PIPEPLUS code. Constructed finite element (FE) model of GDH connection with ECCS pipelines is shown in Figure 1.

a   b
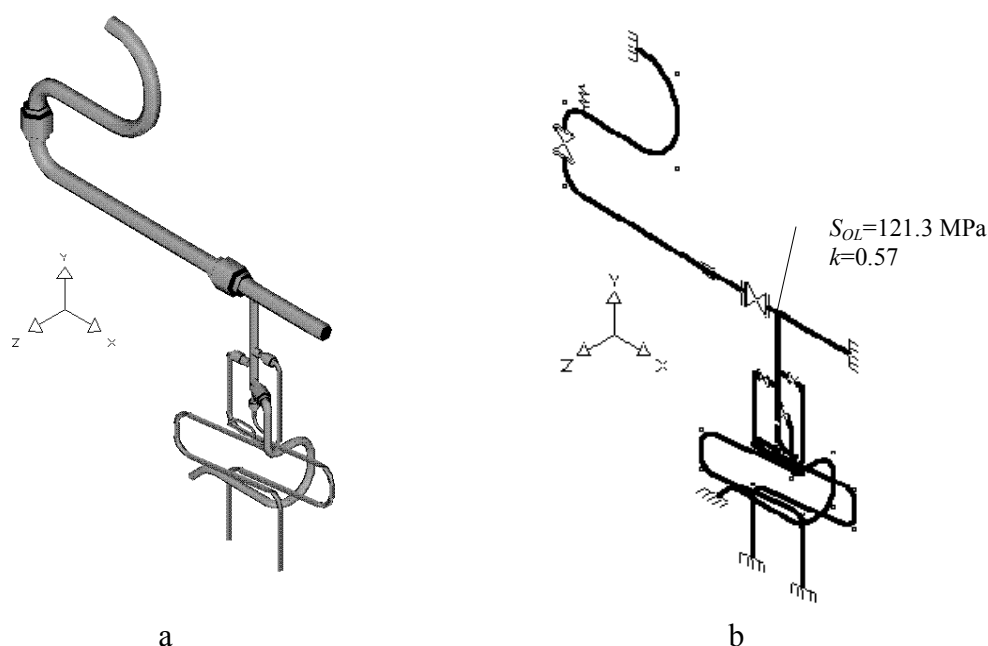
Figure 1: Finite element model ECCS-GDH piping: a – 3-D view, b - model with boundary elements

It was assumed in the calculations that the initial coolant temperature in the GDH-ECCS connecting pipelines is equal to 285 °C while the pressure is equal to 10.12 MPa. Dynamic forces generated by the coolant pressure pulses in the case of waterhammer were calculated using the RELAP5 code. The calculated dynamic force versus time is presented in Figure 2.
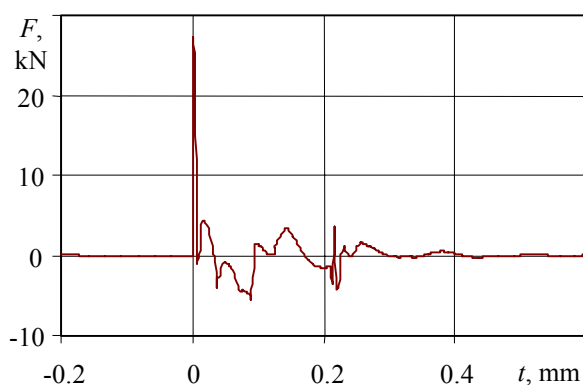
Figure 2: Force history in ECCS-GDH piping during waterhammer event

PIPEPLUS performs time history analysis using the modal superposition method. In order to investigate the correct value of the cutoff frequency, the following equation of motion was used for a single-degree-of-freedom system [1]:

$$\ddot{u} + 2\omega\zeta\dot{u} + \omega^2 u = F(t).$$ (1)

Terms of equation (1) are the following: u is displacement, $\dot{u}$ is velocity of displacement, $\ddot{u}$ is acceleration of displacement, ζ is damping ratio, ω is natural frequency, $F(t)$ is external force function. The cutoff frequency of 400 Hz was used for dynamic analysis.

The SAR report [2] indicates that the equipment and piping of the Ignalina NPP primary circuit are classified as a system of the second safety class except the fuel channels and the drum separators, which are referred to the first safety class. Therefore, ASME III Subsection NC [3] (class 2 components) criteria were used for strength evaluation of ECCS-GDH piping connection under waterhammer event.

According to ASME III Subsection NC [3] the effects of pressure, weight, other sustained loads, and occasional loads, including non-reversing dynamic loads, for which Level B service limits are designated, must meet the requirement of equations (2)

$$S_{OL} = B_1 \frac{P_{max} D_o}{2t} + B_2 \left(\frac{M_A + M_B}{Z} \right) \leq 1.8 S_h \quad \text{and} \quad S_{OL} < 1.5\sigma_y$$ (2)

Terms of equations (2) are the following: S_{OL} is stress due to effects of pressure, weight, other sustained loads, and occasional loads, including non-reversing dynamic loads; B_1, B_2 are primary stress indices for the specific product under investigation; P_{max} is peak pressure, D_o is outside pipe diameter; t is nominal wall thickness; M_A is resultant moment loading on cross section due to weight and other sustained loads; M_B is resultant moment loading on cross section due to non-reversing dynamic loads; Z is section modulus; S_h is allowable stress of material at temperature consistent with the loading under consideration; σ_y is yield strength of material at temperature consistent with the loading under consideration.

The pipelines upstream of GDH and ECCS are produced from austenitic steel 08Ch18N10T, the allowable stress of which is S_h=118 MPa at temperature T=285 °C.

Strength evaluation results of ECCS-GDH piping connection under waterhammer event according to ASME III Subsection NC criteria are presented in TABLE 1 and Figure 1. Static forces and moments acting on the ECCS-GDH piping connection are part of the strength analysis obtained the PIPEPLUS code. These loads are used in 3-D ECCS-GDH piping connection model constructed for the analysis of stress distribution through the thickness, the results of which are used in the crack analysis.

TABLE 1
STRENGTH EVALUATION RESULTS OF ECCS-GDH PIPING CONNECTION
UNDER WATERHAMMER EVENT

S_{OL}, MPa	$1.8S_h$, MPa	$k=S_{OL}/(1.8S_h)$
121.3	212.4	0.57

The results of strength calculations (TABLE 1) show, that ECCS-GDH piping connection meets ASME III Subsection NC strength criteria under waterhammer event.

CRITICAL CRACK SIZE CALCULATIONS

The purpose of postulated crack analysis was to determine the most dangerous crack type, size and location for ECCS-GDH piping connection under waterhammer event. Cracks of three types were postulated:
1) Crack in the corner (Figure 3 a),
2) Finite axial semi-elliptical internal surface crack in the weld (Figure 3 b),
3) Axial embedded crack in the weld (Figure 3 c).

Circumferential cracks were not analyzed because stresses in axial direction are lower than in circumferential and, therefore, critical axial crack size will be less than critical circumferential crack size.
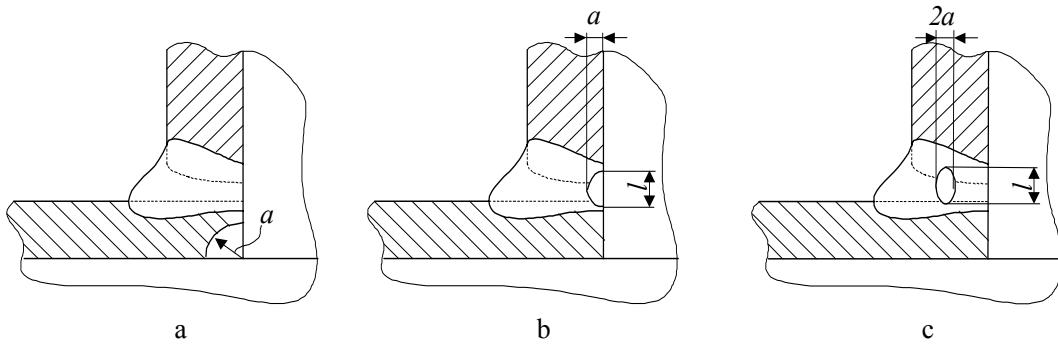
Figure 3: Postulated cracks: a - corner crack; b - finite axial semi-elliptical internal surface crack in the weld; c - axial embedded crack in the weld

The critical sizes of postulated cracks were calculated by R6 method [4] using computer program SACC 4.0 [5]. In the SACC program it is assumed that a stress is obtained under the linear elastic behavior of material. Detailed stress analysis of ECCS-GDH piping connection was performed in order to have through-wall stress distribution for critical crack size calculations. The 3-D finite element model of ECCS-GDH piping connection using 8-node isoparametric brick elements was constructed using computer code ALGOR (Figure 4 a). The forces and moments acting in ECCS-GDH piping connection under waterhammer event calculated in stress analysis by PIPEPLUS code were included in the model.
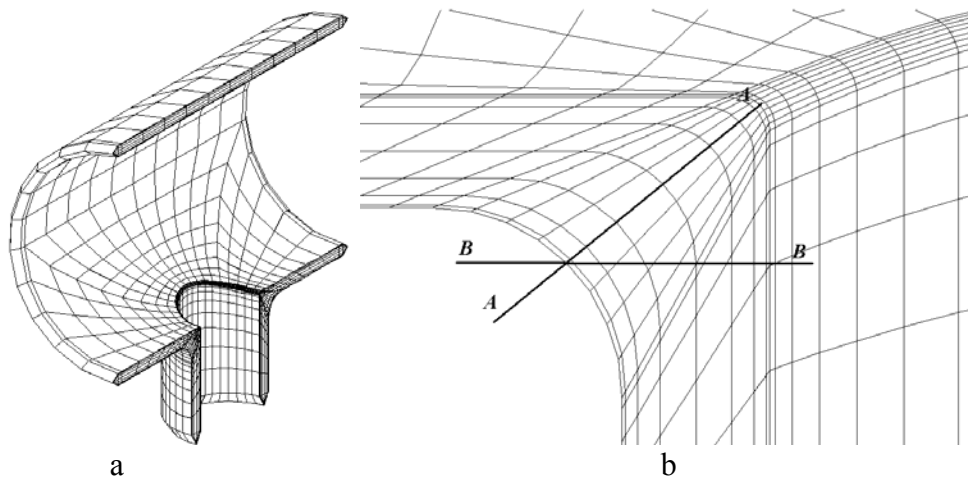
Figure 4: ECCS-GDH piping connection: a - 3-D FE model, b - location of sections A-A and B-B

Stress distribution in section A-A (Figure 4 b) is used for the analysis of postulated crack in the corner (Figure 3 a). Stress distribution in section B-B (Figure 4 b) is used for the analysis of postulated finite axial semi-elliptical internal surface crack in the weld (Figure 3 b) and axial embedded crack in the weld (Figure 3 c). For the calculation of critical crack size through-section stresses are resolved to membrane stresses and bending stresses. Membrane stress is considered as primary stress and bending stress is considered as secondary stress.

The calculated critical crack in the corner (Figure 3 a) size is a_{cr}=13.2 mm. For the calculation of critical crack size of the finite axial semi-elliptical internal surface crack in the weld (Figure 3 b) and axial

embedded crack in the weld (Figure 3 c) different ratios of crack length l and depth a are assumed. Calculation results of finite axial semi-elliptical internal surface crack in the weld (Figure 3 b) and axial embedded crack in the weld (Figure 3 c) as critical crack depth versus length are presented in Figure 5. Embedded crack analysis in program SACC is limited by crack depth and wall thickness ratio $2a/t \leq 0.9$ and crack depth and length ratio $l/2a \geq 1$. Semi-elliptical internal surface crack analysis is limited by crack depth and wall thickness ratio $a/t \leq 0.8$ and crack depth and length ratio $2 \leq l/a \leq 10$. Thus in Figure 5 maximum depth of embedded crack with ratio $l/2a < 1$ conservatively is assumed the same as the embedded crack with ratio $l/2a = 1$. Maximum depth of semi-elliptical crack with ratio $l/a < 2$ conservatively is assumed the same as semi-elliptical crack with ratio $l/a = 2$.
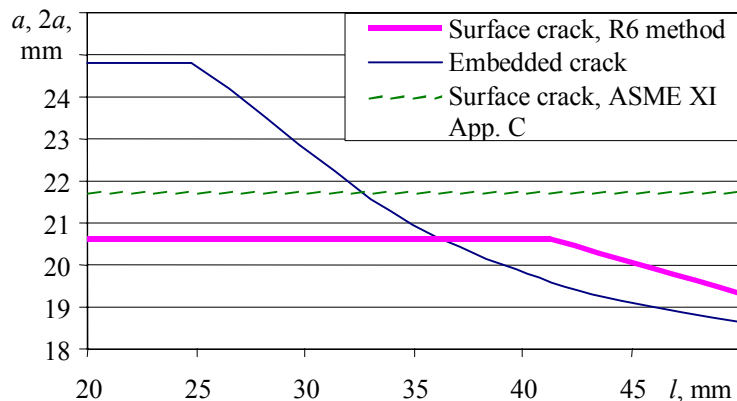
Figure 5: Critical crack depth versus crack length

For comparison sake semi-elliptical internal surface crack in the weld (Figure 3 b) critical crack size was calculated according to ASME XI Appendix C methodology [6]. Different ratios of crack length l and depth a were assumed. For all l/a ratios under consideration calculations reaches crack size limitations, i.e. crack depth reach 75% of wall thickness (dotted line in Figure 5).

The results of crack analysis shows, that even if the length of axial embedded crack in the weld and finite axial semi-elliptical internal surface crack in the weld are exceeding weld limits, critical crack depth is much larger than critical depth of crack in the corner. A crack in the corner of ECCS-GDH piping connection is the most dangerous crack for this construction.

CONCLUSIONS

The strength analysis of Ignalina NPP ECCS-GDH piping connection showed that calculated stresses do not exceed allowable stresses according to ASME III Subsection NC, i.e. structural integrity of ECCS-GDH piping connection will not be lost under waterhammer event. Crack analysis showed that the most dangerous is corner crack critical depth of which calculated according to the method R6 is $a_{cr} = 13.2$ mm.

ACKNOWLEDGEMENTS

REFERENCES

1. Gupta, A.K. (1993). *Response Spectrum Method in Seismic Analysis and Design of Structures*. CRC Press, Tokyo.
2. (1996). *Ignalina Nuclear Power Plant Safety Analysis Report, Volume 1, Task Group 1, Section 5, Subsection 1, Primary Circuit.* Ignalina NPP, Visaginas.
3. (1995). *Rules for Construction of Nuclear Power Plant Components: ASME Boiler and Pressure Vessel Code, Section III, Division 1, Subsection NC, Class 2 Components*. The American Society of Mechanical Engineers, New York.
4. *Assessment of the Integrity of Structures Containing Defects* (1996). Nuclear Electric Ltd., Gloucester.
5. Andersson, P., Bergman, M., Brickstad, B., Dahlberg, L., Nilsson, F. and Sattary-Far, I. (1996). *A Procedure for Safety Assessment of Components with Cracks - Handbook*. SAQ Kontroll AB, Stockholm.
6. *Evaluation of Flaws in Austenitic Piping: ASME Boiler and Pressure Vessel Code, Section XI, Appendix C* (1995). The American Society of Mechanical Engineers, New York pp. 381-394.

STRENGTH DETERIORATION IN SUBSTRATE FOR SEMICONDUCTOR POWER DEVICES BY THERMAL CYCLIC TEST

N. Okabe[1], M. Tsutsumi[1]*, X. Zhu[1] and Y. Abe[2]

[1] Dept. of Mech. Eng., Ehime Univ., 3 Bunkyo-cho Matsuyama City 790-8577, Japan
[2] Toshiba Corp., Isogo-ku, Yokohama City 235-0032, Japan

ABSTRACT

The fractures in aluminum nitride (AlN)-DBC (Direct Bond Copper) semiconductor substrate are caused by the residual stress due to the thermal stress produced in manufacturing process and thermal cycle. The fractural mechanism and strength were investigated based on fracture mechanics. The results obtained are summarized as follows;(1) The structural reliability of the substrate is influenced by the behavior of the residual stress. The repetition of thermal cycle increases residual stress, and lowers the strength of the substrates. (2) The residual tensile stress is distributed within narrow range of Al_2O_3 formed chemically on the surface of AlN, and its maximum stress is far larger than nominal fracture stress in four-point bending of monolithic AlN. This fact suggests the necessity of the fracture strength evaluation based on stress intensity factor. (3) The fracture of the substrate can be analyzed on the basis of the crack growth mechanism, which depends on stress intensity factor, K. The strength and/or fracture life of DBC substrate with the residual stress can be clarified through the thought mentioned above.

KEYWORDS

Substrate For Semiconductor, Direct Bond Copper, Thermal Cyclic Test Durability

INTRODUCTION

The electric power, consumed in the semiconductor parts for an industrial equipment, increases recently, with increasing in the demand of high-power, high integration, high reliability, modulation, low cost, and so on. Thus aluminum nitride (AlN)-DBC (Direct Bond Copper) semiconductor substrate have been developed and applied to practical parts because of better heat radiation required in practical service. The AlN-DBC semiconductor substrate is the joint body, which is strongly bonded copper plate to the surface of ceramic (AlN) by using Cu-O eutectic layer as a joint substance. The Cu-O eutectic layer is formed by reacting of Cu-O eutectic phase a small amount of oxygen with copper in high temperature (about 1300K) [1, 2]. Therefore, the followings become problems. The first is the fast fracture of ceramic due to generating of thermal stress in manufacturing process by difference of the thermal expansion coefficient between ceramic

and metal. The second is the delayed fracture of ceramic due to thermal cycle stress under practical service condition.

In this study, the thermal cyclic test and four-point bending test were carried out. Moreover, the residual stress was analyzed and strength deterioration due to the thermal cyclic stress was discussed. In addition, the fracture strength of the substrate was evaluated based on fracture mechanics, and the fracture life was estimated from the viewpoint of long-term reliability.

EXPERIMENT PROCEDURE AND ANALYSIS MODEL

Experimental procedure

Two types of tests were conducted to investigate the damage of the DBC substrates subjected to repetitive thermal cycle. The first is four-point bending test against the substrates subjected to 1~5 thermal cycles so as to identify the damage as the reduction of bending strength, compared with the virgin substrates. The second is the test to examine the fracture life due to thermal cycle, which is defined as cycle's number until fracturing of substrates. Two types of DBC substrate as shown in Figs.1(a)and(b) were prepared for each test. Thermal cycles against substrates are given by a to-and-fro motion of conveyer between heater box and freezer box under electric-timer-control. One thermal cycle was the sequence of heating (398K, 30min), cooling (room temperature, 10 min), cooling (243K, 10min) and heating (room temperature, 10 min) as shown in Fig.2. Four-point bending inner span was 10mm, and outer span was 30mm. The fracture of substrate in cycle life test was detected noticing the rapid fluctuation obtained by monitoring an output of strain gage putted on the Cu part.

Analysis model

The residual stress produced in thermal cyclic test as well as manufacturing process was analyzed by FEM. The stress analysis was conducted under plain strain condition by using the model consisting of 3parts such as Cu plate, AlN plate and Al_2O_3 layer, bonding chemically each other as shown in Fig.3. As the first stage, the residual stress caused by bonding was analyzed within temperature range from 1323K to 293K. The change of the residual stress due to thermal cycle into the next stage was analyzed taking the stress caused by bonding into consideration. The thermal cycle conditions were agreed with experimental one. On evaluating the measured stress during the four-point bending test, the true bending stress by applied loading was added on the residual stress changed in two stages.

The stress intensity factor mentioned after was calculated
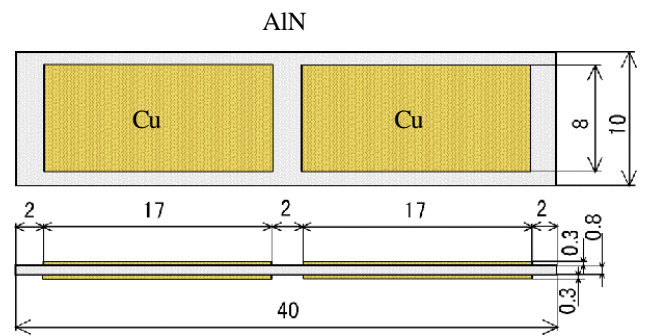
(a) Four-point bending test
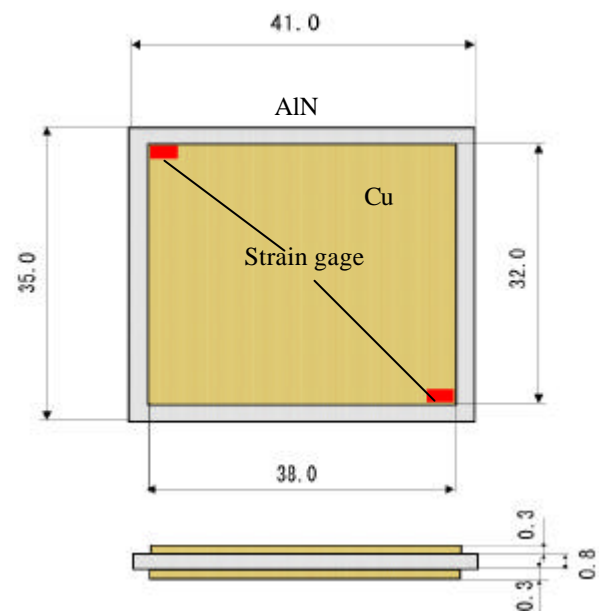
(b) Thermal cyclic test

Figure 1: Specimens
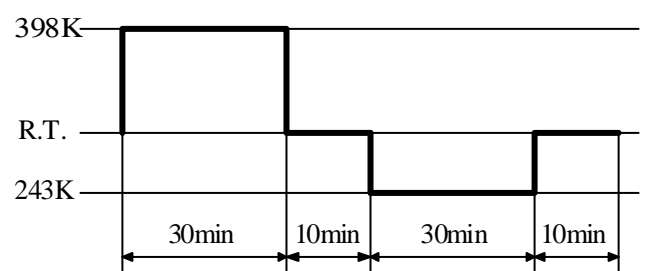
Figure 2: Thermal cyclic pattern

| (a) Whole view | (b) Magnified view |
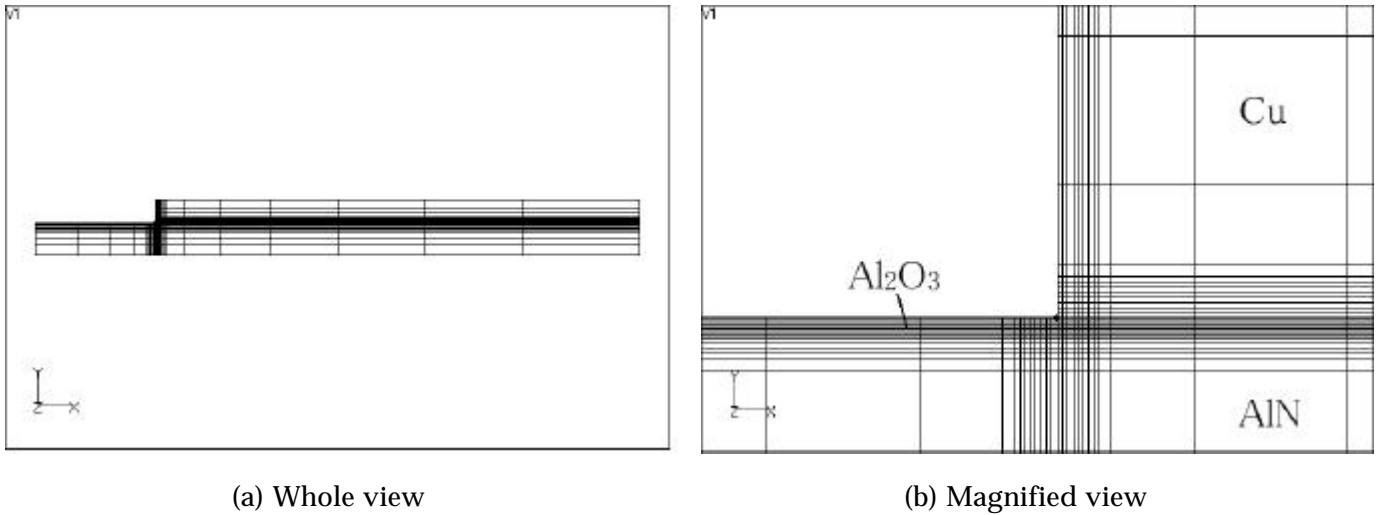
Figure 3: Analysis model

from energy variation of the whole analysis model system before and after of crack growth [3].

RESULTS AND DISCUSSION

Experimental results

Figure 4 shows the relationship between nominal fracture stress in the four-point bending tests and number of thermal cycles. The nominal fracture stress reduced with increasing of thermal cycles, and so it was found to be verified that the damages due to thermal cycles were accumulated with increasing thermal cycle.

The fracture of the substrate in the thermal cyclic life test shows the morphology of exfoliation between Cu and AlN at 140 cycles as Fig.5, and the occurrence of such exfoliation fracture could be detected by monitoring the output of strain gage.

Analytical result

Figure6 shows the distributions of the residual stress obtained through estimating fracture strength by bending tests. In the Fig.6, the stress is expressed as equivalent normal stress. The stress is concentrated within narrow range near the bonding surface of AlN, and reduces rapidly from surface to inner. The maximum stress, called fracture stress in following, is generated at point A in every specimen as shown in Fig.6. Figure7 shows
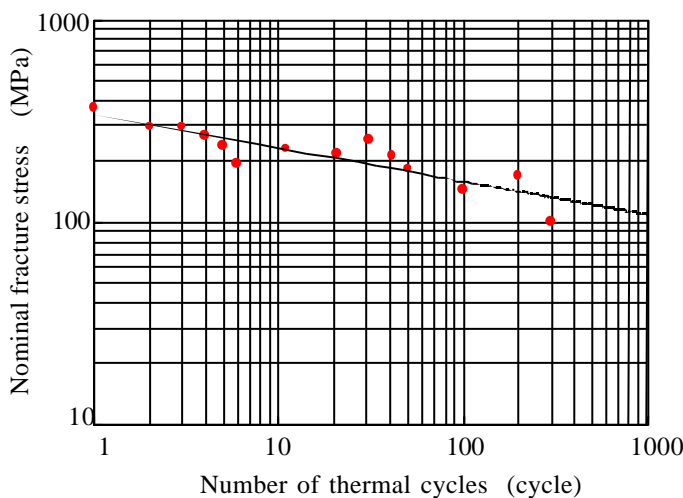
Figure 4: Relationship between nominal fracture stress in the four-point bending tests and number of thermal cycles
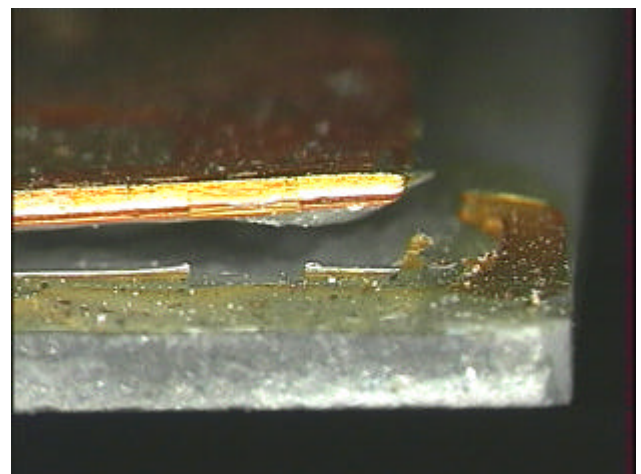
Figure 5: Fracture morphology of the substrate in the cyclic life test
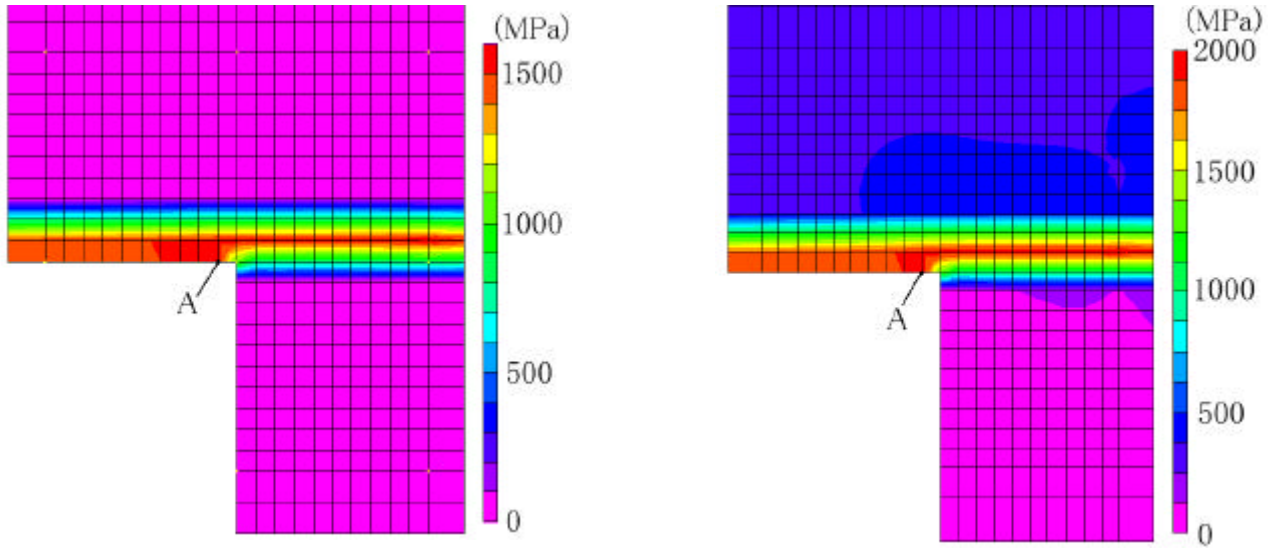
(a) 1 thermal cycle loaded specimen   (b) 5 thermal cycle loaded specimen

Figure 6: The distributions of the residual stress (equivalent normal stress).

relationship between analyzed fracture stress and number of thermal cycles. The true fracture stress is above 1900MPa and far larger than the four-point bending strength of the monolithic smooth AlN plate, 380MPa. Moreover, the stress is not constant and reduces with increasing of thermal cycles. Thus, the maximum tensile stress is not suitable for the criterion of the fracture. Therefore, the following discussions are according to the next assumptions; (1) the fracture occurs from the initial defect existing at the maximum stress point, and the defect can be regarded as initial crack, (2) sizes of initial cracks are almost same in every substrates tested, (3) the crack growth depends on the stress intensity factor, K, (4) unstable fracture occurs on reaching of K to fracture toughness value, K_{IC}.

Discussion based on assumption of crack growth

As for the time dependent crack growth in ceramics, the crack growth rate, *da/dt*, is evaluated as follows

$$\frac{da}{dt} = CK^n = C\left(j\,s_R\sqrt{pa_0}\right)^n = C\left(s_R\sqrt{pa_{eq}}\right)^n \tag{1},$$
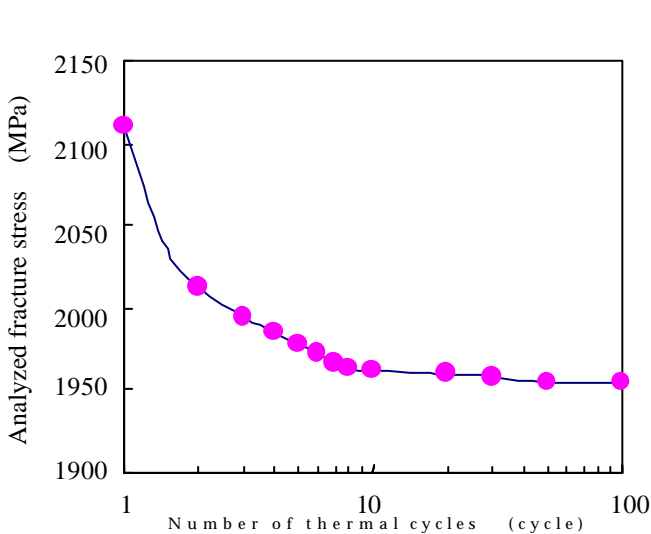
Figure 7: Relationship between analyzed fracture stress and number of thermal cycles
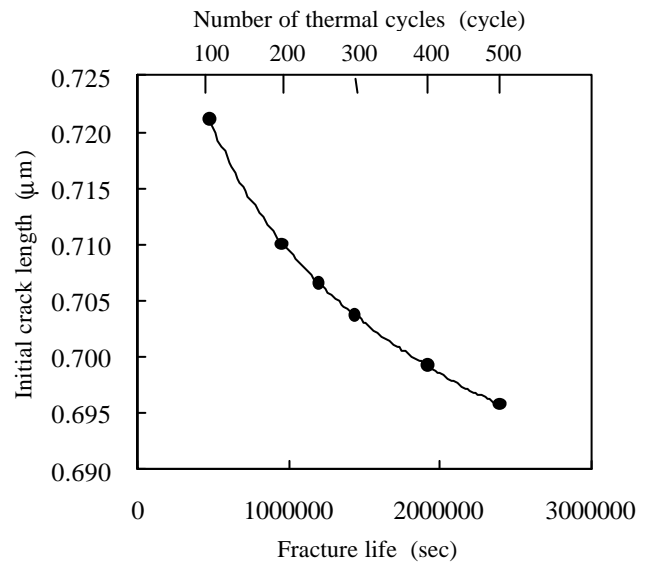
Figure 8: Relationship between the calculated fracture life and assigned initial crack length

(a) Non thermal cycle loaded specimen   (b) 5 thermal cycles loaded specimen
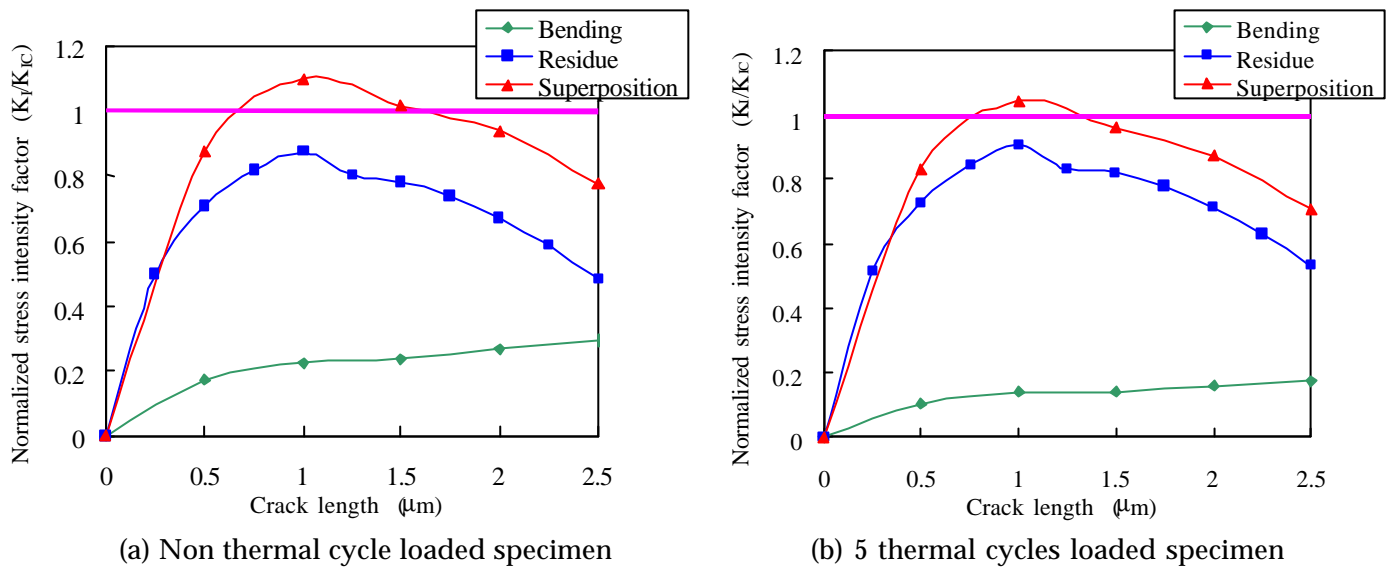
Figure 9: Relationship between normalized stress intensity factor and assigned crack length

where a_0 is initial crack length, C and n, material constants, , shape factor, $_R$, residual stress, $2a_{eq}$, surface crack length of equivalent semi-circular defect. The fracture life is defined as the duration of crack growth from initial length to final one causing unstable fracture of substrates, and so can be calculated by integrating eq.(1). Figure8 shows the relationship between the fracture life obtained by calculation and initial crack length assigned on the substrate as parameter. It was surmised from the number of cycles that the initial crack length is nearly 0.72 micrometer.

Figure9 shows relationship between stress intensity factor normalized by fracture toughness value and assigned crack length on the two specimens, where either thermal cycles of 0 and 5 were conducted. Though, both of residual stress and bending stress are different in either of specimens, the superposition stress intensity factors in both specimens reach fracture toughness value on reaching of crack lengths to 0.6~0.8micrometer. This crack length is well agreement with the crack length evaluated from result obtained in the cyclic life test mentioned above.

As a result, the fracture of the DBC substrates can be analyzed as the crack growth from initial defect depending on stress intensity factor, K. If the size of initial defect is known, the bending strength and/or thermal cycle life is predictable.

REFERENCES

1.   Mizunotani, Y. and Hashima, M. (1986) Toshiba review, 41, 9, 811.
2.   Sugiura, K. and Iwase, A. (1989) Toshiba review, 44, 81 626.
3.   Kobayashi, H. (1993); *Fracture mechanics*; Kyoritsu syuppan, Tokyo

STRESS ANALYSIS AND LIFE ASSESSMENT OF A GAS TURBINE BLADE

M. Mirzaei, R. Karimi

Department of Mechanical Engineering, T.M.U, Tehran, Iran.

ABSTRACT

This paper describes the stress analysis and life assessment of a first-stage air-cooled blade made of the superalloy IN738LC. Three-dimensional finite element thermal and stress analyses of the blade were carried out for the steady-state full-load operation. The results of these analyses were used for determination of the regions where the combination of high temperature and high tensile stress was sufficient for significant creep-fatigue crack growth. Accordingly, a critical point at the leading edge of the airfoil, near the root, was selected for crack modeling. With the assumption of occurrence of small-scale creep and thermal-fatigue during each start-stop cycle, the pertinent crack tip parameters were calculated using the energy domain integral method. An incremental crack growth scheme was considered and the total life for the growth of a 0.5mm surface crack to a 5mm through-thickness crack was calculated.

KEYWORDS: Life Assessment, Fatigue, Creep, Crack Growth, Turbine blade, Finite Element.

INTRODUCTION

The most sever cyclic duty for an industrial turbine blade is the peak-load generation commonly experienced in the utility combined-cycle plants, where the blades are subjected to frequent startups and shutdowns and also large numbers of working hours. Since these blades are made of superalloys and require costly manufacturing processes, they are very expensive to replace. Hence, it is essential to have accurate estimates of their useful life. Turbine blades are highly stressed components and because of their limited tolerance to cracks their life assessment is carried out in terms of crack initiation events [1]. However, the usage of Fracture Mechanics principles for modeling fatigue and creep crack growth can be considered as an important part of a comprehensive life assessment program. The accurate determination of fracture mechanics parameters is essential for modeling fatigue and creep crack growth. The investigation, partly reported in this paper, aims at fatigue and creep life assessment of a first-stage air-cooled blade made of the superalloy IN738LC.

Detailed failure analysis of cracked first-stage blades, for General Electric MS1001E industrial gas turbine, made of IN738LC has been reported by Bernstein and Allen [2]. They observed extensive leading edge cracking for a blade that had experienced 1800 start-stop cycles and 24000 hours of operation, with cracks penetrated through to the leading edge cooling hole. For an 11000-hour blade with 874 start-stop cycles, they observed a 0.5mm crack at the same location. In our investigation, we have tried to model a similar type of crack growth, for Siemens KWU V94 industrial gas turbine, using the results obtained from our finite element analyses and the material properties of the IN738LC obtained from the literature. The details

of the thermal and mechanical stress analyses of the blade without crack were reported in [3,4]. The results of these analyses indicated that the maximum tensile stresses occur at the suction side of the airfoil at the corner of an internal rib. The computation of crack tip parameters for cracks modeled at the suction side of the blade using the point-matching methods was reported in [5]. The calculations of crack growth parameters at this location showed that the crack driving forces are not sufficient for creep crack growth, mainly because of relatively low temperatures. In the current paper, semi-elliptical surface cracks were modeled at a critical region at the leading edge of the airfoil, near the root, which is the hottest region in the blade. The computation of crack tip parameters was performed using the energy domain integral method. With the assumption of occurrence of small-scale creep and thermal-mechanical fatigue during each start-stop cycle, the pertinent crack tip parameters were calculated. An incremental crack growth scheme was considered and the total life was calculated.

STRESS ANALYSIS

The thermal and mechanical stress analyses were carried out using the general-purpose finite element package LUSAS. The finite element models of the blade were constructed using 8-noded and 20-noded brick elements. Figure 1a depicts the finite element mesh of the entire blade. The centrifugal forces were applied as body forces for the rotor running speed of 3000 rev/min. The pressure distribution, obtained from an aerothermal analysis of the turbine, varied between 0.2 to 1 MPa on different locations on the pressure side of the blade. The gas temperature distribution around the blade, also obtained from an aerothermal analysis, varied between 350° to 850°C. Figure 1b shows the distribution of the maximum principal stress component, due to the centrifugal and pressure loadings, in the airfoil. It is clear that the maximum tensile stress occurs at the suction side of the airfoil near the root. However, if the mechanical and thermal stresses are combined, the location of the maximum tensile stress will shift to the corner of an internal rib, which is in fact the coolest point according to the thermal analysis results depicted in Figure 2a. The results also indicate that the leading edge is the hottest region of the blade. Hence, the crack modeling was performed in a critical region of the leading edge near the root, in spite of relatively lower tensile stresses in this region.

(a)   (b)
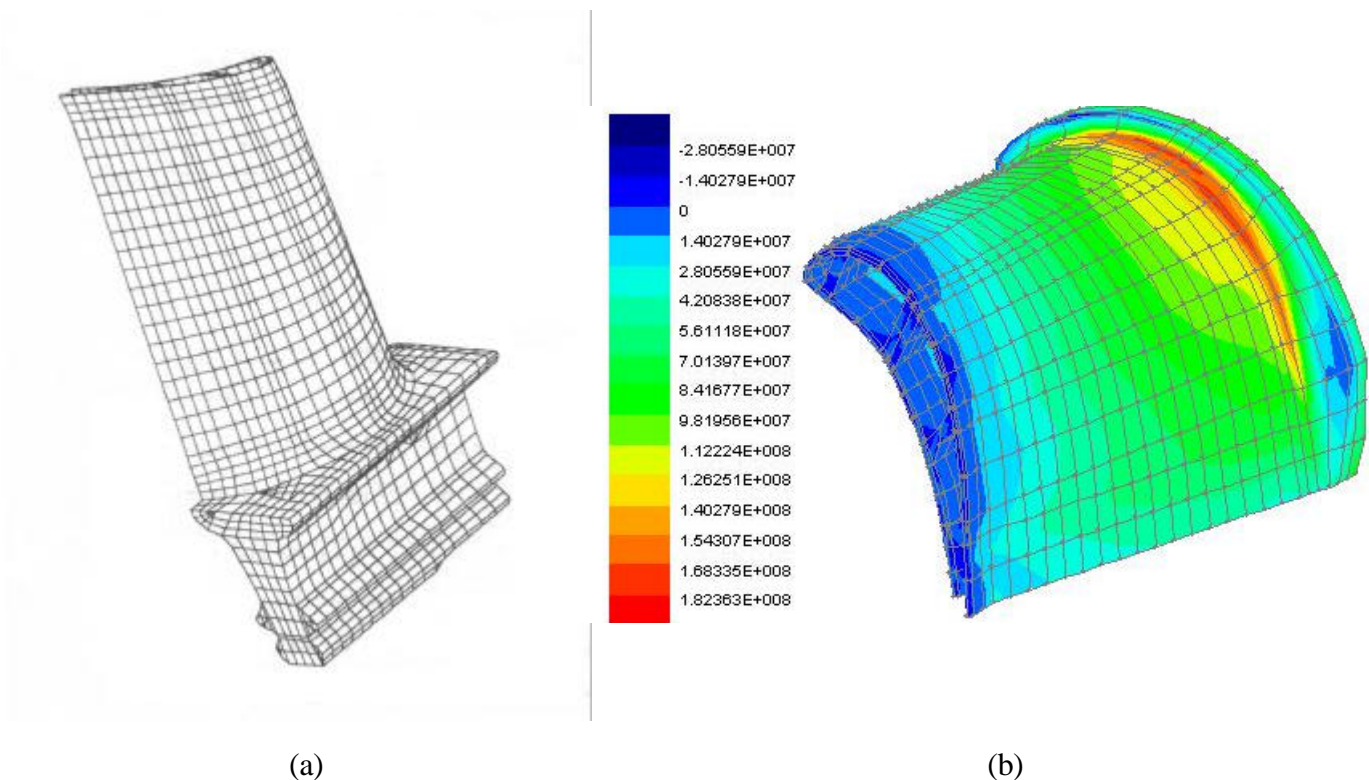
Figure 1: a) Finite Element mesh of the entire blade. b) Contours of maximum principal stress due to the mechanical loadings (stresses are in Pascal).

CRACK GROWTH ANALYSIS

The two major parameters used for correlating creep crack growth data are the stress intensity factor K and the integral C^*. The applicability of K is limited to situations where the size of the crack-tip creep zone is small relative to the crack length and other geometric parameters of the component. This is the so-called Small Scale condition (SSC), as opposed to the Steady State condition (SS) in which the crack propagation is accompanied by extensive creep deformation ahead of the crack tip. In the latter condition, the path-independent integral C^* is usually used. The transition time for SSC condition to turn to SS condition can be estimated by [6]:

$$t_1 = \frac{1+2\,b_n}{n+1}\,\frac{K^2(t_1)(1-n^2)}{C^*(t_1)E} \tag{1}$$

in which â is dependent on the waveform of loading and is defined by:

$$K(t) = K_1 t^b$$

where K(t) is the applied stress intensity parameter as a function of time and K_1 is a constant, í is the Poisson's ratio, E is the elastic modulus, n is the Norton Law exponent, and C^* is the creep integral. If the cycle time t_C is less than t_1 then K is the correct crack tip parameter for correlating creep crack growth. Since the IN738LC is a high-strength creep-resistant material and the start-stop cycle-time of the peak load turbines are usually less than 10 hours, the assumptions of SSC condition and validity of applying K as the correlation parameter were considered in this study. Several procedures are available for numerical evaluation of stress intensity factors. In this study we used the energy domain integral method for calculation of the J integral and the SIF.

Crack Modeling

Figure 2b depicts the section of the airfoil at the crack location, where the mesh was refined for crack modeling. In order to model the crack, new nodes were added on the crack plane. Accordingly, the elements above the crack plane were redefined using the new nodes. In this way semi-elliptical cracks with different lengths from 0.5mm to 5mm were modeled in the area of refined mesh.

(a)   (b)
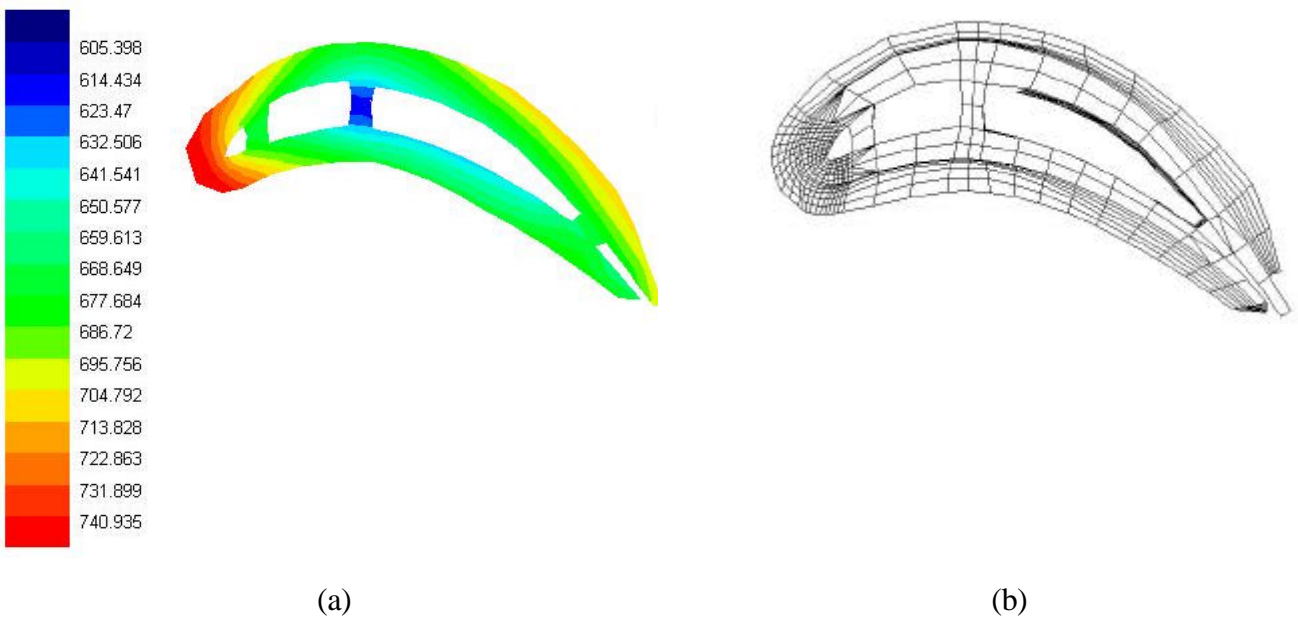
Figure 2: a) Temperature distribution in a section of the airfoil near the root (C°). b) Modified finite element mesh at the same section for crack modeling.

Computation of the J Integral

The general formulation of the energy domain integral method, as proposed by Shih et. al. [7,8], in the absence of plastic strains and crack surface tractions can be written as:

$$J = \int_{A^*} \left\{ \left[\mathbf{s}_{ij} \frac{\partial u_j}{\partial x_1} - W \mathbf{d}_{1i} \right] \frac{\partial q}{\partial x_i} + \left[\mathbf{a} \mathbf{s}_{ii} \frac{\partial \mathbf{q}}{\partial x_1} - F_i \frac{\partial u_j}{\partial x_1} \right] q \right\} dA \tag{2}$$

in which W is the stress work given by: $W = \int_0^{e_{kl}} \mathbf{s}_{ij} d\mathbf{e}_{ij}$

In the above equations A^* is the integration area, σ_{ij} and ε_{ij} are the Cauchy stress and strain tensors, u is the displacement vector, δ is the Kronecker delta, q is an arbitrary function that is equal to unity on $\tilde{A}_0$ and zero on $\tilde{A}_1$ (the inner and the outer integration paths respectively), α is the coefficient of thermal expansion, θ is the temperature, and F_i are body forces. The detailed instructions for the finite element implementation of the domain integral method are described in [9]. In the absence of thermal strains and body forces within the integration area, the discretized form of the domain integral can be written as:

$$J = \sum_{A^*} \sum_{P=1}^{m} \left\{ \left[\left(\mathbf{s}_{ij} \frac{\partial u_j}{\partial x_1} - W \mathbf{d}_{1i} \right) \frac{\partial q}{\partial x_i} \right] \det \left(\frac{\partial x_j}{\partial \mathbf{x}_k} \right) \right\}_P \mathbf{f}_P \tag{3}$$

in which m is the number of Gaussian points per element, $\hat{\imath}_k$ are the parametric coordinates for the element, and ω_p is a weighting factor. The above expression was evaluated for different crack lengths by a computer program [10], using the pertinent values obtained from the output files of LUSAS. Accordingly, the K values were calculated using the following expression:

$$J = \frac{\left(1 - \mathbf{n}^2\right)}{E} K_I^2 \tag{4}$$

Finally, using a regression analysis, the following expression was obtained for the variation of K with the crack length at the desired region:

$$K_I = 58.4 \times a^{0.206} \tag{5}$$

Crack Growth Calculations

The following expressions were obtained for fatigue and creep crack growth rates of IN738LC, based on the data presented in [11,12]:

$$\left. \frac{da}{dN} \right|_{Fatigue} = 6.7 \times 10^{-12} \Delta K^{3.5} \qquad \dot{a}(K) = \left. \frac{da}{dt} \right|_{Creep} = 2.07 \times 10^{-19} K^{7.18} \tag{6}$$

The total crack growth per working cycle, da/dN, was then expressed as:

$$\frac{da}{dN} = \left. \frac{da}{dN} \right|_{Fatigue} + \int_0^{t_C} \dot{a}(K) dt \tag{7}$$

in which, t_C is the holding time during each start-stop cycle. The numerical integration of the above equation between the two crack lengths of 0.5mm and 5mm, for a holding time of 8 hours, resulted in a total life of 11368 hours and 1421 start-stop cycles.

CONCLUSIONS

Three dimensional finite element thermal and mechanical analyses of an air-cooled gas turbine blade were carried out under steady-state full-load operation. It was found that the maximum tensile stress due to the mechanical loadings occurs at the suction side of the airfoil near the root. However, if the mechanical and thermal stresses are combined, the location of the maximum tensile stress will shift to the corner of an internal rib, which is in fact the coolest point of the section. The results also indicate that the leading edge is the hottest region of the blade. Hence, the crack modeling was performed in a critical region of the leading edge near the root, in spite of relatively lower tensile stresses in this region. Since the IN738LC is a high-strength creep-resistant material and the start-stop cycle time of the peak load turbines are usually less than 10 hours, the assumptions of small scale creep condition and validity of applying K as the correlation parameter were considered in this study. The computation of crack tip parameters was performed using the energy domain integral method. An expression for total crack growth per working cycle was obtained using the results obtained from our finite element analyses and the material properties of the IN738LC obtained from the literature. The numerical integration of the fatigue-creep crack growth expression between the two crack lengths of 0.5mm and 5mm, for a holding time of 8 hours, resulted in a total life of 11368 hours and 1421 start-stop cycles. It can be concluded that the blade under study has a very good tolerance to the existence of relatively large and detectable cracks. However, the more reliable predictions of crack growth rates and lifetime assessments require more sophisticated analyses that should consider the effects of thermal transients during each start-stop cycle.

REFERENCES

1. Viswanathan, R., (1989) "Damage Mechanisms and Life Assessment of High-Temperature Components," ASM International, Metals Park, Ohio 44073.
2. Bernstein, H.L., and Allen, J.M., (1992) "Analysis of Cracked Gas Turbine Blades," *Journal of Engineering for Gas Turbines and Power*, Vol. 114, pp. 293-301.
3. Hoseini, S.A. and Mirzaei, M., (1998) "Mechanical Stress Analysis of an Industrial Gas Turbine Blade," Proceedings of the Third International Mechanical Engineering Conference, Tehran, Volume 3, pp. 939-946.
4. Hoseini, S.A. and Mirzaei, M., (1998) "Thermal Stress Analysis of a Gas Turbine Blade," Proceedings of the Third International Mechanical Engineering Conference, Tehran, Volume 3, pp. 947-954.
5. Mirzaei, M., Janbozorgi, A., and Hoseini, S.A., (1999) "Computation of Fracture Mechanics Parameters for an Industrial Gas Turbine Blade," Proceedings of the International Conference on Fracture and Damage Mechanics, Queen Mary and Westfield College, London.
6. Saxena, A., (1988) "Limits of Linear Elastic Fracture Mechanics in the Characterization of High-Temperature Fatigue Crack Growth," Basic Questions in Fatigue, Vol. II, ASTM STP 924, pp. 27-40.
7. Shih, C.F., Moran, B., and Nakamura, T., (1986) "Energy release rate along a three dimensional crack front in a thermally stressed body", *International Journal of Fracture*, Vol.30, pp 79-102.
8. Moran, B., and Shih, C.F., (1987) "A General Treatment of Crack Tip Contour Integrals," *International Journal of Fracture*, Vol. 35, pp. 295-310.
9. Dodds, R.H., Jr. and Vargas, P.M., (1988) "Numerical evaluation of domain and contour integrals for nonlinear fracture mechanics," Report UILU-ENG-88-2006, University of Illinois, Urbana, IL.
10. Karimi, R. (2000), MSc Thesis, Tarbiat Modarres University, Tehran, Iran.
11. Holdsworth, S.R., and Hoffelner, W., (1982) "Fracture Mechanics and Crack Growth in Fatigue," *High Temperature Alloys for Gas Turbines*, Liege, Belgium, pp.495-549.
12. Hoffelner, W., (1986) "Creep Dominated Damage Processes," Riedel Publishing Co., Dordrecht, Holland, pp.413-440.

ORAL REFERENCE: ICF100460OR

Stress Analysis near Crack Tip in Mixed-Mode Condition by Speckle Photography Using an Intelligent Hybrid Method

Kenji Machida [1], Kenji Usui [1] and Hiroyuki Okamura [1]

[1] Department of Mechanical Engineering, Science University of Tokyo,
2641 Yamazaki, Noda-shi, Chiba, 2788510, Japan

ABSTRACT

An experiment was conducted on the compact normal and shear specimen made of homogeneous and dissimilar materials subjected to various kinds of mixed-mode loading. The displacement at any point on the specimen was obtained by pointwise filtering of the specklegram using a thin laser beam. The displacement obtained by speckle photography is not as smooth as that obtained by the finite element analysis. Therefore, the displacement data were smoothed by 2 D FFT filtering and least squares method. Then, stress-intensity factors of the asymptotic solution derived by Sun and Jih were estimated using the displacement data obtained from speckle photography by the least squares method. The displacement of each node was calculated from the asymptotic solution by using stress-intensity factors obtained by the previous process. From the nodal displacement, the stress-strain analysis was conducted by using the latter half of FEM algorithm. Moreover, the stress analysis was carried out using an intelligent hybrid method proposed by Nishioka et al. The contour diagrams of stress and strain obtained by using the raw displacement data of experiment remarkably differed from those obtained by FEM analysis. However, the stresses obtained the present analyzing system were very similar to those obtained by FEM. Consequently, the stresses near the crack tip of homogeneous and dissimilar materials can be evaluated by the present stress-analyzing system.

KEYWORDS

Stress Analysis, Stress Intensity Factor, Finite Element Analysis, Speckle Photography, 2 D Fast Fourier Transform, Young's fringes, Image Processing, Intelligent Hybrid Method

INTRODUCTION

A large amount of displacement data must be taken to investigate the singular field near the crack tip. The Young's fringes analysis procedure is usually time-consuming and tedious. Therefore, image processing is indispensable to carry out fringe analysis with high speed and accuracy. We presented an image-processing system [1][2] for the numerical processing of the diffraction pattern of Young's fringes from a double-exposure speckle photograph. The fringe spacing and orientation are determined using only one Young's fringes pattern without any other diffraction halo patterns. This system is based on the 2 D FFT and iteration using the bounded Newton-Raphson algorithm of the fringe pattern with the resolution of 256x256x8 bits. Therefore, it enables us to automatically analyze the specklegrams of a noisy and poor fringe pattern. The measurement of deformation using laser speckle photography can be carried out with high accuracy, reliability and speed. To date, the stress-intensity factors of homogeneous and dissimilar
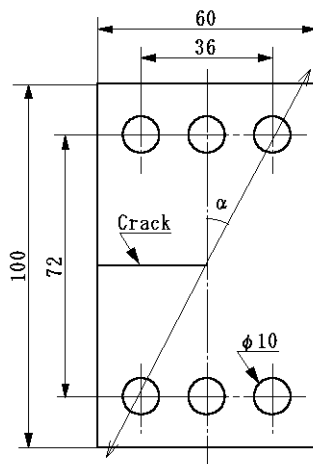
Figure 1: Specimen configuration
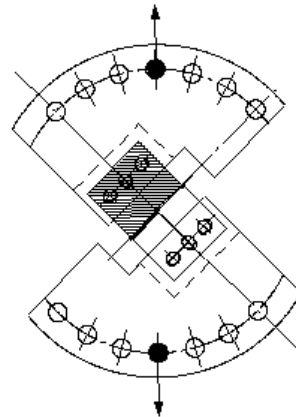
Figure 2: Loading device
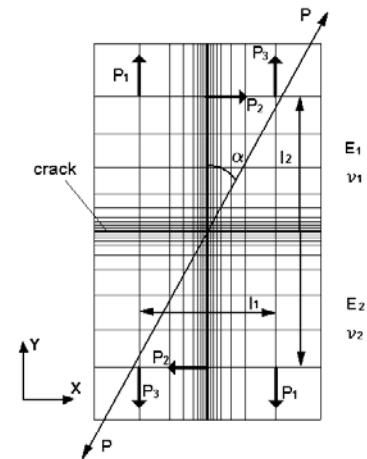
Figure 3: Mesh pattern and loading condition

materials have been evaluated with high accuracy by measuring the displacement along the crack-line on the specklegram [3]-[5]. In this study, the displacements near the crack tip of the homogeneous and dissimilar material CNS (compact normal and shear) specimens subjected to the mixed-mode loading was measured by the speckle photography. By setting up the mesh pattern similar to that in the finite-element analysis, the displacement of each nodal point was measured. The displacement data were smoothed by the 2 D FFT filtering and least squares methods. Then, stress-intensity factors of the asymptotic solution derived by Sun and Jih [6] were evaluated using the displacement data obtained from speckle photography by the least squares method. The displacement of each node was calculated from the asymptotic solution using stress-intensity factors obtained by the previous process. From the nodal displacement, the stress-strain analysis was conducted by using the latter algorithm of FEM. Finally, the stress-strain relationship was discussed in terms of comparison between the speckle photography and finite-element analysis. Moreover, the intelligent hybrid method proposed by Nishioka et al. [7][8] was applied to the stress analysis.

SMOOTHING OF DISPLACEMENT DATA

The displacement data obtained using speckle photography show so little scattering that the error must be removed. Thus, the smoothing process was carried out on the displacement components (u, v) in the x and y directions. Two smoothing methods were employed. One was the masking method using the 2 D FFT. Another was the line-smoothing method using the least squares method. In conventional image processing, the smoothing is carried out by removing the high-frequency component in the FFT. However, even the main data are destroyed in the case of small pixel data. Therefore, the frequency components were omitted except on the main axes. This method enables us to remove the large error without destroying the main data. A 2 D FFT of 4x4 displacement data was carried out, and then a 2 D inverse FFT was carried out by setting the real and imaginary parts of the low power spectrum at zero. This filtering process was performed by moving the mask step-by-step from the left to the right, and then was performed downward in turn. This process was carried out by moving the mask over all data one to four times. The protruding data were removed without destroying the main frame by this process. A small error of data on the mesh line was removed by the polynomial approximation of the least squares method. In addition, the lost data can be complemented using the least squares method during image processing.

EXPERIMENT

The two kinds of specimens that were made of the acrylic homogeneous and acrylic-aluminum dissimilar materials were used for the measurement of displacement around the crack-tip. Young's modulus and Poisson's ratio of aluminum and acrylic resin were 67.3GPa, 0.33 and 3.06GPa, 0.38, respectively. The

configuration of specimen is shown in Fig. 1. The thickness of homogeneous and dissimilar materials was 16 mm and 15 mm, respectively. First, the upper and lower parts of the specimen were machined separately and then two pieces were bonded. A crack was introduced by introducing a Teflon sheet of 0.02 mm thickness between the two pieces during bonding. The mixed-mode loading was applied to the specimen using a device proposed by Richard and Benitz [9] as shown in Fig. 2. This device enables us to carry out the experiments under the seven kinds of mixed-mode loading. The displacement at any point on the specimen was obtained by pointwise filtering of the specklegram using a thin laser beam. For a full field analysis, the specklegram was mounted on an X-Y stage driven by stepping motors controlled by microcomputer. The displacement data were taken in the area of 10 mm(H) x12.8 mm(W) around the crack tip.

MODEL FOR ANALYSIS

The 3 D FEM model was generated by developing the 2 D mesh as shown in Fig. 3 to the thickness direction. One-half portion of the specimen was modeled by the symmetry with respect to the midsection of the specimen by using the isoparametric elements of 20 nodes. The layer division ratio was 1:2:3:4:5 from the free surface and number of elements and nodes was 2400 and 11969, respectively. The same loading condition as Kishimoto et al. [10] was employed for the mixed-mode loading. The materials 1 and 2 denote the upper and lower parts of the specimen, respectively. The homogeneous material is an acrylic resin. The material 1 is aluminum and material 2 is acrylic resin for the dissimilar material. The stress-intensity factor was evaluated by the virtual crack extension method (VCEM).

RESULTS AND DISCUSSIONS

Comparison between stress-intensity factors

To simplify the comparison between stress-intensity factors, the non-dimensional stress-intensity factors was evaluated as follows:

$$F_j = \frac{K_j}{\dfrac{P}{WB}\sqrt{\pi a}} \qquad (j = I, II) \tag{1}$$

Here, P is the load, W and B are the width and thickness of the specimen, respectively.
Figure 6 shows the variation of the stress-intensity factors by the experiment and FEM with a load application angle α of acrylic homogeneous material (a) and acrylic-aluminum dissimilar material interface

(a) Homogeneous material   (b) Dissimilar material
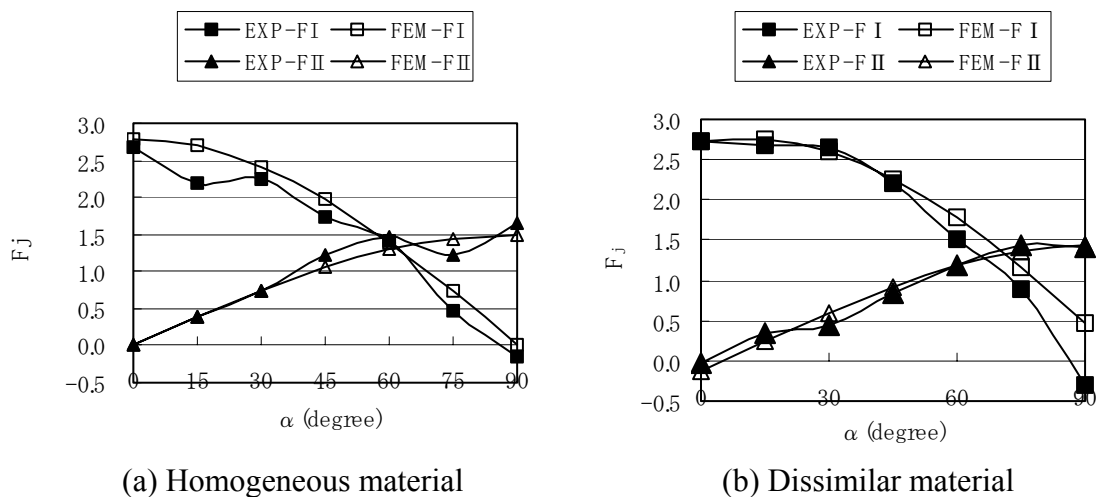
Figure 6: Variation of stress-intensity factors with a load application angle α.

<table>
<tr><td>(a) EXP</td><td>(b) FEM</td></tr>
</table>
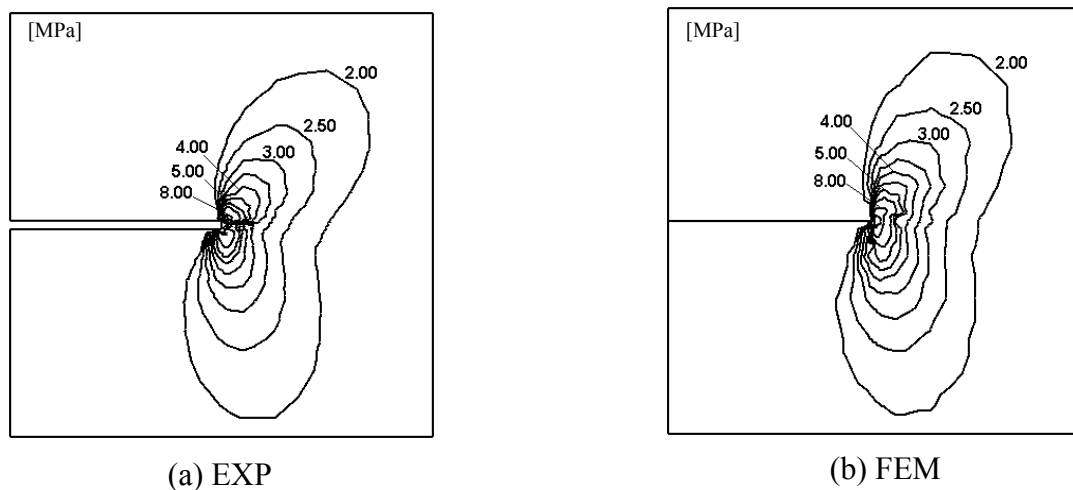
Figure 7: Contour map of σ_y (Homogeneous)

<table>
<tr><td>(a) EXP</td><td>(b) FEM</td></tr>
</table>
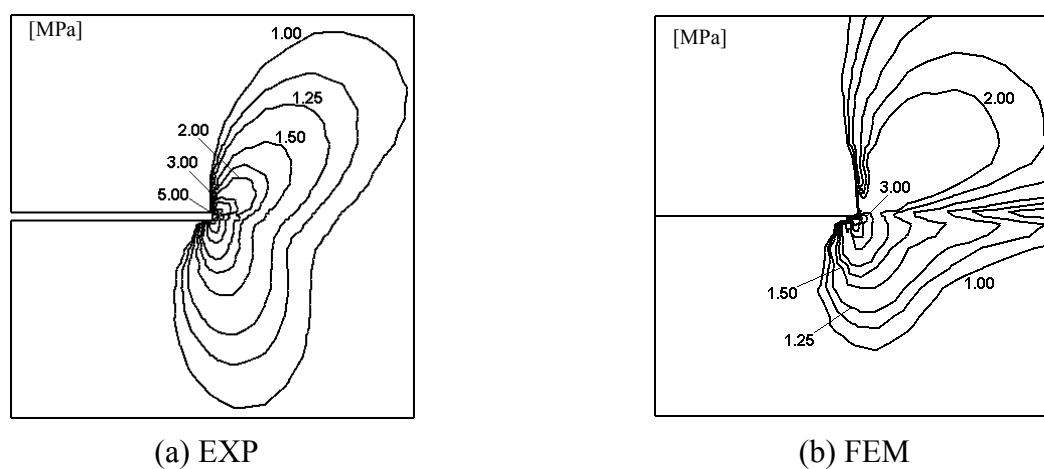
Figure 8: Contour map of σ_y at free surface (Dissimilar)

crack (b). Although some scatter can be seen, F_I decreases while F_{II} increases with an increase in α. This tendency can be seen in both experiment and FEM. However, at $\alpha= 90$ degrees, F_I showed zero or less in homogeneous material, and the large difference is seen in F_I of dissimilar material. It is considered that the same loading condition as FEM could not be performed in the experiment.

Contour map of σ_y

Figure 7 shows the contour map of σ_y (normal stress in the y direction) within 5 mm(W)x5 mm(H) at the free surface and $\alpha=45$ degrees of homogeneous material. Figures 7a and 7b were obtained from the experiment which assumed the plane stress and FEM, respectively. Although the stress state of the experiment is slightly lower than that of FEM, the similar distribution can be seen in the experiment and FEM. Moreover, similar tendency was seen in the distribution of σ_x and τ_{xy}.

Figure 8 shows the contour map of σ_y at the free surface obtained by the experiment assumed a plane stress(a) and FEM (b) at $\alpha=45$ degrees of dissimilar material. The upper and lower parts of this figure are aluminum and acrylic resin, respectively. Although the stress-intensity factors were nearly close, both contour map of σ_y are quite different in the dissimilar material. The stress in the experiment was calculated by the 2 D approximation assuming the plane stress or plane strain condition. However, both of the results differed from FEM. On the other hand, the 3 D analysis was carried out in FEM as mentioned above. The difference in a material constant between material 1 and material 2 causes the large difference of the displacement of the thickness direction. This is considered to have affected the stress distribution in FEM greatly.

<table>
<tr><td>(a) EXP (Plane strain)</td><td>(b) FEM (Midsection)</td></tr>
</table>
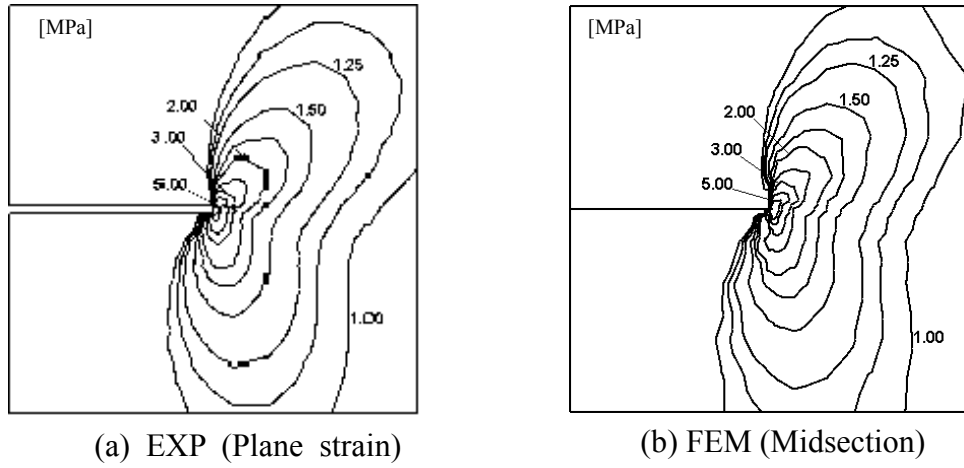
Figure 9: Contour map of σ_y (Dissimilar)

Figure 9 shows the contour map of σ_y at α=45 degrees of dissimilar material. Figure 9a is a contour map at the free surface obtained from the experiment by assuming the plane strain. Figure 9b is a contour map at the central part of the specimen obtained from FEM. K_I and K_{II} at the free surface assuming the plane strain were about 24% and 10% higher than those at the central part of the specimen, respectively. Although the stress value of Fig. 9a is slightly low, the shape of distribution is very similar to that of FEM (Fig. 9b). Therefore, it was revealed that the asymptotic solution of Sun and Jih is applicable to evaluate the stress field from the surface to the inside in homogeneous material and the inside except the surface in dissimilar material.

Intelligent hybrid method

The intelligent hybrid method proposed by Nishioka et al. was applied to the analysis of stress-strain from the displacement data obtained by speckle photography. Figure 10 shows the contour map of σ_y obtained from raw displacement data (a) and intelligent hybrid method (b) at the surface and α=45 degrees of homogeneous material. The raw data obtained from speckle photography were smoothed by the 2 D FFT filtering and least squares methods. However, it is difficult to evaluate the stress-strain accurately using the raw displacement data as shown in Fig. 10a. The experimental displacement field contains measurement errors so that one obtains the following finite element equation:

$$[K]\{Q^{\mathrm{mod}}\} = \{F\} - [K]\{Q^{\mathrm{exp}}\} \tag{2}$$

where $\{Q^{\mathrm{mod}}\}$ and $\{Q^{\mathrm{exp}}\}$ are the nodal displacement vectors of the modifying and experiment fields in entire hybrid analysis area. $[K]$ and $\{F\}$ are the global stiffness matrix and the global nodal force vectors, respectively. First, we calculate the following equation.

$$\{R\} = \{F\} - [K]\{Q^{\mathrm{exp}}\} \neq 0 \tag{3}$$

where $\{R\}$ is the restoration forces. The modifying displacement field can be evaluated by solving the following equation.

$$[K]\{Q^{\mathrm{mod}}\} = \{R\} \tag{4}$$

$\{Q^{\mathrm{mod}}\}$ can be obtained from 2 D FEM by putting R as the nodal load and constraining all nodes at the outer boundary in x and y directions. Finally, the true displacement field is obtained by the following equation.

$$\{Q\} = \{Q^{\mathrm{exp}}\} + \{Q^{\mathrm{mod}}\} \tag{5}$$

(a) Raw data   (b) Hybrid method
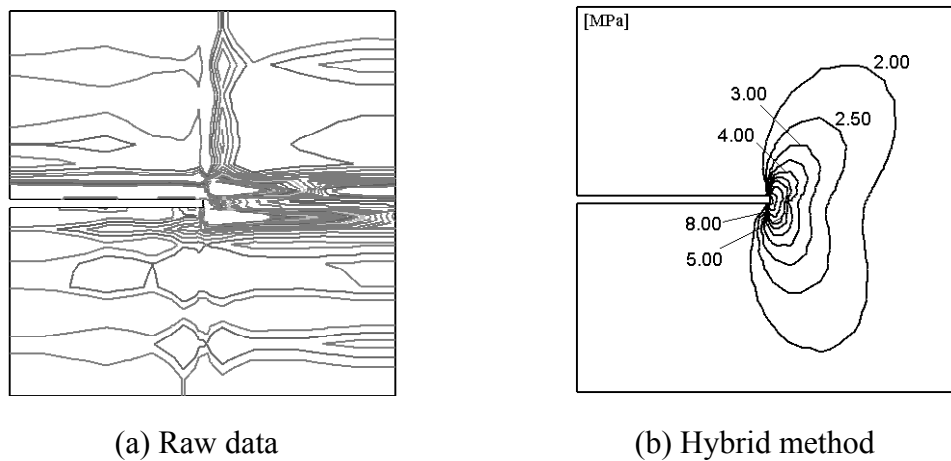
Figure 10: Contour map of σ_y. (Homogeneous)

Figure 10a and 10b show the contour maps of σ_y obtained using raw data and hybrid method at the free surface and α=45 degrees of homogeneous material, respectively. Figure 10a shows the damaged stress distribution while Fig. 10b shows the quite similar distribution to that obtained by FEM.

The stress-strain near the crack-tip was evaluated by two methods; the asymptotic solution derived by Sun-Jih and the intelligent hybrid method. The asymptotic solution is not applicable to the general problem while the hybrid method is applicable to all problems. Therefore, the hybrid method is very useful to the stress analyzing system by experiment.

CONCLUSION

(1) The stress-intensity factors of Sun and Jih can be evaluated with high accuracy using speckle photography.
(2) The asymptotic solution derived by Sun and Jih can evaluate the stress-strain of homogeneous material with high accuracy.
(3) The intelligent hybrid method can be applied to the displacement measurement and stress-strain analysis of speckle photography.
(4) Although the asymptotic solution of Sun and Jih cannot evaluate the stress-strain of the surface of dissimilar material with an interface crack, it is applicable to stress field of the inside except the surface.

ACKNOWLEDGEMENT

References

1. Machida, K. Kikuchi, M. Sawa, Y. and Chiang, F.P. (1994) *Trans. Jpn. Soc. Mech. Eng.*, 60-573A, 1294.
2. Machida, K. Kikuchi, M. Sawa Y. and Chiang, F.P. (1994) *Optics and Lasers in Engineering,* 21-3, 151.
3. Machida, K. (1997) *OPTICAL REVIEW*, 4-2, 253.
4. Machida, K. (1997) *Trans. Jpn. Soc. Mech. Eng.*, 63-6060A, 308.
5. Machida, K. (1998) *Trans. Jpn. Soc. Mech. Eng.*, 64-618A, 284.
6. Sun, C.T. and Jih, C.J. (1987) *Eng. Fract. Mech.* 28-1, 13.
7. Nishioka, T. Ikekita, H. and Tamai, K. (1997), *Comp. Mech.*, 20, 101.
8. Nishioka, T. Kurio, K. and Nakabayashi, H. (2000), *Exp. Mech.*, 40-2, 170.
9. Richard, H.A. and Benitz, K. (1983) *Int. J. Fract.* 22, R55.
10. Kishimoto, K. Fukano, H. Yoshida, T. and Aoki, S. (1990) *Trans. Jpn. Soc. Mech. Eng.*, 56-524, 957.

Stress analysis of beam-to-column connection for earthquake-resistance welded steel structure based on FEM

Zhang Yufeng, Yao Guochun, Huo Lixing, Yang Xinqi, Jing Hongyang

College of Material Science & Engineering, Tianjin University, Tianjin 300072, China

Abstract:

Brittle fracture of beam-to-column connection in steel construction under earthquake loading is affected greatly by the type of welded joints. In this study the artificial crack is formed by lack of fusion in the flange weld of beam in the beam-to-column connection, based on the model of typical beam-to-column connection in China, the stress distributions of connections have been computed by three-dimensional finite element method. It is concluded that stresses of connections could be reduced by connection reinforcement. Among reinforcements it is the most effective way to improve stress concentration at the root of flange weld by adding upstanding ribs on outside beam flange. In addition, stresses of hot spots in the connection without crack were computed first, then based on the driving force of crack calculated by formula of SIF, the stress intensity factors, K_I are obtained for cracks with 3 or 6 mm deep and with the length equal to width of beam web under two states, with or without residual stresses. Load equal to plastic moment of beam was assumed on this beam end to simulate moment loading under earthquake. Meantime the least fracture toughness of reinforced connection with cover plate to avoid brittle fracture is given among several reinforced forms. The analysis results can be used for earthquake-resistance design of beam-to-column connection of steel structure.

Key Words:

Beam-to-column connection, Earthquake-resistance, Stress intensity factor

1. Typical model of beam-to-column connection in China

In steel structure of high-rise buildings beam-to-column connections, which are joined by method of combining weld with bolt, are usually rigid. In these connections beam flanges are connected with column by grooved penetration weld, while beam web bolted by high-strength bolts with shear plate, which is connected to column with weld. Shear plate is used to carry shear force, while flange weld to carry moment loading. From the experiences of the well-known earthquakes of America and Japan, it can be seen that damages of steel structures due to failure of beam-to-column connection often took place at the root of flange weld, and that the initiation points of failure were more often at bottom flange weld than at top flange weld. To ensure the quality of weld, backing bar is used to support weld puddle of flange weld so that artificial crack is formed at the intersection of backing bar and column flange because of lack of fusion.

The examples of rigid beam-to-column connection used for FEM computation in this investigation are taken from Manual of anti-earthquake design of construction [1]. The intersection of beam and column are

Table 1: Mechanic property of weld and base metal of Q235B

Material	σ_y(MPa)	σ_u (MPa)	δ (%)
Q235B base metal	267	444	36.0
Q235B weld metal	372.8	492.2	36.4

hot-rolled type-H steel HK400×300×13.5×24 and HZ550×210×11.1×17.2 respectively. The span of beam is 7.2 meters. Table 1 shows mechanic property of material steel Q235B for column and beam,. Beam flanges are joined with column by penetration weld, while beam web is connected to column by shear plate, which is bolted with high-strength bolt, M20, Grade10.9. Fig.1 shows the detail of beam-to-column connection.

2. FEM analysis

Connection type with beam web unconnected to column is dealt as original type. When beam web connects with column flange thoroughly, it is equal to all-welded structure. In this case moment of structure mainly carried by flange weld will be reduced. Stress status of actual structure is between that of original type and all-welded type.
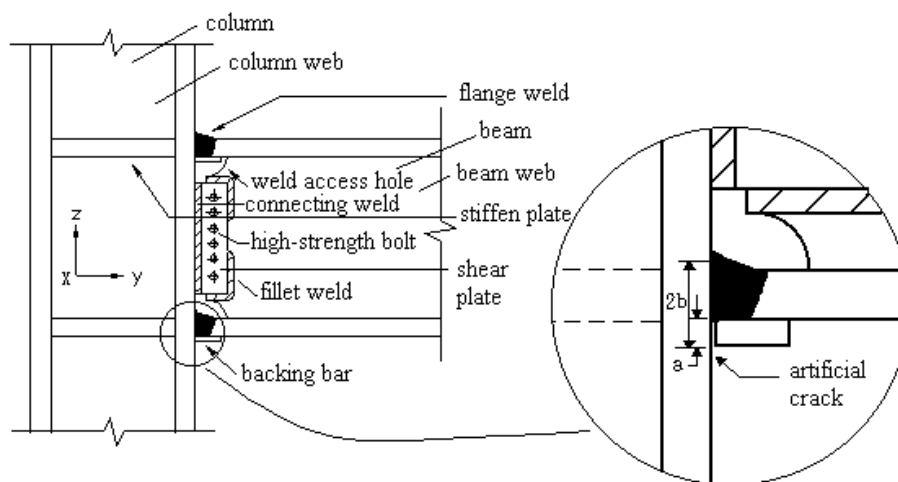
Figure 1: Detail of structure of beam-to-column connection

In addition to structure above, reinforced connections include connection with cover on flange, with stiffened rib inside beam and with upstanding rib on flange. Five alternative types of beam-to-column connection were modeled and analyzed as fellows:

Case one：Original structure (with artificial crack),
Case two：All-welded structure (with artificial crack),
Case three：Reinforced connections with cover plate(with artificial crack),
Case four：Reinforced connections with stiffened rib(with artificial crack),
Case five：Reinforced connections with upstanding rib(with artificial crack).
As examples, The sketch maps of three types of reinforced connection are shown in fig.2.

The example was modeled on eight-node brick elements using three-dimension elastic-plastic finite element program Algor-Feas. The material properties were modeled by Von Mises yield criterion with associated plastic flow rules. In order to mesh the structure, some simplification of bolted joint and weld shape was made. For its symmetry about plane perpendicular to X-axis, half of structure was used. Fig. 3 shows 3D mesh of beam-to-column connection. Artificial crack was treated as notch, which about 0.02 mm wide was at the root of flange weld.
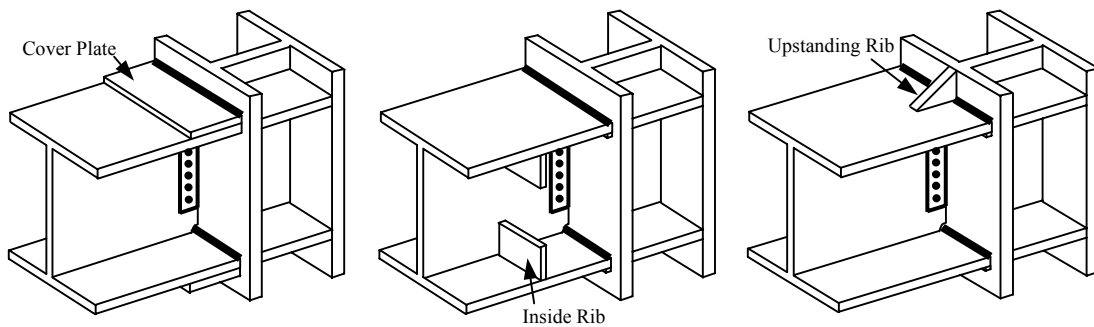
Figure 2: Three types of reinforced beam-to-column connections

3. Analysis result

From FEM computation, stress distribution of flange weld of different types could be obtained. As the stress in the symmetry plane of beam is higher than that of any other place, along beam width away from
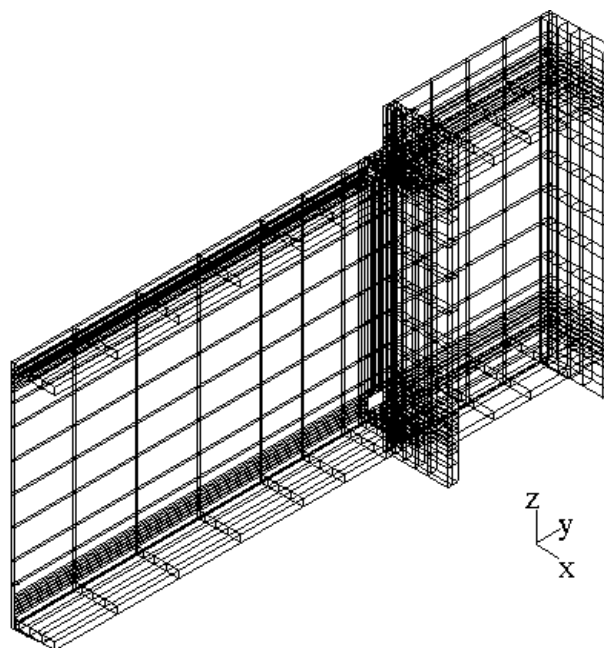
Figure 3: Three-dimensional mesh of beam-to-column connection

symmetry plane the stress reduces. There are high stress in the middle of flange weld of intersection of beam

and column and intersection point between flange and web at the weld access hole. These hotspots where exist stress concentration are weak point of structure, such as point A, B and C that corresponds to maximum stress of artificial crack. The subscript 1 and 2 to point A, B and C are used to specify top and bottom flange weld, respectively. Table 2 lists stress concentration and stresses of weak point.

It concludes from the comparison as fellow:

[1] It is useful to reduce the stress of weak point, such as intersection of weld access hole and middle point at flange weld, through strengthening connection by adding cover plate on flange weld, stiffened rib inside beam or upstanding rib outside beam flange.

[2] It is also proved by actual earthquake that floor which usually connects the top beam flange acts as cover plate, so fracture rarely initiated from top flange.

[3] It also concludes that adding upstanding rib outside beam flange is the most effective measure to improve stress concentration of flange weld.

[4] That no matter which type of connection is taken stress of bottom flange is always higher than that of top flange also accords with that fracture inclined to take place at the root of bottom flange on actual earthquake.

However, extend of amelioration of stress concentration is limited, because the supposition of exiting of artificial crack is more stringent than actuality.

Table 2 Stress concentration factor or Mises stress of weak point of different structure forms

SCF	A1	B1	A2	B2	Stress (C1) (MPa)	Stress (C2) (MPa)
Type one	1.43	2.33	1.25	2.38	114.0	370.0
Type two	1.52	3.83	1.44	3.98	367.5	372.0
Type three	1.42	2.52	1.25	2.12	86.45	371.6
Type four	1.40	2.04	1.31	2.06	114.0	371.9
Type five	—	—	—	—	101.0	200.6

4. Fracture mechanics analyses

The methods of fracture mechanics are used to estimate the acceptability of a crack in a structure. The use of the fracture mechanics approach has given useful results for required toughness [2]. Firstly, these calculations are based on the finite element analysis results. Secondly, fracture toughness determination involves more parameters in real materials and assumptions have had to be made about residual stresses and defect size. The finite element calculations were only elastic. This fracture mechanics assessment gives strong support for more detailed research on the reinforced connections.

Stresses of hot spots in the connection are used to compute the driving force of crack by the fracture mechanics formula. In this study only elastic FEM analysis was carried out. Five alternative types of beam-to-column connection were modeled and analyzed again. Analysis models by FEM are the same as above, but this time the calculation is without crack.

Finite element analysis was performed to determine the distribution of stresses in beam-to-column connections when subjected to moment loading as would arise under earthquake loading. The magnitude of the loading used was intended to make the beam reach its full plastic moment capacity. The moment load was formed by applying opposite surface stress to upper beam flange and lower beam flange. The values of surface stress equals to yield stress of beam, about 267N/mm^2.

The patterns of the stress distribution along the intersection face of beam flange and column flange showed peak values close to the centerline of the beam web which reduced towards the edge of the flange. The results are given in Table 3 and Table 4 in the form of peak stress concentration factors, i.e. the ratio of the maximum stress at the center of the beam width to the remote uniform tension stress.

Of the several Northridge researchers, Kaufmann and Fisher [3] investigated weld defects from the fracture surfaces of damaged connections and tested specimens. Defects [4] observed in the damaged

connections were believed to have had an initiate depth of 3-6mm and their initiate length would have been approximately equal to the web thickness, about 11mm in this paper. In calculations defects are supposed to be semi-ellipse surface crack to compute stress intensity factors through fracture mechanics equation [5].

Zhang and Dong [6] used (2-D) thermo-mechanical simulations of the multi-pass welding procedure for the lower flange connection to provide the first quantitative descriptions of the residual stress fields. It pointed out that at the top of or root of the butt flange weld there are residual tensile stress, but in the middle of flange weld stressed are compressive. The tensile stress at the top or at the root of flange weld could be at the level of the yield strength of the weld metal. In this paper residual tensile stress are assumed to equal to 300N/mm^2.

The results for SCFs at center of beam flange width and the required fracture toughness are listed in tables 3 to 4 where the following categories are distinguished:

- Defect with depth 3mm without residual stress (σ res=0)
- Defect with depth 6mm without residual stress (σ res=0)
- Defect with depth 3mm with residual stress (σ res=300N/mm^2)
- Defect with depth 6mm with residual stress (σ res=300N/mm^2)

Tab.3: Required fracture toughness with defect size 3mm or 6mm and without residual stress

	SCF	Required fracture toughness (N mm$^{-3/2}$) a=3mm, σ_{res}=0	Required frcture toughness (N mm$^{-3/2}$) a=6mm, σ_{res}=0
Case 1	2．22	1875.2	2362.5
Case 2	1．88	1584.2	1996.0
Case 3	1．37	1154.2	1454.2
Case 4	1．76	1489.4	1876.5
Case 5	1．78	1502.0	1892.4

Tab.4 Required fracture toughness with defect size 3mm or 6mm and with residual stress

	SCF	Required fracture toughness (N mm$^{-3/2}$) a=3mm, σ_{res}=300MPa	Required fracture toughness (N mm$^{-3/2}$) a=6mm, σ_{res}=300MPa
Case 1	2．22	2823.8	3557.7
Case 2	1．88	2532.9	3191.2
Case 3	1．37	2102.8	2649.4
Case 4	1．76	2438.0	3071.7
Case 5	1．78	2450.7	3087.6

5. Conclusion

From the analysis above, conclusions can be reached.

[1] Area of high stress concentration exits at the root of flange weld from the study of stress distribution. The stress concentration at the root of bottom beam flange weld is obviously higher than that of top beam flange weld. At the same time, stress concentration also exits at the intersection point between beam flange

and web near the weld access hole.

[2] The experience showed that brittle fracture under earthquake load was the combined effect of weld defects and stress concentration. To improve property of beam-to-column connection, stress concentration must be reduced from design point of view. As the backing bar exits, the artificial crack is origin of stress concentration at the root of flange weld. Therefore to ensure carrying capability of important structure, penetrated flange weld, removing backing bar or weld all around backing bar should be taken to reduce the effect of defect.

[3] The action of reducing stress concentration through reinforcement of connections by adding cover plate, inside rib or upstanding rib is effective. Among the reinforcement of connection, effect of reducing stress concentration is remarkable by using upstanding rib. Improvement of stress concentration will be significant, if other actions, such as raise the fracture toughness of material and decrease the defect, can be taken in company with reinforcement in the meantime.

[4] The finite element analysis revealed the presence of a stress concentration factor of 2.22 at the center of the beam flange to column joint. The reinforced connection with cover and stiffened rib gave low level of stress concentration at critical area, and particularly reinforced connection with cover plate required toughness is least.

Acknowledgement

References

1. Editorial committee of practical manual of anti-earthquake design of construction, Practical manual of anti-earthquake design of construction. Beijing：Publishing company of construction of China, 1997, in Chinese.
2. F.M. Burdekin, A.Pardali, Considerations of design, material properties and inspection requirements for earthquake resistant steel frame connections. Task Group B Draft, IIW JWG on Brittle Fracture of Moment Connection in Seismically Affected Structures, 1999,5.
3. Kauffmann EJ, Fisher JW. A study of the effects of material and welding factors on moment frame weld joint performance using a small scale tension specimen. Technical Report SAC 95-08, 1995.
4. Changbin Joh, Wai-Fah Chen, Fracture strength of welded flange-bolted web connections, Journal of Structure Engineering, Vol.125, No.5: 565~571.
5. Zhang J, Dong P, Residual stress in welded moment frames and implications on structural performance. J. of Struct Engng, ASCE, 1999 [in press].
6. Shen Chengkang，Fracture mechanics，Publishing house of Shanghai Tongji University，1996, in Chinese.

Stress Corrosion Crack Growth Behaviour of Austenitic Stainless Steels in Hot Concentrated Chloride Solution

H. Shaikh[1], H. S. Khatak[1] and P. Rodriguez[2]

[1]Corrosion Science and Technology Division
Indira Gandhi Centre for Atomic Research
Kalpakkam – 603 102, India

[2]Chairman, Recruitment and Assessment Centre
Defence Research and Development Organisation
Lucknow Road, Timarpur
New Delhi – 110 054, India

ABSTRACT

The stress corrosion crack (SCC) growth behaviour of austenitic stainless steels (SS) in different metallurgical conditions was studied by the fracture mechanics (FM) approach. Threshold stress intensity parameters, K_{ISCC} and J_{ISCC}, and plateau crack growth rate (PCGR) were determined in boiling $5M\ NaCl+0.15M\ Na_2SO_4+2.5\ ml/l\ HCl$ solution for AISI type 304N SS, AISI type 316 SS, and for AISI type 316 LN SS in different metallurgical conditions. Sensitisation of AISI type 304N SS and type 316 SS doubled the PCGR and decreased K_{ISCC} and J_{ISCC} to about 0.6 to 0.7 times the value of annealed material. Cold working (CW) of type 304N SS reduced K_{ISCC}, J_{ISCC}, and PCGR to less than those of sensitised SS. In type 304N SS, activation energy of 65 kJ/mol for the SCC process, crack growth in bursts, and crack arrest marks on the fracture surface indicated that hydrogen played a role in the cracking process. The values of K_{ISCC} and J_{ISCC} were about four times higher and the PCGR was nearly one order of magnitude lower for AISI type 316 LN austenitic stainless steel base metal vis-à-vis its weld metal. The higher K_{ISCC}, J_{ISCC} and lower PCGR for type 316 LN stainless steel vis-à-vis type 316 stainless steel signified the beneficial effect of nitrogen addition in improving SCC resistance. Higher K_{ISCC}, J_{ISCC} and lower PCGR for type 316 LN SS as compared to type 304 LN SS indicated the beneficial effect of Mo addition on SCC resistance.

KEYWORDS: Stress corrosion cracking, K_{ISCC}, J_{ISCC}, cold work, delta-ferrite, sensitisation, plateau crack growth rates, austenitic stainless steels

INTRODUCTION

A wide variety of industries, including the nuclear industry, employ austenitic SS as construction materials because of their excellent resistance to general corrosion, adequate high temperature mechanical properties and good fabricability. However, these SS are susceptible to localised corrosion attacks. Amongst the various microstructures encountered in an austenitic SS weldment, the sensitised heat affected zone (HAZ) has the lowest SCC resistance [1].

The resistance of these steels to sensitisation is increased, without sacrificing the strength levels, by reducing the carbon content and enhancing the nitrogen content [2]. The improved resistance to localised corrosion attacks has made nitrogen-added austenitic SS an attractive candidate material in a wide variety of industries. Information available in literature on SCC crack growth behaviour of austenitic SS with high nitrogen contents by using the fracture mechanics (FM) approach is insignificant. Most research on SCC of austenitic SS using a FM approach has been carried out in $MgCl_2$ solution [3]. However, $MgCl_2$ solution is insensitive [4]; while NaCl is sensitive [5]; to the effects of chromium depletion or impurity segregation in austenitic SS. Moreover, NaCl environment is most often encountered in nature. All the crack growth data on austenitic SS has been generated using the FM approach in conjunction with the constant load (CL) and constant strain (CS) testing techniques. Similar data can be generated in a relatively short time using the slow strain rate testing technique (SSRT).

Although the SCC behaviour of base metal of austenitic SS has been thoroughly investigated, studies on weld metal and weld joints have been few and far between. The SCC behaviour of base and weld metals differ depending on chemical composition, environment and testing techniques [6,7]. δ-ferrite alters both the SCC resistance and crack morphology of weld metal. The SCC resistance of weld metal depends on the content, distribution and solidification mode of δ-ferrite. No crack growth data has been published on weld metal of austenitic SS.

In this study, SCC crack growth data (K_{ISCC}, J_{ISCC} and PCGR) were generated in boiling 5M $NaCl+0.15M$ $Na_2SO_4+2.5$ ml/l HCl solution for AISI types 316 and 304N SS, in various metallurgical conditions, using a combination of constant load and constant strain techniques, and for AISI type 316 LN SS and its weld metal, using the SSRT technique.

EXPERIMENTAL PROCEDURES

10 mm thick compact tension (CT) specimens from base metal of types 304N, 316LN and 316 SS, and 7.5 mm thick CT specimens with side grooves from weld metal of type 316N SS, were machined as per ASTM E 399. The chemical compositions of all the SS of the present study are presented in Table 1. SCC data was generated for annealed, cold worked and sensitised type 304N SS, for annealed and sensitised type 316 SS, and for annealed type 316 LN SS and its weld metal. Welding was carried out by depositing type 316N SS electrodes, using the manual metal arc welding process, in V-groove joint of type 316LN SS base metal with 20 mm root gap.

SCC tests were conducted in a boiling solution containing 5M NaCl + 0.15M Na_2SO_4 + 2.5 ml/l HCl (b.p = 381 K, pH = 1.3). SCC tests were carried out on AISI type 304N SS, in SA, 10% cold worked and sensitized conditions, at 363, 373 and 381 K. For the other two SS, the tests

were carried out in boiling solution at 381.5 K. AISI type 304N and type 316 SS were tested using a combination of constant load and constant strain (wedge-loading) techniques. AISI type 316 LN SS and its weld metal were tested by SSRT technique at a constant extension rate of 10μm/hour to pre-specified values of load. The SCC-failed samples were subjected to fractographic examination in a scanning electron microscope (SEM).

TABLE 1
CHEMICAL COMPOSITIONS IN WEIGHT PERCENT OF AISI TYPE 304N, AISI TYPE 316LN AND ITS WELD METAL, AND AISI TYPE 316 STAINLESS STEELS

Weight % of Element	C	Cr	Ni	Mo	Mn	Si	N	S+P
Type 304N SS	0.04	18.3	9.2	--	1.6	0.37	0.086	0.026
Type 316 SS	0.054	16.5	11.4	2.3	1.7	0.64	--	0.031
Type 316 LN Base Metal	0.027	17.4	11.2	1.8	1.6	0.65	0.11	0.039
Type 316N Weld Metal	0.061	19.7	10.7	1.8	2.0	0.7	0.14	0.034

RESULTS AND DISCUSSIONS

The results are discussed in terms of three parameters viz. threshold stress parameters, K_{ISCC} and J_{ISCC}, and plateau crack growth rates, PCGR. The values of these parameters for the different SS studied are listed in Table 2. The maximum valid value of K_I (K_Q), calculated based on linear elastic fracture mechanics, and J_I (J_Q), calculated based on elastic-plastic fracture mechanics, has assessed the applicability of the FM approach in the range of loads of the tests.

TABLE 2
SCC GROWTH DATA FOR THE THREE STAINLESS STEELS IN DIFFERENT METALLURGICAL CONDITIONS IN 5M NaCl + 0.15M Na_2SO_4 + 2.5 ml/l HCl

Parameters	SA 304N SS	10 %CW 304N SS	20 %CW 304N SS	Sensitised 304N SS	SA 316 SS	Sensitised 316 SS	316 LN BM	316 N WM
K_{ISCC} (MPa.m$^{0.5}$)	17.0	9.0	3.0	11.0	13.0	10.5	22.38	5.79
J_{ISCC} (kPa.m)	0.9	0.45	0.15	0.5	1.0	0.6	2.601	0.233
da/dt (m/s)	1.3E-8	4.0E-9	8.0E-9	2.3E-8	4.0E-9	1.0E-8	1.75E-9	2.8E-8
K_Q (MPa.m$^{0.5}$)	18.0	32.0	42.0	17.0	11.2	13.28	18.0	24.0
J_Q (kPa.m)	240.0	220.0	275.0	230.0	74.8	84.0	112.0	122.0

SA → solution annealed; BM → base metal; WM → weld metal

Sensitisation decreased K_{ISCC} and J_{ISCC} and increased the PCGR of annealed type 304N and type 316 SS, as shown in Table 2, due to grain boundary Cr-depletion which resulted in weaker

passive film in the regions along the grain boundary. The higher PCGR for sensitised material was due to the presence of pre-existing active paths coupled with lesser stress relaxation, due to lesser branching.

Cold work reduced K_{ISCC} and J_{ISCC} and also PCGR of annealed type 304N SS (Table 2). The reduction in K_{ISCC} and J_{ISCC} increased with increasing degree of CW. The decrease in K_{ISCC} and J_{ISCC} was attributed to increased density of metallurgical defects, which provided pre-existing sites for crack initiation, and increased dissolution rate due to increased strain energy. The higher strength of the CW material, vis-à-vis annealed SS, caused lower strain rates at crack-tip, leading to reduced PCGR.

Weld metal of type 316N SS showed lower K_{ISCC} and J_{ISCC} than the type 316 LN base metal it joined (Table 2 and Figure1). This was because the microstructural and microchemical heterogeneities in the weld metal, caused by the presence of δ-ferrite, and segregation of S & P at the δ-ferrite/γ interface along with the high concentration of microscopic and macroscopic defects in the weld metal, resulted in formation of uneven and weakly adherent passive film on its surface vis-a-vis base metal. The higher PCGR for the weld metal vis-à-vis the base metal was attributed to the higher yield strength (YS) and lower ductility of the former due to the presence of delta-ferrite [8] and cold work [9]. The poorer SCC resistance of high YS materials was attributed to lesser stress relaxation and, thus, reduced branching ahead of the crack-tip [4].
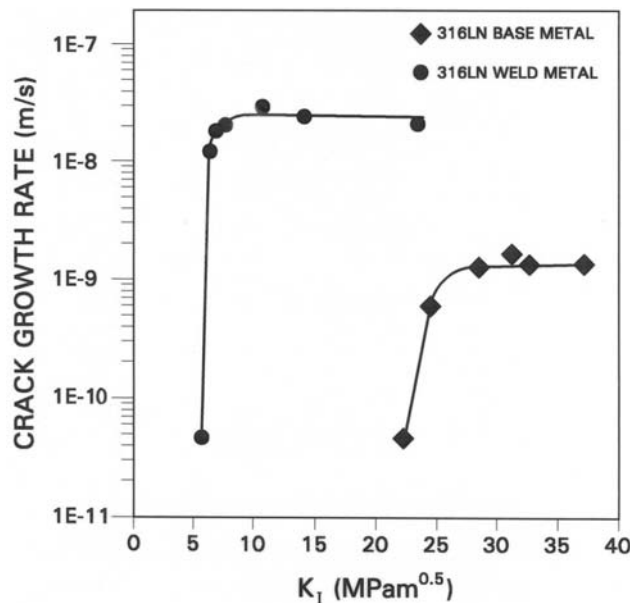
Figure 1: K_I vs. da/dt curves for type 316LN SS and its weld metal
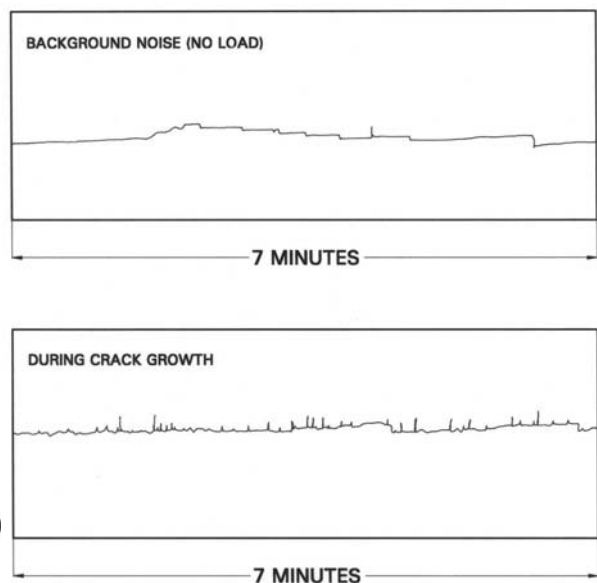
Figure 2: A typical record of acoustic events during crack growth for annealed type 304N SS

Comparison of the crack growth behaviour of types 316LN, 304N and 316 SS (Table 2), shows that type 316LN SS has higher K_{ISCC} and J_{ISCC} and lower PCGR than type 316 SS because of lower carbon and higher nitrogen contents in the former. Usually, SCC of austenitic SS in boiling acidified concentrated NaCl solution initiates through pits, which act as precursors to SCC. Thus, increase in resistance to SCC initiation is explained based on improved pitting resistance of nitrogen-added SS due to improved passive film stability, which also aids in decreasing the PCGR of type 316LN SS vis-à-vis type 316 SS. Type 304N SS had lower values

of K_{ISCC} and J_{ISCC}, and higher PCGR than type 316 LN SS due to the role of Mo in improving SCC resistance through its influence on improving pitting resistance.

Comparison of crack growth data (Table 2) of types 316 and 304N SS gives an insight to the effects of Mo and N on the SCC behaviour of 18-10 austenitic SS. In this study, the Ni content was higher by 2%, Cr content was lower by 2% and carbon content was higher by 0.01% in the former. Presence of higher Ni and lower Cr would nearly neutralise any beneficial or detrimental effects of these additions on the SCC properties of 18-10 SS. Type 316 SS showed a lower PCGR and lower K_{ISCC} and J_{ISCC} than type 304N SS. This suggested that nitrogen imparted better resistance to SCC initiation, as compared to Mo, in 18-10 SS due to a more adherent passive film that it formed. However, Mo imparted better resistance to crack growth for an 18-10 SS. This was because of the effect of nitrogen in lowering the stacking fault energy, which, in turn, would promote planar slip. Planar slip accelerates SCC crack growth. However, the presence of both these elements synergistically improves the SCC resistance of austenitic SS as evidenced by better SCC properties for type 316 LN SS as compared to the other two SS.

The acoustic emission (AE) data on annealed, sensitized and 10% cold worked type 304N SS indicated that the crack growth was discontinuous, as seen in Figure 2 and Table 3. In the plateau region, crack growth per acoustic event varied from less than a micron to 15 μm. These observations and crack arrest marks on the surface (1 to 7 μm) (Figure 3), suggested that cracking occurred by discontinuous jumps of the order of a few microns. Activation energies of cracking were determined by using the PCGRs of annealed, 10% cold worked and sensitised type 304N SS at 163, 173 and 181 K, in the Arrhenius rate equation. The plot of PCGR and 1/T, shown in Figure 4, showed activation energy of the cracking process to be in the range of 50-65 kJ/mol, which corresponded to the diffusion of hydrogen in iron and steel. Table 3 also shows hydrogen diffusion distances per event time for the plateau region of the crack growth curves calculated using the equation $X = Dt^{1/2}$, where $D = 1.76 * 10^{-10}$ for hydrogen diffusion in austenitic SS [10]. It is seen that hydrogen diffuses more than the crack growth per event. This suggests that cracking occurs only when a critical concentration of hydrogen accumulates ahead of the crack-tip. From the above observations it was concluded that hydrogen played a vital role in the cracking of type 304N SS.
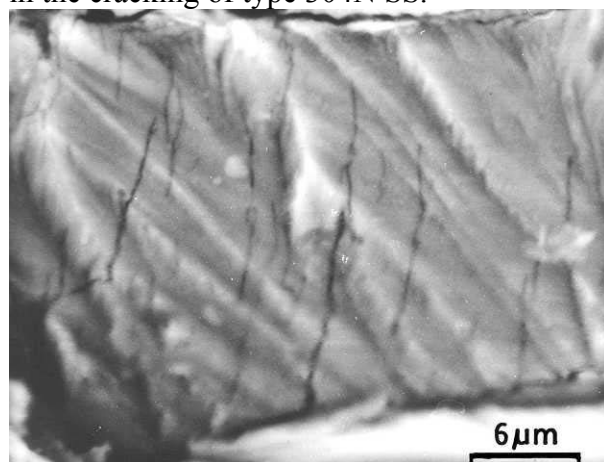
Figure 3: Fractograph showing crack arrest marks
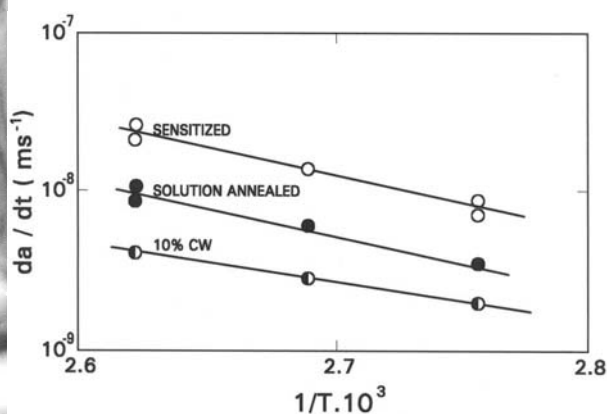
Figure 4: Dependence of da/dt on temperature for type 304N SS

TABLE 3
ACOUSTIC EMISSION DATA MEASURED DURING CRACK GROWTH

Sl. No.	Material Condition	Range of K_I (MPa.m$^{0.5}$)	da/dt (m/s)	Crack growth/event (μm/N)	Time period per event (s)	Hydrogen diffusion distance (μm/event)
1.	SA	33-46	1.1E-8	0.55	50	13
2.	SA	24-30	1.6E-8	1.15	72	159
3.	SA+sensitised	15-25	8.6E-9	2.3	375	360
4.	10% CW	18-20	7E-10	0.27	380	1000
5.	10% CW	43-80	4.8E-9	15	2870	---
6.	10% CW	24-43	3.6E-9	11	3120	1040

CONCLUSIONS

K_{ISCC} and J_{ISCC}, and PCGR were determined in boiling 5M NaCl+0.15M Na_2SO_4+2.5 ml/l HCl solution for NA types 304 and 316L SS and AISI types 316 SS in various metallurgical conditions. The following conclusions were drawn:

1. Sensitisation of annealed types 316 and NA type 304 SS lowered K_{ISCC} and J_{ISCC} by about 60 to 70 %, and increased the PCGR by 2 to 3 times.
2. K_{ISCC} and J_{ISCC} were about four times higher and PCGR was nearly one order of magnitude lower for base metal vis-à-vis the weld metal of AISI type 316 LN SS.
3. Results of AE, fractography and activation energy measurements during SCC of type 304N SS showed that hydrogen played a vital role in the cracking.
4. Comparisons of K_{ISCC} and J_{ISCC} and PCGR of base metals of types 316 LN and 316 SS, indicated the influence of nitrogen on improving the SCC properties of the former. Comparison of K_{ISCC} and J_{ISCC} and PCGR of types 304N and 316 SS indicated that nitrogen influenced to resist crack initiation while Mo functioned to resist crack growth.

REFERENCES

1. Shaikh, H., Khatak. H. S. and Gnanamoorthy, J. B. (1987) *Werkstoffe und Korrosion* 38, 183
2. Dutta, R. S., De, P. K. and Gadiyar, H. S. (1993) *Corrosion Science* 34, 51
3. Russel, A. J. and Tromans, D. (1979) *Metallurgical Transactions A* 10A, 229
4. Shaikh, H., Khatak, H. S., Seshadri, S. K., Gnanamoorthy, J. B. and Rodriguez, P. (1995) *Metallurgical and Materials Transactions A* 26A, 1859
5. Hanninen, H. E. (1979) *International Metals Review* 24, 85
6. Baeslack III, W. A., Lippold, J. C. and Savage, W. F. (1979) *Welding Journal* 58,168-s
7. Baeslack III, W. A., Duquette, D. J., and Savage, W. F., *Corrosion* 35, 45
8. Ward, A. L. (1974) *Nuclear Technology* 24, 201
9. Shaikh, H., Vinoy, T.V. and Khatak, H. S. (1998) *Materials Science and Technology* 14, 129
10. Louthan Jr, M. R. and Devrick R. G. (1975) *Corrosion Science* 15, 565

Stress corrosion cracking mechanism on the basis of the interaction model of dislocation and hydrogen around a crack tip

A. T. Yokobori, Jr.[1], J. C. Ha [2], T. Shoji [1], N. Taketomi[1] and G. F. Li[1]

[1] Fracture Research Institute, Tohoku University, Sendai, #980-8579, Japan
[2] Faculty of Science and Engineering, Teikyo University, Utsunomiya, #320-8551, Japan

1. Introduction

Mechanisms of dissolvent anodic chemical reaction and hydrogen embrittlement were proposed as stress corrosion cracking mechanics (SCC). The former is feasible for the case of plastic deformation dominant metals and the latter is for high strength metals such as high strength steels.

However, in spite of low yield stress, a discontinuous cleavage-like fracture is sometimes observed during SCC for ductile fcc alloys.

In this paper, we proposed stress corrosion cracking model on the basis of interaction of dislocation and hydrogen around a crack tip to predict discontinuous cleavage-like fracture during SCC for ductile fcc alloys. Furthermore, we conducted numerical analyses using this proposed model.

2. Results and Conclusion

The physical model is shown in Fig. 1. Brittle fracture is considered to be induced by inverse pile-up with high dislocation density emitted from a stressed source. For ductile materials such as pure iron, the maximum dislocation density at the end of the dislocation free zone (DFZ) is not so high as shown by the dotted line in Fig. 2.

However, when hydrogen cluster exists near the slip line, the inverse pile-up with high dislocation density occurs at the site of hydrogen cluster, as shown by the solid line in Fig. 2. This will cause cleavage fracture. That is, when hydrogen cluster originated by dissolvent chemical reaction exists near the dislocation slip line, the subcritical cleavage fracture can be observed even for such ductile materials. This result is in good agreement with experimental result obtained by other literature.
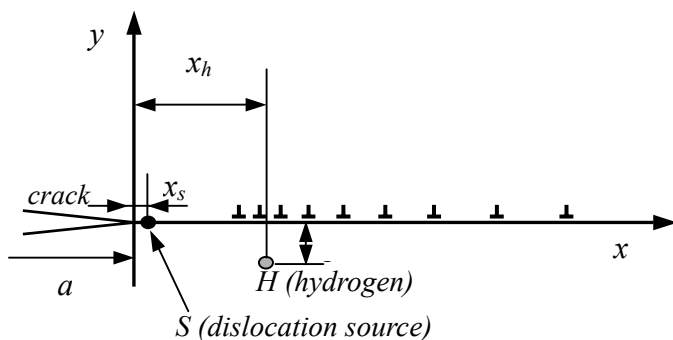
Fig.1 Proposed model in which the source emitting the dislocation group is located at the tip of the crack under hydrogen atmosphere condition.
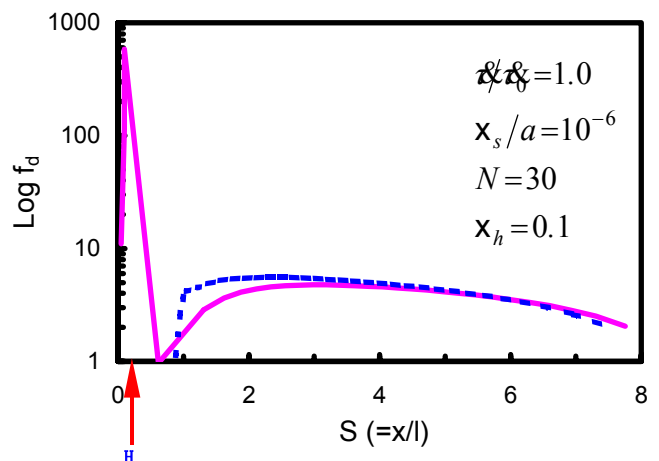
Fig.2 Numerical results on dislocation distribution under the interaction between crack, dislocation groups and hydrogen.

STRESS INTENSITY FACTOR ERROR INDEX
FOR FINITE ELEMENT ANALYSIS
WITH SINGULAR ELEMENTS

T. Meshii[1] and K. Watanabe[2]

[1] Department of Mechanical Engineering, Fukui University,
Bunkyo, Fukui, Fukui, 910-8507, Japan
[2] 1st Division, Institute of Industrial Science, University of Tokyo,
Komaba, Meguro-ku, Tokyo, 153-8505, Japan

ABSTRACT

An error index for the stress intensity factor (SIF) obtained from the finite element analysis (FEA) results using singular elements is proposed. The index was developed by considering the facts that the analytical function shape of the crack tip displacement is known and that the SIF can be evaluated from the displacements only. The advantage of the index is that it has the dimension of the SIF and converges to zero when the actual error of the SIF by displacement correlation technique converges to zero. Numerical examples for some typical crack problems, including a mixed mode crack, whose analytical solutions are known, indicated the validity of the index. The degree of actual SIF error seems to be approximated by the value of the proposed index.

KEYWORDS

Fracture Mechanics, Stress Intensity Factor, Finite Element Method, Error Index, Singular Element

INTRODUCTION

It is popular to evaluate the integrity of a cracked structure under arbitrary loads by comparing the stress intensity factor (SIF) for the crack with the critical value peculiar to the material. The SIF is often evaluated from finite element analysis (FEA) results and it is effective particularly when the SIF solution for the crack under specific load condition is not known, while the error estimation of the obtained SIF is very important.

In the past, many techniques have been proposed for FEA of a cracked structure in order to express and evaluate the stress singularity of the stress at the crack tip. Among these, one of the most popular techniques is to apply singular element (SE), which Barsoum [1] and Henshell and Shaw [2] proposed independently, to realize the crack tip stress singularity. In this case, the SIF is usually evaluated by Tracey's formula [3] (Displacement Correlation Technique, hereafter referred to as DCT). The feature of this technique is that a SIF of practical accuracy can be obtained by comparatively coarse mesh division. So, many researchers have been trying to answer the question "how coarse the SE can be to secure the SIF accuracy?" However, the

load conditions as well as the SE size has become known to affect the SIF accuracy. Thus, it is generally accepted that an optimum SE size that satisfies arbitrary conditions does not exist [4].

Generally the accuracy of the SIF solution by FEA is improved by increasing the number of elements. However, since it is an engineering problem (and especially to take advantages of SE), it is desirable to obtain sufficiently accurate SIF by a mesh division as coarse as possible. This will be possible if we can estimate the error of the SIF obtained from one trial analysis. We can make corrections or judge whether the obtained SIF solution is applicable from a practical viewpoint. Fuenmayor et al. [5] applied the error index (expressed through the energy norm) which Zienkiewicz and Zhu [6] proposed for estimating errors in FEA results. However, since the error index is not expressed in terms of the SIF, one can only expect that the SIF error will be small when the index becomes small. We cannot know the degree of the actual SIF error. So we developed a new SIF error index that has the dimension of the SIF, based on the following three facts: (i) The analytical function forms of the crack tip displacements are known. (ii) Though incomplete, displacements on a SE represent a part of the analytical displacement distribution. (iii) The SIF can be evaluated from the displacements of crack tip elements.

In the following, we will first explain the concept of the error index which we have developed, and then demonstrate its validity by comparing our error index with the actual error for two typical crack problems whose analytical solutions are known.

PROPOSAL OF DCE (DISPLACEMENT CORRELATION ERROR) INDEX

Consider a polar-coordinate system (r, θ) as shown in Figure 1 where the crack tip is chosen as the origin and the crack surfaces as $\theta = \pm\pi$. In this case, the relative displacements $u^*(r, \theta)$ and $v^*(r, \theta)$ in the x and y directions between two symmetric points across the x axis can be related to only mode I and mode II deformations [7], respectively, and, by applying the asymptotic solutions of the displacements $u(r, \theta)$ and $v(r, \theta)$ in the x and y directions, are given as

$$\begin{bmatrix} u^*(r,\theta) \\ v^*(r,\theta) \end{bmatrix} \equiv \begin{bmatrix} u(r,\theta)-u(r,-\theta) \\ v(r,\theta)-v(r,-\theta) \end{bmatrix} = \sum_{n=1}^{\infty} \frac{r^{\frac{n}{2}}}{G} \begin{bmatrix} -A_{\mathrm{II}\,n} f_{\mathrm{II}\,u\,n}(\theta) \\ A_{\mathrm{I}\,n} f_{\mathrm{I}\,v\,n}(\theta) \end{bmatrix} \tag{1}$$

where G is the shear modulus and the functions $f_{\mathrm{I}\,v\,n}$ and $f_{\mathrm{II}\,u\,n}$ are defined as follows:

$$\begin{bmatrix} f_{\mathrm{I}v n}(\theta) \\ f_{\mathrm{II}u n}(\theta) \end{bmatrix} = \begin{bmatrix} \dfrac{n}{2}\sin\left(\dfrac{n}{2}-2\right)\theta - \left(-\kappa + \dfrac{n}{2} + (-1)^n\right)\sin\dfrac{n\theta}{2} \\ -\dfrac{n}{2}\sin\left(\dfrac{n}{2}-2\right)\theta + \left(\kappa + \dfrac{n}{2} - (-1)^n\right)\sin\dfrac{n\theta}{2} \end{bmatrix} \tag{2}$$

Here, suffixes I and II indicate the corresponding crack opening modes, and suffixes u and v represent the quantities corresponding to the displacements u and v, respectively. κ is $(3-4\nu)$ for plane strain or $(3-\nu)/(1+\nu)$ for plane stress when ν is Poisson's ratio. Note that the SIFs are given as $K_{\mathrm{I}} = \sqrt{2\pi}\,A_{\mathrm{I}\,1}$ and $K_{\mathrm{II}} = -\sqrt{2\pi}\,A_{\mathrm{II}\,1}$.

On the other hand, when $U(r, \theta)$ and $V(r, \theta)$ are the displacements of SEs from FEA, corresponding relative displacements $U^*(r, \theta) \equiv U(r, \theta) - U(r, -\theta)$ and $V^*(r, \theta) \equiv V(r, \theta) - V(r, -\theta)$ related to mode I and mode II deformations, respectively, are given by
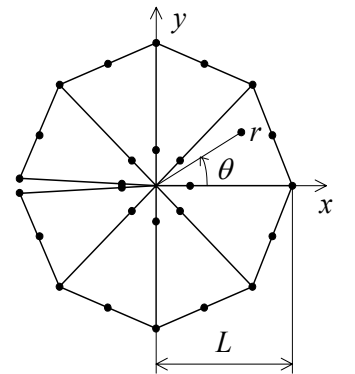
Figure 1: Singular crack tip elements

2

$$\begin{bmatrix} U^*(r,\theta) \\ V^*(r,\theta) \end{bmatrix} = \begin{bmatrix} 4U^*(L/4,\theta)-U^*(L,\theta) \\ 4V^*(L/4,\theta)-V^*(L,\theta) \end{bmatrix}\sqrt{\frac{r}{L}} + \begin{bmatrix} -4U^*(L/4,\theta)+2U^*(L,\theta) \\ -4V^*(L/4,\theta)+2V^*(L,\theta) \end{bmatrix}\frac{r}{L} \qquad (3)$$

The Tracey's formula [3] is frequently used to evaluate the SIF from FEA results. That is, the SIF K_{DCT} is evaluated by letting Eqn. (3) correspond to the first two terms of Eqn. (1) on the crack surfaces ($\theta=\pi$) and it is given concretely, considering $f_{I\ v\ 1}(\pi) = f_{II\ u\ 1}(\pi)=\kappa+1$, $A_{I\ 1} = K_{I\ DCT}/(2\pi)^{1/2}$, $A_{II\ 1} = -K_{II\ DCT}/(2\pi)^{1/2}$ and setting $G' \equiv (2\pi/L)^{1/2}G/(1+\kappa)$, as

$$\begin{bmatrix} K_{II\ DCT} \\ K_{I\ DCT} \end{bmatrix} = G'\begin{bmatrix} 4U^*(L/4,\pi)-U^*(L,\pi) \\ 4V^*(L/4,\pi)-V^*(L,\pi) \end{bmatrix} \qquad (4)$$

Note that the K_{DCT} in Eqn. (4) is evaluated for $\theta=\pi$. It generally differs from the SIF evaluated in a similar way for other $\theta(\neq\pi)$, because SE displacements are not guaranteed to satisfy the angular characteristics which analytical expressions may show.

When we think of a sufficiently small region around a crack tip, terms higher than $O(r^{3/2})$ can be neglected in Eqn. (1). The relative displacements can be accurately expressed by the first two terms of Eqn. (1). If the true SIFs K_I and K_{II} are known, Eqn. (1) can be deduced for the crack surfaces, with $f_{I\ v\ 2}(\pi) = 0$ and $f_{II\ u\ 2}(\pi)=0$ as follows.

$$\begin{bmatrix} u^*(r,\pi) \\ v^*(r,\pi) \end{bmatrix} = \frac{1}{G'}\sqrt{\frac{2\pi r}{L}}\begin{bmatrix} -A_{II\ 1} \\ A_{I1} \end{bmatrix} = \frac{1}{G'}\sqrt{\frac{r}{L}}\begin{bmatrix} K_{II} \\ K_I \end{bmatrix} \qquad (5)$$

On the other hand, the corresponding expressions $U^*(r, \pi)$ and $V^*(r, \pi)$ for the SEs are deduced, by substituting the SIFs $K_{I\ DCT}$ and $K_{II\ DCT}$ in Eqn. (4), as

$$\begin{bmatrix} U^*(r,\pi) \\ V^*(r,\pi) \end{bmatrix} = \frac{1}{G'}\sqrt{\frac{r}{L}}\begin{bmatrix} K_{II\ DCT} \\ K_{I\ DCT} \end{bmatrix} + \frac{2r}{L}\begin{bmatrix} U^*(L,\pi)-2U^*(L/4,\pi) \\ V^*(L,\pi)-2V^*(L/4,\pi) \end{bmatrix} \qquad (6)$$

The nodal displacements in FEA are obtained by determining the unknown coefficients in the adopted displacement function through potential energy minimization process and Eqn. (3) does not necessarily coincide with Eqn. (1). Thus, the coefficients of r/L in Eqn. (6) are not zero unless the adopted displacement function can express the true displacement solution. However, since the SEs under consideration are conformal elements [1], FEA displacements tend to the exact solutions when the size of the elements approaches zero (note that the element size has to be decreased not only in the r direction but also in the θ direction). Then, the second term in Eqn. (6) converges to zero and K_{DCT} to the true value. This suggests the possibility of the second term in Eqn. (6) to become a SIF error index. We will now multiply the coefficient for r/L in Eqn. (6) with $(-G'/2)$ and name it DCE index (Displacement Correlation Error Index) ΔK_{DCE}, which now has the dimension of a SIF.

$$\begin{bmatrix} \Delta K_{I\ DCE} \\ \Delta K_{II\ DCE} \end{bmatrix} = G'\begin{bmatrix} 2V^*(L/4,\pi)-V^*(L,\pi) \\ 2U^*(L/4,\pi)-U^*(L,\pi) \end{bmatrix} \qquad (7)$$

Strong points of the DCE index, the proposed error index, are that (i) it can be directly calculated from the nodal displacements on the SEs, (ii) it converges to zero when the size of the SEs approaches zero and (iii) it has the dimension of a SIF. Thus, the DCE index differs from conventional error indexes, which generally focus on the convergence during iterative mesh refinements. The DCE index may therefore give a SIF error estimate from a single FEA results. This suggests the possibility of dramatically reducing efforts and costs in SIF analysis.

3

NUMERICAL EXAMPLES

In this section, FEA for two typical crack problems, whose analytical SIF solutions K_{ref} are known, were conducted by using SEs. Here the K_{DCT} is a SIF computed with DCT (Eqn. (4)) and ΔK_{DCE} is a DCE Index evaluated from the FEA results. Finally, $K_{error} = (K_{DCT} - K_{ref})$ was compared with the corresponding ΔK_{DCE}. In all cases, shearing modulus G of 79 GPa and Poisson's ratio ν of 0.3 were used. The number m of SEs investigated was 8 [8], 16, 24 and 30. For each m, a normalized SE size L/a of 1/3, 1/6, 1/12 and 1/24 was considered, approximately corresponding to the guideline proposed in the early days [8] (only the SEs were re-divided).

Circumferential Crack in a Cylinder under Uniform Tension

A circumferential crack in a cylinder under remote uniform stress $\sigma = 9.8$ MPa as in the left of Figure 2 was considered first. The dimensions of the cylinder were $R_m = 95$ mm in mean radius, $W = 10$ mm thick and $H = 16W = 160$ mm long. The crack length was $a = 1$ or 3 mm. $K_{I\,error}$ was obtained by using Nied's analytical solution $(a/W, K_{I\,ref}$ MPam$^{1/2}) = (0.1, 0.636), (0.3, 1.324)$ [9]. It was compared with $\Delta K_{I\,DCE}$ in the right of Figure 2 ($m = 16$).
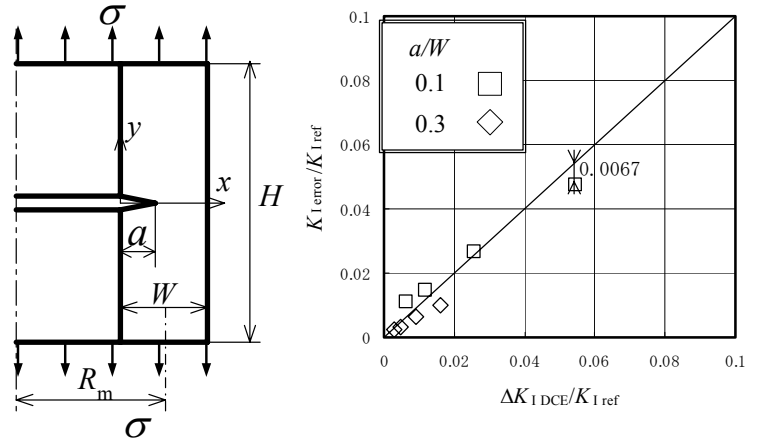
Figure 2： Actual SIF error $K_{I\,error}$ and DCE Index $\Delta K_{I\,DCE}$ ($R_m/W = 9.5$, $H/W = 16$, $m = 16$, $\nu = 0.3$)
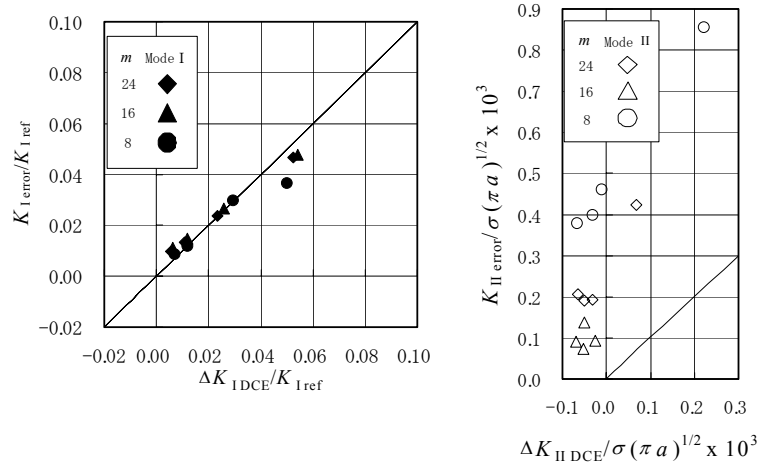
Figure 3: Effect of SE number m on actual SIF error K_{error} and DCE Index ΔK_{DCE} (for $a/W = 0.1$ in Figure 2)

There are four results for each a/W in Figure 2 and each result corresponds to the normalized SE size L/a, which has a positive correlation with the $\Delta K_{I\,DCE}$. The maximum difference between $K_{I\,error}$ and $\Delta K_{I\,DCE}$ in the figure is seen to be 0.67% of $K_{I\,ref}$ for the mark corresponding to $a/W = 0.1$ and $L/a = 1/3$. The figure shows the tendencies of $\Delta K_{I\,DCE}$ and $K_{I\,error}$ to decrease while L/a is made small. In addition, $\Delta K_{I\,DCE}$ and $K_{I\,error}$ are not very different for this problem.

Here as in the right of Figure 2, $m = 16$ was chosen without special notification. The effects of m on mode I and II K_{DCT}s for the case of $a/W = 0.1$ are summarized in Figure 3 left and right, respectively. Figure 3 left explains why we selected this specific m. There are four data for each three marks in Figure 3.

In the problem here, the analytical SIF for mode II is zero, so that $K_{II\,error} = K_{II\,DCT}$. Therefore $K_{II\,ref} = \sigma(\pi a)^{1/2}$ was used to normalize $K_{II\,error}$ and $\Delta K_{II\,DCE}$ in Figure 3 right. We see from Figure 3 right that an increase in m does not necessarily contribute to the decrease in $K_{II\,error}$. It seems that this is due to the fact that the mode II SIF is zero for this problem, and that the tendency expected for conformal elements does not appear for small K_{II}, unless m and L are decreased together smoothly. On the other hand, we see from Figure 3 left that if we choose m to be 16 or more, the vertical distance between a mark and a line of unit slope crossing the origin (the difference between $K_{I\,error}$ and $\Delta K_{I\,DCE}$) becomes approximately constant. Thus, the effect of m on the mode I SIF can be disregarded.

Center Slant Cracked Rectangular Plate Subjected to Uniform Tension

The problem of a center slant cracked rectangular plate under uniform stress $\sigma = 9.8$ MPa in Figure 4 left was considered. The dimensions of the plate were $2W = 30$ mm wide and $2H = 60$ mm high. The crack had a length of $2a = 6$ or 12 mm and an angle of $\alpha = 30^o$. K_{error} was obtained by using Kitagawa's analytical solution $(K_{I\ ref}, K_{II\ ref}) = (0.735, 0.415), (1.138, 0.605)$ MPam$^{1/2}$ [10]. It was compared with $\Delta K_{I\ DCE}$ in the right of Figure 4. This figure is the result for $m = 24$.

The effects of m on mode I and II K_{DCT}s for the case of $a/W = 0.6$ are summarized in Figure 5 to explain why we selected $m = 24$. There are four data for each mark in the figure. As we see from the figure, there was a difference in the mode I $\Delta K_{DCE}/K_{ref}$ and mode II $\Delta K_{DCE}/K_{ref}$ of up to 2.74% for $m = 8$. We thought that the error index $\Delta K_{DCE}/K_{ref}$ for each mode should not show such a large discrepancy, because we estimate the SIF and its error only from FEA displacements. Thus, we set a guideline for this mode I and II $\Delta K_{DCE}/K_{ref}$ discrepancy to be lower than 1.5% and selected $m = 24$ for the problem under consideration. Note that the mode I $\Delta K_{DCE}/K_{ref}$ changed slightly as m increased.

As in the right of Figure 2, there are four marks for each a/W in Figure 4 and each mark corresponds to the normalized SE size L/a, which has a positive correlation with ΔK_{DCE}. The maximum difference between K_{error} and ΔK_{DCE} in the figure can be read as 3.40% of K_{ref} for mode II. The figure shows the tendency of ΔK_{DCE} to decrease while L/a is made small and K_{error} to decrease accordingly.

Figure 4: Actual SIF error K_{error} and DCE Index ΔK_{DCE} ($H/W = 2$, $m=24$, $\alpha=30^o$, $v = 0.3$)

Figure 5: Effect of SE number m on actual SIF error K_{error} and DCE Index ΔK_{DCE} (for $a/W = 0.6$)

DISCUSSIONS

The DCE Index ΔK_{DCE}, which we proposed in this paper, is intended to give a rough idea of the error of the SIF obtained from FEA results. When we refine the crack tip SEs in both r and θ direction with proper correlation (or in terms of the previous section, decrease L/a and $1/m$), the plot (ΔK_{DCE}, K_{error}) on a plane is expected to approach the origin. That is, ΔK_{DCE} is expected to converge to K_{error}. This characteristic of ΔK_{DCE} is similar to that of the error index proposed in the past [5], [6] which was based on the energy norm. However, we think that ΔK_{DCE} is advantageous because it has the dimension of a SIF and the SIF error can be discussed directly.

When we refine the crack tip SEs, we had better reduce the element size in both r and θ directions properly by correlating two parameters L/a and $1/m$. However, because this makes the finite element division quite difficult, we first fixed the number of elements in the θ direction m and reduced the element size in the r direction in the numerical examples shown in the previous section. The results showed that K_I is relatively insensitive to mesh refinements in the θ direction, thus, we can concentrate on refining the mesh in the r

5

direction once we choose m larger than a certain value. On the other hand, the situation differs with regard to K_{II}; that is, the convergence of K_{II} by varying m should be confirmed. In any case, the validity of m can be judged by the discrepancy between plots on a figure like Figure 5 and the origin when L/a is made small, in case that analytical SIF solutions are known. Note that the m presented in the numerical examples in this paper satisfies this condition (at least for K_I whose accuracy is important for practical problems) and that our error index approximates the SIF error closely for $|\Delta K_{I\,DCE}/K_{I\,ref}| < 0.05$. Next, what about the cases for which the analytical solutions are not known (that is, cases the error index is meant to be developed for)? We think that the results for K_I show (though some more study might be necessary) that when we choose $m \geq 16$ and consider a case under $|\Delta K_{I\,DCE}/K_{I\,DCT}| < 0.05$ instead of $|\Delta K_{I\,DCE}/K_{I\,ref}| < 0.05$, our error index gives an approximate evaluation of the SIF error itself and that there is a possibility to compensate the error in $K_{I\,DCT}$. Regarding to K_{II}, as shown in Figure 5, the plots (K_{error}, ΔK_{DCE}) moves closer to the origin when L/a is made small and m is increased. From this, we expect that an error estimation procedure similar to that for K_I just mentioned can be applied to K_{II}, if we use large m. However, applying large m is not necessarily realistic. In this sense, what we refer to as a SE may not necessarily be suitable for K_{II} evaluation. Nevertheless, if we use this SE for the K_{II} evaluation, a candidate for the m selection criteria is $|\Delta K_{I\,DCE}/K_{I\,ref} - \Delta K_{II\,DCE}/K_{II\,ref}|$ as shown in the previous section, because a discrepancy in accuracy of K_I and K_{II} is not desirable. In situations where the analytical solution is not known (the cases for which the error index was developed), the criteria will be $|\Delta K_{I\,DCE}/K_{I\,DCT} - \Delta K_{II\,DCE}/K_{II\,DCT}|$ instead.

Recently, Rahulkumar et al. [11] proposed an approach to use higher order SEs for an accurate SIF evaluation with a coarse mesh division. However, judging from the results of mixed mode problems discussed in the previous section, it still remains necessary to try to find a proper mesh refinement in the θ direction (selection of m) even though higher order elements are used. For this case too, we think it will be effective to first select m for Barsoum's SE by applying ΔK_{DCE} as proposed in this paper.

CONCLUSIONS

In this paper, an error index for SIF obtained from the FEA results using SEs was developed and was named DCE (Displacement Correlation Error) index. The DCE index was developed as a SIF error index that has the dimension of a SIF, based on the following three facts: (i) The analytical functional form of the crack tip displacements are known. (ii) Though incomplete, displacements on a SE represent a part of the analytical displacement distribution. (iii) The SIF can be evaluated from the displacements of crack tip elements. In spite of the DCE index not being a SIF error itself, the presented numerical results (for the problems whose analytical solutions are known) for appropriate mesh divisions in the θ direction show that the DCE index is close to the actual SIF error, especially for mode I SIF evaluations whose accuracy is important for practical problems and that error compensation might be possible in an engineering sense.

REFERENCES

1.   Barsoum, R.S. (1976) *Int. J. Numer. Methods Eng.* 10, 25.
2.   Henshell, R.D. and Shaw, K.G. (1975) *Int. J. Numer. Methods Eng.* 9, 495.
3.   Tracey, D.M. (1976) *Int. J. Numer. Methods Eng.* 10, 401.
4.   Harrop, L.P. (1982) *Int. J. Numer. Methods Eng.* 17, 1101.
5.   Fuenmayor, J., Domínguez, E., Giner, E. and Oliver, J.L., *Fatigue Fracture Eng. Materials* (1997) 20, 813.
6.   Zienkiewicz, O.C. and Zhu, J.Z. (1987) *Int. J. Numer. Methods Eng.* 24, 337.
7.   Ishikawa, H., Kitagawa, H. and Okamura, H. (1980) *Proc. 3rd Int. Conf. Mechanical Behaviour of Materials*. 3, 447.
8.   Saouma, V.E. and Schwemmer. (1984) *Int. J. Numer. Methods Eng.* 20, 1629.
9.   Nied, H.F. and Erdogan, F. (1983) *Int. J. Fracture*. 22, 277.
10.   Murakami, Y. et al. (1987). *Stress Intensity Factors Handbook*, Pergamon, London.

11.   Rahulkumar, P., Saigal, S. and Yunus, S. (1997) *Int. J. Numer. Methods Eng.* 40, 1091.

STRESS INTENSITY FACTOR OF 3D PLANE CRACKS UNDER MODE I LOADING

V. Lazarus

Laboratoire de Modélisation en Mécanique,
Université Pierre et Marie Curie,
4 place Jussieu, 75252 Paris Cedex 5, France

ABSTRACT

In this paper, a numerical method for the determination of the mode I stress intensity factor of an arbitrary plane crack embedded in an infinite isotropic elastic body, is proposed.

This method is based on the three-dimensional weight-function theory of Bueckner-Rice, that gives the variation of the stress intensity factor along the crack front arising from some small arbitrary coplanar perturbation of the front. It is closely linked to previous works of Bower and Ortiz but much simpler in its numerical implementation.

The main advantage is that only one dimensional integrals along the crack front are involved so that only the one dimensional meshing of the crack front is needed, and not the 3D meshing of the whole body as in the finite-element method.

Applications include the asymptotic behavior of the stress intensity factor along the crack front near an angular point and the fatigue propagation path of mode I plane cracks undergoing a large number of loading cycles.

KEYWORDS

Linear elastic fracture mechanics, stress intensity factor, mode I crack, 3-D weight function, 3-D plane/flat crack, perturbation method, angular point, fatigue propagation path.

INTRODUCTION

Let us consider a plane crack with arbitrary contour $\mathcal{F}$, embedded in an infinite isotropic elastic body and loaded in pure mode I through some uniform stress σ_∞ applied at infinity (see fig. 1). The aim of this paper is to determine the mode I stress intensity factor (SIF) along $\mathcal{F}$. A classical method would be to use the finite element method (FEM), but here we propose an alternative method whose main advantage is to restrict the meshing operations to that of the front instead of the whole body. It is based on the three-dimensional weight-function theory derived by Gao and Rice : in [7] the half plane crack is studied, in [4] the penny shaped one and finally, in [8] the theory for any plane crack is presented. It was used by Bower and Ortiz [1, 2, 3] to study several problems concerning a half plane crack. However, the originality of our work lies in the simplification of the numerical implementation and in the applications studied : the asymptotic behavior of the SIF near an angular point of the front and some examples of fatigue propagation paths.
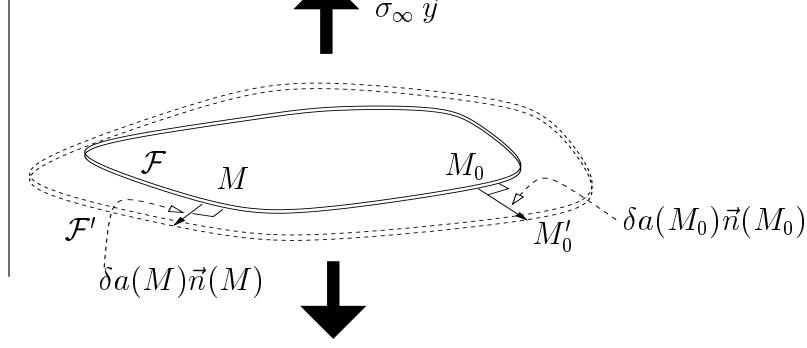
Figure 1: Arbitrary plane tensile crack in an infinite body under uniform stress σ_∞.

PRINCIPLE OF THE METHOD

Three-dimensional weight-function theory

As the crack advances, under constant loading, by a small distance $\delta a(M)$ in the direction perpendicular to the front $\mathcal{F}$ like in figure 1, Rice [8] has shown that to first order in δa, the SIF at point M_0' of the new front defined by

$$\overrightarrow{M_0 M_0'} = \delta a(M_0)\vec{n}(M_0), \tag{1}$$

can be approximated by $K(M_0) + \delta K(M_0)$ where

$$\delta K(M_0) = \frac{1}{2\pi} PV \int_{\mathcal{F}} \frac{W(M, M_0)}{D^2(M, M_0)} K(M)[\delta a(M) - \delta_* a(M)]\mathrm{d}M \tag{2}$$

$D(M, M_0)$ is the distance between the points M and M_0, $W(M, M_0)$ is a two-variable function linked to the weight function of the crack[1]. The function W along the new crack front can be, itself, updated by $W(M_0, M_1) = W(M_0, M_1) + \delta W(M_0, M_1)$ where the variation of W is given, also to first order in δa, by :

$$\delta W(M_0, M_1) = \frac{D^2(M_0, M_1)}{2\pi} PV \int_{\mathcal{F}} \frac{W(M, M_0)}{D^2(M, M_0)} \frac{W(M, M_1)}{D^2(M, M_1)}[\delta a(M) - \delta_{**} a(M)]\mathrm{d}M \tag{3}$$

These formulae are legitimate for special normal advances $\delta_* a(M)$ and $\delta_{**} a(M)$ that preserve the shape of the front and such that $\delta_* a(M_0) = \delta a(M_0)$, $\delta_{**} a(M_0) = \delta a(M_0)$ and $\delta_{**} a(M_1) = \delta a(M_1)$ so as to ensure the existence of the Principal Value (PV) integrals. One can always define some combination of translatory motion, rotation and scaling that verifies all these conditions.

As the quantities in right-hand side of Eqn. 2 and 3 concern only the front $\mathcal{F}$, this theory allows to calculate the SIF and function W along the perturbed one $\mathcal{F}'$ if the SIF and function W are known for the initial one $\mathcal{F}$.

Determination of the SIF and of the function W

Assume now that the functions $K(M)$ and $W(M, M_0)$ are known for one crack shape $\mathcal{C}$ and that a succession of very close to each other, intermediate cracks $\mathcal{F}_k$, $k = 0 \ldots n$, such that $\mathcal{F}_0 = \mathcal{C}$ and $\mathcal{F}_n = \mathcal{F}$, can be constructed. Then by applying Eqn. 2 and 3 successively between $\mathcal{F}_0$ and $\mathcal{F}_1$, between $\mathcal{F}_1$ and $\mathcal{F}_2$, ... and finally between $\mathcal{F}_{n-1}$ and $\mathcal{F}_n$ the SIF $K = K + \delta K$ and the function $W = W + \delta W$ along $\mathcal{F}_1,\mathcal{F}_2$, ... and finally $\mathcal{F}_n = \mathcal{F}$ can be obtained.

---

[1]More exactly to the SIF at the point M of $\mathcal{F}$ induced by unit point forces exerted on the point M' of the crack lips in the direction $\pm\vec{y}$, when M' approaches M_0 (see Rice [8] for the exact definition).

In the sequel, we restrict our attention to a bounded plane crack $\mathcal{F}$ that can be derived from a penny shaped one $\mathcal{C}$ of center O and radius R for which $K(M) = 2\sigma_\infty \sqrt{R/\pi}$ and $W(M, M_0) = 1$ (see for instance, Rice [8]), but each crack shape for which the functions $K(M)$ and $W(M, M_0)$ are known could be chosen as starting point (see [1, 2, 3] for the half plane crack).

Meshing

The initial crack front $\mathcal{F}$ is meshed with N points P_i, $i = 0 \ldots N - 1$. The N nodes P_i^0 of the reference front $\mathcal{C}$ are constructed through intersection of $\mathcal{C}$ with the lines (OP_i). The segments $[P_i^0 P_i]$ are then cut into n pieces to create $n - 1$ intermediate meshes $\mathcal{F}_k$, $k = 1, n - 1$ with nodes $P_{j, j=0, N-1}^k$. As the
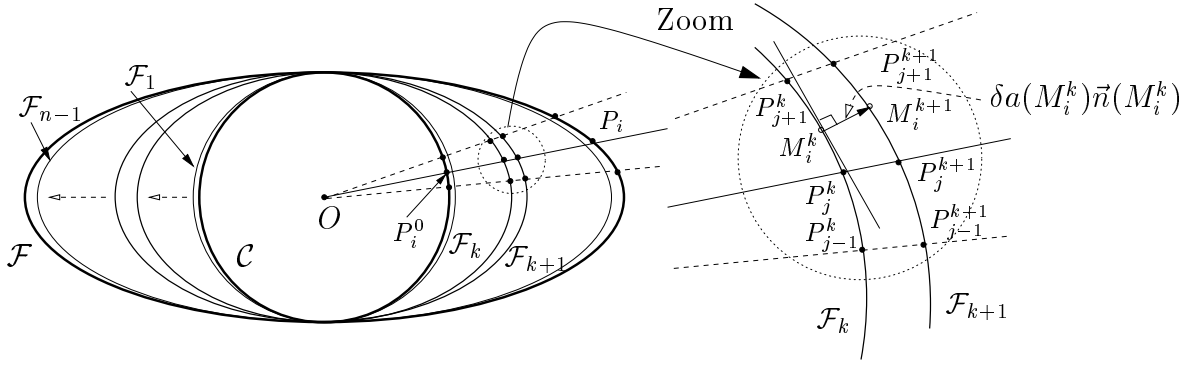
Figure 2: Intermediate cracks between the reference front $\mathcal{C}$ and the final one $\mathcal{F}$.

vector $\overrightarrow{P_j^k P_j^{k+1}}$ is not in general normal to the front $\mathcal{F}_k$ (see fig. 2), the Eqn. 2 and 3 don't give the SIF at point P_j^{k+1} as a function of its values on nodes $P_{i,i=0,N-1}^k$ of $\mathcal{F}_k$. Therefore a second set of meshes $M_{i,i=0,N-1}^k$ of $\mathcal{F}_k$, $k = 0, n$ is constructed by projection of the nodes M_i^k of $\mathcal{F}_k$ onto the arc of a circle passing through the 3 successive nodes P_{j-1}^{k+1}, P_j^{k+1}, P_{j+1}^{k+1}, of $\mathcal{F}_{k+1}$ with, as initialization, $M_i^0 = P_i^0$, $i = 0, N - 1$. The stress intensity factor and function W are then computed on the nodes $M_{i,i=0,N-1}^k$, $k = 1, n$ of this set of meshes. If the meshes become too distorted, remeshing is done.

Calculation of the integrals involved

To calculate each $\delta K(M_i^k)$, the PV part, around M_i^k, is extracted from Eqn. 2 and rewritten in the form (by taking into account the fact that $D(M, M_i^k) \sim |s(M) - s(M_i^k)|$ in the neighborhood of M_i^k) :

$$PV \int_{[M_{i-1}^k M_{i+1}^k]} a \frac{(s(M) - s(M_i^k))(s(M) - b)}{(s(M) - s(M_i^k))^2} \mathrm{d}s(M) =$$

$$a \left[s(M_{i+1}^k) - s(M_{i-1}^k) + (s(M_i^k) - b) \ln \frac{s(M_{i+1}^k) - s(M_i^k)}{s(M_i^k) - s(M_{i-1}^k)} \right] \tag{4}$$

where a, b are interpolation constants, $s(M)$ some curvilinear abscissa along the crack front. The integral over the rest of the front is regular and calculated by quadratic interpolation over each interval.

To calculate $\delta W(M_i^k, M_j^k)$, a similar procedure is employed. Nevertheless, attention must be paid to the fact that the PV concerns both points M_i^k and M_j^k.

One should notice that the procedure is less complicated than the one used by Bower and Ortiz [1], but gives comparable results, as shown below.

The elliptical crack

For an elliptic crack with major axis b and minor axis a subjected to some uniform tensile loading σ_∞, Irwin [6] has shown that :

$$K(M) = \frac{\sigma_\infty \sqrt{\pi a}}{\mathrm{E}(k)} \left(\frac{\sin^2(\theta) + \alpha^4 \cos^2(\theta)}{\sin^2(\theta) + \alpha^2 \cos^2(\theta)} \right)^{1/4} \quad \text{with} \quad \mathrm{E}(k) = \int_0^{\pi/2} (1 - k^2 \sin^2 x)^{1/2} \mathrm{d}x \qquad (5)$$

where θ is the polar angle of M, $\alpha = a/b$, $k = \sqrt{1 - \alpha^2}$ and $\mathrm{E}(k)$ denotes the elliptic integral of the second kind. The numerical results obtained for different values of α are in good agreement with this analytical result.
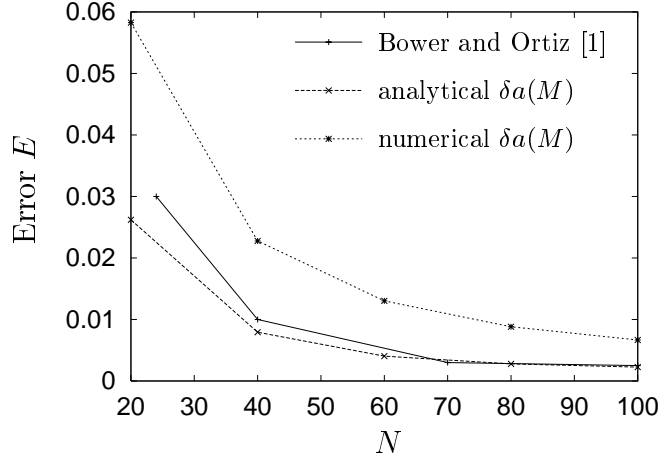
Figure 3: Error E obtained by different methods.

To compare our results to those of Bower and Ortiz [1], the case $\alpha = 1/3$ is considered. Figure 3 shows the value of the error E, defined by :

$$E = \sqrt{\frac{1}{\text{perimeter}} \int_{\mathcal{F}} \frac{(K_{num}(M) - K_{exact}(M))^2}{K_0^2} \mathrm{d}M} \qquad (6)$$

as a function of the number of nodes N, a constant maximum step size of $0.005a$ between the intermediate fronts $\mathcal{F}_k$ and $\mathcal{F}_{k+1}$ being used. K_0 denotes the uniform SIF along the initial penny-shaped crack $\mathcal{C}$ of radius a. When the advance of the front is given analytically like in the work of Bower and Ortiz, E is of the same order although our procedure of integration is simpler. However, when the advance is computed numerically, the error is obviously slightly increased, but reasonable enough to allow us to study cracks with more complex shapes.

Asymptotic behavior of SIF near an angular point of the front

The stress intensity factor along the front of several "heart shaped cracks", like the ones depicted in figure 4(a), with different opening angles Φ is given in figure 4(b).
Leblond and Leguillon [5] have shown that near the angular point O of the front, the SIF behaves in the following manner :

$$K(M) \propto |s(M) - s(O)|^{1/2 + \alpha} \quad \text{when} \quad M \to O, \qquad (7)$$

where α depends only on the opening angle Φ and verifies $\alpha < -1/2$ so that the SIF becomes infinite at the notch point. The peak in figure 4(b) is the numerical manifestation of this propriety.
The scalar α can be computed by fitting the behavior 7 with the results, around the corner point O, of figure 4(b). The values obtained are given in figure 5 for several angles Φ. Errors are due to the dependence of the results upon the points chosen for fitting and to the numerical errors in the computation of the SIF. They are all the greater as the shape of the crack is more different from the

(a) Shape

(b) SIF
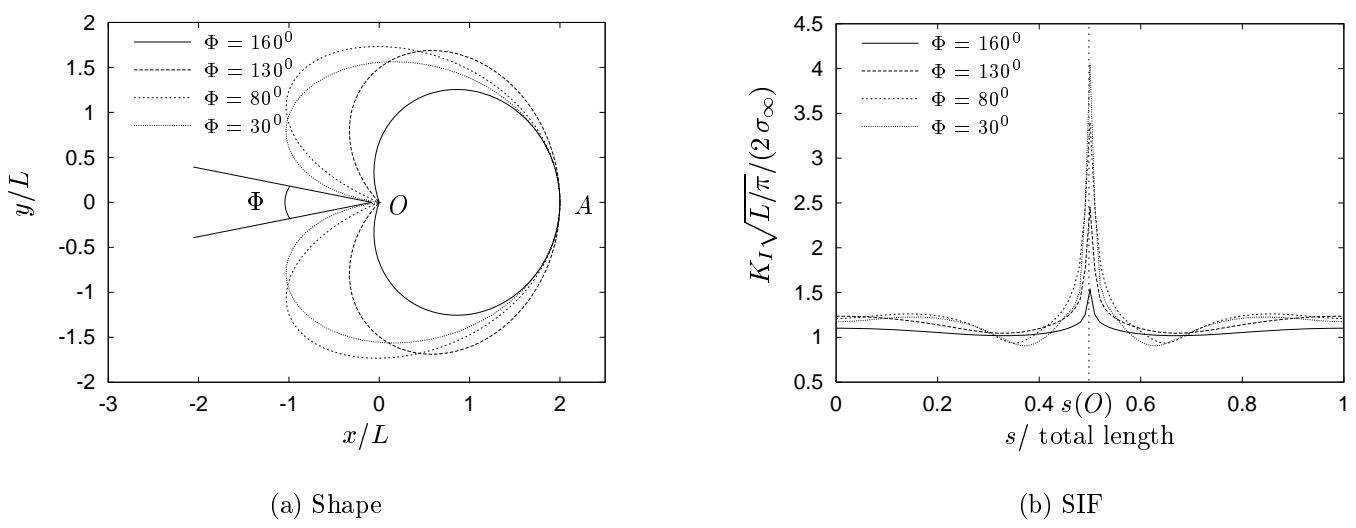
Figure 4: Heart shaped cracks

initial circle $\mathcal{C}$ i.e. as Φ is smaller. Nevertheless, our values are relatively close to the ones obtained by Leblond and Leguillon [5] by a more precise method in spite of the uncertainties linked to our method.
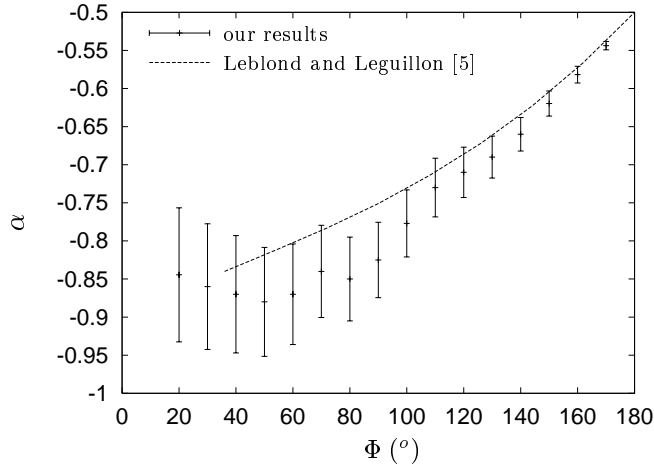
Figure 5: Computed values of the exponent α

SOME EXAMPLES OF FATIGUE PROPAGATION PATHS

Let us now consider a bounded plane crack $\mathcal{F}$ loaded in pure mode I through some uniform cyclic tensile stress applied at infinity. Suppose that the crack propagation rate is given by Paris' law and that during a few, say n_c cycles, the variation of mode I intensity factor $\Delta K(M)$ along the front remains constant so that :

$$\frac{\mathrm{d}a(M)}{\mathrm{d}n} = C(\Delta K(M))^{\beta} \implies \delta a(M) = n_c.C.(\Delta K(M))^{\beta} \tag{8}$$

where C and β are material constants and $\delta a(M)$ the normal crack advance after n_c cycles at the point M of the front.

Once the SIF and W are computed for the initial front $\mathcal{F}$ as explained above, the propagation path of this flaw can be determined by

1. applying Eqn. 8 to determine the displacement $\delta a(M)$ of the front;

2. using Eqn. 2 and 3 to update the SIF and the function W, and Eqn. 1 to obtain the new front;

3. repeat, as many times as required, the two preceding operations.

(a) Ellipse   (b) Rectangle   (c) "Heart"
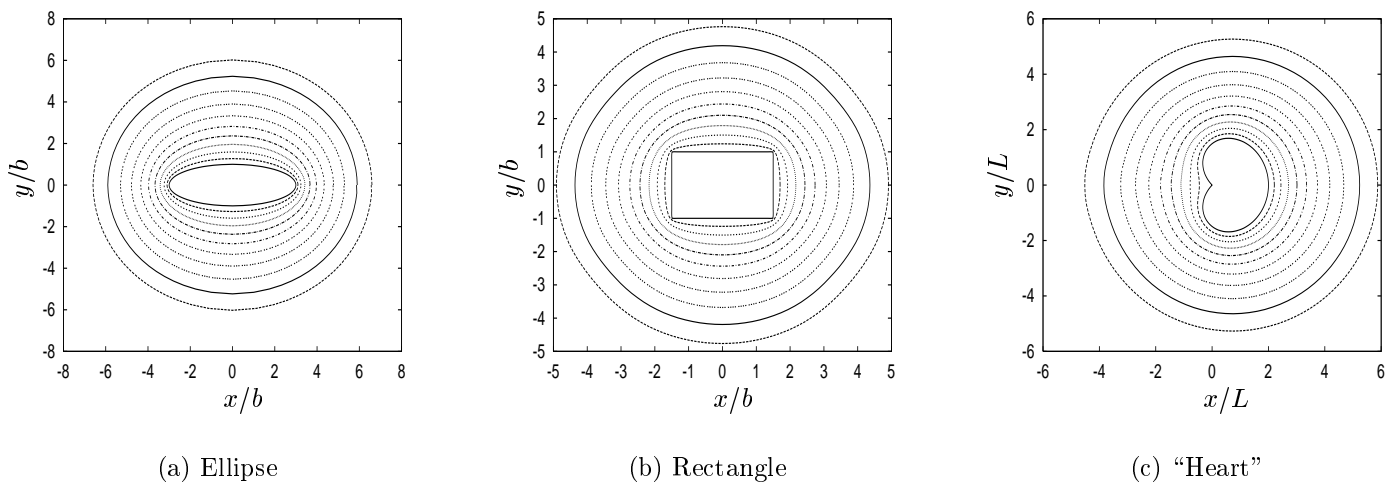
Figure 6: Propagation of some cracks for ($\sigma_\infty = 1$ Pa, $n_c C = 0.005$ Pa^{-2}, $\beta = 2$).

Figure 6 shows, as typical examples, positions of the front during the propagation of initially elliptic, rectangular and heart shaped cracks each $20 n_c$ cycles of loading. It appears that the crack becomes and remains circular after a certain time. This seems to be a general feature of the fatigue propagation of *bounded* mode I cracks embedded in an infinite body.

CONCLUSION

Since only the meshing of the initial front is needed, the procedure depicted above is an efficient tool for solving problems concerning a flat crack subjected to mode I loading. For instance, we have seen that the asymptotic behavior of the SIF near an angular point of the front and the fatigue propagation path of bounded cracks over a large distance can easily be computed.

Nevertheless, it would be interesting to extend the method to finite bodies to broaden the field of applications. But we do not know yet how to take into account boundary effects.

REFERENCES

1. Bower A.F. and Ortiz M. (1990). *J. Mech. Phys. Solids* 38, 443.

2. Bower A.F. and Ortiz M. (1991). *J. Mech. Phys. Solids* 39, 815.

3. Bower A.F. and Ortiz M. (1993). *ASME J. Appl. Mechanics* 60, 175.

4. Gao H. and Rice J.R. (1987). *ASME J. Appl. Mechanics* 54, 627.

5. Leblond J.B. and Leguillon D. (1999). *Eur. J. Mech. A/Solids* 18, 135.

6. Irwin G.R. (1962). *ASME J. Appl. Mech.* 29, 651.

7. Rice J.R. (1985). *ASME J. Appl. Mech.* 52, 571.

8. Rice J.R. (1989). In: *Fracture Mechanics : Perspectives and Directions (Twentieth Symposium), ASTM STP 1020*, pp. 29-57, Wei R.P. and Gangloff R.P., Eds., American Society fot Testing and Materials, Philadelphia.

STRESS SINGULARITIES WITHIN THE CELLULAR CORE OF A SANDWICH PLATE

W. Becker[1], J. Hohe[1], and S. Goswami[2]

[1] Institute of Mechanics and Control Engineering, University of Siegen, Paul-Bonatz-Str. 9-11, D-57068 Siegen, Germany

[2] College of Aeronautics, Cranfield University, Cranfield, Bedfordshire, MK 430 AL, UK

ABSTRACT

Structural sandwich panels with two-dimensional cellular core are subject to an increased delamination hazard compared to layered materials consisting solely of homogeneous materials. The increased delamination hazard is induced by an incompatibility in the modes of deformation of the cellular core and the facesheets which causes singular stress fields in the interface between the layers. A closed-form analytical and a numerical investigation show that the singularity is of the pure non-oscillatory power-law type. The order of the singularity as well as the associated stress intensity factor depend on the cell wall angle and on Poisson's ratio of the cell wall material.

KEYWORDS

Sandwich, cellular core, delamination, stress singularity, complex potential, stress intensity factor

INTRODUCTION

Sandwich plates and shells are widespread structural elements in lightweight construction with superior specific strength and stiffness characteristics. In essence, a sandwich consists of three layers, two homogeneous facesheets of high stiffness and strength and an intermediate low density core, see fig. 1. As typical core material often two-dimensional cellular structures are employed. Whereas the main task of the facesheets is to carry the inplane forces and bending moments the task of the core is to maintain the distance betweeen the facesheets and it is to carry the transverse forces.

For the proper function of a sandwich the integrity of the facesheet/core bonding is of essential importance. The problem of relatively large facesheet/core debondings or delaminations has already been considered by various authors as e.g. [1], [2], [3]. The case of a beginning delamination in sandwich plates with a hexagonal cellular core has been investigated by [4]. A detailed analysis of the mechanical situation along the adhesive bond of a hexagonal core without delamination has been performed by [5].

In comparison to the case of a homogeneous sandwich core in the case of a hexagonal cellular core
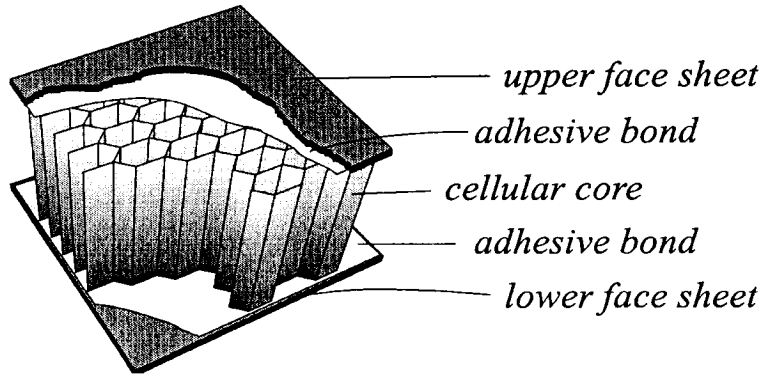
Figure 1: Sandwich construction principle

there is a somewhat increased delamination tendency which results from the incompatibility of the deformation modes of the cellular core and the facesheets respectively. Within the integrated sandwich compatibility is, however, enforced by the bond with the consequence of significant local stress concentrations in the vicinity of those interface locations where three cellular walls are joined to the facesheets. These stress concentrations have a singular character even in the absence of any delamination and thus are critical locations for the onset of delaminations.

The present work is concerned with this kind of singular stress concentration. By a closed-form asymptotic analysis it will be shown that the stress singularity is of a pure non-oscillatory power-law type. This is in good agreement with finite element analyses which in addition yield the according stress concentration factor.

CLOSED-FORM ANALYTICAL APPROACH

Fig. 2 shows the geometry of the hexagonal core of a sandwich plate to be considered. The cellular core is supposed to be doubly symmetric with two cell wall angles of the same size α. From manufacturing reasons the diagonal cell walls of fig. 2 are of simple thickness t whereas the horizontal cell wall has the thickness $2t$. For analysis reasons the coordinates x_1, x_2, r_I, φ_I, r_{II}, and φ_{II} shown in fig. 2 are introduced. As given loading a prescribed effective strain $\tilde{\varepsilon}_{11}$ is presumed.

For the closed-form analytical approach two simplifying assumptions are made. First, it is assumed that the facesheets due to their superior stiffness within the immediate vicinity force the cell walls to follow their deformation, in accordance with the underlying homogeneous effective strain $\tilde{\varepsilon}_{11}$. Second, the bending stiffness of the cell walls due to the small cell wall thickness is neglected. Then
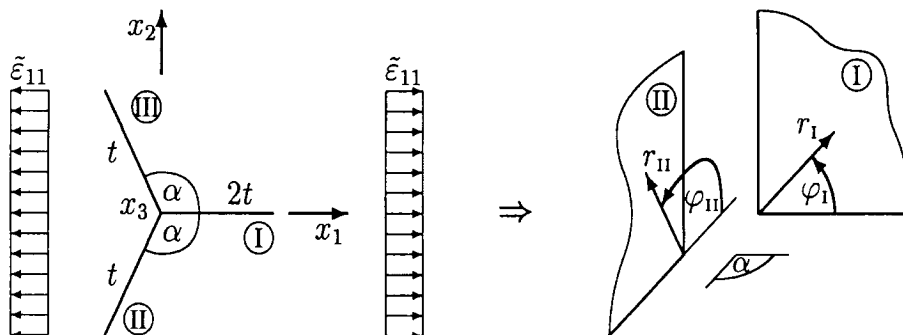
Figure 2: Cellular geometry and employed coordinates

the description of the mechanical field quantities within the cell walls can be accomplished by plane elasticity theory. For symmetry reasons it is sufficient to consider only two cell walls. With the local coordinates r and φ shown in fig. 2 the local stress and displacement fields can be represented through the formulas of Kolosov-Muskhelishvili [6]:

$$\sigma_{rr} + \sigma_{\varphi\varphi} = 2\left(\Phi'(z) + \overline{\Phi'(z)}\right) \quad,$$

$$\sigma_{\varphi\varphi} - \sigma_{rr} + 2i\sigma_{r\varphi} = 2\left(z\Phi''(z) + \frac{z}{\bar{z}}\Psi'(z)\right) \quad, \tag{1}$$

$$2G(u_r + iu_\varphi) = \left(\kappa\Phi(z) - z\overline{\Phi'(z)} - \overline{\Psi(z)}\right)e^{-i\varphi} \quad,$$

$$\text{with} \quad G = \frac{E}{2(1+\nu)} \quad, \quad \kappa = \frac{3-\nu}{1+\nu} \quad \text{(for plane stress conditions)},$$

where the quantities Φ and Ψ are complex potentials of the complex variable $z = e^{i\varphi}$, and the quantities E and ν are Young's modulus and Poisson's ratio, respectively.

In the present situation the following general representation is chosen for the complex potentials:

$$\Phi(z) = Az^\lambda + Cz^\lambda \ln z \quad,$$
$$\Psi(z) = Bz^\lambda + Dz^\lambda \ln z \quad, \tag{2}$$

where the complex constants A, B, C, and D and the order $\lambda - 1$ of the singularity are still undetermined. The stress and displacement components σ_{ij} and u_i have to satisfy the following boundary and compatibility conditions for an arbitrary radius r (for details see [8]):

$$u_r^I(\varphi = 0) = \tilde{\varepsilon}_{11}r \quad,$$
$$u_\varphi^I(\varphi = 0) = 0 \quad,$$
$$u_r^{II}(\varphi = \frac{\pi}{2}) = u_r^I(\varphi = \frac{\pi}{2}) \quad,$$
$$u_\varphi^{II}(\varphi = \frac{\pi}{2}) = (-\cos\alpha)u_\varphi^I(\varphi = \frac{\pi}{2}) \quad,$$
$$(-\cos\alpha)\sigma_{\varphi\varphi}^{II}(\varphi = \frac{\pi}{2}) = \sigma_{\varphi\varphi}^I(\varphi = \frac{\pi}{2}) \quad, \tag{3}$$
$$\sigma_{r\varphi}^{II}(\varphi = \frac{\pi}{2}) = \sigma_{r\varphi}^I(\varphi = \frac{\pi}{2}) \quad,$$
$$u_r^{II}(\varphi = \pi) = \tilde{\varepsilon}_{11}(\cos^2\alpha)r \quad,$$
$$u_\varphi^{II}(\varphi = \pi) = 0 \quad.$$

As these conditions have to be fulfilled for all radii r the inhomogeneous set of equations can be transferred into a set of homogeneous equations by double differentiation. As the 8 equations (3) contain all two different kinds of functional dependences on r (with and without logarithmic dependence) they give in total 16 homogeneous equations for the 16 unknown real and imaginary parts of the complex constants A to D for the two considered cell walls I and II (see fig. 2). Conditions for the existence of non-trivial solutions for homogeneous systems of equations of the present kind have been given by [7]. These conditions comprise a zero-determinant of the coefficent matrix for the case of a pure power-law singularity. In addition the $(8-m)$th derivative of this determinant has to vanish, where m is the rank of the corresponding coefficient matrix. The determination of the eigenvalue λ from these conditions can be done numerically. When solving the system of equations no values λ with $\mathrm{Re}(\lambda) < 0$ are permitted for energetic reasons. On the other hand also solutions λ with $\mathrm{Re}(\lambda) > 1$ are excluded because these would belong to non-singular stress fields. By a correspondingly restricted numerical investigation it turns out that within the relevant range $0 < \alpha \leq \pi$ and $0 < \nu \leq 0.5$ there is no common solution with non-vanishing constants C and D. Thus, it can be concluded that $C = D = 0$ and the stress singularity is of a pure power-law type. Considering the eigenvalues λ they are all found to be real, so that the singularity in any case is non-oscillatory. With the eigenvalue

λ for a given cell geometry with cell wall angle α and a given cell wall material with Poisson's ratio ν then the real and imaginary parts of the remaining complex constants A and B can be calculated from the corresponding homogeneous system of equations, so that finally the stress and displacement components are available in the form

$$
\begin{aligned}
\sigma_{ij}(r,\varphi) &= K^* r^{\lambda-1} f_{ij}(A,B,\varphi) \quad, \\
u_i(r,\varphi) &= \frac{1}{2G} K^* r^{\lambda} g_i(A,B,\varphi) \quad.
\end{aligned}
\tag{4}
$$

with appropriately defined angular functions f_{ij} and g_i. The quantity K^* in (4) denotes a stress intensity factor that cannot be determined by an asymptotic analysis but results from the surrounding far field. Due to the different order of singularity it is to be noted that the stress intensity factor K^* cannot be compared directly with the well-known stress intensity factors K_I, K_{II}, and K_{III} of common fracture mechanics. The actual numerical exploitation of relations (4) reveals that in general all stress components σ_{rr}, $\sigma_{\varphi\varphi}$, and $\sigma_{r\varphi}$ are non-zero for $\varphi = 0$ and $\varphi = \pi$ which can be interpreted as the presence of a mixed mode stress singularity.

NUMERICAL APPROACH

In addition to the closed-form asymptotic analysis a numerical investigation has been performed by means of finite element method. To that end a detailed finite element model has been set up for a representative volume element of the given microstructure. The cell walls and the facesheets have been modelled by standard four-node shell elements in an enhanced-strain formulation with a mesh refinement in the region of the singularity. On the surfaces of the representative volume element periodic boundary conditions have been applied. The loading is given by prescribed displacements on the facesheets and along the outer cell wall edges of the representative volume element. The order $(\lambda - 1)$ of the singularity can be determined from the displacements u_1 of the nodal points along the cell wall junction. The exponent λ is obtained as the slope of u_1 as a function of the radial distance in a double-logarithmic representation.

Beyond this the stress intensity factor K^* can be determined from the stresses $\sigma_{\varphi\varphi}$ along the interface of cell wall I with the upper facesheet in the following way:

$$
K^* = \lim_{r \to 0} \frac{\sigma_{\varphi\varphi}(r, \varphi = 0)}{r^{\lambda-1}}.
\tag{5}
$$

Within the numerical analysis this relation is used for the second to fifth element along the cell wall/facesheet interface. A convergence study gives stable results for a discretization of about 16000 finite elements for both the order of singularity and the stress intensity factor K^*. A comparison of the finite element results for the order of singularity shows very good agreement with the closed-form asymptotic analysis.

RESULTS

The presented closed-form asymptotic analysis reveals that the order $\lambda - 1$ of the considered singularity depends on both the cell wall angle α and Poisson's ratio ν of the cell wall material. The impact of α and ν on the exponent λ is shown in fig. 3, whereas fig. 4 shows the dependence of the stress intensity factor as it comes out from the performed finite element analyses. Obviously, the exponent $\lambda - 1$ vanishes for the limit case $\alpha \to \pi$ of a straight cell wall. On the other hand, the strongest singularity occurs in the case of a vanishing cell wall angle $\alpha = 0$. The impact of Poisson's ratio on the exponent λ is relatively weak, at least in the typical range $\nu = 0.2 \dots 0.4$. For the stress intensity factors K^* smaller cell wall angles lead to significantly larger values, in particular when Poisson's ratio
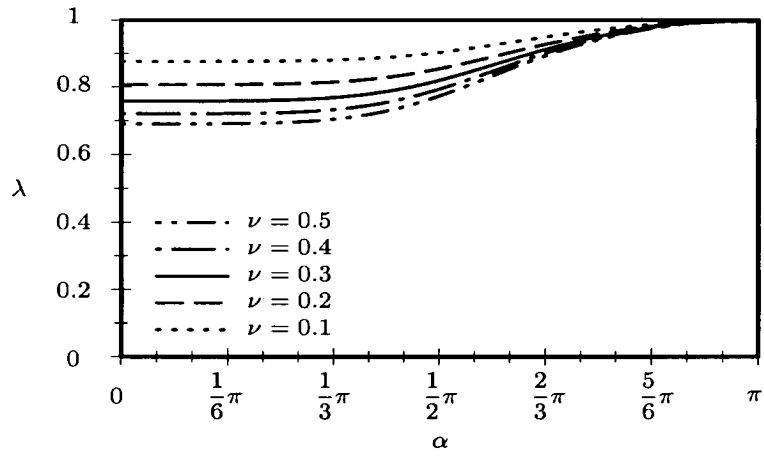
Figure 3: Order λ of the singularity as a function of α and ν
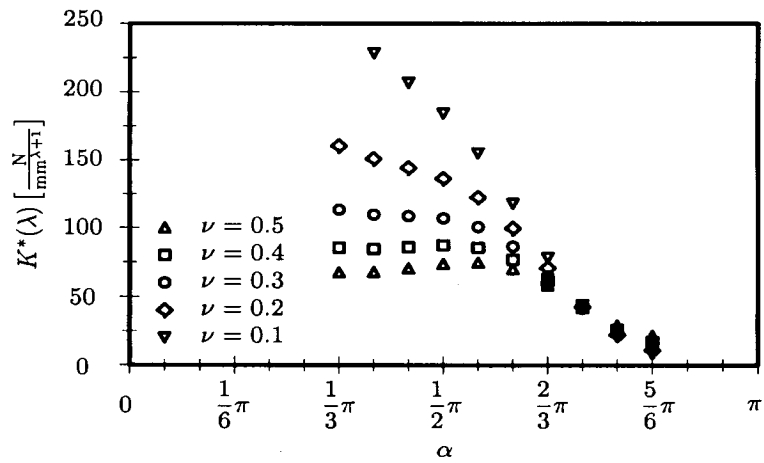
Figure 4: Stress intensity factor K^* as a function of α and ν

is small. Thus, with decreasing cell wall angle α the considered stress singularity increases in terms of the stress singularity exponent $\lambda - 1$ as well as in terms of the stress intensity factor K^*.

In addition to the variation of the cell wall geometry and Poisson's ratio of the cell wall material the influence of the stiffness of the facesheets has been investigated, too. In this regard the result is that there is no significant impact of the facesheet stiffness on the order of singularity $\lambda - 1$ and on the stress intensity factor K^* as long as Young's moduli E_f of the facesheets and E_c of the cell wall material and the thicknesses t_f of the facesheets and t_c of the cell walls are in the order of magnitude that is realistic for actual applications ($E_f \geq 50\text{GPa}$, $t_f \geq 1\text{mm}$, $E_c \approx 70\text{GPa}$, $t_c \leq 0.1\text{mm}$).

CONCLUSIONS

A corner singularity has been investigated that occurs at the junction of the cell walls of a hexagonal cellular core with the facesheets. It has been shown that this singularity is of a pure non-oscillatory power-law type with an order of singularity $\lambda - 1$ that depends on the cell wall angle α and Poisson's ratio ν of the cell wall material. These two quantities have also a significant impact on the resultant stress intensity factor K^*. The thickness and stiffness of the faceheets, on the other hand, have only a minor influence.

A fracture mechanical assessment of the delamination tendency is not directly possible on the basis of the available stress intensity factors as these correspond to varying orders of singularity. Some transfer of fracture mechanical concepts is however possible by means of a critical distance from the cell wall triple points. Beyond this, the calculated local stress fields can be employed as a basis for the analysis of hypothetical delamination cracks.

References

[1] Triantafillou, T. C. and Gibson, L. J. (1989). *Mat. Struct.* 22, 64.

[2] Prasad, S. and Carlsson, L. A. (1994). *Eng. Frac. Mech.* 47, 813.

[3] Cantwell, W. J., Scudamore, R., Ratcliffe, J., and Davies, P. (1999). *Compos. Sci. Tech.* 59, 2079.

[4] Goswami, S. and Becker, W. (2000). *Compos. Struct.* 49, 385.

[5] Burton, W. S. and Noor, A. K. (1997). *Fin. Elem. Anal. Des.* 26, 213.

[6] Muskhelishvili, N. I. (1975). *Some Basic Problems of the Mathematical Theory of Elasticity.* Noordhoff International Publishers, Leyden.

[7] Dempsey, J. P. and Sinclair, G. B. (1979). *J. Elast.* 9, 373.

[8] Hohe, J., Goswami, S., and Becker, W. (2001). *Accepted for publication in Compos. Struct.*

STUDIES ON DEFORMATION AND FRACTURE BEHAVIOUR OF WELDED PLATE FOR A SUPER STEEL

Fuqiang Tian[1], Yaowu Shi[1], Xiaoyan Li[1], Yongping Lei[1] and Xinping Zhang[2]

[1]School of Materials Science & Engineering, Beijing Polytechnic University,
100 Ping Le Yuan, Chaoyang District, Beijing 100022, China
[2]Centre of Expertise in Damage Mechanics(CoE-DM)/ Centre for Advanced Materials Technology(CAMT)
Dept.of Mechanical & Mechatronic Engineering, The University of Sydney, N.S.W 2006, Australia

ABSTRACT

In the present investigation, stress-strain field and fracture parameters as CTOD and J integral of practical overmatched welded plate made of a super steel SS400 is computed using MARC finite element program in 3D condition. The results of the computation show that mechanical heterogeneity has obvious influence on the shape and size of plastic zone. CTOD and J integral of the welded plate are smaller than those of the whole base metal plate in the same tension. Thus, the anti-fracture property of overmatched welded plate is better than that of the whole base metal plate.

KEY WORDS

Super steel SS400, Welded joint, Full yield, CTOD, J integral

INTRODUCTION

Welded joints is a mechanical heterogeneous body which is composed of base metal, heat affected zone (HAZ) and weld metal. Mechanical heterogeneity has important influence on the fracture behavior of structures. In most of studies, welded joints are assumed to be two parts of base metal and weld metal [1,2]. However, for practical welded joints HAZ is often weaker and is sensitive to defects. Therefore, the effect of HAZ is obvious, particularly for the thin plate. Super steel is newly developed steel material with super high strength, super fine grain and super clean micro-structure. The influence of welding on fracture behavior gain special attention.

Soete[3] suggests that allowed defect size can be determined on a basis of strain in large mark distance of wide plate in tension. That is, if a specimen containing a notch is under the action of perpendicular stress and the specimen is under condition of full yield or the whole elongation in the marked distance is up to 1~2%, this type of defect is allowed. Such an assessment standard for the acceptance of flaw in wide plate test is simple and suitable for engineering practice, for it is with a view to whole plasticity of specimen rather than local deformation. Experiments[4] show that overmatching welded joints is apt to attain full yield than

homogeneous base metal, so its limit crack size is large and its anti-fracture behavior is enhanced.

In the present investigation, stress-strain field and fracture parameters as CTOD and J integral of practical overmatched welded plate made of super steel SS400 is computed. According to the full yield criterion, overmatched welded joint has better anti-fracture behavior than homogeneous material. The results also show the effect of HAZ on the shape of plastic zone ahead of crack tip and fracture parameters.

COMPUTATION MODEL

Chemical compositions and mechanical properties of a super steel SS400 are given in Table 1 and Table 2, respectively.

TABLE 1
CHEMICAL COMPOSITIONS OF THE SUPER STEEL SS400 (w.t.%)

C	Si	Mn	P	S	Al	Cu	Cr	Mo	Ni
0.171	0.09	0.36	0.013	0.013	0.025	0.01	0.02	0.01	0.03

TABLE 2
MECHANICAL PROPERTIES OF THE SUPER STEEL SS400

Material	Tension strengthσ_b(MPa)	Yield strengthσ_s(MPa)	Elongation δ_5(%)
SS400	480	365	31

The plate is welded by a pulse metal arc gas (PMAG) shielded welding process. The welding wire used is JS40Cu and the welding heat input is 3.0KJ/cm. The distribution of hardness of the practical welded joint is shown in Figure 1.
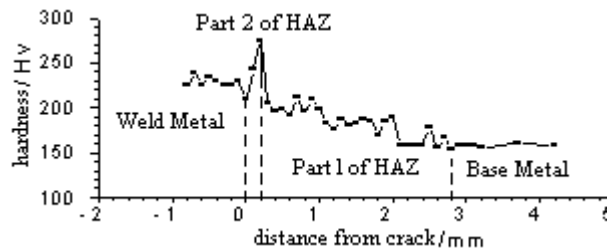
Figure 1: Hardness distribution of the practical welded joint

It can be seen from Figure 1 that the welded joint is composed of base metal, heat affected zone (HAZ) and weld metal. HAZ contain two parts approximately with different hardness, the softer part near base metal is labeled as Part 1 and the harder part near weld metal is labeled as Part 2.

The computation model is a thin plate and big size of wide plate specimen under tension, which is shown in Figure 2. Thickness of the plate is 2.8mm. Crack is located in the interface between Part 2 of HAZ and weld metal.

For the symmetry of specimen, only 1/4 of the whole specimen is computed. 20 nodes hexahedron element is used in the computation. Finite element mesh is shown in Figure 3. The mesh of weld metal and HAZ is dense. Crack tip use obtuse model with radius of 0.002mm. On the direction of thickness two layers of elements are meshed, and the elements of the layer near the center of plate is thinner. The mesh has a total of

14104 elements and 78625 nodes.
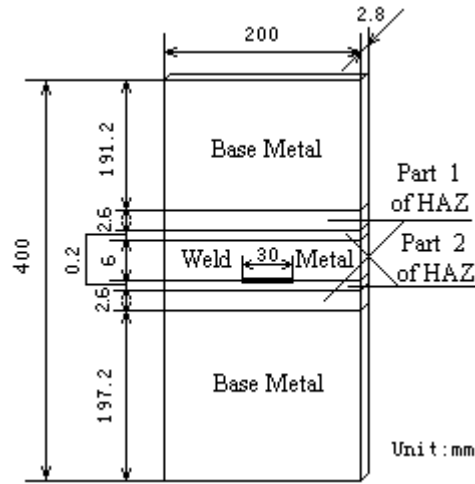
Figure 2: Sketch map of computation model

(a) Whole mesh   (b) Local mesh
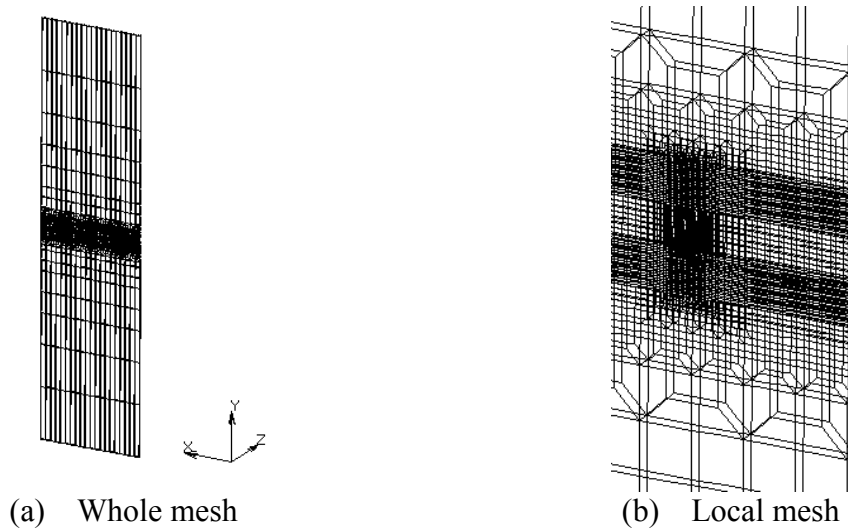
Figure 3: Mesh for finite element computation

Yield strength of the super steel SS400 base metal is 365Mpa based on the result of test, and the yield strength of other parts of welded joint is estimated according to the hardness distribution tested. For the simplification of computation, hardness distribution model showing in Figure 4 is used.
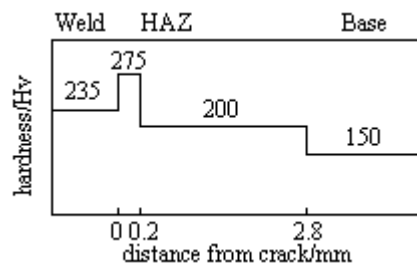
Figure 4: Simplified hardness distribution model of welded joint

In the computation, it is assumed that the whole model consists of four parts as base metal, Part 1 of HAZ, Part 2 of HAZ and weld metal. The uniaxial tensile stress-strain relation follows the pure power hardening law, which is given as,

$$\varepsilon / \varepsilon_y = \alpha \left(\sigma / \sigma_y \right)^n \tag{1}$$

Where ε, σ are the true strain and true stress, respectively, and ε_y, σ_y are the yield strain and yield stress, respectively. α is the hardening coefficient, and n is the power hardening exponent, which is assumed to follow the empirical equation[5],

$$n = 1/\left[k \ln\left(1390/\sigma_y\right)\right] \qquad (2)$$

where k is the constant which is equal to 0.12. Table 3 shows σ_y and n value of each part of welded joint. It is assumed that elasticity module is the same for different part and is equal to 210,000MPa and Possion ratio is 0.3.

TABLE 3

VALUES OF σ_y AND n IN EACH PART OF WELDED JOINT FOR STEEL SS400

	Base Metal	Part 1of HAZ	Part 2 of HAZ	Weld Metal
σ_y (MPa)	365	487	669	572
n	6.23	7.95	11.4	9.39

For contrast, wide plate tension specimen of whole SS400 base metal with same size and same mesh is computed.

The present 3D FEM computations are performed using a software of MARC. Stress loading is used, and the maximum stress is 440MPa which is about $1.2\sigma_y$ where σ_y is yield stress of SS400. J integral is calculated using DeLorenzi Virtual Crack Extension (VCE) method, and CTOD is measured using 45° angle method.

RESULTS AND DISCUSSIONS

Figure 5 shows yield zones of 17th to 20th computation steps of the wide plate tension model for welded joint and whole base metal. Yield zones are expressed by equivalent strain on the mid-section in thickness direction. Applied loads are 340MPa, 360MPa, 380MPa and 400MPa respectively for the relevant loading step.

It can be seen from Figure 5 that ligament yield takes place at the 18th step and full yield takes place at the 19th step for both welded joint and whole base metal. At the 17th step, the yield zone of welded joint plate is smaller than that of whole base metal plate, because the yield strength of the base metal is lower than that of weld metal and HAZ. At the 19th step, the full yield zone in the part of base metal of welded joint plate is bigger than that in whole base metal plate. The reason is that the harder weld metal and HAZ is difficult to deform under the protection of softer base metal, thus it is expected that the anti-fracture performance of welded joint plate is enhanced.

Figure 6 shows the local yield zone of weld metal and HAZ for welded joint plate, where for the whole base metal plate is at the 19th loading step. The contour of yield zone breaks in the interface between parts of materials with different strength, and the shape of yield zone is asymmetry due to the strength difference. The influence of HAZ on the contour of yield zone can also be seen from Figure 6(a).

CTOD and J integral of welded joint plate and those of whole base metal plate in the same tension are compared in Figure 7. The values of both CTOD and J integral of welded joint plate are lower than those of whole base metal plate, and the difference between them becomes larger with increasing load, and J integral increases in approximately same trend as CTOD with increasing load. The reason is that yield strength of

material near crack tip in welded plate is higher, thus crack tip is difficult to stretch. This indicates that driving force to fracture for welded joint plate with overmatched weld metal is smaller than that for whole base metal plate.

(a) 17th step for welded joint plate (b) 18th step for welded joint plate (c) 19th step for welded joint plate (d) 20th step for welded joint plate

(e) 17th step for base metal plate (f) 18th step for base metal plate (g) 19th step for base metal plate (h) 20th step for base metal plate
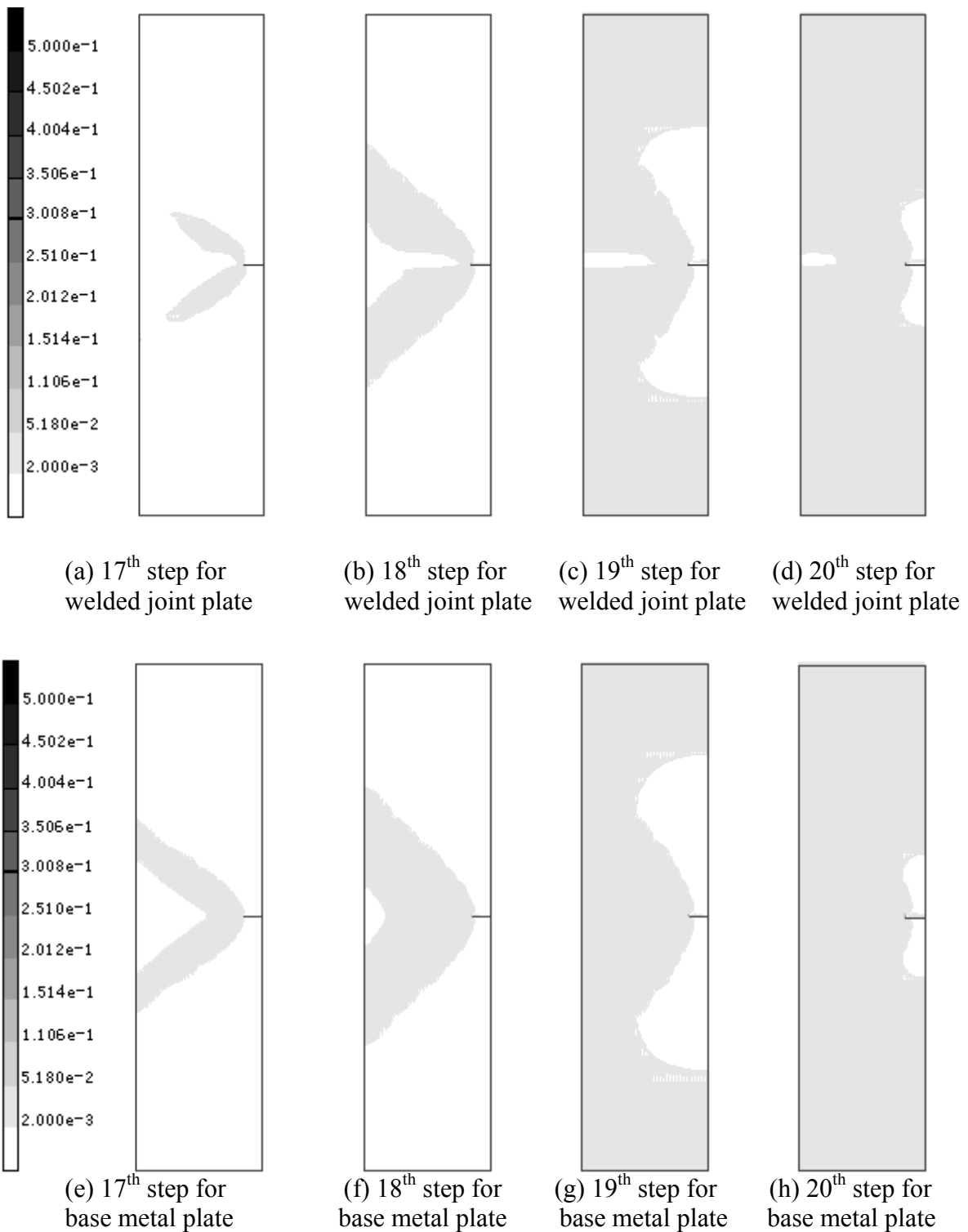
Figure 5: Yield zone of 17th to 20th step of wide plate tension model for welded joint and whole base metal

CONCLUSIONS

The present simulation of practical welded joint in tensile plate for super steel SS400 shows that existence of weld metal and HAZ in welded joint has important influence on the stress-strain field near crack tip, and yield zone is discontinuous when it passes through different parts of joint.

The computation results show that full yield is easier to take place in welded joint tensile plate than whole base metal plate, and driving force to fracture for welded joint plate is smaller than that for whole base metal plate.

(a) Welded joint plate   (b) Whole base metal plate
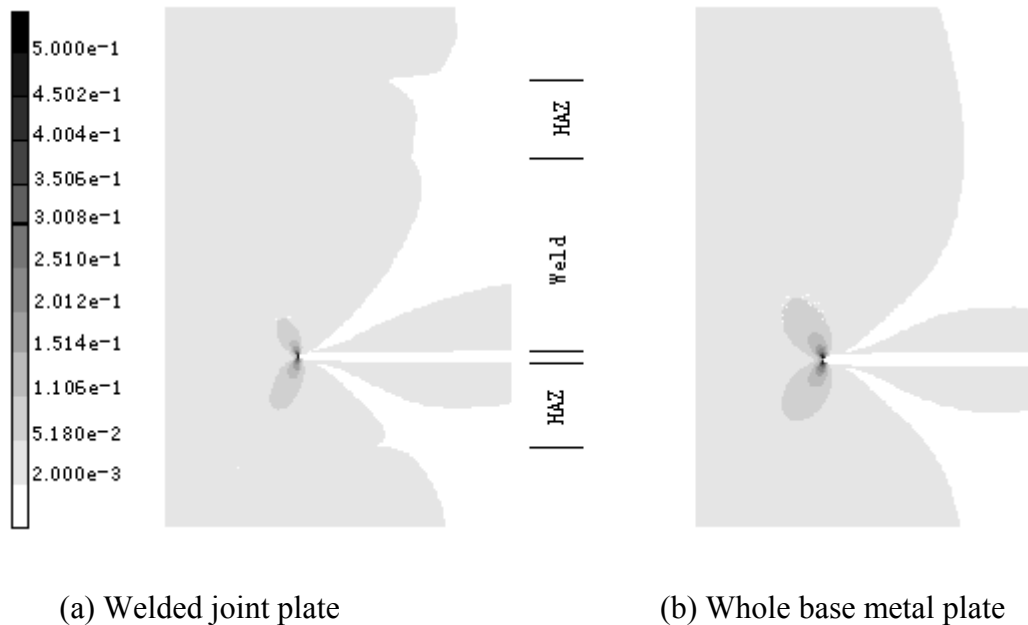
Figure 6: Comparison of the local yield zone of weld metal and HAZ
for welded joint plate and whole base metal plate

(a) Comparison of CTOD   (b) Comparison of J integral
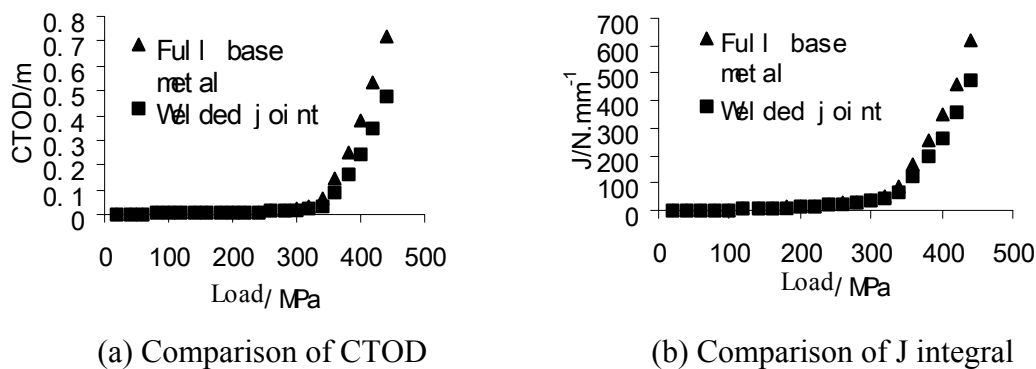
Figure 7: Comparison of CTOD and J integral for welded joint plate and whole base metal plate

REFERENCES

1. Ma, W. , Zhang, S. and Tian, X. (1987) Trans of the China Welding Institution. 8, 89. In Chinese.
2. Zhang, J. , Shi, Y. and Tu, M. (1991) Trans of the China Welding Institution. 12, 221. In Chinese.
3. Soete, W. and Denys, R. (1976). In: *Welding of HSLA structural steels*, pp. 63-84, Rothwell, A. B. and Gray, J. M. (Eds). Metals Park, Ohio.
4. Huo, L. (1995). Engineering Strength of Welding Structures, Mechanical Industry Press, Beijing. In

Chinese.

5. Ueda, Y. , Shi, Y. , Sun, S. and Murakawa, H. (1997) Trans. JWRI. 26,133.

STUDIES ON INITIATION TOUGHNESS AND TEARING RESISTANCE IN WELD JOINTS OF AN OFFSHORE STRUCTURAL STEEL

R.K. Pandey, G.K. Purohit and R.S. Parmar

Dept. of Applied Mechanics, Indian Institute of Technology
Hauz Khas, New Delhi- 110016, INDIA

ABSTRACT

The crack initiation toughness and tearing resistance studies have been conducted in a microalloyed steel weldment, a material for offshore structure and oil - gas pipeline. The CTOD resistance curves were obtained for the base metal, weld metal (WM) and the heat affected zone (HAZ) along weld direction (i.e. long transverse direction) and the thickness direction of crack propagation. The initiation toughness and tearing modulus were compared for the different zones of the weld joint and correlated with corresponding microstructural features and strength properties.

KEYWORDS

Tearing modulus, Heat affected zone, Weldment, CTOD toughness

INTRODUCTION

The microalloyed steel finds extensive application in the manufacture of offshore structures, oil and gas pipelines, pressure vessels, storage tanks for chemical and petrochemical industries etc. where fabrication is done mostly using welding process. The weld joint behaves like a composite material comprising of weld metal (WM), heat affected zone (HAZ) and the base metal (BM). The susceptibility to crack initiation and stable tearing therefore varies, from one zone to another .The present investigation is conducted to study the cracking behaviour of different regions of the joint in a microalloyed steel with C-0.22%, Mn-1.80%, Si-0.35%, S-0.04%, P-0.04%, Nb, V-0.20%.

WELD PARAMETERS

The joints were prepared by single bevel butt welding using single wire DC submerged arc welding machine along the long transverse direction of the plate .The welding conditions were optimized (Purohit, 1995) and presented in Table1.

Table 1. Details of Welding Parameters

Wire – 3.15mm diameter solid wire with composition C: 0.08-0.16%, Mn: 1.60-1.80%, Si: 0.05- 0.25%, S, P: 0.03%.	
Welding Current	250-375 A
OCV	40-45 V
Arc Voltage	26-28 V
Welding speed	50-70 cm/min
Heat input	5.6-12.6 kJ/cm
Nozzle to plate distance	35 mm
Polarity	DCEP
Interpass temperature	150 ^{o} C

The post welding heat treatment (PWHT) i.e. stress relieving was done as per ASM recommendations at 650 C followed by furnace cooling to room temperature.

TENSILE TEST

The tensile tests were conducted on base metal (BM) and the weld metal (WM). Round bars of 5.06 mm diameter and 17.9 mm gauge length were employed. The results on tensile properties are given in Table 2.

Table 2. Tensile Properties

	Base Metal	Weld Metal (All-weld)	Joint
Yield strength (MPa)	526	485	523
Tensile strength (MPa)	709	587	629
% Elongation	32	29	19
Strain hardening exponent	0.223	0.188	-

FRACTURE MECHANICS TEST

Fracture mechanics tests were conducted to investigate behaviour of crack growth and tearing resistance of steel in the BM, WM and the HAZ . In case of BM, crack propagation along rolling direction as well as long transverse direction were investigated, whereas in case of WM and the HAZ studies were made in weld direction and transverse to weld direction (i.e. thickness direction).

The tests were conducted as per ASTM Standard (ASTM E 1290, 1993) using single edge notch (SEN) bend type specimens of dimensions 10mm (thickness, B)   20 mm (width, W)   80 mm (span length, S) for crack propagation studies along the weld direction and 10 mm   10 mm   80 mm for studies along thickness direction. Tests were conducted using MTS machine under three point bending at ambient temperature. Load (P) vs. Crack mouth opening displacement (CMOD) diagrams were obtained and some typical ones are shown in Fig.1.

MICROSTRUCTURAL STUDIES

Microstructural examinations were conducted from the BM, WM and the HAZ. The BM microstructure consists of proeutectoid ferrite (about 80%) along with pearlite .The WM microstructure in low heat input condition consisted of polygonal ferrite (PF) accompanied with side plate ferrite (AC) and acicular ferrite (AF).The corresponding microstructure of HAZ revealed bainitic structure as well as fine pearlitic structure . Under condition of higher heat input large proportion of grain boundary ferrite (GBF) and some AF were noticed in the WM. The HAZ microstructure on the other hand consisted of both martensitic structure as well as ferrite carbide aggregate.

ELASTIC- PLASTIC CRACK INITIATION TOUGHNESS AND RESISTANCE CURVES

The CTOD initiation toughness, $_i$ were obtained for BM, WM and HAZ in different orientations as per ASTM standard. The values of initiation toughness are reported in Table 3 corresponding to 0.2 mm of crack growth. The CTOD values at crack initiation are shown in a bar chart in Figure 2. The CTOD resistance curves i.e.   -R curves were obtained for different regions of the weld joint. Typical   -R curves are presented in Fig. 3.

The   -R curves were fitted in the form of equation, $d = a(b + \Delta a)^g$ where   ,   and   are constants. The representative equations of R curves are presented in Table 4.

Table 3. CTOD Initiation Toughness ($\Delta a = 0.2$ mm)

Material	δ_i μm	Material	δ_i μm
BL	236	BB	209
WL	201	WB	148
WLR	166	WBR	149
HL	195	HB	119
HLR	141	HBR	144
NB B,W,and H in the beginning connote base metal ,weld metal and HAZ respectively. These are followed by L and /or B which indicate weld longitudinal and thickness direction of crack growth respectively. Symbol R towards the end stands for stress relieved condition of the joint.			

Table 4. δ-R Curve Equations

Longitudinal direction		Thickness Direction	
BL	$\delta=0.523(0.107+\Delta a)^{0.675}$	BB	$\delta=0.560(0.041+\Delta a)^{0.690}$
WL	$\delta=0.452(0.100+\Delta a)^{0.672}$	WB	$\delta=0.356(0.032+\Delta a)^{0.603}$
WLR	$\delta=0.332(0.040+\Delta a)^{0.483}$	WBR	$\delta=0.340(0.041+\Delta a)^{0.580}$
HL	$\delta=0.433(0.040+\Delta a)^{0.557}$	HB	$\delta=0.425(0.080+\Delta a)^{1.000}$
HLR	$\delta=0.392(0.026+\Delta a)^{0.685}$	HBR	$\delta=0.420(0.094+\Delta a)^{0.872}$
δ and Δa are in mm			

EVALUATION OF TEARING MODULUS (TM)

The tearing resistance of joint can be quantified in terms of the 'tearing modulus'(T_M) which is given as

$$T_M = \frac{E}{\sigma_f}\frac{d\delta}{d\Delta a}$$

where E is the elastic modulus. and σ_f is flow stress which is given as,

$$\sigma_f = \frac{\sigma_{ys} + \sigma_{UTS}}{2}$$

The tearing modulus were evaluated by obtaining $d\delta/d\Delta a$ from the equations of δ-R curves at different level of crack growth (Purohit, 1995). The tearing modulus is indeed found to depend on the amount of crack growth and it decreases with increasing crack extension. The representative variation of T_M with Δa is presented in Fig. 4 and the values of 'tearing modulus' at initiation of crack growth (i.e. $\Delta a \approx 0.05$mm) and also at $\Delta a = 0.5$mm are shown in Table 5.

DISCUSSION

From Table 2. It is observed that the base metal possesses higher yield and tensile strength as compared to all – weld metal. The lower value of strength properties for the WM is mostly due to presence of coarse grain boundary ferrite and polygonal ferrite in large proportion. This structure is unfavourable both for the strength and fracture toughness. The hardness profile indicated almost similar hardness value (=250VHN) for the WZ and the HAZ, though the base metal showed a somewhat lower hardness (=230VHN).

In general it is found that (Table 3) the initiation toughness, $_i$ is lower in thickness direction as compared to the weld direction of cracking. The higher $_i$ of BM as compared to WM and the HAZ is attributed to its favourable inclusion morphology and their orientation as well as refined grain structure of ferrite and pearlite (Sundaram et al, 1987). The banded structure of ferrite–pearlite does also appear to be advantageous in this respect as the crack initiation was to take place in a direction transverse to the banded ferrite-pearlite structure. The CTOD toughness of HAZ is lower than that of BM and the WM. Presence of somewhat coarse martensite and AC structure are considered to be responsible for reduced toughness of HAZ. In addition, microcracks were also noticed in HAZ which are likely to bring down its toughness (Parmar, 1993). In case of WM, presence of large proportion of GBF and scattered spherical inclusions are detrimental to fracture toughness; though presence of acicular ferrite is expected to have some favourable effect on toughness (Pandey, 1989).

Table 5: Tearing Modulus in Weld Joint

Material Condition	T_m		Material Condition	T_m	
	Initial	a=0.5mm		Initial	a=0.5mm
BL	200	141	BB	241	159
WL	221	143	WB	188	103
WLR	232	082	WBR	208	100
HL	261	115	HB	155	155
HLR	223	120	HBR	164	146

The T_m values can be used to assess integrity of structures where some amount of crack growth is permissible. Based on initial T_m values, it is observed from Table 5 for the longitudinal direction of crack growth that the as-welded HAZ provides the maximum resistance to tearing and is followed by the stress-relieved weld metal. The tearing resistance in other conditions is almost the same. On the other hand for the thickness direction crack growth the trend of tearing resistance is reversed. The BM possesses the maximum resistance to tearing whereas the HAZ has the minimum value. At a = 0.5 mm, it may be noticed that the stress relieved weld metal provides interestingly the minimum tearing resistance for both the longitudinal and thickness direction of tearing initiation. In general, the stress relieving heat treatment does not appear to have much beneficial effect on the crack growth resistance of the weld joint especially when the crack growth is significant (0.5 mm or more) although during the initial stage of crack growth it does produce some positive effects.

The stress relieving PWHT is believed to reduce the level of residual stress. However in the present case, the WM and the HAZ toughness remained practically unaffected after PWHT. Apparently, the 650 C heat treatment causes simultaneously microstructural changes such as carbide precipitation, coarsening of fine carbides etc. leading to deterioration of strength and toughness. This partly negates the beneficial effects of the PWHT.

CONCLUSIONS

1. The -R curves for the microalloyed steel can be expressed in the form of = (+ a) where , , are lying in the range of 0.33-0.56, 0.03-0.10 and 0.48-1.0 respectively.
2. The base metal possesses higher initiation toughness ($_i$) and yield strength values as compared to WM and the HAZ for both as weld condition and the PWHT condition and the HAZ has generally the minimum toughness. Also the weld direction toughness is higher than the thickness direction toughness.
3. The TM decreases with a in all cases. The as-welded HAZ provides maximum TM value followed by stress relieved WM for weld direction crack growth. In the other direction, the BM shows maximum TM

whereas the HAZ shows the minimum. The behaviour of initiation toughness and the tearing resistance has been correlated with microstructure.

REFERENCES

1. ASTM E 1290-93 (1993) Standard Test Method for CTOD Fracture Toughness Measurement, ASTM, Philadelphia.
2. Pandey, R.K. (1989), Fracture toughness- microstructure investigation of hyperbarically welded joint in offshore applications, Engng Fracture Mechanics, **34**, 1119-29.
3. Parmar R.S. (1993) Welding Processes and Technology, Khanna Publishers, New Delhi.
4. Purohit, G.K. (1995) Fracture and Fatigue Characteristics of Arc-Welded Structural Steels, Ph.D. Thesis, IIT Delhi.
5. Sundaram, P., Pandey, R.K. and Kumar A.N., (1987). Effect of welding process and heat input on the fracture toughness of welded joints in HSLA steels, Materials Science & Engg., **91**,29.

CMOD, mm
FIG 1. TYPICAL LOAD VS CMOD DIAGRAMS IN MICROALLOYED STEEL

Study on the effects of notch tip and crack tip plasticity
on small fatigue crack growth

W. F. Li and X. P. Zhang

Department of Mechanical and Mechatronical Engineering,
The University of Sydney, NSW 2006, Australia

ABSTRACT

The experimental investigation and modelling of short fatigue crack propagation in single edge notch specimens of a low strength aluminum alloy were carried out to characterize effects of notch-tip plasticity, crack-tip plasticity and crack closure on short fatigue crack growth within notch plastic zone. The applied loads were intentionally chosen to generate an enough large notch plastic zone where a short fatigue crack initiates and propagates. Different matches of testing conditions, specimens with notches and removing notches after pre-cracked at the stress ratio of R=0, were employed to clarify the influence of notch plastic zone, crack tip plastic zone, and crack closure on short crack growth behaviour. The experimental results show that small crack growth either in notch specimen or in smooth specimen has the common trend: first deceleration then acceleration. The analytical results show that plasticity and plasticity induced crack closure make the different contribution to small crack propagation at different growth stages. It is clear that crack-tip plasticity and notch-tip plasticity influence small crack growth via both plasticity and plasticity induced crack closure mechanisms. The high plastic stress and strain ahead of crack tip due to notch root plasticity or crack tip plasticity directly enhance crack driving force, thereby resulting in fast crack growth; while residual plastic strain due to notch-tip plasticity or crack-tip plasticity left behind crack tip would result in a transition of normalized crack opening stress from closure-free zone at the beginning to saturated zone around notch-tip plastic zone boundary. It can be concluded that the effects of notch-tip plasticity and crack tip plasticity on small fatigue crack growth are tow-hold, plastic deformation in the front of crack tip at maximum load increases crack growth driving force due to the increase in plastic component, while plastic deformation left in the wake of crack tip at minimum load decreases crack driving force due to the decrease in effective components.

Keywords: Notch tip plasticity, Crack tip plasticity, Plasticity induced crack closure, Short fatigue crack growth.

INTRODUCTION

Since small fatigue crack issue was first addressed by Pearson [1], considerable efforts have been expended in the investigation and analysis of its abnormal growth behavior, and it has been found that the majority portion of total fatigue life would often be spent with small crack growth stage. As almost all engineering structures and components contain geometric notches or other notch-like features, and these stress raisers have been recognized to be a main site for small fatigue crack initiation, propagation, and even final failure, the study of the fatigue behavior of notched members has been of prime interest to many researchers and engineers in various fatigue small crack problems. It is well documented that the observed growth of small

cracks emanating from notches have remarkably similar trend: first deceleration and then acceleration. It is first known that concentrated stress gradient ahead of notch root is a direct reason to cause decrease in fatigue small crack growth rate at notch, since a decrease in local plastic strain decreases occurs simultaneously. The second reason is most often proposed, i.e., crack closure. Meantime, a variety of mechanism and corresponding analytical methods for fatigue small growth emanating notch root have been introduced. However, the difficulty in testing and analyzing short fatigue crack growth is still existing and becomes evident when considering the growth of short fatigue crack emanating from plastic notch field. Owing to difficulties in experimental measurement, there are few experimental results available. Furthermore, the two main models for a short crack embedded in notch plastic zone have been proposed, which are plastic shear displacement model due to Miller [2], to account for plasticity only, and crack closure model due to Newman [3], to consider crack closure only. As a result these approaches are still open to discussion from an academic perspective, and additionally represents an area where a contribution to the practical use of these results in engineering application can be made.

Accordingly, one main objective of this study is to show the major role of notch tip and crack tip plasticity in accounting for the abnormal growth behavior of short fatigue crack. The results reported here were obtained as a part of our extensive study on the effects of notch root plasticity and crack tip plasticity on small crack nucleation and propagation. This paper is only restricted to the initiation and growth behavior of short fatigue cracks on low strength aluminum alloy.

EXPERIMENTAL PROCEDURE AND ANALYTICAL PROGRAM

Material, specimen, and experimental procedures
The test material is 5005 aluminum alloy with a yield stress of σ_{ys}=128 MPa and a Young's modulus of 60 GPa as-provided rolled sheet 3 mm thick. Its chemical composition is shown in Table 1. Single edge U-shape-notched (2 mm deep with the radius of 0.7 mm) fatigue specimens with the length of 150 mm, thickness of 3 mm and widths of 20 and 24 mm were prepared. All specimens were mechanically polished, followed by an electrolytic polishing both to remove the residual stresses which may be introduced by rolling and machining processes, and to provide a smooth surface for microscope examination and video recording. Prior to testing, the special fixtures gripping the specimen were carefully aligned with specimens to prevent rotational and lateral bending.

Table 1. Chemical composites of AA5005 (wt%)

Mg	Si	Fe	Mn	Cu	Cr	Zn	Al
1.10	0.30	0.70	0.20	0.20	0.10	0.25	Balance

The fatigue crack propagation tests were performed at a frequency of 10 Hz in sinusoidal waveform pulsating tension loading mode with a stress ratio of R=0, by an Instron 8501 servo-hydraulic testing machine at room temperature in air under constant load control. The applied maximum stresses were deliberately chosen as 0.40, 0.55 and 0.70 of σ_{ys}, or as corresponding local stresses of $1.75\sigma_{ys}$, $2.41\sigma_{ys}$ and $3.07\sigma_{ys}$ to introduce tensile notch plastic zones, and reversal notch plastic zones with different sizes. At least four specimens were tested at each condition of stress amplitude and specimen configuration. The cracking and propagation at different deformation stages were recorded by an imagine recording and measurement system, which consists of 50× microscope, CCD, video recorder, personal computer and imaging analyzer. In order to clarify the influences of notch root plastic field, crack tip plasticity and crack closure on growth behavior of short fatigue crack, the comprehensively comparative studies were carried on by adopting different matches of testing conditions, specimens with notches and removing notches after pre-cracked The difference of crack growth rates between short and long cracks may represent the effect of crack tip plasticity and crack length-dependent crack closure, while the difference of short crack growth rates between notch and smooth specimens may represent notch root plasticity effect. A series of fatigue tests were carried out to understand the growth behavior of short fatigue cracks from either notch specimens or smooth specimen obtained via removing notch left a short crack or long crack, including: (1)Short fatigue crack growth from notch specimen. This is to assess the effect of notch root plasticity on

short crack growth under the high applied stress. (2)Short fatigue crack growth from smooth specimen without residual stress field, which were realized by removing specimen notch and the original notch root plastic field but leaving the specimen with short crack only. This is to evaluate the large crack tip plasticity effect on short crack growth. (3) Long fatigue crack growth. In order to compare short crack growth behavior with that of long crack, the tests of long fatigue crack growth were carried out to establish a baseline crack growth data. The long crack specimens were obtained by pre-cracking on notch specimen and fatiguing short crack.

Analytical program

A general commercial finite element method code ANSYS 54 was chosen to make elastic-plastic finite element analysis of stress/strain distribution ahead of notch root, notch plastic field, and crack closure. Due to the geometric symmetry of the specimen only half of the specimen was used. The meshes were composed of a two dimensional, six-node triangular isoparametric elements and represented a rectangular plate with a crack emanating from single edge U shape notch of a root radius 0.7 mm. The material model employed elastic/perfectly-plastic property with von Mises yield criterion. The number of nodes and elements were 2369 and 4920, respectively, for the notch specimen. Since it has been recognized that under high applied stress levels the crack tip plasticity has a key influence on accelerated small fatigue crack growth, in this work the crack tip plastic zone size was determined using analytical approaches based on Dugdale model.

RESULTS AND DISCUSSIONS

Comparison of growth behavior between short and long fatigue cracks

The growth rates of short cracks (through-thickness crack, $a \approx 0.1 \sim 0.2$ mm) in notch-removed specimens against stress intensity factor range, ΔK, are shown in Fig.1(a), as a comparison to that of long through-thickness crack ($a > 2$mm). The results after accounting for crack closure, in term of ΔK_{eff}, are also shown in Fig.1(a). Inspection of short fatigue crack growth data in Fig.1(a) reveals that at the same applied K levels, the growth rates of the short cracks in three different stress levels exceed those of corresponding long cracks by up to one order of magnitude; even those of crack closure corrected long cracks. The latter implies that along with crack closure, there must be other factor to accelerate small crack growth.

The numerical results of crack tip plastic zone size are showed in Fig.1(b), and indicate that the ratio of crack tip plastic zone size to crack length is dependent on applied stress levels. It is as small as 0.1 at $0.25\sigma_{ys}$ loading level (in figures σ_{ys} is denoted by Sys), but gradually rises from 0.26 at $0.40\sigma_{ys}$, 0.49 at
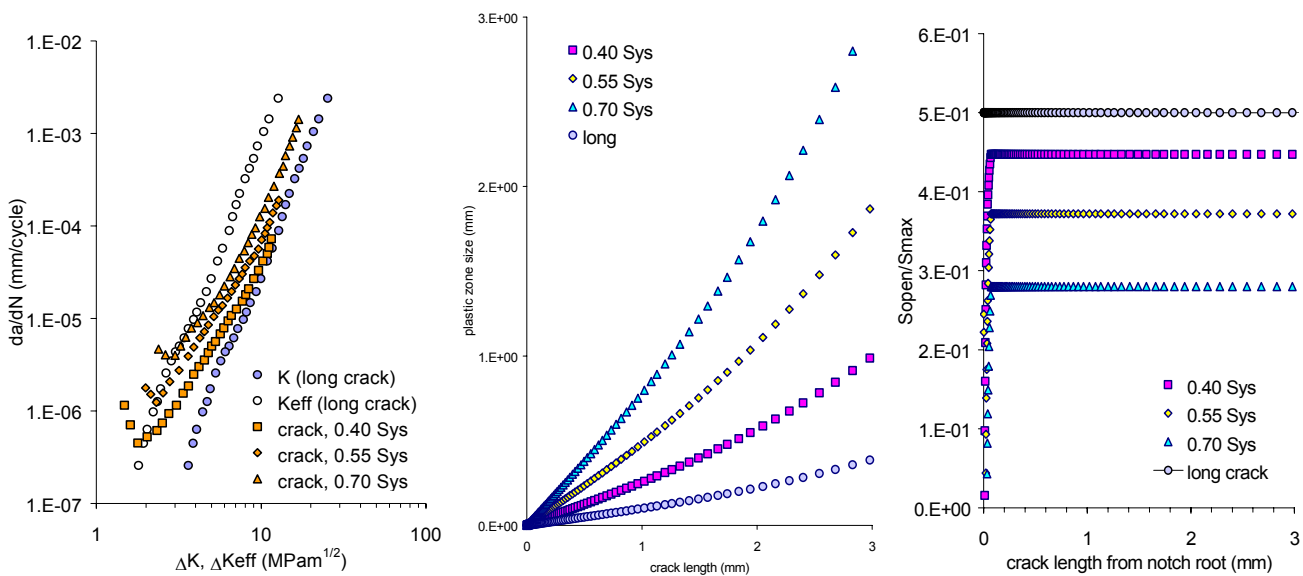
(a) Crack growth rates   (b) Crack tip plastic zone sizes   (c) Crack opening stresses

Fig. 1 Comparison between short and long crack $0.55\sigma_{ys}$, to 0.8 at $0.70\ \sigma_{ys}$.

The calculation of the ratio of crack opening stress(S_{open}) to the maximum applied stress(S_{max}), i.e. the crack closure degree, as a function of crack length a, is shown in Fig.1(c). The initial crack would not close. As the crack grows, however, the newly created crack surfaces close and the crack opening stresses rapidly rise over less than 0.1 mm and reaches a stable value for large crack growth.

1) Effect of crack tip plasticity on growth behavior of small and long cracks from smooth specimens
An important reason generating small crack growth acceleration from smooth specimens is the crack tip plasticity. The current results shown in Fig. 1(a) indicate that with an increase in applied stress level, the corresponding difference between short and long crack growth rates also rises, this coincides with the increase in the ratio of crack tip plastic zone size to crack length. Physically, large crack tip zone size will result in large plastic deformation, and corresponding fast crack growth. This is consistent with many other experimental results. Rice [4] has quantitatively shown that when the applied stress reaches $0.5\sigma_{ys}$, the calculated ratio of plastic zone size to crack length will increased from the small scale yielding condition. Further, it has been shown experimentally by Ritchie [5] that accelerated short crack growth does not necessarily result simply from lager crack tip zone size than crack length, even when crack tip plastic zone size is far less than small crack length (10 μm:200 μm), so-called anomalous behavior still occurred.

2)Effect of crack closure on growth behavior of small and long cracks from smooth specimens
Closure or, more properly, the absence of crack closure, has been frequently suggested as a reason for the accelerated growth of very small cracks in unnotched members. The Fig.1(a) showed that all short crack growth rate data fall between baselines of long crack growth rates against ΔK and ΔK_{eff}, where ΔK_{eff} is the effective stress intensity factor range. Transition of the crack closure as shown in Fig.1(b) should be a main reason, since the initial gradual reduction in growth rate of short cracks is consistent with the corresponding progressive increase in crack opening stress. Another reason is the lower saturated crack opening stress with increasing stress levels, leading the entire short fatigue crack growth curve shift towards the left. However, it can be found that well beyond crack closure transition zone of 0.1 mm, short crack growth data from smooth (notch-removed) specimens are very close to or even exceed to free-closure corrected long crack growth data especially at high stress level. This suggests that beyond crack closure transition zone, other should become dominant factor to affect short crack growth.

Comparison of short crack growth between notch specimens and notch removed smooth specimens
The comparison of short fatigue crack behavior including crack closure degree between notch specimens and notch-removed specimens are shown in Fig.2. Fig.3 shows the numerical results of variation of notch root plasticity zone size under different loading levels of maximum stress. From Figs. 2 and 3, it is characterized that there are three typical stages for fatigue crack propagation: (1)crack initiation zone; (2) small crack propagation zone (within notch plastic zone); and (3)long crack propagation zone (out of notch plastic zone), respectively corresponding to (1)closure-free zone; (2)closure transition zone; and (3)closure saturated zone.

1) Effect of notch root plasticity on small crack initiation
As shown in Fig. 2, at a given load level the short crack initiated from notch root plastic field grows at a much higher rate than that of smooth specimen (i.e. notch-removed specimen), and the growth rate increases with raising loading level. In addition, the crack growth driving force for the short crack in notch specimen is very high, thus resulting in fast crack growth. Analytical results shown in Fig.2(c) manifest that the plastic components of J-integral, J_p, caused by notch plasticity, are strongly dependent on applied stress levels. For example, J_p is zero at $0.40\sigma_{ys}$, but J_p is non-zero positive value at $0.55\sigma_{ys}$, and much more higher at $0.70\sigma_{ys}$. While crack closure level is near zero at crack initiation, thereby producing very high initial crack driving force and corresponding initial crack growth rate. It is noted that such a non-zero cyclic plastic component due to notch plasticity exists only when applied stress level is larger than half yielding stress, or local stress at notch root is larger than 2 times yielding stress, a condition of producing reversed notch plastic zone. And such a plastic component due to notch plasticity is, of course, absent for smooth specimen.

Another factor often ignored is the surface influence on crack initiation. Small cracks invariably initiate at specimen surface where plane stress conditions prevail and material flow resistance or yield stress is reduced compared to the bulk, so resulting in a plastic zone size that is larger compared to those found in the interior which is subjected to plane strain conditions. It should be noted that such a surface effect is particularly important for crack initiation as it greatly enhances plastic deformation at crack tip within surface layer, though it is still not available to accurately describe stress and strain on surface layer of micro-scale, for example, a grain size, which is is independent of applied stress. There are many experimental evidences that short surface fatigue crack grow very much more quickly than short through fatigue crack growth, even if allowing for crack closure effect.

| (a) Crack growth rate | (b)Crack opening stress | (c)Plastic component of J-integral |
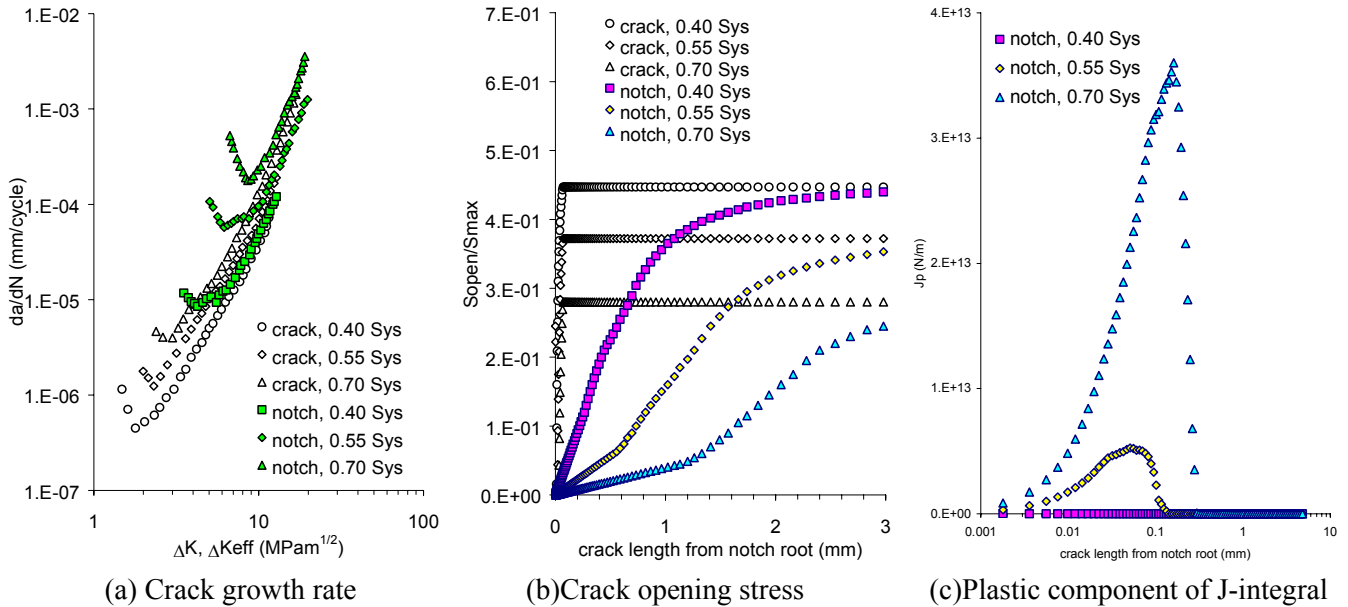
Fig. 2. Comparison of short fatigue crack growth between notch specimens and smooth specimens

| (a) 0.397 mm at $0.40\sigma_{ys}$ | (b) 0.912mm at $0.55\sigma_{ys}$ | (c) 2.05mm at $0.70\sigma_{ys}$ |
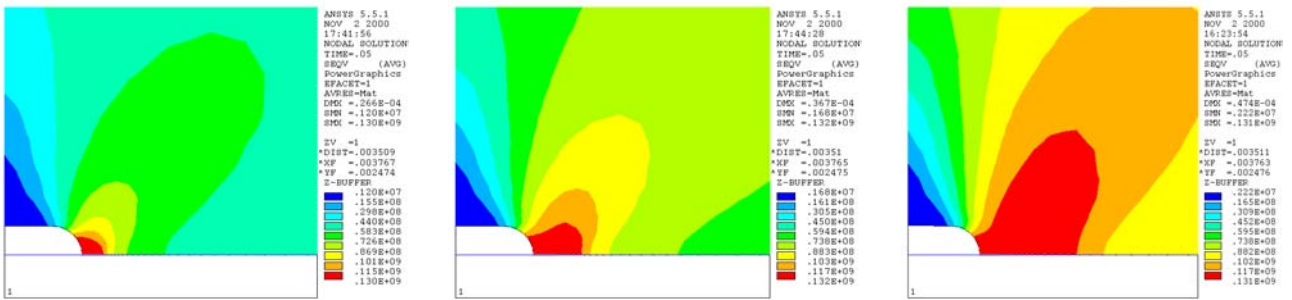
Fig.3 Variation of notch plastic field sizes under different loading levels of maximum stress

Further, plastic strain sharply drops over a short distance, slightly larger than reversed notch plastic field. Meantime, surface effect also reduces quickly since its range is on a micro-scale. While crack closure begins to increase but slowly due to reversed plastic yielding, which is the same as a low crack closure level at R=-1 due to reversed plastic yielding. Therefore, the decrease of growth rate and the presence of 'dip' in crack growth curve is directly attributable to the decrease in tensile and reversed notch plastic strain, resulting a minimum point in the crack propagation curve at about boundary of reversed plastic strain. So, this is a reversed plasticity and surface affected region.

2) Effect of notch root plasticity on small crack propagation
Out of reversed plastic field, notch root plasticity effect decreases, while crack tip plasticity has very quickly increased up to a content where crack tip plastic zone boundary is coincident with the original notch plastic boundary. It implies that the crack tip self-generated plasticity begins to dominate crack tip field. On the other hand, crack closure stress increases with increasing crack tip plasticity, but it is still low.

Thus, at this stage, increase in crack tip plasticity is mainly responsible for median short crack slow growth, while notch root plasticity is also one important affecting factor.

3)Plasticity effect on long crack propagation region
Comparing Figs. 2 and 3, it can be seen that when a short crack approaches the boundary of notch root plastic and elastic field, as expected, notch root plasticity effect on crack growth is disappearing, instead elevated notch elastic stress/strain influence on crack growth is appearing. Crack closure degree begins increasing faster due to quick decreasing of notch elastic stress and strain, and reaches to stable value little beyond original notch plastic field. After then, the crack closure degree basically keeps constant. Thus effective crack driving force is no longer reduced by crack closure, and crack propagation becomes faster, and another transition point occurs. At this region, notch elasticity has great influence on crack growth, and fast transition of crack closure causes a transient point.

CONCLUSIONS

1) Short fatigue crack growth from smooth specimens is much faster than long fatigue crack, caused by both large crack tip plasticity and crack tip plasticity induced crack closure.
2) Crack tip plasticity and plasticity induced crack closure are dominant at crack initiation at smooth specimen, while crack tip plasticity is governing at short crack propagation as crack opening stress reaches a saturated level after a short distance.
3) Short fatigue crack growth from notch specimens is much faster than short fatigue crack growth from smooth specimens, caused by both notch plasticity induced component of crack driving force and notch plasticity induced crack closure.
4) Notch plasticity effect is dominant in reversed notch plastic zone; slightly beyond the reversed notch plastic zone, the crack tip plastic zone boundary coincides with the notch plasticity boundary and crack tip plasticity becomes important; a little bit beyond the tensile notch plastic zone, plasticity induced crack closure is determinative where crack closure transition is faster and finally reaches a stable level.
5) Surface effect on short fatigue crack initiation and very early propagation is very important.

ACKNOWLEDGEMENT

REFERENCES

1. Pearson, S., (1975) Engineering Fracture Mechanics, Vol.7, 2, 235-247
2. Mammouda, M. M., Smith, R.A., and Miller, K.J., (1979) Fatigue of Engineering Materials and Structures, Vol.2, 139-154.
3. Newman, J. C. Jr., X. R. Wu et al, (1994) Small crack effects in high strength aluminum alloys, A NASA/CAE cooperative program.
4. Rice, J. R., (1967) Fatigue Crack Propagation, ASTM STP 415, 247-311.
5. Ritchie, R.O. and Yu, W., (1986) Short crack effects in fatigue, Small Fatigue Cracks, Met. Soc. AIME, Warrendale, PA, 167-189.

STUDY ON CRACK-NUCLEATING DAMAGE
OF HYDRAULIC CONCRETE

Zhang Lixiang[1]，Feng Bohao[1] and [2]Li Qingbin

[1]Department of Hydraulic Engineering, Kunming University of Science and Technology,
Kunming 650051, China.
[2]Department of Hydraulic Engineering, Tsing Hua University, Beijing 100084, China

ABSTRACT

Based on the concept of renormalization group, a methodology of crack-nucleating damage of hydraulic concrete is studied in this paper. Damage state depended on the jump of multi-scaling and two-leveling phase changes is defined by a fractal. The damaging models of considering the influences of aggregate size, aggregate interface, crack nucleation, fractal dimension, etc. on the damage are established by energy-equilibrium relationship under the state in the crack-nucleating damage.

1. INTRODUCTION

Concrete is a makeup material that is made of cement, sand, gravel, and water, etc. The interfaces between the different mediums create lots of inherently weak joints and/or micro- and macro-cracks, as well as voids, or say defects in generality. A concrete body contaminated by the defects informs a non-ordered system. The damage [1-3] gets up firstly at the weakly jointed places at which the crack nucleation is produced by a crack-nucleating mechanism [4], and the damage evolution starts and diffuses with growth of the micro-cracks after nucleating. Thus, the concrete is furthermore described as a man-made material whose physical structure is discontinuous, non-homogeneous, and irregular. The damage and the damaged diffusion in concrete may be categorized by a multi-scale-level mechanism, and the configuration of the damaged front is defined as a fractal. Following these definitions, the makeup of the concrete is shown in figures 1a-1c.

2. FRACTAL LENGTH OF DAMAGE-NUCLEATING CRACKS

At arbitrary damage-scaling level D_i, let the activated micro-cracks in concrete inform a set called as Group, $\Re_i$. To a defect as shown in figure 1d, its configuration is assumed to be a fractal round, whose circumference is featured with a fractal line [5].
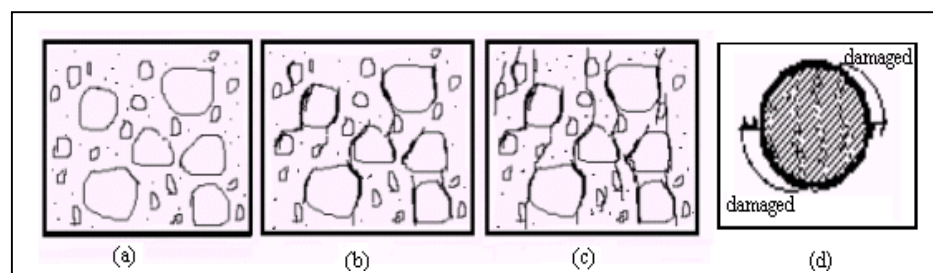
Figure 1 Concrete defects, nucleating and developing damage, and fractal round

The nucleating damage, going with nucleation of the micro-cracks, starts firstly at a place in the circumference of the fractal rounds when the strain or the stress exceeds the nucleating-damage threshold of the concrete. Let the fractal round be a damaged unit consisting of 4 quadrants, and a micro-crack appears stochastically at arbitrary quadrant. Obviously, if the micro-cracks are simultaneously produced at 4 quadrants, the damaged unit is in damaged state. Subsequently, if the micro-cracks are measured at the symmetrical quadrants, say quadrant 1 and 3 or quadrant 2 and 4, the damaged unit is also considered to be in damaged state. Thus, using the concept of the K. G. Wilson's renormalization group, a twice magnification transformation of renormalization group is created as:

$$p_i' = \Re_{i+2}(p_i) = p_i^4 + 2 \times 2 p_i^2 (1 - p_i^2) \tag{1}$$

in which p_i is priori crack-nucleating probability, p_i' is probability after twice renormalization magnification. A physical interpretation of this semi-group transformation is a twice-amplifying relationship of the measuring scale of the cracks. Therefore, the critical jump point of damage phase change can be obtained by the following formula:

$$p_c^4 + 2 \times 2 p_c^2 (1 - p_c^2) - p_c = 0 \tag{2}$$

Its closed solutions are $p_c = 0$, 1, 0.618 -1.618, respectively. It is clearly that the solutions 0, 1 represent the zero-damaged and certainly damaged states, respectively, whilst minus number should be dropped out because of no physic meaning（a probability does not appear in a minus number）. Thus, the probability of the damage phase change is $p_c = 0.618$, and the expectation value of nucleating damage at the defined damaged unit is stated as the following:

$$E_c = \left[4 p_c^4 + 2 \times 2 p_c^2 (1 - p_c^2) \right] / p_c = 4 p_c \tag{3}$$

The value, substituting the critical value $p_c = 0.618$, is $E_c = 2.472$. One can note that $E_c = 2.0$ can be obtained to the classical fracture mechanics.

Assuming the measuring scale δ is as much as n^{-1} times of the diameter of the fractal round studied，namely $d = n\delta$, the fractal dimension of the damage group, D_f, can be expressed as:

$$D_f = \frac{\ln E_c}{\ln n} = \frac{\ln E_c}{\ln \dfrac{d}{\delta}} \tag{4}$$

The relationship between the fractal dimension and the measuring scale is shown in figure 2.
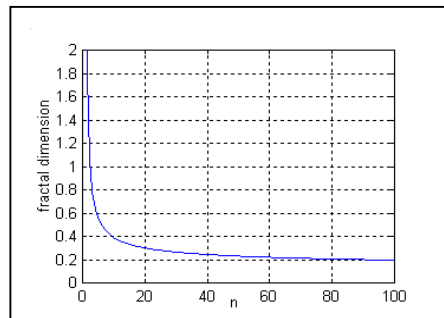
Figure 2 Fractal versus measuring scale

It follows the Mandelbort's definition of fractal line, herein the circumference, L_f, of the fractal round can be stated as:

$$L_f(\delta) = L_0(\delta)\delta^{1-D_f} \tag{5}$$

As an example, if the nucleating cracks appear at the quadrant 1 and 3 of the fractal round shown in figure 1d, the length, $L_c(\delta)$, of the micro-cracks after nucleating is as following:

$$L_c(\delta) = \frac{1}{2}L_0(\delta)\delta^{1-D_f} \tag{6}$$

If $L_0(\delta)$ is defined as the circumference length of the regulation round, namely $L_0(\delta) = \pi n \delta$, the expectation length of the micro crack at the damaged unit is written as:

$$L_c(\delta) = E_c \pi n \delta^{2-D_f} / 4 \tag{7}$$

Taking，one can get a formula that expresses the crack length in respective with the measuring scale and the fractal dimension, namely:

$$L_c(\delta) = 0.618\pi n \delta^{2-D_f} \tag{8a}$$

or,

$$L_c(\delta) = 0.618\pi n^{D_f-1} d^{2-D_f} \tag{8b}$$

3. DAMAGE-NUCLEATING MODELING

In case of the state of crack-nucleating damage, the equilibrium condition of the unit-thicken concrete body can be stated as:

$$\left(\frac{\delta_0}{d}\right)^2 \sigma_f + \sigma\left(C_3 + \frac{4}{\pi}\sqrt{\frac{\delta_0}{d}}(1-C_3)\right)^2 = \sqrt{\frac{4E\psi \cdot 1}{\pi(1-v^2)L_c}} \tag{9}$$

in which δ_0 is the thickness of cement-grouting film between the defect (fractal round) and concrete, σ_f failure strength of concrete, σ loading stress, C_3 material constant to be determined by test, ψ energy containing in unit volume of concrete, v Poisson's ratio, and E initial elastic modulus. It can be seen that the right-hand side of the equation is defined by simulating Griffith's law. Introducing the foregoing definitions to the fractal round and the length of the micro-crack, equation (9) can be changed as:

$$\left(\frac{\delta_0}{d}\right)^2 \sigma_f + \sigma\left(C_3 + \frac{4}{\pi}\sqrt{\frac{\delta_0}{d}}(1-C_3)\right)^2 = \sqrt{\frac{6.472E\psi \cdot 1^{2-D_f}}{\pi^2 n(1-v^2)\delta^{2-D_f}}} \tag{10a}$$

or,

$$\left(\frac{\delta_0}{d}\right)^2 \sigma_f + \sigma\left(C_3 + \frac{4}{\pi}\sqrt{\frac{\delta_0}{d}}(1-C_3)\right)^2 = \sqrt{\frac{6.472E\psi.1^{2-D_f}}{\pi^2 n^{D_f-1}(1-v^2)d^{2-D_f}}} \tag{10b}$$

If the problem studied is focused on a big scale granule diameter of concrete aggregate, namely

considering $d \gg \delta_0$, the first term of the left hand side of equation (10a) or (10b) can be dropped out, and a crack-nucleating damage formula is obtained as:

$$\sigma_{dc} = \left(C_3 + \frac{4}{\pi} \sqrt{\frac{\delta_0}{d}} (1 - C_3) \right)^{-2} \sqrt{\frac{6.472 E \psi. 1^{2-D_f}}{\pi^2 n^{D_f-1} (1-v^2) d^{2-D_f}}} \tag{11}$$

The energy stated in equation (11) can be divided into two parts. One is of a contribution of deteriorated damage, due to deterioration of the material characteristics by crack nucleation; other is of releasing energy due to formation of the micro-cracks at the damaged area. To the former, Helmholtz's free-energy expression is employed, namely:

$$\rho \psi_d = \frac{1}{2} (\lambda + 2\mu) \varepsilon_{ii} \varepsilon_{jj} - \mu \left(\varepsilon_{ii} \varepsilon_{jj} - \varepsilon_{ij} \varepsilon_{ji} \right) + C_1 D_{di} \varepsilon_{ij} D_{dj} \varepsilon_{kk} + C_2 D_{di} \varepsilon_{ij} \varepsilon_{jk} D_{dk} \tag{12}$$

in which ρ is mass intensity of material, λ, μ stand for Lame' constants, and C_1, C_2 represent material parameters to be determined by test and related to the damaged extent. For the sake of simplification, the tension stress state is only considered in this paper, and after a lengthily deducing, the deteriorated damage strain energy, ψ_d, can be got as:

$$\psi_d = \frac{E(1-v)}{(1+v)(1-2v)} \left[\frac{1}{2} \left(1 - \frac{2v^2}{1-v} \right) \varepsilon^2 + \frac{C_1 + C_2 - 2vC_1}{3(B_1 - B_3)} \varepsilon^3 - \frac{1-v}{8} \frac{C_1^2}{(B_1 - B_3)^2} \varepsilon^4 \right] \tag{13}$$

and the releasing energy due to cracking as:

$$\psi_c = \frac{\pi E(1-v)^2 L_c}{4(1+v)^2 (1-2v)^2} \left[\left(1 - \frac{2v^2}{1-v} \right) \varepsilon + \frac{C_1 + C_2 - 2vC_1}{(B_1 - B_3)} \varepsilon^2 - \frac{1-v}{2} \frac{C_1^2}{(B_1 - B_3)^2} \varepsilon^3 \right]^2 \tag{14}$$

in which B_1, B_3 are material parameters. If the hyperbolic damage surface [6] is employed to express developing damage inside concrete body with loading, the following relationship is used, namely:

$$(B_1 - B_3) = \frac{\varepsilon}{D_d^2} \tag{15}$$

Thus,

$$\psi_d = \frac{E(1-v)}{(1+v)(1-2v)} \left[\frac{1}{2} \left(1 - \frac{2v^2}{1-v} \right) + \frac{(C_1 + C_2 - 2vC_1)}{3} D_d^2 - \frac{(1-v)}{8} C_1^2 D_d^4 \right] \varepsilon^2 \tag{16}$$

$$\psi_c = \frac{\pi^2 E(1-v)^2 n^{D_f-1} d^{2-D_f}}{6.472(1+v)^2 (1-2v)^2} \left[\left(1 - \frac{2v^2}{1-v} \right) + (C_1 + C_2 - 2vC_1) D_d^2 - \frac{1-v}{2} C_1^2 D_d^4 \right]^2 \varepsilon^2 \tag{17}$$

Substitution of equation (16) and/or (17) into equation (11) obtains the following damage constitute models describing concrete in tensile state.

Model I, unique consideration of damage-nucleating energy (by substituting equation (17) only)

$$\sigma_{dI} = \frac{\left[\left(1 - \frac{2v^2}{1-v} \right) + (C_1 + C_2 - 2vC_1) D_d^2 - \frac{1-v}{2} C_1^2 D_d^4 \right]}{(1+v)(1-2v) \left(C_3 + \frac{4}{\pi} \sqrt{\frac{\delta_0}{d}} (1 - C_3) \right)^2} \sqrt{\frac{1-v}{1+v}} E\varepsilon, \quad \varepsilon \geq \varepsilon^{th} \tag{18a}$$

Model II, non-consideration of damage-nucleating energy (by substituting equation (16) only)

$$\sigma_{II} = \sqrt{\dfrac{6.472\left[\dfrac{1}{2}\left(1-\dfrac{2v^2}{1-v}\right)+\dfrac{\left(C_1+C_2-2vC_1\right)}{3}D_d^2-\dfrac{\left(1-v\right)}{8}C_1^2D_d^4\right]}{\pi^2 n^{D_f-1}\left(1+v\right)^2\left(1-2v\right)d^{2-D_f}\left(C_3+\dfrac{4}{\pi}\sqrt{\dfrac{\delta_0}{d}}\left(1-C_3\right)\right)^4}}E\varepsilon, \quad \varepsilon \geq \varepsilon^{th} \qquad (18b)$$

Model III, integrated damage (by substituting equations (16) and (17))

$$\sigma_{dIII} = \sqrt{\sigma_{dI}^2 + \sigma_{dII}^2} \qquad (18c)$$

4. DISCUSSIONS OF PARAMETERS C_1 AND C_2

To illustrate the procedure to determine the material parameters of C_1 and C_2, 32 concrete specimens of 70.7mm×70.7mm×212.1mm, were done by a machine of MTS 810 TestStar, and 3-parameter Weibull distribution is used to describe the probabilistic characteristics of the strains. Based on the definition of the $P-D_d-\varepsilon$ curve of concrete [7], a regressive curve on $D_d-\varepsilon$, corresponding to the expectation probability $E_c = 50\%$ (closely to the foregoing theoretical value of 0.618), is obtained as:

$$\varepsilon = 803D_d^3 - 910D_d^2 + 501D_d + 73 \qquad (19)$$

It is clearly when $D_d = 0$, the threshold strain of the damage is $\varepsilon^{th} = 73\mu\varepsilon$. In considering the case of $D_d = 0.2$, one can easily get the relevant value of the strain from equation (10) as $143.2\,\mu\varepsilon$. Thus, dynamic stress corresponding to this strain is approximately got as 2.7MPa by test constitutive relationship [8]. Taking $\delta_0/d = 0.001, C_3 = 0.2$, $v = 0.16, E = 2.1\times10^4\,\text{MPa}$, as well as $d = 0.01\text{m}, n = 10$, and $D_f = 0.393$, the relationships between C_1 and C_2 are obtained, from equation (18a) and (18b), and shown in figures 3a and 3b, respectively, as:

$$C_1^2 - 4C_1 - 5.97C_2 + 133.4 = 0 \qquad (20)$$

$$C_1^2 - 54.33C_1 - 79.60C_2 - 2802.98 = 0 \qquad (21)$$

(a) (b)
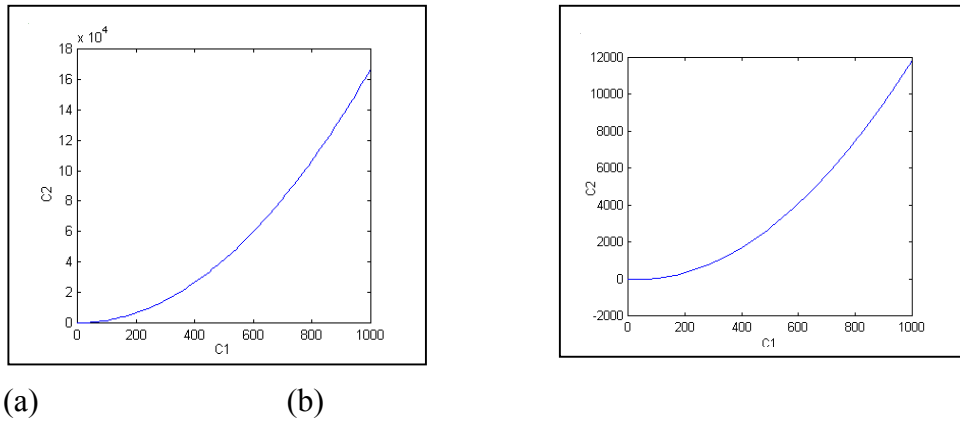
Figure 3 C_1 versus C_2 in case of the above conditions

5. CONCLUSIONS

In consideration of the special characteristics of concrete makeup, a combination of the mechanisms of both damage and micro-crack nucleation is a way to study crack-nucleating damage of the hydraulic concrete. From the theoretical viewpoints, the crack-nucleating damage models established in this paper are suitable. It is surely that a result closer to the practice damage and fracture in engineering can be well predicted by the viewpoints subjected, if the further work is done, especially in experimental and comparing studies.

ACKNOWLEDGEMENTS

REFERENCES

[1] L. M. Kachanov. Introduction of continuum damage mechanics. Martinus Nijhoff Publishers, Dordrecht, 1986

[2] R. Ilankamban and D. Krajcinovic, A constitutive theory for progressively deteriorating brittle solids. Int. Journal of Solids Structures, 23,1987, pp.1521-1534

[3] A. Dragon and Z. Mroz, A continuum model for plastic-brittle behavior of rock and concrete. Int. Journal of Engineering Sciences, 17, 1979, pp.121-137

[4] K. F. Ha. Basics of fractured physics, Scientific Press, Beijing, 2000

[5] B. B. Mandebrot. The fractal geometry of nature, W. H. Freeman and Co., San Francisco, Calif., 1982

[6] D. Krajcinovic and G. U. Fonseka. The continuous damage theory of brittle materials-Part I: general theory, ASME Journal of Applied Mechanics, 48, 1981, pp.809-815

[7] Zhang Lixiang, Zhao Zaodong, and Li Qingbin. $P - D - \varepsilon$ curve and cumulative damage of concrete in fatigue, to be published in Journal of Engineering Mechanics.

[8] Li Qingbin, Zhang Chuhan and Wang Guanglun. Dynamic damage constitutive model of concrete in uniaxial tension, Engineering Fracture Mechanics, 53, 1996, pp.449-455

STUDY ON CRACKPATH STABILITY OR INSTABILITY IN A BODY

D.A. Zacharopoulos

School of Engineering
Democritus University of Thrace
GR 671 00, Xanthi, Greece

ABSTRACT

The crackpath prediction plays an essential role in the estimation of the final shape of broken solids and structures. Furthermore, the study of the crackpath in broken specimens renders the loading conditions just before fracture. Experiments on brittle materials, pre-cracked specimens of the same geometry, under similar loading conditions, occasionally resulted in different trajectories of the crack propagation. The already proposed theories for the prediction of the crackpath stability or instability are based on the perturbation method in combination with analytical and finite elements methods; however, they require the knowledge of the toughness equations. Therefore they can only be applied in specimens with uncomplicated geometry on straightforward loadings. In the present paper the problem of the crackpath stability or instability, is approached from a different viewpoint. The method of dealing with the problem using the estimation criterion is described. Using a finite element program the stress field is calculated and consequently a plotting program constructs the contours map of the strain energy density on the idealization geometry of the specimen or structure. The contours map recovers the stress field on the instance that the crack begins the unstable propagation. For the determination of the predicted trajectory of the crack propagation of the existing crack, the minimum of the strain energy density criterion (SED) is used. The forecasted trajectory appears with the drawing of the "gorge" on the contour map of the strain energy density. Based on the estimation criterion, which claims that the degree of stability is a function of the sharpness of the gorge plot, we can predict the degree of the crackpath stability. Therefore, this simple method offers a good reliability in the prediction of the crackpath stability for problems with complex geometry structures and random loadings. The above consideration offers a classification of the crackpath stability or instability in the following cases: (i) The predicted propagation crackpath is stable for symmetric geometry and loading $(K_{II}=0)$, and has the shape of a straight line or a curve outside its initial direction. (ii) The predicted propagation crackpath is unstable, and follows many discrete curves, including the straight line. In order to clarify the suggested prediction method, we apply it on DCB-type specimens, where a rich international theoretical and practical experience exists. The results on the crackpath stability presented in this work are in good agreement with experimental observations.

STUDY ON PROPAGATION LAW OF SURFACE FATIGUE CRACK AT NOTCH ROOT IN LOW CYCLE FATIGUE UNDER IN-PLANE BENDING

K. Shingai, Y. Yosii, D. Fukui

Department of Mechanical Systems Engineering, Faculty of Engineering, Nagasaki University, 1-14 Bunkyoumachi Nagasaki, 852-8521, JAPAN

ABSTRACT

The fatigue test of the surface crack propagation was conducted on the plate specimen with a small hole at a notch root in the low cycle fatigue region under the reversed deflection control of the in-plane bending load. The surface fatigue crack occurs from a small hole of a notch root center and propagates along a notch root toward both edges of the plate thickness. Cyclic strains at a notch were measured by strain gages and the cyclic strain behavior has been shown as the relationship between the strain and the number of cycle. The strain range at a notch root remains constant as the number of cycle increases, but the mean strain at a notch root increases as the number of cycle increases. It is found that the propagation rate of a surface fatigue crack is expressed as the mth power of the range of the strain intensity factor. The strain intensity factor is defined as the parameter multiplied the strain range at a notch root by root of the half length of a surface crack length. The value of m is 2 in the center and is more than 2 in the edge of the plate thickness. This propagation law of a surface crack can be applied to any radius of notch roots.

KEYWORDS

Surface Fatigue Crack at Notch, Strain Intensity Factor, Propagation Law of Surface Fatigue Crack, Low Cycle Fatigue, Large elastic-plastic strain

INTRODUCTION

The fatigue life of structures and machine parts in the low cycle fatigue region are determined by the initiation life and the propagation life of surface fatigue cracks at notch roots. In case of larger strain range, the main

life of the fatigue life becomes the propagation life of the surface fatigue crack. Therefore, we need the propagation law of the surface fatigue crack at a notch root under the large elastic-plastic cyclic strain.

Generally, in case of a small scale yield in front of a crack, the propagation law of the fatigue crack is expressed as the mth power of the range of the stress intensity factor in the linear fracture mechanics as everybody knows [1],[2],[3]. In case of large elastic-plastic state in front of a crack, the propagation rate of a fatigue crack is related to the range of J-integral[4],[5], COD range and the strain intensity factor range [6],[7],[8]. These propagation laws have been obtained usually from tests of the through thickness crack of a plate and a tube etc..

Recently, authors have investigated the cyclic strain behavior of notched specimens under the cyclic in-plane bending load by using strain gages [9],[10]. From results of these studies in low cycle fatigue region, we have found that the cyclic creep occurs at a notch and Coffin-Manson rule is applied to the relationship between the strain range at a notch root and the number of cycles to the initiation of a surface fatigue crack . We should investigate further the propagation law of the surface fatigue crack at a notch root. But up to now, the propagation law of a surface crack at a notch root has been seldom presented. This cause is that the linear fracture mechanics can not be applied to this kind of crack and the cyclic large strain behavior at a notch root is not understood.

In this study we conducted the propagation test of the surface fatigue crack from a small hole at a notch root center and the strain measurement at a notch by using strain gages under the cyclic in-plane bending load. In this report we present the behavior of the surface fatigue crack, the cyclic strain behavior at a notch and the propagation law of the surface fatigue crack.

MATERIAL, SPECIMEN AND EXPERIMENTAL PROCEDURE

Chemical composition and mechanical properties of the carbon steel annealed are shown in Table 1 and Table 2 respectively. Specimens with notches are shown in Fig.1. A small hole (the diameter of 0.5 mm and the depth of 0.5 mm) is drilled at one notch root center and a strain gage is attached to other notch root. The length of a surface fatigue crack is measured on fine lines drawn on a notch root by the CCD camera. The strain gage with gage length of 0.2 mm is attached to a notch root and strain gages with gage length of 1 mm are attached in front of a notch at distance of 1 or 2 mm. The test have been conducted by the fatigue apparatus of in-plane

TABLE 1

CHEMICAL COMPOSITION(%)

C	Si	Mn	P	S	Ni	Cr	Ca
0.24	0.22	0.50	0.012	0.016	0.07	0.15	0.13

TABLE 2

MECHANICAL PROPERTIES

Modulus of elasticity	199 GPa
Yield stress	273 MPa
Tensile strength	457 MPa
Elongation	38 %

R : 4, 8, 12 mm   D : 4, 8, 12 mm

detail of small hole
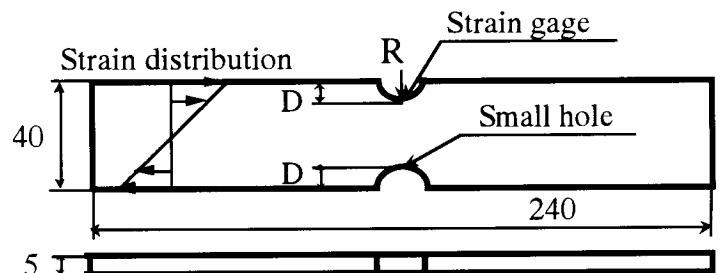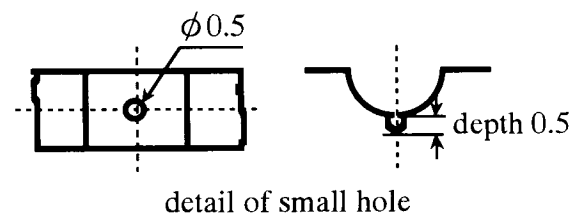
Figure 1 : Specimens with notches

bending with constant deflection control by the eccentric cam and strains have been measured at proper number of cycle using the dynamic strain recorder. Here, the strain distribution by in-plane bending load is shown in a specimen in Fig.1. Experimental conditions are the room temperature, the reversed control of in-plane bending deflection and 72 cpm of the frequency. Test condition of each specimen is shown in Table 3. R is a notch radius. C2, C3 etc. are cam number and the displacement control of the in-plane bending load is determined by cam number. ε_R is the strain range at a notch root measured by a strain gage.

<div align="center">

TABLE 3

TEST CONDITION OF EACH SPECIMEN

Notch root radius R (mm)	Cam No	Strain range measured ε_R (%)
R8	C2	3.05
R8	C4	1.03
R8	C5	0.45
R4	C3	1.60
R12	C2	1.70

</div>

EXPERIMENTAL RESULTS AND DISCUSSIONS

CYCLIC STRAIN BEHAVIOR AT NOTCH

Fig.2.a shows the relationship between the maximum strain, the minimum strain at a notch root and the number of cycle, and Fig.2.b shows the relationship between the strain range, the mean strain at a notch root and the number of cycle. The cyclic creep occurs at a notch root and strains increases toward the tension as the number of cycle increases. The strain range remains constant during cyclic loading, but the mean strain increases as the number of cycle increases. From this result, we think that the surface fatigue crack at a notch root opens during the reversed in-plane bending. Therefore, we think that the full range of the strain intensity factor is useful to the propagation of the surface fatigue crack in the propagation law of the crack in equation (1) mentioned later.

Fig. 3 shows the changes of the strain distribution at 10 cycles and at 100 cycles. It is found that the strain distribution changes drastically as the number of cycle increases.

From these results, it is found that the cyclic strain behavior at a notch shows the complex behavior.

a. ε_{max}, ε_{min} vs N

b. ε_R, ε_m vs N
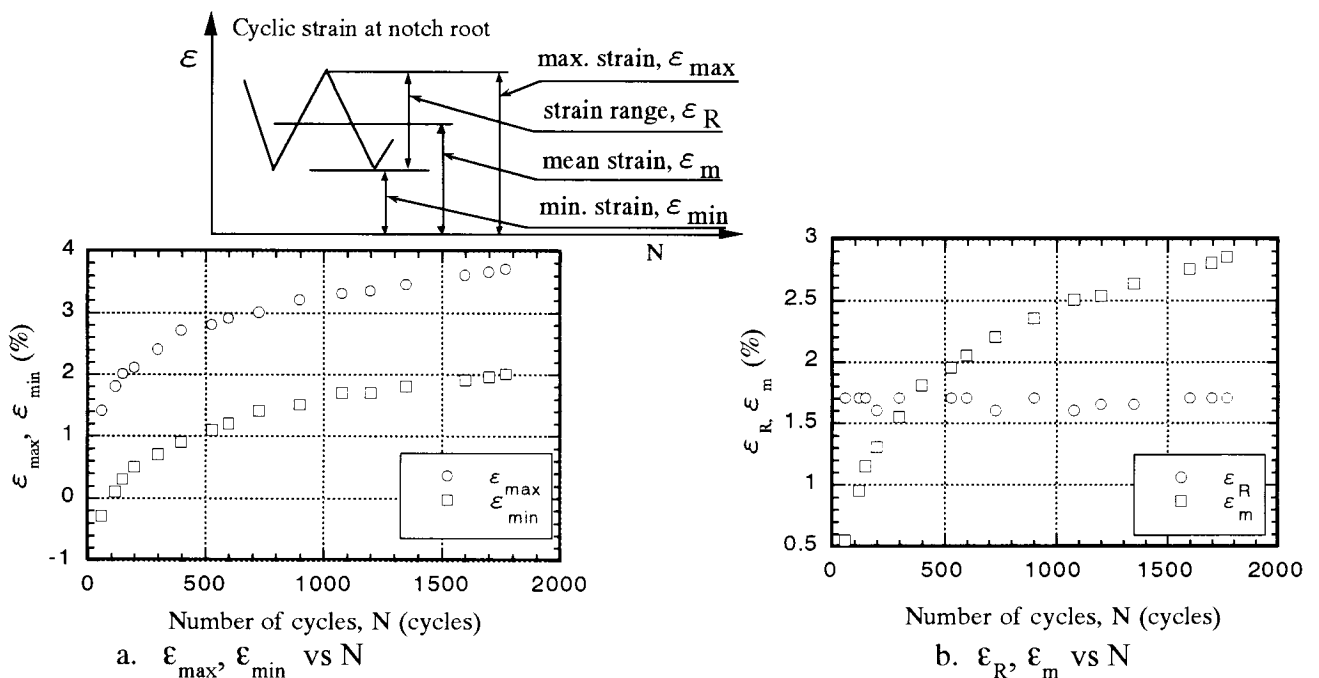
Figure 2 : ε_{max}, ε_{min}, ε_R, ε_m vs N
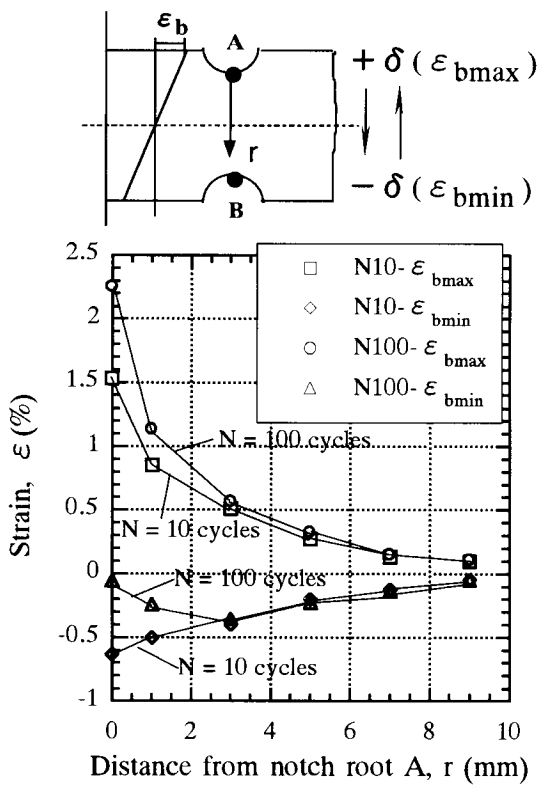
Figure 3 : Change of strain distribution
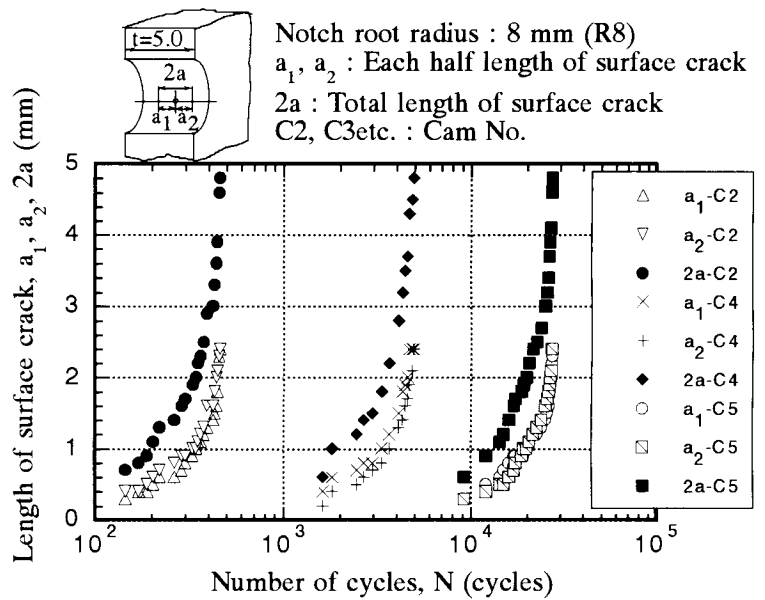
Figure 4 : Relatonship between surface crack length and number of cycles

PROPAGATION LAW OF SURFACE FATIGUE CRACK AT NOTCH ROOT

Fig. 4 shows the relationship between the length of a surface fatigue crack and the number of cycle.

Fig. 5 shows the propagation path model of the surface fatigue crack at a notch root. The region A is the typical surface crack in the center part of the plate thickness and the region B is the surface crack influenced by the edge of the plate thickness.

Fig. 6 shows the relationship between the propagation rate of the surface fatigue crack and the half crack
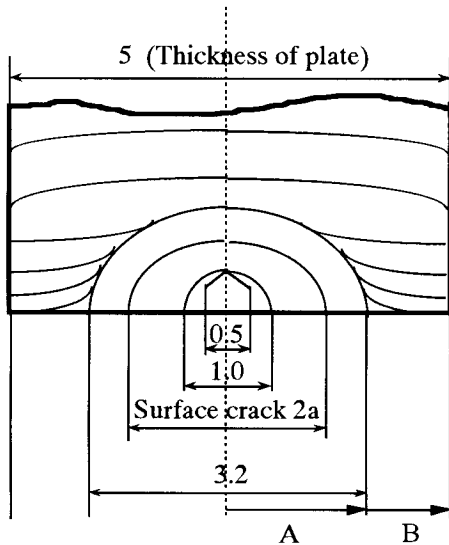
Figure 5 : Path model of surface fatigue crack
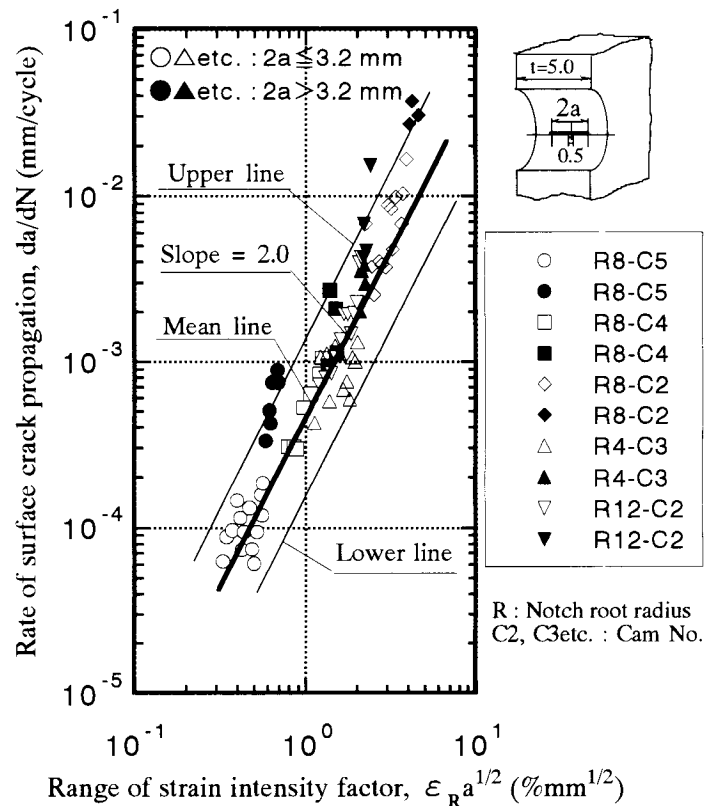
Figure 6 : Relationship between rate of surface fatigue crack propagation and range of strain intensity factor

length. The propagation rate of a crack in the center of the plate thickness is proportional to the half crack length because the slope is 1.0 in a smaller crack than 3.2 mm of a crack length. But one in the edge of the plate thickness is not proportional to the half crack length because the slope is larger than 1.0 in a larger crack than 3.2 mm of a crack length. The reason of regions A and B in Fig. 5 is due to this matter.

Fig. 7 shows the relationship between the propagation rate of a surface fatigue crack and the range of the strain intensity factor. The strain intensity factor is defined as the parameter multiplied the strain range at a notch root by root of the half length of a surface crack length. It is found that the propagation rate of a surface fatigue crack is expressed as the 2nd. power of the range of strain intensity factor in white mark data in the region A. This experimental equation in the region A is expressed as Eq. (1) as follows :

$$da/dN = C \, (\varepsilon_R \, a^{1/2})^2 \tag{1}$$

　　　　da/dN : the propagation rate of a surface fatigue crack (mm/cycle)

　　　　C : the material constant

　　　　ε_R : the strain range at a notch root (%)

　　　　a : the half crack length of a surface fatigue crack (mm)

　　　　$\varepsilon_R \, a^{1/2}$: the range of the strain intensity factor (% $mm^{1/2}$)

The slope in black mark data of the region B is larger than 1.0 in the region A and the propagation rate in the region B is higher than one in the region A. This law can be applied to any notch radius because the data obtained from 4, 8, 12 mm of notch radiuses is within the scattered band.

Fig. 8 shows the elastic-plastic state of the surface crack at a notch root. The elastic-plastic strain is cycled at a notch root and the plastic zone extends in front of a notch. The high strain at a surface crack is composed of the strain concentration by a notch and the strain concentration by a crack. The linear fracture mechanics can

Figure 7 :　Relationship between rate of surface fatigue crack
propagation and range of strain intensity factor
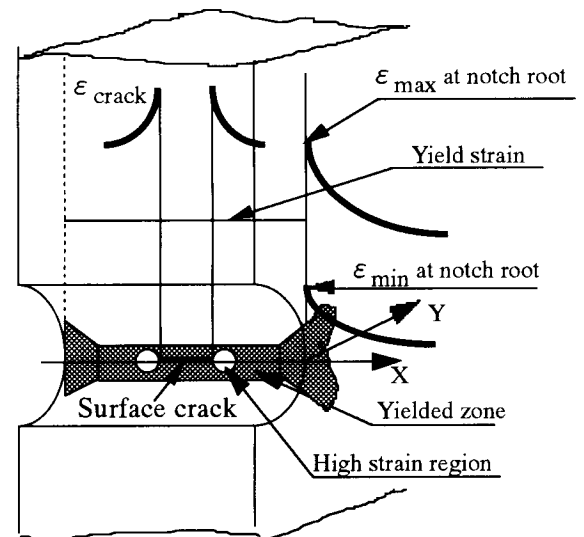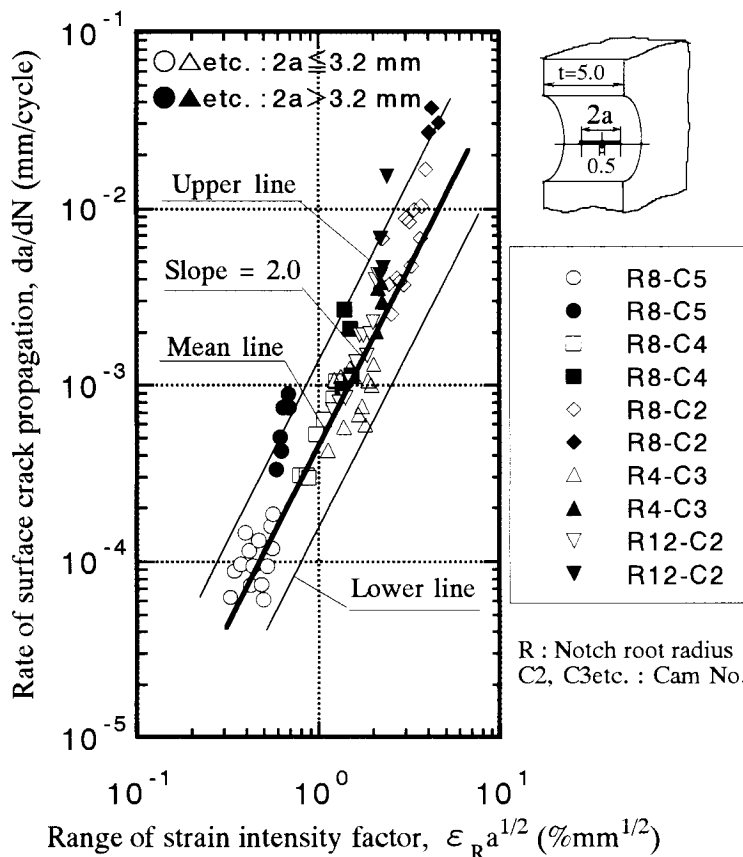
Figure 8 :　Strain state of surface crack
at notch root

not be applied to this crack. The author thinks that the strain intensity factor defined in this paper can be applied to this crack. The strain intensity factor is equivalent to the stress intensity factor in case of the small scale yield in the linear fracture mechanics. Therefore, the strain intensity factor can be applied to a crack from the state of the small scale yield to one of the large scale yield.

Authors [6] have shown already that the strain intensity factor similar to one in this paper has been applied to the through edge crack propagation of a plate specimen under the control of the bending angle of in-plane bending. Therefore, the strain intensity factor can be applied to the propagation of a surface crack at a notch root and one of a through edge crack for the plate specimen.

This propagation law of a surface crack at a notch root may be applied to the estimation of surface crack propagation of the real structures with notches, because strains at notch roots in the real structures can be measured easily by strain gages and can be calculated by the finite element method etc..

CONCLUSIONS

1. The propagation rate of a surface fatigue crack at a notch root is expressed as the mth power of the range of strain intensity factor. The strain intensity factor is defined as the parameter multiplied the strain range at a notch root by root of the half length of a surface crack length. The value of m is 2 in the center and is more than 2 in the edge of the plate thickness. This propagation law of a surface crack can be applied to any radius of notch roots.

2. The cyclic creep occurs at a notch root and strains increases toward the tension as the number of cycle increases. The strain range remains constant during cyclic loading, but the mean strain increases as the number of cycle increases. The strain distribution changes drastically as the number of cycle increases. From these results, it is found that the cyclic strain behavior at a notch shows the complex behavior.

REFERENCES

1.   Paris, P. C. and Erdogan, F. (1963) Trans. ASME, Ser.D, 85-4, 528
2.   Shingai, K. and 2 persons (1973) J. Eng. Fract. Mech., 5, 528
3.   Kobayashi, H. and 5 persons (1977) JSME, 43-366, 416
4.   Dawling, N. E. (1976) ASTM STP 590, 82 and ASTM STP 601, 19
5.   Asada, Y, Yuuki, R., Shingai, K and 5 persons (1980) I. Mech. E., C52/80, 347
6.   Nisitani, H. and Shingai, K. (1968) JSME, 34-258, 224
7.   Hirano, K and 2 persons (1976) JSME, 42-361, A, 2673
8.   Oominami, M and Sakane, M (1977) JSME, 43-375, 3955
9.   Shingai, K. (1997) Proc. of ICF9, 3, 1421
10. Shingai, K. and 2 persons (1999) Proc.of FATIGUE'99,4-2, 1181

STUDY ON SUPERLONG LIFE FATIGUE IN HIGH STRENGTH STEELS

Yasuo Ochi

Department of Mechanical Engineering and Intelligent Systems,
University of Electro-Communications, Tokyo
1-5-1, Chofugaoka, Chofu, Tokyo 182-8585, Japan

ABSTRACT

Recently, superlong life fatigue over 10^7 cycles whcih was assumed to be a fatigue limit of steel materials, has been noticed. One of the reason is the aged industrial structures and materials such as railways wheels and rails, engine components, load bearing parts of automobile industry, etc., have to endure up to $10^8 \sim 10^{10}$ load cycles, and the other is that several unexpected failure have been occurred in severe environmental use of many industrial structures and materials in superlong life fatigue regime. However, most experimental investigation have been limited to testing periods up to 10^7 cycles, and the collecting and the arrangement of the testing data of superlong life fatigue regime have been insufficient until now.

This paper firstly introduces recent several joint research projects being related with superlong life fatigue in JSME (the Japanese Society of Mechanical Engineers), HPIJ (the High Pressure Institute of Japan), JWES (the Japan Welding Engineering Society), and round robin tests of RGSAMS (the Research Group for Statistical Aspect of Materials Strength), JSMS (the Society of Materials Science, Japan) in Japan.

Then, the study of the superlong life fatigue in high strength steels were reviewed briefly, and some results of the progressing round robin tests are shown. From the results, the S-N curves in high strength steels have not clear fatigue limit, and show basically typical doubly deflected or the duplex S-N curves which have a first slope, an intermediate horizontal portion and a second slope in the superlong life regime. And, the fracture mode is divided into two types; the former is the surface fracture mode in the shorter life regime before about 10^5 cycles, and the latter is the internal fracture or the fish-eye fracture mode after about 10^7 cycles.

From SEM observations of fracture surfaces, the crack initiation sites in the surface fracture mode are the surface slip or the inclusions on/near surface, and in the internal fracture, they are mostly non-metallic inclusions, and the fracture surface gives a typical fish-eye fracture mode. The rough grander area RGA are observed in the vicinity around the inclusions, being the crack initiation sites. And lastly, some proposals which are suggested to interpret the mechanism for the formation of the RGA in the superlong life regime.

SUBCASE CRACK PROPAGATION THRESHOLD AND MICROHARDNESS PROFILE INFLUENCE IN ROLLING CONTACT FATIGUE OF CARBURISED COMPONENTS

G. Donzella, A. Mazzù and L. Solazzi

Dipartimento di Ingegneria Meccanica, Università degli Studi di Brescia,
Via Branze 38, 25073 Brescia, ITALY

ABSTRACT

A new experimental methodology was employed to study the subcase cracks propagation in surface hardened components under rolling contact fatigue: some micro-holes were drilled by electron discharge machining on one of the flat faces of carburised disks, at different depths under the surface. Under cyclic contact tests carried out at different contact pressure levels, some micro-cracks nucleated from the holes border and grew mainly in mode II due to the compressive residual stress state present in the hardened layer. These tests simulate the actual subcase fatigue phenomenon, which starts from inclusions present in the material. The experimental results, calibrated with FEM analyses, gave an indication on the fatigue threshold as a function of defect size and material hardness. The definition of a propagation index allowed to assess the subcase fatigue limit, taking explicitly in to account the hardness profile.

KEYWORDS

Rolling contact fatigue, subcase fatigue, short cracks, hardened components

INTRODUCTION

A lot of components subjected to rolling contact are carburised. This treatment (and generally speaking a surface hardened treatment) limits wear and surface fatigue, so that subsurface fatigue (also said subcase fatigue) becomes more important and probable [1,2]: the cracks propagate almost parallel to the surface in the interface zone between core and hardened case, until they branch and emerge to the surface. In some cases the path covered by the cracks under the surface can be very long, thus producing serious damage at the failure instant.

This paper deals with the evaluation of a threshold of this dangerous damage mechanism in carburised disks, taking in to account the determining role played by the hardness profile along the depth. This role can be understood in a simplified manner, thinking the phenomenon of the subcase fatigue as a competition between contact shear stresses, varying along the depth, and material shear fatigue limit, which depends on the hardness and therefore on the depth again. Some design criteria based on this approach have been proposed in the past. Inherent defects in the material were however recognized to constitute preferential initiation points of subsurface cracks [3,4]: their effect must be therefore taken in to account to predict the development of a subcase fatigue phenomenon. Non-metallic oxide inclusions are particularly dangerous:

they are often present in form of clusters, thus originating greater "SIF equivalent defects". The basis of the work here presented is the short cracks theory. Following this theory, and in particular the Murakami approach [5], the subcase fatigue limit is defined as the propagation threshold of small defects inherent in the material. The results available from the short cracks theory regards however quantitative estimation of mode I threshold: in particular, following the Murakami's relationship, it depends on crack dimension and material hardness in the form:

$$\Delta K_{Ith} \propto (HV + 120) \cdot \left(\sqrt{A}\right)^{1/3} \qquad (1)$$

Many difficulties arise in determining the threshold of subcase fatigue cracks, because they propagate mainly in mode II [1,6,7,8] and it is not easy to reproduce this propagation mode in laboratory tests, due to its strong instability [9,10,11]. Some attempts were made on long cracks by Murakami et al. [10] using V-notched cantilever specimens and by Otsuka et al. [6] using clamped specimens. This last work showed in particular that a T-stress (i.e. a compressive stress along the crack direction) acts in stabilising the mode II propagation. A similar condition is present in the rolling contact phenomenon, especially in surface hardened components, were a significant compressive residual stress parallel to the surface is generated by the hardening treatments. The idea followed in the present work was therefore to introduce artificial micro-holes in some carburised disks and to follow their propagation under a RCF test. In such a way, the presence of inherent defects in the material can be simulated, also studying the influence of their dimension and position on the subcase fatigue strength.

EXPERIMENTAL TESTS

The experiment here described was carried out on a carburised disk (120 mm in diameter, 10 mm in thickness) made of 18NiCrMo5 steel, whose hardness profile HV is shown in fig.1.
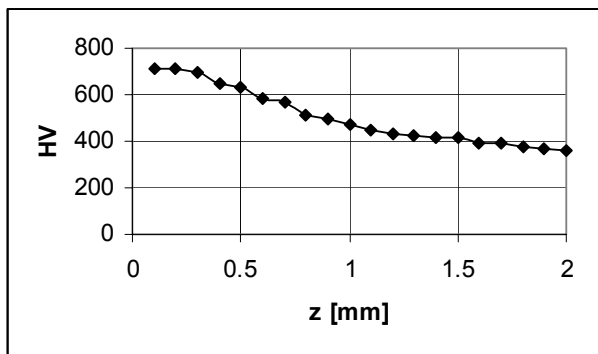
Figure 1: hardness profile of the disk
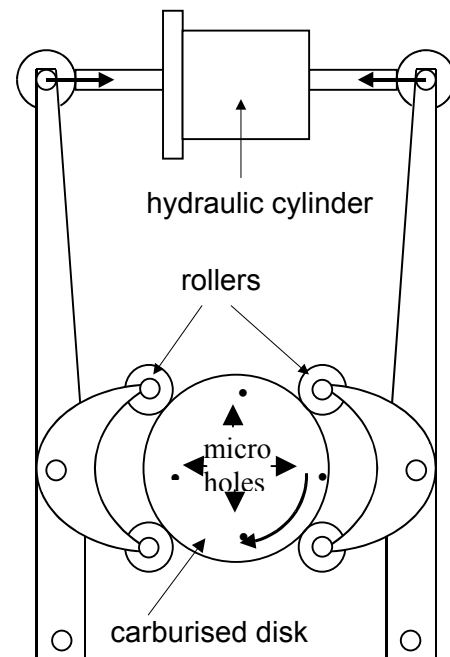
Figure 2: testing apparatus

Four blind micro-holes called A, B, C and D, 130 μm in diameter and 300 μm in length, were machined by electron discharge on one of the flat planes of the disk at different depths z, respectively 250 μm, 380 μm, 510 μm and 620 μm from the surface to the hole axis, in order to study the effect of the hardness gradient. The RCF tests were carried out in pure rolling and lubricated condition with the testing machine, designed at the University of Brescia, schematically shown in fig.2. A constant hertzian pressure p_o was applied during the test, periodically stopping it and examining the disk with an optical microscope. If no crack propagation was detected in $2 \cdot 10^6$ load cycles, the pressure level was incrementally increased by steps of 100 MPa.

NUMERICAL ANALYSES

The aim of the numerical analyses was to calculate the SIFs range during a load cycle for the cracks emanating from the holes, in order to calibrate the experimental results and to determine in this way the correspondent threshold levels. Several plane stress models were employed, simulating the four micro-holes with different crack orientation and length and moving the pressure distribution along the contact surface. The SIFs were calculated from the nodal displacements near the crack tip [12], verifying in every case they respect the singularity field. The submodeling technique, allowed by ABAQUS code, was used for these calculation in order to refine accurately the mesh near the crack tip (fig.3).
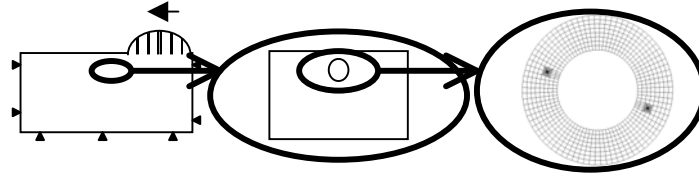
Figure 3: numerical models, using the submodeling technique

RESULTS

No crack propagation from the micro-holes was observed up to a pressure of 2100 MPa. At a pressure of 2200 MPa some micro-cracks started from the holes border. In particolar, from each hole two almost symmetrical cracks appeared, at a direction comprised in the range from 10° to 30° with respect to the surface direction (see fig. 4a). In some cases multiple cracks initiated with various directions, but mainly again in the range from 10° to 30°, as shown in fig. 4b.
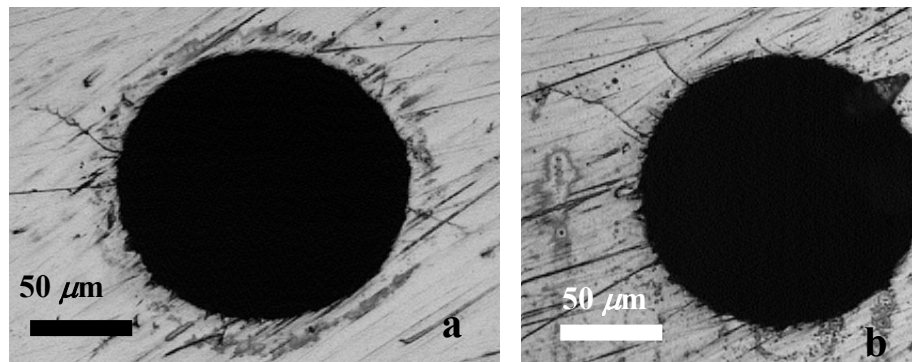
Figure 4: first stage of crack propagation from micro-holes

The numerical analyses showed a clear dominant mode I for the first stage of propagation of these micro-cracks (see fig.5a), but the correspondent calculated SIF is not significant, because near the hole border it is modified by the unknown tensile residual stresses due to electron discharge machining.
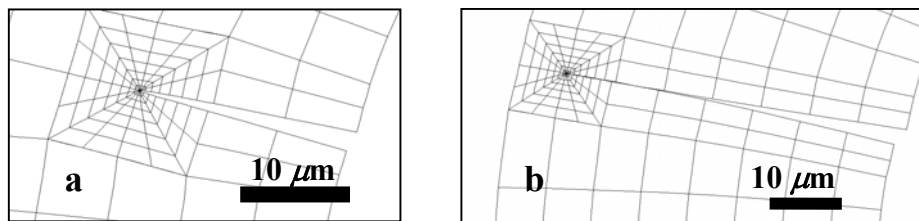
Figure5: deformed meshes of cracks with different length

In the case of multiple cracks, many of these stopped after a few tens of microns (typically 20 μm), going away both from the residual stress zone and from the stress concentration zone around the hole, thus reducing their ΔK_I below ΔK_{Ith}. Only a couple of them for each hole continued growing: the propagation was easier for cracks less inclined with respect to the surface direction. The numerical analyses showed that just for these directions ΔK_{II} reaches its maximum values (see fig. 6) and it increases with the crack length. So, generally speaking we concluded that as a crack starting from the hole border continues growing after 20

μm, the dominating propagation mode in this second stage becomes the mode II, as is also put in evidence by the deformed mesh in fig.5b and by the multiple branching shown in fig.7. A similar result was found numerically by Melander [13].
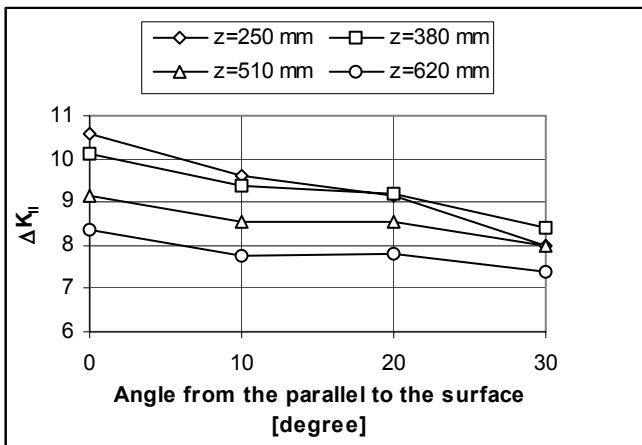
Figure 6: ΔK$_{II}$ versus crack orientation (crack length: 20 μm)
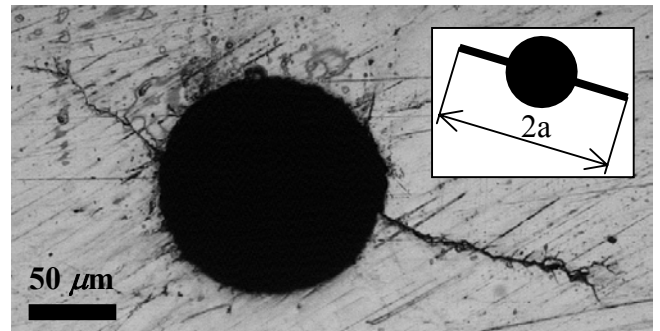
Figure 7: second stage of crack propagation from micro-holes

The cracks propagating from deeper micro-holes (C and D) stopped when they reached a total length 2a (defined as shown in fig.7) of about 250-300 μm, while the cracks propagating from the micro-holes A and B, closer to the surface, continued growing up to $2 \cdot 10^6$ load cycles, after which the test was stopped. In fig.8 the crack length 2a is reported as a function of the cycles number for the four micro-holes. A linear approximation shows that the growth rate is in the range of the threshold.
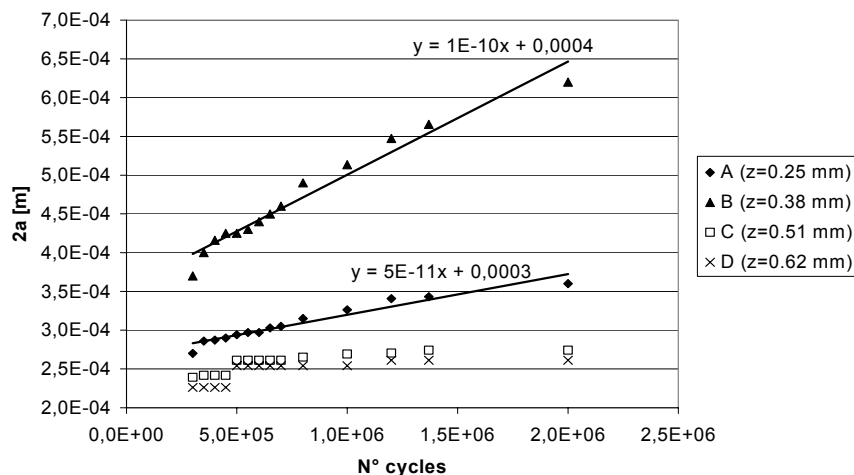
Figure 8: crack growth from micro-holes at different depths

DISCUSSION

In fig.9, the ΔK$_{II}$ for the experimentally propagating and non-propagating cracks, calculated by the fem analyses at the correspondent lengths and orientations, is reported as a function of the total crack length 2a. The first calculations were made for cracks of length 2a=170 μm (i.e. 20 μm from the hole border). In the case of multiple cracks emanating from a hole, those stopped after about 20 μm have been considered as "non-propagating". For the propagating cracks reported in fig.8, further calculations were carried out with increasing length, up to the lenghts observed at the end of the test. For the cracks emanating from holes C and D, the last calculations were made at the length correspondent to their arrest and results were indicated as "non-propagating" in the diagram. In the same figure, for each hole is reported in solid line a curve proposed to describe the mode II threshold [12].
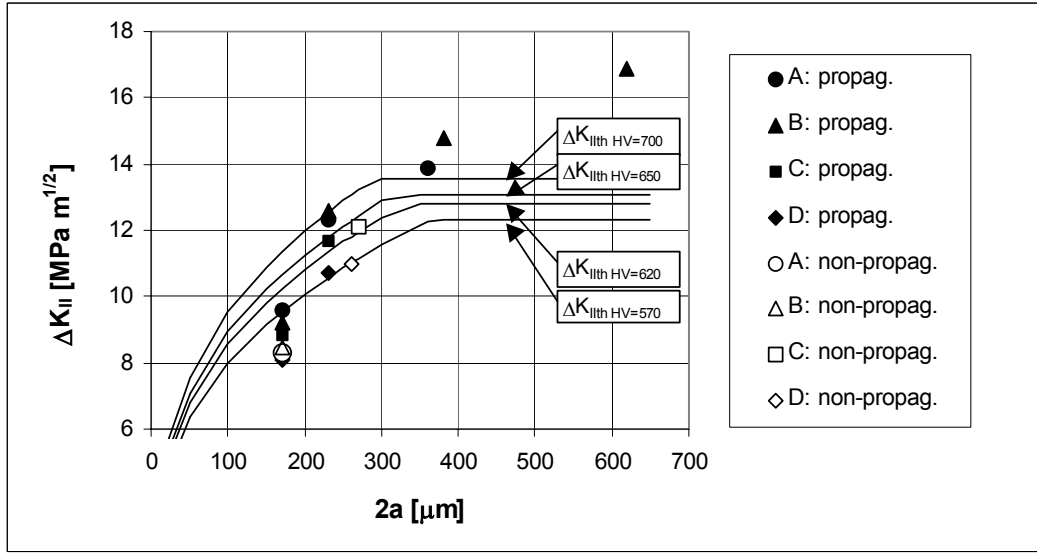
Figure 9: experimental results and proposed threshold curves

Each threshold curve is composed by two parts. The first one, depending on the crack length in the short cracks range:

$$\Delta K_{IIth} = 2.5 \cdot 10^{-3} \cdot (HV + 120) \cdot \left(\sqrt{A}\right)^{1/3} \tag{2}$$

with $\sqrt{A} = 2a$, based on the hypothesis that the influence of hardness and defect dimension on the mode II threshold is the same as the Murakami's mode I relationship (1), where the coefficient 2.5 has been determined on the basis of the study of Beretta et al. [14] on carburised steels. A "closure" effect also in mode II is implicitly hypothesised in this way; it can be mainly attributed to roughness or oxide entrapment between the crack faces. The second one, independent on the crack length in the long cracks range:

$$\Delta K_{IIth} = 6.86 + 9.55 \cdot 10^{-3} \cdot HV \tag{3}$$

based on the study of Kato et al. [15] on carburised steel and the results of Sakae et al. [8], Murakami et al. [10] and Otsuka et al. [6] on hardened steels. It allows to taken in to account the influence of the hardness and also agrees with the results of Hellier et al. [16] and Lunden [17] on carbon steels for rails and railway wheels. The agreement between the present experimental results and the threshold curves proposed above is not so good for smaller cracks: more verifications and refinements, both experimentally (tests with smaller micro-holes) and numerically (3D models) are necessary. From the experimental results, it appears however interesting that smaller cracks seem to present smaller mode II threshold, thus indicating also for this propagation mode a "short cracks" effect. In this sense, the proposed relationships can represent a rough tool to predict the subcase fatigue limit in a rolling contact phenomenon, in terms of the maximum contact pressure which can be applied without determining crack propagation from inherent defects. In particular, for an herztian contact, a propagation index can be defined in the form:

$$I = \frac{\Delta K_{II}(p_0, b, a, z)}{\Delta K_{IIth}(HV(z), a)} \tag{4}$$

where p_0 is the nominal contact pressure, b the contact area half-length, 2a the maximum expected defect dimension (which can be evaluated by means of the statistics of extreme values) and HV(z) the hardness profile. A simplified form for ΔK_{II} is [12]:

$$\frac{\Delta K_{II}}{p_0(\pi a)^{1/2}} = \left(c_0 + c_1 \cdot \frac{z}{b} + c_2 \cdot \left(\frac{z}{b}\right)^2 + c_3 \cdot \left(\frac{z}{b}\right)^3 + c_4 \cdot \left(\frac{z}{b}\right)^4 \right) \tag{5}$$

with $c_0 = 0.21632$; $c_1 = 1.49316$; $c_2 = -2.7232$; $c_3 = 1.97346$; $c_4 = -0.5284$. In fig. 10 is reported an example of the propagation index determination with two different hardness profiles, having equal surface and core levels. Representing I as a function of the depth, it is possible to evaluate the risk of subcase fatigue failure and its location. The strong influence of the hardness profile can be so put in evidence.
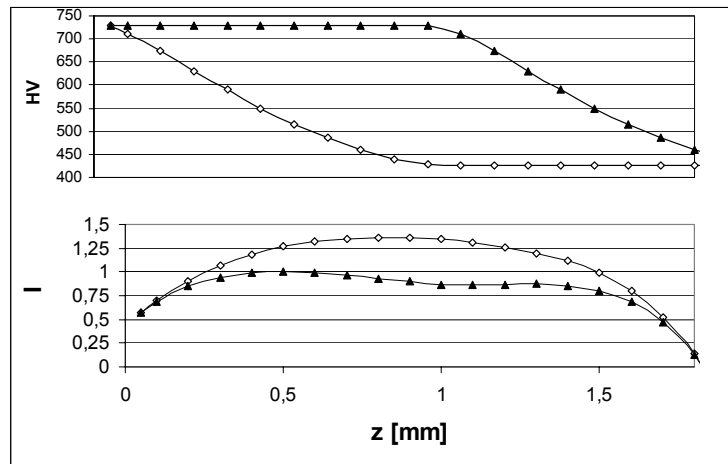
Figure 10: propagation index with different hardness profiles

CONCLUSIONS

- Experimental tests on the carburised disk shown that when the crack extends from the hole border, it passes from a zone dominated by opening stresses (stage I, mode I), to a zone dominated by shear stresses (stage II, mode II). After the first stage, it can therefore continue growing only if $\Delta K_{II} > \Delta K_{IIth}$. This happens preferentially for cracks slightly inclined with respect to the contact surface direction.
- The mode II threshold of the cracks emanating from the micro-holes appears to increase with the crack size, thus indicating a "short cracks" effect also for this propagation mode.
- The proposed "propagation index" allows to take in to account the hardness profile, thus evaluating its effect on the subcase fatigue limit.

References
1. Hyde, R.S. (1996). In: *ASM Handbook*, 19.
2. Voskamp, A.P. (1998). In: *Bearing Steels: Into the 21st Century*, ASTM STP 1327, Hoo & Green (Eds). ASTM.
3. Nelias, D., et al. (1999) *Journal of Tribology* 121, 240
4. Auclair, G., et al. (1997) *5th Int. Symposium on Bearing Steels*, ASTM STP 978. New Orleans.
5. Murakami Y. and Endo, M., (1994) *Fatigue* 16, 163
6. Otsuka, A., Sugawara, H. and Shomura, M. (1996) *Fatigue Fract. Engng. Mater. Struct.* 19, 1265
7. Salehizadeh, H., Saka, N. (1992) *Journal of Tribology* 114, 690
8. Sakae, C., Ohkomori, Y. and Murakami, Y. (1999) Internal report, Kyushu University
9. Melin, S. (1986) *Int. Journal of Fracture* 30, 103
10. Murakami, Y., Sakae C., Hamada S. (1999). In *Mechanism of Rolling Contact Fatigue and Measurement of ΔK_{IIth} for Steels, Engineering Against Fatigue* Beynon et al. (Eds). A.A. Balkema. Rotterdam & Brookfield.
11. Pook, L.P. (1989) In: *Biaxial and Multiaxial Fatigue*, EGF 3, Brown & Miller (Eds), Mechanical Engineering Publications.
12. Donzella G., Mazzù A., Pola A., Solazzi L. (2000) *Atti XXIX Conv. Nazionale AIAS*, Lucca, pp.407-416.
13. Melander, A. (1997) *Int. Journal of Fatigue* 19, 13
14. Beretta, S., Clerici, P. and Guagliano, M. (1998) *XXVII Convegno Nazionale AIAS,* Perugia, pp.249-258
15. Kato, M., Deng, G., Inoue, K. and Takatsu, N. (1993) *JSME Int. Journal* 36, 233
16. Hellier, A.K., McGirr, M.B. and Corderoy, D.J.H. (1991) *Wear* 144, 289
17. Lunden, R. (1992) *Int. Wheelset Congress*, Sydney, pp.163-167

SUPPRESSION OF TRANSVERSE CRACKS IN CFRP LAMINATES WITH EMBEDDED SMA FOILS

N. Takeda[1], M. Kobayashi[1] and T. Okabe[2]

1. Department of Advanced Energy
Graduate School of Frontier Sciences, The University of Tokyo,
c/o Komaba Open Laboratory (KOL), Takeda Lab.
4-6-1 Komaba, Meguro-ku, Tokyo 153-8904, Japan
2. Smart Structure Research Center, National Institute for Advanced Industrial Science and Technology
(AIST), 1-1-1 Umezono, Tsukuba city 305-8568, Japan

ABSTRACT

The present paper experimentally studies the microscopic damage in the Shape Memory Alloy (SMA) foil-CFRP composite system, and proposes an appropriate transverse crack evolution model with Monte Carlo simulation based on the Weibull-Poisson flaw statistics and a modified shear-lag model considering the stress transfer due to the phase transformation. The predictions are found to have good agreement with the experimental results, and show that recovery stresses due to SMA foil suppress the multiplication of the transverse cracks.

KEYWORDS

Composite, Shape Memory Alloy, Transverse crack

INTRODUCTION

SMAs with shape memory mechanism and psuedoelasticity has been widely used as actuators in smart material and structural systems. Especially, in order to suppress the microscopic damage in the composite, the SMA-FRP composite system has been expected to be useful in the engineering application including the aerospace field. Although many studies for SMA composites have been reported, most of them address the SMA wire reinforced composite [1,2]. In a view of preventing the microscopic damage occurring in the composite, SMA foil is considered to be more effective than SMA wire.

In the present paper, we experimentally observe the microscopic damage in the composite and propose an appropriate transverse crack evolution model with Monte Carlo simulation based on the Weibull-Poisson flaw statistics and a modified shear-lag model considering the stress transfer due to the phase transformation. The predictions are found to have good agreement with the experimental results.

Surface and Interface Characterization of Ferritic Stainless Steel by ^{57}Fe Conversion Electron Mössbauer Spectroscopy (CEMS)

Kiyoshi Nomura, Takayuki Terai, and Tsuguo Sawada

School of Engineering, The University of Tokyo

Hongo 7-3-1, Bunkyo-ku, Tokyo, 113-8656

The surface and interface on ferritic stainless steel heated at various high temperatures were characterized by Conversion Electron Mössbauer Spectroscopy. The iron oxides (α-Fe$_2$O$_3$) were mainly produced by heating below 600°C and the chromium oxides were produced with fine paramagnetic iron oxides species above 700°C. The interface of stainless steel beneath the oxide films was especially characterized as the hyperfine field distributions. CEMS is effective for simultaneous and non-destructive characterization of both oxides surface and alloy interface layers of ferritic stainless steel.

1. Introduction

Stainless steel is widely used in many fields. However, there are a few applications of oxide films prepared intensively on stainless steel. We have shown that the oxide film of austenitic SUS316 (18Cr+8Ni+3Mo+Fe balance) treated chemically is a practical pH sensor with a quick response [1]. The oxide film on stainless steel heated in advance is useful for vacuum vessels because there is few gas absorption [2]. In addition, ferritic stainless steel (such as SUS430: 18Cr+Fe balance) is one of candidate materials for high-temperature container, heat exchange vessel of nuclear fusion. For example, low activation ferritic stainless steel is expected as the liquid blanket and container material of LiF-BeF$_2$ molten salt, which is considered as a coolant and a breeder material of tritium [3]. The surface study on stainless steel is important.

On the other hand, the oxidized states of iron steel surfaces have been analyzed using conversion electron Mössbauer spectroscopy (CEMS) [4]. There are few applications of CEMS to characterization of oxide surface of stainless steel [5]. After Mössbauer effect of ^{57}Fe, 7.3 keV K-electrons (80%), 13.6 keV L-electrons (8%) and 5.5 keV auger electrons (63%) are emitted together with the secondary electrons of reemitted 6.3 keV Kα X-rays (23%) and 14.4 keV γ-rays (10%). Although these electrons can be distinguished with high performance electron analyzers such as XPS, the electron spectroscopy with high energy-resolution are not practically so useful for CEMS from the viewpoint of detection efficiency. It is known that the 65% of all conversion electrons emitted from Fe metal is within 60 nm in depth and the 90 % is

within 300 nm in depth [6]. Concerning the interface between coating and substrate steel, we have first reported that the relative intensity ratio between sextet peaks of iron substrate became from 3:4:1:1:4:3 close to 3:2:1:1:2:3 with the increase of dipping time in the phosphated bath [7]. This is mainly caused by the increase of roughness at the interface by the long term of chemical treatment. When analyzed the complex CEMS and XMS spectra of the carbonitride coatings of stainless steel in 1996 [8], we could not find the state transition of the base stainless steel by integral CEMS.

The thin interface of ferritic stainless steel beneath the oxide layers was especially estimated from the hyperfine field distributions of three different energy CEMS spectra by using a He gas proportional counter. As the results, the different hyperfine fields were obtained.

2. **Experimental**

Some SUS430 plates were oxidized by heating in air atmosphere for 1 hour at 400, 500, 600, 700, and 800°C.   Radiation source used was 1.85GBq ^{57}Co(Cr). The γ-rays were perpendicularly irradiated to a sample plane. CEMS spectra were measured using a 2π back scattering type of gas flow counter, flowing He+5%CH$_4$ gas at 15cc/min and applying high voltage at 950 V. A He gas counter has poor energy and time (μsec) resolutions, but high efficiency of 2π stradian to detect all conversion electrons together with the insensitivity against incident γ and X rays.   The typical electron energy spectrum is shown in Fig.1.
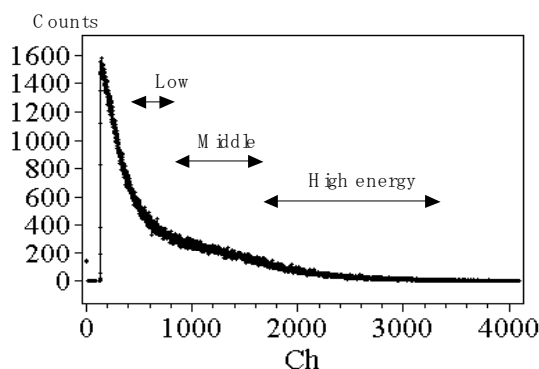
Fig.1 PHA spectrum of conversion electrons detected by a gas flow counter, flowing He+5%CH$_4$ gas at 15 cc/min. HV: 950V, Source: ^{57}Co (Cr), Sample: Stainless steel (^{57}Fe;2.1%, natural abundance)

Three Mössbauer spectra were simultaneously obtained by discriminating the energy of emitted electrons into three regions such as the high, middle and low energy. This method can provide the rough layer-by-layer analysis within about 100nm. MossWinn program [9] was used for the analysis of CEMS spectra and the hyperfine fields distributions.

3. Results

3.1 Depending of CEMS on different energy electrons detected.

The typical CEMS spectra of the stainless steel (SUS430) heated at $500^{\circ}C$ for 1 hour are shown in Fig.2. Three spectra were simultaneously obtained by discriminating three different electron energy regions. It was found that a magnetic sextet (H_{in}=52T) observed is assigned to an antiferromagnetic iron product of hematite (α-Fe_2O_3). The higher contents of hematite produced at the top layers were observed in CEMS spectra obtained by detecting the higher energy electrons. It was confirmed that the rough layer-by-layer analysis by a gas counter is possible. CEMS spectra obtained by the detection of low energy electrons were not so good for the peaks to back grounds. It is why many non-resonant secondary electrons due to photoelectron effect and Compton effect contribute to low energy regions.

The sextet of the original ferritic stainless steel consisted of broad peaks because the iron internal magnetic fields were influenced due to the various numbers of nearest neighbor Cr atoms around an Fe atom. These broad peaks were analyzed using an internal magnetic field distribution by the method of Hesse and Rubartsch [10]. Since the direction of magnetic moment is parallel in-plane in the most thin surface of ferromagnetic materials such as an iron foil, the area intensity ratio between sextet peaks becomes 3:4:1:1:4:3 for γ-ray vertical incidence. However, the internal magnetic field distributions were analyzed assuming that the magnetic splitting components in the surface region observed by integral CEMS had average intensity ratio of 3:3:1:1:3:3 because the best fitting of Mössbauer spectrum of non-treated sample was obtained using this ratio. As shown in the right figures of Fig. 2, it is clear that the internal magnetic field distributions of the stainless steel substrate were strongly affected by discriminating the electron energy. The peaks of 270 and 310 kOe were observed in the hyperfine distributions of high energy CEMS although the peak of hyperfine field distributions was 290 kOe before treatment as shown in Fig.3a). The distributions in low energy regions became similar to that before treatment. Those results suggest that the composition ratio of Fe and Cr is different from that of the bulk at the near interface layers beneath the oxides layers. It is known that the magnetic phase diagram of Fe-Cr alloy consists of a ferromagnetic component for Fe concentration in excess of 19 at.% [11]. The elemental Fe and Cr have similar lattice structures of BCC with close lattice constants, and the local magnetic moment of Fe and Cr depends on their local environment of Cr next neighbors rather than the average electric properties. In the ferromagnetic region, the average local moment is reduced when the Fe-Cr coupling is ferromagnetic, although the Fe local moment increases slightly when the coupling is

antiferromagnetic [12]. It is known that the magnetic hyperfine field at the Fe site decreases with the decrease of Fe concentration [13, 14].

a) 500 $^{\circ}$C H

b) 500 $^{\circ}$C M

c) 500 $^{\circ}$C L
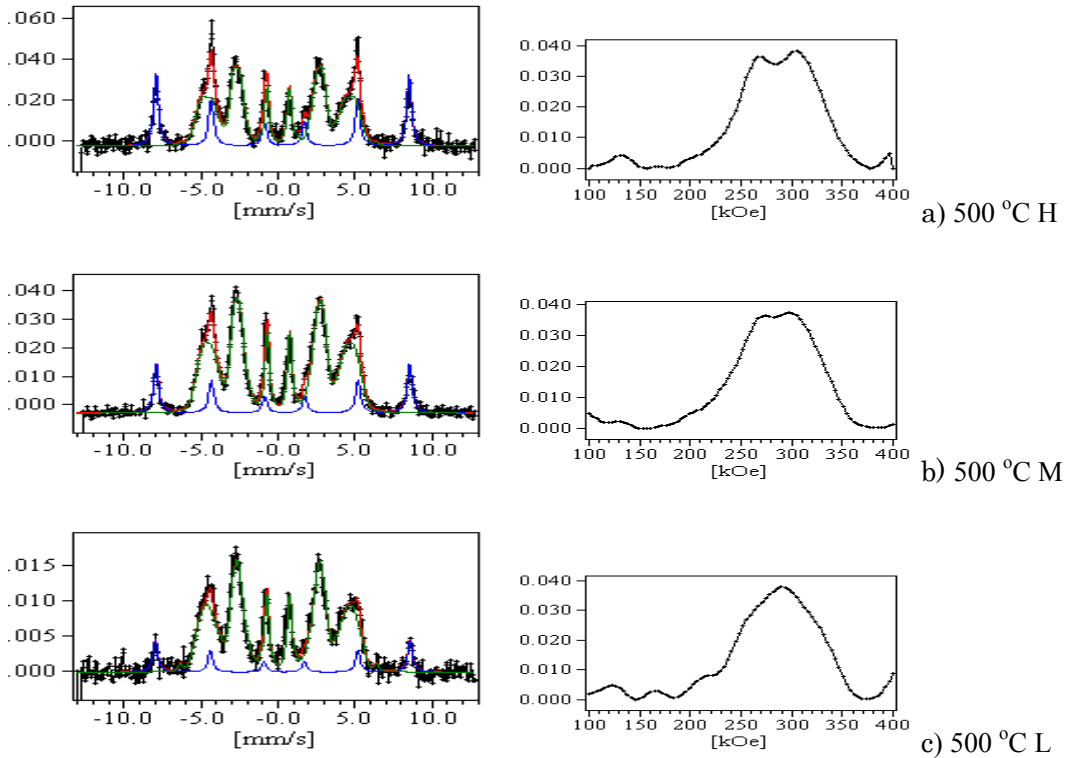
Fig. 2 CEMS and hyperfine distributions of SUS430 heated at 500°C for 1 hour. a) high energy electrons, b) middle energy electrons, and c) low energy electrons detected.

3.2 Temperature dependence on oxide surface and interface layers

Fig.3 shows CEMS spectra of the stainless steel heated at various temperatures, which were obtained by addition of high energy CEMS to middle energy CEMS spectra. The peak at 33T with relatively high intensity was observed in the hyperfine magnetic field distribution of the sample oxidized at 700°C. This indicates that the chromium depletion occurs at the interface of the substrate beneath oxide layers. In the hyperfine field distribution of the sample oxidized at 800°C, the peak at 33T became low again, and lay close to the original hyperfine field distribution. It means that the composition at the substrate interface approximates the original bulk composition of SUS430 with the diffusion of bulk Cr atoms to the interface to form Cr oxide surface layers at the higher temperatures. It was found that Cr depleted layer could be detected by CEMS measurement of the interface of stainless steel heated at high temperatures.

From the relative peak intensity ratio of iron oxides and stainless substrate, it was found that iron atoms were diffused to form top oxide layers up to 600°C and chromium

oxides were grown in the top oxide layers at 700°C or higher. At 800°C, the intensity of hematite became small, and the paramagnetic peaks with IS=0.33mm/s, QS=0.33mm/s were observed. This is reduced in the small particles of hematite or $(Cr,Fe)_2O_3$ doped with Cr.
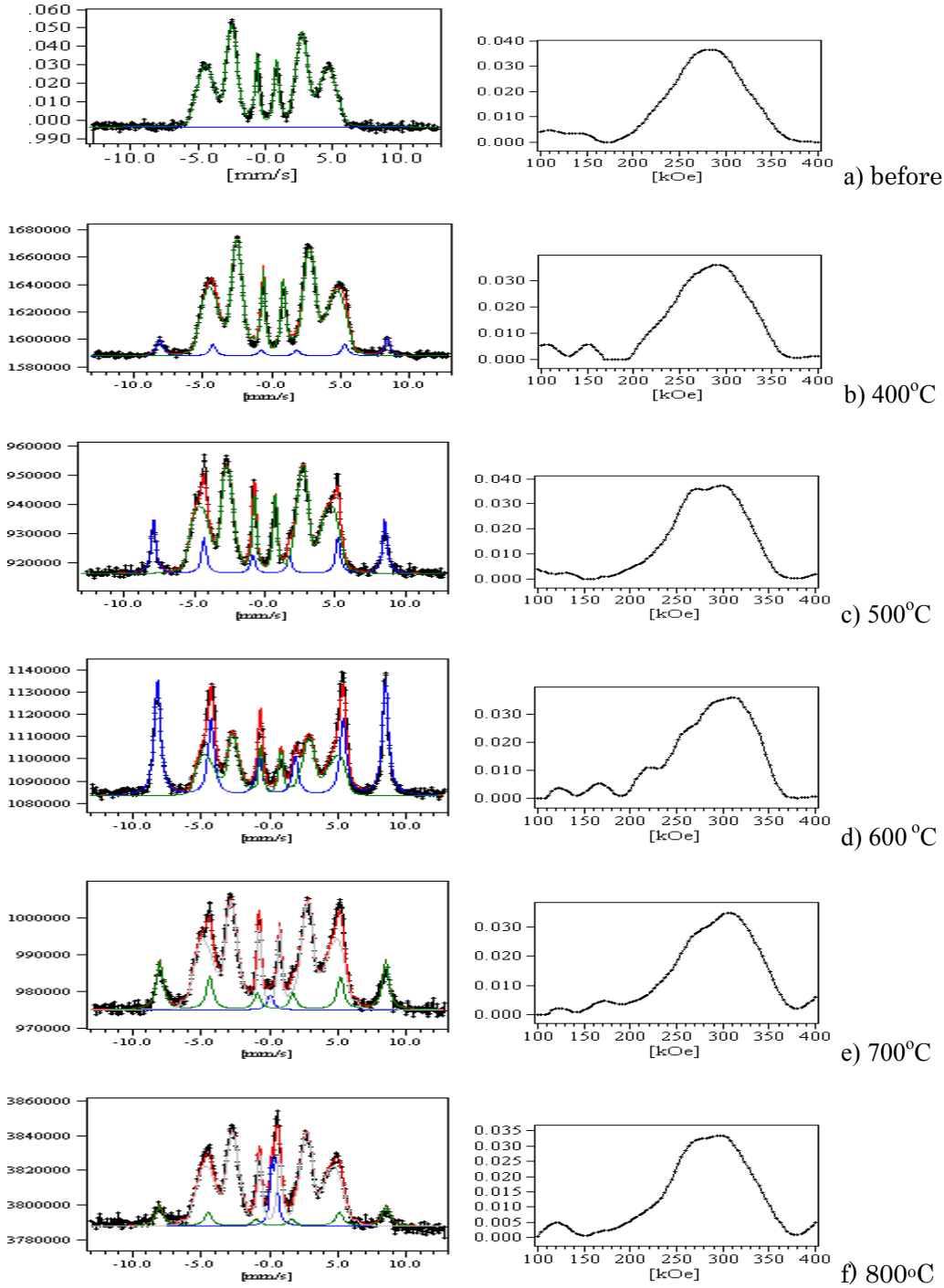
Fig.3 CEMS and hyperfine distributions of SUS430 heated at various temperatures for 1 hour in air. a) before and after heating b) 400°C, c) 500°C. d) 600°C, e) 700°C and f) 800°C.

The schematic diagram of the oxide layers produced on stainless steel and the probing depth by detecting low, middle, and high energy CEMS are shown in Fig.4.
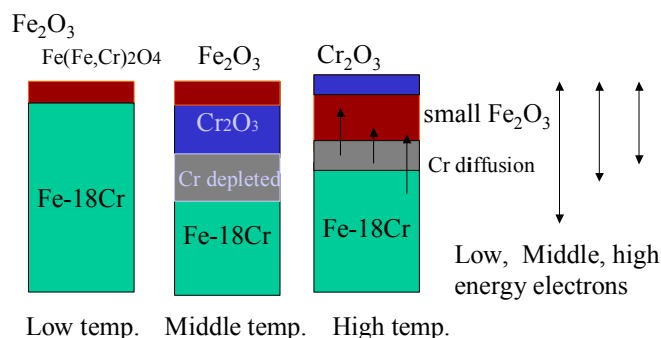
Fig. 4, Schematic cross sections of oxide layers produced on ferritic stainless steel and the detection depth by three different energy CEMS.

3. Conclusions

Depth selective CEMS by a He gas flow counter could not only determine the iron products on steel surface within about 100nm but also simultaneously detect the degradation of composition of Cr and Fe in the interface substrate beneath the surface products by analysis of the magnetic hyperfine distributions.

Reference

1) K. Nomura, and Y. Ujihira, *Analytical Chemistry*, **60**(1988) 2564.

2) B. Cho, E. Choi, S. Chung, K. Kim, T. Kang, C.park, B.Kim, *Surface Science*, 439(1999)L799.

3) K. Nomura, Y. Hosoya, H.Nishimura, T. Terai, *Czechoslovakia J. of Phys.*, 2001 , in press.

4) K. Nomura, Y. Ujihira, A. Vertes, *J. Radioanaly. and Nucl. Chem., Articles*, **202**(1996) 103.

5) K. Nomura, Y. Ujihira, *J. Materials Science*, **25** (1990) 1745.

6) I. Stwert, M.J.Tricher, Corrosion Science, **26**(1986) 1041.

7) K. Nomura, Y. Ujihira, Y.Matsushima, R. Koshima, Y.Sugawara, *Jap. J. of Chem.*, 1372 (1980).

8) K. Kurosawa, M. Hoshino, H.Li, Y. Ujihira, K. Nomura, *Hyperf. Interact.*, **112**(1998) 269.

9) Z. Klencsar, E. Kuzmann, A.Vertes, *Hyperf. Interact.*, **202**(1996) 103.

10) J. Hesse, A. Rubartsch, *J. Phys. E: Science Instruments*, **7** (1974) 526.

11) V.I.Anisimov, V.P.Antrov, A.I.Liechtenstein, V.A.Gubanov, A.V.Postnikov, *Phys. Rev.* B**37** (1988) 5598.

12) M.E.Elzain, J. Phys. *Condes. Matter*, **3**(1991) 2089.

13) H. Kuwano, K. Ono, *J. Phys. Soc. Japan*, **42**(1977) 72.

14) M. Shiga, and Y. Nakamura, *J. Phys. Soc. Japan*, **49**(1980) 528.

TEMPERATURE AND AGING EFFECTS ON ULTIMATE BEARING STRENGTH AND FATIGUE OF POLYMERIC COMPOSITE JOINTS

W. S. Johnson and W. A. Counts

G.W. Woodruff School of Mechanical Engineering
Georgia Institute of Technology
Atlanta, GA 30332-0245 USA

ABSTRACT

The ultimate bearing strength (UBS) and fatigue performance of IM7/PETI-5 composite materials in a quasi-isotropic lay-up, 64 plies thick was determined using a compressive bearing test set-up. Strength testing was performed at room temperature, 177°C (350 ^{o}F) and –50°C (-58 ^{o}F). Fatigue tests were performed at 177°C (350 ^{o}F). Some specimens were thermally aged at 177°C (350 ^{o}F) for up to 10,000 hours. It was found that the IM7/PETI-5 composite material's UBS and fatigue performance was essentially unaffected by the thermal aging. The elevated temperature tests resulted in a lower UBS and the cold temperature tests resulted in a slightly higher UBS. However, the cold temperature bearing failure was quite dramatic, resulting in widespread delamination due to the brittleness of the matrix.

KEYWORDS

 ply buckling, thermal aging, durability, compression

INTRODUCTION

The high strength to weight ratio of composite materials makes them attractive for aerospace applications. In some of these applications, it may be necessary to use mechanical fasteners to assemble composite structures on aircraft. As new aircraft are designed and built to fly faster and higher, the temperature range over which the composite joint will be exposed also increases. At supersonic cruise, the exposure temperature can reach as high as 177°C (350°F), while during subsonic cruise, the exposure temperature can become as low as –50°C (-58°F). As part of a larger program on the mechanical properties of composite joints, the authors had already investigated composite bearing fatigue [1], fastener fatigue [2], composite bearing creep [3] and bearing strength [4]. This paper presents a review of the temperature and aging effects on the bolt bearing strength and fatigue behavior.

Polymer matrix composites have long been recognized as an attractive structural material. The concerns in high temperature applications are (1) the time dependent creep concerns and (2) degradation in mechanical properties due to the extreme temperatures and thermal aging. Previous work by the authors [3] have shown that bolt bearing creep is not an issue at 177°C (350°F) at bearing stresses up to 383 MPa (56 ksi). The concerns addressed in this paper are the fatigue and strength properties under bearing loads at extreme temperatures and after aging for 10,000 hours at 177°C (350°F)

APPROACH

Elevated temperature, 177°C (350°F), bearing fatigue tests were conducted on IM7/PETI-5, using a traditional double shear test set-up by the authors [1,3]. During the course of these fatigue experiments, the high strength steel fastener used to apply the load to the composite failed before the composite. In order to increase the applied load a compression test set-up with a fully supported bolt was adopted. The compression test set-up was based in concept on Wang's test set up but was slightly modified to use existing fixtures and run at low and elevated temperatures [5].

By fully supporting the bolt in the compression test set-up, higher bearing stresses could be applied to the composite without greatly increasing the stress in the steel fastener. However, to fully support the bolt, the applied bearing load had to be changed from tension to compression. In previous work, Eriksson [6] had shown the loading direction had a minimal effect on the bearing properties.

A picture of the specimen is shown in Figure 1 with a schematic of how the load was applied. The edge and width distance of the compression specimen are also included on the figure and were chosen such that bearing failure was the preferred failure mode. One advantage of the compression set-up over the traditional double shear test set-up is the smaller specimen size. The compression set-up specimen was roughly a quarter of the size of the double shear specimen. Consequently, the compression test set-up can decrease the amount of material needed for bearing tests and thus decrease
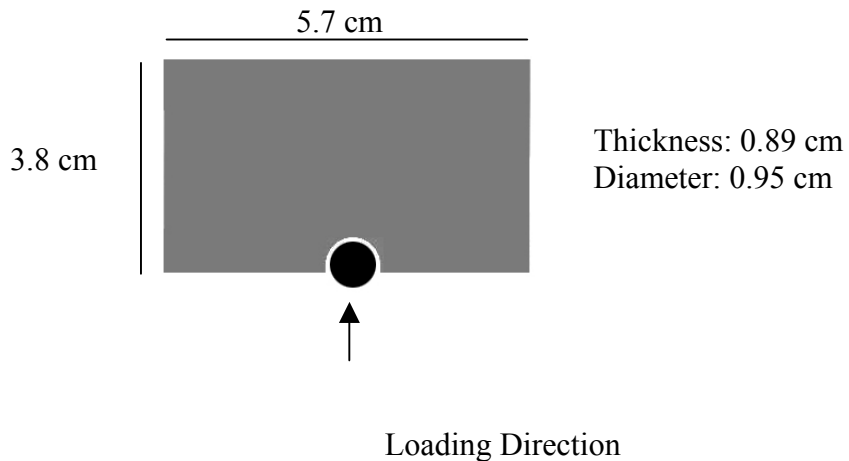
the cost of testing.

Figure 1 Compression Specimen Geometry

MATERIAL

IM7 carbon fibers in a PETI-5 slightly crosslinked polyimide matrix (manufactured by Cytech Fiberite) was made into laminates of 64 plies in a quasi-isotropic lay-up ($[\pm45°/90°/0°]_{8s}$). One panel of IM7/PETI-5 was placed in a forced air aging oven for 10,000 hour aging at 177°C (350°F) to simulate exposure conditions in an aircraft travelling at supersonic cruise.

TEST PROCEDURE

The parameters for all the bearing strength tests were conducted in displacement control, at a rate of 1.41×10^{-3} cm /sec (5.54×10^{-4} in/sec), using the compression test set-up. Also, all of the composite specimens were tested without any clamp up. By not clamping up the composite, the results presented are the natural bearing strength of the composite and provide a worst case scenario for the composite joint.

Two aging conditions were tested: (1) as received and (2) 10,000 hour (1.1 years) aging at 177°C (350°F). At least three UBS tests were conducted per aging condition at each temperature and the results of the UBS tests were averaged.

The original failure criteria for all composite joint testing was 4%, or 0.038 cm (0.015"), permanent bolt hole elongation, as per Mil-Handbook-5. During the first ultimate bearing strength (UBS) tests, it became clear that maximum load was reached well before the bolt hole permanently elongated 0.038 cm (0.015"). The permanent bolt hole elongation at failure as approximately 0.023 cm (0.009"), well below the 4% permanent hole elongation failure criterion. Therefore, failure in the UBS tests was redefined at the maximum load.

The bearing fatigue failure criterion was based on the failure displacement observed during ultimate bearing strength (UBS) testing. To ensure that the fatigue specimens had failed, an additional 0.03 cm (0.01") was added to the 0.07 cm (0.03") overall, not permanent, UBS failure displacement to determine the fatigue failure criteria of 0.1 cm (0.04") of displacement. All of the fatigue tests were duplicated (2 tests at each condition).

RESULTS AND DISCUSSIONS

Ultimate Bearing Strength

Ultimate bearing strength (UBS) tests were run on IM7/PETI-5 unaged and aged at 177 $^{\circ}$C (350 $^{\circ}$F) for 10,000 hours. UBS tests were run at elevated temperature, room temperature, and low temperature to determine the effect of testing temperature and aging on the strength of the composite.

All bearing stresses were calculated using equation 1

$$\sigma_b = \frac{P}{td} \qquad (1)$$

where P = load   t = thickness   d = hole diameter.

UBS tests run on aged and unaged IM7/PETI-5 reveal that the UBS is unaffected by 10,000 hours aging regardless of the test temperature. The results of the UBS tests are shown in Figure 3. The UBS in all three cases was slightly higher in the unaged case, but the greatest observed difference between the two was 5%, which occurred at low temperature. At room temperature, there was virtually no difference, within 1%, and at elevated temperature, there was only a 3% difference. Thus the UBS of IM7/PETI-5 is unaffected by 10,000 hour elevated temperature aging between -50°C (-58°F) and 177°C(350°F).

While aging did not affect the UBS of IM7/PETI-5, temperature did affect the UBS. As expected, the room temperature UBS was higher than the elevated temperature UBS. For both the unaged and aged composites, the elevated temperature UBS dropped 20-25% compared to the room temperature UBS. This reduction in bearing strength was primarily due to matrix softening at elevated temperature. However, at low temperature, the UBS of IM7/PETI-5 increased 3-5% compared to the room temperature. This increase in UBS is consistent with the results of other composite systems at low temperature.

While the UBS was not greatly affected by low temperature, the failure mode was greatly affected by low temperature. A number of bearing stress vs. displacement curves for room temperature (RT) tests and low temperature (LT) tests are shown in Figure 4.
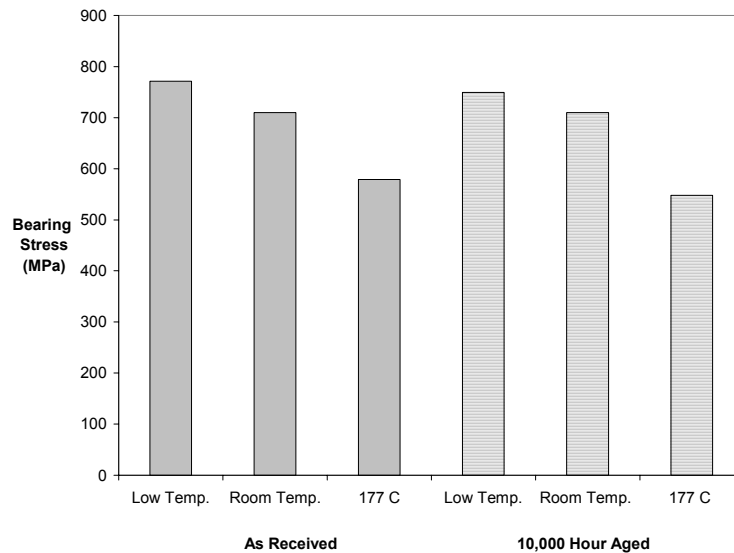
Figure 3 – Effect of Temperature on the UBS of IM7/PETI-5

Notice how much the load drops for the low temperature tests after bearing failure compared to the room temperature data. After failure, the load carrying capability of the composite tested at room temperature dropped about 20%. For the composites tested at low temperature, the load carrying capability dropped about 50% and in some cases as much as 80%. This large drop in load carrying capability after failure at low temperature is due to the brittle nature of the matrix material at these low temperatures. The resulting delaminations due to bearing failure are much more extensive at the low temperatures. was caused by delaminations. The damage on the free edge is extensive. Large cracks on each side propagate from the bolt hole to the specimen edge. During testing, this splitting of the specimen was audible. The damage on the free edge of the failed elevated temperature, room temperature, and low temperature specimens is shown in Figure 5.
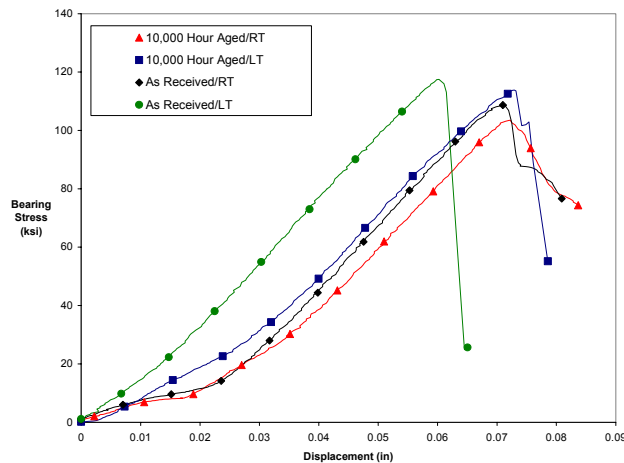
Figure 4 – Comparison of low temperature and room temperature stress vs. displacement curves.

Fatigue Behavior

To determine the effect of aging on the bearing fatigue life of the composite joint, fatigue tests were run on 10,000 hour aged material and compared to fatigue results of as received material. All the tests were run on IM7/PETI-5 material at 177°C (350°F), 10 Hz, and R=0.1. The results of the 10,000 hour aged and as received fatigue tests are shown in Figure 6.

4
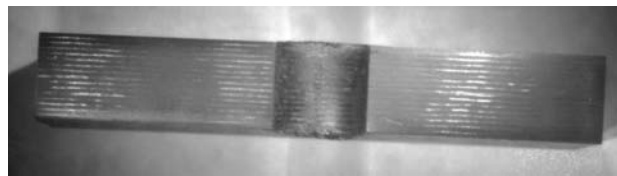
(a) Elevated Temperature
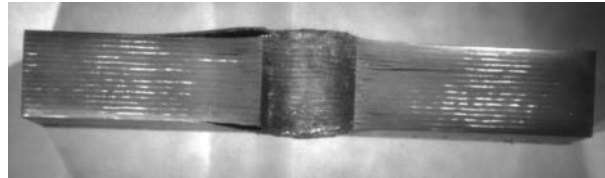
(b) Room Temperature

(c) Low Temperature
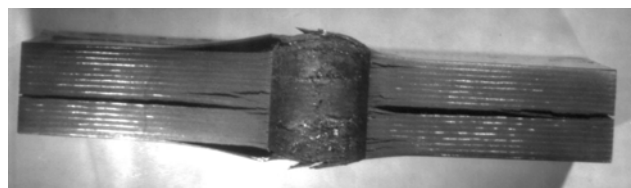
Figure 5 – Free Edge of the Failed UBS Specimens
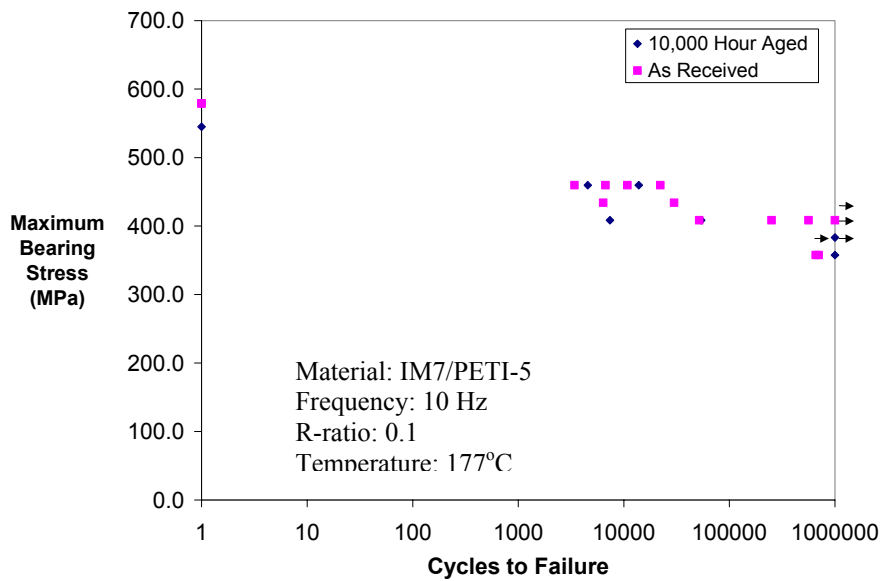
Figure 6 Aging Effect on fatigue

The results of the 10,000 aged and as received fatigue tests show that the fatigue lives of both materials fall in the same general area on the S-N plot with neither data set forming individual scatter bands. The run-out stress level for aged material was around 400 MPa (58 ksi), which is similar to that for the as received material. Therefore, aging up to 10,000 hours does not affect the bearing fatigue life of IM7/PETI-5.

SUMMARY

IM7/PETI-5 composite material with 64 plies in a quasi-isotropic lay-up were tested in static bolt bearing to determine the ultimate bearing strength, UBS, and under fatigue loading. Bearing strength tests were conducted at room temperature (RT), 177°C (350°F), and −50°C (-65°F) while all

fatigue tests were conducted at 177°C (350°F). Some of the specimens had experienced thermal aging up to 10,000 hours at 177°C prior to testing. The following conclusions were reached:

1. IM7/PETI-5 composite materials experienced no decrease in UBS after 10,000 of thermal aging at 177°C (350 °F).
2. IM7/PETI-5 composite materials experience a 26% reduction in UBS when tested at 177°C (350 °F) compared to room temperature.
3. IM7/PETI-5 composite materials showed a small increase in UBS when tested at –50°C (-58 °F) compared to room temperature data. However, the bearing failures at cold temperature were much more dramatic, resulting in much more local delamination/damage. This was attributed to the matrix material being much more brittle at the low temperatures.
4. Fatigue performance was not significantly influenced by thermal aging at 177°C (350°F) for 10,000 hours.

The IM7/PETI-5 composite material has been shown to retain significant UBS and fatigue performance at elevated temperature and long term thermal aging at 177°C. Thus IM7/PETI-5 is an excellent candidate for long term structural applications at temperature. However one must be aware of the reduction in interlaminar toughness that result in some very dramatic failure under bolt bearing at low temperatures.

ACKNOWLEDGEMENT

REFERENCES

1. Counts, W.A., Johnson, W.S., "Bolt bearing fatigue of polymer composites at elevated temperature," submitted to the *International Journal of Fatigue*, June 2000.
2. Counts, W.A., Johnson, W.S., Jin,O., "Assessing Life Prediction Methodologies of Fasteners Under Bending Loads," *Structural Integrity of Fasteners: Second Volume, ASTM STP 1391*, P.M. Toor, Ed., American Society for Testing and Materials, West Conshohocken, PA., pp.3-15.
3. Counts, W.A., Johnson, W.S., "Evaluation of Bolt Bearing Creep Behavior of Highly Loaded Composite Joints at Elevated Temperature," *Journal of Composite Technology and Research*, Soon to be published.
4. Counts, W. A. and Johnson, W. S. Johnson, "Temperature Effect on Ultimate Bearing Strength of Polymer Composite Joints," submitted to the *Journal of Composites Technology and Research*, Dec. 2000.
5. Wang, H.S., Hung, C.L., Chang, F.K., "Bearing Failure of Bolted Composite Joints. Part I: Experimental Characterization," *Journal of Composite Materials*, Vol. 30, 1996, pp. 1284-1313.
6. Eriksson, I., "On the Bearing Strength of Bolted Graphite/Epoxy Laminates," *Journal of Composite Materials*, Vol. 24, 1990, pp. 1246-1269.

Temperature Dependence of Damage Behavior in a Silicon Nitride for Gas Turbine by Spherical Particles

Yoshio Akimune[1],   N. Tooyama[1], F. Munakata[2]. N. Hirosaki[3]

[1]Agency of Industrial Science and Technology, Tsukuba-city, Japan
[2]Nissan Motor Co., Ltd., Yokosuka-city, Japan
[3]National Institute for Research of Inorganic Materials, Tsukuba-city, Japan

ABSTRACT

Model experiment for examining impact damage dependence on temperature is conducted on silicon nitride. It was found that steel and zirconia(PSZ) spheres caused Hertzian cone crack, resulting from the elastic response of the material in accordance with the Hertzian cone crack theory at the room temperature. In contrast, alumina and sialon spheres induced both median-radial crack system at low impact velocity range and Hertzian cone crack at high impact velocity range.

At the elevated temperature, the experimental results indicate that a generated crack system changes from a Hertzian cone crack to median crack in accordance with the experimental temperature change for the case of PSZ spheres. It is explained that the hardness degradation at $1200℃$ generated a change in the stress field from elastic/plastic to plastic, resulting from softening of grain boundary glassy layer for silicon nitride. We can conclude response behavior change in the relation of Ht/Hp ratio caused by temperature change.

KEY WORDS
Impact Damage, Elastic Response, Elastic/Plastic Response, Hertzian Cone Crack, Median Crack, Silicon Nitride

1. Introduction

It has been known that in ceramics, owing to its brittle nature, cracks extended under localized load or stress may trigger instantaneous fracture. A typical example of this effect is fracture in a

ceramic blade of gas turbine caused by impact of oxide scale particles, which has been recognized as one of serious problems [1,2].

For impacts of the same types of impacting particles, the response behavior and failure behavior of a ceramic target are reported to relate to the properties of the target material such as its hardness [3,4]. Studies have also been presented which described differences in damage behavior according to two types [2] and three types of impactors [4]. The relationship between damage under the impact site and material properties of the impactors and target has not been fully explored. Shockey et al.[5] have used a silicon nitride (Si_3N_4) specimen with a tungsten carbide (WC) spheres, and demonstrated elastic repulsion remaining ring cracks on the surface at the room temperature, which turned into elastic-plastic response impressing radial cracks on the surface at high temperatures, however, they did not mention about internal cracks.

The present study concerns a model experiment in which oxide scales striking at the turbine blade are simulated by four types of particles shot to Si_3N_4 specimen at the room temperature and by zirconia particle at 1200℃. In this way, the temperature dependence of impact damage is evaluated by comparing damage morphology at the room temperature with that at 1200℃.

2. Experiment on Impact Damage with Particles

2.1 Materials Preparation

Commercially available gas-pressure-sintered silicon nitride (EC152: NGK Spark Plug Co., Ltd.: Komaki, Japan) was used in this study. Steel, partially stabilized zirconia (PSZ: Toso Co.,Ltd., Tokyo, Japan), alumina (Shinagawa Refractories Co., Ltd., Tokyo, Japan), and sialon (Shinagawa Refractories Co., Ltd., Tokyo, Japan) spheres 1.0 mm in diameter, the size used in the literature [4], were used as impactors. Silicon nitride specimens, 50x8x3 mm, were polished with diamond paste [6 μ m and 3 μ m] to obtain flat and parallel surfaces by eliminating machining damage. The material properties are listed in Tables 1 were taken from suppliers catalogs.

A disk-shaped specimen of 14 mm diameter and 2.0 mm thickness was used for high temperature test. And its surface was polished with diamond paste [6 μ m and 3 μ m] to eliminate machining damage.

2.2 Particle Impact Experiment

The experimental apparatus used a helium gas pistol and the test procedure was almost the same as that described in the literature[6]. The velocity was measured at each sabot firing based on the time-of-flight principle using piezoelectric sensor. The impact damage was examined by means of the fluorescence flaw detection, followed by morphological observation of surface craters and internal cracks under an optical microscope and by measurement of crater diameter and depth by use of a needle-probe profilometer.

A schematic diagram of the impact apparatus is shown in Fig. 1, which consists of a particle launcher of gas-gun type and a specimen holder installed in a furnace [7]. A target, Si_3N_4 disk, is mounted in the specimen holder within the furnace and the same impact test was conducted at 1200℃. As an impact sensor cannot be used in the high temperature experiment, the impact velocity is to be read from a working curve with velocity calibrated against helium gas pressure. In the

present experiment, the impact velocity was available in 500 m/s.

3. Experimental Results

3.1 Surface Damage and Internal Crack

With the steel spheres and PSZ spheres Hertzian cone cracks (Fig. 2B) were initiated high impact velocity range over 330 m/s & 383m/s, respectively. Although   alumina and sialon (Figures 2C, 2D) spheres produced Hertzian cone cracks in the   high impact velocity range (>500m/s), two types of cracks were observed at intermediate impact velocities (300-500m/s) depending on the response behavior. Median/radial crack (Fig. 3) caused by elastic/plastic behavior [8,9] were observed in the low impact velocity range (<300m/s).

In view of materials parameters   listed in Table 1, the ratio of target hardness (Ht) to particle hardness (Hp) for steel and zirconia spheres, i.e., Ht/Hp, is >1.25, which is within a range to produce elastic response. The ratio(Ht/Hp) of sialon and alumina, its become less than 1.0, response behavior becomes elastic-plastic response with median crack formation.

On the other hand, when the target was impacted with particles at 500 m/s velocity and at 1200℃, the surface damage consisted of a porous zone and radial cracks (Fig. 4 (A)), while the internal crack was composed of median crack (Fig. 4 (B)) representing the elastic-plastic response. According to the parameter list in Table 1, the ratio Ht/Hp was 0.75, falling in a range of elastic-plastic response (Ht/Hp < 1.0) [5,7].

3.2 Measurement of Impact Damage to Define Response Behavior

3.2.1 Crater Diameter

The morphology of impact damage at the surface of the target was measured by   using a needle-probe profilometer.(Fig.5) The good   agreement of experimental values at the room temperature with theoretical   ones suggests a state of contact where the materials give elastic response.   At 1200℃, however, the crater size was somewhat greater than the   calculated values, which may be attributed to larger contact diameter associated with deeper penetration of spheres into the materials. The   calculation formula derived from Hertz's theory is as shown below [10],

$$D_a = 2R(5 \pi V^2 \rho k/4)^{1/5} \qquad (1)$$

where D_a stands for contact diameter [m], k is given by $k = (1 - \nu_1^2)/E_1 + (1 - \nu_2^2)/E_2$ [GPa^{-1}], ν_1 is Poisson's ratio of target material, ν_2 Poisson's   ratio of sphere, R is sphere diameter (= 500 μ m), E_1 is Young's modulus of target material, E_2 Young's modulus of sphere (listed in Table 1), ρ is density of sphere (ρ =6.05 x 10^3 kg/m^3), and V is impact velocity of   sphere.

3.2.2 Crater Depth

The crater depth was 1 to 4 μ m at the room temperature, while that at 1200℃ was 8 to 13 μ m (Fig. 6). Data at the room temperature demonstrates   experimentally the occurrence of plastic deformation, though as small as a   few μ m, in contradiction to Hertzian contact theory, where no plastic change is admitted. While a small plastic deformation may affect the elastic stress field [5], the agreement of ring crack morphology at the surface with the contact area shown in Fig. 5 suggests

the formation of elastic stress field   just like that predicted from the theory.

On the other hand, the morphology of internal crack at high temperatures (median crack) indicates that the spherule penetrates into the materials by 8 to 13 μ m in the course of time from coming in contact with the surface to   collapse of sphere, probably owing to softening of glassy phase at the grain boundary of materials. Consequently, the materials take elastic-plastic stress state, forming a median crack and a porous zone   immediately below it with intersecting micro-cracks [11].

4. Response Behavior depending on Temperatures

The Hp/Ht ratio [3] determines   the response behavior. Elastic response occurred when the ratio was less than 0.8, and both elastic/plastic and elastic responses occurred when it was over 1.0. Response behavior changed according to the   Hp/Ht ratio and impact velocity. These ratios differed from the values cited in the literature [4,5], but as suggested by Cook and Pharr [12] crack and damage morphologies are completely material dependent and correlate closely with the ratio of Young's modulus and hardness.

At high temperatures, as the hardness of materials is reduced, resulting in Ht/Hp ratio smaller than 1.0 median cracks are formed through the elastic-plastic rebound. This effect may be attributed to change in the response behavior of materials softened at high temperatures, into which a sphere of room temperature is shot (Fig. 7).

5. Conclusion

In the present study, damage caused by the bombardment of ceramic sphere was examined in model experiment of impact caused by oxide scale hitting the   actual turbine blade. It was found that steel and PSZ particles caused Hertzian cone cracks resulting from the elastic response of the material in accordance with the Hertzian contact theory. In contrast, alumina and sialon particles induced median/radial crack systems showing elastic/plastic response in the intermediate velocity range and also induced Hertzian cone cracks resulting from elastic response in the high impact velocity range. When a zirconia sphere was shot into a target of silicon nitride, the damage in the target was Hertzian cone crack at the room temperature, while it turned into median crack at 1200℃. This may be attributed to change in response behavior to impact from elastic to elastic-plastic, owing to reduced hardness caused by softening of glassy phase at the grain boundary of silicon nitride at 1200℃.

References
[1]K. C. Dao, D. A. Shockey, L. Seamon, D. R. Curran, and D. J. Rowcliff, Annual Rep., Part III, Office of Naval Research, Contract No. N00014-76-057, May 1979.
[2]J. Cuccio and H. Fang, " Impact Damage Study of Silicon Nitride," Proceedings of the 26th Automotive Tech. Development Coordination Meeting, Soc. Automotive Engineers, Pa (1988).
[3]Y. Akimune, Y. Katano, and K. Matoba, J. Am. Ceram. Soc., 72[8]1422-28 (1989).

[4]H. Tsuruta, M. Masuda, T. Soma, and M. Matsui, J. Am. Ceram. Soc., 73[6]1714-18 (1990).

[5]D. A. Shockey, D. C. Erlich, and K. C. Dao, J. Mat. Sci., 16, 477-82 (1981).

[6]Y. Akimune, Y. Katano, K. Matoba, pp.1495-1507 in the Proceedings of the 3rd International Symposium of Ceramic Materials and Components for Engines, edited by V. J. Tennery, The American Ceram. Soc., Ohio, 1989.

[7]Y. Akimune, Y. Katano, Y. Okamoto, and N. Hirosaki,J. of Ceramic Soc. Japan,102[11]1042-46(1994)

[8]B. R. Lawn and T. R. Wilshaw, J. Mat. Sci., 10[6]1049-81 (1975).

[9]A. G. Evans and T. R. Wilshaw, J. Mat. Sci., 12, 97-116 (1977).

[10]H. R. Hertz, Hertz's Miscellaneous Papers, Chapters 5 and 6, Macmillan, London, England, 1896.

[11]D. A. Shockey, D. J. Rowcliff, K. C. Dao, and L. Seamon, J. Am. Ceram. Soc., 73, 1613-19(1990).

[12]R. F. Cook and G. M. Pharr, J. Am. Ceram. Soc., 73[4]787-817 (1990).

Table.1. Material Properties

	Si_3N_4		PSZ	Steel	Al_2O_3	Sialon
	RT	1200 °C	RT	RT	RT	RT
Density ($\times 10^3$ Kg/m^3)	3.26	3.26	6.05	7.86	3.88	3.23
Poisson's Ratio	0.25	0.25	0.3	0.3	0.23	0.27
Young's Modulus (GPa)	318	296	200	200	370	320
Vicker's Hardness (GPa)	15.0	9.0	12.0	7	18	16
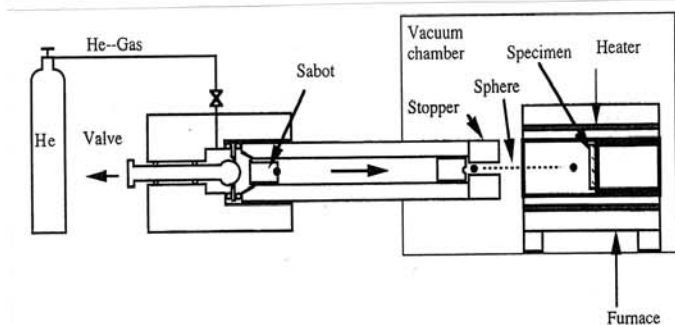
Fig.1.   Experimental apparatus for high temperature test.
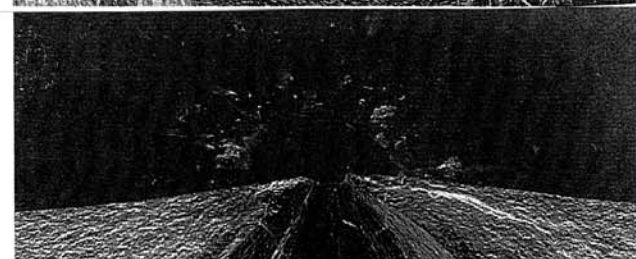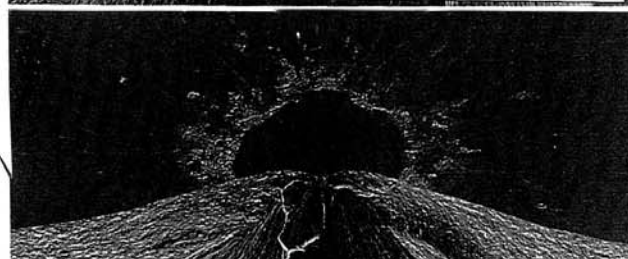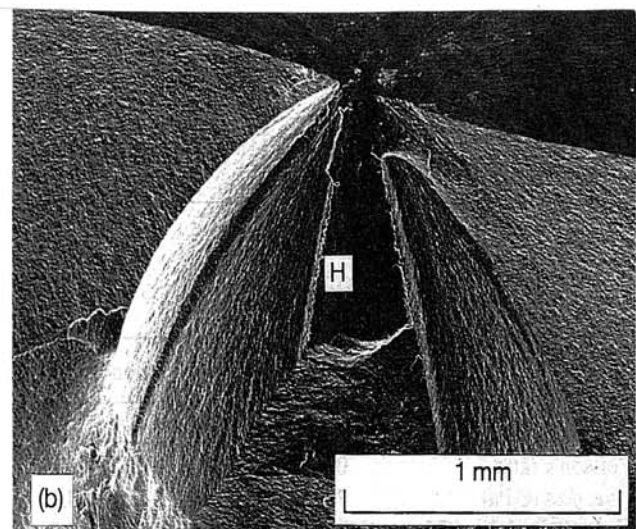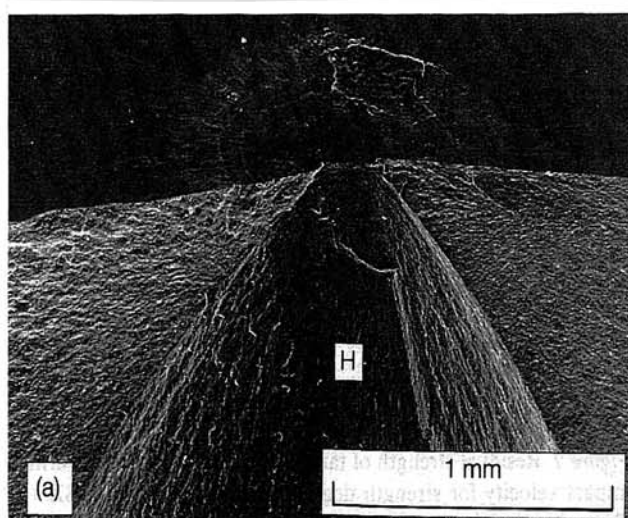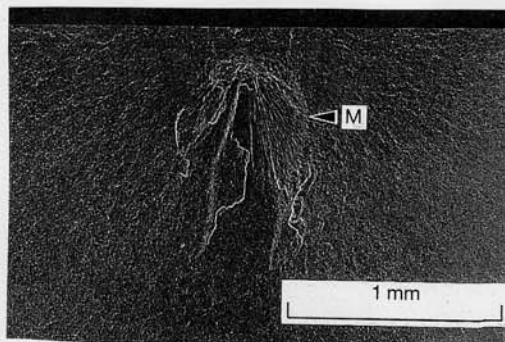
Fig.3.　Medial/Radial cracks
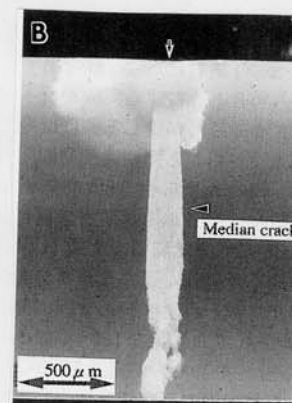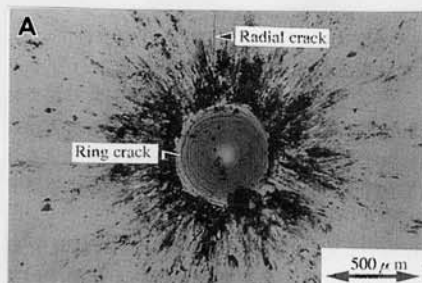
Fig.4.　Surface Damage tested at 1200℃　(A Radial Crack, B: Median cracks)

Fig.5.　Crater Diameter

○Theoretical contact diameter at RT
△Theoretical contact diameter at 1200℃
●Crater diameter at RT
▲Crater diameter at 1200℃
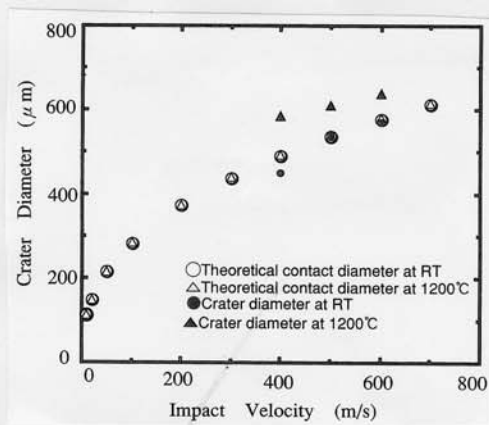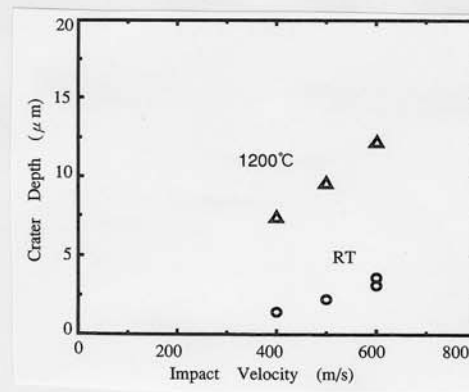
Fig.6.　Crater Depth
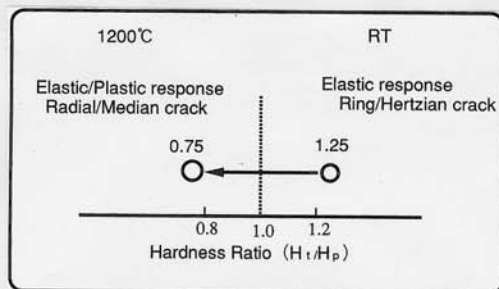
Fig.7.　Response Behavior Change with temperature

TEMPERATURE DEPENDENCE OF FRACTURE TOUGHNESS IN A MICRO-SIZED Ni-P AMORPHOUS ALLOY

R. Tarumi[1], M. Shimojo[1], K. Takashima[1] and Y. Higo[1]

[1] Precision and Intelligence Laboratory, Tokyo Institute of Technology,
4259 Nagatsuta-cho Midori-ku, Yokohama, 226-8503, Japan

ABSTRACT

Temperature dependence of fracture toughness has been studied on micro-sized Ni-P amorphous alloy specimens. The material used in this study was a Ni-11.5wt%P amorphous thin film. The specimens were prepared in a cantilever beam type configuration of dimensions of $10 \times 12 \times 50$ μm^3 by focused ion beam machining. Fatigue pre-cracks were introduced into all the specimens. Temperature was controlled using a newly developed specimen holder from room temperature to 473 K. Compared with room temperature, fracture toughness was increased approximately 36 % at 373 K but decreased 16 % at 473 K. From the transmission electron microscope (TEM) observation, no precipitation of crystalline phase was observed in plastically deformed regions tested at 373 K. Differential scanning calorimetry (DSC) measurement also revealed that no crystallization occurred at a temperature range from 300 to 473 K. From these results it is considered that fracture toughness of an amorphous alloy may be changed due to short or medium range order structural relaxation caused by heating.

KEYWORDS

temperature dependence of fracture toughness, amorphous alloy, micro-sized material, structural relaxation

INTRODUCTION

Microelectromechanical systems (MEMS) are expected to be applied to many industrial fields such as biomedical, semiconductor, telecommunication, aerospace, etc [1]. The size of the components used in these devices will become less than a micron or sub-micron which is smaller than the grain size of conventional crystalline metals. The anisotropic mechanical properties are not negligible, which depends on crystallographic orientation. Furthermore, the mechanical properties of such micro-sized materials are considered to be different from those of bulk materials because of the surface effects. It is therefore unreliable to apply the mechanical properties measured using bulk materials, such as elastic constants, yield stress, fracture toughness, etc., to design the micro-sized machines or MEMS devices. Because of these requirements for micro-sized materials, direct measurements of mechanical properties on micro-sized materials are essential for practical applications of such MEMS devices.

Amorphous alloys have high strength and isotropic mechanical properties because of the absence of long range ordering [2]. Thus it is expected to be used as a structural material for micro machines or MEMS devices. Several mechanical properties such as fracture toughness [3], fatigue life and crack growth properties [4] and corrosion fatigue properties [5] of a micro-sized amorphous alloy have already measured by our group at room temperature. In particularly, fracture toughness is one of the most important parameters to design actual micro-sized machine or MEMS devices. The case of practical applications, however, temperature is considered to be increased. Amorphous alloys are in a thermally non-equilibrium and meta-stable state so that structural relaxation (including crystallization) may occur with increasing temperature [6-8]. Structural relaxation may change the fracture toughness of amorphous alloys. The dependence upon temperature of fracture toughness, however, has not been measured even though temperature in such micro machines may increase under practical applications. In this study, temperature dependence of fracture toughness on micro-sized amorphous alloy has been investigated with a temperature range from 300 K to 473 K. Furthermore, structural changes in plastically deformed regions were also investigated using a transmission electron microscope (TEM).

EXPERIMENTAL PROCEDURE

The mechanical testing machine used in this study was micro fatigue testing machine (MFT2000), which can apply static and cyclic loading. The specimen can be positioned with an accuracy of 0.1 µm using a precise X - Y stage. The load resolution is 10 µN, and the displacement resolution is 5.0 nm.

The material used in this study was a Ni-P amorphous thin film prepared by electro-less deposition on an Al-Mg based substrate. This material has been used for hard disk substrates. This material is mass-produced with uniform quality. The roughness of the surface is in the order of nano-meters. From these features, this material is considered to be one of the suitable materials for the testing of micro-sized material. Crystallization temperature of this material was 639.5 K, which was determined from a differential scanning calorimetry (DSC) measurement at a constant temperature increasing rate of 20 K/min.

The amorphous thin film was separated from a substrate using an NaOH aqueous solution. This material was cut mechanically into a semicicular disk with a diameter of 3.0 mm. Micro-sized cantilever beam type specimens were prepared near the straight edge of the semicircular disk using a focused ion beam (FIB) machine. Figure 1 shows a scanning electron microscope (SEM) image of the specimen observed from the thickness direction (B) of the specimen. The dimensions of the specimens were 50 (l)×10 (W)× 12 (B) µm^3. A notch was introduced into each specimen by FIB machining with a notch tip radius of 0.25 µm. The distances of loading point and notch point were 30 µm (L) and 10 µm from the root of the specimen, respectively. According to our previous study [9], it is necessary to introduce a fatigue pre-crack for fracture toughness measurements because the notch tip radius (=0.25 µm) is not sufficiently small. It is therefore fatigue pre-crack was introduced into all the specimens, using an MFT2000 at a constant ÄK of 2.0 MPa m and a cyclic frequency of 10 Hz.

Fracture toughness, K, of the cantilever beam type specimen can be calculated from the following equation.

$$K = \frac{6PL}{W^2 B} \sqrt{p\,a}\ F(a/W), \quad (a/W < 0.6) \tag{1}$$

where,

$$F(a/W) = 1.22 - 1.40(a/W) + 7.33(a/W)^2 - 13.08(a/W)^3 + 14.0(a/W)^4 \qquad (2)$$

In eq. (1), a represents the crack length and P represents the load at which crack started to propagate.
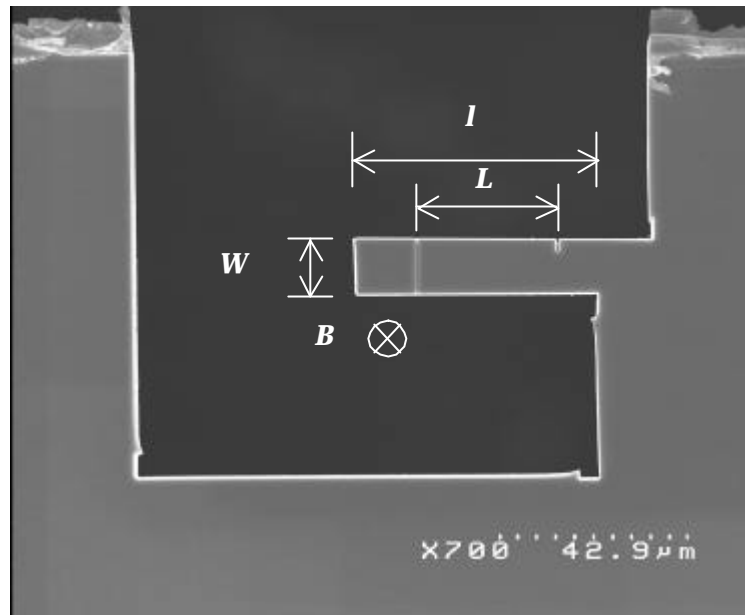
Figure 1 SEM image of a micro-sized cantilever beam type specimen prepared by FIB machining observed from the thickness direction of the specimen.

Fracture toughness measurements were also performed using the MFT2000 in laboratory air. Bending stresses were applied at a loading point with a constant displacement rate of 22 μm/min. The temperature of the specimen was controlled using newly developed special heating equipment installed in the specimen holder of the MFT2000. This heater can control the temperature of the specimen up to 773 K. After the fracture toughness measurements, scanning electron microscope (SEM) and transmission electron microscope (TEM) observations were performed to investigate the shape, fracture surface and structural changes of the specimens.

RESULTS AND DISCUSSION

Figure 2 shows a SEM image of a specimen after the fracture toughness measurement at a temperature of 473 K. It was confirmed from this figure that specimen was failed at the notch position. It was confirmed that other specimens were also failed at the notch position. Figure 3 shows a fracture surface of the specimen tested at 473 K. In front of the notch introduced by FIB machining, flat fracture surface was observed. From the high magnification observation, the formation of striations was observed in front of the notch. The formation of striations was also observed in other specimens. These results indicate that fatigue pre-cracks were introduced into all the specimens.

From the SEM observation a vein pattern [10], a typical fracture surface of amorphous alloys, was clearly observed in the fracture surfaces of all specimens. Moreover, on both sides of the fracture surfaces, the formation of shear lips were observed. This result indicates that the plane strain dominant region existed even in the micro-sized specimen.
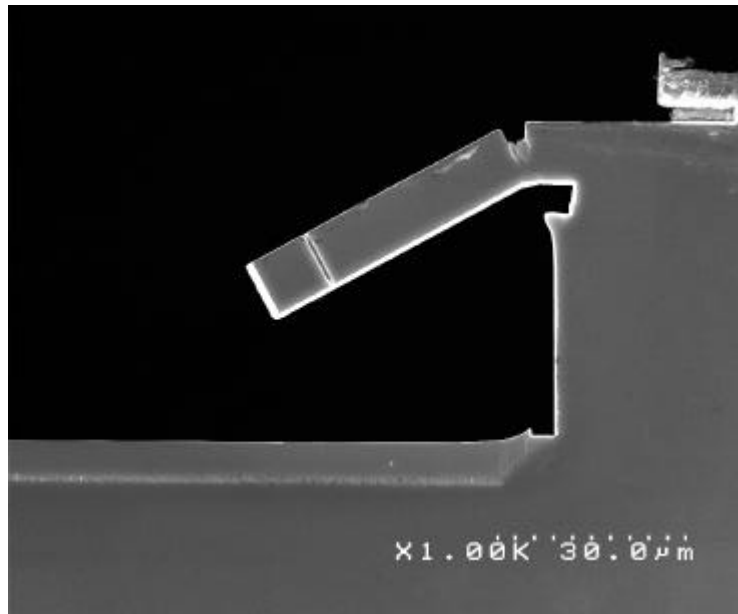
Figure 2 SEM image of micro-sized cantilever beam type specimen after the fracture toughness test observed from the thickness direction of the specimen.
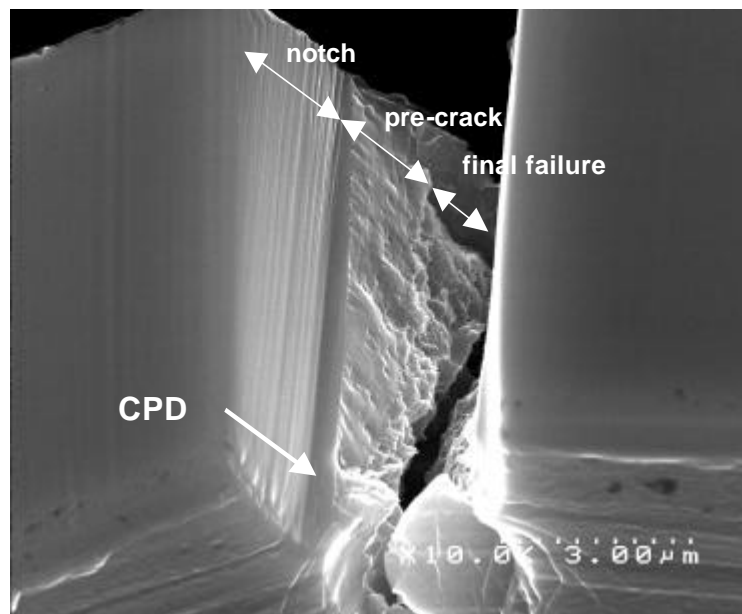
Figure 3 SEM image of fracture surface of the specimen tested at 473 K. Formation of fatigue pre-crack was confirmed in front of the notch tip. CPD in the figure indicates the crack propagation direction.

Figure 4 shows the load and displacement curves obtained at temperatures of 373 and 473 K. The maximum bending load (P_{max}) was 7.82 and 6.06 mN for 373 and 473 K, respectively. Correct value of P at which crack started to propagate could not be determined. Thus, the maximum load values in load and displacement curves were employed for the fracture toughness calculation.
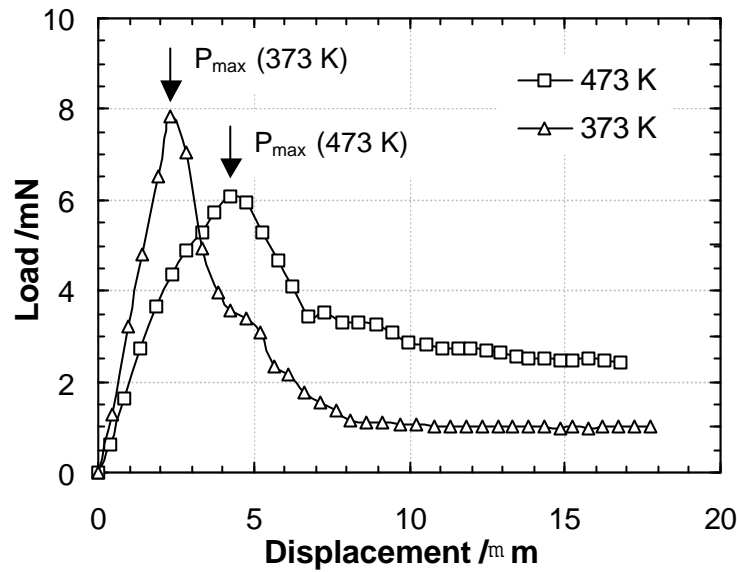
Figure 4 Load and displacement curve obtained at temperatures of 373 and 473 K. The maximum load values were employed for the calculation of fracture toughness.

Temperature dependence of fracture toughness calculated from eq. (1) is shown in fig. 5. In this figure, fracture toughness at room temperature is plotted [3] for the comparision. Measured fracture toughness at a room temperature was 4.33 MPa m. The measured fracture toughness at 373 K was 5.89 MPa m, which is approximately 36 % higher than that at room temperature. On the contrary, at 473 K, fracture toughness was only 3.71 MPa m, which is approximately 14 % smaller than that at room temperature. In the case of this amorphous alloy, fracture toughness does not increase with increasing temperature.
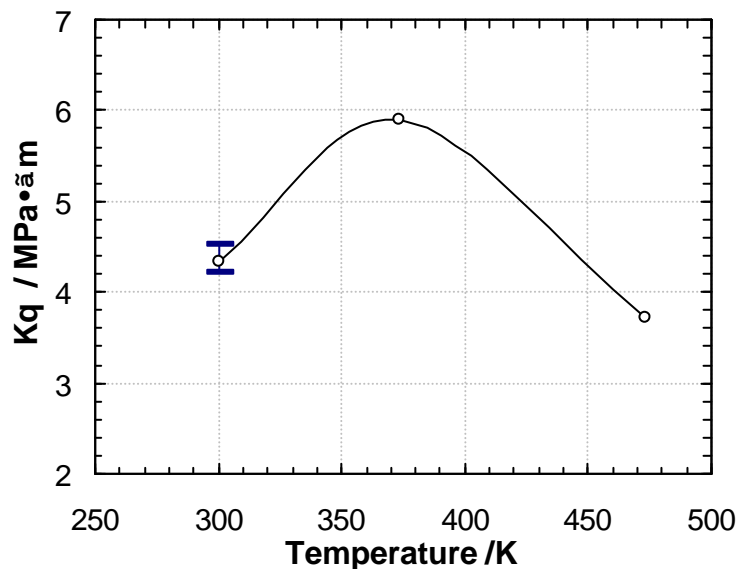
Figure 5 Temperature dependence of fracture toughness calculated from the eq. (1).

To investigate the reason for the abnormal temperature dependence of fracture toughness, TEM observation was performed on the plastic deformed region tested at 373 K. However, no precipitation of crystalline phase was observed. According to the DSC measurement, no heat flow was observed from 300 to 473 K. This result indicates that only the short or medium range structural relaxation was occurred in this temperature range. From these results it is considered that fracture toughness of an amorphous alloy may be changed due to short or medium range order structural relaxation caused by heating.

CONCLUSIONS

Temperature dependence of fracture toughness on a micro-sized amorphous alloy has been investigated at a temperature range from 300 to 473 K. Compared with room temperature, fracture toughness increased approximately 36 % at 373 K, but decreased approximately 14 % at 473 K. The reason for the abnormal temperature dependence of fracture toughness is considered to be caused by the structural relaxation of the amorphous alloy.

REFERENCES

1. S.M.Spearing, Acta Mater. (2000) 48 179
2. A.Inoue, Acta Mater. (2000) 48, 279
3. A.Ogura, Y.Ichikawa, M.Shimojo, K.Takashima, Y.Higo and M.V.Swain, (2000) Proc. 3rd Int. Conf. and Poster Exhibition Micro Materials, 547
4. K.Takashima, S.Maekawa, Y.Ichikawa, M.Shimojo, Y.Higo, S.Sugiura and M.V.Swain (2000) Proc. 3rd Int. Conf. and Poster Exhibition Micro Materials,526
5. Y.Mizutani, Y.Higo, Y.Ichikawa, A.Morita, K.Takashima, (2000) MRS 2000 fall meeting Abst., 574
6. A.I.Taub and F.Spaepan, (1980) Acta Metall. 28, 1781
7. A.van den Beukel and S.Radelaar, (1983) Acta Metall. 31, 419
8. V.A.Khonik, A.T.Kosilov, V.A.Mikhailov and V.V.Svirdov, Acta Metall. (1998) 46, 3399
9. K.Takashima, S.Maekawa, M.Shimojo, Y.Higo, M.V.Swain, (1999) Materials Research Society 1999 Fall Meeting Abst., 682
10. S.Takayama and R.Maddin, (1975) Phil. Mag. 32, 457
11. M.L.Sui, K.Lu and Y.Z.He, (1991) Phil. Mag. B 63, 993

TENSILE AND FATIGUE FRACTURE OF DISCONTINUOUSLY REINFORCED ALUMINUM (DRA)

N. Chawla, J.J. Williams, G. Piotrowski, and R. Saha

Department of Chemical and Materials Engineering
Arizona State University
Tempe, AZ 85287-6006, USA

ABSTRACT

The tensile and fatigue fracture processes in discontinuously reinforced aluminum (DRA) are described in this paper. In tension DRA exhibits planar fracture of the brittle reinforcement particles and ductile microvoid growth and coalescence in the aluminum matrix. Particle strength, strength of the particle/matrix interface, and matrix strength control the tensile behavior of the material. Fatigue fracture is controlled by surface defects and rogue-inclusions, particularly if they are larger than the reinforcement particle size. At elevated temperature, creep-fatigue interactions contribute to an enhancement in damage, particularly in the form of diffusion-assisted void growth and cavity formation.

KEYWORDS

Tension, fatigue, fracture, metal matrix composite, discontinuously reinforced aluminum.

INTRODUCTION

Discontinuously reinforced aluminum (DRA) alloys provide significantly enhanced properties over conventional monolithic aluminum, such as higher strength, stiffness and fatigue resistance, while still maintaining weight savings over other structural materials [1-4]. While continuous fiber reinforcement provides the most effective strengthening (in the direction of the reinforcement), particle reinforced composites are more attractive because of their cost-effectiveness, isotropic properties, and their ability to be processed using similar technology used for monolithic materials. In this paper, we provide an overview of the fracture behavior of discontinuously reinforced aluminum, with an emphasis on the tensile and fatigue fracture behavior of particle reinforced systems.

TENSILE FRACTURE

The reinforcing phase in DRA, typically a ceramic, is much stiffer than aluminum. Thus, a significant fraction of the applied load is initially borne by the reinforcement, by load transfer from the matrix. Since the ceramic phase has a much lower strain to failure than the metal matrix, the particles will fracture prior to failure of the composite, provided that the particles have a critical aspect ratio for load transfer to take place. If the particle/matrix interface is weak,

1

however, interfacial debonding and particle pullout is the preferred damage mechanism. The incorporation of particles in the matrix also results in an increase in "apparent work hardening." The term "apparent" is used here because the higher observed work hardening rate is a simple function of lower matrix volume (by incorporation of the particles) and not necessarily due to a change in work hardening mechanisms. Thus, the higher work hardening rate observed in the composites is due to geometric constraints imposed on the deformation of the matrix by the presence of the reinforcement. When the matrix is significantly work hardened, the matrix is placed under a very large degree of constraint with an inability for strain relaxation to take place by deformation. This causes the onset of void nucleation and propagation, which take place at a lower far field applied strain than that observed in the unreinforced material.

Figure 1 shows the mating surfaces obtained after tensile fracture of an Al-Cu-Mg (2080)/SiC/20$_p$-T6[1] composite (average particle size of 23 µm). The SiC particles fracture in a planar, brittle fashion, while evidence of microvoid growth and coalescence is observed in the matrix. Notice that the particle/matrix interface remains intact, indicating that the shear strength at the interface was higher than the particle tensile strength. Due to the angular nature of the particles, mating fracture surfaces must be observed to ensure that particle fracture did indeed take place.
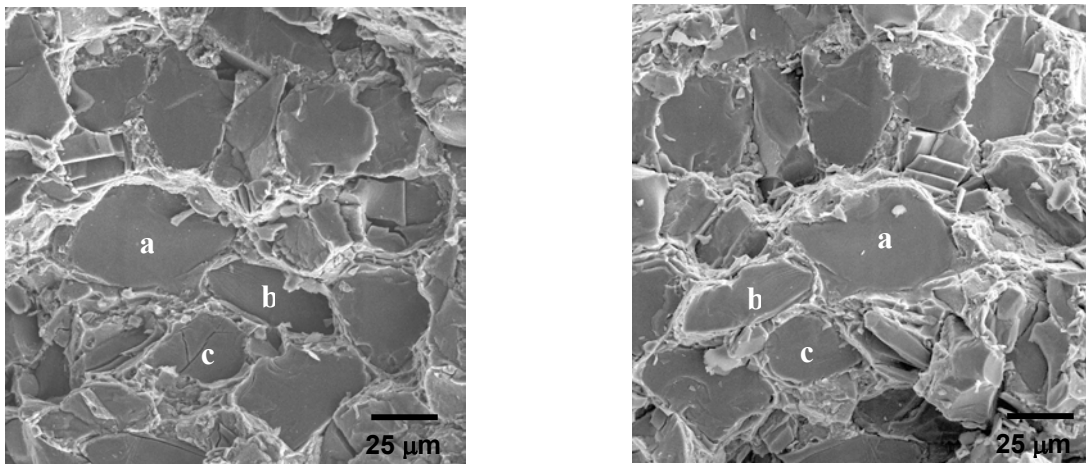
Figure 1: Tensile fracture in DRA. Planar fracture is observed in the particle, accompanied by ductile fracture in the matrix. Mirror images from mating surfaces are shown. The letters indicate examples of mating particles.

Table I shows the tensile strength and fraction of particles pulled-out, for a given particle size and matrix aging treatment. It is well known that the strength of ceramics is controlled by flaws, and that the probability of a strength-limiting flaw being present increases with material volume. Thus, the larger the particle size, the lower the particle strength, and the lower the ultimate tensile strength of the composite. It is interesting to note, however, that particle size itself does not completely control the ultimate tensile strength of the composites. This is readily apparent by the significant decrease in composite strength with severity of overaging, for a given particle size. The rate of strength decrease with overaging is almost identical for both composites. Clearly, as the matrix becomes weaker, dislocation bypass of the precipitates in the matrix

---

[1] We follow the standard notation for metallic composites designated by the Aluminum Association. The matrix alloy is followed by the reinforcement composition. The latter is denoted as a particulate reinforcement by the subscript 'p.' The volume fraction can also be introduced in this notation followed by the heat treatment, e.g. 2080 matrix reinforced with 20% SiC, peak-aged, would be denoted as 2080/SiC/20$_p$-T6.

becomes more predominant, and void nucleation and matrix tearing take place at lower applied stresses.

Table I. Effect of Particle Size and Overaging on Tensile Strength and Particle Fracture Characteristics of 2080/SiC/20$_p$-T8 Composites

Average Particle Size	Aging Treatment	Tensile Strength (MPa)	Fraction of Particles Pulled-out (%)
6 μm	T8-peakage	576	7.8
6 μm	peak + 24 h at 200°C	489	8.5
6 μm	peak + 24h at 225°C	410	9.5
23 μm	T8-peakage	484	5.7
23 μm	peak + 24h at 200°C	414	5.1
23 μm	peak + 24h at 225°C	348	5.6
23 μm	peak + 24h + 250°C	290	5.5

A very small fraction of particles is pulled out in both composites. Since the particle strength is lower than the interface strength, particle fracture will take place first and particle pullout will not be predominant. With an increase in particle strength (a decrease in particle size), a larger fraction of the particles will have a higher strength than the interfacial strength, so a slightly larger fraction of particles are pulled out. It is interesting to note that the extent of pullout does not change significantly with severity of overaging, indicating that, while the matrix strength is lowered significantly, that the interfacial bond strength remains relatively unchanged. It should be noted that the fraction of fractured particles decreases significantly with an increase in distance from the fracture surface [5]. This can be attributed to the large local plastic strain on the fracture plane [6]. A slight overestimation of the extent of particle fracture may take place since the crack takes a path of least resistance resulting in a non-planar fracture surface. Recent results from polished cross-sections taken from the center of the gage section of the tensile specimens, however, indicate that while the extent of particle fracture is significantly reduced immediately below and with increasing distance from the fracture plane, the trends are consistent with those shown in Table I [5].

FATIGUE FRACTURE

Ambient temperature fatigue fracture

Fatigue fracture in monolithic alloys is typically controlled by defects or inclusions, often at the surface of the material [7]. This phenomenon is also quite prevalent in DRA [8-11]. Processing-related defects in the form of exogeneous inclusions (frequently Fe-rich) or particle clusters play a significant role in controlling fatigue strength, particularly when the inclusion is much larger than the SiC particle size. The rogue inclusions act as stress concentrators that increase the local stress intensity in the material and promote easy crack nucleation. Crack initiation during fatigue takes place at these defects, which are typically located at the surface of the specimen, Fig. 2. This is because inclusions at the surface are more highly stressed than inclusions completely within the matrix, so a higher stress concentration and, thus, higher probability for crack initiation is present
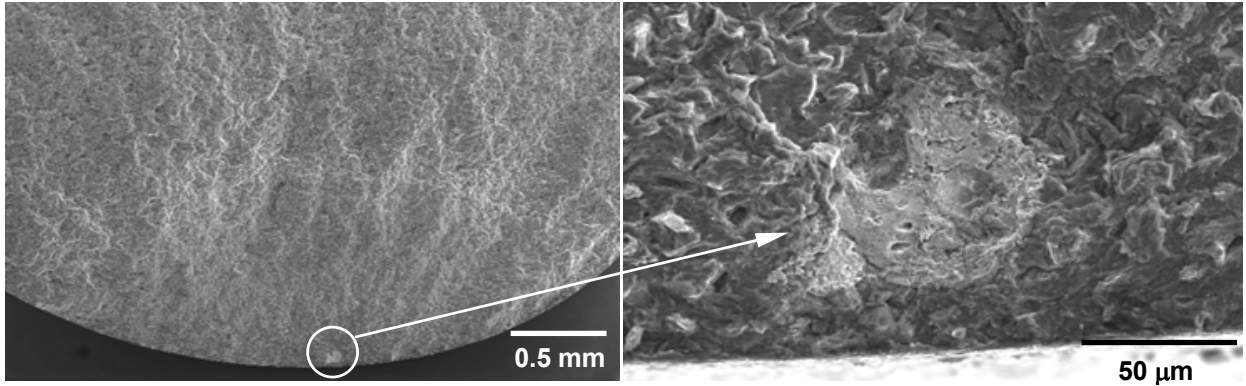
Figure 2: Fatigue fracture in DRA. Crack initiation takes place at rogue inclusions, primarily at the specimen surface.

at the surface. A given inclusion in the composite, however, will be subjected to a lower stress than in the unreinforced alloy, due to "load sharing" by the reinforcement particles. In extruded materials, the overall size of inclusions is also lower in composites since the ceramic reinforcement particles break the brittle inclusions into smaller sizes during extrusion.

Fatigue fracture of DRA exhibits two distinct fracture morphologies, Fig. 3. In the propagation region (region 1 in Figure 3) striations are often observed. After stable crack propagation, a fast fracture region is typically observed (region 2 in Figure 3). Because of the high crack velocity associated with this portion of the fracture surface, large-scale particle fracture takes place. The propensity for striation formation is controlled by the particle size, and thus, the interparticle spacing. As the interparticle spacing decreases, the degree of constraint due to triaxality of stress increases, so striation formation is hindered and the dominant damage mechanism changes to void formation [12]. Striation orientation and spacing in DRA seem to depend on individual matrix grain orientation with respect to the loading axis, Fig. 4. Figure 4 also shows the larger striation spacing in the low cycle fatigue regime, as compared to a specimen fractured in the high cycle fatigue regime. As the magnitude of stress increases, the step-like crack growth will be of a larger amplitude.
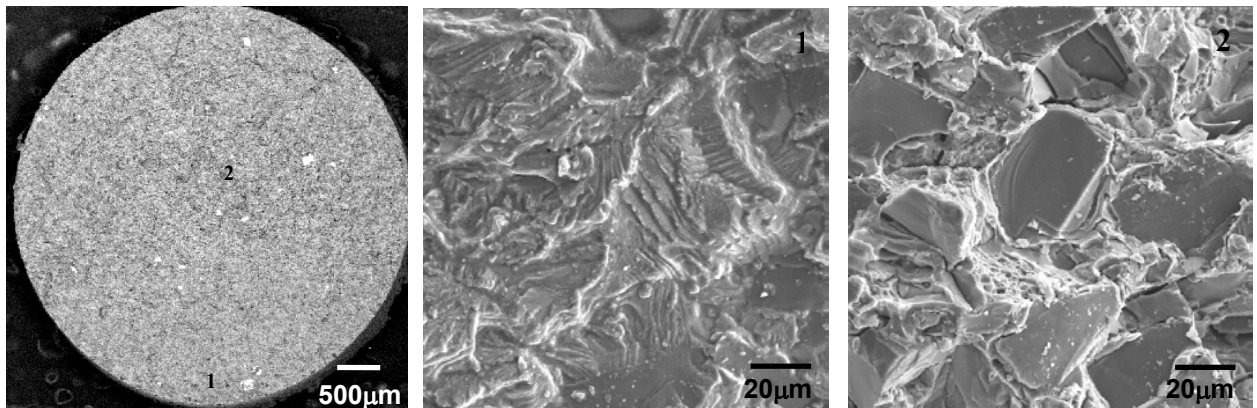
Figure 3: Fatigue morphology in DRA. Striations are observed in the stable crack propagation region (marked 1), while particle fracture is predominant in the fast fracture region (marked 2).

4
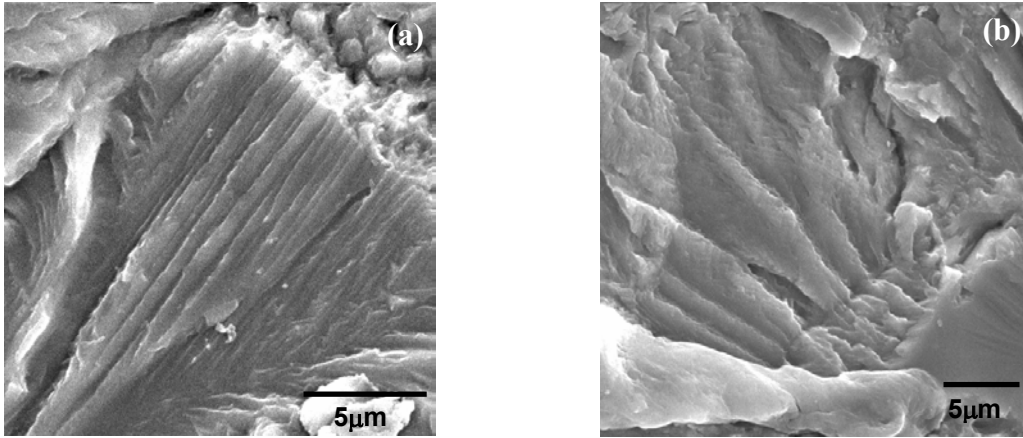
Figure 4: Fatigue striations in the matrix of DRA: (a) Finer striation spacing in high cycle fatigue and (b) larger spacing in low cycle fatigue.

It is interesting to note that in the low cycle regime, cracks seem to originate relatively early in fatigue life (around 10% of total life). In the high cycle regime, on the other hand, crack initiation can occur quite late (after about 70-90% of the life of the specimen). Figure 5 shows data on two different composites systems [9,10]. The transition from crack propagation becomes dominant in the low cycle regime, compared to most of the fatigue life being spent initiating a crack in the high cycle fatigue regime. While crack growth is relatively unimpeded in unreinforced materials, Fig. 6(a), crack growth is hindered by mechanisms such as crack deflection and crack trapping in the composite, Fig. 6(b).
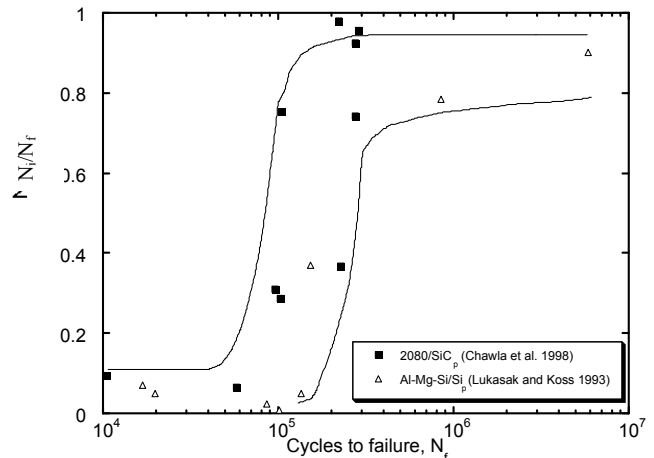
Figure 5: Ratio of cycles to initiation to cycles to failure (N_i/N_f) versus fatigue life for two different composites systems. Notice the transition from crack propagation being dominant in the low cycle regime, compared to most of the fatigue life being spent initiating a crack in the high cycle fatigue regime.

Crack propagation is more significant in the low cycle fatigue regime, since a much greater fraction of the life is spent in propagating the crack.
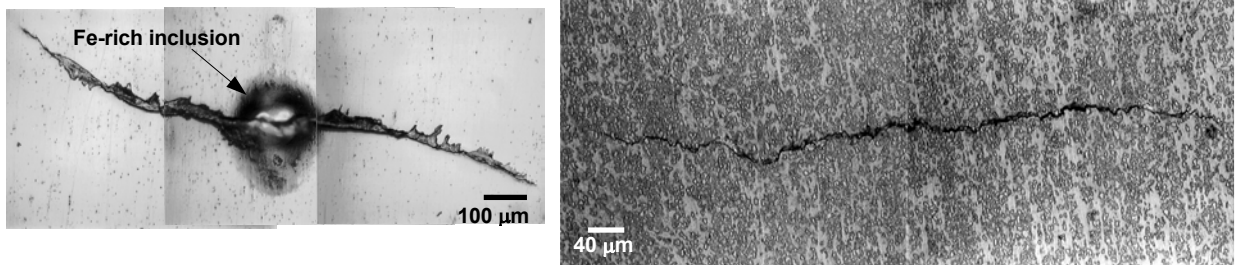
Figure 6: Fatigue crack initiation and growth in (a) unreinforced 2080 Al and (b) in 2080/SiC$_p$ composite. Notice that crack growth is hindered by mechanisms such as crack deflection and crack trapping in the composite.

Elevated temperature fatigue fracture

At elevated temperature, diffusion-assisted processes combine with fatigue processes. Interfacial decohesion and void growth at the particle/matrix interface and particle corners, as well as in the matrix of the composite take place, Fig. 7. It appears that microvoid nucleation and coalescence in

the matrix also seem to have taken place prior at fracture. During the fatigue process, void growth also takes place at angular corners of the particles, the particle/matrix interface, and in the matrix, Fig. 7. It may be reasonable to speculate that cavity growth at elevated temperatures is further enhanced by cyclic loading via diffusion and cyclic slip mechanisms. It should be noted that at elevated temperatures (150-170°C) the decrease in fatigue strength is more significant than the decrease in the yield strength. Thus, some of the proposed mechanisms described above, e.g., diffusion-assisted void growth at elevated temperature, may be responsible for the higher decrease in fatigue strength versus yield strength.
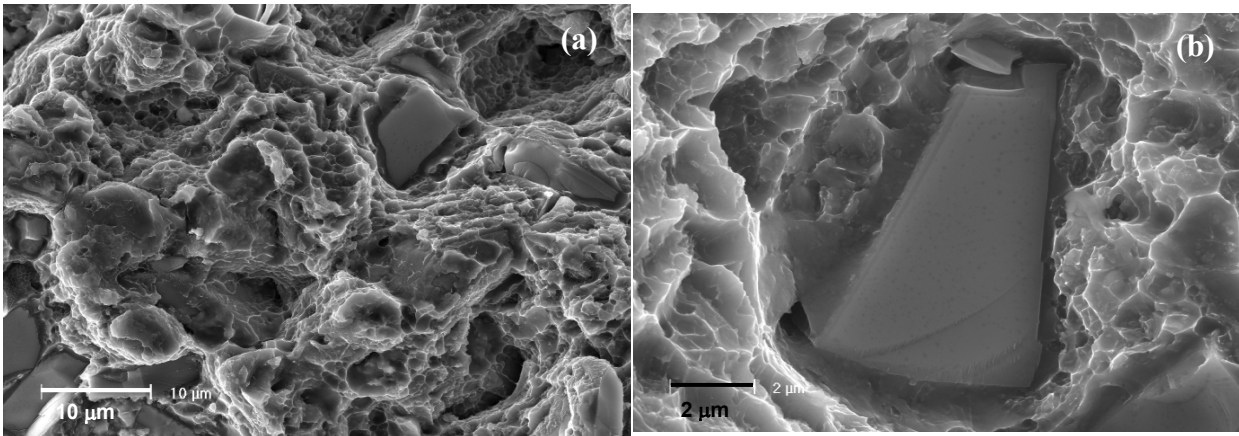
Figure 7: Elevated temperature fatigue fracture in DRA: (a) Diffusion assisted void growth in the matrix and (b) evidence of void growth at stress concentrations, such as sharp particle corners.

REFERENCES

1. Chawla, K.K. (1997). *Composite Materials - Science and Engineering*. 2nd edition, Springer-Verlag, New York.
2. Clyne, T.W. and Withers, P.J. (1993). *An Introduction to Metal Matrix Composites*. Cambridge University Press, Cambridge.
3. Lewandwoski, J.J. (2000). In: *Comprehensive Composite Materials*, pp. 151-187, Kelly, A. and Zweben, C. (Eds.). Elsevier Press, Oxford.
4. Chawla, N. and Allison, J.E. (2001). In: *Encyclopedia of Materials: Science and Engineering*, (2001), in press, Ilschner, B. and Lukas, P., (Eds.). Elsevier Press, Oxford.
5. Williams, J.J., Piotrowski, G., Saha, R., and Chawla, N., (2001) unpublished work.
6. Singh, P.M., and Lewandowski, J.J., (1993) *Metall. Trans*. 24A, 2531.
7. Suresh, S. (1998). *Fatigue of Materials*, p. 132. Cambridge University Press, Cambridge.
8. Chawla, N. and Shen, Y.L. (2001) *Adv. Mater. Eng.* 3, 00.
9. Chawla, N., Andres, C., Jones, J.W., and Allison, J.E. (1998) *Metall. Mater. Trans*. 29A, 2843.
10. Lukasak, D.A. and Koss, D.A. (1993) *Composites* 24, 262.
11. Chawla, N., Jones, J.W., and Allison, J.E., (1999). In: *Fatigue '99*, Wu, X.R. and Wang, Z.G. (Eds.). EMAS/HEP.
12. Sugimura, Y. and Suresh, S. (1992) *Metall. Trans. 23A*, 2231.

ACKNOWLEDGMENTS

TENSILE AND LOW CYCLE FATIGUE STANDARD TESTING FOR SOLDERS
- JSMS Recommendation -

Masao Sakane [1], Haruo Nose [2], Makoto Kitano [3], Hiroyuki Takahashi [4], Minoru Mukai [5] and
Yutaka Tsukada [6]

[1] Department of Mechanical Engineering, Ritsumeikan University,
1-1-1 Nojihigashi Kusatsu-shi Shiga 525-8577, Japan
[2] Department of Mechanical Engineering for Transportation, Osaka Sangyo University
3-1-1 Nakagaito Daito-shi Osaka 574-8530, Japan
[3] R&D Planning Office, Mechanical Engineering Research Laboratory, Hitachi, Ltd.
502 Kandachi-cho Tsuchiura-shi Ibaragi 300-0013, Japan
[4,5] Corporate Research & Development Center, Toshiba Corporation
1 Toshiba-cho Komukai Saiwai-ku Kawasaki-shi Kanagawa 212-8582, Japan
[6] IBM Japan Ltd. Yasu,
800 Ichimiyake Yasu-cho Yasu-gun Shiga 520-2362, Japan

ABSTRACT

This paper proposes the tensile and low cycle fatigue standard testing for lead and lead-free solders. There is no standard method for solder testing, which causes a large scatter in material data of solders. The solder strength working group in the committee on high temperature strength of materials, Japan Society of Material Strength, issued the tensile and low cycle fatigue standards for solder testing. The standards recommend the casting method, specimen shape and heat treatment, strain rate and other testing methods needed for tensile and low cycle fatigue testing of solders. Benchmark testing using Sn-37Pb and Sn-3.5Ag solders, based on the standard methods, demonstrated that these standards generate the reliable data with a small scatter. The tensile and low cycle fatigue database was built based on the standards for the two solders.

KEY WORDS

Solder, Standard testing, Tensile test, Low cycle fatigue test, High temperature

INTRODUCTION

Solders have been used as a connection material for electric and electronic devices. Recent compact mounting technology raises the temperature of the devices which induces more severe damage into solder connections.

Material testing was carried out to obtain mechanical properties of solders but a large scatter in test results was reported due to the difference of testing method. A standard testing method has been needed for generating the stable and reliable material data. The solder strength working group in the committee on high temperature strength of materials, Japan Society of Materials Science, was organized in 1997 and published the two standards in 2000 based on the extensive experiments and discussion. This paper presents the outline of the tensile and low cycle fatigue (LCF) standard testing methods. The standards are applicable to lead and lead free solders in the temperature range of 233K-398K.

TEST SPECIMEN

Specimens have to be cast using a round hollow mould of type 304 stainless steel, cast iron or carbon with 15 mm wall thickness at 100 K higher temperature above the melting point of solders. Inner diameter of the mould should be 20 mm larger than the diameter at the gage section of specimens, which is to exclude the texture developed during casting from the gage section. Specimens are turned from the cast and should be annealed for an hour at 0.87 T/Tm for stabilizing the microstructure of solders ; T is the absolute annealing temperature and Tm the absolute melting temperature. This heat treatment was determined from the extensive aging experiments and corresponds with 5-10 years exposure at room temperature.

TENSILE TEST

Round bar specimen shown in Fig.1 was recommended for tensile testing. Temperature of specimens must be controlled during tensile testing because mechanical properties of solders are sensitive to testing temperature. The allowable variation of temperature along gage length is ±5.0K for the temperature range of 233K-302K and ±1.5K for 303K-398K. Temperature must be raised in more than 30 min and must be stabilized for 15 min before starting tensile test.

Extensometer is attached to the two pyramid collars of the specimen in Fig.1. The specimen with no collars was also recommended to tensile testing. In this case, careful extensometry is necessary not to make any scratch and flaw on the specimen surface when attaching an extensometer.
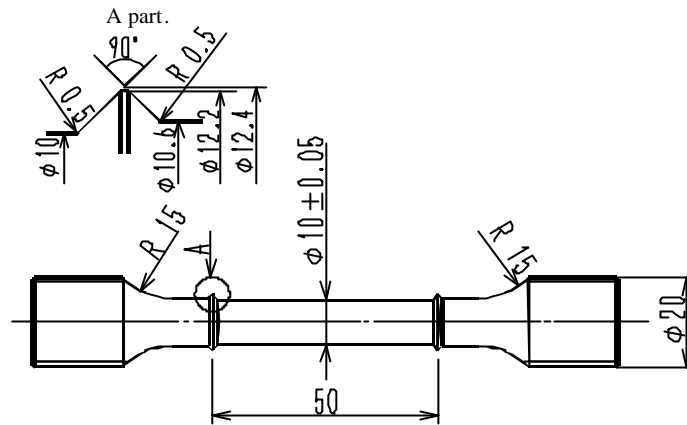
Figure 1: Shape and dimensions of the tensile standard specimen.

Strain rate in tensile test must be 2.0%/s to exclude creep deformation from tensile data. Figure 2 shows the effect of strain rate on the stress-strain relationship of Sn-37Pb used for deciding the tensile strain rate. Flow stresses at 0.5%/s and 1.0%/s are smaller than those at 2.0%/s and 10.0%/s and the flow stress at 2.0%/s is almost same as that at 10.0%. The experimental results indicate that the flow stress saturates at the strain rate of 2.0%/s and that the strain rate faster than 2.0%/s is necessary to exclude the creep deformation from the stress-strain relationship. Almost the similar experimental results were also obtained for Sn-3.5Ag at 398K. Based on the experimental results, the strain rate of 2.0%/s was employed as a strain rate for tensile testing in the standard.

Tensile test results be reported are Young's modulus, proportional limit, 0.02% and 0.2% proof stresses, maximum tensile strength and elongation. The 0.02% proof stress is newly defined be reported because solders have relatively small proportional limits and large strain hardening. The 0.2% proof stress is too high compared with the proportional limit in the case of solders.

LOW CYCLE FATIGUE TEST

Material preparation for LCF tests is exactly the same as that for tensile tests. Button head specimen with straight gage part shown in Fig.3 was recommended for LCF testing in the standard. An extensometry making no flaws on the specimen surface is essential in LCF testing to avoid crack nucleation from the flaws. To achieve this, two small pyramids of epoxy resin are put on the specimen surface and extensometer rods are pressed on the pyramids, Fig.4. Besides the LCF specimen shows in Fig.3, an hourglass shaped specimen was also recommended in the standard for high strain range test to avoid buckling of the gage part. Radial strain is controlled for the case of the hourglass specimen.

Strain controlled LCF test was recommended in the standard with a fully reversed triangular strain wave at a strain rate of 0.1%/s. Since solders significantly creep even at room temperature, creep damage is included into the LCF test results at this strain rate. However, LCF lives in symmetrical triangular strain waves are not reduced by lowering the strain rate so that the strain rate of 0.1%/s was recommended in the standard,

considering that much faster strain rates have a difficulty in experiments. Temperature of specimens should be monitored and controlled during LCF tests. The allowable variation of the temperature along the gage length is ±5K. Temperature must be stabilized for 30mm before LCF testing.

The number of cycles to failure is defined as the cycle of 25% tensile stress drop from that at a half life, Fig.5. This method requires iteration in a couple of times but has an advantage to produce the same failure cycle for given data independent of researcher. The numbers in circles in the figure show the sequence of determining the failure cycle.
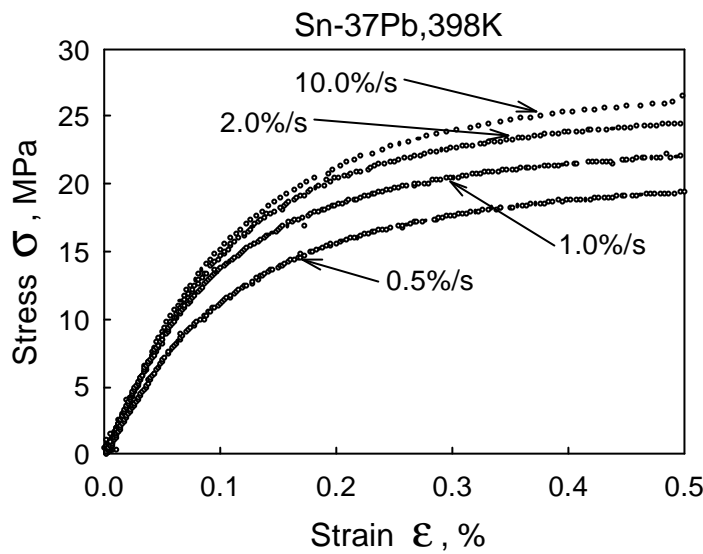
Figure 2:Stress-strain relationship up to 0.5% for Sn-37Pb at the four strain rates at 398K.
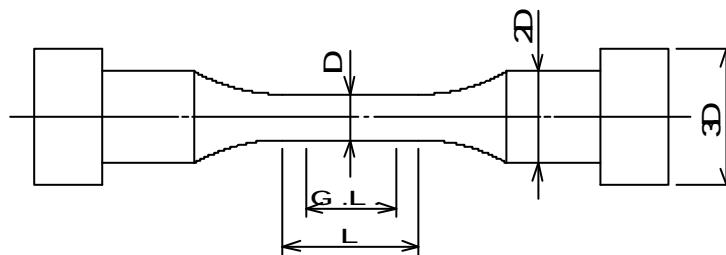
Figure 3:Shape and dimensions of the low cycle fatigue standard specimen.
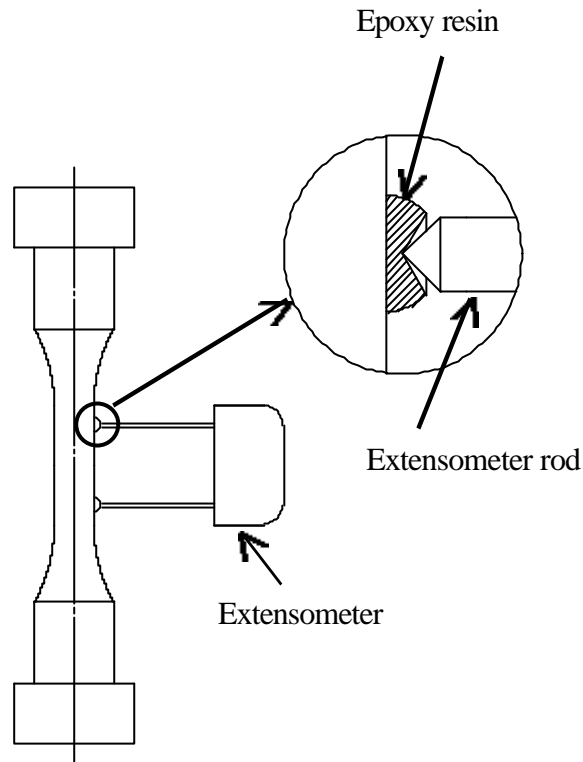
Figure 4: Extensometry using epoxy resin pyramids.
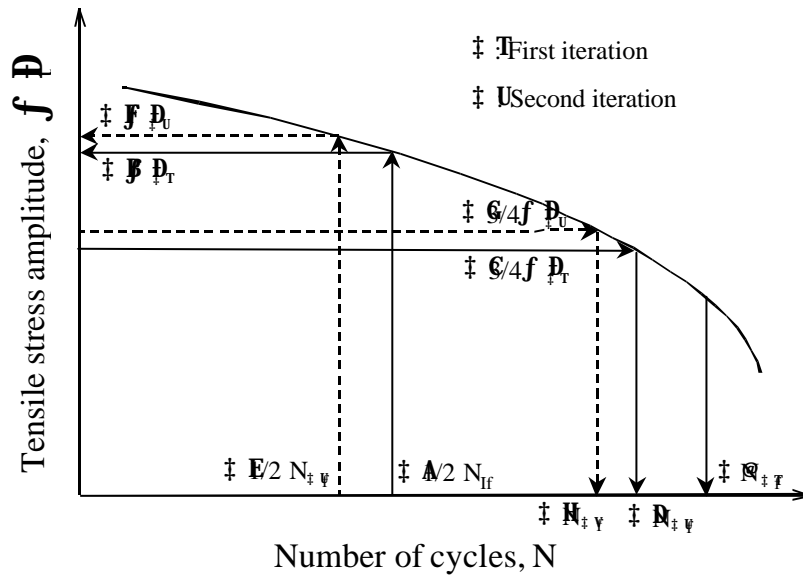
Figure 5: Calculation method of determining the number of cycle to failure.

LCF test results be reported are total strain range-failure cycle relationship, inelastic strain range-faiture cycle relationship, hysteresis loops and cracking site. The strain ranges at half life should be used as a representative value. Photographs of fracture surface is subsidiary recommended to report.

TENSILE AND LOW CYCLE FATIGUE DATABASE

Tensile and LCF database were generated for Sn-37Pb and Sn-3.5Ag solders based on the standards. The database contains, Young's modulus, yield stress, proof stresses, elongation, stress-strain curves at 233K, 253K, 313K and 353K. Low cycle fatigue data were also collected into the database for the two solders at 313K and 353K. The database has not only the failure cycle but also the variation of stress amplitudes and cyclic stress-strain relationships.

CONCLUSION

The outline of the tensile and low cycle fatigue standards for solder testing was presented. The standards recommend the specimen preparation, temperature control, strain rate, definition of failure cycle and so on. The standards were demonstrated to generate the stable tensile and low cycle fatigue data of solders. The database of Sn-37Pb and Sn-3.5Ag in tensile and low cycle fatigue was introduced.

ACKNOWLEDGEMENT

The authors express their gratitude to all the members of solder strength subcommittee for the helpful activities for standardization.

TENSILE FRACTURE AND CREEP-RUPTURE BEHAVIOR OF SiC FIBERS

Hee Mann Yun and James A. DiCarlo

NASA Glenn Research Center, Cleveland, Ohio 44135

ABSTRACT

In order to better understand the fiber role for fracture and rupture of SiC fiber-reinforced ceramic matrix composites (CMC), mechanical tests were performed on single filaments, multifilament tows, and multi-tow fabrics of different types of SiC fibers: near-stoichiometric Hi-Nicalon Type S, Tyranno SA, Sylramic, Sylramic-iBN, and non-stoichiometric Hi-Nicalon and Tyranno ZMI. All fibers were sized with a low molecular weight polymer, and also were tensile fracture tested after coating with a thick and compliant layer of BN. Creep-rupture data were obtained at 1400°C in air and in argon. For the near-stoichiometric SiC tow and fabric with rough surfaces, the sizing and coating significantly affected the room temperature tensile fracture characteristics. Based on simple bundle theory, measured tensile fracture strengths for sized tows, coated tows, and fabrics of all fiber types were in general agreement with the single fiber results. Even though the final fracture behavior and strength properties of some fiber types showed strong effects on the testing environments and fiber specimen form, the initial surface flaw that was introduced during fiber fabrication and the creep-induced cavity growth by stress and time were the most crucial factor for the as-produced room temperature tensile strengths and the high-temperature creep-rupture. In this regard, the treated Sylramic-iBN and Hi-Nicalon Type S fibers showed the best fracture and rupture resistant behavior.

KEYWORDS

SiC fiber, SiC fabric, SiC/SiC composite, tensile fracture, creep rupture

INTRODUCTION

Continuous silicon carbide (SiC) fibers have been developed for reinforcement of ceramic matrix composites (CMC) for high temperature structural components. Small diameter SiC fibers produced by polymer pyrolysis possess high stiffness, high room temperature strength, and high thermal stability. The near-stoichiometric Sylramic fiber and the non- stoichiometric Hi-Nicalon fiber (excess carbon and trace oxygen) are leading candidates for high temperature CMC because they have displayed thermostructural behavior superior to that of the high-oxygen containing Nicalon SiC fiber [1,2]. In contrast to non-stoichiometric SiC fibers, the Sylramic fiber showed no weight loss, grain growth, or contraction below 1500°C. The Hi-Nicalon Type S and Tyranno SA are other near-stoichiometric fibers, whose grain sizes and tensile strengths are similar to those of the Sylramic fiber. More recently, improved tensile and creep-rupture behavior have also been achieved for the Sylramic-iBN fiber, which is derived from the Sylramic fiber by special developmental processes that yield microstructures with smaller boron content [3]. Thus there exists various process routes and microstructural possibilities for thermally stable stoichiometric SiC

fibers.

The properties of the small-diameter SiC fibers are typically measured using single fibers removed from multifilament tows containing ~400 to 1600 fibers. However, since CMC are almost always constructed using woven or braided tows, mechanical tests on either coated and/or uncoated tightly-packed multifilament tows or even woven fabrics that have been exposed to simulated CMC process and service conditions should be more useful for understanding fiber performance within CMC than single fiber tests. These tow or fabric tests not only allow the evaluation of many fibers in the structural forms used in CMC, but also permit a better understanding of the various fiber surface and load transfer interactions that may occur within the CMC. The objective of this study was therefore to understand SiC fiber performance in CMC by measuring the tensile strength and creep-rupture properties of multifilament tows and fabrics consisting of various non-stoichiometric and stoichiometric SiC fibers.

EXPERIMENTAL PROCEDURE

Six types of SiC fibers available as continuous-length multifilament tows were examined: the non-stoichiometric Hi-Nicalon and ZMI fibers, and the stoichiometric Hi-Nicalon Type S, Tyranno SA, Sylramic, and Sylramic-iBN fibers. This last fiber not only has less boron content in the fiber bulk than the precursor Sylramic fiber, but also has a thin (~150 nm) crystalline BN layer on the fiber surface [4]. Table 1 lists typical properties of all the fiber types. In the as-produced condition, the tows for each type were sized with a polymer-based material (see Table 1). These tows were then utilized to fabricate 0/90-degree satin weave fabric by a commercial weaving vendor. This fabric is the basic fiber structure used in most commercial CMC today [5]. For fabric testing, specimen strips, ~13mm wide (10 tows) and ~150mm long, were cut from the fabric cloth and mounted onto paper tabs. Detailed procedures for tow and fabric preparation and testing are reported elsewhere [6]. To determine tensile strength, all fiber types were tested to fracture at room temperature using a 25 mm grip to grip length and a constant displacement rate of 1.27 mm/min. The average cross-sectional area for the multifilament specimens was assumed to be equal to the filament-count times the average fiber area based on the average diameter for each type. The creep-rupture properties were determined for tows and fabrics using the same fiber creep-rupture facilities and procedures previously reported on the single fiber [6]. Creep deformation versus time was recorded at a constant deadweight load using either 25mm or 100mm hot zone lengths for the air furnace.

RESULTS AND DISCUSSION

The room-temperature tensile strengths are shown in Fig. 1 for (a) single fibers, (b) tows, and (c) woven fabrics in their as-produced condition, either sized or BN coated, and after exposure at 1000°C for 3 hours in vacuum or at 1400 °C for 1 hour in argon. These exposure conditions were chosen to simulate those typical of interphase and matrix formation, respectively, for current SiC/BN/SiC composites [7]. Fig. 1a shows that the average tensile strength for the as-processed Sylramic, Syl-iBN, and ZMI single fibers were the highest, above 2700 MPa; while those of the SA and Hi-Nicalon-S fibers were below 1900 MPa. The low strength of the SA fiber is due to mainly large initial flaws that could be related to the fact that it has the largest grain size among all fibers. After inert exposure, the average strengths of single fibers from all fiber types decreased. The degree of degradation is strongly dependent on the type and content of impurities on its surface plus the chemical composition of the exposure environment. This strength degradation under inert conditions is due to changes in the fiber surface morphologies and chemistries by the exposure environment [8].

In general, the average strengths of single tows, as shown in Table 2 and Fig. 1b, were either lower or in good agreement with those of the 10-tow fabrics (Fig. 1c); and the strength ranking for different fiber types was similar to that of the single fiber. The highest tow and/or fabric strength was ~1800 MPa for the Sylramic and Hi-Nicalon fibers; while the lowest was ~500 MPa for the SA fiber. The coated tows showed a similar strength to the as-produced/sized tows. As with single fibers, strengths of multifilament fibers in forms of

tow or fabric also decreased after exposures at 1000°C, and decreased further at 1400°C with some types losing, up to 50 % of their initial strengths.

To better understand the strength of the as-produced multi-fibers, it can be assumed that the individual fibers fractured independently, so that multi-fiber strengths could be calculated using the single fiber results and simple bundle theory assuming the same gauge length of 25 mm [9]:

$$\sigma_b / \sigma_f = (1/(m\,e))^{(1/m)} / \Gamma\,((m+1)/m) \tag{1}$$

Here σ_b is the predicted multi-fiber bundle strength, σ_f is the average measured strength for the single fibers, e is the natural logarithm base, Γ is the gamma function, and m is the Weibull modulus that characterizes the strength distribution of the single fibers. For each SiC fiber type in the as-produced condition, Table 2 shows the calculated and the measured average multi-fiber strength using the Weibull modulus and average strength for the single fibers, and assuming the same gauge length of 25mm. In Table 2, it can be seen that the measured and predicted fabric strengths were generally agreed to the predicted. This was probably due to fabric gauge length being smaller than the grip-to-grip length due to the initial 90-degree tow. However, some as-produced tow with no inter-laced tow showed lower strengths than expected from simple bundle theory, suggesting that the fibers within the tows did not fracture independently. Two possible mechanisms for non-independent fracture are (1) fiber-fiber interaction due to mechanical abrasion and (2) fiber-fiber interaction due to chemical bonding. In both cases, the fracture of the weaker fibers causes premature fracture of the stronger fibers, resulting in a reduced strength for the multi-fiber specimens. The lower tow and fabric strengths for the near-stoichiometric Sylramic and Syl.-iBN fibers with rough surfaces and for the SA fiber with excess sizing can be explained by mechanisms 1 and 2, respectively (see Table 1). Both mechanisms could also explain the loss in multi-fiber strengths after the inert treatments since removal of the fiber sizings may result in more fiber-fiber abrasion and changes in the BN-coatings may result in fiber-fiber chemical bonding.

After air exposure for 100 hours from 400 to 1000°C, room-temperature tow and fabric strengths decreased as shown in Fig. 2a for the stoichiometric SiC fibers, and Fig. 2b the non-stoichiometric fibers, and also included the CVI-BN coated fibers. The air exposures were used to simulate effects from CMC cracking under oxidizing service conditions and from CMC fabrication conditions in which the tows are inadvertently exposed to oxygen, such as during BN interphase deposition at intermediate temperatures. Typically the tow strengths for all fiber types, including the coated fibers, started to drop at ~200°C, and then leveled off at ~ 600°C to ~50 to 80% of their as-produced strengths. Near 1000°C, the strengths of all tows dropped to about the same low level of <~400 MPa. The BN-coated tows appeared to degrade at even lower temperatures, indicating easier fiber-fiber bonding because of tight tows and boron-enhanced silica formation on the fiber surfaces. Contrary to the tows, which have loosely touching fibers during air exposure, the fabrics with tight tows due to interlacing displayed a more rapid strength loss with temperature, so that near 600°C, the strengths of all fabrics dropped to about the same low level of <~400 MPa, nearly 10% of their as-produced values. However, the Syl.-iBN fabric degraded only to a level of ~2/3 of its initial strength. The developmental Syl.-iBN fiber with reduced boron and a crystalline BN surface appears to measurably reduce oxidation-induced bonding at intermediate temperatures. For the Hi-Nicalon fiber, previous TGA studies [4] suggest that the sharp strength drop from ~500 to 600°C were probably due to oxidative removal of sizing and perhaps intrinsic carbon on the fiber surface. The intrinsic carbon on the Hi-Nicalon may have not only healed surface flaws, but also allowed compliant interaction between fibers. For the other tow fiber types, strength degraded slowly in a continuous manner up to ~800°C. For the Sylramic tow, the small increase in strength near 900°C appears to be caused by the formation of a borosilicate glass surface layer which, if thin enough, appears to be able to heal surface flaws without chemically bonding the fibers together. Indeed, due to the presence of boron and TiB_2 on the fiber surface [9], larger TGA weight increases were observed at intermediate temperatures for the Sylramic fiber [5]. Above 1000°C, all tow fibers began to rapidly form silica on their surfaces, which effectively bonded all the fibers together. This gives rise to tow strengths of <~400 MPa.

In support of a chemical bonding issue during multi-fiber air exposures, the general fracture surfaces for the

low strength tows showed (1) localized failure with many groups of fibers bonded together and (2) one or more fracture planes depending upon degree of fiber-fiber bonding. Typical fracture surfaces for the Hi-Nicalon and Sylramic fibers, tow and fabric, are shown in Figs. 3a and 3b before and after a 700°C air exposure, respectively. The single fibers, not shown here, before and after exposure showed no significant alteration of the fracture origin, mainly surface flaws. The tow and fabric fracture surfaces showed two different types: either a bulged explosion style fracture with independent fiber fracture, or a bonded non-explosion style fracture with correlated fiber fracture. The fracture surfaces of the fabric specimens changed from an independent to the dependent fracture mode after air exposure. For CMC, the oxidation results clearly point to the need for some fiber separation within woven tows, plus minimal contamination with oxygen during the interphase coating process or during composite application.

Plots of applied stress versus average rupture time are shown in Fig. 4 for Hi-Nicalon and Sylramic tows and single fibers at 1400°C in (a) air and (b) argon for the as-produced and BN-coated conditions. The time rate of rupture strength degradation for the tows was much weaker than that for the single fibers. The degradation rate for the BN-coated specimens was more rapid than that of the un-coated specimens. At short times (or high stresses), the Hi-Nicalon and Sylramic tows displayed lower rupture strengths (or shorter rupture times) than the single fibers. At long times (or low stresses), the un-coated tows displayed higher rupture strengths (or longer rupture times) than the single fibers or coated tows. Also shown in Fig. 5 is the rupture strength behavior of single Syl.-iBN fibers, which is significantly different in air and argon. In air, this fiber type shows reduced creep and the most rupture-resistant behavior observed to date for all SiC fiber types [11]. Apparently in air, oxide formation allows better creep resistance and blunts strength controlling flaws on the Sylramic-iBN fiber surfaces; while in argon, creep is enhanced and flaw blunting by silica formation is not available. The exact mechanisms for these environmental effects are still unknown. Thus, the general trends observed at 1400°C, which also occurred at 1200°C, are currently creating difficulties for understanding the creep-rupture behavior not only of tows and fabrics, but also of single fibers.

SUMMARY AND CONCLUSIONS

Tensile strengths of as-produced tows or fabric specimens containing various types of SiC fibers can be predicted in most cases by bundle theory in which it is assumed that all fibers fracture independently. In those cases where the measured strengths were lower than predicted, effects due to adverse fiber-fiber mechanical and chemical interactions appeared to be existent. These issues became more prevalent after multi-fiber tow and fabric specimens were subjected to inert thermal treatments or to air exposures at intermediate temperatures. TGA studies suggest that the primary strength degradation mechanism was sizing removal for the inert treatment, and fiber-fiber bonding by surface oxide growth and surface carbon layer removal for the air treatments. Contrary to the room-temperature strength results, the high temperature creep-rupture strengths of tows and fabrics were generally higher than those of single fibers, with environmental effects playing a strong role. Clearly more studies are needed to understand the high-temperature creep-rupture results.

REFERENCES

(1) J.A. DiCarlo and S. Dutta: Continuous Ceramic Fibers for Ceramic Composites. HANDBOOK ON CONTINUOUS FIBER REINFORCED CERAMIC MATRIX COMPOSITES, eds. R.Lehman, S.El-Rahaiby, and J.Wachtman, Jr., Ceramic Information Analysis Center, Purdue University, West Lafayette, Indiana, 1995.
(2) K. Okamura,"Ceramic Fibers from Polymer Precursors", Composites, 18, 2, 1987, pp 107-120.
(3) H.M. Yun and J.A. DiCarlo, unpublished work, 1997.
(4) H.M. Yun and J.A. DiCarlo, "Comparison of the Tensile, Creep, and Rupture Strength Properties of Stoichiometric SiC Fibers", NASA TM 209284, 1999.
(5) J.A. Dicarlo and H.M. Yun: "Fiber Test Development for Ceramic Composite Thermomechanical properties", ASTM STP 1392, 1999, edited by M.G. Jenkins, E.L-Curzio, and S.T. Gronczy.
(6) H.M. Yun and J.A. DiCarlo, "Thermomechanical Behavior of Advanced SiC Fiber Multifilament Tows", Cer. Eng. and Sci. Proceedings, 17A, 1996, pp. 61-67.
(7) D. Landini and P. Gray: private communications to HACI, 1999.

(8) F. Rebillat, A. Guette, L. Espitalier, and R. Naslain, "Chemical and Mechanical Degradation of Hi-Nicalon and Hi-Nicalon S Fibers under CVD/CVI BN Processing Conditions", HIGH TEMPERATURE CERAMIC MATRIC COMPOSITES III, The Ceramic Society of Japan, 1998, pp 31-34.

(9) B.W. Rosen, "Thermomechanical Properties of Fibrous Composites", Proc. Roy. Soc. Lond. A. 319, 1970, pp. 79-94

Table 1. NOMINAL PROPERTIES OF SiC FIBERS

Trade Name	Hi-Nicalon	ZMI	Hi-Nicalon S	SA	Sylramic	Syl.-iBN
	non-stoichiometric SiC		near-stoichiometric SiC (C/Si ~1.0)			
Manufacturer	Nippon Carbon	Ube Industries	Nippon Carbon	Ube Industries	Dow Corning	Dow Corning + NASA
Avg. Grain Size*, nm	4(XRD)	-	22 (XRD)	> ~150	~100	~100
Second Phases or Impurity Conc. (wt.%)	0.5 O, 36 C	8.3 O, 35 C, 2 ZrX	O(0.2)	Al(<2), O(0.3)	TiB2, B	Reduced B, TiB2, B-N
Avg. Diam., μm	14	11	13	10	10	10
# of Filaments per tow	500	400	500	800	800	800
PVA Sizing, wt.%	>1	(~1.0)#	1.2	(~1.0)#	~0.2	-
Modulus at RT GPa)	270	200	400-420	375	~400	>400
Tensile Strength, MPa	2800	2700	~2500	2800	3200	~3200
Tensile Elongation, %	~1.0	1.7	~0.6	~0.7	~0.8	<~0.8

*MEASURED ON TEM MICROSTRUCTURES. # PEO SIZING

Table 2. Strength Characteristics of SiC Single Fibers, Tows, and Fabrics

Fiber Type	Avg. tensile strength (MPA) at room temperature, As-Produced Condition				
	Single Fibers	(m)	Tows	Fabrics	Predicted Tow Strength*
Hi-Nic.	2240	6	1960	2200	1520
ZMI	2700	5	1770	-	1740
Hi-Nic. S	1900	3	1450	1610	1060
SA	1430	3	280	1340	800
SYLRAMIC	2800	4	1550	1850	1700
SYL.-iBN	3060	4	1270	1840	1860

* PREDICTED BY BUNDLE THEORY, Eq.(1), + NO SIZING
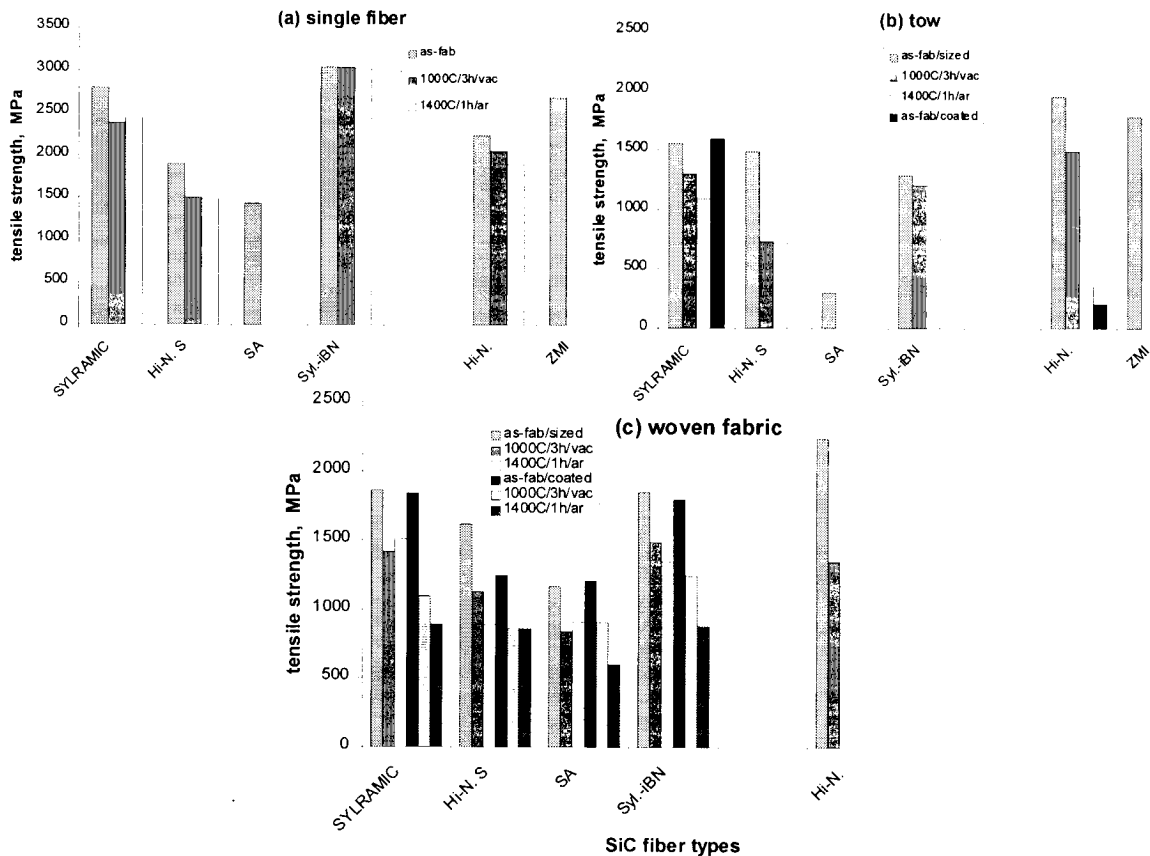
Fig. 1 Tensile fracture strength of SiC fibers, as-fabricated and BN-coated
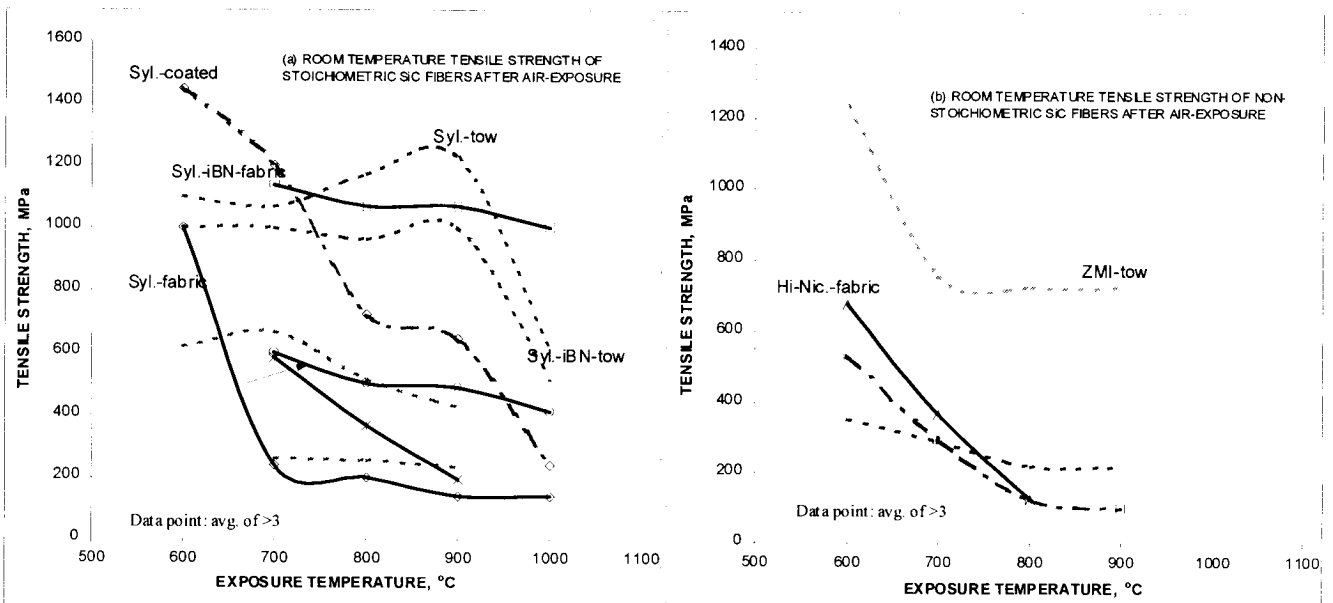
Fig. 2 Retained tensile fracture strength of SiC fibers after 100hr-air exposure.
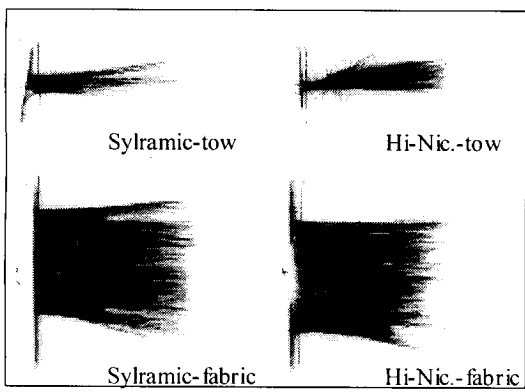
(a) R.T. tensile fracture, as-fabricated
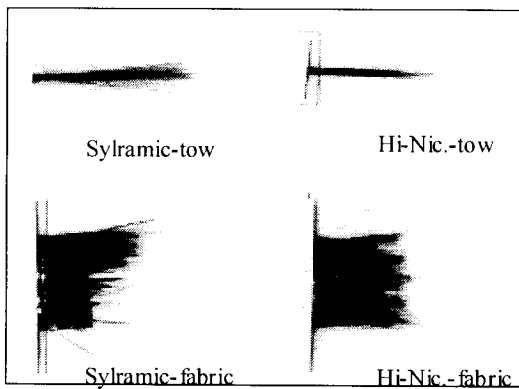
(b) R.T. tensile fracture after 700C/100hr/air exposure

Fig. 3 Typical tensile fracture surfaces of dependent and independent fiber failures.
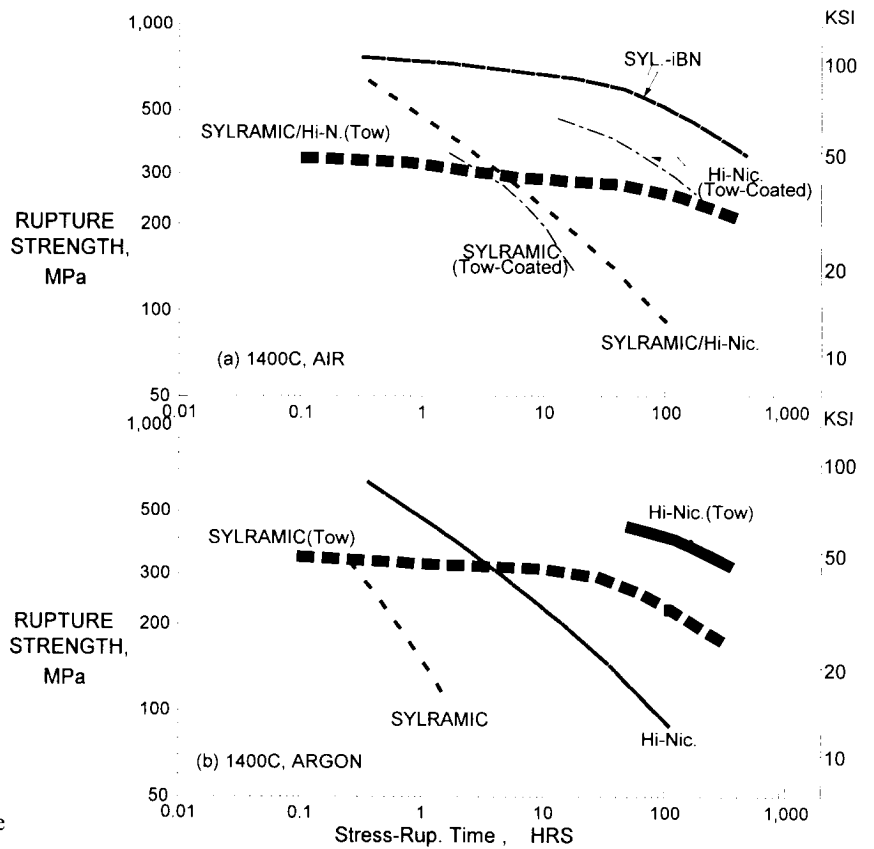
Fig. 4 1400 C creep-rupture strength of SiC fibers, tested in (a) air and (b) argon

TENSION FATIGUE ANALYSIS OF WOVEN COMPOSITE LAMINATES

Rajiv A. Naik

Pratt & Whitney – United Technologies Corporation, East Hartford, CT 06108 USA

ABSTRACT

The three major fatigue damage mechanisms of transverse yarn cracking, inter-yarn debonding, and delamination in a 5-harness satin woven graphite/epoxy composite were modeled using simple mechanistic models. Each of the three models was able to capture the salient features of the woven fabric architecture and also the physics of the damage mechanism. The interaction between the three damage mechanisms was implicitly modeled by including (i) the effect of matrix cracking in the stiffness model for inter-yarn debonding and (ii) the effects of matrix cracking and inter-yarn debonding in stiffness model for delamination. These models were used to determine the effect of the three major damage mechanisms on the laminate stiffness loss during fatigue. The predictions for laminate stiffness loss were compared with tension-tension fatigue test data. By using these damage mechanism models together with interlaminar fatigue delamination growth data (da/dN), it was possible to assess the fatigue life of the woven composite laminate. The fatigue life predictions compared reasonably well with test data. The present fatigue modeling technique should be very useful in designing with woven composite laminates, especially since it can provide estimates of both the fatigue stiffness degradation and the fatigue life.

KEYWORDS

Damage, life, failure mechanism, delamination, matrix cracking, debonding, stiffness degradation, polymer.

INTRODUCTION

Woven polymeric composites are currently being used on several aircraft components. However, there is a lack of fatigue analysis methodology for such woven composites. This analytical capability is critical in the design of aircraft and aero-engine components. There have been very few investigations in the past on the fatigue damage mechanisms of woven graphite/epoxy composites. In two recent studies, Patel and Case [1, 2] investigated the microcracking response, residual strength, fiber-matrix debonding, and dynamic stiffness loss response under fatigue of a woven graphite/epoxy composite. There have been even fewer efforts in the past on the modeling of fatigue damage mechanisms of a woven composite. Kumar and Talreja [3] recently presented a damage mechanics based model for predicting the stiffness properties of a woven composite with transverse cracking. Naik, *et al.* [4] presented simple mechanism-based models to characterize the major fatigue damage mechanisms of a woven graphite/epoxy composite.

In the present study, the three major damage mechanisms of transverse yarn cracking, inter-yarn debonding, and delamination in a 5-harness satin woven graphite/epoxy composite were modeled using simple mechanistic models. Each of the three models was able to capture the salient features of the woven fabric architecture and also the physics of the fatigue damage mechanism. The interaction between the three damage mechanisms was implicitly modeled by including (i) the effect of matrix cracking in the stiffness model for inter-yarn debonding and (ii) the effects of matrix cracking and inter-yarn debonding in stiffness

model for delamination. These models were used to determine the effect of the three major damage mechanisms on the laminate stiffness loss during fatigue. The predictions for laminate stiffness loss were compared with test data. By using these damage mechanism models together with interlaminar fatigue delamination growth curves (da/dN), it was possible to assess the fatigue life of the woven composite laminate. Fatigue life predictions using the present analysis compared reasonably well with test data.

MATERIAL, TESTING, AND FATIGUE DAMAGE MECHANISMS

The material used in this study was AS4/PR500 graphite/epoxy woven composite. A 5-harness satin woven fabric (5HS) constructed using 6k (6000 filaments) yarns of the AS4 fibers at a spacing of 4.724 yarns/cm (12 yarns per inch) was used for each of the plies. The laminate consisted of 8 warp-aligned plies and was fabricated using resin transfer molding (RTM). The nominal thickness of the panels was 2.896 mm (0.114 inch) and the composite fiber volume fraction was 55%. Fatigue testing [1, 2] was performed at 10 Hz and an R-ratio of 0.1. The major initial damage mechanisms were transverse yarn cracking followed by debonding at the yarn cross-over regions (see Fig. 1). Such inter-yarn debonding at the yarn cross-over regions was termed as "meta-delamination" by earlier researchers [1, 2]. This initial damage was followed by delamination, which emanated from the tips of the transverse yarn cracks and also the specimen edges.

MODELING OF FATIGUE DAMAGE MECHANISMS AND FATIGUE LIFE

The transverse yarn cracking in the 5HS woven composite was modeled by considering the repeating unit cell for the 5HS weave architecture (Fig. 2). This unit cell was further idealized as a [0/90] laminate [4]. The inter-yarn debonding failure mechanism was modeled by representing the debonded regions in the repeating pattern of the 5HS weave by an "equivalent" debonded region (Fig. 3). The edge delamination observed during fatigue was modeled using the classic O'Brien model [5] with appropriate extensions to a woven composite laminate.

Transverse Yarn Cracking Model

The transverse yarn cracking model in Fig. 2 was idealized as a [0/90] laminate in which the stiffness, E_1, of the 0-deg layer was calculated as the "effective" stiffness of the warp yarns after accounting for yarn undulations. The stiffness of the 90-deg layer, E_2, was computed as the "effective" combined stiffness of the transverse yarns and the interstitial matrix. The normalized stiffness, E_{mN}/E_o, for a [0/90] laminate with transverse cracks is given by [4]:

$$\frac{E_{mN}}{E_o} = \frac{\left[\dfrac{\sigma_{tr}}{\sigma_a} - \dfrac{E_2}{E_o}\right]}{\left[\dfrac{\sigma_{tr}}{\sigma_a}\left(\dfrac{5}{3}\dfrac{E_2}{E_1} + 1\right) - \dfrac{E_2}{E_o}\left(\dfrac{E_2}{E_1} + 1\right)\right]}$$

(1)

where E_{mN} is the laminate longitudinal stiffness after N cycles, E_o is the undamaged laminate longitudinal stiffness, σ_{tr}, is the maximum cyclic transverse stress in the transverse yarns between adjacent transverse cracks, and, σ_a, is the maximum applied cyclic stress. Equation (1) was based on a simplified form of the shear-lag expressions derived by Lee and Daniel [6] for a [0/90] composite laminate. It was shown in Ref. [4] that for different applied stresses, σ_a, the variation of, (σ_{tr}/σ_a), as a function of fatigue cycles could be represented by a single curve. This empirical curve was given by [4]:

$$\frac{\sigma_{tr}}{\sigma_a} = A\,N^{-d}$$

(2)

Using Eqs. (1) and (2), it is possible to determine the variation of the normalized stiffness, E_{mN}/E_o, for a transversely cracked woven composite laminate as a function of fatigue cycles.

Inter-Yarn Debonding or "Meta-Delamination" Model

As shown in Fig. 1, the woven composite exhibits inter-yarn debonding at the yarn crossover regions. This damage mechanism is unique to woven fabric- reinforced composites. A simple model was used to account for the longitudinal stiffness loss resulting from this damage mechanism. Figure 3 depicts an equivalent inter-yarn debonding model that was used to represent the debonding at the crossover regions in the repeating unit cell (of length, L) of a 5-harness satin weave composite. By assuming that the composite displacements are the sum of the displacements [5] in the undamaged region of length, L-a, and the locally debonded region of length, a, an expression can be derived for the stiffness, E_{md}, of the locally debonded composite as:

$$\frac{1}{E_{md}} = \frac{(1-a/L)}{E_{mn}} + \frac{(a/L)}{E_{LD}} \qquad \text{i.e.,} \qquad \left(\frac{E_{md}}{E_o}\right) = \frac{(E_{LD}/E_o)(E_{mn}/E_o)}{\frac{E_{mn}}{E_o}\left(\frac{1}{n}\right) + \frac{E_{LD}}{E_o}\left(1-\frac{1}{n}\right)} \qquad (3)$$

where, E_{mN}/E_o, is the normalized stiffness loss due to transverse cracking (given by Eq. (1)) and, E_{LD}, is the stiffness of the locally delaminated region. In the present analysis, E_{LD}, was assumed to be $E_1/2$, where E_1 is the equivalent longitudinal stiffness of the warp yarns. For a woven composite with a "*n* x *n*" repeating weave pattern, where *n* fill yarns interlace with *n* warp yarns (in the unit cell), the ratio (a/L) is given by (1/*n*). For the 5-harness satin weave, (a/L) = (1/5). Note that Eq. (3) includes the effect of the transverse yarn cracking given by the, E_{mN}/E_o, terms.

Edge Delamination Model for a Woven Composite

The edge delamination damage mechanism was modeled, in the present study, using an analysis similar to O'Brien's [5] edge delamination model for laminated composites. The longitudinal stiffness of the edge delaminated laminate in Fig. 4, can be derived by assuming that the total load on the laminate is the sum of the loads in the edge delaminated region (of width, c) and the rest of the laminate (of width, 2b-2c). The longitudinal laminate stiffness, E_{ed}, can be derived as:

$$E_{ed} = A_D E^* + (1 - A_D)E_{md} \qquad ; \ A_D = (m\,c/b) \qquad (4)$$

where, A_D, is the delaminated area fraction defined as the ratio of edge delaminated area to the total surface area of the laminate. It is assumed that edge delaminations initiate and grow equally at all ply interfaces in the woven composite. The symbol, m, represents the number of sublaminates formed by these delaminations. For the 8-ply laminate considered here, m = 7. The delamination length, c, represents the length of the delaminations at each of the, m, ply interfaces. It is also assumed that the delamination lengths, c, on both edges of the laminate are equal. E^* is the stiffness of the delaminated region. In the present study E^* was assumed as $E_1/2$, where E_1 is the equivalent longitudinal stiffness of the warp yarns. E_{md} is the stiffness of the laminate which has no edge delamination, and is given by Eq. (3). This region contains damage in the form of inter-yarn debonding and matrix cracking.

Stiffness Degradation and Fatigue Life Model

The stiffness evolution and fatigue life were determined using an empirical growth law for the delamination growth rate. The delamination growth rate, $(dc/dN)_{ed}$, was assumed to follow a power law relationship as:

$$\left(\frac{dc}{dN}\right)_{ed} = B\,G_{ed}^{\beta} \qquad (5)$$

where, G_{ed}, is the strain energy release rate and the parameters, B, and, β, are determined using delamination growth tests. The strain energy release rate, G_{ed}, for edge delamination was also derived using an extension of O'Brien's [5] model as:

$$G_{ed} = \frac{t\sigma_a^2}{2mE_o}\left(\frac{E_{md}}{E_o} - \frac{E^*}{E_o}\right) \tag{6}$$

where, t, is the laminate thickness (Fig. 3), σ_a is the maximum applied cyclic stress, and (E_{md}/E_o) is computed using Eq. (3).   Note that Eq. (6) is a function of (E_{md}/E_o) which is a function of the evolution of transverse yarn cracking. If we assume that the transverse yarn cracking essentially reaches a plateau and does not propagate after the onset of delamination, then (E_{md}/E_o) can be replaced by it's value at delamination onset, (E_{md}/E_o)$_{do}$, and G_{ed} will remain constant throughout the delamination propagation stage.

Equation (5) was integrated to give an expression for the delamination length, c, in terms of, G_{ed}. The unknown constant of integration was determined from the condition that $c \approx 0$ when $N = N_{do}$, where N_{do} is the cycles required for edge delamination onset. This resulted in the following expression for the delamination length, c:

$$c = B\,G_{ed}^{\beta}\left(N - N_{do}\right) \tag{7}$$

The variation of the laminate normalized stiffness, (E_{ed}/E_o), can then be expressed using Eqs. (4) and (7) as:

$$\frac{E_{ed}}{E_o} = \frac{mBG_{ed}^{\beta}\left(N - N_{do}\right)}{b}\left(\frac{E^*}{E_o} - \left(\frac{E_{md}}{E_o}\right)_{do}\right) + \left(\frac{E_{md}}{E_o}\right)_{do} \tag{8}$$

Note that Eq. (8) includes the effects of both transverse yarn cracking (until delamination onset) and inter-yarn debonding.

The criterion used in the present analysis for fatigue failure was based on the maximum cyclic strain, ε_a, in the laminate and was given by:

$$\varepsilon_a = \frac{\sigma_a}{E_{ed}} \geq \varepsilon_{cr} \tag{9}$$

Using Eqs. (8) and (9) the fatigue life of a woven composite laminate can be expressed as:

$$N = N_{do} + \frac{b}{mBG_{ed}^{\beta}\left(\left(E^*/E_o\right) - \left(E_{md}/E_o\right)_{do}\right)}\left(\frac{\sigma_a}{\varepsilon_{cr}E_o} - \left(\frac{E_{md}}{E_o}\right)_{do}\right) \tag{10}$$

RESULTS AND DISCUSSION

The models described in the previous section were used to analyze the stiffness degradation and the fatigue life of the AS4/PR500, 5HS composite. The effective axial stiffness of the undulating yarns, $E_1 = 119.3$ GPa, was calculated using the rule of mixtures and the measured [1, 2] value of $E_o = 64.12$ GPa and the estimated value of $E_2 = 9.03$ GPa. E_2 was estimated using constituent graphite fiber and epoxy matrix properties along with micromechanics and textile mechanics analyses described in Refs. [7, 8]. The parameters, A and d, in Eq. (2) were determined in Ref. [4] as, 0.0883 and 0.0083, respectively. The parameter, $\beta = 5.25$, in Eq. (5) was obtained from Ref. [9] which tested a similar RTM graphite/epoxy composite under mode II fracture conditions. The parameter, $B = 8.3 \times 10^{-18}$, in Eq. (5) was selected to match the average measured stiffness degradation rate at 70% of ultimate tension strength (UTS). The value of, N_{do}, was estimated using an initial crack size of 0.3 mm in Eq. (5). The predicted stiffness degradation using Eq. (9) is shown in Fig. (5) and it correlates reasonably well with the measured stiffness degradation.

The critical maximum cyclic strain, ε_{cr}, under fatigue was estimated using $N = N_{do}$ in Eq. (10) for a maximum fatigue cyclic stress of 80% UTS. It was assumed that at this high stress level delaminations would become unstable as soon as they were initiated. Figure 6 shows that the predicted fatigue life (S-N curve) compares reasonably well with test data.

SUMMARY

Simple mechanism-based models were developed for the effects of matrix cracking, inter-yarn debonding, and delamination on the longitudinal stiffness of a woven composite. Using these models it was possible to predict both the stiffness loss and the life of a woven AS4/PR500, 5HS graphite/epoxy composite at room temperature under tension-tension fatigue loading. The present analysis predicted the trends in the stiffness degradation and the fatigue life reasonably well. The present fatigue modeling technique should be very useful in designing with woven composite laminates, especially since it can provide estimates of both the fatigue stiffness degradation and the fatigue life.

REFERENCES

1. Patel, S. R. and Case, S. W., "Durability of a Graphite/Epoxy Woven Composite Under Combined Hygrothermal Conditions," International Journal of Fatigue, Vol. 22, No. 9, 2000, pp. 809-820.
2. Patel, S. R. and Case, S. W., "Durability of a Woven Polymer Matrix In Aerospace Applications," Proceedings of the 41st AIAA/ASME/ASCE/AHS/ASC Structures, Structural Dynamics, and Materials Conference, Atlanta, GA, 3-6 April, 2000, AIAA-2000-1680.
3. Kumar. R. and Talreja R., "Fatigue Damage Evolution in Woven Fabric Composites," Proceedings of the 41st AIAA/ASME/ASCE/AHS/ASC Structures, Structural Dynamics, and Materials Conference, Atlanta, GA, 3-6 April, 2000, AIAA-2000-1685.
4. Naik, R. A., Patel, S. R., and Case, S. W., "Fatigue Damage Mechanism Characterization and Modeling of a Graphite/Epoxy Woven Composite," Submitted to the Journal of Thermoplastic Composite Materials, Feb. 2001.
5. O'Brien, T. K., "Analysis of Local Delaminations and Their Influence on Composite Laminate Behavior," *Delamination and Debonding of Materials, ASTM STP 876*, W. S. Johnson, Ed., 1985, pp. 282-297.
6. Lee, J-W. and Daniel, I. M., "Progressive Transverse Cracking of Crossply Composite Laminates," 1990, *J. of Composite Materials*, Vol. 24, November 1990, pp. 1225-1243.
7. Naik, R. A. and Crews, J. H., "Micromechanical Analysis of Fiber-Matrix Interface Stresses Under Thermomechanical Loadings," *Composite Materials: Testing and Design (Eleventh Volume), ASTM STP 1206*, E. T. Camponeschi, Ed., 1993, pp. 205-219.
8. Naik, R. A., "Analysis of Woven and Braided Fabric-Reinforced Composites," *Composite Materials: Testing and Design (Twelfth Volume), ASTM STP 1274*, R. B. Deo and C. R. Saff, Eds., 1996, pp. 239-263.
9. Vinciquerra, A. J., Davidson, B. D., Schaff, J. R., and Smith, S. L., "An Improved Methodology for the Determination of Mode II Fatigue Delamination Growth Rates Using the End-Notched Flexure Test," Proceedings of the American Society for Composites, 15th Technical Conference, Sept. 25-27, 2000, College Station, Texas, pp. 999-1007.
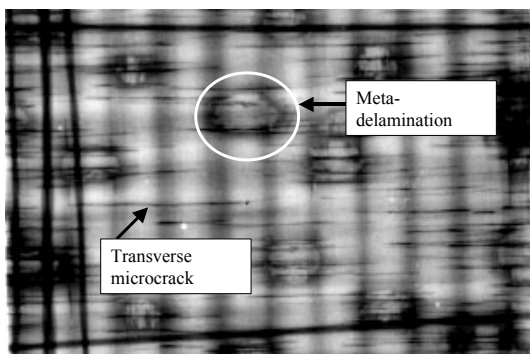
Figure 1: Radiograph showing the transverse yarn cracking and 'meta-delamination' damage.
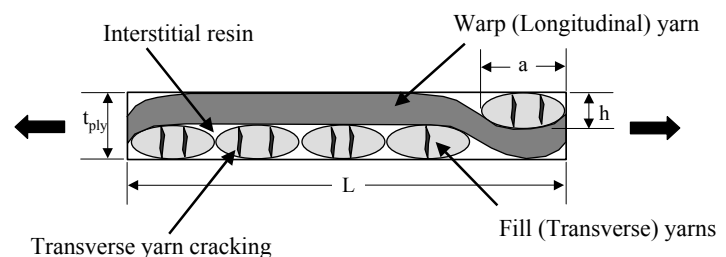
Figure 2: Transverse yarn cracking model showing repeating unit cell of a 5-harness satin weave ply.
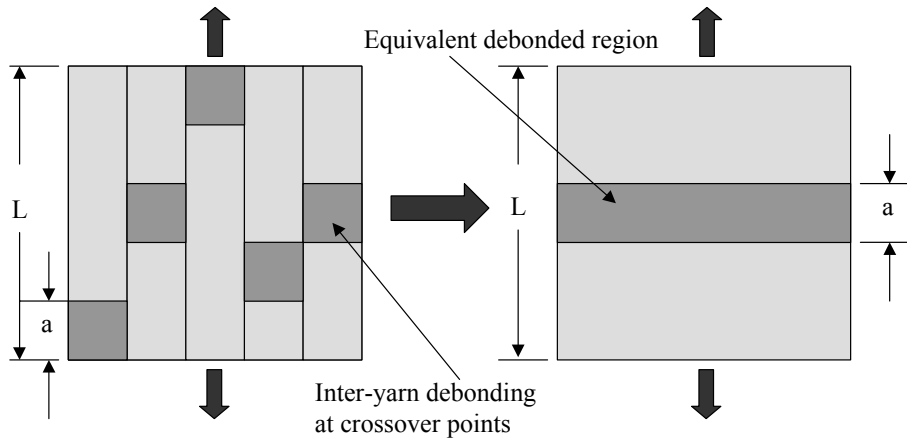
Figure 3: Equivalent inter-yarn debonding model for a 5-harness satin weave composite ply.
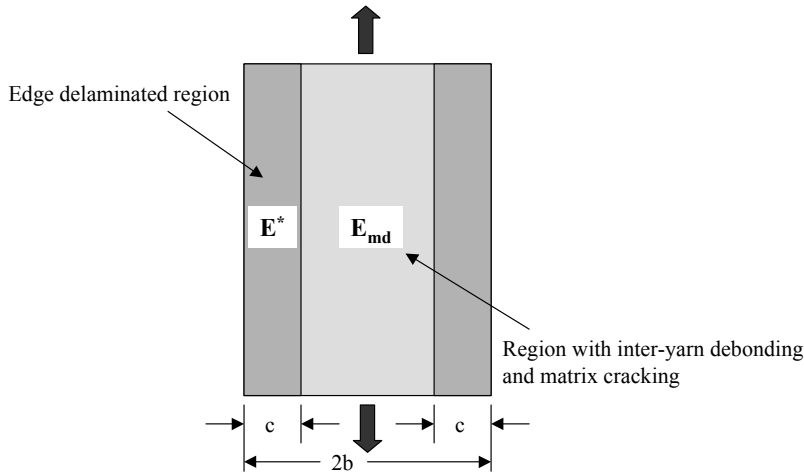
Figure 4: Edge delamination model for a woven composite laminate.
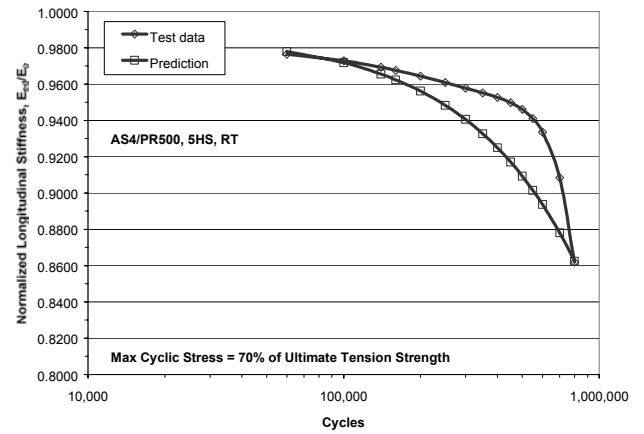
Figure 5: Comparison of predicted and measured normalized stiffness loss during fatigue.
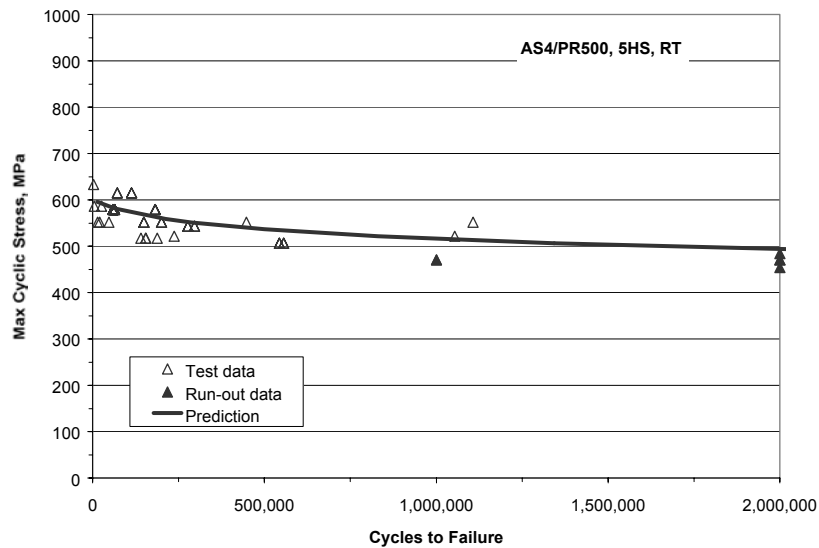
Figure 6: Comparison of predicted fatigue life S-N curve with test data.

THE ANALYSIS OF THE COMPLIANCE CHANGE PRIOR TO THE ONSET OF CRACK GROWTH

A.Neimitz

Department of Mechatronics and Machines Design, Kielce University of Technology, Al. 1000 lecia P.P.7, 25-314 Kielce, Poland.

ABSTRACT

Experimental results presented in this paper show that, for certain steels, the compliance of the specimens containing cracks, measured during the partial unloading, decreases during the first stage of loading and reachs the minimum value. After the minimum is reached, the compliance rises along with the growing crack. The theoretical model to find when this situation may happen is presented. Both the experimental analysis and the theoretical model suggest that the minimum is reached for these materials at the onset of the crack growth.

KEYWORDS

Compliance change, stable crack growth, onset of crack growth.

INTRODUCTION

The method of compliance change is considered as one of the most important in the experimental methodology to measure a critical value of the J- integral (J_{IC}) or to determine J_R curves. Compliance of the specimen during unloading is a function of the elastic properties of a material as well as the length and the net cross section of the specimen. Growing crack changes the net cross section in front of it thus, the crack extension can be expressed as a function of the compliance change. However, in most cases, the onset of crack growth can not be determined using the compliance change technique. Thus, the value of the J_{IC} determined according to this technique or the potential drop technique is not a value of J at the critical moment. It is the value, which is at most, according to certain conventions, close to this point. If one knew the onset of crack growth he would compute the critical value of J using the well known, simple Rice's formula [1]. However, according to the author's experimental observations, there are steels, for which the compliance change technique can be used to determine the onset of crack growth. When the pre-cracked specimens made of these materials are repeatedly unloaded from the very beginning of the loading process (displacement control loading process) the reduction of the compliance is first observed until the minimum value is reached.

EXPERIMENTAL OBSERVATIONS

The force, P, displacement, u, diagrams, $P=P(u)$, are always recorded to determine the J_R curves for the specimens containing cracks. The shapes of these diagrams can be classified, according Turner [2], into two groups: *pagoda roof*- type and *round house*-type. As representatives of these groups two steels have been selected: the 40HMNA steel (according to the Polish standards, similar to the ASTM 4340 steel) and the 18G2A steel. The yield stress of the 40HMNA steel varied from 1083 to 1217 MPa, depending on heat

treatment. The ultimate strength varied from 1176 to 1294 MPa, the Ramberg – Osgood exponent, *n*, was equal to 53. The yield stress of the 18G2A steel was 363 MPa, the ultimate strength was 573 MPa and the Ramberg – Osgood exponent was equal to 11. The CCT (central crack tension), DENT (double edge notched tension), SENB (single edge notched bend) specimens were machined and pre-cracked to obtain different in-plane and out-of-plane constraints. For the 40HMNA steel for all heat treatments (quenching and tempering) and for all specimen configurations the shape of the *P=P(u)* diagrams were of the *pagoda roof* type (Fig.1a). For the 18G2A steel the *P=P(u)* diagrams were always of the *round house* shape (Fig.1c).

The analyses of the fractured surfaces of the broken specimens have been performed with the help of the scanning microscope. Characteristic features of these fractographs were always similar. The fractured surfaces of the specimens made of the 40HMNA steel contain both cleavage and ductile domains (Fig.2a). The cleavage domains are distributed either arbitrarily as "islands" surrounded by voided regions or as sequential brittle and ductile regions. The fractographs taken from the specimens made of 18G2A steel indicate a pure ductile mechanism of fracture (Fig.2b) (voids) with shear lips of different size depending on the specimen thickness for the non-side-grooved specimens. Similar fractographs can be presented for side-grooved specimens. The above observations suggest that the shapes of the *P=P(u)* diagrams depend on the mechanism of fracture. From a simple phenomenological model of the specimen containing the growing crack [3] one can conclude that the shapes of the *P=P(u)* diagrams (*pagoda roof* or *round house*) depend on the crack growth equation *a=f(u)* where *a* is an actual crack length. For the very slow crack extension after the onset of crack growth the *round house* shape is observed. For the fast at the beginning and slowing down afterwards crack extension process the *pagoda roof shape* is observed.

The *round house* shape of the *P=P(u)* curves is usually associated with the "plastic" materials for which the large scale yielding is observed in front of the growing crack. The *pagoda roof* shape of the *P=P(u)* curves is usually observed for the small scale yielding in front of the growing crack. The shape of the *P=P(u)* diagrams helps the experimenter to predict the mechanisms of fracture, the general structure of the crack growth equation and, to some extend the microstructure of the material. Moreover, the shape of the *P=P(u)* curves indicates for which materials one can expect the reduction of the compliance of the specimen during unloading before the onset of crack growth. If this reduction is observed, it happens for the materials characterized by the *pagoda roof* shape of the *P=P(u)* diagram. In the Figs 1a and 1b two typical *P=P(u)* curves for the CCT and SENB specimens made of the 40HMNA steel are shown along with the *C=C(u)* diagrams, where *C* is the compliance measured during unloading. In the Fig. 1c the corresponding curve is presented for the 18G2A steel. The minimum of the *C=C(u)* diagrams for the 40HMNA curves can be identified with the onset of the crack growth. It has been confirmed by numerous measurements using the potential drop and multi – specimen techniques. For the *pagoda roof P=P(u)* diagrams the sudden change of the $\Delta\phi=f(u)$ slope (Fig. 3), where $\Delta\phi$ is the potential drop, is observed at the same displacement, *u*. For the *round house P=P(u)* diagrams neither minimum along the *C=C(u)* curves nor the sudden change of the $\Delta\phi=f(u)$ slope can be observed.
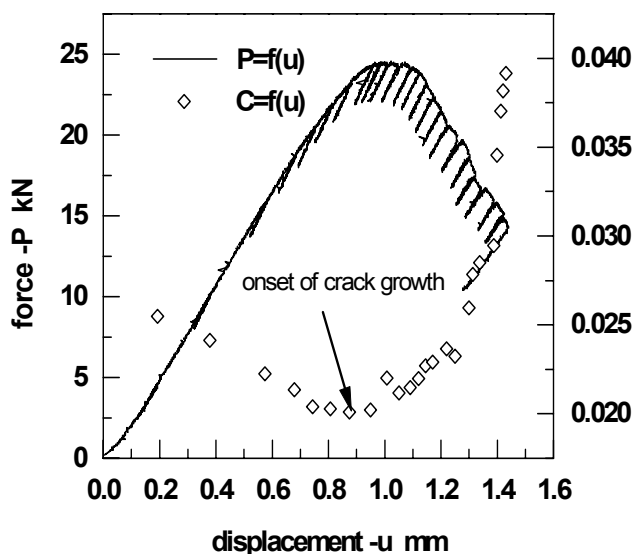
Fig.1a. The *pagoda roof* shape of the *P=P(u)* curve and *C=C(u)* curve. SENT specimen. 40HMNA steel.
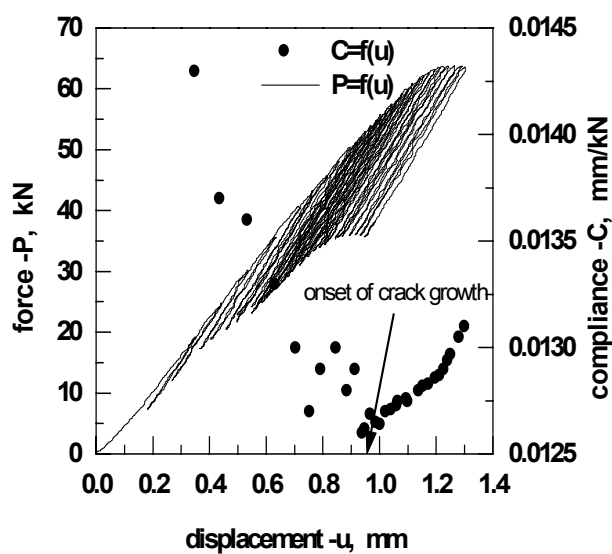
Fig.1b. The *P=P(u)* curve and *C=C(u)* curve. CCT specimen. 40HMNA steel.
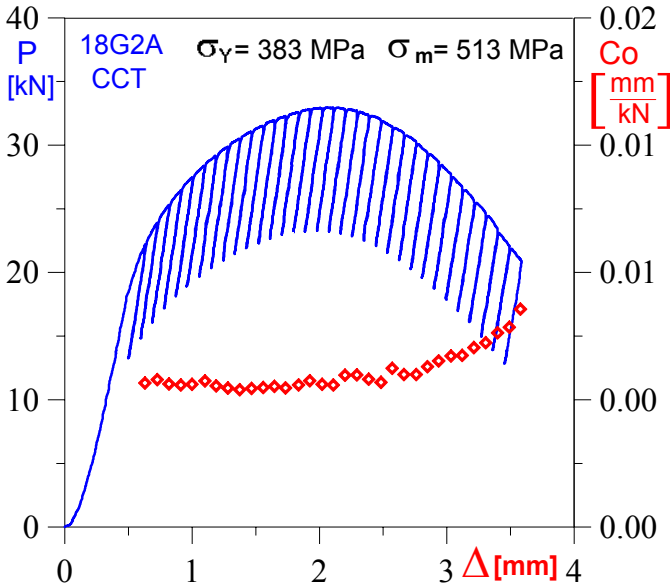
Fig.1c. The *round house* shape of the $P=P(u)$ curve and $C=C(u)$ curve. CCT specimen, 18G2A steel.

Fig.2a. Fractured surface of the 40HMNA steel, SENB specimen.
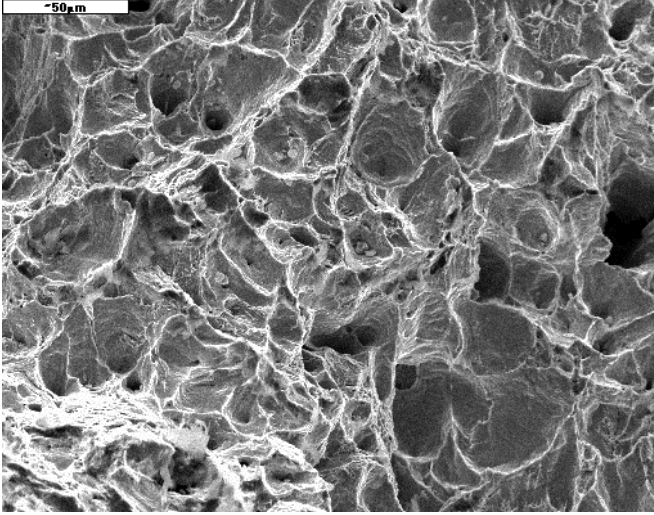
Fig.2a. Fractured surface of the 18G2A steel, SENB specimen.
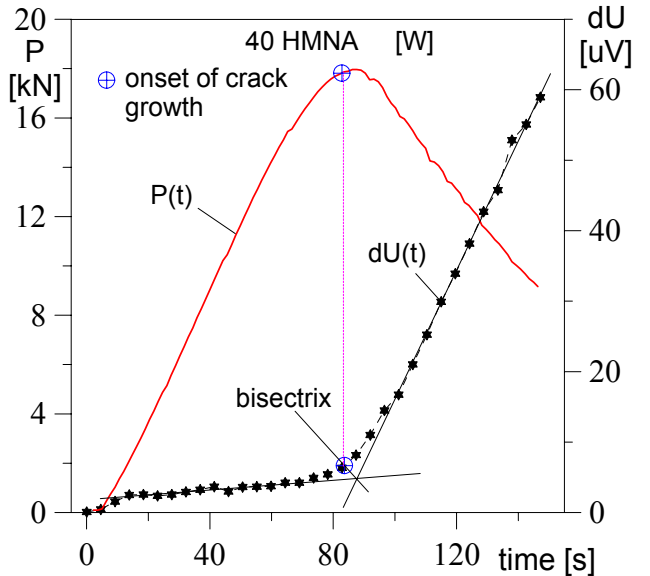
Fig.3. The *pagoda roof house* shape of the $P=P(u)$ curve and potential change $\Delta\varphi=f(u)$ curve

THEORETICAL ANALYSIS

Theoretically obtained $P=P(u)$ curves with the help of the phenomenological model [3] are presented in the Figs 4a and 4b. To obtain such curves from the model, the material properties (yield stress, σ_y, the Young's modulus, E), geometrical characteristics of the specimen (e.g. for CCT specimens there are: thickness, B, width, $2W$, length, L and the initial crack length, $2a_0$) and the crack growth equation should be introduced. In the case presented here, the following crack growth equation was used::

$$a(u) = a_0 + \psi u H(u_i - u) + [\psi u_i + \beta(u - u_i)^\alpha]H(u - u_i).. \tag{1}$$

The second term in Eq. (1) represents the blunting process, the third - actual crack growth; α, β, ψ, are some constants (at least in this paper; in general they may be the functions of specimen dimensions and material properties), u_i denotes the load point displacement at the onset of crack growth. $H(-)$ is the Heaviside's step function. The power α assumes positive values. In the author's opinion, it may depend on the mechanisms of crack growth.

To obtain the *pagoda roof* shape of the $P=P(u)$ diagram, the exponent α should be less than 1 and greater than 1 for the *round house* curves. In the model the point of the crack growth initiation is known thus

it can be precisely pointed out in the $P=P(u)$ and $C=C(u)$ diagrams. Also the extension of the plastic zone can be traced. From the Fig. 4a one can observe that the minimum along the $C=C(u)$ curve coincides with the onset of the crack growth. It is not so for the *round house $P=P(u)$* diagram (Fig.4b). In this case the very weak minimum along the $C=C(u)$ diagram can be observed for the moment of the rapid extension of the plastic zone (in this case the strip yield zone), not at the onset of crack growth. Such a weak minimum can not usually be observed experimentally.
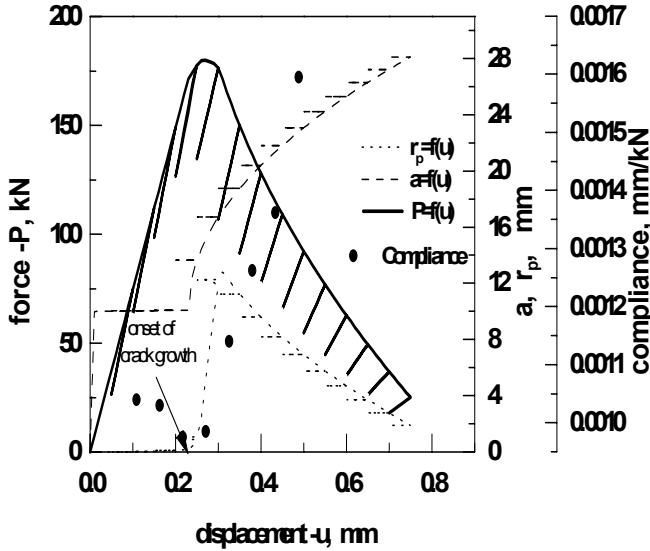
Fig.4a. *Pagoda roof* curve obtained from the phenomenological model. $C=C(u)$ points.
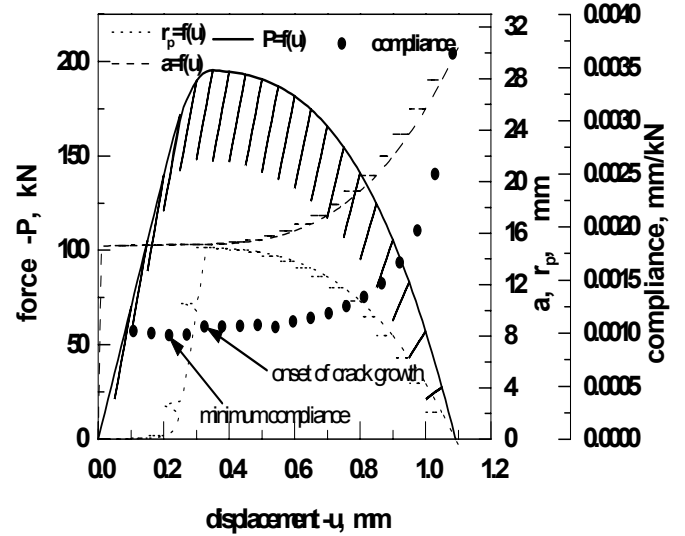
Fig.4b. *Round house* curve obtained from the phenomenological model. $C=C(u)$ points.

The theoretical model confirmed the experimental observations. However, there is still the important question open: why it happens? Below, a simple model and computations will be presented. To some extend they answer this question.

When the specimen is loaded the plastic zone evolves in front of the crack. It is assumed first that we observe the small scale yielding situation *SSY*. All computations will be performed for the SENB specimen with the standard proportions for the basic specimen dimensions ($W=2B$, $L=4W$, $0.45<a_0/W<0.65$). The results of the experimental measurements of the compliance for the 40HMNA steel and the SENB specimen are shown in Fig.1a. The SENB has been selected because of very simple basic formulas for the stress intensity factor.

Without the plastic zone in front of the crack the compliance during loading and unloading is constant and can be computed from the formula:

$$C = \frac{u}{P} = \frac{16}{EB}\left(1 + \frac{ah_3L}{23.28b_0^2}\right),$$
(2)

where $b_0=W-a_0$. To obtain this formula the following procedure and assumptions have been made: It was assumed that the total load point displacement is:

$$u_{Tot} = u_{ncr} + u_{cr},$$
(3)

where: u_{ncr} is deflection of the specimen without a crack, u_{cr} is deflection of the specimen due to the existing crack. To compute u_{ncr} the simplest elementary formula has been used. u_{cr} has been computed from the relation [4]:

$$u_{cr} = \alpha \frac{\sigma_y}{E} a_0 \left(\frac{P}{P_0}\right)^n h_3(n, a/W)$$
(4)

Where $n=1$ for an elastic material, P_0 is a limit load which in this case has been computed for the plane strain situation and the Huber-Mises-Hencky yield criterion, h_3 can be found in Kumar et al. [4]. For $0.45 < a_0/W < 0.65$ this function is equal to a constant: $h_3 = 4.65$ with the maximum error about 4 per cent.

When the plastic zone is introduced in front of the crack the original crack length can be replaced with the effective crack length.

$$a_{eff} = a_0 + r_p \tag{5}$$

Now, the total deflection of the specimen is:

$$u_{Tot} = \frac{16P}{EB}\left(1 + \frac{(a_0 + r_p)Lh_3}{23.28(b_0 - r_p)^2}\right). \tag{6}$$

We assume the formula for the length of the plastic zone in the form:

$$r_p = \beta\left(\frac{K_I}{\gamma\sigma_y}\right)^2, \tag{7}$$

where $\beta = 1/2\pi$ for Irwin's model, $\beta = \pi/8$ for Dugdale's model, γ defines the level of the out-of-plane constraints
. It is equal to unity for plane stress or $\sqrt{3}$ for plane strain situations. More general definition for γ was given by Wang et al. [5]. The formula (6) can also be extended to take into account the effect of strain hardening [6]. Now the "local" compliance during the *loading* process can be written in the form:

$$C_{load} = \frac{du_{Tot}}{dP} = \frac{16}{EB}\left\{\left(1 + \frac{\varepsilon(a_0 + r_p)}{(b_0 - r_p)^2}\right) + 2\beta\varepsilon P\left[\frac{2(a_0 + r_p)}{(b_0 - r_p)^2}\right]\frac{\left(0.995\frac{L}{\sigma_0 B}\right)^2}{(b_0 - r_p)^2(b_0 - 4r_p)}\right\}, \tag{8}$$

where $\varepsilon = \frac{h_3 L}{23.28}$. To compute the compliance during elastic unloading, C_{unl} the following procedure has been assumed: The total energy of the deformation process can be computed from Fig.5 and the formula:

$$E_{Tot} = area(OAC) = Pu_{Tot} - \int_0^P u_{Tot}\,dP. \tag{9}$$

The total elastic energy is equal:

$$E_{elast.} = area(CAB) = \frac{1}{2}C_{unl}P^2. \tag{10}$$

The amount of dissipated energy is equal:

$$E_{dissip.} = area(OAB) = E_{Tot} - E_{elast.} = V_{pl}\xi, \tag{11}$$

where ξ is the average specific energy of the plastic and process zones formation. It is not unreasonable to assume that for the stationary crack and *SSY* this quantity is a constant. The volume of the plastic zone can be approximated by a simple formula:

$$V_{pl} = \psi B r_p^2 . \tag{12}$$

The constant ψ defines how much the shape of the real plastic zone differs from the cylinder. It is also assumed that for the stationary crack and SSY the shape of the plastic zone does not change. Introducing Eqs 9, 10, 12 into Eq.11 one can easily obtain the formula for the compliance during elastic unloading:

$$C_{unl} = \frac{32}{EB}\left[1 + \frac{\varepsilon(a_0 + r_{pk})}{(b_0 - r_{pk})^2}\right] - \frac{32}{P^2}\int_0^P \frac{P}{EB}\left[1 + \frac{\varepsilon(a_0 + r_{pk})}{(b_0 - r_{pk})^2}\right]dP - 2\xi\psi\frac{Br_{pk}^2}{P^2} . \tag{13}$$

The actual length of the plastic zone r_{pk} can be computed by the iterative procedure starting from $r_{p0}=0$. For k=3 the error is less than 3 per cent. Computations has been made for 40HMNA steel with the following data: L=100mm, B=20mm, W=25mm, a_0=12.5mm, E=215000 MPa, σ_y=1100 MPa, ν=0.33. It turns out that the compliance during unloading may increase or decrease depending on the product $\psi\xi$. For the above data this product should be greater than $2 \cdot 10^4$ MPa in order to observe a decreasing compliance during unloading. The results presented in Fig.6 have been obtained for $\psi\xi$=$3 \cdot 10^4$. The above results suggest that the compliance reduction before the onset of the crack growth can be observed if the specific energy of the plastic and process zones formation is sufficiently high.

The computations performed for the same specimen but for the case when the whole ligament is in plastic state (the Kumar et al. [4] formulas were used) do not lead to the compliance change before the onset of the crack growth.
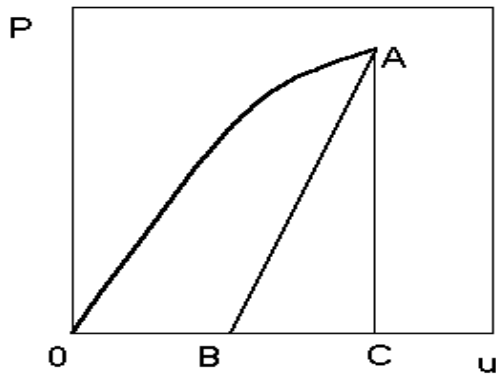
Fig.5. Schematic $P=P(u)$ diagram
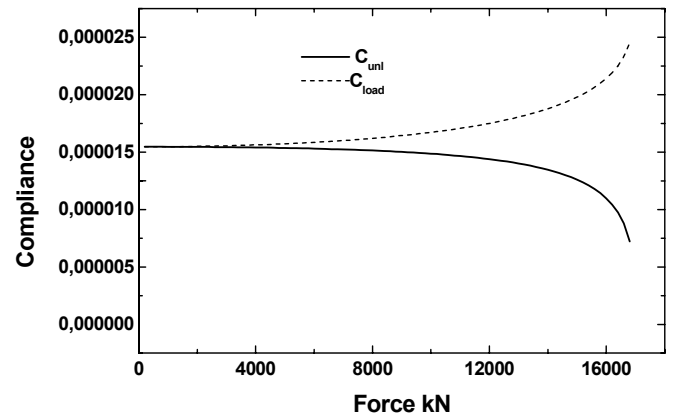
Fig.6. Compliance of the specimen during loading and unloading as a function of the external force

REFERENCES

1. Rice, J.R., (1968), *Journal of Applied Mech.*Vol.35, pp.379-386
2. Turner, C.E. (1990) In: Fracture Behaviour and Design of Materials and Structures, 8th European Conference on Fracture (ed. D.Firrao), Vol.II, EMAS, Warley, UK,pp.933-968.
3. Neimitz, A. (2000), In: *Advances in Mechanical Behaviour, Plasticity and Damage,* (Ed. D.Minnay, P.Costa, D.Francois, A.Pineau), Elsevier, Vol.II, pp. 1505-1510
4. Kumar V., German, M.D., Shih C.F. (1981), In: *An Engineering Approach for Elastic Plastic Fracture Analysis,* Electric Power Research Institute, Inc. Palo Alto, Ca, , EPRI Raport NP. – [67]
5. Wang, J., Shen, Y.P., Wanlin, G., (1998), *Engineering Fracture Mechanics,* Vol. 21, pp. 1389-1401,

THE ANTI – PLANE SHEAR FIELD FOR CRACK IN INFINITE SLAB OF A NONLINEAR DAMAGE MATERIAL

L.Q. Tang, H.J. Chen and Y.H. Cai

College of Civil Engineering, Harbin Engineering University, Harbin   150001 ,China

ABSTRUCT

In this paper, the constitutive equation of nonlinear damage material is given .The basis equation for founding solution of mode III crack is established, using transformation of coordinates .The analytical and numerical results are obtained .The shape and the scale of damage zone where the material completely fails are determined.

KEY WORDS

Nonlinear damage material, solution of near tip crack for Mode III crack

INTRODUCTION

The field of stress and strain near tip-crack is an important research problem of fracture mechanics because it controls the crack growth. There are many kinds of structures of crack –tip field [1-3] , that depend upon the material nature and the loading condition .All of the existing solutions to the crack tip fields are based on the singular analysis, i.e. either stress or strain possesses singularity at the crack tip. But the real behavior of materials does not permit the singular, at finite stress and strain the material always fails. Therefore, the singular solution is not valid when the crack tip is really approached. In order to reveal the true feature of the crack tip fields, we must consider the real character of materials. When strain reaches certain critical value, the strength of material will completely vanished, so that the concept of damage mechanics mast is introduced [4].

There are continuous models of internal damage parameters, which can be incorporated into crack analysis. For instance, Bui and Ehrlachar[5] Proposed a simple model to analysis the dynamic steady state propagation of a damage zone in elastic and plastic solids and got exact solutions for the small scale damage model in elastic material and for the strip problem, in mode III loading. There was not singularity in the solution of stresses and strains. With Krajcinovic's[6] assume, Popelar and Hoagland[7] discussed distribution of damage field of mode   III crack ,where the relation of damage variable and strain is linearity.

This paper is concerned with an infinite slab containing a semi – infinite crack, which is subjected to the anti – plane shear K_{III} field at infinity. First, the constitutive equation of nonlinear damage material is given, which is that $\boldsymbol{t} = G(1 - D^{n})\boldsymbol{g}$, where $\boldsymbol{t}$ is the effective stress, n is the softening parameter, damage

factor D, depends on the effective strain, $D = (G\mathbf{g}/k)$, where G is the shear module, k is the damage module and the $\mathbf{g}$ is effective strain.. When $n = 1$, the material is linear damage material[6]. Secondly, the basis equation is given for founding solution of mode III crack, using transformation of coordinates. Finally, the analytical and numerical results are obtained .The shape of damage zone; stress distribution and the scale of damage zone are discussed. When $n = 1$, the result is same as that given by C.H.Popela[5]

THE BASIS EQUATION

The constitutive equation

The evolvement equation given by Krajcinovic [6] is

$$\mathbf{s} = E(1-D)\mathbf{e}$$

$$D = E\mathbf{e}H(\mathbf{e})/K \qquad\qquad 1$$

Where E is Young's modulus $H(\mathbf{e})$ is Heaviside's function. This constitutive equation describes damage process of concrete, rock and brittle materials. We assume that the constitutive equation of materials in the uniaxial tension case is

$$\mathbf{s}_e = E(1-D^*)\mathbf{e}_e$$

$$D^* = \left(\tfrac{E}{K}\mathbf{e}_e\right)^n = D^n \qquad\qquad (2)$$

where $\mathbf{s}_e$ is effective stress $\mathbf{e}_e$ is effective strain in the uniaxial tension case, Eq. 2 is

$$\mathbf{s}/_K = D(1-D^n) \qquad\qquad 3$$
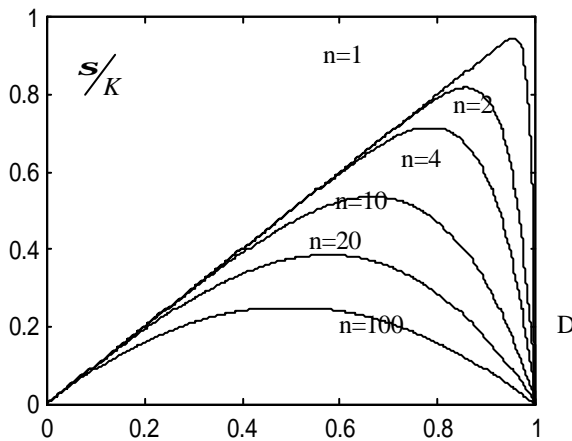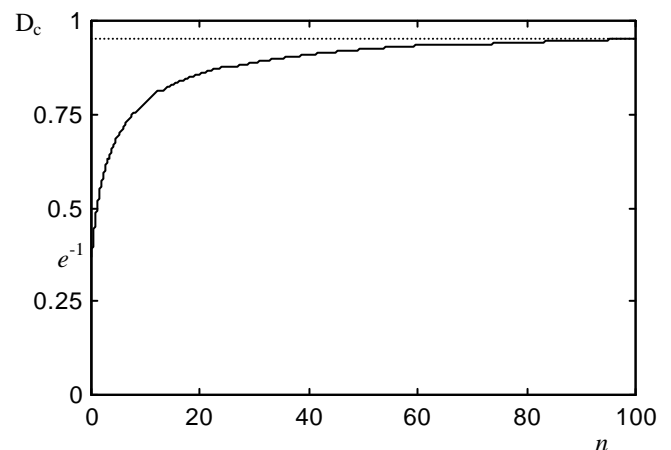
Figure 2: the relation of n and the damage critical

Figure 1 Curve of $\mathbf{s}/_K \sim D$

Curve of $\mathbf{s}/_K \sim D$ (Eq. (3)) is given by Fig.1.When stress reaches extremism the material is in

Unstability State, soft and fails .The damage critical value satisfies that $\dfrac{d\mathbf{s}}{dD} = 0$, then

$$D_c = \left(\tfrac{1}{n+1}\right)^{\frac{1}{n}} \qquad\qquad\qquad 4$$

As n increases, D_c increases   the relation of n and the damage critical value is given by Fig.2

The basis equation of problem of Mole III crack

In anti-plane problem, stresses, $t_{xz} = t_x, t_{yz} = t_y$ satisfy the equilibrium equation:

$$\frac{\partial t_x}{\partial x} + \frac{\partial t_y}{\partial y} = 0 \qquad\qquad\qquad 5$$

The strain and displacement, $W = W(x, y)$, are given by

$$g_{xz} = g_x = \tfrac{\partial W}{\partial x}$$
$$\qquad\qquad\qquad 6$$
$$g_{yz} = g_y = \tfrac{\partial W}{\partial y}$$

The compatibility equation is

$$\frac{\partial g_x}{\partial y} = \frac{\partial g_y}{\partial x} \qquad\qquad\qquad 7$$

The constitutive equation:

$$t_x = G\left(1 - D^n\right)g_x$$
$$\qquad\qquad\qquad 8$$
$$t_y = G\left(1 - D^n\right)g_y$$

Where g is effective shear strain, $g = \left(g_x^2 + g_y^2\right)^{\frac{1}{2}}$ and

$$t = G\left(1 - D^n\right)g \qquad\qquad\qquad (9)$$

Where $D = \left(\tfrac{G}{K}g\right)$

The boundary conditions are

$$t_q = 0 \qquad\qquad on \qquad q = p$$

$$t_y - it_x \to \frac{K_{III}}{\left[2p(x - iy)\right]^{\frac{1}{2}}} \qquad when \quad |x + iy| \to \infty \qquad (10)$$

$$W = 0 \qquad\qquad on \qquad q = 0$$

THE BASIS SOLUTION OF MODE III CRACK

Using transformation of co-ordinates (Fig.3), we can take variable (g_x, g_y) instead of (x, y) [8].
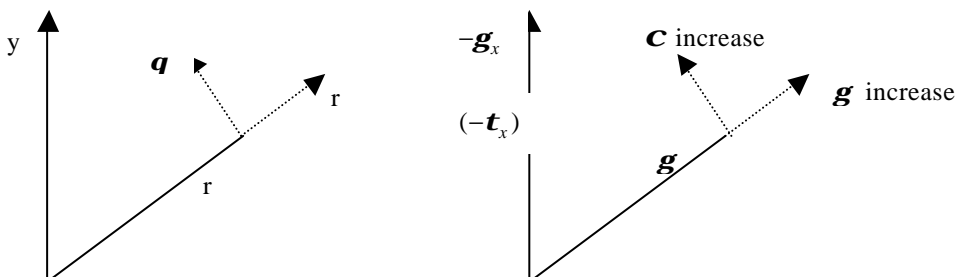
The equilibrium equation 5 becomes

$$\frac{\partial x}{\partial t_x} + \frac{\partial y}{\partial t_y} = 0 \qquad\qquad 11$$

The compatibility equation 7 is

o $\quad\searic$ $\boldsymbol{q}$ ⟶x   o $\quad\searic$ $\boldsymbol{c}$ ——— $\boldsymbol{g}_y(\boldsymbol{t}_y)$
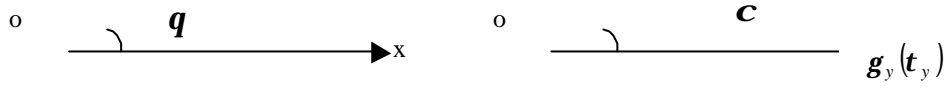
Fig.4 Physics and strain plane

$$\frac{\partial x}{\partial \boldsymbol{g}_y} = \frac{\partial y}{\partial \boldsymbol{g}_x} \qquad\qquad 12$$

Introducing the strain function $y(\boldsymbol{g}_x, \boldsymbol{g}_y)$

$$x = \frac{\partial \boldsymbol{y}}{\partial \boldsymbol{g}_x} \qquad y = \frac{\partial \boldsymbol{y}}{\partial \boldsymbol{g}_y} \qquad\qquad 13$$

Then Eq. 12 is satisfies. Taking note of transformation of co-ordinates, we have express of x and y

$$x = -\sin\ \boldsymbol{c}\frac{\partial \boldsymbol{y}}{\partial \boldsymbol{g}} - \frac{\cos x}{\boldsymbol{g}}\frac{\partial \boldsymbol{y}}{\partial x}$$

$$y = \cos x\frac{\partial \boldsymbol{y}}{\partial \boldsymbol{g}} - \frac{\sin\ x}{\boldsymbol{g}}\frac{\partial \boldsymbol{y}}{\partial x} \qquad\qquad 14$$

In the problem of mode III crack, $y(\boldsymbol{g}, x)$ satisfies

$$\frac{1-D^n}{1-(n+1)D^n}\frac{\partial^2 \boldsymbol{y}}{\partial D^2} + \frac{1}{D}\frac{\partial \boldsymbol{y}}{\partial D} + \frac{1}{D^2}\frac{\partial^2 \boldsymbol{y}}{\partial \boldsymbol{c}^2} = 0 \qquad\qquad 15$$

When $D < D_c$ $\quad \frac{d\boldsymbol{t}}{d\boldsymbol{g}} > 0$ Eq. 15 is elliptic and a well-behaved small-scale yielding solution is attainable. Assume that

$$\boldsymbol{y} = f(D)\sin\ \boldsymbol{c} \qquad\qquad 16$$

Where $f(D) = D\boldsymbol{j}(D)$ and $\boldsymbol{j}(D)$ satisfies

$$\frac{d\boldsymbol{j}}{dD} = \frac{A}{D^3(1-D^n)} \qquad\qquad 17$$

A is unknown constant. We can obtain solution of Eq. 17 .

When $n = 1$, we have

$$\boldsymbol{j}(D) = -\frac{1}{2D^2} - \frac{1}{D} + \ln\left(\frac{D}{1-D}\right) + C \qquad\qquad 18$$

When $n = 2$, we have

$$\boldsymbol{j}(D) = -\frac{1}{2D^2} + \ln D - \frac{1}{2}\ln\left(1 - D^2\right) + C \qquad\qquad 19$$

When $n \neq 1,2$ we have $nm - 3 \neq -1$ i.e. when $n \neq 1,2$ there are not terms of D^{-1}, we have

$$\frac{1}{D^3\left(1 - D^n\right)} = D^{-3} + D^{n-3} + D^{2n-3} \cdots\cdots + D^{nm-3} + \cdots\cdots \qquad 0 < D < 1$$

$$\boldsymbol{j} = C - \frac{1}{2D^2} + \frac{D^{n-2}}{n-2} + \frac{D^{2n-2}}{2n-2} + \cdots\cdots + \frac{D^{Mn-2}}{Mn-2} + \cdots\cdots \qquad\qquad 20$$

Where C is unknown constant, and series in Eq. (20) is convergence, when $D \in (0,1)$.

DISCUSSION

The shape of damage zone

With Eq. 14 and 20 we have

$$x = X(D) + R(D)\cos 2\boldsymbol{c} \qquad\qquad (21)$$
$$y = R(D)\sin 2\boldsymbol{c}$$

Where
$$X(D) = -\frac{G}{2K}(f' + f/D)$$
$$R(D) = \frac{G}{2K}(f' - f/D)$$

The damage zone, defined by (21), is a set of circles for $0 < D < D_c$ with their centers on x>0 ,y=0. There are two unknown constants , A and C, in solution ,which are determined by boundary condition and the damage zone where the material completely fails, respectively. By Eq. 10 , we have

$$A = \frac{K_{III}^2}{2\boldsymbol{p}\,KG} \qquad\qquad 22$$

When $D = D_c$ by $X(D_c) = R(D_c)$ C satisfies

$$\frac{df}{dD} = 0 \qquad\qquad 23$$

When n=1 $C = -4$,this is same as result in [7]

Fields of stresses and strains

With Eq. (21 and expression of y we obtain

$$\sin(2c - q) = b\sin q$$
$$r = R(D)[b^2 + 2b\sin(2c) + 1]$$

24

Where $\quad b = X(D)/R(D)$

$$g_r = g\sin(q - c)$$
$$g_q = g\cos(q - c)$$

25

For certain geometry point, (r, q) by Eq. 24 , (c, D) are determined and the field of strains is given.

As n increases $R(D_c)$ decreases. When $n \to \infty$

$$R(D_c) = \frac{K_{III}^2}{2pK^2}$$

26

If we take that $K = t_s$, the yield strength when $n \to \infty$ the material is elastic then the radius of damage zone is the same as of the plastic radius in the elastic perfectly plastic material[3].

References

1.Gao , Y.C.(1987), *Int. J. Of Fracture*, **34**,111
2.Chen, H.J. and Tang, L. Q. (2000) *Mesomechanics 2000 ,* Xi'an , P.R.China ,Vel.**1**,305
3.Rice,J.R.(1967) *J. of Appl. Mech.* , **34**,287
4.Kachanov, L.M.(1961) *in Problems of continuum mechanics, SIAM*, Philadelphia,306
5.Bui, H. and Ehrlachar, A. (1981) *Proc.of Fifth Intter.Conf. on Fracture,*Vel.**2,**533
6.Krajcinovic,D.(1979) *J. of Appl. Mech.,* **46,**592
7.Popelar. C.H.and Hoagland. R.G.(1986) *Eng. Fracture Mech., ,*23,131
8.Hwang,K.Z. and Yu,S.W.(1985),Elastic plastic Fracture Mechanics, *Tsinghua University Press.* Beiging , China.

THE CORRELATION BETWEEN TEMPERATURE, LOADING RATE, AND MICROSTRUCTURE OF POLYMER BLENDS

T. Vu-Khanh

Université de Sherbrooke - Faculté de genie
2500 boul. de l'Université
Sherbrooke, Quebec, Canada, J1K 2R1

ABSTRACT

The study of polymer blends is probably the most active area of polymer research. In this work, the effects of morphology on fracture performance of both uncompatibilized and compatibilized polymer blends have been investigated over a large range of loading rates and temperatures. For this purpose, blends of different concentrations were studied at various test conditions. The focus is put on the time – temperature dependence of fracture performance of these blends. The results show that the organization of the blend structure play an important role in the dependence of fracture behavior on time and temperature. For instance, the co-continuous morphology of an uncompatibilized nylon 6/ABS blend gives an optimum fracture performance at a fracture test-speed of 2.5 m/s at room temperature. However this 'optimum' property disappears when the test speed is reduced to 100 mm/min at room temperature or when the temperature is lowered to -40°C at 2.5 m/s. The addition of compatibilizers such as interfacial agents makes polymer blends more ductile. The time-temperature dependence of the brittle-ductile transition is controlled by an energy activation process. Adding the interfacial agent lowers the temperature at brittle-ductile transition and reduces the energy barriers controlling two relaxation mechanisms called a and β , that act in parallel and affect both yielding and fracture behaviors.

KEYWORDS

Polymer, Blend, Fracture, Yielding, Relaxation, Morphology, Brittle-Ductile Transition.

INTRODUCTION

Blending existing polymers together has long been known to be an effective, low-cost way of developing novel materials and polymer alloys and blends represent one of the fastest growing sectors of the plastics industry. Block copolymers have been shown to be effective interfacial agents for many incompatible blends of homopolymers. They are known to reduce the interfacial tension, homogenize the morphology and improve adhesion between the phases. This effect results in an improvement in mechanical properties and fracture performance.

The emulsification curve, which relates the average minor phase particle diameter to the concentration of interfacial agent added, has been used to quantify the effect of the interfacial agents on the blend morphology [1, 2]. It displays some key characteristics, an initial significant drop in the size of the dispersed phase with the addition of the copolymer followed by an equilibrium diameter value at high concentrations of modifier once

interfacial saturation has been obtained. This drop in particle size is the result of reduced coalescence and interfacial tension due to the presence of the interfacial modifier [2].

The addition of an interfacial modifier to an incompatible polymer blend, though widely and successfully used in industry, can introduce certain complications into the processing, such as an additional compounding step, and increases the production costs, since modifiers are usually expensive. A clear economic advantage can result if the mechanical properties of a blend can be controlled and improved to an acceptable level without the addition of an interfacial modifier. The morphology of immiscible blends is also highly dependent on the concentration of the dispersed phase, particularly in the absence of an interfacial modifier. In recent detailed studies [3], image analysis has shown that both the size and size distribution of the dispersed phase increase rapidly with composition. At a given concentration, at the point of phase inversion, a co-continuous morphology is observed.

The influence of the above microstructures on physical properties still remains largely an unknown in the scientific literature. This paper presents the results of an investigation on the effects of morphology on fracture and yielding behaviors in compatibilized and uncompatibilized blends. The compatibilized blend consists of 80 volume % polystyrene (PS) and 20 volume % ethylene- propylene rubber (EPR) compatibilized by two triblock copolymers of styrene/ ethylene- butylene/ styrene (SEBS) of different molecular weights. The uncompatibilized blend consists of nylon 6 and ABS (Acrylonitrile-Butadiene-Styrene). The focus is put on the correlation between time, temperature and microstructure.

EXPERIMENTAL

Blends of various compositions of nylon 6 and ABS (both polymers were supplied by Monsanto) have been prepared by extrusion. The properties and blending procedure are given in [4]. Each prepared blend is designated by S_n in which n corresponds to the weight fraction of ABS. For example, S_{10} contains 10% in weight of ABS, S_{80} contains 80 wt% of ABS etc.

The compatibilized blend investigated consists of a polystyrene matrix (PS), supplied by Dow Chemical (Styron D685), and a minor phase of ethylene-propylene rubber (EPR), a random copolymer containing 54% ethylene, supplied by Exxon Chemical (Vistalon V-504). The interfacial agents were supplied by Shell: they consist of two styrene/ ethylene- butylene/ styrene (SEBS) triblock copolymers (Kraton 1651 and Kraton 1652, referred to as K1 and K2, respectively), containing 29% styrene. The number average molecular weights of K1 and K2 are 174,000 and 50,000 g/mol, respectively. Some properties of these materials are presented in [5]. Blends were prepared with various interfacial agent concentrations, based on the minor phase. Thus, the sample denoted as K1 10 has the following composition: 80 parts PS, 20 parts EPR, and 2 parts (10% of EPR content) Kraton 1651. Likewise, K2 20 has a composition of 80 parts PS, 20 parts EPR, and 4 parts (20% of EPR content) Kraton 1652.

RESULTS AND DISCUSSIONS

Figure 1a shows the variation of the measured fracture energies at crack initiation as a function of ABS concentration. It can be seen that, with increasing ABS content, fracture is brittle up to about 70wt% and then becomes ductile with a significant jump in fracture energy. The morphological analysis of the blends [4] revealed that phase inversion occurs around 70wt% ABS, where a co-continuous morphology is observed. The change in mechanical performance of the blend and the peak in fracture energy at this composition were therefore attributed to this co-continuous morphology. However, further fracture tests at low loading rates have shown that the peak in fracture energy does not always occur around 70wt% ABS but its location varies with the loading rate of the fracture test. Figure 1b shows an example of variation of fracture energy with ABS content at a cross-head speed of 100 mm/min. In this case, the peak in fracture energy occurs at about 10wt% ABS, with the same change in fracture type from brittle to ductile. In polymer blends, it has long been shown that the morphology strongly controls fracture performance and optimum microstructure has always been researched for good performance. Figure 2 shows the variation of the ABS content at the peak of fracture energy, as a function of the loading speed of fracture test. It clearly indicates that optimum morphology depends on loading rate. The rate dependence of physical and mechanical properties of polymer

has always been attributed to an energy activation process. It can therefore be expected that the optimum morphology also depend on temperature. To confirm this effect, fracture tests were then carried out at lower temperatures. Measurement of the impact fracture energy at $-40°C$ for the two constituent polymers and three selected blends S_{10}, S_{40}, and S_{70} revealed that the above peaks in fracture energy disappear, suggesting a strong dependence of these peaks with temperature.
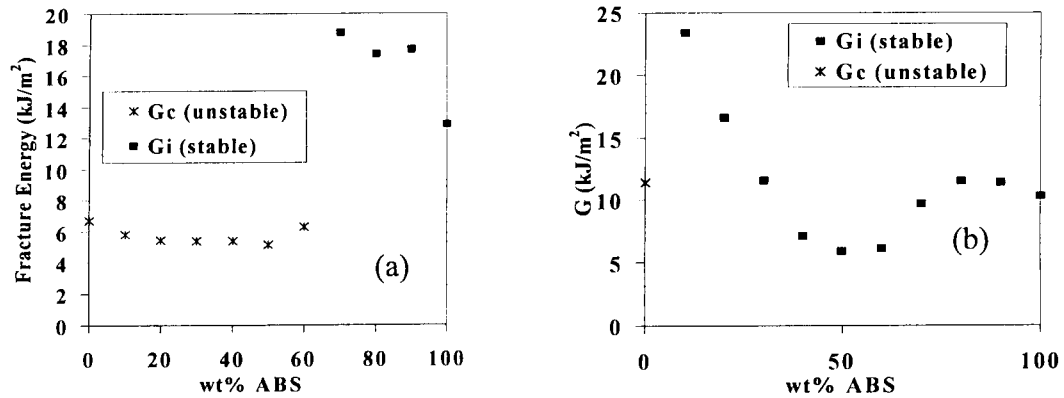
Figure 1: Fracture energies versus ABS content at impact speed of 2 m/s (a) and 100 mm/min (b).
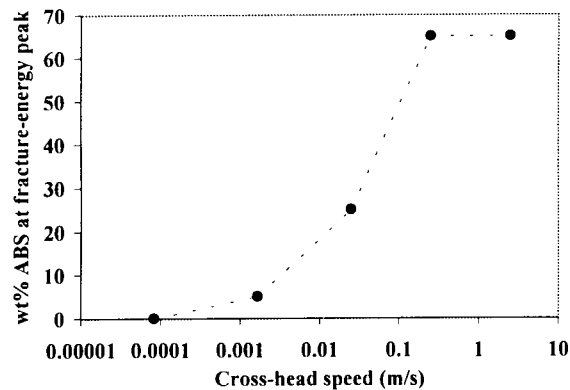
Figure 2: ABS content at the peak of fracture-energy, as a function of loading speed.

The time and temperature dependence of the properties of polymers is known to be due to the molecular relaxation. In immiscible polymer blends, the phase separation usually results in clear and distinct molecular relaxation corresponding to each constituent of the polymers present. The relaxation time or temperature has been found to be an intrinsic property of the polymer. The organization of the blend structure at a larger scale does not affect the relaxation processes. Multiple impact peaks have been reported for several polymers [6-8] and, although it is still a controversial subject, attempts have been made to relate the observed impact peaks to the molecular relaxation peaks of the polymer. A peak in the fracture energy is always observed at the brittle-ductile transition temperature. For toughened polymers, the cause of ductile-brittle transition has often been attributed to the glass transition of the rubbery phase [9]. The brittle-ductile transition in a rubber-toughened nylon 66 (Zytel ST-801) and a High Impact Polystyrene (HIPS) have been analyzed as a function of the molecular relaxation mechanisms of the rubbery and matrix phases in these materials [7]. It has been found that the type of molecular relaxation with lower activation energy seems to be related to the brittle-ductile transition phenomenon. In the case of HIPS, the relaxation process involved seems to be the glass-rubber transition of the polystyrene matrix. In the case of Zytel ST-801, the β transition of the Nylon 66 seems to be related to the brittle-ductile transition of fracture [7].

Unlike these effects, the results on the nylon-6/ABS blend suggest that the organization of the blend structure plays an important role in the dependence of fracture behavior on time and temperature. The co-continuous morphology at about 70wt% ABS gives an optimum fracture performance at a fracture test-speed of 2.5 m/s at room temperature. However this 'optimum' property disappears when the test speed is reduced to 100 mm/min (at the same room temperature) or when the temperature is lowered to $-40°C$ (at the same loading

speed of 2.5 m/s). It is worth mentioning that other mechanical properties such as Young modulus, yielding or strength do not show any peak when the ABS concentration increases. The yield stress of the blend continuously decreases with increasing ABS content. A reduction in the loading rate also results in a continuous decrease in the yield stress of the blend as expected.

In the PS/EPR blends, fracture also exhibits a brittle, semi-ductile, or ductile behavior, depending on the temperature and loading speed. Figures 3 shows the variation of various fracture energies as a function of temperature at 100 mm/min and 2.5 m/s, for the K1 30 sample. The transition from brittle to ductile behavior occurs with a peak in the measured value of fracture energy. As the temperature increases, a semi-ductile behavior is generally observed at the region of the peak, before the onset of ductile fracture. In the semi-ductile behavior, a certain amount of stable crack propagation occurs in the sample before the onset of unstable fracture. The reported value corresponds to the fracture energy at instability. It should be noted [8, 10] that one cannot base only on the initiation value of fracture energy to determine the fracture performance but the type of crack propagation should also be considered. With the same value of fracture at crack initiation the material exhibiting a stable crack propagation performs better in terms of impact resistance since after initiation, fracture can only continue with further supply of energy by external loads. However, in the case of brittle fracture, the crack accelerates without any additional supply of energy from the external forces.
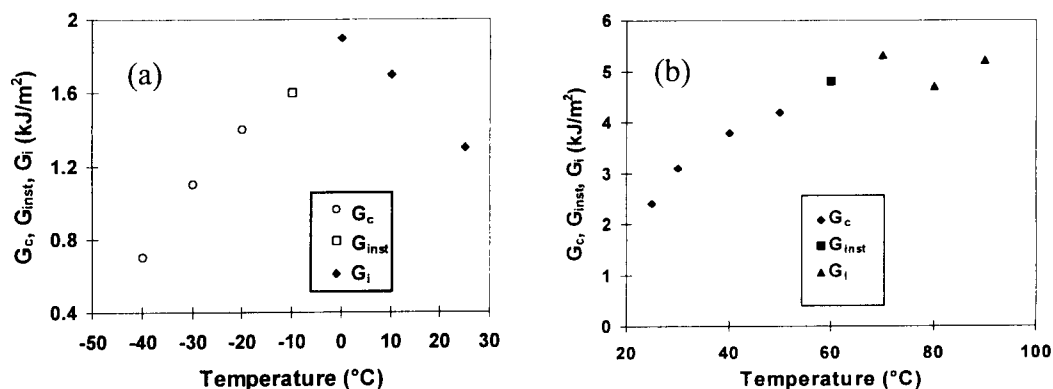
Figure 3: Fracture energy versus temperature for K1 30 sample at: a) 0.0067 m/s; and b) 2.5 m/s.

Table 1 summarizes the temperature at brittle-ductile transition at loading speeds (v) of 100 mm/min and 2.5 m/s for the non compatibilized (NC), K1 30 and K2 30 samples. Ductile behavior of fracture is observed at higher temperatures for the non compatibilized sample. Adding an interfacial agent results in a lower temperature at brittle-ductile transition. This effect is also much more pronounced with the K2 interfacial agent. With an impact loading of 2.5 m/s, the brittle-ductile transition occurs at around 0°C for the K2 30, 65°C for the K1 30, and 80°C for the NC samples. Furthermore, the dependence of fracture behavior on loading rate and temperature also depends on the molecular weight of the interfacial agent. When loading speed increases from 100 mm/min to 2.5 m/s, the shift in the transition temperature, ΔT, is less significant in the K2 30 sample. The result is rather surprising since it has been generally recognized that the effects of loading rate and temperature on the mechanical properties of polymers are mainly controlled by molecular relaxation.

TABLE 1
APPROXIMATE TEMPERATURE AT BRITTLE-DUCTILE TRANSITION

Blend	NC	K1 30	K2 30
v = 100 mm/min (0.00167 m/s)	0°C	-10°C	-20°C
v = 100 mm/min (0.00167 m/s)	80°C	65°C	0°C

The above results indicate that morphology and interfacial strength also have a significant effect on the time-temperature dependence of fracture behavior. The differences in morphology and interface of these samples have been presented in [5]. It has been shown that adding these interfacial agents results in a continuous decrease in the diameter of the minor phase, and the lower molecular weight interfacial agent K2 results in a

more important reduction in this diameter. In this case, the volume average particle size is reduced from 2.72 to around 0.55 μm, a decrease of nearly 80%, whereas the K1 copolymer only decreased it to about 1.1 μm.

In terms of fracture performance, secondary transitions have often been found to play an important role and the energy barrier controlling the time temperature dependence of the fracture process can be estimated using the Arrhenius equation [7, 8]. The energy barrier ΔH controlling the time temperature dependence of the brittle-ductile transition in the fracture process can been estimated using a set of data of the temperatures and the average times to fracture measured at this transition. Table 2 summarises the effect of K1 and K2 on the activation energy (ΔH) controlling the brittle-ductile transition in the fracture process. Increasing the amount of interfacial agent decreases the diameter of the minor phase and the value of ΔH. Smaller diameters of the minor phase associated with K2 also results in a lower value of the activation energy.

TABLE 2
ACTIVATION ENERGY OF BRITTLE-DUCTILE TRANSITION

Blend	NC	K1 2.5	K1 10	K1 20	K1 30	K2 2.5	K2 15	K2 30
ΔH (kJ/mol)	42.3	71.87	52.08	50.56	39.6	45.21	38.37	32.10

The yielding process of a polymer is usually regarded as a momentary condition of pure viscous flow because it denotes the point at which the change of stress with strain is zero for a given strain rate. It has been thus considered to be a thermally activated process involving inter-and intramolecular motion and has been described by Eyring's viscosity theory. Ree and Eyring [11] have suggested later that the yielding behavior of polymers could be controlled by two relaxation processes (α and β) acting in parallel. The equation governing the yield stress and the two molecular relaxation processes has been expressed by:

$$\frac{|\sigma_y|}{T} = \frac{|\sigma_{y\alpha}|}{T} + \frac{|\sigma_{y\beta}|}{T} = \frac{R}{V_\alpha^*} \left[\frac{\Delta H_\alpha}{RT} + 2.303 \log\left(\frac{2\dot{\varepsilon}}{\dot{\varepsilon}_{0_\alpha}}\right) \right] + \frac{R}{V_\beta^*} \sinh^{-1}\left[\frac{\dot{\varepsilon}}{\dot{\varepsilon}_{0_\beta}} \exp\left(\frac{\Delta H_\beta}{RT}\right) \right]$$

where ΔH denotes the activation energy of the yielding process, T the absolute temperature, $\dot{\varepsilon}$ the strain rate (proportional to the cross-head speed). V^* is known as the activation volume, $\dot{\varepsilon}_0$ is the pre-exponential factor and R is the universal gas constant. The symbols α and β refer to α and β relaxation process respectively. In order to verify the Ree-Eyring model, compression tests have been carried out over a wide range of temperatures. The yield stress in uniaxial compression was measured at different temperatures from -75°C to 100°C and over nearly four decades of loading rate from 0.1 to 200 mm/min. An example for the time-temperature dependence of the yielding behavior of the K1 2.5 blend is shown in Figure 4.
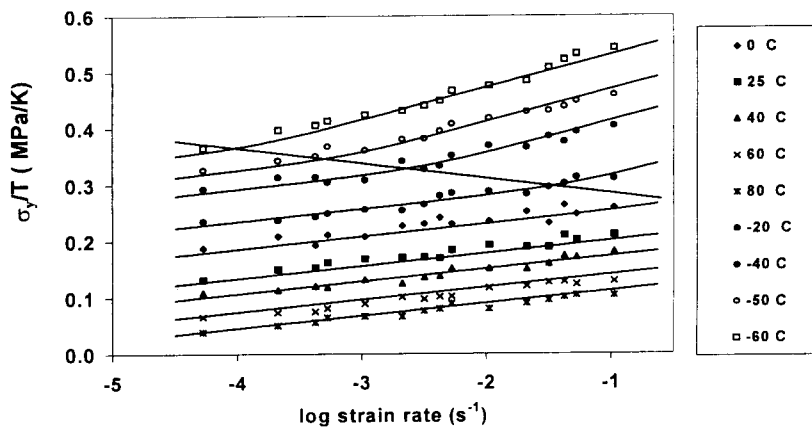
Figure 4: Time - temperature dependence of yield stress for K1 25 sample.

It can be seen that the diagram of σ_y/T versus logarithm strain rate can be separated into two regions: region I at high temperature and low loading rate where the process α dominates; and the region II at low temperature and high loading rate where the process β is activated. Between the regions α and β, the curve of σ_y/T as a function of logarithm strain rate shows a noticeable variation in slope. This variation can be used to find the transition boundary between these two regions by standard mathematics or using the procedure proposed in [12]. In Table 3, the values of the parameters (V_α^*, ΔH_α, $\dot{\varepsilon}_{0_\alpha}$, V_β^*, ΔH_β, $\dot{\varepsilon}_{0_\beta}$) characterizing the yielding behavior of the blend with three compositions; K1 2.5, K1 10 and K1 20, are presented. It can be seen that the addition of interfacial agent results in an increase in the activation volume V^* and a reduction of the activation energy ΔH for both α and β processes. The results also show that the values of energy barrier controlling the β process are close to those presented in Table 2, measured by the brittle-ductile transition of the fracture tests. This suggests that the brittle-ductile transition in fracture behavior is controlled by a secondary relaxation of the polymer molecules. Furthermore, the plasticizing effect of the interfacial agent also reduces the energy barrier of the secondary motions that occur at low temperatures and high loading rates. The correlation between the activation energy of the β process and the energy barrier controlling the brittle-ductile transition suggests therefore that there is an implicit correlation between yielding and the fracture behavior.

TABLE 3

PARAMETERS CONTROLLING THE α AND β PROCESSES IN YIELDING

Blend	ΔH_α (kJ/mol)	V_α^* (nm^3/segment)	ΔH_β (kJ/mol)	V_β^* (nm^3/segment)
K1 2.5	145	1.43	66	0.89
K1 10	138.3	1.46	61.1	0.91
K1 20	133.5	1.58	58	1.13

CONCLUSION

The organization of polymer blend structure plays an important role in the dependence of fracture behavior on time and temperature. The time-temperature dependence of the brittle-ductile transition in fracture performance of the blend is controlled by an energy activation process and can be predicted by the Arrhenius equation. The yielding behavior of the blend is controlled by two processes (α and β) acting in parallel and can be predicted by the Ree-Eyring model. It has also been found the value of energy barrier controlling the β process in yielding is close to the energy barrier controlling the brittle-ductile transition in fracture. The results suggest an implicit correlation between yielding and fracture behavior.

REFERENCES

1. Matos, M., Favis, B.D. and Lomellini, P. (1995) *Polymer*, 36, 3899.
2. Lepers, J-C., Favis, B.D. and Tabar, R.J. (1997) *J. Poly. Sci.: Poly. Phys.*, 35, 2271.
3. Willis J.M., Caldas V. and Favis B.D. (1991) *J. Mat. Sci.* 26, 4742.
4. Mamat A., Vu-Khanh T., Cigana P., Favis B., J. Polym. Sci. Part B: Polym. Physics, 35, 2583-2592, 1997.
5. Cigana, P., Favis, B.D., Albert, C. & Vu-Khanh, T. (1997) Macromolecules, 30(14), pp. 4163.
6. Woo L., Westphal S., and Ling M. T. K. (1994) Polym. Eng. Sci., 34, 420.
7. Vu-Khanh T., Yu Z (1997) *Theor. Appl. Fract. Mech.*, 26, 177.
8. Vu-Khanh T. (1998) *Theor. Appl. Fract. Mech*, 29, 75.
9. Bucknall B. (1988) *Makromol. Chem., Makromol. Synp.*, 16, 209.
10. Vu-Khanh T. (1997) *Trends in Polym. Sci.*, 5, 356.
11. Ree, T. & Eyring, H. J. Appl. Phys., 26, p. 793, 1955.
12. Bauwens-Crowet, C. (1973) J. Mater. Sci., 8, 968.

The Dynamic Mechanical Respondence of Weldment with Mechanical Heterogeneity by SHPB Testing

J.X.Zhang[1], S.L.Gong[2]

[1]Welding Research Institute, Xi'an Jiaotong University, Xi'an, China
[2]Northwest Institute of Nuclear Technology, Xi'an, China

ABSTRACT

A large number of research reports about dynamic mechanical behaviors with the metal and nonmetallic materials have been published in domestic and international publications. The studied results made it known that the dynamic mechanical behaviors of the majority of metals and alloys have the close relationships with the strain rate. The weldment is widely used in some important structures with a dynamic loading especially an impacting in earthquake. The dynamic mechanical respondence of a pressure vessel steel and its weldment with mechanical heterogeneity were investigated by means of Split Hopkinson Pressure Bar (SHPB) testing with different loading rates. The results show that the loading strain rate will affect the dynamic strength of the weldment, that the dynamic respondence of the weldment with mechanical heterogeneity is sensitive to the direction of loading. A testing procedure with SHPB is proposed in order to get reasonable results to describe the dynamic property of weldment with mechanical heterogeneity.

KEY WORDS: SHPB testing, Weldment, Dynamic Mechanical respondence

INTRODUCTION

Much attention has been taken into the mechanical properties of weldment with mechanical heterogeneity, and a lot of numerical and experimental researches are relating with the behavior of mis-matched weldment[1-3]. In general, the strength of mis-matched weldment has much relation with the size of weld metal. The narrower the weld metal is, the higher the strength of weldment at static situation. A few works are down relating with the dynamic respondence of weldment with mechanical heterogeneity, although a large number of researches have been down about the dynamic mechanical behaviors with the metal and nonmetallic materials[4-5]. It is getting more and more important and necessary to study the dynamic respondence of weldment as the increase usage of welded structures in some important structures suffering the dynamic loading such as earthquake and so on. The studied results made it known that the dynamic mechanical behaviors of the majority of metals and alloys have the close relationships with the strain rate. The dynamic mechanical respondence of a pressure vessel steel and its weldment with mechanical heterogeneity were investigated by means of Split Hopkinson Pressure Bar (SHPB) testing with different impacting rates in this paper. The dynamic stress of base metal, weld metal and weldment is recorded and discussed. Some important conceptions are built thought the basic experiment.

MATERIALS AND TESTING

The material used in the SHPB experiment is a pressure vessel steel, 16MnR with 16mm thickness. Its chemical compositions and mechanical properties are shown in table 1. The specimens for welding with

16x50x500 mm are welded manually with J507 electrode (Chinese standard). The welding conditions are the following: welding current 120A, welding voltage 25V and welding speed 120 mm/min. The J507 electrodes were preheated at 350°C with 2 hours before welding. Three kinds of impacting specimens of base metal, weld metal and weldment were extracted from the welded specimens according to the specimen scheme shown in Fig.1. The specimens extracted were machined to the size of $\phi30 \times 15$. The weldment specimen contains three region, weld metal base metal and HAZ(heat Affected Zone).

The test devise is a kind of Split Hopkinson Pressure Bar testing equipment called as SHPB testing and the measuring system is illustrated in Fig.2. The pressure bars, input pulse bar and output pulse bar, are made of 40Cr alloy steel and the size of input pulse bar is $\phi40 \times 800mm$. The experiments are done in room temperature and the impacting rates are near 18 m/s, 23m/s and 39m/s respectively.

RESULTS AND DISCUSSION

Fig.3 shows the dynamic stress of the base metal with different loading rates. It is shown in Fig.3 that the maximum value of the dynamic stress becomes larger as the increase of loading rate and that stress curve at loading rate 39.4 m/s is delayed largely. The dynamic stress of the weld metal is indicated in Fig.4 for different loading rates. It is also shown in Fig.4 that the larger dynamic stress is correspondent with the larger loading rate. Comparing with Fig.3 for near same loading rate, there are two conclusions that the maximum stress of base metal is larger than that of weld mental at loading rate 39.6m/s and the contrary at near 23m/s. Although the yielding stress and tensile stress of the base metal(16MnR) and weld metal(J507) are almost the same in static situation, the dynamic stresses are not the same. It means that the matching property of weldment is changing with dynamic loading situation. The large loading rate will change the matching property of the weldment from the other words. Fig.5 expresses the dynamic stress of weldment with different loading direction at the same loading rate. The type C specimen is taken in the experiments. The specimen consists of the weld metal and the base metal. There exists so called HAZ(Heat Affect Zone) between the base metal and weld metal. Two type of loading directions are used in the testing. One type is from the base metal to the weld metal and the other is from the weld metal to the base metal. It can be seen from the Fig.5 that there is different dynamic stress for two directions. The dynamic stress from base metal to weld meta is larger than that from weld metal to base metal. Comparing with Fig.3 and Fig.4, it can be understood that the dynamic mechanical respondence of weldment with mechanical heterogeneity is different with homogeneous materials. And the mechanical heterogeneity of weldment will affect the dynamic respondence of weldment. Therefore, the mechanical heterogeneity of weldment should be taken into account in designing the welded structure with dynamic loading.

CONCLUSION

The dynamic mechanical respondence of a pressure vessel steel and its weldment were investigated by means of Split Hopkinson Pressure Bar (SHPB) testing with different loading rates. The results show that the dynamic respondence with mechanical heterogeneity is sensitive to the loading direction, the maximum dynamic stress becomes larger with the loading rate, and the matching property of weldment at dynamic situation would be affected by the dynamic loading rate and direction.

REFERENCES

[1] F.M.Burdekin, A comparision of methods for assessment of the significance of the defects in weled structures, IIW Colloquium on Significance of Defects, Bratislava(1979)

[2] J.X.Zhang, Y.W.Shi, and M.J.Tu, Factors Affecting the Estimation of Fracture Mechanics Parameters of Center-cracked weldment, Engineering Fracture Mechanics, Vol50, No.4, pp537-543, (1995)

[3] J.Carlsson, Fracture Mechanics for cracks in weldments, In Advances in Fracture Research (Ed. By S.R.Valluri et.al.), Pergamon Press, Oxford(1984)

[4] J.Harding, In Explosive Welding, Forming and Compaction, T.Z.Blazynski(Ed). Applied Science Publishers, London & New York, (1983)

[5] T.Nakamura, C.F.Shin, and L.B.Freund, Analysis of a Dynamically Loaded Three-Point-Bend Ductile Fracture Specimen,   Engineering Fracture Mechanics, Vol.25, pp323-329, (1086)

Table 1   The chemical composition and mechanical properties of 16MnR ateel

C	Mn	Si	S	P	σ_b(Mpa)	σ_s(Mpa)	δ(%)
0.19	1.4	0.45	0.023	0.015	540	340	21
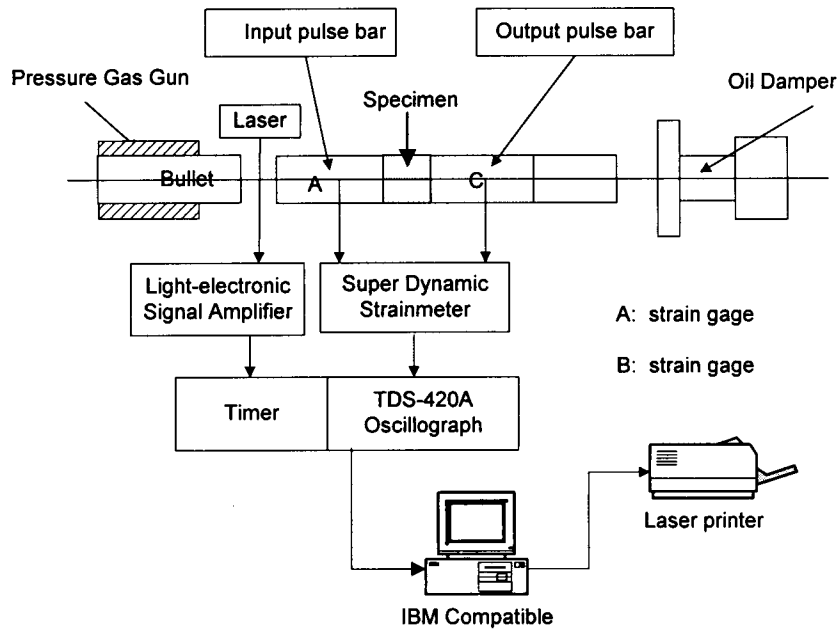
Fig.1 Illustrition of the equipments and measurement system in SHPB
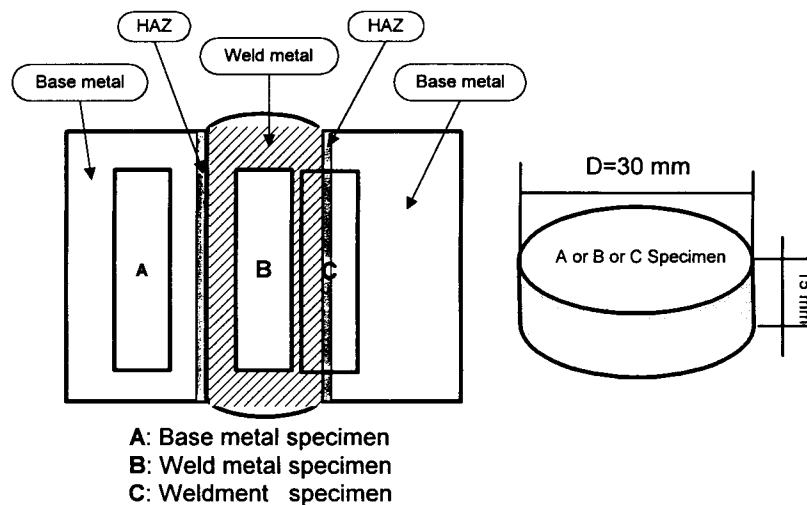
Fig.2 Illustrition of speciments used in SHPB experiments
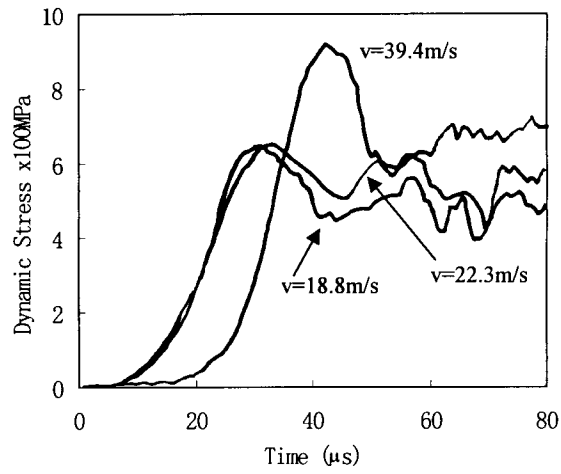
Fig.3 Dynamic stress of base metal with different loading rates
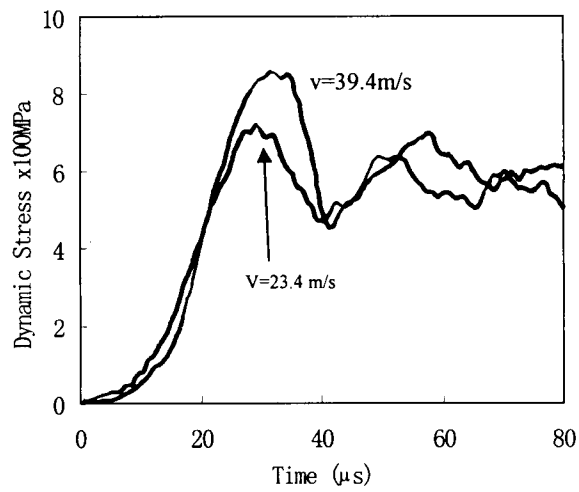
Fig.4 Dynamic stress of weld metal with different loading rates
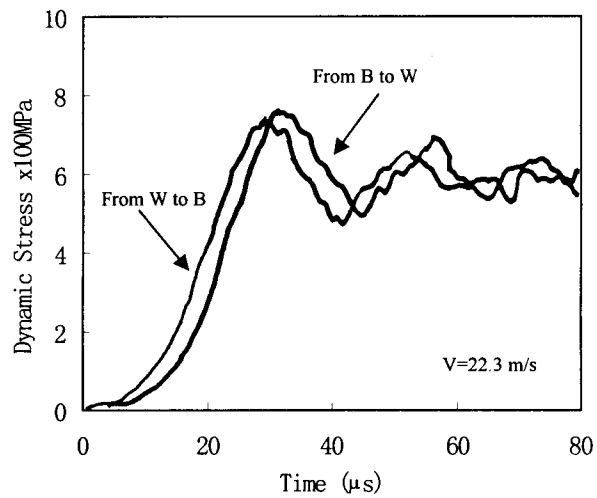
Fig.5 Dynamic stress of weldment with two loading directions

The Dynamic Punch Test in Isotropic and Composite Materials *

C. Rubio-Gonzalez[1] [†]and J. J. Mason[2]

[1]Centro de Ingenieria y Desarrollo Industrial
Pie de la Cuesta 702, Desarrollo San Pablo
76130 Queretaro, Qro., Mexico

[2]Department of Aerospace and Mechanical Engineering
University of Notre Dame. Notre Dame, IN 46556. U.S.A.

Abstract

An experimental investigation is conducted on the two-dimensional punch problem for isotropic and unidirectional fiber-reinforced composite materials under quasi-static and impact loading. Singular estresses are generated in the especimen near the punch corners and the stress intensity factor K_I is introduced to describe such singular stress field. Laser interferometry was used to measure in-plane stresses (transmission mode) and out-of-plane displacements (reflection mode), and then estimate the stress intensity factor. In the dynamic case, a high speed photography technique was employed to capture the transient response of the specimen and measure $K_I(t)$ just after the impact. In all the cases a good agreement between the measurements of K_I and the theoretical predictions was found.
Keywords: stress intensity factor, dynamic fracture, coposite materials, punch test.

1 Introduction

The potential use of composite materials in the construction of defense structures makes it necessary to understand the initiation of damage in the composite as caused by impacting fragments. Typically, this kind of damage initiation is simulated in the laboratory by the punch test. In such a test, fiber-reinforced epoxy matrix composites will develop a limited amount of plasticity before failure occurs. This fact suggests an elastic solution of the stress field will play an important role in understanding and predicting the behavior of composites under punch test, impact conditions.

Like in fracture mechanics, a stress intensity factor K_I is introduced in this work to characterize the behavior of the singular stresses around the punch corners. This parameter is measured experimentally using laser inteferometry and then compared with theoretical predictions. The experimental investigation is conducted on the quasi-static and dynamic punch test for isotropic and orthotropic materials. A rigid punch impacts (in the dynamic case) one side of the specimen, figure 1. The lateral shearing interferometer of coherent gradient sensing (CGS), in conjunction with high speed photography will be used to obtain real time interferograms of the singular stress field generated near the corner of the punch.

The application of the CGS method in the punch test is new. Here, results for isotropic as well as for composite materials are reported. In the isotropic case, the material selected was PMMA (polymethyl methacrylate) a transparent acrylic for which the CGS method in transmission mode is suitable. For the orthotropic case, the material chosen was a unidirectional graphite-epoxy composite with fiber volume density of 0.65. In this case the CGS method in reflection mode was used.

The CGS method has been applied successfully in dynamic fracture experimentation of isotropic materials (Tippur, Krishnaswamy & Rosakis 1991, Mason, Lambros & Rosakis 1992) and fiber reinforced composite materials (Lambros & Rosakis 1997a, Lambros & Rosakis 1997b).

In the quasi-static test, K_I is compared successfully with known solutions of the punch problem for isotropic and orthotropic materials. In the dynamic case, each photograph taken by the high speed camera is digitized and $K_I(t)$ is then measured. The time evolution of K_I agrees very well with the theoretical predictions for the dynamic punch problem developed in Rubio-Gonzalez (1999).

A detailed explanation of the analysis and results for the dynamic test is included in the following sections.

2 Elastodynamic Analysis of the Finite Punch Problem

The punch problem is of great importance in solid mechanics for its multiple technical applications including ballistic impact, metal forming and manufacturing operations such as punching and blanking.

The problem of a *finite*, rigid and flat punch impacting an orthotropic half-plane has been analyzed by Rubio-Gonzalez (1999) using integral transforms and the Wiener-Hopf technique. A solution for the dynamic stress intensity factor $K_I(t)$ was developed which is valid while the dilatational wave travels the punch width ($2l$) twice. That is

$$K_I(t) = \begin{cases} K_I^{(0)}(t) & \text{for } 0 < t < 2l/c_d \\ K_I^{(0)}(t) + K_I^{(1)}(t) & \text{for } 2l/c_d < t < 4l/c_d \end{cases} \tag{1}$$

where $K_I^{(0)}(t)$ and $K_I^{(1)}(t)$ may be called contributions of zero and first orders respectively.

For isotropic materials, the zero order contribution is (Freund 1990)

$$K_I(t) = 2\sigma_0 \frac{\sqrt{c_d(1-2\nu)/\pi}}{(1-\nu)} \sqrt{t}. \tag{2}$$

2

which coincides with the dynamic stress intensity factor for a semi-infinite crack under uniform impact load, σ_0, applied on the crack faces in mode I.

The expression $K_I^{(0)}(t)$ for orthotropic materials has been developed by Rubio-Gonzalez & Mason (2000)

$$K_I(t) = 2\sigma_0 \sqrt{\frac{2c_s\xi}{\pi\sqrt{c_{22}}}} \sqrt{t}. \tag{3}$$

In both cases, the velocity $c_d = \sqrt{c_{11}}c_s$ represents the dilatational wave speed along the x−axis. The constant ξ is given by

$$\xi = \frac{\beta\sqrt{\frac{c_{22}}{c_{11}}}}{\sqrt{\beta - 2\frac{c_{12}}{c_{22}} + 2\sqrt{\frac{c_{11}}{c_{22}}}}}, \quad \text{with} \quad \beta = \frac{c_{11}c_{22} - c_{12}^2}{c_{22}} \tag{4}$$

and $c_s = \sqrt{\mu_{12}/\rho}$ represents the velocity of the in-plane shear wave propagating along the the principal material axes and ρ is the mass density. The non-dimensional constants c_{ij} may be written in terms of engineering constants see (Rubio-Gonzalez & Mason 2000)

3 Dynamic Punch Test

The specimen was impacted on one side by a rigid projectile made of hardened steel as shown schematically on figure 1.
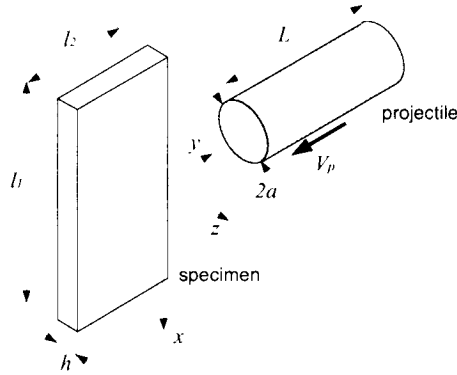
Figure 1: Specimen and projectile geometry in the dynamic punch test.

3.1 Isotropic Materials

The projectile is shot by an air gun as shown schematically in figure 2(b). The apparatus consists primarily of an air gun, a Cordin 330 high speed camera and a coherent argon-ion laser pulsed for 10ns. Once the projectile is launched it travels along the barrel and activates two infrared detectors, this signal is used to trigger the camera and laser controllers and to determine the projectile velocity, V_p. The speed of the camera was set to $5.2\mu s$

3

between pictures or 192,300 frames/sec. The specimen dimensions were 127x50x6.3mm, the grating pitch was $p = 0.0254$ mm and the distance between gratings was $\Delta = 30$ mm. A 50 mm-diameter collimated laser beam was used. The projectile length was $L = 145$ mm and $2a = 25.4$ mm, the velocity $V_p = 16$ m/s.

Figure 2(a) shows a series of some CGS interferograms for the dynamic test. Note that the size of the lobes increases and then decreases with time. Such a behavior is expected for the stress intensity factor as well. An analysis of each photograph leads to the determination of the time evolution of the stress intensity factor $K_I(t)$ for the punch test.
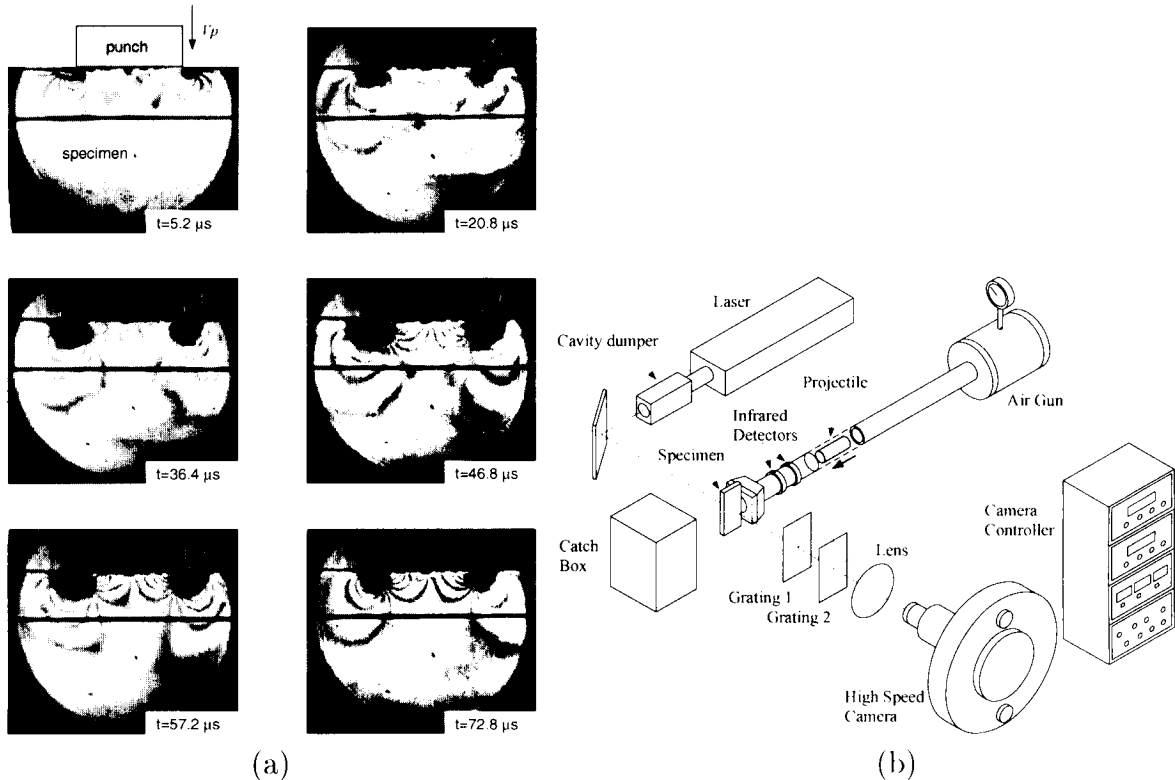
Figure 2: (a) Sequence of CGS interferograms for the dynamic punch test. Transmission mode, isotropic materials, (b) Schematic illustration of CGS set-up in transmission mode for use in the dynamic punch test.

Figure 3(a) shows the dynamic stress intensity factor for the dynamic punch test. Note a good agreement in the loading zone between experimental results and the theoretical prediction for the semi-infinite punch.

3.2 Orthotropic Materials

The dynamic punch test was conducted on graphite-epoxy composite material using the CGS method in reflection. For a detailed explanation of specimen preparation and characterization see (Rubio-Gonzalez & Mason 1999). The fiber orientation of the specimen was along the x-axis. The x-gradient was considered, e.i., $\partial w/\partial x$ was measured. The projectile impacted the specimen (with dimensions 101x50x6.5mm) at the velocity $V_p = 11.5$m/s. The grating

4

pitch was $p = 0.0254$mm and the distance between gratings was $\Delta = 36$mm. The speed of the camera was set to $4\mu s$ between pictures or 250,000 frames/sec.

The normalized dynamic stress intensity factor for the punch test is shown in figure 3(b). The normalization factor is $K_0 = \sigma_0 C_I \sqrt{2a/c_{d,y}}$, where $\sigma_0 = \rho c_{d,y} V_p$, being $c_{d,y}$ the dilatational wave speed for wave propagation along the $y-$axis. An increase in $K_I(t)$ is noted and then a decrease occurs when the dilatational wave reflected from the opposite side of the specimen arrives at the punch corners. The solid line corresponds to the stress intensity factor for the semi-infinite punch problem under impact load $\sigma_0 H(t)$ applied during a time interval $0 < t < t^*$

$$K_I(t) = \sigma_0 C_I \left[\sqrt{t} H(t) - \sqrt{t - t^*} H(t - t^*) \right] \tag{5}$$

where C_I is a material dependent parameter derived in Rubio-Gonzalez & Mason (2000) and given by

$$C_I = 2\sqrt{\frac{2c_s\xi}{\pi\sqrt{c_{22}}}}. \tag{6}$$
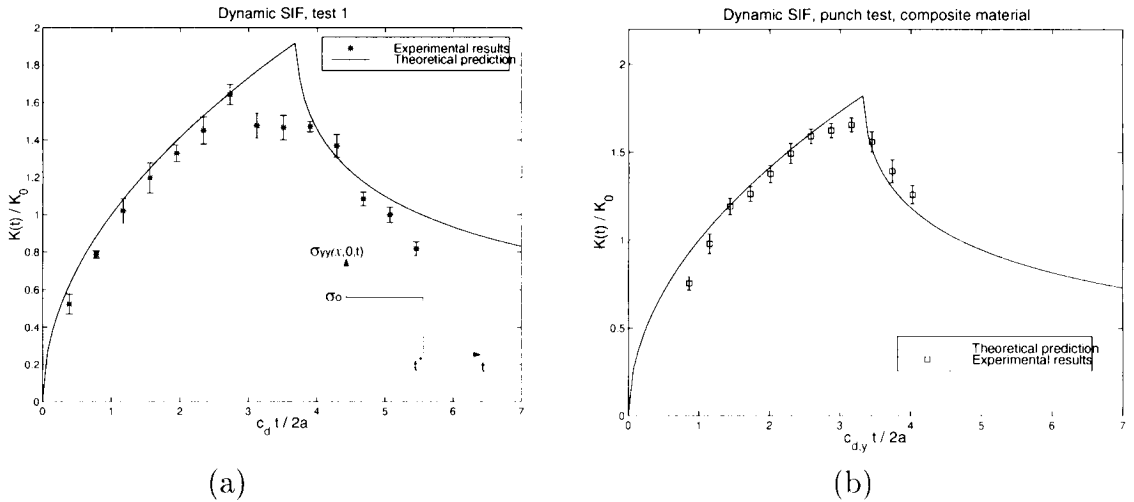
Figure 3: Normalized dynamic stress intensity factor for the punch test. (a) Isotropic materials, (b) Composite materials

4 Conclusions

Like in fracture mechanics, the stress intensity factor K_I has been introduced to characterize the severity of the singular stresses around the punch corners in the punch test. Quasi-static and dynamic punch tests were performed on PMMA and unidirectional graphite-epoxy composites to measure K_I. Laser interferometry was used to measure in-plane stresses (transmission mode) and out-of-plane displacements (reflection mode), and then estimate the stress intensity factor. In the dynamic case, a high speed photography technique was employed to capture the transient response of the specimen and measure $K(t)$ just after the impact. Each photograph of the CGS fringe pattern was digitized. A fitting procedure based

on the least squares method was used to estimate K_I from the fringe pattern. In all the cases a good agreement between the measurements of K_I and the theoretical predictions was found. The theoretical prediction for the dynamic case on composites is just an extension of the solutions developed in Rubio-Gonzalez (1999) and Rubio-Gonzalez & Mason (2000) for orthotropic materials.

References

Freund, L. B. (1990), *Dynamic Fracture Mechanics*, Cambridge University Press. New York, NY.

Lambros, J. & Rosakis, A. (1997*a*), 'Dynamic crack initiation and growth in thick unidirectional graphite/epoxy plates', *Composites Sci. and Tech.* **57**, 55 65.

Lambros, J. & Rosakis, A. (1997*b*), 'An experimental study of dynamic delamination of thick fiber reinforced polymeric matrix composites', *Experimental Mechanics* **37**(3), 360 366.

Mason, J., Lambros, J. & Rosakis, A. (1992), 'The use of a coherent gradient sensor in dynamic mixed-mode fracture mechanics experiments', *J. Mech. Phys. Solids* **40**(3), 641 661.

Rubio-Gonzalez, C. (1999), Dynamic Fracture Initiation in Composite Materials, PhD thesis, University of Notre Dame.

Rubio-Gonzalez, C. & Mason, J. (1999), 'Experimental investigation of the dynamic punch test in isotropic and composite materials', *Submitted to Experimental Mechanics*.

Rubio-Gonzalez, C. & Mason, J. (2000), 'Dynamic stress intensity factors at the tip of a uniformly loaded semi-infinite crack in an orthotropic material', *J. Mech. Phys. Solids* **48**(5), 899–925.

Tippur, H., Krishnaswamy, S. & Rosakis, A. (1991), 'A coherent gradient sensor for crack tip measurements: Analysis and experimental results', *Int. J. fracture* **48**, 193 204.

The Dynamics of Multiple Neck Formation and Fragmentation in High Rate Extension of Ductile Materials

P.R. Guduru and L.B. Freund

Division of Engineering, Brown University, Providence, RI 02912

ABSTRACT

Dynamic necking bifurcation in rapidly extending cylindrical rods is investigated. It has been found that both short wavelength and long wavelength perturbations are suppressed by inertia and an intermediate wavelength is favored. The analysis predicts an increase in the number of necks and an increase in the bifurcation strain with increasing extension rate, in agreement with the experimental observations. In terms of the number of necks formed as a function of extension rate, good agreement has been found between the experiments and the analysis. At any given aspect ratio, the model also predicts that the number of necks increases rapidly beyond a critical extension rate. Currently no experimental results are available to verify this prediction.

KEYWORDS
Necking bifurcation, ductility, fragmentation, plasticity.

INTRODUCTION

The necking instability in rods under quasi-static uniaxial loading has been studied by Miles[1], Cheng et al. [2], Hutchinson & Miles [3] and Hill & Hutchinson [4]. The general approach has been to use perturbation analysis in order to determine the critical stress state at which a non-homogeneous, neck-like deformation field can exist. Hutchinson and Miles [3] showed that such a deformation field can exist at a critical stress, which is greater than the stress at maximum load, and the lowest critical stress corresponds to the longest wavelength perturbation, in other words, a single neck is formed at this critical stress. However, fragmentation experiments of Grady & Benson [5] and Altynova *et al.* [6] have demonstrated that rapidly expanding rings form multiple necks and some of these necks fail, leading to fragmentation of the rings. Shenoy and Freund [7] generalized the perturbation analysis of Hill and Hutchinson [4] to study a rectangular block of material, dynamically loaded in plane strain, using a hypoelastic constitutive relation. They examined the growth rate of neck-like perturbations and found that short as well as long wavelength perturbations are suppressed and intermediate wavelengths have the highest rate of growth. Their analysis captured the qualitative features of the experimental observations such as the increasing number of necks and the increasing ductility with an increase in extension rate. However, direct comparison with experiments could not be performed as it was a plane strain analysis. In this paper, the perturbation analysis of Shenoy and Freund [7] is adapted to an extending cylinder in order to facilitate comparison with experiments. This work is a generalization of the analysis of Hutchinson and Miles [3] to include inertial effects. The next section discusses the homogeneous solution to the extending rod problem, followed by a section on perturbation analysis. Results and a brief discussion are presented at the end.

HOMOGENEOUS DEFORMATION

Consider an incompressible cylindrical rod of radius A and length 2L, undergoing homogeneous deformation in the axial direction, as shown in Fig. 1. The ends of the rod move with a speed v_0 as shown. Denoting the reference coordinates as (R, Θ, Z) and current coordinates as (r, θ, z), the deformation is described as

$$r = \lambda^{-1/2} R, \qquad z = \lambda Z \qquad (1,2)$$

where
$$\lambda = 1 + v_0 t / L \qquad (3)$$

with t representing time. Using eq. (1)-(3), the velocity field corresponding to the homogeneous deformation state is

$$v_r = -\frac{v_0}{2L}R\left(1+\frac{v_0}{L}t\right)^{-3/2}, \qquad v_z = \frac{v_0}{L}Z \qquad (4,5)$$

The fields $v_r(R,Z,t)$ and $v_z(R,Z,t)$ are the radial and axial components of velocity. The Cauchy stress ($\boldsymbol{\sigma}$) for this homogeneous 1-D deformation is

$$\boldsymbol{\sigma} = \begin{pmatrix} 0 & 0 & 0 \\ 0 & 0 & 0 \\ 0 & 0 & \sigma \end{pmatrix} + \begin{pmatrix} -p & 0 & 0 \\ 0 & -p & 0 \\ 0 & 0 & -p \end{pmatrix} \qquad (6)$$

where σ is the axial stress due to strain history and p is the hydrostatic stress due to particle acceleration (see eq.(4)). Using the equation of motion in the radial direction and the condition that $p=0$ at $R=A$, p can be determined to be [7]

$$p = \frac{3}{8}\rho\left(\frac{v_0}{L}\right)^2\frac{(A^2-R^2)}{(1+v_0t/L)^3} \qquad (7)$$

In the above equation, ρ is the mass density. Eq. (4) and (5) describe the deformation state and σ is not known since no constitutive relation has been used yet. The stability of this deformation state is analysed next. In other words, if the velocity field given by eq. (4) and (5) is slightly perturbed in a way that is consistent with the boundary conditions, we examine if such a perturbation grows in time and, if it does, what is its rate of growth.

LINEAR PERTURBATION ANALYSIS

The equations of motion in the rate form in terms of the components of the first Piola Kirchoff stress $\boldsymbol{T}$ are

$$\dot{T}_{Rr,R} + \dot{T}_{Zr,Z} + (\dot{T}_{Rr} - \dot{T}_{\Theta\theta})/R = \rho\ddot{v}_r \qquad (8)$$

$$\dot{T}_{Rz,R} + \dot{T}_{Zz,Z} + \dot{T}_{Rz}/R = \rho\ddot{v}_z \qquad (9)$$

All derivatives with respect to Θ are set to zero in writing these equations. The boundary conditions are

$$v_z(R,\pm L,t) = \pm v_0, \qquad \dot{T}_{Zr}(R,\pm L,t) = 0 \qquad (10,11)$$

$$\dot{T}_{Rz}(A,Z,t) = 0, \qquad \dot{T}_{Rr}(A,Z,t) = 0 \qquad (12,13)$$

In the above equations, $\dot{\boldsymbol{T}}$ can be expressed in terms of the current stress and deformation quantities using

$$\dot{\boldsymbol{T}} = \boldsymbol{F}^{-1}(\hat{\boldsymbol{\sigma}} - \boldsymbol{D}\boldsymbol{\sigma} - \boldsymbol{\sigma}\boldsymbol{W}) \qquad (14)$$

where $\boldsymbol{F}$ is the deformation gradient, $\hat{\boldsymbol{\sigma}}$ is the Jaumann rate of Cauchy stress, $\boldsymbol{D}$ and $\boldsymbol{W}$ are the symmetric and antisymmetric parts of the velocity gradient. The material is assumed to follow the hypoelastic constitutive relation developed by Storen and Rice [8], which in the present context becomes

$$\hat{\sigma}'_{rr} = (h+h_1)D_{rr} + (h-h_1)D_{\theta\theta} \qquad (15)$$

$$\hat{\sigma}'_{\theta\theta} = (h-h_1)D_{rr} + (h+h_1)D_{\theta\theta} \qquad (16)$$

$$\hat{\sigma}'_{zz} = 2hD_{zz} \qquad (17)$$

$$\hat{\sigma}'_{rz} = 2h_1D_{rz} \qquad (18)$$

where prime denotes the deviatoric component. In writing eq. (15)-(18), it was assumed that $v_\theta = 0$, all derivatives with respect to θ are zero and $D_{rr} + D_{\theta\theta} + D_{zz} = 0$. Here h and h_1 are the tangent modulus and the secant modulus of the graph of equivalent stress $\sqrt{\sigma'_{ij}\sigma'_{ij}/2}$ vs. equivalent strain $\sqrt{2\varepsilon_{ij}\varepsilon_{ij}}$. This curve reduces to the shear stress – shear strain curve in pure shear. It can be verified that the homogeneous solution given by eq. (4)-(7) satisfies eq. (8)-(18). In addition, σ at any time can be calculated by integrating eq. (15)-(18).

Introduce, at some time τ, a perturbation velocity field (v_r', v_θ', v_z') such that $v_\theta'=0$, and v_r' and v_z' do not depend on θ. Then, it can be seen that this perturbation velocity field, along with the corresponding perturbation stress field satisfies eq. (8)-(18), with eq.(10) modified as

$$v'_z(R,\pm L,t)=0 \tag{19}$$

Dropping the prime for convenience, eq.(8)-(9) and eq. (11)-(19) are the governing equations for the perturbation velocity field and the task is now reduced to analyzing the evolution of this field. Without loss of generality, τ can be set to zero, so that $F=1$ and the reference and current configurations coincide with each other. Note that eq. (15)-(18) do not determine the hydrostatic component of the stress rate and, in order to eliminate it, eq. (8) is differentiated with respect to z and eq. (9) with respect to r and subtracted from one another. This results in

$$\left(\dot{T}_{rr}-\dot{T}_{zz}\right)_{,zr}+\dot{T}_{zr,zz}+\left(\dot{T}_{rr}-\dot{T}_{\theta\theta}\right)_{,z}/r-\dot{T}_{rz,rr}-\dot{T}_{rz,r}/r+\dot{T}_{rz}/r^2=\rho\left(\ddot{v}_{r,z}-\ddot{v}_{z,r}\right) \tag{20}$$

Since the material is incompressible, v_r and v_z can be written in terms of a potential $\varphi(r,z,t)$ as $v_r=-\varphi_{,z}$ and $v_z=\frac{1}{r}(r\varphi)_{,r}$. Defining $\alpha=\frac{3}{4}\rho(v_0/L)^2$ and using eq. (14)-(18), eq. (20) becomes

$$\frac{1}{2}(\sigma-2h_1)\varphi_{,rrrr}-\frac{1}{2}(\sigma+2h_1)\varphi_{,zzzz}-(3h-h_1)\varphi_{,rrzz}+\frac{1}{r}(\sigma-2h_1)\varphi_{,rrr}-\frac{1}{r}(3h-h_1)\varphi_{,rzz}-$$
$$\frac{3}{2r^2}(\sigma-2h_1)\varphi_{,rr}+\left(\frac{3h-h_1}{r^2}-\alpha\right)\varphi_{,zz}+\frac{3}{2r^3}(\sigma-2h_1)\varphi_{,r}-\frac{3}{2r^4}(\sigma-2h_1)\varphi=$$
$$\rho\left(-\ddot{\varphi}_{,rr}-\ddot{\varphi}_{,zz}-\frac{\ddot{\varphi}_{,r}}{r}+\frac{\ddot{\varphi}}{r^2}\right) \tag{21}$$

Assuming a separable solution of the form

$$\varphi(r,z,t)=\psi(r,z)T(t) \tag{22}$$

results in an equation for $\psi(r,z)$ as

$$\frac{1}{2}(\sigma-2h_1)\psi_{,rrrr}-\frac{1}{2}(\sigma+2h_1)\psi_{,zzzz}-(3h-h_1)\psi_{,rrzz}+\frac{1}{r}(\sigma-2h_1)\psi_{,rrr}-\frac{1}{r}(3h-h_1)\psi_{,rzz}+$$
$$\left(\rho\theta^2-\frac{3}{2r^2}(\sigma-2h_1)\right)\psi_{,rr}+\left(\frac{3h-h_1}{r^2}+\rho\theta^2-\alpha\right)\psi_{,zz}+\left(\frac{3}{2r^3}(\sigma-2h_1)+\rho\theta^2/r\right)\psi_{,r}-$$
$$\left(\frac{3}{2r^4}(\sigma-2h_1)+\rho\theta^2/r^2\right)\psi=0 \tag{23}$$

where $\theta^2=\frac{\ddot{T}}{T}$, is the separation constant. If θ^2 is real and positive, the perturbation field is unstable. Assume a separable solution once again.

$$\psi(r,z)=g(r)\cos(\gamma z) \tag{24}$$

In order to satify the boundary condition eq.(19),

$$\gamma=\frac{\pi q}{2L}, \quad q=1,3,5,\ldots \tag{25}$$

Using eq.(24) in eq. (23), the governing equation for $g(r)$ is obtained as

$$g''''+\frac{2}{r}g'''+\left(\frac{\gamma^2(3h-h_1)+\rho\theta^2}{\sigma/2-h_1}-\frac{3}{r^2}\right)g''+\left(\frac{\gamma^2(3h-h_1)+\rho\theta^2}{r(\sigma/2-h_1)}+\frac{3}{r^3}\right)g'-$$
$$\left(\frac{\gamma^2(3h-h_1)+\rho\theta^2}{r^2(\sigma/2-h_1)}+\frac{3}{r^4}+\frac{\gamma^2(\rho\theta^2-\alpha)+\gamma^4(\sigma/2+h_1)}{\sigma/2-h_1}\right)g=0 \tag{26}$$

Assuming a power law type uniaxial stress-strain relation,

$$\sigma=k\varepsilon^n \tag{27}$$

where k and n are material constants, n denoting the strain hardening exponent. Also, $n=h/h_1$. By defining

$$b=[3-1/n+12N(v_0/v_p)^2/(\pi^2q^2n(ns)^{n-1})]/(3s-2/n)$$

$$c=[(1/n+3s/2)+3(4N-3)(v_0/v_p)^2/(\pi^2q^2n(ns)^{n-1})]/(1/n-3s/2)$$

in which $s = \sigma / 3h$, $v_p = \sqrt{k / \rho}$ and $N = (L\theta / v_0)^2$, eq.(26) can be written as

$$\boldsymbol{L}^2(g) + 2b\gamma^2 \ \boldsymbol{L}(g) + c\gamma^4 g = 0 \tag{28}$$

where the operator $\boldsymbol{L}$ is defined by $\boldsymbol{L}(g) = g'' + g'/r - g/r^2$. Further, by setting $\rho_1^{\ 2} = b - \sqrt{b^2 - c}$ and $\rho_1^{\ 2} = b + \sqrt{b^2 - c}$, eq.(28) can be represented as

$$\left(\boldsymbol{L} + \gamma^2 \rho_1^{\ 2}\right)\left(\boldsymbol{L} + \gamma^2 \rho_2^{\ 2}\right)g = 0 \tag{29}$$

The boundary conditions eq. (12) and (13) give

$$g''(A) + \frac{1}{A}g'(A) + \left(\gamma^2 - 1/A^2\right)g(A) = 0 \tag{30}$$

$$g'''(A) + \frac{2}{A}g''(A) + \left(2b\gamma^2 - 1/A^2\right)g'(A) + \left\{\frac{1}{A^3} + \frac{2\gamma^2}{A}\left(b - \frac{h_1}{\sigma/2 - h_1}\right) + \frac{\gamma^2 \alpha A}{\sigma/2 - h_1}\right\}g(A) = 0 \tag{31}$$

Nontrivial solutions of eq. (29) are sought subject to constraints eq.(30) and (31). The solution to eq.(29) has different forms depending on the complex character of $\rho_1^{\ 2}$ and $\rho_2^{\ 2}$. The relevant case here is the one when $\rho_1^{\ 2}$ and $\rho_2^{\ 2}$ form a complex conjugate pair, in which case eq.(29) admits a solution of the form

$$g(r) = BJ_1(\gamma\rho r) + \overline{B}\ J_1(\gamma \bar{\rho} r) \tag{32}$$

where bar denotes complex conjugate, B is an arbitrary complex constant, ρ a square root of either $\rho_1^{\ 2}$ or $\rho_2^{\ 2}$ and J_n is the Bessel function of order n. Subject to eq. (30) & (31), the condition for the existence of a non-trivial B is

$$\boldsymbol{Im}\left\{\left(1 - \bar{\rho}^2\right)J_1(\gamma\bar{\rho}A)\left[\left(C_1 - C_2\right)J_1(\gamma\rho A) + \gamma\rho A\left(C_3 - \rho^2\right)J_0(\gamma\rho A)\right]\right\} = 0 \tag{33}$$

where

$$C_1 = \frac{\frac{9}{4}(A/L)^2(v_0/v_p)^2}{n(ns)^{n-1}(3s/2 - 1/n)}, C_2 = \frac{2}{(3ns/2 - 1)} \text{ and } C_3 = \frac{3(1 - s/2)}{(3s/2 - 1/n)} + \frac{12N(v_0/v_p)^2}{\pi^2 q^2 n(ns)^{n-1}(3s/2 - 1/n)}$$

In the above equations, N represents the rate of growth of the perturbation relative to the background homogeneous rate of stretch. N is required to be large compared to 1 for a perturbation mode q to result in multiple necking. For a given strain hardening exponent n, stress s, aspect ratio A/L, extension speed v_0/v_p and perturbation mode q, eq.(33) determines the rate of growth N.

RESULTS AND DISCUSSION

The calculation procedure is described first. For a given n, aspect ratio $\beta = A/L$, stress s and extension rate v_0/v_p, eq. (33) is solved for N as a function of q. The value of q corresponding to the maximum value of N (N_{max}) is termed q_{max} and it represents the dominant perturbation mode for these conditions. However, we require $N_{max} \gg 1$ for this perturbation mode to turn in to a necking mode. Hence, a given mode q_{max} is supposed to satisfy a failure criterion when $N_{max} = N_C$, where N_C is an arbitrarily chosen large number. In the following analysis, N_C is chosen to be 200. If $N_{max} < N_C$, s is increased gradually until $N_{max} = N_C$. The corresponding s is the critical stress (s_c) for necking bifurcation. The fragmentation experiments of Grady & Benson [5] and Altynova et al. [6] show the following qualitative features. (i) The number of necks/fragments increases with an increase in extension rate. (ii) The fracture strain increases with an increase in extension rate. The current analysis quantifies these observations, as illustrated in Fig. 2 and Fig. 3. Fig. 2 shows the number of necks as a function of extension rate, for different hardening exponents. The analysis predicts that the hardening exponent has little effect on the number of necks, within the range of v_0/v_p plotted in Fig. 2. Fig. 3 shows an almost linear increase in critical strain, which is again independent of the hardening exponent. One of the drawbacks of the analysis presented above is the arbitrary choice of N_C. However, the number of necks is weakly dependent on N_C. An increase in N_C from 100 to 2000 results in an increase in the number of necks by a factor of 2-3. Thus, a judicious choice of N_C could possibly be made from an appropriate comparison with experiments. Comparison

of the perturbation analysis results with those of the experiments requires information about the constitutive behavior of the material at the high strain rates. Typical strain rate in the experiments of Grady and Benson [5] on aluminum and copper rings was around 10^4/s. For these materials, this is also the strain rate around which there is a sharp increase in the flow stress. Thus, the accuracy of the constitutive data available places a limitation on the comparison with the experimental results. Fig. 4 compares the number of necks observed in the fragmentation experiments of Grady & Benson [5] on OFHC copper rings with the model predictions, for four different choices of N_C. Constitutive parameters used are $k=760MPa$ and $n=0.49$ (strain rate 1.2 x 10^4 /s, Follansbee [9]). A value of 125-200 for N_C appears to fit the experiments well. Similar comparison for 1100-O aluminum is shown in Fig.5. Constitutive parameters used are, $k=230MPa$ and $n=0.33$ (strain rate 10^3 /s, Pao & Gilat [10]). A choice of 150-250 for N_C appears to yield god agreement. Figs. 6 and 7 show the comparison between the bifurcation strain from the analysis and the fracture strain measured by Grady and Benson [5] for the same materials. Fracture strain, defined as the change in the total length of all fragments with respect to the initial ring length, always overestimates the bifurcation strain. In spite of that, the model captures the magnitude and the trend of fracture strain quite well. Fig. 8 shows the variation of the number of necks over a larger range of extension rate, for several aspect ratios. The number of necks is seen to increase rapidly beyond a critical extension rate and this rate decreases as the aspect ratio increases. As the number of necks increases rapidly, the stress is seen to saturate at the same value for all aspect ratios and this level is found to be a decreasing function of the hardening exponent. However, no experimental results are currently available to test the validity of this prediction.

CONCLUSIONS

A linear perturbation analysis of extending cylindrical rods has been carried out and it captures all the qualitative features of the fragmentation experiments, such as the increase in the number of fragments and fracture strain with increase in extension speed. Good quantitative agreement between the model predictions and the experimental results has been found for a choice of N_C in the range of 100-250. Moreover, the choice of the range of N_C that yields good agreement with experiments for two different materials is almost the same. This implies a predictive capability for the current analysis. The constitutive law for the materials used in the experiments is very rate sensitive at the strain rates encountered during rapid extension. Thus, the accuracy of constitutive data is an important ingredient in using the perturbation analysis. The model also makes other predictions on the effect of aspect ratio on the number of necks and fracture strain and the effect of the extension speed on the number of necks beyond a critical speed. More detailed experimental results are necessary to test these predictions.

References
[1] Miles J.P. (1970). *J. Mech. Phys. Solids*. 19, 89-102.
[2] Cheng S.Y., Ariaratnam S.T. and Dubey R.N. (1971). *Quart. Appl. Math* 29, 41-51.
[3] Hutchinson J.W. and Miles J.P. (1974). *J. Mech. Phys. Solids*. 22, 61-71.
[4] Hill R. and Hutchinson J.W. (1975) *J. Mech. Phys. Solids*. 23, 239-264.
[5] Grady D.E. and Benson D.A. (1983) *Exper. Mech*. 12, 393-400.
[6] Altynova M., Hu X. and Daehn G.S. (1996) *Metall. Mater. Trans*. 27A, 1837-1844.
[7] Shenoy V.B. and Freund L.B. (1999) *J. Mech. Phys. Solids*. 47, 2209-2233.
[8] Storen S and Rice J.R.(1975) *J. Mech. Phys. Solids*. 23, 421-441.
[9] Follansbee, P.S. (1986) In *Metallurgical Applications of Shock-wave and high-strain-rate phenomena*, ed. Murr, L.E., Staudhammer, K.P. and Meyers, M.A., p. 451.
[10] Pao Y.H. and Gilat A. (1989) *Int. J. Plasticity*. 5, 183-196.
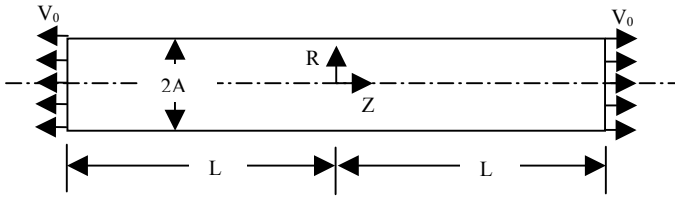
Figure 1. Geometry of the deforming cylinder
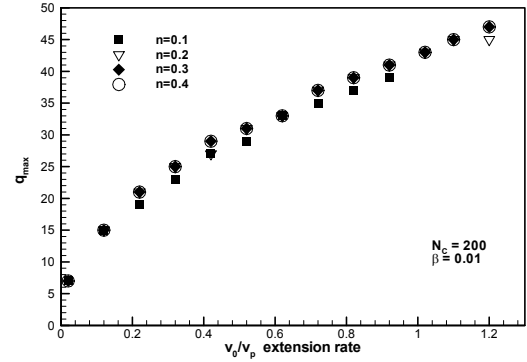
Figure 2. Number of necks as a function of extension rate.
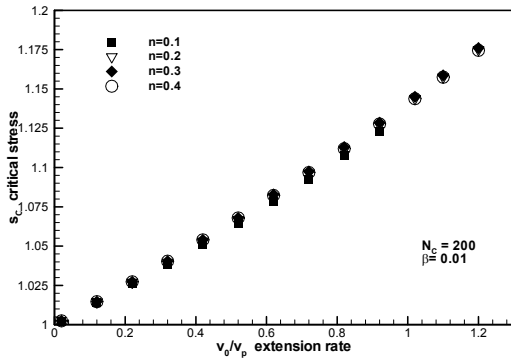
Figure 3. Variation of critical stress with extension rate
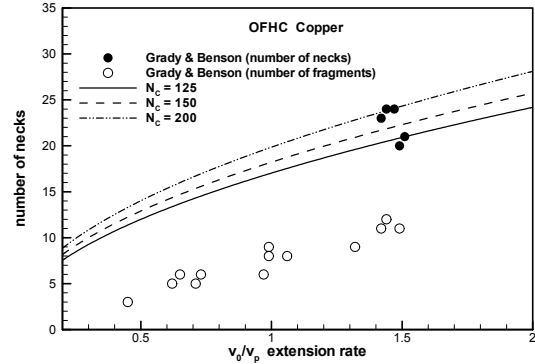
Figure 4. Comparison with experiments for OFHC copper
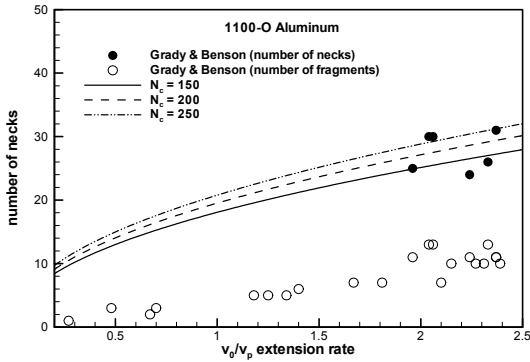
Figure 5. Comparison with experiments for 1100-O aluminum
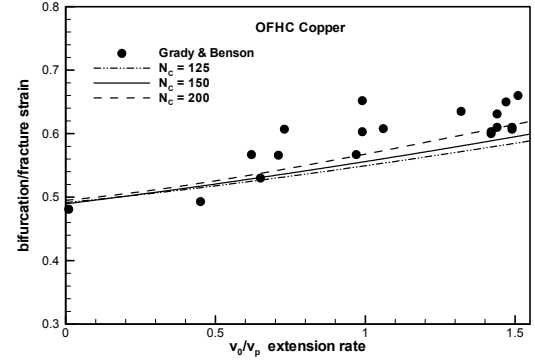
Figure 6. Fracture strain comparison for OFHC copper
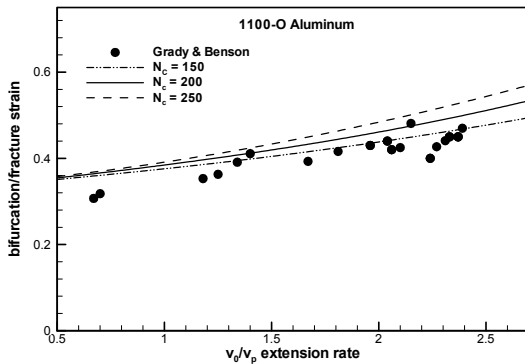
Figure 7. Fracture strain comparison for 1100-O aluminum
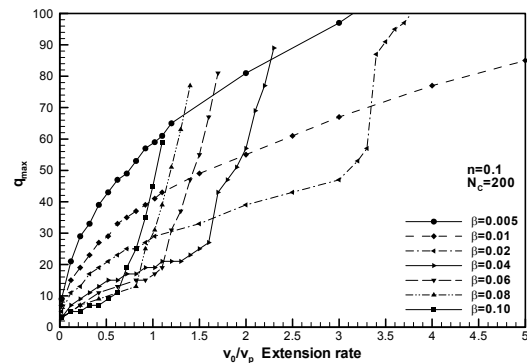
Figure 8. Variation of number of necks at high extension rates

THE 10TH INTERNATIONAL CONGRESS OF FRACTURE

The effect of cold expansion on fatigue resistance of fastener holes

Dr J. Vogwell, T Navid-Chakherlou

Faculty of Engineering & Design
University of Bath,
UK

Prof J. M. Minguez

Departamento de Fisica Aplicada II
Universidad del Pais Vasco
Bilbao, Spain

Key Words :   Cold Expansion, Residual Stress, Fatigue Resistance.

Abstract

It has long been known that cold expansion of fastener holes (as used on bolted or riveted metal joints) can be used as a means of improving the resistance of the hole to failure by fatigue. However, the fatigue resisting behaviour can be unpredictable as tensile fatigue tests carried out on batches of specimen made of aircraft grade aluminium alloy and containing a central hole has shown. Those subjected to the ballising method of cold expansion did not result in any noticeable improvement in fatigue life. This finding is partly supported by recently published research findings where finite element models have been used to predict residual stress distributions. Results have shown that sometimes positive, rather than negative, residual stresses can result at the edge of a hole after cold forming under certain conditions and this helps explain why the anticipated improvement in fatigue strength sometimes does not materialise.

This paper describes the results of a study that has sought to clarify the situation with regard to amount of interference and fastener material thickness. Results are presented of a two dimensional axisymmetric finite element study, which has accurately modelled the cold expansion process and the elastic/plastic isotropic material behaviour. It has confirmed that under certain circumstances positive tangential residual stresses are indeed possible at the critical edge of hole location and these will increase, rather than reduce, the possibility for fatigue damage.

1   INTRODUCTION

The cold expansion process involves expanding the hole beyond local yield with the aim of producing compressive tangential residual stresses around the inner circumference once the load causing the expansion is removed. If this is achieved it is generally very desirable under tensile loading as it helps counter the localised stress concentration effect and thus reduce the likelihood of fatigue damage. When hole diameters are large then sufficiently high pressure can be applied to cause tangential yielding but when diameters are small, as with bolt and rivet holes, the required pressure would be excessive and so an expansion device is necessary.

There are many practical examples where a cold expansion technique has been used to help improve the resistance of a fastener hole to fatigue damage. For example, the practise was once used in railway applications with the bolt holes of the lap-joint brackets used for fastening lengths of railway track together [1]. It is also widely used in aircraft construction at vulnerable bolt and rivet holes and special cold expansion devices are produced for this purpose [2]. Some devices rely on an oversize ball bearing (ballising) or use a pin that is directly forced through

the hole whereas other devices use the expanding wedge principle. Although seeking to achieve the same function, the resulting residual stress distribution and consequent fatigue resisting strength may be very different as this paper reports.
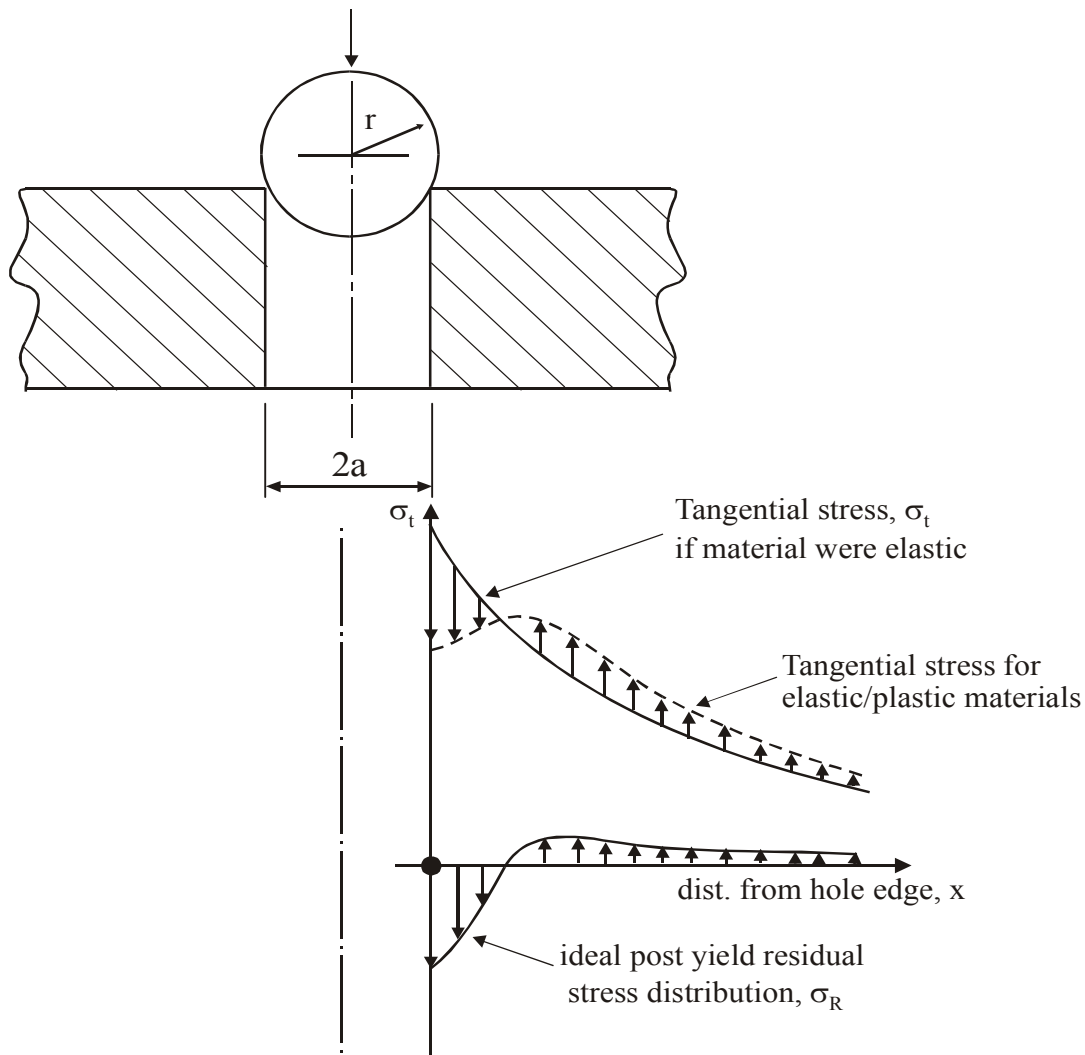
Figure 1   Hole Ballising and the Ideal Tangential Residual Stress Distribution

2   THE IDEAL STATE

The ballising method of cold expansion is illustrated in Figure 1. The oversized ball is forced through the hole causing the hole diameter to expand as the ball passes through. If the amount of interference (the difference between ball and hole diameters) is relatively small then the expansion occurs within the elastic range of the material and so the hole returns to its original size and unstressed state. However, if the amount of diametral interference is sufficiently large to cause localised yielding then the hole will not return completely to its original size. The tangential stress distribution also does not return to the unstressed state and ideally varies from compression at the edge of the hole changing to tension away from the hole (thus maintaining equilibrium) as shown in Figure 1. This ideal state is what is obtained from applying the Wohler hypothesis [1]. This predicts that the resulting residual stress magnitude, σ_R is the difference between the actual tangential stress that occurs during expansion (based on the actual

stress/strain relationship as idealised in Figure 2) and the 'hypothetical' stress that would have resulted had the material continued to behave elastically. This difference is shown on revised axes on Figure 1. Generally, it is found, the greater the amount of interference, the greater the region of yielding that occurs and the larger the magnitude of the compressive residual stress at the hole edge.
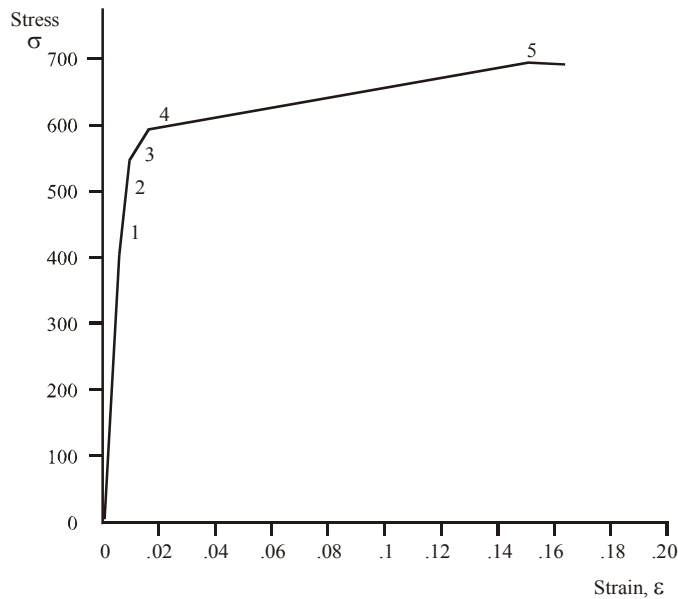
Figure 2   Idealisation of Aluminium Alloy 7075 True Stress – Strain Behaviour

3   EXPERIMENTAL TESTS

Static tensile and fatigue tests have been carried out to support the finite element study. The material used for the plate was aluminium alloy 7075 T6. This is an aircraft specification, light alloy material and has been assumed to be isotropic for simplicity. The ball was made from steel with an elastic modulus, $E = 210$ GPa and $\upsilon = 0.3$.

Two batches of ten fatigue test specimen were produced from aluminium alloy 7075 T6 2 mm thick sheet material cut into 25 mm widths and 150 mm in length. A 2.9 mm diameter hole was drilled through the centre of all specimen and for one batch a 3 mm diameter, steel ball was forced through the holes; this equates to an interference of 3.3 %. The test specimen were then fatigue tested in an Amsler Vibrophore, resonant frequency machine at 90 Hz and the resulting semi-stress amplitude/fatigue life performance is displayed in Figure 3. As can be seen in this S – N diagram there is no discernible difference in behaviour between the best fit curves for the two sets of results beyond the normal scatter inherent with this type of test.
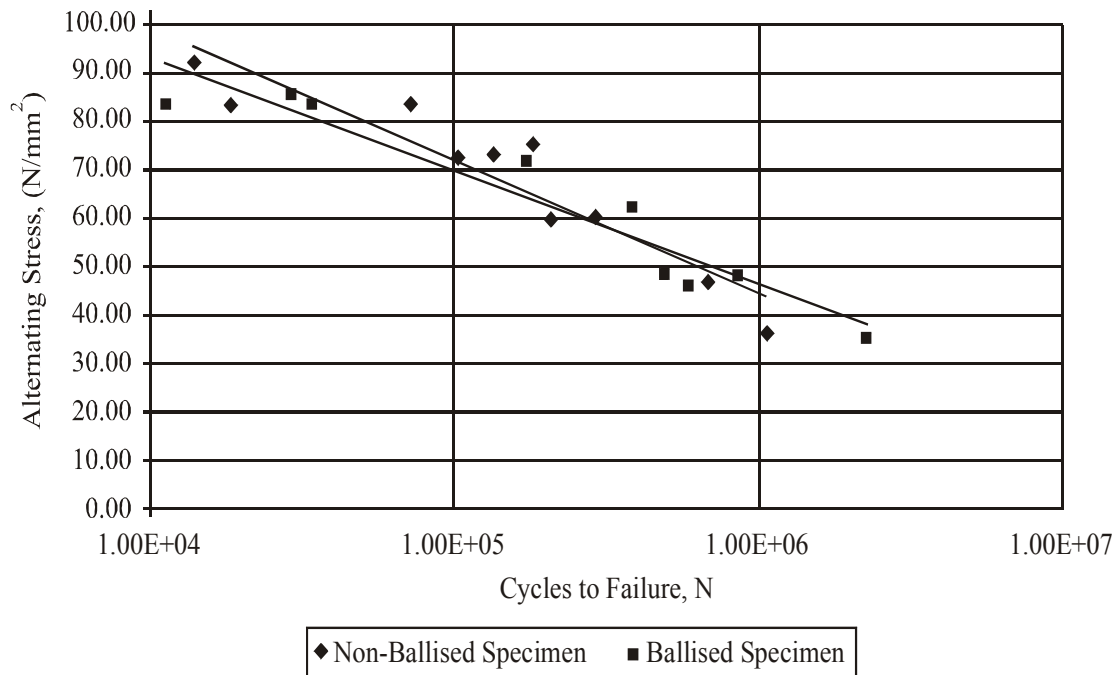
Figure 3   **Effect of Ballising on Fatigue S – N Diagram**

4   FINITE ELEMENT MODEL

An annular shaped plate was chosen for the finite element model - rather than a rectangular plate with a central hole (as used for the test specimen) because it enabled an axisymmetrical element mesh to be used, as shown in Figure 4. This was felt justified because the stress behaviour in the region of the hole is much the same in both plate shapes and the ease in modelling a circular plate offers considerable advantages. Four node quadrilateral elements have generally been used (with 2 x 2 Gaussian integration points) and also contact elements are used at the surfaces to correctly allow positive pressure to be transferred between contacting surfaces.

The annular plate model has been constrained in the vertical direction around the 50 mm outer circumference. This avoided having any localised support reaction effects influencing the residual stress distributions in the region of the hole as would occur had the plate been supported close to the exit region of the hole as would happen in practice. The ball was constrained from moving horizontally and was forced through the hole in 150 incremental step displacements to its top node; this was a sufficient number to reach convergence. Zero friction between steel ball and light alloy plate was assumed.

Finite element analyses have been carried out for nine variants - three different plate thickness' (T = 2, 5 and 10 mm) and with three different cold expansion interference magnitudes (I = 2%, 4% and 6%) to show the changing trends. The ANSYS finite element package [3] was used.
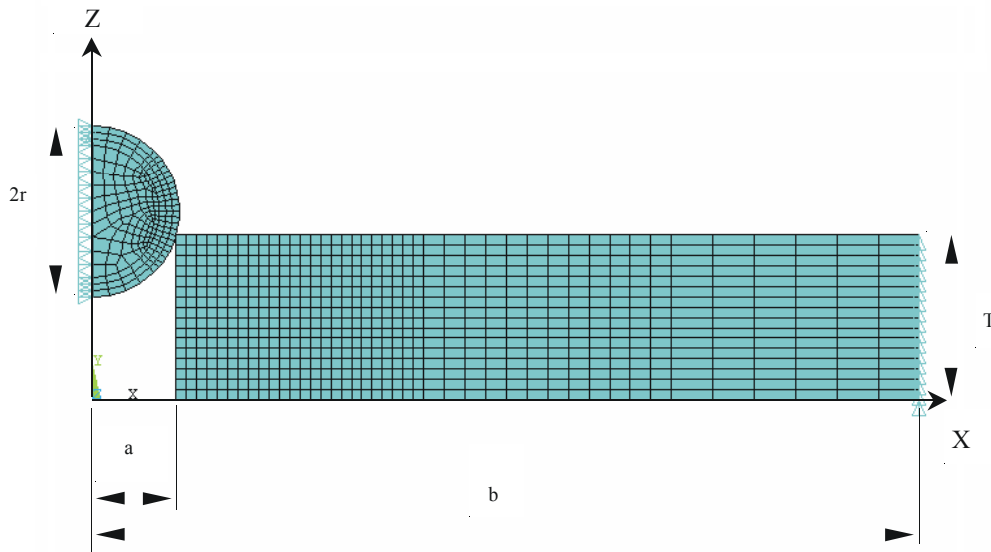
Figure 4   Axisymmetric Finite Element Mesh

5   DISCUSSION OF RESULTS

The tangential residual stress distributions obtained by finite element analysis are displayed in Figure 5. This figure shows that residual stress magnitudes are different at the entrance face, mid-thickness and exit faces for each of the three plate thickness' and three interference cases considered. With the exception of the smallest material thickness and least interference case, tensile residual stress occurs at the edge of the hole at the entrance surface. This is contrary to the ideal state as shown in Figure 1 and is of concern because residual stress magnitudes up to 500 MPa are reached. This can have a profound influence on the likelihood of a fastening hole initiating and propagating a fatigue crack under cyclic loading conditions and would help explain why there was no advantage gained in increased fatigue life from the ballised specimen. This result supports similar finding by Pavier [4] and Papanikos [5].

6 CONCLUSIONS

This study has shown that when cold forming is achieved by directly force fitting a ball through a hole it is possible that substantial tensile residual stresses can occur at a hole entrance location. Rather than nullifying the stress concentration effect of the hole, as intended, this can have the opposite effect and exaggerate the stress raiser. This can thus reduce the fatigue strength of a fastener hole rather than increase it.

Fatigue experiments completed on aluminium alloy 7075 T6 specimen have shown that a hole which has been ballised does not lead to a noticeable improvement or reduction in fatigue life beyond the normal scatter inherent with such experiments.
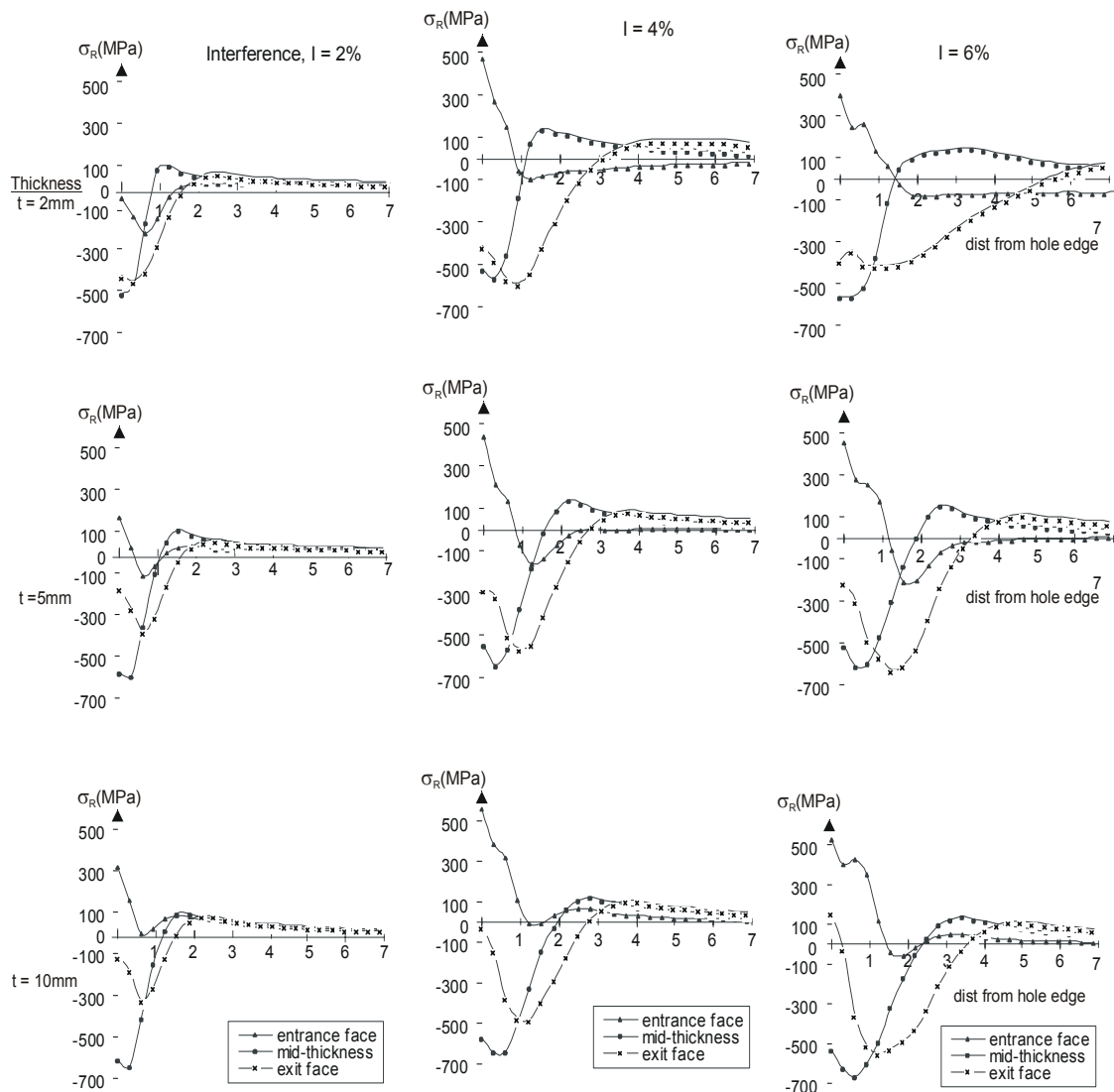
Figure 5   Tangential Residual Stress Distributions due to Ballising for Different Plate Thickness and Hole Interference

7   REFERENCES

[1]   Cannon DF, Sinclair J, Sharp KA   Improving the fatigue performance of bolt holes in railway rails by cold expansion   Proceedings A.S. Metals Conference editor VS Goel pp 353 – 363   1965

[2]   Poussard C Pavier MJ, Smith DJ   Analytical and finite element predictions of residual stresses in cold worked fastener holes   Journal of Strain Analysis Vol. 30 No. 4 pp 291-304 1995

[3]   Swanson Analysis Systems Inc. ANSYS version 5.4

[4]   Pavier MJ, Poussard DJ, Smith DJ   A finite element simulation of the cold working process for fastener holes   Journal of Strain Analysis Vol. 32 No. 4 pp 287-300 1997

[5]   Papanikos P, Meguid SA   Three dimensional finite element analysis of cold expansion of adjacent holes   Int. Journal of Mech. Science   Vol. 40 No. 10 pp 1019-1028, 1998

THE EFFECT OF CONSTRAINT ON THE FIELD OF INTERFACE CRACKS BETWEEN STRENGTH MISMATCHED MATERIALS IN ELASTIC-PERFECTLY PLASTIC PLANE STRAIN CONDITIONS

K. A. Lowe, J. Li and J.W. Hancock

Department of Mechanical Engineering, University of Glasgow, Scotland, G12 8QQ, U.K.

ABSTRACT

The structure of the elastic-perfectly plastic plane strain fields for a crack located on the interface between elastically similar but strength mismatched elastic-perfectly plastic materials has been investigated. Attention is focussed on the role of the non-singular T stress on the structure of the near mode I asymptotic fields. Analytic solutions have been developed by expressing the fields as combinations of elastic and plastic sectors. In the plastic sectors, the stresses are analysed in terms of slip-line field theory while the stresses in the elastic sectors are determined from semi-infinite elastic wedge solutions. The analytic solutions have been verified numerically using plane strain modified boundary layer formulations.

KEYWORDS

Mismatch, T stress, elastic-perfectly plastic, slip-line fields

INTRODUCTION

Fracture mechanics originates from studies of cracks in isotropic homogeneous solids. However, in welded structures defects may occur on the interface between solids which are elastically similar but plastically dissimilar. Mismatch problems of this type have been investigated for strain hardening materials by Zhang and co-workers [1], and are widely discussed by Schwalbe and Koçak [2]. Insight into the structure of the fields can however be obtained by simplifying the plastic response to perfect-plasticity. In this context Sham, Li and Hancock [3] have developed analytic solutions for the contained yielding fields of an interface crack between strength mismatched solids for the complete range of normal versus shear tractions on the interface. In the limit, when the yield strengths are identical these solutions make contact with known homogenous elastic-plastic solutions. Notably in mode I the Prandtl field which is the non-hardening limit of the HRR fields is recovered. Similarly in mode II the Hutchinson [4] field is recovered. It is however known that for homogenous solids, the mode I fields are not unique, and depend on a non-singular terms in the Williams expansion [5], which Rice [6] has denoted T.

The possibility that plasticity might not always encompass the tip, allowing the possibility of elastic sectors, was originally discussed by Nemat-Nasser and Obata [7]. In this context Du and Hancock [8] demonstrated that

the Prandtl (or HRR) field only occurs when the T stress is positive and plasticity encompasses the crack tip. If T is non-positive elastic sectors appear on the crack flanks and lead to a loss of constraint (mean stress) in the sectors ahead of the crack. In the strength mismatch problem Ganti and Parks [9] have shown that the near mode I fields are also affected by the T stress. The present work examines the role of T on the near mode I fields for strength mismatched solids. Analytic solutions are developed which are compared with numerical solutions from modified boundary layer formulations.

GEOMETRY AND MATERIAL RESPONSE

A crack is defined along the interface between two elastically similar but strength mismatched solids under plane strain conditions. Cylindrical axes (r,θ) are centred at the crack tip with the crack flanks located at $\theta = \pm \pi$. The material above the crack $(\pi \geq \theta \geq 0)$ has a uniaxial yield stress σ_0, while the material below the crack, $(\pi \leq \theta \leq 0)$ has a higher yield stress $M\sigma_0$ $(M \geq 1)$. Both materials are elastic-perfectly plastic, obeying a Mises yield criterion and an associated flow rule. The solids are elastically identical with a shear modulus G and an elastic response close to incompressibility. Solutions are initially presented for the homogeneous problem, M = 1 and an example is given of the mismatch problem, M = 1.2. Fuller sets of solutions are presented by Lowe and Hancock [10]. For both the homogeneous and the mismatch problem the role of the non-singular T stress has been examined.

ANALYTIC METHOD

The analytic solutions derive from an analysis by Rice [11] which describe the asymptotic field in terms of elastic and plastic sectors. Rice [11] shows that the assumption that the crack tip stresses are finite allows the equilibrium equations and the plane strain yield criterion to be written in the form;

$$\frac{\partial \sigma_m}{\partial \theta} \cdot \frac{\partial \sigma_{r\theta}}{\partial \theta} = 0 \tag{1}$$

This allows two possible forms for the plastic sectors. The first possibility is the mean stress, σ_m, is independent of angle and the Cartesian stresses are constant, defining a constant stress region characterised by straight slip lines. The second possibility is that the shear stress, $\sigma_{r\theta}$ is constant which gives rise to centred fans. When the yield criterion is not satisfied, an elastic sector occurs and the stresses can be derived from the semi-infinite wedge solutions of Timoshenko and Goodier [12]. The sectors are assembled in a manner consistent with continuity of tractions $\sigma_{\theta\theta}$ and $\sigma_{r\theta}$. Although continuity of stresses is not enforced, it may be shown that the sector boundaries within the same material require continuity of all stresses, while discontinuities in σ_{rr} and σ_{zz} across the interface are permitted. Mismatch problems are inherently mixed mode and although the remote elastic loading comprise pure mode I field the local field is mixed mode. To date no analytic ways of connecting the mixity of the remote and local fields have been proposed. However, this is straight forward in numerical solutions, and so the analytic solutions for the low levels of mismatched problems originate from defined ratios of shear to normal traction on the interface and the mean stress on the interface . In the homogeneous fields it is straightforward to determine values of T associated with different levels of mean stress ahead of the crack, but fully analytic ways of making this connection have not yet been developed. Thus the homogeneous solutions start from defined levels of the mean stress or constraint ahead of the crack.

NUMERICAL METHOD

A finite element method has been used to validate the analytical solutions by modelling the crack tip region as a modified boundary layer formulation, (Rice and Tracey [13]). The mesh consisted of 24 concentric rings of second order elements focussed on the crack tip. The tip was defined as the focus of a ring of collapsed elements with coincident but independent nodes. On the remote boundary of the model, Cartesian displacements, u_x, u_y, corresponding to the first two terms of the Williams expression [5] were applied.

$$u_x = \frac{K}{2G}\left(\frac{r}{2\pi}\right)^{\frac{1}{2}}\cos\left(\frac{\theta}{2}\right)\left[\eta-1+\sin^2\left(\frac{\theta}{2}\right)\right]+\frac{1+\eta}{8G}rT\cos\theta \tag{2a}$$

$$u_y = \frac{K}{2G}\left(\frac{r}{2\pi}\right)^{\frac{1}{2}}\sin\left(\frac{\theta}{2}\right)\left[\eta-1+2\cos^2\left(\frac{\theta}{2}\right)\right]+\frac{\eta-3}{8G}rT\sin\theta \tag{2b}$$

Here $\eta = 3 - 4\nu$, G is the shear modulus and ν is Poisson's ratio. K is a loading parameter established by the far field conditions while three representative values of T have been chosen as 0, $+0.4\sigma_0$ and $-0,4\sigma_0$, where σ_0 is the uniaxial yield stress. All calculations were performed with a non-hardening elastic/perfectly plastic incompressible response at constant values of T. Stresses were extrapolated to the crack tip along radial lines at an angular frequency of 7.5 degrees around the tip. In order to permit stress discontinuities in the radial stress at the interface the extrapolation to the interface nodes was made from element sets completely contained within either the harder or softer materials, allowing the possibility of stress discontinuities at the interface.

RESULTS

The solutions to the homogeneous mode I problem are given in Figure 1 for three different levels of T stress. When the T stress is positive the fully constrained Prandtl field is recovered. This is the non-hardening limit of the HRR fields and is a fully constrained field characterised solely by J. However, when the T stress is non-positive, a family of unconstrained fields arise, as discussed by Du and Hancock [8] and Li and Hancock [14]. Crack tip constraint is lost ahead of the crack and an elastic wedge appears on the crack flanks. These unconstrained fields require a two parameter characterisation using either T, (Betegón and Hancock [15]) or Q, (O'Dowd and Shih, [16]) to characterise the level of constraint. The numerical and analytic solutions to the homogeneous mode I problem can be seen to agree very closely. Although only mode I solutions are presented here, similar solutions to the mixed mode problem have been given by Li and Hancock [14].

Lowe and Hancock [10] have developed a full range of analytic solutions to elastic-perfectly plastic mismatch problems with remote mode I loading. The problems considered span a wide range of mismatch, but the examples presented in the present work are restricted to relatively low levels of mismatch. Interest is focussed on a mismatch, M=1.2, shown in Figure 2. The fields can be seen to be simple variants of the homogeneous fields given in Figure 1. Plasticity surrounds the crack tip when the T stress is positive, and elastic wedges appear on the crack flanks when T is non-positive. The angular span of the wedges increases as T becomes more negative, as in the homogeneous field. The non-singular T stress is shown to have a constraint effect on the structure of the fields, in agreement with Ganti and Parks [9]. Although the remote loading is pure mode I, the interface exhibits both normal tractions and shear stresses. Equilibrium requires that the hoop and shear stresses are continuous across the interface however there is an allowable jump in the radial stress and a necessary discontinuity in the slip-lines across the interface.

As with the homogeneous problem, crack tip constraint is lost when the non-singular T stress is zero or negative. The extent of constraint loss is similar to that observed in the homogeneous problems (Zhang et al, [1]. Constraint loss is also accompanied by the appearance of elastic wedges on the crack flanks, as in the homogeneous problem. Sham, Li and Hancock [3], developed a set of fields which agreed closely with analytic solutions for almost the complete range of remote mixed mode loading. However discrepancies between the

analytic solutions and the accompanying numerical solutions were noted for near mode I problems. Sham et al [3] attributed this to constraint effects associated with T. The present work confirms this conclusion and shows that the Sham, Li and Hancock solutions make full contact with the T positive fields in the near mode I region. As T becomes negative the angular span of the wedge increases. The T stress also has a weak but noticeable effect on the ratio of shear to normal tractions directly ahead of the crack. At high levels of mismatch the fields change from those shown in Figure 2. Elastic sectors appear even in the T positive loading cases, however the dominant feature that the Sham, Li and Hancock fields make contact with the T positive fields is retained while non-positive T stresses lead to both a loss of constraint and a change in the structure of the fields, as discussed in detail by Lowe and Hancock [10].

ACKNOWLEDGEMENTS

REFERENCES

1.   Zhang, Z. L., Hauge, M., Thaulow, C. (1997). In: Proceedings of the Ninth International Conference on Fracture, 5, 2643-2650. Karihaloo, B.L., et al (Eds).
2.   Schwalbe, K.-H, and Koçak, M., (1994). Mismatching of Welds. International Symposium on Mismatching of Welds – Performance of Strength-Mismatched Welded or Bonded Joints, Germany. ESIS Publication 17.
3.   Sham, T.-L., Li, J. and Hancock, J.W. (1999). J. Mech. Phys. Solids 47, 1963.
4.   Hutchinson, J.H. (1968). J. Mech. Phys. Solids 16, 13.
5.   Williams, M. L. (1957). J. Appl. Mech. 24, 109.
6.   Rice, J.R. (1974). J. Mech. Phys. Solids 22, 17.
7.   Nemat-Nasser, S. and Obata, M. (1984). Mechanics of Materials 3, 235.
8.   Du, Z. Z. and Hancock, J. W. (1991). J. Mech. Phys. Solids 39, 555.
9.   Ganti, S. and Parks, D., M. (1997). In: Recent Advances in Fracture, 13-25, Mahidara, K. et al (Eds). The Minerals, Metals and Materials Society.
10.   Lowe, K and Hancock, J. W. (2001). Uni. Of Glasgow Research Paper.
11.   Rice, J.R., (1982). Mechanics of Solids – The Rodney Hill 60th Anniversary Volume, 539-562. Hopkins, H.G. and Sewell, M.H. (Eds). Pergamon Press, Oxford.
12.   Timoshenko, S.P. and Goodier, J. N. (1970). Theory of Elasticity 3rd Edition. McGraw-Hill, New York.
13.   Rice, J.R. and Tracey, D.M., (1973). Numerical and Computational Methods in Structural Mechanics. Academic Press, New York.
14.   Li, J. and Hancock, J.W. (1999). Int. J. Solids and Structures 36, 711.
15.   Betegón, C. and Hancock, J.W. (1991). J. of Appl. Mechs. 58,104.
16.   O'Dowd, N.P., and Shih, C.F. (1991). J. Mech. Phys. Solids 39, 989.
17.   ABAQUS V.5.8, (1999). ABAQUS Manual. Hibbitt, Karlsson and Sorenson Inc., Providence, RI.
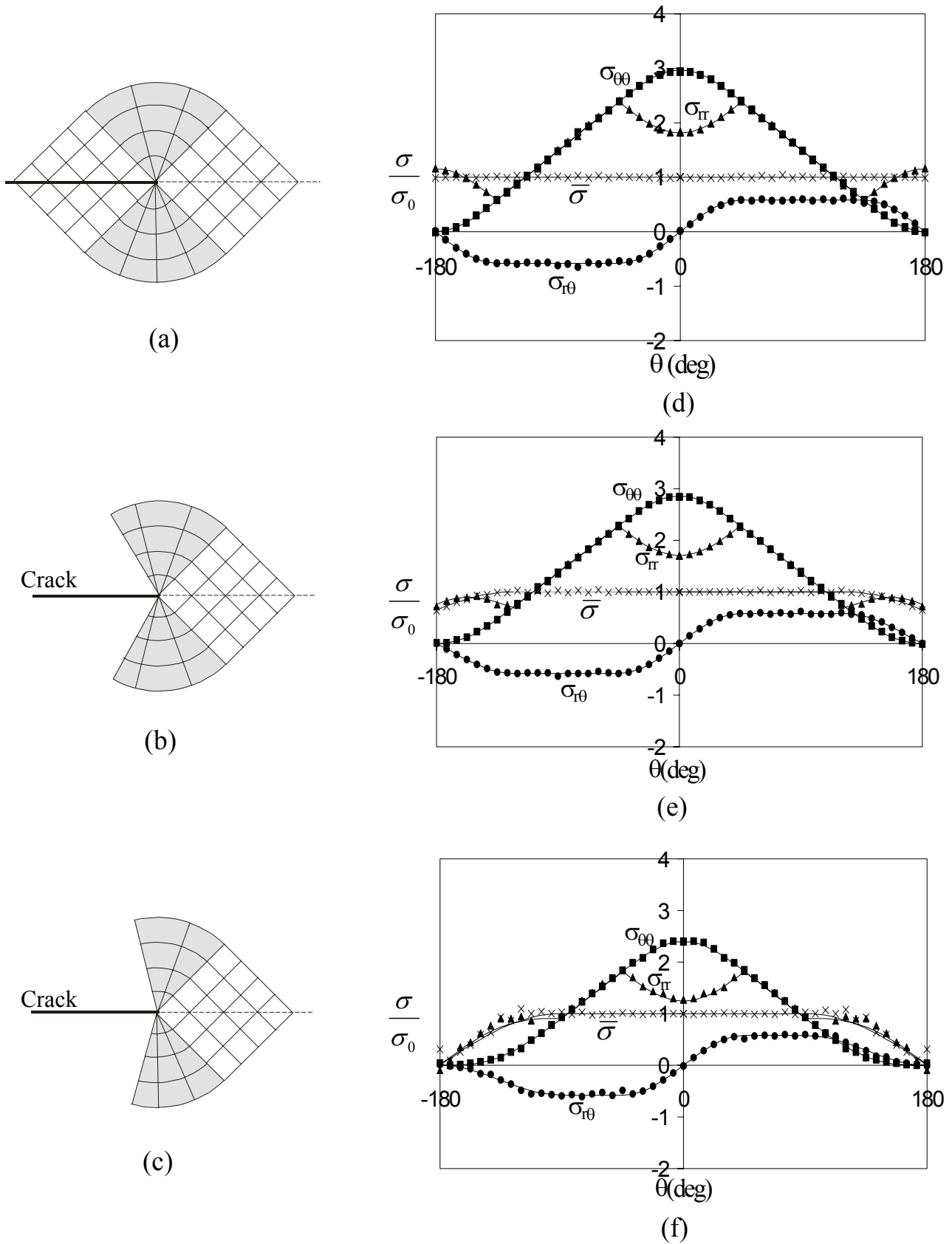
Figure 1   Slip-line fields for M=1 for (a) Positive T stress, (b) Zero T stress and (c) Negative T stress and asymptotic stress fields for M=1 for (a) Positive T stress, (b) Zero T stress and (c) Negative T stress. The solid lines represent the results from the analytic solutions, the symbols the results from the computational analysis.
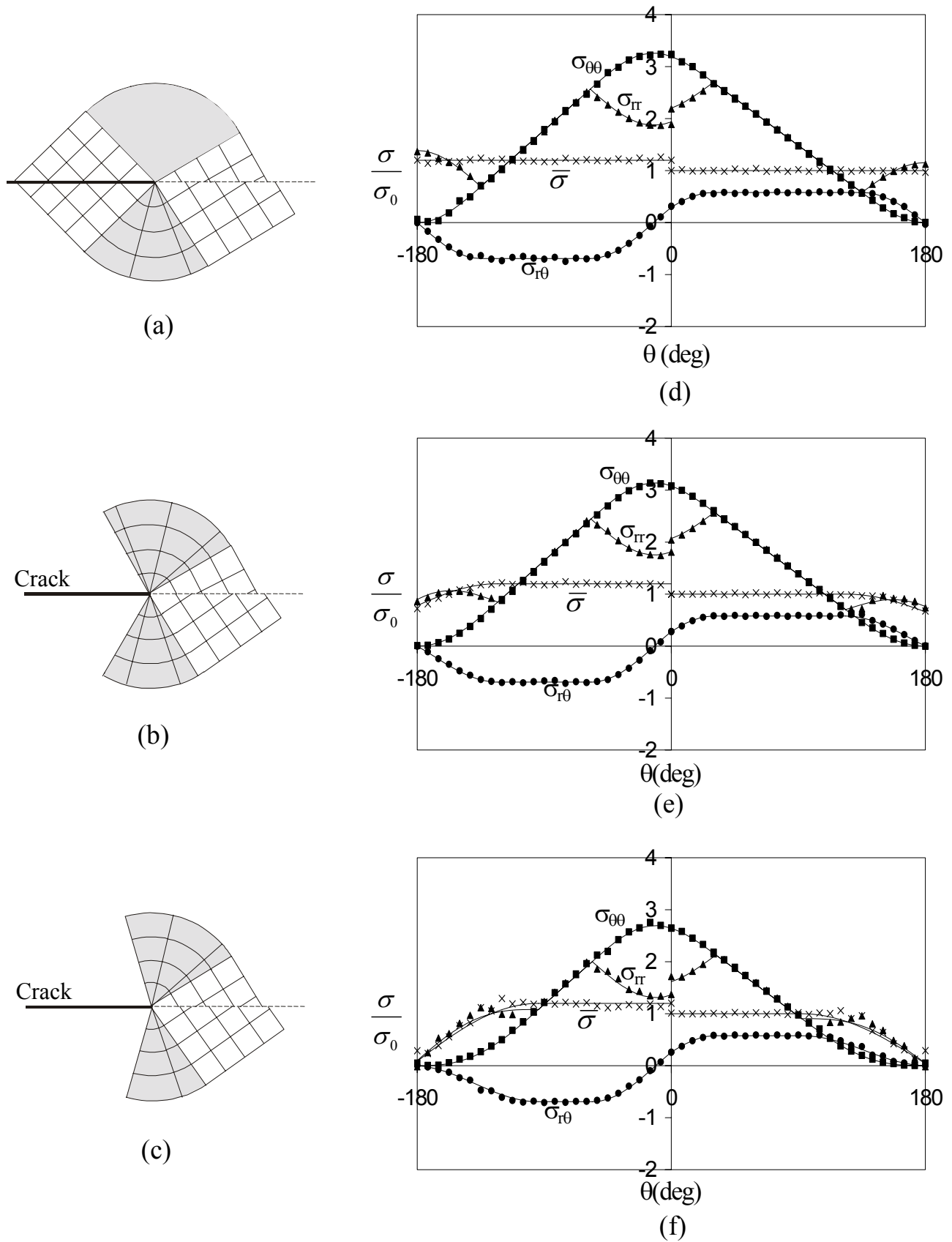
Figure 2   Slip-line fields for M=1.2 for (a) Positive T stress, (b) Zero T stress and (c) Negative T stress and asymptotic stress fields for M=1.2 for (a) Positive T stress, (b) Zero T stress and (c) Negative T stress. The solid lines represent the results from the analytic solutions, the symbols the results from the computational analysis.

THE EFFECT OF HYDROGEN-INDUCED SOFTENING ON THE DEFORMATION AT A CRACK TIP: IMPLICATIONS FOR FRACTURE

Y. M. Liang and P. Sofronis

Department of Theoretical and Applied Mechanics,
University of Illinois at Urbana-Champaign,
Urbana, IL 61801, USA

ABSTRACT

The hydrogen concentrations in equilibrium with local stress and plastic straining are studied in conjunction with large elastic-plastic deformation in the neighborhood of a blunting crack tip. The hydrogen effect on material behavior is modeled through the hydrogen-induced volume dilatation and the reduction in the local flow stress. Plane strain finite element analysis shows that stress relaxation due to solute hydrogen decreases the extend of plastic yielding whereas hydrogen-induced material softening causes the deformation to center in the region directly ahead of the crack tip. The consequence of this result on the hydrogen-induced fracture processes is discussed.

KEYWORDS

Hydrogen, diffusion, plasticity, softening, fracture

INTRODUCTION

Of the many suggestions for the explanation of the hydrogen related failures, the mechanism of **hydrogen-enhanced localized plasticity** (**HELP***)* appears to be a viable one [1]. Arguments in support of the HELP mechanism are based on experimental observations [2] and theoretical calculations [3] that in a range of temperatures and strain rates, the presence of hydrogen in solid solution decreases the barriers to dislocation motion, thereby increasing the amount of deformation that occurs in a localized region adjacent to the fracture surface [4]. The underlying principle in the HELP mechanism is the shielding of the elastic interactions between dislocations and obstacles by the hydrogen solutes [2, 3]. Reduction of the interaction energies between elastic stress centers results in enhanced dislocation mobility, i.e., decreased material local flow stress [4].

Nonetheless, significant issues remain to be resolved. Among these are: i) what is the detailed mechanism by which the enhanced dislocation mobility causes fracture in bulk specimens? ii) does the fracture occur by microvoid coalescense, formation of a Stroh crack or some other mechanism? iii) can the contribution of the plastic deformation to the fracture energy be established as a function of the hydrogen concentration? In view

of these questions, the prime goal of this paper is to address the effect of hydrogen-induced softening on the stress and deformation fields around a blunting crack tip. In a continuum sense material softening can be described through a local flow stress that decreases with increasing hydrogen concentration. It is important to emphasize that the term "flow stress" denotes the intrinsic flow characteristics of a small volume of material at the microscale around a crack tip where hydrogen concentrates as the material deforms. The amount of hydrogen concentration in the specimen is calculated by considering the effect of plastic straining (trapped hydrogen) and hydrostatic stress (normal interstitial lattice site hydrogen). In view of the very high mobility of the hydrogen solute, hydrogen concentration in trapping sites is assumed always in equilibrium with hydrogen in interstitial sites, which is also assumed to be in equilibrium with local hydrostatic stress. The calculated total hydrogen concentration is then used to estimate the material softening along the lines proposed in the work of Sofronis et al. [5] on the basis of the experimental observations of Tabata and Birnbuam [6]. It is emphasized that the present equilibrium calculation of the hydrogen concentrations, stress, and deformation fields is fully coupled. It should also be pointed out that the numerical predictions for our chosen model system, i.e. niobium, turn out to be independent of the amount of trapped hydrogen. Therefore, the present numerical results can be considered as an assessment of the synergism between the local hydrostatic stress and hydrogen-induced softening ahead of a crack tip. However, in view of the generality of the present approach, the current treatment can be easily applied to other systems with different trapping characteristics.

HYDROGEN CONCENTRATION AND CONSTITUTIVE LAW

Hydrogen is assumed to reside either at normal interstitial lattice sites (NILS) or reversible trapping sites at microstructural defects generated by plastic deformation. Hydrogen concentration in NILS is studied under equilibrium conditions with local stress σ_{ij}, and the occupancy of NILS sites, θ_L, is calculated through the Fermi-Dirac form in terms of the stress-free lattice concentration c_0 and stress [5]. Hydrogen atoms at trapping sites are assumed to be always in equilibrium with those at NILS according to Oriani's theory [7], and the trapping site occupancy is given by $\theta_T = \theta_L K / (1 - \theta_L + \theta_L K)$, where $K = \exp(W_B / RT)$, W_B is the trap binding energy, R is the gas constant, and T is the temperature. Thus the total hydrogen concentration (in trapping and NILS) measured in hydrogen atoms per solvent atom (H/M) is calculated as $c = \beta \theta_L(\sigma_{kk}) + \alpha \theta_T(\theta_L) N_T(\varepsilon^p) / N_L$, where N_T is the trap density which is a function of the effective plastic strain ε^p, N_L is the number of host metal atoms per unit volume, and α, β are material constants.

Sofronis et al. [5] based on the calculations of Sofronis and Birnbaum [3] and on microscopic studies of the effect of hydrogen on dislocation behavior in iron [6] argued that a continuum description of the hydrogen effect on the local flow stress σ_Y can be stated as $\sigma_Y = \sigma_0^H \left(1 + \varepsilon^p / \varepsilon_0\right)^{1/n}$, where σ_0^H is the initial yield stress in the presence of hydrogen that decreases with increasing hydrogen concentration, ε_0 is the initial yield strain in the absence of hydrogen, and n is the hardening exponent that is assumed unaffected by hydrogen. In this equation, the hydrogen effect on the local continuum flow characteristics is modeled through the initial yield stress which is assumed to be given by $\sigma_0^H = \phi(c)\sigma_0$, where $\phi(c)$ is a monotonically decreasing function of the local hydrogen concentration c and σ_0 is the initial yield stress in the absence of hydrogen. A possible suggestion for $\phi(c)$ is a linear form $\phi(c) = (\xi - 1)c + 1$, where the parameter ξ which is less than 1 denotes the ratio of the yield stress in the presence of hydrogen, σ_0^H, to that in the absence of hydrogen, σ_0, at the maximum hydrogen concentration of 1.

The total deformation rate tensor (symmetric part of the velocity gradient in spatial coordinates) is written as the sum of an elastic part (which is modeled as hypo-elastic, linear and isotropic), a part due to the presence of hydrogen, and a plastic part: $D_{ij} = D_{ij}^e + D_{ij}^h + D_{ij}^p$. The mechanical effect of the hydrogen solute atom is purely dilatational and is phrased in terms of the deformation rate tensor as $D_{ij}^h = \Lambda(c)\dot{c}\delta_{ij}/3$, where $\dot{c}$ is the time rate of change of concentration c, $\Lambda(c) = \lambda/\left[1 + \lambda(c - c_0)/3\right]$, $\lambda = \Delta v / \Omega$, Δv is the volume change per atom of

hydrogen introduced into solution that is directly related to the partial molar volume of hydrogen $V_H = \Delta v N_A$ in solution, Ω is the mean atomic volume of the host metal atom, c_0 is the corresponding initial concentration in the absence of stress, and δ_{ij} is the Kronecker delta. The material is assumed to be rate independent, flow according to the von Mises J_2 flow theory, and harden isotropically under plastic straining. Thus,

$$D_{ij}^p = \frac{1}{h}\left(\frac{3\sigma_{kl}'}{2\sigma_e} + \mu \delta_{km}\delta_{lm}\right)\frac{3\sigma_{ij}' \overset{\triangledown}{\sigma}_{kl}}{2\sigma_e} \tag{1}$$

where $\sigma_e = \left(3\sigma_{ij}'\sigma_{ij}'/2\right)^{1/2}$ is the von Mises equivalent stress, $\sigma_{ij}' = \sigma_{ij} - \sigma_{kk}\delta_{ij}/3$ is the deviatoric stress, $h = \frac{\partial\sigma_Y}{\partial\varepsilon^p} + \frac{\partial\sigma_Y}{\partial c}\frac{\partial c}{\partial\varepsilon^p}$, $\mu = -\frac{\partial\sigma_Y}{\partial c}\frac{\partial c}{\partial\sigma_{kk}}$, $\varepsilon^p = \int\sqrt{2D_{ij}^p D_{ij}^p/3}\,dt$ is the effective plastic strain, and the superposed $\triangledown$ denotes the Jaumann stress rate that is spin invariant.

NUMERICAL RESULTS

Solutions to the boundary value problem for the equilibrium hydrogen concentration coupled with material elastoplasticity are presented in the neighborhood of a blunting crack tip under plane strain mode I opening. Small scale yielding conditions were assumed and the system's temperature was 300K. The material used in the simulations was niobium, as this metal is a high H solubility system, suffers from embrittlement at room temperature, and experimental data are readily available. Displacement boundary conditions of the singular linear elastic field were imposed at a circular boundary at a distance $L = 15$cm from the tip. The ratio of L/b_0, where b_0 is the initial crack opening displacement, was taken equal to 30,000. The finite element mesh is described in the work of Sofronis and McMeeking [8]. Before the application of the external load, the specimen was assumed to be stress free and at a uniform initial hydrogen concentration c_0. Upon loading, uniform redistribution of the H solute occurs within the solid so that hydrogen is always under quasi-static "local equilibrium" conditions with local stress and plastic strain as discussed in the previous section. Since hydrogen is assumed to be provided by a chemical reservoir, an arrangement corresponding to "far field concentration" kept constant at c_0, the calculation corresponds to a constant chemical potential for the hydrogen solute. Hydrogen was assumed to expand the lattice isotropically and its partial molar volume in solution was $V_H = 1.88\,\text{cm}^3/\text{mole}$ which corresponds to $\lambda = 0.174$. The molar volume of niobium was $10.852 \times 10^{-6}\,\text{m}^3/\text{mole}$ which implies that the number of the available NILS was $N_L = 5.55 \times 10^{28}$ solvent lattice atoms per m^3. The hydrogen trap sites were associated with dislocations in the deforming metal. Assuming one trap site per atomic plane threaded by a dislocation, one finds that the trap site density in traps per cubic meter is given by $N_T = \sqrt{2}\rho/a$, where ρ is the dislocation density and a is the lattice parameter. The dislocation density ρ, measured in dislocation line length per cubic meter was considered to vary linearly with logarithmic plastic strain ε^p so that $\rho = \rho_0 + \gamma\varepsilon^p$ for $\varepsilon^p < 0.5$ and $\rho = 10^{16}$ for $\varepsilon^p \geq 0.5$. The parameter $\rho_0 = 10^{10}$ line length/m^3 denotes the dislocation density for the annealed material and $\gamma = 2.0 \times 10^{16}$ line length/m^3. The trap binding energy was taken equal to $W_B = 29.2\,\text{kJ/mole}$ [5], the parameter β was set equal to 1 and this corresponds to a maximum NILS concentration of 1 H atom per solvent lattice atom, and the parameter α was also set equal to 1 which denotes 1 trapping site per trap. The lattice parameter was $a = 3.3 \times 10^{-10}\,\text{m}$, Poisson's ratio $v = 0.34$, Young's modulus $E = 115\,\text{GPa}$, the yield stress in the absence of hydrogen $\sigma_0 = 400\,\text{MPa}$, the hardening coefficient $n = 10$, and the softening parameter ξ was set equal to 0.1.

In Figure 1, the normalized stress σ_{22}/σ_0 and normalized hydrogen concentration c/c_0 are plotted against normalized distance R/b from the crack tip along the axis of symmetry at an initial hydrogen concentration $c_0 = 0.1\,\text{H/M}$.
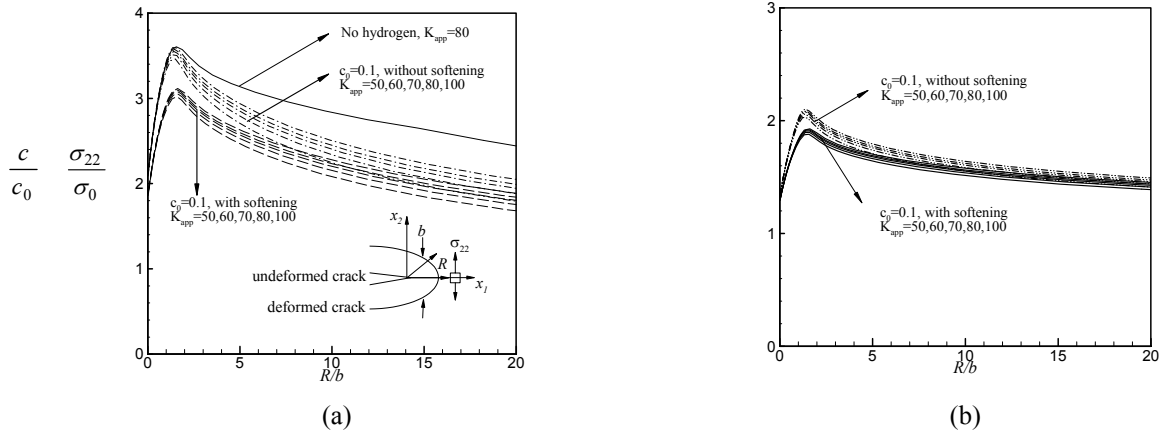
Figure 1. (a) plot of the normalized stress σ_{22}/σ_0 vs normalized distance R/b along the axis of symmetry ahead of the crack tip for various applied stress intensities measured in $MPa\sqrt{m}$. The parameter R denotes the distance of a point from the notch root in the undeformed configuration and b is the current crack opening displacement; (b) plot of the normalized hydrogen concentration c/c_0 vs normalized distance R/b.

Clearly, at a given initial hydrogen concentration c_0, the hydrogen concentration profiles are shown in Fig. 1b to scale with the applied load in accordance with the formula $c = c\left(\sigma_{kk}, \varepsilon^p\right)$ and the well known corresponding scaling [9] of the stress and effective plastic strain in the small scale yielding solution. Lattice dilatation by H is accompanied with stress relaxation in the area ahead of the tip. As shown in Fig. 1a, this relaxation is more pronounced in the region $R/b > 1.6$ where the plastic strain in the absence of hydrogen is small in comparison to the plastic strain in the region close to the crack tip ($R/b < 1.6$). Hydrogen-induced softening decreases the local flow stress ahead of the crack tip, thus resulting in a reduced hydrostatic stress (Fig. 1a) and increased plastic strain. Since the hydrogen concentration profiles are dominated by the hydrostatic stress, the hydrogen concentration profile ahead of the tip is lower for a material undergoing softening due to hydrogen than for a material in the absence of any softening effect (Fig. 1a). It should also be mentioned here that the reduced hydrogen populations in the softened material are associated with a stronger stress relaxation than in the material without softening under the same applied load. Thus, the overall stress relaxation ahead of a crack tip is dictated by the synergism between material softening and relaxation due to hydrogen-induced dilatation.
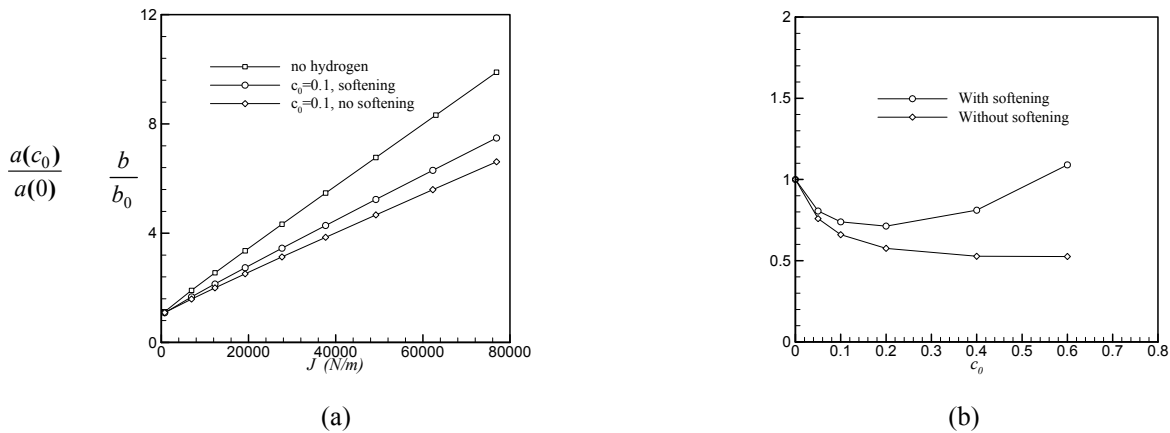
Figure 2: (a) Plot of normalized crack opening displacement b/b_0 against the applied $J = \left(1-\nu^2\right)K_{app}^2\big/E$ integral. The parameter b_0 denotes the crack opening displacement in the undeformed configuration; (b) Plot of $a(c_0)/a(0)$ against the initial hydrogen concentration c_0, where $a(c)$ is defined through $b/b_0 = a(c)J + 1$
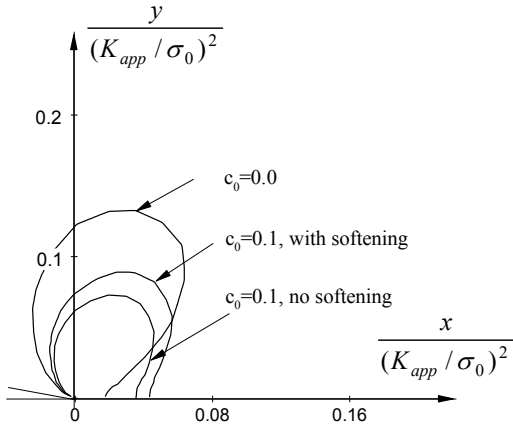
Figure 3: Superposed plastic zones ahead of a crack tip: for the hydrogen free material, $c_0 = 0.1$ and with no softening, and $c_0 = 0.1$ and with softening.

In the absence of hydrogen, there exists a linear relationship between the crack tip opening displacement (CTOD) and the applied J integral, namely $b/b_0 = aJ + 1$ [9], where a is a constant. In the presence of hydrogen, the numerical results of Fig. 2a show that for both hydrogen-induced softening and in the absence of any softening effect, this linear relationship between b and J continues to hold. This is a direct consequence of the fact that scaling of the stress and deformation fields ahead of the tip with the applied load continues to hold in the present case of equilibrium hydrogen concentrations. Figure 2a shows that at a certain applied load and initial hydrogen concentration, hydrogen tends to close the crack, i.e., decrease the parameter a. This is because hydrogen-induced lattice dilatation relaxes the stresses around the crack tip, thus leading to reduced plastic strains behind the tip and smaller plastic zones (see Fig. 3). Furthermore, hydrogen-induced softening causes a to be greater than that without softening because the plastic zone and strains are larger in the former case than in the latter (Fig. 3). It can be deduced that softening increases the parameter a (i.e. increases the CTOD) whereas relaxation due to dilatation decreases (i.e. decreases the CTOD) it. Also, comparing the cases with no hydrogen and hydrogen-induced softening, one sees that the softening effect is overridden by the relaxation effect at the concentration of 0.1 H/M as shown in Fig. 2a.

The dependence of the parameter a (i.e., the CTOD) on the initial hydrogen concentration c_0 is shown in Fig. 2b for the cases with and without hydrogen-induced softening. For the case without softening, a decreases with increasing c_0 and asymptotes a nearly constant value at large initial hydrogen concentrations. This is because for $0 < c_0 < 0.4$, numerical results show that the hydrogen concentration enhancement $\Delta c = c - c_0$ ahead of the crack tip increases with c_0, thereby resulting in increased stress relaxation and in turn, in decreasing $a(c_0)/a(0)$ (CTOD) with increasing c_0. However, for initial concentrations $0.4 < c_0 < 0.6$, Δc is almost insensitive to c_0, in particular for $R/b > 20$, and hence $a(c_0)/a(0)$ is nearly constant.

(a)

(b)
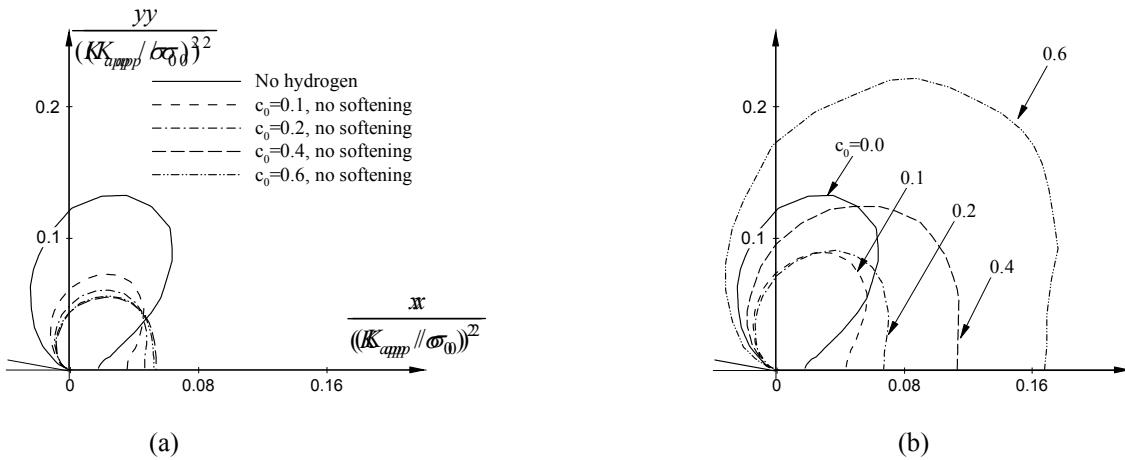
Figure 4: (a) Superposed plastic zones ahead of the crack tip at various initial hydrogen concentrations c_0 for the case (a) without softening; and (b) with softening.

In the case of hydrogen-induced softening and $c_0 \leq 0.2$, $a(c_0)/a(0)$ decreases with increasing c_0 because the relaxation due to $\Delta c = c - c_0$ overrides the relatively small softening effect associated with concentrations $c_0 < 0.2$. In contrast, for $c_0 > 0.2$ the corresponding relaxation is mild due to the small increases in Δc, and

this mild relaxation is overridden by the strong softening effect associated with these large initial concentrations.

The numerical results for the effect of hydrogen on the shape and size of the plastic zone in the neighborhood of the crack tip are shown in Fig. 4. First, hydrogen-induced lattice dilatation relaxes the stresses ahead of the tip and as a result, the plastic zones are shown spread and confined directly ahead of the tip and smaller (Fig. 4a) than in the absence of hydrogen. In the case of no-softening, Figure 4a shows that as the initial hydrogen concentration increases, the plastic flow of the material continues to concentrate in the region ahead of the crack tip while the plastic zone shrinks in the directions along the normal to the axis of symmetry and behind the crack tip. Shrinking of the plastic zone behind the crack tip with increasing initial hydrogen concentration (Fig. 4a) yields reduced crack opening displacements in agreement with the trend shown in Fig. 2b. For $c_0 = 0.4$ and $c_0 = 0.6$, both the plastic zone shape and size are almost the same (Fig. 4a), and this also corresponds to the nearly constant $a(c_0)/a(0)$ shown in Fig. 2b in the absence of softening. In the presence of hydrogen-induced softening, the plastic zones are shown expanding in every direction relative to the case with no softening (Figs. 3, 4b) as the initial concentration increases. Since $c_0 = 0.1$ is a relatively low initial concentration at which the softening effect on spreading the plasticity is dominated by the local expansion and confinement of the plastic flow ahead of the tip due to the dilatation-induced relaxation, the plastic zone size continues to be smaller than that in the absence of hydrogen (Fig. 3). However, at much larger initial concentrations (e.g. $c_0 = 0.6$), the softening effect results in much larger plastically deforming regions (Fig. 4b) and this is in accordance with the behavior of $a(c_0)$ shown in Fig. 2b.

CONCLUDING DISCUSSION

The present finite element calculations of coupled elastoplasticity with hydrogen concentration development in equilibrium with local stress and plastic strain show that that hydrogen concentration profiles ahead of a crack tip scale with the applied load for both hydrogen-induced softening and with no softening effects (Fig. 1). Dilatation-induced relaxation causes the plastic zone to expand and be confined ahead of the crack while it shrinks in all other directions. This reduces the crack tip opening displacement. In contrast, hydrogen-induced softening causes the plastic zone to expand in all directions and the CTOD to increase. At small initial concentrations ($c_0 < 0.2$), stress relaxation dominates whereas softening prevails at larger initial concentrations ($c_0 \geq 0.2$). As a result, the plastic zones are smaller in the former case than in the latter. However, in all cases, there is substantial plastic flow that takes place directly ahead of the crack tip which is not the case in the hydrogen free material (Fig. 4b). Therefore, one may identify the role of hydrogen with promoting intensification of the ductile fracture processes (e.g. void opening and inter-void ligament fracture by shear localization) that occur directly ahead of the crack tip. This is particularly true at small c_o (~0.1H/M) at which the hydrostatic stress, assisting void growth, is not substantially relaxed even in the case with softening.

REFERENCES

1. Birnbaum, H.K. and Sofronis, P. (1994) *Mater. Sci. & Eng.* A176, 191.
2. Sirois, E. and Birnbaum, H.K. (1992) *Acta Metall.* 40, 1377.
3. Sofronis, P. and H. K. Birnbaum (1995) *J. Mech. Phys. Solids* 43, 49.
4. Robertson I.M. and Birnbaum, H.K. (1986) *Acta Metall.* 34, 353.
5. Sofronis, P., Liang, Y. M. and Aravas, N. (2001) Submitted to *European Journal of Mechanics A: Solids*.
6. Tabata, T. and Birnbaum, H.K. (1983) *Scripta Metall.* 17, 947.
7. Oriani, R.A. (1970) *Acta Metall.* 18, 147.
8. Sofronis, P. and McMeeking, R.M. (1989) *J. Mech. Phys. Solids* 37, 317.
9. McMeeking, R.M. (1977) *J. Mech. Phys. Solids* 25, 357.

THE EFFECT OF PROCESSING ON TENSILE STRENGTH AND FRACTURE BEHAVIOR OF CFRP SMART COMPOSITES WITH EMBEDDED SHAPE MEMORY ALLOY WIRES

Byung-Koog Jang, Ja-Ho Koo, Ya Xu, Nobuyuki Toyama, Hitoshi Yoshida, Yoshio Akimune and Teruo Kishi

Smart Structure Research Center
National Institute of Advanced Industrial Science and Technology (AIST)
Tsukuba Central 2, 1-1-1, Umezono, Tsukuba-City, Ibaraki, 305-8568, JAPAN

ABSTRACT

TiNi/CFRP composites were fabricated by hot pressing in the temperature range of 130~180°C, by controlling the applied pressure. The TiNi wires were embedded as an 1mm interval into the center of CFRP layers and CFRP host materials were stacked as 0, 30, 60 and 90 degrees configuration on tensile direction, respectively. The stress-strain curve and tensile strength of composites strongly depends on stacking direction of carbon fibers. The tensile strength of TiNi/CFRP composites with stacking direction of 0 and 90 degrees configuration are about 1.2GPa and 50MPa, respectively. The microstructural properties of TiNi/CFRP composites were observed by SEM. Pore and/or voids were found to congregate near the embedded TiNi wire and they increased in proportion to stacking direction of carbon fibers. Larger pores and interfacial cracks were also observed at interface between TiNi wires and epoxy resin. Furthermore, the fracture behavior was studied by one-dimensional AE source location during tensile test, to analyze the fracture mode. It was confirmed that the extensional mode for 0 degree composites and the flexural mode for 90 degrees composites are predominant, respectively.

KEYWORDS

TiNi shape memory alloy, CFRP (carbon fiber reinforced plastics), tensile strength, microstructure, AE (acoustic emission), Lamb wave, fiber breakage, smart composites.

INTRODUCTION

Recently, many research work regarding smart composites by incorporation of functional materials into structural material were reported. Smart composites have proven to be a promising new material system and many applications have been found like as sensors, actuators, and control

processors. Shape memory alloy (SMA), optical fiber, and piezoelectric materials, have been found to be capable for fabrication of smart composites [1, 2]. Among such functional materials, SMA is good candidate material because it exhibits various properties of actuator, super-elastic response, high damping and self-recovery function. Specially, TiNi shape memory alloy is attractive because of the large shape memory effect, high damping capacity and high stiffness at the austenite state. Various kinds of smart composites having new functional properties have been investigated by incorporated materials of SMA with various shape such as fibers, wires, ribbons, particles and thin films [3, 4]. The SMA reinforced smart composites can be manufactured with conventional polymer matrix composite fabrication method, by laying the SMA wires with the reinforcing shape into the CFRP prepreg matrix and then using either hot-pressing or an autoclave and several different types of cure cycles. However, manufacturing by autoclave has several demerits such as high cost, high material loss, and low work efficiency. Very little research has been done regarding processing effects on mechanical properties and fracture behavior in TiNi SMA embedded composites. Therefore, this work focuses on effect of processing regarding mechanical properties of CFRP smart composites incorporating TiNi wires of shape memory alloy by using hot pressing. It was also investigated the fracture mode due to separation of Lamb wave by one-dimensional AE source location using the notched tensile specimens attaching two AE sensors.

EXPERIMENTAL PRODECURE

It was designed a TiNi/CFRP composite by sandwiching the TiNi wires between layer of CFRP prepreg. Stacks are composed of CFRP prepreg and embedded TiNi wire and then stacked together. The different stacking direction for carbon fibers such as 0, 30, 60 and 90 degrees configuration on tensile direction are chosen to establish the optimal design for fabrication of TiNi/CFRP composites. CFRP prepreg had been cut in size of 200×105 mm. During the lamination procedure, the TiNi wires were carefully embedded into CFRP prepreg as an 1mm interval into the center of 8 sheets of CFRP layer and those were laid in the 0 degree configuration on tensile direction using the special steel jig. Anti-heat vinyl sheets were used to prevent the flow of epoxy resin of CFRP prepreg during heating. Stacked bodies with CFRP prepreg and TiNi wires were laid up in the steel mold. TiNi/CFRP smart composites could be fabricated by curing at hot-press. Curing was accomplished for 2hr, in range of 130~180°C by controlling the applied pressure in range of 0.03~0.3 MPa. After curing, hot-pressed specimens allowed cooling to room temperature. The hot-pressed TiNi/CFRP composites were cut by diamond blade and prepared as a tensile test specimen according to the standard of JIS-K 7073. It was induced notch having a dimension of 3×0.3 (L×t) at both side of specimens using diamond wheel as shown in Figure 1.
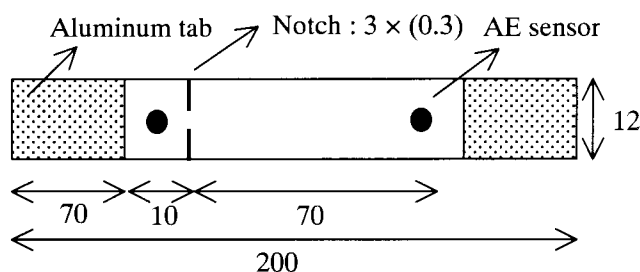
Figure 1: Schematic drawing of notched tensile specimen

2

The AE (acoustic emission) technique was applied to investigate the fracture mode of TiNi/CFRP composites and was conducted using two channel monitoring system. One AE sensor was attached near notch area and another AE sensor was attached opposite area of notch for classifying the AE signal, easily. Detected AE signals were filtered to avoid the noise and were analyzed by a computer. The microstructural properties of TiNi/CFRP composites such as observation by SEM and optical microscopy were also investigated.

RESULTS

Microstructure

The SEM micrograph of the polished surfaces for TiNi/CFRP composite hot pressed at 180°C, 0.3MPa regarding the different stacking direction of carbon fibers are shown in Figure 2. The brightly big circle materials are an embedded TiNi wire and surrounding materials are CFRP matrix.
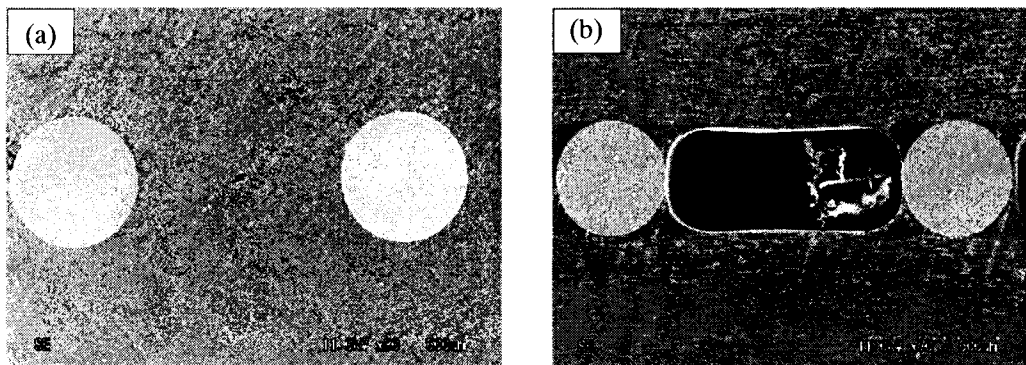
Figure 2: SEM micrographs of TiNi/CFRP composites with different stacking direction
of carbon fibers : (a) 0 and (b) 90 degrees configuration on tensile test direction

Pore and/or voids could not almost detected in composites stacked as 0 degree configuration of carbon fibers, whereas big voids existed at around TiNi wire and matrix in composites stacked as 30 degrees configuration of carbon fibers. For composites stacked as 60 and 90 degrees configuration of carbon fibers respectively, bigger void existed at interfacial matrix between TiNi wires. The averaged pore and/or void size of composites stacked as 0 degree configuration were smaller than those of composites stacked as 30~90 degrees configuration. Combining the data from all cross-sections, the average void size for specimen stacked as 0 degree configuration was found to be below 20 µm, whereas that for specimen stacked as 90 degrees configuration was found to be up to 600 µm, respectively. It seems that the mass transport of epoxy resin for composite with various stacking direction may be inhomogeneous during curing, resulting in defect formation. These results indicate that a more uniform microstructure can be obtained for stacked bodies as 0 degree configuration. Based on result of pore and/or voids distribution, it could be understood that the microstructure of TiNi/CFRP composites strongly depend on stacking direction of carbon fibers. These results suggest that stacking design for manufacturing of composites should be carefully carried out in order to obtain the TiNi/CFRP composites with defect free. Also, it may be that the embedded TiNi wires act as an impurity sites for the formation of pore and/or voids. Pore and/or voids fraction also increased in proportion to volume of the embedded TiNi wire location. Based on this work, By properly designing a stacking configuration of carbon fibers, internal defects may be reduced or controlled.

Mechanical Properties

The detected various defects induced during processing can significantly degrade the mechanical properties of SMA composites. So, the tensile strength was experimentally investigated as shown in Figure 3. It was found that the tensile strength of composites stacked as 0 degree was higher than those for various 30~90 degrees configuration. The reason of the degradation in tensile strength resulted from increase of internal defects such as pore or voids fraction as well as a little fiber breaking. These results mean that the tensile strength of TiNi/CFRP composites has strongly depended on the stacking direction of carbon fibers and tensile strength precisely showed the remarkable decrease with increasing stacking direction of carbon fibers for TiNi/CFRP composites. In addition, CFRP monolithic without TiNi embedding is 1.3 GPa, whereas TiNi embedded composites is below 1.1 GPa. The reason for the degradation in tensile strength of TiNi/CFRP composites is attributed to the fact that the material defects are generated in the matrix by incorporation of TiNi into the CFRP matrix. It is considered if volume fraction of TiNi embedded into CFRP matrix is increased, it may be more decreased the tensile strength.
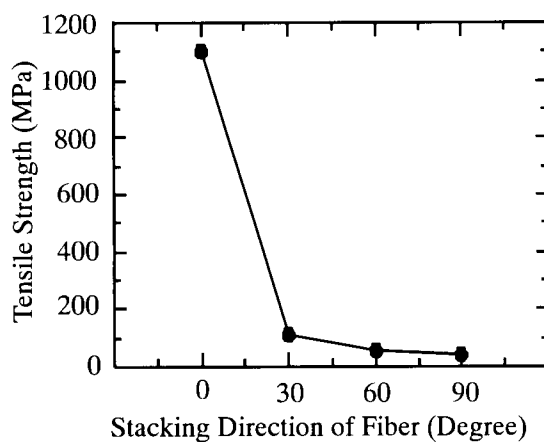
Figure 3: Tensile strength of TiNi/CFRP composites with different stacking direction of carbon fibers
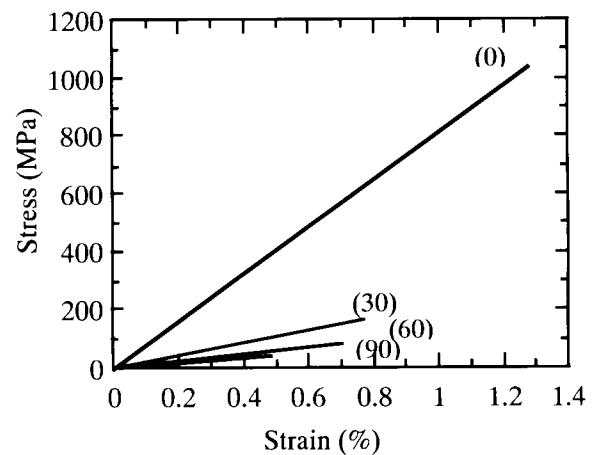
Figure4: Stress-strain curves of TiNi/CFRP composites with different stacking direction of carbon fibers

The relationship of the stress-strain (S-S) curves during tensile test is plotted in Figure 4. All stress-strain curves have tendency to be steadily linear until fracture at maximum load. As expected, stress-strain curves decrease with increasing the stacking direction of carbon fibers. For TiNi/CFRP composites stacked as 0 degree configuration, a strain increases gradually with increasing stress. The tendency of largely linear stress-strain curve for 0 degree configuration, also means the existence of carbon fiber breakages arising at carbon fibers, because embedded carbon fiber direction is 0 degree against tensile direction. S-S curve results indicate the low inclination for specimens stacked as 30~60 degrees configuration and it shows the extremely lower inclination for 90 degrees configuration. The Young's modulus can be measured from the S-S curve. It is expected that composites of 0 degree configuration having the higher inclination in results of S-S curve show the higher Young's modulus, whereas composites of 30~90 degree configuration with lower inclination correspond to the lower Young's modulus. The average Young's modulus of specimens stacked as 0 and 90 degrees configuration, were estimated as 75 GPa and 8 GPa, respectively.

Analysis of Fracture Behavior by One Dimensional AE Source Location

The fracture mode of a fiber reinforced composites depends on its embedded direction in the specimen. Different fracture mode, such as matrix crack, debonding, fiber breakage and buckling,

may complicatedly occur due to tensile, compressive, shear or a combination of these stresses. Generally, the AE technique proved to be effective for investigating the fracture process of fiber reinforced plastic composite materials. The generated AE events resulted from the generation of micro-fracture such as carbon fiber breaking, debonding and matrix micro cracking during tensile test. However, AE characteristics of these fracture modes associated with embedded direction are rarely investigated. In order to investigate the fracture mode in TiNi/CFRP composites, AE measurements have been coupled using notched tensile specimens applying the AE source location. Figure 5 shows the representative results of Lamb wave generated by one-dimensional AE source location from detected AE signals. Generally, AE signals propagate as the extensional and flexural plate modes in thin composite plates and plate-like geometries such as shells, pipes and tubes. The relative amplitude of the two modes depends on the directionality of the source motion [5, 6]. Therefore, if specimen is plate with thin thickness like in the present specimen, detected AE signal correspond to Lamb wave. Lamb wave can be also divided to two kinds, that is, the extensional mode and flexural mode as shown in Figure 5.

(A) Extensional mode   (B) Flexural mode
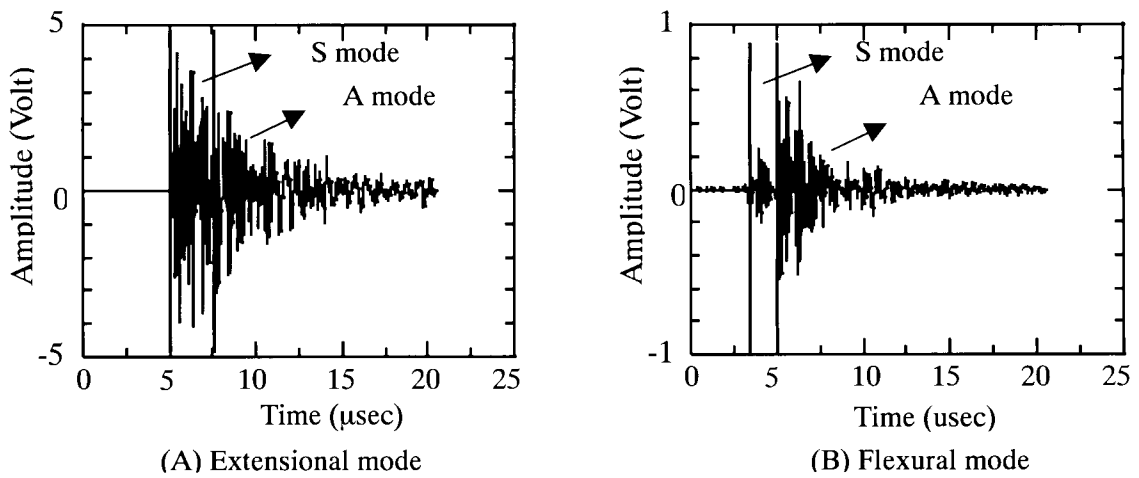
Figure 5: Lamb wave of AE signal generated by tensile test using notched tensile specimens of TiNi/CFRP composites: (A) Extensional mode and (B) Flexural mode
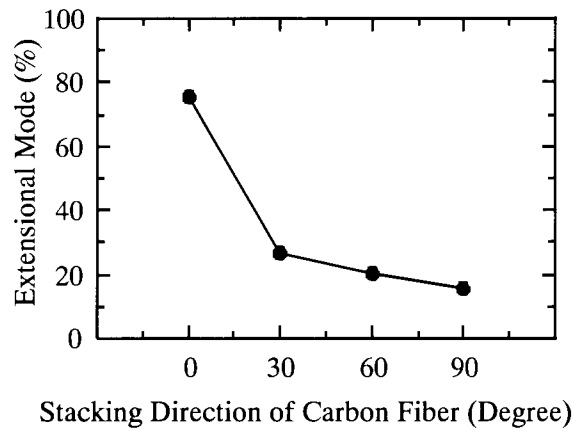
Figure 6: Extensional mode ratio by separation of Lamb wave
for notched tensile specimens of TiNi/CFRP composites

From analyzing results of AE wave, the extensional mode shows that S mode of wave is relatively large amplitude and A mode shows small amplitude. However, the flexural mode shows that S mode of wave is low-level amplitude and A mode relatively shows large amplitude. Furthermore, the extensional mode corresponds to generation of mainly fiber breakings, whereas the flexural mode correspond to generation of mainly debonding and micro cracking. Figure 6 compares an extensional mode ratios based on one-dimensional AE source location using notched tensile specimens. The detected AE signals were collected total 10mm range area including notch center, because this notch area generated many AE events during tensile test. The extensional mode ratio is derived from value that extensional mode is divided by sum of extensional mode and flexural mode. Extensional mode ratio of 0 degree specimen is about 80%. However, various 30~90 degrees composites shows very low extensional mode. This demonstrates that the generation of fiber breakings for specimen with 0 degree is predominant during tensile test. However, in case of 30~90 degrees composites, the generation of flexural mode is predominant rather than extensional mode. Consequently, this means that the generation of fiber breakings is very few. These results demonstrate that fracture mode in TiNi/CFRP composites can classify by one-dimensional AE source location using notched tensile specimen.

CONCLUSIONS

TiNi SMA wires embedded CFRP smart composites with free of pores or voids, were successfully fabricated. Stacking direction of carbon fibers is more important processing parameter for obtaining the dense composite. Pore and/or voids rarely existed in composites stacked as 0 degree configuration of carbon fibers, whereas bigger voids mainly existed near TiNi wires with increasing the stacking direction. With increasing the stacking direction of carbon fibers, the tensile strength and Young's modulus of composites decrease. The fracture mode of TiNi/CFRP composites depends on its stacking direction of fibers from the results of one-dimensional AE source location using two AE sensors. TiNi/CFRP composites with 0 degree predominantly show the extensional mode, corresponding to fiber breakages.

ACKNOWLEDGEMENTS

REFERENCES

1. Mall, S., Dosedel, S.B. and Holl, M.W. (1996) *Smart Mater. Struct.*, 5, 209-215.
2. Galea, S. C., Chiu, W.K. and Paul, J.J. (1993) *J. Intell. Mat. Sys. Struc.*, 4, 330-336.
3. Eppa, J. and Chandra, R. (1997) *Smart Mater. Struct.* 6, pp. 251-264.
4. D.A. Hebda, M.E. Whitlock, J.B. Ditman and S.R. White (1995) *J. Intell. Mat. Sys. Struc.* 6, 220-228.
5. Gorman, M.R., (1991) *J. Acoust. Soc. Am.*, 90(1), 358-364
6. Prosser, William H., Gorman, Nichael R. and Doighi, (1992) *J. of Com. Mat.*, 26, 2016-2027

THE EFFECT OF RESIDUAL STRESSES AND STRAINS ON FATIGUE CRACK PROPAGATION: MEASUREMENT AND MODELLING

D. Nowell, L.J. Fellows, D.A. Hills, and Y. Xu

Department of Engineering Science, University of Oxford,
Parks Road, Oxford, OX1 3PJ, UK

ABSTRACT

Moiré interferometry provides an accurate means of measuring residual displacements around a propagating fatigue crack. From these displacements, crack closure behaviour and residual stresses may be determined. This paper describes the construction and operation of an in-situ moiré interferometer, mounted on a servohydraulic fatigue machine. Photoresist gratings were applied to fatigue specimens of Ti 6/4 and these proved durable under fatigue loading. Crack closure data is presented for a number of loading conditions, including constant amplitude loading and a single overload cycle. The results obtained are compared to the predictions of a plane stress boundary element model, based on the concept of strip yield. Encouraging agreement is obtained, particularly for the case of constant amplitude loading.

KEYWORDS

Fatigue, crack closure, residual stress, moiré interferometry.

INTRODUCTION

It has long been recognised that plasticity in the region of the crack tip is an important aspect of the fatigue process in most engineering materials. The existence of such regions of plasticity implies that there are also residual stresses and strains close to the crack tip and, in the case of a propagating fatigue crack, these remain behind as the crack grows so that a region of residually strained material exists along the crack flanks. Elber [1,2] was the first to report the phenomenon of plasticity-induced crack closure where, even in purely tensile loading, the tip of a fatigue crack is found to be closed for part of the loading cycle. This phenomenon is important, since it provides a means of explaining experimental observations that crack growth rate depends on loading history as well as nominal ΔK. In order to exploit this phenomenon for improved predictions of crack propagation life, two key techniques are reguired:

(i) A convenient and accurate means of measuring crack closure, residual stresses, and residual strains for cracks under controlled loading.

(ii) A model which is sufficiently detailed to predict the important aspects of the observed behaviour, yet simple enough to allow modelling of representative loading histories in a reasonable timescale.

Techniques have not yet been developed which can fully meet these requirements, but a range of approaches are now available which can go some way towards the objectives. Traditional means of monitoring crack

closure, such as compliance measurements with crack mouth gauges or strain gauges, electrical resistance, etc have now been complemented by full field techniques such as moiré interferometry [3] or photoelasticity [4]. Moiré provides surface information only, but in principle may be applied to any material. Photoelasticity does offer the possibility of through thickness measurements, but only for a restricted range of materials. Thus, for use on engineering materials, moiré interferometry provides the best current technique for obtaining full field displacement measurements, although alternatives such as laser speckle interferometry are under investigation. Modelling of fatigue crack closure can be carried out using finite element methods [5], but the computational resources required for simulation of practical load cycles have led to the development of simplified boundary element methods such as that proposed by Newman [6]. These simplified models often use an approximation for the basic plasticity mechanism such as the Dugdale strip yield assumption [7].

The current paper describes work carried out on the aerospace alloy Ti-6Al-4V. Full-field displacement measurements were made around the tip of a growing fatigue crack using moiré interferometry. From these it was possible to determine residual strains and crack opening. A simple boundary element model was then used to compare the experimental measurements with predictions.

EXPERIMENTAL WORK

Fatigue cracks were grown in small 4-point bend specimens of Ti-6Al-4V. Specimens were 8mm deep by 7mm thick and the inner and outer support spacing was 60mm and 110mm respectively. In order to measure the displacements at any point of the fatigue cycle (including cycles with positive R-ratio), an in-situ interferometer was built adjacent to the servo-hydraulic fatigue machine. The design and operation of the interferometer is described fully by Güngör and Fellows [8]. Interference gratings of 1200 lines per mm were applied to the surface of the specimen to give a displacement sensitivity of 0.417μm per fringe order. In our earlier work [3], these were applied using a standard replication technique to produce aluminium gratings bonded by an epoxy resin. It was found in practice that the quality of these gratings deteriorated quite rapidly with fatigue cycling, usually by debonding of the adhesive, so that they were not suitable for tracking the specimen through a number of load cycles. An improved grating system was therefore developed based on a polymer photoresist (Hunts 514 [8]). The photoresist was applied to the specimens by dipping and then exposed to a laser interference pattern in order to produce the grating. After development the gratings were coated with a thin layer of gold to improve reflectivity. Interference patterns were collected by the temporal phase-stepping method [9], giving values of intensity $I(x,y)$ at each spatial point in the region of interest for five different phase differences, δ_i. Data was collected from a 256 x 256 array over a region close to the crack tip, with a pixel spacing of about 9μm. Determination of the phase, ϕ, of the interference pattern at each point was carried out by a least squares technique using the equation

$$I_i(x,y) = a(x,y) + b(x,y)\cos(\phi(x,y) + \delta_i) \tag{1}$$

where $a(x,y)$ is the local background intensity and $b(x,y)$ is the contrast. Values of ϕ vary between $-\pi$ and π between one fringe order and the next. An unwrapping routine [10] is therefore used to determine absolute phase, from which the u or v displacement component can be obtained. The displacements need to be measured relative to an arbitrary datum and, in our experiments, the interferometer was adjusted to give a null field at the lowest load in the cycle. Displacements of opposite sides of the crack line could then be monitored at a number of steps during the loading cycle. Any increase in relative displacement of the two crack faces was interpreted as an opening of the crack.

MODELLING

Modelling of crack behaviour was carried out using a boundary element strip yield model which is physically similar to Newman's [6]. The principal innovation in the model was the use of a quadratic

programming formulation [11] which automatically determined the appropriate boundary condition in each region, i.e. along the crack faces:

$$\sigma_{xx} = 0, \quad b > 0, \quad (Crack\ open) \tag{2}$$

$$\sigma_{xx} < 0, \quad b = 0, \quad (Crack\ closed) \tag{3}$$

where b is the crack opening, and within the yield zone:

$$\sigma_{xx} = \sigma_y, \quad \Delta b > 0, \quad (Tensile\ yield) \tag{4}$$

$$-\sigma_y \leq \sigma_{xx} \leq \sigma_y, \quad \Delta b = 0, \quad (No\ yield) \tag{5}$$

$$\sigma_{xx} = -\sigma_y, \quad \Delta b < 0, \quad (Compressive\ yield) \tag{6}$$

Here, Δb is interpreted as the change in plastic displacement in the yield strip during the current load step and σ_y is the yield stress. The material is modelled as elastic/ideally plastic. Several hundred elements are used along the crack and in the yield strip and a focussed mesh is employed so that greater definition is obtained close to the crack tip. Typical output from the model is shown in Figure 1, where σ_{xx} and crack shape are plotted along the crack line ($x = 0$). Full field displacements and stresses may also readily be obtained.

RESULTS

A range of results were collected for different load conditions as shown in Table 1.

TABLE 1
LOAD CONDITIONS INVESTIGATED

Test No	Ref. No	Maximum Load (P_{max}/P_y)	Minimum Load (P_{min}/P_y)	Overload (P_{ovl}/P_y)	R-Ratio	Crack Length (mm)
1	17	0.529	0.0	-	0.0	0.842
2	17a	0.529	0.0	-	0.0	1.704
3	22	0.529	-0.529	-	-1.0	1.040
4	55	0.705	0.282	-	0.4	1.235
5	51	0.529	0.0	0.881	0.0	0.438
6	53	0.265	0.0	0.529	0.0	1.881

Loads given in the table have been normalised with respect to P_y, the load required to produce first yield in an uncracked specimen.

Constant amplitude loading

Tests 1 to 4 were carried out by subjecting the specimen to constant amplitude loading. Cracks initiated and grew from a starter notch and, since the remote load was constant, were subject to a slowly increasing ΔK. At an appropriate crack length a series of moiré interferograms were taken at different loads during the cycle, both during the loading and the unloading parts. The discontinuity in displacement across the crack was extracted from the raw displacement data and plotted against position along the crack for each load step. It should be remembered that the initial grating was applied to the undeformed and uncracked specimen. Thus, the displacement data collected at the minimum load step incorporates residual deformation caused by
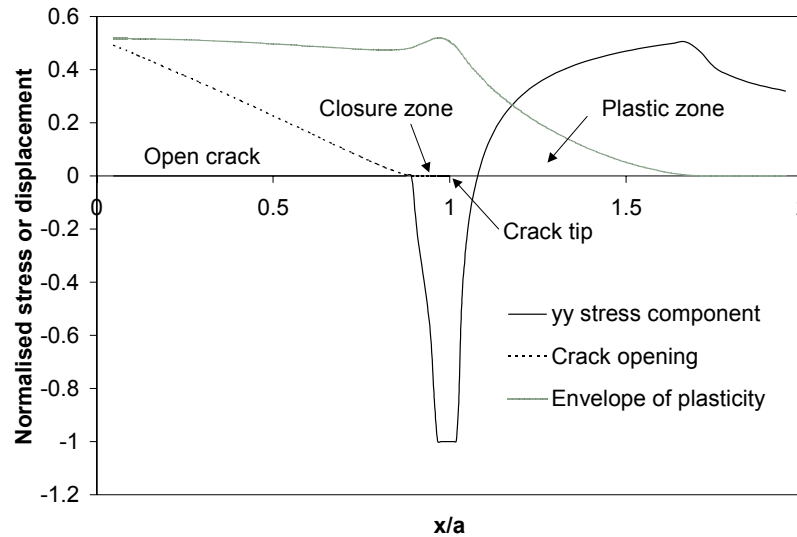
Figure 1: Typical output from boundary element model for a partially-closed crack,
$R = 0.0$, $P_{max}/P_y = 0.6$, constant amplitude load.

crack tip plasticity as the crack grows. Grating damage was observed close to the crack faces, so that the displacement could not be measured right up to the crack face. Consequently there was some displacement discontinuity across the crack even at zero load when portions of the crack might be expected to be closed. The following procedure was therefore adopted to determine the extent of crack closure.

    (i)   Moiré displacement data was collected at n load steps during the loading cycle

    (ii)   For each load step i, the displacement discontinuity $\delta_i(x)$ across the crack was determined and plotted against position along the crack

    (iii)   For i >0, the change in displacement discontinuity from minimum load, $d_i(x)$ was calculated by subtracting the value at minimum load, $\delta_0(x)$. i.e. $d_i(x) = \delta_i(x) - \delta_0(x)$.

    (iv)   Where $d_i(x)$ was found to be close to zero it was assumed that the crack faces had not moved relative to each other since minimum load and that the crack was therefore closed in this region.
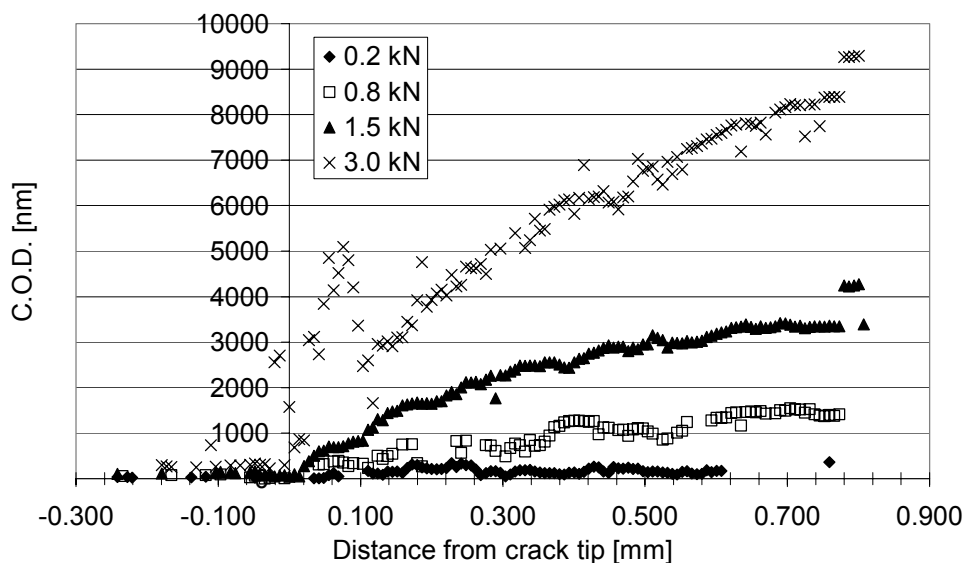
Figure 2: Measurements of crack face displacement during loading phase (test 1)

Typical output data from this procedure is shown in Figure 2, for Test 1 during the loading half of the cycle. It may be seen that the crack is closed at the tip until a load of 1.5kN is applied. Some evidence of crack tip

opening displacement is visible at maximum load, although this is partly obscured by excessive scatter in the data points close to this region. Figure 3 shows the corresponding output from the model. It can be seen that there is surprisingly good agreement between the experimental data and model predictions. Figure 4 shows the variation of percentage of the crack which is open against load for the same test. Tests 2, 3, and 4 show a similar pattern of agreement between experiment and model.

Overload tests

Some difficulty was experienced in carrying out the overload tests due to crack branching which occurred at the higher load levels. Nevertheless, some useful data were obtained. Figure 5 shows crack shape immediately after the overload. Both experimental data and the model predict that the crack is fully open in this case. It should be noted that the apparent difference between model predictions and measurements ahead of the crack tip is a consequence of the concentration of plasticity in a thin strip in the model, whereas in reality it is distributed over the entire plastic zone. The overloaded crack was then grown on and displacement readings taken at crack lengths of 0.654, 0.700, 0.916, and 1.158 mm. Even for the longest of these, normal closure behaviour had not been re-established.
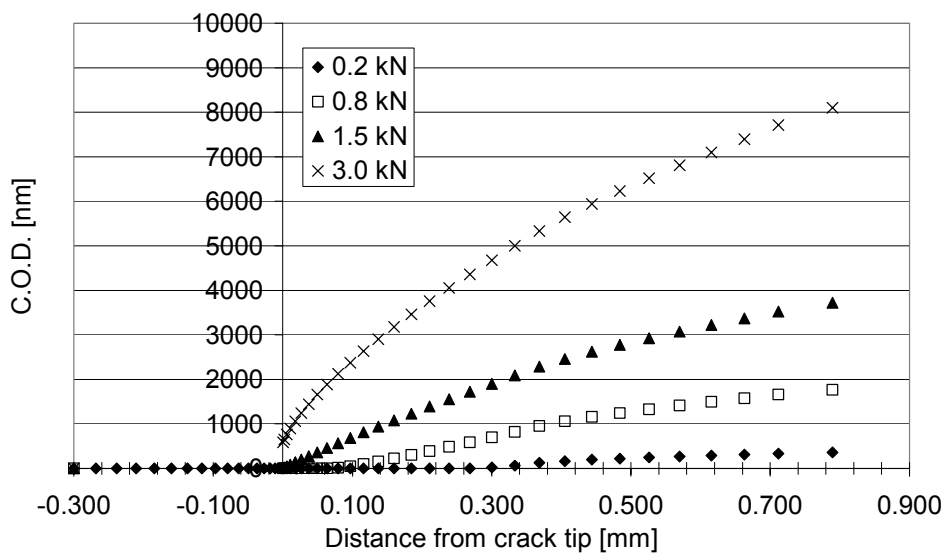
Figure 3: Predictions of crack face displacement from the model, corresponding to the measurements shown in Figure 4.
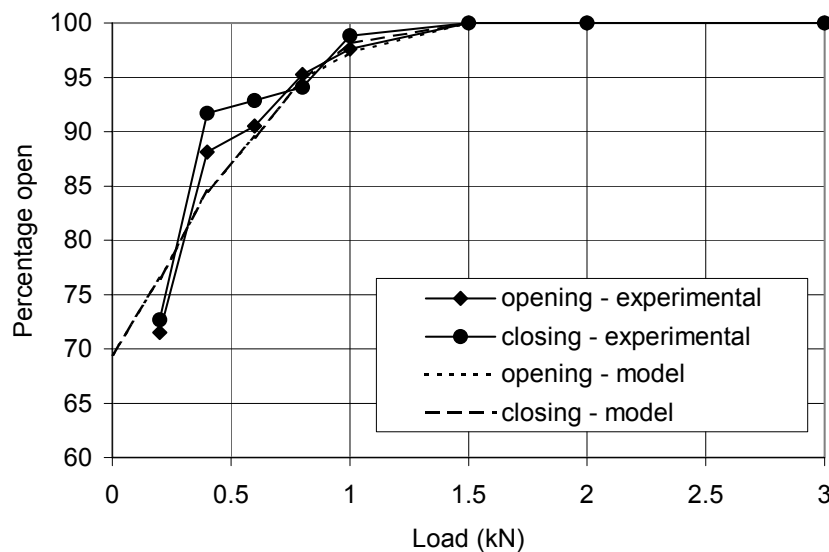
Figure 4: Variation of proportion of crack open with load for test 1

DISCUSSION AND CONCLUSIONS

Model predictions and experimental measurements of crack profiles show surprisingly good agreement for constant amplitude loading. Predictions of the distribution of strain ahead of the crack are, of course, much less satisfactory, due to the concentrated plasticity assumptions inherent in the strip yield model. The model is appropriate to a two-dimensional plane stress situation. Although the moiré displacement readings are taken on the surface, it should be remembered that the specimen is fully three-dimensional and the surface displacements will be influenced by conditions remote from the surface. The agreement between the model and experimental data is less satisfactory for the single overload tests carried out. This may be due to the higher levels of plasticity involved during the overload cycle, which can be less satisfactorily modelled using the strip yield assumption. However, the experimental data does demonstrate that, as predicted by the model, the effects of an overload persist, even when the crack tip has completely traversed the overload plastic zone. Overall the predictions of the model are encouraging and suggest that such simplified models might form the basis of enhanced life prediction methods. More work needs to be done, however, particularly in understanding three-dimensional effects, since most real cracks contain a portion of the crack front which is essentially plane strain.
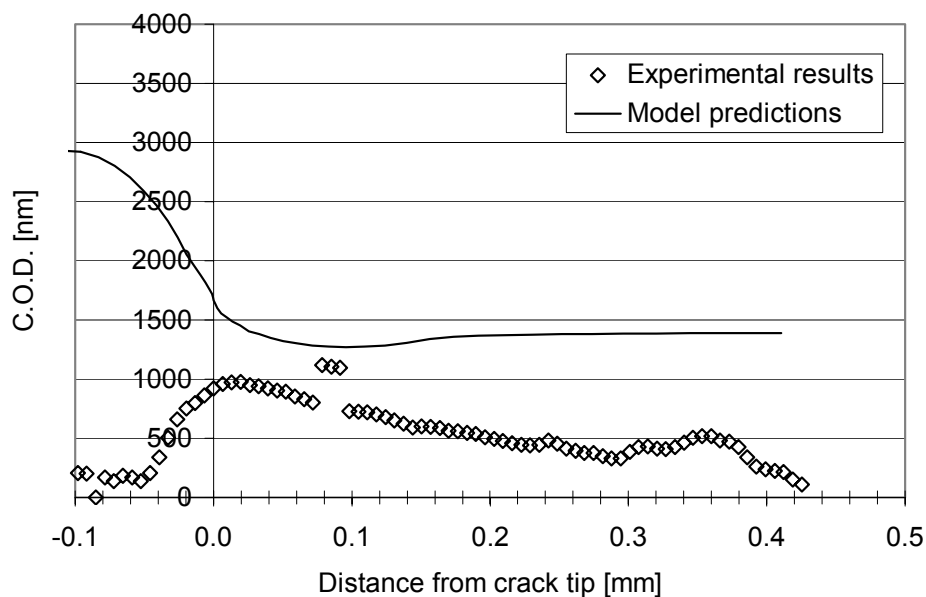
Figure 5: Crack face displacement for test 5 immediately after overload at zero load

REFERENCES

1. Elber, W. (1970). *Eng. Fract. Mech.* 2, 37.
2. Elber, W. (1971). In: *Damage tolerance in aircraft structures*, ASTM STP 486, pp 230-247. ASTM, Philadelphia.
3. Fellows, L.J., Nowell, D., and Hills, D.A., (1997). In: *Advances in Fracture Research*, pp 2551-2558, Karihaloo B.L., Mai, Y-W, Ripley, M.I., and Ritchie, R.O., Eds, Pergamon, Oxford.
4. Pacey, M.N., Patterson, E.A., and James, M.N. (2001). *Proc. Roy. Soc.,* under review.
5. Chermahini, R.G. and Blom, A.F., (1991). *Theoretical and Applied Fracture Mechanics,* 15, 267.
6. Newman, J.C. Jr., (1981). In: *Methods and models for predicting fatigue crack growth under random loading*, ASTM STP 748, pp53-84, Chang J.B., and. Hudson, C.M., Eds. ASTM, Philadelphia.
7. Dugdale, D.S. (1960). *Jnl Mech. Phs. Solids*, 8, 100.
8. Güngör, S., and Fellows, L. (1998) In: *Experimental Mechanics: Advances in Design, Testing, and Analysis*, pp1071-1076, Allison, I.M., Ed, Balkema, Rotterdam.
9. Poon, C.Y., Kujawinska, M., and Ruiz, C., (1993). *Exp. Mech.*, 33, 234.
10. Takeda, M., Ina, H., and Kobayashi, S. (1982). *Jnl Opt. Soc. Amer.,* 72, 156.
11. Nowell, D., (1998) *Fatigue and Fract. of Eng Mats and Structs*, 21, 857-871.

ICF100432PR

THE EFFECT OF SPECIMEN THICKNESS DURING FATIGUE OF S 355 CONSTRUCTION STEEL

F.A.Veer[1], J.Zuidema [2], P.A. Houdijk[2]
'Faculty of Architecture , Delft University of Technology, NL
[2]Laboratory of materials science, Delft University of Technology, NL
Email : f.a.veer@bk.tudelft.nl, J.Zuidema@tnw.tudelft.nl

ABSTRACT

One of the problems in developing fatigue crack growth rate models is allowing for the effect of specimen thickness on the fatigue crack growth rate. Although a lot of data is available on similar materials tested in different thicknesses the inherent scatter in fatigue crack growth rates prevents a proper comparison. To make a good comparison blanks for CCT and CT specimens were cut out of the middle of 30 mm thick S335 steel blocks using the spark discharge technique. This resulted in CCT specimens with thicknesses of 2, 6 and 10.3 mm and CT specimens of 10.3 and 25 mm. CA fatigue tests were conducted at different load ratios to look at the relation between the specimen thickness and the crack growth rate. The results showed that thicker specimens had higher growth rates. Comparison of CCT and CT specimens of the same thickness showed that there are systematic differences in the da/dN versus AK relation between these two specimen types.

KEYWORDS

fatigue, crack closure, thickness effect, steel

INTRODUCTION

The thickness effect in fatigue is phenomenon that is found by many authors. Research has been done, notably by Fleck [1], that suggests that thick specimens have higher crack growth rates than thinner specimens. The usual explanation for this is the difference in plane strain and plane stress plastic zone sizes which causes differences in plasticity induced crack closure. The problem in determining the effect of specimen thickness is that usually specimens from different plates are taken which have slightly different compositions and mechanical properties. As the effect of thickness which is reported is not very big compared to the normal scatter in fatigue is was decided to investigate this effect by producing tests specimens by cutting them out of the centre of 30 thick S 335 steel plates. This steel is a construction steel commonly used in the offshore industry. The original plates had been homogenised to ensure constant through thickness properties. Using CCT and CT specimens allowed for a range of thickness varying from 2 to 25 mm to be tested. CCT specimens of more than 10.3 mm thickness could not be tested on the available equipment. By conducting tests in this way the actual effects of thickness on the fatigue crack growth rate and on the crack closure level can be determined with adequate accuracy.

EXPERIMENTS

Blanks were cut from 30 mm S355 steel plates using spark discharging to cut plates of thicknesses 2.2, 6.2, 10.5 and 25.2 mm from the centre of the plates. Composition and properties of the S 355 steel used are given in tables 1 and 2.

Table 1 : Chemical composition of S 335 steel used (%)

C	Mn	Si	Al	Cu	N	P	S	Nb	Fe
0.187	1.297	0.398	0.048	0.014	0.005	0.014	0.007	0.029	Bulk

Table 2 : Mechanical properties of S 335 steel used

yield stress	460 MPa
ultimate tensile stress	630 MPa

These blanks were ground down to 2,6,10.3 and 25 mm in accordance with the guidelines laid down in ASTM E647-91,[2]. From these blanks CCT specimens of length 340 mm and width 100 mm and CT specimens of length 125 mm and height 120 mm were produced. These specimens were fatigue tested in an MTS 350 kN fatigue testing machine. Pre-fatiguing with load shedding was conducted to ensure the absence of overload effects at the start of the CA test. The crack length was measured using a Howden pulsed direct current potential drop apparatus. Crack growth rates and stress intensities were calculated using the guidelines provided by ASTM E 647-91, [2]. Crack closure measurements were done using an Elber clip on CCT and CT specimens and back face strain gages on CT specimens.

Table 3 : CA tests conducted on CCT specimens, σ_{max}= 113 MPa

Thickness (mm)	Load ratios				
2	0.1	0.3	0.4	0.5	0.7
6	0.1	0.2	0.3	0.5	0.7
10.3	0.1	0.2	0.3	0.5	0.7

Table 4 : CA tests conducted on CT specimens

Thickness (mm)	Maximum load (kN)	Load ratios			
10.3	8.4	0.1	0.3	0.5	0.7
25	20.4	0.1	0.3	0.5	0.7

RESULTS

The tests were conducted in five groups separating them to thickness and specimen size. Each group will be dealt with separately. In addition crack closure measurements were done on some tests.

Results for CCT specimens

The fatigue crack growth rates of the tests on 2 m specimens show a significant dependency on the load ratio, a shown in figure 1. The crack growth rate at load ratios of 0.5 and 0.7 shows significant differences. This suggests that plane stress crack closure is working at this thickness.

The fatigue crack growth rates of the tests on 6 mm specimens, shown in figure 2 show a smaller load ratio dependency. The crack growth rates at R=0.3 and higher overlap suggesting that crack closure is disappearing.

The 10. 3 mm specimens have crack growth rates almost independent of the load ratio, as shown in figure 3. This suggest that there is no active crack closure in this thickness.
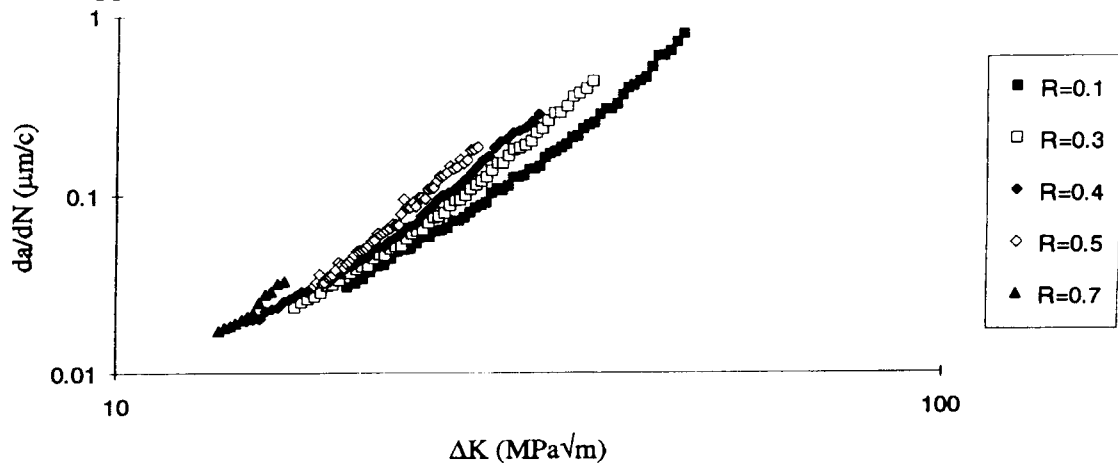
Figure 1: CA Crack growth rate of 2 mm thick CCT specimens at different load ratios
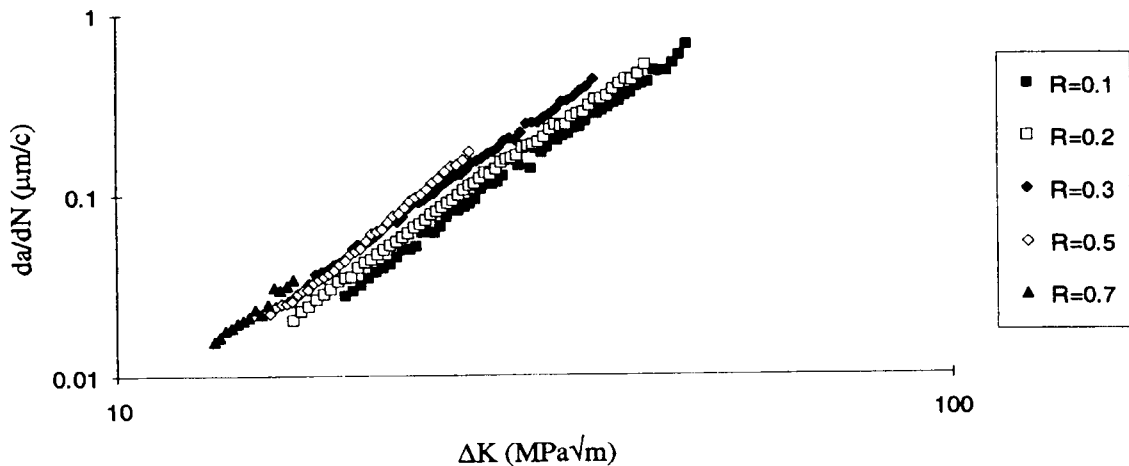
Figure 2: CA Crack growth rate of 6 mm thick CCT specimens at different load ratios
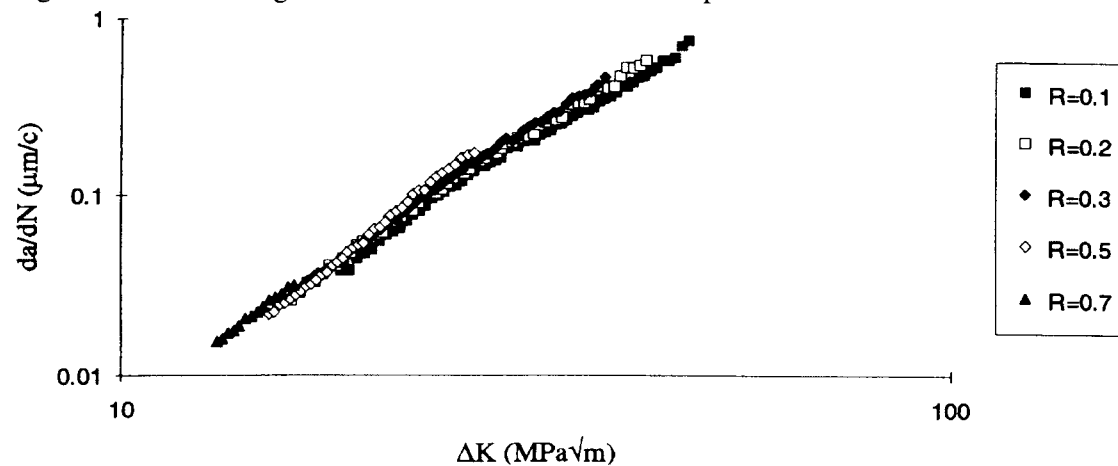
Figure 3: CA Crack growth rate of 10.3 mm thick CCT specimens at different load ratios

Results for CT specimens

The results of the 10.3 mm CT specimens are shown in figure 4 and are similar to those of the 10.3 mm CCT specimens although the load ratio effects appear to be slightly less than in the CCT specimens.

The results from the 25 mm CT specimen, shown in figure 5 are strange in that they show significant load ratio effects at low ΔK but no load ratio effect at high ΔK. These tests were conducted at the same ΔK range as the 10.3 mm specimens using similar pre-fatiguing procedures. Thus overload effects at the start of the CA tests cannot explain the observed differences.
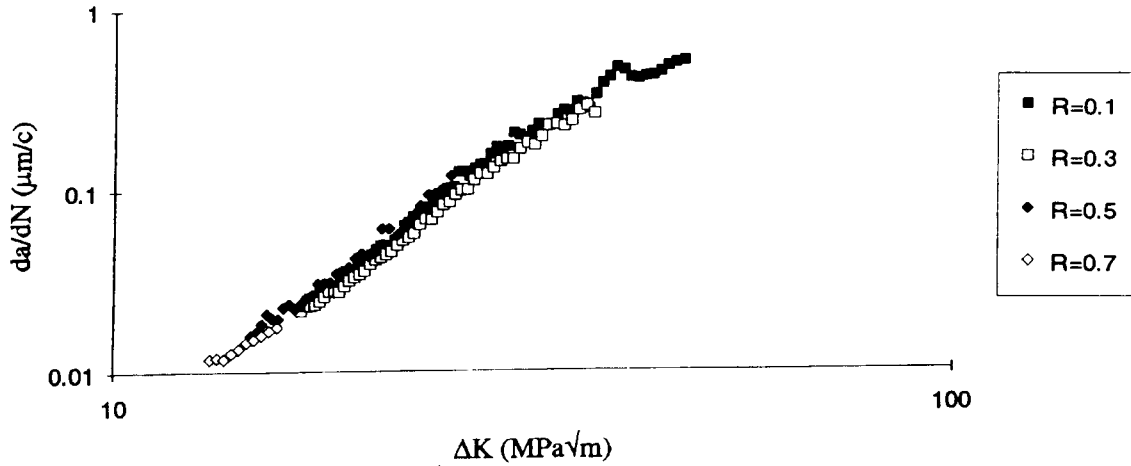
Figure 4: CA Crack growth rate of 10.3 mm thick CT specimens at different load ratios
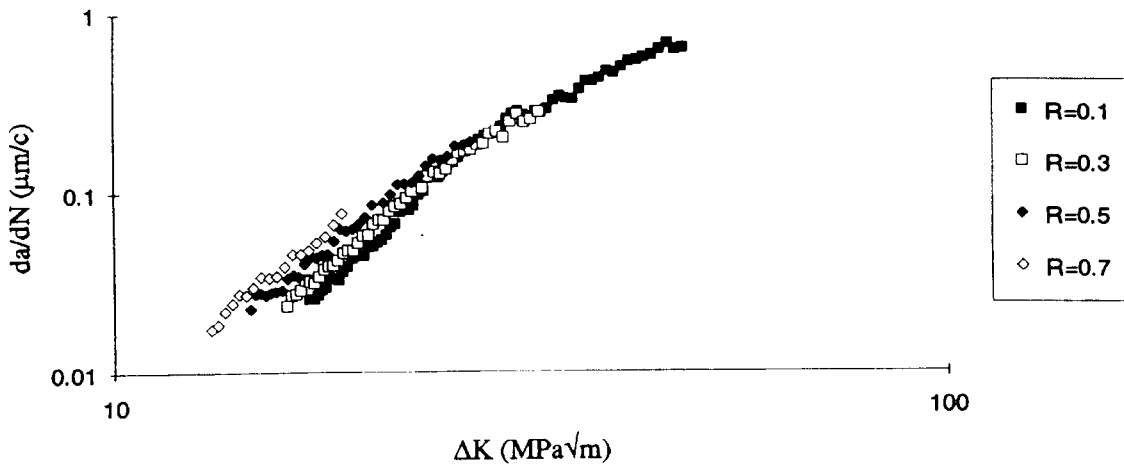
Figure 5: CA Crack growth rate of 25 mm thick CT specimens at different load ratios

Results of crack closure measurements

The crack closure measurements were confusing. The Elber clip suggested the presence of crack closure at low load ratios even on thick specimens. Figure 6 shows the results of an Elber clip measurement and a back face strain measurement on a 10.3 mm CT specimen tested at load ratio 0.1. The crack growth rates in this thickness is independent of the load ratio suggesting the absence of crack closure, which is confirmed by the back face strain gage. The Elber clip suggests the presence of significant crack closure at low load ratios, even in thick specimens. This suggests that the Elber clip is only reliable in specimens of 2 mm thickness or less.
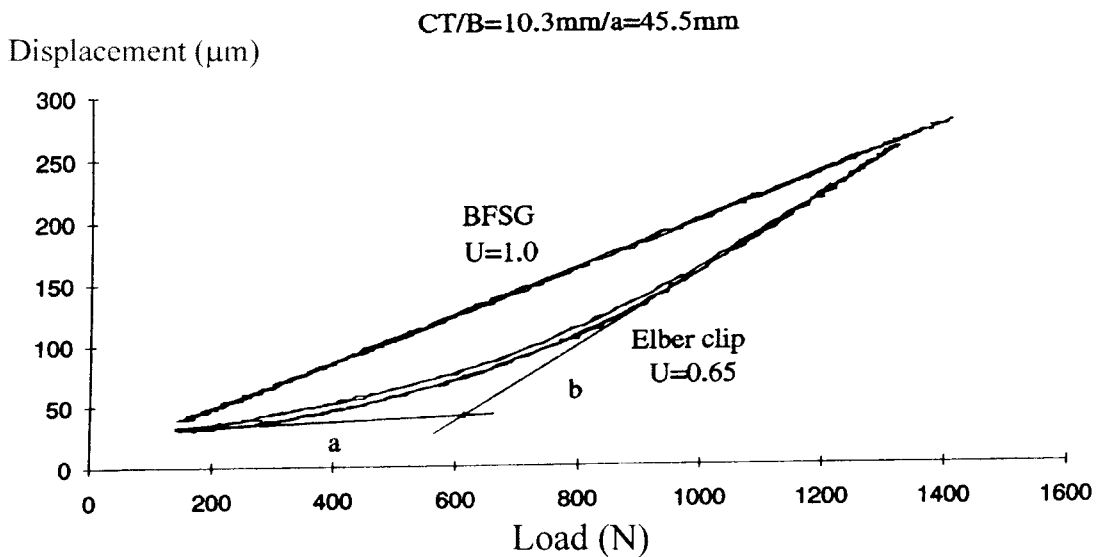
Figure 6: Crack closure measurement results in 10.3 mm thick CT specimen tested at R=0.1

DISCUSSION

The thickness effect is as expected going from 2 mm thickness to 10.3 mm thickness. This can be explained by crack closure changes going from plane stress domination in 2 mm specimens to plane strain domination in specimens of 10.3 mm. The crack closure measurements and the dependency of the crack growth rate on the load ratio support this view. The unexpected presence of a load ratio effect on the crack growth rate in the 25 mm thick specimens at growth rate of less that 0.15 µm/c suggests the situation is more complicated.

Another puzzling result is that the crack growth rates between the 10.3 mm CCT and CT specimens show a systematic difference as shown in figure 7. The CCT specimens have an increased crack growth rate at crack growth rates less than 0.2 µm/c. This small difference is reproducible and suggests a small error in the stress intensity, either in the formulation or possibly in the clamping of the CT specimens.
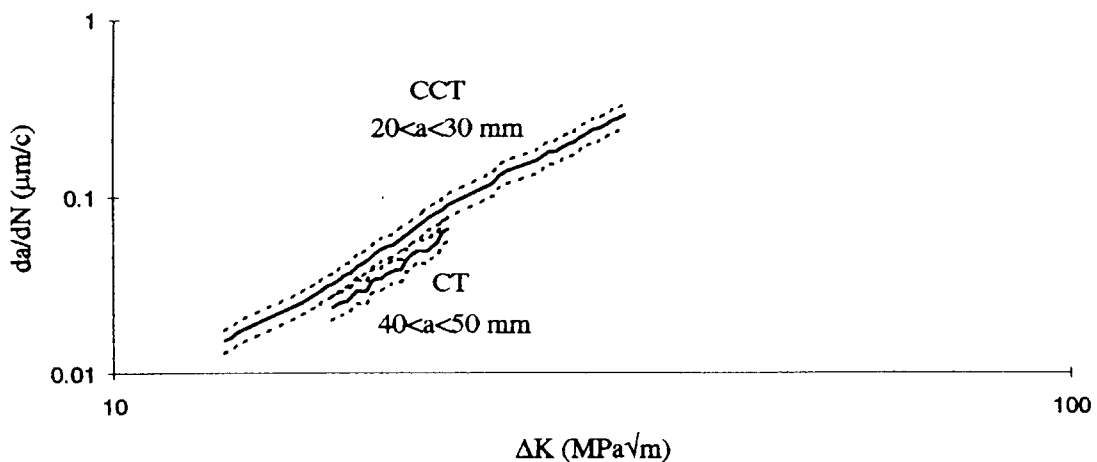
Figure 7 : Crack growth rates in 10.3 mm CCT and CT specimens

Another puzzling result is that the load ratio dependency in 2 mm thick CCT specimens can be described by a single relation such as proposed by Schijve, [3], for aluminium alloys.

$$U=0.5 + 0.5R - 0.35 \, R^2 \, , \, 0.1 \leq R \leq 0.7 \quad (1)$$

Using this relation to calculate ΔK_{eff} allows us to plot all crack growth rates on a single curve, as is shown in figure 8.
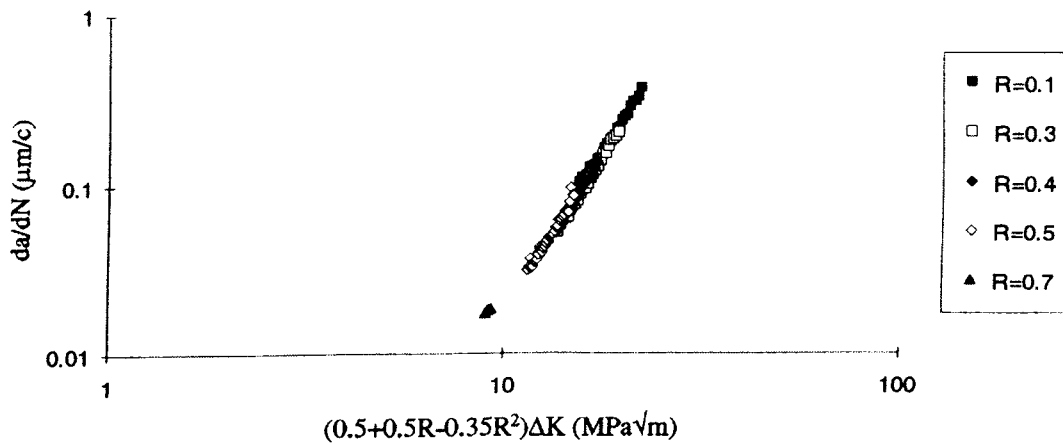
Figure 8 : Crack growth rate in 2 mm CCT specimens plotted against ΔK_{eff}

Puzzling is why S355 steel CCT specimens of 2 mm should show behaviour so similar to that of other alloys, while thicker specimens of the same steel show different behaviour. In Aluminium 2024-T351 the load ratio effect is the same in CCT specimens of 2 mm, 6 mm and 10.3 mm, as shown by Veer, [4]. As this steel was specially selected for its homogeneity through the thickness and all specimens thus have an identical micro-structure the observed differences should be the result of mechanistic effects. These will be the object of further study.

CONCLUSIONS

- There is a significant effect of the thickness on the crack growth rate.
- This effect from 2 mm to 10.3 mm can be explained by the changes in crack closure going from dominant plane stress to dominant plane strain.
- The load ratio effects found in the 25 mm thick specimens cannot be explained by crack closure changes.
- The Elber clip method of measuring crack closure is unreliable except for thin specimens.
- The load ratio effects in 2 mm thick specimens can unified to a ΔK_{eff} calculated using an quadratic U relation similar to that introduced by Schijve for Aluminium alloys.

REFERENCES

1   N.A. Fleck, "An investigation of fatigue crack closure", PhD thesis, Cambridge university, Great Britain, November 1983.

2   1991 Annual book of ASTM standards, vol. 3, Philadelphia, 1990

3   J. Schijve, "fatigue crack closure : observations and technical significance", ASTM STP-982, Philadelphia, 1988

4   F.A.Veer , "The effect of shear lip, loading transitions and test frequency on constant ΔK and constant load amplitude fatigue tests, PhD thesis, Delft University of Technology, Delft, the Netherlands, 1993.

The effect of thickness and crack geometry on material fracture toughness of high-toughness pipeline steels

Huiru Dong[1,2], Wanlin Guo[1,3]

1) The State Key Laboratory of Mechanical Structural Strength and Vibration, Xi'an Jiaotong University, Xi'an, 710049, China

2) Engineering College, Engineering University of Air Force, Xi'an, 710043, China

3) Department of Aircraft Engineering, Nanjing University of Aeronautics and Astronautics, Nanjing, 210016, China

Abstract   The fracture toughness of all sort of crack forms of a kind of pipeline steel were investigated experimentally by using through-cracked specimens with thickness of 3,6,9,12,15mm, surface cracked panels, single and double corner cracked panels. The coupled effects of specimen thickness and delamination upon fracture toughness and the mechanism of delamination are revealed; the general role of delaminations and geometry configurations on fracture toughness is found out; the initiation stress intensity factors and fracture toughness are determined. It is very dangerous to predict critical load for no-through cracked bodies by using test data from through crack. The initiation stress intensity factors of no-through and through cracks can be unified by the three dimensional fracture theory.

Keywords   three-dimensional crack, delamination, constraint, fracture toughness, pipeline steel

1. Introduction

Thick wall and relatively high-toughness pipeline steels are widely used. However, it has been recognized by fracture mechanics community that the fracture toughness curve is not really a material constant, and that its value may decrease with increasing thickness in metal materials [1,2]. On the other hand, most of the existing cracks are not through the pipe wall but in the form of internal or external surface cracks or embedded cracks. In this paper, detailed experimental investigations will be conducted by use of tensile specimens with through cracks of varying thickness, semi-elliptical surface cracks and corner cracks of different configurations. The purposes are to reveal coupled effects of specimen thickness and delamination upon fracture toughness and the mechanism of delamination in part-through cracked pipes, to find out the general role of delaminations and geometry configurations on fracture toughness, and to determine whether the cracking resistance of a no-through crack in pipelines can be predicted by the fracture toughness obtained from through-thickness cracked specimens.

2. Experiments

2.1 specimen preparation and testing

The material pieces were directly cut from a pipe structure with 700mm diameter and 18mm-thick wall. The yield stress of the material σ_{ys}=500MPa, the limit stress $\sigma_u \geq$620MPa, the Young's modulus E=210GPa, the Poisson's ratio is equal to 0.3. CT specimens with width W=60mm are prepared with the crack along the axial direction. Microstructure was found homogeneous along thickness. Mechanical milling thinned the wall pieces and six thicknesses were obtained: 3, 6, 9, 12 and 15 mm. The in-plane geometry is the same as that of the ASTM E561 standard [3] CT specimen; five specimens for each thickness were prepared; the final crack length to width ratio of $a_0/W \approx$0.47 for each specimen. To simulate the various possible forms of crack in practical pipelines, single edge corner cracked (SECC), double edge corner cracked (DECC) and center surface cracked (CSC) tensile specimens are prepared. The size of the pre-fatigued cracks are given in table 1 where WCSC denotes the CSC from a rib with 10mm-width which leads to a final ratio c/a≈0.2, and NCSC denotes the CSC from a rib with 6mm-width which leads to a final ratio c/a≈0.3. All of the pre-fatigue tests were performed on a MTS810 100kN machine.

After fatigue pre-cracking, all the specimens were loaded monotonically to fracture at room temperature on a MTS 810 100kN TestStar controlled fatigue testing system under displacement control mode with a loading speed of 0.05mm/sec. A MTS 633.030-01 COD gauge was used for crack-mouth opening displacement (COD) measurement. Data were captured using the TestStar computer-testing system and were triggered every 0.05mm of displacement.

2.3 Testing Phenomena and analyses

2.3.1 CT through-thickness specimens

(1) Delamination exists in all CT through-thickness specimens. Although no obvious delamination appears in the 3mm-thick specimens, under SEM, small delaminations can also be found in them. Multiple delaminations occur in thicker specimens. As the out-of-plane constraint is highest at the center of the specimen the delaminations in the middle part of all specimens are most severe.

(2) Delamination originates before crack initiates, and with the thickness increases, the size and depth of delaminations at the center of the specimen increase. In the 15mm-thick specimen, a large delamination starts from the initial crack front and grows with crack extension to the final separate point. This implies that the constraint at the growing crack front is like that in two 7.5mm-thick plates. Secondary delaminations turn up at 1/4 thickness from the free surfaces, and similar to the main delaminations in 6mm- and 9mm-thick specimens. The main reason for this phenomenon is that the overall out-of-plane constraint and the size of high constraint zone increases with thickness. The main delamination at the center of thick plate

releases the out-of-plane constraint completely on the middle plane, and the second peak of constraint move to 1/4 thickness with lower levels.

(3) All the delaminated cracks, in spite of the size, are opened and necking occurs between the delaminations. This means that extensive plastic deformation is accompanied the cracking and the delaminations can reduce the out-of-plane constraint effectively. Both necking and delamination will greatly reduce the effect of thickness on cracking resistance.

2.3.2 Part-through thickness specimens

As can be seen in Fig.1, there is no delamination in the first few millimeters crack growth, the initiation of the corner crack occurs at 45°. However, once the crack grows through the thickness and further expands through the remaining ligament, large delaminations formed at the center of the plate, similar to that observed in CT specimens. The fracture profiles of the DECC is similar to that of SECC in Fig.1.

Typical fracture profiles of the WCSC specimens are shown in Fig.2. It can be seen that the crack grows through the thickness firstly and then expands to two sides as a through crack with company of large delaminations, the initiation the surface crack is at 75°-90° to the front surface. In both stages, strong residual deformation has been formed. As all the fracture section except the pre-fatigue cracked area was seriously deformed, it can be deduced that before crack growth, large plastic deformation has occur and the stable crack growth stage is very short. This is in coincidence with the phenomena observed during the test. Large plastic deformation and crack blunting made the final rupture of the specimens insensitive to the existed initial crack.

Fig.1 Macro-profile of the fracture surface of a SECC specimen
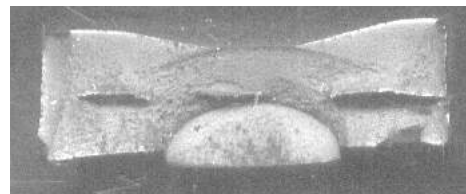
Fig.2 Fracture profile in a WCSC specimen

3. Experimental Results and Analyses

3.1 Load-displacement results

Typical measured load-COD curves for each thickness of CT specimens are plot in Fig.3. Figure 4 shows the effect of crack geometry on the load-COD curves. From the figure
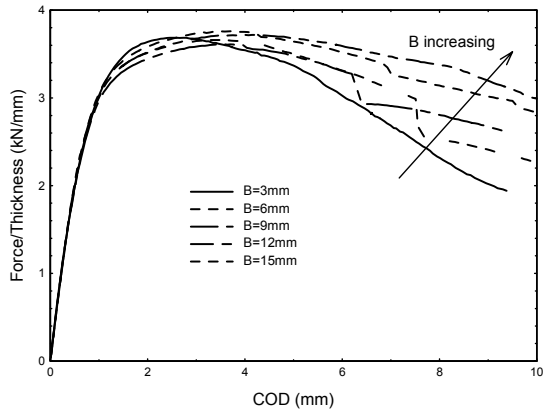
Fig.3 Typical load versus crack open displacement (COD) curves for different thickness of CT specimens
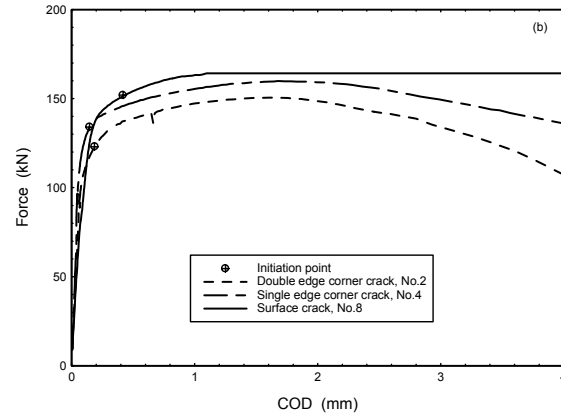
Fig.4 The load-COD curves

it can be found that before crack initiation, plastic deformation is limited. After initiation large deformation occurs before unstable crack growth but the increment of load is relatively small, about 8% to 30% of the initiation load.

3.2 Measurement of critical stress strength

The initial loads and J assessment can be obtained from the load-COD curves. The effective stress strength factor K_e and a J-based SIF $K_J(K_J=(EJ)^{1/2})$ can then be attained in through-thickness specimens. For no-through thickness specimens, the initiation toughness K_i along the crack front and K_{zi} assessed according to the three-dimensional fracture theory[4] are calculated, K_{imax} is the maximum of K_i. They are listed in table 1.

4. Conclusions
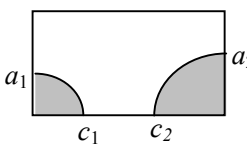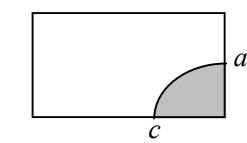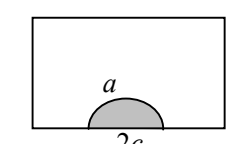
(1) Delaminations exist not only in through-thickness specimens but also in no-through thickness specimens; it is characteristics of this material. Delamination originates before crack initiates in through-cracked specimens; however, inverse phenomena appear in others' specimens. Strong coupled effects of specimen thickness and delaminations dominate the fracture behavior of this steel. Formation of delaminations and has close relation to the relative orientation between the directions of crack growth and thickness.

(2) As the out-of-plane constraint keeps low in spite of the specimen thickness B. The conservative plane strain fracture toughness K_{IC} or J_{IC} can not be approached by increase of B as the multi-delaminations will reduce the "effective local thickness" and enhance the nominal toughness. When the through-thickness toughness is used to safe assessment of general 3D cracked bodies, delaminations may be dangerous.

(3) As the out-of-plane constraint keeps higher in the interior of the part-through

cracks, the fracture initiation toughness is much lower than that of the through-thickness cracked specimens. The traditional fracture toughness K_i is not a proper material toughness parameter. The three-dimensional parameter K_{zi} proposed by Guo[5] is proven to be a material constancy independent of geometry configurations. The toughness K_i of part-through cracks can be predicted well by the three-dimensional theory and test data of through cracks provided there is no delamination.

REFERENCES

[1] Schwalbe, K.-H., Influence of stress state on static crack growth in AlZnMgCuO.5, *Engineering Fracture Mechanics*, 1977, **9**, 557-583.

[2] Anderson, T.L., Fracture Mechanics-Fundamental and Application. CRC Press, Boca Raton, 1995.

[3] ASTM E561–81, Test method for determining R curve, 1981

[4] Guo W L, Pitt S D, Jones R. Three dimensional strength assessment for damage tolerant structures, Strength Theory. Science Press, Beijing and New York; 1998: 799

[5] Guo, W., Three dimensional study for the effects of sheet thickness on fracture toughness of materials, *Acta Mechanica Solida Sinica*, 1995, **16**(S.I.), 1-9.

Table 1. Geometry of the specimens and experimental results

Specimen Number	Crack configuration	Crack size mm	Initiation					Maximum				
			Initiation load P_i kN	K_{imax}		K_{zimax}		Maximum load P_{max} kN	K_{cmax}		K_{zCmax}	
				MPam$^{1/2}$	θ°	MPam$^{1/2}$	θ°		MPam$^{1/2}$	θ°	Mpam$^{1/2}$	θ°
No.0	Double edge corner cracks (DECC)	a_1=6.5, c_1=6.5 a_2=9.5, c_2=10	125	91.2	0	107.8	0	135	98.5	0	116.6	0
No.1		a_1=6, c_1=7 a_2=7.4, c_2=8.5	132	70.3	0	106.6	45	148.75	78.8	0	112.4	45
No.2		a_1=5.5, c_1=6 a_2=7, c_2=8	123	61.2	0	89.2	45	150.78	74.9	0	111.6	45
No.3	Single edge corner crack (SECC)	a=7, c=7.7	139	68.4	0	100.8	45	164.67	81.0	0	114.5	45
No.4		a=7, c=7.3	134	64.9	0	102.1	45	159.90	77.4	0	110.6	45
No.5		a=7, c=6.4	145	69.5	0	100.6	45	165.66	79.4	0	109.5	45
No.6	Center surface crack (CSC)	a=3.5, 2c=11	158	49.5	90	106.9	75	180.20	56.5	90	128.6	75
No.8		a=4, 2c=11.5	152	49.8	90	111.5	75	176.84	57.9	90	130.8	75
No.12		a=4, 2c=7.5	151	49.2	0	100.6	80	188.91	61.5	0	116.8	80
No.13		a=4, 2c=8	150	44.9	0	100.9	80	186.95	56.0	0	116.8	80
No.14		a=4, 2c=9	136	41.6	0	100.0	75	178.00	54.4	0	119.7	75

The Effect of Thickness on the Characterization of Crack Tip Opening Angle for 2024-T351 Aluminum Alloy

Samer Mahmoud and Kevin Lease

Department of Mechanical and Nuclear Engineering, Kansas State University, Manhattan, KS 66506, USA

ABSTRACT

The crack tip opening angle (CTOA) parameter has been shown to be well suited for modeling stable crack growth and instability during the elastic-plastic fracture process. Furthermore, this parameter, implemented in both 2D and 3D elastic-plastic FEM codes, has been successfully applied to stable tearing and stability analyses of some very complex structural configurations made of thin-sheet 2024-T3 aluminum alloy. However, the effect of material thickness on the characterization of this parameter has not been thoroughly evaluated. Therefore, an investigation was conducted to assess the effect of material thickness on the characterization of the CTOA parameter for 2024-T351 aluminum alloy. Stable tearing fracture tests were conducted on C(T) specimens in four thicknesses (2.28, 6.35, 12.7, and 25.4 mm), with all specimens taken from a single 25.4 mm thick plate. Overall, the average experimental surface critical CTOA (ψ_C) values obtained from the current work were found to decrease with increasing specimen thickness. The amount of crack extension necessary for the transition to a fairly constant CTOA value was not characterized by the specimen thickness for the three largest thicknesses tested in this research, as observed in the earlier thin-sheet tests. As the specimen thickness increased, discrepancies between the experimental (surface) CTOA values and those obtained computationally were shown to increase. More thorough experimental and computational investigations into the effects of surface vs. interior CTOA values and/or crack tunneling must be performed before CTOA characterization can be directly applied to thicker specimens.

KEYWORDS

fracture-experimental, fracture-computational, stable crack growth, crack-tip opening angle

INTRODUCTION

One of the most promising parameters that have been introduced to simulate the elastic-plastic stable tearing process is the crack tip opening angle (CTOA) defined at a specified distance (d) from the crack tip. Numerous investigators [1-6] have characterized and evaluated (both experimentally and computationally) the CTOA parameter and have found that it is nearly constant after a small amount of crack extension. The non-constant CTOA region (measured at the free surface) has been shown [1,2] to be associated with severe crack tunneling during the initiation of stable tearing. These characterization results have also been utilized in numerous finite element-based fracture analyses to simulate the stable tearing and stability of both simple and complex structures with excellent results [2-5]. The majority of these CTOA characterization and

analysis studies have focused on aluminum alloys in thin-sheet form in support of the aerospace industry's damage tolerant and aging-aircraft efforts. This paper describes an experimental/computational investigation into thickness effects on the characterization of the crack tip opening angle (CTOA) fracture parameter in 2024-T351 Aluminum. The experimental portion of the current project consisted of conducting stable tearing fracture tests using C(T) specimens of various thicknesses. These tests provided measurements of CTOA and crack extension on the surface of the specimen as well as load and load line displacement history through out the stable tearing process. The computational portion of this work involved three-dimensional finite element based CTOA fracture analyses to simulate the stable tearing process in the test specimens. These analyses were used iteratively to obtain the mid-thickness critical CTOA (ψ_C) value that produced the closest agreement between the predicted maximum applied load and the experimentally measured values.

MATERIAL, SPECIMEN, AND EXPERIMENTAL PROCEDURES

The 2024-T351 Aluminum alloy was chosen for this study in order to allow for the direct comparison to, and extension of, the previous CTOA characterization work on thin-sheet (1.0, 1.6, 2.3 mm thickness) form of the 2024-T3 alloy [6]. The thickness range chosen for this research included 2.3, 6.35, 12.7, and 25.4 mm. The 2.3 mm thickness was chosen to correspond to the thickest specimens evaluated in the previous thin-sheet 2024-T3 work. Compact tension (C(T)) specimens (W = 203 mm) with a chevron starter notch were used for all fracture testing in this study. All specimens were machined out of a single 25.4 mm thick plate of 2024-T351 in the L-T orientation. Uniaxial tensile tests were conducted (in the L-T orientation) to determine the monotonic stress-strain properties for the acquired 2024-T351 plate. The test set up for all stable tearing fracture tests consisted of a material testing machine, clevis grips, a microscope, a CCD camera, a VCR, and computer hardware/software for controlling the machine and facilitating the image acquisition. Anti-buckling guide plates were used with the 2.3 mm and he 6.35 mm thick specimens. All specimens were pre-cracked to provide an initial crack length to specimen width ratio of 0.4 using an R = 0.1 sinusoidal loading and keeping K_{max} below 13 MPa$\sqrt{m}$. The actual stable tearing fracture tests consisted of an incremental displacement controlled ramp waveform (rate = 0.002 mm/sec) that would pull the specimen apart until a stable tearing event was detected visually. At this point, the test was temporarily paused to record load, load line displacement, and VCR counter, and to reposition the microscope as needed to track the crack tip. After manual data logging, the ramp test was resumed until another crack growth increment was observed, repeating this process until complete specimen fracture occurred. Along with the video-taped history of the surface cracking behavior, automated logging of load and load line displacement was obtained by the testing machine internal data acquisition system.

A commercial digital image analysis software package with integrated length and angle measurement tools was used to measure CTOA and crack extension for each stable tearing event. To perform a single CTOA measurement, a series of frames ranging from just prior to just after the onset of stable tearing were transformed from the VCR tapes into an image sequence file. The image sequence file was then played at a slow speed and the frame containing the image showing the specimen surface at the onset of a tearing event was selected for measuring the CTOA. As outlined by Dawicke *et al.* [1], CTOA measurements were made at a distance behind the crack tip ranging between 0.25-1.0 mm. Six to ten angle measurements were made and the average of the measurements was selected as the representative critical CTOA (ψ_C) for that particular crack length. By once again reviewing the image sequence file, the image corresponding to the end of the current stable tearing event was then determined. Using the crack tip location from the previously selected image and the final crack tip location the crack extension was measured, using the length measurement tools, and recorded for each stable tearing event.

COMPUTATIONAL PROCEDURE

The computational phase of this project involved three-dimensional finite element based CTOA fracture analyses to simulate the stable tearing process in the test specimens. By modifying the input critical CTOA (ψ_C) value, these analyses were used iteratively to determine the mid-thickness critical CTOA (ψ_C) value

that produced the closest agreement between the predicted maximum applied load and the average experimentally measured values. The three-dimensional elastic-plastic finite element-based fracture analyses were performed using the ZIP3D program [7]. A discretized, multi-linear representation of the tensile stress-strain curve obtained for the 2024-T351 plate was used to incorporate the material properties into the simulation. To implement the critical CTOA (ψ_C) fracture criterion, ZIP3D calculates the CTOD/CTOA value at the first central free node behind the current crack tip (1 mm behind the current crack tip). When the CTOA value at this node reaches the specified critical value, ZIP3D releases the next set of tied nodes. It should be noted that the critical CTOA (ψ_C) value input to ZIP3D specifies the critical CTOA (ψ_C) at the center of the specimen, whereas the experimentally measured CTOA behavior corresponds to the specimen surface. However, the CTOA values for all crack front nodes across the specimen thickness can also be obtained from the ZIP3D output, facilitating at least a partial comparison of measured and calculated surface CTOA values. The 3D mesh of the C(T) specimen used in this study was generated by extruding a 2D mesh in the thickness direction to produce five layers of eight-noded isoparametric elements, producing a total of 13662 nodes and 10790 elements. The elements at the crack face were 1 mm long. Only one fourth of the 203 mm C(T) specimen was modeled due to symmetry about the crack plane and the mid-thickness of the specimen.

RESULTS

Figure 1 shows the experimentally measured surface CTOA versus crack extension behavior for all four thicknesses of the 2024-T351 alloy evaluated in this study. As can be seen, all four specimen thicknesses exhibited similar behavior with the CTOA starting at a high value followed by a rather rapid decrease to a fairly constant value after a small amount of crack extension. In Figure 1(a) (2.3 mm thickness) experimental data from the earlier thin-sheet 2024-T3 work is also included for comparison purposes. As can be seen, this data compares quite closely to the data obtained in the current work for this thickness. The scatter in Figure 1 was generally within ±1.5 degree and the amount of scattering appears to decrease with increasing specimen thickness. Also, the amount of crack extension necessary to transition to a fairly constant CTOA value is seen to decrease with increasing specimen thickness. This is in contrast to the observation in the earlier thin-sheet 2024-T3 work [1, 2] that this transition crack extension was characterized roughly by the specimen thickness. The horizontal solid line in each plot in Figure 1 represents the numerical average of the data points in the constant (or "critical" CTOA) region. The dashed vertical line, designated as "Max Load" in each plot, indicates the amount of crack extension where the maximum fracture load occurred.

Figure 2 provides a comparison between the experimental and calculated critical CTOA (ψ_C) values for all four thicknesses of the 2024-T351 alloy evaluated in this study. Also shown in this figure are the calculated results from the earlier 2024-T3 thin-sheet study (1.0, 1.6, and 2.3 mm thickness) [6]. As can be seen from this figure, the experimentally determined surface critical CTOA (ψ_C) value for the 2.3 mm thickness compares quite closely to the computational result from the earlier thin-sheet study for this thickness. Furthermore, the overall trend of the critical CTOA (ψ_C) value decreasing with increasing specimen thickness that was shown in the earlier thin-sheet study was also shown in the results of the current work. The experimentally determined surface critical CTOA (ψ_C) values from the current study appear to imply that a lower limiting value of surface critical CTOA (ψ_C) may exist for this alloy. For the thicknesses evaluated in this study, two sets of calculated CTOA values are shown in Figure 2. The first set corresponds to the ZIP3D center node (mid-thickness) values. These correspond to the actual ZIP3D input values that produced the closest correlation between the calculated and experimental maximum fracture loads. The second set of calculated CTOA values in this figure correspond to the ZIP3D surface CTOA value at the moment that the center node (mid-thickness) value reached the input critical value. As can be seen, the experimentally determined surface critical CTOA (ψ_C) values fall between the mid-thickness and surface CTOA values calculated from ZIP3D for each thickness. Moreover, the difference between the interior and exterior CTOA value increases with increasing specimen thickness. While the calculated surface values in this figure show a decreasing trend that mirrors that of the experimentally determined surface CTOA values,

the calculated mid-thickness CTOA values do not show a definite trend. It should be noted that the CTOA computed at the surface of the specimen is for a stationary (non-tearing) straight (non-tunneling) crack front.

Figure 3 compares the measured and computed load vs. crack extension curves for all four thicknesses of the 2024-T351 alloy evaluated in this study. It should be noted that the computational curves shown in this figure were obtained from the ZIP3D analyses with the critical input mid-thickness CTOA (ψ_C) value (solid diamonds in Figure 2) that produced the best correlation between the measured and calculated maximum fracture loads. For all four thicknesses it can be seen that the predicted curve either matches or slightly under-predicts the experimental behavior prior to the maximum load and then either matches or over-predicts the experimental behavior after the maximum load. As indicated in Figure 3(a), scattering of the experimental data for the 6.35 mm thick specimens occurred due to the fact that one of the specimens had a slightly longer initial crack length (a/w=0.416) while another specimen exhibited a change in crack growth orientation from across to along the grain after a short amount of stable crack extension.

CONCLUSIONS

Thickness effects on the characterization of the CTOA parameter were investigated using 203 mm C(T) specimens fabricated from 2024-T351 Aluminum alloy in the L(T) orientation. The experimental results obtained in this study for the 2.3 mm thickness compared quite closely to the published values [1, 2, 6] for this thickness. Experimental results also show that the amount of crack extension necessary for the transition from an initially high CTOA to a fairly constant critical value decreases with increasing specimen thickness and overall the critical CTOA (ψ_C) value decreases with increasing thickness. The experimentally determined surface critical CTOA values fall between the mid-thickness and surface CTOA values calculated from ZIP3D for each thickness. Moreover, the difference between the interior and exterior CTOA value increases with increasing specimen thickness. More thorough experimental and computational investigations into the effects of surface vs. interior CTOA values and/or crack tunneling must be performed before CTOA characterization can be directly applied to thicker specimens.

REFERENCES

1. Dawicke, D.S., and Sutton, M.A., "Crack-Tip Opening Angle Measurements and Crack Tunneling Under Stable Tearing in thin Sheet 2024-T3 Aluminum Alloy," NASA CR 191523, NASA Langley Research Center, Hampton, VA 23681, September 1993.
2. Newman, J.C., Jr., Dawicke, D.S., and Bigelow, C.A., "Finite-element Analyses and Fracture Simulation in Thin-Sheet Aluminum Alloy," NASA TM August, 1992.
3. Chen, C.S., Wawrzynek, P.A., Ingraffea, A.R., "Residual Strength Predictions of Fuselage Structures with Multiple Site Damage," Proceedings from the Second Joint NASA/FAA/DoD Conference on Aging Aircraft, Williamsburg, VA, August 31 - September 3, 1998.
4. Gullerud, A.S., Dodds, R.H. Jr., Hampton, R.W., Dawicke, D.S., "3-D Finite Element Modeling of Ductile Crack Growth in Thin Aluminum Materials," *Fatigue and Fracture Mechanics: 30th volume,* K.L. Jerina and P.C. Paris, Eds., American Society for Testing and Materials, 1998.
5. Dawicke, D.S, Newman J.C., Jr., "Evaluation of Various Fracture Parameters for Predictions of Residual Strength in Sheets with Multi-site Damage," First Joint DoD/FAA/NASA Conference on Aging Aircraft, Ogden, Utah, July 8-10, 1997.
6. Dawicke, D.S., A presentation on NASA Aging Aircraft Activities. Wide Spread Fatigue Damage Evaluation, 5th Semi-Annual Review. NASA Langley Research Center, Hampton, VA. February 1999.
7. Shivakumar, K.N., Newman, J.C., "ZIP3D − An Elastic and Elastic-Plastic Finite-Element Analysis Program For Cracked Bodies," NASA Langley Research Center, Hampton VA 23665-5225, 1990.
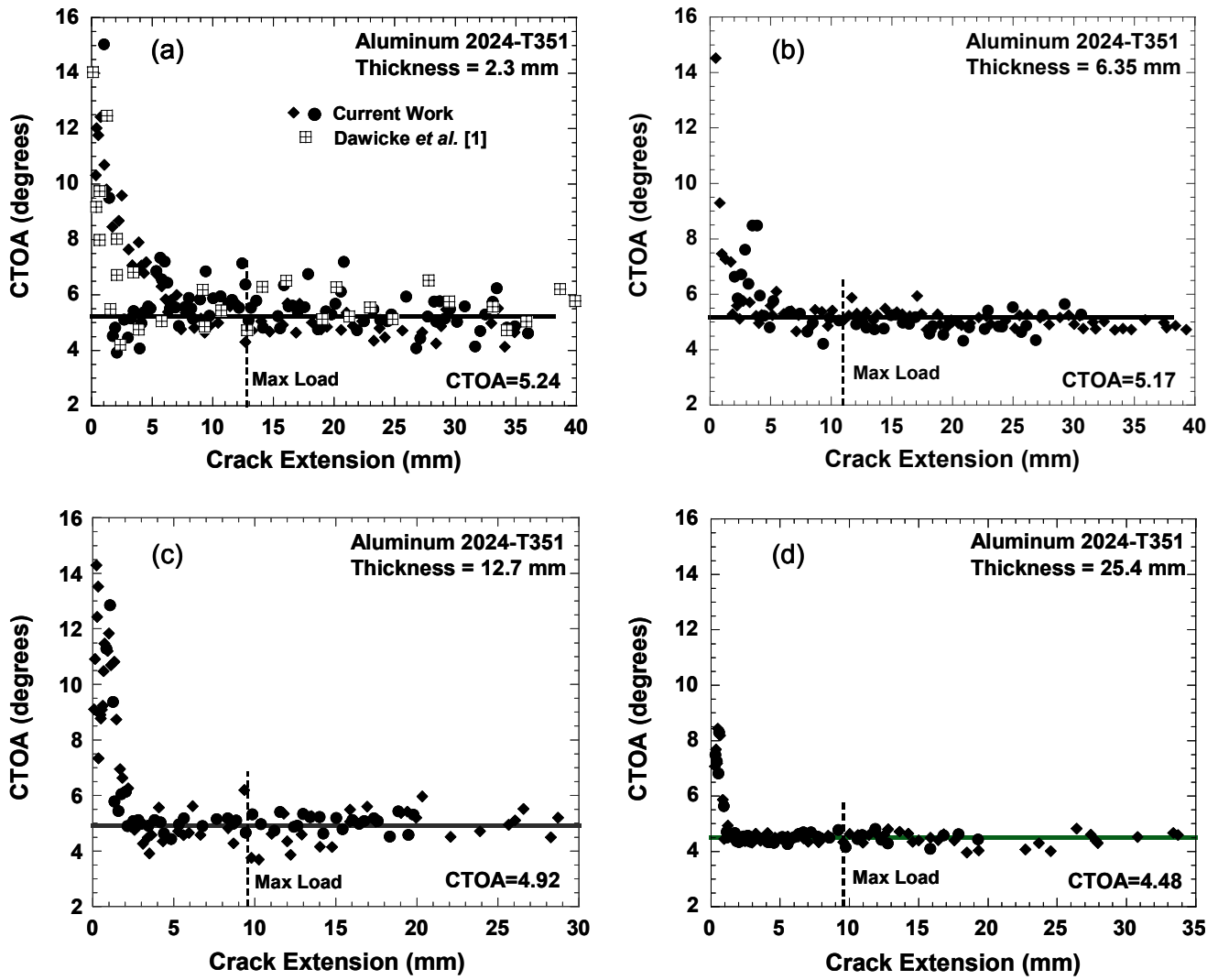
Figure 1: Experimental surface CTOA versus crack extension behavior for all four thicknesses of the 2024-T351 (L-T) Aluminum alloy evaluated. (a) 2.3 mm (b) 6.35 mm (c) 12.7 mm (d) 25.4 mm
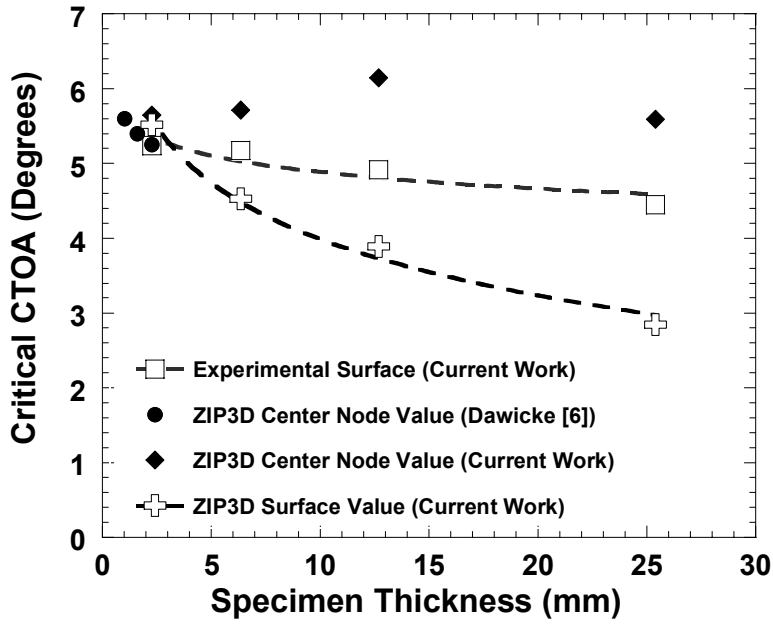
Figure 2: Experimental and computational (ZIP3D) critical CTOA values as a function of specimen thickness for the 2024-T351 (L-T) Aluminum alloy.
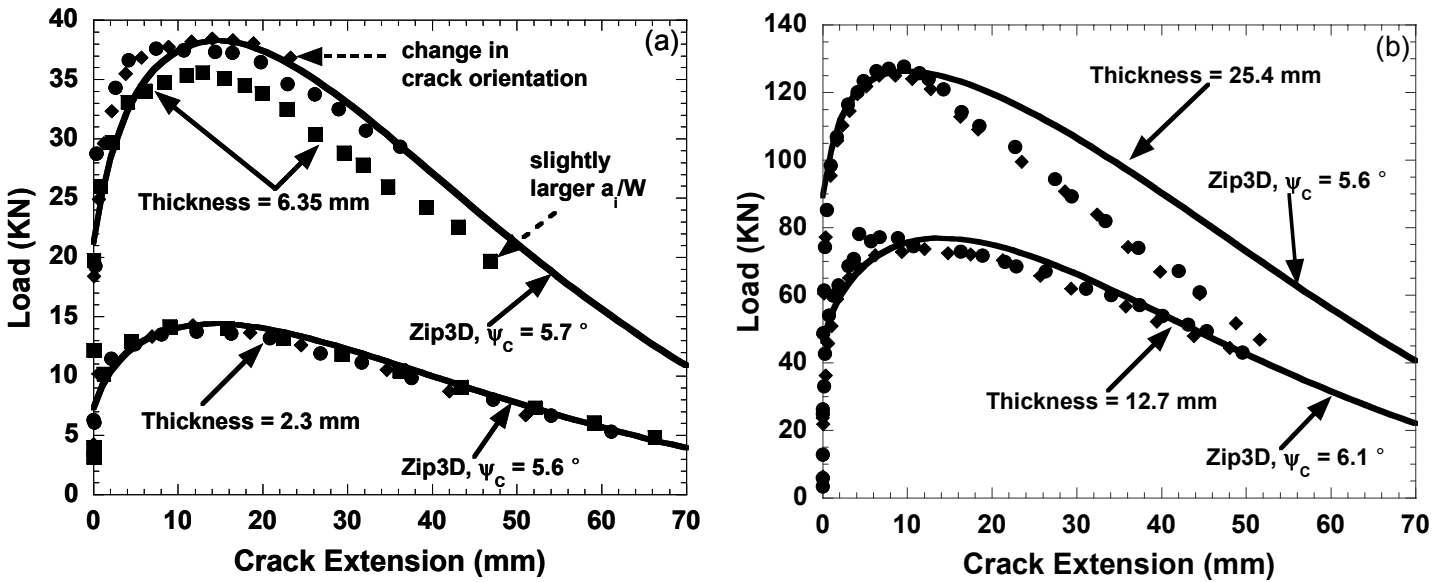
Figure 3: Experimental (symbols) and ZIP3D computational (solid lines) load versus crack extension behavior for all four thicknesses of the 2024-T351 (L-T) Aluminum alloy evaluated. (a) 2.3 and 6.35 mm (b) 12.7 and 25.4 mm

EFFECTS OF DIFFUSION ON INTERFACIAL FRACTURE OF MULTILAYER HYBRID MICROCIRCUIT FILMS

N. R. Moody, *D. P. Adams, D. Medlin, **A. Volinsky , N. Yang, **W. W. Gerberich

Sandia National Laboratories, Livermore, CA 94551-0969
*Sandia National Laboratories, Albuquerque, NM 87185-0959
**University of Minnesota, Minneapolis, MN 55455

ABSTRACT

In this study, the effect of diffusion on gold-chromium film durability was determined from interfacial fracture energy measurements on laboratory samples aged to simulate long term service. The samples were prepared by sputter deposition of gold films and chromium adhesive layers on sapphire substrates. Some films were left in the as-deposited condition while others were given an accelerated age to drive the chromium off the interface. Stressed overlayers and nanoindentation were then used to induce interfacial delamination and blister formation from which interfacial fracture energies were determined using mechanics-based models. The results clearly showed that diffusion-induced changes in composition and structure of the films markedly alter susceptibility to interfacial fracture.

KEYWORDS: Gold films, gold-chromium films, stressed overlayers, nanoindentation, interfacial fracture

INTRODUCTION

Interface structure and composition are two of the most important factors controlling the performance and reliability of thin film devices [1,2]. They are particularly important in gold-chromium hybrid microcircuits which consist of an alumina substrate, a thin chromium layer for adherence, and a gold layer for conductance to connect components on the microcircuit [3-5]. During post deposition annealing, lead-frame bonding and service at elevated temperature, diffusion and segregation change the composition and structure of the films and interfaces [3-7]. This has caused significant concern as to the long-term effects of chromium migration on film performance and durability and has motivated numerous studies on diffusion processes and their effects on film properties and performance. These tests have repeatedly shown that chromium diffusion continues until the chromium adhesion layer has been depleted. Nevertheless, the effect of these changes on film adhesion is not well defined due to limitations in quantitative test and analysis techniques [8-10]. These measurements are made even more difficult for ductile films where extensive plasticity limits the stress that can be applied at the film-substrate interface [8]. Recent work by Kriese and coworkers [8,10] following earlier work of Bagchi et al. [11,12] shows that this limitation can be overcome by deposition of a hard highly stressed overlayer. This overlayer applies a uniform stress to the ductile films while constraining out-of-plane plasticity [11-13]. We used this approach to study how changes in composition and structure of gold-chromium films affect susceptibility to interfacial fracture. The results clearly show that chromium promotes

adhesion. More interestingly, the strong increase in fracture resistance observed accompanying chromium layer depletion suggests that the relationship between interface structure and deformation dictates film performance.

MATERIALS AND PROCEDURE

In this study, thin gold and gold-on-chromium films were sputter deposited onto polished single crystal (0001) sapphire. Deposition began by heating the substrates to 700˚C in vacuum to drive off moisture followed by a cool to room temperature. The films were deposited on the substrates using chromium and gold targets and argon as the carrier gas. Chromium was deposited first to a thickness of 6 nm. This was followed by gold deposition to a thickness of 200 nm. A gold-on-sapphire film was created for reference.

The gold-on-chromium film samples were then divided into three groups. One group was left in the as-deposited condition. A second group was heated at 400˚C for 2 hours in air at which point chromium had begun to come off the sapphire interface in many regions. The third group was then heated at 400˚C for 8 hours in air after which all the chromium had migrated off the interface. During heating, chromium diffused through the gold to the surface leading to Cr_2O_3 formation upon exposure to air. This oxide was removed using a solution of ceric ammonium nitrate prior to any subsequent fabrication or testing process.

Mechanical properties were determined for each film system using the continuous stiffness option on a Nano Indenter II™ and a Berkovich diamond indenter. All measurements were conducted at an excitation frequency of 45 Hz and displacement of 3 nm. Following nanoindentation, tantalum nitride (Ta_2N) overlayers were deposited on all films to provide a uniform compressive stress for fracture testing. These films were deposited using a tantalum target, argon as a carrier gas, and controlled additions of nitrogen. 450 nm-thick Ta_2N overlayers were sputtered on the gold-on-chromium films. An overlayer 275 nm thick was deposited on an as-deposited gold film to explore the minimal stress needed to cause buckling when chromium was not present.

RESULTS AND DISCUSSION

Structure
The structure and composition of the films were determined using x-ray diffraction and Transmission Electron and Scanning Auger Microscopy. Figure 1 shows that the as-deposited gold and gold-chromium films formed fine scale structures along the substrate interfaces. In the gold films the structure was characterized by formation of 5-nm-thick (111) interface twins parallel with the substrate interface. Continued deposition led to extensive through thickness twinning. In the gold-chromium films, the 5-nm-thick chromium adhesive layer formed the fine scale structure. No long interface twins formed in the gold on the chromium but extensive through thickness twinning did occur within the gold film.

Scanning Auger Microscopy of the films showed a well-defined chromium peak at the interface with the sapphire substrate corresponding to the chromium adhesive layer. (Figure 2.) Aging at 400˚C for 2 hours led to through thickness migration of chromium and partial depletion of the adhesive layer. This was confirmed by backside optical examination where a thin translucent chromium layer covered the substrate interface. In contrast, long term annealing led to complete depletion of the chromium adhesive layer creating a uniform through thickness gold-chromium solid solution. Backside optical examination did not reveal any evidence of a chromium interlayer. The structure and stresses within the tantalum nitride overlayers were characterized using a Rigaku X-ray diffraction (XRD) system with a thin film detection system and Cu-Kα radiation. The patterns showed a randomly oriented polycrystalline structure for these overlayers, typical for sputter-
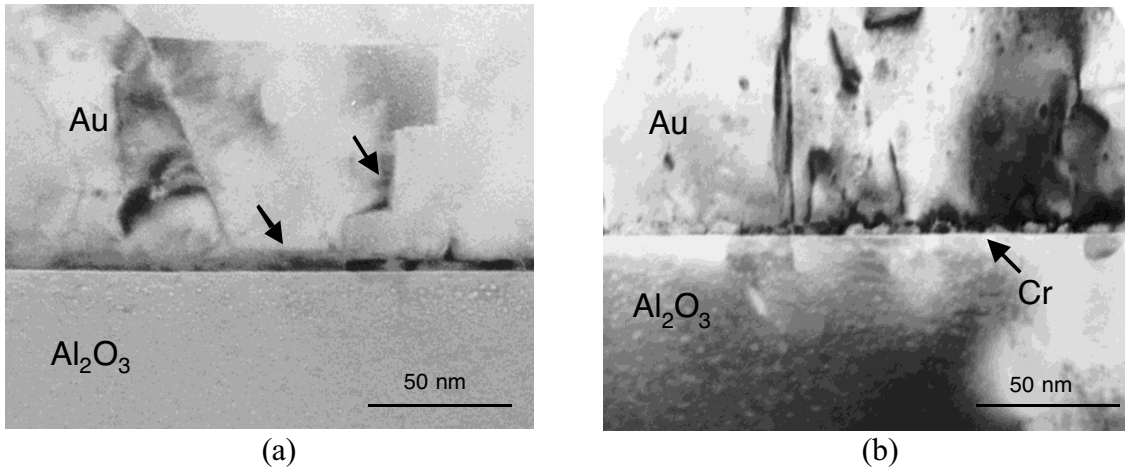
Figure 1. (a) Interface twins formed in the gold along the sapphire substrate during deposition. Continued deposition led to extensive through thickness twinning. (b) Only through thickness twins formed in the gold on chromium films during deposition.

deposited tantalum nitride. Out-of-plane strain, indicated by shifts in the 2θ peak position for (101), (110), and (211) planes, was then used to calculate the in-plane residual stress assuming isotropic elasticity [14-16]. This gave a compressive stress value of 2.5 GPa which was subsequently confirmed using an inclined angle method for measuring residual stress [16].

Fracture

Previous work [17] showed that deposition of the tantalum nitride overlayers triggered extensive delamination and telephone cord blistering on the as-deposited gold film sample and to a lesser extent over the as-deposited gold-on-chromium film sample. (Figure 3a) The blistered material readily spalled away exposing the lower fracture surface. High resolution SEM coupled with energy dispersive spectroscopy revealed that fracture had occurred along the film-sapphire interface. The freshly exposed sapphire surfaces under the telephone cord and the circular blisters were visually smooth at 50kX and showed no evidence of gold or chromium indicating that fracture occurred by interfacial decohesion. [18,19]
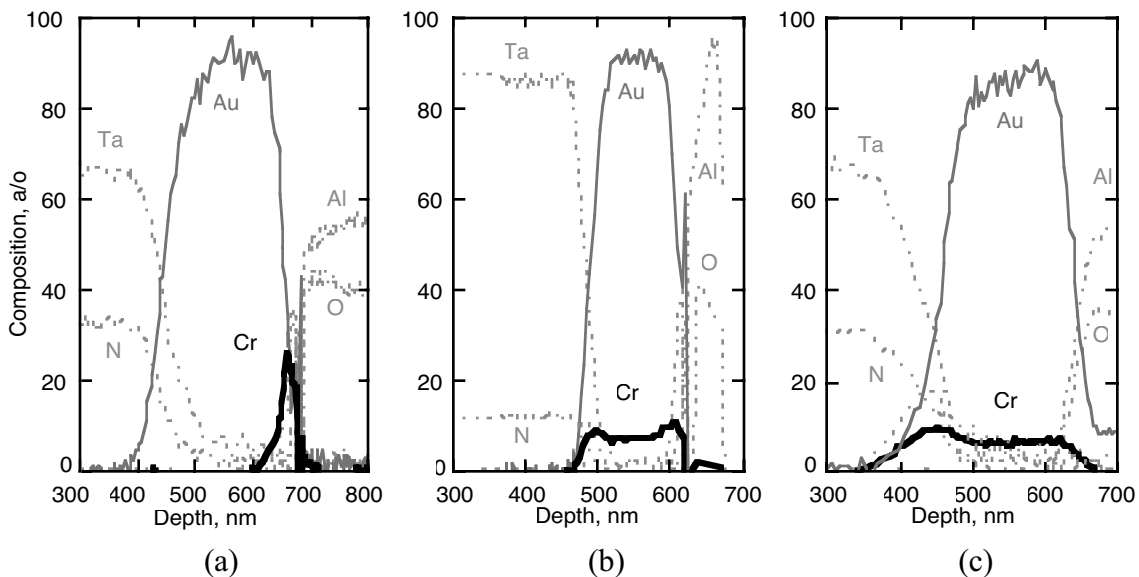
Figure 2. Composition profiles of the (a) as-deposited film, (b) the film annealed at 400˚C for 2 hours and (c) the film annealed at 400˚C for 8 hours show that diffusion during annealing has depleted the continuous chromium adhesive layer.

(a)	(b)
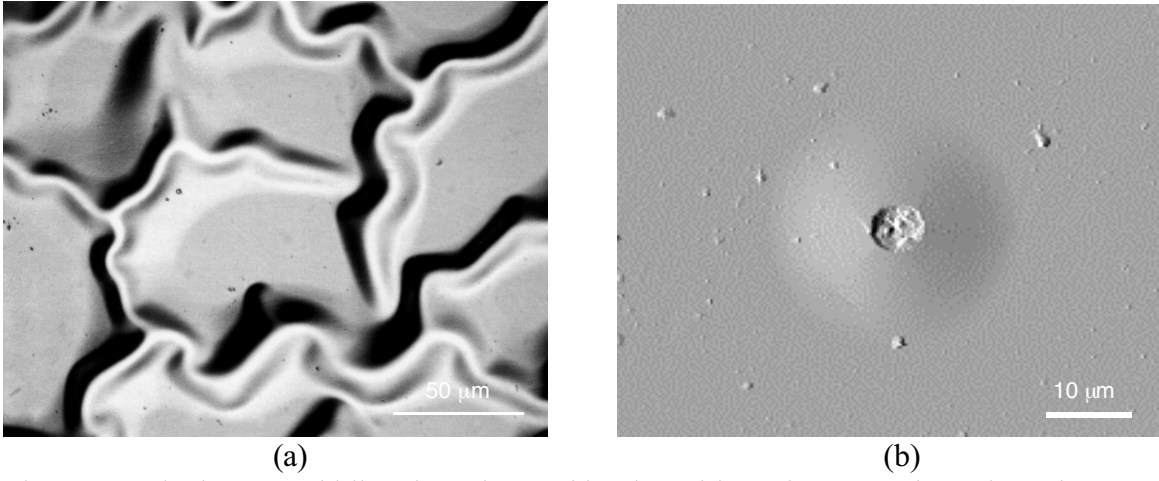
Figure 3. Telephone cord blistering triggered by deposition of a stressed overlayer is shown for the (a) as-deposited gold film. A circular blister triggered by nanoindentation is shown for the (b) 400°C/2h annealed gold-chromium film.

Nanoindentation was then used to induce interfacial fracture in the annealed films where telephone cord blistering did not occur. (Figure 3b) These tests triggered formation of large circular spalls. In all cases fracture occurred by reverse or double buckle formation during indentation with the material under the indenter pinned to the substrate [9]. The fractures in the partially annealed samples also occurred along the chromium-substrate interface. In contrast, all fractures in the long term annealed sample occurred along the tantalum nitride-gold interface. Moreover, the size of the blisters were smaller and the loads at fracture higher than observed in the partially annealed samples indicating that these samples were more resistant to interfacial fracture than any of the other samples tested.

Fracture Analysis
The uniform width and circular blisters provide the data from which interfacial fracture energies can be obtained using solutions for film systems where residual stresses dominate fracture behavior. These solutions were originally derived for single layer film-on-substrate systems [20-22]. Work by Bagchi et al. [11,12] and more recently by Kriese et al. [8] extended these solutions to multilayer systems by treating the multilayer film as a single film of the same total thickness with a transformed moment of inertia. The approach and results for the as-deposited films is presented in previous work.

Failure in the as-deposited gold and gold-chromium films occurred by telephone cord blistering. Under steady state conditions, the width of the telephone cord blister remains fixed creating a straight-sided blister with growth occurring along the more or less circular end of the blister. This gives a steady state fracture energy, Γ_{ss}, as follows [21],

$$\Gamma_{ss} = \left[\frac{(1 - \bar{\upsilon}^2)h\sigma_r^2}{2\bar{E}} \right] \cdot \left(1 - \frac{\sigma_b}{\sigma_r} \right)^2 \tag{1}$$

where h , E and ν are the multilayer film thickness, elastic modulus, and Poissons' ratios respectively, σ_b is the stress for delamination modified for multilayer films, and σ_r is the average residual stress.
Failure in the accelerated aged samples required nanoindentation to trigger delamination and circular blister formation. In all blisters, the center is constrained giving rise to a reverse or double buckle configuration. Following the analyses of Marshall and Evans [21] and Evans and Hutchinson [22], the strain energy release rate for formation of a circular blister at fracture due to residual and indentation stresses, $\Gamma(\psi)$, is given by

$$\Gamma(\psi) = \frac{(1 - \bar{\upsilon}^2)h\sigma_v^2}{2\bar{E}} + (1 - \alpha)\frac{(1 - \bar{\upsilon}^2)h\sigma_r^2}{\bar{E}} - (1 - \alpha)\frac{(1 - \bar{\upsilon})h(\sigma_v - \sigma_c)^2}{\bar{E}} \tag{2}$$

TABLE I.

FRACTURE ENERGY RESULTS FOR AS-DEPOSITED GOLD AND GOLD-CHROMIUM FILMS.

Film	h_{Au} (nm)	h_{Ta_2N} (nm)	2b/2c (μm)	σ_b/σ_c (μm)	σ_r (GPa)	$\Gamma_{ss}/\Gamma(\psi)$ (J/m^2)	ψ	Γ_I (J/m^2)
Au								
As-deposited	200	275	28.8	0.3	-1.4	1.3	-75	0.5
Au-Cr								
As-deposited	200	450	57.8	0.1	-1.8	2.9	-82	0.9
400˚C/2h	200	490	29.9	0.5	-1.8	2.8	-67	1.3
400˚C/8h	200	490	15.4	5.6	-1.8	11.8	-68	5.3

where $\alpha=1-[1+0.902(1-\nu)]^{-1}$ [20], σ_c is the stress for delamination, and σ_v is the stress from indentation.

The uniform width and circular blister fracture energies are mixed mode values consisting of shear and normal contributions. The normal contribution is critical to understanding mechanisms controlling susceptibility to interfacial fracture. Of the criteria proposed to describe the relationship between mixed mode and mode I contributions, $\Gamma_I=\Gamma(\psi)/[1+\tan^2\{(1-\lambda)\psi\}]$ [20,23], is most often used. In this equation, λ is a material parameter equal to 0.3 for most materials, and ψ is the phase angle of loading.

Average blister widths and diameters, delamination stresses, residual stresses, mixed mode and mode I fracture energies, and phase angles of loading are given in Table I for the uniform width blisters in as-deposited gold and gold-chromium films and circular blisters in the annealed gold-chromium films. The as-deposited gold film fracture energy of 0.5 J/m^2 is in very good agreement with the true work of adhesion from contact angle measurements of gold on sapphire. [18] This is consistent with the observation that fracture occurred along the film substrate interface. The fracture energies for the gold-chromium films on sapphire are two times greater than for pure gold clearly demonstrating the better adhesion properties of chromium interlayers. Interestingly, the fracture energies increase slightly for samples where the chromium interlayer is reduced in size. Complete depletion of the chromium adhesive layer led to a marked increase in fracture energies. In addition, the fracture path changed from along the film-substrate interface to along the overlayer-gold film interface. Diffusion has replaced the thin hard chromium adhesive layer with a solid solution of gold and chromium in the lattice and enhanced concentrations of chromium along the gold grain boundaries. Gone also is the resistance to deformation that nanometer scale features possess. The solid solution of gold and chromium deforms much more readily than the chromium interlayer facilitating crack tip plasticity and dislocation emission. Moreover, it appears that crack nucleation has become much more difficult without the hard interlayer. It is unlikely that adhesion improved with the transition from a continuous chromium interlayer to a gold-chromium solid solution. There are no reactions between film and substrate at these temperatures or in samples held at high temperatures for much longer times. [24] As a result, the increase in fracture resistance following annealing appears attributable to the effects of interfacial structure on deformation and fracture while chromium in solution remains as effective an adhesion promoting agent as it is forming a continuous interlayer.

CONCLUSIONS

In this study, highly compressed overlayers were combined with nanoindentation to study the effects of diffusion during post deposition annealing on susceptibility to interfacial fracture of gold and gold-chromium films used in hybrid microcircuits. The gold films formed with 5-nm-thick twins along the substrate interface while the chromium interlayers formed a complementary structure along the substrate interface in the gold-chromium films. Highly stressed overlayers were combined with nanoindentation to induce delamination and blister formation from which fracture energies were determined. The results on as-deposited films showed that chromium increased the work of adhesion from 0.5 to 0.9 J/m^2. Tests on the annealed films showed that the films remained bonded at a similar strength level as long as the adhesive layer remained essentially continuous along the substrate. However when diffusion led to chromium layer

depletion, fracture changed from the film-substrate interface to the overlayer-film interface accompanied by a three-fold increase in fracture energies. This change in fracture path and increase in fracture energies appears attributable to formation of a gold-chromium solid solution that promotes deformation while inhibiting interfacial fracture.

ACKNOWLEDGMENTS

REFERENCES

1. Mittal, K. L. (1976) *Electrocomponent Science and Technology*. 3, 21..
2. Mattox, D. M. (1973) *Thin Solid Films*. 18, 173.
3. Munitz, A. and Komem, Y. (1976) *Thin Solid Films*. 37, 171.
4. Thomas, R. E. and Haas, G. A. J. (1972) *Appl. Phys*. 43, 4900.
5. Rairden, J. R., Neugebaur, C. A. and Sigsbee, R. A. (1971) *Metall. Trans*. 2, 719.
6. George, M. A., Glaunsinger, ,W. S., Thundat, T. and Lindsay, S. M. (1990) *Thin Solid Films*, 189, 59.
7. Munitz A. and Komem, Y. (1980) *Thin Solid Films*, 71, 177.
8. Kriese, M. D., Gerberich, W. W. and Moody, N. R. (1999) *J. Mater. Res*. 14, 3007.
9. Moody, N. R., Hwang, R. Q., Venkataraman, S., Angelo, J. E., Norwood, D. P. and Gerberich, W. W. (1998) *Acta mater*. 46, 585.
10. Kriese, M. D., Moody, N. R. and Gerberich, W. W. (1998) *Acta mater*. 46, 6623.
11. Bagchi, A.and Evans, A. G. (1996) *Thin Solid Films*. 286, 203.
12. Bagchi, A., Lucas, G. E., Suo, Z. and Evans, A. G. (1994) *J. Mater. Res*. 9, 1734.
13. He, M. Y., Evans, A. G. and Hutchinson, J. W. (1996) *Acta metall. mater*. 44, 2963.
14. Moody, N. R., Medlin, D., Boehme, D. and Norwood, D. P. (1998) *Engng. Fract. Mech*. 61, 107.
15. Sun, R. C., Tisone, T. C. and Cruzan, P. D. (1975) *J. Appl. Phys*. 46, 112.
16. Cullity, B. D. (1956) *Elements of X-Ray Difffraction*. Addison-Wesley Publishing Co., Reading, MA.
17. Moody, N. R., Adams, D. P., Volinsky, A. A., Kriese, M. D. and Gerberich, W. W. (2000) In: *Interfacial Engineering for Optimized Properties II*, Briant, C., Carter, C., Hall, E., and Nutt, S. (Eds.)., Mater. Res. Soc. Proc. 494, pp. 195-205, Pittsburgh, PA.
18. Reimanis, I. E., Dalgleish, B. J., Brahy, M, Ruhle, M. and Evans, A. G. (1990) *Acta metall. mater*. 38, 2645.
19. Reimanis, I. E., Dalgleish, B. J. and Evans, A. G. (1991) *Acta metall. mater*. 39, 3133.
20. Hutchinson, J. W. and Suo, Z. (1992) In: Advances in Applied Mechanics. 29, pp. 63-191, Hutchinson, J. W. and Wu, T. Y. (Eds.) Academic Press Inc., New York.
21. Marshall, D. B. and Evans, A. G. (1984*) J. Appl. Phys*. 56, 2632.
22. Evans, A. G. and Hutchinson, J. W. (1984) *Int. J. Solids Struct*. 20, 455.
23. Thouless, M. D., Hutchinson, J. W., and Liniger, E. G. (1992) *Acta metall. mater*. 40, 2639
24. Zhao, X.-A., Kolawa, E. and Nicolet, M.-A. (1986) *J. Vac. Sci. Technol. A*. 4, 3139.

THE FATIGUE DAMAGE OF CONSTRUCTION MATERIALS

S. Shamirzaev [*1], Sh.Ganihanov[2] and G. Shamirzaeva[2]

[1] Physical Technical Institute of Academy of Sciences, Uzbekistan
[2] Tashkent State Aviation Institute; Uzbekistan

ABSTRACT

Construction material's fractures are due to various imperfections. In a real material there are different types of micro-imperfections. They form an intricate potential relief, which moves in space of material under random fatigue loading [1-3]. As a result material becomes more harder or more looser. The physical model of how it occurs is the main object of this poster. We have found the common law ruled the migration of complex of defects and used the full orthonormal set of functions $\{\varphi_n, 1\}$ which are the state functions of the operator of "age" [4]. It gives us opportunity to create the new way of fatigue damage analysis of construction materials.

KEYWORDS

Fatigue damage, sensors, quantitative model, time series, monitoring

INTRODUCTION

The damage of construction material (CM) units which undergo repetitive or random loads relates to fatigue. But up to recent time neither a quantitative model of the initial stage of material fatigue damage nor reliable sensors to record it have been developed. It is connected with the fact that damage is not formed by a single defect but a complex of defects which are generated by random loads, migrate and gather in material of construction forming unordered structures preceding the damage. The duration of process, measured by the number N – cycles of loading (when the forming of cracks is held and the 1st stage of their growth is realized) is compared with the duration of processes on the second stage (the growth of macroscopic cracks).The features of structure of polycrystal alloys are reflected on the structures of their potential reliefs that are originated by both a residual deformation and an imposed fatigue deformation. In local regions of polycrystal material (PM) which undergoes fatigue loads a wide spectrum of strongly exited states arises [3]. These states can not be described by traditional methods of a perturbation theory. With the help of mechanics methods of damage one can study only the growth of macroscopic cracks (second stage) using empirical – formula dependencies describing the growth of a crack.

Contrary to the traditional methods of damage mechanics we use both the methods of theory of chaos and one dimensional time series that are formed by suitable experimental data [3,4]. It permits us to model the features of structure of potential relief of a construction material (CM) and to study its transformation under imposed both the selected single deformation and a fatigue in limit cycle regime. **Objects under study** are Aluminum alloy's samples with the SEs rigidly installed on them. *The same spectrum of deformation imposed on both of them.*

Aluminum alloy's samples. Brittle and hard inter-metal combinations originate in Aluminum alloys. The fastness of aluminum alloys (for example, AlCuMg) are raised after its quenching. Selected alloys of Aluminum consist of various types of grains: Al_2Cu – in Al&Cu alloy ; Al_3Fe – in Al&Fe alloy; Mg_2Si, $MgZn_2$ and Cu_2NiAl_7 in multi-compound alloys of Aluminum. These hard fine grains, taking place in a relative soft base material, implement the high resistance to wear of a material. The plastic CMs possess ample types of local structures which readily rearranged to each other at the local zones. Whereas a brittle CMs possess only a single local structure. A lattice can not be rearranged under cycles loading so there is a cracking process. As an example, pure NiTi possess closely adjacent B2 structure and B19 structure which readily rearranged to each other at the local zones. As a result pure NiTi is perfect plasticity material. But NiTi<Fe> becomes a brittle material possessing very stable B2 structure. Below we will present the experimental way of describing these alloys. The various impurities in Aluminum implement the various resistance to fatigue of an Aluminum alloy's samples. The same situation one has in heterogeneous materials, that are used to form the sensitive elements (SEs) for fatigue gages [1]. Further we will also deal with the fatigue features of a SEs, which have a various impurities.

The SE has small weight (no more than 5g) and either 3D or film geometry. They are produced either by the method of powder metallurgy (cold pressing with the subsequent agglomeration in a quartz ampoule) or by thermal vacuum evaporation of the charge onto the polyamide support. The charge consists of a finely dispersed mixture of various initial components, e.g., a mixture of granular $Bi_{2-x}Te_{3+x}$ and $Sb_{2-y}Te_{3+y}$ with carbonyl iron. The fatigue processes in the selected SEs as well as in Aluminum alloys are sensitive to vary impurities and are similar to each other. It gives one the opportunity to develop different type of the SEs for adaptive forecast of fatigue damage of the CMs, subjected to random loads.

Simple model of SE . Resistance, R_{eff}, of SE is simulated by lattice at the corners of which randomly located resistance - r_i (i = 1,2,3,..., K ; K - total number of grains [or clusters] of SEs). r_i is the resistance of the grains of the SEs randomly connected with neighboring grains. In that model lattice one may find a simple module in Fig.1 Model lattice consists of L modules, of this kind , each having index - k, (k = 1,2,...., L). At equilibrium state the effective resistance R [a-b] = R_{eff} of such module is independent on the value of resistance r_5 = R[γ-δ], intervened between γ and δ points (Fig.1). The electric balance is disturbed under loading cycle (irreversible) of deformation. So, R[a-b] varies according to quantity of resistance r_5 = R[γ-δ]. It is the simplest model of high sensitivity of SEs [1].
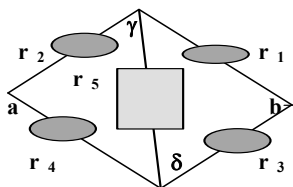
Figure 1. R_{eff} = R **(a-b)** - resistance of module is measured by use **a** and **b** points. For equilibrium situation electric potential in γ and δ points are equal (balanced points); so R(a-b) becomes independent on the value of resistance r_5. It is valid also if r_5 =0. (Electrical Wheatstone bridge).

Our aims are to represent both the quantitative model of initial stage of materials' fatigue and the new way of fatigue damage analysis of construction materials by using SEs .

The ways of realization. Effective rheological output parameters (J_{eff} and η_{eff} or Q^{-1}_{eff} - coefficient of nonlinear internal friction) of a real construction beam are also modeled by lattice in the knots of which rheological elements – elasticity (J_k, k = 1,2,…,K_{cm}; K_{cm} – the total number of granules [or clusters] of CM) and /or viscosity (η_k) are randomly located. J_k and η_k – are elasticity and viscosity of CM granules which are randomly connected with neighboring granules [3].

Real CM has an intricate potential relief. So in it there are couples of points (**balanced points**) with identical potential. Their space function of distribution f_n (x, y, z) can be presented by the complete orthonormal series of functions ({ φ_ν , 1 } ; $-\infty < \nu < +\infty$), which obey the baker (**B**) transformation [3,4]. After the loads being imposed some of balanced points migrate in the CM space. Their space function of distribution f_n also obeys baker transformation (See Fig. 3a, 3b, 3c). It gives the possibility to determine common law controlling the migration of defects complex.

Ample grains do not take part in fatigue process of both a polycrystal CM and a SE. Along with growth of the number of strongly deformed grains in polycrystal CM as well as in SE there are also an ample grains possess their original state. The simple model (See Fig.2) describes these situations is given in [3]. There is also next sufficient **conclusion** : *When random deformation process taking place at regular (unit) intervals of time - τ, the CM's and the SE's responses at both a fast ($\tau << \tau_c^{(SE)}$) and a slow*

*($\tau > \tau_c^{(CM)}$) loads can be found by using distribution function f_n (x, y, z; τ). Their distribution functions $f_n(x, y, z; \tau)$ can be expanded to the series by full orthonormal set of functions $\{\varphi_v, 1\}$[3,4] . $\{\varphi_v, 1\}$ are eigenfunctions of the operator of "age" is, by definition, a self – adjoint operator **T** [4] : **T** $\varphi_v = v * \varphi_v$, v = 0, ±1, ±2,......, ± ∞. $\{\varphi_v, 1\}$ also suit to baker's transformation (**B**). It gives one the opportunity to simulate a fatigue process in both the CMs and SEs. And it is the main reason why for all kinds of imposed deformation (extension-compression; bending variations with different coefficients of asymmetry; various spectra of imposed deformation), at which the output parameters (electric resistance R_n for SE and internal friction Q_n for CM) of materials are recorded in equal time (τ) intervals, the next recurrent relations take place:*

$$R_{n+1}[\sigma] = \mathbf{O}_n * R_n[\sigma] = B_n * R_n + (1-B_n)*M_n \; ; \tag{1}$$

$$Q^{-1}_{n+1}[\sigma] = \mathbf{O}_n * Q^{-1}_n[\sigma] = b_n * Q^{-1}_n + (1-b_n)*m_n \; . \tag{1a}$$

Here: R_n is the electric resistance of SE measured under the same state of the environment; n is the ordinal number of measurement (n = 1,2,3, ..., g); g is the maximum number of the measurement performed; $\mathbf{O}_n$ is the loading operator transferring the SE resistance from R_n-th state to R_{n+1} -th state ; σ is a complicated
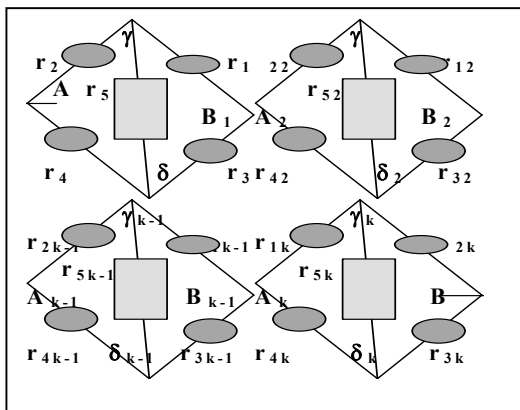
Fig.2. One port network resistance $R_{eff} = R$ **(A-B)**
Some of grains do not take part in R_{eff} performance. $\Delta R(\sigma, N) = R_{eff} (\sigma, N) - R_{eff} (\sigma, 0)$;

$$\Delta R(\sigma, N) = \sum_{k=1}^{L} [g_k * \Delta R_k (\sigma, N)] ; \quad \sum_{k=1}^{L} g_k = 1.$$

*I) Equilibrium situation - **active module :***
$$R (A-B_1) \equiv R^*_{20} ;$$
*II) Non equilibrium situation –**passive module:***
$$R (A-B_1) \equiv R^*_{10} > R^*_{20}$$
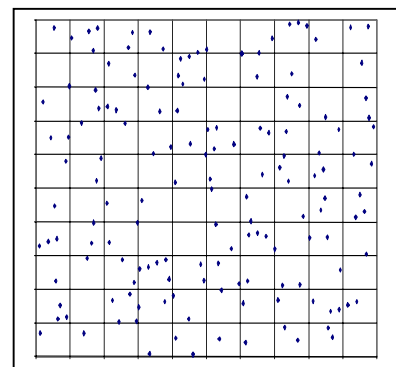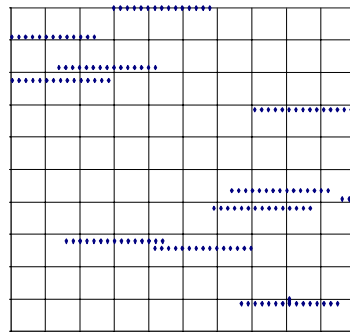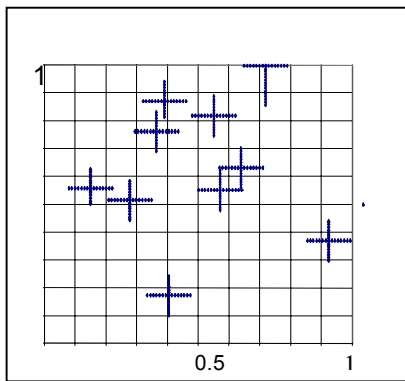
a)

b) **B^1**

c) **B^8**
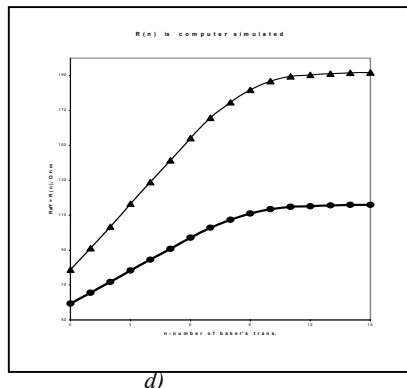
d)

Fig. 3a. N_e - original equilibrium points are arbitrary located at a SE' space. $N_e = 10$; $N_1 = 15$; $N_2 = 15$; N_1 – compressible subset (contains active module – R^*_{20}); N_2 -expandable subset (contains passive module – R^*_{10})

Fig.3b. SE's state after 1 baker transformation: $N_e = 10$; $N_1 = 15$; $N_2 = 15$;

Fig.3c. SE's state after 8 baker transformations: $N_e = 10$; $N_1 = 15$; $N_2 = 15$;

Fig.3d SE's R_{eff} versus number n discrete deformation process taking place at regular intervals of time - τ. . Simple mode of loading. $R_{eff} = R_v$ - is computer simulated:1) $R_{1,0} = 120$ Ohm ; $R_{2,0} = 40$ Ohm;
2) $R_{1,0} = 200$ Ohm ; $R_{2,0} = 40$ Ohm

parameter to characterize the type of imposed deformation ; the "time series", composed of experimental data of the types:

$$R_1, R_2, \ldots, R_{n-1}, R_n, R_{n+1}, \ldots, R_g ; \tag{2}$$

$$Q^{-1}{}_1, Q^{-1}{}_2, \ldots, Q^{-1}{}_{n-1}, Q^{-1}{}_n, Q^{-1}{}_{n+1}, \ldots, Q^{-1}{}_g . \tag{2a}$$

By using the Grassbereger and Procaccia [6] procedure, efficient phase dimensionalities K_g of the time series (2) is calculated. K_g is integer and, in general, depends on the magnitude of the chosen interval (τ).

Taking into account the numerical value of K_g, formulas (1) for R_n, and using formulas of regression, we can find the dependence of parameters B_n and M_n on $n*\tau$ ($n > K_g > 2$).

The relationships

$$B_n = B_{n-1} = B_{n-2} = \ldots = B_{n-Kg+1} ; \quad \text{and} \quad M_n = M_{n-1} = M_{n-2} = \ldots = M_{n-Kg+1} \tag{3}$$

take place. As a result R_{n+1} can be forecasted from previous values of R_n (2) (See Fig.4, Fig.6).
The same procedure can be used to find b_n, m_n, and to forecast $Q^{-1}{}_{n+1}$ having time series (2a) (See Fig.8)
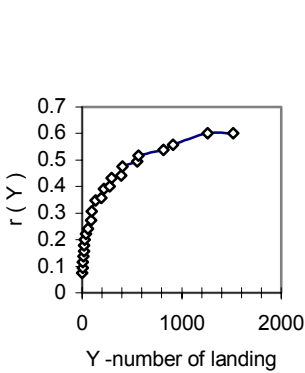
Fig.4 Irreversible random (TU-154B wing spectrum) deformation r-Y. Here Y is number of plane landing;
$r(Y) = (R_{Y,eff} - R_{0,eff}) / R_{0,eff}$
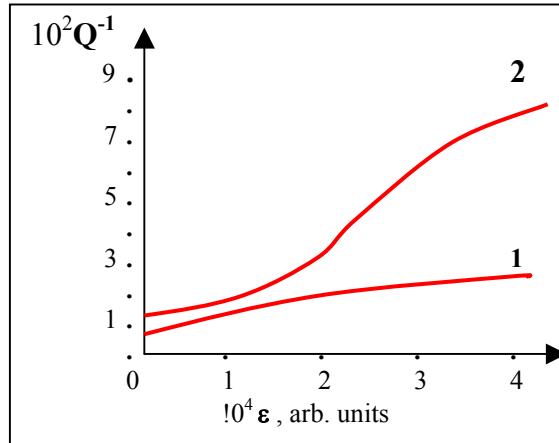
Fig. 5 Internal friction of alloy's sample Q^{-1} versus on imposed deformation ε.
1– After imposed 500 cycles of 25 kg/mm^2 load
2 - After imposed 10^4 cycles of 25 kg/mm^2 load
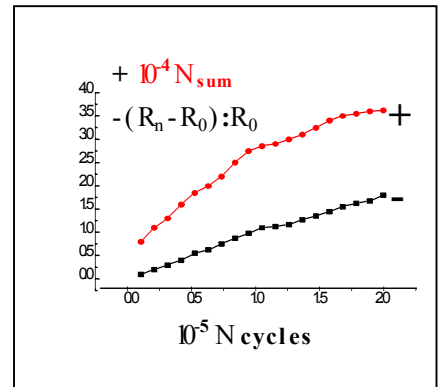
Fig.6 SE resistance [$(R_n - R_o) / R_o$] and total acoustic emission N_{sum} of the D-16T spesimen versus number of cycles N of the imposed deformation corresponding to a 25 kg/ mm^2 load. The asymmetry coefficient is unity (m =1).
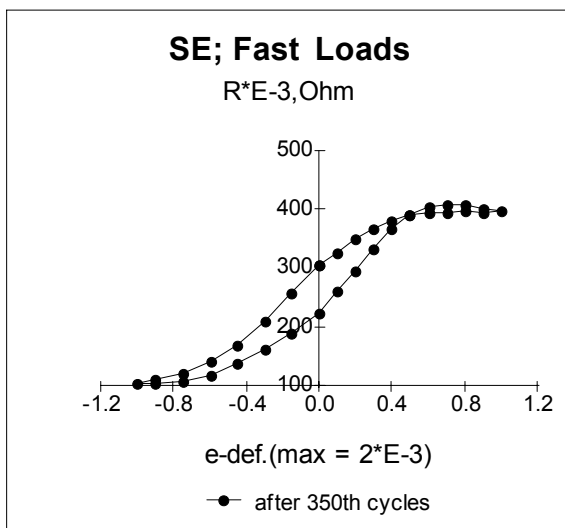
Fig 7. SE's resistance R_{eff} versus on imposed deformation ε, after imposed 350 cycles of fatigue loads, the single fast cycle is imposed. The R_{eff} - ε curve was automatically recorded within this fast cycle.
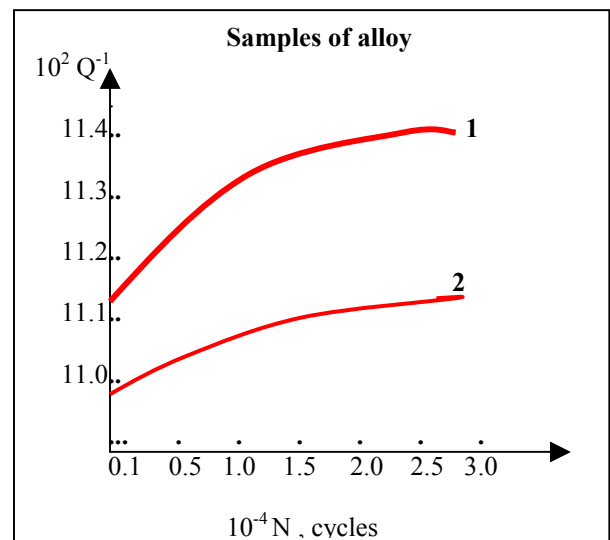
Fig. 8 Internal friction of alloy's sample Q^{-1} versus on number N cycles of the imposed deformation corresponding to both 32 kg/mm^2 (1) and 26 kg/ mm^2 (2) loads. The asymmetry coefficient is unity (m =1).

To gain a greater insight into why the R_{eff} - N dependence has the form given in Fig.4,6 assume that for every module (Fig.1)

$$\Delta R_k (\sigma, N) = \begin{cases} G(\sigma, m)*N & \text{if } N \le N_k \\ \\ G(\sigma, m)*N_k & \text{if } N \ge N_k \end{cases} \tag{4}$$

takes place; N_k varies in value. A scale factor - $G(\sigma, m)$ is the same for each module of the SE and depend on the amplitude - σ and degree of asymmetry - m of the imposed regular cyclic deformation.

Each module (Fig.2) will be able to contribute to the ΔR_{eff} in accordance with statistic g_k [7]:

$$\Delta R(\sigma, N) = \sum_{k=1}^{L} [g_k * \Delta R_k (\sigma, N)] ; \quad \sum_{k=1}^{L} g_k = 1. \tag{5}$$

$\Delta R_k(\sigma, m; N)$ - variation of resistance of a k-th module depend on the amplitude - σ and degree of asymmetry - m of the superimposed regular cyclic deformation. N is the number of cycles. For the sake of convenience, assume that $\Delta R_{max} = M_g (\sigma, m)$ and

$$Z_k = G(\sigma, m)*N_k / M_g (\sigma, m) \quad , (k = 1, 2, 3, ..., L). \tag{6}$$
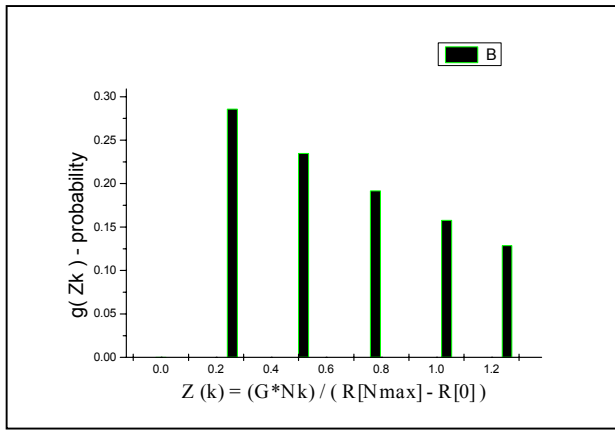
a)
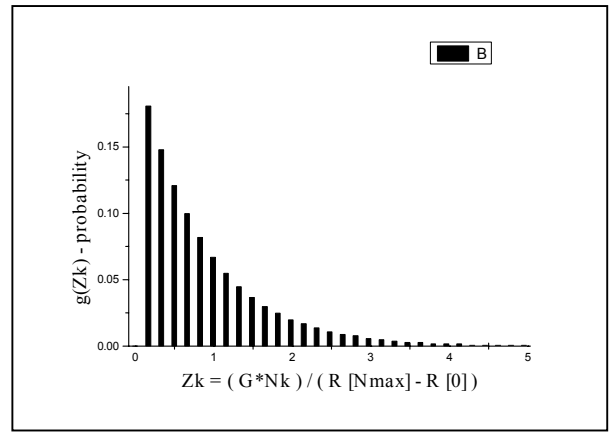
b)

Fig. 9 . The state of SM-film after be loaded : a) 250 and b) 1000 cycles of regular deformation :
(σ_{eff} = 17 Kg/mm^2); σ_a = 7.42 Kg/mm^2 ; σ_m = 12.04 Kg/mm^2
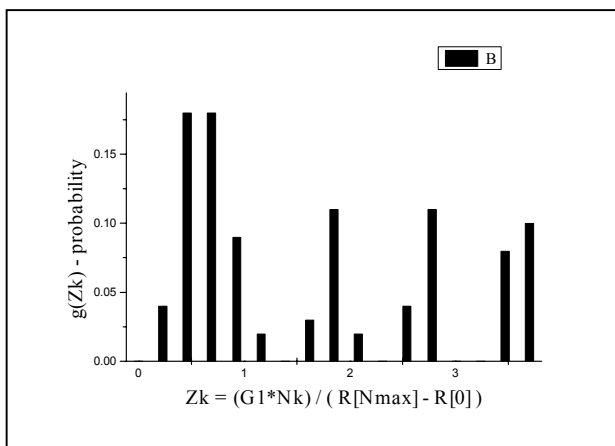
Fig.10. The state of SM-film after be loaded 800 cycles of arbitrary deformation (σ_{eff} = 20.02 Kg/mm^2)
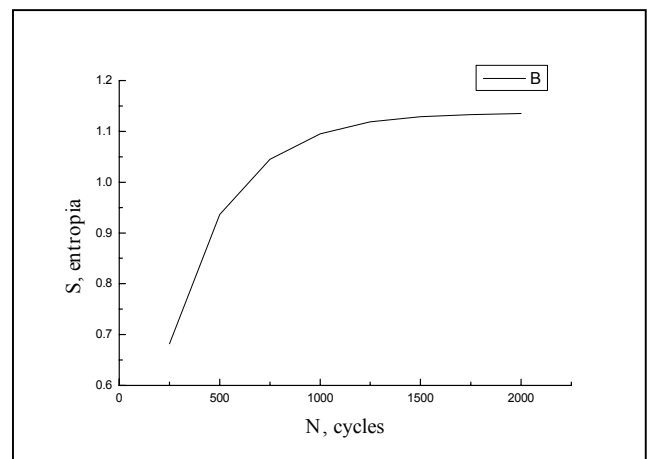
Fig.11 . The increase of entropy (S) versus (N) regular cycles.

Z_k and g_k can be found from experimental data, Fig.4 (or Fig.6, or Fig 8). Proceed as follows:

$$\Delta R(N) = G*N* \sum_{k=1}^{L} g_k = G*N, \qquad\qquad 0 \le N \le N_1$$

$$\Delta R(N) = G*N_1*g_1 + G*N*\{1-g_1\} \qquad\qquad N_1 \le N \le N_2$$

$$\Delta R(N) = G * N_1 * g_1 + G * N_2 * g_2 + G * N * \{1 - g_1 - g_2\}; \qquad N_2 \leq N \leq N_3$$

$$..$$ (7)

$$\Delta R(N) = G * \sum_{k=1}^{L} [N_k * g_k] \qquad\qquad N_L \leq N$$

Notice that $N_1 < N_2 < N_3 < ..... < N_L$ and N vary in each of interval of $[N_k, N_{k+1}]$. Let us take a derivative of $\Delta R(N)$ with respect to N in each of (7) equalities. Then each subsequent equality can be subtracted from the preceding one. As a result one find all quantities of g_k, N_k, as well as $G(\sigma, m)$ and $M_g(\sigma.m)$. Figure 9 (a,b) and Fig.10 present the states of SE - film after both various number of cycles and value of the imposed deformation. Information entropy S

$$S = \sum_{\hat{e}=1}^{L} [g_k * Ln\, g_k].$$ (8)

is a measure of the amount of disorder (different states) in SE states.

The way mentioned above can also be used to find from experimental data (as Fig. 8) the features of the CMs, possess both the various types of grains and the various types of local structures which readily rearranged to each other at the local zones.

This model admits control of the structure mutations in both a CM and a SE after N cycles of imposed regular deformation. Fig. 9a – 9b show the regular decrease of probability g_k for modules having a big value Z_k (see (6)). For non-regular deformation there is other situation (see Fig.10). The increase of entropy S (see (8)) of SE is presented on Fig.11.

Conclusion. The various impurities in Aluminum implement the various resistance to fatigue of an Aluminum alloys' samples. The same situation one has in heterogeneous materials, that are used to form the sensitive elements (SEs) for fatigue gages [1,2]. The SEs are rigidly installed on the Aluminum alloys' samples and the same spectrum of deformation imposed on both of them. We have educed that the fatigue features of a SEs, which have a various impurities, can be reflected on each other [1].

After imposing a limit number of cycles of fatigue deformation, that change both the CM's structure and the SE's structure, the single fast cycle of deformation with selected value of amplitude is imposed on the sample. The R - ε (R – electrical resistance of SE and ε - value of imposed deformation) curve, that was automatically recorded within this fast cycle of deformation, permits one to bring out the forthcoming structures of SE and its features, that will take place at the near future cycles of imposed deformation. Reiteration of these processes also for Q^{-1} - ε curves gives the chance to do the monitoring of fatigue features of polycrystal alloys' samples .

REFERENCES

1. Shamirzaev S. (1998) MHMs FOR FATIGUE GAGE. *Published by The Iron and Steel Institute of Japan Proceedings of the 7th International conference, STEEL ROLLING'98, November, 9-11, 1998, Makuhari, Chibo, Japan, pp. 844-849.*
2. Shamirzaev S.(1999) RESPONSE OF MHFMs AT A FAST AND A SLOW OPERATIONAL LOADS. *A collection of technical papers of the 1999 AIAA/ASME/ASCE/AHS/ASC Structures, Structural Dynamics, and Materials Conference and Exhibit, St. Louis, MO, USA, 12-15 April,1999; volume 3, pp.1717-1726.*
3. Shamirzaev S. and Shamirzaeva G. (2000) THE RHEOLOGICAL MODEL OF FATIGUE DAMAGE OF CM. *Proceedings of the XIIIth INTERNATIONAL CONGRESS ON RHEOLOGY. Cambridge, United Kingdom, 20 [th] to 25th August, 2000. Published by the British Society of Rheology. Volume 3, pp. 377-379.*
4. Nicolis G., Prigogine I. (1989) EXPLORING COMPLEXITY. An Introduction. *W.H. Freeman and Company.*
5. Dubrov V.E., Levinstein M.E., Shur M.S.(1976) . *JETP, v. 70, **no**.5, p.2014.*
Grassberger P., Procassia I., (1983). *Physica, v. 9D, pp.189-208.*

THE FORMULAE OF FATIGUE CRACK PROPAGATION IN POLYMETHYL METHACRYLATE

WANG Hong, YAN Junhui and ZHENG Xiulin

Department of Material Science and Engineering, Northwestern Polytechnical University, Xi'an 710072, P.R.China

Abstract: The formula for cyclic fatigue crack propagation (fcp) of PMMA derived from the static fracture model and modified to include the critical condition of fcp was deduced in this study. The formula can be used to represent the test results of cyclic fcp of four types of PMMA in near-threshold-, intermediate- and rapid crack propagation regions well. The correlation between the fcp rate and the stress intensity factor (ΔK), the fcp coefficient (B), the fcp threshold (ΔK_{th}) and the fracture toughness (K_{1c}) was revealed in the formula. The value of fcp coefficient can be calculated by Young's modulus as $B=15.9/E^2$. So the coefficient and the parameters involved in the formula all have definite physical meaning. Therefore, the above mentioned formulae could be thought as the almost perfect formulae for cyclic fcp of PMMA. The governing parameters of fcp of PMMA are, respectively, the effective stress intensity factor ($\Delta K-\Delta K_{th}$) in near-threshold region and intermediate region, and the difference between the fracture toughness and the maximum value of stress intensity factor ($K_{1c}-K_{max}$) in rapid crack propagation region. The fcp coefficient (B) and the ratio of fcp threshold to fracture toughness ($\Delta K_{th}/K_{1c}$) are the governing parameters in intermediate region. Comparing with those of the normal PMMA, the lower fcp rate of oriented PMMA mainly results from the higher values of fcp threshold, higher fracture toughness and the smaller ratio value of fcp threshold to fracture toughness.
Key words: PMMA, fatigue crack propagation, threshold, fracture toughness

1. Introduction

The explosion accidents due to crack in the aircraft cabin cover made of PMMA exist commonly after a certain period of service of PMMA. The results of cabin outfield employing show that the no crack life-span is always difficult to be predicted because of its large scatter. On the other hand, the safe application life is always composed of fatigue crack propagation (fcp) life, which is much longer than the crack initiation life in cabin sometimes. So, for economic and reliability reason, it is very important to accurately estimate the residual life of pieces having cracks and scientifically work out the schedule of checking period for cabin. Studies have shown that the life of fatigue crack propagation (fcp) has less scatter than that of fatigue crack initiation [1]. If a formulae can well describe the behavior of crack propagation of PMMA, the problem mentioned above can be solved. So the comprehensive and valid formulae is very important for estimating the residual life of pieces having cracks. The test results of the fatigue crack propagation rates of PMMA were fitted and

expressed by using Paris' equation [2-4]. However, Paris' equation can not be used to fit the test results in near-threshold region and rapid region of the fatigue crack propagation, and the coefficient and the exponent in Paris' equation have no definite physical meaning [5]. In the present study, the test results show three regions of PMMA fatigue crack propagation and attempts are made to propose expression to fit those.

2. The materials and experiments

Four types PMMA are used in this study, i.e., two kinds of normal PMMA (type No: YB-3 and YB-4) and two kinds of oriented PMMA (type No: DYB-3 and DYB-4). The dimensions of the specimens are 400mm×100mm×10mm, and a center penetrate crack $2a_o=10\sim15$mm was prefabricated. The temperature of the test is at 23 ± 2℃, and the sine wave load with 2.5Hz frequency and 0.1 stress ratio are employed in these fcp experiments. Figure 1 and Table 1 show the test results of fcp rate with test dots and the tensile properties respectively.

3. The basic formulae introduced to describe the fcp of PMMA

Even though the fcp rates of PMMA are mach higher than that of metallic materials, but when the test results were normalized by the parameter ΔK/E(the ratio of stress intensity factor range to Young's modulus), the data of both kind of materials are scattered in almost a similar curve band [2]. On the other hand, striations were found in fatigue fracture surface of PMMA.[6] That is very similar to the ductile striation mechanism in fcp of metals. Thus, it may be also assumed that the crack propagation in PMMA occurs due to the fracture of the material elements located ahead of the crack tip, or the crack tip could not advance if the material elements ahead of the crack tip do not fracture under applied load. Based on this static fracture model for fcp in metals, the formulae introduced in this study was the expression derived by Zheng and Hirt as follows [5,8]:

$$\frac{da}{dN} = B(\Delta K - \Delta K_{th})^2 \tag{1}$$

Where ΔK$_{th}$ is the fcp threshold defined as the value of ΔK below which no fcp will occur, and B is the fcp resistance coefficient depending on the fcp mechanism and the tensile properties,

$$B = 1/2\pi\sigma_{ff}^2 \tag{2}$$

Where σ_{ff} is the effective fracture stress of the material elements ahead of the crack tip. For metals, 0.1E may be taken as the estimated value of the effective fracture stress, and if the fatigue crack propagation by ductile striation mechanism we have:

$$B = 1/2\pi(0.1E)^2 = 15.9/E^2 \tag{3}$$

E is Young's modulus. Because of the similar striation propagation mechanism is of PMMA and metal, the basic formulae mentioned above was introduced to describe the fcp of PMMA:

$$\frac{da}{dN} = \frac{15.9(\Delta K - \Delta K_{th})^2}{E^2} \tag{4}$$

From the fcp test results shown in fig.1, it can be seen that the whole fcp test dots of PMMA consist of three regions, i.e., the near-threshold region, the intermediate region and rapid crack propagation region, which are similar to those of fcp curve of metals. As it has been pointed out in Refs. [5,8], eqn. (4) can be used only to describe the fcp in near-threshold region and intermediate region, see curves in figure 1. This is because eqn.(4) does not include the upper limit of fcp, i.e., the

condition of critical propagation of fatigue crack when $K_{max} = K_{Ic}$, where K_{1c} is the fracture toughness of materials; K_{max} is applied maximum stress intensity factor.

(a)   (b)
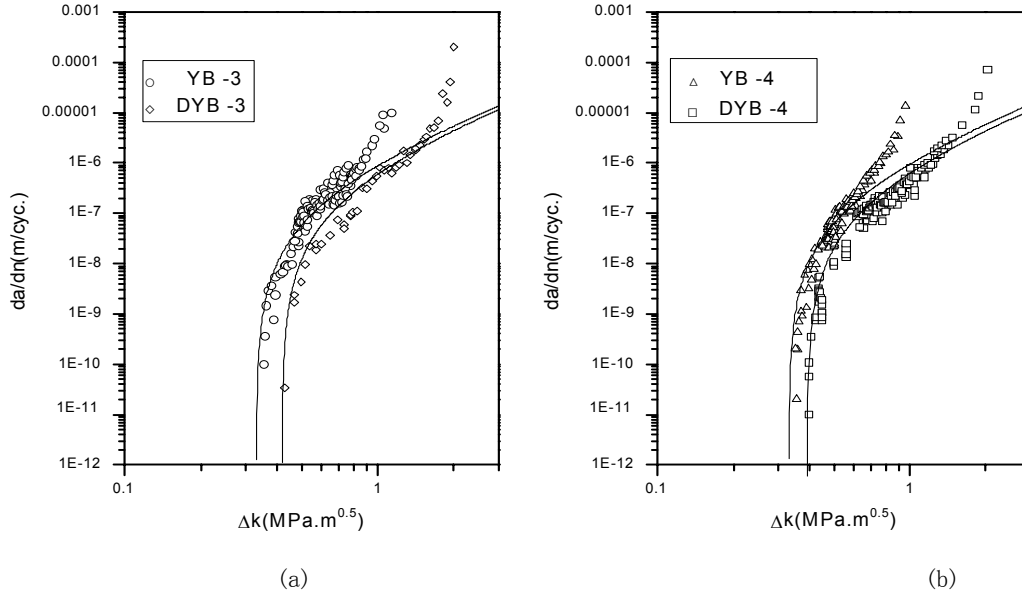
Figure 1 The Test Data of Four Types of PMMA and the Curves Obtained from Formula (4)

4. Modification to the formula

In order to enable eqn.(1) to describe the whole fcp curve of PMMA and to include the condition of critical crack propagation, eqn.(1) should be modified as follows [9]:

$$\frac{da}{dN} = B(\Delta K - \Delta K_{th})^2 f\left[\frac{K_{max} - (K_{max})_{th}}{K_{1c} - K_{max}}, \frac{(K_{max})_{th}}{K_{1c}}\right] \tag{5}$$

Where $(K_{max})_{th}$ is the fcp threshold defined as the value of K_{max} below which no fcp will occur.

Compared with the different（$K_{max})_{th}$/K_{1c} values of metals (0~0.2), ceramics (0.4~0.8) and PMMA (0.2~0.4), the slope of fcp curve is closely related with the value of（$K_{max})_{th}$/K_{1c}. So the parameter（$K_{max})_{th}$/K_{1c} should be located at the exponent place in the formula. Then we get eqn.(6):

$$\frac{da}{dN} = B(\Delta K - \Delta K_{th})^2 \left[\frac{(\Delta K - \Delta K_{th})/(1-R)}{K_{1c} - \Delta K/(1-R)}\right]^{\frac{\Delta K_{th}}{(1-R)K_{1c}}} \tag{6}$$

Where R is the stress ratio and the more details about this formulae can be found in Refs.(10). Figure 2 show the fcp curves drawn according to eqn.(6) and the test dots of test results. As it may be seen, eqn.(6) can well express the whole fcp curve of PMMA, including all three regions mentioned above, and it may be thought an almost perfect formula for fcp of PMMA.

5. Discussions

By analyzing the formula (6) and the slope of the curves in figure 2, It can be seen that:

1）the fcp rate of PMMA at near-threshold and intermediate regions are mainly controlled by the fcp coefficient (B) and the effective stress intensity factor (ΔK-ΔK_{th}). Because there is little difference of young's module (E) among different types of PMMA at room temperature, there is little difference of fcp coefficient too (B=15.9/E^2). So, the effective stress intensity factor (ΔK-ΔK_{th}) is the governing parameters of fcp in near-threshold region and intermediate

3

region of PMMA.

2） The exponent $(\Delta K_{th}/K_{1c})$ of the formula modifies the shape of whole fcp curve. The higher of the value of $(\Delta K_{th}/K_{1c})$ the shorter of the intermediate region and the higher value of the curve slope. Comparing with normal PMMA, the lower fcp rate of oriented PMMA mainly results from the smaller ratio value of fcp threshold to fracture toughness $(\Delta K_{th}/K_{1c})$ as well as the higher values of fcp threshold and higher fracture toughness.

3） Every parameter in eqn.(6) has its certain physical meaning and the dimension relation between the both sides of the equation is the same. The material constants, ΔK_{th}, K_{1c} and B（or E） are the governing factors of fcp curve of PMMA, and if the value of these constants are known, the expressions of fcp curves of PMMA can be easily obtained without experiment.

Table 1 The Values of Young's Modulus, Fracture Toughness, Crack Propagation Threshold and Fcp Coefficient

Materials	E (GPa)	K_{1c} (MPa.m$^{0.5}$)	ΔK_{th} (MPa.m$^{0.5}$)	B (MPa^{-2})
YB-3	2.9	1.25	0.33	1.89E-6
DYB-3	3.1	2.23	0.42	1.65E-6
YB-4	2.8	1.10	0.33	2.03E-6
DYB-4	3.1	2.20	0.39	1.65E-6

(a)   (b)
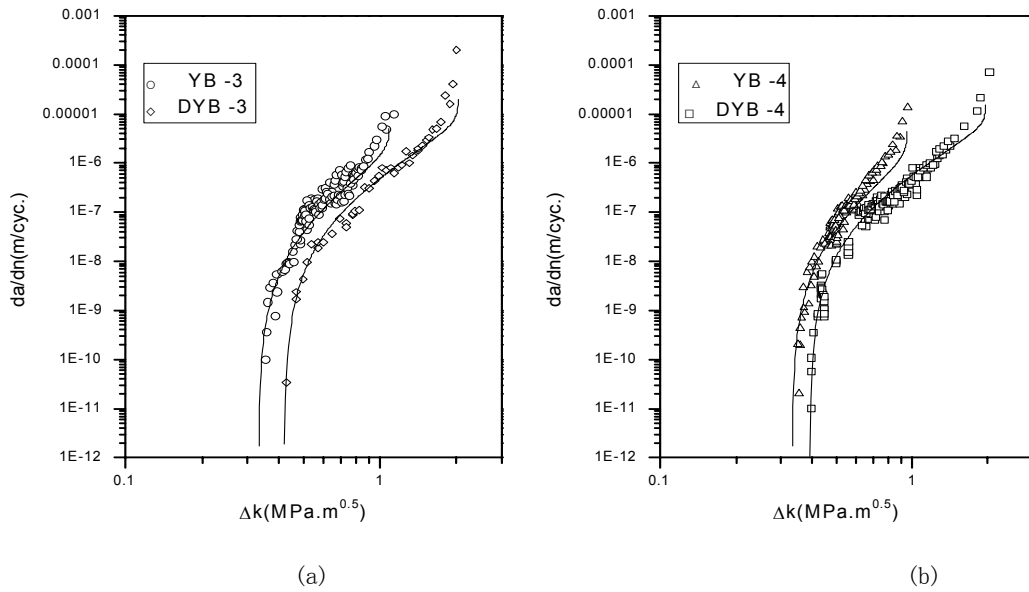
Figure 2 The Test Data of Four Types of PMMA and the Curves Obtained from Formula (6)

6. Conclusions

1） Eqn.(6) can be used to represent the test results of cyclic fcp of four types of PMMA in near-threshold-, intermediate- and rapid crack propagation regions well. This formula revealed the correlation between the fcp rate (da/dN) and the stress intensity factor (ΔK), the fcp coefficient (B), the fcp threshold (ΔK_{th}) and the fracture toughness (K_{1c}).

2） The value of fcp coefficient can be calculated by Young's modulus as B=15.9/E^2. So the coefficient and the parameters involved in the formula all have definite physical meaning. Therefore, the above mentioned formulae could be thought as the almost perfect formulae for cyclic fcp of PMMA.

3） The governing parameters of fcp of PMMA are, respectively, the effective stress intensity factor (ΔK-ΔK_{th}) in near-threshold region and intermediate region, and the difference between

the fracture toughness and the maximum value of stress intensity factor (K_{1c}-K_{max}) in rapid crack propagation region. The fcp coefficient (B) and the ratio of fcp threshold to fracture toughness ($\Delta K_{th}/K_{1c}$) are the governing parameters in intermediate region.

4）Comparing with those parameters of the normal PMMA, the lower fcp rate of oriented PMMA mainly results from the higher values of fcp threshold, higher fracture toughness and the smaller ratio value of fcp threshold to fracture toughness.

Reference

[1] Jiang Jun. The study of fatigue standard deviation and scatter factor in aviation polymethyl methacrylate. Airplane Design,1990,49(1): 50~60 (in chinese)

[2] Manson J.A., Hertzberg R.W. and Bretz P.E. Normalization of fatigue crack propagation behavior in polymers. In Advances in Fracture Research,1981,vol.1:443-448

[3] Abo-El-Ezz Aly Elsayed, Abd-El-Hakeem Hany Mohamed, Takahashi Kiyoshi. Study of fatigue crack propagation in a glassy polymer by the optical method of caustics. JSME Mechanics and Material Engineering, 1994,37 (4): 466~471

[4] Shiraishi Tetsuro, Ogiyama Hiroyuki, Tsukuda Hitoshi. Effect of compressive stress on fatigue crack propagation i n polymers. Journal of the Society of Materials Science. Japan, 1997, 46(11): 1255~1260

[5] Zheng Xiulin, M.A.Hint. Fatigue Crack Propagation in Steels. Eng. Fract. Mech., 1983,18(5)：965~973

[6] Gao Zhentong. Fatigue datum and Fracture Surface Photos of PMMA. Beijin: Science Publishing Company, 1987. 26~53 (in chinese)

[7] Lal D W, Weiss V. Metal. Trans., 1978, 9A(2)：413~416

[8] Zheng Xiulin. Mechanical model for fatigue crack propagation in metals. Handbook of fatigue crack propagation i n metallic structures. (Ed. By A. Carpinteri), Elsevier Science B V, 1994. 363~396

[9] J.K. Forman, V.E. Kearney, and R.M. Engle, Numerical Analysis of Crack Propagation in Cyclic Loaded Structures. J. Basic Engng(ASME), 89,459-464(1967)

[10] WANG Hong, YAN Junhui and ZHENG Xiulin, Formulae and Governing Parameters of Fatigue Crack Propagatio n in Polymethyl Methacrylate. ACTA AERONAUTICA ET ASTRONAUTICA SINICA, 2001, 22(1):83~86(in chinese)

THE FRACTURE OF GEOPOLYMERS

F. J. Silva and C. Thaumaturgo

Material Science and Mechanics Engineering Department(DE/4), Militar Engineering Institute (IME)
Pç. Gal. Tibúrcio, 80, Praia Vermelha, CEP 22290-270, Rio de Janeiro, RJ, Brazil.
e-mail: imes4cle@epq.ime.eb.br

ABSTRACT

The alkaline activation of Portland cement based composites, granulated blast-furnace slag and pozzolans opens new opportunities for the manufacture of special cements with properties different from those presented by the ordinary Portland cement.

In this work, a polymeric inorganic cement based on metakaolin, of early-high compressive strength and curable at room temperature called geopolymer[1], was obtained and the mechanical strengths were evaluated.

In order to stabilize the geopolymer cement matrix and improve its fracture toughness, micro-fibers of natural wollastonite were used in volumes from 0 to 5%. The methodology used was based on the non-linear fracture mechanics, developed for quasi-brittle materials[2]. The properties of fracture toughness, represented by the G_I^s curves, the fracture parameters K_{Ic}^s and $CTOD_c$ as well as the compressive, flexural strength and indirect tensile strength were evaluated and compared with those of a reference Portland cement composite with the same volumes of fibers.

The addition of wollastonite micro-fibers as stabilization elements and reinforcement yielding satisfactory results as to the improvement of the mechanical properties of the geopolymer cement composites. The results showed that the wollastonite micro-fibers are compatible with the alkaline matrix and develop a interfacial transition zone (matrix/fiber) as dense as the matrix. Toughness increase (K_{Ic}^s and $CTOD_c$) of the order of 26%, obtained for a fiber volume of 2%, were considered significant, when compared with the 8% gain obtained in the Portland cement composite. The effective critical crack extension (Δa_c) also showed a significant improvement. All the other mechanical properties were optimized, including the compressive strength, with addition of wollastonite.

keywords: geopolymer, nonlinear fracture mechanics, composite.

INTRODUCTION

The geopolymers, also called poly(sialate)s, are a new family of materials based on the oxide-aluminosilicates (pozzolans) polymerization, obtained by a similar process to that employed in the synthesis of crystalline zeolites [1]. The process consists of the hydrothermal polymerization of the pozzolan in a highly alkaline environment (pH ~14). The time of reaction depends on the processing temperature and of the radiation frequency used [2].

Depending on the Si/Al ratio, it is possible to obtain products with different characteristics. A 3D arrangement, with cross-linked bonds is formed when the Si/Al ratio is the equal or higher than 2. The polymeric mineral with those atomic ratios is called poly(sialate-siloxo), or PSS, and can be used a binder material in high-performance concretes and mortars [3].

When materials rich in amorphous silica (pozzolans) are added to the Portland cement, they react with the $Ca(OH)_2$, liberated during the formation of C-S-H by the hydration of C_3S and βC_2S, generating an extra production of C-S-H, even so, with more larger Si/Ca ratio. The consumption of $Ca(OH)_2$ and the extra formation of C-S-H, increase the matrix density and it contributes to the maintenance of a lower pH and therefore, more stable[3]. Even so, these alterations in the matrix increase its sensibility to such sharp defects as internal microcracks. Several researchers reveal that when reinforcement elements in the form of fibers are incorporated in the matrix, notable improvement in toughness is obtained.

In the case of the PS, countless microcracks are formed in the matrix due to the gradient of tensions generated during the polymerization. The employment of mineral fillers, in the form of fine particles minimizes those effects. In mortars and concretes, the stabilization can be associated to the reinforcement of the matrix, when particles in form of fibers are incorporate.

The RILEM Technical Committee 89 – Fracture Mechanics of Concrete – Test Methods[4], recommends the employment of the two-parameter fracture model (TPFM) based on the studies of Jeng and Shah[5] for determination of the fracture toughness of quasi-brittle materials such as mortars and concretes. The model considers the elasto-plastic deformations happening ahead of the tip of a macrocrack induced by a notch. The unloading compliance (C_u) measure in the unloading at 95% of the maximum load (post-peak load) in diagrams Load versus CMOD (crack mouth opening displacement) it allows the determination of the fracture properties of the material, indicated by the critical stress intensity factor (K_{Ic}^S), the critical crack tip opening displacement ($CTOD_c$) and the critical crack effective extension, $\Delta a_c = (a_c - a_0)$. The compliance in the initial loading (C_i) it supplies the modulus of elasticity (E) of the composite. The results obtained were used to calculate the deformation energy release rate (G_I^S).

This work presents a study of the fracture toughness of a mortar composite of PSS cement matrix with ratio Si/Al = 3, reinforced with natural wollastonite ($Ca[SiO_3]$) micro-fibers, a natural mineral of high modulus of elasticity (120 GPa) and aspect ratio (10-20) employed in the ceramic industry as a reinforcement and stabilization element. The volumes of fibers studied were of $V_f = 0\%$ (pure matrix) at $V_f = 5\%$. The fracture parameters were measured and compared with the results obtained with the Portland cement mortar composites.

MATERIALS AND METHODS

In order to obtain PSS, the main source of aluminum and silicon was the metakaolin obtained by the kaolin calcination from Rio Grande do Norte (RN), Northeast of Brazil. The time and the temperature of calcination were objects of initial study, because they depend on the purity and of the degree of crystallinity of the kaolin. The calcination to 12 hours at 700 ^{o}C promote the desidroxilation of the kaolinite and the conversion of aluminum coordination number from VI to IV, disordering the lattice. Since the ratio between the silicon and the aluminum in the metakaolin is smaller than 3, an extra source of silicon, a commercial alkaline polysilicate was used. With the purpose of obtaining the necessary pH of 14, to initiate the polymerization, potassium hydroxide (Vetec P.A.) was also used as a complementary alkali source. The calcium source was granulated blast furnace slag (GBFS) supplied by Belgo Mineira S.A. In this work, the geopolymer studied was the sodium, potassium and calcium poly(sialate-siloxo), Na,K,Ca-PSS.

The reference Portland cement was the CPIIE-32 (type II of ASTM C 150), of marks Campeão/Mauá and the fine aggregate was the river sand supplied by IPT S.A. (Normal Brazilian sand). The proportion between binder and aggregate was 1:3, in weight for all the composites and the water/binder dry was 0,48 for the Portland cement composite and 0,38 for the PSS composite. The consistency index (flow table - ASTM C 230) for both composites it was of 165 $\pm$ 5 mm , with $V_f = 0\%$.

The wollastonite used was the NYAD-G$^®$ grade (Figure 1) of Nyco Minerals Inc. (New York - USA). The Table 1 shows the main characteristics of the raw materials used in this study.
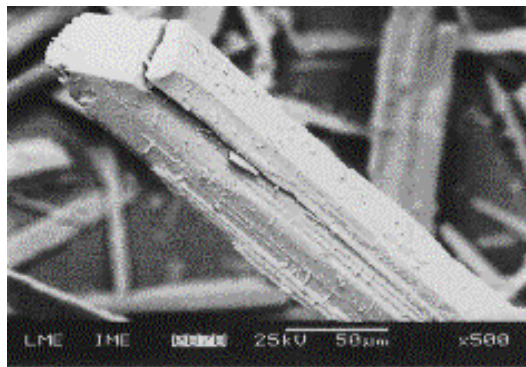
Figure 1 – Micrograph (SEM) of wollastonite micro-fibers used (500 X).

Table I – Chemical composition and physical properties.

Materials	Chemical Composition (%)									L.O.I.	Specific Area Blaine	Specific Weight
	CaO	MgO	Na$_2$O	K$_2$O	Fe$_2$O$_3$	SO$_3$	Al$_2$O$_3$	TiO$_2$	SiO$_2$	(%)	(m^2.Kg^{-1})	(g .cm^{-3})
Metakaolin	< 0,01	0,01	0,04	0,33	0,30	-	39,8	0,11	44,4	14,4	1060,76	2,56
Na-Silicate	-	-	17,3	-	-	-	-	-	35,6	44,3	-	1,75
GBFS	47,8	0,63	0,21	0,26	0,72	0,47	13,0	0,38	39,7	0,14	345,43	2,98
Wollastonite	46,55	0,15	0,01	0,05	0,75	-	0,28	0,04	51,37	0,34	-	2,90
CPIIE-32	60,4	1,4	-	-	1,6	3,9	5,0	-	20,0	6,30	349,92	3,04

Strength Activity Index (ASTM C 618) of pozzolan $\varnothing$ < 0,074 mm = 107,88%.
% Retained in the sieve # no. 325 Tyler-Mesh = 12,35%.
Aspect ratio of wollastonite: 10 to 20.
CPIIE-32 – Bogue composition (ASTM C 150): 46,60% C$_3$S; 22,18% βC$_2$S; 10,54% C$_3$A; 4,87 C$_4$AF.

The mixture of the basic constituent and the moldings of the specimens followed the procedures described in the NBR 7215 Brazilian standard. The wollastonite was dispersed in the water before mixing with other materials. Cylindrical test specimens of ($\varnothing$10x20)cm for compressive strength (ASTM C 39) and splitting test (ASTM C 496) were moulded. To determination of the fracture toughness, the procedures established by TC-89 FMT of RILEM were adopted as already mentioned. The dimensions of the test specimens of toughness and the experimental configuration are shown in the Figures 2 and 3. The Na,K,Ca-PSS cement composites was cured to the air at 25 $\pm$ 2 $^{\circ}$C, and the Portland cement composites was cured immerged in water at 22 $\pm$ 2 $^{\circ}$C until the date of the tests. The G_{Ic}^s values were calculated based on relationship:

$$G_{Ic}^s = \frac{\left(K_{Ic}^s\right)^2}{E}$$

and G_I^s curves were obtained as function of Δa by interation.

After determination of the mechanical properties, samples of pastes and mortars were selected for scanning electron microscopy (SEM – Jeol 5800 LV) to identify the failure mechanisms.
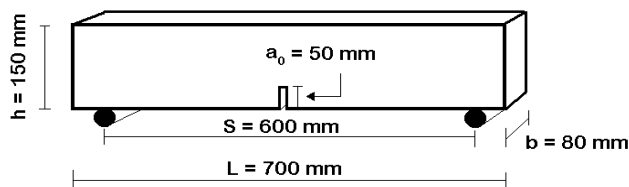
Figure 2 – Geometry and dimensions of the beams tested under 3-point bend.
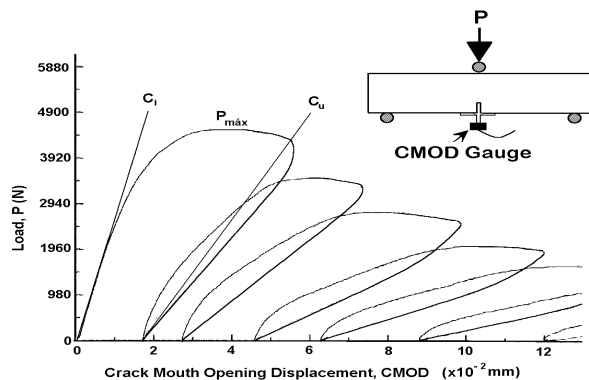
Figure 3 – A typical Load versus CMOD curve obtained from 3-point bend tests. The maximum load (P_{max}), initial compliance (C_i) and unloading compliance (C_u) are obtained from the graph and used as input for the TPFM.

RESULTS AND DISCUSSIONS

The Figures 4 and 5 show the results of characterization of the two matrices studied. The results reveal that the microstructure of the poly(sialate-siloxo) cement is formed by phase of sodium, potassium and calcium aluminosilicate - Na,K,Ca-PSS, without any traces of $Ca(OH)_2$, commonly present in the Portland cement matrix.
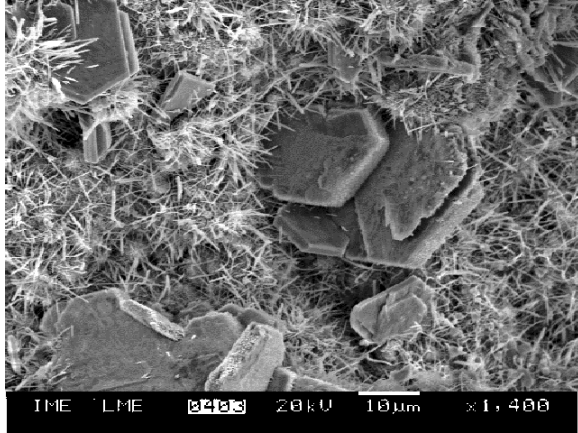
Figure 4 – Micrograph (SEM) of Portland cement composite bulk matrix (1400X). The big polygonal phases are $Ca(OH)_2$ crystals and the needle-like crystals are C-S-H particles.
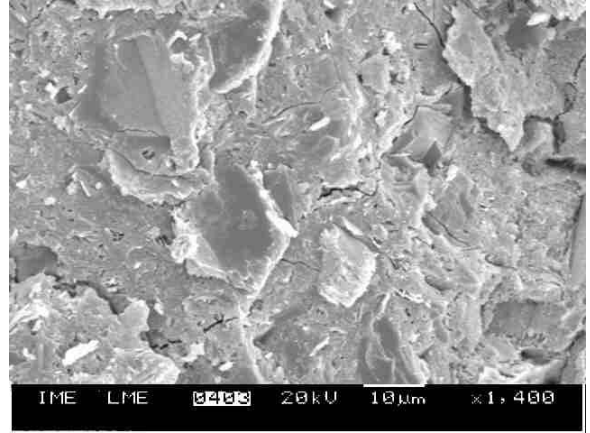
Figure 5 – Micrograph (SEM) of Na,K,Ca-PSS cement composite bulk matrix (1400X). Note as the microstructure is homogeneous and dense, but with microcracks.

The compressive strength tests results of normal mortar of cement CPIIE-32 and of cement Na,K,Ca-PSS specimens, without fiber reinforcement ($V_f = 0\%$), as function of age are shown in the Figure 6. When the Na,K,Ca-PSS is cured at 65 ^{o}C to 4 hours, it reaches an early compressive strength of 45 MPa. This same strength level is reached at three days of age, when the cure is realized at room temperature. At 28 days of age, a compressive strength of 60 MPa is reached, largely overcoming the Portland cement mortar.

Figure 7 shows the flexural strength and splitting tests results at 28 days of age, as a function of fibers volume. It can be noted that the optimum fiber volume and that presents the best results was of 2%. Above this value, there was strength reduction due to what may be an increase of mixture porosity, since the water/binder ratio stayed constant and chemical admixture was not used.

The Figures 8 and 9 show the results obtained in the three-point bend beam tests, for determination of modulus of elasticity (E) and of the toughness properties (K_{Ic}^{s}, $CTOD_c$ and Δa_c).
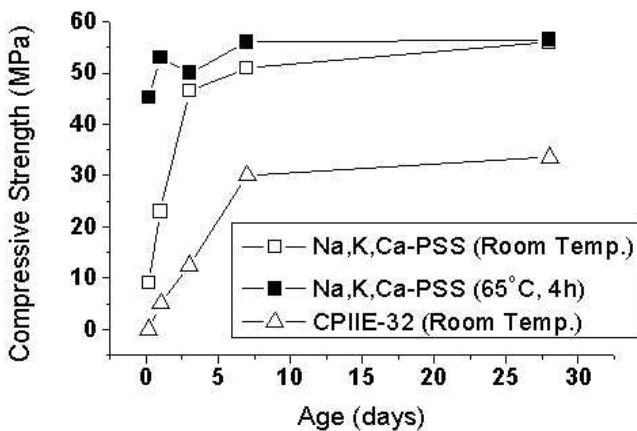
Figure 6 – Compressive strength of poly(sialate-siloxo) composite matrix and Portland cement composite matrix as function of the time and temperature.
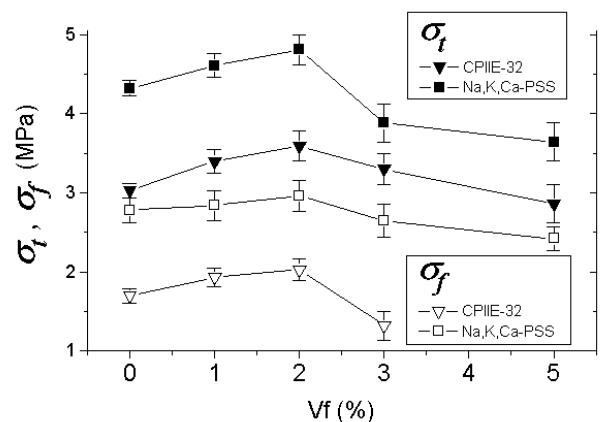
Figure 7 – Variation of tensile and flexural strengths as function of fiber volume. (at 28 days of age)

As shown in Figure 8, in both composites, K_{Ic}^s values increased until 2%. The toughness increase was of 26% to PSS composite and 8% to PC cement. The $CTOD_c$ values always growing with fiber addition. In the Portland cement composites, the $CTOD_c$ values decreased up to $V_f = 2\%$. Only to $V_f = 3\%$ that there was improvement of $CTOD_c$, however the values were low than the matrix with $V_f = 0\%$. Here is noted the importance of determination of two fracture parameters, because with only one these means, a equivocal can be performed in quasi-brittle materials toughness analysis. The addition up to 2% increased the modulus of elasticity to both composites system. However, above this fiber volume, there was decrease of E values, probably due the excessive porosity of the mixture.
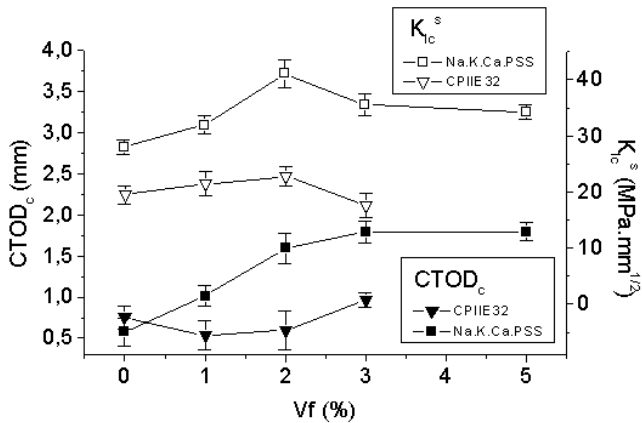
Figure 8 – Variation of $CTOD_c$ and K_{Ic} as function of fiber volume.
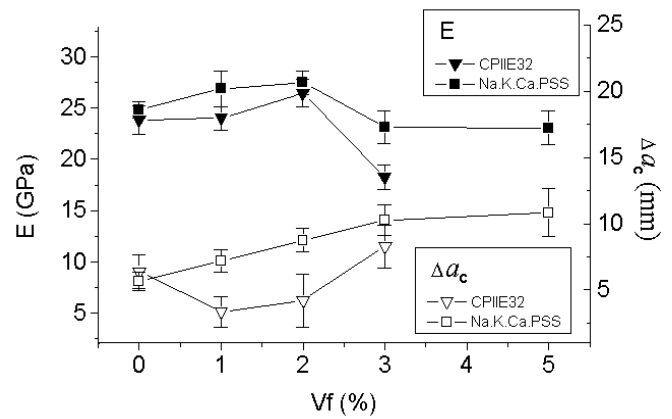
Figure 9 – Variation of modulus of elasticity and critical crack effective extension as function of fiber volume.

The critical effective crack extension increased to all fiber volume in the PSS cement composites. However, in the Portland cement composites, was observed a decrease in Δa_c to $V_f = 1$ and 2 %. These results indicates different actuation of wollastonite micro-fibers, depending of composite matrix. The G_I^s values obtained by PSS composites show its high performance. The fracture toughness determined by G_{Ic}^s for PSS was 100% higher than to presented by PC, for all fiber volumes, as shown in Figures 10 and 11.
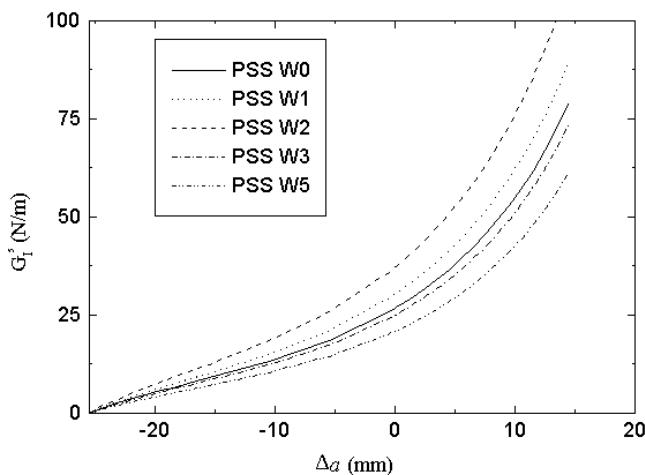
Figure 10 – Variation of deformation energy release rate, G_I^s as function of effective crack extension, Δa to PSS geopolymer cement with $V_f = 0\%$ to 5%.
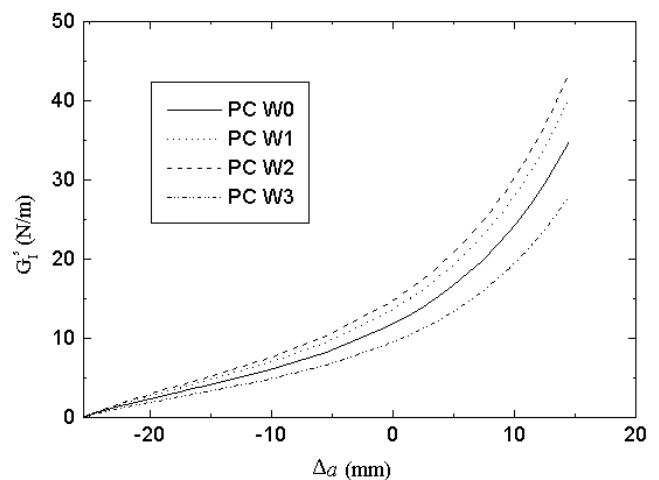
Figure 11 – Variation of deformation energy release rate, G_I^s as function of effective crack extension, Δa to CPIIE-32 Portland cement with $V_f = 0\%$ to 3%.

The Figure 12 shows a micrograph (SEM), obtained by secondary electrons of the fracture surface of the PSS composite. To notice the presence of fibers broken in traction in the level of the fracture surface and other, had gone pull-out of matrix. Figure 12 shows a micrograph (SEM) obtained by backscattering electrons of the polished surface, revealing the change happened in the crack trajectory when intercepting the

fiber. These observed mechanisms are the main ones responsible for the increasing of toughness of the material. The critical crack effective extension (Δa_c) increased 50% in PSS composite with $V_f = 2\%$. In Portland cement composite, increasing occurs of 10% in Δa_c only occurs with at $V_f = 3\%$.
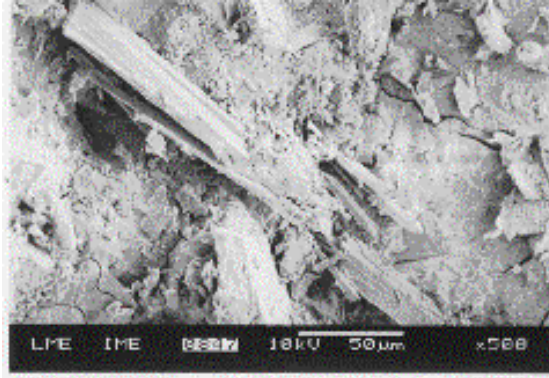
Figure 10 – Micrograph (SEM) of Na,K,Ca-PSS cement composite with 2% of wollastonite micro-fibers (500X).
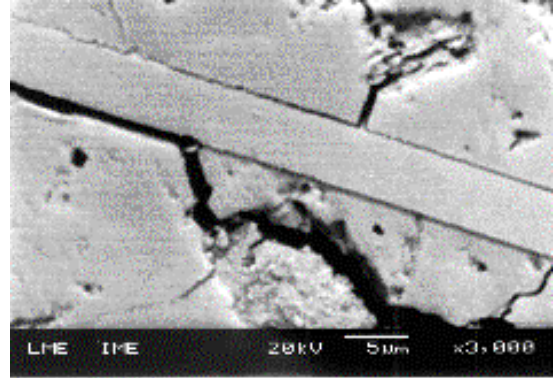
Figure 11 – Micrograph (SEM) of Na,K,Ca-PSS cement composite fracture surface polished. Note as the crack trajectory is modified by fiber (3000X).

CONCLUSIONS

The addition of wollastonite micro-fibers as reinforcement elements, supplies satisfactory results as the improvement of the mechanical properties of the geopolymeric composite type Na,K,Ca-PSS. The results reveal that the wollastonite micro-fibers present total compatibility with the alkaline matrix (pH = 13) and, they develop a interfacial transition zone (matrix/fibre) that is as dense as the bulk of the matrix. Increases of fracture toughness (K_{Ic}^{s} and $CTOD_c$) of the order of 26% to $V_f = 2\%$ were registered. The critical crack effective extension (Δa_c) also showed a significant improvement. The G_I^{s} curves calculated by K_{Ic}^{s} and $CTOD_c$ values showed the high performance of geopolymeric composites, always 100% higher the Portland cement composites to all fiber volumes. The other mechanical properties too were optimized with addition of wollastonite, including the compressive strength.

References

1 – Davidovits, J.. Geopolymer'88, Vol. 1, 6, (1988)
2 – Davidovits, J.. J. Thermal Analysis, 27, 1633-1656 (1991)
3 - Neville, A.; Aïtcin, P-C. Materials and Structures, 31, 111-117 (1998)
4 - RILEM - TC89-FMT. Materials and Structures. 23, 457-460, (1990)
5 -Jeng, Y.; Shah, S.P.. Journal of Engineering Mechanics. 11 (10), 1227(1985)

THE FRACTURE TOUGHNESS OF SOME METAL MATRIX COMPOSITES - COMPARISON OF TECHNIQUES

G. L. Heness[1] and Y-W Mai[2,3]

[1] Department of Chemistry, Materials & Forensic Science, University of Technology, Sydney, PO Box 123, Broadway, NSW, 2007, Australia
[2] Centre for Advanced Materials Technology, University of Sydney, NSW, 2006, Australia
[3] MEEM, City University of Hong Kong, Tat Chee Avenue, Kowloon, Hong Kong

ABSTRACT

The ability to measure plane strain fracture toughness on small specimens, such as biomaterials and developmental alloys, and on materials that do not lend themselves to fatigue pre-cracking is becoming increasingly important, especially with the profusion of "advanced" materials now being developed. The short rod and short bar chevron notched specimens address this. This paper looks at the correlation between valid K_{Ic} data and short rod fracture toughness (both K_{Iv} and K_{Ivm}) for a series of metal matrix composites. It is shown that the relationship between these values form part of a family of curves that exist for monolithic alloys. The relationship appears to be independent of the use of maximum or critical load values in the calculation of short rod fracture toughness.

KEYWORDS

Metal matrix composites, chevron notch fracture toughness, short rod fracture toughness

INTRODUCTION

In 1977 Barker [1] proposed the short-rod specimen for determining plane strain fracture toughness and this has since been extensively studied. Since then Barker made considerable progress in developing the parameters behind chevron notch fracture toughness [2] testing and in 1978 [3,4] proposed a rectangular cross-section specimen (short bar).

During the early 1980's a number of investigators, for example [5, 6, 7] worked on analysing the chevron notch geometry with a good review of the work until 1984 given by Newman[8]. In 1992, the

original analysis was revisited [9]. Much of the work was concerned with comparing fracture toughness measurements with plane strain fracture [10].

The first standard for short rod and short bar specimens, despite the title, was introduced into the ASTM standards in 1987: ASTM B771-87, "Short Rod Fracture Toughness of Cemented Carbides". In 1989, ASTM E1304-89, "Plane Strain (Chevron-Notch) Fracture Toughness of Metallic Materials" was introduced. Due to the fact that this method makes use of a steady state slowly moving crack as opposed to the start of crack extension from a fatigue precrack (ASTM E399), K_{Ic} cannot be used and K_{Iv}: is used to denote the plane strain (chevron-notch) fracture toughness

The lack of a need for fatigue pre-cracking allows for simpler testing procedures. This has resulted in a large variety of materials being tested using this technique for a number of materials [11]. For example poly(methylmethacrylate), (PMMA); polystyrene; polysulphone and polycarbonate [12], silicon nitride and [13], commercially available aluminas [14], a number of biomaterials [15, 16], dental amalgams [17]M-50 bearing steel, alumina, silicon carbide, monolithic silicon nitride and in situ toughened silicon nitride [18] and delamination fracture toughness of several unidirectional, continuous reinforced graphite/epoxy and graphite/PEEK polymer matrix composites [19]. The last four here were tested using modified specimen geometries. Bond strength of thermal barrier coatings [20] and interface toughness of dentin-composites [21], even multiyear sea ice [22], have all had their fracture toughness measured using this technique.

EXPERIMENTAL PROCEDURE

Three types of metal matrix composites (MMCs) were investigated.
- Comral 85, nominally 20 vol% spherical ceramic particles
- Duralcan 20, nominally 20 vol% irregular shaped alumina particles
- Duralcan 10, nominally 10 vol% irregular shaped alumina particles

The matrix was a 6061 aluminium alloy for all MMCs.

The compact tension specimen data were supplied by Hardianfard [23]. All specimens were fatigue pre-cracked and tested in accordance with ASTM 399 Plane-Strain Fracture Toughness of Metallic Materials and the measured fracture toughness is referred to as "K_{Ic}".

The chevron notch specimens were tested in accordance with ASTM E1304-89 Plane-Strain (Chevron-Notch) Fracture Toughness of Metallic Materials and the measured fracture toughness is referred to as "K_{Iv}".

RESULTS

The data obtained for the MMCs via ASTM E399 (compact tension specimens) and ASTM 1304 (short rod geometry) are given in Table 1. A range of fracture toughness values was obtained through heat treatment of these age hardenable materials. The terms UA, PA and OA refer to under-aged, peak-aged and over-aged tempers respectively.

There is good agreement between the values obtained from pre-cracked CT specimens and chevron-notched short rod specimens with an average difference of 3.7%. The short rod results generally fell below the values obtained from compact tension specimens.

TABLE 1

FRACTURE TOUGHNESS VALUES OBTAINED FROM SHORT ROD (K_{IV}) AND COMPACT TENSION (K_{IC}) GEOMETRIES.

Material	Temper	K_{Iv} MPa√m	K_{Ic} MPa√m
Duralcan 0%*	PA	-	30
Duralcan 10%	UA	25.7±0.3	26.1±0.3
	PA	23.1±0.3	24.2±0.6
	OA	21.3±0.1	22.0±0.7
Duralcan 20%	UA	24.4±0.5	23.6±0.2
	PA	21.8±0.3	22.8±0.2
	OA	19.7±0.2	21.7±0.9
Unreinforced COMRAL-85 alloy	PA	-	27
COMRAL-85	UA	19.6±0.6	19.0±0.4
	PA	19.0±0.6	18.7±0.6
	OA	17.9±0.2	18.4±0.5

* Data from Duralcan Composites Mechanical and Physical Property Data Sheet, 1990.

For sufficiently brittle materials it has been shown that the short rod result, K_{Iv}, is numerically equal to K_{Ic} [6]. There is a possibility that although there is some good agreement between K_{Ic} and K_{Iv}, the chevron-notched specimen can give a non-conservative measure of toughness when rising R-curve behaviour occurred or there is sample heterogeneity. Marschall et al. [24] found that chevron-notched specimens consistently gave results 18% higher than K_{Ic}. They attributed this to the difference in crack extension in the two specimen geometries and not to any metallurgical differences.

The body of statistical comparisons of K_{Iv} and K_{Ic} are for high strength aluminium alloys. As an example, when differences from metallurgical heterogeneity were removed from the results for a series of high strength heat-treatable aluminium alloys good correlation was found between K_{SB} and K_{Ic}. For a variety of alloys and tempers Brown reported [196]:

$$K_{SB} = 1.017(\pm 0.014) \, K_{Ic} \qquad (1)$$

for values of K_{Ic} up to 40.7 MPa√m, where K_{SB} is the fracture toughness obtained form the short bar geometry.

Re-arranging Brown's relationship to give

$$K_{Ic} = 0.983(\pm 0.014) \, K_{SB.} \qquad (2)$$

Using the same data compilation technique as Brown a good fit with his relationship is achieved and is shown in Figure 1. The slope of the resultant curve for the data in this study results in

$$K_{Ic} = 0.985 K_{Iv}. \qquad (3)$$

This compares well with the reported relationship of Brown.
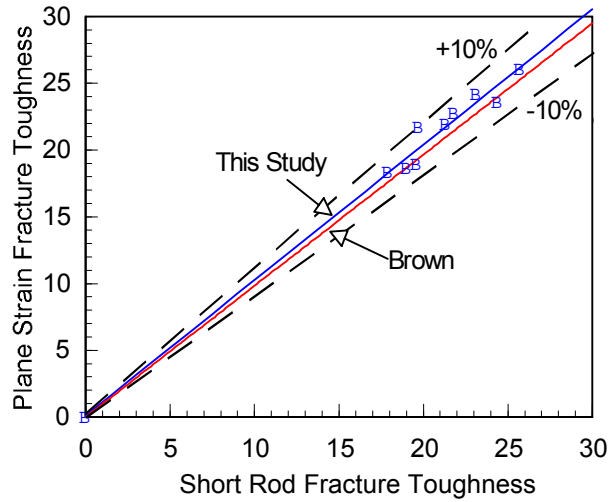
Figure 1. Relationship between K_{Iv} and K_{Ic} for the materials in this study compared to Brown's relationship for a series of aluminium alloys.

Examination of Brown's graphs show that the curve tends to level off at values of fracture toughness above ≈ 35 MPa√m. This may be the reason that the slope obtained for that data is lower than the slope obtained for the MMCs whose maximum value is <30 MPa√m. Despite this reasonable agreement is obtained for the two sets of data.

Other investigators have also tried to develop a relationship to predict K_{Ic} values from short rod or short bar data. These have been based on the calculation of short bar toughness from maximum loads. For example, Bray investigated the use of K_{Ivm} to predict K_{Ic} for a series of aluminium alloys, tempers and orientations in the toughness range of 24-95 MPa√m. Using a linear regression the following relationship was found:

$$K_{Ic} = 0.681(K_{Ivm}) + 9.259 \ (R^2 = 0.929) \tag{4}$$

Using the short rod fracture toughness data calculated from maximum load the following relationships were obtained for the data in this study:

$$K_{Ic} = 0.75 K_{Ivm} + 5.3 \ (R^2 = 0.814) \tag{5}$$

The Comral-85 short rod specimens had a a 2mm wide particulate rich zone was observed running through the centre, parallel to the extrusion direction, of each specimen and represented some 30% of the crack front width at the critical crack length. This resulted in the temper having little effect on the measured fracture toughness. This has been attributed to the cause of the Comral-85 specimens, in general, having a higher K_{Iv} than K_{Ic} as opposed to the Duralcan materials [11].

If the Comral-85 composites are disregarded due to their inhomogeneity, the Duralcan composites provide a relationship:

$$K_{Ic} = 0.687 K_{Iv} + 7.83 \ (R^2 = 0.85) \tag{6}$$

which compares reasonably well with that obtained by Bray for aluminium alloys. The larger difference for the Bray analogy and the lower correlation coefficient is due to the use of K_{Ivm}, fracture toughness based on maximum load, and indicates the value of the validation checks in K_{Iv} determinations.

None-the-less, if the gradient for each of the relationships found in this and previous studies is plotted against the respective y-intercept a linear relationship of:

$$Y = -26.69G + 26.8 \tag{7}$$

(where Y = y-intercept and G= gradient of the K_{Ic} versus K_{Iv} or K_{Ivm} curves) is obtained suggesting that Y and G for these composites form part of a family of curves that exist for monolithic alloys, as opposed to parallel shifts that might have existed and is shown in Figure 3.
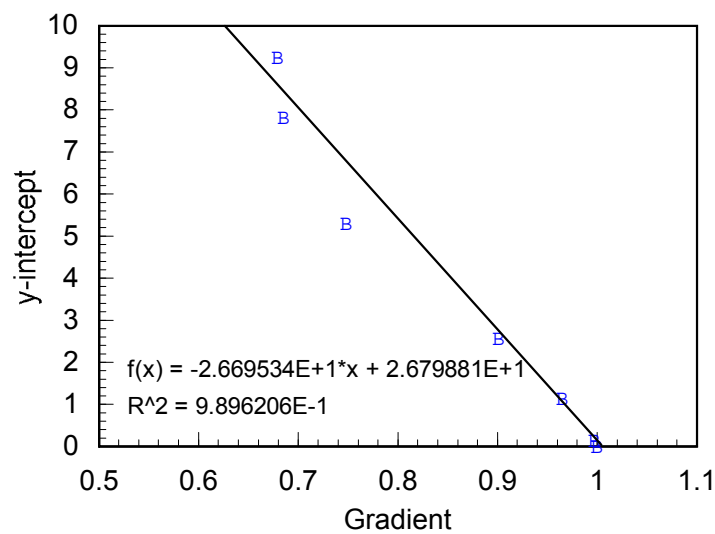
Figure 3. Correlation between gradient and y-intercept for the relations of this study and others.

This relationship appears to be independent of the use of maximum or the critical load to calculate fracture toughness for the chevron-notched specimens. It can be seen that the maximum load values, the first two on the graph, do suffer from the lack of validity checks. For values using K_{Iv} a very good fit is observed.

CONCLUSION

The ability to measure the plane strain fracture toughness of a material in a less expensive manner than generated by ASTM E 399, Standard Test Method for Plane Strain Fracture Toughness of Metallic Materials has been of interest since the 1960's. Most notable of these is the notched tension test, however, there is generally poor correlation with K_{Ic}. Unlike this test the chevron-notched test provides a relative measure of the plane strain fracture toughness.

ACKNOWLEDGEMENTS

REFERENCES

1   Barker, L.M., (1977). *Eng. Frac. Mech.,* 9, 361.
2   Barker, L.M., (1979). *Int. J. Fract*., 15, 515.
3   Barker, L.M., (1979). In: *ASTM STP 678, Fracture Mechanics Applied to Brittle Materials*, pp. 73-82.
4   Barker, L.M., (1983). *Eng. Frac. Mech*., 17, 289.
5   Munz, D., Bubsey, R.T. and Srawley, J.E., (1980). *Int. J. Frac.,* 16, 359.
6   Beech, J. F. and Ingraffea, A.R., (1982) *Int. J. Frac.,* 18, 217
7   Raju, I. and Newman, J., (1984). In: *ASTM STP 855,* Underwood, J.H., Freiman, S.W. and Baratta, F.I., (Eds). American Society for Testing and Materials, Philadelphia*., pp. 32-48.
8   Newman, Jr. ,J.C. (1984). In: *ASTM STP 855,* Underwood, J.H., Freiman, S.W. and Baratta, F.I., (Eds). American Society for Testing and Materials, Philadelphia.
9   Yin, X. and Chen, T., (1992). *J. Test. & Eval*., 20, 239.
10   Barker, L.M. and Baratta, F.I., (1980). *J. Test. and Eval*., 8, 97.
11   Heness, G. L. (1996). PhD Thesis, University of Sydney, Australia
12   Watson, T., Jolles, M., Peyser, P. and Mostovoy, S., (1987). *J. Mater. Sci*., 22, 1249.
13   Salem, J.A. and Shannon, Jr., J.L., (1987). *J. Mater. Sci*., 22, 321.
14   Barker, L., (1978). In: *Fracture Mechanics of Ceramics*, 3, pp. 483-494,
15   Pilliar, R.M., Vowles, R. and Williams, D.F., (1987). *J. Biomed. Mater. Res*., 21, 145.
16   Wang, C.T. and Pilliar, R.M., (1989). *J. Mater. Sci*., 24, 3725.
17   Mueller, H., (1992). In: *Chevron-Notch Fracture Test Experience: Metals and Non-Metals, ASTM STP 1172*, Brown, K. and Baratta, F., Eds., American Society for Testing and Materials, Philadelphia, pp. 74-88.
18   Salem, J., Shannon, Jr., J. and Jenkins, M., (1992). In: *Chevron-Notch Fracture Test Experience: Metals and Non-Metals, ASTM STP 1172*, Brown, K. and Baratta, F., Eds., American Society for Testing and Materials, Philadelphia, pp. 9-25.
19   Lucas, J., (1992). In: *Chevron-Notch Fracture Test Experience: Metals and Non-Metals, ASTM STP 1172*, Brown, K. and Baratta, F., Eds., American Society for Testing and Materials, Philadelphia, pp. 74-88.
20   Jordan, E., Gell, M. Pease, D., Shaw, L., Clarke, D., Gupta, V., Barber, B., Vaidyanathan, K., (1997), Am. Soc. Mech. Eng. ASME, New York, NY,
21   Tam, L.E. and Pilliar, R.M., (2000). *J. Dentistry*, 28, 487.
22   Sammonds, P.R., Murrell, S.A.F. and Rist M.A., (1998). *J. Geophysical Res.-Oceans*, 103(C10) 21795.
23   Hardianfard, J., Personal Communication
24   Marschall, C., Held, P. and Dolan, F., (1992). In: *Chevron-Notch Fracture Test Experience: Metals and Non-Metals, ASTM STP 1172*, Brown, K. and Baratta, F., Eds., American Society for Testing and Materials, Philadelphia, pp. 144-156.

THE HIGH TEMPERATURE FATIGUE OF A NICKEL-BASE SUPERALLOY : THE INFLUENCE OF WAVEFORM VARIABLES

D.M. Knowles* and D.K. Skelton*

*Department of Materials Science and Metallurgy, University of Cambridge,
Cambridge, UK, CB2 3QZ

ABSTRACT

The drive for improved understanding of turbine disc alloys at elevated temperatures has led to an increased interest in the contribution of time-dependent mechanisms to high temperature fatigue crack growth. A study has been conducted on a new powder disc alloy to investigate the contribution of these mechanisms when the applied waveform is varied in terms of ramp rates and hold periods. Variable waveform tests performed in air and vacuum at 725°C have indicated that the hold period at maximum load causes the greatest acceleration in growth rate. In air, the ramp up is slightly more damaging than the ramp down and it is suggested that this is due to a fatigue/environment interaction. In vacuum no difference between ramp up and ramp down is observed, but at low stress intensity, a hold at minimum load was observed to cause retardation in crack growth, which may be attributable to either a blunting or crack tip annealing process. An extension of the duration of the hold at maximum load was observed to cause an acceleration in crack growth but not to induce intergranular cracking. It is suggested that the effects may be attributed to the influence of creep on the crack growth process. The linear summation model was shown to accurately predict growth rates in air but to over predict in vacuum.

KEYWORDS

High temperature, fatigue crack growth, nickel superalloy, waveform, vacuum

INTRODUCTION

The drive for improved gas turbine engine performance has led to an increase in the required temperature capability of the turbine disc alloys namely the polycrystalline nickel-base superalloys. As operation temperatures increase, time-dependent mechanisms begin to contribute to the fatigue crack growth process and growth rates per cycle (da/dN) increase.

The environment is well known to have a significant effect on the growth rate of fatigue cracks through polycrystalline nickel base superalloys, especially at lower frequencies [1,2,3]. Frequency, and cycle waveform can have a profound effect on measured crack growth rates, their influence being functions of temperature, alloy composition, grain size and heat treatment. Often an increase in growth rate is associated with a transition in the crack path from transgranular to an intergranular mode as the crack follows embrittled grain boundaries [1,4,5,6]. A previous study [7] conducted by the authors has

demonstrated the influence of frequency on crack growth behaviour of a nickel based superalloy manufactured via a powder metallurgy route and the ability of a simple linear summation in predicting the effect of frequency on crack growth rates. Predictions in air were generally good but an under prediction observed on reduction in frequency at a stress intensity of 17 MPam1/2 and R ratio of 0.5 was proposed to be due to an environmental/fatigue interaction occurring during the loading or unloading part of the cycle. Understanding of the influence of waveform on the FCG of nickel base superalloys is relatively limited. In particular there has been little research into the effect of strain rate on crack growth. The literature suggests the importance of the ramp up over the ramp down during loading [8] and a mechanism has been proposed previously by Clavel et al. [9] based on the planarity of slip that may explain the effect of frequency on FCG modes and rates. More literature exists to explain the influence of dwell time on FCG [5,10] . The addition of hold time at maximum load allows processes such as creep and environmental damage which are not only time dependent but also dependent on stress state at the crack tip to be enhanced. In the majority of cases, this leads to acceleration in crack growth rate. However, studies by Sadananda et al [11] on Inconel 718 show that time dependent mechanisms which cause a transition to intergranular growth which can lead to crack closure, branching or deflection, may result in a reduction in growth rate per cycle.

This paper presents results from a continuing investigation into high temperature fatigue of a new fine grained nickel based superalloy produced by a powder metallurgy route, specifically addressing the influence of waveform variables and comparing the experimental results with predictions made using a linear summation model.

EXPERIMENTAL PROCEDURE

The material used throughout the course of this work was produced via a powder route with a composition limit listed in table 1 and had been supplied in the forged and heat treated condition. This gave it a 0.2% proof stress of 1020MPa at 725°C. Optical microscopy was carried out following electrolytic etching with 10% phosphoric acid in distilled water. For fatigue crack propagation tests a single edge notch (SENB) specimen geometry was used throughout the programme. Testing was conducted using a computer controlled servo-hydraulic 150 kN 'Mand' machine. The direct current potential difference (dcpd) technique was used to monitor crack growth and throughout testing, temperature, cycle count, notch voltage, maximum and minimum load and elapsed time were monitored and logged by a computer control and data acquisition system. High temperature testing was conducted using a quartz lamp heating arrangement within a vacuum chamber capable of maintaining a pressure of 10^{-6} mbar at temperature.

TABLE 1
COMPOSITION RANGE OF DISC ALLOY

Element	Cr	Co	Mo	Al	Ti	Ta	Hf	Zr	C	B
Wt%	14.35	14	4.25	2.85	3.45	1.35	0	0.05	0.012	0.01
	15.15	19	5.25	3.15	4.15	2.15	1.0	0.07	0.033	0.025

Constant stress intensity factor range (ΔK) tests at varying cycle period were conducted using a trapezoidal waveform, with an R-ratio of 0.5. This waveform consists of a cycle that contains a linear ramp up to maximum load, a hold period, a ramp down to minimum load and a hold time at the minimum level. The four stages of the load cycle were altered independently to investigate the influence of each of the waveform variables. Total cycle period of 12 and 21 seconds were employed in this process, the time period of all variables but one being held at 1 second and the variable of interest changed to either 9 or 18 seconds (depending on cycle period). The tests were conducted in air and vacuum at 725 °C at ΔK values of 30 and 17 MPa$^{1/2}$.

Fractography was performed on a Jeol 6340F SEM. Side profile micrographs were taken using the SEM at an angle of approximately 65° to the fracture surface and this enabled one to establish more clearly the prominent crack growth mode.

RESULTS

A typical optical micrograph of the material is illustrated in figure 1. It generally consists of a uniform fine grain size of 15 microns. Large primary γ' particles exist at the grain boundaries which have not been dissolved by the solution heat treatment. The total γ' volume fraction consisted of around 50% with a typical secondary size of 300-350nm [7]
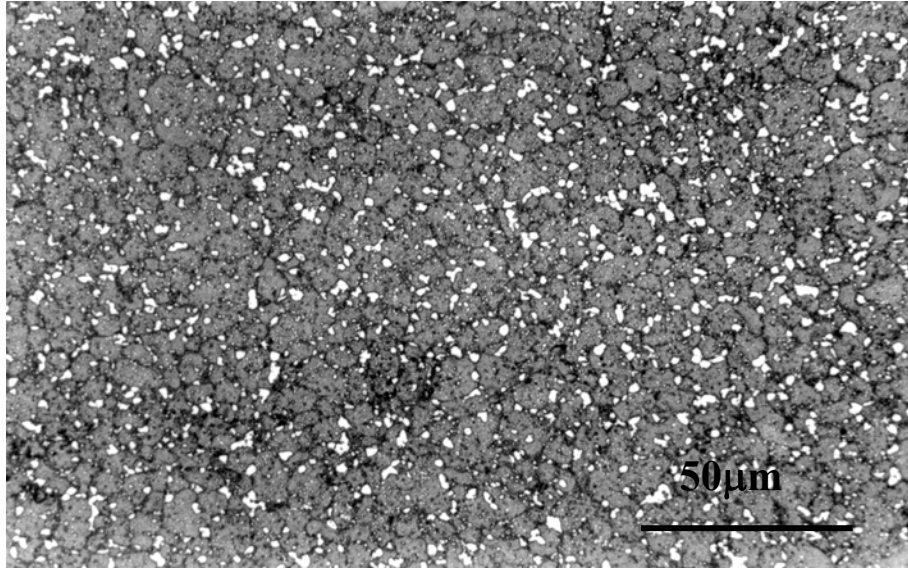
Figure 1: Optical micrograph of alloy

The results of the variable frequency constant $\Delta K=17\&30$ MPam$^{-1/2}$ tests conducted in air and under vacuum at 725°C and associated predictions are illustrated as a composite plot in figure 2. The data is arranged in sets corresponding to the environment, stress intensity range and cycle period conditions. Also included on this figure are predictions of growth rates using a simple linear summation model:

$$\frac{da}{dN} = \int_{t=0}^{t=1/\upsilon} \frac{da}{dt}(t)dt + \frac{da}{dN_{cyclic}} \tag{1}$$

In this model, static crack growth rates as a function of stress intensity factor K have been taken from a previous study on the material where they have been shown to follow the form:

$$\frac{da}{dt} = CK^n \tag{2}$$

in both air and vacuum. The values for the cyclic portion of the model have been taken as the measured growth rates at 20 Hz.

The fatigue crack growth results presented in figure 2 demonstrate that under any set of loading conditions the crack growth rates in vacuum are lower than those observed in air (in this figure A and V refer to air/vacuum, subsequent numbers relate to ΔK and the cycle period). At the lower ΔK this extends to over two orders of magnitude. Consideration of the effect of each waveform variable during this investigation demonstrates clearly that the application of a hold at maximum load caused the greatest acceleration in crack growth rate irrespective of the loading and environment conditions. Furthermore, in

air, crack growth rates for the standard baseline 1-1-1-1 (0.25 Hz) cycle period data were significantly lower than that of the 12 and 21 second data, i.e. a hold at maximum or minimum load or a ramp up or down caused an increase in the crack growth rate per cycle when compared to the baseline. In vacuum this discrepancy was not so large and at $\Delta K=17$ MPam$^{1/2}$ crack growth rates relating to the standard 0.25 Hz data were actually greater than those rates observed when a hold was applied at minimum load.
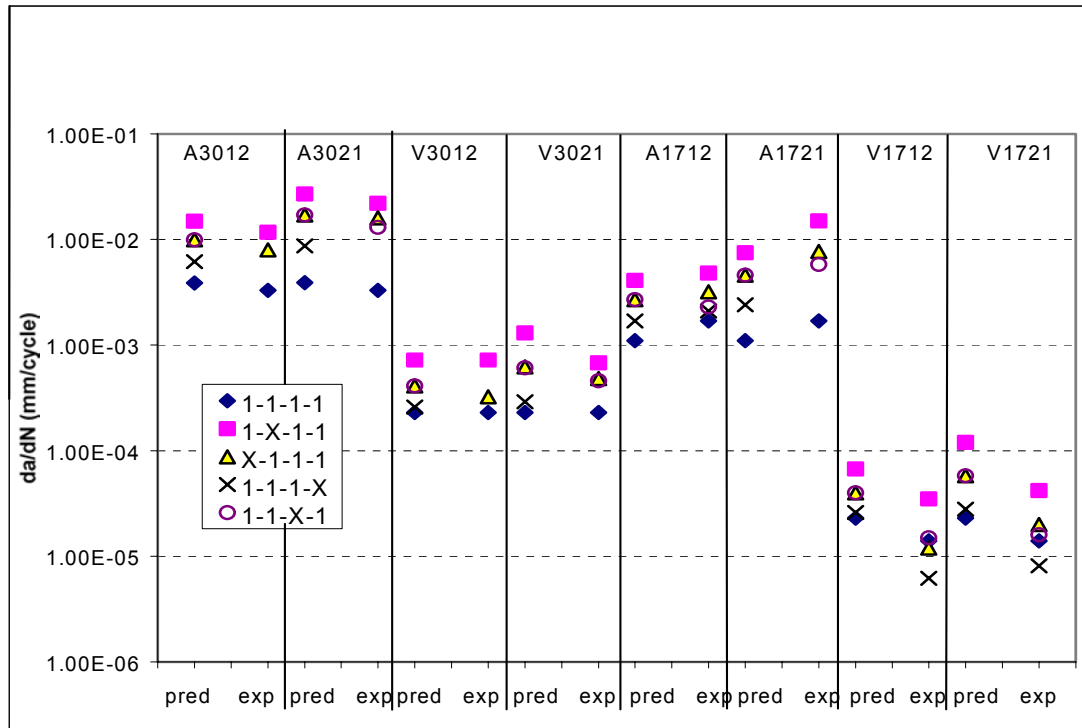
Figure 2: Results of variable waveform tests along with predictions from linear summation model as marked at the bottom of the columns. References at the top of the columns refer the air/vacuum, ΔK and total cycle period respectively.

The ramp to maximum load leads to a higher growth rate than the ramp down, when testing is conducted in air. This is most prominent for the lower ΔK test. In vacuum there is a negligible difference between growth rates for either ramp over all the tests undertaken within experimental error.

TABLE 2
SUMMARY OF THE CRACK MORPHOLOGY FOR EACH OF THE WAVEFORM VARIABLE CONDITIONS.
I=INTERGRANULAR, M=MIXED MODE, T=TRANSGRANULAR.

	A3012	A3021	V3012	V3021	A1712	A1721	V1712	V1721
1-1-1-1	I	I	M	M	I	I	T	T
X-1-1-1	I	I	M	I	I	I	T	T
1-X-1-1	I	I	I	I	I	I	T	T
1-1-X-1	-	I	-	I	I	I	T	T
1-1-1-X	-	-	-	-	I	I	T	T

The crack growth modes in this material can be difficult to discern due to the fine nature of the microstructure, particularly in the regime of mixed mode. Detailed fractography on both surface and side profiles is summarised in table 2 as either predominantly transgranular (T), intergranular (I) or mixed mode (M). Intergranular has been defined when no definite areas of transgranular cracking have been observed. The table indicates that mixed mode cracking was visible in vacuum for the standard baseline test and where a 9 second ramp to maximum load was applied at $\Delta K=30$ MPam$^{1/2}$. Apart from these instances the mode of failure could be clearly separated into the two distinct regimes of inter or transgranular crack growth. All the tests conducted in air displayed fully intergranular growth although this was associated with differing degrees of crack bifurcation, which was observed to increase as the

hold time was extended. In contrast for the vacuum tests at $\Delta K=17MPa^{1/2}$ all the observed fracture profiles were transgranular, despite the fact that there existed a discernible influence of hold time on growth rates.

DISCUSSION

At maximum load the crack tip opening displacement is at its greatest, maximising the extent of the strain field ahead of the crack tip. In air oxygen can sweep in along slip planes and the application of a hold allows deeper oxygen penetration. The longer the time available for the ingress of oxygen the more damage that can be accumulated in the form of internal oxidation and grain boundary embrittlement. This leads to intergranular cracking as has been observed in this study and an acceleration in the crack growth per cycle. As the extent of the hold is increased a larger amount of grain boundary embrittlement is able to occur throughout the strain field. This manifests itself as an increase in the degree of intergranular and secondary cracking, crack bifurcation and crack growth as observed in the current study. These observations support of the work by James [6] and Branco et al [10] where, following their logic it can be concluded that the tests have been conducted below the base cycle frequency sufficient to induce intergranular cracking. Although in air the hold time is the dominant parameter, which is no doubt an influence of both the high temperatures employed and the fine grain size of the material, a measurable difference in growth rate between ramping up and down was also observed in air. Although much shorter ramp times are employed and a high test temperature is used, these observations support the conclusions of Byrne et al [8] on Waspaloy although the differences measured are much less pronounced. Although it is difficult to draw definitive conclusions it is likely that oxygen is being swept in along slip planes during the ramping up section of the waveform that subsequently interacts with the fatigue process reducing the crack growth resistance [5]. Naturally the simple linear summation model does not pick up the influence of ramp rate. It assumes that transgranular and intergranular processes occur independently. The comparisons shown in figure 4 demonstrate that such a model is able to make a reasonably good approximation to experimental growth rates for all the variable waveform conditions. The model mirrored trends observed on alteration of the waveform and there is a reasonable close correlation between experimental and predicted growth rates, especially in regard to the typical levels of scatter associated with such testing. It is thought that this arises because time dependent mechanisms are dominating crack growth in air under these conditions [7].

Previous analysis using the linear summation model demonstrated that over prediction of growth rates in vacuum was a general observation [7]. This was attributed to the fact that in the sustain load crack growth tests initial transients were observed owing to a delay in rates reaching stable values on application of a load as would occur in the fatigue conditions experienced at the crack tip here. In effect the linear summation model assumes immediate stability of crack growth during the hold periods and it is this which leads to the over prediction. Figure 2 demonstrates that this was the case when attempting to predict the crack growth rates observed in vacuum for variable waveform conditions. The only exception appears to be at $\Delta K=30$ MPam$^{-1/2}$ for the 9 second hold. This would appear to be an anomaly associated with scatter as it is not reflected in the longer hold where over prediction again occurs although a more accurate result would be expected from the longer hold time. Unlike air the vacuum data shows no definite trend in the crack growth rates for ramping up and down. This supports the view that environmental rather than creep processes must be influencing the ramping sections of the waveform in air. Crack growth rates increase with hold time and if time dependent growth mechanisms are in operation this often manifests itself in the form of intergranular regions, however all the fracture surfaces in this instance were transgranular. As discussed by Crompton and Martin [12] creep relaxation could increase the plastic zone size if there is sufficient time for creep processes to occur. Crack tip plasticity is associated with the yield stress and it is conceivable that under conditions where creep is able to occur, longer hold periods will lead to higher crack tip strain ranges. If this occurs an acceleration of crack growth rate per cycle would be observed for a transgranular growth mode. Interestingly a hold at minimum load at $\Delta K=17$ MPam$^{1/2}$ led to a decrease in growth rates. The reasons for this again may well be associated with creep as postulated by Shahinian et al [13] leading to blunting during the minimum

load hold, which serves to impede the progress of the crack. Alternatively one could consider that recovery processes could be operating which anneal out damage due to strain hardening. Crack growth during transgranular cracking is dependent on the reversibility of slip so an increase will reduce the crack growth resulting from cyclic deformation at the crack tip lowering growth rates. Pressure welding of asperities during the minimum hold is also a possibility die the high temperatures and low vacuums involved, but this is unlikely to be possible at such high R-ratios which would hold the crack tip faces apart.

CONCLUSIONS

Variable waveform tests performed on a powder disc alloy in air and vacuum at 725°C demonstrated that the hold at maximum load caused the greatest acceleration in growth rate. In air, the ramp up has been shown to be more damaging than the ramp down and it is suggested that this is due to a fatigue/environment interaction. In vacuum at low stress intensity, a hold at minimum load was observed to cause a retardation in crack growth which may be attributable to a blunting or crack tip annealing process. An extension of the duration of the hold at maximum ramp up or down was observed to cause an acceleration in crack growth but not to induce intergranular cracking. It was suggested that the affects were due to the influence of creep on the crack growth process. The linear summation model was shown to accurately predict growth rates in air but to over predict in vacuum.

ACKNOWLEDGEMENTS

REFERENCES

1. Pedron, J. P. and Pineau, A., (1982) *Mater. Sci. Engng,* 56, 143
2. Gayda, J., Gabb, T. P. and Miner, R. V., (1988), Low Cycle Fatigue, ASTM STP 942, Eds H D Sobran et al., ASTM, 293
3. Gabrielli, F. and Pelloux, R. M., (1982) *Met. Trans. A*, 13A , 1083
4. Andrieu, E., Molins, R., Ghonem, H. and Pineau, A., (1992) *Mater. Sci. Engng.*, A154, 21
5. Lynch, S. P., Radthe, T. C., Wicks, B. J., and Byrnes, R. T., (1994), *Fatigue Fract. Engng. Mater. Struct.*, 17, No 3, 297
6. James, L. A., (1986), *Engng Fract. Mech.*, 25, No 3, 305
7. Knowles, D.M. and Skelton, D.K., (2001), submitted to *Mater. Sci. Tech.*
8. Byrne, J., Hodkinson, V. and Tong, J., (1999), Fatigue '99, 2171, Wu, X.R. and Wang, Z.G. (Eds).,Higher Education press EMAS, Beijing.
9. Clavel, P and Pineau, A, (1978), *Met. Trans. A.,* 9A, 471
10. Monra Branco, C., Byrne, J and Hodkinson, V., (1996) Mechanical Behaviour of Materials at High Temperature, Ed. Monra Branco C. et al (Eds), NATO ASI Series, 93, Portugal
11. Sudananda, K. and Shahinian, P., (1981), *Metallurgical Society of AIME*, 86.
12. Crompton, J. S. and Martin, J. W., (1984), *Mater. Sci. and Engng.,* 64, 37.
13. Shahinian, P. and Sudananda, K., (1979), *Transactions of the ASME*, 101, 224.

THE INFLUENCE OF DYNAMIC TESTING ON THE J - R RESISTANCE CURVE BEHAVIOUR OF MEDIUM DENSITY POLYETHYLENE

J. T. Dutton, D. M. Shuter and W. Geary

Health and Safety Laboratory, Broad Lane, Sheffield S3 7HQ, UK.

ABSTRACT

The dynamic fracture behaviour of medium density polyethylene has been investigated using an instrumented drop weight machine. Quasi-static and dynamic J - R resistance curves were obtained on both the parent and weld material. Three point bend specimens were used with a width of 30mm and a thickness of 15mm. All specimens were sidegrooved to a depth of 10% on each side. In the case of the welded specimens the notches were located in the weld centre line. All tests were carried out in accordance with the ESIS protocol on R curve testing of plastics. Dynamic tests were carried out over a range of impact velocities between 0.5 and 1m/sec. Load time data were obtained using a piezoelectric force transducer and displacement was derived from the double integration of the acceleration. Energy to maximum displacement was used to calculate J. Little difference was observed between the parent and the weld materials under both quasi-static and dynamic test conditions. Impact loading significantly reduced the level of the J - R curves for both the parent and weld materials particularly at higher values of Δa. $J_{0.2}$ values were reduced by up to 50%. The results were rationalised in terms of increased constraint resulting from the elevation of tensile properties under dynamic test conditions.

Keywords: Polyethylene, J – R curves, Welds, Dynamic Tests, Quasi-Static Tests.

INTRODUCTION

The increasing uses of polymers in many industrial sectors for a wide range of components and structures has resulted in a need to develop a better understanding of the failure characteristics of these materials. One area of particular concern is the fracture behaviour of medium density polyethylene, due to its widespread use in gas and water transmission, and the requirement to carry out engineering critical assessments (ECA) of components containing defects. One of the principal requirements of an ECA is some value of fracture toughness. Firstly, there is a need to establish test methodologies that allow fracture toughness data to be generated and secondly, to quantify those variables that influence fracture behaviour.

Early work [1] in this area established the J integral method for polymers and J was shown to be a useful parameter for determining the plain strain fracture toughness of high density polyethylene. The multiple specimen method was found to be a reliable technique for generating J-R resistance curves and thus for establishing $J_{IC.}$ More recently standard procedures [2] and protocols [3] for J-R resistance curve

determination, which can be used to define J_{IC}, and which go a considerable way towards providing the necessary methodologies have been developed. A reasonable amount of data exists in the literature on specimen size effects [4,5], for example, but there is little work on the influence of a number of experimental variables including temperature, dynamic effects and sidegrooving. In addition the influence of welds on fracture behaviour of these materials needs to be quantified.

EXPERIMENTAL

A length of polyethylene pipe (PE 80) was obtained from the manufacturer. From this material a number of notched three-point bend specimens having a width (W) of 30 mm and a thickness (B) of 15 mm were machined from the pipe wall in the axial direction. A similar length of PE pipe containing a circumferential butt weld, manufactured in accordance with British Gas guidance, was also obtained. From this pipe, specimens were manufactured such that the weld was positioned along the centreline, allowing the notch to be positioned in the centre line of the weld. Sidegrooves with a depth of 10% of the specimen thickness and a 45° angle were prepared in accordance with the ESIS protocol [3]. Pre-cracks were introduced by tapping a razor blade into the base of the notch to give an (a_0/W) of approximately 0.5.

All the dynamic tests were conducted on a instrumented falling weight impact machine. Tests were conducted at impact velocities in the range 0.5 - 1m/s. Impact forces were measured using a piezoelectric force transducer mounted just behind the striker mass. The displacement during the test was obtained from a double integration of the acceleration. Quasi-static tests were carried out on a 10kN servo-hydraulic test machine using a ramp rate of 1mm/min.

Extraneous displacements, such as roller indentations on the test specimen, were measured by loading an un-notched blank specimen, in a rig with the bottom rollers held together. The resultant load-displacement data was used to determine the energy lost due to this extraneous displacement and was subtracted from the total energy calculated for each specimen. The indentation energy obtained during these tests, however, was negligible, much less than 1% of the total energy (due to the small drop heights used) and was therefore excluded from any subsequent energy calculations. In all cases the energy to maximum displacement (U) was used in the calculation of the fracture resistance, J :

$$ J = \frac{\eta U}{B_N(W-a_o)} $$

where $\eta = 2$ for three point bend specimens
B_N = net thickness of sidegrooved specimens
W = specimen width
a_0 = initial crack length (to the tip of the pre-crack)

In all cases, a nine point average method was used to determine the amount of ductile crack growth (Δa).

RESULTS AND DISCUSSION

A summary of results obtained at 20^oC are given in Table 1, in terms of Power Law fits to J-Δa data and $J_{0.2}$.

Sidegrooving

Sidegrooved specimens exhibited much straighter crack fronts than those obtained in the non-sidegrooved specimens. This was anticipated since the increase in constraint and plain strain conditions promoted by sidegrooving would be expected to produce a more uniform crack front [6]. The effect of sidegrooving on the dynamic J-R curve characteristics of the parent material tested at 20^oC is shown, for example, in Figure 1. It is evident from the reduction in the power law exponent that the shape of the R-curve is significantly affected by using sidegrooved specimens.

TABLE 1
SUMMARY OF J-Δa DATA OBTAINED AT 20^oC

Specimen Type	Loading Conditions			
	Dynamic		Quasi-Static	
	Power Law Fit	$J_{0.2}$ (kJ/m^2)	Power Law Fit	$J_{0.2}$ (kJ/m^2)
Parent	$J = 4.22(\Delta a)^{0.709}$	1.35	$J = 5.244(\Delta a)^{0.849}$	1.34
Parent, Sidegrooved	$J = 3.592(\Delta a)^{0.569}$	1.44	$J = 5.077(\Delta a)^{0.656}$	1.77
Weld	$J = 3.972(\Delta a)^{0.813}$	1.07	$J = 5.751(\Delta a)^{0.930}$	1.29
Weld, Sidegrooved	$J = 3.524(\Delta a)^{0.647}$	1.244	$J = 5.117(\Delta a)^{0.505}$	2.27
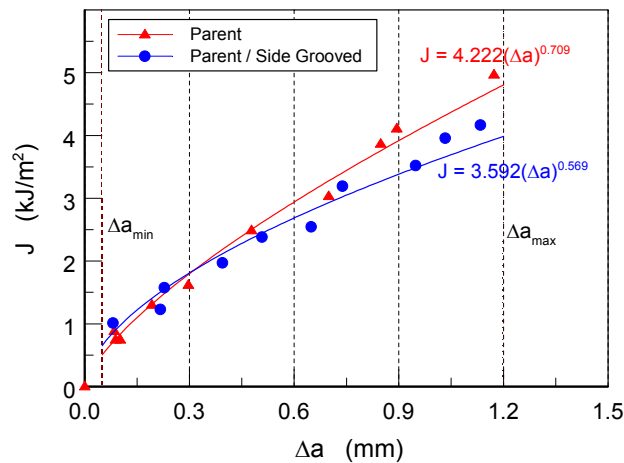
Figure 1 : Effect of Sidegrooving on Dynamic J-R Curve (Parent Material, 20^oC)

The toughness exhibited by sidegrooved specimens at longer crack lengths is somewhat lower than non-sidegrooved specimens which is explained by the increase in constraint and crack front straightness associated with sidegrooving [7]. These observations are consistent with data on high density polyethylene [5] which showed that sidegrooving lowered the R curve and reduced the amount of scatter. In this case it was argued that the plastic deformation at the shear lips accounted for a large part of the energy put into the system. Sidegrooving was also shown to promote crack tip triaxiality and reduce crack front curvature. The shape of the R curve for the sidegrooved material reported here is more consistent with what is known about R curve behaviour in polyethylene [5], other polymeric materials [7] and metals [8]. Some earlier round robin work on polyethylene [9] had found that the crack front profile was too curved for valid testing and relaxing the requirements led to inconsistencies in the J-R curves. $J_{0.2}$ values reported here were slightly larger for the sidegrooved specimens. Therefore it is recommended that sidegrooved specimens be used in all cases where significant crack front bowing is encountered.

Welding

Figure 2 shows the J-R curves obtained for non-sidegrooved parent and welded specimens tested under quasi-static loading conditions at 20^oC. At the lower end of the curve where crack initiation is important, both the parent and welded specimens exhibited similar toughness characteristics. However, as the crack extension approaches the maximum of $0.1(W-a_0)$, which in this case is approximately 1.2 mm, the welded material appears to be slightly but not significantly tougher.
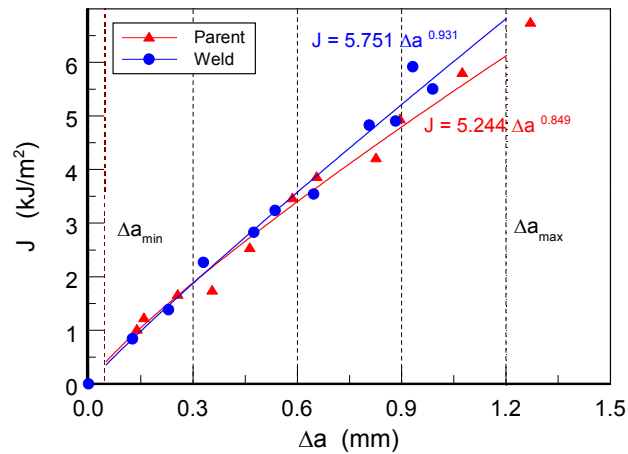
Figure 2 : Effect of Welding on Static J-R Curve (20°C)

Under dynamic loading conditions, the welded material exhibited somewhat lower toughness across the range of crack growth investigated.

For the non-sidegrooved welded specimens significant bowing of the crack front was apparent. In most cases the degree of bowing fell outside that allowed by the protocol and therefore, in this respect, the data were outside the valid range of behaviour.

Impact Loading

The effect of impact loading, at velocities between 0.5 and 1m/s, on the J-R curve characteristics of parent material is shown in Figure 3. Compared to data obtained under quasi-static loading conditions it is evident that impact loading reduces the toughness significantly (predominantly at longer crack lengths), illustrated by a reduction in the power law exponent obtained for the dynamic J-Δa curve. Similar results were obtained for non-sidegrooved welded specimens, underlining the strain rate sensitivity of this material.
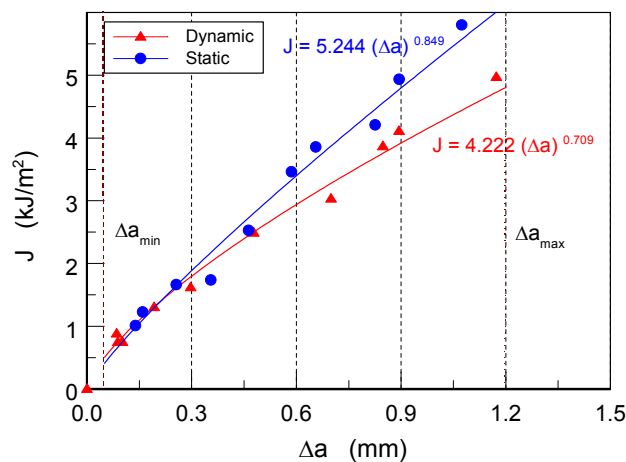
Figure 3 : Effect of Impact Loading on J-R Curve (Parent Material, 20°C)

It should be noted that at shorter crack lengths (<0.3mm), however, toughness remains largely unaffected by variations in applied strain rate, with similar $J_{0.2}$ values being obtained under both static and dynamic loading conditions. Similar fracture surfaces, showing bowed crack fronts, were obtained under both static and dynamic conditions, for non-sidegrooved parent and non-sidegrooved welded specimens.

Results obtained from both quasi-static and dynamic tests performed on sidegrooved parent and sidegrooved weld material, again showed that the effect of impact loading is to reduce the toughness. Lower $J_{0.2}$ results

were obtained for both parent and weld material under dynamic loading conditions, with the effect becoming more pronounced at larger crack lengths, as was the case for non-sidegrooved specimens. The reduction in the slope of the R curves under dynamic conditions is consistent with the higher constraint of these specimens resulting from an elevation of the tensile properties.

Temperature Effects

The influence of temperature on the J-R curve obtained for parent material tested under static loading conditions is shown in Figure 4. Similar results were also obtained for welded material. It is clear that a reduction in temperature of 20°C has a significant influence on behaviour. An R curve with a lower slope is anticipated since, at the lower temperature, an increase in tensile properties is expected, analogous to the influence of impact loading discussed in the previous section, and this produces an increase in specimen constraint. Similar trends have been observed in high density polyethylene [4].
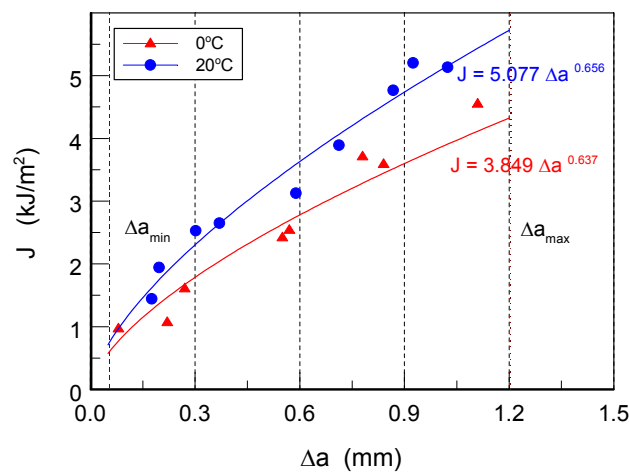
Figure 4 : Effect of Temperature on Static J-R Curve (Parent Material)

Under dynamic conditions, little difference between the curves generated at $+20^{\circ}$C and 0°C for either the parent material or the welded material, was observed. It was evident from a comparison of the static and dynamic curves obtained at 0°C that there was a small reduction in toughness associated with the dynamic tests, however, a much larger reduction is apparent for the tests conducted at 20°C. It is likely that the constraint changes associated with the reduction in temperature and the impact test rate are not simply additive. Further work in this area is justified to quantify the synergistic effects on constraint of temperature and dynamic rates of testing.

ESIS J-R Protocol

Both the static and dynamic tests were carried out in accordance with the ESIS draft protocol [3] with the exception of pre-crack and ductile crack growth measurement. The protocol recommends the use of a three point average to establish the pre-crack length and a 'subjective' average of ductile crack growth by positioning the cross-hair of a travelling microscope at the centre of the crack front. These methods were thought to be open to error and variability, so a nine point average (as used in other J-integral test standards, e.g. [10]) was considered to be the most appropriate technique to quantify both the original crack length and the amount of ductile crack growth.

The protocol specifies that the difference between the mean crack growth and any measurement point should be less than 30% otherwise sidegrooved specimens must be used. The 'subjective' measurement of ductile crack growth used in the ESIS protocol does not allow this analysis to be carried out and thus a nine point average was used. When this criterion was used to analyse the results reported here for both the sidegrooved and non-sidegrooved specimens, it was found that the majority of the specimens failed to meet this criteria. This was due to a small amount of additional crack growth observed at the edges of the fracture surface adjacent to the sidegrooves. Using a nine point average [10] (i.e. the average of the two near-surface

measurements at 0.1B and 0.9B, combined with the average of the seven remaining crack lengths) the majority of the sidegrooved specimens fell inside the 30% validity limit. For the non-sidegrooved specimens, however, the majority of specimens remained outside the 30% limit.

CONCLUSIONS

The data showed that there was little difference in resistance curve behaviour between the parent and the weld material.

Sidegrooving increased the specimen constraint and reduced crack front bowing leading to lower, more conservative, R curves. The shape of the curve for the sidegrooved specimens was more consistent with data obtained for other materials.

Impact loading produced a reduction in the slope of the R curve and lower toughness values, particularly at longer crack lengths. This data was consistent with an increase in specimen constraint resulting from the elevation of tensile properties.

A reduction in test temperature led to a reduction in the slope of R curve and this is likely to be due to the increase in specimen constraint associated with an increase in tensile properties. The effects of impact rate and temperature are not simply additive and further work is needed to quantify the influence of these variables.

The ESIS draft protocol is generally fit for purpose, however, a more rigorous method of determining the amount of ductile crack growth is needed. A nine point average method such as that used in ASTM 1737-96 is suggested.

ACKNOWLEDGEMENT

REFERENCES

1. Chan M. K. V and Williams J. G. (1983). Int. J. of fracture. pp145-159
2. ASTM D - 6068-96 (1996). American Society for Testing and Materials, D-6068-96.
3. ESIS J-R Protocol (1995). ESIS Technical Committee on Polymers and Composites (TC4)
4. Frassine R., Rink M. and Pavan A. (1997) Fat. Fract. Eng. Mat. Struct. 20, 8, pp1217-1223.
5. Chung W. N. and Williams J. G. (1990) in: Fracture behaviour and design of materials and structures (ECF8), Torino, Italy.
6. Etemad M R and Turner C E. (1985) Journal of Strain Analysis. 20, 4, pp201.
7. Huang D.D. (1993) American Chemical Society. Advances in Chemistry Series. 233, p39.
8. Schwalbe K.-H.and Heerens J. (1998) Fat. Fract. Eng. Mat. Struct. 21, pp1259-1271
9. Sehanobish K., Bosnyak C.P. and Chudnovsky A. (1993) Use of plastics and plastic composites: materials and mechanics issues. MD 46, ASME.
10. ASTM E1737 -96 (1996) American Society for Testing and Materials, E1737-96.

THE INFLUENCE OF LATTICE DISTORTION REGION NEAR THE GRAIN BOUNDARY ON MECHANICAL PROPERTIES IN NANO-CRYSTALLINE MATERIALS

Xiaowei Wang[1,2], J.Y. Wang[1,2], J. Rifkin[3], D.X. Li[2]

[1]International Centre for Materials Physics, Institute of Metal Research,
Chinese Academy of Sciences, Shenyang 110016, China
[2] Shenyang National Laboratory for Materials Science, Institute of Metal Research,
Chinese Academy of Sciences, Shenyang 110016, China
[3] Institute of Materials Science, University of Connecticut, USA

ABSTRACT

In this paper, the distortion structure in nano-crystalline NiAl is studied using molecular dynamics simulation. In these simulations the lattice structures within these small grains show a distortion relative to the large grained lattice structure. They are mainly located near grain boundary. Our results show that rounded grain boundaries in these nano-grains (as opposed to the planar faceted grain boundaries found in conventional-sized grains) are a direct factor in the production of the observed lattice distortion. The grain size directly affects the volume fraction of the distorted lattice in the nano-grain. The smaller the grain sizes, the larger the distortion region contributes to improved mechanical properties.

KEYWORDS: Molecular dynamic simulation, Nano-crystalline, Distortion

INTRODUCTION

Research on the structure of nano-crystalline materials is motivated by their advanced properties. The influence of grain size on mechanical properties is first considered as the most important influential factors. Except for a number of experimental observation, previous computer simulation studies have focused on the relation between grain size and properties of nano-crystalline. For example, Schiøtz *et al.* [1] studied the softening of nano-cystalline metals at small grain size. In their work, the conventional faceted grain boundary is studied. In fact, the types of the interface structure between

nano-grains is also an very important factor. Li *et al.* [2] reported results from high-resolution electron microscopic (HREM) observation in nano-crystalline materials. Their results indicate that there are three types of interface structures. The first is similar to the planar, faceted interfaces in conventional coarse grains. The second type of interface structure exhibits an imperfect or disordered grain boundary region. The third type is a rounded grain boundary (as opposed to a planar, faceted grain). HREM observation clearly shows a lattice distortion near grain boundary for the last two types of grain boundaries, the disordered grain boundary and the rounded grain boundary, but not for the conventional faceted grain boundary. Otherwise, the existence of this distortion region is also supported by X-Ray diffraction observations (Sui *et al.* [3]). These observations show lattice distortions in individual grains as an average result, but cannot determine where in the grain the distortions are located, nor even if the distortions are localized. The influence of distortion structure on properties of materials and how these lattice distortion region form have not been studied specially in previous works.

The present work concentrates on the character of the lattice distortion region near the grain boundary and the formation of this region. This paper aims to show the influence of the lattice distortion region on the mechanical behavior of nano-crystalline grain and its forming mechanism.

SIMULATION METHOD

The atomic configuration is designed to model nano-crystalline grains with rounded grain boundaries, it consists of a number of small spherical nano-grains embedded in an amorphous matrix. Each simulation contains eight equal-sized nano-grains arranged in a closed packed structure. The initial configuration is shown in Figure 1. Periodic boundaries condition are used in all three directions.

(a)   (b)
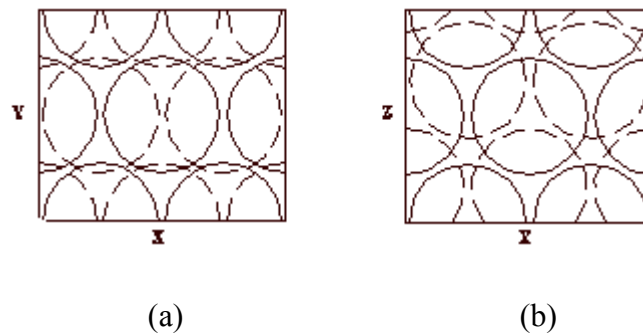
Figure 1: Initial simulated nano-crystalline configuration.The system contains 8 equal-sized grains arranged in 3-layer close packed structure. The solid line corresponds to the first and third layer of grains. The dashed line corresponds to the second layer of grains. Two projective directions, (a) and (b), is selected.

Simulations are done for varying sizes of nano-grains, but with a fixed separation between grain boundaries. In other words, the width of the amorphous region between grains remains fixed. This was done to judge the effect of grain size and by extension, the grain boundary curvature on the intergranular region.

The simulation was done using the XMD molecular dynamics program. NiAl alloy was selected as the material simulation. The Embedded Atom Method potential due to Voter and Chen [4] was used. The grain diameters used in the simulations are 3.8nm, 6.2nm and 8.7nm, corresponding to 30 327, 131

227 and 344 534 atoms per simulation. The initial percentage of atoms residing in the interface are 34.7%, 35.8% and 36.8%. Four different lattice orientations are used to orient the grains, they are

$$(1\ 1\ 1)\quad (1\ 1\ \bar{2})\quad (1\ \bar{1}\ 0)$$
$$(1\ 1\ 1)\quad (4\ 1\ \bar{5})\quad (2\ \bar{3}\ 1)$$
$$(3\ 1\ 2)\quad (1\ 1\ \bar{2})\quad (\bar{2}\ 4\ 1)$$
$$(2\ 2\ \bar{3})\quad (3\ 3\ 4)\quad (1\ \bar{1}\ 0)$$

These orientations ensure that there is a common lattice plane between two adjacent grains, this makes it easier to analyze the change of lattice structure between grains.

These nano-grains of defect free lattice are constructed. It is assumed that grains under this small size could not maintain internal defects because any such defects would easily migrate to the nearby grain boundary and reduce the lattice energy.

RESULTS

For the three different initial grain sizes described above we performed a static relaxation of the initial system. This was done using XMD's QUENCH command with a time step of 2E-15 and for 1500 time steps. For each grain size the relaxation shows a reduction in the lattice volume with the corresponding growth of the amorphous region. In addition, within the lattice closest to the amorphous region there formed a distorted region. For future reference we called these three regions as follows: the 'grain' is the undistorted lattice, the 'distortion region' is the distorted lattice, and the 'interface region' is the amorphous region. The 'grain' is a roughly spherical region surrounded by a spherical shell of 'distortion region', which in turn is embedded in the 'interface region'. The volume fraction respectively occupied by three region is shown in Figure2 as a histogram.
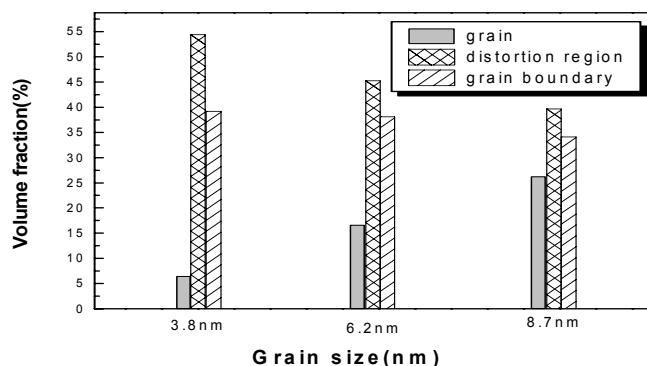
Figure 2:   The volume fraction respectively occupied by distortion region, interface region and grain.

Figure 3 gives another indication of the distortion region. It shows the average nearest neighbor distance (nnd) as a function of the distance from the center of interface region to the center of grain. The nearest neighbor distance is expressed in units of the nearest neighbor distance in the bulk d_0. The sharp upturn in the graphs as one travels from the grain to the interface region gives a clear indication of the presence of the distortion region.
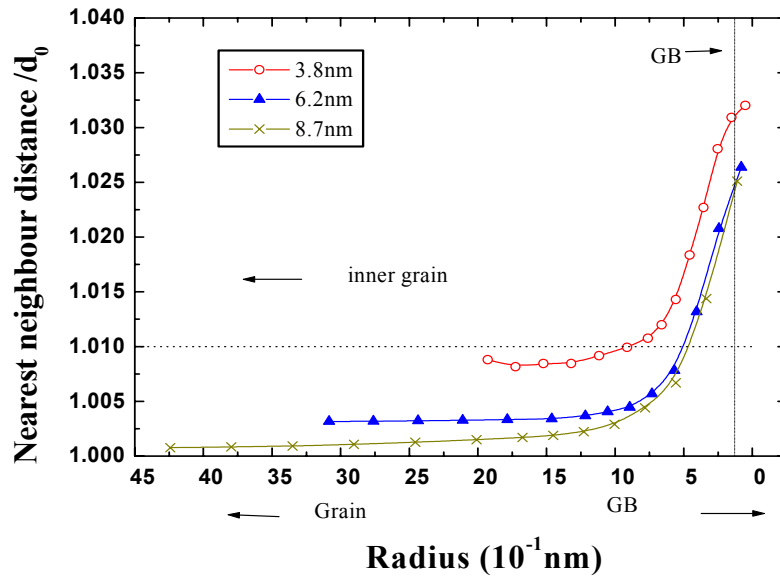
Figure 3: The relationship between the distance from the center of the interface region and the average atomic nearest neighbor distance

Figure 4 shows the deformation behavior of the nano-grains in the amorphous matrix. The horizontal axis displays the amount of uniaxial strain of the system, the vertical axis shows the resulting internal tensile stress. For each data point the atomic system is stretched in one direction while being compressed in the other two directions. Repeating boundary conditions are imposed with these new dimensions and the system is quenched. The resulting internal stress is plotted. This was done for each grain size, and the difference in elastic behavior and yield stress is plainly shown.
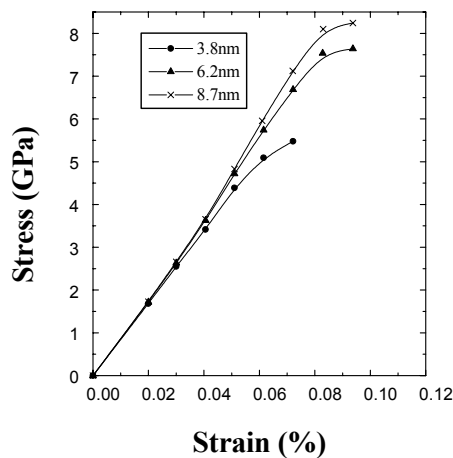
Figure 4: Grain size dependence of tensile Deformation.
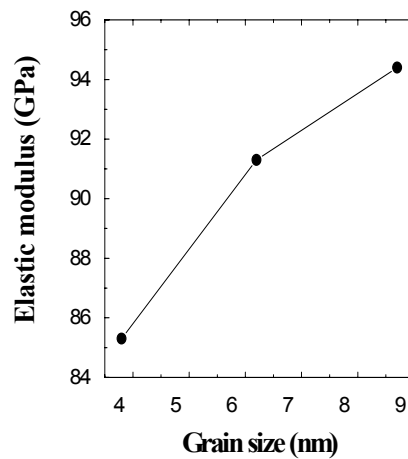
Figure 5: Grain size dependence of elastic modulus.

The results of elastic modulus are given in Figure 5. This is mainly calculated by the slope change of stress-strain curves.

DISCUSSION

Based on the observations of HREM, it is obvious that the structure of nano-crystalline materials (NC) differ from those of coarse grain materials. The distortion region is a transition structure between the perfect NC and the amorphous-like interface. It is also a metastable region in terms of the energy distribution. Therefore, it should be sensitive to a change in external conditions. The presence of the distortion region should have an important influence on the strength of NC. The results of Figure 2 shows clearly the effect of the distortion region and grain size when other conditions are fixed - the smaller the grain size, the higher the proportion of distortion.

Past works have focused on the influence of the grain boundary structure, the distortion structure of NC has received much less attention. But research into the excess enthalpy of NC has exposed a feature of that is different from coarse grain materials. Tschöpe *et al.* [5] showed the unrelaxed strain and non-equilibrium boundary structure in nano-grain are thought to be an important factor that produces the excess enthalpy. Lu *et al.*'s [6] study indicated further two things, (1) that the effective grain boundary energy in NC is smaller than in coarse grain materials despite the fact that the total enthalpy is greater and (2) that the grain boundary energy decreases with decreasing grain size. The excess enthalpy arises mainly from the distortion of the lattice structure. The present work demonstrates that the distortion region near the grain boundary is where the micro-strain is located. This distortion structure is a factor - in addition to the high percentage of grain boundary - that affects the mechanical properties of NC.

The results showed in Figure 4 and Figure 5, the change of deformation behavior with grain size, arise from two factors: the grain size and the size of the distortion region. These two factors have different influence on mechanical behavior. The decrease of grain size causes the increase of distortion region. The change of grain size and distortion region are a correlative factors to affect the yield stress and the elastic modulus of nano-crystalline. When the grain size is smaller, the kind of grain which have the rounded grain boundary will have produced larger distortion region and increased the energy of grain. When we consider the mechanism of deformation in nano-crystalline, the change of distribution of distortion energy is also an important factor except for the change of grain size.

ACKNOWLEDGEMENTS

REFERENCES

1. Schiøtz, J., Di Tolla F. D. and Jacobsen, K. W., (1998) *Nature*, **391**, 561.
2. Li, D.X., Ping, D.H., Ye, H.Q., Qin, X.Y.,and Wu, X.J., (1993) *Mater. letter*, **18**, 29.
3. Sui, M.L. and Lu, K., (1994) *Mater. Sci. Eng.* A, **179/180**, 541.
4. Voter, A. and Chen, S.F., (1987) *MRS Symposia Proceedings*, **82**, 175.
5. Tschöpe, A., Birringer, R. and Gleiter, H., (1992) *J. Appl. Phys.* **71**, 5391.
6. Lu, K. and Sun, N. X., (1997) *Phil. Mag. Lett.*, **75**, 389.

THE INFLUENCE OF THE IN-PLANE CONSTRAINT ON THE J RESISTANCE CURVES

A.Neimitz, J.Galkiewicz, R.Molasy

Department of Mechatronics and Machines Design, Kielce University of Technology.
Al. 1000 lecia P.P. 7, 25-314 Kielce, Poland

ABSTRACT

The results of the experimental investigation on the influence of the specimen size and geometry (four specimen configurations) on the J_R curves for two different steels are presented. Side-grooved and non-side-grooved specimens were tested. Two-dimensional finite element modeling (both plane stress and plane strain) of the experimentally tested specimens has been performed. The Q–stresses were determined among other results. The correlations between the trends of the J_R curves and the trends of the $Q=f(a/W)_{J=const}$ or $Q=f(J)_{a/W=const}$ are discussed.

KEYWORDS

J_R curves, Q-stress, stable crack growth, in-plane constraint.

INTRODUCTION

The nature of the stable crack growth is relatively well understood. It is a dissipative process-taking place close to the thermodynamic equilibrium. Thus, the crack growth equation can be considered as the equation representing the sequence of equilibrium states. In principle, this equation can be expressed in a general form:

The crack driving force = The crack growth resistance force

Various quantities were used in the literature as the *crack driving force*. Among them the most popular is the *J* integral understood as a global quantity not being the path independent or the amplitude of the singular HRR field. Recently, another quantity has been promoted as a good candidate to be utilized in the crack growth equation. It is dissipation rate, *R* [1] that is considered to have better physical meaning than the *J* integral. However, it does not solve the basic practical problem, which has been met using both quantities. This problem concerns the quantity called here *the crack growth resistance force.* In both cases it is not a material constant (or better – a material function; since it is a function of the crack extension). It depends not only on the material but on the specimen geometry and size as well as the mode of loading. Numerous experimental and theoretical researches have been undertaken to propose the universal J_R key curves for given materials in order to assure the transferability of results from one to another geometry of the specimen. According to the author's knowledge no full success has been reached so far. The present author and his coworker, following the theoretical analysis [2], proposed the methodology to normalize the J_R curves [3] in order to obtain the transferability of the results. This methodology has been successfully verified experimentally for two materials but only for the one specimen geometry: SENB (single edge notch bending) and for the two extreme cases: the small scale yielding and the fully plastic situation (prior the onset of crack growth). In this method the crack extension *Δa* was normalized by the length of the ligament

b_0, and the J integral was divided by the quantity proportional to the volume of the plastic zone. For the small scale yielding this quantity was r_p^2, where the r_p is the length of the plastic zone. For the fully plastic case it was the product b_0B, where B is the specimen thickness.

An extensive research has been undertaken to generalize these results to the other specimen configurations and sizes (some of the results of this research are presented in this paper). However, the results obtained were not satisfactory. The main reason for the failure of the methodology proposed is, in our opinion, disability to obtain a closed form formula to compute the volume of the plastic zone for various in- and out-of-plane constraints. Thus, we were not able to compute the quantity, which is necessary to normalize the J integral. The extent of the plastic zone depends on the in- and out-of-plane constraints. The in-plane constraint can be quantified, to some extend, by the Q–stresses [4]. If the Q-stresses, computed prior to the onset of the crack growth, varied according to the similar pattern with changing geometry and sizes of the specimens as the J_R curves it would mean that they could be used to normalize the J_R curves. The appropriate numerical computations have been performed using the ADINA finite element method code. Some of the results obtained are presented in the paper.

THE J_R CURVES – EXPERIMENTAL RESULTS.

The CCT (central crack tension), DNT (double notch tension), SENB (single edge notch bend) and SENT (single edge notched tension) specimens (side-grooved and non side-grooved) were machined and pre-cracked to obtain different in-plane and out-of-plane constraints. More than 120 specimens were tested. They were made of the 40HMNA steel (according to Polish standards, similar to the ASTM 4340 steel) and the 18G2A steel. The chemical composition of both steels and their mechanical properties are shown in Tables 1 and 2. All specimens made of the 40HMNA steel satisfied requirements of the plane strain. Non side-grooved CCT, DNT and SENT specimens made of the 18G2A steel satisfied requirements of the plane stress.

Table.1 Chemical composition

steel	C	Mn	Si	P	S	Cn	V	Cr	Ni	Mo	Cu	Al
18G2A	0.18	1.41	0.38	0.020	0.010	<0.05		<0.05	<0.05	<0.05		<0.025
40HMNA	0.41	0.66	0.25	0.026	0.003		0.01	0.71	1.35	0.20	0.12	

Table.2 Mechanical properties

Steel	σ_0 [MPa]	σ_m [MPa]	A5 [%]	Z [%]
18G2A	383	573	32	68
40 HMNA [N]	1217	1294	9.6	52.6
40HMNA [S]	1173	1247	11.4	53.3
40HMNA [W]	1086	1176	14.1	54.6

The single specimen technique to determine the J_R curves was used. The crack extension was measured using both potential drop and compliance change techniques. The J_R curves for SENB and SENT specimens were determined using the standard formula:

$$J_{i+1} = \left[J_i + \left(\frac{\eta}{b} \right)_i \frac{A_{i,i+1}}{B} \right] \left[1 - \frac{\gamma}{b_i} (a_{i+1} - a_i) \right] \qquad (1)$$

where $A_{i,i+1}$ is the part of the area under the $P=P(u)$ curve, between the ith and $i+1$ points along the $P=P(u)$ diagram, u is the load point displacement, B is the specimen thickness, $b=W-a$, W is the width of the specimen, a is the crack length. $\gamma = 1$, $\eta = 2$ for SENB specimens for a/W greater than 0.282. For a/W less than 0.282 η and γ were computed from the formulas known in the literature [5]. From the same source the formulas defining η and γ for SENT specimens were adopted.

For CCT and DNT specimens the following formulas were used:

$$J_i = J_{i-1}\left(1 - \frac{\Delta b}{b_{i-1}}\right) + \frac{1}{Bb_{i-1}}\left(P_{i-1}\Delta u - u_{i-1}\Delta P + \Delta P \Delta u\right), \qquad (2)$$

where

$$J_0 = \frac{1}{Bb_0}\left(2\int_0^{u_0} P_0 \, du - P_0 u_0\right). \qquad (3)$$

The subscript *0* denotes the point of the crack growth initiation.

Only some of the results obtained for the non side-grooved specimens are presented in this short article. For the side-grooved specimens the J_R curves follow the same pattern as for the non side-grooved specimens however they fall lower than for the non side-grooved specimens. For the CCT and DNT
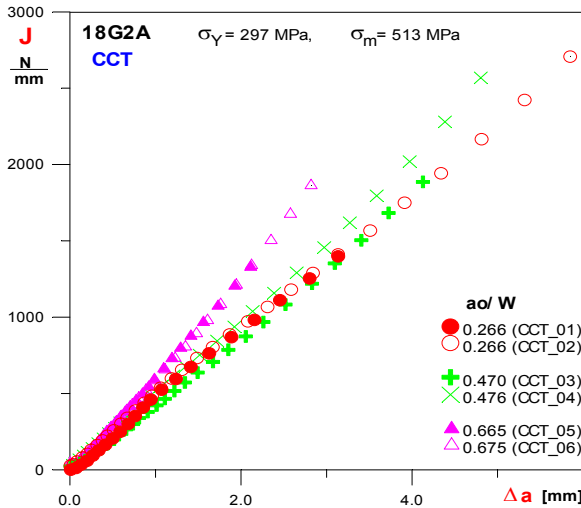
Fig.1a.The J_R curves for the CCT, non – side-grooved specimens made of 18G2A steel. *B*=3mm.
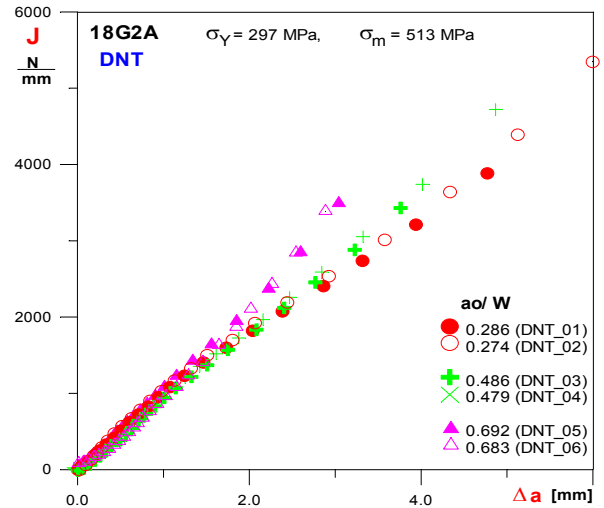
Fig.1b. The J_R curves for the DNT, non-side-grooved specimens made of 18G2A steel. *B*=3mm.

specimens the longer the initial length of the crack is the higher the J_R curve rise (Figs 1a and 1b). Similar trend was observed for the side-grooved specimens and for the both types of the specimens made of the 40HMNA steel. However, for this steel and both specimens configurations a very short stable crack growth had always been observed before the unstable, cleavage fracture occurred. Different trend was observed for the SENB specimen as shown in Fig.2a. In this case, for both side-grooved and non side-grooved specimens and both steels the J_R curves rise as the crack length decreases. For both types of the SENB specimens and for both steels a long stable crack growth was always observed.
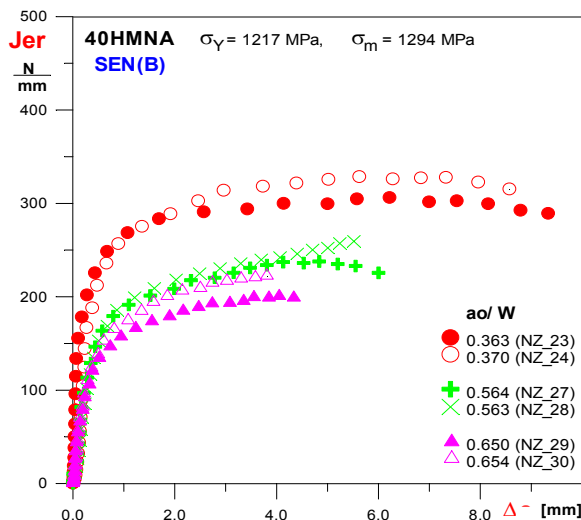
Fig.2a. The J_R curves for the SENB, *B*=15 mm, 40HMNA steel non-side-grooved specimens
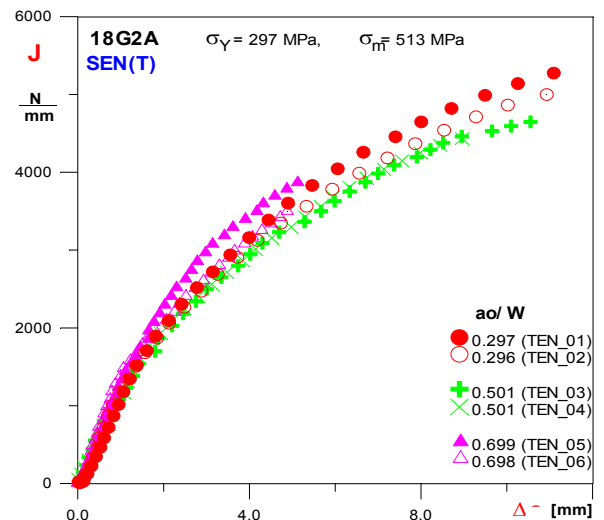
Fig.2b. The J_R curves for the SENT, *B*=3 mm, 18G2A steel, non-side-grooved specimens

For the SENT specimens the J_R curves run close to each other (Fig.2b) and no particular influence of the initial crack length is observed. It is probably due to the changing mode of loading from the predominantly tensile to bending.
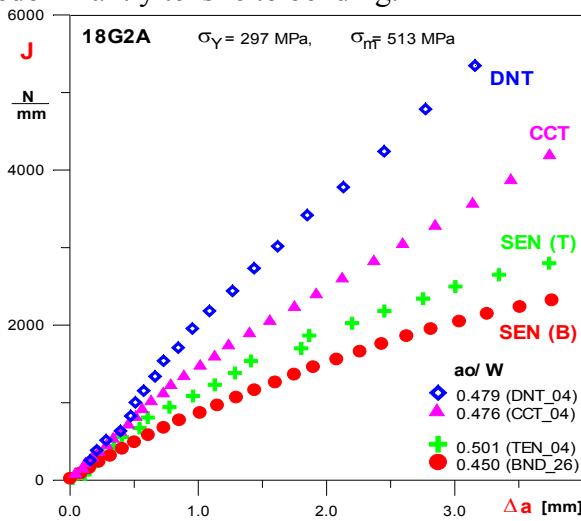
Fig.3. Comparison of the J_R curves for different specimen configurations for the 18G2A steel.
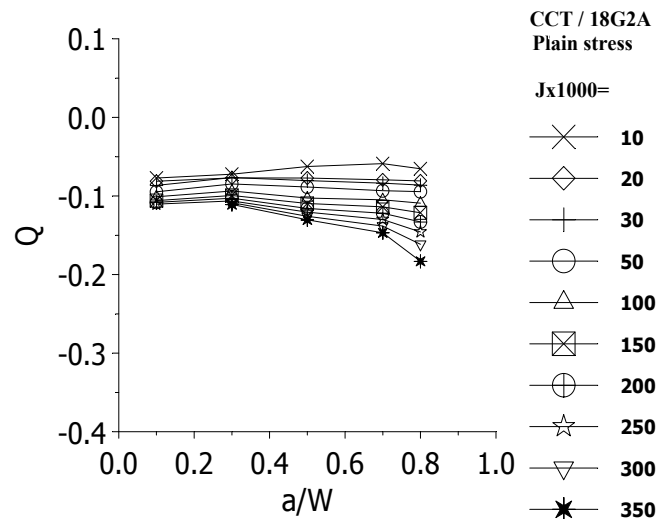
Fig.4. Selected numerical results of the Q-stress computations for the CCT specimens

In Fig.3 the typical trends of the J_R curves for the four specimen configurations are shown. Similar trend was observed for the side-grooved specimens.

NUMERICAL COMPUTATIONS OF THE Q – STRESS.

The finite element computations were carried out with ADINA version 7.4 computer code. All experimentally tested specimens were modeled and computations were made both for the plane strain and plane stress situations for small and finite strains (180 various examples were considered). The finite element meshes were similar to ones used by O'Dowd and Shih [4,6]. Also the methodology to compute the Q–stress followed suggestions of these authors (for the plane stress the similar methodology was used). The Ramberg – Osgood exponents were different for both tested materials. For the 40HMNA steel it was equal to 53 and for the 18G2A steel it was equal to 11. The Q – stresses were computed at the distance $r=2J/\sigma_o$ from the crack tip. In addition to the Q–stresses the stress distributions in front of the cracks were computed as well as the shapes and extents of the plastic zones according to the Huber-Mises-Hencky hypothesis. The results obtained were analyzed along with the experimentally obtained J_R curves. Because of the limited length of this article only few, selected $Q=f(a/W)_{J=const}$ curves are presented for both materials and tested specimens to demonstrate general trends of these curves (Figs 4 and 5). Discussion is included in the next section.

DISCUSSION

In the series of papers by O'Dowd and co-workers (e.g. [4,6]) and other authors the important observations have been made concerning the interrelation between the level of the Q-stress, the extent of plastic deformation and fracture mechanisms. Shortly, the lower the Q-stresses are the less constraint against plastic deformation is observed. With some simplification it may be said that the micro-cracks are generated by high stresses and voids by large strains with a strong shear component. Voids are expected to occur at a high degree of overall (macroscopic) plastic flow, and micro-cracks at a stress build-up without significant relief of plastic flow. In general, both micro-cracks and voids grow inside the grains, thus eventually producing transgranular fracture (Broberg[7]).

One of the aims of the research performed in this project was to compare the behaviour of the J_R curves for various specimen sizes and configurations with the trends of the $Q=f(a/W)_{J=const}$ and $Q=f(J)_{a/W=const}$ functions computed prior to the onset of crack growth for the same specimens. It turns out that many conclusions concerning the stable crack growth can be drown from the shapes of the $Q=f(a/W)_{J=const}$ or $Q=f(J)_{a/W=const}$ curves in accordance with the registered J_R curves and the fractographs. However, it is not so for all types of the specimens tested. Distinct exceptions are the DNT specimens.
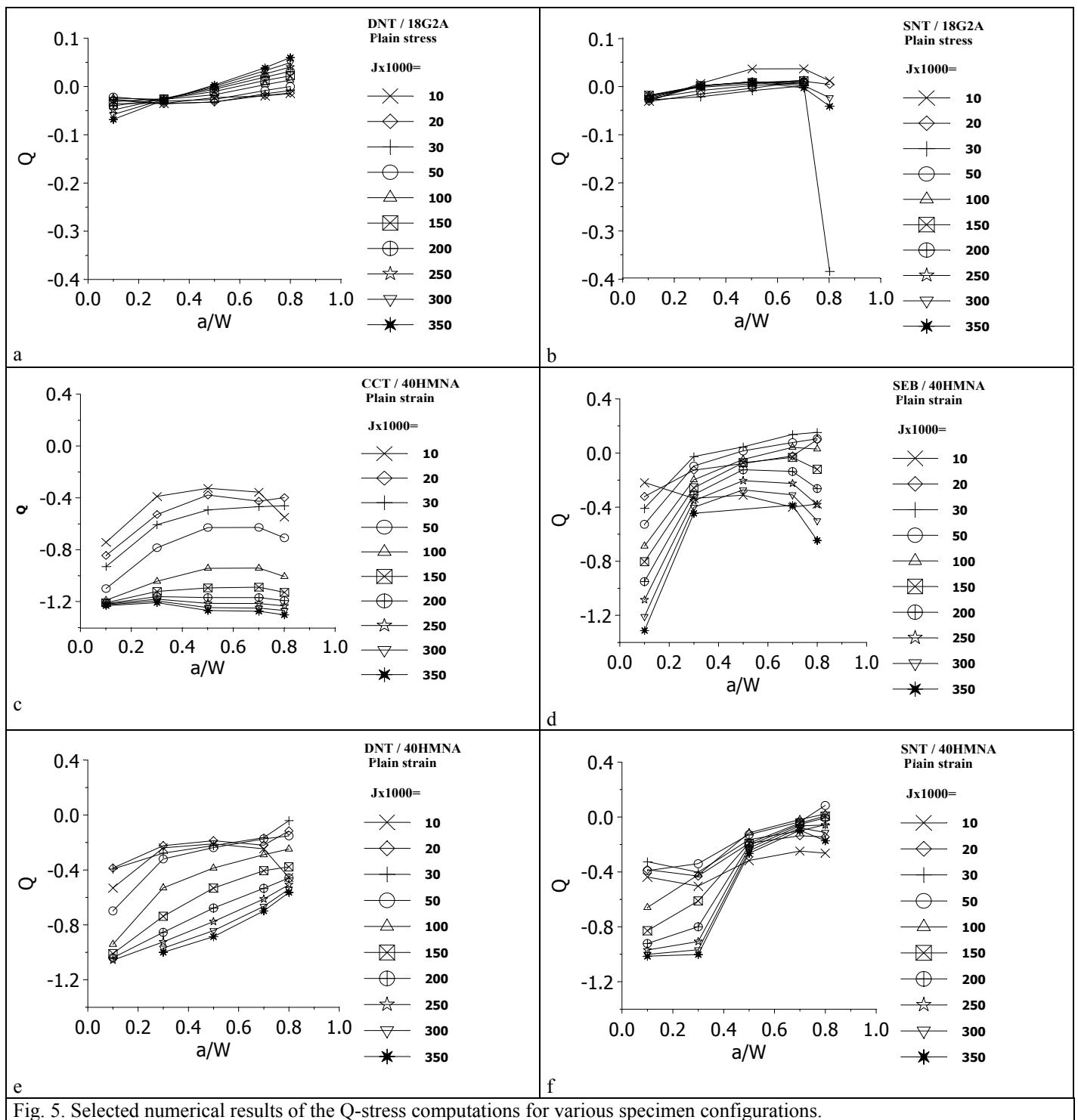
Fig. 5. Selected numerical results of the Q-stress computations for various specimen configurations.

Because of the limited space only few general conclusions can be listed here.

a) For the CCT specimens (plane stress, 18G2A steel, the $J_{IC} \cong 300$ kN/m) the J_R curves rise higher as the initial crack length increases (Fig. 1a). It follows from the numerical computations that the normal stresses as well as the Q-stresses decrease (Fig. 4) in front of the crack when the initial crack length and the J integral increase. Assuming that the similar behaviour may happen for growing cracks, the J_R curves should follow the same pattern as observed experimentally (the smaller Q the less constraint and more dissipation due to the plastic deformation). Sizes of the voids should increase with the crack length. It is also observed experimentally (because of the limited volume of the paper the fractographs are not shown here). The J_R curves for the side-grooved specimens followed the same pattern although they run lower than for the non-side-grooved specimens. The normal stress components for side-grooved specimens are higher than for the plane stress situation. Moreover, the plastic deformation is more

localized because of the stronger geometrical constraints. Plastic dissipation is less for these specimens thus, the J_R curves run lower than for the non-side-grooved specimens.

b) For the SENT specimens (plane stress) the Q stresses are close to zero (Fig. 5b) and they do not change much with the initial crack length. One could conclude that the J_R curves should not be much dependent on the a_o/W. Indeed, we observed such a trend of the J_R curves for this specimen configuration (Fig.2b). The J_R curves for the SENT specimens (plane stress) should run below the curves for the CCT specimens since the normal stresses and the Q-stresses in front of the crack are higher for the former specimens. This behaviour was also observed experimentally (Fig.3).

c) For all types of the specimens considered the lowest J_R curves are for the SENB specimens (Fig.3). It also can be predicted from the analysis of the normal stress components in front of the crack. However, in this case the results for the plane strain (SENB specimen) and plane stress (other specimen shapes) must be compared.

d) For the SENB specimens J_R curves follow different pattern than for the CCT specimens. For the shortest crack the J_R curves rise highest (Fig.2a). This phenomenon can also be explained through the analysis of the normal stresses or the Q-stresses in front of the crack. For the SENB specimen geometry the Q-stress increases with the a_o/W.

Above observations would suggest that the Q-stress could have been considered a proper parameter to be used to normalize the J integral along ordinate in order to assure transferability of the J_R curves. However, the numerical results obtained for the DNT specimens lead to the conclusions which are in the total conflict with experimental observations. For the DNT specimens (plane stress, 18G2A steel) the Q-stresses are negative and close to zero (Fig.5a) for small a_o/W and increase for greater a_o/W reaching positive values. The Q-stresses for the DNT specimens are greater than for CCT and SENT ones. Thus, one could expect that the J_R curves for the DNT specimens should run below the J_R curves for the CCT and SENT specimens. In fact it is inversely (Fig. 3).

Since the Q-stresses increase with a_o/W (for the DNT specimens) one could expect that the J_R curves should follow the pattern similar to the SENB specimens (the highest curves for the shortest crack). It is again inversely. However, the sizes of the voids, observed in the fractographs, decrease with increasing a_o/W and this is the only observation, which agrees with the theoretical prediction (the greater Q the smaller void diameter). The only qualitative explanation, so far, of this exceptional (among tested specimen configurations) behaviour of the DNT specimens follows from the analysis of the shapes and sizes of the plastic zones in front of the crack. Detailed numerical analysis of this problem has been performed. For the material tested (18G2A steel, plane stress) and for the loading close to the critical one the plastic zone grows bigger than for the CCT and SENT specimens and it is not limited to the well defined shapes and sizes following from the size and shape of the specimens. Thus, one could conclude that the Q-stress alone is not able to give the full information on the loss of the in-plane constraint for all geometrical shapes of the specimen.

REFERENCES

1. Turner, C.E. (1990) In: *Fracture Behaviour and Design of Materials and Structures, 8th European Conference on Fracture* (ed. D.Firrao), Vol.II, EMAS, Warley, UK,pp.933-968.
2. Neimitz, A., (1996). In: *Constitutive Relation in High/very High Strain Rates*, (ed. K.Kawata and J.Shiori), Springer-Verlag, Tokyo, pp. 92-104
3. Neimitz, A. Molasy, R. (1998),.In: *Fracture from Defects, 12th European Conference on Fracture* (ed. M.W.Brown, E.R. de los Rios and K.J.Miller), EMAS, pp. 787-812,
4. O'Dowd, N.P., Shih, C.F. , (1991), *J.Mech. Phys. Solids,* Vol.39, No.8, str. 989-1015,
5. Link, R.E. and Joyce, J.A.,(1996), *Application of Fracture Toughness Scaling Models to the Ductile-to-Brittle Transition,* NUREG/CR-6279, U.S.Nuclear Regulatory Commission, NRC Job Code J6036, Washington
6. O'Dowd, N..P., (1995), *Engineering Fracture Mechanics* Vol.52, No.3, str. 445-465.
7. Broberg, K.B., (1999), *„Crack and Fracture",* Academic Press

THE INFLUENCE OF THERMAL RESIDUAL STRESSES AND FRICTION ON FATIGUE CRACK GROWTH IN FIBRE-REINFORCED INTERMETALLIC MATRIX COMPOSITES

G. Rauchs, P.F. Thomason, P.J. Withers

Manchester Materials Science Centre, University of Manchester,
Grosvenor Street, Manchester, M1 7HS, UK

ABSTRACT

A three-dimensional model of a compact tension specimen consisting of a Ti-6-4 matrix reinforced with unidirectional, continuous SiC fibres is investigated. The influence of post-processing thermal residual stresses and friction on the crack growth behaviour during monotonic and cyclic loading is assessed. It was found that the bridging fibres strongly reduce the crack-tip stress intensity factor. The thermal residual stresses produce a load of the crack tip in the absence of an external load and have an impact on the crack tip load ratio. The results are compared to investigations resulting from the modelling of crack-tip shielding by fibre-induced bridging tractions on the crack-face using the weight function method. Reasonable agreement was found between the two methods used.

KEYWORDS

Composites, Fibre reinforcement, Cyclic fatigue, Finite element modelling, Thermal residual stresses

INTRODUCTION

The relatively low fracture toughness in some metallic and intermetallic materials can often be improved by incorporating unidirectional fibre reinforcement [1-3]. One example is given by fibre-reinforced titanium matrix composites (TMCs) [2,3]. The cyclic fatigue of this material is also improved by the addition of unidirectional fibres to the matrix material. Experiments have shown that crack-tip shielding by fibre bridging can lead to crack arrest [2,3]. Several numerical studies have investigated the fracture behaviour of fibre reinforced materials, both for monotonic and cyclic loads [4-7]. Nevertheless most of these investigations rely heavily on the weight function method to assess the crack-tip shielding. This method is used within the context of continuum fracture mechanics wherein the bridging fibres are treated as a perturbation of the tractions acting on the faces of the matrix crack [5-9]. Therefore, the local traction transfer mechanism is smeared over the bridged area in the wake of the crack. Whereas elastic mismatch is accounted for in this approach, thermal expansion mismatch is mostly neglected. In recent years, finite element models of push-out tests have been developed to model the influence of debonding and friction on the material behaviour of fibre-reinforced materials [10,11]. Debonding has been modelled either by a quadratic failure criterion [11] or a Coulomb friction law [10], while interface friction has been included through the Coulomb friction law.

By using a finite element model, the mechanisms governing local stress transfer by bridging can be better resolved by modelling the individual bridging fibres and the fibre-matrix interface. The effects of elastic and thermal mismatch on fracture behaviour can also be investigated. In this study, this approach is used on a cracked compact tension specimen to investigate the cyclic fatigue behaviour of fibre-reinforced Ti-6Al-4V using a simple debonding criterion and friction model.

NUMERICAL MODELS

In the present study, a compact tension (CT) specimen of square shape with a sidelength of d=25 mm consisting of a Ti-6Al-4V matrix reinforced with continuous, unidirectional SiC-fibres normal to the crack surface is modelled using ABAQUS 5.8. The fibres have a diameter, d_f, of 0.1 mm and the fibre volume fraction f is 31%. Both matrix and fibres have purely linear-elastic material behaviour (Young's moduli E_m=115000 MPa, E_f=400000 MPa, Poisson's ratios ν_m=0.3, ν_f=0.17, CTE's α_m=10x10^{-6} 1/K, α_f=5x10^{-6} 1/K). Assuming that fibre bonding is weak, the debonding of the fibres is modelled by using the Coulomb friction law:

$$\tau \leq \mu\sigma_N \tag{1}$$

where τ is the interface shear stress, μ the friction coefficient and σ_N the normal compressive stress. Calculations for different interface strengths are performed by using different magnitudes for the friction coefficients μ. In order to model a true fibrous material rather than a layered composite, and to include the radial clamping stresses σ_N caused by thermal residual stresses and necessary for the debonding criterion used, a three-dimensional finite element analysis is necessary. Due to the small size of the fibres compared to the specimen, the size of the finite element model has been reduced considerably by using the embedded cell method. At the crack-tip, a microstructural region 20 fibres is modelled, while the remainder of the CT-specimen is modelled as a uniform continuum material with transversely isotropic material parameters representative of the composite properties. The growth of a crack around a fibre often leads to a curved crack front [12]. However here the model was simplified by assuming a straight crack at mid distance between two fibres, fully located in the matrix. The crack-tip stress intensity factor was calculated by the J-integral method. This is acceptable in our case for cyclic loads because of the linear-elastic behaviour of the matrix material. Because the stress intensity factor varies locally at the crack front, the average stress intensity factor was calculated from the values at each node on the crack front. In the model, crack growth is considered over a range of 10 fibres, with the crack length ranging from that of a half-cracked specimen +/- 5 fibres. This means that for the initial crack length a_0, 5 fibres remain in the wake of the crack and for the maximum crack length, 5 fibres remain in the unbroken ligament. This allows one to include the effects of the fibres for the minimum and maximum crack length and ensures that stress fluctuations from the transition from the embedded cell to the surrounding homogeneous bulk material do not seriously influence the magnitude of the stress intensity factor. It should be noted that the initial crack a_0 is unbridged, i.e. the fibres in the wake are cut. During crack growth, the fibres are assumed to remain intact and bridge the crack, with the crack growing only through the matrix.

The loads are applied in 3 steps. In the first step, the uncracked specimen is cooled down from the stress-free processing temperature to room temperature (ΔT=900K) to generate the initial residual stresses from the thermal expansion mismatch. In the second step, the initial crack, a_0, is introduced into the specimen by the node release technique. In the third step, the actual external load is applied. The magnitude of the external load is calculated in such a way as to obtain a constant applied stress intensity factor, K_{appl}, for all crack lengths using geometry functions Y(a/W) for CT-specimens taken from literature [13]. When considering cyclic loads, first the external load is applied, then the specimen is unloaded. The crack is then grown to the next crack location by the load release technique. This process is repeated until the maximum crack length is reached.

For the analytical model using the weight function method, the crack-tip stress intensity factor K_{tip} and the shielding K_{sh} have been calculated using a method of [8]. The bridging tractions, σ_{br}, including the effect of

thermal mismatch, are related to the crack-tip opening displacement u [9], using the fibre and matrix Young's modulus E_f and E_m, the fibre and matrix thermal expansion coefficient α_f and α_m, the temperature T with reference to the stress-free state, the rule-of-mixture Young's modulus E of the composite and a constant interface frictional stress τ, whose magnitude is derived by Eqn.1 from the interface pressure from the finite element results:

$$u = \frac{d_f(1-f^2)E_m^2}{4f^2E^2E_f\tau}\left[\sigma_{br} + f(E_f(\alpha_f - \alpha_m)T)\right]^2 \tag{7}$$

The crack-tip opening displacement u at the location x on the crack with crack length a has been calculated using the weight function h(a,x) by:

$$u(x) = \frac{2}{E}\int_x^a h(a',x)\left[K_{appl}(a') + \int_{a_0}^{a'} h(a',x')\sigma_{br}(x')dx'\right]da' \tag{8}$$

In an iterative procedure, the crack-tip opening profile is calculated using Eqn.7 and 8. The crack tip stress intensity factor is calculated by using the applied crack tip stress intensity factor K_{appl} and the bridging stresses resulting from the crack-tip opening profile over the bridged crack length ranging from a_0 to a:

$$K_{tip} = K_{appl} + \int_{a_0}^a \sigma_{br}(x)h(a,x)dx \tag{9}$$

RESULTS

Effect of Thermal Residual Stresses
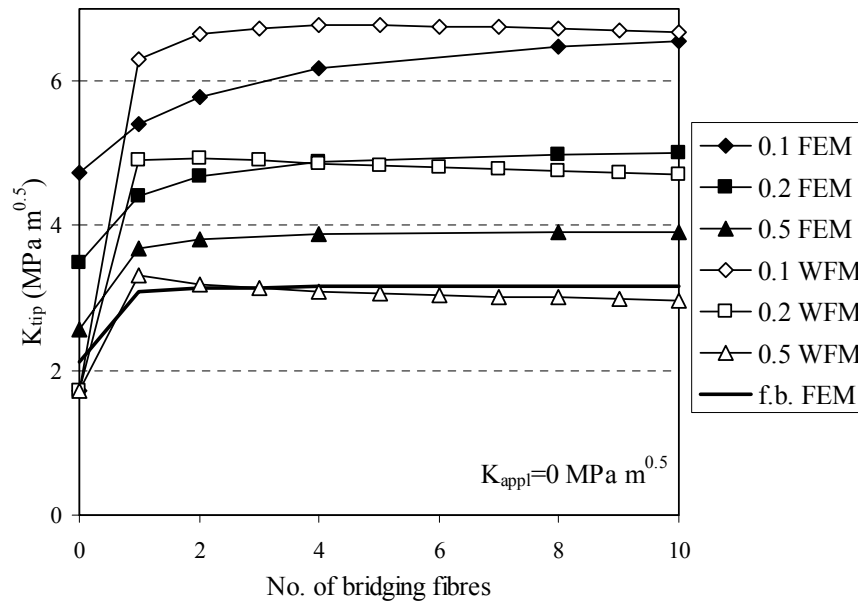
Figure 1: Comparison of results from finite elements and weight function method for thermal residual strains for several friction coefficients (0.1, 0.2 and 0.5).

It was found that after the cooling process, substantial thermal residual stresses occur in the composite. In the direction of the fibre axis, the fibres have a compressive stress of –899 MPa and the matrix has a tensile stress of 395 MPa. This is in good agreement with those measured by neutron diffraction (360 MPa in the

matrix and -720 MPa in the fibres [14]). After the introduction of the initial crack, the crack-tip experiences a considerable load resulting from the thermally induced residual stresses. It can be seen in Fig.1 that after crack growth, the thermally induced stress intensity factor, K_{th}, is magnified by the presence of one bridging fibre in the wake of the crack. The variation in stress intensity factor for different friction coefficients is caused by the varying debonding lengths of the non-bridging fibres, which increase as μ decreases. During further crack growth, the crack-tip stress intensity factor increases strongly for a friction coefficient $\mu=0.1$, whereas for higher friction coefficients, the increase is small. It can be assumed that the bridging fibres inhibit the rotation of the crack face, which leads to an applied bending moment on the crack face resulting in an increase of the crack-tip stress intensity factor. This is underlined by the fact that the tensile stresses in the fibre are superimposed by bending stresses. This effect predominates in the case of one single bridging fibre. The increase of the crack-tip stress intensity factor with decreasing friction coefficient results from the larger debonding length. With a larger debonding length, the matrix in the cracked segment, which is under axial tension from the residual stresses, can contract more, which leads to an increase in crack-tip opening displacement and consequently in a higher stress intensity factor. It has to be noted that the results of the weight function method are considerably higher than those from the finite element calculations. This might be caused by the fact that the bridging stress profile used in the weight function method does not include the bending stresses found in the fibres in the finite element analysis.

Cyclic Fatigue
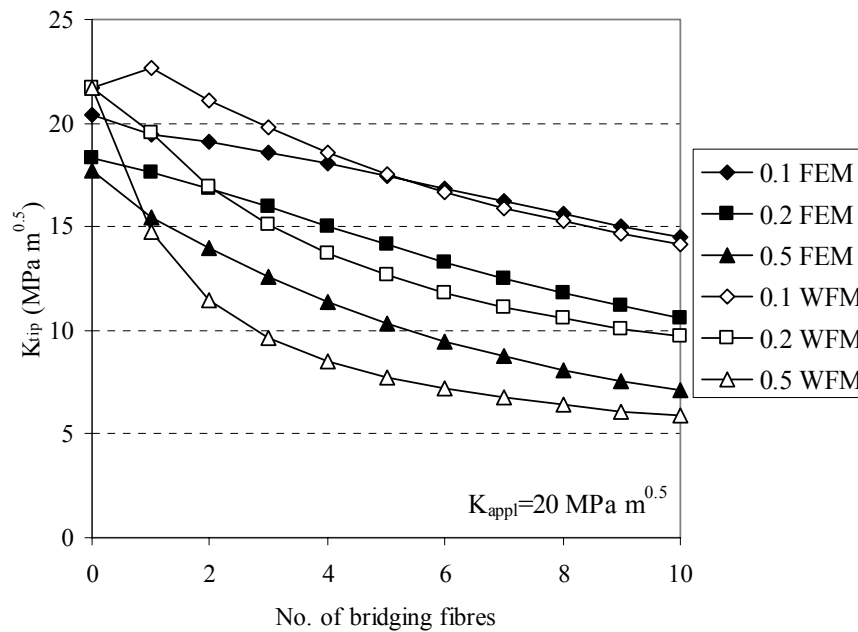
Figure 2: Comparison of crack-tip K_{max} from finite elements and weight function after an external load has been superposed on the thermal residual strains load for several friction coefficients.

In Fig.2, the K_{tip} recorded at maximum load is represented for both finite element and weight function method. Both sets of results show a reasonable agreement. Nevertheless, it has to be pointed out that the decrease of the crack-tip stress intensity factor is steeper for the weight function method. This is probably due to the constant frictional shear stress used in that analysis, compared to the variation of the frictional shear stress caused by Poisson contraction of the matrix, which affects Eqn.1 used in the finite element calculations. For all friction coefficients, the crack-tip stress intensity factor decreases with the increase in the number of bridging fibres during crack growth. Higher friction coefficients produce a larger decrease of the crack-tip stress intensity factor. This is again due to the smaller debonding length and thus smaller thermal stress relaxation induced contraction of the matrix. For an applied stress intensity factor range of $\Delta K_{appl}=10 MPa\sqrt{m}$, a similar trend was found, but the magnitude of the change in crack-tip stress intensity factor was smaller. During the finite element analysis, K_{min} and K_{max} have been calculated and the local crack-tip stress intensity factor range, shown in Fig.3, has been derived. In Fig.3, it is clear that the crack-tip stress intensity factor range decreases strongly with the increasing number of bridging fibres during crack

growth. The difference between the different friction coefficients is much smaller than for the respective K_{max} and K_{min} values. Nevertheless, it can be seen that higher friction coefficients lead to a smaller stress intensity factor range. At $\Delta K=10MPa\sqrt{m}$, ΔK_{tip} decreases, but the reduction is smaller than for $\Delta K=20MPa\sqrt{m}$.
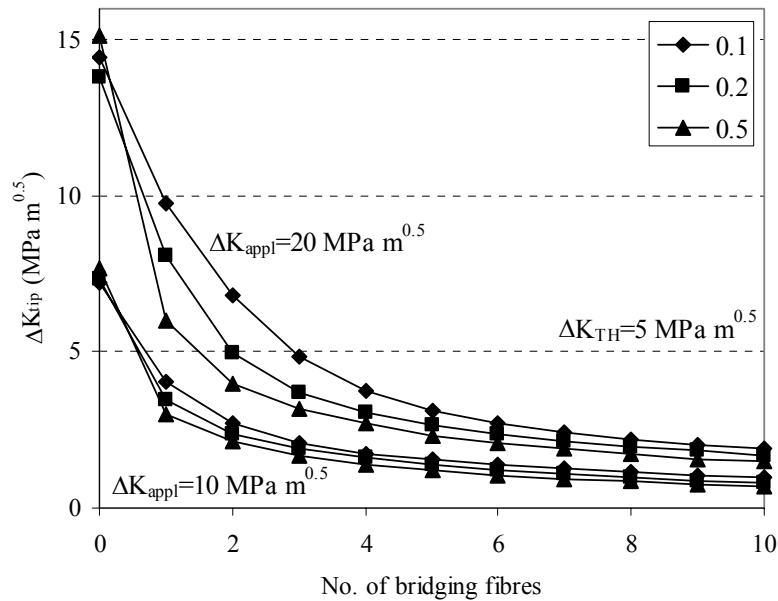
Figure 3: Crack-tip stress intensity factor range for two different applied load levels for friction coefficients of 0.1, 0.2 and 0.5.
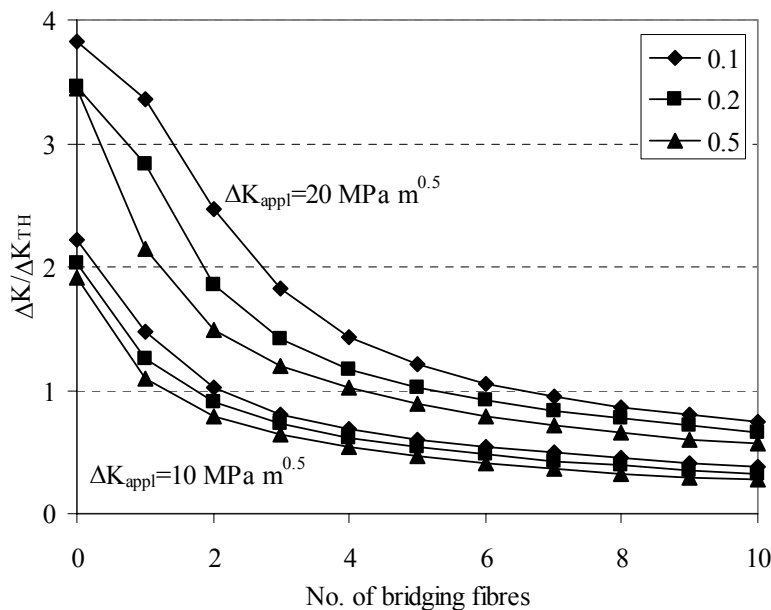
Figure 4: Crack growth criterion including the effect of the crack-tip load ratio on ΔK_{TH} for friction coefficients 0.1, 0.2 and 0.5.

For the applied external load, the load ratio R equals 0. For this load ratio, a threshold stress intensity factor $\Delta K_{TH}=5MPa\sqrt{m}$ has been reported for Ti-6Al-4V alloy [15]. Introducing this value into Fig.3, it can be inferred that for an applied load of $\Delta K=10MPa\sqrt{m}$, the crack would not progress beyond the first fibre, whereas for the load level of $\Delta K=20MPa\sqrt{m}$, the crack would progress only one or two fibres before crack arrest ($\Delta K/\Delta K_{TH}<1$). Crack growth is higher for lower friction coefficients. Due to the presence of thermal residual stresses and frictional interface shear stresses, the actual crack-tip load ratio is different from the applied load ratio. In fact, the crack-tip load ratio increases rapidly from between 0.2-0.4 towards a plateau

of approximately 0.8. By interpolating ΔK_{TH} values from [15] (ΔK_{TH}=4.6, 2.9 and 2.6 MPa$\sqrt{m}$ for R=0.1, 0.5 and 0.8), the maximum crack extension can be calculated using the failure criterion $\Delta K/\Delta K_{TH}$. It can be seen in Fig.4 that by including the dependence of ΔK_{TH} on the crack-tip load ratio, crack arrest occurs at higher crack lengths compared to the values obtained for the load ratio R=0. For an applied stress intensity factor range of ΔK=10MPa$\sqrt{m}$, the crack would not grow beyond one or two fibres, depending on the friction coefficient. For a stress intensity factor range of ΔK=20MPa$\sqrt{m}$, the crack would not grow beyond 4 fibres for μ=0.5 and beyond 6 fibres for μ=0.1.

CONCLUSIONS

The analysis presented in this paper provides some important insights into the crack-tip stress intensity factors expected when frictional fibre bridging occurs during cyclic loading. It was found that in this fibre-reinforced composite, residual stresses arising from thermal expansion mismatch generate a crack opening load on the crack-tip in the absence of an applied load. This increase in the stress intensity factor is offset by the elastic transfer of load towards the fibres when an external load is applied so that $K_{tip} < K_{appl}$. For this reason, the bridging fibres produce a substantial reduction of the crack-tip stress intensity factor. With decreasing friction coefficient, the debonding length increases, which leads to an increase in the crack-tip stress intensity factor. In fact, relaxation of thermal stresses over longer debonding lengths leads to a more extensive matrix contraction locally, which results in a higher crack-tip stress intensity factor. It was found that under cyclic loading, the bridging mechanism is predicted to have a strong impact on crack growth. In fact, the high crack-tip shielding leads to crack arrest. Additionally, thermal residual stresses and fibre bridging have a strong impact on the crack-tip load ratio. Therefore, the variation of the fatigue threshold limit with the load ratio has to be incorporated into the crack growth criterion. Reasonable agreement has been found between the results from the finite element method and the weight function method.

REFERENCES

1. Venkateswara Rao, K.T., Siu, S.C. and Ritchie, R.O. (1993) Metallurgical Transactions 27A, 721-734
2. Cotterill, P.J. and Bowen, P. (1996) Mat. Sci. Tech. 12, 523-529
3. Barney, C., Ibbotson, A. and Bowen, P. (1998) Mat. Sci. Tech. 14, 658-668
4. Bao, G. and McMeeking, R.M. (1994) Acta Metall. Mater. 42, 2415-2425
5. Begley, M.R. and McMeeking, R.M. (1995) Comp. Sci. Tech. 53, 365-382
6. Ghosn, L.J., Kantzos, P. and Telesman, J. (1992) Int. J. Fract. 54, 345-357
7. Cox, B.N. and Lo, C. (1992) Acta Metall. Mater. 40, 1487-1496
8. Fett, T. (1994) KfK-Report 5291, Kernforschungszentrum Karlsruhe
9. Bao, G. and McMeeking, R.M. (1995) J. Mech. Phys. Solids 43, 1433-1460
10. Dinter, J., Peters, P.W.M. and Hemptenmacher, J. (1996) Composites 27A, 749-753
11. Ananth, C.R. and Chandra, N. (1996) Composites, 27A, 805-811
12. Zhao, D. and Botsis, J. (1996) Int. J. Fract. 82, 153-174
13. Tada, H., Paris, P.C. and Irwin, G.R. (1985) The stress analysis of Cracks Handbook, Del Research, St. Louis, MO
14. Withers, P.J. and Clarke, A.P. (1998) Acta Mater. 46, 6585-6598
15. Ritchie, R.O., Boyce, B.L., Campbell, J.P., Roder, O., Thompson, A.W. and Milligan, W.W. (1999) Int. J. Fatigue 21, 653-662

THE LOAD CARRYING-ABILITY OF PMMA FLEXURAL SPECIMENS WITH BLUNT NOTCHES

A.J. Heidweiller

Faculty of Design, Engineering and Production, Delft University of Technology, Delft, The Netherlands

ABSTRACT

The effect of blunt notches on the load carrying-ability of poly(methyl methacrylate) flexural specimens was investigated. A large number of three-point bending tests were carried out on specimens with various notch radii and notch depths. Four different loading rates were applied. The results were analyzed in terms of nominal strength. Furthermore, apparent blunt notch values for critical strain energy release rate G_b and critical stress intensity factor K_b were determined. The latter approach was applicable to the relatively deeply notched specimen. The reduction of the load carrying-ability of the specimens with shallow notches and notch radii greater than 0.1 mm followed the stress concentration factor quite well.

KEYWORDS

Blunt notch, PMMA, strain energy release rate, stress intensity factor, stress concentration factor.

INTRODUCTION

Geometry transitions often are weak parts of products due to a local appearance of peak stress combined with a tri-axial stress state. It was tried to model the effect of stress concentrations with the concept of notch factors [1]. A notch factor is defined as the ratio between the load carrying ability of a component with a geometry transition and without a geometry transition. However, the relation between notch factors and geometrical stress concentration factors could not be described by simple parameters and besides, this relation depends on temperature and loading rate as well [2].

Models based on a critical stress were also proposed. E.g., a maximum principal stress was proposed in [3] and in [4] was concluded from the results of plane strain tests and an analytical analysis based on the theory of slip line fields, that craze formation in glassy polymers could be described on the basis of a critical value for the mean normal stress. In general, polymer products have thin walls and therefore geometry transitions often are not in plane strain conditions, but finite element method techniques might be applied to evaluate the maximum mean stress. Plati and Williams [5] applied the concept of fracture mechanics to specimens with blunt notches. There method was based on Linear Elastic fracture Mechanics (LEFM). They assumed, a critical value of the (Dugdale) plastic zone size, whether or not the plastic zone was caused by a crack or a blunt notch. For deep blunt notches a simple relation was derived between the notch radius, the critical plastic zone size and the critical strain energy release rate of blunt notches (G_{BI}) or cracks (G_{CI}). Their tests
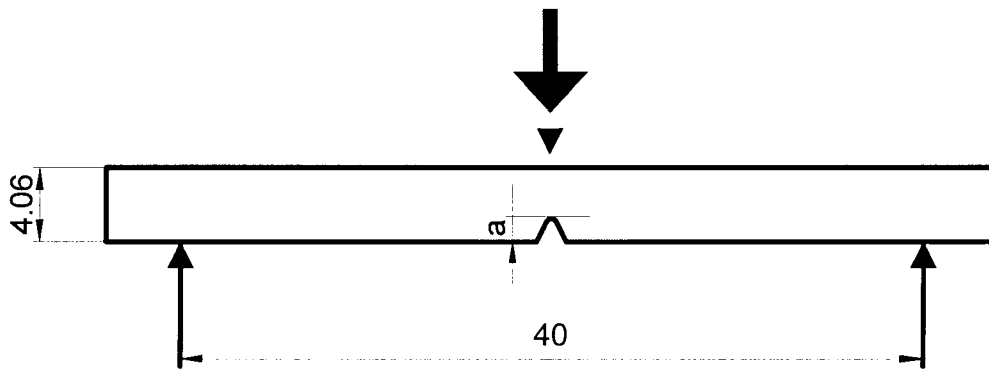
Figure 1: three-point bending set up

showed good correspondence between theory and experimental results in the range of notch radii between 0.2 and 1 mm.

The present study is part of our research concerning the effect of geometry changes on the load carrying ability of plastic products. The method of [5] is applied to study the effect of blunt notches in flexural specimens of PMMA. The effect of loading rates also was studied.

EXPERIMENTAL

Three point bending tests on injection molded poly (methyl methacrylate) (PMMA) specimens were carried out. The test set up is shown in figure 1. The specimen width was about 4.06 mm and the thickness about 6.1 mm. To correct for the small spread of the dimensions, the cross section of all specimens was measured. Specimens were notched applying 5 notch radii (see table 1). The notch depths varied from about 0.1 mm till about 2.5 mm. The cracks (notch radius of 0 mm) were formed by a razor blade, which was hit by a falling weight. The blunt notches were formed with a special notch device. Repeatedly a thin layer of the specimen was scraped away by a steel bar with the appropriate profile till the desired notch depth was reached. The blunt notch depth could be determined from the notch device. The depth of the razor blade notch was determined from the fracture surface using a microscope. Smooth specimens also were tested.

Four tup velocities were applied. The velocity of 0.1 m/s is missing for the razor blade notches and the velocity of 0.001 m/s for the smooth specimens. The test temperature was 23 °C. The tests were performed on a hydraulic set up. Both the displacement (LVDT) and the force (piëzo element) were measured as a function of time during the test. From this the load – displacement relation was established. The number of tests was between 20 and 40 for each combination of notch radius and tup velocity.

TABLE 1
NOTCH RADII AND TUP VELOCITY OF TEST SERIES

radius [mm]	tup velocity			
	10^{-4} m/s	10^{-2} m/s	10^{-1} m/s	1 m/s
0	x	x	x	
0.01	x	x	x	x
0.1	x	x	x	x
0.3	x	x	x	x
1	x	x	x	x
smooth		x	x	x

2
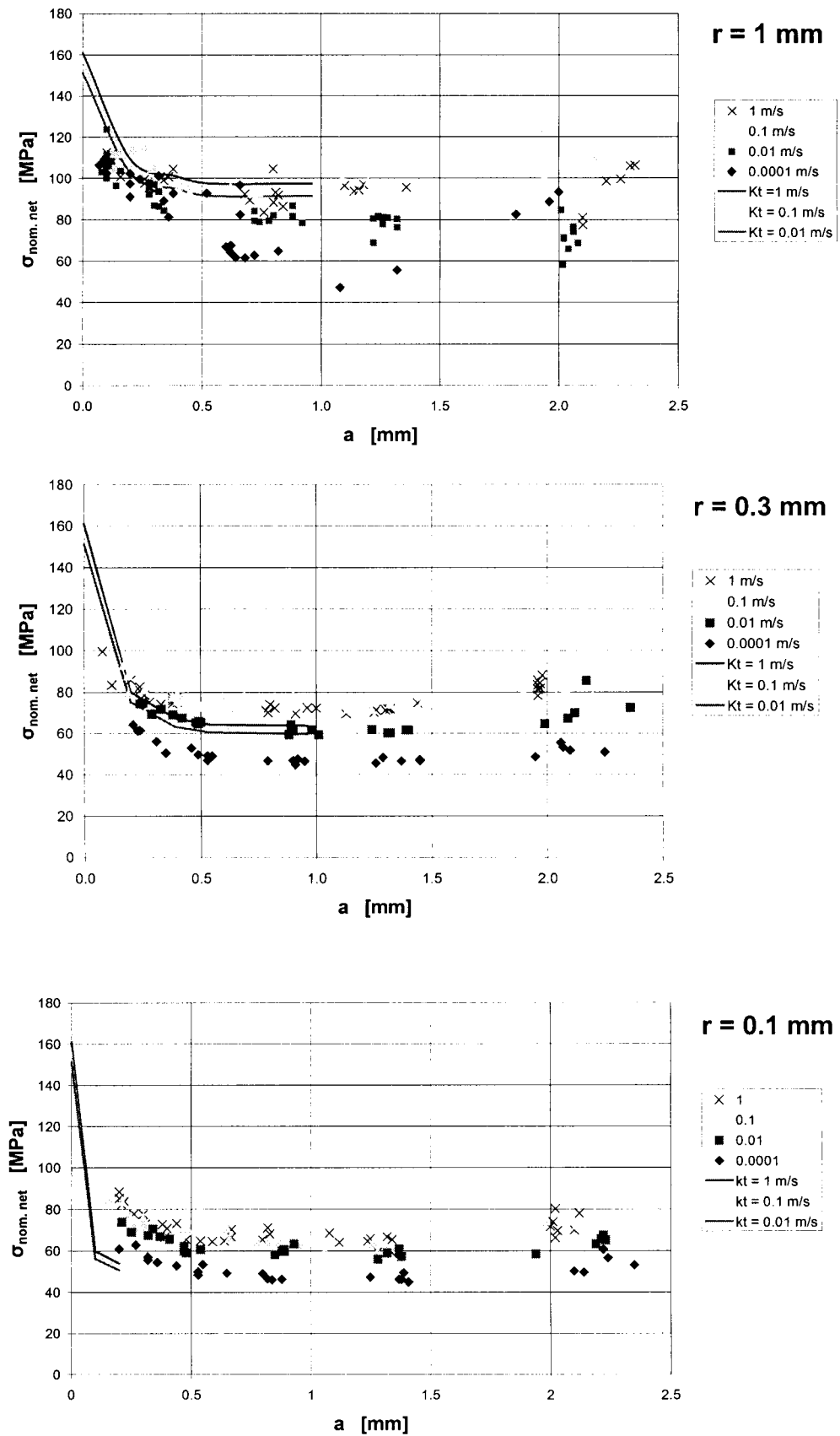
Figure 2: Nominal strength related to notch depth for three (out of the series of five) notch radii. The results of all four tup velocities are indicated in each diagram. The lines indicate the ratios of nominal smooth specimen strength over stress concentration factor K_t for tup velocities of (in order of decreasing nominal strength) 1 m/s, 0.1 m/s and 0.01 m/s.

RESULTS AND ANALYSIS

Nominal strength

The nominal strength, $\sigma_{nom.\ net}$ was defined as the maximum stress working on the net-section according to linear-elastic theory, but leaving out the effect of stress concentrations. It holds:

$$\sigma_{nom.\ net} = M_{max} / (1/6 * B * (D-a)^2) = 60F_{max} / (B*(D-a)^2) \tag{1}$$

Where M_{max} is maximum moment in specimen, B is specimen thickness, D is specimen width, a is notch depth and F_{max} is maximum force during the test. In figure 2 the nominal strength related to the notch depth a is shown for notch radii of 1, 0.3 and 1 m/s. Additionally, the ratio of nominal smooth specimen strength over the stress concentration factor is indicated for shallow notches in the graphs. This ratio can be considered as a prediction of nominal strength based on linear elastic theory. The stress concentration factors were taken from [6].

The following could be concluded from the nominal strength results:

– The shallow blunt notches caused a considerable reduction in nominal strength. The graphs of notch radii 1 and 0.3 mm show, that the strength reduction for notch depths smaller than the notch radius could be described by the stress concentration factor.
– The spread in nominal net stress sometimes was very high. E.g. for deep notches with radius 1 mm.
– The tup velocity is positively correlated with the nominal strength as well as for notched as for smooth specimens.
– The increase of the nominal stress for notch depths greater than 2 mm probably was due to some plastic hinge effect.

Analysis based on LEFM

From the load – displacement curves apparent values for both the critical strain energy release rate, G_B and the critical stress intensity factor, K_B were established for all tested specimens. The subscript B indicates that these parameters refer to blunt notches. The values of K_B were determined from the maximum load during the tests. The values of G_B were determined from the work performed to fracture as was proposed by [5]:

$$G_{IC} \text{ or } G_{IB} = W / (B * D * \varphi) \tag{2}$$

Where W is the area under load deflection curve (work performed to fracture) and φ is a geometrical factor, which was determined using an approximation of the geometry factor Y, supplied by [7]. G_B was estimated from the slope of the straight line fit of W related to $BD\varphi$. K_B was estimated from the slope of the straight
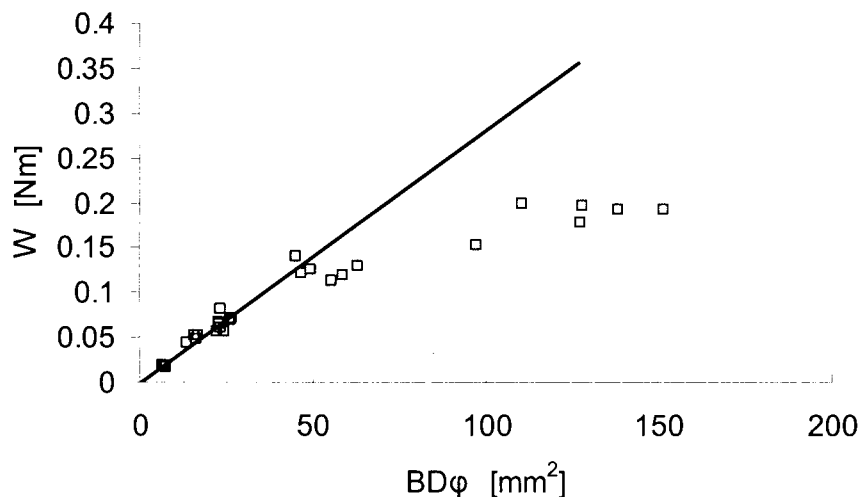
Figure 3: Typical diagram for determining G_B (notch radius 1 mm and tup velocity 1 m/s)

4
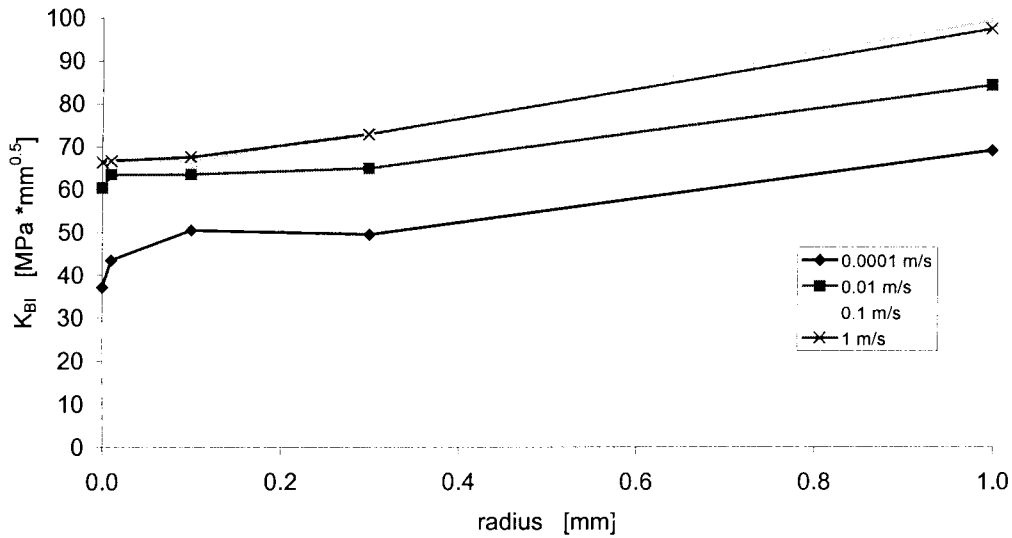
Figure 4: K_B related to notch radius at four different tup velocities
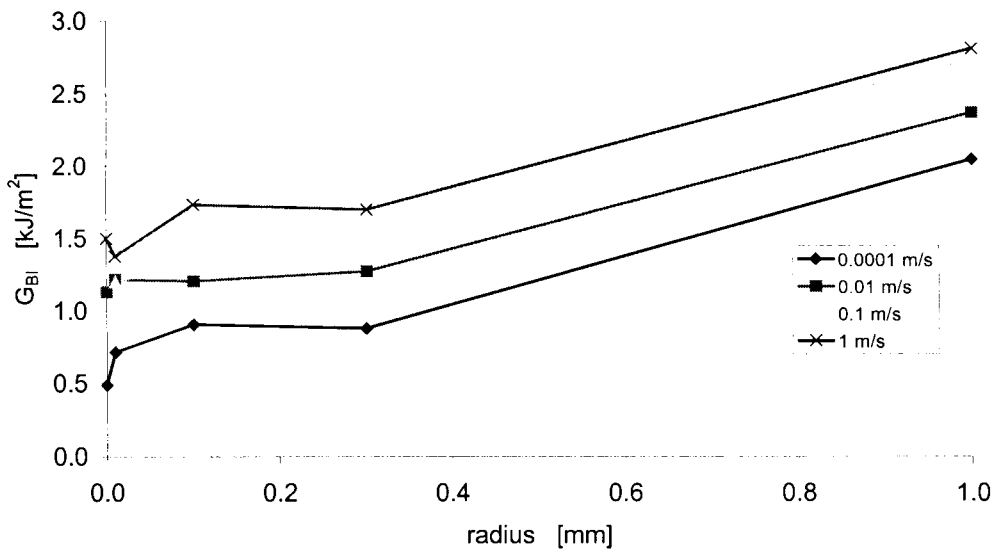
Figure 5: G_B related to notch radius at four different tup velocities

line fit of $\sigma^2 * Y^2$ related to $1/a$. A typical example of this procedure is given in fig. 3 for a notch radius of 1 mm and a tup velocity of 1 m/s. Generally, the best fit to a straight line did not intersect the axis in the origin. Often a small negative or positive intercept was found. Sometimes, the line could be shifted to the origin by applying a plastic zone size correction, but not always the same plastic zone size was found for K and G_b. Therefore, we did not apply such a correction. The results were fitted to a straight line that starts from the origin. Only the results of relatively deep notches were used. For the analysis of fig. 3 only the results of notches with a depth of 0.7 mm or more were used (r = 1 mm). In case of smaller notch radii the results of smaller notch depths were used with a minimum depth of 0.3 mm. From the results of these fits was concluded, that a K_b and G_b value could be applied to deep blunt notches, where a plane strain condition was present.

Fig. 4 and 5 show K_B and G_B related to the notch radius for different tup velocities. There is a positive correlation between the notch radius and K_B or G_B. However, the differences are very small up to a notch radius of 0.3 mm. An explanation for the small differences might be the effect of blunting, but it might also be the result of crazing induced during blunt notch machining or a combined effect. The range between 0.3 and 1 mm notch radius showed a greater increase of K_B and G_B. The increase was almost the same for the four tup velocities. However, according to the above-mentioned method of [5] the increase of G_b is rather small. Application of their model resulted in relatively high plastic zone sizes r_p. The tup velocity of 10^{-4} m/s

5

resulted in a plastic zone size r_p = 0.06 mm. The size increases up to r_p = 0.19 mm for the tup velocity of 1 m/s. According to [5] this must be caused by crazing induced during forming the blunt notches. Figure 5 and 6 show, that an increase of K_B and G_B is caused by an increase of the tup velocity. Only the graphs of 0.1 and 1 m/s were rather close, especially the graph for K_b. This could not be explained. If we take the ratio G^2 /K_B as a measure of the modulus, than the modules increases with the tup velocity, except for the range from 0.1 m/s to 1 m/s, where it decreases.

CONCLUDING REMARKS

It was shown, that in case of shallow notches up to a depth of about the notch radius the stress concentration factor reasonably well described the strength reduction of the flexural specimens with the two greatest notch radii (1mm and 0.3 mm). For the deep blunt notches the concept of G_B and K_B could be used. Increase of the tup velocity caused increase of the nominal strength and K_B and also of G_B. The tests show an increase of K_B and G_B as the notch radius increases, but a higher increase was expected. The applied blunt notch forming technique probably caused more crazing than the mill technique used in [5].

REFERENCES

1. Takano, M. and Nielsen, L.E. (1976) J. Appl. Polym. Sci. 20, 2193.
2. van der Zwet, M.J.M., Heidweiller, A.J. (1998) J. Appl. Polym. Sci. 67, 1473.
3. Vincent, P.I., (1961) Plastics 26.
4. Narisawa, I., Ishikawa, M. and Ogawa, H. (1980) J. Mater. Sci, 15, 2059.
5. Plati, E., Williams, J.G. (1975) Polym. Eng. Sci. 15, 470.
6. Peterson, R.E. (1974) Stress Concentration Factors. John Wiley & Sons, New York (1974).
7. Brown, H.F., Srawley, J.E. (1966), A.S.T.M., STP 410.

THE MECHANICAL BEHAVIOR AND FRACTURE OF THIN WALL IRON UNDER QUASI-STATIC AND DYNAMIC LOADING CONDITIONS

K. K. Schrems, J. A. Hawk and Ö. N. Do_an

U.S. Department of Energy, Office of Fossil Energy, Albany Research Center
Albany, Oregon 97321, USA

ABSTRACT

The use of cast iron in automotive applications in this era of increasing fuel efficiency requires the ability to cast very thin sections (2-7 mm). The mechanical properties of thin wall ductile iron castings are strongly affected by the thickness of the castings because thinner castings cool at a faster rate. In this study, strength properties were found to decrease as a reciprocal function of thickness. Strain properties were found to increase as a linear function of thickness. Determining quasi-static and dynamic mechanical properties is difficult due to the thin section sizes. Experiments relating mechanical properties with casting thickness will be discussed, including non-standard fatigue tests. Various means of verifying the non-standard tests will also be discussed.

KEYWORDS

ductile iron, mechanical properties, fatigue, thin section castings

INTRODUCTION

Iron-based castings will have some degree of pearlite in the microstructure, depending upon the processing conditions and cooling rate. As the percentage of pearlite increases, the strength increases and ductility decreases. Traditionally, castings have been produced with thick walls (greater than 7 mm), which results in a large percentage of the softer, more ductile ferrite. The mechanical properties of a keel block poured at the same time and from the same heat as a casting have been sufficient to represent the mechanical properties of the casting in general [1]. Mechanical properties are dependent on processing parameters, including the chemical composition, cooling rate, inoculation, solidification rate [1], and many other variables. The high cooling rate of thin-wall ductile iron is reported to result in a decrease in mechanical properties, specifically, ductility and toughness [1]. Thin sections of castings have been shown to have a larger amount of pearlite than thicker sections within the same casting [4], Figure 1. Whereas the keel block is sufficient to represent the properties for thick castings, it may not be for thin castings.

In order to effectively use thin wall castings, design properties pertinent to their processing conditions need to be available. No test methodology exists for thin wall iron, however, so a program is needed to develop the quasi-static and dynamic properties of thin-wall iron. To address this need, a program was undertaken to develop test specimen configurations, test procedures, and sampling recommendations. The results of the quasi-static testing are presented. The results from the quasi-static tests are then used to predict fatigue behavior.

EXPERIMENTAL PROCEDURE

Three heats of ductile cast iron were produced using an open ladle treatment. The final chemistries of the three heats are listed in Table 1. The treated irons were poured into resin-bonded dry sand molds. The irons were post-inoculated using two methods: for heat 6, a lump of 75% foundry grade ferrosilicon was placed in the mold, and for heats 8 and 9, 75% foundry grade ferrosilicon was added to the stream during pouring. The test castings were thin strips (referred to as singles) approximately 25 mm wide by 100 mm long, with a 25 mm x 25 mm x 35 mm runoff and a step plate (referred to as stepblock) consisting of joined strips approximately 25 mm wide by 100 mm long. The nominal thicknesses of the strips were 1.5, 2.0, 2.5, 3.0, 3.5, 4.0, 5.0, and 6.0 mm. Microstructure of the castings was characterized using image analysis software and an optical microscope [4].

The specimen blanks were machined into flat tensile bars approximately 75 mm long with a 25.4 mm reduced gage section. The width of the test section was approximately 6.35 mm with a thickness that depended on the original cast dimension. A taper of less than 0.1 mm was created from the shoulder to the center of the gage length. Approximately 0.25 mm of the broad surface was removed by grinding, effectively removing the as-cast surface. The tensile samples were tested on a screw-drive universal testing machine at 0.5 mm/min. Details of this testing procedure are published in [1].

From the stress-strain data, monotonic (quasi-static) design properties were calculated [1]. These design properties include reduction in area (%RA), elongation (%elo), true fracture ductility (ε_f), modulus of elasticity (E), yield strength (σ_y), ultimate tensile strength (s_u), true fracture strength (σ_f), strain hardening exponent (n), and strength coefficient (K).

TABLE 1
FINAL COMPOSITION OF TREATED IRONS (wt%)

Element	Heat 6	Heat 8	Heat 9
C*	3.80	3.71	3.76
Si	2.74	2.67	2.67
Mn	0.22	0.20	0.21
Cu	0.15	0.10	0.14

Cr	0.05	0.04	0.04
Mg	0.020	0.021	0.021
S	0.006	0.006	0.009

* calculated (base iron carbon content - 0.13 wt%)

Strain-life curves for eight different thicknesses of ductile cast iron were constructed using the strain-based four-point method [1]. The coordinates of the four points can be constructed from quasi-static properties by the following estimates:

where the first coordinate is the value in cycles to failure, N_f, and the second coordinate is the value of the strain range, $\Delta\varepsilon$. Points P_1 and P_2 define the elastic strain line. Points P_3 and P_4 define the plastic strain line. The sum of the two lines creates the fatigue curve for the alloy. Point P_4 is determined by the intersection of the elastic and plastic curves at the transition fatigue life, N_t, and is estimated to be 10^4.

RESULTS

The mechanical properties were plotted as a function of as-received thickness. Properties that are a measure of

strain, such as reduction in area, elongation (Figure 2), and true fracture ductility, were observed to have a linear relationship with the as-received thickness. Properties that are a measure of stress, such as yield strength, ultimate tensile strength (Figure 3), and true fracture strength were observed to have a reciprocal or inverse relationship with the as-received thickness. In addition, the two properties derived from the stress-strain curve, e.g., the strain hardening exponent and the strength coefficient, as well as one property often related to strength, e.g., hardness, were also found to have an inverse relationship with the as-received thickness. Modulus of elasticity was a constant value, independent of the as-received thickness.

Multiple linear regression was used to describe the results obtained from the mechanical testing campaign. The strain properties were evaluated for a fit against the following general model:

where μ is the mean value of reduction in area, elongation, or strain to failure. The model determines if there is a difference between the baseline value and any of the explanatory variables, which in this case is the as-received thickness. The coefficient β_0 is the mean value for the property at a thickness of zero. If the coefficient for thickness, β_1, is found to be statistically significant, then the mechanical property depends on the as-received thickness. The thickness coefficient was found to be significant for all measures of strain. Properties that appeared to have a reciprocal (inverse) relationship with the as-received thickness were

evaluated with a slightly different model:

The coefficient β_3 is the mean value for the property at an infinite thickness. The coefficient for the inverse thickness, β_3, was found to be significant for measures of stress, strain hardening exponent, strength coefficient, and hardness. The only property where thickness was not found to be significant was modulus of elasticity, which is a constant value of 158 GPa.

The multiple linear regression equations can also be used to predict the mean value of the property at a given thickness. These results are presented in Table 2.

TABLE 2
MEAN VALUES OF MECHANICAL PROPERTIES

t (mm)	% RA	% elo.	ε_f	σ_y (MPa)	s_u (MPa)	σ_f (MPa)	n^*	K^* (MPa)	HRG
2.0	1.9	1.6	0.024	485	597	596	0.28	2180	80
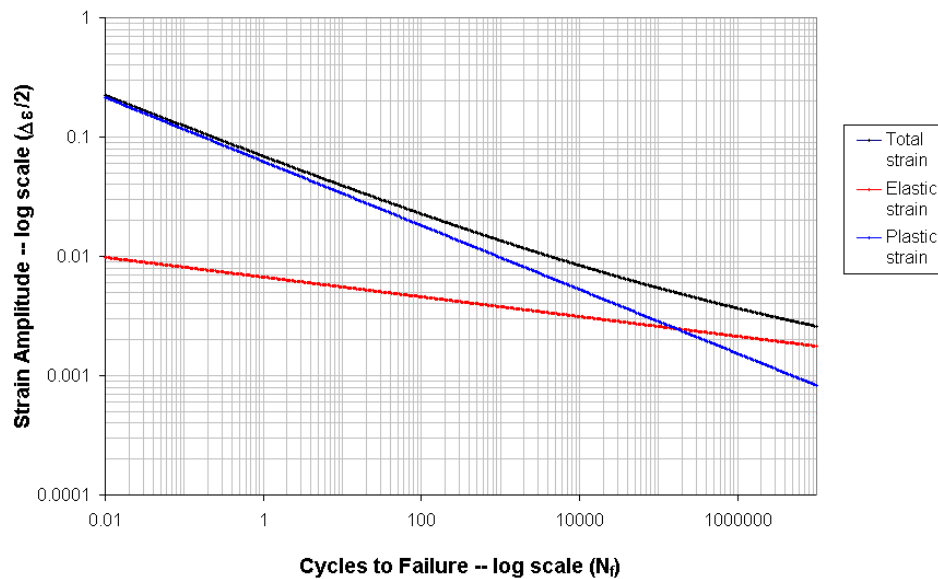
2.5	2.4	2.1	0.028	450	558	563	0.24	1770	75
3.0	2.8	2.5	0.033	427	532	541	0.22	1500	72
3.5	3.2	3.0	0.037	411	513	525	0.20	1310	70
4.0	3.7	3.5	0.042	399	499	513	0.19	1170	68
5.0	4.6	4.4	0.051	381	480	497	0.17	960	66
6.0	5.4	5.3	0.060	370	467	486	0.16	830	65
7.0	6.3	6.2	0.069	362	457	478	0.15	730	64

* values calculated from yield to 1% strain.

The strain-life curve constructed from these values for a sample 7.0 mm thick is shown in Figure 4.

DISCUSSION

Elongation and other measures of strain followed a linear relationship with respect to the as-received thickness of the ductile iron tensile specimen. Ultimate tensile strength and the other stress-related properties followed an inverse relationship with respect to the as-received specimen thickness. Since cooling rate is a function of the surface area divided by volume (mm^2/mm^3), it follows that the inverse thickness relationship (1/mm) closely approximates cooling rate when trying to explain the behavior of the stress-related properties. The inverse thickness effect is also seen in the pearlite percentages in Figure 1, which had been attributed to cooling rate.

The linear relationship between strain and thickness can be attributed to anomalies within the castings [1]. Any inconsistency in the microstructure or defects in the volume can be expected to alter the mechanical properties to a greater extent than the volume fraction of the inconsistency would suggest. For example, one sand grain may be present within the entire gage length, yet the specimen will break at the location of the sand grain with a lower tensile strength than that of the matrix. This effect was observed in the thin-wall ductile iron test specimens.

Based on the quasi-static results, it is expected that the fatigue properties of thin-wall castings will also differ from those of the bulk due to the combination of cooling rate and microstructural anomalies. Fatigue tests are planned to validate these predictions. A flat specimen with a 25 mm gage length will be used to determine low and high cycle fatigue properties. One of the assumptions of the predicted fatigue curves is that life transitions from plastic strain-controlled to elastic strain-controlled behavior at a lifetime of 10^7 cycles. This assumption, in particular, needs to be verified.

CONCLUSIONS

·   Reduction in area, elongation, and true fracture ductility were observed to have a linear relationship with the as-received thickness of thin wall castings. This is attributed to the presence of microstructural anomalies.
·   Yield strength, ultimate tensile strength, true fracture strength, strain hardening exponent, strength coefficient, and hardness were observed to have a reciprocal or inverse relationship with the as-received thickness. This is attributed to the faster cooling rate of the thinner sections producing larger amounts of pearlite.
·   Thin wall castings have properties that differ from the bulk. Accurate mechanical properties of thin wall cast iron may require testing specimens from the desired thickness. Additional testing is planned to correlate thin wall casting properties with those from keel blocks.
·   Fatigue properties can be predicted from the quasi-static mechanical properties. Testing is planned to verify the transition life, as well as the validity of the curves.

ACKNOWLEDGMENTS

REFERENCES

1.   Jenkins, L.R. and Forrest, R.D. (1990). In: *Metals Handbook, Tenth Edition. Volume 1: Irons, Steels, and High-Performance Alloys*, pp. 33-55. ASM International, Materials Park, OH.

1. O'Rourke, R. (2001) *Adv. Matls & Proc.*, January, 65.

1. Javaid, A., Davis, K.G., and Sahoo, M. (2000) *Modern Casting*, June, 39.

1. Schrems, K.K., Do_an, Ö.N., and Hawk, J.A., to be published: *J. Test. Eval.*

1. SAE J1099: Technical Report on Fatigue Properties (1975). Society of Automotive Engineers, Warrendale, PA.

1. (1996). In: *Metals Handbook, Tenth Edition. Volume 19: Fatigue and Fracture*, pp. 963-979. ASM International, Materials Park, OH.

1. Schrems, K.K., Hawk, J.A., and Do_an, Ö.N., submitted to: *Met. Trans. A.*

THE MOBILITY OF NON-PLANAR DISLOCATIONS AHEAD OF A CRACK TIP

A.H.W. Ngan

Department of Mechanical Engineering, The University of Hong Kong,
Pokfulam Road, Hong Kong, P.R. China

ABSTRACT

In this paper, we first show using a generalised Peierls-Nabarro dislocation model that, if the cause of the low mobility of a dislocation is due to the need to transform the core from a non-planar configuration to a planar one, then this transformation will be greatly enhanced in the vicinity of a crack tip. The physical reason is that, being a free surface, the presence of the crack tip will reduce the mechanical rigidity of the matrix in which the dislocation is situated. We then present atomistic simulation results on screw dislocations in iron to show that this mobility enhancement effect is indeed a real one. The results suggest that there exists a critical stress intensity factor K_{mc} of the order of $\sim 0.15\ \mu\sqrt{b}$ (μ = shear modulus, b = Burgers vector), such that if the applied stress intensity factor is larger than this value, all dislocations ahead of the crack tip would be planar and mobile. K_{mc} is found to be lower than the critical stress intensity factor for nucleation from crack-tip, and so crack-tip emission is nucleation rather than mobility controlled.

KEYWORDS

Dislocation, crack-tip plasticity, atomistic simulation, brittle-to-ductile transition

INTRODUCTION

The brittle-to-ductile transition (BDT) has been a problem of considerable practical and theoretical interest. It is generally believed that BDT will occur when dislocation sources near the crack tip can send out dislocations quick enough to shield the crack tip [1], or when dislocations can emanate quick enough from the crack tip itself to shield or blunt it. In the latter case, Weertman [2], Schoeck [3,4], Rice [5,6], and Xu et al [7] have investigated the problem of dislocation emission from crack tips. In their work, the process of gradually forming a dislocation from zero to unit Burgers vector content is considered in detail, and the relative ease of dislocation nucleation in competition with crack cleavage is studied. In the incipient process considered by these authors, the dislocation is assumed to have a planar core. In particular in Rice's model, a J-integral was used to evaluate the fault energy change as the dislocation forms from the crack tip. This results in the model's inability to account for any lattice friction that might act on the dislocation during the incipient process. In materials exhibiting the BDT, the intrinsic Peierls

stress is high and so lattice friction should not be neglected *a priori* in a satisfactory treatment on crack-tip plasticity.

In the present paper we focus on the interaction between the ½<111> screw dislocation and a mode III crack tip in the body-centred cubic (BCC) structure. The ½<111> screw dislocation has a three-fold non-planar core and is therefore representative of a system with a large friction stress. We will first use a semi-continuum approach based on a generalised version of the Peierls-Nabarro model [8] which can cater for non-planar dissociation of the dislocation core. This is then followed by atomistic simulation which serves to verify the conclusions reached by the semi-continuum model.
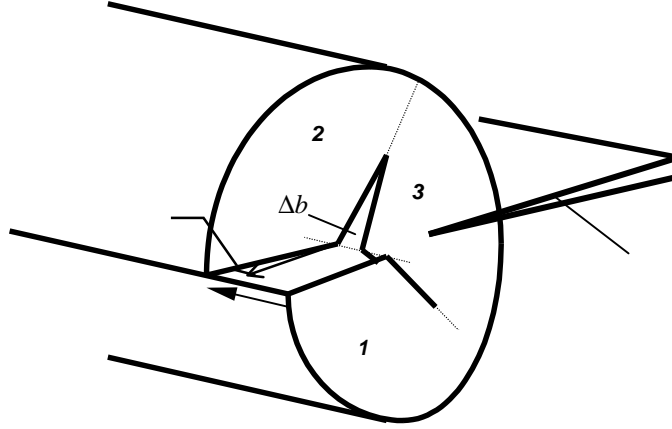
Figure 1: Three-fold screw dislocation ahead of a mode III crack tip

SEMI-CONTINUUM MODEL

In the generalised Peierls-Nabarro model, the ½<111> screw dislocation is modelled as elastically strained wedges joined together at surfaces parallel to the dislocation line over which atomic misfit takes place (Figure 1). The force law operating across the misfit surfaces is non-linear and may be assumed to have a simple Frenkel form

$$\gamma = \frac{\mu b}{4\pi^2}\left[1 - \cos\left(\frac{2\pi\Phi}{b}\right)\right], \tag{1}$$

where μ is the shear modulus, b the Burgers vector and Φ the misfit displacement. When the screw dislocation is situated at a distance x ahead of a mode III crack tip, the total energy E_{tot} may be expressed as

$$
\begin{aligned}
E_{tot} = \frac{3\mu}{2\pi} \int_0^\infty \int_0^\infty &\{ \frac{2\eta^2}{(\eta^3 - \xi^3)}\sqrt{\frac{\xi^3 + x^3}{\eta^3 + x^3}}\, u_{3-}{}'(\xi)u_{3-}(\eta) + \frac{\sqrt{\eta}}{\eta^{3/2} + \xi^{3/2}}\left[u_{2-}{}'(\xi)u_{2+}(\eta) + u_{2+}{}'(\xi)u_{2-}(\eta)\right] \\
&+ \frac{\sqrt{\eta}}{\eta^{3/2} - \xi^{3/2}}\left[u_{2+}{}'(\xi)u_{2+}(\eta) + u_{2-}{}'(\xi)u_{2-}(\eta)\right] \} \, d\eta d\xi \\
&+ 2\int_0^\infty \gamma[\Phi = \Delta b - u_{3-}(r) - u_{2+}(r)]\,dr + \int_0^\infty \gamma[\Phi = (1-2\Delta)b - 2u_{2-}(r)]\,dr \\
&- 2\int_0^\infty \tau_c(r)[u_{3-}(r) + u_{2+}(r)]\,dr + 2\int_0^\infty \frac{K_{III}}{\sqrt{2\pi(r+x)}}u_{2-}(r)\,dr
\end{aligned}
\tag{2}
$$

where K_{III} is the applied stress intensity factor and $\tau_c(r) = K_{III}\cos(\psi/2 + \pi/3)/\sqrt{2\pi\rho}$, $\rho = \sqrt{r^2 + x^2 - rx}$, $\psi = \tan^{-1}[\sqrt{3}r/(2x-r)] \in [0,\pi]$. In this expression, the double integral term is the strain energy, the

terms involving γ the misfit energy and the last two terms the work-done against applied stress. $u_{i\pm}(r)$ is the displacement function of the boundary marked by + or - of wedge i relative to the wedge tip position (see Figure 1). Δ is the Burgers vector content of the misfit surface 2|3 or 3|1, and can be used as a parameter specifying the degree of recombination of the core into the planar state. In the absence of the crack-tip, the core configuration should be symmetrically three-fold, and Δ will assume the value 1/3, and when the core is totally constricted into the planar state, Δ will become 0. The boundary displacements are subject to $u_{3-}(0) = 0$, $u_{3-}(\infty) = b/2$, $u_{2-}(0) = 0$, $u_{2-}(\infty) = (1/2-\Delta)b$, $u_{2+}(0) = 0$, $u_{2+}(\infty) = (\Delta-1/2)b$ because of the necessity to match with the Volterra solution in the long-range.

The stable configurations of the dislocation core under various conditions were obtained by minimising E_{tot} in eqn. (2) with respect to Δ, u_{3-}, u_{2+} and u_{2-} by variational means. More details about the methodology used are given in ref. [9]. Figure 2 shows the relation between the fractional Burgers vector Δ and the applied load at different values of distance x between the dislocation and the crack tip. It can be seen that with increasing stress, Δ initially decreases gradually. However, as soon as Δ decreases beyond ~ 0.25, the conversion towards the planar configuration speeds up quickly, implying that as long as the Burgers vector content in the 1|2 branch parallel to the crack plane reaches about 0.5, the core transforms very quickly to the planar state. As comparison, the behaviour of the screw core without the presence of the crack tip has also been investigated by Ngan [8,9]. In this case, the total energy functional is simpler than that shown in eqn. (2) but because of limitation of space it is not reproduced here. Figure 3 shows the relation between the fractional Burgers vector Δ and the stress applied along the Burgers vector on the 1|2 plane. It can be seen that Δ drops gradually with increasing stress and a rapid transformation to the planar state at $\Delta \approx 0.25$ does not occur in the crack-free situation. The rapid transformation to the planar state at $\Delta \approx 0.25$ in the presence of the crack in Figure 2 can be understood from the γ force law expressed in eqn. (1), in which the misfit energy attains a maximum when Φ equals $0.5b$. Thus as soon as the tip of the 1|2 branch opens by more than $0.5b$, corresponding to Δ falling below 0.25, the misfit force law exerts a force trying to enlarge the opening along the 1|2 branch. In the absence of a crack, the enlargement of branch 1|2 is resisted by the associated strain energy rise mainly in wedge 3 and so no instability situation arises. However, if wedge 3 is cracked as shown in Figure 1, it will become much less rigid and so the misfit energy may prevail. To prove that $\Delta \approx 0.25$ indeed marks an instability point in the cracked situation, stress removal tests were performed. It was found that if the core is stressed to any configuration with $\Delta > 0.25$, the configuration will return to the stress-free stable configuration upon removal of the applied load. However, if the core is stressed to beyond the $\Delta \approx 0.25$ point so that it has become planar, then upon removal of stress, the core will remain in the planar configuration with $\Delta \approx 0$. This shows that the planar state is a metastable state.
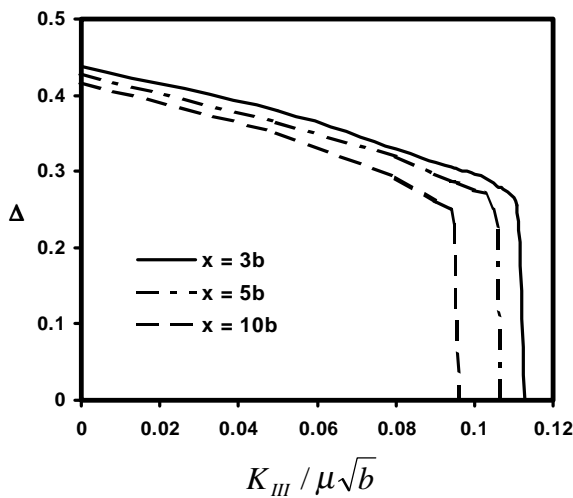
Figure 2: Core behaviour ahead of crack tip
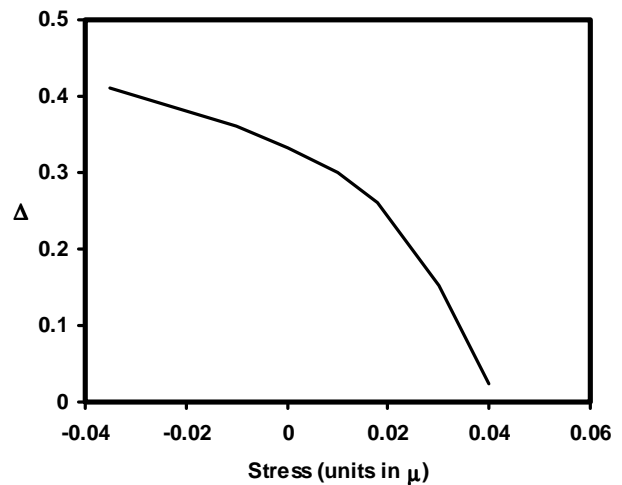
Figure 3: Core behaviour in bulk crystal

The above results suggest that the mobility of the screw dislocation is greatly enhanced ahead of a crack tip. To estimate the effective Peierls stress τ_p in the presence of a crack tip, we write

$$\frac{K_m}{\sqrt{2\pi x}} = \tau_p + \frac{\mu b}{4\pi x} \tag{3}$$

where K_m is the value of K_{III} needed to move the dislocation against τ_p and the image stress. In our current Peierls-Nabarro picture, K_m can be taken to be the critical K_{III} required to convert the core into the planar, mobile state obtainable as the intercepts of the curves at $\Delta = 0$ in Figure 2. In Table 1 are shown these K_m values at various values of x. By fitting eqn. (3) to these data points, we find that τ_p is $\sim 0.004\mu$ ahead of a crack tip. The value of τ_p for a dislocation in the bulk can be estimated to be 0.04μ from Figure 3. Thus, a screw dislocation situated in front of a crack tip is predicted to have an effective Peierls stress one order of magnitude lower than if it is situated in a perfect crystal.

TABLE 1
EFFECTIVE PEIERLS STRESS AHEAD OF CRACK TIP FROM PEIERLS-NABARRO MODEL

$\dfrac{x}{b}$	$\dfrac{K_m}{\mu\sqrt{b}}$	$\dfrac{\tau_p}{\mu} = \dfrac{K_m}{\mu\sqrt{2\pi x}} - \dfrac{b}{4\pi x}$
3	0.113	~ 0
5	0.107	0.003
10	0.096	0.004

ATOMISTIC SIMULATION

The atomistic simulation was set up by placing a mode III crack plane on a {110} plane with the crack tip parallel to a <111> axis. A ½<111> Burgers vector screw dislocation was also introduced parallel to the same <111> axis on the same {110} plane at a distance x from the crack front. This is similar to the situation in Figure 1. In the MD simulation, an iron-like potential was used and fuller details are given in ref. [10]. The relaxation region was composed of a circular cylindrical crystallite with radius $25a$ (a is the lattice parameter). Periodic boundary conditions were applied along the <111> dislocation direction. In the other two orthogonal directions, the displacement of the boundary region was fixed according to the elasticity solution of the dislocation-crack system.

We have simulated the effects of an applied stress on the core configuration with and without a crack tip in the vicinity of the dislocation. In the crack-free situation without an applied stress, spreading of the core is confined mainly to three intersecting {110} planes. When a shear stress is applied along one of these {110} planes, the spreading on this plane will extend while that on the other two {110} planes will retract. When the configuration is almost planar, the core starts to move. In our simulation, this occurs at a critical applied stress of about 0.027μ, which agrees well with the result reported by Duesbury et al [11] and reasonably well with the value of 0.04μ in Figure 3.

In the presence of a stress-free crack tip, the main effect on the dislocation core is the image force. At distances $x < 5b$ from the crack-tip, because of the large magnitude of the image force, no stable core configuration can be found in our simulation if no applied stress is exerted. For $x \geq 5b$, the dislocation configuration near the unstressed crack tip is similar to that in the bulk but with a negative stress acting. A more or less symmetrical three-fold state as similar to that in the unstressed bulk crystal can however be produced by exerting a positive K_{III} load on the crack so as to counteract the image force. An example of this is shown in Figure 4, which shows the core structure at $x = 8b$. The core spreading configuration at $K_{III} = 0$ (Figure 4(a)) has a turning point on the lower inclining branch and is similar to the structure found

in the crack-free situation with a negative applied shear stress. At $K_{\text{III}} = 0.067\,\mu\sqrt{b}$ (Figure 4(b)) the configuration appears very similar to that in the unstressed bulk crystal. The core begins to move at a higher load of $0.170\,\mu\sqrt{b}$. Denoting by K_i the critical load required to completely balance the image force so as to make the core structure appear like that in the unstressed bulk crystal, K_i is given in the Volterra model by

$$\frac{K_i}{\sqrt{2\pi x}} = \frac{\mu b}{4\pi x}. \tag{4}$$
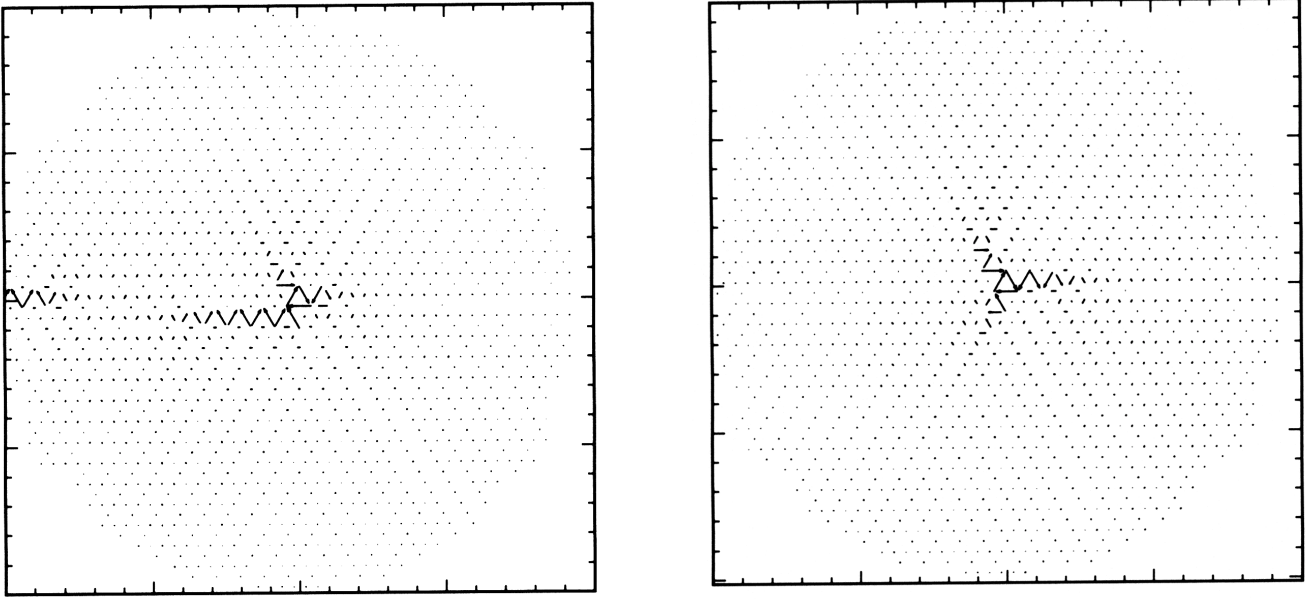
Figure 4: Atomistic core structure when the dislocation is situated at $x = 8b$ from the crack tip.
(a) $K_{\text{III}} = 0$, (b) $K_{\text{III}} = 0.067\,\mu\sqrt{b}$.

Table 2 shows the values of K_i estimated from our atomistic results for $x \geq 5b$. It can be seen that eqn. (4) agrees very well with the atomistic results. This means that at $x \geq 5b$, the crack-tip stress field and the image force can be accurately represented by the elastic K-field and the Volterra dislocation field respectively.

TABLE 2
EFFECTIVE PEIERLS STRESS AHEAD OF CRACK TIP FROM ATOMISTIC SIMULATION

x	"atomistic" K_i ($\mu\sqrt{b}$)	$\dfrac{2\sqrt{2\pi x}\,K_i}{\mu b}$ ($= 1$ in elastic model eqn. (4))	"atomistic" K_m ($\mu\sqrt{b}$)	$\dfrac{K_m}{\mu\sqrt{2\pi x}} - \dfrac{b}{4\pi x}$ ($= \tau_p/\mu$ in elastic model eqn. (3))
$5b$	0.09	1.01	0.15	0.0108
$8b$	0.07	0.99	0.17	0.0140
$12b$	0.06	1.04	0.18	0.0141

The critical load K_m required to move a dislocation core as determined from the atomistic simulation is also listed in Table 2. From the conclusion above, we are confident that the K-term and the image term in eqn. (3) are valid for $x \geq 5b$. The Peierls stress for a dislocation in the bulk crystal is $\sim 0.027\mu$ as

mentioned above. However, as can be seen from Table 2, if eqn. (3) is to be obeyed, the effective τ_p ahead of a crack-tip is about 0.014 μ which is only half of the bulk value of 0.027μ. The effective Peierls stress from the atomistic simulation is higher than that calculated from the semi-continuum model in Table 1, but both indicate an enhancement of dislocation mobility ahead of a crack-tip.

DISCUSSION AND CONCLUSION

The semi-continuum results in Figure 2 suggest that the critical load K_m to move the dislocation core decreases slightly as x increases, and that if K_{III} is larger than about 0.12 $\mu\sqrt{b}$, a dislocation that has been freshly emitted from the crack tip (with $x \sim 0$) and all dislocations situated further away would have planar cores and are thus mobile. The atomistic results in Table 2 indicate K_m to be more or less the same at 0.15-0.18 $\mu\sqrt{b}$, which is of similar magnitude as the 0.12 $\mu\sqrt{b}$ from the semi-continuum model. These results therefore suggest the existence of a critical stress intensity factor K_{mc} such that if the applied K_{III} is higher than this value, then all dislocations would be mobile. If the applied K_{III} is lower than K_{mc}, then an immobile zone would exist ahead of the crack tip, the size of which would increase as the difference ($K_{mc} - K_{III}$) increases. A dislocation situated within this zone would require thermal activation for motion. Rice [5] has suggested the existence of a critical load K_e for dislocation nucleation directly from crack tip and $K_e = \sqrt{2\mu\gamma_{us}}$, where γ_{us} is the unstable stacking fault energy. Taking γ_{us} to be the maximum value of the γ-force law in eqn. (1), $\gamma_{us} = \mu b/(2\pi^2)$, and so $K_e \approx 0.3$ $\mu\sqrt{b}$. K_e is therefore of similar magnitude but about one time higher than K_{mc} for motion, implying that nucleation from crack-tip would be more difficult than subsequent motion. Thus, if dislocations can be nucleated from the crack-tip, they should be able to move away from it, implying that crack-tip emission is nucleation rather than mobility controlled.

ACKNOWLEDGMENT

REFERENCES

[1] Hirsch, P.B. and Roberts, S.G. (1991) *Phil. Mag. A*, 64, 55.
[2] Weertman, J. (1981) *Phil. Mag. A*, 43, 1103.
[3] Schoeck, G. (1991) *Phil. Mag. A*, 63, 111.
[4] Schoeck, G. (1996) *J. Mech. Phys. Solids*, 44, 413.
[5] Rice, J.R. (1992) *J. Mech. Phys. Solids*, 40, 239.
[6] Rice, J.R. and Beltz, G.E. (1994) *J. Mech. Phys. Solids*, 42, 333.
[7] Xu, G., Argon, A.S. and Ortiz, M. (1995) *Phil. Mag. A*, 72, 415.
[8] Ngan, A.H.W. (1997) *J. Mech. Phys. Solids*, 45, 903.
[9] Ngan, A.H.W. and Zhang, H.F. (1999), *Mech. Mater.*, 31, 367.
[10] Zhang, H.F. and Ngan, A.H.W. (1999), *Scripta Mater.*, 41, 737.
[11] Duesbury, M.S., Vitek, V. and Bowen, D.K. (1973) *Proc. R. Soc. Lond. A*, 332, 85.

THE QUASI-STATIC FRACTURE BEHAVIOR OF 7034 ALUMINUM ALLOY REINFORCED WITH SILICON CARBIDE PARTICULATES

T. S. Srivatsan[1], Meslet Al-Hajri[1] and M. Petraroli[2]

[1]Department of Mechanical Engineering, The University of Akron
Akron, Ohio 44325-3903, USA
[2]The Timken Company, 1835 Dueber Avenue, S.W.,
P.O. Box 6930, Canton, Ohio 44706-0930, USA

ABSTRACT

The quasi-static response of aluminum alloy 7034 discontinuously reinforced with particulates of silicon carbide was studied at room and elevated temperatures, in both the under-aged and peak-aged conditions, with the objective of documenting the influence of microstructure and temperature on tensile properties and intrinsic fracture behavior. Test results reveal the elastic modulus and strength of the aluminum alloy-based metal matrix composite to decrease with an increase in temperature, while the ductility, quantified in terms of elongation-to-failure and reduction-in-area, revealed significant improvement. Fractures on a microscopic scale was dictated by events that resulted in the failure of the brittle reinforcing silicon carbide particulates by cracking and decohesion at the matrix-particulate interfaces.

KEYWORDS: *Aluminum alloy composite, microstructure, tensile properties, fracture*.

1.   INTRODUCTION

Twenty-first century aerospace systems have mission requirements that will demand advanced materials, such as metal matrix composites, to have the potential to meet the demands of present and future aerospace vehicles. In the time period spanning the last two decades, metal matrix composite (MMCs) have been a promising and often-promised, structural materials solution. Reinforced metal-matrices are highly versatile engineering materials that offer the potential for improvements in efficiency, strength, stiffness coupled with good wear and corrosion resistance over the newer generation monolithic alloys of aluminum and titanium and even organic matrix composites [1-5]. Besides, they have the ability to be processed and finished using conventional metal processing. In fact the technology of discontinuously-reinforced aluminum alloy based composites has matured to the point where components are now being produced for aircraft structures, gas turbine engines, automobiles, electronics, spacecraft and even recreational goods [6].

This paper examines the influence of silicon carbide particulate (SiC_p) reinforcements and aging condition on the tensile properties and fracture behavior of 7034 aluminum alloy based MMC. The tensile properties and fracture behavior of the composite, at both room and elevated temperatures, are compared in order to rationalize microstructure and test temperature influences on deformation and fracture.

2.   MATERIAL

The aluminum alloy MMC used in this research investigation was made using the spray processing technique and provided as an extruded billet by the Air Force Materials Laboratory (Dayton, Ohio, USA). The billet

was obtained by extruding the consolidated sample through a standard shear-face die. The as-received billet was subject to the following heat treatment: (a) solution heat treated at 490°C for 4 hours, (b) immediately quenched in cold water, and (c) artificially aging at the following temperatures: (1) 120°C for 30 minutes to get the under-aged (UA) condition, and (2) 120°C for 24 hours to get the peak-aged condition. The composites are referred to henceforth in this manuscript as 7034/SiC/15p-UA and 7034/SiC/15p-PA.

3. EXPERIMENTAL PROCEDURES

Samples were cut from both the 7034/SiC/15p –UA and 7034/SiC/15p-PA composites and prepared by standard metallographic procedures for observation in an optical microscope. The reinforcing silicon carbide particulate morphology, their size and distribution in the aluminum alloy metal matrix and other coarse microstructural features were examined in an optical microscope and photographed using a bright-field technique.

Tensile test specimens were precision machined from rectangular blanks (l: 150 mm x w: 20 mm x t: 20 mm), using a diamond coated saw blade, with the stress axis parallel to the extrusion direction. To minimize the effects of surface irregularities and finish, final surface preparation was accomplished by mechanically polishing the entire gage section of the test specimens through 600 grit silicon carbide paper and then finish polished to remove all circumferential scratches and surface machining marks. The specimens were deformed at a constant strain rate of 0.0001 s^{-1} on a fully automated, computer controlled servohydraulic test machine equipped with a 22,000-kg load cell (INSTRON: Model 8500 Plus). The tests were performed at room temperature (27°C) and elevated temperature of 120°C. The elevated temperature tests were performed in an environmental changer (Type: INSTRON Model 3111). The temperature was controlled with the aid of a temperature controller linked to thermocouple fixed on the surface of the specimen. Maximum temperature variation along the gage section of the specimen was + 2°C. Fracture surfaces of the deformed tensile specimens were examined in a scanning electron microscope (SEM) to characterize the predominant fracture mode and the fine-scale features on the fracture surface.

4. RESULTS AND DISCUSSION

4.1 *Initial Microstructure*
The optical micrographs illustrating the microstructure of the 7034/SiC/15p-UA and 7034/SiC/15p-PA composites are shown in Figure 1. The SiC$_p$, in the 7034 metal matrix, were non-uniform in size, irregularly shaped and randomly dispersed. At regular intervals, a clustering or agglomeration of the SiC particulates, of varying sizes, was observed resulting in SiC particulate rich and SiC particulate depleted regions. An agglomerated site consisted of the smaller SiC$_p$ intermingled with few larger SiC$_p$. No attempt was made to determine the particle size distribution for the two microstructures.

4.2 *Tensile Properties*
Test results reveal that at the elevated temperature of 120°C the elastic modulus of the 7034/SiC/15p-PA composite is marginally lower that at the ambient temperature (27°C), and marginally higher for the 7034/SiC/15p-UA counterpart. The yield strength, defined as the stress corresponding to a plastic strain of 0.2 percent, decreased with an increase in test temperature for both the peak-aged (PA) and under-aged (UA) test samples. The observed decrease was as high as 13% for the 7034/SiC/15p-PA microstructure and only 9% for 7034/SiC/15p-UA counterpart. For both aging conditions the ultimate tensile strength (σ_{UTS}) of the 7034/SiC/15p composite is marginally higher than the tensile yield strength (σ_{YS}) indicating that the work hardening rate past yielding is low. The ultimate tensile strength followed the same trend as the yield strength of the composite. The decrease in ultimate tensile strength with an increase in test temperature from 27°C to 120°C was around 11% for the 7034/SiC/15p-UA and 7034/SiC/15p-PA microstructures.

The ductility as measured by: (a) tensile elongation over a 12.7 mm gage length of the test specimen, and (b) reduction in cross-sectional area, increased with an increase in test temperature. The increase was as high as 40% for the PA microstructure and only 3% for the UA microstructure. The reduction-in-area increased with an increased in test temperature by as much as 110% for the 7034/SiC/15p-PA and only 25% for the 7034/SiC/15p-UA condition. The observed increase in strain-to- failure and reduction-in-area with an increase in test temperature is consistent with the degradation of strength at the higher test temperature.

4.3 *Tensile Deformation and Fracture Behavior*

At both room (27°C) and elevated (120°C) test temperatures the 7034/SiC/15p composite exhibited essentially limited ductility, on a macroscopic scale, with fracture occurring on a plane normal to the far-field tensile stress axis. However, examination of the tensile fracture surfaces at higher magnifications revealed features reminiscent of locally ductile and brittle mechanisms. Representative fractographs of the tensile fracture surface of the 7034/SiC/15p-UA and 7034/SiC/15p-PA composites are shown in Figures 2 and 3.

A: *7034/SiC/15p-UA Composite*

At both test temperatures the tensile fracture surfaces of this microstructural condition was flat and normal to the tensile stress axis when viewed on a macroscopic scale but rough when viewed on a microscopic scale (Figure 2a). The aluminum alloy metal matrix revealed combinations of tear ridges (Figure 2b), failure of the reinforcing SiC_p by cracking (Figure 2c) and decohesion at the interfaces with the matrix (Figure 2c). Following the early initiation of damage, subsequent accumulation, growth and eventual linkage in the matrix resulted in brittle failure (Figure 2c). At the higher test temperature the degree of particulate failure both through cracking and decohesion at its interfaces with the metal matrix increased (Figure 2d). The matrix of this composite was covered with pockets of shallow dimples. Multiple microscopic cracks were observed in regions of particulate agglomeration, which is responsible for the inferior ductility of the composite.

B: *7034/SiC/15p-PA Composite*

At ambient temperature (27°C) the fracture surfaces revealed the SiC particulates surrounded by ductile regions described as tear ridges (Figure 3b), particulate failure through cracking (Figure 3c) and decohesion or separation at the matrix-particulate interfaces (Figure 3d). No major difference in tensile fracture features was evident at the higher test temperature (120°C). The matrix of the composite was covered with a population of microscopic voids of varying size and isolated pockets of shallow dimples. The submicrometer-sized dimples are indicative of the improved ductility of this composite at this temperature.

The constraints imposed on mechanical deformation by the presence of brittle and essentially elastically deforming SiC_p in a soft, ductile and plastically deforming aluminum alloy metal matrix and the concomitant development of a local triaxial stress state, in the matrix, aids in limiting flow stress of the composite microstructure and thus favors: (a) void initiation and growth in the matrix, and (b) debonding at the matrix-SiC_p interfaces. As a direct consequence of deformation constraints induced by the hard and brittle SiC_p reinforcements, a higher applied stress is required to initiate plastic deformation in the aluminum alloy metal matrix. This translates to a higher yield strength and higher elastic modulus of the composite microstructure. Under the influence of a far-field tensile load the voids appeared to have undergone limited growth confirming a possible contribution from particulate-constraints induced triaxiality on failure of the composite matrix. The local plastic constraints are particularly important for the larger-sized SiC particulates and for SiC particulate clusters during composite fracture [7,8]. Examination of the fracture surfaces revealed damage to be highly localized at the SiC reinforcing phase through: (a) cracked particulates and (b) interfacial failure or decohesion. This suggests that plastic strain become localized during the early stages of tensile deformation. Few of the microscopic voids, generated by SiC particulate cracking, did not grow extensively in the tensile stress direction, which is generally the case for ductile fracture of unreinforced aluminum alloys [6]. The lack of extensive void growth in this particulate-reinforced aluminum alloy metal matrix also suggests that both void nucleation strain and associated linkage strain critically control the fracture strain.

5. CONCLUSIONS

The following are the essential findings of this study:

1. The microstructure of the two composites, Underaged and peaked, revealed a non-uniform dispersion of the reinforcing SiC particulates. At regular intervals, an agglomeration of the reinforcing particulates, of varying size, was observed.
2. The modulus and strength of the two composite microstructures decreased with an increase in temperature. The ductility, quantified in terms of elongation-to-failure and reduction in area decrease with an increase in temperature.

3. Fracture of the reinforcing SiC particulates coupled with decohesion at its interfaces with the matrix permits the microscopic cracks to grow and link by fracture through the matrix resulting in macroscopically brittle appearance and resultant low ductility.

ACKNOWLEDGEMENTS

TABLE 1: THE TENSILE PROPERTIES OF THE 7034/SiC/15p COMPOSITE**

Aging Condition	Temperature (°C)	E (GPa)	Yield Strength (MPa)	Ultimate Tensile Strength (MPa)	Elongation (%)	Reduction-in-Area (%)
UA	27	90	662	709	1.8	2.4
	120	86	574	604	2.5	5.1
PA	27	91	612	683	1.9	3.3
	120	90	562	611	1.9	4.0

** Results are the mean values based on duplicate tests.

6. REFERENCES

1. Srivatsan, T.S., Sudarshan, T.S., and Lavernia, E.J. (1995) *Progress in Materials Science*, 39, 317**.**
2. Lewandowski, J.J., in *Comprehensive Composite Materials*, (editors: A. Kelly and C. Zweben).
3. Lewandowski, J.J., in Metal Matrix Composites: Volume 3 (editors: T.W. Clyne), Elsevier Publishers, pp. 151-187, 2000.
4. Taya, M., and Arsenault, R.J., (1989) Metal Matrix Composites, Pergamon Press, Elmsford, New York, 1989.
5. Hunt, Jr., W.H., Cook, C.R., and Sawtell, R.R., (1991) SAE Technical Paper Series 91-0834, Society of Automotive Engineers, Warrendale, PA, USA.
6. Maruyama, B., (1998) *The AMPTIAC Newsletter*, Vol. 2, Number 3.
7. Lewandowski, J.J., Liu, C and Hunt, W.H., *Materials Science and Engineering*, A107, 1989, pp. 241-255.
8. Argon, A.S., Im, J., and Safoglu, R., (1975) *Metallurgical Transactions*, Vol. 6A, pp. 825.
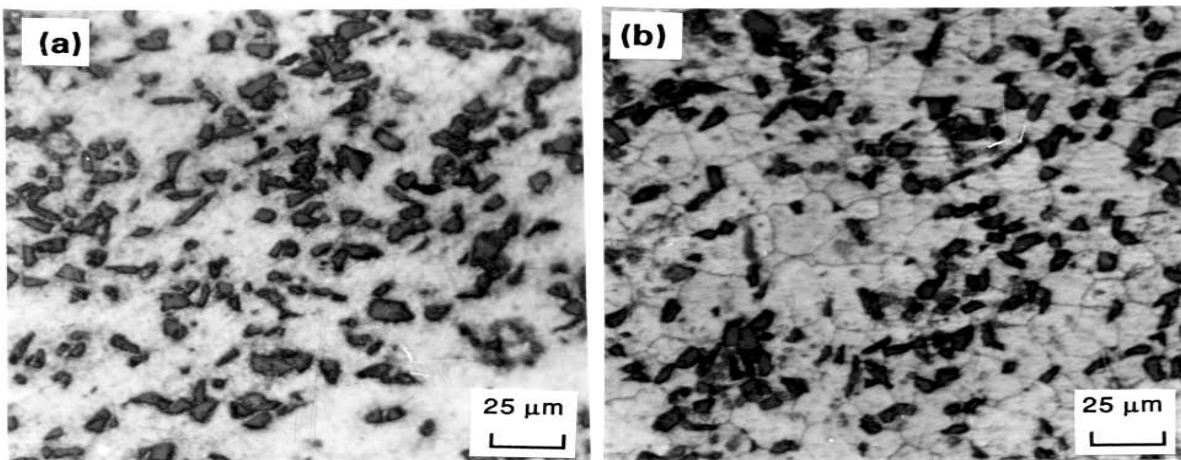
Figure 1.   Optical micrographs showing the microstructure of the 7034/SiC/15p composite for: (a) under-aged (UA) and (b) peak-aged (PA).
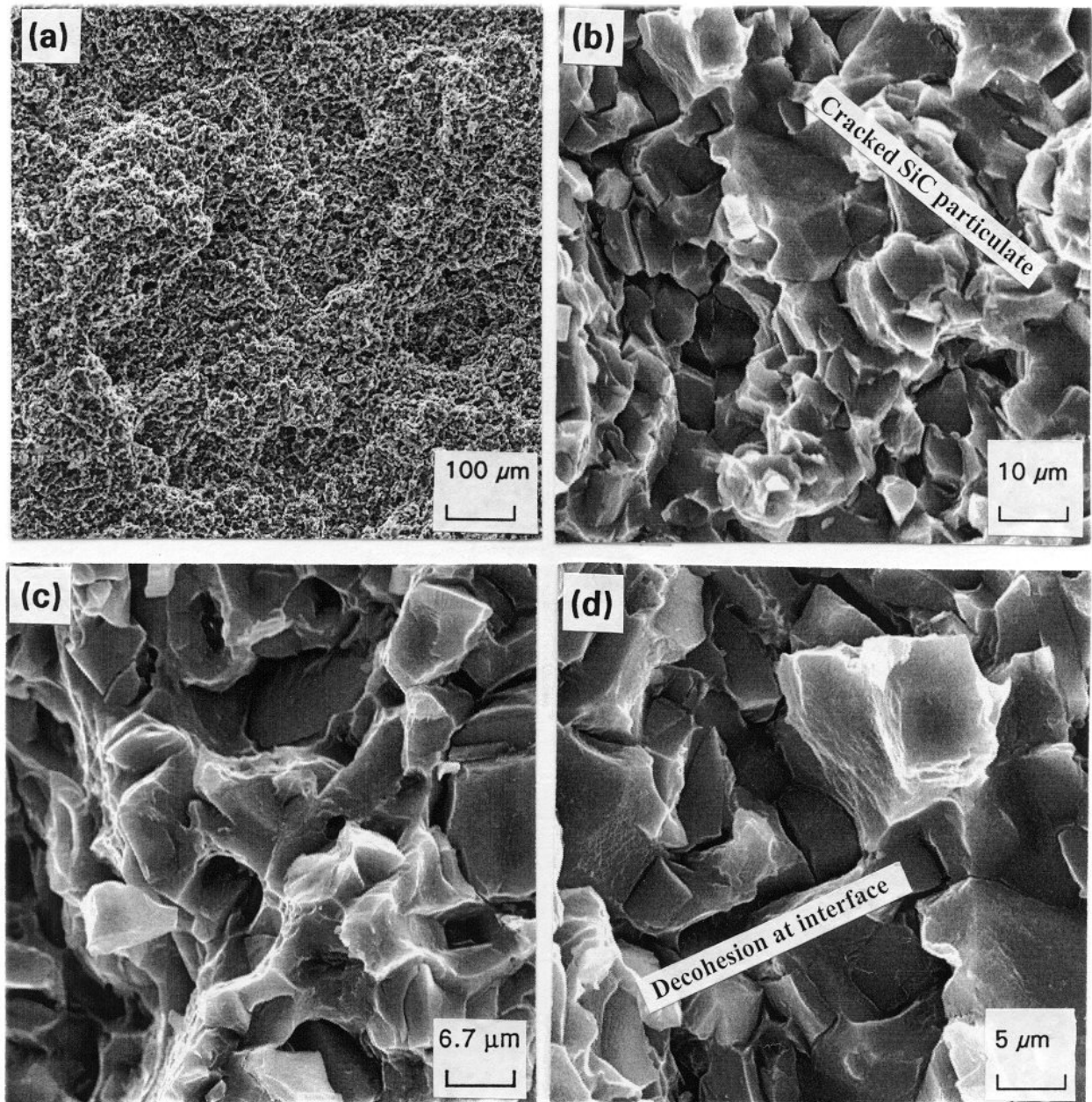
Figure 2. Scanning electron micrographs of the 7034/SiC/15p-UA composite deformed at 27°C and showing the following features: (a) overall morphology, (b) tear ridges, (c) cracked SiC particulates and decohesion at matrix-particulate interfaces, (d) microscopic features of fracture at the higher test temperature (120°C).

5
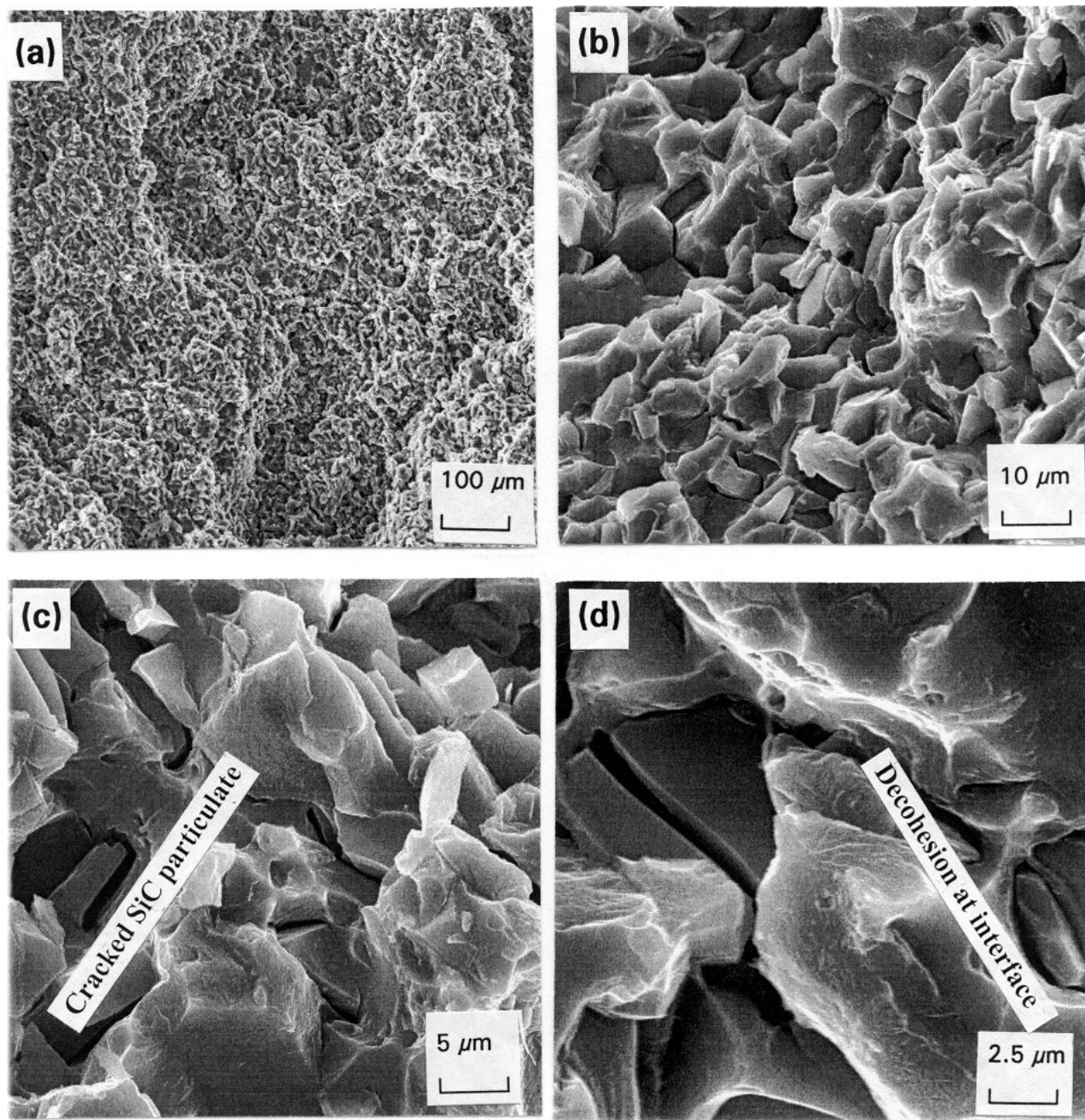
Figure 3. Scanning electron micrographs of the 7034/SiC/15p-PA composite deformed at 27°C and showing the following features: (a) overall morphology, (b) tear ridges, (c) cracked SiC particulates, and (d) decohesion at matrix-particulate interfaces.

THE RELATIONSHIP BETWEEN THE MEDIAN/RADIAL AND LATERAL CRACKS OF VICKERS INDENTS IN SODA-LIME-SILICA GLASS

B. R. Whittle and R. J. Hand

Department of Engineering Materials, University of Sheffield, Sir Robert
Hadfield Building, Mappin Street, Sheffield, S1 3JD, UK

ABSTRACT

The surface traces of Vickers indentations made in soda-lime-silica glass at loads varying between 5 kg and 16 kg showed good adherence to accepted models. The surface trace length of the median/radial cracks extended in the week after indentation relieving some of the residual stress resulting in an increase in the strength of the indented specimens. Specimens indented with less than 5 kg showed less adherence to the pattern of one median/radial crack at each corner of the indentation impression. A study of 10 kg indentations using confocal laser scanning microscopy showed that the sub-surface structure of the crack system is not adequately explained by present models. Although beneath the median/radial cracks the lateral crack rises towards the surface, between the median/radial cracks it propagates away from the surface meaning that they cannot be responsible for material removal around indentations. It is concluded that although the surface traces of Vickers indent flaws appear to be adequately rationalised and modelled, the shape of lateral crack and its interaction with the median/radial cracks is not yet understood nor even accurately recorded.

KEYWORDS

Vickers indentation, lateral crack, radial, median, glass, confocal microscopy

INTRODUCTION

Vickers indenters are frequently used to introduce a strength limiting flaw into brittle mechanical test specimens. In doing so the scatter observed in the results is reduced. Vickers indentations are a common method of introducing controlled damage because it is possible to precisely control the location and size of the critical flaw. Furthermore, the geometry of the cracks arising from indentation with a Vickers indenter is very reproducible and behaves in a manner representative of naturally arising flaws [1]. The system of cracks is commonly depicted as two semicircular cracks perpendicular to the surface and each other. They grow in depth during the loading phase of the indentation cycle and break through to the surface at some point during the unloading phase. Early work concerning indentation flaws considered the cracks which form on loading (median cracks) and the cracks which form on unloading (radial cracks) as separate phenomena but the current understanding is that median cracks can develop into radial cracks or radial cracks can develop into median crack shapes or that median cracks and radial cracks can develop

independently and combine [2]. In the present work the cracks perpendicular to the surface are referred to as median/radial (M/R) cracks because they share characteristics of both types of crack. A third type of crack associated with Vickers indentations forms nearly parallel to the surface and is known as the primary lateral crack. This crack is widely believed to have an inverted conical form, propagating slightly towards the surface from an initiation point directly beneath the region of glass plastically deformed by the indenter and is independent of the M/R cracks [3].

Several studies have attempted to delineate the sequence of crack formation during and after indentation although the present state of understanding is that the extent and sequence of cracking is related to the maximum indentation load and hence there is no universal sequence of cracking. The formation and growth of M/R cracks has been extensively studied and predictive equations relating the indentation load to the M/R crack diameter have been demonstrated to be accurate. The lateral cracks have traditionally been less thoroughly investigated partly because they do not directly affect the strength of indented articles, partly because the stress field controlling their formation is complex and not straightforwardly modelled and partly because of difficulties in imaging the flaws. Nevertheless, an understanding of the lateral crack system is necessary since lateral crack chipping is thought to be responsible for material removal around indent sites [3]. In this paper we first show that the indentations used conform to the acknowledged relationship between load and size and the phenomenon of post-indentation crack growth. It is then demonstrated that there is an intrinsic link between these predictable M/R cracks and the lateral cracks. Furthermore, with the use of confocal laser scanning microscopy (CLSM) it is shown that the formation of lateral cracks and material removal are not linked.

EXPERIMENTAL PROCEDURE

Soda-lime-silica glass microscope slides (37 x 25 x 1.1 mm) were indented with a Vickers hardness testing machine for the standard duration of the Vickers hardness test, roughly 10 seconds. The diagonals of the indenter were aligned perpendicular to the longest edges of the specimen. The samples were then annealed at 540°C for 60 minutes, then cooled at 1°C/min. The length of the M/R surface trace was measured using Foster Findlay image analysis software. Samples for which the post indentation crack growth was monitored were not annealed but aged in laboratory conditions (22°C and 50 % relative humidity) for prescribed periods of up to two weeks.

Samples which had been indented and aged for one week were prepared for CLSM by being sprayed with a fluorescent dye (Neopen W/W). The dye was allowed to penetrate the flaws for 15 minutes before being rinsed away by spraying with water. The samples were examined with a Leica TCS 4D confocal laser scanning microscope equipped with an argon laser which emits at a wavelength suitable for the excitation of the fluorescent dye. The top and bottom of the indent were identified and twelve micrographs were taken at intervals between these depths. The distance between the optical sections was of the order of 13-23 μm giving a total analysis depth of around 200 μm.

Vertical sections through the crack system away from the M/R cracks were prepared by indenting the sample then scoring across the indent using a diamond impregnated tungsten carbide cutting wheel. The samples were then snapped by hand and inspected to ensure that the fracture had followed the scored line and not deviated along a M/R crack. The resulting crack surfaces were polished so that the lateral crack profile could be seen.

RESULTS AND DISCUSSION

Normal indentation crack systems show a M/R crack propagating at each corner of the contact impression. Figure 1 shows the cross section of an indentation made at 10 kg. It is representative of the morphology of cracks formed at all loads of 5 kg and above. Its shape differs somewhat from the often reported morphology of indentation flaws but is in agreement with the results of Sglavo & Green [4] and Smith & Scattergood [5]. The lateral crack constrains the base of the M/R crack and as a consequence the downwards

propagation of the M/R crack is curtailed and it assumes a semielliptical form. Indentations made with loads of less than 5 kg were not as reproducible as those made at higher loads. In many instances fewer than four M/R surface traces were recorded for 1 kg and 2 kg indentations and the cross-sections of these flaws frequently did not resemble the widely recognised appearance. Those indentations which did have properly developed M/R cracks tended to be less semielliptical than the cracks in Figure 1.
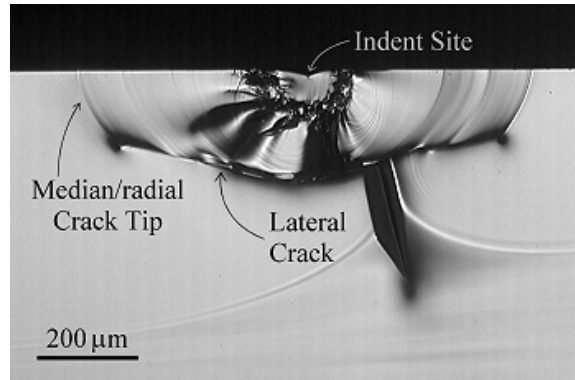
Figure 1 : Cross section of a 10 kg indentation aged for 1 week

Lawn *et al.* [6] predict that the length of the surface trace of M/R cracks after the removal of the indenter is given by

$$d = \left[\frac{\chi_r P}{K_{IC}} \right]^{2/3}$$ (1)

where d is half the crack diameter, K_{IC} is the fracture toughness of glass, P is the indentation load and χ_r is a dimensionless indenter-material constant for the residual component of the stress field. The relationship for the median component of the crack and the radial component have different values of χ_r. It is the radial component which is used here because the growth of the surface trace of the M/R crack is an aspect of radial crack behaviour. χ_r for the radial component is 0.049 ± 0.004. Figure 2 shows the results from the present investigation and the predicted values using Eqn. 1. There is close agreement between the model and the experimental results suggesting that the indentations resemble those observed in previous investigations.
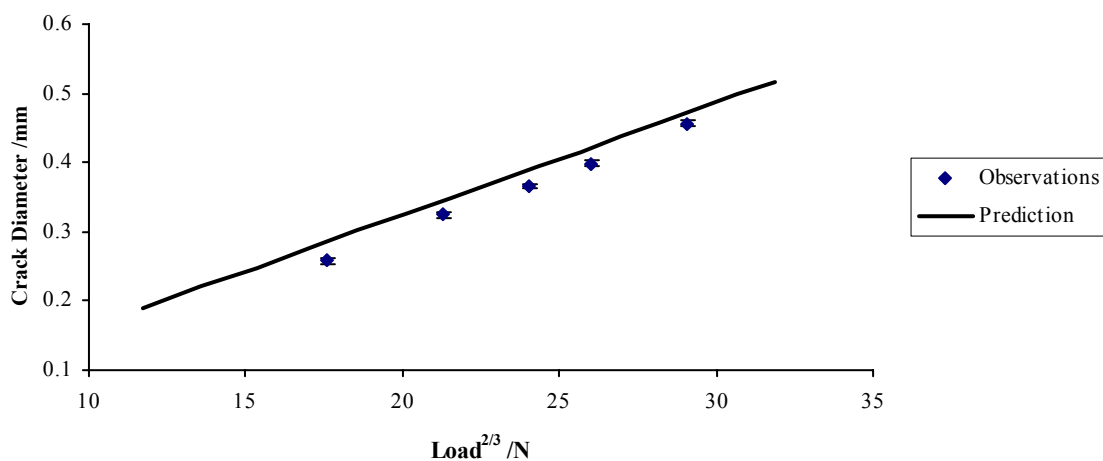
Figure 2 : Comparison of experimental observations with Eqn. 1

Residual stresses arise from indentations because the region directly beneath the contact area between the indenter and the glass plastically deforms resulting in permanent deformation. The material around the plastically deformed region is elastically deformed during indentation and attempts to recover when the indenter is removed. The residual stress is responsible for post indentation crack growth of both M/R and lateral cracks. Upon ageing the M/R cracks grow in length by almost 20 %. Figure 3 shows that the growth

was initially rapid and saturated after a period of approximately one week. This broadly agrees with the work of Lawn *et al.* [7] although it is difficult to qualify exactly when growth has saturated. This further emphasises that the indentations investigated in this study behave in the same way as those which have been studied in previous investigations.
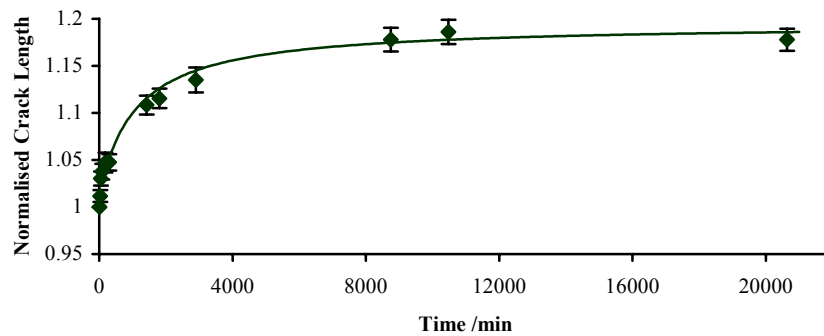
Figure 3 : Post indentation growth of the median/radial surface trace of a 10 kg indentation. The line is for guidance only.

Lateral cracks are often linked with material removal since it is popularly believed that they rise to intersect with the surface. While this is undoubtedly true for secondary lateral cracks which nucleate on the periphery of the contact site close to the surface, the results of this investigation indicate that the primary lateral cracks which form underneath the plastically deformed region do not propagate to the surface. Figure 4 shows 12 confocal micrographs focussed at depths increasing in 14.6 µm increments.
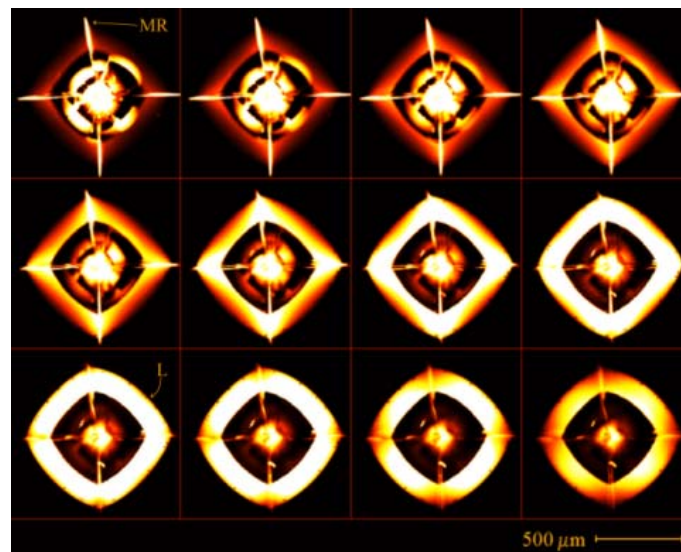
Figure 4 : Confocal images of a 10 kg indentation at depth increasing in 14.6 µm increments. MR indicates the median/radial and L indicates the lateral crack.

Confocal microscopes display images as light or dark depending on whether the corresponding part of the image is in focus. The parts of each micrograph which appear bright are the parts which lie within the focal plane. Between the M/R cracks the ring delineating the lateral crack appears bright at the inner edge before the outer edge indicating that the inner edge is shallower than the outer edge and thus showing that the lateral crack is extending away from the surface. This appears to contradict Figure 1 since this micrograph clearly shows the lateral crack following the base of the M/R crack towards the surface. However, this is merely indicative of the complex three-dimensional form of the lateral crack. Figure 4 does not contradict Figure 1. It simply demonstrates that the lateral crack does not have a uniform profile in rotation. Beneath the M/R cracks it propagates towards the surface. Between the cracks it propagates away from the surface.

As the analysis depth increases the signal from the lateral crack increases in intensity in the region between the perpendicular M/R cracks which shows that the lateral crack is furthest away from the surface at this point. Figure 5 shows sections cut through a 10 kg indentation which show the profile of the lateral crack. They confirm the trends indicated by the confocal results. Figure 5b particularly shows that the lateral crack dips away from the surface between the M/R cracks. Figure 5c shows that the lateral crack profile beneath the contact point curves sharply away from the surface. This is not well illustrated by Figure 4 because, it is believed, when the excess fluorescent dye was removed from the surface of the specimens, the dye in the widest parts of the crack was also flushed away.
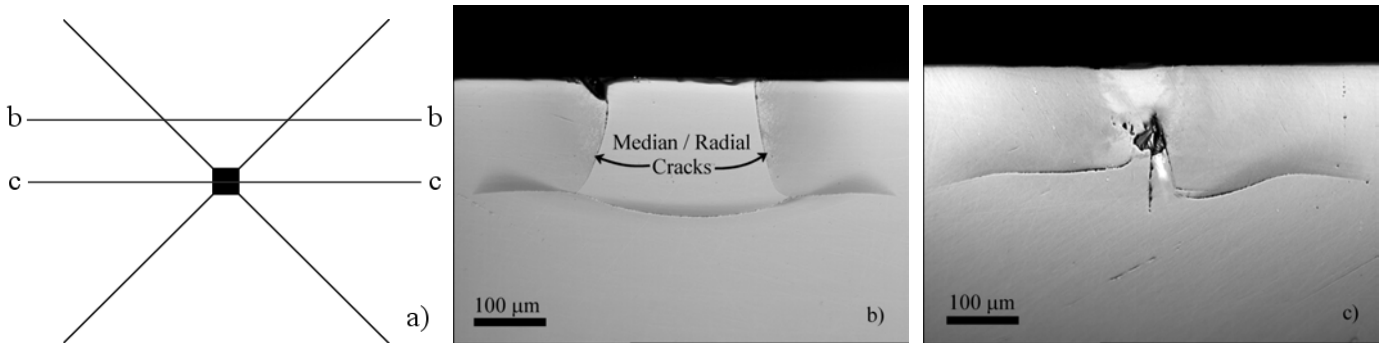
Figure 5 : Vertical sections through a 10 kg indentation flaw. a) shows the section paths where line b-b indicates the section in b) and line c-c indicates the section in c)

The complex shape of the lateral crack in relation to the M/R cracks is shown schematically in Figure 6.
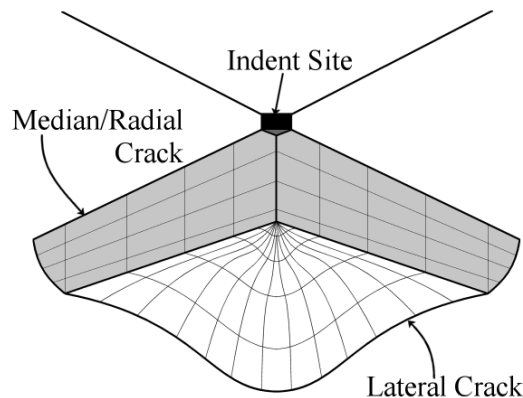
Figure 6 : Schematic diagram of the shape of the lateral crack in relation to the median/radial cracks.

It has previously been thought that the extension of the lateral cracks should not be influenced by the presence of M/R cracks [3] however these results show that this is not the case. The proximity to the M/R cracks has changed the direction of crack propagation since no other factor can account for the localised perturbation of the crack direction towards the surface. This is because the stress field far from the indent site is independent of the shape of the indenter [8]. The lateral crack is not perfectly circular. It has extended further along the M/R cracks than between them. It is interesting to note that both Figure 1 and Figure 4 show that the tip of the M/R crack and the lateral crack beneath it are exactly coincident. No circumstances were encountered where the lateral crack and the M/R crack did not share the same terminus. This does not contradict the observations of Lawn *et al.* [7] and Ritter *et al.* [9] who both observe that initially the lateral crack diameter grows faster than the M/R crack until the diameters are almost equal. Despite observing different initial growth rates, the position of the M/R and lateral crack tips can still be coincident. This is because the M/R crack grows in a semicircular shape but is truncated by the intersection with the lateral crack and thus becomes more semielliptical. Figure 7 illustrates how this truncation results in the lateral crack diameter growing faster than the M/R crack diameter.
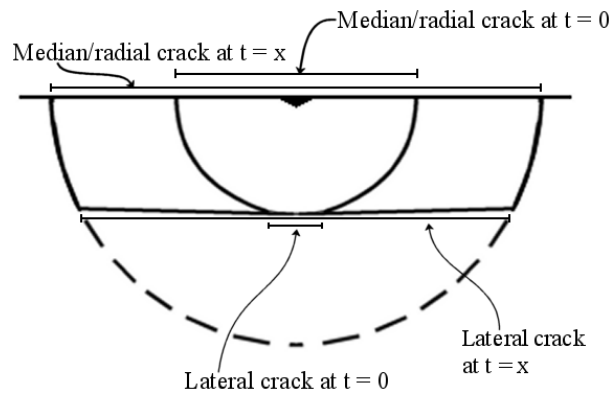
Figure 7 : Diagram of an indentation before and after post indentation crack growth showing the relative sizes of the median/radial and lateral cracks.

CONCLUSIONS

In this investigation indentations in soda-lime-silica glass made with a Vickers indenter at a variety of loads have been closely observed. Lateral cracks have been shown to propagate away from the surface between the M/R cracks. This means that they are not responsible for material removal around indentation sites. The difference should be recognised between the primary lateral cracks, which are as reproducible as M/R cracks, and the secondary lateral cracks which form much more randomly close to the surface and result in material removal. Since the extent of secondary lateral cracking has not been demonstrated to be explicitly dependent on the degree of primary lateral cracking it is erroneous to link material removal to the formation of primary lateral cracks beneath the deformed region of the indent.

It has also been demonstrated that the M/R cracks cause deflections in the direction of lateral crack propagation since beneath M/R cracks the lateral crack is drawn towards the surface. The tips of the lateral and M/R cracks are always coincident which is concordant with a model of M/R and lateral crack growth where the M/R crack grows as a semicircle truncated by an expanding lateral crack.

The above conclusions contradict two tenets of the current understanding of lateral crack behaviour. The new observations brought to light in this investigation cannot be dismissed by arguing that the indentation flaws studied were not the same as those used to generate the accepted models because of the adherence to acknowledged post indentation crack growth behaviour and the relationship between indentation load and surface trace diameter. Although the surface traces of Vickers indentations appear to be adequately rationalised and modelled, the shape of the lateral crack and its effect on the M/R cracks is not yet understood nor even accurately recorded.

REFERENCES

1. Marshall, D.B. and Lawn, B.R. (1985). In: *Strength of Inorganic Glass,* pp. 171, Kurkjian, C. R. (Ed) Plenum, New York.
2. Cook, R.F. and Pharr, G.M. (1990) *Journal of the American Ceramic Society* 73, 787.
3. Marshall, D.B., Lawn, B.R. and Evans, A.G. (1982) *Journal of the American Ceramic Society* 65, 561.
4. Sglavo, V.M. and Green, D.J. (1996) *Engineering Fracture Mechanics* 55, 35.
5. Smith, S.M. and Scattergood, R.O. (1992) *Journal of the American Ceramic Society* 75, 305.
6. Lawn, B.R., Evans, A.G. and Marshall, D.B. (1980) *Journal of the American Ceramic Society* 63, 574.
7. Lawn, B.R., Jakus, K. and Gonzalez, A.C. (1985) *Journal of the American Ceramic Society* 68, 25.
8. Chiang, S.S., Marshall, D.B. and Evans, A.G. (1982) *Journal of Applied Physics* 53, 298.
9. Ritter, J.E., Mahoney, F.M.J. and Jakus, K. (1986) *Fracture Mechanics of Ceramics* 8, 213.

THE ROLE OF CONSTRAINT IN MIXED MODE I AND II DUCTILE FRACTURE

T.D. Swankie[1], and D.J. Smith[2]

1. Structural Integrity Technology Group, TWI Ltd., Cambridge, CB1 6AL, UK
2. Department of Mechanical Engineering, University of Bristol, Bristol, BS8 1TR, UK

ABSTRACT

There is a wealth of experimental data that demonstrates that the resistance to mode I ductile tearing is dependent on specimen dimensions and crack depth. For mode II there is significantly less data. In this paper, the results of a series of mode II and mixed mode I and II experiments, using A508 Class 3 ferritic steel at ambient temperature, are summarised. Tests were carried out using single edge notched specimens and a special fixture. As expected for mode I loading, specimens with low constraint resulted in high resistance to tearing. In contrast, for mode II the tearing resistance was lower than for fully constrained mode I and was not influenced by specimen constraint. For mixed mode loading, the transition from mode I to mode II was a strong function of constraint. In some specimens, additional shear reduced constraint, but in other specimens of different dimensions additional shear led to lower tearing resistance.

KEYWORDS

Mixed mode, steel, ductile, R-curve, constraint

INTRODUCTION

More recently there have been extensive studies [1-3] on the mixed mode ductile fracture of steels in an attempt to provide information for assessing the integrity of real components. However, the method for inferring the integrity of real components is uncertain. This is because the behaviour of laboratory test specimens is known to be dependent on specimen size. For example, in mode I many results [4,5] have demonstrated that ductile fracture toughness varies considerably when the crack length remains the same and the specimen dimensions are changed. The general approach for mode I loading is to consider the effects of specimen dimensions and geometry through a measure of crack tip constraint. Two parameter methods such as K-T [6] and J-Q [7] have been developed, where the second terms provide a measure of constraint. In this paper a summary of the results of an experimental study [1] are provided. The aim is to obtain an understanding of the role of shear and constraint in ductile fracture for combinations of tension (mode I) and shear (mode II) loading on a ferritic steel.

EXPERIMENTAL METHODS

Material and specimens

The material for the experiments was A508 Class 3 steel. The chemical composition, in wt% is; 0.16 C, 1.34 Mn, 0.007 S, 0.004 P, 0.22 Si, 0.67 Ni, 0.17 Cr, 0.51 Mo, 0.06 Cu, 0.004 Sb, 0.01 Al, 0.004 Sn, 0.019 As, <0.01V, <0.01 Ti and <0.01 Nb. The S-L orientation was chosen for the fracture tests since earlier studies [2] identified this as the least tough orientation. The basic tensile properties at ambient temperature are 430 MPa, 561 MPa and 201 GPa, yield and tensile strength, and elastic modulus respectively.

Plain sided, single edge notch (SEN) specimens were used. The specimen thickness B was varied from 10 to 40mm and width W from 20 to 80mm. The normalised crack depth, a_o/W ratio was 0.5 for all tests. In each test the load was applied directly through the crack tip.

Test Fixture and Procedure

Mixed mode I/II loading was applied using a test fixture (Fig.1) clamped around the SEN specimen, similar to that designed by Davenport [2]. The fixture is described in detail elsewhere [1]. All fracture tests were carried out in air at ambient temperature in a servohydraulic test machine. The tests were done under displacement control at a constant rate of approximately 0.5mm/min.
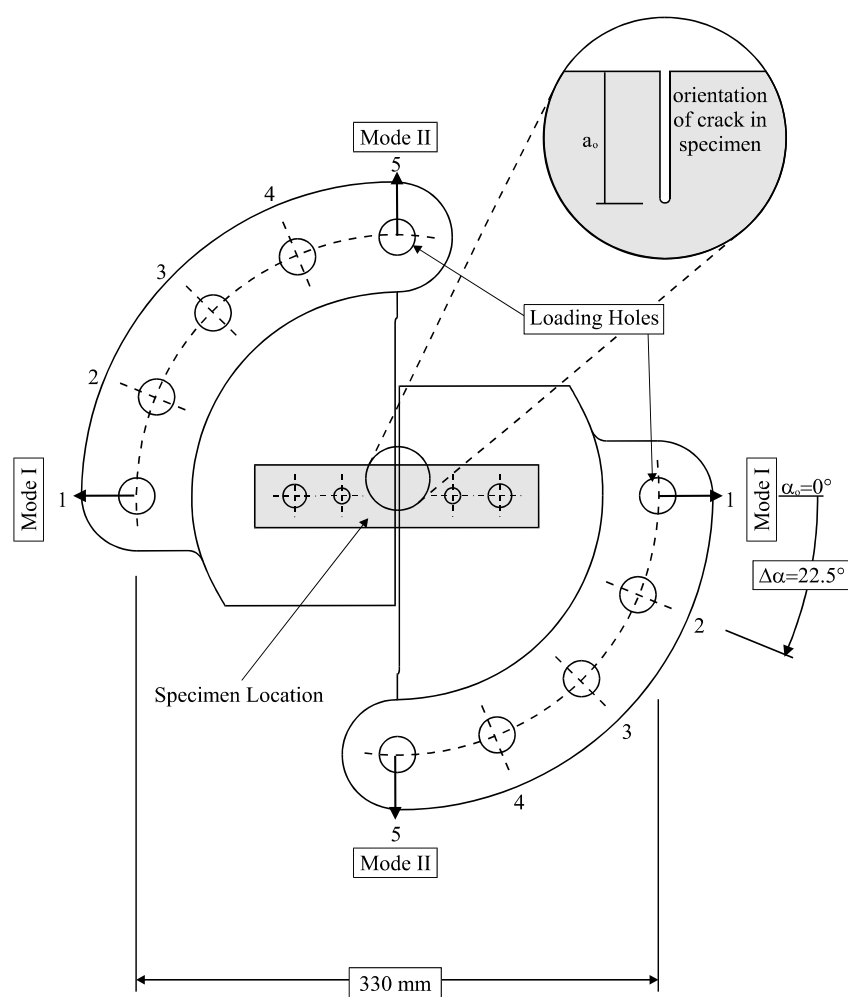
Fig.1. Layout of mixed mode test fixture

The elastic-plastic fracture toughness was calculated in terms of J from the area beneath the loading portion of the applied load versus load line displacement curve [8]. For a given mixed mode loading angle α (see Fig.1), J was calculated using,

$$J_T = \frac{P_{max}^2 \left(1 - v^2\right) \left\{ f\left(\dfrac{a_o}{W}\right)_I^2 + f\left(\dfrac{a_o}{W}\right)_{II}^2 \right\}}{B^2 W E} \left\{ 1 - \frac{\eta_p}{\eta_e} \right\} + \frac{\eta_p}{B\left(W - a_o\right)} \left\{ U_T - \frac{P_{max}^2}{2k} \right\} \qquad (1)$$

where P_{max} refers to maximum load, $f(a_o/W)$ and η are geometry dependant functions, U is the plastic energy and k is a machine stiffness function. Values of $f(a_o/W)$ and η were calculated from plane strain finite element studies, using ABAQUS, and values of k for a given α were determined experimentally. The subscripts I and II refer to mode I and mode II respectively, and e and p denote elastic and plastic respectively.

RESULTS

A total of 109 specimens of varying thickness, B (10mm, 20mm and 40mm) and width, W (20mm, 40mm and 80mm) were tested; 32 specimens in mode I ($\alpha=0.0°$), 35 in mode II ($\alpha=90.0°$), and 42 in mixed mode loading (11 at $\alpha=22.5°$, 19 at $\alpha=45.0°$ and 12 at $\alpha=67.5°$). From each set of tests (corresponding to a particular size of specimen) multi-specimen crack growth resistance curves (R-curves) were generated using the following power law expression,

$$J = C_1 \left(\Delta a\right)^{C_2} \qquad (2)$$

where, Δa is the increment of crack growth, and C_1 and C_2 are curve fitting parameters which were derived from an initial first order fit of all applicable data for a specific specimen size and mode of loading.

The R-curves for mode I loading are shown in Fig.2. As can be seen, for W=20mm specimens tested in mode I, the effect of thickness (10mm$\leq$B$\leq$40mm) on crack initiation toughness, J_{init}, measured at $\Delta a=0.2$mm, and tearing resistance (measured by the slope of the R-curve, dJ/da) was negligible. However, J_{init} and dJ/da decreased significantly as W increased for a given B.
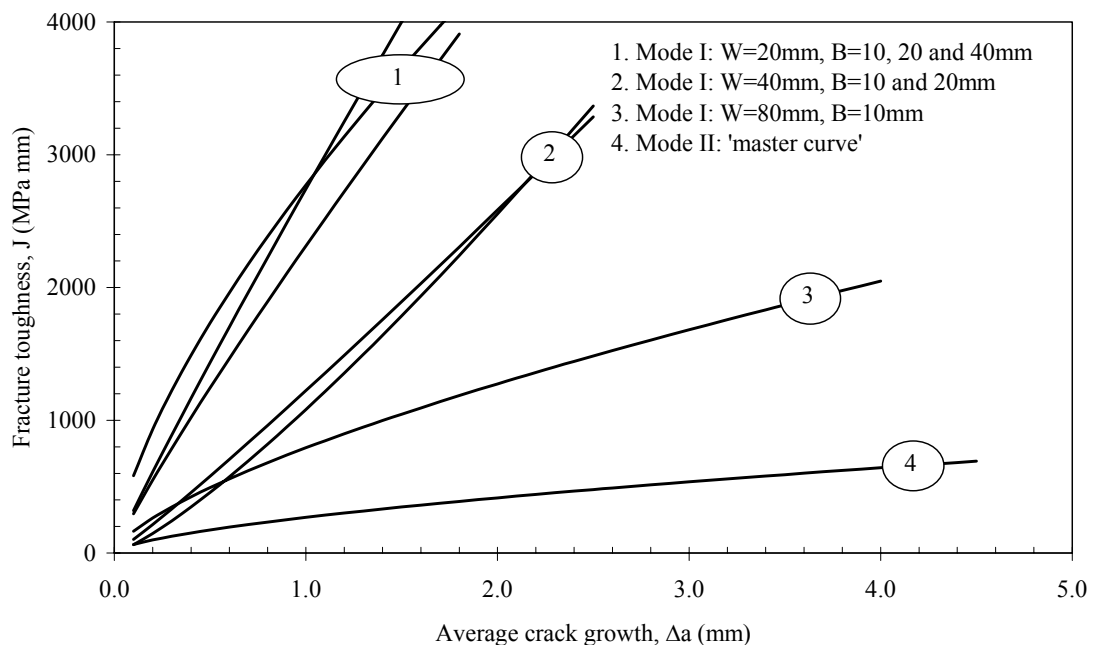
Fig.2 mode I and mode II R-curves: effect of specimen size

All mode II data, regardless of specimen size, can be described by a single curve (a 'master curve'), thus suggesting that the ductile tearing resistance for mode II loading is size independent. The mode II master curve is also shown in Fig.2. Both J_{init} and dJ/da were lower for mode II loading than for mode I.

To investigate the effect of mixed mode loading, 10mm thick specimens were used. This is because the range of specimen thickness tested in both mode I and mode II demonstrated that thickness effects were negligible, in terms of J_{init} and dJ/da. For each combination of tensile and shear loading (α=22.5°, 45.0° and 67.5°), specimens with W=20mm, 40mm and 80mm were tested. An additional 4 tests were done for α=45.0° on B=40mm specimens (W=20mm), to establish whether the negligible effect of thickness seen in the pure mode studies could be confirmed.

R-curves for a given B and W are shown in Fig.3 (B=10mm, W=20mm) and Fig.4 (B=10mm, W=80mm) for different combinations of tension and shear. For B=10mm, W=20mm (see Fig.3) the R-curves steadily decrease with increasing mode II. However, at Δa=0.2mm, J_{init} for mode I loading is similar to J_{init} for α=45.0°. For B=10mm, W=80mm (see Fig.4) the R-curve for mode I loading lies between the R-curves for α=45.0° and 67.5°. At Δa=0.2mm, J_{init} for mode I loading is similar to J_{init} for α=67.5°. The R-curve for α=22.5° is the highest and with increasing mode II the R-curves steadily decrease. Although not shown, the R-curves for B=10mm, W=40mm also decrease with increasing mode II, and at Δa=0.2mm, J_{init} for mode I loading is similar to J_{init} for mode II.
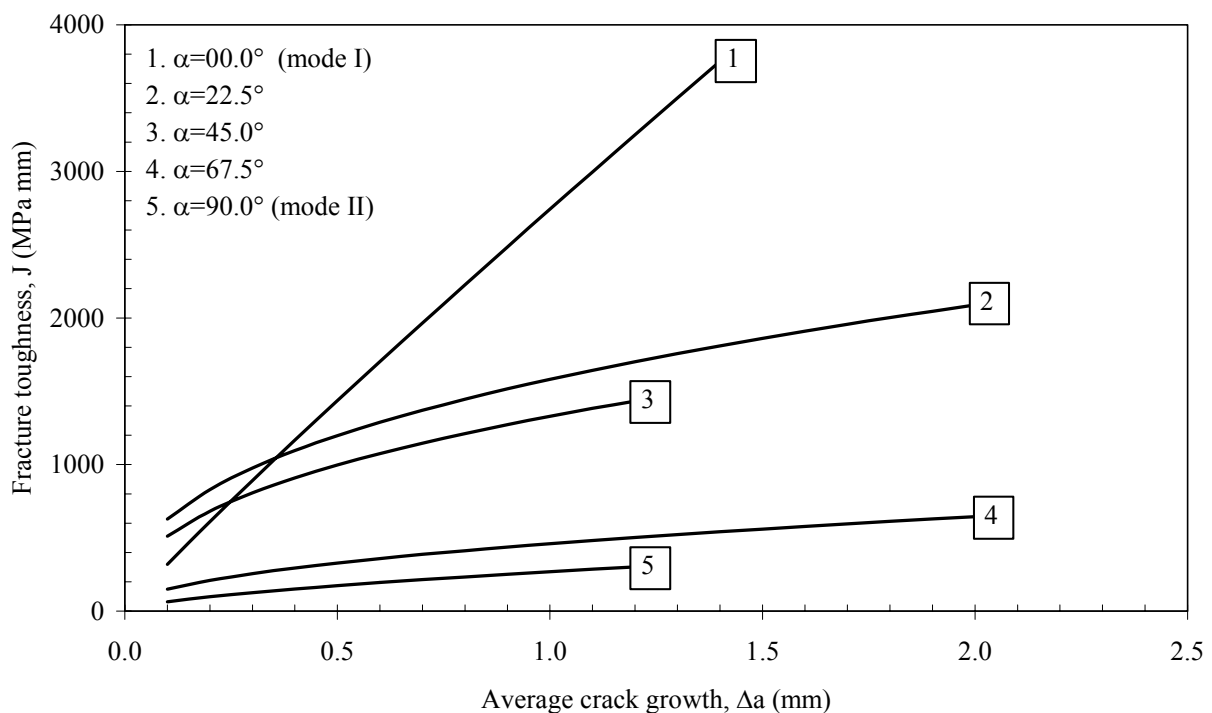
Fig.3 Mixed mode I/II R-curves: W=20mm, B=10mm

DISCUSSION

Initial studies have investigated the effect of specimen size when the crack tip is subject to conditions of pure mode I loading for a crack depth ratio, a_o/W of 0.5. The experiments demonstrate that an increase in specimen thickness has a negligible effect on J_{init} and dJ/da in mode I (see Fig.2). This is in agreement with Joyce and Link [5] who tested HSLA HY100 using SEN specimens up to 50mm thick. In contrast a number of investigators, also examining C-Mn steels [9-11], have found that an increase in specimen thickness causes dJ/da to decrease but the reported effects on J_{init} are varied.
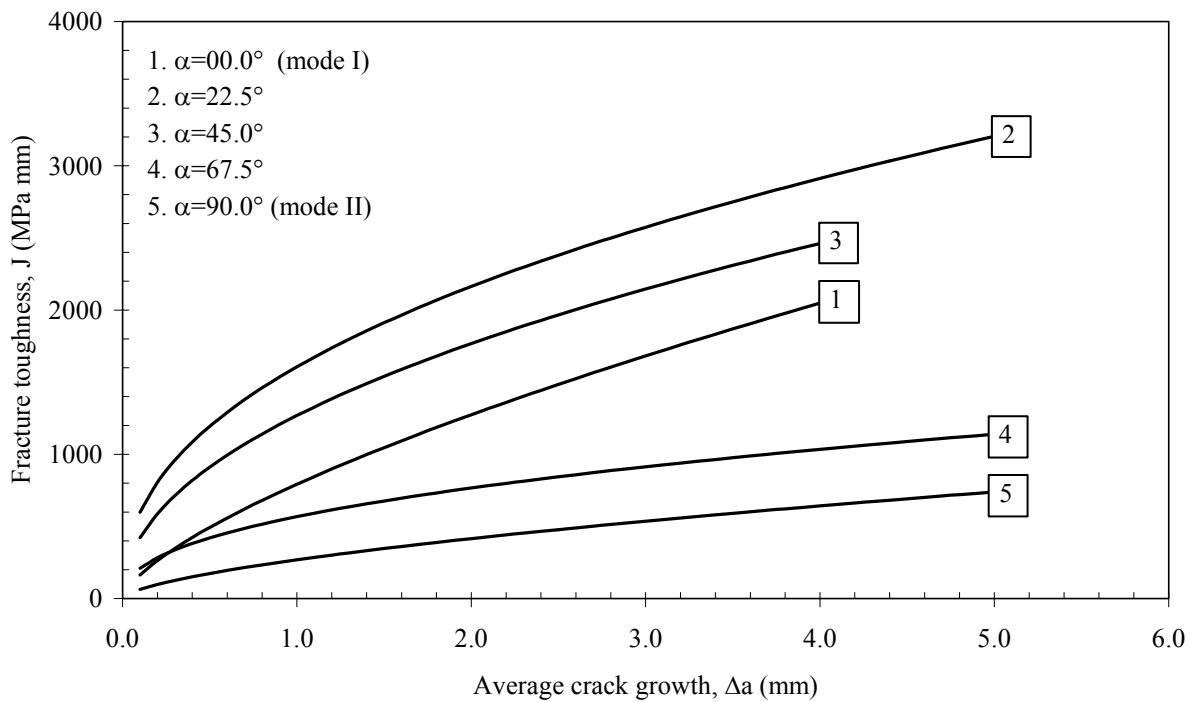
Fig.4 Mixed mode I/II R-curves: W=80mm, B=10mm

The effect of the variation in specimen width is also shown in Fig.2. Width has a significant effect on both J_{init} and dJ/da since J_{init} for W=20mm is greater than for W=80mm (which is similar to W=40mm), and dJ/da for W=20mm is greater than for W=80mm (which is less than for W=40mm).

The mode II experiments demonstrate that specimen size has a negligible effect on J_{init} and dJ/da, and microscopic examination has shown that failure is due to shear localisation. Unlike mode I, at the onset of shear loading asymmetric blunting of the notch tip causes one side to blunt and the other to sharpen. Similar features have been observed by Aoki et al. [12] who demonstrated that the strain and void volume fraction were higher at the sharpened corner with increasing load due to the distribution of equivalent plastic strain. In the present experiments a higher density of microvoids nucleated at the sharpened corner where the localisation of plastic strain was high. This led to a loss in stress carrying capability and subsequent failure of the ligament between neighbouring voids by a localised shear mechanism.

Mixed mode loading causes asymmetric blunting of the crack tip where the angle of the blunted tip, caused by the forward rotation of the upper crack flank in relation to the lower, corresponds approximately to the mixed mode loading angle, α. For α=45.0° and 67.5°, shear cracks initiated at the blunt side of the deformed notch. In contrast, competing failure mechanisms were observed for loading through α=22.5°. This was due to the variation in specimen width causing a change in constraint such that the wider specimens (W=80mm) failed in a manner similar to that observed in mode I while the smaller width specimens (W=20mm) failed by shear localisation.

Figure 3 (W=20mm) shows a proportional decrease in both J_{init} and dJ/da with increasing mode II until the limiting condition of pure mode II is reached. With the exception of the mode I R-curve, the R-curves for W=80mm also follow this trend as shown in Fig.4. However, the mode I R-curve is no longer an upper bound curve. The increase in constraint associated with an increase in specimen width is reflected only in the mode I R-curve and not when a component of mode II is present. The mode I R-curves suggest that in addition to tensile loading at the crack tip, a proportion of this load is attributed to bending. Bend loading

is not reflected in the curve for W=20mm but becomes increasingly effective as W increases. The mixed mode R-curves for W=40mm show a similar trend to those for W=80mm, although the decrease in dJ/da is not as great.

CONCLUSIONS

1. Mode II resistance to ductile tearing for A508 Class3 steel was found to be independent of specimen size and can be characterised by a "master-curve". The mode II master curve was lower than the mode I R-curve for high constraint.
2. For mode I loading there was an increase in constraint with increasing specimen width in mode I loading such that the slope of the R-curve decreased. The effect of increasing specimen thickness was negligible.
3. For some mixed mode loading conditions and larger specimen sizes, the application of shear loading decreased constraint and increased the resistance to ductile tearing.
4. For smaller specimens subjected to mixed mode loading, there was a proportional decrease in tearing resistance from mode I to mode II with an increase in shear loading.

ACKNOWLEDGEMENTS

REFERENCES

1. Swankie, T.D. (1999). PhD Thesis, University of Bristol, UK.
2. Davenport, J.C.W. (1993). PhD Thesis, University of Bristol, UK.
3. Laukkanen, A., Wallin, K., and Rinitimaa, R. (1999) In *Mixed-Mode Crack Behaviour*, ASTM STP 1359
4. Gibson, G.P., Druce, S.G., and Turner, C.E. (1987). *International Journal of Fracture*, 32, pp.219-240
5. Joyce, J.A. and Link, R.E. (1995). In *Fracture Mechanics: Twenty-sixth Volume*, ASTM STP 1256,142-177
6. Betegon and Hancock (1991), *Journal of Applied Mechanics*, 58, 104-110
7. O'Dowd and Shih (1992), *Journal of the Mechanics and Physics of Solids*, 40, 989-1015
8. Sumpter, J.D.G. and Turner, C.E. (1976) In *Cracks and Fracture*, ASTM STP 601, 3-18
9. Andrews, W.R. and Shih, C.F. (1979). In *Elastic-Plastic Fracture*, ASTM STP 668, 426-450
10. G.P. Gibson, G.P (1986), In *Size Effects in Fracture*, I.Mech.E., 33-36
11. Turner, C.E. (1986) In *Size Effects in Fracture*, I.MechE., 25-32
12. Aoki, S., Kishimoto, K., Yoshida, T. and Sakata, M. (1987*), Journal of the Mechanics and Physics of Solids*, 35, 431-455

The role of deformation twins

in a ductile to brittle transition and brittle fracture of ferritic steels

Tibor ŠMIDA, Ján BOŠANSKÝ, Welding Research Institute, Bratislava, Slovak Republic

Key words: ductile to brittle transition, brittle fracture, deformation twins, ferritic steels

Abstract: The fundamental question which basic factors determine the temperature and shape of the brittle to ductile transition remains unanswered, Hirsh [1]. According to Thomson and Knott [2] the calculations of experimentally-measured values of fracture stresses indicate that inherent nuclei of cleavage microcracks with length of the order of several ìm should be present in ferritic steel. Our experimental results indicate that:

1. in various ferritic materials and under various deformation conditions there is a correlation between the deformation mode (twinning) and the fracture mode (cleavage)

2. in the transition temperature region deformation twinning represents an integral part of deformation processes ahead of the growing crack tip

3. the intersections of active slip systems with unfavorably oriented deformation twin boundaries act as nucleation sites for cleavage fracture nuclei (pre-cleavage microcracks)

Based on experimental results we propose:

1. change of fracture mode of ferritic steels in ductile to brittle transition temperature region is a direct consequence of the change of deformation mechanism from deformation by slip of matrix dislocations to deformation by slip *and* twinning

2. brittle/cleavage fracture is governed by the nucleation of pre-cleavage microcracks (PCMCs) on deformation twins ahead of the growing crack tip, deformation twins thus acting as inherent nuclei of cleavage in ferritic steels

[1]   P. B. Hirsch, Mat. Trans. JIM 30 (1989) 841.

[2]   A.W.Thompson, J.F.Knott, Metall.Trans.A, 24A (1993) 523.

Details of submitting author

Title: The role of deformation twins in a ductile to brittle transition and brittle
         fracture of ferritic steels

Authors: Tibor ŠMIDA, Ján BOŠANSKÝ, Welding Research Institute,
         Bratislava, Slovak Republic

Presenting author: Tibor ŠMIDA, MSEE, Ph.D.

Mailing address: Welding Research Institute
         Raèianska 71
         832 59 Bratislava
         Slovak Republic

Tel.:   +421 7 49 24 64 88
Fax: +421 7 49 24 62 69
E-mail: smida.tibor@vuz.sk

The paper is proposed for oral presentation

THE ROLE OF MONAZITE IN OXIDE CERAMIC MATRIX COMPOSITES

J. B. Davis, D. B. Marshall, and P. E. D. Morgan

Rockwell Science Center
1049 Camino Dos Rios
Thousand Oaks, CA 91360

ABSTRACT

Rare-earth orthophosphate (monazite and xenotime) fiber-matrix interphases allow debonding and sliding of fibers in oxide-oxide ceramic fiber-matrix composites (CMCs).[1-10] Rare-earth orthophosphates are refractory (LaPO$_4$ mp = 2072°C)[11] and compatible in high temperature oxidizing environments with many oxides that are available as reinforcing fibers.[2, 3] For refractory materials they are also relatively soft (LaPO$_4$ hardness of 5 GPa, Moh's scale hardness of 5).[1, 12] The most refractory of these, and the most thoroughly investigated, is LaPO$_4$ (La-monazite). Monazite has been demonstrated to enhance the performance of some porous matrix fiber-reinforced oxide composites. In addition, the use of a monazite interphase represents the most likely approach for a successful dense fiber-reinforced oxide composite. In this paper, the properties of monazite-containing composites will be reviewed and the role of monazite discussed.

KEYWORDS

monazite, fiber/matrix interphase, oxide composite, fiber debonding, damage tolerance

1. INTRODUCTION

The limited creep resistance and microstructural stability of fine-grained oxide fibers impose restrictions on composite processing conditions. Few refractory oxide materials can be sintered to full density at pressures and temperatures that do not degrade fiber properties. Consequently, all oxide composites developed so far have porous matrices (with the exception of hot-pressed composites containing very low volume fractions of single crystal fibers). In some cases, a virtue has been made of this necessity and porous matrices have been used to impart damage tolerance without the need for a weakly bonded interphase.[13, 14] Although matrix porosity provides the mechanism for decoupling matrix and fiber fracture, monazite interphases enhance the performance of some materials of this type. Specifically, monazite coatings have prevented fiber strength loss at high temperatures in some matrices and enhanced non-linear behavior.[6, 15] Furthermore, monazite-matrix composites have been developed with the requisite thermal stability and mechanical performance for use as constituents in durable thermal protection systems for spacecraft re-entry.[16, 17]

Although porous matrix composites are suitable for some applications, composites with strong, dense matrices are still needed, especially for service in erosive and chemically corrosive environments (e.g., high gas flow rates with salt spray and H$_2$O vapor). In composites with strong or fully dense matrices, a weak interface or interphase between the fibers and matrix is needed to decouple the fracture processes in the matrix and fibers.[18] The condition for initial debonding is well-defined in terms of a critical interfacial fracture energy.[19] The condition for continued debonding and sliding is less well-defined. When the

interface is not perfectly smooth (usually the case), a means of accommodating the asperity contact during constrained sliding is needed, either by elastic strains or by a secondary damage mechanism.

Evidence for such damage mechanisms in $LaPO_4$ interphases has been found from fiber push-out tests in dense composites. The debonding and sliding of four La-monazite coated fibers (alumina and mullite single crystal, YAG/Al_2O_3 and Al_2O_3/ZrO_2 eutectic) have been investigated. The coated fibers were hot-pressed with a matrix of polycrystalline Al_2O_3. Debonding and sliding were assessed using indentation fracture and push-out techniques. Deformation in the La-monazite coating by wear and abrasion during push-out was observed by scanning electron microscopy.

2. POROUS MATRIX COMPOSITES

Monazite coatings improve the high temperature capability of porous matrix composites. However, the effectiveness is very sensitive to processing conditions; some coating processes can lead to degraded fiber properties. Many precursor chemistries and infiltration techniques for fiber coatings have been investigated in our laboratory and elsewhere.[6, 20, 21] Tensile strength measurements of coated, heat-treated single-filaments or fiber tows have been used as screening tests to evaluate the effect of each coating composition on the properties of fibers. In general, the loss of fiber strength during processing has been a major impediment to the use of liquid precursor routes for monazite coatings with the extent of fiber strength loss dependent on the fiber composition for identical coating formulations. Studies to correlate the coating microstructure and stoichiometry to retained fiber strength have identified several potential causes for the degradation, although no conclusive results exist. However, the strength loss appears to be associated with the precursor chemistry in combination with polycrystalline fibers: it does not occur for solution precursors with single crystal fibers or for polycrystalline fibers coated with monazite powder slurries.[17, 21]

Although the cause of fiber degradation by monazite solution precursors is not fully understood, we have discovered that the strength loss for Nextel 610 fibers (3M Company) is significantly reduced with alumina powder additions to the precursor solutions.[6] Adding buffering powders to other precursor chemistries and oxide fibers has also met with some success.[20] The addition of the powder fillers help to distribute the monazite at fiber surfaces, essentially forming the interphase *in situ*.

Composites have also been produced by laminating fabrics infiltrated with powder-filled (Sumitomo AKP50) solution precursors (produced from La-nitrate and phytic acid). The laminated composite consisted of 2-D fabrics (8-harness satin weave) of Nextel 610 (10 plies, each 15 cm X 15 cm) which were dip-coated with slurry and stacked together while wet. The assembly was subsequently placed in a vacuum bag and dried at low temperature (60°C) in an hydraulic press under a slight pressure (~0.2 MPa). The dry composites were then removed from the vacuum bags and sintered, without pressure, at 1100°C for one hour in air. The composites contained ~40% Nextel 610 fiber by volume with half oriented parallel to the loading direction during tensile testing. Composites were not re-infiltrated after sintering and typically contained ~20-25% porosity.

After sintering, the composites were cut into tensile test specimens with fibers oriented 0/90° to the tensile test direction by diamond sawing. Double-edge notched specimens were evaluated as well as straight-sided specimens. Tests were conducted at room temperature for specimens in the as-processed condition (1100°C; 1h) as well as for specimens subjected to high temperature aging heat treatments (1100°C; 24h). Additional tensile tests to temperatures of 1025°C were conducted using quartz lamp arrays to heat the specimen.

Stress-strain traces obtained from monotonic tensile loading of 0/90° laminates showed an initial linear regime (E~ 90 GPa) to stress levels of approximately 150 MPa followed by considerable nonlinearity prior to the peak stress (220-250 MPa). Similar curves were obtained for notched composites tested in the as-sintered and thermally-aged condition tested at room temperature and for notched composites tested at 1025°C. The stress values were determined from the measured loads divided by the composite net-section area between the notches. Strengths for specimens with no notches at both room and elevated temperatures were essentially the same as the notched specimen values. In fact, all net-section strengths were

approximately equivalent regardless of notch dimensions and test conditions (Fig.1). Normalizing the peak load value by the total aligned fiber cross-sectional area indicated fiber strength values of ~1.1-1.3 GPa.
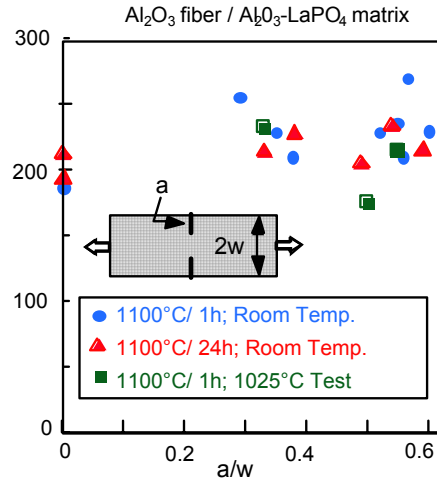

Figure 1. Net-section strength values of porous matrix composite containing monazite.

Coatings produced from monazite powders provide the best fiber strength retention during fiber tests as previously mentioned.[21] Furthermore, fiber coatings of this type have been used successfully to improve the properties of porous alumina matrix composites containing various types of oxide fibers (Nextel 610, 650 and 720).[15] In all cases, unidirectional composites containing coated fibers and heated to temperatures of 1200°C exhibited higher strengths than control specimens containing uncoated fibers. The strength improvement was most significant for the Nextel 610 and 650 fibers.

Monazite powder slurries have also been used to produce oxide composites for durable thermal protection systems (TPS). Thermal protection blankets, consisting of refractory fiber batting sandwiched between two sheets of woven ceramic fabric, are of interest as a lower cost alternative to rigid tiles for protection of re-entry vehicles. These blankets require an outer woven sheet coating that infiltrates and stiffens the fabric to provide an aerodynamic surface. The coating must act as a "high temperature starch" without embrittling the fabric. Since the coated fabric layer is essentially a thin ceramic matrix composite (the infiltrated coating being the matrix), the requirements for blanket durability are the same as those for damage tolerance in structural CMCs: a weak bond is needed between the matrix and the fibers to prevent embrittlement. The upper surface of the orbiter is protected by blankets that consist of silica-based fabric, insulation and coating. At temperatures above ~700-800°C, the silica-based coating bonds strongly to the fibers, embrittling the outer fabric and limiting its lifetime. Development of more refractory blanket fabrics and compatible coatings such as monazite with temperature capability to the range of 1000-1200°C would allow use of blankets over a larger fraction of the vehicle surface.

Comparisons of retained strengths for fiber tows and fabrics (Nextel 440 and 610) coated with monazite powder slurry and the baseline silica system indicated that, for high temperature applications (up to 1300°C), the preferred material system is Nextel 610 fabric infiltrated with monazite.[17] To assess the performance of these materials under relevant thermal and acoustic load conditions, small blanket test specimens were fabricated with Nextel 440 and 610 facesheets coated with monazite powder slurry, and exposed to various tests.

A modulated wind tunnel was used to expose the coated, radiantly heated (1100°C/30 min.) blankets to aerodynamic flow and a fluctuating pressure that simulates the acoustic loading of reentry. Tests were conducted for 600 seconds. The stiffened outer blanket surface performed well under acoustic loading during the wind tunnel testing. In no case was any evidence of coating degradation detected by visual inspection during or after the tests. Out-of-plane displacements ("pillowing") of the fabric during the tests were minimal.

Exposures to higher surface temperatures in flowing gas were conducted on the Nextel 610 fabric/monazite

coating system using the Panel Test Arc Jet Facility at NASA Ames. A test panel with a surface area of approximately 30 cm x 30 cm was infiltrated with monazite powder slurry and subsequently exposed to two heating cycles, giving surface temperatures of 1200°C for 10 min and 1300°C for three minutes.

Post-test evaluations included x-ray diffraction analysis, which indicated that no reaction phases had formed during exposure, and measurement of the retained mechanical performance of the coated fabric facesheet. Impact resistance measurements were conducted using a drop-weight impact tester with a hemispherical projectile tip of radius 0.64 cm. An impact energy of 1.4 J was used and data was obtained from five measurements. Limited coating damage and no fabric penetration were observed for the monazite-coated Nextel 610 surface. This represents a significant improvement over Nextel 440 fabrics coated with a silica-based composition and exposed to 1200°C in the arc jet. Optical micrographs shown in Figure 2 depict the difference in the level of impact damage incurred by both systems after impact under identical conditions.
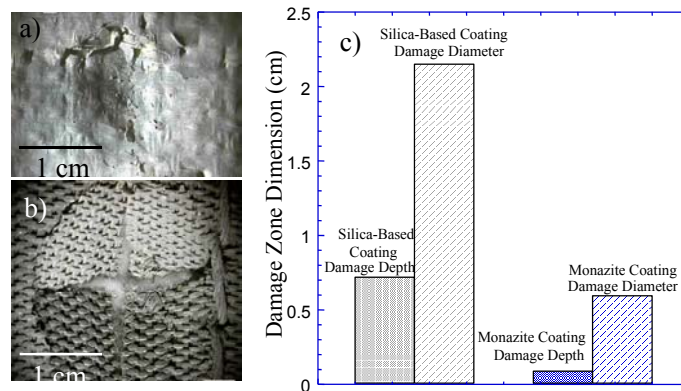
Figure 2. Showing impact damage to arc jet tested blankets with facesheets of a) Nextel 610 fabric/ monazite coating b) Nextel 440/ silica-based coating and c) impact test results.

3. DENSE MATRIX COMPOSITES

The debonding and sliding of four types of La-monazite coated fibers, chosen to provide different residual stress states and interface morphology and embedded in a dense alumina matrix have been investigated and provide evidence for the utility of monazite interphases in dense composites.

Four different single crystal or eutectic oxide fibers (alumina and mullite single crystal, YAG/Al_2O_3 and Al_2O_3/ZrO_2 eutectic, grown at NASA-Glenn by a laser float-zone technique [22, 23]), were coated with $LaPO_4$ by dip coating in a rhabdophane (hydrated $LaPO_4$) slurry. The coating thicknesses were nonuniform (between ~ 1 μm and 5 μm) and largest along fiber surfaces parallel to the hot-pressing direction. The coated fibers were embedded in α-alumina powder (Sumitomo AKP50) and hot-pressed in graphite dies for 1 h at 1400°C. Uncoated fibers were included in the same specimen as controls. No reactions were observed between $LaPO_4$ and the fibers. The fibers had different surface morphology and thermal expansion coefficients, thus allowing some assessment of the effects of interface morphology and residual stress on debonding and sliding (Table I).

The $LaPO_4$ coatings protected all fibers from penetration of matrix indentation cracks whereas uncoated fibers were always penetrated by the indentation cracks. The cracks generally penetrated through the $LaPO_4$ coating and arrested at the coating/fiber interface, causing debonding (Fig 3a). In a few cases ZrO_2/Al_2O_3 fibers debonded at both interfaces (matrix/coating and coating /fiber). The former response was observed previously with coated sapphire fibers[1] and was consistent with the debond criterion of He and Hutchinson[19] and the measured fracture toughnesses of the fibers, coating, and interface. Although the fracture toughnesses of the YAG/$LaPO_4$ and mullite/$LaPO_4$ interfaces have not been measured, the present observations suggest that they are similar to those of the alumina/$LaPO_4$ interface (~4.5 J/m^2).

All of the fibers debonded during fiber push-out experiments. Sliding occurred unstably over ~5 to 10 μm at a critical load between 10 and 20 N. The average shear stress (load divided by fiber surface area) at the critical load was 130 ± 10 MPa for the sapphire fiber; 200 ± 20 MPa for the mullite fiber; 190 ± 20 MPa for the YAG/Al_2O_3 fiber; and 255 ±30 MPa for the Al_2O_3/ZrO_2 fiber.

TABLE I Representative* residual stresses (MPa) for monazite-coated fibers in a dense polycrystalline Al_2O_3 matrix.

Stress component	Fiber			
	Sapphire	Mullite	YAG/Al_2O_3	Al_2O_3/ZrO_2
Radial (coating/fiber)	15	-720	130	240
Radial (matrix/coating)	25	-630	140	240
Hoop (coating)	300	420	290	280
Axial (fiber)	7	-1160	240	420

*These values are intended only as rough guide for stresses. They were calculated using a coaxial cylinder analysis,[24, 25] assuming a temperature change of ΔT = 1000°C, coating thickness 2 μm, zero volume fraction of fibers, and the following Young's moduli and thermal expansion coefficients (nominal isotropic, temperature-independent values): polycrystalline Al_2O_3 (400 GPa, 8 x 10^{-6} °C^{-1}); sapphire (400 GPa, 8 x 10^{-6} °C^{-1}); mullite (200 GPa, 4 x 10^{-6} °C^{-1}); Al_2O_3/ZrO_2 (300 GPa, 9 x 10^{-6} °C^{-1}); and YAG/Al_2O_3 (350 GPa, 8.5 x 10^{-6} °C^{-1}).[26, 27]

Extensive wear tracks observed in the $LaPO_4$ coating for both eutectic fibers indicate that sliding involved plastic deformation (Fig. 3b). The plane of sliding was mostly adjacent to the fiber-coating interface, although smeared $LaPO_4$ coating fragments remained on the fiber surface. In some regions sliding occurred near the matrix-coating interface. Transmission electron microscopy observations have shown the presence of extreme deformation by dislocation generation, cleavage and twinning.[28]
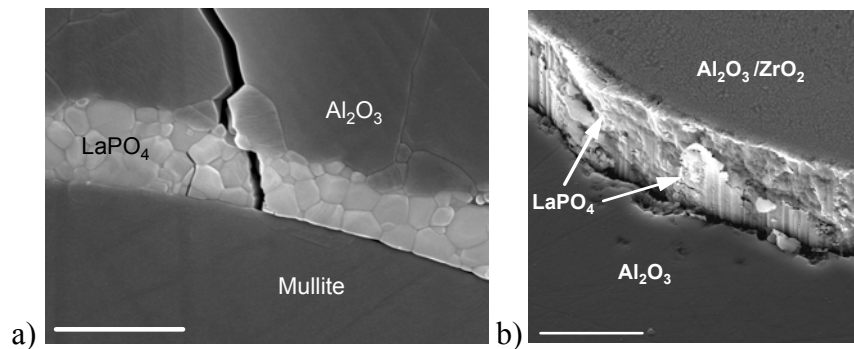
Fig. 3. a) Debonding at $LaPO_4$/mullite interface. B) Deformed $LaPO_4$ coating on a eutectic fiber pushed through a dense alumina matrix.

4. DISCUSSION AND CONCLUSIONS

Monazite fiber coatings and interphases have been demonstrated to improve the properties of some porous matrix oxide composites. However, control of the chemistry, processing and morphology of the coatings are needed to avoid degrading the fiber strength during the processing or during subsequent thermal exposure.

Monazite interphases exhibit characteristics necessary to allow damage tolerance in dense matrix composites. La-monazite is compatible with potential advanced fiber materials such as mullite, YAG, ZrO_2 and Al_2O_3. The interfaces between La-monazite and these materials debond when a crack approaches the interface from monazite. This occurs even when there is significant compressive stress normal to these interfaces, as in the case of mullite fibers in an alumina matrix. The ability of La-monazite to deform plastically relatively easily at low temperatures during fiber push-out may be critical for its use as a composite interface.

REFERENCES

1. P. E. D. Morgan and D. B. Marshall, *J. Am. Cer. Soc.*, **78** [6] 1553-1563 (1995).
2. P. E. D. Morgan, D. B. Marshall, and R. M. Housley, *J. Mat. Sci. Eng.*, **A195** 215-222 (1995).
3. D. B. Marshall, P. E. D. Morgan, R. M. Housley, and J. T. Cheung, *J. Am. Ceram. Soc.*, **81** [4] 951-956 (1998).
4. D. B. Marshall, J. B. Davis, P. E. D. Morgan, and J. R. Porter, *Key Engineering Materials*, 27-36: Trans Tech Publications, Switzerland, 1997.
5. J. B. Davis, D. B. Marshall, and P. E. D. Morgan, *J. Eur. Ceram. Soc.*, **19** 2421-2426 (1999).
6. J. B. Davis, D. B. Marshall, and P. E. D. Morgan, *J. Eur. Ceram. Soc.*, **20** [5] 583-587 (2000).
7. K. A. Keller, T. Mah, E. E. Boakye, and T. A. Parthasarathy, *Cer. Eng. Sci. proc.*, **21** [4] 525-534 (2000).
8. T. A. Parthasarathy, E. Boakye, M. K. Cinibulk, and M. D. Petry, *J. Am. Ceram. Soc.*, **82** [12] 3575-3583 (1999).
9. S. M. Johnson, Y. Blum, C. Kanazawa, H.-J. Wu, J. R. Porter, P. E. D. Morgan, D. B. Marshall, and D. Wilson, *Key Engineering Materials*, **127-131** 231-238 (1997).
10. S. M. Johnson, Y. D. Blum, and C. H. Kanazawa, *Key. Eng. Mat.*, **164-165** 85-90 (1999).
11. Y. Hikichi and T. Nomura, *J. Am. Cer. Soc.*, **70** [10] C252-C253 (1987).
12. W. A. Deer, R. A. Howie, and J. Zussman, pp. 339-346 in *Rock Forming Minerals Vol. 5: Non-Silicates*; John Wiley and Sons, New York, 1963.
13. W.C. Tu, F.F. Lange and A.G. Evans, *J. Am. Ceram. Soc.,* **79** [3] 417-424 (1996).
14. C.G. Levi, J.Y. Yang, B.J. Dalgleish, F.W. Zok and A.G. Evans, *J. Am. Ceram. Soc.,* **81** [8] 2077-2086 (1998).
15. K.A. Keller, T. Mah, T.A. Parthasarathy, E.E. Boakye, M. Cinibulk, "Evaluation of All-Oxide Composites Based on Coated Nextel 610 and 650 Fibers," submitted to *Cer. Eng. Sci. Proc.*
16. J.B. Davis, D.B. Marshall, K.S. Oka, R.M. Housley and P.E.D. Morgan, *Composites A*, **30** 483-488 (1999).
17. J.B. Davis, D.B. Marshall, P.E.D. Morgan, K.S. Oka, A.O. Barney and P.A. Hogenson, "Damage Tolerant Thermal Protection Systems," Manuscript #AIAA-2000-0172, proc *Space 2000*, AIAA, Long Beach, CA, 2000.
18. A.G. Evans and D.B. Marshall, *Prog. Mat. Sci.,* **33** 85 (1989).
19. M.Y. He and J.W. Hutchinson, *Int. J. Sol. Struc.* **25** 1053-1067 (1989).
20. R.S. Hay, E.E. Boakye, "Monazite Coatings On Fibers: I, Effect Of Temperature And Alumina-Doping On Coated Fiber Tensile Strength," submitted to *J. Am. Ceram. Soc.*
21. E.E. Boakye, R.S. Hay, P. Mogilevsky, and L.M. Douglas, "Monazite Coatings On Fibers: II, Coating Without Strength Degradation," submitted to *J. Am. Ceram. Soc.*
22. A. Sayir, In *Computer Aided Design of High Temperature Materials*, edited by A. Pechenik, R. Kalia and P. Vashishta, 197-211: Oxford University Press, 1999.
23. A. Sayir and S. C. Farmer, *MRS Symp. Proc.*, **365** 11-20 (1995).
24. N. J. Pagano and G. P. Tandon, *Compos. Sci. Tech.*, **31** 273 (1988).
25. N. J. Pagano and G. P. Tandon, *Compos. Sci. tech.*, **38** 1 (1990).
26. Y. S. Touloukian, R. K. Kirby, R. E. Taylor, and T. Y. R. Lee, *Thermal Expansion - Non-Metallic Solids*; Plenum Press, 1977.N.J. Pagano and G.P. Tandon, *Compos. Sci. Tech.*, **31** 273 (1988).
27. S. Geller, G. P. Espinosa, and P. B. Crandall, *J. Appl. Cryst.*, **2** 86-88 (1969).
28. J.B. Davis, R.S. Hay, D.B. Marshall, P.E.D. Morgan and A. Sayir, "The Influence of Interfacial Roughness on Fiber Sliding In Oxide Composites with La-Monazite Interphases" *in preparation*.

THE ROLE OF PARTICLES IN FATIGUE CRACK PROPAGATION OF ALUMINUM ALLOYS

Z.Z.Chen[1], K.Tokaji[2] and T.Horimoto[1]

[1] Graduate Student, Gifu University, 1-1 Yanagido, Gifu 501-1193, Japan
[2] Department of Mechanical and Systems Engineering, Faculty of Engineering,
Gifu University, 1-1 Yanagido, Gifu 501-1193, Japan

ABSTRACT

Fatigue crack propagation (FCP) in two aluminum alloys (casting alloy, AC4CH, and aluminum alloy, A2024, reinforced with $5\,\mu$ m SiC particulates) was studied to understand the role of SiC and Si particles. In the SiC$_P$/Al composite, there were few particles appeared on the fracture surfaces even at high ΔK region, indicating that cracks propagated predominantly within the matrix avoiding SiC particles because of the high strength of the particles and the strong particle/matrix interface. In the casting alloy, Si particle debonding was more prominent. When compared with the SiC$_P$/Al composite, the casting alloy exhibited lower FCP rates, but had a slight steeper slope in the Paris region. Crack deflection and branching were found to be more remarkable in the casting alloy than in the SiC$_P$/Al composite that may contribute to better FCP resistance in the former alloy.

KEYWORDS: Aluminum matrix composite, Casting alloy, Fatigue crack propagation, Particle

INTRODUCTION

Aluminum-based matrix composites reinforced with silicon carbide particulates (MMCs) have received more attention in the past decade because the conventional metallurgical and machining processing techniques, such as direct casting, powder metallurgy, rolling, forging, and extrusion can be applied for their fabrication. Although the second phase additions can cause reduced tensile ductility, lower fracture toughness, and in some cases, decreased fatigue resistance compared with the constituent matrix alloy, SiC$_P$/Al composites still have potential in structural applications because of considerable weight saving due to their specific properties. On the other hand, the outstanding mechanical, physical, and casting properties of Al-Si-Mg alloys make them attractive for use in cheaper and lighter engineering components. The eutectic Si particles in Al-Si-Mg alloys can be considered as a reinforcement whose size, distribution and volume fraction may affect strongly

fatigue properties just like SiC particulates in SiC$_P$/Al composites. Some studies have been done to understand the effects of SiC and Si particles on fatigue resistance and fatigue crack propagation (FCP) in SiC$_P$/Al composites and in Al-Si-Mg casting alloys [1-6], but further studies are still needed to clarify the role of SiC and Si particles in FCP.

In the present study, FCP tests were conducted on casting alloy, AC4CH, and SiC$_P$/Al composite, and the role of SiC and Si particles in FCP and the mechanisms are discussed on the basis of detailed fractographic examination.

EXPERIMENTAL PROCEDURES

Materials

The materials used are aluminum casting alloy, AC4CH, and aluminum alloy 2024 reinforced with 10wt.% SiC particulates, the average particle size of 5μm, hereafter denoted as SiC$_P$/Al. The SiC$_P$/Al composite is fabricated by powder metallurgy. The chemical compositions (wt.%) are; Si 6.67, Mg 0.36, Fe 0.07, Ti 0.13, Sb 0.10, balance Al for the casting alloy, and Si 0.13, Fe 0.24, Cu 4.57, Mn 0.63, Mg 1.65, Cr 0.01, Zn 0.091, Ti 0.02, balance Al for the SiC$_P$/Al composite. The mechanical properties are listed in Table 1. The SiC$_P$/Al composite exhibits higher 0.2% proof stress, tensile strength and Young's modulus and lower elongation and reduction of area than the casting alloy. Figure 1 shows the microstructures. It can be seen that SiC particulates are well-distributed and tend to be weakly aligned to the extrusion direction (Figure 1(a)), while eutectic Si particles distribute to form dendrite cells (Figure 1(b)).

TABLE 1

MECHANICAL PROPERTIES OF ALLOYS

Alloy	Tensile strength (MPa)	0.2% proof stress (MPa)	Elongation (%)	Reduction of area (%)	Elastic modulus (GPa)
AC4CH	289	235	7	24	64
SiC$_p$/Al	462	365	5	8	71
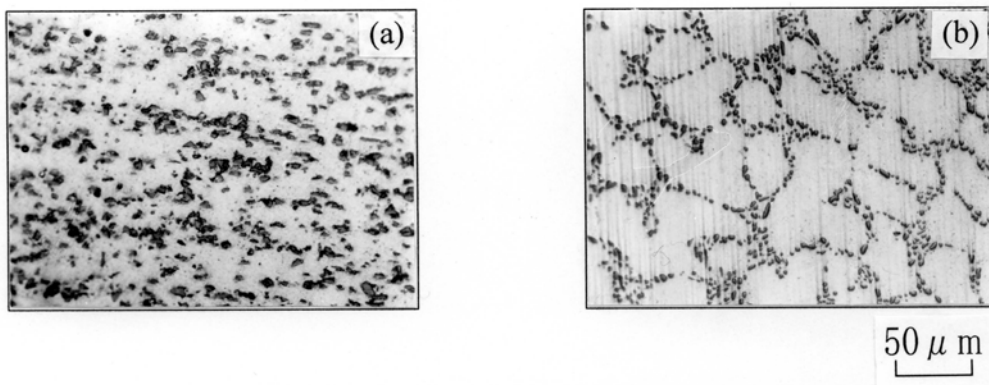
Figure 1: Microstructures: (a) SiC$_P$/Al, (b) AC4CH.

Test Methods

The casting alloy was solution treated at 530℃ for 6hrs followed by aging at 160℃ for 6hrs. The SiC$_P$/Al composite was also solution treated at 495℃ for 1h, quenched in water and then aged at 190℃ for 5hrs. CT specimens (*W*=24mm, *B*=5mm) were prepared after heat treatment. Experiments were conducted on an electro-servohydraulic fatigue testing machine operating at a frequency of 10Hz under load control with sinusoidal wave form in laboratory air at ambient temperature. Stress ratios were 0.05 and 0.7. Crack length was measured by a traveling microscope and crack closure was monitored by a compliance method using a strain gauge mounted on the back of the specimens. In the near threshold region, load shedding technique was employed to gradually decrease the FCP rate while keeping the stress ratio constant. In the region of d*a*/d*N* >10^{-8} m/cycle, constant load amplitude tests were used. The d*a*/d*N* and ΔK curves were obtained using a five points polynomial method. Crack path and fracture surfaces were examined using optical microscope and scanning electron microscope (SEM), respectively.

RESULTS AND DISCUSSION

FCP rate

Figure 2(a) and (b) show the relationships between d*a*/d*N* and ΔK at *R*=0.05 and *R*=0.7 in both alloys, respectively. In Figure 2(a), the casting alloy exhibits a better FCP resistance than the SiC$_P$/Al composite and has a higher threshold value of approximately 5.2MPam$^{1/2}$ compared with 4.5MPam$^{1/2}$ in the SiC$_P$/Al composite. In d*a*/d*N*>10^{-8}m/cycle, the d*a*/d*N*-ΔK relationships of both alloys can be expressed by the Paris law, while the casting alloy shows a slightly higher slope and the parameters of the Paris law, *C* and *m*, are 1.22×10^{-14} and 6.46 for the casting alloy and 6.64×10^{-12} and 4.24 in the SiC$_P$/Al composite, respectively. As can be seen in Figure 2(b), the FCP rates of both alloys are the same. Since crack closure was not recognized at *R*=0.7, the observed differences in FCP rate between both alloys in Figure 2(a) may be attributed to crack closure.
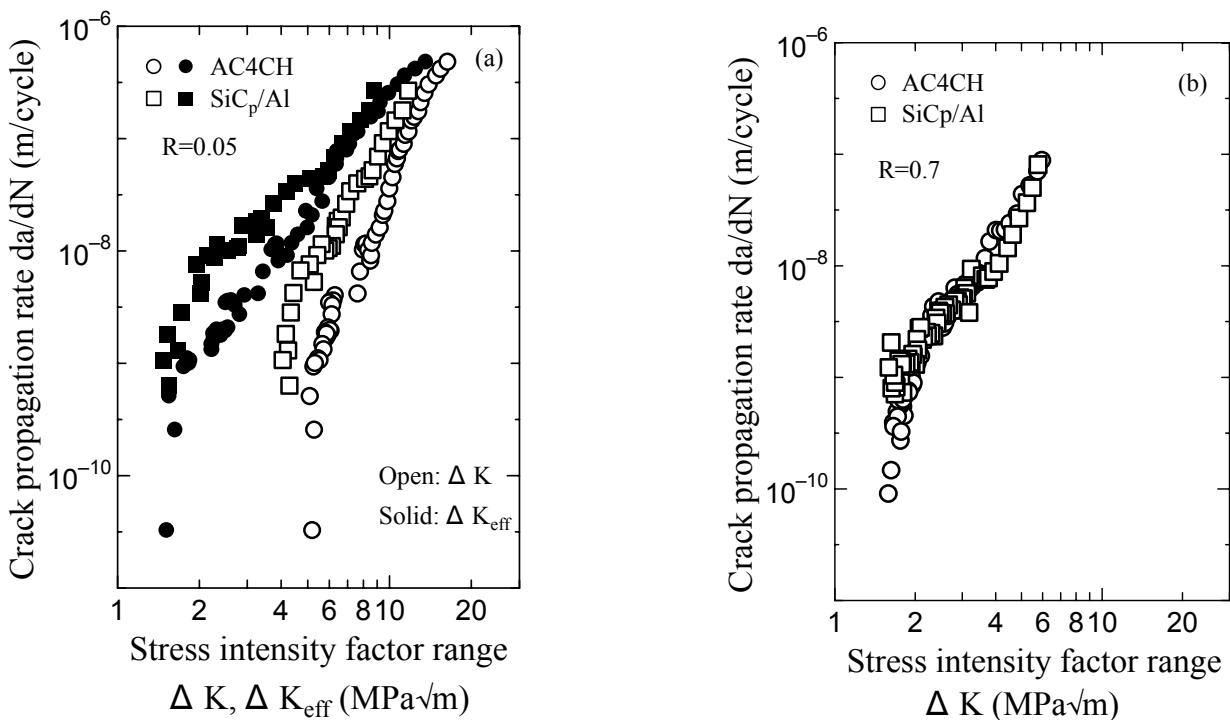
Figure 2: Relationships between d*a*/d*N* and Δ*K*: (a)*R*=0.05, (b)*R*=0.7.

Crack closure behavior, K_{op}/K_{max}, is shown in Figure 3 as a function of K_{max}. It can be seen that the casting alloy shows higher closure levels than the SiC_p/Al composite in the intermediate K_{max} region, but the closure levels in both alloys are almost identical at high and low K_{max} regions. After allowing for crack closure, *i.e.* in terms of the effective stress intensity factor range, ΔK_{eff}, there exist still differences in FCP rate between both alloys (see Figure 2(a)), but it should be noticed that the threshold value is nearly the same. Comparison between Figure 2(a) and (b), the da/dN-ΔK relationship at $R=0.7$ in the casting alloy is consistent with the da/dN-ΔK_{eff} relationship at $R=0.05$, while the differences in FCP rate between both can be seen in the SiCp/Al composite.
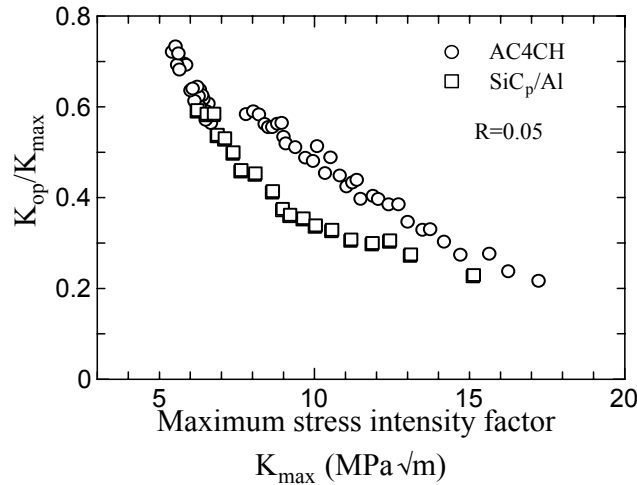
Figure 3: Crack closure behavior.

Crack path profile

Figure 4 reveals the crack paths at different FCP rates, *i.e.* ΔK levels, in both alloys. The crack paths of the SiC_P/Al composite are rather smooth regardless of ΔK. On the contrary, the casting alloy exhibits remarkable crack deflections and the crack paths are much more tortuous compared with the SiC_P/Al composite. As ΔK increases, the fracture surface roughness decreases. Therefore, the better FCP resistance in the casting alloy may be attributed to crack deflection *i.e.* fracture surface roughness, because of the higher crack closure levels and the reduction in the actual crack driving force at the crack tip [7]. Branching and bridging due to particle debonding can also be seen in the casting alloy, which can contribute to higher FCP
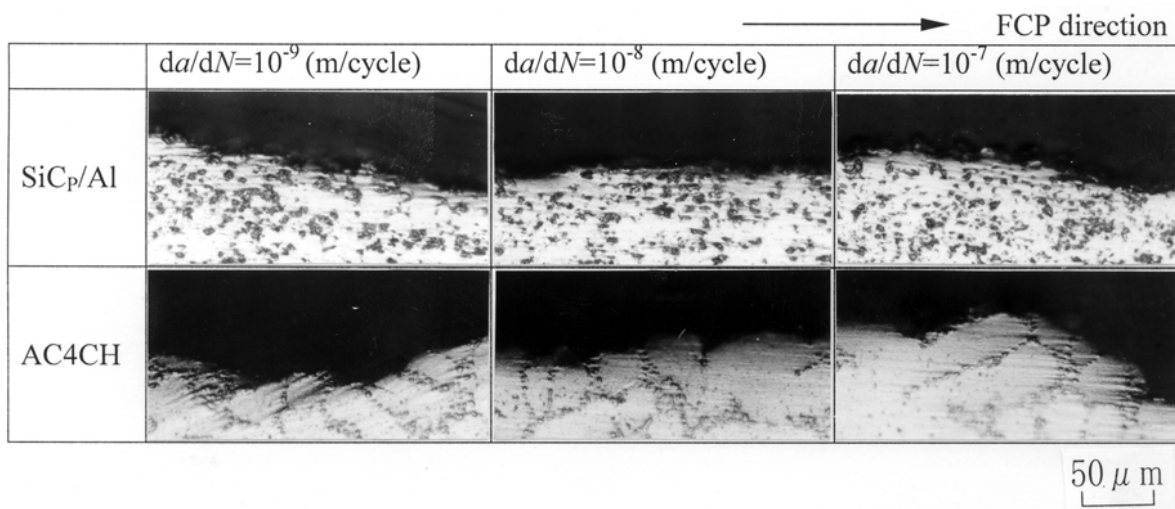
Figure 4: Optical micrographs of crack path profiles in SiCP/Al and AC4CH.

resistance. Furthermore, there exist a lot of porosity defects in the casting alloy that enhance FCP rate by coalescence/linkage of those defects. Contrarily, those defects may also cause crack deflections that can promote crack closure, in turn leading to decreased FCP rate.

Fractographic analysis of fracture surfaces
SEM micrographs of fracture surfaces of the SiC_P/Al composite and the casting alloy are shown in Figure 5. In the SiC_P/Al composite, the main features are hills and concavities that are caused when cracks propagate enveloping or avoiding SiC particles. Exposure of bare SiC particles on the fracture surfaces is very rare, indicating a good interfacial bond between SiC particle and matrix. However, debonded coarse SiC particles can be seen occasionally, particularly in high ΔK region. Around debonded coarse SiC particles, secondary crackings can be seen that may be the result of the thin matrix layer's enveloping SiC particles being torn. In the casting alloy, the facet is main feature on fracture surface at low ΔK region, while the secondary crackings can be observed at intermediate and high ΔK regions. Debonded eutectic Si particles are clearly seen, especially in low ΔK region and the debonded Si particles along the dendrite cells are just like that observed in Figure 1, suggesting that cracks propagated along the boundaries of dendrite cells. Few fractured Si particles are observed even at high ΔK regions. Decohesion of Si particles from the surrounding matrix is the main mode of fracture in this case. It should be noticed that eutectic Si particles appeared on the fracture surfaces tend to decrease as ΔK increases, *i.e.* FCP rate increases. This implies that cracks often grow in the matrix at high ΔK region, leading to smoother crack paths, as shown in Figure 4.
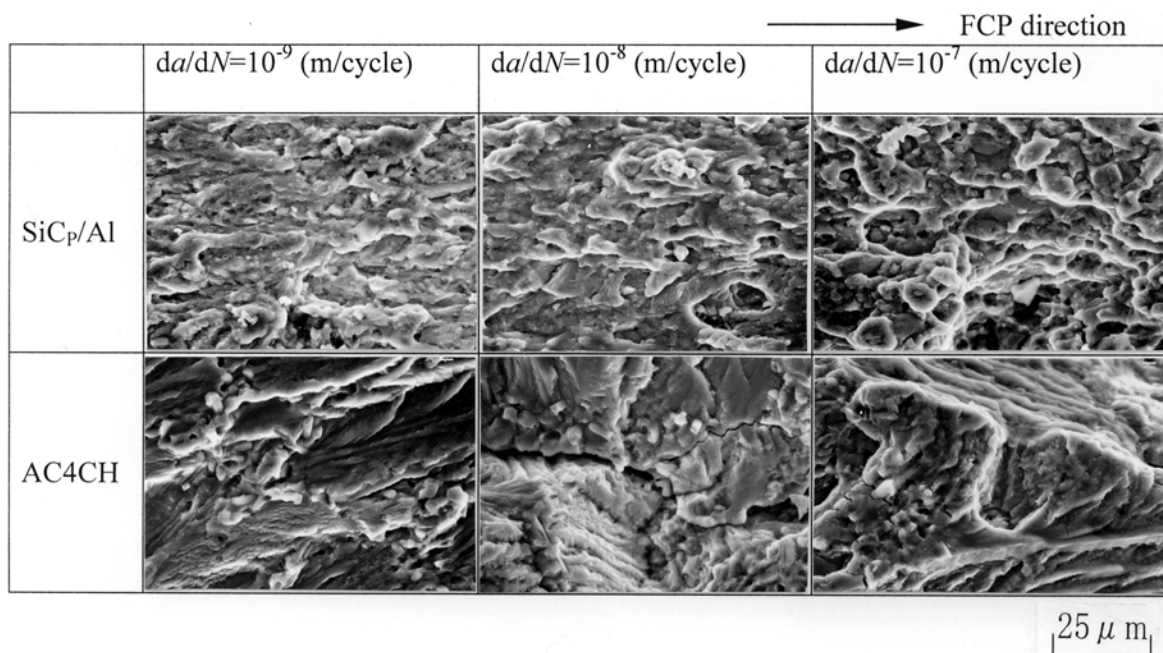
Figure 5: SEM micrographs of fracture surfaces in SiC_P/Al and AC4CH.

Crack growth mechanisms
In the SiC_P/Al composite, cracks grow preferably in the matrix avoiding SiC particles regardless of ΔK, because of a good interfacial bond between SiC particles and matrix and high strength of SiC particles. The particle size is small, thus the fracture surfaces become smooth. On the contrary, in the casting alloy, cracks propagate along the dendrite cells due to the debonding of Si particles in low ΔK region. In this case, there are two factors that may affect crack propagation; the first is that the cluster distribution causes the Si particles debonding easier and the second is that the Si particles along the dendrite cells may act as an "egg-shell" [4]. In the latter, cracks will need extra stress to advance into the next dendrite cell compared with propagating along the boundaries of dendrite cells. Whether cracks propagate along or through the

dendrite cells depend strongly on the crack-tip driving force and the strength of "egg-shell". In low ΔK region, cracks prefer to propagating along the boundaries of dendrite cells because Si particles provide a weak path, while in high ΔK region, cracks can break the "egg-shell" and thus grow into the inside of the next dendrite cell.

CONCLUSIONS

FCP tests were conducted on casting alloy, AC4CH, and SiC_P/Al composite, and the role of SiC and Si particles in FCP and the mechanisms are discussed on the basis of detailed fractographic examination.

1. Both alloys showed considerable differences in FCP behavior that was mainly attributed to the difference in particle distribution.
2. The casting alloy showed lower FCP rates compared with the SiC_p/Al composite, but had a slightly steeper slope in the Paris region.
3. After allowing for crack closure or in the crack closure-free FCP behavior, there were no significant differences in FCP rate between both alloys, indicating that the higher FCP resistance in the casting alloy was attributed to crack closure.
4. In the SiC_P/Al composite, cracks propagated avoiding SiC particles and predominantly within the matrix, while in the casting alloy, debonding of eutectic Si particles was the main feature and cracks grew to link debonded particles along dendrite cells that caused remarkable crack deflections.

REFERENCES

1. CHITOSHI MASUDA, YOSIHISA TANAKA, *etc*. (1994) *Adv. Composite Mater.* **3 No.4**, 319.
2. F.T. LEE, J.F. MAJOR, and F.H. SAMUEL. (1995) *Fatigue Fract. Engng Mater. Struct.* **18 No.3**, 385.
3. S. Kumai, K Yoshida, Y. Higo and S. Nunomura. (1992) *Int. J Fatigue,* **14 No.2**, 105.
4. ZHIRUI WANG and RUBY J. ZHANG. (1994) *Acta metal. Mater.* **42**, 1433
5. O.BOTSTEIN, R.ARONE and B.SHPIGLER. (1990) *Mater. Sci. Eng.* **A128,** 15.
6. KEN GALL, NANCY YANG, *etc*. (1999) *Metal. Mater. Trans.* **30A**, 3079.
7. S. SURESH. (1983) *Metal. Trans. A* **14A**, 2375.

The Simulations of the Void Initiation from the multiple seeds by Molecular Dynamics and the FEM

T. Tsuji[1] and N. Noda[1]

[1]Department of Mechanical Engineering, Shizuoka University,
Johhoku 3-5-1, Hamamatsu, 432-8561, Japan

ABSTRACT

We have been studied the void formation from the single seed by using MD. Moreover, the same model has been simulated by using FEM. In this paper, as the next step, which will connected to the mezzo-scopic and the macroscopic fracture, we study the void initiation from multiple seeds. A square unit cell with some atom defects is constructed with nickel atoms and is subjected to the tensile load by using Molecular Dynamics. A same configured model with some small voids is simulated by using FEM. In this simulation, the mechanical properties, which are given by the potential function of the Molecular Dynamics, are used. When there is only one seed, one void grows simply from the seed. If there are multiple seeds, we observe the void growth and the void vanishing by the influence from the other voids. The behaviors of the voids initiation by the two methods, which are microscopic and macroscopic method, are compared to each other.

KEYWORDS

Molecular Dynamics, void initiation, FEM, computational simulation, Ni.

INTRODUCTION

Formation of a void is a considerable feature for a number of engineering materials, because failure by coalescence of the voids is an important fracture mechanism in ductile solids. There are some theoretical solutions of the void formation for nonlinear elastic solid. On the other hand, it is important to study microscopic void formation, in order to consider the initiation of the void. We have been studied the void formation from the single seed by using Molecular Dynamics (MD) [1-3]. There are many studies about crack simulations by MD. But, we think that the atom order crack can not grow and exists as steady state. If

an atomic order crack exists, it will immediately close by the inter-atomic power. Moreover the optimum configuration of the very small defect should be sphere by surface tension. By our void growth simulation, the atom order void can exist in steady state by reducing the load. On the other hand, the atom order void can not grow to the macroscopic void, although the void in the liquid can grow to very huge. Thus, we think that the following scenario to the destruction of a solid.

1) The atom order void initiation and growth.
2) The mezzo-scopic crack initiation by chaining the atom order voids.
3) The macroscopic destruction by the crack growth.

The step 2) might be denoted as phase changing from simple voids to a complex crack. We have been studied the step 1) [1-3]. In this paper, as the next step, which will connected to the mezzo-scopic and the macroscopic fracture, we study the void initiation from multiple seeds. A square unit cell with some atom defects is constructed with nickel atoms and is subjected to the hydrostatic tensile load by using Molecular Dynamics. A same configured model with some small voids is simulated by using FEM. In this simulation, the mechanical properties, which are given by the potential function of the Molecular Dynamics, are used. If there is only one seed, one void grows simply from the seed. In this study, we observed the void growing and the void vanishing by the influence from the other voids. The behaviors of the voids initiation by the two methods, which are microscopic and macroscopic method, are compared to each other.

SIMULATIONS BY FEM

The void formations in an infinite long compressible elastic cylinder under axis-symmetric stretch are examined by Biwa [4]. In this theory, the strain energy function W for homogeneous isotropic nonlinear elastic solid is given as constitutive relation.

$$W\left(\lambda_1,\lambda_2,\lambda_3\right) = \frac{\mu}{k}\left|\lambda_1^{-k}+\lambda_2^{-k}+\lambda_3^{-k}-3+k\left(\lambda_1\lambda_2\lambda_3-1\right)\right| \tag{1}$$

where, λ_i ($i=1, 2, 3$) is the principle stretches. Young's modulus, the bulk modulus and Poisson's ratio of Ni can be given as 110[GPa], 180[GPa] and 0.398 for EAM potential, respectively. Then, the material constants μ and k are set to 154[GPa] and 0.513, respectively. We consider the square plate, which side length is denoted as A, and make five holes with radius B_i ($i = 1, 2, 3, 4, 5$), as shown in Fig.1.
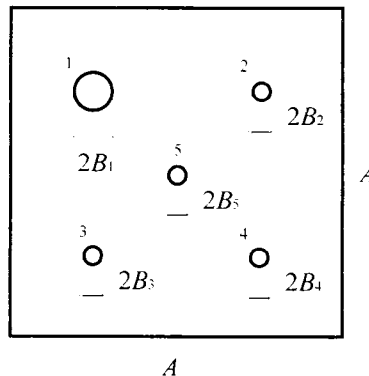
Figure 1: Simulation model.

By using the energy function W as shown in Eq.(1), FEM simulations are proceeded with plain strain condition. The stepwise uniform stretch is applied by moving boundary of this square in plane strain condition. Two types of radius $Bi/A = 0.002145$ or 0.00357 are used as the initial void. The number of combination to set two radii to five holes is twelve in consideration with symmetry. We tried every combinations and the typical results are shown in Fig. 2.

| Stretch = 1.171 | 1.206 | 1.240 |

(a) $B_1/A = B_2/A = B_3/A = B_4/A = B_5/A = 0.002145$

| Stretch = 1.171 | 1.206 | 1.240 |

(b) $B_1/A = 0.00357$, $B_2/A = B_3/A = B_4/A = B_5/A = 0.002145$

| Stretch = 1.171 | 1.206 | 1.240 |

(c) $B1/A = B2/A = B4/A = B5/A = 0.00357$, $B3/A = 0.002145$
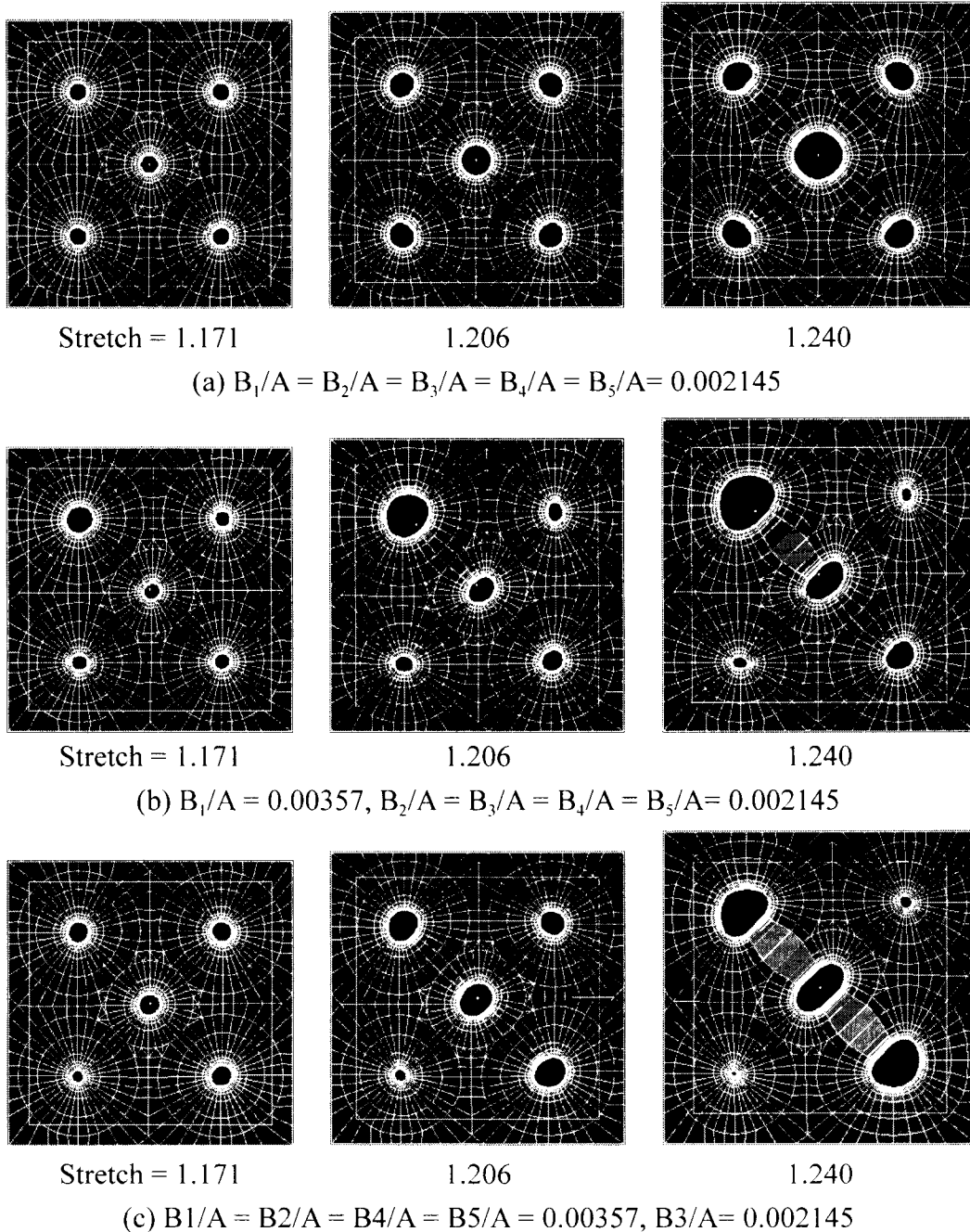
Figure 2: Void growth from the five seeds.

We found that, the void in the neighborhood of the slightly big void, that is void along the diagonal line, grows into bigger. The other voids are growing within small stretch, but they are shrinking by the growth of the bigger voids. Figure 3 shows relationships between the stretch and the radius of the voids for case (a), (b) and (c) in Fig.2. The growth of the void is reduced by growing of the void in diagonal line. For example, the radius of void B_2 in (b) and (c) is reducing after stretch 1.2 by growing of void B_1.
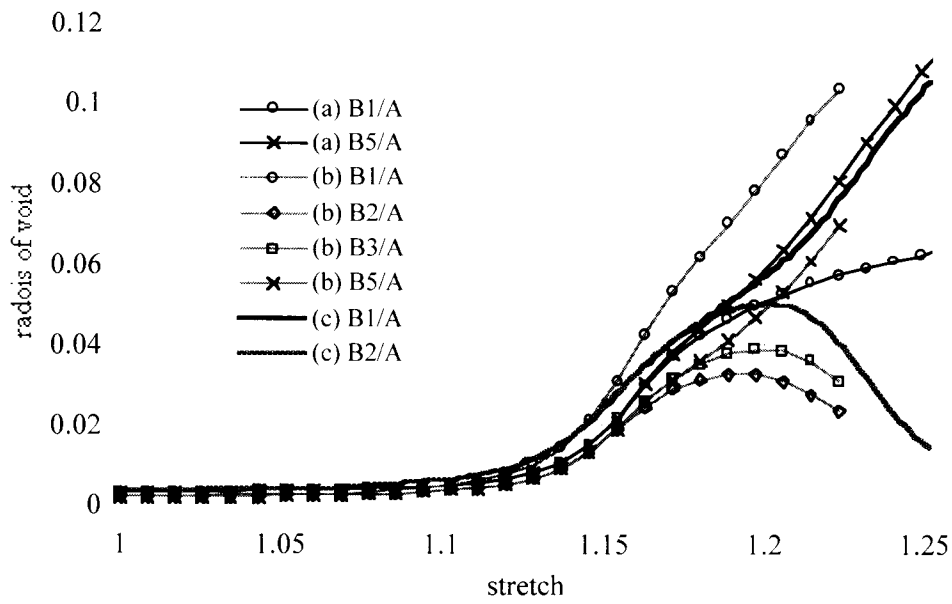
Figure 3: Relationship between stretch and radius of the voids with the initial hole radius as (a) $B_1/A = B_2/A = B_3/A = B_4/A = B_5/A = 0.002145$, (b) $B_1/A = 0.00357$, $B_2/A = B_3/A = B_4/A = B_5/A = 0.002145$ and (c) $B_1/A = B_2/A = B_4/A = B_5/A = 0.00357$, $B_3/A = 0.002145$.

SIMULATIONS BY MD

The simulation model is constructed with fcc crystal of Ni atoms. The axial direction is set along [111] direction. By applying the periodical boundary condition with periodic length 6.097 Å to the axial direction, the model forms the infinite long bar with square cross section 100.6 × 100.6 Å. The number of atoms without void is 5692. The equilibrium lattice constant at the absolute temperature 0K is 3.52Å. The movement of atoms, which constructs the outer surface of the bar within 4 Å from the edge, is fixed in order to apply the stretch. Two types of the initial void, as shown in Fig. 4, are introduced by taking the atoms. The time step $\Delta t = 0.001$ [ps] and the stretch 1.001 is applied by every 100 time steps, that is, the relaxation time 0.1 [ps] is applied by every stretch step. Embedded Atom Method [5] is used as the inter-atomic potential. At first, the simulation model is relaxed at the initial temperature 0K. Next, the model is subjected to the uniform stretch by moving the fixed atoms along the cross section of the bar. While the external load is applied, the temperature control is not carried out.
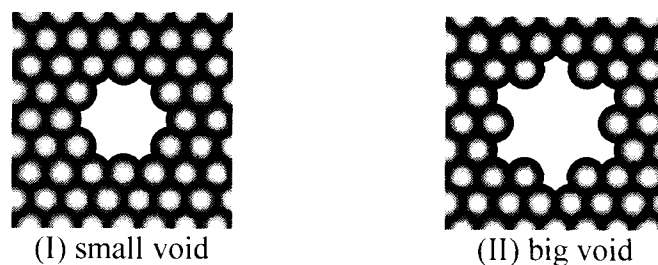
(I) small void   (II) big void
Figure 4 : Two types of initial void.

Figure 5 shows the snapshots of the simulations with the stretch 1.051, 1.105 and 1.139. We can observe the similar manner of the voids growing to the results by FEM in Fig. 2. In this MD simulation, smaller initial void can not grow. In case (c), such the void is vanished by growing of the other voids. The radius of the initial voids is relative to the width of this plate with about 0.04. Thus, this relative radius of the initial voids is ten times larger than the one in the FEM simulations. Then, the growth of the small void is disturbed by

the big voids at smaller stretch.

| Stretch = 1.051 | 1.105 | 1.139 |

(a) All holes are type I (small).

| Stretch = 1.051 | 1.105 | 1.139 |

(b) The hole 1 is type II (big), and the other holes are type I (small).

| Stretch = 1.051 | 1.105 | 1.139 |

(c) The hole 2 is type I (small), and the other holes are type II (big).
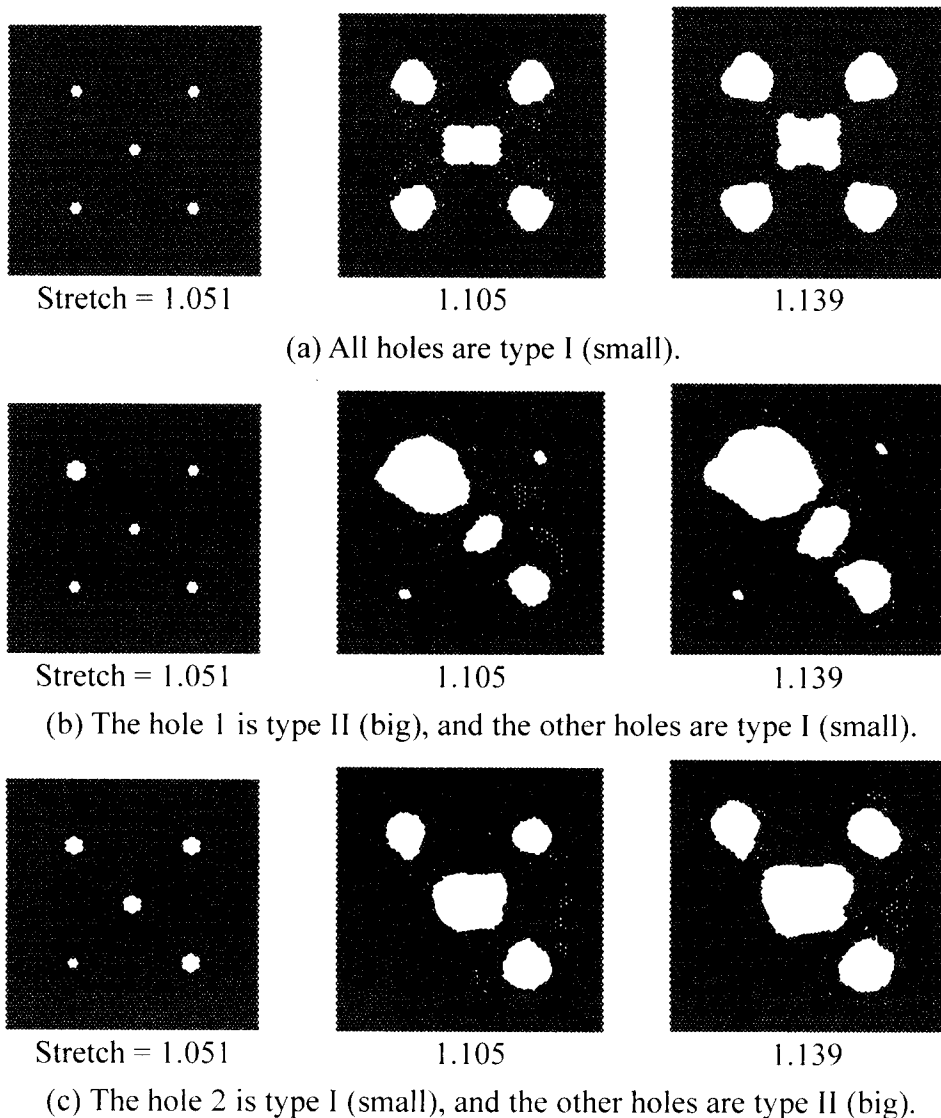
Figure 5: Void growth from the five origins.

CONCLUSIONS

The growth of five initial seeds, whose radius is slightly different, in the square plate is simulated by FEM and MD. Very different void growth by the difference of the initial void radius could be observed. Moreover, the manner of growth by FEM is similar to the one by MD, although the scale and the method of the simulation are very different. It might be some formulas in the growing of the void from multiple seeds. If we can find such the formulas, it could be possible to discover the process from micro to mezzo.

REFERENCES

1. Makino, M., Tsuji, T. and Noda, N. (1998) *Proc. JSSUME'98 (ISBN 89-7581-073-9 93550)*, 53.
2. Makino, M., Tsuji, T. and Noda, N. (2000) *Computational Mechanics*, 26, 281.
3. Tsuji, T., Makino, M and Noda, N. (2000) *Advances in Comput. Eng. & Sciences*, II, 1168.
4. Biwa, S. (1995) *Int. J. Non-Linear Mech.*, 30-6, 899.
5. Foiles, S.M., Baskes, M.I. and Daw, M.S. (1986) *Phys. Rev. B*, 33, 7983.

THE TUNNEL-CRACK WITH A SLIGHTLY WAVY FRONT UNDER SHEAR LOADING

V. Lazarus and J.-B. Leblond

Laboratoire de Modélisation en Mécanique, Université Pierre et
Marie Curie (Paris VI), 8 rue du Capitaine Scott, 75015 Paris, France

ABSTRACT

One considers a planar tunnel-crack with a slightly wavy front in an infinite body, loaded in mode II+III through uniform remote shear stresses, such as a geophysical fault. The distribution of stress intensity factors along the perturbed front is determined using Bueckner-Rice's weight function theory. From there, one addresses the following bifurcation and stability problems: (i) is there a non-rectilinear configuration of the front for which the energy release rate is uniform along that front? (ii) is the rectilinear configuration of the front stable versus small coplanar perturbations? The answer to question (i) is positive. The "critical", bifurcated configuration is sinusoidal; both its wavelength and the "phase difference" between the fore and rear parts of the crack front depend upon the ratio of the initial (prior to perturbation of the front) mode II and III stress intensity factors. The answer to question (ii) depends upon the wavelength of the perturbation envisaged; stability prevails for wavelengths smaller than the critical one and instability for larger ones. This conclusion is similar to those arrived at by Gao and Rice and the authors for analogous problems.

KEYWORDS

Tunnel-crack, slightly perturbed front, shear loading, Bueckner-Rice theory, bifurcation, stability

INTRODUCTION

Consider a plane crack with arbitrary contour $\mathcal{F}$ in an arbitrary body Ω. Slightly perturb the crack front, within the crack plane, by an amount $\delta a(s)$, where s denotes the curvilinear distance along $\mathcal{F}$. Then the variations $\delta K_\alpha(s)$ ($\alpha = I, II, III$) of the stress intensity factors (SIF) are given, to first order in the perturbation, by the following formula, which was first established by Nazarov [1] and Rice [2] in situations of pure mode I, and later extended by Leblond *et al.* [3] to arbitrary mixed mode conditions:

$$
\begin{aligned}
\delta K_\alpha(s) &= [\delta K_\alpha(s)]_{\delta a(s') \equiv \delta a(s)} + N_{\alpha\beta}(0) K_\beta(s) \frac{\mathrm{d}\delta a}{\mathrm{d}s}(s) \\
&+ PV \int_{\mathcal{F}} Z_{\alpha\beta}(\Omega; s, s') K_\beta(s')[\delta a(s') - \delta a(s)] ds'
\end{aligned}
\tag{1}
$$

where Einstein's implicit summation convention is employed for the index $\beta = I, II, III$. In this equation, the $K_\beta(s)$ are the initial (prior to perturbation of the crack front) SIF; $[\delta K_\alpha(s)]_{\delta a(s') \equiv \delta a(s)}$ denotes the value of $\delta K_\alpha(s)$ for a *uniform crack advance* equal to $\delta a(s)$ ($\delta a(s') = \delta a(s), \forall s'$); the $N_{\alpha\beta}(0)$ are the components of a *universal* (valid in all circumstances) operator which has been calculated by Gao and Rice [4]; and finally the $Z_{\alpha\beta}(\Omega; s, s')$ are the components of an operator which depends upon (in addition to s and s') the entire geometry of the body and the crack considered, and diverges like $(s' - s)^{-2}$ for $s' \to s$, so that the integral in Eqn. 1 makes sense as a Cauchy principal value (PV).

Equation 1 was applied by Leblond *et al.* [5] to the study of a planar tunnel-crack with a slightly wavy front in an infinite body, loaded in pure mode I through some uniform remote tensile stress. Using an original method based on the work of Rice [2], these authors first evaluated the geometry-dependent operator component $Z_{I,I}(\Omega; s, s')$ for the configuration envisaged. Then they studied problems of configurational bifurcation and stability of the crack front during propagation. The bifurcation problem is the following one. Does there exist, in addition to the trivial, rectilinear configuration of both parts

of the crack front, some non-trivial, curved configuration for which the energy release rate is uniform along that front in spite of its curvature? The answer was shown to be "yes"; the "critical", bifurcated configuration was symmetric with respect to the middle axis of the tunnel-crack and sinusoidal, its wavelength being a characteristic multiple of the crack width. The stability issue was as follows: if both parts of the crack front are slightly perturbed within the crack plane, will the perturbation decay or increase as propagation proceeds? It was shown that stability prevails for sinusoidal perturbations of wavelength smaller than that of the critical perturbation, and instability for wavelengths larger than it. This finding was compatible with the conclusions of Rice [6] and Gao and Rice [7, 8] concerning other types of cracks loaded in mode I.

The aim of this paper is to consider the same problem, but for a shear (mode II+III) loading. Propagation will still be assumed to be coplanar; this is reasonable provided that the crack is channeled along a planar surface of low fracture resistance, which can be the case for instance for a geological fault. Also, propagation will be considered to be governed by the (local) energy release rate, the critical value of which will be assumed to be independent of the ratio of the mode II and III SIF. Again, this is reasonable (Rice, private communication) for coplanar propagation along a weak surface, since energy dissipation occurs through the same physical mechanisms (shear and friction) in both modes II and III. It will be shown that there again exists a critical, bifurcated configuration of the front. Again, this configuration is sinusoidal and its wavelength is a multiple of the width of the crack, but this wavelength now depends upon the ratio of the mode II and III initial (prior to perturbation of the front) SIF. Also, it is symmetric with respect to the middle axis of the crack only for initial conditions of pure mode II or pure mode III; for mixed mode II+III conditions, there is a "phase difference" between the bifurcated configurations of the fore and rear parts of the crack front. The stability issue will be addressed only in the case where the phase difference between the perturbations of both parts of the front takes some special values. It will be shown that in the most interesting case, stability prevails only if the wavelength of the perturbation is smaller than the critical one. This conclusion is the same as in pure mode I (Leblond *et al.* [5]), and also as in mixed mode for other crack shapes (Gao and Rice [9], Gao [10]).

STRESS INTENSITY FACTORS FOR A PERTURBED TUNNEL-CRACK

Consider now (Figure 1), within an infinite body, a tunnel-crack of half-width a loaded through uniform remote shear stresses $\sigma_{xy}^\infty, \sigma_{yz}^\infty$. The orientations of the fore $(+)$ and rear $(-)$ parts of the crack front being chosen as identical, this loading generates a uniform SIF $K_{II} = \sigma_{xy}^\infty \sqrt{\pi a}$ and opposite SIF $K_{III}^+ = \sigma_{yz}^\infty \sqrt{\pi a}$, $K_{III}^- = -K_{III}^+$ on them. Now slightly perturb the fore and rear parts of the crack front, within the crack plane, by the amounts $\delta a(z^+)$, $\delta a(z^-)$ respectively. Using then Eqn. 1, the values of the $N_{\alpha\beta}(0)$ provided by Gao and Rice [4], "symmetry" properties of the $Z_{\alpha\beta}(\Omega; s, s')$ established by Leblond *et al.* [3] and elementary symmetry considerations for the crack configuration envisaged, one gets for the perturbations of the SIF on the fore part of the crack front:

$$\delta K_{II}(z^+) = K_{II}\frac{\delta a(z^+)}{4a} - \frac{2}{2-\nu}K_{III}^+\frac{\mathrm{d}\delta a}{\mathrm{d}z}(z^+)$$

$$+PV\int_{-\infty}^{+\infty}\left[f_{II,II}\left(\frac{z'-z}{a}\right)K_{II} + f_{II,III}\left(\frac{z'-z}{a}\right)K_{III}^+\right]\left(\delta a(z'^+) - \delta a(z^+)\right)\frac{dz'}{(z'-z)^2} \qquad (2)$$

$$+\int_{-\infty}^{+\infty}\left[g_{II,II}\left(\frac{z'-z}{a}\right)K_{II} + g_{II,III}\left(\frac{z'-z}{a}\right)K_{III}^-\right]\delta a(z'^-)\frac{dz'}{a^2}\ ;$$

$$\delta K_{III}(z^+) = K_{III}^+\frac{\delta a(z^+)}{4a} + \frac{2(1-\nu)}{2-\nu}K_{II}\frac{\mathrm{d}\delta a}{\mathrm{d}z}(z^+)$$

$$+PV\int_{-\infty}^{+\infty}\left[-(1-\nu)f_{II,III}\left(\frac{z'-z}{a}\right)K_{II} + f_{III,III}\left(\frac{z'-z}{a}\right)K_{III}^+\right]\left(\delta a(z'^+) - \delta a(z^+)\right)\times \qquad (3)$$

$$\times\frac{dz'}{(z'-z)^2} + \int_{-\infty}^{+\infty}\left[-(1-\nu)g_{II,III}\left(\frac{z'-z}{a}\right)K_{II} + g_{III,III}\left(\frac{z'-z}{a}\right)K_{III}^-\right]\delta a(z'^-)\frac{dz'}{a^2}\ .$$

In these expressions, the $f_{\alpha\beta}$ and $g_{\alpha\beta}$ are functions which depend solely upon (in addition to the

argument $(z' - z)/a)$ Poisson's ratio ν; $f_{II,II}$, $f_{III,III}$, $g_{II,II}$, $g_{III,III}$ are even, and $f_{II,III}$, $g_{II,III}3$ odd. The values of $\delta K_{II}(z^-)$, $\delta K_{III}(z^-)$ are given by the same expressions, with the obvious substitutions $\delta a(z^+) \to \delta a(z^-)$, $\delta a(z'^\pm) \to \delta a(z'^\mp)$, $K_{III}^\pm \to K_{III}^\mp$. The functions $f_{\alpha\beta}$ and $g_{\alpha\beta}$ $(\alpha, \beta = II, III)$ can be
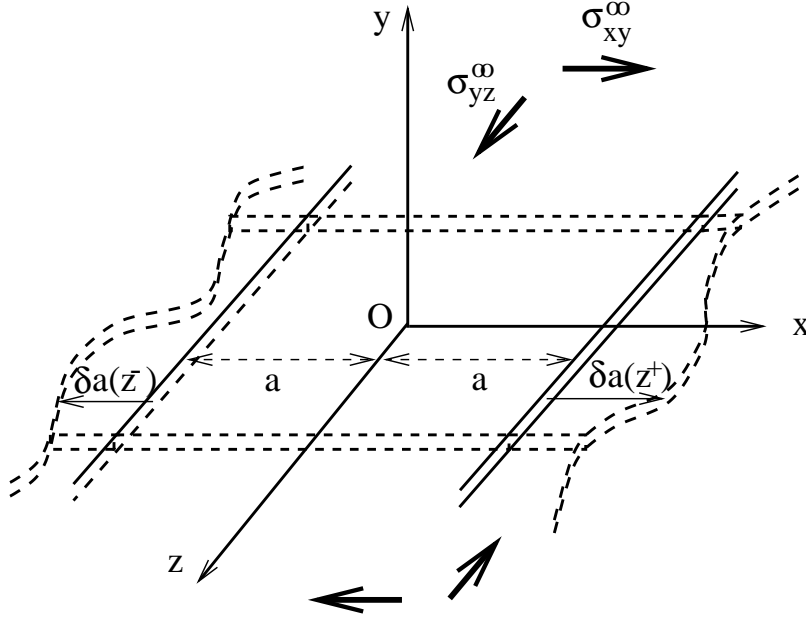
Figure 1: Tunnel-crack with a slightly wavy front loaded in shear

determined in a similar way as the corresponding functions for mode I (Leblond *et al.* [5]). The method combines the relation between the $Z_{\alpha\beta}(\Omega; s, s')$ and Bueckner's crack-face weight functions (Leblond *et al.* [3]), and Eqn. 1 applied to some special motions of the crack front preserving the shape of the crack while modifying its size and orientation. It yields integro-differential equations on the $f_{\alpha\beta}$ and $g_{\alpha\beta}$, which are transformed into ordinary differential equations through Fourier transform along the z−direction, and then integrated numerically for any value of ν.

BIFURCATION OF THE STRAIGHT CONFIGURATION OF THE FRONT

Consider a slightly curved configuration of both parts of the crack front defined by

$$\delta a(z^+) = \alpha \cos(kz) \; ; \; \delta a(z^-) = \alpha \cos(kz + \varphi) \tag{4}$$

where α, $k > 0$ and $\varphi \in [-\pi, \pi)$ are parameters. Using Eqns. 2 and 3 and Irwin's formula, one obtains the following expression of the perturbation of the energy release rate $\mathcal{G}$ on the fore part of the crack front:

$$\delta\mathcal{G}(z^+) = 2\frac{1 - \nu^2}{E}\frac{\alpha}{a}K_{II}^2[(F + G\cos\,\varphi + H\sin\,\varphi)\cos(kz) + (-G\sin\,\varphi + H\cos\,\varphi)\sin(kz)] \; . \tag{5}$$

In this expression, E is Young's modulus and $F \equiv F(K_{III}^+/K_{II}, p)$, $G \equiv G(K_{III}^+/K_{II}, p)$, $H \equiv H(K_{III}^+/K_{II}, p)$ the quantities given by

$$F = \bar{f}_{II,II}(p) + \frac{1}{1 - \nu}\frac{K_{III}^{+2}}{K_{II}^2}\bar{f}_{III,III}(p) \; ;$$

$$G = \bar{g}_{II,II}(p) - \frac{1}{1 - \nu}\frac{K_{III}^{+2}}{K_{II}^2}\bar{g}_{III,III}(p) \; ; \; H = 2\frac{K_{III}^+}{K_{II}}\bar{g}_{II,III}(p) \tag{6}$$

where the "reduced" wavevector p (> 0) and the functions $\bar{f}_{\alpha\beta}$, $\bar{g}_{\alpha\beta}$ are defined by

$$p = ka \; ; \; \bar{f}_{\alpha\beta}(p) = \frac{1}{4} + 2\int_0^{+\infty} f_{\alpha\beta}(u)(\cos(pu) - 1)\frac{du}{u^2} \; ,$$

$$\bar{g}_{\alpha\beta}(p) = 2\int_0^{+\infty} g_{\alpha\beta}(u)\cos(pu)du \qquad ((\alpha, \beta) = (II, II) \text{ and } (III, III)) \; ; \tag{7}$$

$$\bar{g}_{II,III}(p) = 2\int_0^{+\infty} g_{II,III}(u)\sin(pu)du \; .$$

The expression of $\delta\mathcal{G}(z^-)$ is given by the same formula 5 as $\delta\mathcal{G}(z^+)$ with the substitutions $\cos(kz) \to \cos(kz + \varphi)$, $\sin(kz) \to -\sin(kz + \varphi)$.

For $\mathcal{G}$ to be uniform along both parts of the crack front, the terms proportional to $\cos(kz)$ and $\sin(kz)$ in the expression of $\delta\mathcal{G}(z^+)$, and those proportional to $\cos(kz + \varphi)$ and $\sin(kz + \varphi)$ in the expression of $\delta\mathcal{G}(z^-)$, must be zero. This leads to the following conditions:

$$F + G\cos\varphi + H\sin\varphi = 0 \ ; \ \tan\varphi = H/G \ . \tag{8}$$

Using Eqn. 8_2 in Eqn. 8_1, one gets $\cos\varphi = -FG/(G^2 + H^2)$, $\sin\varphi = -FH/(G^2 + H^2)$. Use of the relation $\cos^2\varphi + \sin^2\varphi = 1$ then yields

$$F^2 = G^2 + H^2 \ \Rightarrow \ F = \pm\sqrt{G^2 + H^2} \ ; \ \cos\varphi = -\frac{G}{F} \ ; \ \sin\varphi = -\frac{H}{F} \ . \tag{9}$$

For a given ratio K_{III}^+/K_{II}, 9_2 is an equation on p the solution of which is the critical reduced wavevector; Eqns. 9_3, 9_4 then define the corresponding critical phase difference between the configurations of the fore and rear parts of the crack front.

It can be shown that for $p = 0$, $F = G = \frac{1}{4}\left(1 + \frac{1}{1-\nu}\frac{K_{III}^{+2}}{K_{II}^2}\right)$, $H = 0$, and that for $p \to +\infty$, $F \to -\infty$, $G \to 0$, $H \to 0$. Therefore, if one chooses the sign $+$ in Eqn. 9_2, the solution is obviously $p = 0$, and it then follows from Eqns. 9_3, 9_4 that $\varphi = -\pi$, so that by Eqns. 4, $\delta a(z^+) = -\delta a(z^-) = Cst$. This is a trivial bifurcation mode which merely corresponds to some translatory motion of the crack in the x−direction. On the other hand, if the sign $-$ is selected in Eqn. 9_2, there is a non-zero solution p_c and a corresponding angle φ_c, which define a non-trivial bifurcation mode. It can be shown that $\cos\varphi_c = -G/F > 0$ so that $\varphi_c \in (-\pi/2, \pi/2)$.
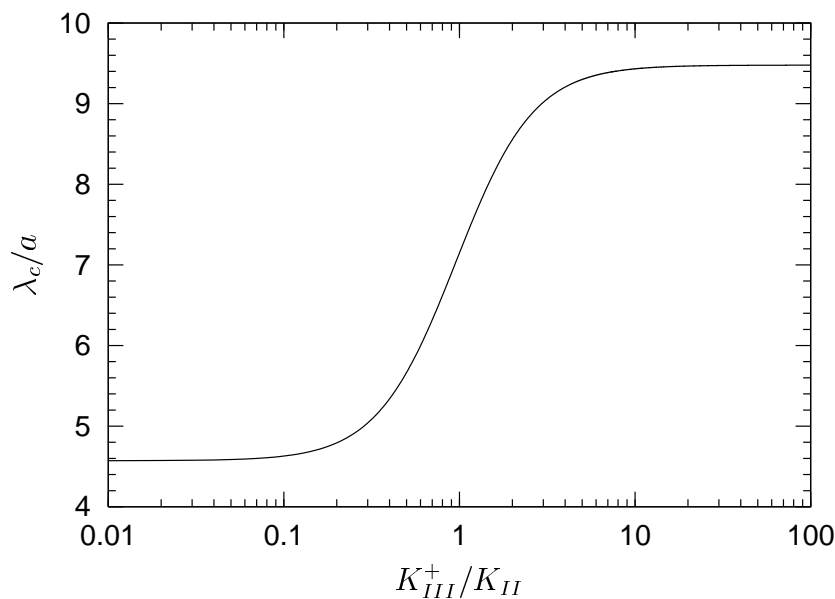
Figure 2: Critical reduced wavelength versus the ratio of the initial SIF

For each value of the ratio K_{III}^+/K_{II}, Eqn. 9_2 (with the sign $-$) can be solved numerically, using the values of the functions $f_{\alpha\beta}$, $g_{\alpha\beta}$ determined as sketched in the preceding section. Figures 2 and 3 represent the critical reduced wavelength $\lambda_c/a = 2\pi/p_c$ and the critical phase difference φ_c of the bifurcated mode, as functions of this ratio, for $\nu = 0.3$. (K_{III}^+/K_{II} is assumed here to be positive; it is obvious that if it changes sign, λ_c remains unchanged while φ_c changes sign). One sees that the critical wavelength is larger in pure mode III than in pure mode II. Also, the critical phase difference vanishes in pure mode II and III, that is, the bifurcated configuration becomes symmetric with respect to the middle axis Oz of the crack in these cases. It is recalled that the bifurcation mode was also found to be symmetric for a pure mode I loading (Leblond et al. [5]).
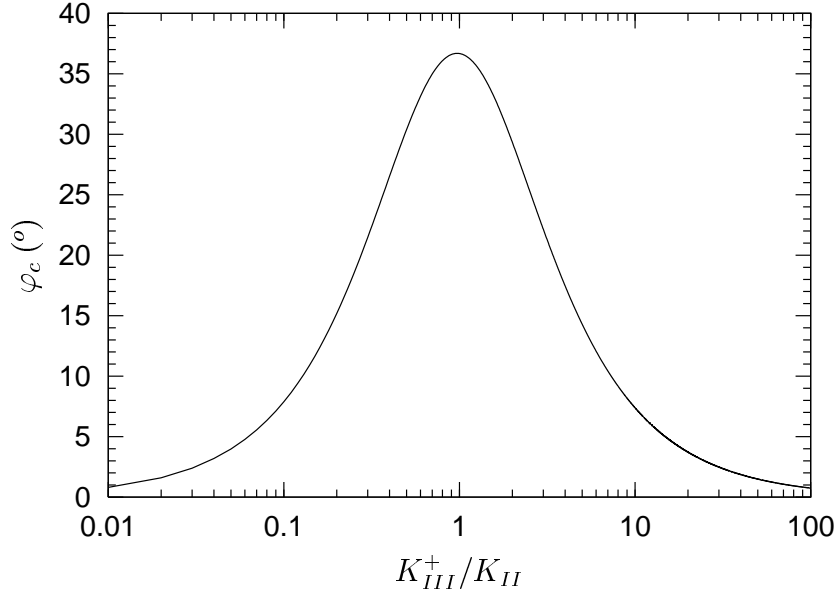
Figure 3: Critical phase difference versus the ratio of the initial SIF

STABILITY OF THE STRAIGHT CONFIGURATION OF THE FRONT

The issue of configurational stability of the crack front is easily dealt with only if the extrema of $\delta\mathcal{G}(z^+)$ coincide with those of $\delta a(z^+)$, and similarly for those of $\delta\mathcal{G}(z^-)$ and $\delta a(z^-)$; then one gets stability if the maxima of $\delta\mathcal{G}(z^+)$ and $\delta\mathcal{G}(z^-)$ correspond to the minima of $\delta a(z^+)$ and $\delta a(z^-)$, and instability if they correspond to the maxima of $\delta a(z^+)$ and $\delta a(z^-)$. We thus assume that the terms proportional to $\sin(kz)$ and $\sin(kz+\varphi)$ in the expressions of $\delta\mathcal{G}(z^+)$ and $\delta\mathcal{G}(z^-)$ vanish, *i.e.* that the phase difference φ is given (in terms of K_{III}^+/K_{II} and p) by Eqn. 8_2. Then stability prevails if the cofactors of $\cos(kz)$ and $\cos(kz+\varphi)$ in the expressions of $\delta\mathcal{G}(z^+)$ and $\delta\mathcal{G}(z^-)$ are negative:

$$\text{Stability} \quad \Leftrightarrow \quad F + G\cos\varphi + H\sin\varphi < 0 \quad (\text{with } \tan\varphi = H/G) . \tag{10}$$

Let us for instance assume K_{III}^+/K_{II} to be positive. Then it can be checked that $\tan\varphi = H/G \geq 0$ so that $\varphi \in [0, \pi/2)$ or $\varphi \in [-\pi, -\pi/2)$. Note that if $p = p_c$, $\varphi = \varphi_c$ in the first case and $\varphi = \varphi_c - \pi$ in the second one.

* The more interesting case corresponds to $\varphi \in [0, \pi/2)$. Then, for $p = 0$, $F = G > 0$ and $H = 0$ (see above) so that $\varphi = 0$ and $F + G\cos\varphi + H\sin\varphi = F + G > 0$. On the other hand, for $p \to +\infty$, $F \to -\infty$, $G \to 0$, $H \to 0$ (see above) so that $F + G\cos\varphi + H\sin\varphi \sim F < 0$. Finally, for $p = p_c$, $\varphi = \varphi_c$ so that $F + G\cos\varphi + H\sin\varphi = 0$. Thus $F + G\cos\varphi + H\sin\varphi$ is positive for $p < p_c$, zero for $p = p_c$ and negative for $p > p_c$: *stability prevails for wavelengths smaller than the critical value λ_c and instability for wavelengths greater than it.* This finding is similar to those of Leblond *et al.* [5] in pure mode I, and Gao and Rice [9] and Gao [10] for semi-infinite and penny-shaped cracks in mode II+III.

* In the less interesting case where $\varphi \in [-\pi, -\pi/2)$, for $p = 0$, $\varphi = -\pi$ so that $F + G\cos\varphi + H\sin\varphi = F - G = 0$; for $p \to +\infty$, $F + G\cos\varphi + H\sin\varphi < 0$; finally, for $p = p_c$, $\varphi = \varphi_c - \pi$ so that $F + G\cos\varphi + H\sin\varphi = F + G^2/F + H^2/F = -2\sqrt{G^2 + H^2} < 0$. Thus $F + G\cos\varphi + H\sin\varphi$ is always negative, and stability prevails for all wavelengths.

REFERENCES

1. Nazarov, S.A. (1989). *Mech. Solids*, 24, 145.

2. Rice, J.R. (1989). In: *Fracture Mechanics: Perspectives and Directions*, ASTM STP 1020, pp. 29-57, Wei, R.P. and Gangloff, R.P. (Eds.). ASTM, Philadelphia.

3. Leblond, J.-B., Lazarus, V. and Mouchrif, S.-E. (1999). *Int. J. Solids Structures*, 36, 105.

4. Gao, H. and Rice, J.R. (1986). *ASME J. Appl. Mech.*, 53, 774.

5. Leblond, J.-B., Mouchrif, S.-E. and Perrin, G. (1996). *Int. J. Solids Structures*, 33, 1995.

6. Rice, J.R. (1985). *ASME J. Appl. Mech.*, 52, 571.

7. Gao, H. and Rice, J.R. (1987). *Int. J. Fract.*, 33, 155.

8. Gao, H. and Rice, J.R. (1987). *ASME J. Appl. Mech.*, 54, 627.

9. Gao, H. and Rice, J.R. (1986). *ASME J. Appl. Mech.*, 53, 774.

10. Gao, H. (1988). *Int. J. Solids Structures*, 24, 177.

THE USE OF A WATER-BASED EPOXY RESIN COATING FOR STRENGTHENING GLASS

B. R. Whittle, J. D. Whittle, R. J. Hand and B. Ellis

Department of Engineering Materials, University of Sheffield, Sir Robert Hadfield Building, Mappin Street, Sheffield, S1 3JD, UK

ABSTRACT

A water-based emulsion consisting of an epoxy resin and a polyamidoamine hardener has been developed which is capable of strengthening soda-lime-silica glass containing artificially introduced flaws via a bridging mechanism. It is less effective on naturally occurring damage although significant increases in strength are observed. The epoxy resin coating has poor hydrolytic resistance resulting in rapid loss of strengthening unless a silane coupling agent is incorporated into the formulation whereupon ageing in humid environments for up to 64 days no longer affects the strength. X-ray photoelectron spectroscopy showed that accelerated ageing of the coating was accompanied by the diffusion of sodium from the substrate through polymer layer to the surface. It was also demonstrated that polymer undergoes some degradation. The presence of the coupling agent did not significantly influence these effects. The coupling agent therefore, provides hydrolytically stable linkages between the glass and the resin but does not alter the durability of the resin network nor does it prevent sodium extraction from the underlying glass substrate.

KEYWORDS

Strengthening, glass, silane, epoxy resin, ageing, hydrolytic durability.

INTRODUCTION

Soda-lime-silica glass may be strengthened by the application of an epoxy resin coating. The coating infiltrates and bridges the flaws on the surface of an item and upon curing these flaws are healed to some extent, thus reducing the apparent severity of the damage [1]. Coatings consisting of only epoxy resin and hardener suffer from hydrolytic degradation of the interfacial bond between the resin and the substrate resulting in the loss of the strengthening effect. By incorporating a silane coupling agent however, the hydrolytic stability of the glass-polymer bond is improved. Hand *et al.* [2] have developed a system of bisphenol A epoxy resin and an amine hardener containing an aminosilane which exhibits exceptional resistance to hydrolytic degradation as well as an improvement in the initial strength of coated specimens. However, the system uses acetone as the solvent which is a significant disadvantage with respect to health and environmental regulations.

We have developed a similarly effective system consisting of an emulsion of epoxy resin in an aqueous solution of a polyamidoamine hardener. Using this formulation we have compared the hydrolytic ageing

characteristics of formulations of the coating with and without a silane addition which enables us to report some interesting observations concerning the influence of the silane on the ageing process.

EXPERIMENTAL PROCEDURE

Soda-lime-silica glass microscope slides (37 x 25 x 1.1 mm) were indented with a Vickers hardness testing machine with a 10 kg mass such that the diagonals of the impression were perpendicular to the longest edges of the specimen. Following indentation, the specimens were allowed to age for one week in laboratory conditions. This procedure results in a well characterised, reproducible system of cracks known as the median/radial and lateral cracks which measure approximately 1 mm in diameter [3,4].

Two coating formulations were used. The first formulation, coded EH, was prepared by mixing 5 g of a bisphenol A/F blend of epoxy resin (Ciba-Geigy PY 340-2) with 7.5 g of a polyamidoamine hardener (Ciba-Geigy HZ 340). 50 g of deionised water was then slowly added to create an emulsion and mixed for 10 minutes. The second formulation contained γ-glycidoxypropyltrimethoxy silane and was coded EHS. 0.8g of the silane was added to 50 g of deionised water and mixed for two hours. 4.4 g of the resin was mixed with 7.5 g of the hardener and then the water/silane solution was gradually incorporated and mixed for 10 minutes. The coating was applied to the samples by dipping and withdrawing at 1.2 mm s^{-1}. After drying at room temperature for 30-90 minutes, the samples were cured at 220°C in a fan-assisted oven.

After curing the samples were given an accelerated ageing treatment of 24 hours at 52°C in an atmosphere of 96 % relative humidity. This was achieved by suspending the samples above a saturated potassium sulphate solution inside a desiccator jar and placing the desiccator jar in an oven. Control samples were aged for 24 hours in laboratory conditions (roughly 22°C and 50 % r.h.). The strength of the samples was measured in four-point bending with the indent in tension on a Mayes SM 200 universal testing machine. A strip of adhesive tape was used to contain the fractured fragments. A stressing rate of approximately 35 MPa s^{-1} was used.

X-ray photoelectron spectroscopy (XPS) was performed with a VG Clam 2 X-ray photoelectron spectrometer using MgKα x-rays. Survey scans were taken at a pass energy of 100 eV and experimentally calculated sensitivity factors were used to determine the composition. Core level scans of the C1s region of the samples were performed at a pass energy of 20 eV and Gaussian-Lorenzian component peaks were fitted using Scientia software (Uppsala, Sweden) to estimate the distribution of carbon bonding environments.

Strips of soda-lime-silica float glass were used to test the effectiveness of the coating on naturally occurring edge flaws. The glass had been cut into strips measuring approximately 200 x 20 x 3.9 mm and the cutting process had been carefully controlled to ensure that one of the long sides of the strip contained damage typical of that which might be formed by the selvedge removal process. These samples were hand-dipped into a batch of the EHS coating formulation and cured in the manner described above. Ten indented samples were also coated in the same batch of coating to enable the performance of the coating on the natural flaws and artificially introduced flaws to be more rigorously compared. The float glass samples were fractured in four point bending with the spans at separations of 100 mm and 160 mm and at a loading rate of approximately 35 MPa s^{-1}. Adhesive tape was used to contain the resulting fragments.

RESULTS AND DISCUSSION

Figure 1 shows that the EH and EHS coatings dramatically improve the strength of indented samples. The EH coating improves the strength by 160 % and the EHS coating by 130 %. There is a certain amount of variability between different batches of nominally the same formulation. Improvements in strength of more than 210 % have been noted with EH formulations prepared on several different occasions. It is an encouraging strengthening effect but investigations have previously shown that silane-containing systems should be stronger than systems consisting of epoxy resin and hardener alone [5,6]. The present results do not concur with these investigations but this may be explained by considering the locus of failure within the

resin layer. Previous investigations have demonstrated that the failure of epoxy/substrate bonds occurs at the interface. Examination of opposing fragments from the present investigation shows a complimentary morphology indicative of the failure path being within the resin layer itself. Therefore the silane coupling agent, which strengthens the interfacial bond, would not be expected to increase the strength beyond the level of the EH samples.
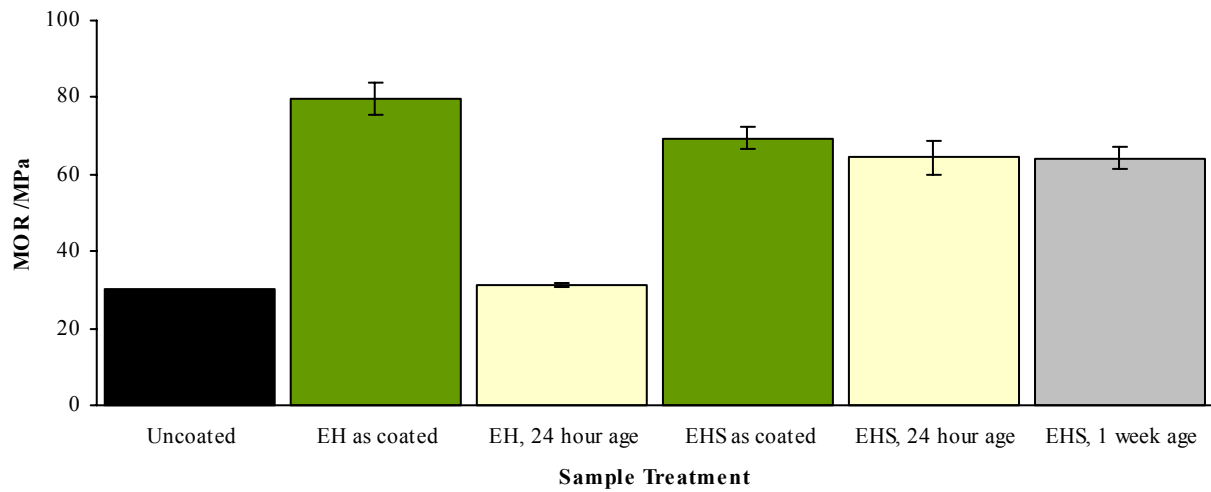
Figure 1 : Effect of accelerated ageing on the strength of EH and EHS coatings

Although impressive improvements were made to the strength of indented samples, float glass samples containing natural damage were not so effectively improved. Figure 2 illustrates that whereas the strength of artificially flawed specimens was improved by around 170 % from 30 MPa to 81 MPa, the strength of the float glass strips with the scoring damage were improved by only 41 % from 50 to 71 MPa. Kingston and Hand [7] have demonstrated that epoxy resin coatings are more effective on certain types of flaw. The effectiveness of the coating could simply be a function of the flaw size. The coating has an ability to penetrate flaws only down to a certain width due to the physical size of the resin and hardener molecules therefore, a large flaw may be reinforced over a greater fraction of its length than a small flaw hence large flaws would be expected to be strengthened to a greater extent. Flaw size may not be the only factor affecting the effectiveness of the coating. A different flaw geometry could be responsible for impeding the ingress of the emulsion, or the loading mechanism could change the way that the stresses are applied through the coating leading to premature failure.
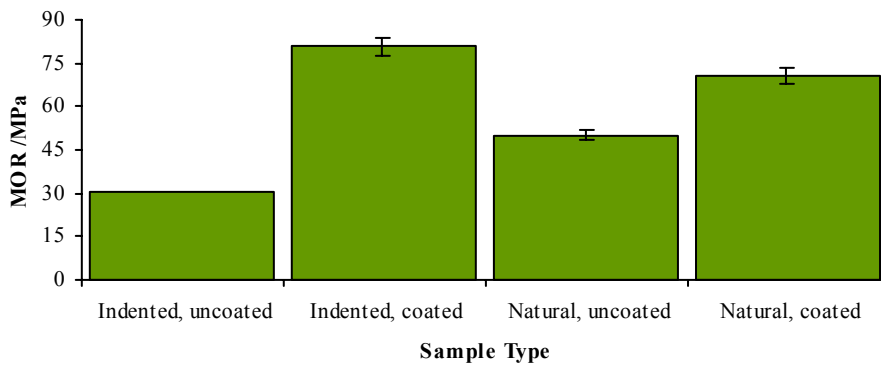
Figure 2 : Comparison of the effect of an EHS coating on artificial and naturally arising flaws

With any strengthening treatment it is hoped that when it is applied to a population of samples, the low-strength tail is eliminated. Since the coating is more effective in strengthening large flaws than small flaws it might be expected that by coating the specimens the distribution of strengths is reduced but unfortunately this is not the case. At this stage of development ensuring perfect and uniform penetration of the coating into all the flaws has not been achieved. Consequently the Weibull modulus of a set of coated specimens is reduced compared to the Weibull modulus of the uncoated specimens. The Weibull modulus of the indented

specimens typically falls from around 25 (the exceedingly high value for a brittle material being testament to the reproducibility of the median/radial crack system produced by indentation) to 7.3 ± 0.5. For natural flaws there is no change and the Weibull modulus remains at 4.3 ± 0.1.

Whereas prior to ageing the performance and behaviour of the EH and EHS coatings is similar, after accelerated ageing the behaviour of the coatings diverge. Figure 1 shows that the accelerated ageing treatment entirely negates the effect of the EH coating yet the EHS coating retains most of its strengthening characteristics. A further experiment showed that after a period of 64 days at 52°C and 96 % r.h. a different batch of EHS specimens retained a 200 % improvement in strength. Examination revealed that the EH coating had failed interfacially whereas the EHS coating retained the cohesive failure pattern observed in the unaged samples. The silane at the interface changes the bonding mechanism between the glass substrate and the polymer. Epoxy resin/amine hardener systems bond to glass via hydrogen bonding between amine groups on the hardener and hydroxyl groups on the substrate. These bonds are susceptible to hydrolytic degradation [8]. The bonding of polymers via silanes is more complex and involves the condensation of surface Si-OH groups with Si-OH groups on the silane molecules [9]. The resulting Si-O-Si linkages are non-polar and therefore hydrolytically more stable.
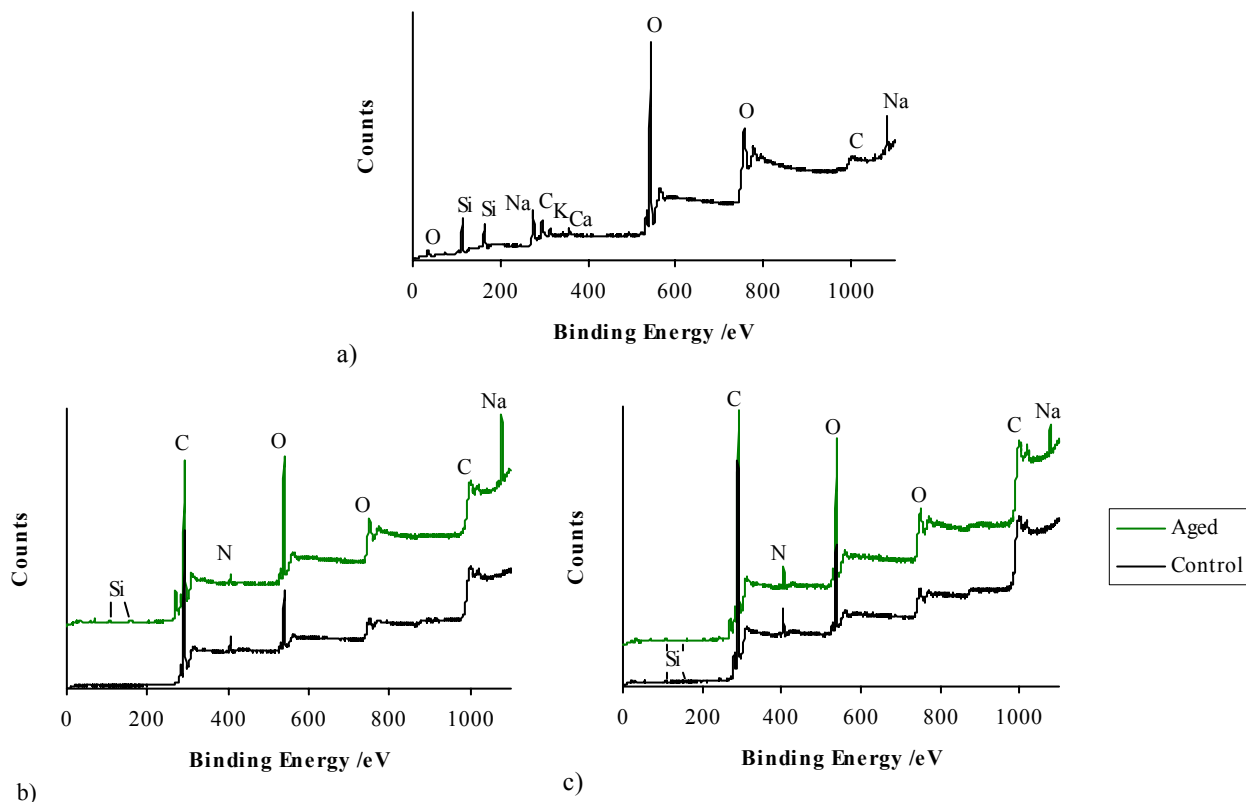
Figure 3 : Survey scans of a) uncoated glass, b) EH coating and c) EHS coating

XPS revealed that even though the silane addition had inhibited the effect of humidity on the strength of the coated specimens, reactions were still taking place within the bulk of the resin. Figure 3 shows the survey scans from EH and EHS coatings after 24 hours of laboratory ageing and accelerated ageing. Comparing the data for the unaged coatings to the data for uncoated glass it is clear that a coherent layer has been deposited on the glass since there is no signal corresponding to calcium, potassium or sodium.

The ageing treatment has affected both the EH and EHS coatings. Most apparent is that sodium is now detectable at the surface. Table 1 displays the chemical composition of the EH and EHS surfaces. It shows that there is more sodium than silicon detectable at the surface of the aged specimens. This indicates that the sodium signal is not due to pinholes in the coating since if this were the case then the silicon signal would be stronger than the sodium signal. The sodium must have been extracted from the underlying substrate since it

is well known that hydroxonium ions can exchange with sodium ions. It therefore may be stated that neither the EH or the EHS coating can completely protect the underlying substrate from water vapour.

Naturally both the unaged and the aged EHS samples contain a small amount of silicon, however it is interesting to note the appearance of silicon on the EH sample following ageing. This is an indication that there has been some dissolution and diffusion of silicon through the epoxy layer. Since there is essentially no change in the silicon concentration of the EHS coatings this dissolution process must be specific to the EH coating system. It is tentatively speculated that as the interface of the EH coating is hydrolysed, the liberated amine groups increase the local pH to a level where silica dissolution may take place. Since the EHS interface remains intact during the ageing process the pH remains unchanged and silica dissolution does not take place.

TABLE 1
COMPOSITION OF EH AND EHS COATINGS DETERMINED BY XPS

Specimen	Composition, atomic %				
	C	O	N	Na	Si
EH	80.5	14.0	5.5	0	0
EH, aged	72.8	20.8	2.2	3.3	0.9
EHS	81.2	12.6	5.8	0	0.3
EHS, aged	77.4	17.5	3.7	0.9	0.5

Narrowscans of the C1s regions of the samples can be used to show how the ageing treatment alters the nature of the carbon bonding in the coatings. Figure 4 shows the C1s narrowscans of the EH and EHS coatings before and after ageing. The unaged EH and EHS spectra are very similar, which is to be expected since the silane only contains carbon in epoxide groups exactly the same as those on the epoxy resin molecules.
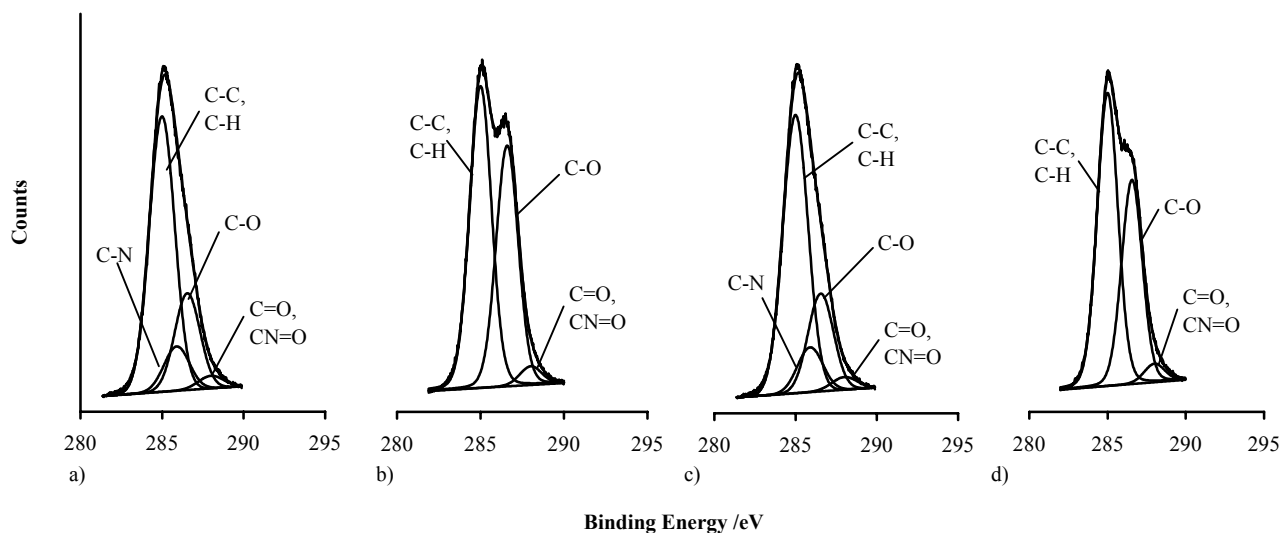
Figure 4 : C1s core level scans of a) EH sample, laboratory aged b) EH sample, accelerated aged c) EHS sample, laboratory aged d) EHS sample, accelerated aged

After the accelerated ageing treatment the C1s signals of both the EH and EHS samples exhibit a change which may be attributed to an increase in the proportion of C-O bonds surely corresponding to an increase in the population of C-OH groups. Note also that Figure 3 and Table 1 indicate an increase in the concentration of oxygen from chemisorbed water. The C-OH groups are the probably the result of

hydrolysis reactions of secondary and tertiary amine crosslinking sites, a theory also proposed by Xiao *et al.* [10]. An intriguing point to note is that even though the EHS coating has apparently degraded in the same way as the EH coating, the strength is maintained. This suggests that the resin on the EH samples retains most of its strength and it is only the interfacial bonds which lose integrity due to ageing.

CONCLUSIONS

It has been shown that on large Vickers indent flaws improvements in strength of around 200 % are achievable by using epoxy resin coatings. Promising increases in the strength of naturally occurring flaws have also been demonstrated and it is believed that by improving the application method further improvements will be made. The disadvantage of poor hydrolytic durability leading to a reduction of strength was overcome with the addition of a silane coupling agent. With such an addition periods of accelerated ageing of up to two months did not result in a loss of strength. The silane addition does not curtail all the effects of ageing in humid conditions however. The evidence presented showed that water still interacts with the glass substrate resulting in the extraction of sodium ions. XPS also showed that the cured resin network is affected by the humidity. Secondary and tertiary amine crosslinking sites suffer from hydrolytic scission resulting in an increase in the population of C-OH groups but curiously not a decrease in the strength of the coated specimens.

After ageing of EH coatings the failure path changes from the bulk of the resin to the interface between the resin and the glass. The failure of EHS coatings is always cohesive. Since in all other respects the ageing characteristics are the same it is concluded that the hydrolytic degradation only has a detrimental effect on the strength of the polar interfacial bonds of the EH coatings which are replaced with non-polar bonds by the addition of the silane. The function of the silane therefore, is not to render the epoxy resin network immune to hydrolysis or to protect the underlying substrate but to provide hydrolytically stable linkages between the inorganic substrate and the resin matrix.

REFERENCES

1. Wang, F.H., Hand, R.J., Ellis, B. and Seddon, A.B. (1995) *Physics and Chemistry of Glasses* 36, 201.
2. Hand, R.J., Wang, F.H., Ellis, B. and Seddon, A.B. (1998) *Journal of Sol-Gel Science and Technology* 13, 695.
3. Marshall, D.B., Lawn, B.R. and Evans, A.G. (1982) *Journal of the American Ceramic Society* 65, 561.
4. Lawn, B.R., Evans, A.G. and Marshall, D.B. (1980) *Journal of the American Ceramic Society* 63, 574.
5. Walker, P. (1991) *Surface and Interface Analysis* 17, 465.
6. Hand, R.J., Wang, F.H., Ellis, B. and Seddon, A.B. (1998) *Physics and Chemistry of Glasses* 39, 301.
7. Kingston, J.G.R. and Hand, R.J. (2000) *Physics and Chemistry of Glasses* 41, 1.
8. Clark-Monks, C. and Ellis, B. (1972) *Canadian Journal of Chemistry* 50, 907.
9. Erickson, P.W. and Plueddemann, E.P. (1974). In: *Interfaces in Polymer Matrix Composites,* pp. 1, Plueddemann, E. P. (Ed) Academic Press, New York.
10. Xiao, G.Z., Delamar, M. and Shanahan, M.E.R. (1997) *Journal of Applied Polymer Science* 65, 449.

Thermal cycle fatigue behavior on the dissimilar material joint

Y. Fukuzawa, S. Nagasawa, H. Takahashi and S. Hikotani

Department of Mechanical Engineering, Nagaoka University of Technology,
Kamitomioka, Nagaoka, 940-2188, Japan

Abstract

As many types of dissimilar material joint are fabricated in high temperature atmosphere, the tensile residual stress occurs around the interface during cooling procedure due to the difference of mechanical and physical properties between dissimilar materials. Various researches have been performed in order to relax the tensile residual stress and enhance the bonding strength on the bonded dissimilar materials. The interface shape is one of the most effective factor to obtain the high bonding strength. On the other hand, the interface strength decreases under the thermal cycle fatigue condition, due to the increasing of the residual stress for every thermal cycle. In this study, to obtain the long thermal fatigue life the interface shape effects on the bonding strength under thermal cycle fatigue condition was researched. Ceramics-metal joints that were machined to the proper interface shape by Electrical Discharge Machining Method were fabricated. The variations of bonding strength were estimated on the thermal cycle test practically. Also the analysis of the residual stress value and distribution around the interface was carried out with FEM. Comparing with results of the experimental and numerical analysis, suitable interface shape for dissimilar material joint under thermal cycle condition was discussed.

Keywords: Dissimilar joint, Interface shape, Interface strength, residual stress, thermal cycle fatigue, Electrical discharge machining

1. Introduction

When the ceramics-metal joint is fabricated by the diffusion bonding method at high temperature, the tensile residual stress is generated during the cooling process at the bonding interface, due to the difference of mechanical properties between dissimilar materials such as thermal expansion coefficients and Young's modulus. It reduces the bonding strength to the below of the interface strength. Therefore, it is important to estimate the residual thermal stress value and it's distribution by experimental and analytical method. The effects of interface shape for the bonding strength have been reported by FEM analysis and practical tensile tests[1-3]. Though joint was cooled under inhomogeneous temperature field in practice, many studies of the FEM analysis have been carried out in the uniform cooling conditions. On the inhomogeneous temperature it was assumed that the heat transfer occurred from exterior and osculating plane to inside of joint body. So sometime the experimental data did not coincide with the FEM analysis. It was also considered that the residual stress generation process would be much change on the

thermal cycle tests.

In this study, to clarify the effect of thermal cycle fatigue behavior on the bonding strength considering the interface shapes, FEM analysis and tensile tests were carried out.

2. Experimental

2-1 Specification of experiment

Sintered Si_3N_4 (ceramics) which is square plate (the side length: $2R_1=20$[mm] and, thickness: $Z_1= 7$[mm] and commercial pure Ni (metal) which is a cylindrical bar (Diameter: $2R_2=10$[mm], height: $Z_2= 23$[mm]) are bonded by diffusion method with Ag (59wt%)-Cu (27.25wt%)-In (12.5wt%)-Ti (1.25wt%) solder in the vacuum furnace. The initial thickness of brazing metal is 0.2[mm]. The bonding conditions are described in Table 1.

Table 1 Joint processing condition

Atmosphere / Torr	Vacuum ($<10^{-6}$)
Joining temperature / K	1123
Joining pressure / MPa	2
Pressing time / sec	600
Furnace heating / K sec^{-1}	0.144
Furnace cooling / K sec^{-1}	-0.1 (1123[K] 723[K]) -0.03 (723[K] 293[K]) [-0.077 (1123[K] 293[K])]

The designed profile of joint is shown in Fig.1. Various spherical interfaces were machined for the joints. The insulating ceramics of Si_3N_4 were machined by the electrical discharge machining (EDM) method, which was proposed and named "assisting electrode method" by authors[4] as shown in Fig.2. The Ni cylinder was machined by lathe machining and used for the electrode of EDM. The joint angle ö was defined as a geometrical angle between the tangential line at the interface edge and the outer surface of metal side. The joint angles $ö_1$ were chosen 33.6,51.2,60,71.8,90 [deg]. The bonding strength of each shapes were evaluated by the tensile test for the jointed material and after thermal cycle treatment at room temperature. The thermal cycle tests were carried out on the following conditions as shown in Fig. 3 and Table 2. The fracture surface profiles were observed by SEM and the fracture angles were measured by optical Microscope .
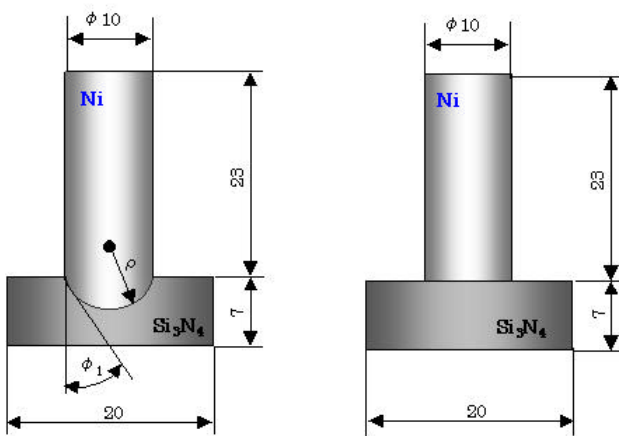
(a) Concave $ö_1$ 90.0[deg.]   (b) Flat $ö_1=90.0$[deg.]

Fig.1 Experimental Si_3N_4-Ni joint model
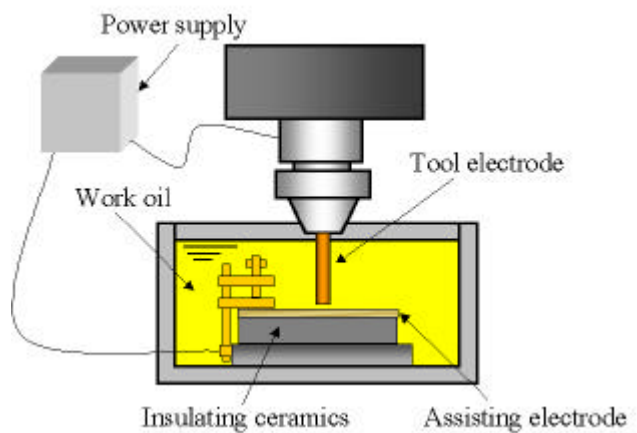
Fig.2 Schematic illustration of EDM method for insulating ceramics

Table 2 Thermal cycle conditions

Thermal cycle temperature / K	473,573,673
Atmosphere	Air
Inside furnace keep time / sec	300
Out of furnace keep time / sec	600
Thermal cycle number / cycle	1,5
Heating speed (293 573K) / K sec^{-1}	3.78
Cooling speed (573 293K) / K sec^{-1}	0.67
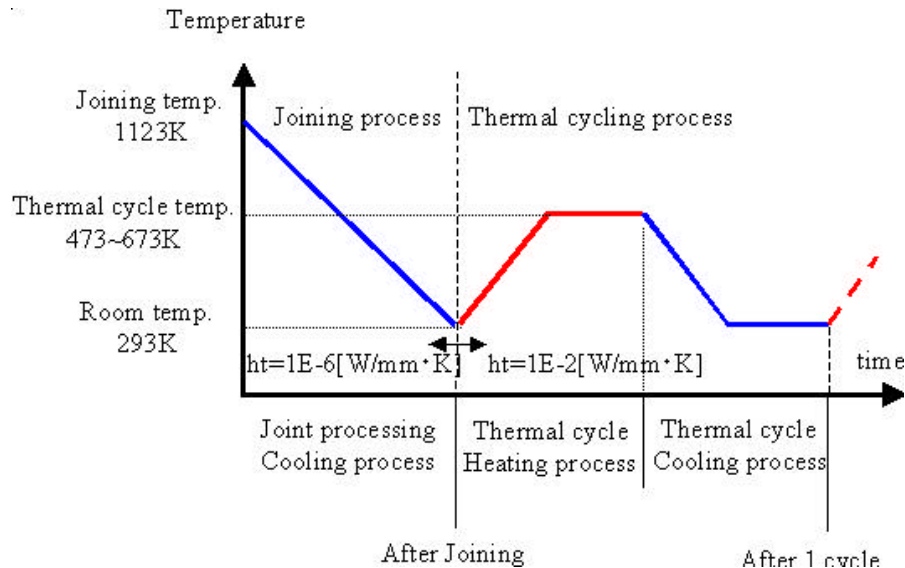
Fig.3 Thermal cycle fatigue diagram

2-2 Numerical analysis model

Si$_3$N$_4$-Ni joint model, which had various spherical shapes, was chosen for FEM analysis. The axisymmetric bonded half of two dissimilar materials were considered with the cylindrical coordinates (z,r). The joint angles ö were selected the same shapes of experimental specimens. A quadrilateral axisymmetric ring element was used in this model, and mesh size of element was highly refined at the edge of interface (number of all elements2304, the minimum subdivided ratio r/R=z/Z=0.001, subdivided ratio of two neighborhood elements: 0.7 as shown in Fig.4 The analysis was carried out on based on following assumptions. (1) Joining process of two isotropic materials was carried out perfectly at the bonding temperature 1123K. (2) The cooling process was carried out from the bonding to the room temperature under the inhomogeneous conditions. (3) Si$_3$N$_4$ was regarded as an elastic body. Ni was regarded as an elasto-plastic body. (4) All the displacement was geometrically considered as large and the strain was considered as finite strain.

Table 3 Mechanical properties of used materials

	Si$_3$N$_4$	Ni
Conductivity / J mm^{-1} sec^{-1} K^{-1}	0.029	0.088-0.0595
Density / 10$^{-6/}$ kg mm^3	3.20	8.90
Specific heat / J kg^{-1} K^{-1}	711.28	435.0-578.0
Young's modulus / GPa	274.59	206.0-107.0
Poisson's ratio / -	0.27	0.30
Thermal expansion / 10^{-6} K^{-1}	3.5	13.4-20.0
Yield strength /MPa	-	539.0-38.0
Coefficient of work-hardening / MPa	-	617.0-0.38
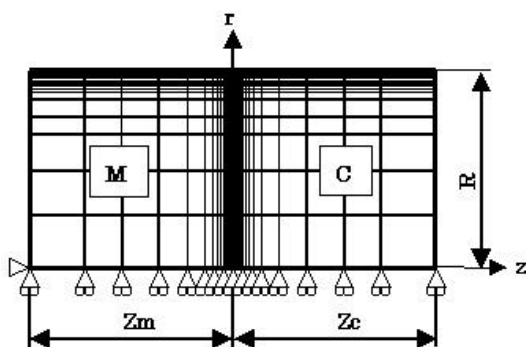
Fig. 4 Subdivided element model of bonded structure (ö1=ö2=90.0[deg.])

The mechanical properties of Ni depend on temperature. The mechanical properties of Si_3N_4 and Ni that were used for this analysis were shown in Table 3. The major discussion has been focused here on the σ_{zz} stress on the ceramics outer surface and interface.

3. Results and Discussions

Fig.5 shows experimental results of tensile strength for after joining treatment on each interface angle θ_1. The maximum bonding strength identified at near the interface angle of 51.8 [deg]. It indicated that the bonding strength depended to the interface angle. Fig.6 shows the typical fracture patterns of joint. The fracture occurred at the bonding interface and internal ceramic side except the interface angle 51.3[deg]. On the 51.3 [deg] the failure propagated to the direction of outer surface of ceramics. It had small interface area. The relation between the fracture and interface angles was shown in Fig.7. The bonding strength increased with decreasing the fracture angle except the angle of 33.8[deg]. It indicated that the bonding strength depended on the crack propagation direction. When the fracture occurred near the outer surface of ceramics, the maximum bonding strength was obtained. Fig.8 shows the relationship between the interface angle and bonding strength on each thermal cycle temperature and cycle numbers. The same relations between bonding strength and interface angle were obtained, but the bonding strength values decreased with increasing the thermal cycle temperature and cycle numbers. The fracture angles of the thermal cycle tests changed comparison with the "after joining body" as shown in Fig.9. On the thermal cycle tests, the fracture propagation angle of outer interface circle became flatter than the "after joining" and turned to spherical shapes at the inside of interface position. In order to compare with the results of bonding strength after thermal cycle treatment and FEM analysis, the distribution of σ_{zz} stresses on the interface ceramics surface was calculated. The results are shown in Fig.10 (a), "after joining", and (b) which is cycle temperature of 673 K and 5 cycles.
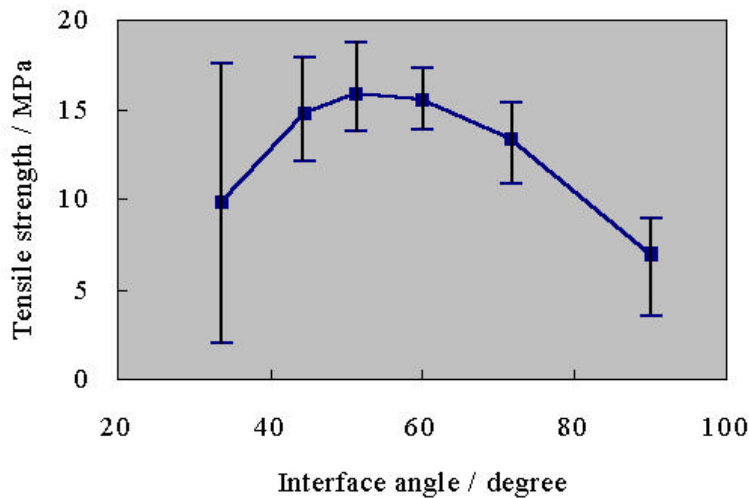
Fig. 5 Relation between interface and tensile strength

(a)33.6[deg.] (b)51.3[deg.] (c)60.0[deg.]

(d)71.8[deg.] (e)90.0[deg.]
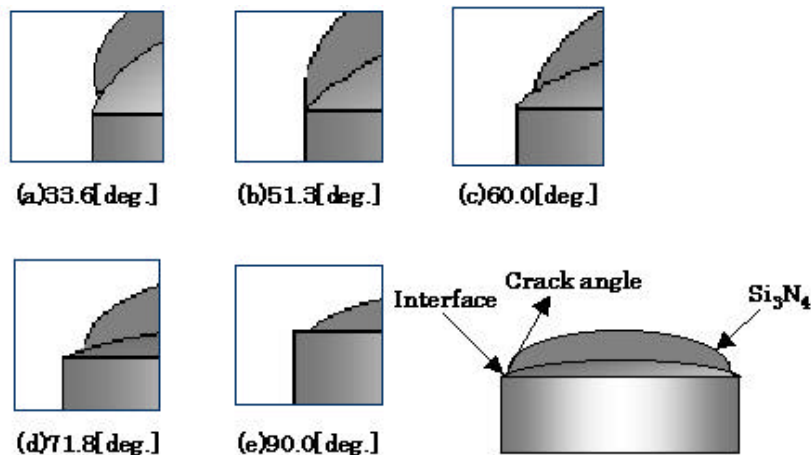
Fig.6 Schematic illustration of fracture surface models
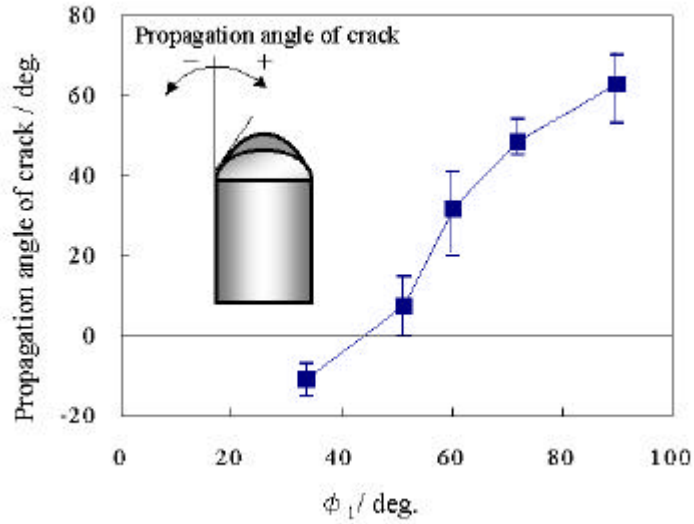
Fig.7 Relation between joint angle ϕ_1 and propagation angle of crack
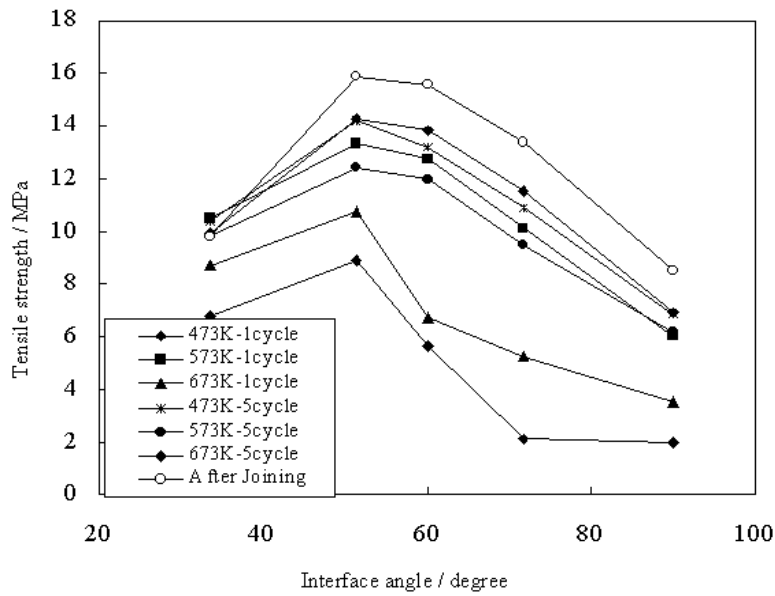
Fig.8 Relation between Interface angle and tensile strength

Fig.9 Fracture surface

(a) After joining   (b) After 5 cycle (673K)
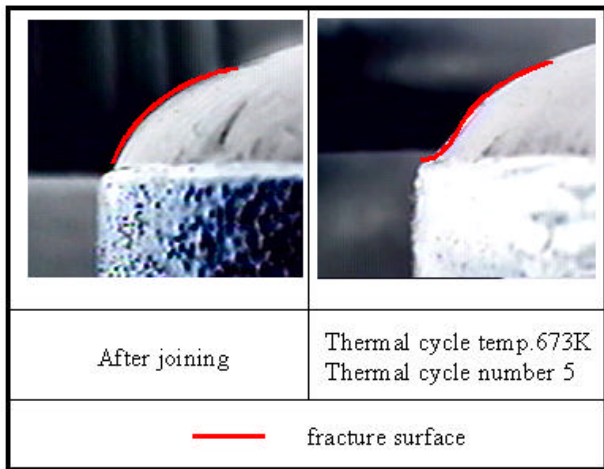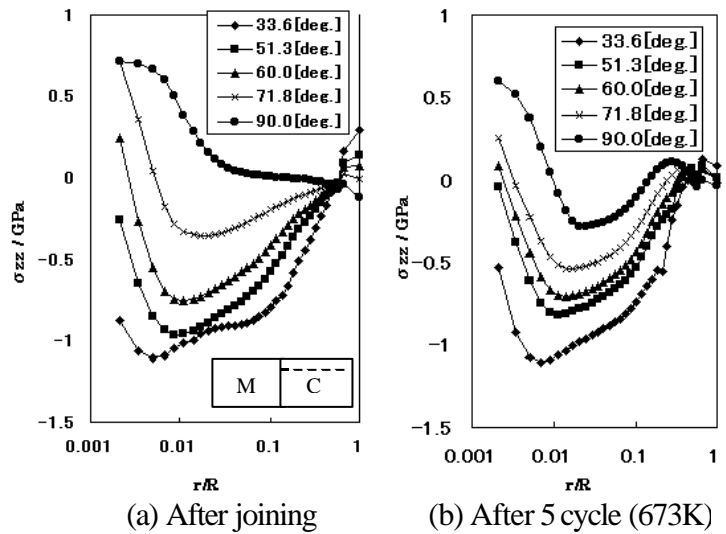
Fig.10 Effect of thermal cycle temperature of σ_{zz} of ceramics side interface
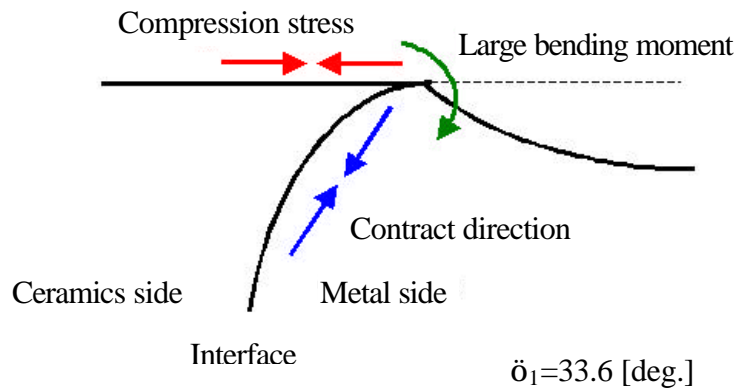
Fig.11 Mechanism of bending by metal contract

As reported before [5], the residual thermal stress values and distribution were varied with the cooling rate and volume of body that was evaluated from the heat transfer coefficient (ht), on the numerical analysis and joint volume. On the joint volume of this experiment, the uniformly cooling condition (furnace cool on the bonding treatment) was accomplished at the heat transfer coefficient value, $ht= 10^{-6}$[W mm^2 K^{-1}] , and $ht= 10^{-2}$[W mm^2 K^{-1}] corresponded to the cooling rate of thermal cycle test in which was inhomogeneous cooling condition. On the above FEM analysis the calculations were carried out with the above ht values for the bonding and thermal cycle treatments. The σ_{zz} distributed from the tensile to compressive region. When the tensile stress was applied, the distribution of σ_{zz} moved to tensile side[6]. In the $\sigma_{zz} - r/R$ curve below $0.1r/R$, the position of minimum σ_{zz} moved to compression side with reducing the interface angle and to the interface surface. The values increased with increasing the cycle temperature and numbers. The inclination of $\sigma_{zz} - r/R$ curve near the interface became large, it corresponded to the reducing bonding strength on the thermal cycle rests. The variations of fractured angle around the outer interface were also explained by the inclination. On the interface angle of 33.6[deg], the bending moment must be considered as shown in Fig.11. So the bonding strength decreased than the 51.8[deg] case.

4. Conclusions

The influence of interface angle for the bonding strength was investigated on the thermal cycle conditions by experimental test and FEM analysis. The following conclusions were obtained.

(1) The relations between the bonding strength and interface shape angle on the thermal cycle fatigue were similar to the after joining. The suitable interface angle for joining was detected on the thermal cycle test also. The bonding strengths decreased with increasing the cycle temperature and numbers.

(2) The fractured angles depended on the interface angle and the thermal cycle conditions.

(3) The fracture behaviors were explained with the FEM analysis, in which the inhomogeneous cooling process was considered.

References

1. S.Nagasawa,Y.Fukuzawa,Y.Yokoyama and M.Tateno,(2000)Adv. In Computational Eng.&Sci. Tech.Sci. Press, pp.1026-1030.

2. M.Tateno,Y.Fukuzawa,S.Nagasawa,H.Sakuta and Y.Kojima, (1993) Trans. Mat. Res. Soc.Jpn. Vol. 16B, pp.1101-1104.

3. Y.Fukuzawa,Y.Kojima,M.Tateno and N.Mohri,(1993) Trans. Mat. Res. Soc.Jpn. Vol. 16B, pp.1097-1100.

4. Y.Fukuzawa,N.Mohri and T.Tani,(1997) Int.J.of Electrical Machining,2,pp.25-30.

5. S.Nagasawa,Y.Fukuzawa, H.Takahashi,T.Yamada, H.Sakuta and M.Tateno,(1997) Joining ceramics, Glass and MetalDVS,120-123.

6. Y.Fukuzawa,S.Nagasawa,H.Takahashi,H.Sakuta,M.Tateno and Y.Kuboyama, (1996) Interface Science and Materials Interconnection Proc.of JIMIS-8 pp.463-466.

THERMAL FAILURE MECHANISM AND THRESHOLD OF SiC PARTICULATE REINFORCED METAL MATRIX COMPOSITES

Y. C. Zhou[1,2], S. G. Long[1], Z. P. Duan[2]

[1]Institute of Fundamental Mechanics and Material Engineering, Xiangtan University, Xiangtan, Hunan, 411105, China
[2]Laboratory for Laser and Dynamics Behaviors of Materials, Institute of Mechanics, CAS, Beijing, 100080, P. R. China

ABSTRACT

Thermal failure of Al/SiC composites induced by coupled loads of laser thermal shock and mechanical load is experimentally and theoretically studied. It is found that the initial crack is occurred in the notched-tip region, wherein the initial crack was induced by void nucleation, growth and subsequent coalescence in the matrix materials or separation of the interface. It is further found that the process of the crack propagation occurred by fracture of the SiC particulate. The damage threshold and completely failure threshold could be described with a plane of far-field load σ_{max} with laser beam energy density E_J. A simple theoretical model was proposed to explain the damage/failure mechanism and to calculate the damage threshold and completely failure threshold.

KEYWORDS

Thermal failure, Particulate-reinforced metal matrix composites, Laser beam, Damage and failure mechanism, Failure threshold

INTRODUCTION

Metal matrix composites (MMCs) are excellent candidates for structural components in the aerospace and automotive industries due to the high specific modulus, strength, and thermal stability [1]. However in aerospace and automotive industries the structural components are often subjected to sever thermal loads that may be produced by aerodynamic heating, by laser irradiation, or by localized intense fire [2-4]. At the same time, there are mechanical loads acting on the structural components. The concentration of thermal stresses around defects often results in catastrophic failure. The damage analysis for these structures exposed to intense thermal shock and mechanical load will be required for MMC design and reliability analysis. In the present paper, the thermal failure mechanism and failure threshold of particulate-reinforced metal matrix composites were experimentally and theoretically investigated.

EXPERIMENTAL METHOD

SiC particulate/6061 Al composite was chosen as a model MMC system for this study. The composites with

15 wt pct SiC were fabricated by melt casting route, and as-cast ingots of the composite were subsequently extruded. Thermal shock is generated by an incident laser beam, which impinges normally to a single-edge notched specimen. The energy E of the laser beam ranges from 1 to 40J, with a power intensity of the order of 1.0×10^4 to $18.0 \times 10^4 W/cm^2$. It is a single pulse Nd:glass laser with a wavelength of 1.06μm. Laser beam was pulsed Nd:glass laser with a wave length of 1.06μm and a full width at half of the maximum (FWHM) of 250μs. The single-edge notched specimen was radiated by laser beam and loaded by a static tensile machine. In this case, the thermal damage and fracture are induced by both laser thermal shock and far-field mechanical load. Figure 1 is a schematic of the specimen configuration and dimensions.
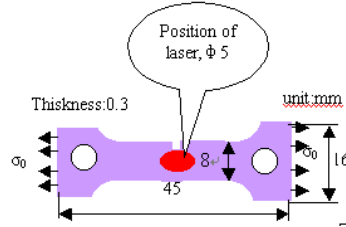
Figure 1: Schematic of the specimen configuration and dimensions

The shape of the notch is U-like. As well known, the maximum stress is located in notched tip with a coefficient of stresses concentration of α_σ=3.2 [3]. Therefore, the maximum stresses at the tip of the notch are $\sigma_{max} = \alpha_\sigma \sigma$. In experiment, the samples were subjected to the different coupled loads of mechanical load and laser shock intensity (σ_{max}, E_J).

EXPERIMENTAL RESULTS

Damage mechanism
When the intensity of the coupled loads (σ_{max}, E_J) were low (i.e. σ_{max} and E_J were lower than critical thresholds), there were not any visible damage and failure phenomenon. However, when the coupled loads were increased to critical thresholds, some visible damage phenomena could be observed by scanning electron microscopy. Figure 2 shows the typical SEM of damage characterization. Figure 2(a) is the micro-voids in the notched-tip region. It is observed that the voids occur in the form of interfacial debonding between the particles and the matrix and the micro-cracks occur in the matrix and interface. When the
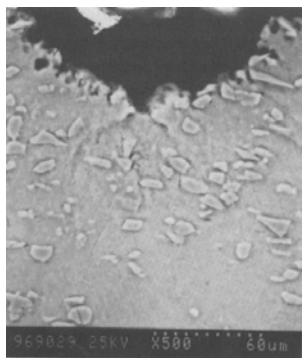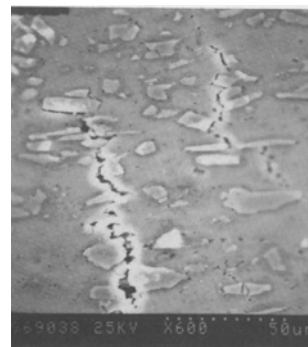
(a) (b)

Figure 2: Damage characterizations: (a) SEM of micro-voids in the notched-tip region, (b) radial cracking showing voids in matrix and the separation between SiC particle and matrix

reinforcement SiC particle is at the crack tip, the SiC particle does not fracture and resist the crack propagation. In order to understand the initial damage behavior of SiC particulate reinforced aluminum alloy matrix composite induced by laser beam thermal shock, the laser beam irradiated region was moved away from the notched-tip region. In this case, the radial crack appeared around the periphery of the laser beam as shown in figure 2(b). The radial crack occurred by the same mechanism as in figure 2(a). Therefore, one can conclude that the initial damage should be produced in the form of the separation of the SiC particle-matrix interface or in the form of void nucleation and growth within the matrix.

Crack propagation

When the thermal shock and mechanical loads were gradually increased, the damage became more and more serious. When the coupled loads (σ_{max}, E_J) were up to critical threshold, the micro-cracks formed in the notched region would grow into macroscopic cracks. The higher magnification SEM micrographs of macroscopic crack tip are shown in figure 3. As shown in the figure, the reinforcement SiC particle fracture is the dominant damage mechanism for macro-crack propagation. The reinforcements are broken by cracks perpendicular to the loading axis, and the fraction of broken reinforcements increases near the crack tip zone as shown in figure 3(b). Note that the SEM in figure 3 is distinct from the SEM in figure 2 for damage mechanism. It is very interesting that although the particles were broken near the macro-crack tip region, there was not damage in matrix and between the interfaces of matrix/particle.

(a)   (b)
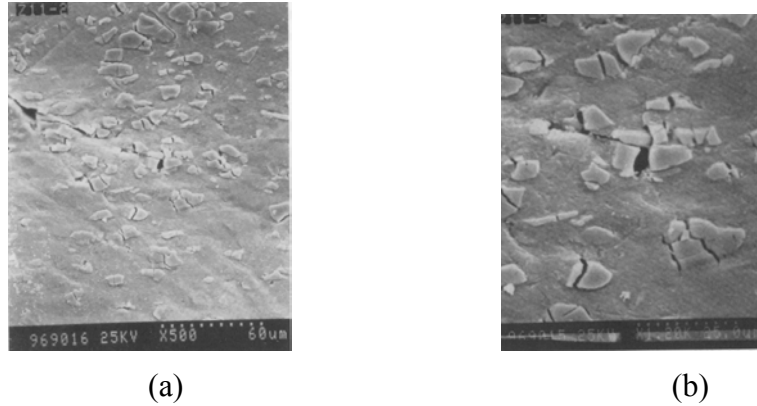
Figure 3: The failure characterizations in crack-tip: (a) macro-crack showing the cracked SiC particles, (b) phenomenon of SiC particles broken and no-damage of matrix in the crack-tip region
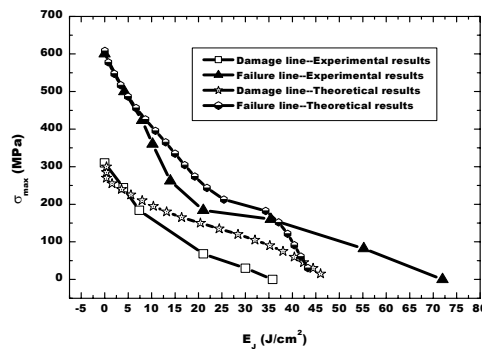
Figure 4: Damage and failure threshold plane

Damage and failure threshold

The damage threshold and completely failure threshold could be described with a plane of far-field load with laser beam energy density, i.e., a plane of σ_{max}-E_J. In the plane σ_{max} is the maximum stress at notched-tip and E_J is the energy density of incident laser beam. The damage occurred in two forms, which were matrix failure as in the form of voids, and particle/matrix interface de-cohesion. The damage threshold was defined as that one could observe voids in matrix or between matrix/particle interfaces for analyzing the SEM micrographs with 500 magnifications. The failure threshold was defined as that when the sample with single-notched was completely fractured. Figure 4 is the experimental results for the plane of σ_{max}-E_J. The damage threshold for mechanical load with no laser beam heating E_J is σ_{max}=300MPa. The complete failure threshold for mechanical load is σ_{max}=600MPa. According to the level of damage and failure, three regions are divided. They are non-damaged region, damaged region and failure region, respectively. The non-damage region is located on the down left of damage line. The damage region is on the region between damage line and failure line. The failure is located on the upper right of failure line. One can see that the contribution of far-field mechanical load and laser beam thermal load to the damage and failure of MMCs is non-linear. In other word,

their contributions are coupled. If the mechanical load is between damage thresholds σ_{max}^{Dth} and complete

failure thresholds σ_{max}^{Fth}, an additional thermal load with a little laser energy density will make the samples

completely failure. This region is called a laser beam sensitive region. On the other hand, when the laser energy density is high enough, additional little mechanical load also makes the samples completely failure.

DISCUSSIONS

Theoretical model
As previously described, the mechanism of initial damage was void formation in matrix and separation of SiC particle-matrix interface. However, the mechanism of crack propagation was dominated by SiC particle fracture. Why is there the difference between the damage mechanism and crack propagation. In this section, a simple theoretical model is proposed to explain the interesting experimental phenomenon and to predict the damage threshold and failure threshold. In the model, the temperature rise and thermal stress was first obtained. The stress-strain relation of MMC is assumed to follow the numerical results obtained by Brockenbrough and Zok[5].The secant Young's modulus E^c of MMC was defined by the ratio of tensile stress to the tensile strain,

$$E^c = \frac{E^m}{1 + \frac{3}{7}\left(\frac{\sigma^m}{\sigma_0^m}\right)^{\frac{1}{N}-1}}\left\{\bar{\rho}(\varepsilon)(1 - \gamma f - \xi f^2) + [1 - \bar{\rho}(\varepsilon)][1 + \bar{\alpha}\tan(3\pi f / 4) + \bar{\beta} f^3]\right\} \tag{1}$$

where the superscript m indicate matrix, σ^m and ε are the axial stress and strain of matrix, respectively; σ_0^m

is its yield stress; N is the hardening exponent, f is particle volume fraction, other variables are coefficients and they are given in [5].

It is well known that the reinforcement of a hard ceramic in a soft metallic matrix produces composites with substantially higher yield strength compared to that of the matrix. The idea of stress transfer for a hard elastic particulate with (E^p, ν^p) embedded in an infinite elastic matrix with (E^c, ν^c) is adopted in the model. The complete solution to this problem was given by Eshelby [6]. They found that then stress and strain fields inside the inclusion were uniform. For tensile loads the largest normal stress always occurs at the poles of the inclusion. The largest shear stress along the interface is always at 45 degrees off the tensile direction. The largest normal stress in the particle and largest shear stress along the interface can easily obtained. The above ideas can be easily explain the damage and failure mechanism, and predict the damage threshold.

In order to predict the failure threshold, the stress intensity for a single edge crack in a finite rectangular

plate should be calculated. The weight function method is used to calculate the stress intensity factor K_I as,

$$K_I = K_I^m + K_I^T \tag{2}$$

where K_I^m is the stress intensity factor induced by the far-field mechanical loading and it is given by the

following expression

$$K_I^m = F_I(\varsigma)\frac{\sigma_{max}}{\alpha_\sigma}\sqrt{\pi c} \tag{3}$$

Here c is the crack length, $\varsigma = c / w$ and w is the width of the sample, the coefficient $F_I(\varsigma)$ was given in [7].

One can obtain the thermal stress intensity factor K_I^T by using Wu's weight function as,

$$K_I^T = \Phi \sigma_0 \sqrt{\pi c} \tag{4}$$

with $\sigma_0 = \frac{1}{2}\alpha E^c \vartheta$ and $\Phi = \frac{1}{\sqrt{2\pi\beta_0(\varsigma)}} \frac{1}{\varsigma} H(\varsigma)$. In the equation, α is thermal expansion coefficient of MMC,

ϑ is temperature rise induced by laser beam thermal shock. The coefficient $\beta_0(\varsigma)$ is given in [8] and the

coefficient $H(\varsigma)$ can easily obtained by integrating Wu's weight function [8] and thermal stress. The stress

intensity factors can be used to predict the completely failure threshold.

Damage mechanism
For a pair of (σ_{max}, E_J), we can obtain the largest shear stress along the interface which is shown in figure 5. The laser beam thermal shock will make the yield strength and tensile strength of matrix degrade at high temperature. It is assumed that the degradation of the reinforcement is negligible and the strength of reinforcement/matrix and the strength of matrix is the same. The interface strength is also shown in the figure.
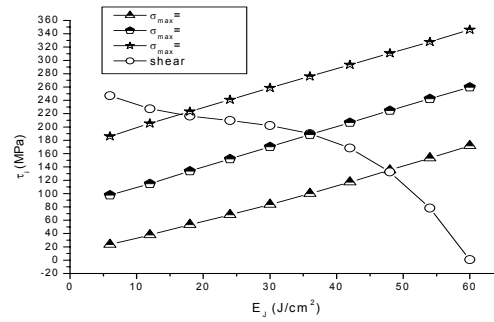
Figure 5: Largest shear stress along interface as a function of E_J for different σ_{max}

It is easily seen that the interfacial shear stresses τ_i may be larger than the tensile strengths of matrix when the coupled loads (σ_{max}, E_J) are more than the thresholds. However, the largest normal stress in particle is lower than the strength of reinforcement SiC particle. The results explain that the initial crack is produced by the mechanism of void formation in the matrix and separation of void formation in the matrix and the reinforcement particles do not fracture. When the MMC is subjected to laser beam heating, the strength of the matrix will be degraded at elevated temperature. In other words, the matrix yield strength decreases. In this case, the particle loading through the interface is so low that the SiC particle cracking does not take place. But the localized thermal stresses due to the rapid changes in temperature may lead to the nucleation of micro-cracks within the matrix/reinforcing phase interface or in the matrix. More commonly, however, these thermal stresses lead to the growth of pre-existing cracks. If the applied stress is sufficiently large, these micro-cracks may grow into macroscopic cracks and lead to the propagation of the macro-crack.

Crack propagation mechanism
When the micro-cracks are formed in the notched region they may grow into macro-crack. As well known, the strain rate at the crack tip is very high in the case of macro-crack propagation. It was found that the strain rate at crack tip is approximately $2.0\sim3.0\times10^3$/s. As a result of the high strain rates or the matrix hardening, the matrix yield stress increases significantly. Equivalently, the axial tensile stresses in reinforcement are so high that the stress intensity factor may exceed the SiC particle strength, i.e., the Griffith criterion.

Damage and failure thresholds
The damage threshold is determined by the criterion that the largest shear stress is high than the interface

strength. For a pair of (σ_{max}, E_J), we can obtain the largest shear stress along the interface. In this case, the damage threshold can easily determined and the results are shown in figure 4. For a pair of (σ_{max}, E_J), we can obtain the stress intensity factor K_I and energy release rate G_I. When the following condition is satisfied the crack will propagate Δc

$$K_I \geq K_{IC} \text{ or } G_I \geq G_{IC} \text{ and } \frac{\partial G_I}{\partial c} \geq \frac{\partial G_{IC}}{\partial c} \tag{5}$$

where the fracture toughness K_{IC} and crack-growth resistance G_{IC} of MMC at high temperature are taken from the [9]. In this case, the failure threshold can be determined and the results are shown in figure 4.

One can see that the theoretical results for both damage threshold and failure threshold are close their experimental results when the laser energy density E_J is low. When the laser energy density E_J is higher and higher, the difference of theoretical results and experimental results become larger and larger. It may be due to the neglect of visco-plastic deformation for MMC at high temperature. One can see the non-linear coupled effect of far-field mechanical load with laser beam thermal load on the MMC failure from the plane of $\sigma_{max} - E_J$.

CONCLUSIONS

The failure of particulate-reinforced metal matrix composites induced by laser beam thermal shock is experimentally and theoretically studied. It is found that the initial crack is occurred in the notched-tip region, wherein the initial crack was induced by void nucleation, growth and subsequent coalescence in the matrix materials or separation of the interface. However, the process of the crack propagation occurred by fracture of the SiC particulate and it is very different from the crack initiation mechanism. The damage threshold and completely failure threshold could be described with a plane of far-field load σ_{max} with laser beam energy density E_J. A simple theoretical model was proposed to explain the damage/failure mechanism and to calculate the damage threshold and completely failure threshold. The model is based on the idea of stress transfer between reinforced-particle and matrix, and the calculation of far-field mechanical stress intensity factor and local thermal stress intensity factor. The theoretical model can explain the experimental phenomenon and predict the damage threshold and failure threshold. The failure of MMC induced by laser thermal shock and far-field mechanical load is non-linear coupled.

REFERENCES

1. Llorca, J. (2001) *Progress in Materials Science*, (in press)
2. Zhou, Y.C. and Duan, Z.P (1998) *Metall. Mater. Trans. A*, 29, 685.
3. Zhou, Y.C. and Long, S.G. (2001) *Trans ASME J. Engng. Materials & Tech.* 123, (in press)
4. Zhou, Y. C., Zhu, Z. M., Duan, Z. P. and Yang, Q. B. (1999). In: *IUTAM Symposium on Rheology of Bodies with Defects*, pp. 121-132, Wang, R. (Eds), Kluwer Academic Publishers
5. Brockenbrough J. R. And Zok, F. W. (1995) *Acta Metall. Mater.* 43, 11.
6. Eshelby, J. D. (1959) *Proc. R. Soc.* 252, 561.
7. Tada, H., Paris, P. and Irwin, G. (1973) *The Stress Analysis of Cracks Handbook*, Del. Research Corp. Hellertown, Pennsylvania, pp.2.10-2.11
8. Wu, X. R. (1984) *Engng. Fract. Mech.* 20, 35.
9. Somerday, B. P., Leng, Y. and Gangloff, R. P. (1995) *Fatigue Fract. Engng. Mater. Struct.*18, 565.

THERMAL FAILURE OF THERMAL BARRIER CERAMIC COATING

Y. C. Zhou[1,2], T. Hashida[1]

[1]Fracture Research Institute, Tohoku University, Sendai, 980-8579, Japan
[2]Institute of Fundamental Mechanics and Material Engineering, Xiangtan University, Xiangtan, Hunan, 411105, China

ABSTRACT

The paper presents the experimental investigation on the fracture of thermal barrier ceramic coating (TBC) at high temperature. The fracture was induced by temperature gradient along TBC system thickness direction and oxidation between TBC and bond coat. Laser heating method was used to simulate the operating state of TBC system. Micro-observation and acoustic emission (AE) detect both revealed that fatigue crack was in two forms: surface crack and interface delamination. One can understand the failure mechanism from the plane of TBC surface temperature and substrate surface temperature. It was found that the life of thermal fatigue was reduced by the formation of alumina at interface. On the other hand, it was found that the temperature gradient between inner and outer surface of specimen accelerates the growth of alumina layer.

KEYWORDS

Thermal barrier ceramic coating, thermal fracture, temperature gradient, oxidation

INTRODUCTION

A thermal barrier ceramic coating (TBC) provides performance, efficiency, and durability benefits by reducing turbine cooling air requirements and lowering metal temperatures. The study of TBC is to develop a technology to protect alloy and make it to operate at 1500^0C and to realize 50% of thermal efficiency. Previous work has demonstrated that there are some important effects on TBC system operating life. The first effect is thermal fatigue [1,2]. High temperature heating and low or fast cooling must induce thermal stress loading and unloading for many cycles. The second effect is thermal growth oxidation (TGO) between bond coat and thermal barrier ceramic coating[3,4]. Generally, the composition of TGO is brittle ceramic, such as alumina (Al_2O_3). The cycles of high temperature loading and unloading not only make TGO to thicken but also make micro-voids and micro-cracks formation in TGO. On the other hand, the degradation of TGO may induce the spallation or delamination of thermal barrier ceramic coatings. The third is the surface roughness of bond coat[5,6]. The effect makes the formation of tensile stress at the peaks of interface undulation or compress stress at the valleys of interface undulation at cooling stage. The fourth is oxygen and sulfur penetration along grain boundaries[7]. Their effect causes the thermal barrier ceramic coatings to thin and consequence the function of TBC is weakened. However, in the real TBC system, the temperature gradient along TBC system thickness direction and TGO between bond coat and ceramic coating are the key factor of TBC system service life[8-10]. In this paper, the failure characteristics of TBC at high temperature induced by temperature gradient and TGO were investigated.

MATETIALS AND EXPERIMENTAL METHOD

Heating Method

In order to study the above-mentioned effects, one needs to design an experimental method to simulate the operating state which has the temperature gradient in the TBC system thickness direction, many cycles of heating/cooling. The simulating system was laser heat method in which heating of specimen surface was accomplished using a continuous CO_2 laser of 10.6μm output wavelength. The unit was nominally specified as a 50W laser. The system was arranged so that the coated specimens could be exposed to a laser beam with a preset size (such as 8mm or 6mm in diameter), duration and intensity. The specimen was internally gas-cooled to achieve various temperature drops within the coating layer. The computer-controlled system shown in Figure 1 allowed heating/cooling processes to be automatically cycled.

The temperatures on ceramic coating surface and on substrate surface were monitored by means of a general infrared radiation pyrometer and thermocouple, respectively. Concurrently with the heating tests, acoustic emission (AE) monitoring was performed to detect the micro-fracture process of the coating materials. The disposition of the two or three transducers enabled the determination of the linear location of the AE sources emitted from the sample. Furthermore, AE signal analysis can be used to provide a way to predict the long term behavior of the TBC under thermal-cycling conditions. AE signals were detected using a broad band piezoelectric transducer with a resonant frequency close to 1MHz. The square of signal peak voltage was used as a measure of AE energy. Impedance spectroscopy (IS) was used to evaluate the formation kinetics and physical properties of the reaction layer between bond coat and ceramic coating. In the evaluations of TBCs degradation, the IS method was developed to detect various defects such as delamination, spallation and cracks and other damages.
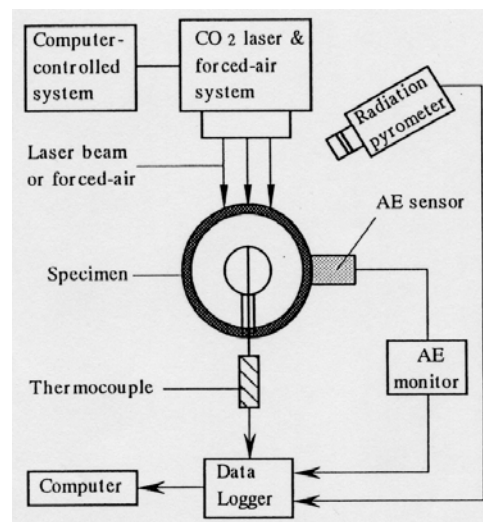
Figure 1: Schematic of the experimental setup for CO_2 laser heating method

Materials and Specimens
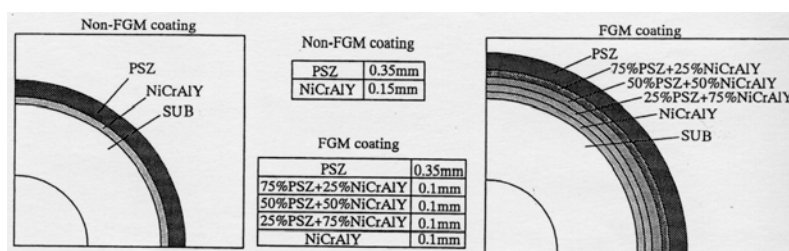
Figure 2: Schematics of the cross-sections of two types of coatings.

Two types of materials samples were prepared. One was conventional coating (non-FGM) which was a two-layer coating system consisting of PSZ layer (partially stabilized ZrO_2 by 8 wt%Y_2O_3) over a NiCrAlY bond coat. The coatings were air-plasma-sprayed onto a substrate. The material of the substrate was cylindrical Ni base superalloy which simulated radius of leading edge for gas turbine blade. Recently,

multi-layer coating system, in particular, the functionally graded material (FGM) coating system has been proposed. The FGM coating was a five-layer coating system of PSZ and NiCrAlY, and the composition was designed to have the same thermal shielding performance as that of the non-FGM coating. Figure 2 shows the schematics of the cross-sections of non-FGM and FGM coatings.

EXPERIMENTAL RESULTS AND DISCUSSIONS

Crack characteristics

SEM (scanning electron microscope) observations indicated that laser heating produced two types of coating damage: vertical (or surface) cracking and interface delamination both in non-FGM and FGM coatings. The vertical cracking and interface delamination for non-FGM and FGM coatings exposed to laser heating are shown in Figure 3. SEM examination of the specimens' cross-sections showed that the delamination cracks in non-FGM coating always occurred just above the interface between bond coat NiCrAlY layer and PSZ layer. On the other hand, one can see that the interface crack kinks out the main crack as shown in the figure. However, the delamination cracks in FGM coating always occurred close to two interfaces: the interface between PSZ layer and 75%PSZ/25%NiCrAlY layer, and between 75%PSZ/25%NiCrAlY layer and 50%PSZ/50NiCrAlY layer. The final complete failure was spallation due to the interface delamination growth.

(a)

(b)
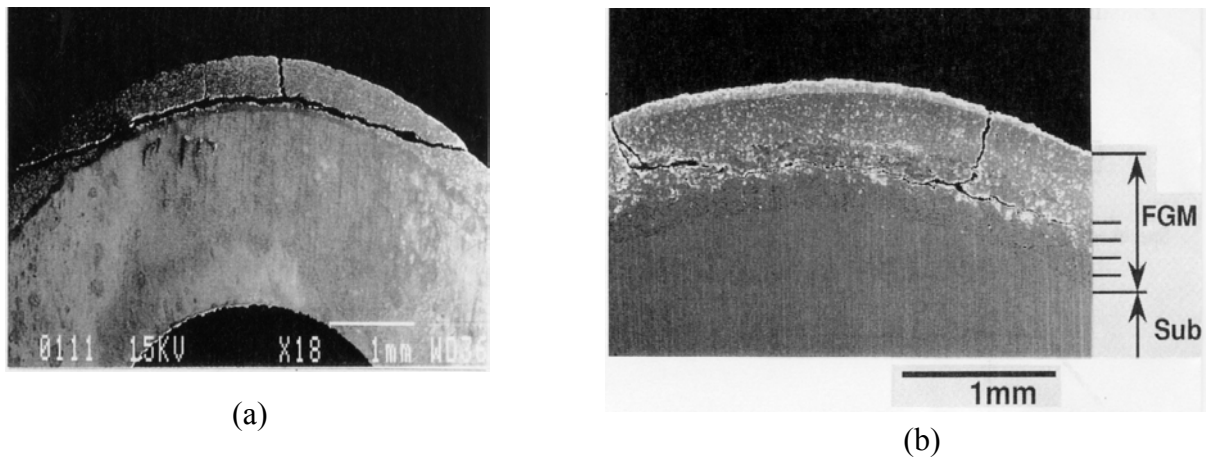
Figure 3. SEM micrographs showing vertical cracking and interface delamination cracking: (a) non-FGM coating subjected to 6 thermal fatigue cycles, where the exposed time for every cycle was 70s and the highest temperature on coating and substrate was 1200^0C and 600^0C, respectively. (b) FGM coating subjected to 10 thermal fatigue cycles, where laser power was 34W.

(a)

(b)
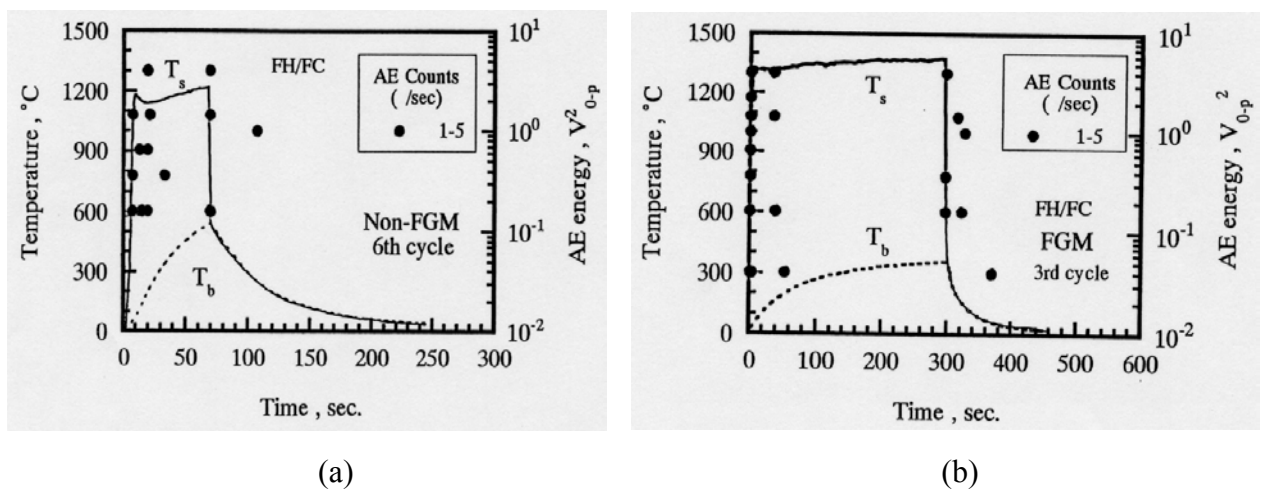
Figure 4: Temperature histories and AE activity in non-FGM and FGM coating during laser heating: (a) non-FGM coating subjected to 6 thermal fatigue cycles, where the exposed time for every cycle was 70s and the highest temperature on coating and substrate was 1200^0C and 600^0C, respectively. (b) FGM coating subjected to 3 thermal fatigue cycles.

Temperature histories and AE monitoring results in the laser thermal fatigue tests were also obtained as shown in Figure 4. It was found that AE signals were recorded most often in the periods of heating or cooling. AE signals were recorded even on the later stage of cooling, i.e., the temperature gradient was zero. The comparison of AE behavior and SEM observation indicated that first AE signal detected corresponds to the vertical cracking. The high energy of AE signals after the first AE signal recorded was associated with interface delamination cracking growth. This means that vertical (or surface) crack can more easily take place than interface delamination cracking. On the other hand, no delamination growth was observed for FGM coating within the tested temperature range where non-FGM coating showed extensive delamination.

Fracture mechanism map

One finds that temperature drop through specimen thickness is an important parameter to analyze failure mechanism such as vertical crack and interface delamination crack. The observed damage modes correlated with temperature conditions, T_s-T_b are shown in Figure 5, where T_s and T_b are, respectively the temperature on the surface of coating and substrate. In the figures, the temperature is maximum values recorded during a heating-cooling cycle. Experimental data for uniform heating are also included, which were obtained from furnace heating-cooling tests. It is convenient to use the T_s-T_b plane to study the failure threshold of TBC system. The physical concept is also clear and the optimum state for temperature range of advanced gas turbine can also be obtained on the T_s-T_b plane. In the plane, one can distinguish three regions which are no crack region, vertical crack region and delamination region. From the T_s-T_b plane, one can have the conclusion that FGM coating has much higher thermal fatigue resistance compared to non-FGM coating system through thermal cycling tests conducted under the simulated advanced gas turbine blade conditions.
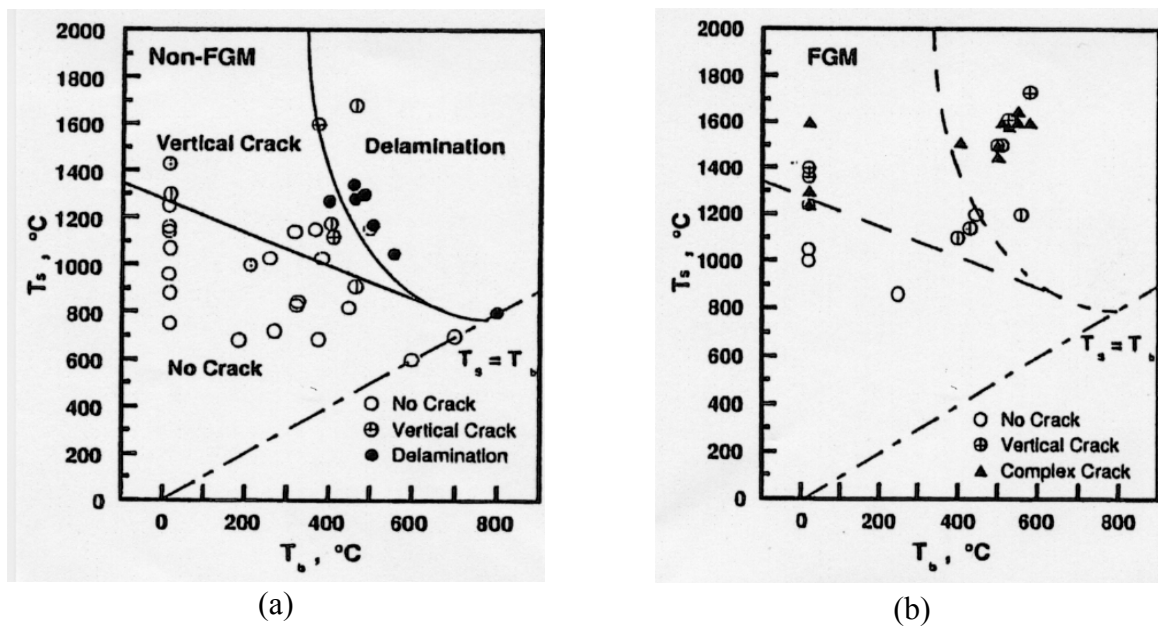
Figure 5: Fracture mechanism map in the T_s-T_b plane, (a) non-FGM coating, (b) FGM coating.

Interface crack

From the AE characteristics of coating failure process it is possible to correlate the sum of AE energy recorded during heating and cooling process with the total length of delamination crack. The correlation is shown in Figure 6(a) and (b) for non-FGM coating and FGM coating, respectively. The total length of the delamination cracks for FGM coating shown in Figure 6(b) is the sum of the length of the delamination cracks at two interfaces as described in the above. It is seen that there is a general correspondence between AE energy and delamination length for two coating systems. For non-FGM coating, the correlation is approximately linear, although considerable experimental scatter is observed. In contrast, the correlation is nonlinear for FGM coating. The data both in Figure 6(a) and (b) are different from each other in different heating or cooling rate and cycle number.
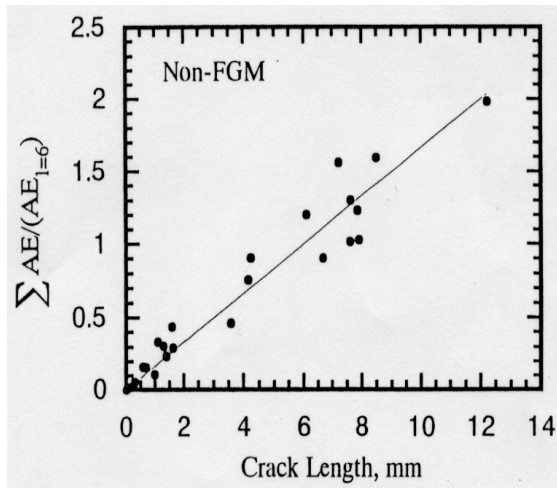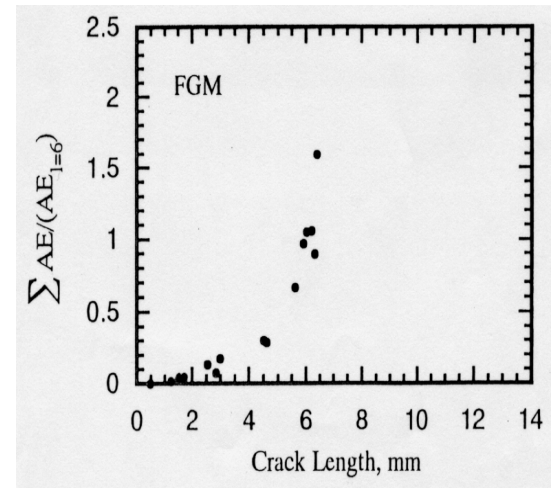
(a) Non-FGM   (b) FGM

Figure 6: Total energy of AE versus total length of delamination, (a) non-FGM coating, (b) FGM coating.

Influence of oxidation on the thermal fatigue failure

In order to understand the effect of TGO on the thermal fatigue properties, thermal fatigue tests were performed heat cycle of simulated real plant with as-received and pre-aged non-FGM specimen. The pre-aged specimen was heated by furnace for 4000 hours at 1000^0C. In this case, the formation of $12\mu M$ thickness oxide was observed at the interface between TBC and NiCrAlY bond coating.
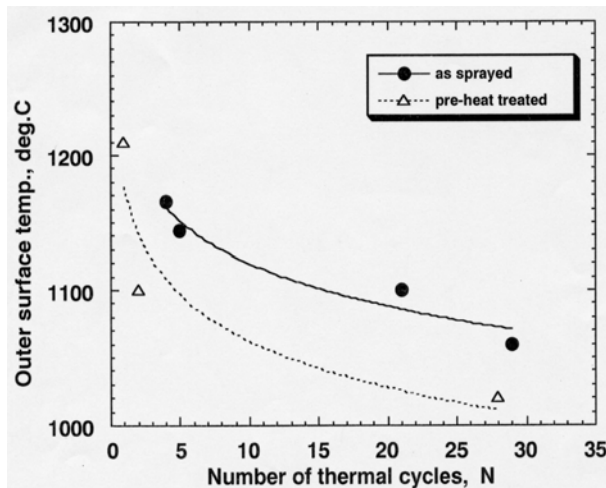
Figure 7: Relationship between surface temperature and fracture cycles of thermal fatigue test.
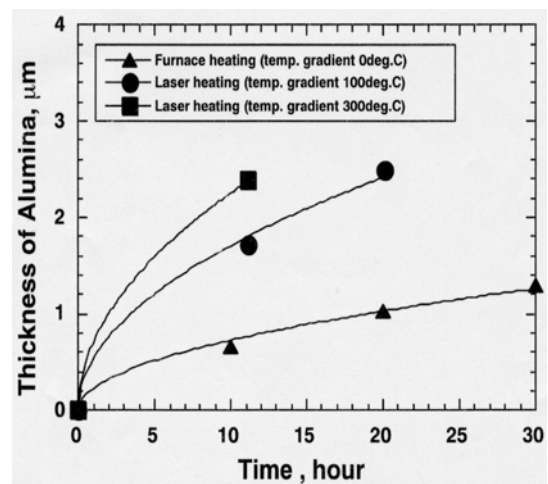
Figure 8: Comparison between furnace and laser heating concerning time dependence of alumina thickness

The relationship between surface temperature and thermal cycle of failure is shown in figure 7. Failure cycle increased accompanied with surface temperature decreased both in received and pre-aged specimen. However, in case of equality in the surface temperature of both, pre-aged specimen was earlier degradation than non-aged specimen. Moreover, almost all cracks formed at interface between top coating YSZ and oxide. These cracks are confirmed by SEM observation. This means that the oxide is bad influence in terms of thermal fatigue properties. Furthermore, the oxide is identified as Al_2O_3 (alumina) by energy dispersive x-ray spectroscopy (EDX). Thermal stress can be induced by the formation of alumina. Consequently, evaluation of oxidation behavior, especially alumina formation and growth, is very important for understanding of coating degradation.

Influence of temperature gradient on oxidation

In order to understand the effect of temperature gradient on the oxide growth, the alumina thickness was measured for the non-FGM specimen heated by CO_2 laser heating or furnace heating. In the former case, there was a temperature gradient along TBC system thickness direction. Moreover, the temperatures were not

only measured on surface and backside but also at interface between YSZ and MCrAlY by thermo-couples. The temperature on backside surface was kept on 800^0C or 600^0C and the temperature at interface was kept on 900^0C. This means that the temperature gradients were 100^0C and 300^0C, respectively. In the later case, there was zero temperature gradient along TBC system thickness direction. In the furnace heating, the temperature was kept 900^0C. The relationship between alumina thickness and aging time was obtained. The result is represented in Figure 8 with result of the uniform heated as for same aging temperature. As the result, in spite of equal YSZ/NiCrAlY interface temperature between the non-uniform heated specimen and uniform heated one, the alumina thickness are markedly different. The alumina is thicker for non-uniform heated case than that for uniform heated case. Namely, smaller temperature gradient forms thicker alumina than large gradient. The reason of the phenomenon is that the diffusion of oxygen through the YSZ accelerates in order to being high temperature concerning YSZ surface in case of laser heating as local heat. Moreover, due to the laser heated specimen has many porosity accompanied by formation of microcracks by virtue of larger thermal stress, oxygen rapidly penetrates interface through microcracks. Accordingly, laser heating which has temperature gradient is more effective condition in order to evaluation of oxidation behavior of real plants.

CONCLUSIONS

The thermal fracture in thermal barrier ceramic coating system was experimentally investigated. The fracture was induced by temperature gradient along TBC system thickness direction and oxidation between TBC and bond coat. Laser heating method was used to simulate the operating state of TBC system. The obtained results are arranged as follows.

(1) The failure of TBC system was in two crack forms: surface crack and interface delamination. The final complete failure was spallation due to the interface delamination growth.

(2) A fracture mechanism map in the T_s-T_b plane was obtained, where T_s and T_b are, respectively the temperature on the surface of coating and substrate. One can understand the effect of temperature gradient on TBC system service life.

(3) The life of thermal fatigue was reduced by the formation of alumina at interface. To sum up, the alumina has a bad influence on thermal fatigue property due to existence of thermal stress.

(4) The temperature gradient between inner and outer surface of specimen accelerates the growth of alumina layer.

ACKNOWLEDGMENTS

REFERENCES

1. Takeuchi, Y. R. and Kokini, K. (1994) *Trans. ASME, J. Engng Gas Turbines Power*, 116, 266.
2. Zhu, D. M. and Miller, R. A. (1998) *Mater. Sci. Engng. A*, 245, 212.
3. Cheng, J., Jordan, E. H., Barber, B. and Gell, M. (1998) *Acta Mater.*, 46, 5839.
4. Tolpygo, V. K., Dryden, J. R. and Clarke, D. R. (1998) *Acta Mater.*, 46, 927.
5. He, M. Y., Evans, A. G. and Hutchinson, J. W. (1998) *Mater. Sci. Engng. A*, 245, 168.
6. Wang, J. S. and Evans, A. G. (1999) *Acta Mater.*, 47, 699.
7. Bernstein, H. L., Allen, J. M. (1992) *J. Engng Gas Turbines Power*, 114, 293.
8. Zhou, Y. C., Hashida, T. (2001) *Int. J. Solids Structures*, 38, 4235.
9. Zhou, Y. C. and Hashida, T. (2001) *Int. J. Fatigue*, (in press)
10. Zhou, Y. C., Hashida, T. (2001) *Trans. ASME J. Engng Gas Turbines Power*, 23, (in press)

THERMAL FATIGUE DISLOCATION STRUCTURES IN 316L STEEL: EXPERIMENTS AND SIMULATIONS

C.F. Robertson[1] M.C. Fivel[2] and A. Fissolo[1]

[1] SRMA CEA/Saclay, 91191 Gif-sur-Yvette, France.
[2] GPM2 CNRS/INPG, BP 46, Domaine Universitaire, 38402 Grenoble, France.

ABSTRACT

In an attempt to better understand damage accumulation mechanisms in thermal fatigue, dislocation substructures forming in 316L steel during a specific test are examined and simulated. Hence, thin foils taken out of massive, tested specimens are observed in transmission electron microscopy (TEM). These observations help in determining an initial dislocation configuration to be implemented in a 3D model combining 3D discrete dislocation dynamics simulation (DDD) and finite element method computations (FEM). It is found that the simulated mechanical behaviour of the DDD microstructure is compatible with FEM and experimental data. The numerically generated dislocation microstructure is similar to ladder-like dislocation arrangements as found in many fatigued f.c.c. materials. Distinct mechanical behaviour for the two active slip systems are shown and deformation mechanisms are proposed. Up to T=650K, no evidence for direct effect of temperature on climb and cross slip phenomenon was found.

KEYWORDS

Multiscale Modelling, 3D Discrete Dislocation Simulation, Fatigue Simulations, TEM, FEM.

INTRODUCTION

Thermal fatigue in the temperature range 300K-700K constitutes typical loading conditions for metallic pressure vessels and piping used in the electric power industry [1]. In these conditions, component material failure results from transgranular crack initiation and propagation [2], regardless of the component surface state finish [3]. Transgranular cracking therefore results from damage accumulation mechanisms operating at a scale much smaller than the metal grain size. Hence, little is known about dislocation based, mesoscopic scale deformation mechanisms in component materials undergoing thermal fatigue. In an attempt to better understand phenomenon involved in thermal induced cyclic plasticity, an innovative investigation approach is proposed here and adapted to a widely used component material, 316L austenitic stainless steel (f.c.c. crystalline structure).

One 'classical' tool to investigate fatigue dislocation substructure is the transmission electron microscopy (TEM) technique [4-8]. Though informative, TEM examinations are very difficult to rationalise in terms of dynamic deformation mechanisms, due to the very large number of dislocations involved. In addition, it is very difficult to establish how the identified mechanisms influence larger-scale mechanical behaviour. One way to cope with these problems is to use numerical modelling that couples information coming from different scales. Modelling reliability can then be established by direct comparisons of numerical results with adequate experimental data. In the present paper, dislocation substructures forming in 316L steel during a

specific test are examined and simulated in order to better understand damage accumulation mechanisms in thermal fatigue. In the next sections, we will describe in detail both the selected experimental setting (thermal fatigue tests, TEM) and the proposed numerical methods (discrete dislocation dynamics, finite element method). In the next section, an application of these methods to a specific thermal fatigue test will be presented and the results given. Information coming out of the proposed approach is summed up in a brief conclusion.

EXPERIMENTS

Thermal fatigue tests

The experimental apparatus is presented in Figure 1(a). Specimens are machined from plates in the solution annealed state. The mean grain size is about 50µm. Portions of the external wall will be extracted after fatigue test for TEM examination. These portions are electropolished before testing. This eliminates any residual plastic deformation that can affects the interpretation of the results. During the test, the external specimen surface is heated by HF induction while the internal surface is continuously cooled by flowing water. This gives rise to a radial temperature gradient between the two walls, enforcing a thermal-induced stress field. Fatigue loading conditions are achieved by switching the heating on and off periodically ($f \approx 8 \times 10^{-3}$ Hz), up to 100 cycles. In these conditions, temperature of the internal wall fluctuates from 22°C to 80°C during the cycle, whereas temperatures of the external wall varies between 32°C and 380°C.
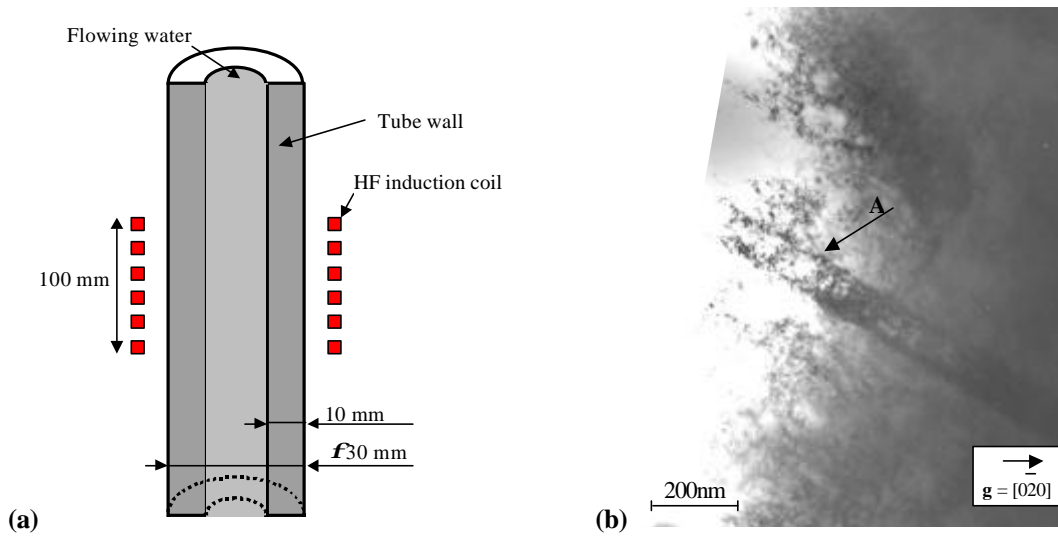
Figure 1: (a)-Experimental apparatus. **(b)-**TEM observation of a surface grain

TEM observations

After test, 2cm×1cm×0.1cm slices from (the electropolished) parts of the external wall surface are cut out of the massive tube specimens, using a rotating precision saw. These slices are further thinned to 100µm by mechanically polishing the back. Then, 3mm disks are punched out. TEM thin foils are prepared using back side electropolishing in a twin jet Tenupol, while the external surface is protected by lacquer. The TEM observations are then made in a CM-20 Philips operated at 200kV.

Out of the observed specimens, a single grain has been selected for a complete indexation, with a view to use these results for DDD simulations. According to electron diffraction pattern analysis, the observed grain plane (the TEM foil top surface) is found to be close to (211).

In Figure 1(b), a pair of 30nm thick parallel bands separated by a 100nm wide channel is shown (letter A). The channel is partially filled with dislocation lines more or less perpendicular to the bands, that are obviously parallel to ($\bar{1}11$) planes. Using the **g.b** = 0 rule, it is found that band and channel dislocations share the same Burgers vector ½[110]. The two possible active slip systems for dislocations present in and between these bands are thus ($\bar{1}11$) [110] and ($11\bar{1}$) [110].

MODELLING

Finite element method (FEM) computations

Strain and stress fields generated during test are computed by FEM, using CASTEM-2000 software. By taking advantage of specimen geometry, the problem corresponding to the experimental setting as shown in Figure 1(a) can be solved with a mesh corresponding to one eighth of the specimen. Eight node cubic elements were used with a mean element width of about 175 µm (see Figure 2(a)). Calculations were done as follows. Experimentally obtained temperatures in specimen internal and external walls are first imposed to the nodes corresponding to these respective walls. Temperature of every node inside the meshing is then computed assuming thermal equilibrium and the mentioned thermal boundary conditions. In the next computing step, the 'complete' thermal field together with suitable mechanical boundary conditions enforce a thermal induced displacement field. Associated strain and stress fields are computed assuming an elastoplastic model involving a linear kinematic yielding criteria that fits experimental fatigue data. Stresses estimated with this model agree with experimental saturation values at 300K.

FEM computations gives an equibiaxial thermal induced stress state ($\sigma_{zz} = \sigma_{\theta\theta} = \sigma$) which is in good agreement with analytical expressions found by Fissolo [2]. The stress amplitude is σ = -230MPa when $T = T_{max}$ and σ = 130MPa when $T = T_{min}$. These conditions are often referred to as 'out of phase' thermal fatigue, i.e. the compressive stress (negative) peaks whereas the temperature is maximal. The mechanical stress-strain curve is plotted in Figure 2(b), for the zz components.
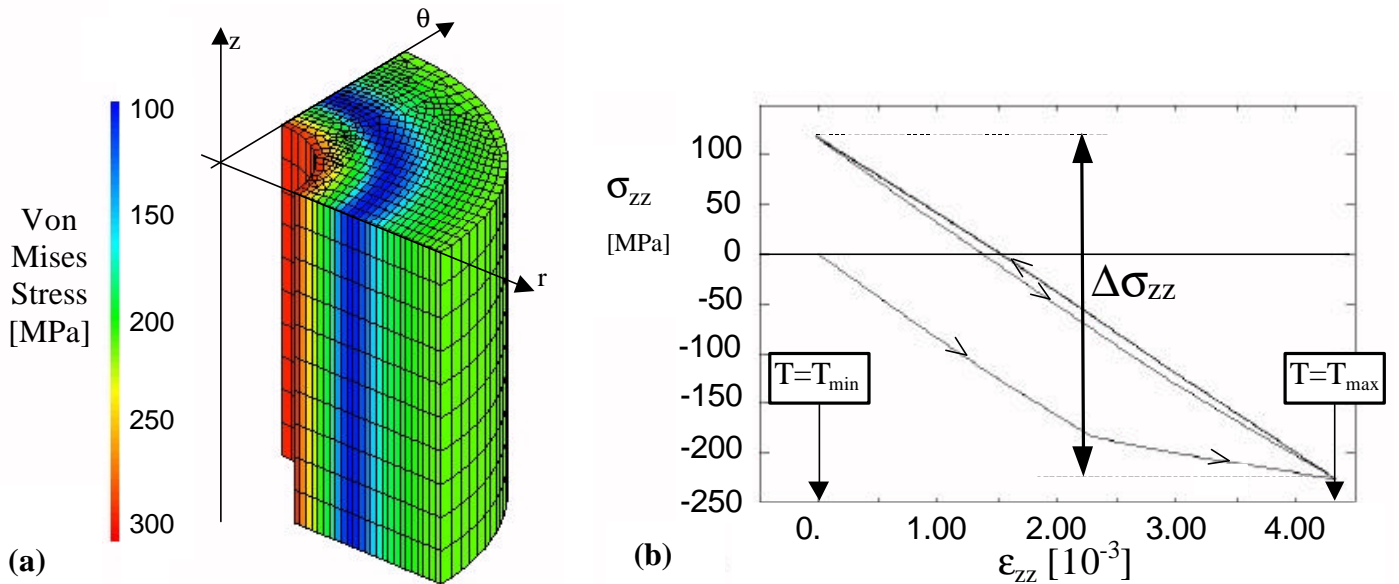
Figure 2: (a)-FEM Von Mises equivalent stress in MPa at maximal temperature T = 653K. The represented mesh corresponds to the part of the specimen located inside the induction coil described in Figure 1(a). Note that the external wall undergoes compressive stress whereas the internal wall is in tension.
(b)-External wall total loading (mechanical+thermal): $\sigma_{zz}(\varepsilon_{zz})$.

The resolved shear stress τ_R are then computed on all the 12 f.c.c. glide system of the grain identified in previous section. It is worth mentioning that $|\tau_R|$ on the $(\bar{1}11)[110]$ and $(1\bar{1}1)[110]$ slip systems (those of the identified 2D bands) are very similar, a condition we will later refer to as 'double' slip.

Discrete dislocation dynamics (DDD) simulation

The constitutive principles of DDD modelling are described in details elsewhere [10]. Numerically generated dislocations inside the simulation box glide in a homothetic 3D f.c.c. lattice, with a lattice parameter of 10b (2.5×10^{-9}m), where b is the Burgers vector magnitude. The dislocation lines are discretised in screw and edge segments, whose displacement occurs over discrete time steps. For each time step, the effective resolved shear stress acting on all the segments are computed. Each segment is then moving at a velocity proportional to the effective stress. The DDD code treats all the possible 3D

annihilation/recombination interactions between the dislocations. A stochastic temperature-dependant cross-slip mechanism is implemented as well.

We will now attempt to simulate the dynamic evolution under cyclic thermal load of the same dislocation band pair as the one described in first section. The DDD simulation box is taken as a faceted cylinder with a selected radius and height of 5µm. The simulation box size is chosen so as to be similar to the experimentally observed separation distance between the selected pair of bands and the pair next to it (2µm). This box represents a part of a 316L grain, with upper and bottom faces parallel to (211) planes. Dislocations that reach the bottom and peripheral cylinder faces are stopped, producing strong barrier effects like dense dislocation walls and/or highly disoriented grain boundaries. The effect of the free surface is accounted for by allowing dislocations reaching the upper face to escape. The initial dislocation microstructure consists of 2 µm long pinned dislocation segments randomly put in the $(\bar{1}11)[110]$ slip system only (43 segments in all), which will be referred to as the primary slip system. Each pinned segment acts as a Frank-Read source with random sign and orientation. The initial sources are positioned at random inside two 30nm wide parallel bands centred in the simulation box and separated by a 100nm wide channel. This initial dislocation microstructure is selected in order to quickly obtain a configuration complying with TEM observations thus, with a known number of cycles N = 100. Of course then, this initial DDD dislocation configuration does not correspond to the microstructure of cycle N = 0 of the performed test, but instead to the Nth cycle, with $0 < N < 100$.
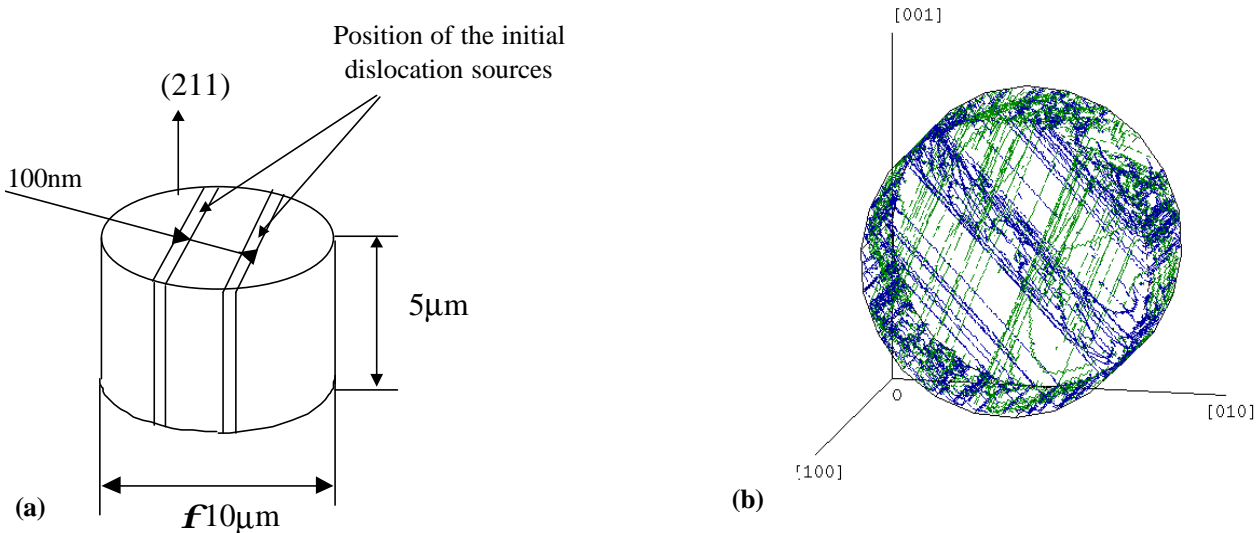
Figure 3: (a)-Schematic representation of the initial dislocation structure. **(b)-**3D dislocation microstructure obtained after 3 simulated cycles.

The numerical fatigue test is performed in imposed applied stress conditions. The *applied* stress field is as determined with the help of FEM computations. This field is assumed to be homogenous inside the whole simulation box, i.e. the same applied stress tensor is used for each dislocation segment. Note that although the applied stress field is homogeneous, the effective stress tensor computed at the middle point of each dislocation segment is heterogeneous due to the contribution of the internal stress field generated by the dislocation segments. In practice, the loading is enforced stepwise, 5MPa by 5MPa. Each time the applied load is changed, dislocations move and multiply over as many computing steps (with $\delta t=10^{-9}$sec) as needed to obtain a stable dislocation configuration, i.e. one that equilibrates the applied load. Therefore, as many as 460MPa/5MPa = 92 stable dislocation configurations have to be determined for each complete thermal cycle. Because one thermal cycle lasts 120 seconds, each stepwise load increase correspond to 120s/92 ~1.3 seconds. As dislocations move much faster than the applied load increase rate, equilibrium is usually achieved within as few as N = 10^2-10^3 time steps, i.e. Nδt ~ 10^{-7}-10^{-6} seconds. At this point, if dislocation climb is neglected, cross slip is the only time-dependant mechanism that can further affect the microstructure inside the simulation box. This means that quasi-static approximation can here be fully assumed provided no more cross slip occurs within the ~1.3 second following stabilisation. This assumption has been checked in a separate paper [11]. Hence, the simulated time can here be converted into an equivalent time corresponding to the actual test duration.

Results

When the initial dislocation sources are placed inside the simulation box and applied load gradually increases, dislocation density in the primary slip system increases smoothly as shown in Figure 4(a). This regime lasts for the first half of the first simulated cycle, i.e. until $T = T_{max}$. At this point, the dislocation density in the deviate slip system (we recall that $\rho_{(t=0)} = 0$ in this slip system) starts increasing due to intense cross slip, until it is about half as large as in the primary slip system.

Over the last simulated applied cycle (third one), the equivalent mechanical strain of the simulation attains $\Delta\varepsilon_{eq} \sim 2\times10^{-3}$. Average dislocation density during that same cycle is around $\sim5\times10^{12}$ m^{-2}. By comparison, the equivalent mechanical FEM strain amplitude is $\Delta\varepsilon_{eq} \sim 2.2\times10^{-3}$ when the thermal expansion contribution is subtracted. However, it seems quite obvious that the straining is not homogeneous inside the simulation box. This is reflected by the heterogeneity of the dislocation densities. For example, the dislocation density computed inside a sphere of radius 500nm located inside the central bands is $\rho\approx5.4\times10^{13}$ m^{-2}. If that same sphere is now positioned outside the bands, the density ρ is reduced down to 7.9×10^{12} m^{-2}. At this stage thus, the DDD strain amplitude reasonably agrees with elastoplastic FEM results although a simplified model has been used: only 2 glide systems are considered, the influence of the image forces is neglected and no internal obstacles such as local twins or misorientation are taken into account. In a forthcoming study, all these points will be implemented and tested.

Interestingly, the mechanical behaviour of the two involved slip systems presents distinct characteristics, as plotted in Figure 4(b). Shear strain γ in the deviate slip system $(1\bar{1}1)[110]$ is periodic and vanishes one time per cycle. It is worth mentioning that a $\gamma = 0$ strain is associated with a non-vanishing dislocation density. This means that dislocations in this system can arrange in low shear strain configurations with a strongly reversible character.

In the primary slip system $(\bar{1}11)[110]$, shear strain accumulates from one cycle to an other, i.e. it is not fully reversible. In addition, dislocation density in the primary slip system is about twice that in the secondary slip system, whereas shear strain associated with the later is three times higher than that associated with the former. Hence, by opposition with the secondary system, the dislocation arrangements in the primary slip system maximize the induced shear strain.
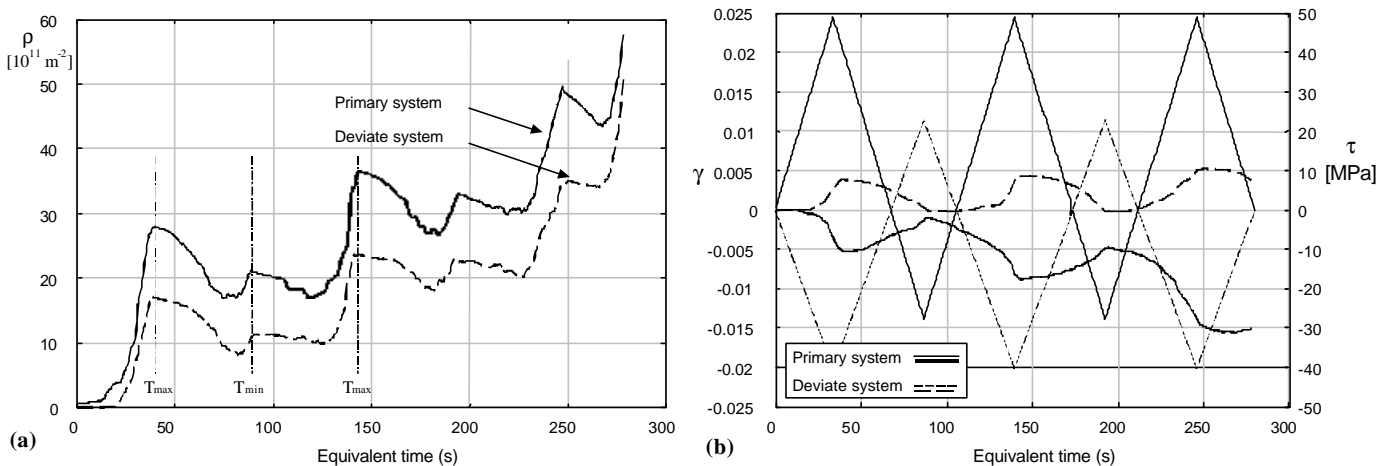
Figure 4: (a)-Dislocation density evolution ρ(time) on primary and deviate slip systems versus time. The plotted densities are associated with the whole simulation box. Local dislocations densities can be much higher. **(b)** Shear strain (left axis–thick lines) and applied shear stress triangular wave (right axis–thin lines).

Incidentally, most of the $(1\bar{1}1)$ slip planes do not cross the crystal top surface whereas dislocations present in these planes keep gliding there until they form stable, low energy dislocation substructures. Indeed, the $(1\bar{1}1)[110]$ dislocations located inside the channel between the two initial bands have a strong edge-edge dipolar character. Dynamic 'in test' observations show dipoles to form in large numbers as soon as the first applied load reversal begins. Obviously though, the cyclic character of the applied load strongly increases the dipole formation probability. Once an isolated dipole has formed, it promotes further dipole formation by capturing additional isolated dislocations. When a few dipole clusters have formed, they rearrange in

dislocation walls perpendicular to the **b** vector [110] common to primary and deviate slip systems, as soon as the applied stress becomes low enough. Secondary dislocations therefore tend to stabilise the primary walls substructure at this particular stage of the cycling. We assume that a secondary wall exists whenever at least 2 dipoles are positioned along [$1\bar{1}2$] direction, inside each 500nm thick (211) slice cut out of the simulation box. Using this criteria, an average wall-wall separation of 250nm is measured. Note that dipole width inside the bands is more or less constant: isolated dipole width distribution is similar to that of dipoles everywhere else in the central bands.

It is worth mentioning that during the presented simulations, new bands spontaneously form at some distance (up to 1,5 µm) from the initial pair position. The new band formation occurs when screw dislocations located in some ($1\bar{1}1$) planes (located out of the initial band pair) cross-slip back into some distant ($\bar{1}11$) planes, near the simulation box edges. Obviously, this band formation mechanism is promoted under the present 'double' slip loading conditions. New band formation can also be assisted by the stress field coming from the accumulated dislocations at the simulation box edges thus, by the presence of a strong barrier.

CONCLUDING REMARKS

Although the present approach seems promising, many remaining questions have to be addressed. For example, how does the simulation box size affects the results? Here, the simulation box size has been chosen according to TEM observed minimal separation distance between two pairs of bands. The boundary conditions in the simulation box do not account for the actual grain boundary in the metal. This could be done by calculating more accurately the stress fields existing inside the grain.

In addition, the top surface of the simulation box, i.e. the external wall of the tested specimen, was not treated in a realistic way: dislocation segments crossing the surface were cut away. A specific treatment of the boundary conditions relevant to the presence of an oxide layer and/or a traction free surface has to be implemented.

Finally, due to the very large computing time, only about 3 cycles have been simulated. The stability of the results with time could be addressed. Therefore improved DDD algorithms have to be developed.

ACKNOWLEDGEMENTS

REFERENCES

1. Sehitoglu, H., ASM Handbook (1996). Vol.19 Fatigue and Fracture, Thermal and Thermomechanical Fatigue of Structural Alloys.
2. Fissolo, A., Marini, B., Wident, P. and Nais, G. (1994) *Soc. Fr. Métall. Matér.*, pp. 513-526.
3. Wareing, J. and Vaughan, H.G. (1979) *Metal Science*, pp. 1-8.
4. Boulanger, L., Bisson, A. and Tavassoli, A.A. (1985) *Phil. Mag A*, 51(2), L5-L11.
5. Obrtlik, K., Kruml, T. and Polak, J. (1994) *Mat. Sci. Eng.* A187, 1.
6. Tavassoli, A.A. (1986) *Phil. Mag A* 54(4), 521.
7. Armas, A.F., Alvarez-Armas, I. and Petersen, C. (1992) *J. Nucl. Mat.* 191-194, 672.
8. Gerland, M., Mendez, J., Violan, P. and Ait Saadi, B. (1989) *Mat. Sc. Eng.* A118, 83.
9. Fissolo, A., Marini, B., Nais., G. and Wident, P. (1996) *J. Nucl. Mat.*, 233-237, 233.
10. Verdier, M., Fivel, M. and Groma, I. (1998) *Modelling Simul. Mater Sci. Eng.*, 6(6), 755.
11. Robertson, C., Fivel, M.C. and Fissolo, A., *Mater. Sci. Eng A.*, in press.

THERMAL SHOCK DAMAGE MECHANISM
OF FIBER BONDED CERAMICS

Y.Kogo[1] and M.Kamiya[2]

[1] Department of Materials Science and Technology,
Science University of Tokyo
2641, Yamazaki, Noda, Chiba 278-8510, JAPAN
[2] Graduate Student, Science University of Tokyo

ABSTRACT

Thermal shock behavior of unidirectionally reinforced Si-Ti-C-O fiber bonded ceramics was experimentally examined. Water quench tests were carried out with various temperature differences (ΔT) up to 800K. Macroscopic cracks were introduced with ΔT of 600K, although no degradation was observed in Young's modulus. With larger ΔT, large cracks were introduced accompanied by the degradation of Young's modulus. SEM observation revealed that microscopic damage near the surface occurred even when ΔT was less than 600K. The microscopic damage might play an important role to release the thermal stresses induced by the thermal shock.

KEYWORD

Thermal Shock, Water Quench Test, Fiber Bonded Ceramics, Micro-damage

INTRODUCTION

Various types of ceramic matrix composites (CMC) have been developed and studied for high temperature applications. Among them, Si-Ti-C-O fiber bonded ceramics (FBC) is one of the promising materials, which possess superior high temperature mechanical properties and long-term durability at elevated temperature [1].

In actual operation conditions, the materials will be exposed to severe temperature changes, which will induce large thermal stresses. Because of this, knowledge of thermal shock resistance is indispensable for structural design. However, thermal shock behavior of the CMCs is generally complicated compared with monolithic ceramics [2-4], and is not fully understood yet. In this study, water quench tests were carried out on the unidirectionally reinforced (UD) FBC to investigate micro- and macroscopic damages induced by the thermal shock. Young's modulus before and after thermal shock tests were also measured to clarify the effect of the thermal shock induced damage on the mechanical properties of the UD FBC.

EXPERIMENTAL PROCEDURE

Materials

Material used in this study was unidirectionally (UD) reinforced Si-Ti-C-O fiber bonded ceramics (FBC) manufactured by UBE Industries [5]. Continuous Si-Ti-C-O fiber was used as the starting material for the manufacturing of the FBC. The fiber was first heat treated in air to form an oxide layer on the fiber surface. The pre-oxidized Si-Ti-C-O fibers were hot-pressed to pack interstices by the oxide material on the fiber surface. A thin carbon layer was formed between the fiber and the oxide layer after the hot-pressing [1]. Typical optical micrograph of as-received UD FBC is shown in Fig.1. Fiber volume faction was approximately 90%, which was much higher than those of other CMCs.

10μm
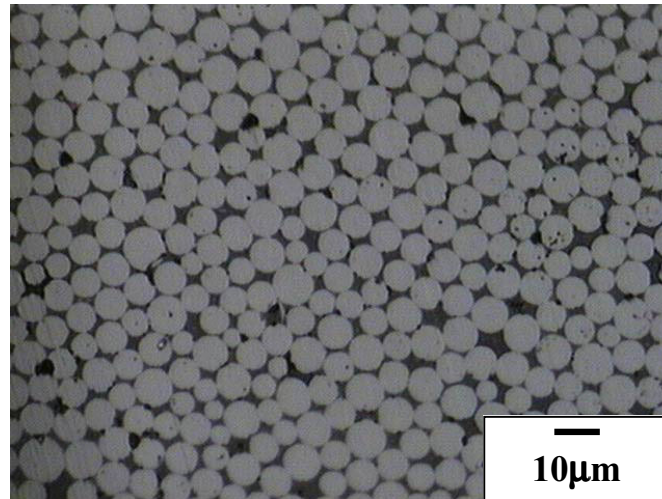
Fig.1 Cross-sectional view of as-received UD FBC.

Thermal Shock Test

The UD FBC plate was machined into rectangular bars, and the wedge made of the UD FBC was bonded to the tip of the specimen. The wedge was necessary to avoid formation of thick air layers on the specimen surface when the specimen entered into the water. As already reported [6,7], heat transfer at specimen surface was increased by attaching a wedge due to change in the boiling condition on the surface. This resulted in more severe thermal shock condition compared with a specimen without a wedge. In the thermal shock test, the specimen was heated in an inert atmosphere and kept for 15 min. at a given temperature (473 K ~ 800 K). Then, the specimen was made to fall freely and stopped in the water bath. Both falling height and falling depth from the water surface were set to 600 mm following the Japanese standard for the thermal shock test of ceramics (JIS-R1615). In order to investigate macro- and microscopic damage induced in the UD FBCs, the dye penetrant test and the SEM observation were carried out on the surface of the thermally shocked specimens. Cross-sections were also observed to estimate depth of the damaged area.

Finite element analyses (FEA) were carried out to estimate thermal stresses induced in the FBC. Two dimensional transient thermal stress analysis was carried out by modeling cross-section of the specimen. Fracture mechanical analysis also carried out to clarify the macroscopic fracture criteria. The boundary conditions were determined by experiments using rod-shaped silver specimens with and without the wedge. A thermocouple was set in the silver specimens to measure the temperature change during the thermal shock test. Because the temperature difference between the center and the surface of the silver specimen was less than 8%, the heat flow at the surface could be estimated assuming uniform temperature distribution in the silver specimen. The heat flow on each silver specimen surface was assumed to correspond to the top surface or the side surface of the FBC specimen.

RESULTS AND DISCUSSION

Thermal Shock Damage Observation

Figure 2 shows a typical thermal shocked specimen (ΔT=800K). Two types of cracks along the fiber direction were introduced in the UD FBC. Type A crack was first observed when ΔT was 600K. With increasing ΔT, the length of Type A crack was increased and Type B crack appeared on the side surface of the specimen. With these results, the critical temperature difference (ΔT_C) of the UD FBC could be determined as 600K.
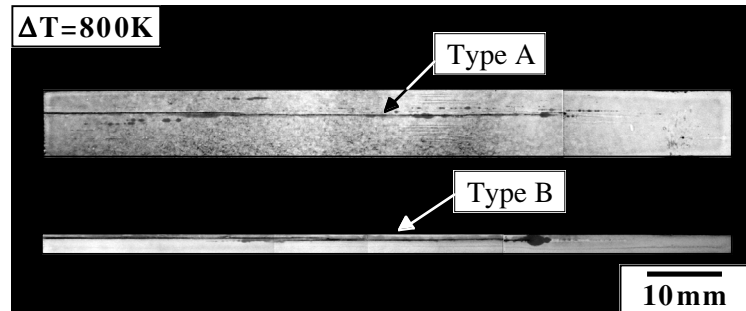

Fig.2 Cracks introduced by thermal shock

Change in the longitudinal Young's modulus was measured by the four-point flexure tests as shown in *Fig.3*. Normalized electrical resistance is also shown in the figure. When ΔT was lower than 600K, the Young's modulus after the thermal shock test was the same with that of the as-received specimen. However, when ΔT was above 600K, the Young's modulus dramatically decreased with increasing ΔT. This was due mainly to formation of Type B cracks in the UD FBC. The electrical resistance also changed drastically above 600K. At ΔT of 800K, the electrical resistance showed ten times larger than that of as-received specimen. These results suggested that the electrical resistance be closely related to the damage induced in the UD FBC. If we pay attention to ΔT lower than 600K, the electrical resistance gradually increased with increasing ΔT, even though no macroscopic damages were observed in the UD FBC.
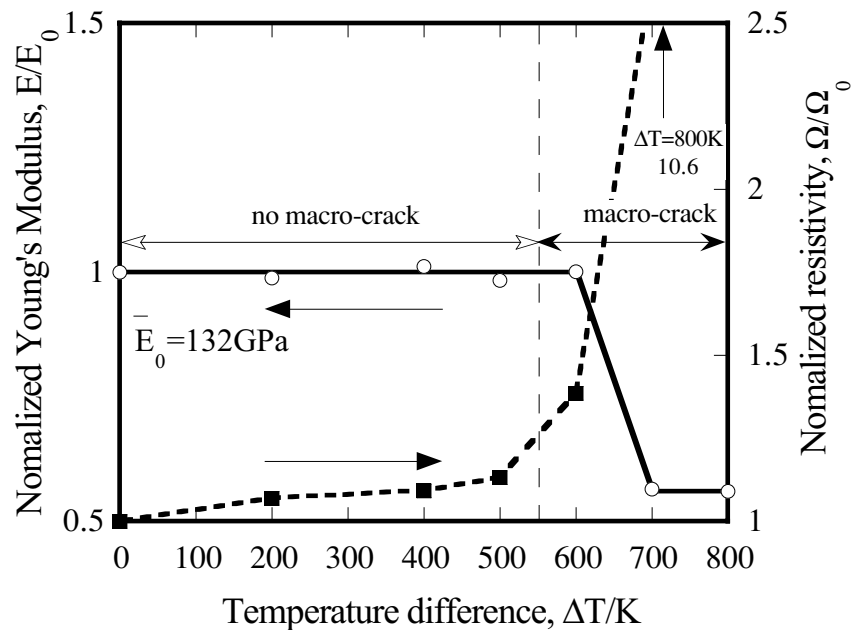
Fig.3 Change in Young's modulus and electrical resistance

Figure 4 shows the typical cross-sectional views of the as-received and the thermally shocked specimens. Even in the specimens tested at the lower ΔT than 600K, fiber spacing near the surface increased. This must be a microscopic damaged area induced by the thermal shock. *Figure 5* shows a microscopic damage area at a higher magnification. Micro-cracks were generated at the fiber/matrix interface.

The depth of microscopic damage area (t_d) was measured at 20 arbitrary points in each specimen, and plotted against ΔT as shown in Fig.12. The t_d increased monotonously with increasing ΔT, and saturated at ΔT_C. These observations suggested that the breakaway of the fibers from the specimen surface and/or delamination at the fiber/matrix interfaces near the surface occur due to the thermal shock even below the ΔT_C. It was also expected that slight increase in the electrical resistance corresponded to formation of the microscopic damage in the UD FBC.
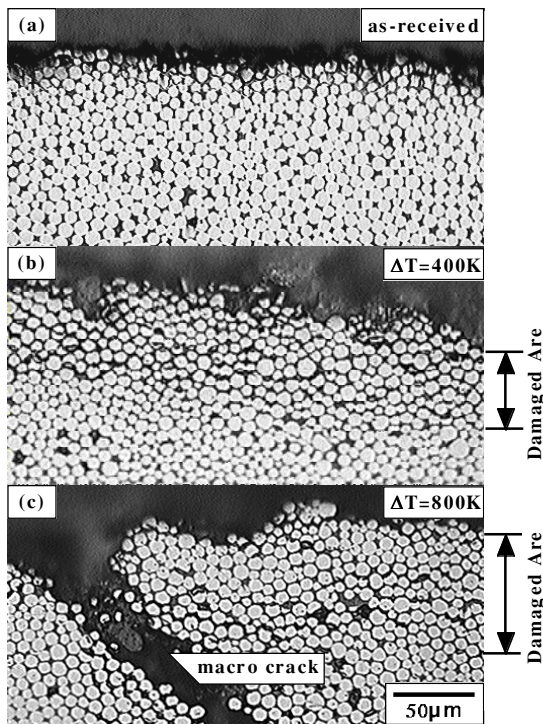
Fig.4 Typical optical micrographs of cross-sectional view of the UD FBC.
(a) before test, (b) ΔT=400K, (c)ΔT=800K
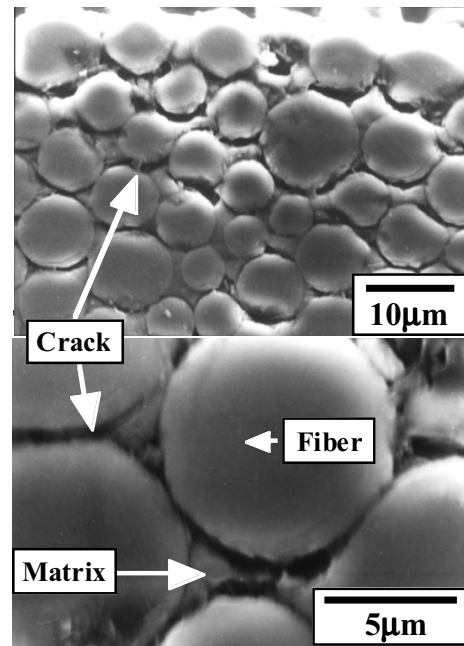
Fig.5 Fiber-matrix interface view of the thermal shocked UD FBC (ΔT=400K).

Thermal Stress Induced by thermal shock

For estimating thermal stress induced in the specimen, finite element analysis was carried out. Linear elastic two dimensional model was used assuming the plane strain condition. The cross section was modeled using 8 nodes isoparametric elements. The transient heat flow can be estimated from the experiments of the silver specimen and considered in the boundary condition.

The calculated maximum thermal stress induced in the UD FBC is shown in Fig.6. Even at ΔT of 200K, the maximum thermal stress was higher than the transverse tensile strength of the UD FBC. These results suggested that macroscopic fracture can not be predicted by the maximum stress criterion. As another approach to predict the macroscopic fracture, fracture mechanical analysis was also carried out by the virtual crack closure method [8]. Energy release rates were calculated for various crack length and various temperature difference. Figure 7 shows the maximum energy release rates in each condition. Results showed that if the initial crack size is less than 100 µm,   crack extension will occur at 600K or higher temperature difference. These calculated results well agree with the experimental results. Form

these analyses, it can by concluded that the fracture toughness criterion can be predict the macroscopic fracture. In addition, it is also expected that the microscopic damage observed near the surface of the UD FBC specimen play an important role to relax thermal stress. This must be an unique stress release mechanism to the UD FBCs.
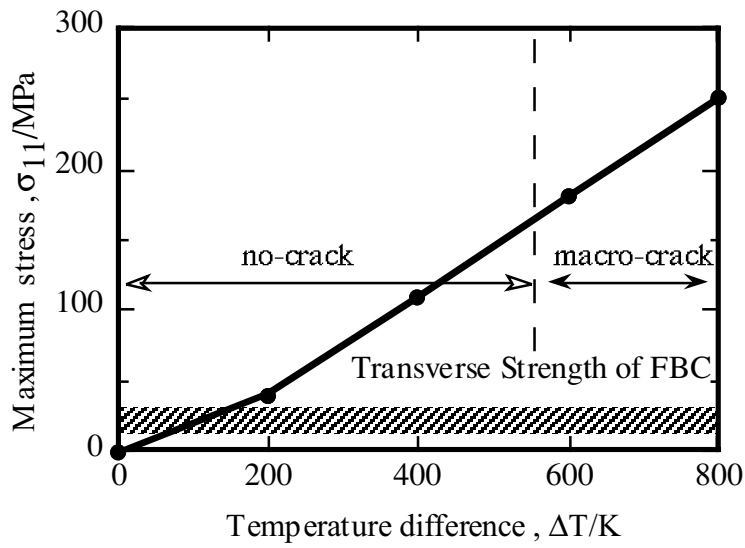

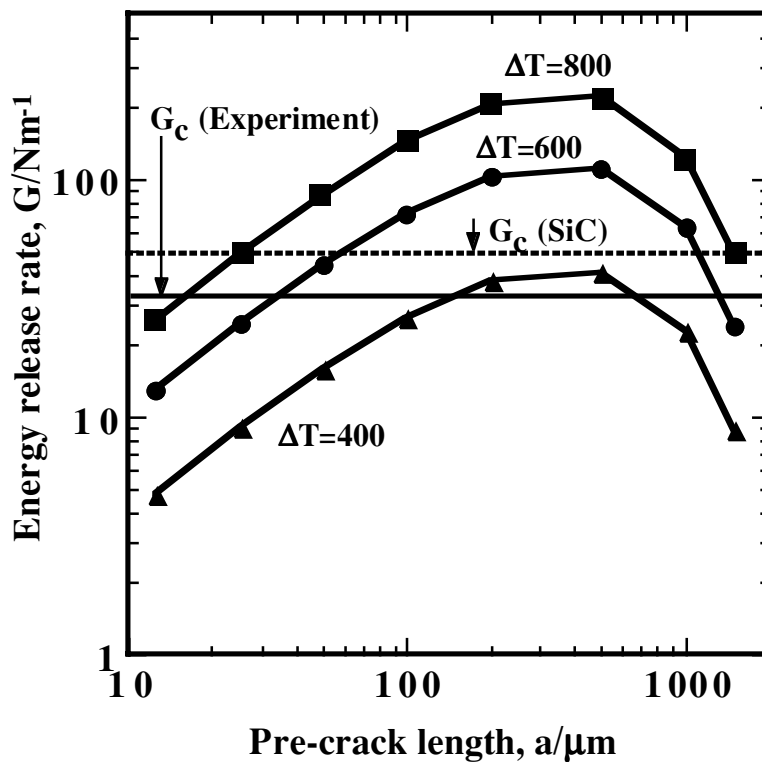Fig.6 Maximum Thermal Stress Induced in the Specimen

Fig.7 Maximum Energy Release Rate during Thermal shock Test

SUMMARY

The thermal shock behavior of the unidirectionally reinforced Si-Ti-C-O fiber bonded ceramics was experimentally examined, and following results were obtained.

1. The critical temperature difference of the unidirectionally reinforced Si-Ti-C-O fiber bonded ceramics was estimated as 600K, which was much higher than those of monolithic ceramics.
2. Even below the critical temperature difference, microscopic damage such as delamination of fiber/matrix interface and/or breakaway of fibers from the surface occurred in the unidirectionally reinforced Si-Ti-C-O fiber bonded ceramics.
3. Macroscopic fracture was controlled by the fracture toughness criterion rather than the maximum stress criterion.
4. The microscopic damage was expected to release the thermal stresses induced in the material. This must be an unique stress release mechanism.

REFERENCE

1. Ishikawa, T., Kajii, S., Matsunaga, K., Hogami, T. and Kohtoku, Y. (1995) *J. Mater. Sci.*, 30, 6218.
2. Kagawa, Y., Kurosawa, N. and Kishi, T. (1993) *ibid.*, 28, 735.
3. Wang, H. and Singh, R.N. (1994) *Int. Mater. Rev.*, 39, 228.
4. Wang, H., Singh, R.N. and Lowden, R.A. (1996) *J. Am. Ceram. Soc.* 79, 1783.
5. Magtsunaga, K., Ishikawa, T., Kajii, S., Hogami, T. and Kohtoku, Y. (1995) *J. Ceram. Soc. Japan*, 103, 288. (*in Japanese*)
6. Sakuma, T., Iwata, U. and Takaku, H. (1991)Trans.Japan Soc.Mech.Eng.A, 57 : 2741-2746.
7. T.Sakuma, U.Iwata and H.Takaku, 1992 *ibid*. 58, 1424.
8. Rybicki, E.F. and Kanninen, M.F. (1977) *Eng. Fract. Mech.*, 9, 931.

THERMAL SHOCK FRACTURE BEHAVIOR OF CERAMICS CHARACTERIZED BY DISK-ON-ROD TESTS

Shuichi WAKAYAMA[1], Kousuke NISHINO[2] and Shinya ARAI[2]

[1] Department of Mechanical Engineering, Tokyo Metropolitan University
1-1 Minami-Ohsawa, Hachioji-shi, Tokyo 192-0397, JAPAN
[2] Graduate Student, Tokyo Metropolitan University

ABSTRACT

New experimental technique for evaluating the thermal shock fracture characteristics of ceramic materials, ***Disc-on-Rod test***, was developed. The specimens have thin disc shape and the 2-dimensional thermal stress field was then obtained. The specimen was heated to high temperature and quenched by means of contacting with the cool metal rod with 4 mm diameter. The temperature distribution of specimen was measured by a high-speed IR camera (30 frames/s) and used for the determination of thermal stress field in specimen using FEM analysis. In order to evaluate the fracture process, AE signals during thermal shock fracture were also detected using an AE sensor attached on the end of the metal rod. It was observed by the video camera system that the maincrack was initiated at the center region subjected to the maximum balanced biaxial stress. On the other hand, the initiated crack was propagated, arrested and re-propagated after several seconds, which showed good agreement with the result of AE analysis.

KEY WORDS

Ceramics, Disc-on-Rod Test, Thermal Shock Fracture, Maincrack Formation, Crack Propagation

INTRODUCTION

The thermal shock fracture behavior of ceramics has been investigated using many traditional thermal-shock-testing methods. One of the most popular thermal shock tests is the water quench [1,2]. The critical temperature difference, where samples are subjected to severe damage, is used as the criterion for the thermal shock resistibility of ceramics. Recently, new experimental methods are proposed and applied to the investigation of thermal shock fracture behavior, based on fracture mechanics [3-5]. However the characterization of microfracture process under thermal shock as well as transient thermal stress field is indispensable, since thermal shock fracture is caused by the accumulation of microscopic damages such as microcrackings due to thermal stress.

In this study, new experimental technique for the investigation of thermal shock fracture behavior, Disk-on-Rod test, is proposed. The temperature fields in the specimen were measured and used to calculate the 2 dimensional thermal stress field. Furthermore, fracture process was evaluated by AE measurement. The formation of maincrack due to propagation and/or microcracks was focused in the present paper. Especially, the critical stress for maincrack formation is evaluated from obtained experimental data and

compared with the results of mechanical biaxial bending tests. Consequently, thermal shock fracture process in ceramics was well understood.


EXPERIMENTAL PROCEDURE

Materials
Two kinds of alumina ceramics (Material A and B) were used in the present study. Material A (own-making) was sintered from high purity alumina powder using a hot-press at 1650 ˚C for 2 hours under the pressure of 40MPa in Ar atmosphere. Material B (ADS-11) was offered from Toshiba Ceramics Co., Ltd. The relative density and mean grain size were 99.3% and 20 μm for Material A, and 97.7% and 6 μm for Material B, respectively. Disk specimens were cut from the rod materials and both surfaces were polished.

Disk-on-Rod Tests
In this study, for characterizing the thermal shock fracture process, new experimental technique, Disk-on-Rod test was developed. A thin disk specimen was heated to the required temperature by an infrared lamp and only the central part of disk was quenched by means of contacting with a Cu rod. The disk specimens have diameter of 20 mm and thickness of 0.6mm, and a contacting area has 4 mm diameter, therefore 2-D thermal stress field was obtained. The apparatus of Disk-on-Rod test and AE measuring system are shown in Figure 1 schematically. Contacting speed was controlled by an air damper to restrain the generation of AE noise due to contacting. And temperature distributions on disk surface were measured by a high-speed infrared camera (30 frames/s). Then thermal stress was calculated from the measured temperature distribution using FEM analysis.

In order to evaluate the fracture process, AE signals during thermal shock fracture were detected by AE sensor attached on the bottom end of metal rod, which was used for both coolant and wave guide. AE sensor, in which amplifier is instrumented, with resonant frequency of 180 kHz was used, then the initiations of microcracks could be detected with excellent sensitivity. The total gain of the AE system was 75 dB (main amplifier; 20 dB and pre-amplifier with sensors; 55 dB) and the threshold level was 40 dB, i.e.18 μV at the input terminal of the pre-amplifier. AE signals were measured by AE analyzer, sent to a computer and analyzed.
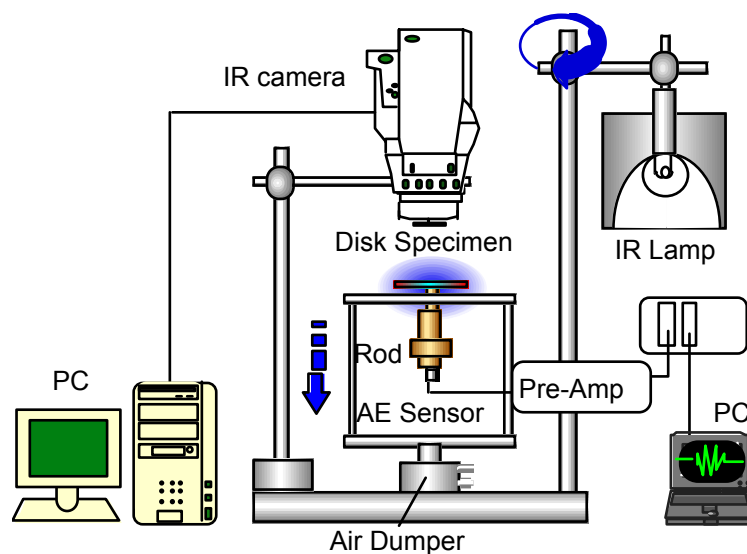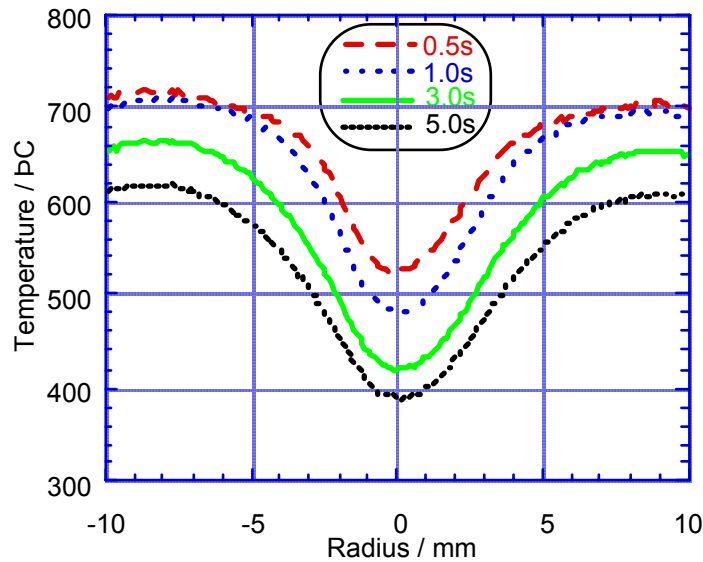
Figure 2: Temperature Distribution during Disk-on-Rod Test of Material B

RESULTS AND DISCUSSION

Determination of Thermal Stress

The temperature on specimen surface was measured by 1/30 s using a high-speed infrared camera system during Disk-on-Rod test and concentric temperature field was obtained. Figure 2 describes the temperature distribution along the specimen diameter for Material B. It can be seen in the figure that there are large temperature gradient in the disk by contacting the metal rod and this gradient becomes maximum at 3s and decreased gradually.

The thermal stress field was computed from the obtained 2-dimensional temperature distribution using FEM code (ANSYS; isoparametric structural shell, 2977 elements, 6082 nodes). The obtained stress field was axi-symmetric according to the concentric temperature distribution. The determined temperature fields were shown in Figure 3 (a), radial stress, and (b), tangential stress. It is understood from the figure that equi-biaxial maximum stress is subjected at the center of the disk and the stresses decrease to the outer region along the radial direction. It is important that radial stress is tension in the whole of disk specimen, while tangential stress has the transition point from tension to compression at 4mm from the center of the disk. Both stresses show the maximum at 3s.
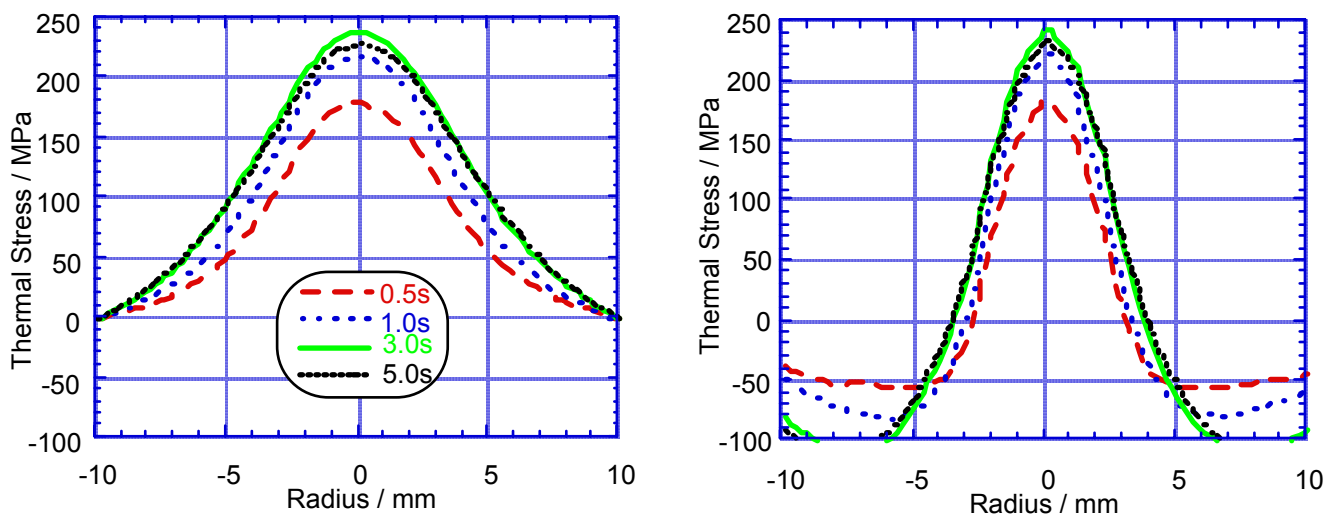
Figure 3: Thermal Stress during Disk-on-Rod Test of Material B.
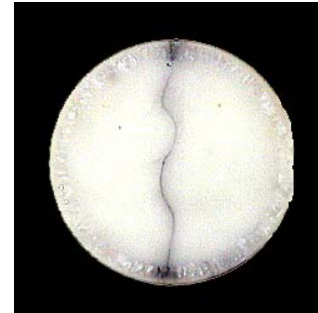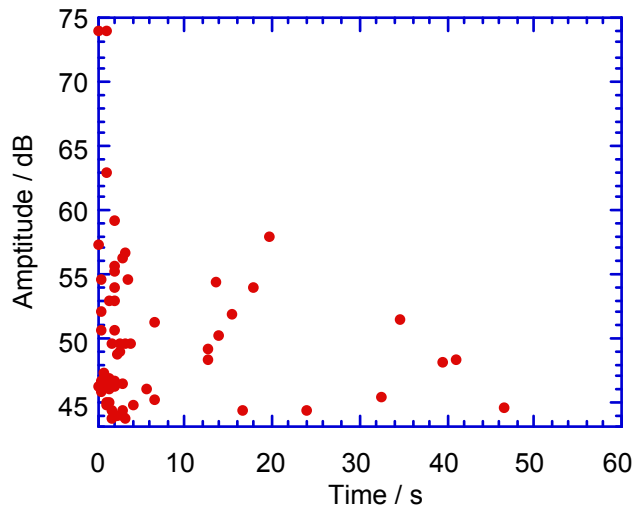
Figure 4: Thermal Stress and AE Behavior during Disk-on-Rod Test and Fractured Specimen.(Material A)

(a) Thermal Stress and AE Behavior   (b) Fractured Specimen

Fracture Behavior during Disk-on-Rod Tests

AE behavior during Disk-on-Rod test of Material A and fractured specimen are shown in Figure 4. In Figure 4 (a), each plot indicates the detected time and amplitude of each AE event. A large number of AE events were detected at $0-7s$ as thermal stress increased. It is important that there are incubation period at $7-12s$ and secondary generation after 12s. AE activity before incubation period is higher than secondary AE. It is then suggested that the crack propagation rate before incubation period is higher. The disk specimen (Material A) after Disk-on-Rod test is shown in Figure 4 (b). It is observed in the figure that maincrack was formed along radial direction at the center of the disk and propagated to the outer region with the deflection to tangential direction, which shows good agreement with the thermal stress field (Figure 3).

On the other hand, Figure 5 shows AE behavior during Disk-on-Rod test of Material B and a fractured specimen. It is recognized in Figure 5 (a) that both cumulative AE events and energy increase remarkably at 1.5 s. Since the formation of maincrack was observed at the AE increasing point, it is understood that the critical stress for maincrack formation during thermal shock fracture, σ_{th}, can be determined by Disk-on-Rod test. Those values for Material B ranged from 250 to 300 MPa. It is worth noting that the incubation period and secondary activity in AE behavior was not observed for Material B.
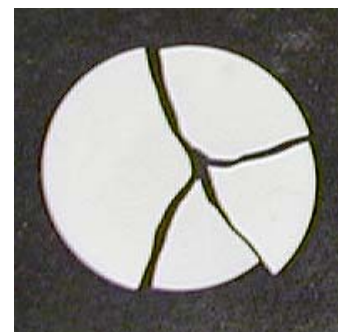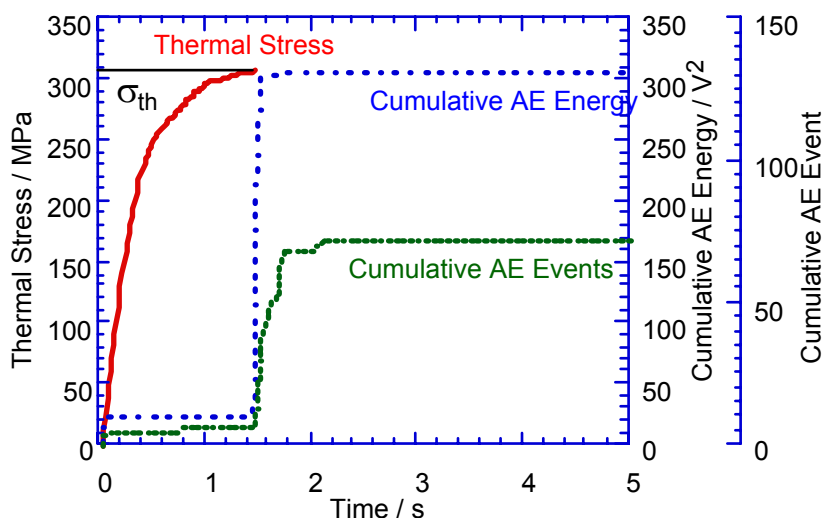
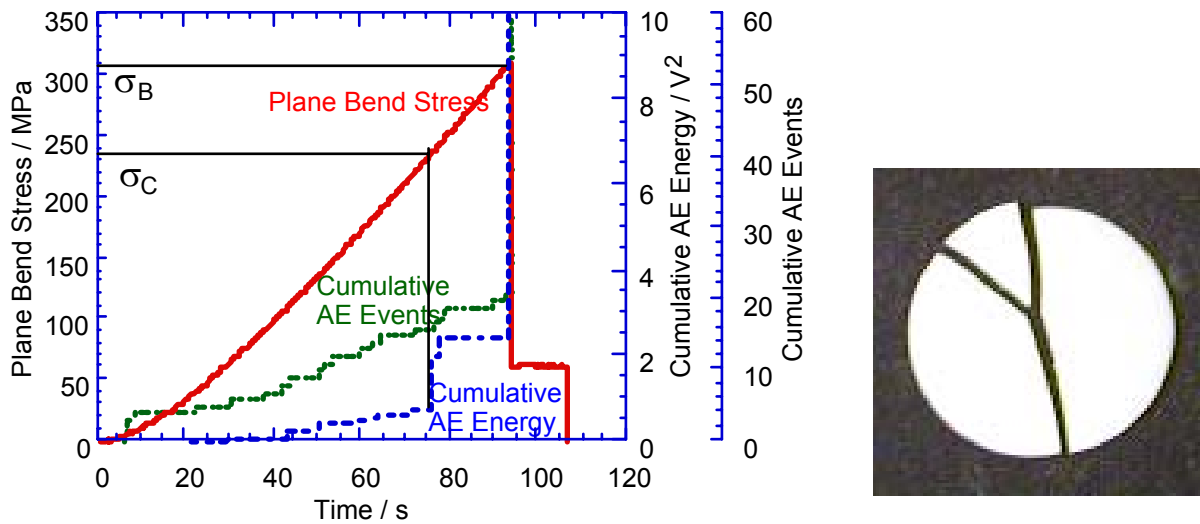Figure 5: Thermal Stress and AE Behavior during Disk-on-Rod Test and Fractured Specimen.(Material B)

Figure 6: Result of Plane Bending Test and Fractured Specimen.(Material B)

The observation of crack path in fractured specimen shown in Figure 5 (b) demonstrates that the deflection of maincrack in Material B is much smaller than Material A and specimen separated into 4 pieces. Therefore it is suggested that the crack propagation in Material B is unstable, while that in Material A is stable (Figure 4 (b)), that might be resulted from the difference in the strength of both materials as mentioned in the following section. Stress and AE Behavior   (b) Fractured Specimen

Facture Process under Thermal Shock

In order to investigate the critical stress for maincrack formation, the plane bending tests were carried out using same geometry specimens and a loading rod with 4mm diameter. Figure 6 shows the result of plane bending test of Material B and a fractured specimen. Similarly to the thermal shock fracture, it is observed in Figure 6 (b) that the maincrack was initiated at the center region of the specimen subjected to equi-biaxial stress. In Figure 6 (a), the AE increasing point can be observed before maximum bending stress, therefore it is understood that the critical stress for maincrack formation under mechanical loading, σ_C, can be determined. Those critical stresses for Material B were evaluated as 180 – 240 MPa; those are lower than the critical stress for maincrack formation under thermal shock as mentioned above. Considering the influence of stress corrosion cracking due to water during bending test at room temperature, it can be concluded that the critical stresses for maincrack formation under thermal shock and mechanical loading are equivalent to each other.

On the other hand, the critical stress for maincrack formation under biaxial mechanical loading was estimated as 80 – 150 MPa elsewhere [6]. Therefore, the strain energy released at the formation of maincrack during thermal shock fracture in Material B may be higher than Material A, which result the deference in crack propagation behavior during Disk-on-Rod tests; stable for Material A (Figure 4) and unstable for Material B (Figure 5).

In the case of Material A, the crack path in outer region is parallel to radial direction although the calculated tangential stress in the outer region was compressive (Figure 3 (b)). Therefore, stress field must be redistributed. It was considered from the incubation period of AE from 7 s to 12 s in the Figure 4 (a) that stress redistribution was not caused by mechanical stress redistribution because mechanical stress redistribution might be caused instantaneously. Therefore, it caused by the redistribution in temperature due to the disturbance of heat flow by maincrack. Consequently, thermal shock fracture process in Material A was understood as followings.

(1) Microcrackings were initiated at the center of the disk due to the thermal shock. Maincrack was then formed by equi-biaxial maximum stress due to the coalescence and propagation of the microcracking.

(2) The maincrack was deflected to the tangential direction due to the radial stress as the maximum principal stress and propagated at high speed.
(3) The crack arrested by the tangential compressive stress at the outer region of the disk.
(4) The temperature and the thermal stress were redistributed and maincrack re-propagated to radial direction by redistributed tangential tensile stress.

It is expected that larger specimen yield the similar fracture process for Material B. Consequently, it should be emphasized that the whole process associated with thermal shock fracture suggested by the unified theory of Hasselman [2], i.e. crack initiation, arrest and propagation, can be characterized during simple Disk-on-Rod test.

CONCLUSIONS

In the present study, new experimental technique, Disk-on-Rod test, was developed and applied to the characterization of thermal shock fracture process in ceramics. The thermal stress fields were computed from temperature distributions measured by high-speed IR camera and fracture process was evaluated by AE measurement, both of which are significant for understanding the thermal shock fracture behavior. From these results, the following conclusions were obtained.

(1) The maincrack was formed at the center of disk specimen subjected to maximum equi-biaxial stress.
(2) The critical stress for maincrack formation was evaluated and it was almost equivalent to the critical stress for maincrack formation in plane bending test.
(3) Thermal shock fracture process consisting of crack initiation, propagation and arrest was well understood.

ACKNOLEDGEMENT

REFERENCES

1. Kingley, W. D. (1955) *J.Am.Ceram.Soc.* 38, 3.
2. Hasselman, D. P. H. (1969) *J.Am.Ceram.Soc.*, 52, 600.
3. Schneider, G. A. and Petzow, G. (1991) *J.Am.Ceram.Soc.* 74, 98.
4. Rogers, W. P. and Emery, A. F. (1992) *J. Mater. Sci.* 27. 146.
5. Mizutani, Y., Nishikawa, N. and Takatsu, M. (1995) *J.Ceram.Soc.Japan* 103 494
6. Wakayama, S. (1998) *Progress in Acoustic Emission* 9, III73.

THERMAL-ELASTIC-PLASTIC COUPLED ANALYSES OF DYNAMIC CRACK GROWTH

F.Xu[1]   W.Guo[1,2]   Y.Y.Liu[3]

[1] State Key Laboratory of Mechanical Structure Strength and Vibration,
Xi'an Jiaotong University, 710049, Xi'an, PR China
[2] School of Aeronautics and Astronautics,
Nanjing University of Aeronautics and Astronautics, 210016, Nanjing, PR China
[3] Department of Aircraft Engineering,
Northwestern Polytechnical University, 710072, Xi'an, PR China

ABASTRACT

Finite Element Analyses (FEA) on dynamic crack growth with different velocity have been conducted on the basis of a strain rate thermal-elastic-plastic coupled model for an aluminum alloy. The dynamic J integral and recently developed incremental path-independent T^* integral are studied and the T^* integral is shown to be a more reasonable parameter in characterizing dynamic crack growth. Although the crack tip stresses and plastic strain decrease with increasing crack growth velocity, the triaxiality stress parameter is nearly unchanged in front of a moving tip. Fluctuant expansion of plastic strain zone for different growing velocities appears in the analyses. Through the cases studied here, the effect of temperature rise on the crack tip field is weaker than that of the strain rate.

KEYWORDS

thermal-elastic-plastic, strain rate, dynamic fracture, incremental path independent integral, temperature rise, crack growth, crack tip fields, triaxiality stress

INTRODUCTION

Dynamic fracture mechanics is a main offshoot of fracture mechanics and considers the effects of inertia of material element and strain rate. Due to the high strain rate near the dynamic crack tip, temperature rise is inevitable which makes the problem more complex and better understanding is necessary.

The J integral has received much attention in monotonic nonlinear fracture mechanics as it can characterize the near tip asymptotic fields. Unfortunately, in company with unloading in crack growth, the theoretical foundation of the J integral does not permit further extension of its utility. Some more reasonable integrals based on the incremental plastic theory have been proposed in recent years. The T^* integral presented by Altluri [1,2] has been developed and found application in a wide range of problems [3,4,5]. Experimental methods to measure the T^* integral have also been developed [6].

Previous works have demonstrated that the temperature rise caused by plastic deformation is significant in some cases. However, simulating model suitable for this phenomenon has not been well established [7,8]. Because the strain rate is very high at the crack tip of high velocity crack propagation, which would affect the yield stress immediately, this factor must be taken into account as well [9,10].

Consequently, this paper focuses on the coupled effect of temperature and strain rate on dynamic crack growth. The J integral and T^* integral are evaluated on the basis of finite element analyses and crack tip

stresses, strains, triaxiality stress and plastic zone are discussed.

ANALYTICAL MODEL
Dependence of the yield stress on temperature and strain rate

Based on micro scale energy transformation analyses in ductile materials, two models among yield stress σ_{ys}, temperature T and strain rate $\dot{\varepsilon}$ are proposed [11] as in the following.

$$\sigma_{ys} = \sigma_a + \sigma_p^*[1 - \frac{kT\ln(A/\dot{\varepsilon})}{\Delta H_0}]^n ,$$ (1)

$$\sigma_{ys} = \sigma_a + \sigma_p^*[\frac{1 - kT\ln(A/\dot{\varepsilon})}{\Delta H_0}] .$$ (2)

where the σ_a is internal stress and stands for non-temperature part, σ_p^* is the equivalent stress under absolute zero temperature, k is Bossman constant. Once the material constants A, σ_a and ΔH_0 are determined, yield stress can be evaluated.

Constitutive relations on the coupled effect of temperature and strain rate

A widely used empirical relationship between yield stress and strain rate is prescribed as [12,13]

$$\sigma = \sigma_G(\varepsilon, T = T_0)[1 - \beta(T - T_0)]\left(\frac{\dot{\varepsilon}_p}{\dot{\varepsilon}_0}\right)^m , \qquad m<<1.$$ (3)

where $\dot{\varepsilon}_0$ is the reference strain rate, T_0 is the reference temperature, σ_G is the yield stress under the reference strain rate, m and β are material constants. In this paper, material constants m and β are determined to be 0.005 and 0.001 by a lot of experimental results for a thin plate aluminum alloy. Recently, the above equation has been used in the study of micro scale dynamic fracture [14].

When the strain rate increases up to a certain value, the heat transformed from the plastic work cannot be exchanged with the environment, which then causes the temperature rise. The temperature rise during the adiabatic process can be calculated from the viewpoint of energy balance as

$$\Delta T = \frac{\chi}{\rho C_p}\int \sigma_{ij}d\varepsilon_{ij}^p .$$ (4)

where ρ and C_p are the density and the specific heat of a material. χ is heat transformation coefficient, which has been demonstrated to be great than 90% for large amount of metal materials once the crack growing velocity is higher than *100m/s* [7,14].

NUMERICAL PROCEDURE
Finite element model and method

The basic geometry of a compact tension (CT) specimen is as follows: length equals 120mm, width equals 110mm, thickness equals 2.8mm and crack length equals 55mm. Only one half of the model is established for the symmetric geometry. About 700 four-node elements are used in the mesh and the minimum element length is 0.25mm. Distributed force is applied to the loading hole. In order to simulate the crack growth well, spring element is used in the ligament.

Fixed mesh method is used to simulate the crack growth in this paper. In order to avoid the sudden jump during the growing process, at every crack increment, i.e. the minimum element length, the node constraint is released for several sub-steps by using the spring elements.

Practical use of the T^* integral parameter

The physical interpretations of the T^* integrals for the circle path or the Dugdale path are different. [1,2] T^* evaluated along a Dugdale path is interpreted as the energy flow into a finite-sized process zone. Dugdale path is chosen here for the sake of the application of the node constraint releasing technique. The features that T^* evaluated along the Dugdale path converges to a finite value, and it is independent on mesh size, are very helpful.

In practical operation, it is easy to perform the calculation by

$$T^*\big|_\varepsilon = T^*\big|_{\varepsilon=0} - \int_{V_\varepsilon} [W_{,1} - (\sigma_{ij}\varepsilon_{ij,1})]dV , \tag{5}$$

$$T^*\big|_{\varepsilon=0} = \int_{\Gamma_f} [Wn_1 - t_i u_{i,1}]d\Gamma + \int_{V_f} [W_{,1} - (\sigma_{ij}\varepsilon_{ij,1})]dV . \tag{6}$$

where Γ_f is a path which circles the crack far from the crack tip, and V_f is the volume within Γ_f. ε is the size of finite buffer zone around the crack. It is convenient to evaluate the integrals using Eqn. 6, and then subtracts out the V_ε term.

RESULTS AND DISCUSSIONS

The J and T^* Integrals

The effect of different paths on the evaluated values of T^* integral is shown in Fig. 1, where the symbols *1,2,3,4,5* and *6* represent paths from the far field to the near tip field. It is obvious that the values of T^* integral are consistent for far-field path marked by *1,2* and *3*. Values of the T^* integral calculated from the middle-field path are the same as that of far-field path before the crack initiation and decrease a little during the crack propagation. Symbol *6* represents the most near-field path, which is only five or six times the minimum element length away from the tip. Since the influence of finite strain is significant in the near tip, the integral values deviate from the far-field one. In the following discussions the results of the far-field integral are used. The effect of buffer zone size ε on the T^* integral is also discussed. In the FE model, which is made of the four-node element, the buffer zone of two or three element length is suggested, which is similar to that of the eight-node element.
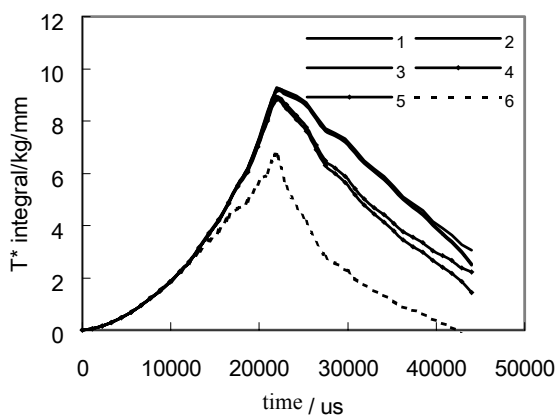
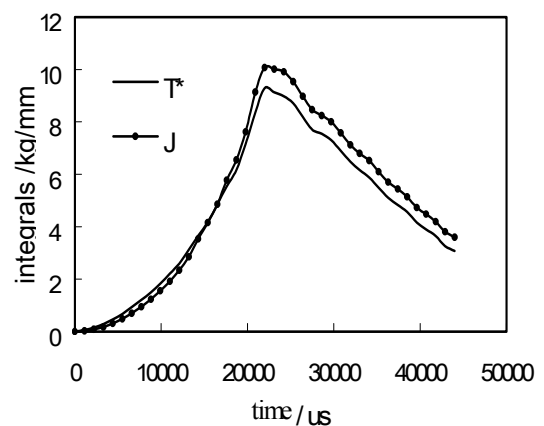Figure 1: The effect of different paths to T^* integral   Figure 2: Comparison between the two integrals

Figure 2 shows a basic feature between the T^* integral and dynamic J integral under the crack growing velocity of *0.3m/s*. The two integrals are consistent, with T^* value being a little smaller than J value. These give the meaning that under the condition of low strain rate, small crack growth, isothermal and isotropic material, monotonic loading, dynamic J integral can be extended to control crack growth for a certain length. Through the analyses of two typical stress states, it is shown that dynamic J integral is of the ability to

control a longer crack length in the state of plane stress than in plane strain.

Figure 3(a) shows T^* integral for five different crack growing velocities. It can be found that the integral decreases as crack growing velocity or growing length increases. The tendency of the T^* integral to the growing velocity is more disciplinary than that of the J integral. Further comparisons between T^* integral and dynamic J integral for different crack growing velocities are shown in Fig. 3(b). When the crack growing velocity is *100m/s*, T^* integral and J integral are consistent for a length after the crack initiate. When the growing velocity increases to *500m/s*, the consistent length is much shorter. When the growing velocity reaches up to *1000m/s*, dynamic J integral is useless. These two groups of curves are not shown for the limited space, but can be found in the reference [15]. It is very interesting that when the growing velocity is *2000m/s*, the two integrals approach again. This phenomenon can be explained by the strong effect of the inertia and stress wave under dynamic condition. The high growing velocity obviously reduces the plastic unloading zone, so the J integral is useful again. Since it is really hard for metals to reach such a crack growing velocity as *2000m/s,* generally speaking, the J control zone decreases as the crack growing velocity increases.

(a) T^* integral   (b) J integral
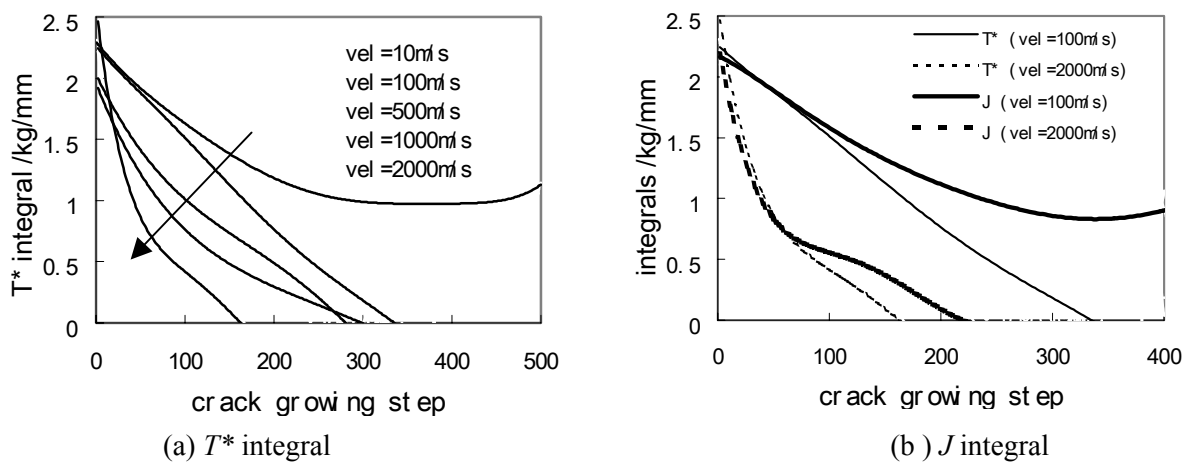
Figure 3: Comparison of integrals for different growing velocity

The effect of temperature rise and strain rate on the integral parameters are shown in table 1. The subscript '*c*' stands for the reference case in which neither temperature nor strain rate is thought of. The subscript '*t*' represents the case that only temperature effect is taken into account. The subscript '*s*' stands for the case that both temperature and strain rate are considered. It can be seen from the table that the T_t^* is slightly smaller than the T_c^*, while the J_t is nearly the same as J_c. This means that the T^* integral is more sensitive to the changes at the crack tip than the J integral. T_s^* and J_s are obviously higher than their reference values in case '*c*'. This illustrate that the effect of the strain rate is much stronger than that of temperature rise in the present calculation.

TABLE 1

THE EFFECT OF TEMPERATURE AND STRAIN RATE ON THE INTEGRAL PARAMETERS

Growing velocity	Jc	Jt	Js	Tc*	Tt*	Ts*
m/s	*kg/mm*	*kg/mm*	*kg/mm*	*kg/mm*	*kg/mm*	*kg/mm*
500	.847	.849	.872	.486	.480	.589
1000	.277	.277	.304	.118	.111	.142
2000	.370	.370	.895	.169	.157	.778

(The growing length simulated by FEA is 30mm for the velocities 500m/s and 1000m/s and 10mm for velocity 2000m/s.)

The stress and strain fields

The study of the crack tip fields is a very important aspect in the fracture mechanics. Since there is no theoretical solution for the open mode elastic-plastic dynamic crack tip fields, the study of the distribution of stresses, strains and other relevant parameters in front of a moving crack tip is essential.

Figure 4 shows the distributions of open stress σ_{yy}, equivalent plastic strain ε_p and triaxiality stress $R_\sigma = \sigma_m / \sigma_e$ in the front of a growing crack at velocity *1000m/s*. The initial position of the crack tip is located at the coordinates *(20,0)*. The crack growing direction is along the positive of the *X* direction. The symbols *1,2,3,4* and *5* represent different crack growing length *2mm, 6mm, 10mm, 14mm* and *18mm* respectively. In order to explain the features of the high velocity crack growing process thoroughly, the stable elastic-plastic crack propagation and the low velocity crack propagation are discussed at the same time, although the results are not shown. (See reference [15].) It can be seen from Fig. 4(a) that the maximum values are stable in crack growing process with high velocity. In contrast, for stable elastic-plastic crack propagation, open stress increases as the crack grows. Although the equivalent plastic strain increases for stable and low velocity crack growth, it decreases during the high velocity crack propagation, as shown in Fig. 4(b). This is due to the delay in development of plastic strain under high strain rate. From Fig. 4(c), a regular pattern can be seen that the triaxiality stress keeps constant for a certain distance in front of a growing crack tip, which exists in all cases of stable, low velocity and high velocity crack propagations. Compared with different growing velocities *100m/s, 500m/s* and *2000m/s*, it can be learned that the stress and strain both decrease when the growing velocity increase, while the maximum triaxiality stress is nearly independent of growing velocity, with the high triaxiality stress region reducing with the growing velocity.

(a) open stress   (b) equivalent plastic strain   (c) triaxiality stress
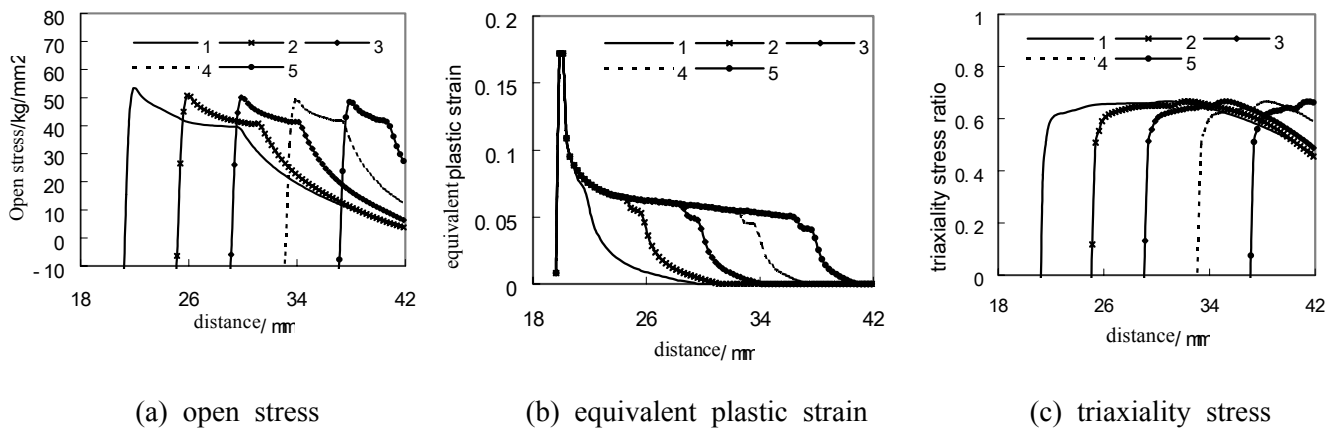
Figure 4: The distribution of stress and strain during the crack propagation
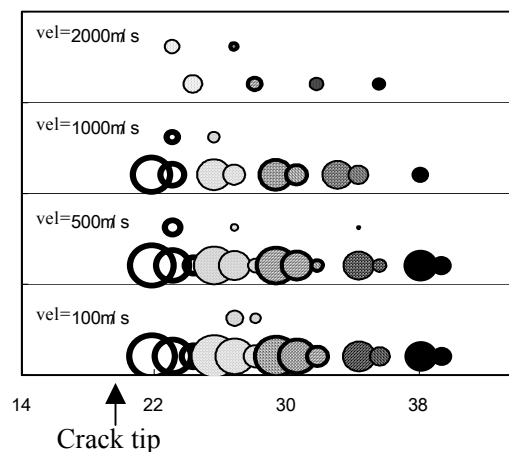

Figure 5: The evolvement of the plastic zone at different growing velocity

Figure 5 shows the evolvement of the plastic zone at different growing velocities, *100m/s, 500m/s, 1000m/s* and *2000m/s* respectively. Five crack growing lengths *2mm, 6mm, 10mm, 14mm* and *18mm* are shown by five types of circles, where the crack initiates at the coordinates of *20mm* on the axis of abscissas. The size of a circle represents the value of the plastic strain and the center of a circle gives the location of the strain. It is obvious that the plastic zone reduces monotonously under high growing velocity, while it firstly increases then decreases under moderate growing velocity. In the case of stable elastic-plastic crack propagation, a monotonous size increment of plastic zone is found.

The effect of the temperature rise and the strain rate on the growing crack tip field is discussed in detail. For the material and the loading condition considered here, the plastic zone is small, then the temperature rise is only *10℃* for a growing velocity, while the temperature drop deduced by the high strain rate is *78℃*. So we can say again that the effect of the strain rate on the crack tip field is stronger than that of the temperature.

CONCLUSIONS

The *T** integral is more reasonable in the analyses for dynamic crack growth than the *J* integral, while the dynamic *J* integral can be extended to control crack growth under certain conditions.

When the crack growing velocity increases, both the stress and the strain at the crack tip decrease, while the triaxiality stress keeps constant in front of the moving crack tip.

When the effects of the temperature and strain rate are taken into account of, it can be found that the strain rate will more strongly affect the crack tip field than the temperature.

The plastic zone evolves monotonously under both stable crack growth and high growing velocity propagation, which expands in the former and shrinks in the latter. Under a moderate growing velocity, the plastic zone increases at first, and then reduces.

REFERENCE

1. Brust, F.W., Nishioka, T. and Altluri, S.N. etc. (1985) *Engng. Fracture Mech.* 22(6), 1079-1103.
2. Altluri, S.N. and Nishioka, T. (1984) *Engng. Fracture Mech.* 20(2), 209-244.
3. Brust, F.W. and Altluri, S.N. (1986) *Engng. Fracture Mech.* 23(3), 551-574.
4. Liu, C.D., Han, Y.F. and Yan, M.G. (1992) *Engng. Fracture Mech.* 43(5), 827-836.
5. Xu, F., Guo, W. and Liu, Y.Y. (2000) *Chinese J. of Applied Mech.* 40(4), 102-106
6. Okada, H., Atluri, S.N. and Omori, Y. (1999) *J. of Plasticity* 15, 869-897
7. Kuang, Z.B and Altluri, S.N. (1985) *J. of Applied Mech.*, Trans. ASTM 52, 274-280.
8. Zehnde, A.T. and Rosakis, A.J. (1991) *J. Mech. Phys. Solid,* 39(3), 385-415.
9. Rice, J.R. and Levy, N. (1969). In: *Physics of strength and plasticity*, MIT, Cambridge, 227-293.
10. Kallivayalil, J.A., Hui, C.Y. and Zehnder, A.T. (1996) *Int. J. solids and structures*, 33(13), 1867-1889.
11. Lie, W.S., Yan, M. and Chen, B.S. (1996) *Engng. Fract. Mech.*, 53(4),633-643.
12. Pan, J., Saje, M. and Needleman, A. (1984) *Acta. Metal.* 32,157-169.
13. Needlimam, A. and Tvergaard, V. (1991) *Int. J. Fract.*, 49,41-67.
14. Sun, D.Z. and Honig, A. etc. (1995) *ASTM STP 1220*, 343-357.
15. Xu, F. (1998). *DSc Thesis*, Northwestern Polytechnical University, China.

THICKNESS DEPENDENCE OF DUCTILE TEARING IN THIN ALUMINIUM PLATES – EXPERIMENTS AND MODELLING

F. Hachez and T. Pardoen

Université catholique de Louvain, Département des Sciences des Matériaux et Procédés, PCIM, Bâtiment Réaumur, 2 Place Sainte Barbe, B-1348 Louvain-la-Neuve, Belgium

ABSTRACT

The tearing resistance of 6082O aluminum panels has been investigated using DENT (Double Edge Notched Tension) specimens of various thicknesses, t. The J_R curves were determined using a multiple-specimens method. Several geometrical parameters were measured on polished section of the unloaded specimens such as crack tip opening displacements and reduction of thickness at the crack tip. In agreement with a previous study, the J-integral at cracking initiation, J_c, and the critical crack tip opening displacement, δ_{CTODc}, were found to increase with thickness (Pardoen *et al.*, *J. Mech. Phy.s Solids* 1999). The tearing resistance also increases with thickness. The potential of a 3D-interface cohesive zone model to predict the crack propagation rates and the thickness effect has been analyzed. An original method is proposed to experimentally determine the work per unit area spent for material separation in the pure plane stress regime. The limit of cohesive zone type of models for covering the full range of thicknesses from plane stress to plane strain is discussed based on considerations related to the void growth micromechanism.

INTRODUCTION

The demand for lighter structures relies on the use of thinner plates, which, in turn, implies the development of both more resistant and damage tolerant alloys and more robust methods for structural integrity assessment. One important open issue about the structural integrity assessment of thin plates concerns the thickness dependence of cracking resistance in the plane stress or approximately plane stress regime. The difficulty with thin ductile plates lies in the 3-D character of the crack tip stress and strain fields. Pure plane stress analysis is only acceptable for thin sheets. Diffuse and localized plastic yielding coexist under the form of a neck at the crack tip surrounded by a large plastic zone. The macroscopic fracture toughness of thin plates, as given by the value of the J-integral at cracking initiation J_c, results from energy spent in the fracture process zone in front of the crack tip. Two contributions can be distinguished:

- the work per unit area for necking which depends on thickness (indeed, the height of the necking zone increases proportionally to the plate thickness);
- the work per unit area for damage until final material separation in a localized band (noted Γ_0). The height of that band is dictated by the fracture mechanism and is thus, in principle, geometry independent.

The fact that J_c includes the work of necking, which can be sometimes much larger than Γ_0, induces the well-known thickness effect [1,2,3]. As long as the stress state is purely plane stress, fracture toughness linearly increases with thickness. As thickness increases, the crack tip stress field evolves towards plane strain and the increase of the fracture toughness slows down, reaches a maximum and decreases finally to the plane strain value. Strictly speaking, J_c is thus not a material property because of the thickness dependence.

Cracking in 6082O aluminum plates has been investigated using DENT specimens of various thicknesses, t, (from 1 to 6 mm) with constant ligament length $l_0/W = 1/3$ (see Fig. 1). In Ref. [4], only the fracture

toughness at cracking initiation has been discussed in terms of J_c and of the critical crack tip opening displacement δ_{CTODc}. A method was proposed for separating the fracture work spent for localized necking and the work for material separation. 3D finite element simulations have been performed in order to investigate the effect of the thickness on the stress triaxiality inside the fracture process zone.

In this report, we present the second part of the study devoted to the characterization and modeling of the effect of the thickness on the tearing resistance. The pertinence of 3D cohesive zone elements for modeling the fracture process is investigated. The fact that the basic cohesive zone formulation does not incorporate any effect of the stress triaxiality will turn out to be a major limitation for its use in thin plate fracture.
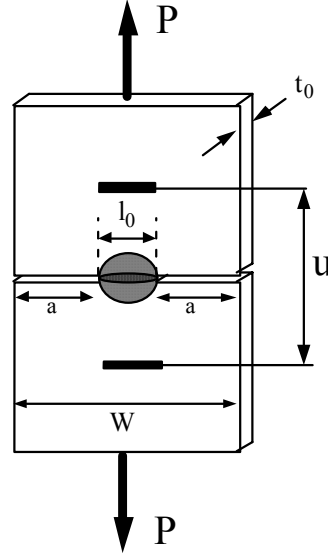
Figure 1. Testing of a DENT specimen

MATERIAL AND EXPERIMENTAL PROCEDURES

The material consists of 6 mm-thick plates of aluminum alloy 6082 in O temper. Low values of hardness (35HBN) and yield stress (σ_0 = 50MPa) are well suited for the purpose of this study. Indeed, high ductility results in a large range of thicknesses for which 3D effects (out-of-plane constraint effects) significantly affect fracture toughness. The flow rule is well represented by a power law curve

$$\sigma = 202.1 \, \varepsilon^{0.247} \, . \tag{1}$$

The Young's modulus is equal to 70 GPa, and the Poisson ratio is equal to 0.34. In order to obtain a wide range of thicknesses without change of the microstructure, the 6mm-thick plates were thinned by mechanical milling. Microstructure was found homogeneous along thickness. In this report, results for 4 different plate thicknesses will be discussed: 0.6, 1, 2 and 4 mm. The other dimensions of the DENT specimens, length and width, were 150 mm x 60 mm. Notches were made by cutting the plate first with a saw and subsequently with a fresh razor blade in such a way as to obtain sharp initial notch tips. The validity of this precracking method is justified by the large values of δ_c. The specimens were strained along the rolling direction for various degree of crack extension Δa. J has been computed from the load-displacement curve using the simple relation derived by Rice *et al.* [5] to evaluate a mean value for the J integral ("mean" because J varies along the crack front)

$$J_{DENT} = \frac{K_I^2}{E} + \frac{1}{l_0 t_0}\left[2\left(\int_0^{u_p} P du_p \right) - P u_p \right] \tag{2}$$

where K_I is the stress intensity factor, E the Young's modulus, P the applied load, and u_p is the plastic displacement. After unloading, the specimens are machined, embedded in an edge-retention resin, ground and polished. Each specimen is ground and polished several times in order to measure Δa through the

thickness, which allows quantifying the magnitude of the tunneling effect. Crack tip opening quantities were also measured in order to estimate the CTOD at crack initiation, δ_{CTODc}, following the method of ref. [6].

EXPERIMENTAL RESULTS

The fracture profile of broken DENT specimens of alloy A6082O presents shear lips restricted only to the surface of the plates. The fracture profile is, for the different plate thicknesses, predominantly flat along the whole ligament length (on a macroscopic point of view). A classical profile with dimples is observed at the microscale. The phenomenon responsible for cracking initiation is mechanism of void growth and coalescence. Shear localization is definitely not the dominant phenomenon (no slant fracture). After a transient of crack extension, the crack tip necking becomes steady-state with a reduction equal to about 60% of the initial thickness [4], independently of the value of the initial thickness.

The J_R curves for thicknesses 0.6, 1, 2 and 4 mm are given on Figure 2. A change of thickness significantly affects both the initiation of cracking and the tearing resistance.
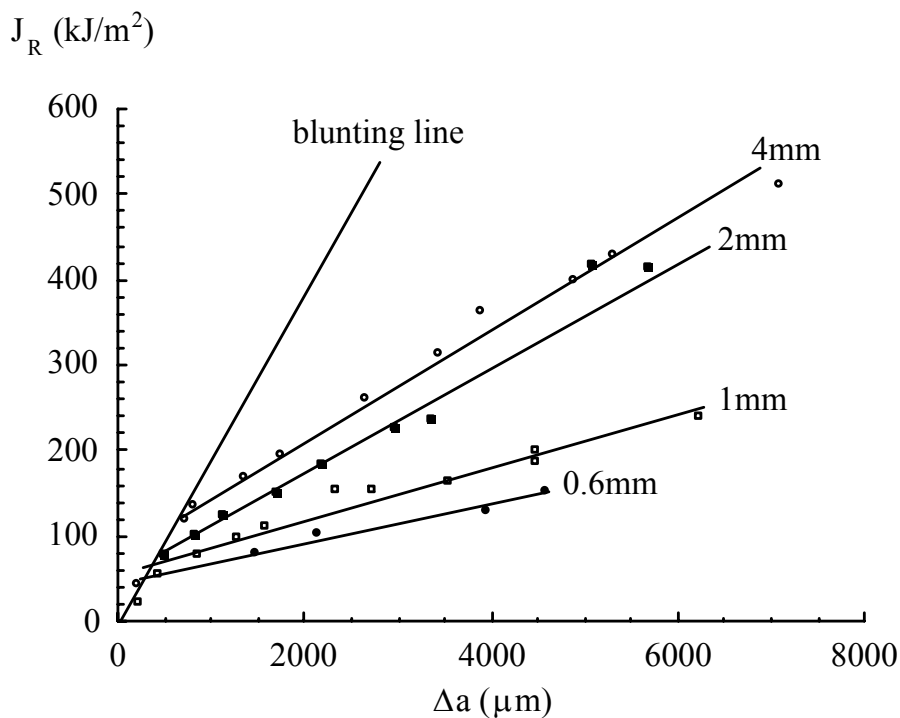
Figure 2: J_R curve for DENT plates with 0.6, 1, 2 and 4 mm thickness
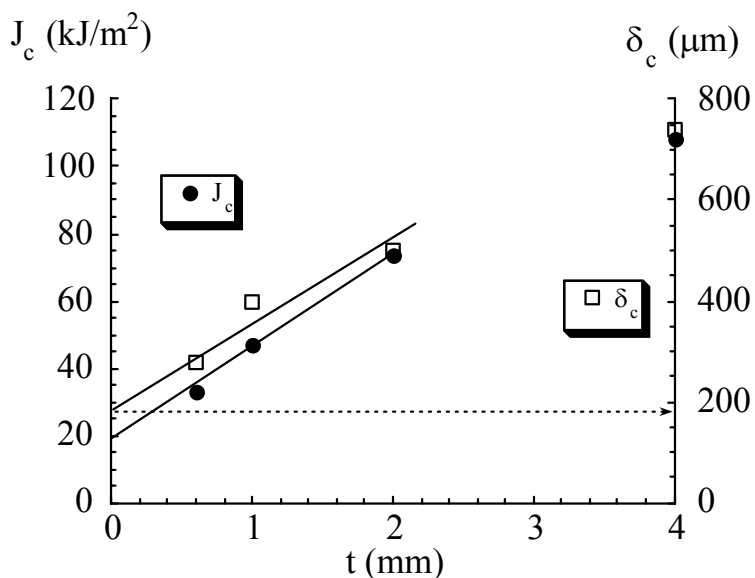
Figure 3: Variation of J_c and δ_{CTODc} as a function of the plate thickness

Figure 3 shows the variation of J_c at cracking initiation (defined in a physical sense as the first cracking event) as a function of thickness. These values of J_c are more accurate than the one obtained in ref. [4] where cracking initiation was detected by means of a camera equipped with a zoom focusing on the midsection of the specimen (the new results naturally give smaller J_c's). Linear regression of the variation of J_c as a function of t (the regression is performed only on data corresponding to small specimen thicknesses which giving rise to near plane stress regime) yields a constant terms equal to about 20 kJ/m², which agrees with the results of ref. [4]. Figure 3 also shows the variation of the CTOD at cracking initiation as a function of the thickness. Linear regression of the variation of δ_{CTODc} as a function of t yields a constant terms equal to 0.18 mm.

In ref. [4,7], it was proposed that this regression allows separation of the fracture work per unit area spent for material separation Γ_0 and the work for necking at the crack tip. The new parameter Γ_0 would correspond to the constant work required for nucleation, growth and coalescence of voids, until final separation in one localized band inside the fracture process zone (FPZ). This fracture work more intrinsically characterizes fracture resistance of thin plates because it does not depend on thickness and it is more directly related to the mechanisms occurring in the FPZ. It can be seen as a "purely plane stress fracture toughness". The pertinence of this idea will be assessed in the next section using the cohesive zone approach. We must stress the fact that this more "intrinsic" work of fracture does not correspond to the work of fracture of very thin plates or sheets, for which the fracture mechanisms are different. In other words, the linear regression cannot be assimilated to an extrapolation of the fracture toughness values at $t = 0$. The same interpretation holds for introducing the concept of a "plane stress crack tip opening displacement" δ_c.

Crack tunneling was found negligible for the 0.6 and 1 mm plates. In the 2 mm and 4 mm plates, the difference in crack extension between the center and the surface in the steady state regime amounts to 0.9 mm and 2 mm, respectively. The important crack tunneling effect in the 4 mm plate demonstrates significant differences of stress states between the center and surface, in agreement with the finite element results obtained in ref. [4] for a static crack.

MODELLING OF DUCTILE TEARING USING 3D SURFACE COHESIVE ELEMENTS

The tensile tests were simulated in 3-D using the general-purpose finite element program ABAQUS (Hibbit, Karlsson & Sorensen, Inc.). The bulk material is modeled by the J_2 flow theory with isotropic hardening. 3D cohesive zone elements were introduced on the plane of symmetry of the plates. The cohesive zone elements were implemented using a User defined Element (UEL). Details about the formulations of 3D cohesive zone elements can be found in [8]. The cohesive zone form (see Figure 4) used in this work can be characterized, in the case of purely mode I loading, by 5 parameters: Γ_0, δ_c, σ^{max}, λ_1, and λ_2 (but only four of these parameters are independent) as proposed by Tvergaard and Hutchinson [9].
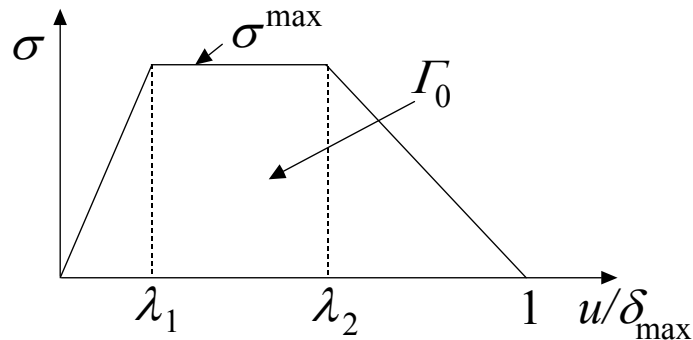

Figure 4: Cohesive zone representation with tensile stress σ as a function of normal displacement u

The parameters of the cohesive zone model were calibrated in the following way. A first set of parameters Γ_0 and δ_c is obtained from the experimental data as explained in the previous section. Then, the results

obtianed for the smallest thickness (i.e. the closest to a pure plane stress state), 0.6 mm in this case, are used to calibrate the maximum stress σ^{max} (by tuning the values of λ_1 and λ_2). Figure 5 show conspicuous agreement between the results of the 3D FE simulation and the experimental J_R curve for the 0.6 mm plate using a peak stress of 200 MPa. The degree of crack tip necking is also correctly reproduced by the numerics.

However, keeping the same set of parameters (δ_c, σ^{max}) to model the cracking of the specimens with larger thickness leads to significant underestimation of the initiation toughness and, to a smaller extent, of the tearing resistance. The best choice of parameters for the other thickness are: for 1 mm, $\delta_c = 0.2$ mm and $\sigma^{max} = 200$ MPa, for 2 mm, $\delta_c = 0.25$ mm and $\sigma^{max} = 220$ MPa. For the 4 mm thickness, a peak stress larger than 220 MPa would be required for matching against the experimental tearing resistance. However, the low constraint close to the specimen surface prevents the tensile stress to reach peak stress larger than 220 MPa. The cohesive elements close to the surface thus never fail for such large peak stresses leading to unphysical results. Consequently, for the 4 mm plate δ_c and σ^{max} have to be tuned along the thickness too.
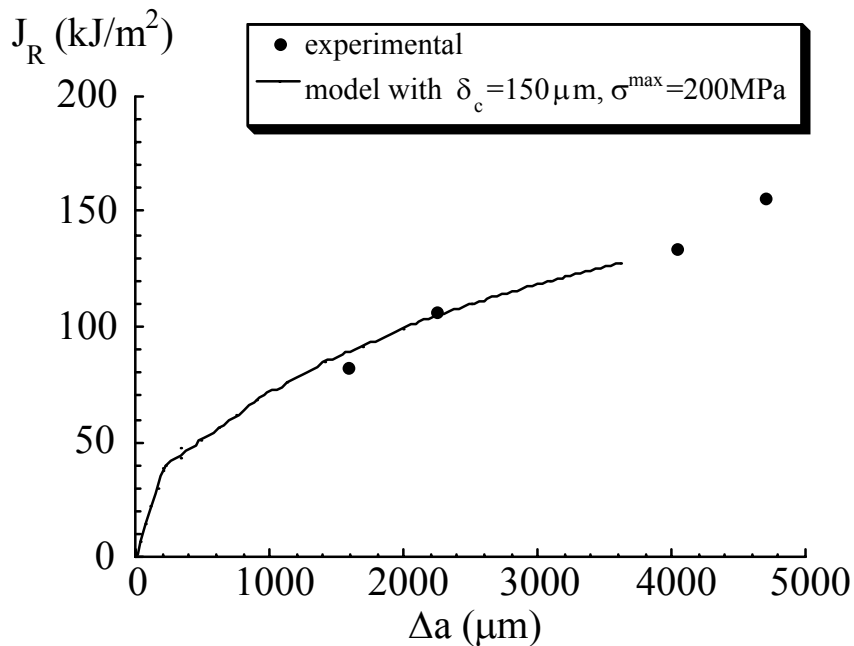
Figure 5: Comparison of the simulated and experimental J_R curve for a 0.6mm thickness DENT plate

DISCUSSION AND CONCLUSIONS

The results presented in Figure 5 suggest that the "intrinsic" critical displacement and fracture work obtained by the linear regression on the experimental fracture toughness data can be used as the maximum opening and the area under the stress / opening curve in a cohesive zone model when modeling plane stress or close plane stress fracture (same for the maximum opening equal to the constant term in the regression on δ_c data).

However, the simple formulation of a stress state independent cohesive zone model is too limited for addressing situations intermediate between plane stress and plane strain. In other words, dependence of the peak stress and of the maximum opening on the stress state is necessary, meaning that the cohesive zone parameters will depend on the thickness and on the location through the plate thickness. This fact has already been recognized by several authors [10,11]. It comes from that the mechanism of ductile fracture is very dependent on the stress triaxiality. The cohesive zone formulation can be enhanced by introducing a link with the local stress triaxiality. However, it is exactly the purpose of full constitutive models such as the various versions of the Gurson model [12,13,14], to take these effects into account based on rigorous micromechanical approach. Furthermore, full constitutive models, in principle, allow dealing with slant fracture, which is also not easy to model with cohesive zone elements.

Cohesive zone approaches remains probably very useful for addressing the two extreme plane stress or nearly plane strain situations, as well many other fracture problems. For theplane strain case, it is important to note that as long as the stress triaxiality is large enough, typically above 2.5, the parameters of the fracture process are almost independent of the stress triaxiality.

REFERENCES

1. Bluhm, J.I. (1961). *ASTM Proc.* **61**, 1324
2. Swedlow, J.L. (1965). *ARL 65-216*, Aerospace Research Laboratories, Office of Aerospace Research, United State Air Force, Wright-Patterson Air Force Base, OH
3. Knott, J.F. (1973). *Fundamentals of Fracture Mechanics*, Butterworth, London
4. Pardoen, T., Marchal, Y., and Delannay, F. (1999). *J. Mech. Phys. Solids* **47**, 2093
5. Rice, J.R., Paris, P.C., and Merkle, J.G. (1973). In: *Progress in Flaw Growth and Fracture Toughness Testing*, ASTM STP 536, American Society for Testing and Materials, Philadelphia, 231-245
6. Pardoen, T. and Delannay, F. (2000). *Engng. Fract. Mech.* **65/4**, 455-466.
7. Pardoen, T., Marchal, Y., and Delannay, F. (2001). *Engng. Fract. Mech.*, accepted for publication
8. Arun Roy, Y., Roychowdhury, S., and Dodds, R.H. (2001) *Int. J. Fract.*, in press
9. Tvergaard, V. and Hutchinson, J.W. (1992). *J. Mech. Phys. Solids* **40**, 1377
10. Siegmund, T. and Brocks, W. (1999). *Int. J. Fract.* **99**, 97
11. Tvergaard, V. and Hutchinson, J.W. (1996) *Int. J. Solids Struct.* **33**, 3297
12. Gurson, A.L. (1977). *J. Engng. Mater. Tech.* **99**, 2
13. Needleman, A. and Tvergaard, V. (1984). *J. Mech. Phys. Solids* **32**, 461
14. Pardoen, T. and Hutchinson, J.W. (2000) *J. Mech. Phys. Solids* **48**, 2467

THREE-DIMENSIONAL FATIGUE FRACTURE IN COMPLEX ENVIRONMENTS

W. Guo[1,2] Ping Wang[2]

[1]Departmant of Aircraft Engineering, Nanjing University of Aeronautics & Astronautics,
Nanjing, 210016, CHINA
[2]Key Laboratory of Mechanical Structural Strength and Vibration, Xian Jiaotong University,
Xian, 710049, CHINA

ABSTRACT

Some important problems in fatigue fracture of metal materials and structures under complex loading conditions and corrosion environments are analyzed on the basis of three-dimensional (3D) elastic-plastic fracture theory and experimental results. Special emphases are given for corrosion fatigue crack growth which is shown to be independent of stress ratio and geometry of specimen when represented by use of the three-dimensional theory. A 3D method for fatigue life prediction was established and life prediction under spectrum loading in corrosion environment can then be performed without requirement of any empirical parameter or extra-parameter to be determined by no standard tests. The prediction of whole fatigue life of structures and the calendric life of machines are discussed along this line. The efforts have been made in this direction by the fatigue fracture community in China are addressed briefly.

KEYWORDS

Three-dimensional constraints, fatigue crack growth, corrosion fatigue, life prediction, calendric life

INTRODUCTION

Fatigue fracture of structures is always analyzed or predicted on the basis of standard material test data obtained in laboratory. From standard specimens to real structures there exist significant differences in geometry configuration, size, stress state, loading configuration as well as environmental factors. Therefore, the reliability of the analysis and prediction is determined by the ability of the applied theory to eliminate these differences. Some of the efforts we have made in this direction are introduced in this paper and researches of the fatigue fracture community in China are addressed briefly.

THEORETICAL FUNDAMENT

For ideally two dimensional sharp crack, the near tip stress field in strain hardening material can be obtained from the HRR solution and the recently developed *J-Q* theory or higher order solutions[1]

$$\sigma_{ij} = \left[\frac{J}{\alpha \varepsilon_0 \sigma_0 I(n) r} \right]^{1/(n+1)} \tilde{\sigma}_{ij}(\theta) + Q\delta_{ij} . \tag{1}$$

3D studies show that crack tip fields are not only dependent on J-integral and in-plane constraint, but also dependent on out-of-plane constraint and in the case of $\partial Tz/\partial z < \infty$, a *J-$T_z$-$Q_T$* description can be proposed [2]

$$\sigma_{ij} = \left[\frac{J}{\alpha \varepsilon_0 \sigma_0 I(n, Tz) r} \right]^{1/(n+1)} \tilde{\sigma}_{ij}(\theta, Tz) + Q_T \delta_{ij} . \tag{2}$$

Here, the *x-y* or *r-θ* plane is coincided with the normal plane at any point P of the crack front line, *z* is along the tangent line of the crack front and *y* perpendicular to the crack plane at P. Then the constraint in the *x-y* plane is the in-plane constraint that can be determined by the *K-T* or *J-Q* theory. The out-of-plane constraint in *z*-direction can be expressed by $T_z = \sigma_{zz}/(\sigma_{xx} + \sigma_{yy}) = \sigma_{zz}/(\sigma_{rr} + \sigma_{\theta\theta})$. In the front of through cracks or notches in finite thickness plate under mode I loading, empirical expression of T_z has been obtained in [2] and [3] respectively.

For a through cracked plate with thickness of *B=2h*, the average tensile stress in the plastic zone ahead of the crack can be expressed as $\sigma_{yy} = \alpha_s \sigma_{ys}$ in a ideally-plastic material obeying Von Mises rule with the stress constraint factor

$$\alpha_s = \frac{1}{\bar{r}_p B} \int_{-h}^{h} \int_0^{r_p} \frac{\sigma_{ys}}{\left[(1 - T_z + T_z^2)(1 + k^2) - (1 + T_z - 2T_z^2)k \right]^{1/2}} dr dz . \tag{3}$$

Where, $k = \sigma_{xx}/\sigma_{yy}$ is dependent on the in-plane constraint *T* or *Q*, σ_{ys} is the yield stress, r_p is the plastic zone size and $\bar{r}_p$ is the through-thickness average of r_p. α_s is found to be a function of $\bar{r}_p/B$ and for strain hardening material of *n* as well. In plane stress state, $T_z = 0$, $k = 0.5$ and $\alpha_s = 1.155$ in perfectly plastic solution. In plane strain state, $T_z = 0.5$, $k = 0.611$ and $\alpha_s = 2.97$ in the perfectly plastic solution.

In corrosion environment, the influence factors on fatigue crack growth are complex. Generally, material degradation caused by the corrosion and the change in effective driving force for crack growth caused by fatigue crack closure are the most important factors. For aluminum alloys, it has been shown that the corrosion environment has no effect on fatigue crack closure [4]. Thus the effective stress intensity factor can be obtained as in laboratory ambient.

It has been proven that plasticity induced fatigue crack closure is dominated by a combining constraint factor α_t [5]：

$$\frac{\alpha_t}{\beta} = \frac{\mu \pi}{(\kappa + 1)\beta \sigma_{ys}} \frac{\delta_0}{r_p} . \tag{4}$$

Where, μ is the Lame constant，$\kappa = \dfrac{3 - v - 4vTz}{1 + v}$，$\beta$ is the stress constraint factor in the reverse yield zone，δ_0 is the crack tip opening displacement. By use of the 3D constraint theory and the Budiansky-Hutchinson model it can be obtained that [5]

$$\frac{K_{open}}{K_{max}} = 1 - \frac{1}{\pi}\int_0^\eta \frac{f_1(\xi) - f_2(\xi)}{\sqrt{\xi}}d\xi, \tag{5}$$

where f_1 and f_2 are known functions and η is a parameter which can be determined as a function of stress ratio R and α_t/β by the following equation set,

$$\begin{cases} R\pi = \dfrac{\beta\pi}{2\alpha_t}\displaystyle\int_0^\eta \sqrt{\dfrac{\eta - \xi}{\xi(\xi - \gamma)}}d\xi + \displaystyle\int_\eta^1 \sqrt{\dfrac{\xi - \eta}{\xi(\xi - \gamma)}}f_1(\xi)d\xi \\[4mm] R\pi = -\dfrac{\beta\pi}{2\alpha_t}\displaystyle\int_0^\eta \sqrt{\dfrac{\xi - \gamma}{\xi(\eta - \xi)}}d\xi + \displaystyle\int_\eta^1 \sqrt{\dfrac{\xi - \gamma}{\xi(\xi - \eta)}}f_1(\xi)d\xi \end{cases}. \tag{6}$$

Solve the integral equations (5) and (6) and fitting the results can lead to an empirical expression of the opening stress ratio:

$$\frac{K_{open}}{K_{max}} = 1 - \sqrt[3]{\eta} \tag{7}$$

$$\eta(R,\alpha_t) = (1 - R^2)^2(1 + 10.34R^2)\left[(1 + 1.67R^{1.61}) + \frac{\beta}{0.15\pi^2\alpha_t}\right]^{-4.66}. \tag{8}$$

For a large range of β/α_t ($1.0 < \beta/\alpha_t < 3.0$) and $R \geq 0$, the fitting error of expression (7) and (8) is less than about 3%. For $R<0$, a linear relationship between the opening stress ratio and R can be assumed.

Under small scale yielding condition, $\alpha_s \approx \alpha_t$. Assume $\beta=1$ and $\alpha=\alpha_t=\alpha_s$, it can be found that the expression (7) and (8) coincides very well with Newman's empirical equation of crack closure [6]. So that Newman's equation is a special case of the present solution. When $R<0$, Newman's equation can be used.

Consequently, under small scale yielding condition the fatigue crack growth rate can be expressed as a function of equivalent stress intensity factor range

$$\Delta K_{eff} = (1 - K_{open}/K_{max})K_{max}, \tag{9}$$

or

$$\frac{da}{dN} = \begin{cases} f\left(\Delta K_{eff}\right) & \text{for} \quad \Delta K_{eff} > \Delta K_0 \\ 0 & \text{for} \quad \Delta K_{eff} \leq \Delta K_0 \end{cases}. \tag{10}$$

Where, ΔK_0 is a material constant.

MATERIAL BASE LINE FOR CRACK PROPAGATION

Material Base Line in Laboratory Ambient

Life prediction is always based on the da/dN-ΔK test curve under constant amplitude loading with standard specimens. This curve changes with stress ratio as well as specimen thickness and is not a material base line as shown in Figure 1. In the figure the da/dN-ΔK curve is obtained from standard compact tension specimens of 2mm and 10mm-thickness machined from a thick LY12-CZ aluminum mother plate. To avoid other influence factors the specimens take from the same position of the mother plate and have the same in-plane geometry with width of 60mm. When ΔK_{eff} obtained from the above 3D closure model is used a unique da/dN-ΔK_{eff} is obtained for both thicknesses. Such da/dN-ΔK_{eff} curve is also independent of stress ratio so that it can serve as the material base line for fatigue crack propagation.
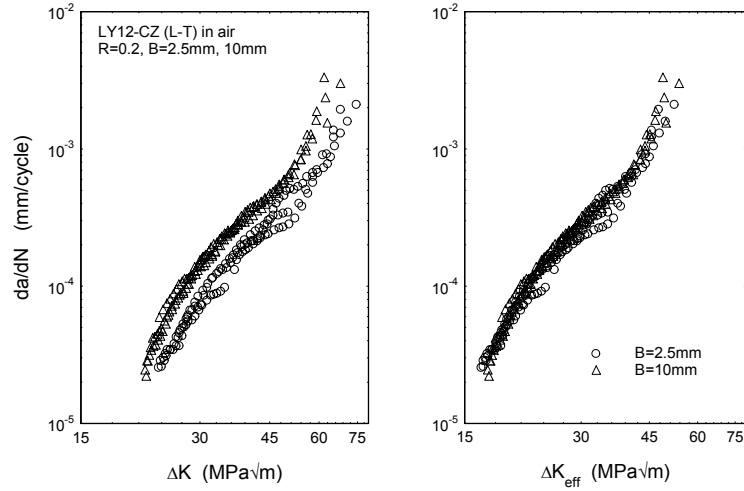
Figure 1: Effect of thickness on fatigue crack growth of LY12 aluminum alloy

Material Base Line for Corrosion Fatigue Crack Growth

Corrosion fatigue curve of da/dN-ΔK is generally higher than that in laboratory ambient and changes with the combination of material-environment-loading-geometry. When the above theory is used the da/dN-ΔK_{eff} curve become independent of loading and geometry parameters and unique for given combination of material-environment. In Figure 2 some typical results are presented for an aluminum alloy. It is shown that corrosion fatigue crack closure can be explained very well by plasticity-induced closure theory.

Figure 2: Effect of stress ratio on corrosion fatigue crack growth curve of 7050 aluminum alloy
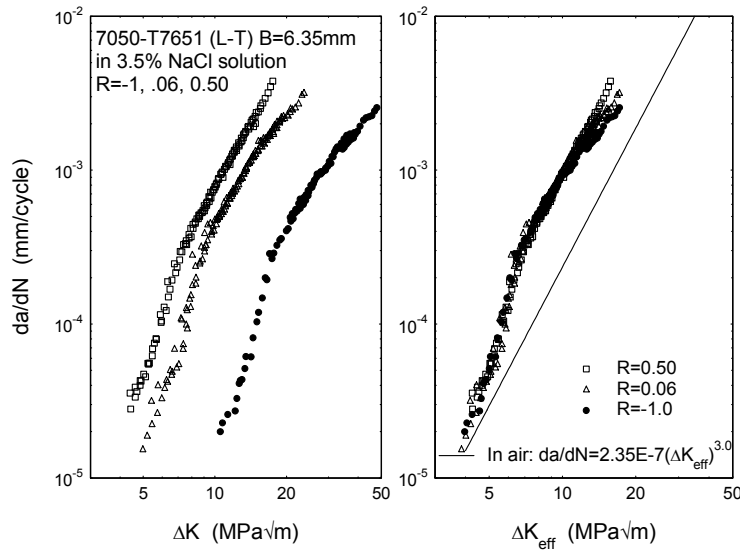
For Al-alloys and Ti-alloys, the effects of frequency is very weak and the expression (10) can be used for given material-environment system. In steels, however, corrosion fatigue crack growth is very sensitive to loading frequency. As the plasticity induced crack closure will not change with frequency (λ), so the da/dN-ΔK_{eff} curve is still free from the stress ratio and geometry. So the crack propagation rate can be expressed in form of variable separation

$$\frac{da}{dN} = \begin{cases} f\left(\Delta K_{eff}\right) \times f_H(\lambda) & \text{for} \quad \Delta K_{eff} > \Delta K_0 \\ 0 & \text{for} \quad \Delta K_{eff} \leq \Delta K_0 \end{cases}. \tag{11}$$

$f_H(\lambda)$ can be determined by experiment.

CORROSION FATIGUE LIFE PREDICTION UNDER SPECTRUM LOADING

Service life of structures can be reduced in corrosion environment mainly for two reasons: reduction of initiation life of a micro-crack by corrosion pitting and rise in crack propagation rate as shown above. The former influence can be represented by a large initial crack size a_0, while the later can be simple predicted by use of the corrosion fatigue crack growth base line (10) or (11). The effective initial crack size a_{0eff} in corrosion environment is a function of time that has to be determined by experiment or survey of aging structures. a_{0eff} is a statistic parameter having close relation with materials, environments, lasting time, interaction of environment and mechanical loading, *et al*.

As the plasticity induced crack closure is not affected by the corrosion environment, load interaction in spectrum corrosion fatigue caused by plasticity can be predicted by the plasticity-induced crack closure model. By use of the corresponding corrosion fatigue curve of da/dN-ΔK_{eff} and the modified FASTRAN-II life prediction code [6], the initial defect size dependent limit stress-life (S_L-N) curve of an aluminum alloy in sump-tank water under fighter spectrum is predicted and the results are presented in Figure 3. In the bi-logarithm coordinates the S_L-N curve is shown to be a linear line for different a_0.

Experiments have been performed on fastener specimens of 7475-T761 aluminum alloy in 3.5% NaCl solution under another kind of fighter spectrum. Specimens with straight hole as well as 90° dimple rivet hole are tested by MTS880 system. It is found that crack initiation always occurs at the intersected corner of the dimple with the hole in form of corner crack in the rivet hole specimen. Stress intensity factor for this kind of crack is calculated by 3D finite element code of ANSYS®. The present life prediction method and the da/dN-ΔK_{eff} curve of long crack of the material in the same environment are used to calculate crack growth life. When the initial defect size a_0 are determined in air and the salt solution by use of the straight hole test data in a manner of trial-and-error, the same a_0 is used to predict the life of the rivet hole specimens. The experiment results as well as the predicted results are drawn in Figure 4. Pretty agreement between the experiment and predicted results can be found.
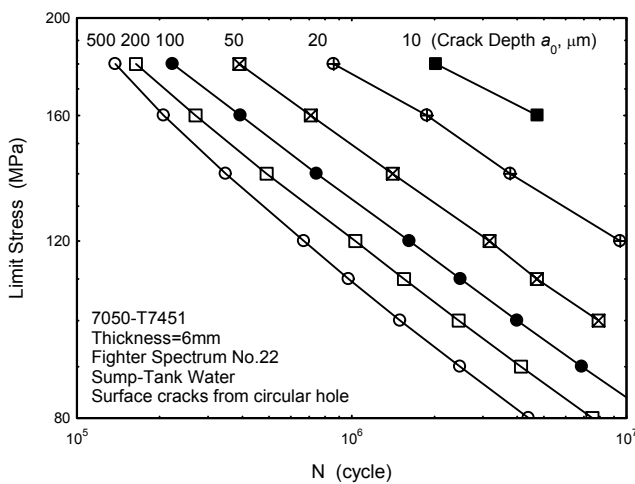
Figure 3: Effect of initial defect size on limit stress-life curve of 7050 Al in sump-tank water
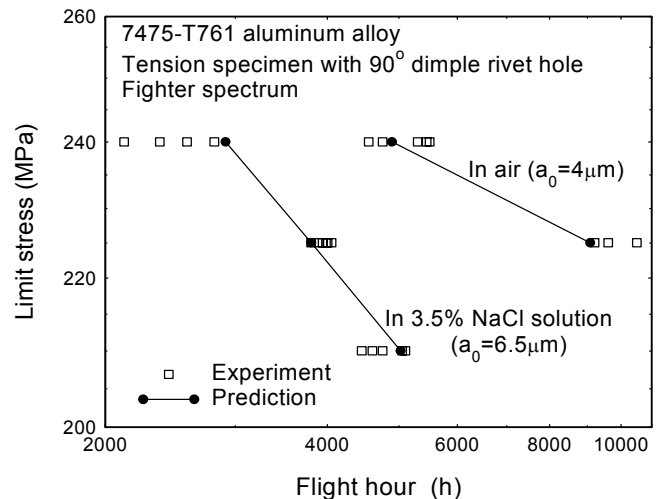
Figure 4: Life prediction for 7475-T761 under spectrum loading in air and 3.5% NaCl solution

It is shown that life of aluminum alloy can be remarkably reduced by the salt solution. The lower the stress level applied, the greater the reduction in life can be found. The initial crack size a_0 in the salt solution is also larger than that in air for the same material. From the viewpoint of life prediction, corrosion environments affect the structure by means of increasing both of the size of defects or corrosion pits and crack growth rate. The essential contents for life prediction in complex environments are illustrated in Figure 5.
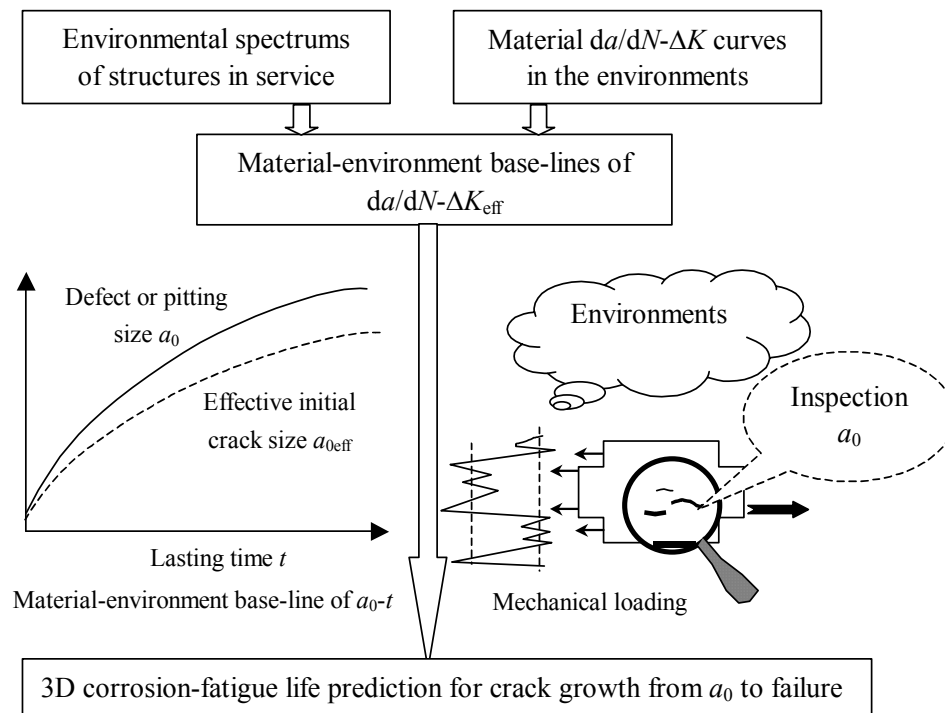
Figure 5: Illustration for life prediction in complex environments

The China community has paid great efforts toward solving the problem mainly in the following areas: 1) Compilation of environmental spectrums for mechanical systems used in different region of China and for different task. A wide range of environments has been surveyed. 2) Material degradation, especially reduction in fatigue strength in out-door air and other natural environments in different region of China has been studied for more than 20 years and it is shown that the reduction in fatigue strength in the first few years may be significant in some regions but the degradation rate slows down with time lasting. Structural materials for aircrafts, pipelines, sea structures and cars are studied extensively. Speeded simulation and damage equivalent study in controlled artificial environment in laboratory are important parts in the program. Inspection and survey of aging aircrafts, sea structures have been in processing. 3) Material base-lines for corrosion fatigue, creep fatigue are in accumulating. New materials and special details of structures such as welds and fasteners are widely studied. 4) Corrosion protection, repair and other surface engineering are studied and widely applied in both civil and defense engineering. 5) Based on these researches, calendric life of aircrafts and other important mechanical systems is intensively studied at present stage in order to extend the service life of aging structures.

ACKNOWLEDGEMENTS

REFERENCES

1   O'dowd.N.P and Shih.C.F. (1991) *J. Mech. Phys. Solids* **39,** 989-1015.

2   Guo W. (2000) *Key Engineering Materials* **183,**193-198.

3   Li Z.H. and Guo W. (2001) *Int.J.Fract.* **107**, 53-71.

4   He B., He J. and Fan W. (1997) *J. Nanjing Univ. Aero-& Astronautics* **29**, 786.

5   Chang T. and Guo W. (1999) *Int.J.Fatigue* **21,** 881-888.

6   Newman J.C.Jr. (1992) FASTRAN-II. *NASA TM* 104159.

THREE-DIMENSIONAL MIXED MODE FRACTURE OF CEMENT MORTAR

K. Zhong, K. W. Lo and T. Tamilselvan

National University of Singapore, 10 Kent Ridge Crescent, Singapore 119260

ABSTRACT

In practice, most engineering components undergo complex three-dimensional loading and contain, or are assumed to contain, cracks or crack-like flaws. However, theoretical and experimental studies on mixed mode I, II and III fracture have only just begun in recent years.

In this study, a generalised criterion for the extension of a mixed mode fracture surface in three dimensions is proposed as an extension of the *unified model*, based on the notion of a simple conversion of pure mode to mixed mode loading energy, in direct proportion to their respective fracture energies. The criterion may be represented as the 3-dimensional surface depicted in Figure 1.

The proposed criterion has been tested against the behaviour of beam specimens (Figure 2) of cement mortar which were subjected to three- or four-point bending, as well as four-point shear. A grooved ligament which was rotated both vertically and horizontally with respect to the beam section was formed in the specimen, where each specimen had different orientations of the ligament and were subject to various loading combinations, so as to provide mixed mode loading conditions at the crack front. In doing so, the crack might be initiated and hence guided to extend along the truncated V-shaped throat segment as a mixed mode fracture, thereby providing a means of verifying the efficacy of the fracture envelope. The stress intensity factors K_I, K_{II} and K_{III}, of the respective modes of deformation were determined by three-dimensional finite element analysis, where the data pre-processing was undertaken by PATRAN, while the solution process was carried out by ABAQUS. The results of the analyses, as well as measurements made on the INSTRON 1334 servo-hydraulic testing machine, will be presented in the following text, and the proposed fracture criterion thereby validated.
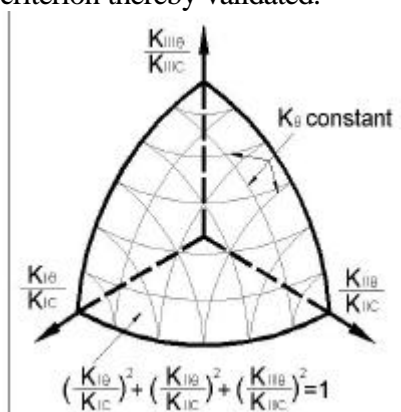
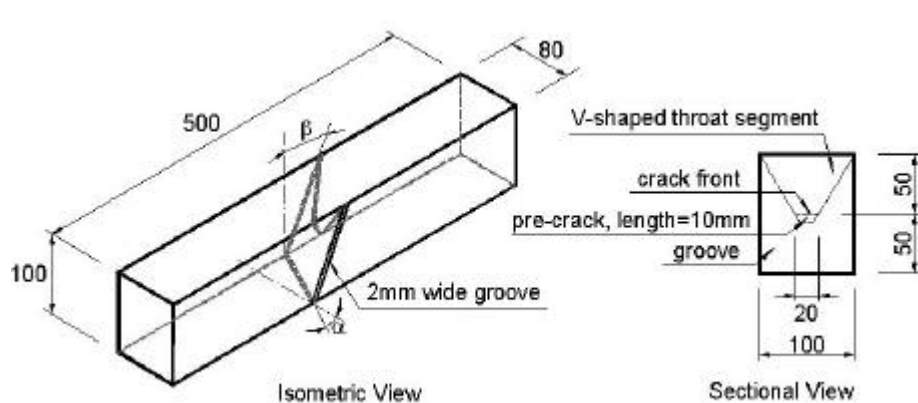**Figure 1:** Unified mixed mode I, II and III fracture envelope

Figure 2: Beam specimen subject to mixed mode I, II and III loading (units in mm)

THREE-DIMENSIONAL MIXED MODE FRACTURE OF CEMENT MORTAR

K. Zhong, K. W. Lo and T. Tamilselvan

National University of Singapore, 10 Kent Ridge Crescent, Singapore 119260

ABSTRACT

A generalised criterion for the extension of a mixed mode fracture surface in three dimensions is proposed. The criterion has been tested against the behaviour of beam specimens of cement mortar which were subjected to three- and four-point bending, as well as four-point shear. A grooved ligament which was rotated vertically as well as horizontally with respect to the beam section was formed in the specimen, where each specimen had different orientations of the ligament, so as to provide differing mixed mode loading conditions at the crack front. In doing so, the crack could be initiated and hence guided to extend along the truncated V-shaped throat segment as a mixed mode fracture, thereby providing a means of verifying the efficacy of the fracture envelope.

The stress intensity factors K_I, K_{II} and K_{III}, of the respective modes of deformation were determined by finite element analysis, where the data pre-processing was undertaken by PATRAN, while the solution process was carried out by ABAQUS. As a result of the analyses, as well as measurements made on the INSTRON 1334 servo-hydraulic testing machine, the proposed fracture envelope was confirmed.

KEYWORDS

Three-dimensional fracture testing, mixed mode fracture criterion, cement mortar specimens, FE analysis.

INTRODUCTION

In practice, most structural components undergo mixed mode loading involving tension as well as in- and out-of-plane shearing. Studies on mixed modes I, II and III fracture have been the subject of research in recent decades. Various fracture criteria have been proposed, among which the maximum tangential stress criterion proposed by Erdogan and Sih [1] and the minimum strain energy criterion proposed by Sih [2] are the more commonly used in the study of mixed mode crack growth. The application of these criteria has been extended to mixed modes I, II and III loading [3]. However, it has been reported that none of the criteria give satisfactory results under all loading conditions [4].

On the other hand, Richard and Kuna [5] have developed a loading device to achieve mixed modes I, II and III, as well as respective pure mode fractures on plexiglass and aluminium specimens, while Hyde and Aksogan [6] have used an axisymmetric bar-type specimen containing conical "crack-like" external flaws to obtain mixed modes I, II and III fracture data. Apart from the foregoing reports, laboratory tests on mixed modes I, II and III fracture are rarely found in the corresponding literature, and this may be due to the complexities of specimen geometries and loading conditions that are involved in such applications.

In the following discussion, a mixed mode I, II and III fracture criterion and test method to verify the criterion, which is based on cement mortar beam specimens, will be proposed. The stress intensity factors of the respective modes of loading have been evaluated numerically from three-dimensional finite element analysis. The results of the analyses and measurements from corresponding laboratory tests will be presented subsequently, and shown to confirm the validity of the proposed fracture criterion.

BACKGROUND OF THEORY

Similarly as in the case of the *unified model* [7], for pure mode III loading, the energy release rate $G_{III\theta}$ along the generalized plane of Figure 1 may be expressed via closure analysis as

$$G_{III\theta} = \frac{1}{\delta a} \int_0^{\delta a} \left[\hat{\sigma}_{\theta z}(r, \theta) \cdot u'_{zz}(\delta a - r, \pi) \right] dr ,$$ (1)

where the $\sigma_{\theta z}(r, \theta)$ is the shear stress along the generalized plane, $u'_{zz}(\delta a - r, \theta)$ the displacement of the crack edge along the z direction, as referred to the kinked branch tip, and δa the length of the kinked branch crack. Next, by adopting $K_{III\theta}$ as the unified mode III stress intensity factor with respect to the generalized plane, it may be shown that

$$K_{III\theta} = \lim_{r \to 0} \tau_{\theta z} \sqrt{2\pi r} = K_{III}(\cos \frac{\theta}{2} \cos \theta + \sin \frac{\theta}{2} \sin \theta) ,$$ (2)

where K_{III} is the mode III stress intensity factor along the self-similar direction, defined as

$$K_{III} = \lim_{r \to 0} \tau_{\theta z}(r,0) \sqrt{2\pi r} .$$ (3)

Since the stress intensity factor K'_{III}, which is referred to the generalised direction of the kinked branch tip, may be specified as

$$K'_{III} = \lim_{(r - \delta a) \to 0} \tau'_{\theta z}(r - \delta a, 0) \sqrt{2\pi(r - \delta a)} ,$$ (4)

in the limiting condition in which $\delta a \to 0$ and K'_{III} would thereby have to be evaluated with respect to the main crack tip, $K'_{III} = K_{III\theta}$. Hence, Eqn. 2 may be simplified as

$$G_{III\theta} = (1 + \nu) \frac{K_{III\theta}^{2}}{E}$$ (5)

(a more detailed derivation may be obtained from reference [8]).

As a result of invoking the principle of superposition, the overall rate of energy release, G_θ, due to crack extension in the generalized plane when subjected to mixed mode I, II and III loading, may be determined as

$$G_\theta = G_{I\theta} + G_{II\theta} + G_{III\theta} ,$$ (6)

where $G_{I\theta}$ and $G_{II\theta}$ are the energy release rates for the tensile and shearing modes of deformation respectively. Therefore, in the state of fracture,

$$G_\theta = G_C,$$ (7)

2

where G_C would be the generalized mixed mode critical rate of energy release. Next, based on a pro-rata energy conversion rate of

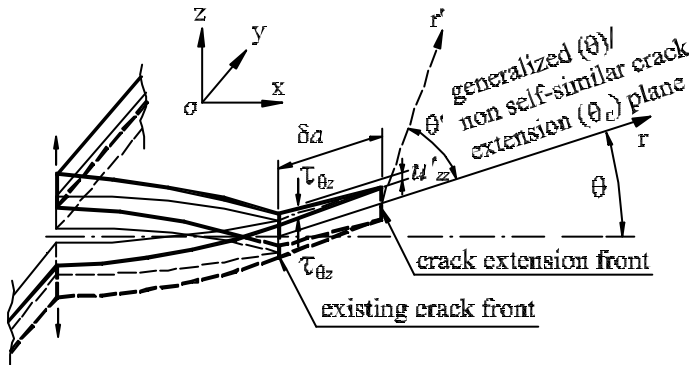$$G_{Iq} + G_{IIq} + G_{IIIq} = G_{Iq}\frac{G_C}{G_{IC}} + G_{IIq}\frac{G_C}{G_{IIC}} + G_{IIIq}\frac{G_C}{G_{IIIC}} , \tag{8}$$

in view of Eqn. 6 and 7, the generalised mixed mode I, II and III fracture criterion may be expressed as

$$\frac{G_{Iq}}{G_{IC}} + \frac{G_{IIq}}{G_{IIC}} + \frac{G_{IIIq}}{G_{IIIC}} = 1 , \tag{9}$$

or alternatively re-stated as

$$\left(\frac{K_{Iq}}{K_{IC}}\right)^2 + \left(\frac{K_{IIq}}{K_{IIC}}\right)^2 + \left(\frac{K_{IIIq}}{K_{IIIC}}\right)^2 = 1 , \tag{10}$$

as depicted by the envelope of Figure 2.

Figure 1: Closure parameters for mode III crack extension
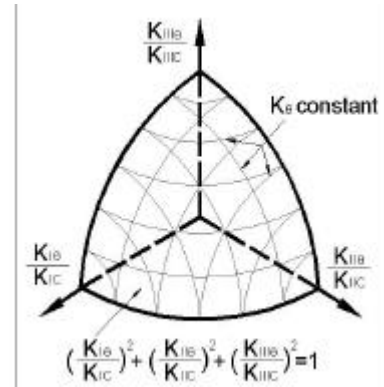
Figure 2: Unified mixed mode I, II and III fracture envelope

LABORATORY TESTING AND FINITE ELEMENT ANALYSIS

Experimental Materials
Ordinary Portland Cement and natural, fine-graded sand were used to cast the mortar specimens. The mix proportions of cement : water : sand by weight was 1.0 : 0.31 : 0.8. The materials were mixed in a drum mixer for a period of not less than 10 minutes to ensure its uniformity. The mean compressive cube strength was measured as 86MPa in tests carried out according to BS 1881: Part 116 [9]. Stainless steel moulds were used for the specimens which were cured in the fog room for 28 days.

Geometry of Specimen
Figure 3 illustrates the design of the beam specimen. The overall dimensions of the specimen was 500mm (length)   100mm (depth)   80mm (width). In order to have a mixed mode I-II-III fracture, a 2mm wide grooved ligament, which was rotated both vertically (angle   ) and horizontally (angle   ) was formed in the specimen, leaving a V-shaped throat segment. This was done by fixing a thin, stainless steel shim, coated with mould oil, to the mould before casting, and then removing it within 3 hours of casting so as not to adhere to the specimen. The ligament was located such that the mid-crack-front coincided with the centre of the specimen. Two values were chosen for   and   , namely 26.56   and 45   respectively. Hence, four groups of beam configuration with differing combinations of   and   values were available for testing.
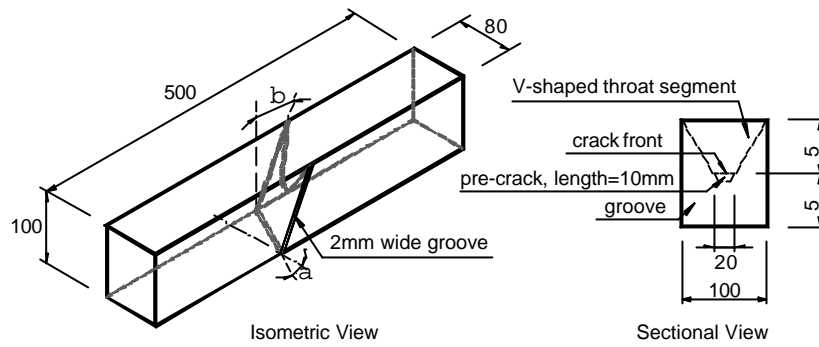
3

Figure 3: Geometry of beam specimen (units in mm)

Laboratory Set-up and Testing Procedures

The tests were conducted on the INSTRON 1334 servo-hydraulic testing machine. In order to achieve different mode I/mode II and mode I/mode III loading ratios, each beam group was subjected to three loading cases, as depicted in Figure 4. In all cases, the specimen was simply-supported.
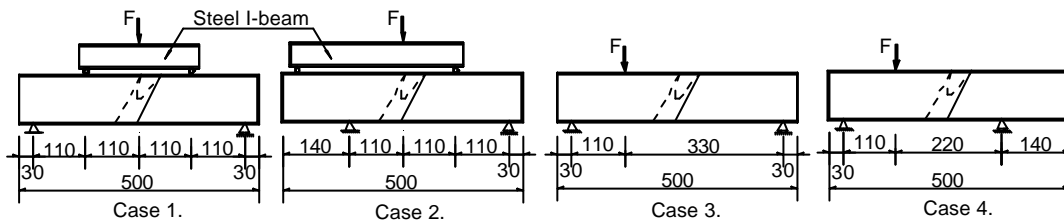

Figure 4: Loading cases used in tests

The load was then applied monotonically at a rate of 0.1mm/min until the specimen failed. The force applied and corresponding stroke displacement was automatically recorded during the entire test.

Determination of Stress Intensity Factors by FE Analysis

Four 3-dimensional finite element models representing the respective beam groups were generated using PATRAN 8.5 [10]. Generally, 20-node second-order quadratic brick elements were used in the model. Around the crack front, however, triangular prismatic elements [11] formed by collapsing one face of corresponding brick elements, and with the four mid-side nodes moved to their quarter points, were employed. Figure 5 shows the entire assembly for a beam group, which consisted of 5944 elements and 27019 nodes.
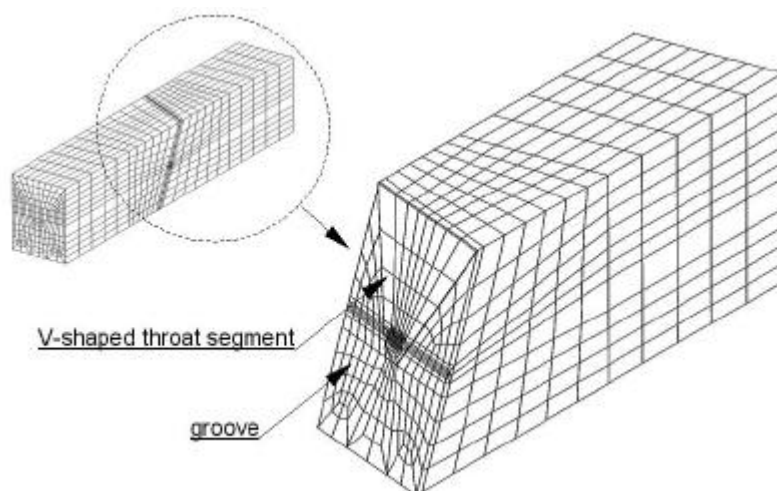
Figure 5: Finite element mesh for beam group A

4

The numerical analyses were carried out by ABAQUS 5.8 [12] and the stress intensity factors, K_I, K_{II} and K_{III}, for each layer of elements across the throat, and in each case of unit loading, were obtained from the corresponding nodal displacements of the crack face. The stress intensity factors along the crack front were thereby obtained. Figure 6 shows the distributions of K_I, K_{II} and K_{III} for one of the beam groups.
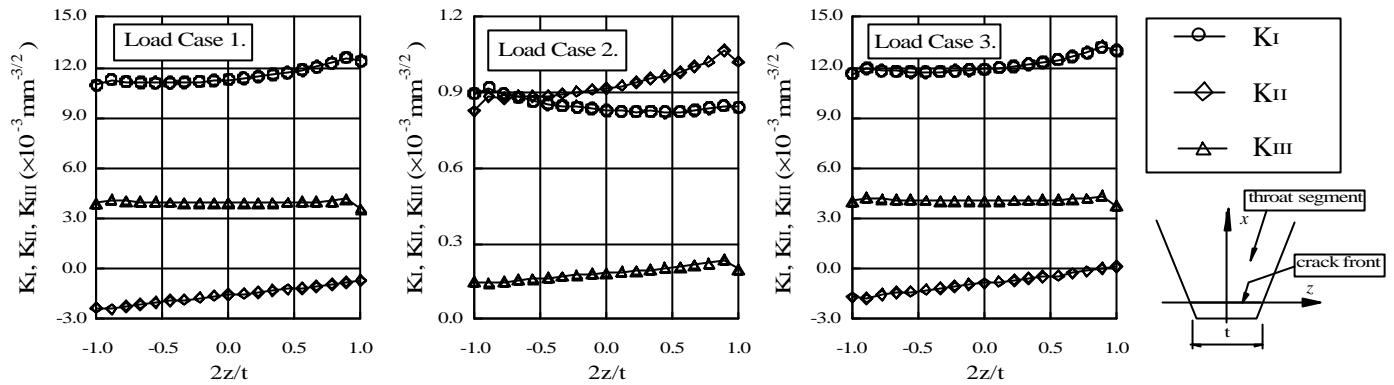

Figure 6: Distributions of tress intensity factors across crack front of beam group

RESULTS AND CONCLUSIONS

For each of the beam groups, three specimens have been tested under each category of loading case. Accordingly, thirty-six beam specimens were tested in all.

In all cases, the load was found to rise with stroke displacement initially. Crack extension started when the load reached its critical value of F_C. As illustrated in Figure 7, the values of F_C were significantly greater under four-point shear loading than under four- or three-point bending. In the cases of three- and four-point bending, the load decreased gradually after F_C, until failure occurred in the specimen. This implies that additional energy was required to maintain crack extension. However, in the case of four-point shear, the peak load dropped suddenly, and the specimen was subjected to sudden failure.

The cracks were found to extend along the grooved segment initially, and after a certain stage, deviated from the throat segment to extend vertically upwards (Figure 8). The reason of such a deviation was that when the crack approached the top face of the specimen, the length of the crack front increased. Thus, by a certain stage, the effect of grooving would not be sufficient to guide the crack along the grooved segment and the crack would extend along the more critical direction, which was upwards.
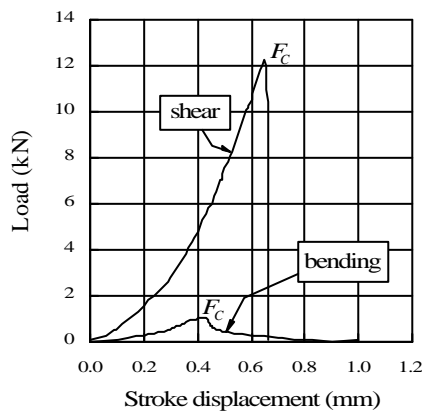

Figure 7: Typical load-stroke displacement curves for bending and shear loading

Figure 8: Failure of specimen

The fracture toughness in pure modes I, II and III had been evaluated in earlier tests on the same material as being 0.468MPa m, 0.759MPa m and 1.12MPa m respectively. For each of the present mixed mode fracture cases, $K_{I\theta}$, $K_{II\theta}$ and $K_{III\theta}$ were obtained via

$$K_{Iq} = K_I \times F_C , \tag{11}$$

$$K_{IIq} = K_{II} \times F_C \tag{12}$$

and

$$K_{IIIq} = K_{III} \times F_C , \tag{13}$$

where K_I, K_{II} and K_{III} were the stress intensity factors obtained from numerical analyses, and F_C the critical load measured in corresponding tests. The test results are depicted in the plot shown in Figure 9. The figure also shows the unified fracture envelope defined by Eqn. 10 superimposed on the results of the fracture tests. Accordingly, the agreement between prediction and experimental results was within 10%.
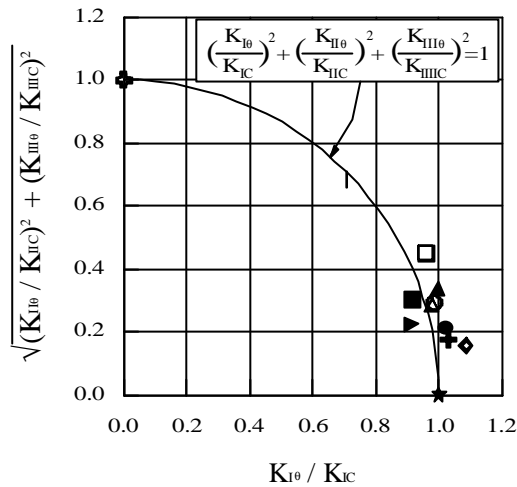
Figure 9: Comparison of unified fracture envelope with test results
(different symbols for various loading and specimen configurations)

In view of the preceding findings, the following conclusion may be drawn: -
A generalized mixed mode I, II and III fracture criterion has been proposed as an extension of the *unified model*, based on the notion of a simple conversion of pure mode to mixed mode loading energy, in direct proportion to their respective fracture energies. A corresponding test method has been proposed to characterize the fracture of material subjected to mixed mode I, II and III loading. On the basis of the proposed fracture criterion and pure mode fracture toughness obtained from earlier tests, the experimental results show reasonably good agreement with the extended *unified model* prediction.

REFERENCES

1   Erdogan, F. and Sih, G.C. (1963) *J. Bas. Eng., ASME Trans.* 85, 519.
2   Sih, G.C. (1974) *Int. J. Fract.* 10, 305.
3   Chen, X.M., Jiao, G.Q. and Cui, Z.Y. (1986) *Eng. Fract. Mech.* 24, 127.
4   Qian, J. and Fatemi, A. (1996) *Eng. Fract. Mech.* 55, 969.
5   Richard, H.A. and Kuna, M. (1990) *Eng. Fract. Mech.* 5, 949.
6   Hyde, T.H. and Aksogan, O. (1994) *J. Strain Analysis*, 29, 1.
7   Lo, K.W., Tamilselvan, T., Chua, K.H. and Zhao, M.M. (1996) *Eng. Fract. Mech.* 54, 189.
8   Lo, K. W., Zhong, K. and Tamilselvan, T. Invited keynote lecture presented at MicroMaterials Conference *MicroMat 2000*, Berlin, April 17-19, 2000.
9   British Standard Institution, BS 1881: Part 116, "Methods for Determination of Compressive Strength of Concrete Cubes", 1983.

10   The MacNeal-Schwendler Corporation. (1999) *PATRAN Version 8.5*. USA.
11   Barsoum, R.S. (1976) *Int. J. Numerical Method in Eng.* 10, 35.
12   Hibbit, Karlsson and Sorensen, Inc. (1998) *ABAQUS Version 5.8*. USA.

TIME DEPENDENT STRESS INTENSITY FACTORS
IN A VISCOELASTIC STRIP

S. Yoneyama [1] and M. Takashi [2]

[1] Department of Opto-Mechatronics, Wakayama University,
930 Sakaedani, Wakayama 640-8510, Japan
[2] Department of Mechanical Engineering, Aoyama Gakuin University,
6-16-1 Chitosedai, Setagaya, Tokyo 157-8572, Japan

ABSTRACT

The time-dependent stress fields around a moving crack tip in a viscoelastic strip is studied. Photoviscoelastic technique using an elliptically polarized white light is employed for the evaluation of the time-dependent stress distribution around a crack tip. The time-dependent stress intensity factor K_I^* which is extended for linearly viscoelastic materials is evaluated using a method based on the least-squares. The results show that the proposed critical stress intensity factor K_c^* for fast crack growth may be considered as a characteristic property of the material under monotonically increasing load.

KEYWORDS

Viscoelasticity, Crack growth, Stress intensity factor, Time- and temperature-dependent properties, Photoviscoelasticity

INTRODUCTION

Reflecting rapid expansion of the application of polymeric materials in various industrial fields, extensive investigations on crack threshold and subsequent growth in linearly viscoelastic materials have been reported from both theoretical and experimental viewpoints [1-8]. Various theories have been developed to describe crack initiation and propagation in such materials. However, the mechanism and the viscoelastic behavior in the fracture process are not yet clear since many difficulties, such as the detection of the initiation of crack growth or the constitutive behavior in the fracture process, still exist in this type of material.

Several optical methods, such as moiré interferometry or photoelasticity, have long been used in experimental mechanics to evaluate the deformation of solids under load and the mechanics of fracture [9]. These optical methods, which are non-contact and full-field measurement techniques, are very valuable in areas where other methods of analysis are not available or impractical. For the fundamental studies on the mechanics of viscoelastic materials, it has been pointed out that the photoviscoelasticity [10] is a very useful experimental method. Using photoviscoelastic technique, time-dependent stress state in the vicinity of crack tip can be calculated from the time-variation of fringe order and the principal direction of birefringence.

In this paper, the time-dependent stress fields around a crack tip at the instant of crack threshold and during subsequent growth in a viscoelastic material are discussed. The time-dependent stress state around a crack tip

is successfully analyzed using photoviscoelastic technique with elliptically polarized white light taking a single shot image [11]. Then, the time-dependent stress intensity factor, which is extended for viscoelastic materials, is evaluated using a method based on the least-squares. The experimental results show that the proposed critical stress intensity factor K_c^* depends on not only the crack growth rate but also the temperature. As a result, the values of the critical stress intensity factor for fast crack growth may be considered as a characteristic property of the material under monotonically increasing load.

EXPERIMENT

Material Properties

The material used in this study is a soft epoxy resin (Epikote 871). This material is linearly viscoelastic, thermorheologically simple and

Figure 1: Master curves of the mechanical and opto-mechanical properties of the material

birefringent. The glass transition temperature is measured as $T_g = 258$ K. Figure 1 shows the mechanical and opto-mechanical properties of the material. In this figure, the mechanical properties, i.e., the master curves of the relaxation modulus $E_r(t')$ and the creep compliance $D_c(t')$ as a function of the reduced time t' are shown by solid lines, and the inverse relaxation stress-birefringence coefficient $C_{\sigma r}^{-1}(t')$ and the inverse creep strain-birefringence coefficient $C_{\varepsilon c}^{-1}(t')$ are represented by broken lines. They are measured and determined through uniaxial tension tests under several constant strain rates at various temperatures, and constructed using the WLF time-temperature shift factor [12] at the reference temperature $T_0 = 308$ K. Then, each master curve is approximated by a Prony series by the collocation method to facilitate the calculation of the convolution integrals involved in the constitutive equations. As seen in Figure 1, the values of the coefficients vary remarkably between the rubbery and glassy states over a wide range of the reduced time on a logarithmic scale.

Experimental Procedure

The specimen adopted is a strip with $w = 80$mm in width, $2b = 40$ mm in length and $t = 0.5$ mm in thickness, having an initial crack $C_0 = 20$ mm from the left edge as shown in Figure 2. The ratio of the initial crack length to the other dimensions of the specimen is chosen to satisfy approximately the condition of a semi-infinite crack [13]. A very sharp initial crack [6] is generated by extending a razor cut pre-crack of 8 mm in length to 20 mm under constant displacement rate loading at a temperature of 273 K, in order to realize good repeatability of crack growth under every test condition. The constant rate displacement loading is applied on the lower edge of the specimen normal to the crack surface under five different rates of the extension $V = 8.33 \times 10^{-3}$, 3.33×10^{-2}, 8.33×10^{-2}, 3.33×10^{-1} and 8.33×10^{-1} mm/s at the temperatures $T = 263$, 268 and 273 K. At these temperatures, the material shows marked viscoelastic behavior. However, the experiment under $V = 8.33 \times 10^{-1}$ mm at $T = 263$ K is excluded since the specimen exhibits brittle fracture under this condition.

Photoviscoelastic fringe patterns are observed through a polariscope arranged for an elliptically polarized white light photoviscoelasticity [11]. A tricolor type fluorescent lamp is used as a light source in order to reduce the attenuation of light intensities of photoviscoelastic fringe pattern. The variations of fringe pattern are recorded on color reversal films periodically. The photographic images of the propagating crack are later digitized into a computer using a film scanner.
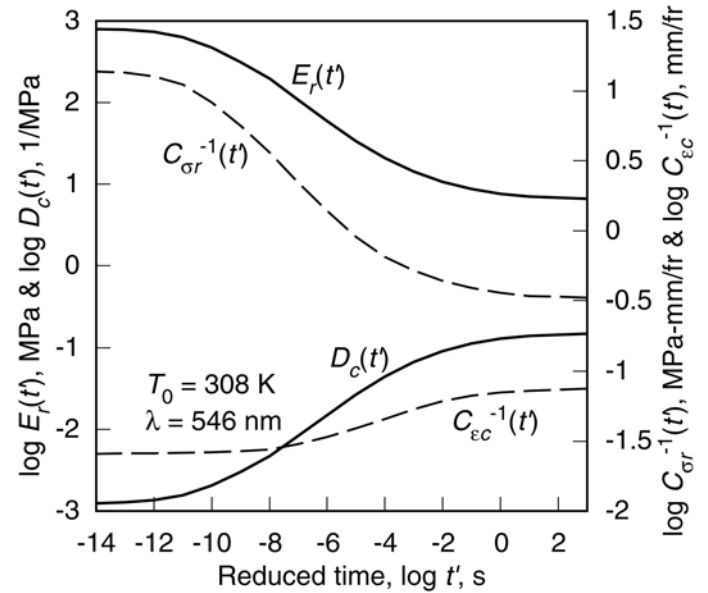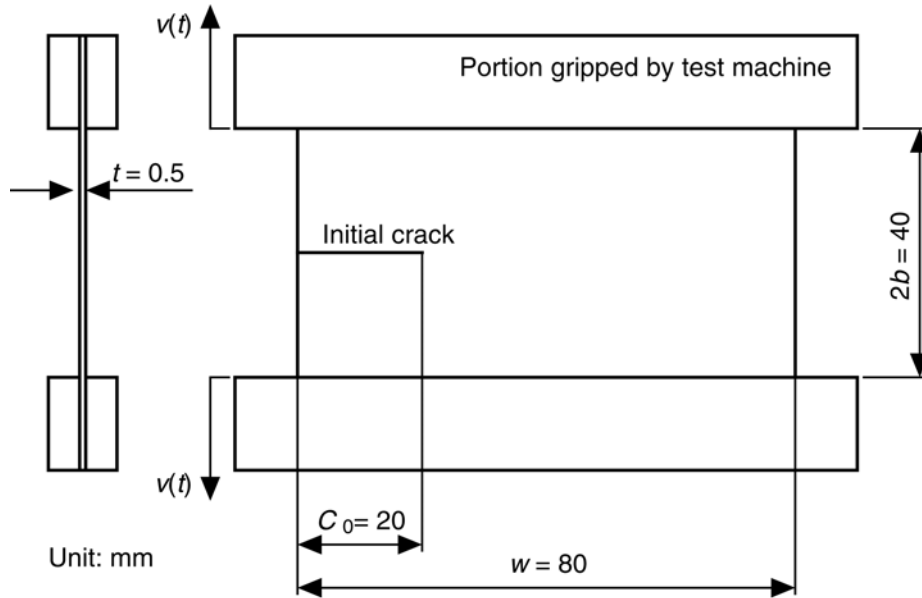
Figure 2: Specimen geometry

RESULTS AND DISCUSSION

Crack Growth Behavior

Figure 3 shows the crack extension curves, i.e., the relation between the increment of the crack growth $a(t)$ and the time t, measured from the careful observation of the photoviscoelastic image data. As reported by several researchers [2,3], the linear relation between the crack length increment and the time in a double logarithmic scale is observed. Thus, each crack growth curve is approximated by a power function as [3],

$$a(t) = \alpha' \, t^{\beta}, \qquad (1)$$

where α' and β' are constants. The crack growth curves approximated by the least-squares method are also shown in the

Figure 3: Examples of the crack extension curves ($T = 273$ K)

same figure. Good correlations are observed. However, it is noteworthy to say that the crack threshold time, i.e., the critical condition for crack threshold cannot be determined from Eqn. (1). This fact is one of the unsolved difficulties in the discussion on viscoelastic fracture problem.

Fringe Pattern and Photoviscoelastic Analyses

Figure 4 shows examples of the photoviscoelastic fringe pattern around the crack tip at $T = 273$ K under the extension rate of $V = 8.33 \times 10^{-3}$ mm/s. Here, the originally colored images are expressed in gray levels. Typical mode I type fringe pattern varies with the movement of the crack tip. However, some of isochromatic fringes still remain at the initial crack tip and on the fracture surface behind the crack tip. This phenomenon indicates one of the features of the viscoelastic behavior.

The photoviscoelastic fringe patterns are analyzed using the method proposed by the authors previously [11]. Applying the procedure to a time-series of the photoviscoelastic images, the time-variation of fringe order and the principal direction of birefringence at selected points are determined. Then, the time variation and the
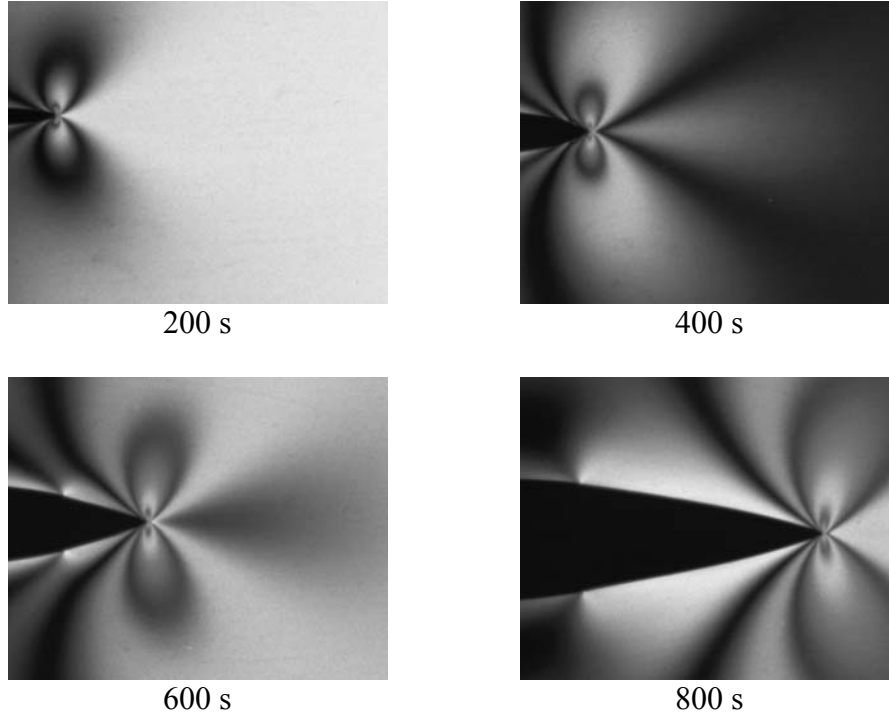
| 200 s | 400 s |

| 600 s | 800 s |

Figure 4: Examples of photoviscoelastic fringe pattern around a crack tip ($T = 273$ K, $V = 8.33 \times 10^{-3}$ mm/s)

distribution of the principal stress difference in the vicinity of the crack tip are calculated using the constitutive equations of photoviscoelasticity [10]. Unlike photoelastic case, the time-history of the variations of the fringe order and the principal direction of birefringence at each point have to be traced in photoviscoelastic case. In this study, to determine the fracture mechanics parameter of the moving crack at any instant, over 400 points on a specimen (19 points for an instant) are selected for tracing the history of the fringe order and the principal direction of birefringence.

Critical Stress Intensity Factor
The viscoelastic fracture studies reported up to date concerning the threshold condition of crack growth tend to search for a fracture mechanics parameter which could hopefully be independent of loading rate and temperature, such as the case of COD [2], M_{Ic} [4] or J_c' [5]. However, since discontinuous critical phenomena have not been observed in crack extension curves as shown in Figure 3, a new approach is developed in this study.

In viscoelastic crack problems, the expressions for stress fields, that is, the relations between stresses and the stress intensity factor, are not given unlike the elastic case. Thus, the conventional formula for extracting the stress intensity factor in photoelasticity does not provide an accurate estimation, except in the case of a stationary crack. In this study, however, since the expressions for stress fields in the vicinity of a running crack tip in viscoelastic materials cannot be obtained in general form, the value calculated by use of the conventional formula [9] is adopted as an apparent stress intensity factor K_I^* which is extended for viscoelastic materials. For the calculation of the viscoelastic stress intensity factor, the over deterministic algorithm based on the method of least-squares proposed by Sanford and Dally [14] is employed. The results of the viscoelastic stress intensity factor at the temperature of 273 K as a function of applied displacement $v(t)$ ($= Vt/2$) is shown in Figure 5. In this figure, curves represent theoretical values for a stationary crack obtained by the following equation.

$$K_I^*(t) = \frac{1}{\sqrt{\left(1 - v^2\right)b}} \left\{ v(0)E_r(0) - \int_0^t E_r(t - \tau) \frac{dv(\tau)}{d\tau} d\tau \right\}, \tag{2}$$

where b represents the half length of the specimen and v is constant Poisson's ratio. Equation (2) can be

obtained by invoking the correspondence principle, since the case of a stationary crack is a type of proportional loading problem.

From Figure 5 it is seen that in the early stage of the tests, the faster the loading rate is applied, the higher the values of K_I^* are observed. This observation is due to the viscoelastic response of the material. In this stage, the theoretical and experimental values show fairly good agreement. As displacement is increased the values of K_I^* initially increase monotonically, until the experimental values of K_I^* become constant, or sometimes decrease suddenly, at a particular value of the applied displacement in each curve. It may be considered that when the experimental value swerves away from the theoretical value, the actual effect of crack length increment on the optical and mechanical entities arises at this instant as an apparent crack threshold. However, the crack threshold time determined by the procedure mentioned

Figure 5: Viscoelastic stress intensity factor as a function of the applied displacement ($T = 273$ K)

above does not give a strict estimation. Judging from the crack extension curves shown in Figure 3, at the point at which the experimental value of K_I^* varies discontinuously, the crack has already grown about 0.9 ~ 1.8 mm, depending on the loading rate. From the viewpoint of the results, however, the stress fields in the vicinity of the crack tip change drastically at that moment. That is to say, the viscoelastic stress intensity factors K_I^* at the time can be evaluated as critical stress intensity factor K_c^* for fast crack growth.
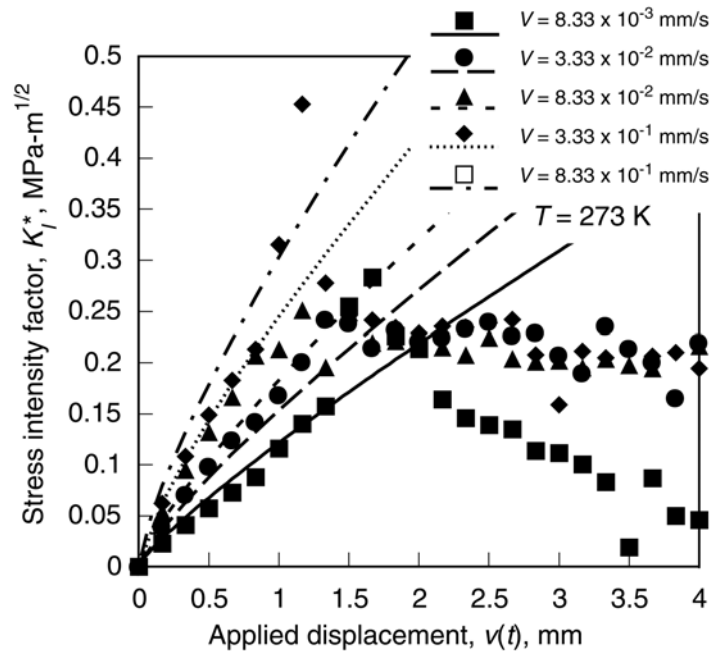
Figure 6 shows a rough estimation of the critical stress intensity factor K_c^* as a function of the crack extension rate $da(t)/dt$, obtained from Figure 5. The crack extension rate is determined by differentiating the crack extension curves in Figure 3. The values of K_c^* increase with the increase of the crack extension rate. Also, the values of K_c^* depend on temperature. Thus, it is expected that a master curve of the critical stress intensity factor K_c^* can be constructed from the curves in Figure 6, in a manner similar to other material properties. Each curve in Figure 6 is shifted by WLF time-temperature shift factor. The results are shown in Figure 7. Here, the abscissa represents the logarithmic scale of the reduced crack growth rate $a'(t)$. As shown in this figure, the plots of the critical stress intensity factor can be approximated by a single curve. As a result, the proposed critical stress intensity factor for fast crack growth may be considered as a characteristic property of the material under monotonically increasing load.

CONCLUDING REMARKS

Using a new fringe pattern analysis method with an elliptically polarized white light and photoviscoelastic technique, an experimental approach to the viscoelastic fracture problem is discussed. The time-dependent fracture mechanics parameter K_c^*, which is extended for linearly viscoelastic materials under various loading rates and at several temperatures, is evaluated. The results are briefly summarized as follows.

1. The experimental values of the viscoelastic stress intensity factor K_I^* shows fairly good agreement with the theoretical values in the early stage of the tests, that is, for a stationary crack.
2. The discontinuous variation of the values of K_I^* is observed at a particular value of the applied displacement.
3. The values of the proposed critical stress intensity factor K_c^* for fast crack growth obtained from the discontinuous change of K_I^* depend on not only the crack extension rate but also the temperature.
4. The proposed critical stress intensity factor K_c^* may be considered as a characteristic property of the
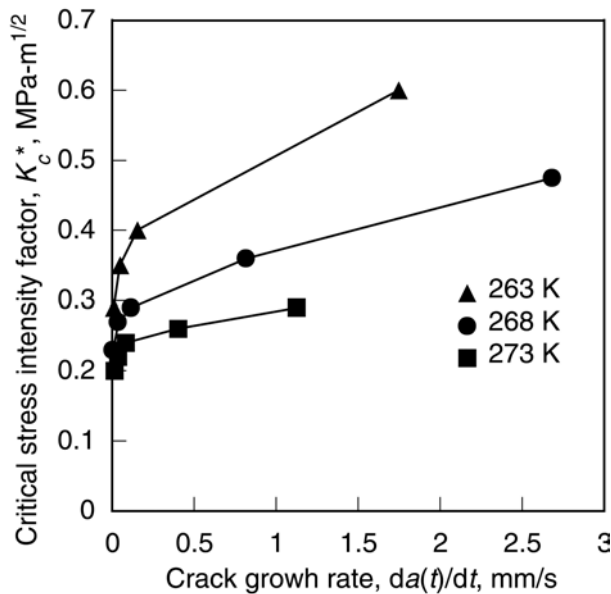
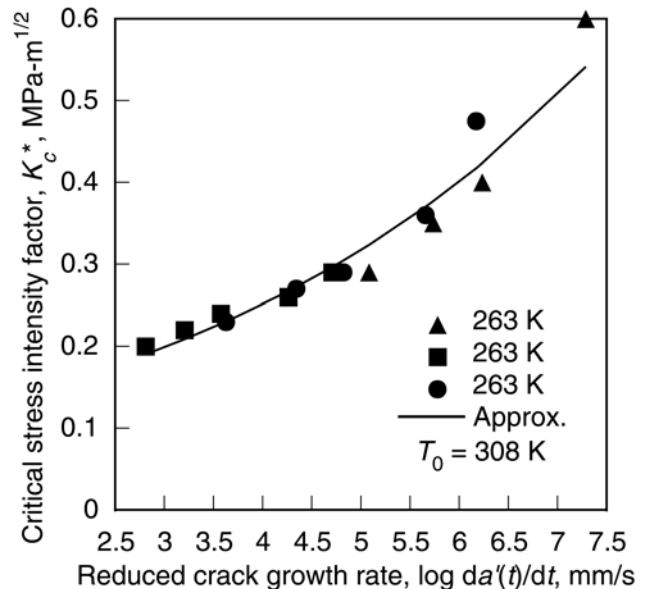**Figure 6**: Critical stress intensity factor as a function of the crack growth rate

Figure 7: Master curve of the critical stress intensity factor

material under monotonically increasing load.

ACKNOWLEDGMENT

REFERENCES

1. Knauss, W.G. (1975). In: *Deformation and Fracture of High Polymers*, pp. 501–541, Kausch, H.H. et al. (Eds). Plenum, New York.
2. Schapery, R.A. (1975) *Int. J. Fract.* 11, 141.
3. Takashi, M., Ohtsuka, H., Misawa, A. and Kunio, T. (1983). In: *Proc. 26th Japan Cong. Materials Res.*, pp. 247–252.
4. Misawa, A., Takashi, M. and Kunio, T. (1984). In: *Advances in Fracture Research*, pp. 2571–2578, Valluri, S. R. et al. (Eds). Pergamon, Oxford.
5. Misawa, A., Takashi, M. and Kunio, T. (1990). In: *Proc. 9th Int. Conf. Exp. Mech.*, pp. 1786–1794.
6. Ogawa, K., Misawa, A. and Takashi, M. (1999) *Int. J. Fract.* 93, 209.
7. Frassine, R., Rink, M., Leggio, A. and Pavan, A. (1996) *Int. J. Fract.* 81, 55.
8. Bradley, W., Cantwell, W.J. and Kausch, H.H. (1998) *Mech. Time-Dependent Materials* 1, 241.
9. Smith, C.W. and Kobayashi, A.S. (1993). In: *Handbook on Experimental Mechanics, 2nd ed.*, pp. 905–968, Kobayashi, A.S. (Ed). VCH, New York.
10. Kunio, T., Miyano, Y. and Sugimori, S. (1990). In: *Applied Stress Analysis*, pp. 588–597, Hyde, T.H. and Ollerton, E., (Eds). Elsevier, London.
11. Yoneyama, S. and Takashi, M. (2000). In: *IUTAM Symp. Advanced Opt. Methods and Applications in Solid Mech.*, pp. 169-176, Lagarde, A. (Ed). Kluwer, Dordrecht.
12. Williams, M.L., Landel, R.F. and Ferry, J.D. (1955) *J. Am. Chem. Soc.* 77, 3701.
13. Knauss, W.G. (1966) *Trans. ASME, J. Appl. Mech.* 33, 356.
14. Sanford, R.J. and Dally, J.W. (1979) *Eng. Fract. Mech.* 11, 621.

TOUGHENING OF NANO-COMPOSITE CERAMICS

D. N. Fang[1], Z. X. Dong [1] and A.K. Soh[2]

[1]Department of Engineering Mechanics, Tsinghua University, Beijing 100084
[2]Department of Mechanical Engineering, The University of Hong Kong, Hong Kong

ABSTRACT

In this paper, the toughening of zirconia ceramics with dispersed silicon carbide nano-particles is studied. Based on both the experimental observations, three effects of nano-particles on the toughness of nano-composite ceramics, namely, nano-particle clustering, crack pinning and transgranular fracture, are identified from both the experimental and analytical studies. And a model considering the above toughening effects is developed to predict the overall toughness of nano-composite ceramics.

KEYWORDS

Toughening mechanism, ceramic, fracture, nano-particle, composite, clustering.

INTRODUCTION

Since nano-composite ceramics were first made in1980's, the experiments carried out by many researchers, e.g., Izaki et al. [1], Niihara [2], Sawaguchi[3], Zhao et al. [4], and Tian [5], have shown that the ceramic matrix can be significantly toughened by dispersing nanometer sized particles in it to form nano-composite ceramics. The toughening mechanisms of such process have attracted the interest of many researchers. Niihara et al. [2] found that not all nano-particles were distributed within the matrix grains but also along the grain boundaries. Niihara et al. [2] and Zhao et al.[4] concluded that the switch of fracture pattern from intergranular to transgranular, due to the existence of nano-particles along the grain boundaries, is the main toughening mechanism. In comparison with the experimental work, there is a lack of theoretical modelling due to mathematical complication. Pezzotti [6] proposed a "bridging" model and argued that the "bridging" effect of the nano-particle near a crack tip is the main toughening mechanism. The most valuable theoretical work on examination of toughening mechanisms was done by Tan and Yang [7] who highlighted some toughening mechanisms. In this paper, the toughening of zirconia ceramics with dispersed silicon carbide nano-particles is studied. Based on both the experimental observations done by

the authors and other researchers and the theoretical modelling proposed by Toya [8], Cotterell and Rice [9], Sumi [10] and Tan and Yang [7], the toughening mechanisms of nano-composite ceramics are analyzed. And a model, in which three toughening effects, i.e., nano-particle clustering, crack pinning, and transgranular fracture induced by nano-particles, is developed to predict the overall toughness of nano-composite ceramics.

EXPERIMENTAL OBSERVATION

The nano-composite ceramics with zirconia (Z_rO_2) matrix and silicon carbide nano-particles were fabricated by the coagulation casting approach [1]. The Young's modulus and Poission's ratio of the zirconia matrix are E_m=400GPa and $v_m = 0.25$, respectively, and the corresponding values of the nano-SiC particles are E_p=440GPa and $v_p = 0.17$.

The zirconia ceramic, which consists of 0% nano-particle, and the nano-composite ceramics with 2%, 5%, 10%, 20% volume fraction of nano-particles were produced at the sintering temperatures of 1600^0C, 1650^0C, 1700^0C,

Fig.1: Strength of the Z_rO_2/nano-SiC ceramics

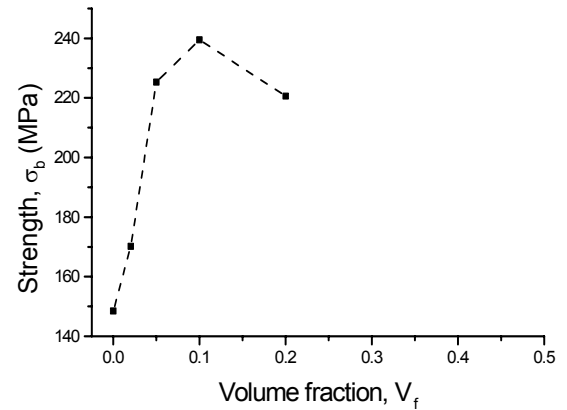1750^0C, and 1800^0C, respectively. The average size of the SiC nano-particle and the zirconia matrix grain were 60 nanometers (nm) and 3 μm, respectively. The strength of the nano-composites with different volume fractions of nano-particles was measured using three-point-bending specimens with length 36mm, height 4mm and thickness 4.0mm. Figure 1 shows the average bending strength of the nano-composite with respect to the volume fraction of the dispersed nano-particles. Note that each experimental point represents the average measured value of nine specimens. The fracture toughness was obtained from the indentation test, which has been accepted as a standard test for toughness measurement of brittle materials [12]. Figure 2 demonstrates the toughness of nano-composites with respect to the volume fraction of the dispersed nano-particles. It can be seen from the experimental data in Fig.1 and 2 that both the strength

Fig. 2 Toughness of the Z_rO_2/nano-SiC ceramics

and toughness increase with increasing volume fraction of nano-particles. However, the strength reaches its highest value at V_f=10%. The fracture surfaces of the specimens used in three-point bending tests were

examined using a scanning electronic microscope. It can be found from SEM observation that the ZrO_2 matrix grains are refined by the addition of nano-particles. The transgranular cracking increases with increasing volume fraction of nano-particles, and the fracture surface at the scale of each grain has many irregular steps, i.e., the fracture surface becomes more blurry. Figure 3 shows the TEM images of ZrO_2/nano-SiC composite ceramics. Figure 3(a) clearly illustrates the clustering of nano-particles within the grains; Fig. 3(b) clearly shows the inter/intra distributions of nano-particles; and Fig. 3(c) reveals crack pinning due to nano-particles.
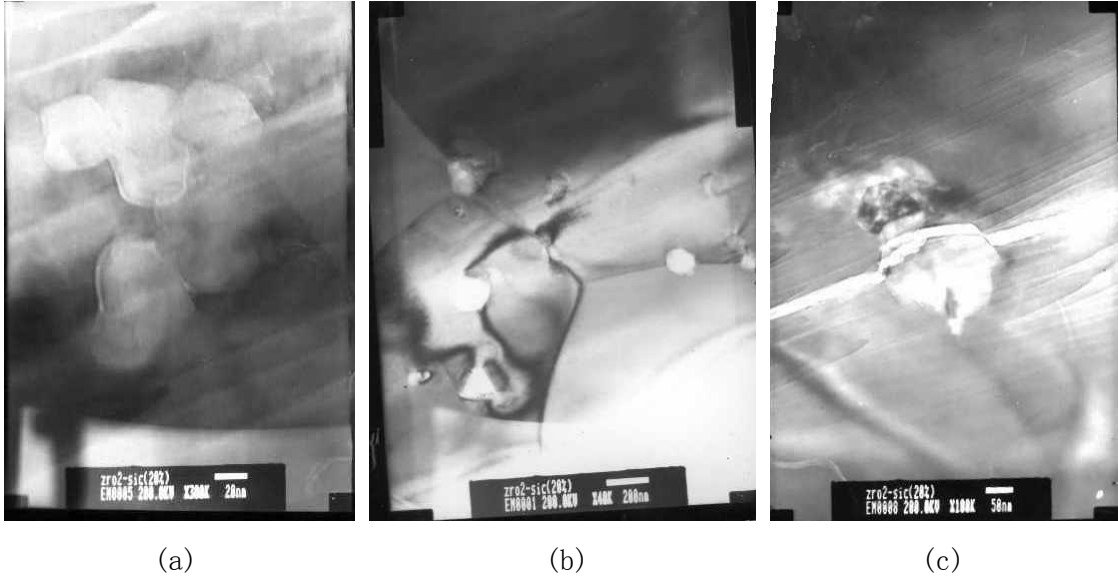
(a)   (b)   (c)

Fig. 3: TEM images of ZrO$_2$/nano-SiC composie ceramics: (a) clustering of nano-particles. within the grains; (b) inter/intra distributions of nano-particles; (c) crack pinning of nano-particles.

ANALYSIS

Effects of nano-particle clustering

Assume that the nano-particles with an average size, d_p, are randomly distributed. The random distribution can be produced in the following manner. At the initial state, the two-dimensional coordinates (x_i, y_i) for each nano-particle with radius, $r_i = r_p$, is introduced into the representative element by a

(a)   (b)

Fig.4: Nano-particle clustering operation for V_f =30%.

randomizer, as shown in the left-hand column of Fig. 4. The plane size of the representative element is $1000 r_p \times 1000 r_p$ in which the total number of nano-particles, N^{total}, is about 320000 when the volume fraction, V_f, reaches 100%. After randomly distributing the nano-particles, an approach is adopted to statistically record the clustering. Two arbitrary nano-particles, i, j, with radii r_i and r_j, respectively, are deemed to be in contact if the coordinates of the two particles satisfy $(x_i - x_j)^2 + (y_i - y_j)^2 < (r_i + r_j)^2$.

When two particles are in contact with each other, a new particle, k, is formed replacing particles i and j. Once two particles are combined, the radius and coordinates of the new particle, k, can be determined by

$$x_k = x_i \frac{r_i^2}{r_i^2 + r_j^2} + x_j \frac{r_j^2}{r_i^2 + r_j^2}, \quad y_k = y_i \frac{r_i^2}{r_i^2 + r_j^2} + y_j \frac{r_j^2}{r_i^2 + r_j^2}, \quad r_k = \sqrt{r_i^2 + r_j^2} \tag{1}$$

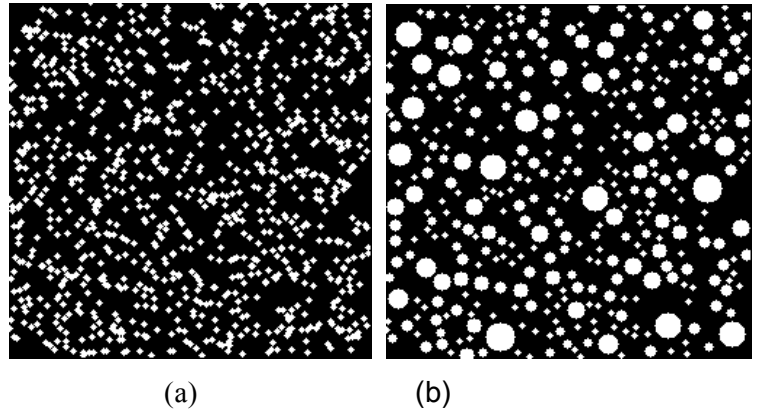This clustering process continues till no particles are in contact with each other. Upon completion of this

process, a new random distribution is formed, as shown in the right-hand column of Fig. 4. Obviously, in the new clustering distribution, the total number of nano-particles becomes lesser while the average size of the particles becomes larger. For an original random distribution of m nano-particles with a given volume fraction V_f, the average radius, $\bar{r}_{clustering}$, of the clustered particles in the new distribution can be calculated

by $\bar{r}_{clustering}(V_f) = \sqrt{\dfrac{V_f A_0}{\pi N^{agg}}}$, where A_0 is the area of the representative element and N^{agg} is the the number

of the clustered nano-particles. Note that each clustered nano-particle may consist of n nano-particles ($n = 1,2,3,........$). For each and every step of the statistical clustering process, two parameters, which are important to the toughening analysis to be carried out later, are to be recorded. One is the volume fraction,

V_f^n, of the clustered nano-particles (with radius $\bar{r}_{clustering}$), each of which consists of n nano-particles with

radius r_p. The volume fraction is given by $V_f^n = nN^n / N^{total}$, where N^n is the number of the clustered

nano-particles, each of which consists of n original nano-particles. It is obvious that $V_f = \sum_n V_f^n$. The other

is the probability of crack pinning, p_n, which defines the chance that a crack is impeded by a nano-particle

and, thus, cannot pass through the nano-particle. The probability is defined as $p_n = \dfrac{1}{n^2}$. If $n = 1$, there is

no clustering, i.e. $p_n = 1$, which means that the crack cannot pass through the nano-particle. The larger the

value n, the smaller is the probability p_n. In other words, the larger the size of the clustered particle, the

more defects it contains and, thus, the easier it is for the crack to pass through the clustered particle.

Therefore, p_n reflects the effect of nano-particle clustering.

Effects of crack pinning of nano-particles
When a main crack is pinned by a nano-particle, the nano-particle may be pulled out from the matrix since the crack cannot penetrate directly through the nano-particle. In the initial pull out stage, an interfacial

arc-crack appears at $\theta = \pm\pi/4$ and $r = d_p/\sqrt{2}$. For an arc-crack subtending an angle 2α, Toya [8] has

established the following formula to calculate the energy release rate J:

$$\frac{J}{J_0} = \frac{k^2}{8}\left(1+4\omega^2\right)\left[1+\frac{(1+\kappa_2)}{(1+\kappa_1)\Gamma}\right]N\exp[2\omega(\pi-\alpha)]\sin\alpha = F(\alpha) \tag{2}$$

where $\kappa_1 = 3 - 4\nu_1$, $\kappa_2 = 3 - 4\nu_2$, $\Gamma = \dfrac{\mu_2}{\mu_1}$, $\omega = -\dfrac{\ln(\nu)}{2\pi}$, and the parameters k, N and ν are given in Toya's

paper [8], μ_1, ν_1 are the shear modulus and Poisson's ratio of the matrix, respectively, and μ_2, ν_2 are the

corresponding values of the nano-particle. The energy release rate for a crack of length d_p in the matrix is

given by $J_0 = \dfrac{(1-v_1)\sigma_y^2 \pi d_p}{4\mu_1}$. When J reaches the critical value J^c at the interface between the matrix and the nano-particle, the main crack will connect to the arc-crack along the interface, leading to the "pull-out" of the nano-particle from the matrix. In this case $J = J^c$, the "pull-out" stress and stress-intensity-factor can be obtained as follows:

$$\sigma_y = \sqrt{\frac{4J^c \mu_1}{(1-v_1)\pi d_p F(\alpha)}}, \quad K_{nano} = \frac{1}{0.593278}\sqrt{\frac{4J^c \mu_1}{(1-v_1)\pi F(\alpha)}} \tag{3}$$

It is obvious that crack pinning gives rise to toughening because a higher stress intensity factor is required for a crack to pass through a nano-particle leading to "pull-out" of the nano-particle. Indeed, the numerical calculation indicates that K_{nano} is much larger than that of the matrix ceramics.

Transgranular fracture induced by nano-particles

The experimental results showed that the nano-particles along the grain boundaries steer the crack to propagate into the matrix grains [3-4,7]. Note that the procedure adopted in the analysis of transgranular fracture is similar to that employed by Cotterell and Rice [9], Sumi [10] and Tan and Yang [7] for the analysis and discussion of kinked and transgranular fractures. By considering the mechanism of transgranular fracture, the overall toughness of the nano-composite ceramic can be expressed as [7]

$$\bar{J} = (f^{ins} + f^{int}V_f)J_1^{ins} + f^{int}(1-V_f)J_1^{int} \tag{4}$$

where J^{int}, J^{ins} denote the fracture energy of the grain boundary and that of the lattice with no existence of nano-particles, respectively. f^{int}, $f^{ins} = 1 - f^{int}$ are fractions of the intergranular and the transgranular fracture, respectively. V_f stands for the area percentage, . For zirconia ceramics, the values are $J_1^{int} = 18.28\,\mathrm{Jm^{-2}}$ and $J_1^{ins} = 48.07\,\mathrm{Jm^{-2}}$ from formula given in [.

Toughening of nano-composite ceramics

The three effects of nano-particles on the toughness of nano-composite ceramics discussed above can be combined to obtain a general formula for calculating the overall toughness of such ceramics. Thus, the critical stress intensity factors for intergranular fracture, K_c^{int}, and transgranular fracture, K_c^{ins}, are given by

$$K_c^{int} = (1-V_f)K_{(1)}^{int} + \sum_n (V_f^n p_n K_{nano} + (1-p_n)V_f^n K_{(2)}), \quad K_c^{ins} = (1-V_f)K_{(1)}^{ins} + \sum_n (V_f^n p_n K_{nano} + (1-p_n)V_f^n K_{(2)}) \tag{5}$$

where subcript 1 and 2 denote the matrix and nano-particle, respectively. Thus, $K_{(1)}$ and $K_{(2)}$ are the critical stress intensity factors of the matrix ceramic and nano-particle materials, respectively. Note that

$$K_{(1)}^{int} = \sqrt{E_1 J_1^{int}/\left(1 - v_1^2\right)}, \quad K_{(1)}^{ins} = \sqrt{E_1 J_1^{ins}/\left(1 - v_1^2\right)} \tag{6}$$

The overall toughness of nano-composite ceramics can be calculated by combining equations (5) and (6) as follows:

$$K^c = \left[\left(1 - f^{int} + f^{int} V_f\right)\left(K_c^{ins}\right)^2 + f^{int}\left(1 - V_f\right)\left(K_c^{int}\right)^2\right]^{1/2} \tag{7}$$

Figure 2 shows that the solid curve, which was plotted using equation (7), for the ZrO_2/nano-SiC composite ceramics agrees with the corresponding experimental data represented by the solid circles. The theoretical prediction indicates that the toughness reaches its maximum value when the volume fraction of the nano-particles equals 25%. Note that in the calculations, the size of the nano-particle was assumed to be 60 nm in average diameter, and that of the matrix grain was 3 μm in average diameter.

CONCLUSIONS

The toughness of nano-composite ceramics may be influenced by many factors, e.g., the size, volume fraction and distribution pattern of the nano-particles, etc.. Three effects of nano-particles on the mentioned toughness, namely, nano-particle clustering, crack pinning and transgranular fracture, are identified from both the experimental and analytical studies. The propagation of a crack may be pinned by the nano-particles near the crack tip. Crack pinning leads to pull-out of a nano-particle. Transgranular fracture increases with the increase of the volume fraction of nano-particles. Since the fracture resistance of the grain boundary is lower than that of the grain lattice, the higher the probability of transgranular fracture induced by nano-particles, the tougher is the nano-composite. Nano-particle clustering, which increases with increasing volume fraction of nano-particles, leads to the reduction of both the strength and toughness of the nano-composite ceramics. The larger the size of the clustered particle, the more defects it contains and, thus, the easier it is for the crack to pass through the clustered particle.

REFERENCES

1. Izaki K., Hakkei K., and Ando K., (1988). *Ultrastructure Processing for Advanced Ceramics*, New York, John Willey & Sons.
2. Niihara K., (1991). *J.Ceram. Soc. Jpn.*, 99: 962~974
3. Sawaguchi A., Toda K., and Niihara K., (1991). *J. Am. Ceram. Soc.*, 74: P1142~44
4. Zhao J., Stearns L.C., Harmer M.P., Chan H.M., Miller G.A., (1993) *J. Am.Ceram. Soc.*, 76: P225~240
5. Tian W., Zhou Y., Zhou W.L., (1998) *J. Mat. Sci.* 33: P797~802
6. Pezzotti G., Nishida T., Sakai M., (1996). *J. Ceramic Soc. of Jpn.* 103: P889~896
7. Tan H.L. and Yang W. (1998) *Mechanics of materials,* 30: P111~123
8. Toya M. (1972) *J. Mech. Phys. Solids,* 22: P325-348.
9. Cotterell B. And Rice J.R., (1980). *Int. J. Fract.,* 116: P155-169.
10. Sumi Y., (1989). In: Micromechanics and Inhomogeneity (Toshio Mura's anniversary volume), P407-419, Weng, G.J., Taya, M., Abe H. (Eds.). Springer, Berlin.
11. Lawn B. R., Evans A.G. and Marshall D.B., (1980). *J. Am. Ceram.Soc.* 62:P574-581.

TRANSITION FROM DUCTILE TO CLEAVAGE FRACTURE
- EFFECT OF SPECIMEN SIZE AND MISMATCH

E. Østby[1], Z. L. Zhang[2], and C. Thaulow[1]

[1]Department of Machine Design and Materials Technology, Norwegian University of
Science and Technology, N-7491, Trondheim, Norway
[2]SINTEF Materials Technology, N-7465, Trondheim, Norway

ABSTRACT

The effect of specimen size and mismatch on the possible transition from ductile crack growth to cleavage is studied for two different specimen geomtries by means of 2D FE analysis. For homogeneous specimen the crack growth resistance is little influenced by specimen size. The stress level displays stronger size dependence resulting in increasing probability of cleavage fracture with increasing specimen size. For mismatch situations the crack growth resistance is only clearly reduced in cases where the crack grows along the interface between the two materials. When crack growth deviation occurs the detrimental effect of mismatch is reduced both with regard to crack growth resistance and susceptibility to cleavage fracture. The crack growth deviation for mismatch cases is mostly dependent on the specimen geometry, and specimens loaded in bending show stronger tendency for deviation than specimen loaded in tension.

KEYWORDS

Ductile crack growth, Cleavage fracture, Size effect, Mismatch, Numerical simulation

INTRODUCTION

In the ductile to brittle transition region cleavage fracture in steels may be preceded by ductile crack growth. Recent progress in modelling of ductile crack growth, using either damage mechanics (see e.g. [1-2]) or cohesive zone models (see e.g. [3-4]), has brought better understanding of both the ductile and cleavage behaviour of steels in this region. Of special interest for the cleavage fracture susceptibility has been the observation that the stress level increases with ductile crack growth, and this has been used as one way of explaining why transition from ductile to cleavage crack growth may happen (see. e.g. [5-6]). In this paper we focus on two aspects regarding ductile crack growth in finite specimens. The first is the effect of the specimen size. The second aspect addressed is the effect of mismatch for cracks initially located on the interface between two materials with different yield stress. This latter aspect is of great interest for prediction of the behaviour of weldments, where often the most critical location of cracks is close to the fusion line between the weld metal and the Heat Affected Zone (HAZ)/base material.

MATERIALS AND FE-DETAILS

The two different finite geometries studied by means of 2D plane strain FE-analysis are shown in Figure 1. One is a shallow cracked specimen (a/W=0.15) loaded in tension, while the other is a deep cracked specimen (a/W=0.5) loaded in bending. The two different geometries are chosen to evaluate the effect of different

constraint levels. The one half of the specimen where the crack growth will take place is referred to as Mat 1, and is modelled as Gurson material. The other half is referred to as Mat 2, and a von Mises constitutive relation is used here. Referring to Figure 1. the mismatch ratio, m, between Mat 1 and Mat 2 is defined as:

$$m = \frac{\sigma_{0,2}}{\sigma_{0,1}} \tag{1}$$

where $\sigma_{0,1}$ and $\sigma_{0,2}$ is the yield stress of Mat 1 and 2, respectively. In the case of no mismatch m=1. The relation between plastic strain and flow stress used for Mat 2 and the matrix in Mat1 is on the form:

$$\bar{\sigma} = \sigma_0 \left(1 + \frac{\varepsilon_p}{\varepsilon_0} \right)^n \tag{2}$$

where $\bar{\sigma}$ is the flow stress, σ_0 is the yield stress, ε_p is the equivalent plastic strain, $\varepsilon_0 = \sigma_0/E$ is the strain at yield, and n is the hardening exponent. The yield stress of Mat 1 is kept fixed at 400 N/mm^2 (with $E/\sigma_0=500$), while the yield stress in Mat 2 is varied according to (1). A value n=0.1 for the hardening exponent is used in all analyses. The yield function of the Gurson model has the following form:

$$\phi(q, \bar{\sigma}, f, \sigma_m) = \frac{q^2}{\bar{\sigma}^2} + 2q_1 f \cosh\left(\frac{3q_2\sigma_m}{2\bar{\sigma}} \right) - 1 - (q_1 f)^2 = 0 \tag{3}$$

where f is the void volume fraction, which is the average measure of the void-matrix aggregate, σ_m is the mean macroscopic stress, q is the conventional von Mises stress, σ is the flow stress of the matrix material. Values of $q_1=1.5$ and $q_2=1.0$ have been used here. An initial void volume fraction of $f_0=0.002$ is assumed. Further, the increase in void volume fraction is assumed to be solely due to growth of existing voids, and no void nucleation is introduced in the analyses. Void coalescence is predicted by a hardening modified version of Thomason's limit load criterion discussed in [7]. Details of the near tip FE mesh are shown in Figure 2. An area with uniformly shaped elements extends 4.8 mm ahead of the crack tip and 0.7 mm to each side of the interface between the two materials. The element size in this area is 0.05x0.1 mm, with the shortest side parallel to the interface. The reason for choosing an aspect ratio of 2 is that this strongly reduces oscillations in the stress field, due to additional constraint at the interface in the mismatch cases, found when using elements with aspect ratio close to 1.
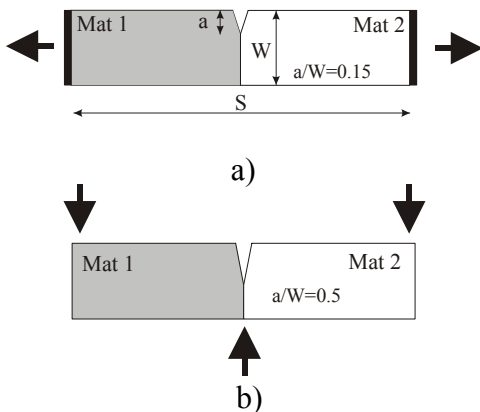

Figure 1. a) Shallow cracked (a/W=0.15) specimen loaded in tension. b) Deep cracked (a/W=0.5) specimen loaded in bending.
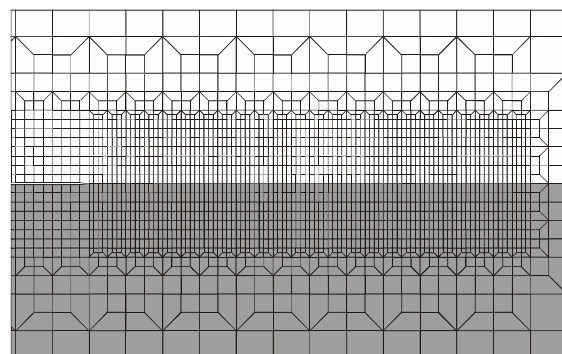
Figure 2. Near tip details of FE-mesh

SIZE EFFECT FOR HOMOGENOUS SPECIMENS

In this section we discuss the effect of specimen size in relation to ductile crack growth. Four different specimen thickness are used: W=25, 50, 100, and 200 mm. Figure 3 a) shows the J-Δa curves for different specimen thickness, W, from the numerical simulations of the shallow cracked specimen (a/W=0.15) loaded in tension. It is evident that the specimen size does not influence the crack growth resistance significantly. Figure 3 b) shows the J-Δa curves for the deep cracked bend specimens (a/W=0.5). Here it can be seen that initial part of the J-Δa curves, up to 1-1.5 mm of crack growth, is more or less independent of specimen size. After further crack growth a more pronounced effect of the specimen size can be seen, with less resistance to crack growth with increasing size. This observation is similar to what was reported in [8] for the same geometry.
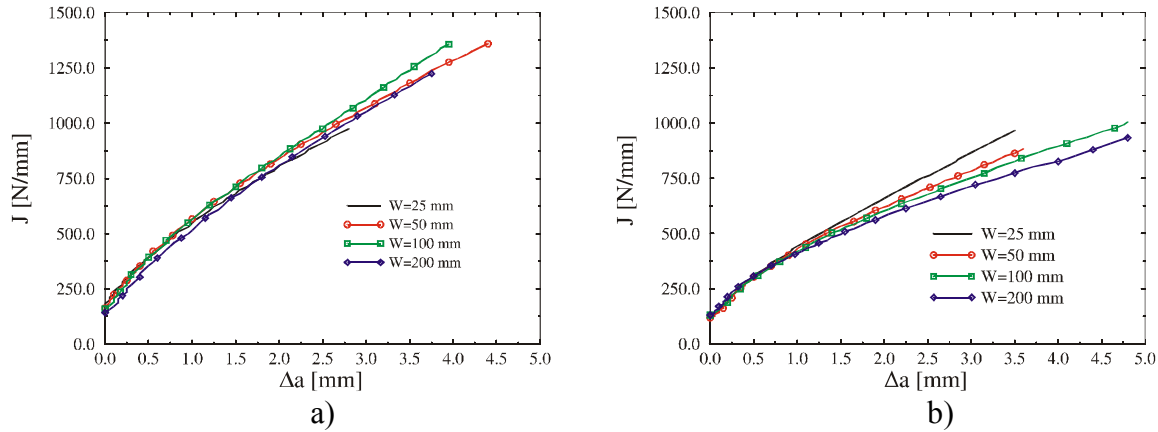
Figure 3. Effect of specimen size on the J-Δa curves. a) Shallow cracked specimen loaded in tension. b) Deep cracked specimen loaded in bending.

The normalised opening stress for different amounts of crack growth for the tensile specimen is compared for the different specimen sizes in Figure 4 a). For a fixed specimen size the peak stress is increasing with crack growth. For the largest specimen (W=200 mm) the increase is about 25% of the yield stress, and slightly less for the smaller specimen. It should also be observed that the major part of the increase in stress happens up to crack growth of about 1 mm, after which only a minor increase in peak stress is seen. An interesting point is the rather large size effect on the stress level, with about 100 N/mm^2 difference between the largest and smallest specimen. The evolution of the normalised opening stress for the deep cracked bend specimen is shown in Figure 4 b). For this high constraint geometry the relative increase in stress with crack growth is smaller than for the tensile specimen. There is also a tendency that the size dependence of the peak stress is somewhat reduced with crack growth. The area of highly stressed material will, however, increase more in the larger specimens due to smaller influence from the global bending field.
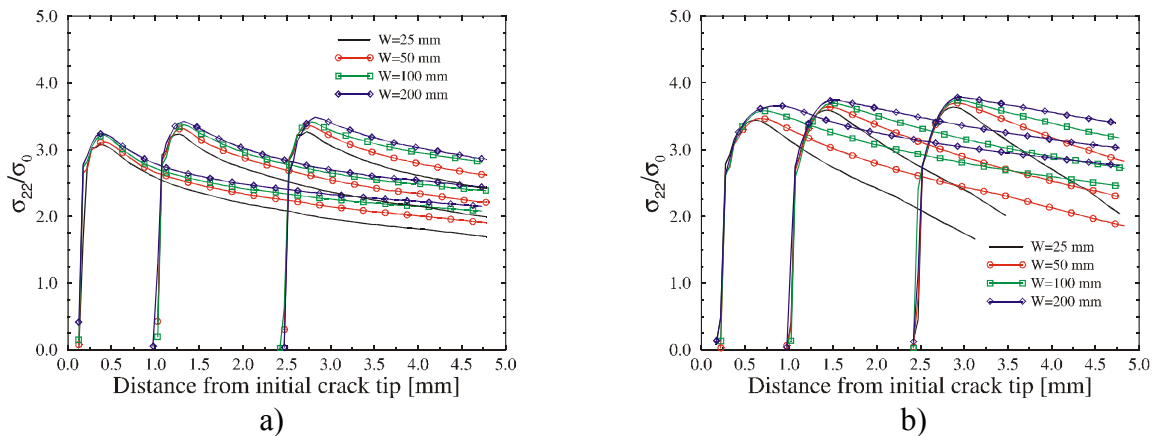

Figure 4. Evolution of normalised opening stress with crack growth. a) Shallow cracked specimen loaded in tension. b) Deep cracked specimen loaded in bending.

The size effect on the susceptibility to cleavage fracture is compared through the Weibull stress, σ_w, (Beremin [9]) calculated according to the following expression:

$$\sigma_w = \sqrt[m_w]{\frac{1}{v_0} \sum (\sigma_{1,i})^{m_w} V_i}$$ (4)

where m_w is the Weibull modulus, v_0 is a scaling volume, $\sigma_{1,i}$ is the average principal stress in element i, and V_i is the volume of element i. The summation is performed over all elements actively yielding. Values of m_w=20 and v_0=0.001 mm^3 have been assumed. The evolution of the Weibull stress as a function of J for the tensile and bend specimens are shown in Figure 5 a) and b), respectively. From Figure 5 a) it can be seen that the Weibull stress is monotonically increasing with J. Also as expected from the stress fields the Weibull stress for a given J is increasing with increasing specimen size. The results thus indicate that the cleavage fracture probability will increase with increasing ductile crack growth, and that the brittle fracture probability for a given J is increasing with specimen size. Similar results are also seen for the bend specimen in Figure 5 b), however, with a stronger size effect due to the influence of the global bending field.
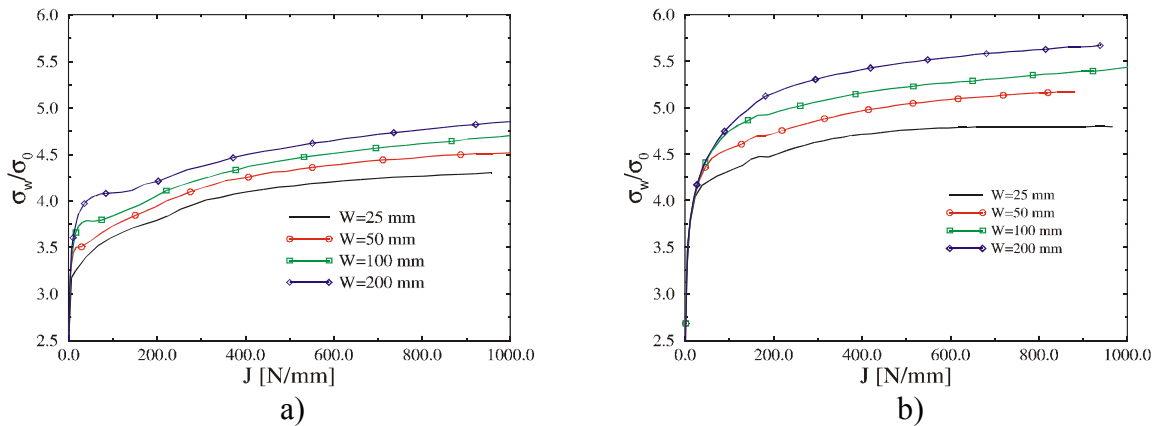

Figure 5. Effect of specimen size on evolution of normalised Weibull stress. a) Shallow cracked specimen loaded in tension. b) Deep cracked specimen loaded in bending

EFFECT OF YIELD STRESS MISMATCH

This section focuses on the effect of mismatch for cracks initially lying on the interface between two materials with different yield stress. The crack is assumed to grow in the material with the lowest yield stress. Three different levels of mismatch, m=1.125, 1,25, and 1.5, are considered both for the tensile and the bend specimen. The specimen thickness, W, is fixed at 50 mm. For the mismatch case the possibility of crack growth deviation away from the interface enters as a new feature compared to simulation of ductile crack growth in homogenous specimens. The effect of mismatch on the J-Δa curve and the crack growth path for the different mismatch levels are shown in Figure 6 a) and b), respectively, for the tensile specimen. From Figure 6 a) it can be seen that mismatch reduces the crack growth resistance. For the two lowest mismatch levels, m=1.125 and 1.25, the reduction compared to the homogenous specimen (m=1) is small. A reason for this can be seen from Figure 6 b) where it is observed that the crack growth does not follow the interface. For m=1.5, however, the reduction in crack growth resistance is significant, following from the fact that the crack grows along the interface. Figure 7 a) shows the effect of mismatch on the crack growth resistance for the bending case, and the crack growth paths are shown in Figure 7 b). By comparing Figure 6 b) and 7 b) it can be seen that the tendency for crack deviation due to mismatch is stronger for the bending than for the tensile specimen. The effect of this stronger tendency to crack deviation is seen on the resistance curves in Figure 7 a), where the curves for m=1.125 and 1.25 displays a slightly higher slope than for the

homogenous specimen. Initially the bend specimen with m=1.5 has crack growth along the interface (up to about 0.5 mm), after which a strong deviation of crack growth path is the case also for this mismatch level.
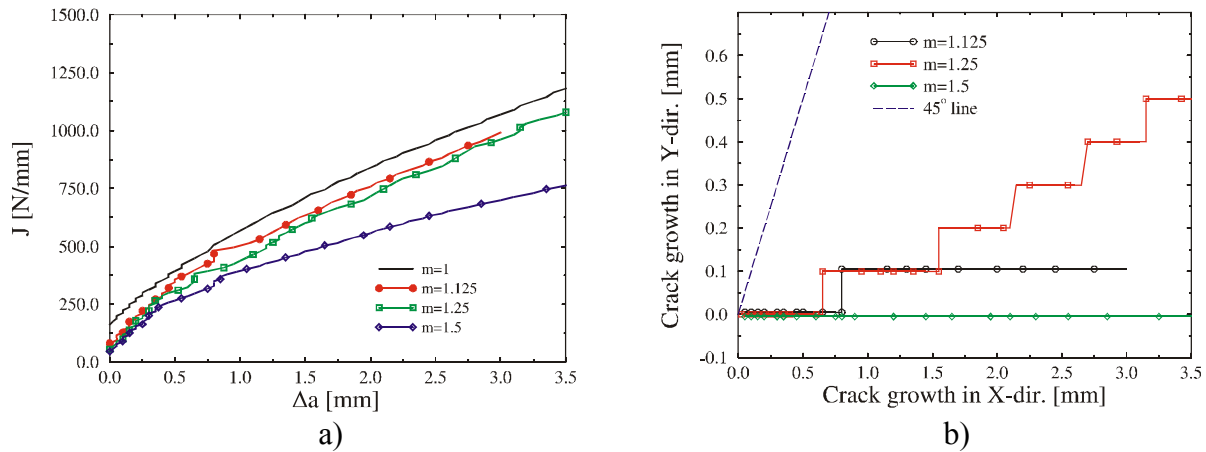

Figure 6. Effect of mismatch on ductile crack growth behaviour for shallow cracked specimen loaded in tension. a) J-Δa curves. b) Crack growth paths.
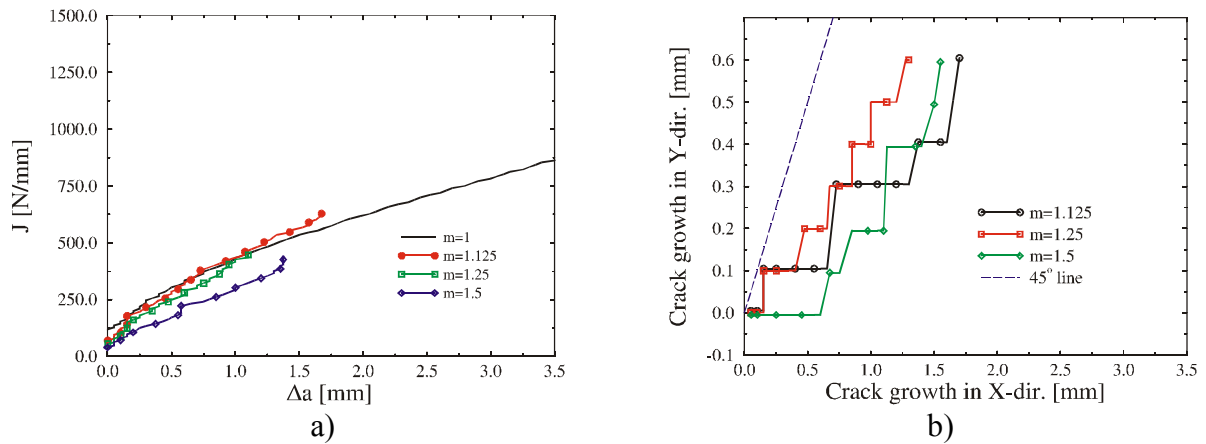

Figure 7. Effect of mismatch on ductile crack growth behaviour for deep cracked specimen loaded in bending. a) J-Δa curves. b) Crack growth paths.

The structure of the stress fields for growing cracks in mismatched specimens becomes complex due to the deviation of the crack growth away from the interface. The effect of mismatch on the brittle fracture susceptibility for ductile crack growth is only discussed through the Weibull stress here. Contribution to the Weibull stress for the mismatched specimens is only calculated in Mat 1, while for the case with m=1 the whole specimen is used. The results for the evolution of the Weibull stress for the different levels of mismatch are shown in Figure 8 a) for the tensile specimen and in Figure 8 b) for the bend specimen. For the tensile case a clear effect with increasing Weibull stress for increasing level of mismatch is seen. This indicates that a detrimental effect of mismatch should be expected on the susceptibility to cleavage fracture for ductile crack growth in specimens loaded in tension. The results for bending also indicate a detrimental effect of mismatch for low load levels. However, it can be seen that the Weibull stress for the mismatch cases displays a lower increase for increasing load compared to the homogenous specimen. Thus, when significant deviation of the crack growth occurs the detrimental effect of mismatch is reduced.
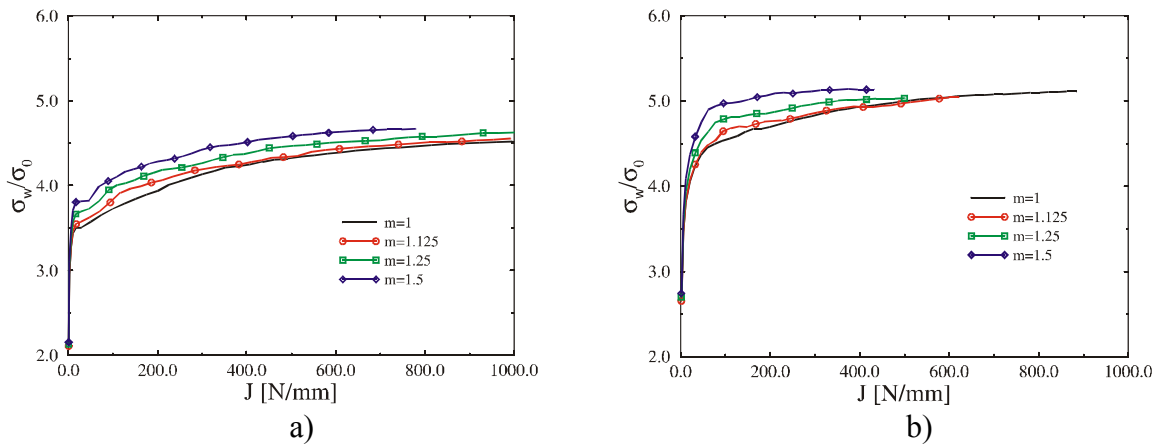
Figure 8. Effect of mismatch on the evolution of the Weibull stress. a) Shallow cracked specimens loaded in tension. b) Deep cracked specimens loaded in bending.

CONCLUDING REMARKS

The numerical simulations indicate that no unique stress field exists for ductile crack growth in a given specimen geometry, and the specimen size, together with the specimen geometry, will influence on the stress level. The size effect appears to be more important with regard to cleavage fracture susceptibility than for ductile crack growth resistance. As for stationary cracks, mismatch will also have a detrimental effect on cleavage fracture probability for interface cracks when ductile crack growth occurs. However, crack growth deviation away from the interface will reduce the detrimental effect of mismatch both for the cleavage fracture susceptibility and the resistance to ductile crack growth. This latter effect appears to be more pronounced for specimens loaded in bending compared to specimens loaded in tension.

ACKNOWLEDGEMENTS

REFERENCES

1. Xia, L. and Shih, C. F., (1995) J. Mech. Phys. Solids, 43, 233
2. Xia, L. and Shih, C. F., (1995) J. Mech. Phys. Solids, 43, 1953
3. Tvergaard, V. and Hutchinson, J. W. (1992) J. Mech. Phys. 40, 1377
4. Tvergaard, V. and Hutchinson, J. W. (1994) Int. J. Solids Structures, 31, 823
5. Xia, L. and Shih, C. F., (1996) J. Mech. Phys. Solids, 44, 603
6. Ruggieri, C. and Dodds, R. H., (1996) Int. J. Fracture (1996), 79, 309
7. Zhang, Z. L., Thaulow, C. and Ødegård, J. (2000) Eng. Frac. Mech. 67, 155
8. Xia, L., Shih, F. C. Hutchinson, J. W., (1995) J. Mech. Phys. Solids, 43, 389
9. Beremin, F. M, (1983) Met. Trans. A, 14A, 2277

ULTIMATE ANALYSIS OF IGNALINA NPP REINFORCED CONCRETE CONTAINMENT SUBJECTED TO INTERNAL PRESSURE

G. Dundulis, E. Uspuras

Lithuanian Energy Institute
3 Breslaujos str. , 3035 Kaunas, Lithuania

ABSTRACT

Numerical analysis are carried out using the NEPTUNE finite element program to predict the ultimate pressure capacity and the failure mode of the RBMK-1500 reinforced containment at Ignalina Nuclear Power Plant. NEPTUNE is a three-dimensional finite element program developed to simulate the response of reactor components in three-dimensional space to design basis and beyond-design-basis loads. It uses reinforced concrete element for analysis of reinforced concrete structures. Material nonlinearity such as concrete tension and compression, yielding of reinforcing steel are simulated with appropriate constitutive models. Calculations for concrete rupture are performed in all the layers of the elements. The results of the analysis for the determination of the Accident Localization System (ALS) failure start with the leakage mode presented in the analysis. Calculations are performed until the appearance of the first crack, which propagates through the all layers of the concrete wall.

KEYWORDS

Finite elements, nonlinear analysis, concrete cracking, stress

INTRODUCTION

The nuclear reactors of the Ignalina nuclear power plant (NPP) belong to the RBMK class of reactors designed and constructed by the Ministry of Nuclear Power Construction of the former Soviet Union. These reactors do not possess the conventional Western containment structure that could confine the radioactive products of a severe nuclear accident. Instead, the Ignalina NPP has a suppression type containment which, for Soviet built reactors, is referred to as the Accident Localization System (ALS) or sometimes as the Accident Confinement System (ACS). The ALS encloses about 65% of the entire cooling circuit, the most dangerous sections of piping to rupture in case of the so-called Loss-Of-Coolant Accident (LOCA).

The ALS reinforced concrete building of the RBMK-1500 reactors is comprised of two (similar in design) towers adjacent to the reactor unit (Figure 1). The ALS towers are interconnected through a system of the leak-tight compartments designed for steam discharge in case of rupture of the primary coolant circuit. The leak-tight compartment system is divided in to following zones: Zone 1 - the pressure-resistant leak-tight compartments, and Zone 2 - compartments of the reactor fuel channel feeder pipes and group distribution headers.
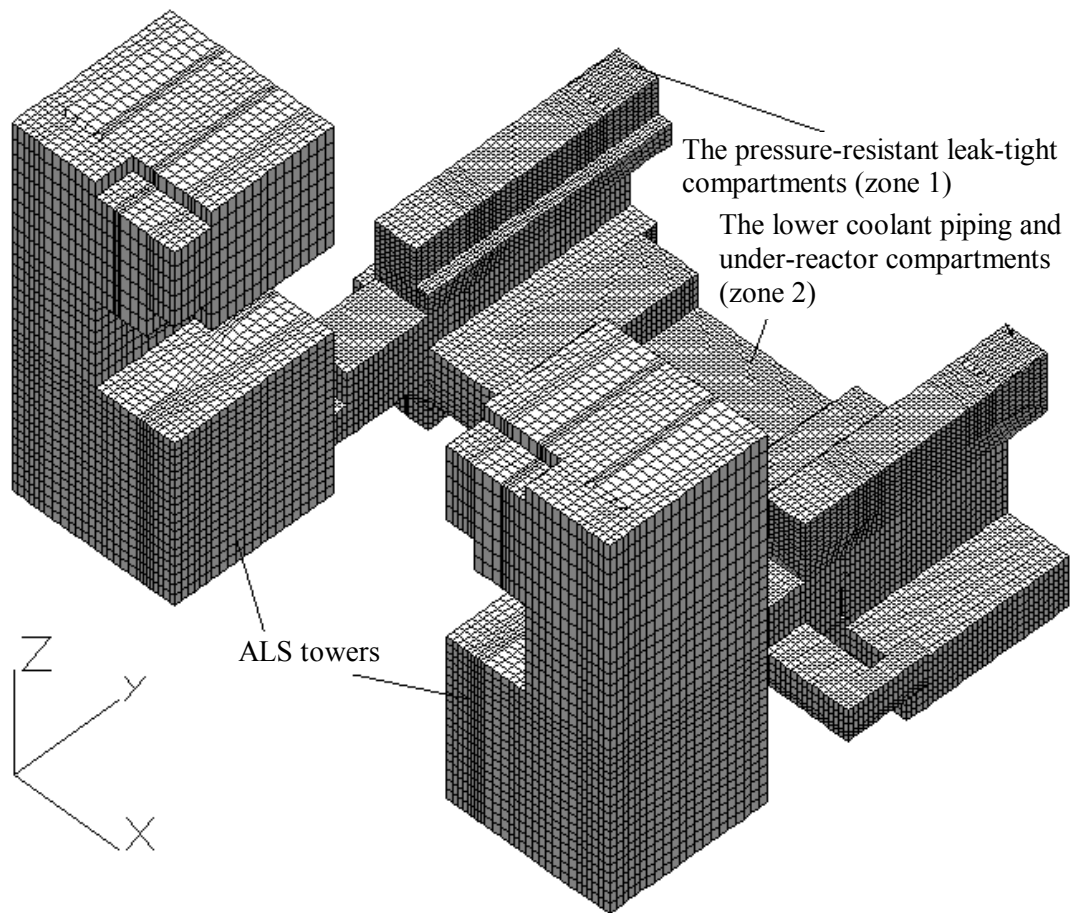
Figure 1: General layout of ALS

In structural integrity analysis of ALS it is important to evaluate strength limit of ALS building structures as well as to establish load at which first through-wall crack appear in the outer wall of ALS. Therefore, it is very important, that available leak-tightness of ALS in case of an accident would not be exceeded and would not release radioactive materials to the atmosphere. In the analysis the standard properties of concrete and rebar steel are applied. The calculations are performed until the appearance of the first crack, which passes through all layers of the concrete wall. The analysis results of the ALS failure (zone 1), when the first through-wall crack appears in the outer wall of ALS, are presented in this paper.

GEOMETRICAL MODEL

Due to symmetry of the ALS (Zone 1) geometry, only one half of the actual building was chosen for the analysis. The basic philosophy creating these models was, at first step, to model separate compartments and then combine the individual models into the entire composite model. This was performed by employing the features of the ALGOR preprocessor [1]. ALGOR/NEPTUNE interface program was created to transform all input variables (nodal coordinates as well as element properties) from ALGOR input to NEPTUNE input [2]. Comparison of ALGOR and NEPTUNE solutions was made [3] for validation.

The geometrical data of compartments (dimensions of the walls and slabs and location of the compartments) were obtained from architectural drawings. The data of reinforced concrete (thickness of walls and slabs, diameters and location of reinforcement bars in the walls and slabs, dimensions and positioning of metallic frames, type of reinforcement bars, concrete and elements of metallic frames) were obtained from reinforced concrete drawings.

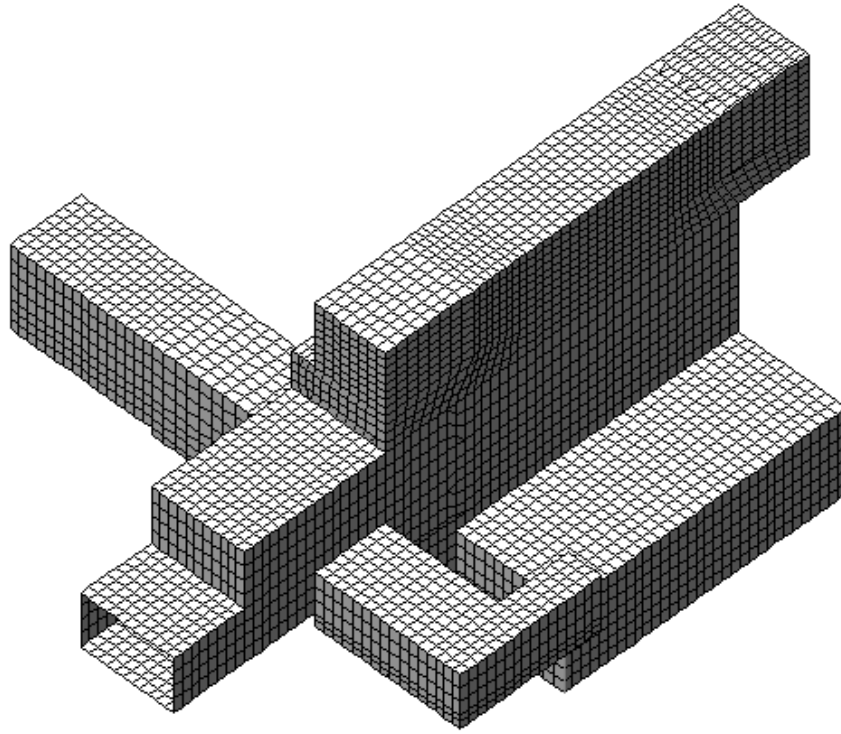The finite element model of the ALS zone 1 is presented in a Figure 2.

Figure 2: Finite element model of zone 1

MODELLING OF REINFORCED CONCRETE WALLS USING FINITE ELEMENTS

The NEPTUNE code model uses four-node quadrilateral plate element developed by Belytschko (Figure 3) [4]. The formulation of this element is based on the Mindlin theory of plates and uses a velocity strain formulation. Kulak and Fiala further developed the element by incorporating the features to represent concrete and reinforcing steel [5]. Subsequently, additional failure criteria were added and this enabled the modified elements to model concrete cracking, reinforcing bar failure and gross transverse failure.
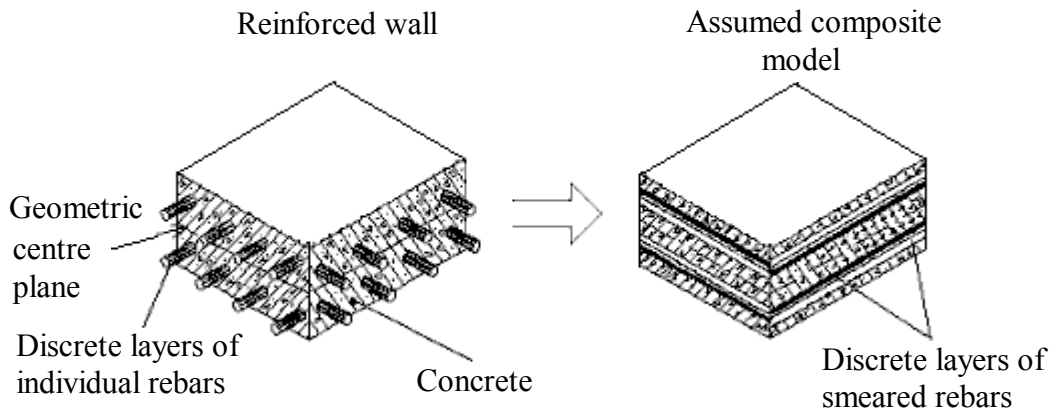

Figure 3: Section through wall/slab and equivalent finite element model with distinct layers of smeared reinforcing bars

The concrete failure model used is the Hsieh-Ting-Chen four–parameter model. The model uses the following four-parameter criterion involving the stress invariants I_1, J_2 and the maximum principal stress σ_1 [5]:

$$f(I_1, J_2, \sigma_1) = a\frac{J_2}{f_c^2} + b\frac{\sqrt{J_2}}{f_c} + c\frac{\sigma_1}{f_c} + d\frac{I_1}{f_c} - 1 = 0 \qquad (1)$$

The four failure parameters (a, b, c, d) are determined so that they represent the following four failure states:

1. Uniaxial compressive strength, f_c;
2. Uniaxial tensile strength, $f_t = 0.1 f_c$;
3. Equal biaxial compressive strength, $f_{bc} = 1.15 f_c$;
4. Combined triaxial compression, $f_{pc} = 0.8 f_c$, $f_{cc} = 4.2 f_c$.

The transverse shear failure of a reinforced concrete slab is considered by an empirical formula [5]:

$$\tau_u = \left(0.05\left(pf_y - \sigma_v\right) + 0.5\right)\sqrt{f_c}; \cdots where \cdots 0.5\sqrt{f_c} \leq \tau_u \leq 4.5\sqrt{f_c} \qquad (2)$$

Terms of equation (1) are the following: σ_y is the normal stress, f_y is the yield strength of reinforcement, p is the reinforcement ratio, f_c is the compressive strength of concrete.

BOUNDARY CONDITIONS OF MODEL AND MECHANICAL PROPERTIES OF MATERIALS

The outside surface of the main ALS is shown in Figure 1. When pressurized, the deformation of this structure is resisted by the outside structures, which are not shown in Figure 1. The outside constraints consist of walls and floor-ceiling slabs of the adjacent structure. Most of the outside nodes of the ALS model are common with those of the external constraints. Because the external constraints should be primarily resisting the ALS deformation in the tension-compression mode, their stiffness should be very large. Therefore, for simplicity, the locations of the external nodes, which in fact are connected to adjacent structures, for the first approximation are assumed completely fixed in translation.

The structural integrity analysis of the ALS was performed using standard material properties the concrete and steel properties of which are presented in Table 1 [6, 7].

TABLE 1

MATERIAL PROPERTIES

Material	Type	Young's modulus, MPa	Poisson's ratio	Yield stress, MPa	Compressive stress (concrete)/ Ultimate stress (steel), MPa	Ultimate strain, %
Concrete	M300	2.7e4	0.2	8.5	17	0.35
Steel	A III	20.5 e4	0.3	392	590	14

THE STRUCTURAL INTEGRITY ANALYSIS OF ALS

The layer element shown in Figure 3 is used in performing calculations by the NEPTUNE code. Five (5) layers are applied in the ALS models for the modelling of concrete. The code determines what layers are subjected to tension and what are subjected to compression and performs calculations subject to the failure surface of the constitutive model. Calculations for tension are performed in all elements of concrete and the possibility of element failure is considered. The code gives the following messages about the element failure:

- Failure surface reached – limit for tension is reached, the concrete cracking begins;
- Completed softening – tension evaluation is completed and the crack in concrete starts to open;
- Crushing of boundary element – element reaches ultimate strength in compression and looses resistance for any loading;
- Rebar failure – the structure looses its integrity.

Rebar failure is assumed not at the ultimate strength but when 5 % of strain is reached. This is related to the ultimate load capacity of two-rebar connector that fails at the specified deformation.

The first event of element failure (failure surface reached) means that tension limit is reached but the leakage is improbable. The calculations are performed up to the pressure at which the ultimate tension strength is

exceeded and the crack opens in all 5 layers of one concrete element (information "completed softening" in all layers of one element is recorded), i.e. the through-wall crack appears in the ALS wall.

The strength calculation of the building structures of ALS zone 1 was performed up to the pressure at which the first through-wall crack in the concrete of the outer ALS wall appears. The stress-strain curve of the reinforcing bar is assumed to be elastic-perfectly plastic, i.e. up to the limit of elasticity of the rebar steel.

The results of the stress state in zone 1 employing code NEPTUNE are presented in Figure 4. The maximum normal stresses at the pressure of 0.284 MPa are 392 MPa for tension and 355 MPa for compression. It is calculated that at this pressure one through-wall crack appears in concrete of the slab in compartment 1 (Figure 5). This picture shows the outside layer of zone 1 and it is assumed that the leakage is possible through this crack.
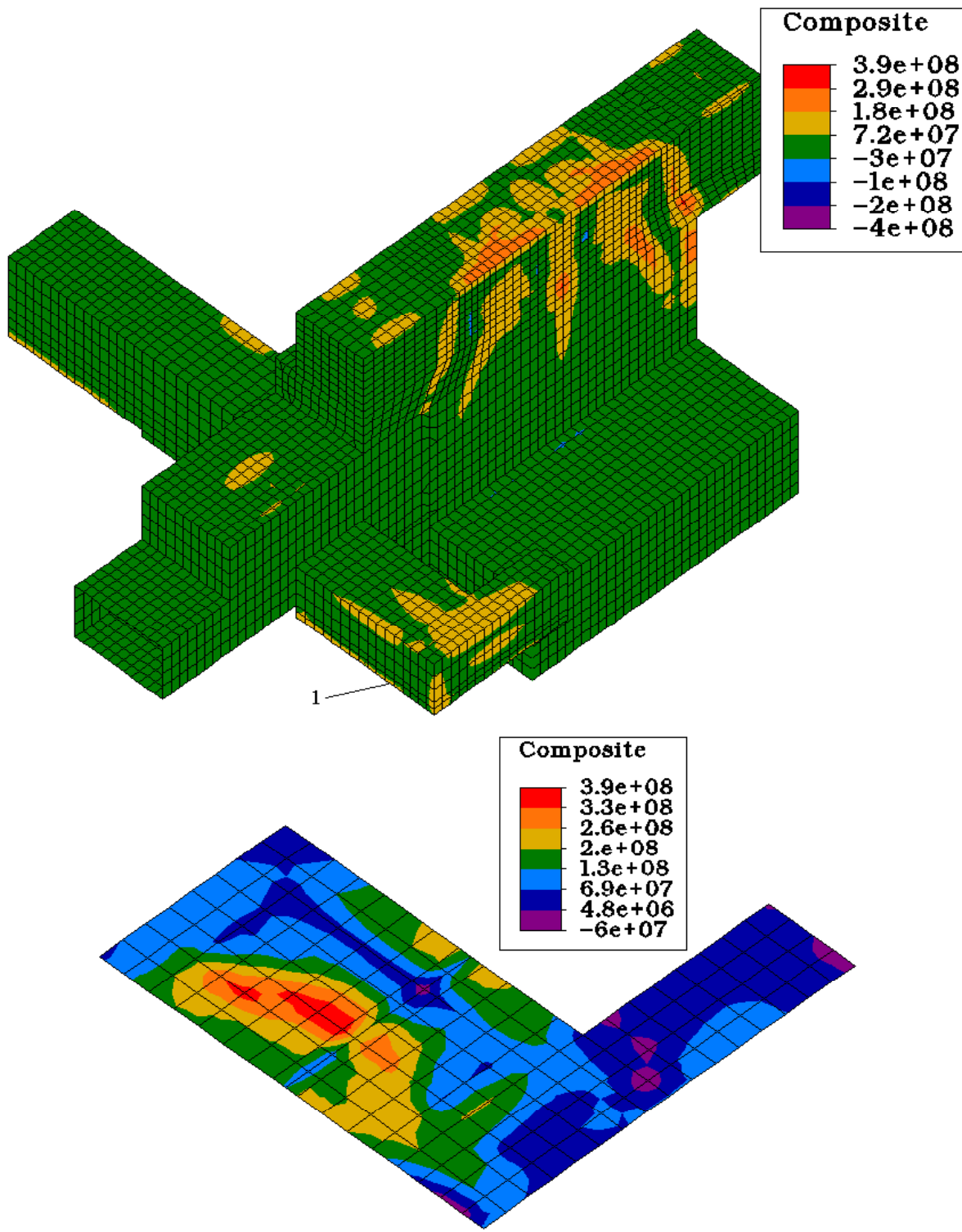

Figure 4: Distribution of the maximum principal stress (Pa) in the outside walls of zone 1 and the slab of compartment 1 (pressure – 0.284 MPa)
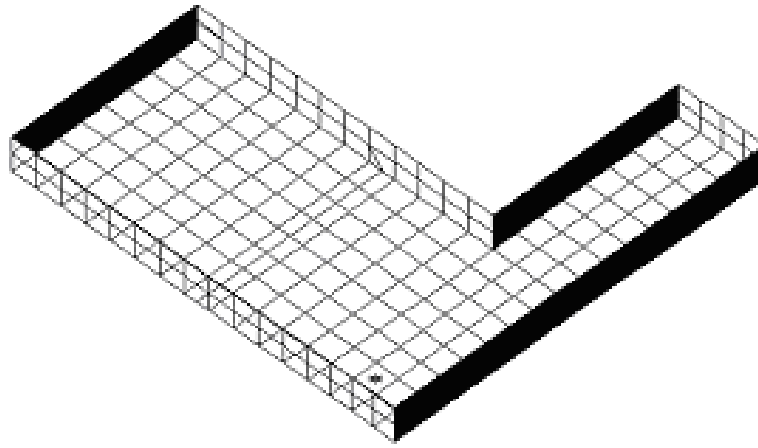
Figure 5: Location of the first through-crack in the slab of compartment 1 (star)

CONCLUSIONS

Analysis of ALS building showed that the first through-wall crack in concrete appears in the slab of compartment 1 (Figure 5) at pressure 0.284 MPa. This slab shows the outer layer of zone 1 and the leakage through this crack is possible. Thermo-hydraulic analysis showed that pressure in case of maximum design basis accident reaches 0.180 MPa. Thus, pressure safety margin exists before the first through-wall crack in the outer walls of ALS appears.

ACKNOWLEDGEMENTS

REFERENCES

1. ALGOR Instruction Manuals (2000). *Algor Finite Element Analysis System*. Algor, Inc. Pittsburgh.
2. Kulak, R.F. and Fiala, C. (1988). *Nuclear Engineering and Design*. 106, 47.
3. Dundulis, G., Narvydas, E., Uspuras, E. and Listopadskis N. (1999). *Transactions of 15th International Conference on Structural Mechanics in Reactor Technology*. VI, 333.
4. Belytschko, T., Lin, J.I. and Tsay, C.S. (1984) *Computer Methods in Applied Mechanics and Engrg.*. 42, 225.
5. Kulak, R.F., Pfeiffer, P.A. and Plaskacz, E.J. (1997). *Nuclear Engineering and Design*. 174, 143.
6. Norms and Rules for Buildings SNiP 2.03.01-84. (in Russian)
7. Baikov, V. N. and Sigalov, E. N. (1991). Reinforced Concrete Structures. Strojizdat, Moscow. (in Russian)

ULTRA-HIGH TEMPERATURE CREEP BEHAVIOR FOR IN-SITU SINGLE CRYSTAL Al$_2$O$_3$/YAG OXIDE CERAMIC EUTECTIC COMPOSITES

Y. Harada, T. Suzuki and K. Hirano

Institute of Mechanical Systems Engineering, National Institute of Advanced Industrial Science and Technology, AIST Tsukuba East, Namiki 1-2, Tsukuba, Ibaraki 305-8564, Japan

ABSTRACT

Creep behavior was undertaken for in-situ single crystal Al$_2$O$_3$/YAG oxide ceramic eutectic composites. Creep tests were conducted in the ultra-high temperature ranging from 1773 to 1873 K under a constant tensile stress ranging from 90 to 160 MPa in air and moisture environments under the water vapor pressure range from 0.06 to 0.6 MPa. Al$_2$O$_3$/YAG eutectic composites exhibited a stress exponent of 8-13. The tensile creep rate in air was about an order of magnitude higher than the compressive creep rate in argon at the same temperature. The presence of moisture enhanced the creep strain and the creep rate significantly. The creep rates increased with increasing the water vapor pressure up to 0.45MPa.

KEYWORDS

Single Crystal Oxide, Eutectic Composites, Ultra-high Temperature, High Pressure, Moisture, Creep Deformation

INTRODUCTION

Advanced ceramics such as SiC/SiC, Si$_3$N$_4$ and oxides are expected to be candidates for the ultra-high temperature structural materials in the field of power generation industries and aerospace industries because of their low density, high melting point, good oxidation resistance and high temperature strength. However, at high temperatures of 1477 K, it has been recently reported the degradation of SiC or Si$_3$N$_4$ in high pressure, moisture-rich environments (0.15 MPa of water vapor carried in air environment at 1.0 MPa of total pressure) [1-3]. Also, poly-crystal Al$_2$O$_3$ tested in water vapor revealed significant changes in weight, volume, microstructure and strength by grain boundary etching and grain growth [4]. These studies agree that the presence of water vapor accelerates the corrosion process.

In-situ single crystal oxide ceramic eutectic composites such as Al$_2$O$_3$/Y$_3$Al$_5$O$_{12}$(YAG), Al$_2$O$_3$/GdAlO$_3$ (GAP) and Al$_2$O$_3$/Er$_3$Al$_3$O$_{12}$(EAG), have newly been investigated and developed [5-9]. Al$_2$O$_3$/YAG eutectic composite has new microstructure in which single crystal Al$_2$O$_3$ and YAG are three-dimentionally and continuously connected. This composite has thermally stable at 1973K in air, excellent flexural strength and compressive creep resistance [5,6]. However, limited investigations have been conducted on the mechanical properties for Al$_2$O$_3$/YAG eutectic composite at ultra-high temperature. Furthermore, in a search of the

literature no reference was found to work investigating only the effect of water vapor on long-term mechanical properties for Al_2O_3/YAG eutectic composite.

Recently, our laboratory has been the first to construct to conduct a material test in simulated severe environments such as high temperature, high pressure or moisture environment [9-11]. This equipment permits mechanical tests at ultra-high temperature up to 1973 K, high pressure as high as 0.98 MPa and air, moisture, O_2 or N_2 environment. In this study, in order to ensure the long-term durability for Al_2O_3/YAG eutectic composite, tensile creep behavior at ultra-high temperature, high pressure, moisture environments was conducted by using the developed materials testing system in simulated severe environments.

EXPERIMENTAL PROCEDURES

Materials

The material investigated in this paper was the Al_2O_3/$Y_3Al_5O_{12}$ (YAG) in-situ single crystal oxide ceramic eutectic composite. Commercial α-Al_2O_3 powder (99.99 %) and Y_2O_3 (99.999 %) powder were pre-melted to obtain an ingot, and then the ingot was placed in a molybdenum crucible. It was fabricated by the unidirectional solidification at a melting temperature of 2173 K by lowering the molybdenum crucible at a speed of 5 mm/h [5,6]. The composition of the binary eutectic composite was Al_2O_3/YAG=67/33 wt.%. Figure 1 shows the microstructure for Al_2O_3/YAG eutectic composite. The microstructure consists of a fine lamellar structure and a three-dimensional network structure containing single crystal YAG phase (bright phase) distributed in a matrix of single crystal Al_2O_3 (dark phase). The homogeneous microstructure exists no pores or colonies in the eutectic composite.

20μ m

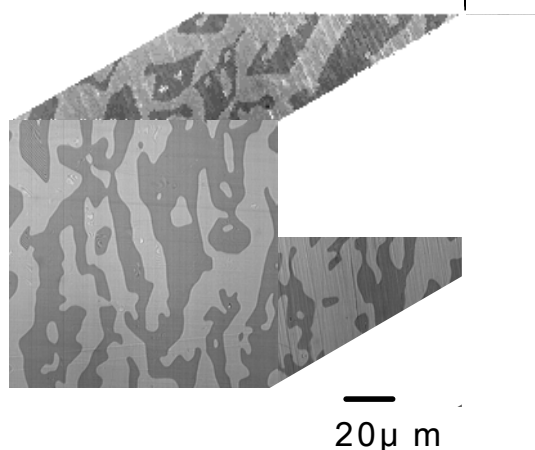Figure 1: Microstructure for Al_2O_3/YAG eutectic composite

Creep test

Tensile creep specimens having a 2.5 mm diameter and 10 mm gage-length were machined with their axis parallel to the solidified direction. In the case of the tensile creep test at 1873K, the flat, dog-bone shaped specimen having a 3×2 mm cross-section and 10 mm gage-length was machined. The overall length of all specimens was 65 mm. After machined, all specimens were homogenized at 1873K for 1 hour in air.

Tensile creep tests were undertaken by using a developed materials testing system in simulated severe environments [9-11]. By using this developed material testing system, tensile creep tests were conducted at 1773 K or 1873 K in air and 1773 K in moisture environments. The test temperature was measured by thermocouples located in the near vicinity of the specimen gage length, which was maintained within 1 K of the set point throughout each test. The constant load was controlled by a closed loop servomotor system. The displacement during creep test was measured by the extensometer using a linear variable differential transducer. Creep strain was measured by assuming that deformation occurred only in the gage section. The strain increment was calculated from the displacement after the deformation of the initial loading. Stress dependence on the creep rate was examined by stepwise loading after a creep curve showed the secondary creep behavior at a lower stress, because of the limited supply of specimens.

In addition, crept specimens were characterized by scanning laser microscopy, scanning electron microscopy

(SEM) and Energy dispersive X-ray spectroscopy (EDS).

RESULTS AND DISCUSSION

Creep curve

Tensile creep tests were conducted at 1773 K and 1873 K in air environment with the applied stresses ranging from 100 to 160 MPa. Figure 2 shows the relationships between the strain increment, $\Delta\varepsilon$, and time for tensile creep of Al_2O_3/YAG eutectic composite at 1773 K and 1873 K in air environment. All creep curves under constant stresses have essentially the same shape and can be divided into primary and secondary creep region. In the initial part of the curve, the creep rate decreases with increasing strain and reached a minimum forming a brief quasi-steady state condition. At the temperature of 1773 K under the stress of 160 MPa, failure occurred in the transient creep region.
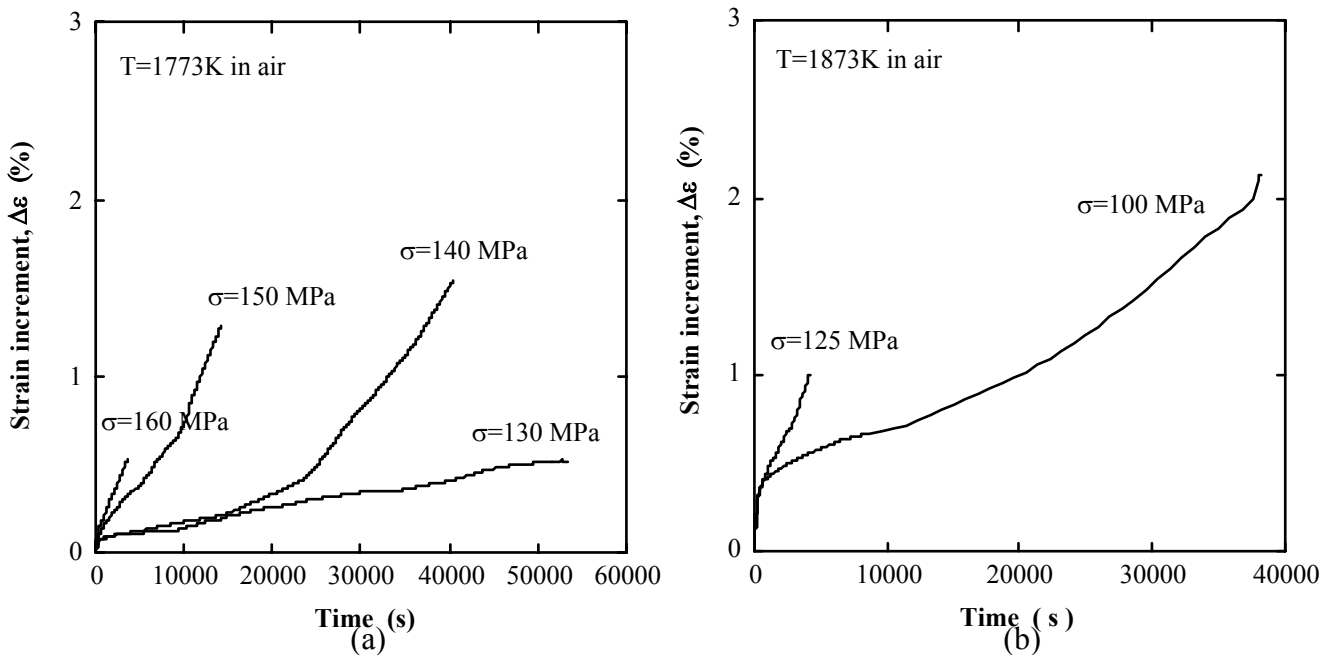

Figure 2: Strain increment as a function of time for Al_2O_3/YAG eutectic composite, (a) 1773 K and (b) 1873 K in air environment
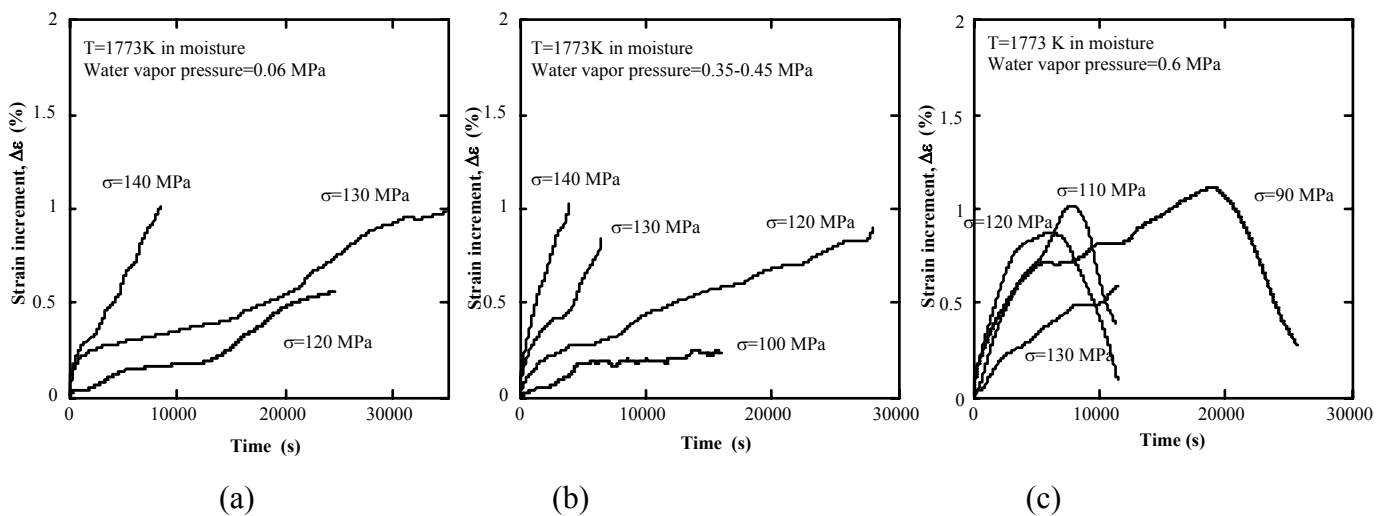

Figure 3: Strain increment as a function of time for Al_2O_3/YAG eutectic composites at 1773 K in moisture environments, under the water vapor pressure of (a) 0.06 MPa, (b) 0.35-0.45 MPa and (c) 0.6 MPa

Tensile creep tests were conducted at 1773 K in moisture environments with applied water vapor pressure ranging from 0.06 to 0.6 MPa. The applied stress was ranging from 90 to 140 MPa. Figure 3 shows the

relationships between the strain increment $\Delta\varepsilon$ and time for tensile creep of Al_2O_3/YAG eutectic composite at 1773 K in moisture environments. Creep curves under the water vapor pressure of 0.06 MPa and 0.35-0.45 MPa have the deformation in primary creep and a stable secondary creep as well as Figure 2. On the other hand, in the case of the water vapor pressure of 0.6 MPa, it can be seen that after the deformation in primary creep have reached at a maximum strain, the specimen begins to contract. This phenomenon defined as short-term negative creep [12,13]. However, under the stress of 130 MPa, as applied load is increased the negative creep is reduced, even disappeared, and failure occurs in the transient creep region. The more details are under investigation.

Stress dependency of the creep rate
The steady-state creep region stated here is the region where the creep curve is a straight line after the leveling treatment. Figure 4 shows the stress dependence of the tensile creep rates for Al_2O_3/YAG eutectic composite at 1773 K and 1873 K in air environment. These creep rates increase linearly with increasing applied stresses on the logarithmic scales. Figure 4 illustrates that the stress exponent is around 8-13 and decreases with increasing temperatures (from n=13 at 1773 K to n=8 at 1873 K). It is assumed to consider a dislocation backstress argument to explain the high stress exponents observed. One possible source for this backstress is an Orowan pile-up and bowing mechanism occurring in the single crystal Al_2O_3 matrix due to the presence of the more creep resistant single crystal YAG phase or the presence of the interphase boundary etching. The more details are under investigation.
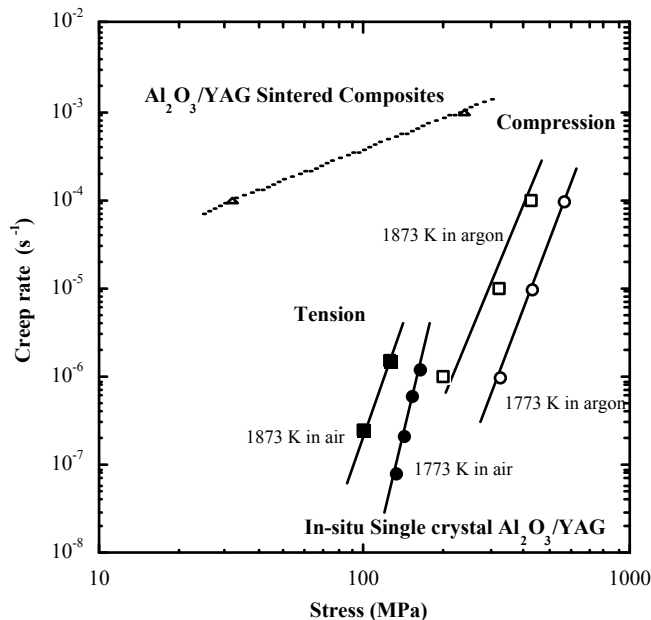

Figure 4: Stress dependence of the tensile creep rate for Al_2O_3/YAG eutectic composite at 1773 K
and 1873 K in air environment, compared with the compressive creep rates for Al_2O_3/YAG
eutectic composite and sintered composite at 1773 K and 1873 K in argon environment

Figure 4 also shows the stress dependence of the compressive creep rates for Al_2O_3/YAG eutectic composite and the sintered composite shared the same composition and constitutional phase at 1773 K and 1873 K in argon gas reported by Waku [5]. The compressive creep rates in argon environment decreases by approximately an order of magnitude compared with the tensile creep rates in air environment at each temperature. The stress exponent varies between 5 and 6. It was reported the compressive deformation mechanism followed the dislocation creep model as observed dislocations in crept specimens [5]. While, for the sintered composite, the compressive creep rate in argon environment is approximately 2.5 orders of magnitude higher than the tensile creep rates or 3 orders of magnitude higher than the compressive creep rates in argon environment for Al_2O_3/YAG eutectic composite. The exponent is close to 1. It is assumed that the creep deformation mechanism followed the diffusional creep such as Nabarro-Herring or Coble creep models.

Effects of moisture environments on creep rate

Figure 5 shows the stress dependence of the tensile creep rate for Al_2O_3/YAG eutectic composite at 1773K in moisture environments without the water vapor pressure of 0.6 MPa. This figure also shows the results for Al_2O_3/YAG eutectic composite at 1773 K and 1873 K in air environment. These creep rates increase linearly with increasing the applied stress on logarithmic scales. The creep rates in moisture environment are larger than that at 1773 K and smaller than that at 1873 K in air environment. Also they increase with increasing the water vapor pressure up to 0.45 MPa. The stress exponent is around 9.4-10 and slightly decreases with increasing the water vapor pressure.
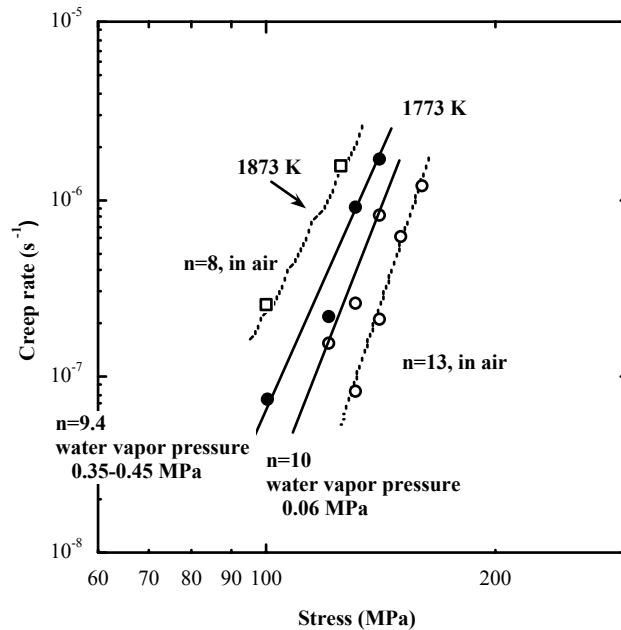

Figure 5: Stress dependence of the tensile creep rate for Al_2O_3/YAG eutectic composite
in air and moisture environments

It was widely recognized that metals, alloys and intermetallics can be severely embrittled by moisture. Impurities in moisture can dissolve in most materials and affect their properties. For instance, the Ni_3(Si, Ti) alloys exhibited substantially reduced tensile ductility and intergranular fracture when tested in air or hydrogen containing environments [14]. In contrast, hydrogen introduced in palladium enhances its deformation by promoting diffusional creep [15]. In the case of single crystal ceramics, it is reported that the presence of water enhanced weakening of sapphire with introduction of water defect as a result of enhanced dislocation mobility [16].

Taking into account these considerations, the accelerating of creep rate in moisture-induced environments may be due to molecular water, hydroxide or hydrogen defect in moisture in crept in Al_2O_3/YAG eutectic composites. These defects could be introduced in the bulk, by complex transport processes (pipe diffusion, solute drag, etc.) and enhance dislocation mobility. An alternative explanation for the accelerating of creep rate in moisture-induced environments may be based on the role of the Peierls potential in controlling dislocation glide and the influence of interstitial hydrogen in moisture which introduces in the specimen. The stress for the deformation is directly due to the nucleation and motion of kink pairs on dislocation. If either kink nucleation or kink motion is enhanced by the presence of interstitial hydrogen, the accelerating creep could be explained. However, the exact mechanism responsible for this accelerating creep in moisture-rich environment needs await precise observations of dislocations in crept specimens.

CONCLUSION

The tensile creep behavior for in-situ single crystal Al_2O_3/YAG eutectic composite was studied in the temperature range 1773-1873 K and the stress range 90-160 MPa in air or in moisture environments under the water vapor pressure of 0.06-0.6 MPa by using the materials testing system in simulated severe environments. The following conclusions can be drawn:

(1) Al$_2$O$_3$/YAG eutectic composite exhibited the same shape creep curve and could be divided into primary and secondary creep region. The tensile creep rates in air environment increased by about an order of magnitude compared with the compressive creep rates in argon environment. The stress exponent was 8-13, and it was assumed to consider a dislocation backstress argument.

(2) It was found that the presence of moisture enhanced the creep strain and the creep rate of Al$_2$O$_3$/YAG eutectic composites significantly. The creep rates increased with increasing the water vapor pressure up to 0.45 MPa. On the oher hand, in the case of water vapor pressure of 0.6 MPa, it was seen the short-term negative creep. As applied load was increased the negative creep was reduced, even disappeared.

REFERENCES

1. Ferber, M.K., Lin, H.T., Parthasarathy, V. and Brentnall, W. (1999) *ASME papers* 99-GT-265.
2. More, K.L., Tortorelli, P.F., Ferber, M.K. and Keiser, J.R. (2000) *J. Am. Ceram. Soc.* 83, 211.
3. More, K.L., Tortorelli, P.F., Ferber, M.K., Walker, L.R., Keiser, J.R., Miriyala, N., Brentnall, W.D. and Price, J.R. (2000) *J. Eng. Gas Turb. Power.* 122, 212.
4. Tai, W.P., Watanabe, T. and Jacobson, N.S. (1999) *J. Am. Ceram. Soc.* 82, 245.
5. Waku, Y., Nakagawa, N., Ohtsubo, H., Ohsora, Y. and Kohtoku, Y. (1995) *J. Jpn Inst. Met.* 59, 71.
6. Waku, Y. and Sakuma, T. (2000) *J. Eur. Ceram. Soc.* 20, 1453.
7. Waku, Y. (2000) *J. Jpn Inst. Met.* 64, 977.
8. Waku, Y. (2000) *J. Jpn Inst. Met.* 64, 101.
9. Hirano, K., Suzuki, T., Kamei, A. and Tamai, F. (2001) *Inter. J. Mater. Prod. Tech.* 16, 276.
10. Suzuki, T., Harada, Y., Hirano, K. and Waku, Y. (2001) *Proc. 7th International Conference on Creep and Fatigue at Elevated Temperatures,* in print.
11. Harada, Y., Suzuki, T., Hirano, K. and Waku, Y. *J. Am. Ceram. Soc.,* to be submitted.
12. Liu, X.C. and Bathias, C. (1994) *J. Mater. Sci.* 29, 4618.
13. Ren, D.G. (1998) *J. Mater. Process. Tech.* 73, 74.
14. Takasugi, T., Liu, C.T., Heatherly, L., Lee, E.H. and George, E.P. (1999) *Intermetallics* 7, 543.
15. Xu, Z.R. and Mclellan, R.B. (1998) *Acta Mater.* 46, 4543.
16. Castaing, J., Kronenberg, A.K., Kirby, S.H. and Mitchell, T.E. (2000) *Acta Mater.* 48, 1495.

Unconventional domain bands near a crack tip

W. Yang, F. Fang, H.T. Wang and Y.Q. Cui

Department of Engineering Mechanics, Tsinghua University,

Beijing 100084, P.R. China

Tel. 86-10-62782642, Fax: 86-10-62781824, e-mail: yw-dem@tsinghua.edu.cn

Abstract

Experiment indicates that unconventional domain band structure appears ahead of an indentation crack tip, and it is caused by the highly localized crack tip electric field. The partially switched ferroelectric grain resembles a banded Eshelby inclusion embedded in a polycrystalline ferroelectric matrix. Mesomechanics analysis quantifies the unconventional domain band structures, including the volume fraction, the thickness, and the orientation of switched domain bands. The interaction between cracking and domain switching in single crystal ferroelectrics is also discussed.

1. Introduction

Ferroelectric ceramics exhibit peculiar behaviors such as fracture near a defect or an electrode under electric load [1]. The intensive electric field near a crack tip stimulates local domain polarization switching that plays a critical role in electric fracture. The switched domains generate incompatible strain under the constraint of un-switched material and consequently alter the stress distribution near the crack. Experiment [2] indicates that unconventional domain band structure appears ahead of an indentation crack tip when subjected to lateral electric field. The band structure is caused by highly localized crack tip electric field. The elastic mismatch energy for a partially switched ferroelectric grain embedded in a polycrystalline ferroelectric matrix is evaluated as a banded Eshelby inclusion. The discussion is extended to the interaction between cracking and domain switching in single crystal ferroelectrics.

2. Microscopy of Crack Tip Unconventional Domain Bands

Experimental observations for domain bands were mostly reported under uniform fields. It was the work in [2] that provided direct evidence for the domain switching near a crack tip subjected to the electric field concentration. The PLZT ceramic samples were mechanically cut and grounded into specimens with the size of 3.5mm×5mm×25mm. XRD revealed an aspect ratio c/a of 1.013, and a spontaneous domain switching strain of 1.3% . The samples were poled under an electric field of 2300V/mm at $120^{o}C$, resulting in the ferroelectric domains to align with a polarization normal to the plane. After poling, indentation is performed, followed by the application of the lateral electric field of $0.6E_c$ (E_c＝1100V/mm) to cause the field concentration near the indenting crack. Fig. 1 provided a SEM image near an indentation crack tip [2]. The

actual crack enters the view from the upper-left, and runs down at about $45°$ degrees. Lamellar $90°$ domain structure appeared as the black and write strips shown in Fig. 1.
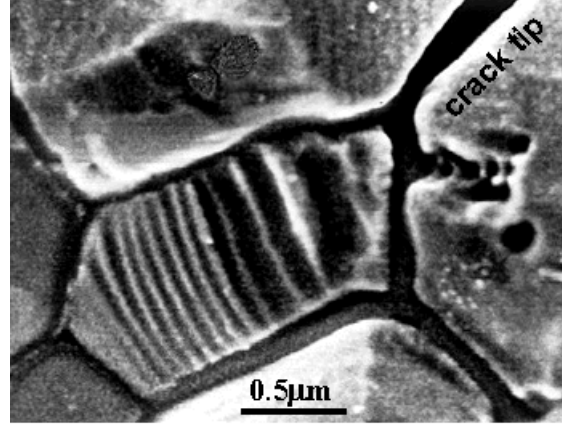

Fig. 1 SEM shows $90°$ domain switching bands near a crack tip.

3. Energetics of Domain Bands

The equilibrium domain assemblies is quantified by the free energy minimization. Consider a ferroelectric grain of volume D^3 embedded within a homogenized ferroelectric matrix. Remote stress $\overline{\sigma}_{ij}$ and electric field $\overline{E}_i$ are applied. The formation of domain band structure in the ferroelectric grain causes the following change in system free energy:

$$\Delta U = \Delta U_{\text{Elastic}} + \Delta U_{\text{Electric}} + \Delta U_{\text{Wall}} - \Delta U_{\text{M}}^{\infty} - \Delta U_{\text{E}}^{\infty}, \tag{1}$$

where $\Delta U_{\text{Elastic}}$ denotes the elastic mismatch energy, $\Delta U_{\text{Electric}}$ the electric depolarization energy, ΔU_{Wall} the domain wall energy, and $\Delta U_{\text{M}}^{\infty}$ and $\Delta U_{\text{E}}^{\infty}$ correspond to the works done by the remote stress and electric fields. Denote the spacing of two adjacent domain plates as $2t$. For the case of an instantaneous $90°$ domain switch, the depolarization energy can be computed as

$$\Delta U_{\text{Electric}} = \frac{2P_s^2 t}{\pi^3 \varepsilon D} f(V_{90}),; \quad f(V_{90}) = \sum_{k=1}^{\infty} \frac{\sin^2(V_{90}k\pi)}{k^3}, \tag{2}$$

where ε denotes the mean square root average of the dielectric constants, P_s the spontaneous polarization, and V_{90} the volume fraction of the switched domain. The domain wall energy has a form of $\Delta U_{\text{Wall}} = \Gamma_{90}/t$, where the $90°$ domain wall energy Γ_{90} is composed of the coherent domain wall energy Γ_{coh} and the energy Γ_{misfit} of misfit dislocations along the domain wall. The quantity Γ_{coh} assumes a value of $\Gamma_{\text{coh}} = 0.002\text{J/m}^2$ for PZT. The switching released works are

given by $\Delta U_{\mathrm{M}}^{\infty} = V_{90}\bar{\sigma}_{ij}\Delta\gamma_{ij}$ and $\Delta U_{\mathrm{E}}^{\infty} = V_{90}\bar{E}_i\Delta P_i$.

4. Banded Eshelby Inclusion

Consider an infinite region with a banded Eshelby inclusion. The self-equilibrium feature of the residual mismatch stress renders the decomposition of the elastic mismatch energy as $\Delta U_{\mathrm{Elastic}} = \Delta U_{\mathrm{LR}} + \Delta U_{\mathrm{SR}}$. The first term signifies the long-range elastic mismatch energy for a uniform transform in the inclusion. Dimensional consideration dictates that

$\Delta U_{\mathrm{LR}} = \alpha(\nu)Y\left(V_{90}\dfrac{c-a}{a}\right)^2$. The transformation strain solution of Eshelby [3] leads to the

dimensionless quantity $\alpha(\nu)$ as $(7-5\nu)/[15(1-\nu^2)]$ for a spherical shape, and the value of

$3/[16(1-\nu^2)]$ for a cylindrical grain unconstrained in axial direction. The short-range mismatch

energy due to the fluctuating mismatch $\tilde{u}_i^*$ along the grain boundary can be computed as

$$\Delta U_{\mathrm{SR}} = -\frac{1}{2D^3}\int_{\partial\Omega}\tilde{t}_i\tilde{u}_i^*\,\mathrm{d}S. \tag{3}$$

The misfit dislocations are used to release the long range strain mismatch within the inclusion caused by misfit strains. The domain misfit energy can be obtained as

$$\Gamma_{\mathrm{misfit}} = \frac{Yl}{8\pi(1-\nu^2)}\left(\frac{c-a}{a}\right)^2\left[\ln\frac{l}{4\pi r_0} - \frac{1}{4(1-\nu)}\right]\frac{\sin^2\phi(1+3\cos^2\phi)}{(1+\cos^2\phi)^2}. \tag{4}$$

where ϕ denotes the top view angle of domain wall. That angle is measured by microscopy of etched specimen as $70°$.

5. Band Parameters near a Crack Tip

The mismatch along the grain boundary can be expanded by sinusoidal Fourier series, the calculation yields

$$\Delta U_{\mathrm{SR}} = \frac{4(1-\nu)Yf(V_{90})}{(1+\nu)(3-4\nu)\pi^3}\frac{(c-a)^2}{a^2}\frac{t}{D}\frac{1+2\cos^2\phi+5\cos^4\phi}{(1+\cos^2\phi)^2}. \tag{5}$$

That leads to a band thickness of

$$t = \sqrt{\frac{\pi^3\Gamma_{90}D}{2f(V_{90})\left[\dfrac{P_s^2}{\varepsilon} + \dfrac{2(1-\nu)Y}{(1+\nu)(3-4\nu)}\dfrac{(c-a)^2}{a^2}\dfrac{1+2\cos^2\phi+5\cos^4\phi}{(1+\cos^2\phi)^2}\right]}}. \tag{6}$$

Substituting the above derivations into (1), one finds the change in system energy as

$$\Delta U = \frac{Y(7-5v)}{15(1-v^2)} \left(V_{90} \frac{c-a}{a} \right)^2 - V_{90} \left[\frac{c-a}{a} (\bar{\sigma}_{22} - \bar{\sigma}_{33}) + P_s (\bar{E}_2 - \bar{E}_3) \right]$$
$$+ \frac{2}{\pi} \sqrt{\frac{2f(V_{90})\Gamma_{90}}{\pi D} \left[\frac{P_s^2}{\varepsilon} + \frac{2(1-v)Y}{(1+v)(3-4v)} \frac{(c-a)^2}{a^2} \frac{1+2\cos^2\phi+5\cos^4\phi}{(1+\cos^2\phi)^2} \right]}. \tag{7}$$

Numerical calculations indicate that the last term only offers an effect of about a few percent in determining the switched volume fraction V_{90}. If that term is neglected, the following explicit expression is derived for V_{90}:

$$V_{90} = \frac{1}{2Y\alpha(v)} \frac{a}{c-a} \left[\bar{\sigma}_{22} - \bar{\sigma}_{33} + \frac{a}{c-a}(\bar{E}_2 - \bar{E}_3)P_s \right]. \tag{8}$$

Fig. 1 indicates that the switched ferroelectric grain ahead of the crack has a shape of $1\times1.5\mu m$ rectangle, and the length D along the crack extension line is approximately $1.5\mu m$, while the theoretical solution for the domain switching zone is a circle of diameter $1.35\mu m$ ahead of the crack but touching the crack tip. The applied field for this case can be evaluated as $2\sqrt{5}E_{app}$, with

$E_{app} = 0.6E_c = 660\text{V/mm}$. Substituting $\bar{E}_2 \approx 2\sqrt{5}E_{app}$ and $\bar{E}_3 = 0$ into (8), one finds that the

volume fraction for switched bands is $\frac{\sqrt{5}}{Y\alpha(v)} \left(\frac{a}{c-a} \right)^2 P_s E_{app}$. For the "soft" ferroelectric ceramics

used in this test, the relevant physical constants are $Y = 33\text{GPa}$, $v = 1/3$, $c/a = 1.013$,

$E_c = 1.1\times10^6\text{V/m}$ and $P_s = 0.3787\text{C/m}^2$. The calculation gives $V_{90} = 0.249$ for fully constrained

spherical grain, and $V_{90} = 0.474$ for cylindrical grain unconstrained in the x_3-direction. The

measured volume fraction of domain switch is $V_{90} \approx 0.35$. The misfit energy is obtained for the

particular domain wall in Fig. 1 as $\Gamma_{\text{misfit}} \approx 0.021\text{J/m}^2$. Consequently, Γ_{90} is about 0.023J/m^2. For

at a volume fraction of $V_{90} \approx 0.35$, it is found that $f(0.35) \approx 0.902$ from (2). The substitution of the

above data, plus $P_s = 0.3787\text{C/m}^2$ and $\varepsilon = 1800\varepsilon_0 = 1.593\times10^{-8}\text{F/m}$, into (6) gives a predicted

domain wall spacing of $t = 0.2178\mu m$. That value is of the same order, but somewhat larger, than

the experiment measurement from Fig. 1.

6. Bands near an Indentation Crack of Poled Single Crystals

Two poling modes are taken prior to Vickers indentation. One is the anti-plane poling whose poling field is normal to the observation plane and directed outward; the other is the vertical poling whose poling field lying in the observation plane and directing upward. For the former case, the effect of poling on the observation plane is isotropic, while anisotropic effect can be observed for the latter case.
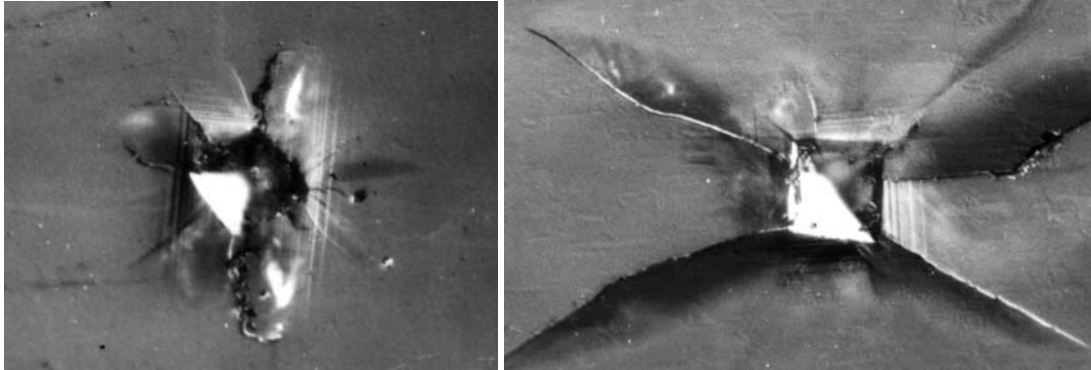

Figure 2 Vickers indents for single crystal barium titanate

Yang *et al*. [4] reported the micrographs of Vickers indents on single crystal barium titanate. Figure 2 shows the micrograph referring to the case of anti-plane poling. Indentation cracks emanated equally from the indenting pyramid in four directions. Domain bands perpendicular to the indenting cracks were formed. Extensions of the indenting cracks trigger the formation of domain bands along their wakes. Since the domain bands are normal to the crack, their switching strains are normal to the indenting crack. Switching strains of this type induce closure and effectively suppress the crack extension. The indentation cracks arrested after small amount of extension.

The right graph of Figure 2 illustrates the microscopy for the case of vertical poling. The cracks extended from the indent pyramid in anisotropic manner. Since the poling is upward, the cracking along the horizontal direction causes less 90° domain switching than the cracking along the vertical direction. Accordingly, the domain switch suppresses the crack growth towards a horizontal direction less than that does the crack growth towards a vertical direction. The cracking tilted to the vertical direction was shorter but triggered a wider switching wake, while the cracking tilted to the horizontal direction was longer but triggered a narrower switching wake. Consequently, the fracture toughness of a ferroelectric single crystal after vertical poling is anisotropic: the value against cracking in horizontal direction is lower than that in vertical direction. An interesting phenomenon happened: the strain mismatch along the phase boundary of horizontal bands and vertical bands induced cracks. Since the horizontal domain bands were wider than the vertical bands, the phase boundary of strain mismatch was tilted toward the

horizontal direction. The influence of habit plane of previously formed domain bands dictated that the subsequent formation of domain bands could only be the same horizontal and vertical family, with the same domain boundary mismatch to drive the crack extension along the phase boundary of different domain bands. Subsequently formed domain bands hardly suppressed the propagation of the tilted cracks but drove them. Those cracks tilted in the horizontal direction gradually became the dominant cracks and enjoyed long extension.

References

1. Winzer, S.R., Shankar, N. and Ritter, A.P., Designing cofired multilayer electrostrictive actuators for reliability, *J. Am. Ceramic Soc.* **72**(1989), 2246-2257.
2. Fang, F., Yang, W. and Zhu, T., Crack tip 90^0 switching in tetragonal lanthanum-modified lead zirconia titanate under an electric field. *Journal of Materials Research*, **14** (1999), 2940-2944.
3. Eshelby, J.D., Determination of the elastic field of an ellipsoidal inclusion and related problems. Proc. Roy. Society London Ser. **A241**(1957), 376-396.
4. Yang W, Fang F, Tao M. Critical role of domain switching on the fracture toughness of poled ferroelectrics. Int. J. Solids & Structs., 38(2001):2203~2211.

Rockwell
Science Center

UNIVERSAL BRIDGING LAWS FOR CRACKS IN CREEPING MEDIA

B. N. Cox and N. Sridhar

Rockwell Science Center
1049 Camino Dos Rios
Thousand Oaks, CA 91360
U.S.A.

ICF100959OR

UNIVERSAL BRIDGING LAWS FOR
CRACKS IN CREEPING MEDIA

B. N. Cox and N. Sridhar

Rockwell Science Center, 1049 Camino Dos Rios, Thousand Oaks, CA 91360, U.S.A.

ABSTRACT

Some theoretical results for bridging traction/crack displacement laws for composite and monolithic materials in which cracks are bridged by rate-dependent ligaments are reviewed. Laws derived from experiments and laws proposed on theoretical grounds for different material systems and for different loading conditions often display similar functional characteristics. It is therefore proposed that engineering creep/fracture tests be analysed by simple, trial bridging laws of the most common functional form, with parameters to be determined by fitting test data such as crack length vs. time and load. A simple bridging law of this kind, with only a few unknown parameters to be evaluated, offers a reasonable balance between consistency with the underlying physical mechanisms and engineering practicality. An approach to engineering certification of damage tolerance for materials containing cracks bridged by rate-dependent ligaments is outlined.

KEYWORDS

Certification, crack bridging, rate dependence, creep, ceramic composite, polymer craze

INTRODUCTION

This paper is motivated primarily by the need to establish certification procedures for fibre-reinforced ceramic matrix composites for high temperature use in applications such as rocket nozzles, turbine engine combustors, and hot airframe components. In many such composites, failure mechanisms involving fibre creep are likely to form a significant part of the boundary of the allowable design space [1,2].

In notched or damaged components, one archetypal problem of interest is that illustrated in the schematic of Fig. 1, where a system of matrix cracks emanates from a stress concentrator. At high temperature, a single dominant crack tends to emerge from the system, the others arresting and remaining relatively short [1,3]. Considerable evidence shows that at least for some important composites the primary rate effect is fibre creep [1-5]. Crack acceleration of the dominant crack results from reduction of the shielding effect at its tip. The essential characteristic of the composite required to model crack growth and eventual failure is the relation between the stress, σ_0, in the fibres on the matrix crack plane and the relative displacement, u, of the fibres and the matrix on the same plane (the matrix crack opening displacement; or more generally the displacement discontinuity across a band of localised damage). If this function (which of course will also involve time and temperature) is known, bridged crack analysis will predict crack propagation.
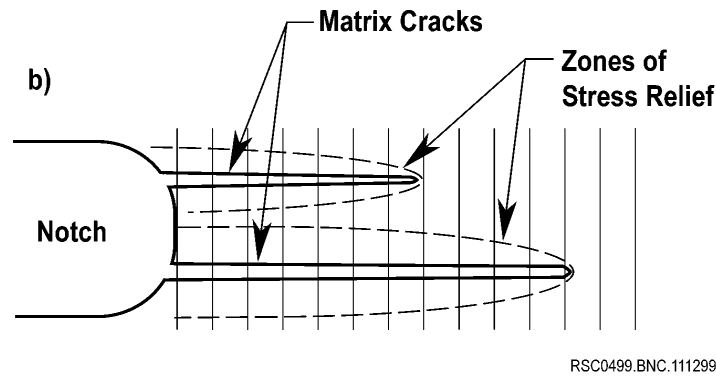
Figure 1: System of matrix cracks emanating from a stress concentrator, with one crack becoming dominant.

A simple model has led to an expression for the differential function $\dot{u}(\sigma_0)$ (the derivative of u with respect to time) [6]. The function bears close similarity to laws found for other material systems, especially polymers. This leads to the conjecture that a method of engineering certification for crack growth in ceramic composites and polymers in the presence of rate-dependent bridging that is based on standardisable tests fitted by a universal canonical traction law might be attainable. Such a method is needed to make the certification problem sufficiently straightforward.

TRACTION LAW FOR CREEP-RUPTURE PROBLEMS IN CERAMIC COMPOSITES

The physics of a creeping fiber being pulled out of an elastic matrix can be summarised by dividing the fibre into three zones in which different mechanisms operate (Fig. 2). Far from the matrix crack plane lies a so-called intact zone ($z > z_2$), where the fibre and matrix have equal strains in the axial direction, z. Displacements remain continuous across the interface in this zone and the loads are assumed to be low enough that the creep threshold of the fibres is not exceeded. Closer to the matrix crack lie two frictional zones, where the fibre has slipped relative to the matrix against the spatially varying friction stress, $\tau(z)$. In the further of these zones from the matrix crack plane (the "friction zone", $z_1 < z < z_2$), the axial stress in the fibres remains below a threshold for creep. Here any variation in the friction stress is caused by elastic contraction of the fibre in the radial direction due to Poisson's effect alone. In the nearer of the zones to the matrix crack plane (the "friction/creep" zone, $d < z < z_1$), the axial stress in the fibre exceeds the creep threshold and fibre shrinkage due to creep also modifies the friction stress. Nearest to the matrix crack a so-called debond zone may exist ($0 < z < d$), where the radial shrinkage of the fibre is so great that contact has been lost with the matrix and so there is no friction. One seeks the time history of the pullout displacement, u_0, for any history of the fibre stress at the fracture plane, σ_0, which is proportional to the bridging traction, p.

For fixed loads, a steady-state configuration exists, in which the friction/creep and friction zones propagate invariantly along the fibre away from the crack plane at a constant velocity, v. Simple analytical results can be obtained for general load histories in the limiting case that changes in stress are sufficiently slow that the solution is always close to the steady-state solution corresponding to the instantaneous value of the load, which will often be the case. In this quasi-steady state condition, the displacement rate for fibers obeying

power-law creep with exponent m, i.e., $\dot{\varepsilon} \propto (\sigma - \sigma_{th})^m$, where σ_{th} is the creep threshold, can be written [6,7][1]

$$\dot{U}_0 = \frac{2\tau_0\lambda}{\gamma_2}\left\{\Sigma_0^m D + \frac{2}{m+1}\Sigma_0^{m+1}\right\} + \frac{2\tau_0}{\gamma_3 E}\frac{d}{d\bar{t}}[\Sigma_0 D] + \eta\frac{2\tau_0}{\gamma_3 E}\left[\frac{\sqrt{\pi}}{2}\frac{\Gamma\left(\frac{m+3}{m+1}\right)}{\Gamma\left(\frac{m+5}{2m+2}\right)}\right]2\Sigma_0\dot{\Sigma}_0 \tag{1}$$

where a dot denotes differentiation with respect to a normalised time variable, $\bar{t} = 2\gamma_2 t/\gamma_3\left(2\tau_0/\gamma_3\right)^{m-1}$; λ is a creep rate parameter; τ_0 is the pristine friction stress; E is the fibre modulus; d is the length of the debond zone (Fig. 2); U_0, D, and Σ_0 are normalised forms of u_0, d, and σ_0; γ_3 and η are elasticity/geometry parameters; and Γ is the Gamma function. The first term on the right hand side of Eq. (1) expresses the contribution of fibre creep to the displacement rate, with the term involving D arising from the debond zone and the term Σ_0^{m+1} from the friction/creep zone; the second term represents elastic stretching of the fibre in the debond zone; and the third term represents elastic stretching of the fibre in the friction/creep zone. The contributions involving D are history dependent, since

$$D = \int_0^{\bar{t}} V d\bar{t} \tag{2}$$

where V is the velocity (rate of self-similar translation) of the friction/creep zone, which is a function of σ_0 and therefore of the normalised time, $\bar{t}$. For the limits used to reduce the results of [6,7] to Eq. (1), one finds that

$$V = \frac{2}{m+1}\Sigma_0^{m+1} \qquad . \tag{3}$$

In the approximation that bridging tractions can be represented by continuous, averaged tractions, p, acting smoothly over the crack faces rather than only at the location of bridging fibres, a traction law, $\dot{u}(p, \dot{p})$, follows from Eq. (1) by substituting $p = f\sigma_0$ where f is the fibre volume fraction. The differential form of Eq. (1) implies that bridged crack problems will have to be solved by integrating over the history of the applied load, while accounting for any crack growth [4,5].

Equation (1) has been derived under the assumptions that fibre/matrix friction is not uniform but is modified by creep shrinkage of the fibres; and that the debond and friction/creep zones evolve in a quasi-steady state condition, which is valid for moderate rates of change of the bridging stress. Begley, Evans, and McMeeking (BEM) derived a bridging law for fibres that undergo linear creep but remain coupled to the matrix by a constant and uniform friction stress, τ_0 [8]. Thus in BEM there is no debond zone (no fibre shrinkage) and the steady-state conditions of the model underlying Eq. (1) cannot be considered. The bridging law of BEM describes the transient response to the first period of loading. In its simplest form (omitting certain terms containing convolutions that are small), BEM reduces to

$$\dot{u}_0 = m_1\sigma(t)_0[\dot{\sigma}_0(t) + m_2\sigma_0(t)] \tag{4}$$

where m_1 depends on elastic constants and the fibre volume fraction and m_2 includes the creep rate constant, λ. The first term in brackets arises from the elastic straining of the fibre in the friction/creep zone. Because the friction stress is constant and uniform in BEM, their law reproduces the familiar quadratic relationship

---

[1] From Eq. (37) of [6] and generalisations for non-linear creep in [7]. An error of sign is corrected and an integral term omitted from the former. The integral term corresponds to an elastic displacement rate arising from the friction zone, which is identically zero since the friction zone is bounded by the fixed stress condition, $\sigma = \sigma_{th}$, and is therefore invariant. The limit is taken here that Poisson's effect causes radial strains in the fibre that are small compared to its shrinkage due to creep.

between crack displacement and load, $u_0 \propto \sigma_0^2$, in the absence of creep. The last term of Eq. (1) refers to the same contribution and has the same form, even though the assumed stress distribution along the fibre is different (because of creep shrinkage). The second term in brackets in Eq. (4) arises from fibre creep in the BEM model. It corresponds to the term $\lambda \Sigma_0^{m+1}$ in Eq. (1), with equality of form in the case of linear creep ($m = 1$). Thus the contribution to the crack displacement of fibre creep within the friction/creep zone has the same functional form in both models.
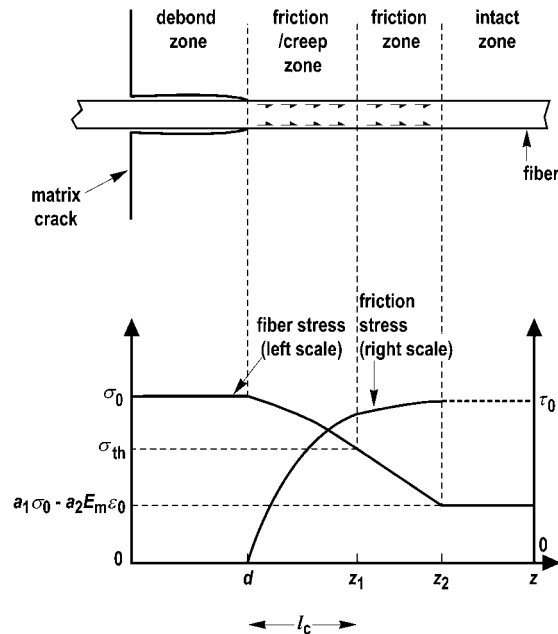

Figure 2: Four zones in a creeping fibre that bridges a matrix crack, with schematics of the axial stress and friction stress variations.

The similarity of the forms of BEM and the model of Eq. (1) when $m = 1$ is quite remarkable, since BEM is essentially a model of transient response, while the quasi-static approximation underlying Eq. (1) depends on the existence of a steady-state crack configuration. Furthermore, the stress distributions along the friction/creep zone in BEM and the model of Eq. (1) are not the same, even in the absence of Poisson's effect, being linear in BEM and nonlinear in the latter, due to non-uniformity of the friction stress. Yet the two models yield identical dependences on the applied load for both the elastic and creep contributions to the total displacement arising from the friction/creep zone. This interesting universality suggests that Eq. (1) might be a powerful basis for crack growth data reduction. The functional form of Eq. (1) is

$$\dot{U}_0 = c_1 \Sigma_0^m D + c_2 \Sigma_0^{m+1} + c_3 \frac{d}{dt}\left[\Sigma_0 D\right] + c_4 \Sigma_0 \dot{\Sigma}_0 \tag{5}$$

This law might be hoped to give good correlation with creep/rupture (crack growth) data for fixed temperature. The coefficients c_1, etc., will of course be different at different temperatures. While the micromechanical basis of Eq. (1) is a model of a single matrix crack, the same law, Eq. (5), is also proposed here for analysing damage bands consisting of multiple matrix cracks, or a non-planar matrix crack, or a crack system with complicated connectivity; and for non-unidirectional reinforcement, including wavy or misaligned fibres, such as in a textile composite, as long as a damage band can still be identified in each case.

RATE-DEPENDENT COHESIVE ZONES IN POLYMERS

The depiction of Fig. 2 for creeping fibres has a close analogy in the drawing and extension of fibrils in a craze zone in a polymer. Two processes dominate the extension of fibrils in a craze zone under normal loads: 1) creep or viscous extension of the fibrils, which is analogous to the creep extension of fibres in the debond zone of Fig. 2; and 2) drawing of new material from the bulk into the fibrils, which is analogous to the process of loss of contact between creep-shrinking fibres and the matrix in the friction/creep zone of Fig. 2. Micromechanical models of fibril drawing give rise to relations between the total displacement rate and the stress and stress-rate in the fibrils, which can be re-arranged to exhibit forms similar to Eq. (5) (e.g., [9,10]). Some quantitative distinctions are worth noting. First, because of the hardening mechanism in drawn polymers, creep extension of the fibrils once they have been drawn tends to be relatively small. Therefore, the first term in Eq. (5) is often omitted in craze models. Second, the stress dependence of the drawing rate in polymers is relatively strong. Thus where a power law relation is used between the stress (σ_0 in the current notation) and the displacement rate due to the drawing of new fibrils, the power is typically of order 10. Fibre creep tends to have milder stress dependence: the power for creeping fibres usually is bounded by $m \leq 4$.[2] Third, because of the dominance of the plastic displacement arising during the drawing process of newly drawn fibril, models of crazes have no analogue of the fourth term in Eq. (5) (elastic strain in the process zone). Thus in polymers, Eq. (5) might reduce to the second and third terms only, with a relatively high power expected in the second term.

FAILURE OF THE BRIDGING MECHANISM

At some point, the creeping fibres (or fibrils in a craze) will rupture, terminating the bridging traction. A plausible criterion for rupture of a creeping fibre is the attainment of either a critical creep strain or a critical stress. For a fibre exhibiting power law creep, $\dot{\varepsilon} \propto (\sigma - \sigma_{th})^m$, the rupture criterion will have the form

$$\int_0^t \left(\Sigma_0 - \Sigma_{th} \right)^m dt = \varepsilon_{crit} \tag{6a}$$

$$\sigma_0 = \sigma_{crit} \tag{6b}$$

for two material constants, ε_{crit} and σ_{crit}. In most cases of interest, Eq. (6a) is likely to be the first failure criterion to be attained: if the most highly-loaded fibres (those at a notch root) do not satisfy Eq. (6b) on first loading, then they never will, since the stress in them relaxes if the applied load is held constant [5].

AN APPROACH TO EMPIRICAL CREEP/RUPTURE LAWS AND CERTIFICATION

Certification of a part against creep-rupture by crack propagation requires a material calibration test that is simple and repeatable, from which any necessary material information can be deduced in a simple form without complicated computational analysis. For failure by crack propagation in the presence of long zones of bridging fibres, the critical material information is the rate dependent traction law, $\dot{u}(\dot{p}, p)$, or equivalently, $\dot{u}(\dot{\sigma}_0, \sigma_0)$, together with a bridging ligament failure criterion, such as Eq. (6).

---

[2] The stress dependence of the rate of drawing of fibrils in crazes is so strong that it has also been modeled as an exponential function [11]. Whether the dependence is exponential or a power law with a power ~ 10, the effective result is that the fibrils will draw almost infinitely fast whenever the stress, σ_0, exceeds some threshold. A traction-displacement relation must result that is not far in its effect on crack growth from a Dugdale model of uniform stress in the cohesive zone.

An engineering certification procedure cannot depend on detailed knowledge of micromechanical mechanisms, such as those treated in deriving Eq. (1) as a problem in materials science. Therefore, Eqs. (5) and (6) are suggested as a parametric form of material data for the creep-rupture problem, with the parameters to be found empirically. Some speculations on the outcome of calibrating tests are as follows. 1) At low or moderate stresses, creep strain will dominate elastic strain and the last two terms of Eq. (5) will be negligible: the coefficients c_3 and c_4 will be difficult to determine. 2) At relatively short times, e.g., if the critical creep strain for rupture is relatively small, any debond zone will remain small and the first term of Eq. (5) will be negligible: the coefficient c_1 will be difficult to determine. At relatively long times, conversely, the first term will become the dominant creep term and the second term will be negligible, with c_2 difficult to determine. 3) The length of the bridging zone will depend on the notch size used in an experiment. With relatively small notches, a long zone of bridging fibres might evolve before the critical creep rupture strain is reached; with a long notch, the fibre at the notch root will be highly stressed and will reach the critical rupture strain while the bridging zone is relatively short. Thus tests for different notch sizes will yield information about different regimes.

CONCLUSIONS

A functional form, Eq. (5), has been suggested for a simple bridging traction law that could serve as the basis for empirical calibration of materials in which cracks are governed by rate-dependent bridging. The law has been derived with the first objective of establishing a certifying procedure for ceramic composites at fixed temperature. However, the law may also be useful for analysing time-dependent notch effects in polymers and the durability of bonded repairs. In different applications, some of the terms of the proposed law might be negligible and therefore could be omitted. The traction law will be complemented in general by a criterion for bridging ligament rupture, Eq. (6).

Acknowledgments

References

1. Henager, C. H. Jr., and Jones, R. H., 1993. *Materials Science and Engineering* **A166**, 211-220.
2. Cox, B. N., Marshall, D. B., McMeeking, R. M., and Begley, M. R., 1997. *IUTAM Symposium on Nonlinear Analysis of Fracture*, ed. J. R. Willis (Kluwer Academic, Dordrecht, 1997) pp. 353-65.
3. Mumm, D. R., Morris, W. L., Dadkhah, M. S., and Cox, B. N., 1996. ASTM STP 1309, ed. M. G. Jenkins *et al.* (ASTM, Philadelphia, 1996).
4. Cox, B. N., and Rose, L. R. F., 1994. *Mechanics of Materials* **19**, 39-57.
5. Begley, M. R., Cox, B. N., and McMeeking, R. M., 1995. *Acta Met. et Materialia* **43**[11], 3927-36.
6. Cox, B. N., Sridhar, N., and Argento, C. R., 2000, *Acta Materialia*, **48**, 4137-50 (2000).
7. Sridhar, N., Cox, B. N., and Samuels, A. Y., 2001. to be submitted to *Acta Materialia*.
8. Begley, M.R., Evans, A.G. and McMeeking, R.M., 1995. *J. Mech. Phys. Solids*, **43**, 727.
9. Socrate, S., Boyce, M. C., and Lazzeri, A., 2001. *Mechanics of Materials*, 33, 155-175.
10. Sha, Y., Hui, C. Y., and Kramer, E. J., 1999. *J. Mater. Sci.*, **34**, 3695-3707.
11. Argon, A. S., and Bessonov, M. I., 1977. *Phil. Mag.*, **35**, 917-933.

USE OF ATOMIC FORCE MICROSCOPY IN ASSESSING SURFACE DAMAGE DUE TO FATIGUE

Laurent Cretegny[1] and Ashok Saxena[2]

[1]GE Corporate R&D Center, Schenectady, NY
[2]School of Materials Science and Engineering, Georgia Institute of Technology
Atlanta, GA 30332-0245, USA

ABSTRACT

Strain controlled fatigue tests were conducted on polycrystalline copper at $\Delta\varepsilon/2$=0.161% and 0.255% to various fractions of fatigue life. Scanning electronic microscope (SEM) and atomic force microscopy (AFM), a relatively new tool that readily provides high resolution digitized images of surface features, were used to describe and quantitatively characterize the evolution of surface deformation during fatigue. To quantify surface deformation, a parameter γ^{irrev} is defined that is a measure of the local slip irreversibility at the surface. This parameter applies to any type of surface deformation feature, is independent of the size of the fields of view and yields information on the distribution of surface strains over the specimen gage length. From this formalism, a criterion for crack nucleation is proposed using actual AFM surface strain measurements.

KEYWORDS

Damage, Fatigue, Copper, AFM, SEM, Extrusions, Protrusions, Slip-bands

INTRODUCTION

Although engineering models for predicting fatigue life are available, damage evolution that leads to the formation of a macro-crack is difficult to predict, because no easily measurable parameter uniquely describes the state of damage during this stage. The objective of this study is to quantitatively describe the evolution of the surface features that develop in copper polycrystals up to crack nucleation. Because fatigue crack nucleation is a surface phenomenon, fatigue damage is better characterized by changes at the surface rather than by alterations in the interior of the material and, therefore, scanning electron microscopy (SEM) and atomic force microscopy (AFM) were chosen as analytical tools to perform this study. AFM is a relatively new technology that provides high-resolution three-dimensional images of the surface and digitized information about the surface topography providing accurate and quantitative measurements of the surface features.

EXPERIMENTAL PROCEDURE

Strain controlled fatigue tests were performed on high purity C101 grade polycrystalline copper (OFHC). The fatigue tests were performed on standard axial specimens with a surface preparation that consisted of a combination of mechanical and electrochemical polish. The grain size of copper was

estimated by mean intercept length method at about 40 μm after a heat treatment of one hour at 500°C. The fatigue tests were conducted using a triangular waveform at a strain rate of 0.005 s⁻¹ and a stress ratio R=-1. The strain amplitudes enforced on specimens during the fatigue tests were 0.161% and 0.255%, and yielded fatigue lives of 75,900 cycles and 6,900 cycles, respectively. Several specimens were tested at each strain amplitude and all but one test was arrested prior to failure to allow the observation of surface topography by AFM at fractions of the fatigue life of about 0.5 and 0.9. Failure was declared once a macroscopic crack was observed at the surface. The fatigue tests were followed by sectioning of the specimens for post-test observations by SEM and AFM. The AFM used in this study was an Aris-3500 with a long range scanning module METRIS-3070. About twenty scans were analyzed along the length and at several positions around the circumference of each specimen. The collection of AFM images was submitted to a verification procedure described elsewhere [1] to ensure that the area covered by the AFM scans was representative of the whole surface.

RESULTS AND DISCUSSION

Characterization of Surface Damage

The most common occurrence of surface deformation in cyclically loaded polycrystalline copper is in the form of slip bands regularly distributed within grains. The slip bands in specimens tested at 0.161% strain amplitude, had heights that varied from 30 nm and 900 nm, Figure 1. Slip bands were observed at both applied strain amplitudes, although towards the end of the fatigue life in 0.255% strain amplitude tests, protrusions became the dominant form of surface damage. According to Suresh's definition [2], a protrusion is a surface upset many μm in height, where a macro-PSB, tens of μm wide and containing tens of matrix and/or PSB lamellae, emerges at the free surface. This definition applies to single crystals, where PSBs span across the entire width of the sample and clusters of similarly oriented slip bands can form over the whole surface. Protrusions with characteristics such as reported by other research groups for copper single crystals [3,4] were obviously not observed in this study with 40 μm grains, but AFM measurements showed that a considerable bulging of the surface (about 1 μm) took place across the width of some PSBs that had covered a significant portion of a grain, Figure 2. The typical width of the protrusions was between 10 and 20 μm, creating a height to width ratio smaller than measured in single crystals. This is consistent with findings on copper single crystals by Hunsche and Neumann [4] that showed a decrease in the height of the protrusions with a reduction of the thickness of the single crystals, explained by availability of less material to produce the upset. In the present study, the term protrusion is used when PSBs occupy the greater part of a grain and the density of the slip bands forming the PSB has reached a high enough level that no band of matrix is visible between the slip bands.

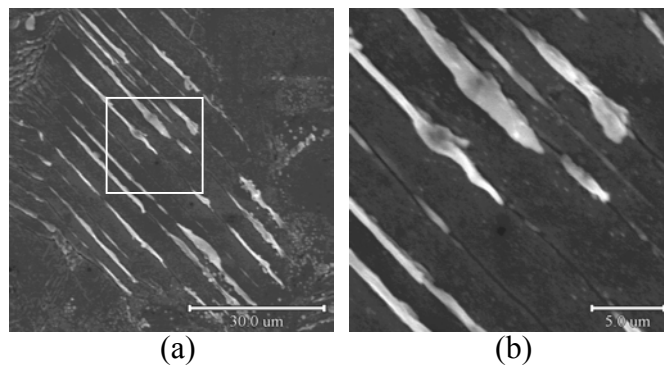(a)   (b)

Figure 1: Typical appearance of slip bands at the surface in large grains in polycrystalline copper cyclically loaded at a strain amplitude of 0.161%. (b) magnified picture of the boxed area in a.

At 0.255% strain amplitude, the average height of slip bands at N/N_f=0.25 is 108 nm, which shows that a significant growth occurs early in the fatigue life and then increases to 247 nm at failure. The latter compares well to the average height of 271 nm obtained at failure for the 0.161% strain amplitude, a fact that actually supports the theory by Essmann et al. [5] that relates the surface roughness to point defect formation

in the bulk, which is limited by the size of the grains in polycrystals. As a result, the growth of slip bands in

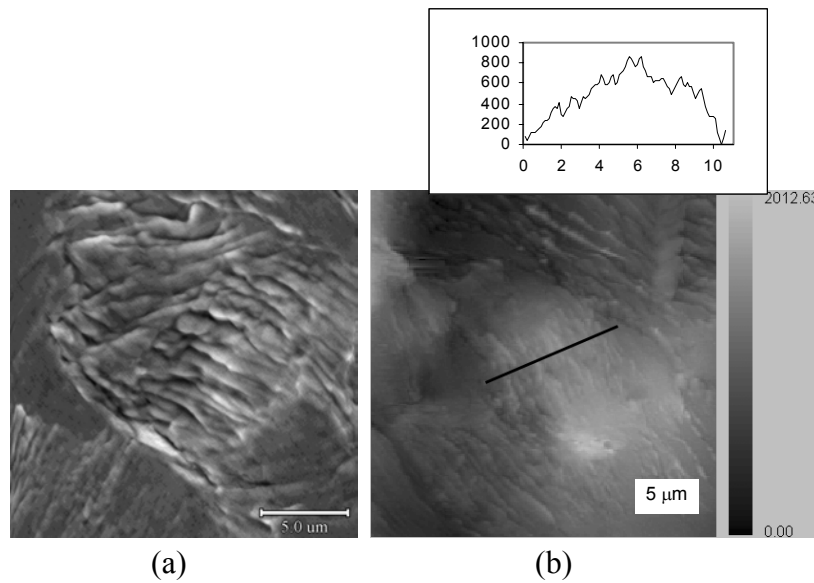(a)   (b)

Figure 2: Example of a protrusion in polycrystalline copper formed during fatigue at a strain amplitude of 0.255% (a) SEM photo and (b) AFM photo. The loading axis is along the vertical and the gray scale to the right of the AFM photo refers to the height of the features.

polycrystalline copper with grains on average 40 μm in diameter seems to saturate at a height of about 250 nm.

Fatigue crack nucleation in copper specimens at both strain amplitude occurred systematically at grain boundaries in regions with significant surface deformation, Figure 3. More specifically, in almost every case, cracks initiate at the boundary between one grain with considerable surface upset and another grain that does not show much trace of surface deformation.

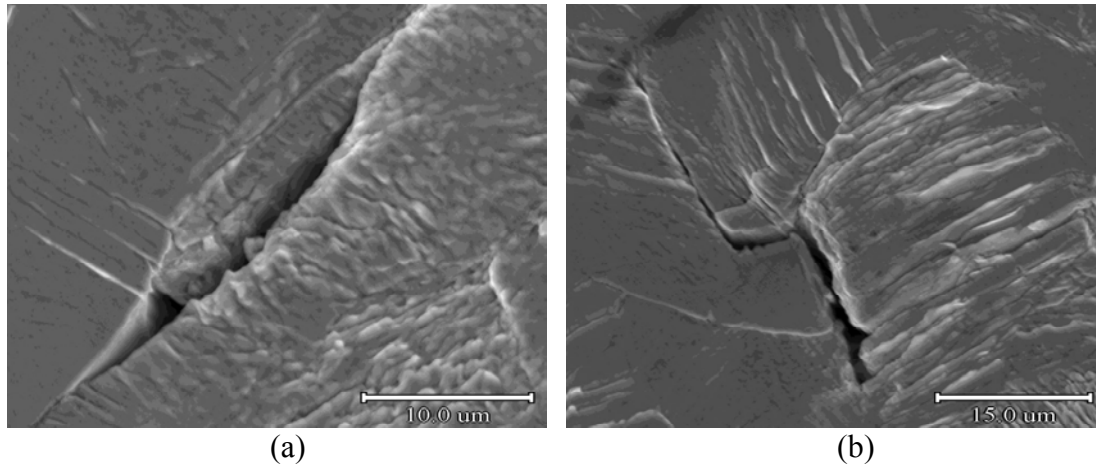(a)   (b)

Figure 3: Typical intergranular cracks in different specimens of Cu cycled at different strain amplitudes. Cracks tend to form on boundaries between grains that show considerable surface deformation and those that are relatively free of deformation.

Criterion for Fatigue Crack Nucleation

The potential of high resolution devices capable of quantitatively describing the surface topography, such as scanning tunneling microscopy (STM) and atomic force microscopy (AFM), was discovered in the early 90's and used for accurately measuring the height of surface features in various materials [6-12]. Quantitative parameters were defined from these measurements to describe the state of surface deformation, such as the average slip distance [6] or the ratio of the average height to the average spacing between the surface features [7] and root mean square (RMS) height of the surface [9]. A direct relationship exists between these parameters and the average accumulation of surface plastic strain, which was exploited in these studies to determine the irreversibility of slip at the surface. Although, the use of average values of

surface parameters is correct to describe the general state of surface damage, the extension of their use to the determination of the onset of the nucleation of fatigue cracks, which is by nature a heterogeneous process, is beyond the capabilities of such parameters. Indeed, microcrack nucleation is always preceded by a local concentration of surface deformation and only the local cyclic plastic strain at this site is representative of fatigue damage, not the average deformation over the entire surface.

This study attempts to remedy the above shortcoming by characterizing the entire distribution of surface displacements instead of just the average value. In addition, the irreversible surface deformation parameter defined in this investigation to quantify surface deformation is not limited to the height or height to spacing ratio, but combines measures of length, height and number per unit area of the surface features and is therefore able to accommodate different types of surface deformation features. Furthermore, it does not rely on spacing between slip bands, which makes it also applicable to surface features that develop individually as was the case with one of the materials studied here. The irreversible surface deformation parameter is defined as follows (a detailed derivation is provided in [13])

$$\gamma^{irrev} = \frac{\sum_{j=1}^{m}\left(\sum_{i=1}^{n} 2|\delta_i|a_i^{norm}\right)_j}{\sum_{j=1}^{m} L_j} \tag{1}$$

where δ is the height or depth of a surface feature, a^{norm} is its length normalized relative to the size of the field of view (FOV), L is the length of the FOV, n is the number of slip bands per FOV and m the total number of FOV. The numerator consists, therefore, of the total amount of normal deformation at the surface, while the denominator represents the total length of the fields of view, which is effectively the gauge length.

When considering the entire surface of a specimen, equation (1) provides an average value of γ^{irrev}, which is not pertinent to the study of the onset of fatigue crack nucleation, because the latter is the result of local surface deformation. Therefore, the measured average values of γ^{irrev} are not reported here, but can be found elsewhere [13]. On the other hand, the following analysis of the distribution of γ^{irrev} can provide valuable information on the onset of fatigue crack nucleation.

Due to the high level of heterogeneity in fatigue surface deformation, it is virtually impossible to predict where the fatal crack will nucleate and monitor changes in topography at that precise location. However, even though the local maximum of γ^{irrev} cannot be directly measured, by statistically characterizing the distribution of surface damage in a large number of FOVs, it is possible to predict the amount of damage in the region with maximum local surface damage, even though that specific region is not directly included in the FOVs. It was found that the distribution of γ^{irrev} resembles a Gaussian distribution where only a few regions have extreme amounts of surface upset (high or low) and the major portion of the surface has a local amount of damage that is close to the sample average [13]. The distribution is in fact adequately modeled by a continuous normal distribution function, which has the advantage that it can be easily integrated and has an area under the curve equal to one, corresponding to 100% of the specimen's surface. Figure 4 shows the distribution of γ^{irrev} with the horizontal axis representing ranges of γ^{irrev} and the distribution indicated on the vertical axis.

Since the normal distribution curves of Figure 4 reveal the extreme values of irreversible surface deformation reached in some regions, these plots directly provide information on the advancement of surface upset in the highly deformed regions. Thus, this data can be used to predict when the material reaches a critical state that will trigger the nucleation of a fatal crack. This analysis is however better performed on the cumulative version of these plots shown in Figure 5, which is simply the integral of the plots in Figure 4. The vertical axis on the left indicates the portion of the surface that contains amounts of irreversible surface deformation between zero and the amounts indicated on the horizontal axis of the graph. Conversely, the vertical axis on the right provides the fraction of the surface that has developed amounts of irreversible surface deformation larger than the amount indicated on the horizontal axis.

The previous AFM and SEM observations clearly showed that fatigue cracks nucleate in regions with significant surface deformation. Therefore, a criterion for crack nucleation may be defined in terms of a critical *local* value of γ^{irrev} necessary for crack nucleation. This critical value of γ^{irrev} can be determined from AFM measurements by measuring the value of γ^{irrev} of FOVs that contain a crack nucleus. Once known, this value can be traced on the normal distribution curves of the irreversible surface deformation, as shown by the vertical lines shown on Figure 5. It was found that the levels of local surface deformation necessary to trigger the nucleation of a fatigue crack are similar between the low and the high amplitude tests in stainless steel but they differ between the two strain amplitudes in copper [13].

It is important to note that the criterion described above does not act like a "failure or no failure" switch that would imply that a crack is always nucleated once the critical value of surface deformation is achieved in a specific location. On the contrary, certain portions of the surface may develop levels of surface deformation well beyond the critical value without nucleating a fatal crack, as observed in all failed specimens and in some specimens tested to 90% of the life. The actual fraction of the surfaces that has reached or exceeded the crack nucleation criterion is indicated by the ordinate of the intersection of the distribution curves with the vertical line that specifies the criterion. Now, if one postulates that the likelihood of nucleating a crack increases with the fraction of the surface over which the critical level of surface deformation is exceeded, the distribution curve of the irreversible surface deformation then provides an estimation of the probability for crack nucleation.

CONCLUSIONS

From the SEM and AFM analyses of the surface deformation of cyclically loaded polycrystalline copper, the following conclusions were drawn.

Extrusions are the principal surface deformation features in copper tested at 0.161% and 0.255% strain amplitudes, with the development of protrusions later in the fatigue life at the higher strain amplitude. Slip bands reach on average 250 nm in height at both strain amplitudes, which tends to indicate that the growth of slip bands saturates at this level in copper with a grain size of 40 μm. In all tests, fatigue cracks nucleated at grain boundaries and seemed to be driven by the strain mismatch between adjacent grains. From the digitized description of the surface topography, a procedure was developed to quantitatively assess surface damage at any given point in the fatigue life.
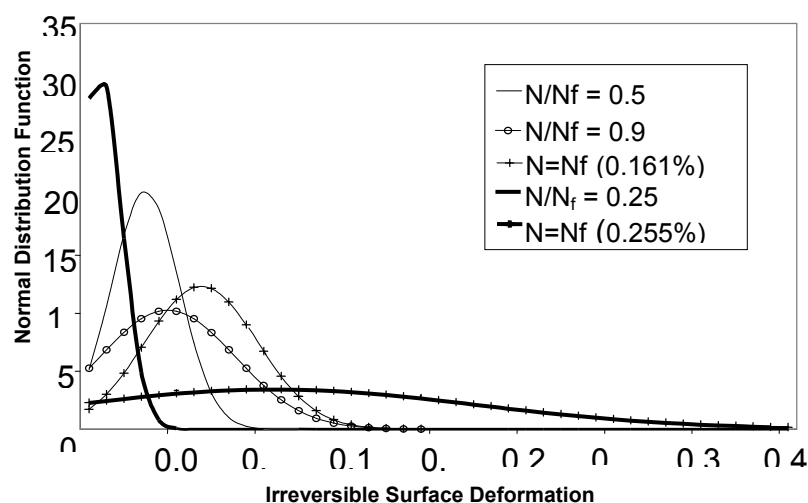
ACKNOWLEDGEMENTS

Figure 4:   Representation of the distribution of the irreversible surface deformation at the surface of fatigue specimens using the normal (Gaussian) distribution function for polycrystalline copper (at 0.161% and 0.255% applied strain amplitude).
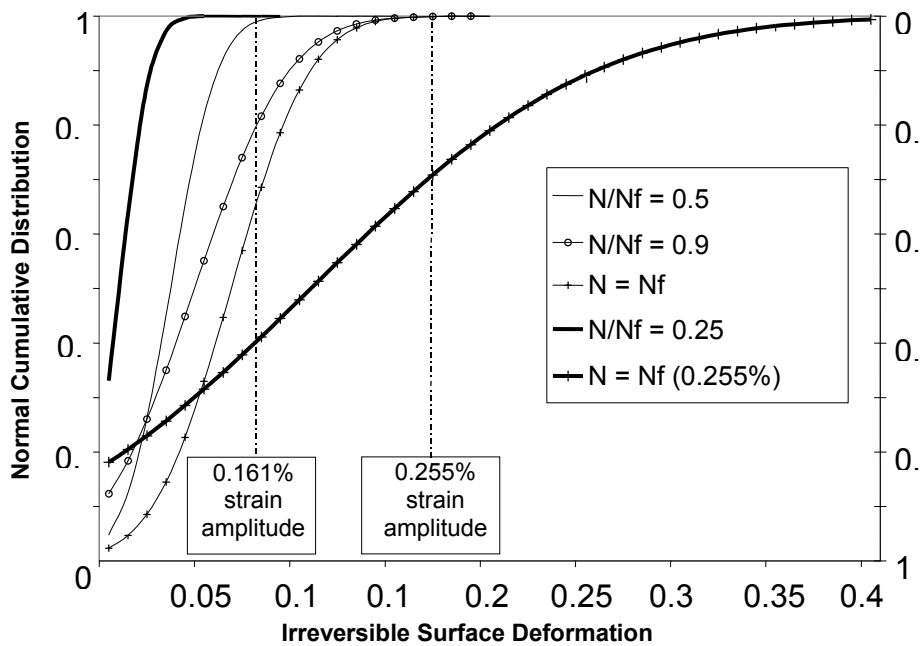
Figure 5: Polycrystalline copper (tested at 0.161% and 0.255% strain amplitude). The right axis corresponds to one minus the left axis, and the vertical dotted lines represent the critical values of the irreversible surface strain.

REFERENCES

1 .   Cretegny, L., Saxena, A., (2000) "Evolution of Surface Deformation during Fatigue using AFM – Part I: Polycrystalline Copper", submitted for publication to Acta Materialia.
2.   Suresh, S., (1998) *Fatigue of Materials*, Second Edition, Cambridge University Press.
3.   Ma, B.T., Laird, C., (1989) *Acta Metallurgica*, 1989, 37, 325.
4.   Hunsche,A., Neumann, P., *Acta Metallurgica*, 34, 207.
5 .   Essmann, U., Gösele, U., Mughrabi, H., (1981) *Philosophical Magazine A*, 44, 405.
6.   Sriram, T.S., Ke, C.M., Chung, Y.W., (1993) *Acta Metall Mater*, 41, 2515.
7.   Harvey, S.E., Marsh, P.G., Gerberich, W.W. (1994) *Acta Metall Mater*, 42, 3493.
8.   Gerberich, W.W., Harvey, S.E., Kramer, D.E., Hoehn, J.W., (1998) *Acta Mater*, 46, 5007.
9.   Yang, F., Saxena, A., (2000) *Proc Instn Mech Engrs*, 214C, 1151.
10.   Saxena, A., Yang, F., Cretegny, L., (1999) *Proc Seventh Int Fatigue Congress*, Editors: X.R. Wu, Z.G. Wang, Beijing, P.R. China, 4, 2777.
11.   Jono, M., (1999) *Proc Seventh Int Fatigue Congress*, Editors: X.R. Wu, Z.G. Wang, Beijing, P.R. China, 4, 57.
12.   Man, J., Obrtlík, K., Lopour, F., Blochwitz, C., Polák, J., (1999) *Proc Seventh Int Fatigue Congress*, Editors: X.R. Wu, Z.G. Wang, Beijing, P.R. China, 4, 157.
13.   Cretegny, L., Saxena, A., (2000) "Evolution of Surface Deformation during Fatigue using AFM – Part III: Criterion for Crack Nucleation", submitted for publication to Acta Materialia.

USE OF SURFACE-TREATMENT LIFE EXTENSION METHODS FOR AIRCRAFT COMPONENTS

Q. Liu, S. A. Barter, P. Baburamani, P. K. Sharp and G. Clark

Airframes and Engines Division, Defence Science and Technology Organisation, 506 Lorimer Street, Fishermans Bend, Victoria 3207, Australia.

ABSTRACT

Surface treatment methods such as shot peening or glass bead peening are well established as methods for extending the fatigue lives of structural details in aircraft. These methods introduce residual stresses in the surface layers that retard the growth of fatigue cracks, similar to the use of cold-expansion methods for fatigue enhancement of fastener holes. While these techniques have been used extensively to achieve satisfactory fatigue lives in individual components that exhibit unexpected fatigue cracking, the difficulty of guaranteeing full coverage and full implementation of the process make it difficult to factor the expected life extension fully into the component's service fatigue life. This paper discusses the development of a mid-life rework method, which can be applied to fatigue-critical aircraft structure. The process involves removing a layer of material from the surface to remove any damage in the form of cracks or flaws from earlier surface treatments. This approach alone will restore fatigue life, and a further life enhancement is achieved by application of an optimised glass-bead peening process. Two key elements are the use of life prediction methods to determine the size of any fatigue cracks developed during earlier service, and the development of a technique for the confident removal of the damaged material. The paper discusses the development of this approach for possible application to a fighter aircraft structural component.

KEYWORDS

Fatigue, peening, cracks, structural integrity, residual stress; 7050 Aluminium alloy; crack growth, life extension.

INTRODUCTION

Mechanical treatments such as radial cold expansion of holes and peening with glass or ceramic beads are used widely for fatigue life-enhancement of aircraft components, usually as part of the manufacturing process. New technologies such as laser shock peening and low plasticity burnishing provide alternative means of fatigue life enhancement and are being considered for application in the manufacture and repair of next generation aircraft. Peening is one of the most effective surface modification processes. It will improve the service life of structural components subjected to dynamic stresses by retarding fatigue crack growth in the early stages of a components service life. This occurs through the development of residual compressive stresses in the surface layers, generally, to a depth of 200μm to 300μm. The beneficial effects of peening surface treatments are dependent not only on the material and the pre and post-peening surface quality, but more importantly on the technique used and close control of the peening parameters. Further, the use of these methods in critical aerospace applications is highly dependent on the reliability of the process.

1

Research by the Defence Science and Technology Organisation (DSTO) examined the influence of material factors and surface condition on the fatigue life of aircraft structural components in the Royal Australian Air Force (RAAF) F/A-18 aircraft [1,2]. The work, which focussed on aluminium alloy 7050, used in the manufacture of F/A-18 wing carry-through bulkheads and other structural components re-emphasised the critical influence of the surface condition on the fatigue life of the component.

While surface modification technologies applied at manufacture are aimed to provide an enhanced fatigue life, there is a strong need for a viable repair/rework technique to restore and, where feasible, extend the fatigue life of components partially damaged by processes such as cracking, corrosion, or mechanical damage during service. The rationale behind the development of a life extension method for partially damaged components is to provide a means of extending the life of any local area that has displayed unexpectedly rapid or early fatigue cracking during service. To address this need, DSTO investigated the life extension potential of a re-work method involving removal of a specified amount of "prior fatigue damaged" material, including any surface damage remaining from manufacture, followed by an optional, controlled peening process using glass beads [3].

This paper discusses the potential application of this rework/repair method to a fatigue-critical region of a component in the RAAF F/A-18 fleet, in which fatigue cracking could lead to unacceptably high levels of inspection and maintenance. The approach is based on estimating the depth of any current cracking developed in service, using life prediction methods, and the development of a technique for confident removal of the damaged material completely, prior to rework by peening or re-peening, using tightly controlled conditions. The method has been developed to allow repeated life extensions of fatigue-critical parts reliably, with reduced maintenance costs being the expected benefits.

INVESTIGATION OF F/A-18 PEENING PROCESS

The fatigue critical areas in the F/A-18 aircraft, made of aluminium alloy 7050-T74511 were peened by the original equipment manufacturer (OEM), to provide additional resistance to fatigue cracking. However, the beneficial effect of peening was not accounted for in the original aircraft life modelling, rather, it was regarded as an added "insurance". At the time of aircraft purchase, local experience with peening high strength aluminium alloys such as AL7050 was very limited. Having recognised that the surface condition of airframe alloys in modern aircraft was critical [4], the DSTO research program focussed initially on assessing the Life Improvement Factor (LIF) associated with the peening treatments used on the F/A-18, under local service loading conditions.

The initial work [5], was aimed at understanding the effectiveness of the peening process used on the aircraft, and the influence of surface condition on a components fatigue life. Based on experiments with various peening conditions, it was shown that any life extension from peening resulted from the sum of two competing effects: the first; a decrease in fatigue crack growth rate associated with sub-surface residual compressive stresses, and the second; life reduction associated with the introduction of laps and folds in the surface during the peening treatment.

Improved Peening Method

During the course of the investigation, a number of refinements to the original (OEM) F/A-18 peening process were suggested to ensure that the maximum realistic LIF could be obtained from the modified peening treatment [6,7], the intention being to use the modified, improved treatment during any modification work performed on the fleet. The main refinements to the peening method recommended by DSTO were:
  a.   using a lower Almen intensity (peening intensity is measured using the bowing of small test strips);
  b.   better control of the bead impact angle;
  c.   better control of nozzle stand-off distance;
  d.   use of non-recycled glass beads, to minimise the impacts from broken or damaged beads.

The refined peening process led to substantially improved fatigue lives and reduced scatter in the fatigue lives due to the reduction in the level of surface damage in comparison with surface damage observed in OEM peened surface [6] ,(Figure. 1). The depth of the damaged layer in the OEM peened surface was 150μm, compared to 80 μm in the DSTO optimised (refined) peening process.
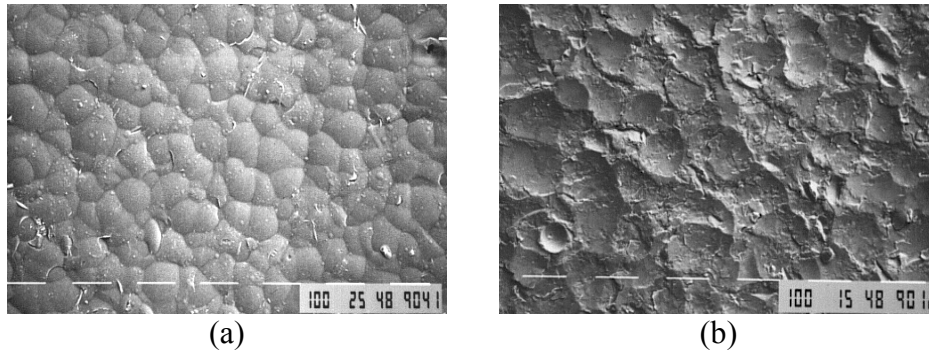
| (a) | (b) |

Figure 1: The improved surface condition resulting from the DSTO-optimised peening method (a), compared with the surface damage observed in fleet aircraft component produced by OEM peening (b).

PEENING AS A LIFE EXTENSION AND RE-WORK TREATMENT

The F/A-18 aircraft has several critical regions, some of which were peened during manufacture. Any mid-life re-work or life extension method must take into account the differences in surface finish and expected fatigue lives in the peened and un-peened regions. Since the original (OEM) peened surface was found to have peening associated surface damage [2], and one proposal was to rework the area by simply peening over the damaged area part-way through life, DSTO compared the laboratory fatigue lives of different peening rework processes performed on the aircraft, using 7050 aluminium alloy test coupons and a spectrum (variable amplitude) loading sequence representative of loads experienced by the aircraft structure during RAAF service [6]. In these experiments, fatigue lives of specimens hand polished to 800# finish and peened to simulate OEM peening were compared with direct over peen of OEM peening, and polish to remove previous surface and cracking damage and peen (DSTO method) treatments. Using a peak spectrum stress level of 410MPa the improvement in the fatigue life using the DSTO method was 50% over the OEM's over-peen approach, ie., peening over previous and possibly damaged peened surface. The results are shown in Figure 2. Based on the findings of these comparison experiments, it was concluded that all traces of the OEM peening should be removed prior to rework peening [6].

Further research established that peening over a surface which contained growing fatigue cracks or embedded damage (which could be a source of cracking), might not be beneficial for life extension. This is illustrated in Figure 3, in which the specimens were fatigue tested to a percentage of total life of the un-peened specimens and then peened before continuing the test until failure; peening of a specimen that has seen less than 50% of its failure life (fatigue damage) can be beneficial. However, if the damage exceeds ~60% of original life, the peening re-work is ineffective in restoring the fatigue life, since the residual stress distribution is less effective once the crack has progressed beyond the compressive residual stress layer (250 to 300μm deep for glass bead peening). Accordingly, if an effective life recovery procedure is to be developed, it will be necessary to remove both any cracking along with other surface damage.
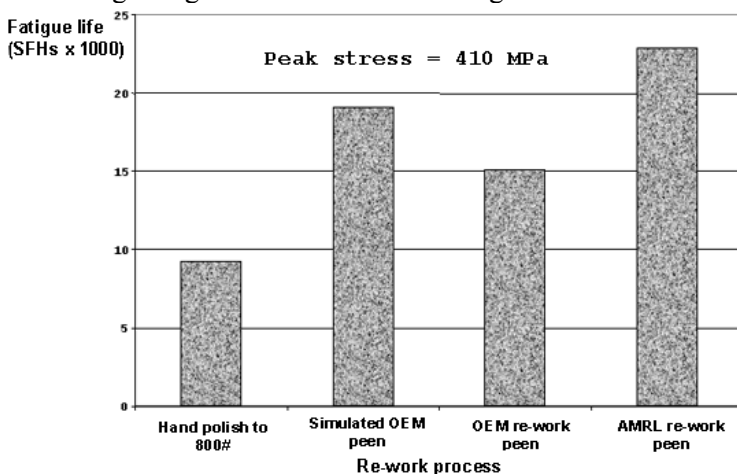

Figure 2. Comparison of fatigue lives (averaged on a log basis) for various re-work peening processes
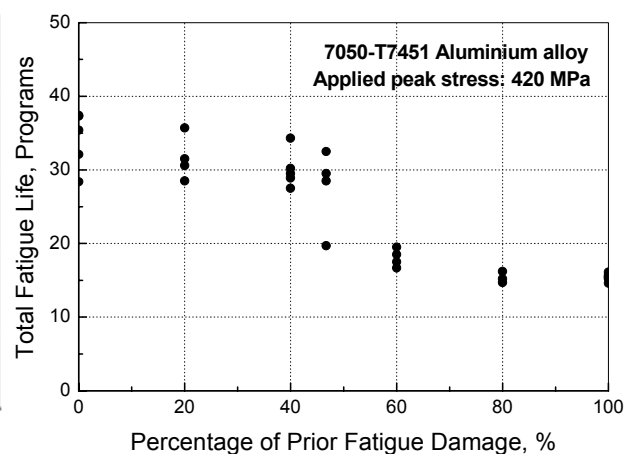

Figure 3: Fatigue life of specimens peened after various levels of prior fatigue damage (% of unpeened life).

Recovery and Extension of Fatigue Life

The first phase of the life-extension method is the effective surface removal of previous surface damage, including any cracking that may be present. Generally, the surface removal in any highly stressed fatigue critical airframe component is considered undesirable, since the amounts of material must be very carefully controlled to avoid major damage, and yet there must be a high level of confidence that the damaged material has in fact been removed.

Recognising that the controlled material removal is a critical aspect of the repair process, DSTO developed a surface removal method [8] to remove both the fatigue cracking which was developing, but was as yet undetectable, and any damaged surface layer. The steps involved in the DSTO surface removal method are shown in Figure. 4.
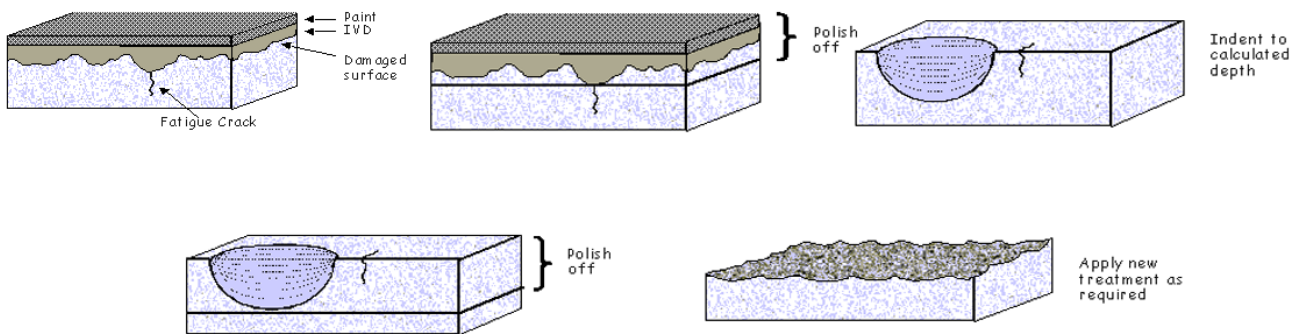

Figure 4:   A step-by-step description of the complete repair process, using indentation to mark the damaged layer and the possible application of a new surface treatment

Rework method summary

Two local-area re-work processes have been identified and developed;

1. Remove the layer of material containing any original surface damage and a further quantity of material which will accommodate any fatigue cracking growing from it, making allowance for variability in the depth of this cracking. This would restore the original un-peened fatigue life. The DSTO surface removal method provides a means of removing thin surface layers on critical parts without risking either excessive or insufficient material removal from the surface.
2. If required, apply the DSTO optimised-peening process over the damage-removed or undamaged surface, as a supplementary life-extension method. Decision-making as to whether this process is desirable needs to balance the life extension against the possibility that introducing a peened surface finish may compromise component inspection.

APPLICATION OF LIFE EXTENSION METHOD TO AIRCRAFT COMPONENTS

The rework procedure was trialed by developing the method for a proposed repair to a critical area; the X-19 pocket one of the wing carry-through bulkheads of the F/A-18, shown in Figure 5 [3,10]. This bulkhead is made from 7050-T7451 aluminium alloy plate. The X-19 pocket area encounters high service stresses and is thought to be developing cracks at a rate faster than desired.

The manufacturer's original process specification does not require peening in the X-19 area (an Engineering Change Procedure implemented later introduced peening for this area). However, the location has a surface coating of Ion Vapour Deposition (IVD) aluminium for corrosion protection. Prior to applying this coating the surface of the component is acid etched. Laboratory fatigue tests and detailed fractographic analysis showed that this etching treatment produced etch-pits, which initiate fatigue cracks [10]. The average fatigue lives of etched specimens were 30% shorter than those of as-machined specimens.
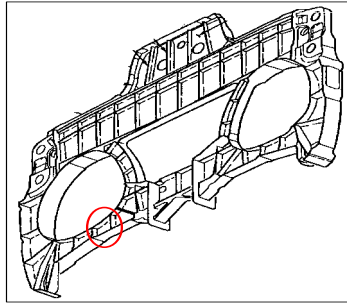
Figure 5   Figure showing the location of the X-19 pocket area (arrowed) of Y470 bulkhead

The amount of material to be removed is dependent on the previous surface treatments, and the extent of cracking, which, in turn, is dependent on the period the component, has been in service and the loading experienced. The two variables to be considered in the material removal are: (i) the initial defect starter size or Initial Discontinuity State (IDS) and (ii) the crack growth rate derived from quantitative fractography on cracked components from full-scale fatigue tests and laboratory etched and peened coupon tests. The IDS distributions – in this case, the distributions of initiating defect sizes for the dominant fatigue cracks were determined from quantitative fractography on etched fatigue loaded specimens backed up by full-scale test examples. The crack growth rate and therefore the depth of fatigue damaged material requiring removal on the X-19 area was also determined from these coupon tests and examples. The depth of a fatigue crack will be the sum of the deepest flaw and the amount of cracking possible at a given life. To determine a (1/1000) crack depth, three approaches are possible:
1. Use the 1/1000 defect as the initial crack depth ($3\log\sigma$) and mean crack growth rate;
2. Use the 1/1000 crack growth rate ($3\log\sigma$) and mean initial defect starter size; or
3. Use a combination of $1\log\sigma$ initial defect starter size coupled with a 1σ crack growth rate.

Graphical representation of the above [3], showed that Case 1 material removal was the most conservative (it provided an upper bound to the 1/1000 cases), for the fatigue lives expended (FLE) by the aircraft.

For an area in the component material that has been peened previously (by OEM), the 1/1000 IDS value was found to be 138μm. For the IVD etched material the 1/1000 IDS was 91μm. To return a AL7050-T7451 surface to its "as new" condition 138μm for a OEM peened surface and 91mm for a IVD etched surface would need to be removed without regard of service fatigue cracking. This is the amount of material that would need to be removed once any surface peening indications (ie dimples) or obvious etch pits have been removed, to ensure t no remnants of the original surface damage (including peening debris, grain boundary etching). A further allowance for service induced cracking would be removed estimated by considering the fatigue crack growth rate for this material under the aircraft-loading spectrum representative of fleet service.
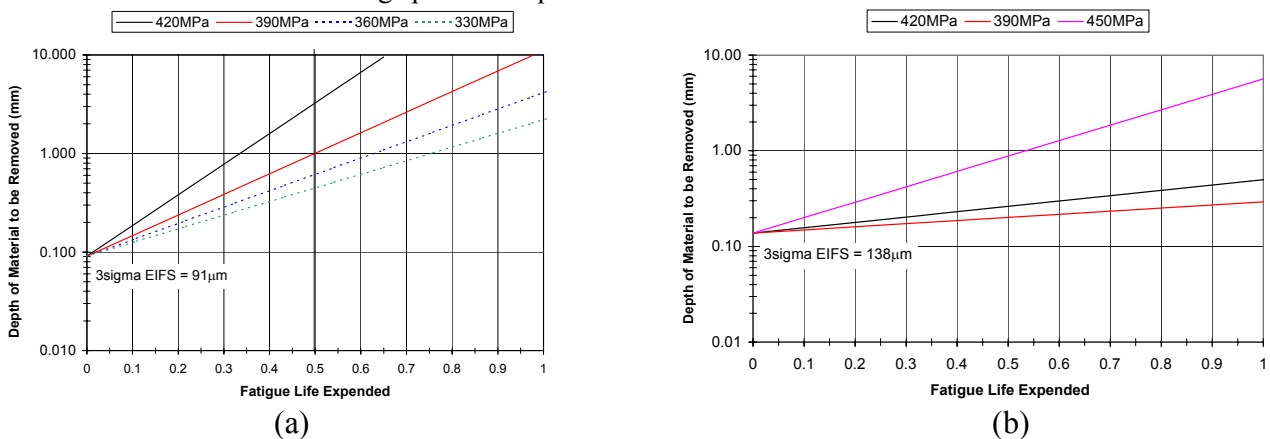

(a)   (b)

***Figure 6**: Material removal versus aircraft FLE ((a) not previously peened and (b) previously peened surface)*

For the proposed repair method, the material to be removed from un-peened and peened surfaces of a fleet aircraft structural component as a function of the FLE with a loading spectra and stress level representative of the area being considered in the aircraft are obtained from the curves [3,10], shown in Figure. 6. These curves were based on an exponential crack growth relationship drawn from the quantitative fractography of numerations coupon and

full-scale fatigue test cracks at several stress levels, with the appropriate curve being used for the stress measured in the item being repaired.

Multiple Re-works

In considering the possible application of the rework method to aircraft, it is necessary to consider the possibility of further reworks later in service life, and to ask whether there is a limit to the number of times an area could be repaired, while still maintaining the required strength. While multiple reworks may protect the surface, they offer no protection against the increasing risk of failure initiating from sub-surface defects. The number of re-works is being examined to determine how many can be applied before sub-surface flaws cause failure.

CONCLUSIONS

This paper has presented the development of a rework/repair method developed at DSTO for application in fatigue-critical aircraft parts in the RAAF F/A-18 fleet. The approach is based on estimating the depth of any current cracking, and removing the damaged layer, prior to rework by peening or re-peening, using tightly controlled conditions. The method has been developed to allow repeated life extensions of fatigue-critical parts reliably and by enhancing the fatigue resistance of the aircraft components; reduced maintenance costs are the expected benefits.

The method involves removal of a layer of material containing any original surface damage and any fatigue cracks growing from it, using the surface removal method developed by DSTO. This should enable restoration of most of the original un-peened fatigue life. The second approach involves the use of DSTO optimised peening process, which could be used on relatively undamaged surfaces, previously peened surfaces or as a supplementary life-extension approach after surface damage removal, to provide additional fatigue life improvement.

REFERENCES

1. Barter, S.A., Bishop, B.C. and Clark, G. (1991). "Assessment of Defects in F/A-18 Bulkhead Test Article", Defence Science and Technology Organisation, Aeronautical Research Laboratory, Aircraft Materials Report, ARL-MAT-R-125, Commonwealth of Australia, August 1991, 26p.
2. Sharp P.K., Athiniotis N., Byrnes R., Barter S.A., Clayton J.Q. and Clark G. (1997). "Assessment of RAAF F/A-18 FS488 Bulkhead Offcuts; Microstructure and Surface Condition", Defence Science and Technology Organisation, Aeronautical and Maritime Research Laboratory Technical Report, DSTO-TR-0326, Commonwealth of Australia, September 1997, 93p.
3. Sharp, P.K, Barter, S.A and Clark, G. (2000). "Localised Life Extension Specification for the F/A-18 Y470 X-19 Pocket", DSTO-TN-0279, Defence Science and Technology Organisation, Aeronautical and Maritime Research Laboratory, 22p.
4. Clark, G. (1990). Defect Assessment: Changing Requirements in Military Aviation, *Materials Australasia* 22 (4) 18-21.
5. Clayton, J.Q. and Clark, G. (1988). The effect of steel shot and glass bead peening treatments on the fatigue resistance of 7050-T76351 aluminium alloy, *Proc. Aust. Fract. Group, "Fracture Mechanics in Engineering Practice"*, Melbourne.
6. Sharp P.K., Clayton J.Q. and Clark, G. (1994). "The Effect of Peening 7050-T7451 Aluminium Alloy on Fatigue Life", Fatigue and Fracture of Engineering Materials and Structures, Vol. 17 No.3, pp 243-52, March 1994.
7. Sharp, P.K. and Clark, G. (1997). "The Effect of Peening on the Fatigue life of Aluminium Alloys", Advances in Fracture Research, Proceedings, ICF 9, Sydney, Vol. 3, 1997, pp 1491-99.
8. Barter, S.A. and Houston, M.I. (1997). Examination of methods to control the depth of surface removal on the F/A-18 488 bulkhead, DSTO-DDP-0192, Department of Defence, Defence Science and Technology Organisation, Aeronautical and Maritime Research Laboratory.
9. Barter, S.A., Molent, L., Sharp, P.K. and Clark, G. (2000). Repair and life assessment of critical fatigue damaged aluminium alloy structure using a peening rework method, Proc Conference USAF Aircraft Structural Integrity Program – ASIP 2000, San Antonio, USA, 5-7th December 2000.
10. Barter, S. A. and Price, J. (2000). "Effect of Surface Preparation Treatments on Fatigue Life of 7050 Aluminium Alloy", Structural Integrity and Fracture 2000, G. Heness (Ed.), Australian Fracture Group Inc. and University of Technology, Sydney, Australia, pp.140-53.

VALIDITY REQUIREMENT FOR THE CNT SMALL SPECIMEN TESTING PROCEDURE TO EVALUATE FRACTURE TOUGHNESS

R N Ibrahim and J W H Price

Mechanical Engineering Department, Monash University

ABSTRACT

This paper presents the cylindrical notched test (CNT) specimen for evaluation of K_{Ic}. The specimen geometry is the smallest which can produce values of K_{Ic} which are very nearly valid in respect to such testing and much smaller than the standard compact tension test (CTT) specimen.

INTRODUCTION

The determination of fracture toughness (characterised by the material property K_{Ic}) is of considerable importance for materials used in mechanical engineering. Fracture toughness is the measure of the material's resistance to crack growth. At present K_{Ic} is determined using standard compact tension test (CTT) specimens which are expensive to manufacture and require relatively sophisticated laboratory equipment.

Because of the inconvenience of the CTT specimen there has been a quest for smaller specimens and a wide variety of smaller tests have been used. Many of the tests such as Charpy, Izod and punch tests can only be described as comparative tests since the geometry of the final crack cannot give valid values of K_{Ic}.

An extensive research program which began in 1985, and is still continuing[123], has indicated the effectiveness of a new small specimen for determining valid fracture toughness values. The cylindrical notched test (CNT) K_{Ic} Fracture Toughness Specimen[4] is now being evaluated as a standard test specimen by the American Society for Testing Materials (ASTM) and could make a major impact on material testing practices. The CNT specimen is shown in Figure 1 and compared to a CTT specimen in Figure 2
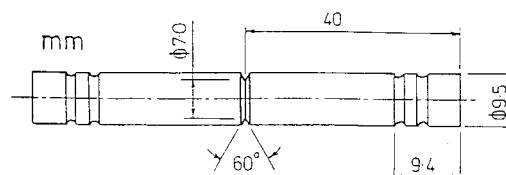

Figure 1. Cylindrical notched test (CNT) specimen. All dimensions in mm.

Figure 2 A valid ASTM CTT specimen (bottom) compared to cylindrical CNT specimen for the same material.

Procedure of CNT tests

The test procedure involves machining the specimen from the material to be tested including a circumferential vee notch as shown on Figure 1. A crack is then grown from the base of the notch in a rotating fatigue machine to provide a sharp crack. The specimen is finally broken in a tensile test, the failure load is recorded and the crack geometry is measured to give the data required to determine K_{Ic}.

The advantages of the CNT specimen

The advantages of the small specimen over existing compact tension testing specimens are its reduced size, ease and economy of manufacture, and ease of testing. In tests conducted, acceptable results have been achieved using a 9.5 mm diameter specimen whereas standard compact tension tests require dimensions varying in thickness from 20 mm up to 80 mm, depending upon the material.

The CNT specimen has a simple cylindrical shape making manufacture in a lathe a simple process. Also the small diameter means that the forces required to produce failure of the specimen are low, simplifying the testing apparatus required.

A further advantage of the much smaller physical size is that it can be used in many applications not possible with the standard CTT specimens. For example, the reduced size means that specimens can be taken from batch production material and from a failed component or structure in a post-mortem analysis to determine the cause of the failure, where the thickness of the components would not allow valid K_{Ic} testing using a CTT specimen.

Current commercial costs to determine K_{1c} for a material using 4 compact tension specimens are in the order of \$5,000. This is a significant impediment to the application of fracture mechanics in industry. The CNT specimen being developed costs about one tenth of the standard specimen

An innovation in the present work is the procedure for growing the circumferential crack using a rotating beam fatigue machine. The methodology for sensing the associated growth of the crack, and further interpreting the results when the final uncracked ligament is eccentric is new. The depth and shape of the crack is not known until the specimen is finally broken in tensile testing to establish K_{Ic}.

Requirements for validity

It is required for valid K_{Ic} testing that only a minimal amount of plastic flow during fracture so that the conditions appropriate to linear elastic fracture exist. Normal compact tension CTT specimens with through-thickness cracks are generally required to be relatively large and bulky in order to satisfy the

high restraint and plane strain requirements for test validity. Due to the axisymmetric symmetry of the CNT specimen, plane strain conditions and low plasticity can be established despite the small size.

Our current work is aimed at determining the correct size of specimen and crack depth for higher toughness materials than originally tested.

Normal compact tension specimens are required to be large to achieve a condition where the free surface regions are negligible compared to the internal plane strain zone. However, in the cylindrical specimen the circumferential crack which is developed at the bottom of the notch has no end or free surface and therefore there is no end to the plane stress zone. In CNT specimens the required minimum depth of this crack is defined by the need to ensure that the crack tip zone is not influenced by the free surface shoulder of the notch from which the crack was grown.

The dimension of the ligament which remains for the final tension test in both the CTT and CNT specimen must be sufficient to ensure that yielding does not occur across the entire section in the cylindrical part of the specimen. Here the cylindrical specimen has a distinct advantage. The von Mises and Tresca criteria for plastic flow depend on the maximum shear stress in the material. For example, by the Von Mises criterion yielding initiates when

$$(\sigma_1 - \sigma_2)^2 + (\sigma_2 - \sigma_3)^2 + (\sigma_3 - \sigma_1)^2 = 2 \sigma_y^2 \qquad (1)$$

where σ_i are the principal stresses and σ_y is the uniaxial yield strength.

Hydrostatic tension is not relevant to yield according to the Von Mises criterion and this is very closely true for metals under most conditions. In the cylindrical specimen lateral contraction in the section of the notch is constrained by the surrounding material in the unstressed shoulder of the notch. As a result a high triaxial state of tension exists reducing the tendency for yielding to occur according to equation 1. The algebraic sum of the principal stresses at the notched section can rise to over 3 times σ_y before limits to elastic behaviour are encountered[5]. This constraint phenomenon greatly increases the ability of the small specimen test to maintain conditions appropriate to the application of linear elastic fracture mechanics at the crack tip.

Initially a finite element study was carried out to compare the finite element solution for the stress intensity factor at the crack tip with known analytical solutions and thus validate the model and the method for determining K_{Ic}. The finite element analysis was in all cases based on three-dimensional, isoparametric hexahedral and pentahedral elements. A specimen with a uniform fatigue crack depth was examined, giving a symmetric geometry and allowing the model to be reduced to a study of a two-degree wedge of the specimen. The specimen modelled was taken from an aluminium alloy Mirage wing spar on which considerable tests had been conducted by the Aeronautical Maritime Research Laboratories. The load used in the finite element analysis was that experimentally recorded at brittle fracture of the specimen. The crack depth is considered to be the combined depth of the notch and the fatigue crack.

Stresses in the axial direction, σ_{YY}, ahead of the crack tip are plotted in Figure 3. For simplicity a direct stress approach was implemented matching the stresses ahead of the crack tip to the analytical formula for plane strain

$$K_1 = \sigma_{YY} \sqrt{(2\pi r)} \qquad (2)$$

An elastic-plastic analysis was then conducted implementing both a linear hardening rule and then perfect plasticity. The results of the first analysis is shown in Figure 4 indicate the plastic zone approximates the plane strain zone size as expected for the cylindrical specimen but that the zone size increases as the crack becomes shallower. on the basis of this result it was decided that the depth for the

fatigue crack had to be at least twice the Irwin plastic correction radius for the crack tip to not be influenced by the free surface shoulder of the machined notch.

The model was then loaded till net-section yielding occurred. It is seen that this required that the stress in the section of the crack had to be raised to almost three times the Uniaxial yield stress of the material confirming the large amount of constraint occurring in the notched specimen. On the basis of these results the diameter required for the notched specimen could be determined and is plotted in Figure 5. The size advantage over the standard test is clearly evident.
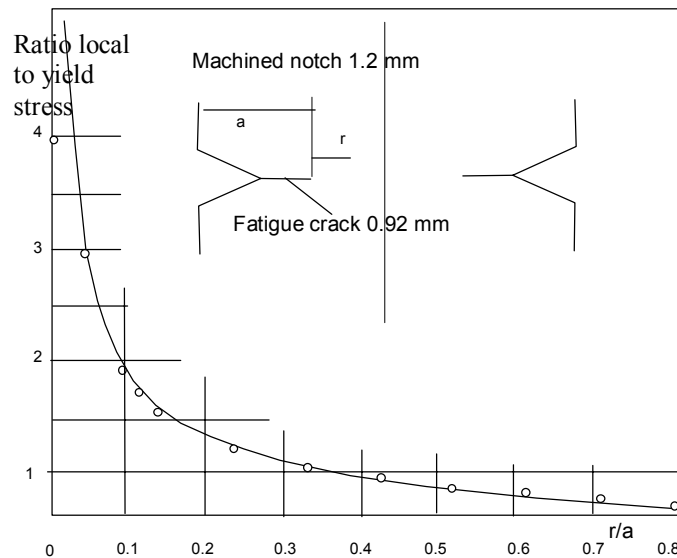
Figure 3 Ratio of local stress (σ_{yy}) to yield stress at a distance r ahead of the crack tip in a **CNT specimen.**
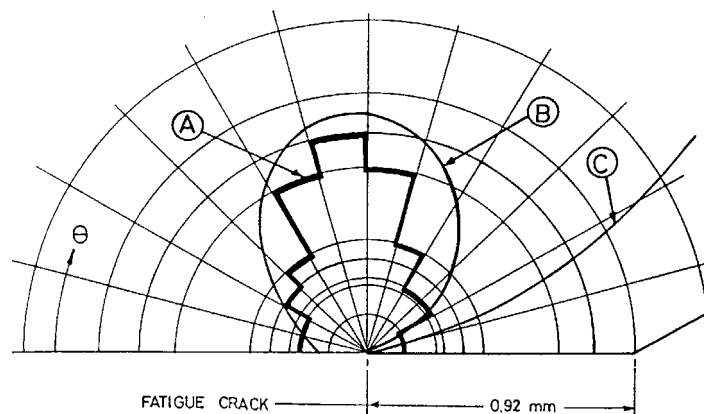

Figure 4 Results of an elastic-plastic analysis with linear hardening rule.

The results indicate that the plastic zone approximates the plane strain zone size for the cylindrical specimen. A is boundary of plastic zone, B. Von Mises approximation of plastic zone for plane strain conditions.

In all these analysis the elements at the crack tip were modified to model the crack tip strain singularity. The mid-side nodes were moved to the quarter side point as suggested in[6]. For the elastic case all elements meeting at the crack tip shared the same nodes giving the $1/\sqrt{r}$ strain singularity expected in linear elastic fracture mechanics. In the perfectly plastic case each element had different nodes allowing crack tip blunting and giving the $1/r$ strain singularity expected in this case[7].
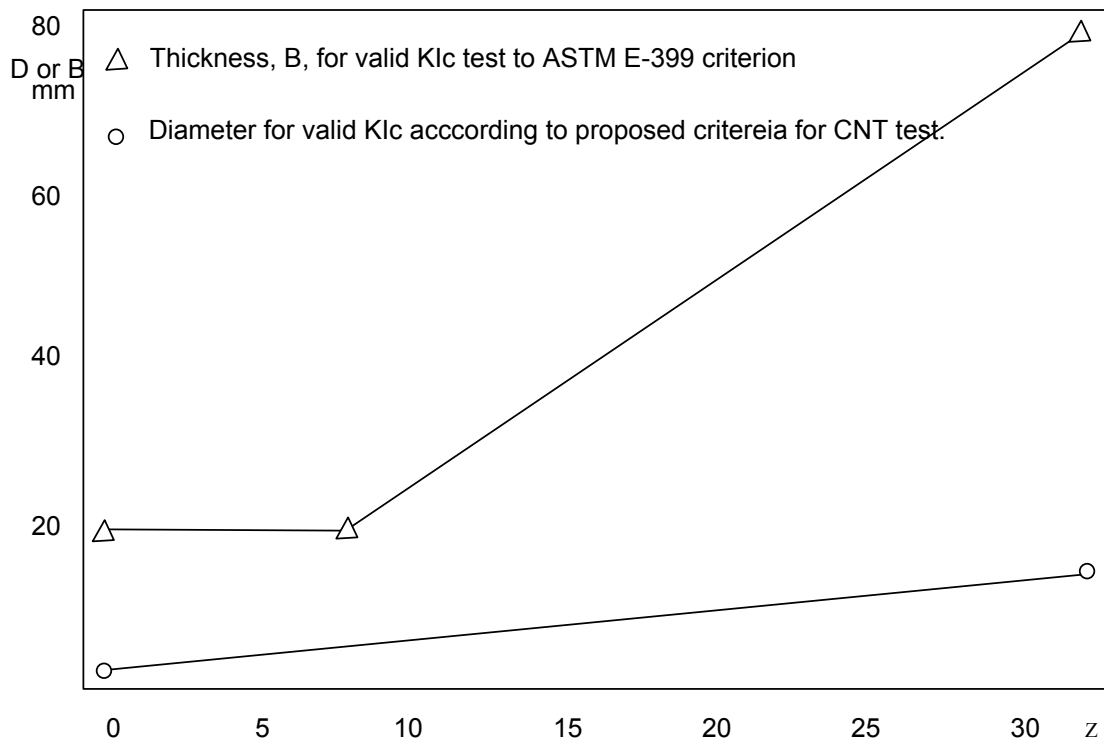
Figure 5 The diameter required for CNT specimens compared to CTT requirements ($Z = (K_{Ic}/\sigma_y)^2$

Experiemntal confirmation

Experimental studies have been conducted for which the results were compared with values obtained from compact tension specimens by the authors and at the Aeronautical and Maritime Research Laboratories in Melbourne[8]. In this work a large batch of 8.4 mm diameter specimens which collectively gave an experimental value for K_{Ic} of 31.6 MPa√m with a standard deviation of 0.98 MPa√m. These values compare with 31.6 with a standard deviation of 0.5 for tests by the AMRL using four 62.5X 60X 25 mm compact tension specimens. The results indicate that the new procedures will provide values of K_{Ic} of acceptable engineering accuracy (within 5%).

Information is currently available to justify the validity for K_{Ic} testing using the cylindrical notched test (CNT) specimen for only two different diameters (8 and 9.5 mm). The current dimensions are too small for valid K_{Ic} testing for high toughness, low yield strength materials with $(K_{Ic}/\sigma_y)^2$ greater than 18 mm. This restriction was satisfactory for the original development of the CNT specimen which was targeted at a hardened aluminium alloy but the restriction excludes materials used in many applications, for example, structural steels such as used in pressure vessels.

Recent tests at Monash have indicated a significant increase of applicability with CNT specimens if they are 15 mm in diameter. This is still small compared to the equivalent standard American Society for Testing Materials (ASTM) specimens which would be up to 200 mm thick. It is very difficult to find material of adequate thickness or testing machines capable of carrying out the ASTM tests. The effect of developing the CNT test to cover materials of higher values of $(K_{Ic}/\sigma_y)^2$ is to increase the usefulness of the test and extend the test to everyday use.

Correction factor to allow for eccentric fatigue cracks

The fatigue crack is grown in the notched specimen to provide a sharp crack for the tension test may not be exactly central to the notch. The crack is grown in a rotating fatigue machine under an applied moment but there is no guarantee that the crack growth will always be constant around the specimen, especially if the material properties are not uniform in the material from which the specimen has been machined. A procedure for correction for this eccentricity has been established[910].

CONCLUSIONS

The small cylindrical notched specimens which are pre-cracked by fatigue in a rotating bending machine which are described as cylindrical notched tesnile (CNT) specimens have been demonstrated to produce valid and reproducible K_{Ic} values over a wide range of toughnesses and materials. Validity limits and corrections for eccentricity of cracking have been developed.

The substantial advantages of the specimens smaller than the standard ASTM 399 type specimen allows testing in a wide range of conditions where K_{Ic} would otherwise be difficult to determine.

REFERENCES

1. R N Ibrahim, Y C Lam, and J W H Price, Effect of residual stresses and defects on the performance of aluminium pressure vessels, *Failure Analysis in Materials Engineering,* Materials Society of the IEAust, Melbourne March 1994.
2. H L Stark and R N Ibrahim, Crack Propagation in aluminium gas cylinder neck at constant load, *Engineering Fracture Mechanics,* Vol 48, pp 569-574, 1992.
3. H L Stark and R N Ibrahim, Estimating fracture toughness from small specimens, *Engineering Fracture Mechanics,* Vol 25, No 4, pp 395-401, 1986.
4. R N Ibrahim and H L Stark, Validity requirements for fracture toughness measurements from small circumferentially notched cylindrical specimens, *Engineering Fracture Mechanics,* Vol 28, No 4, pp 455-460, 1987.
5. J M Barsom and S T Rolfe, *Fracture and failure control in structures,* Prentice-Hall, NJ, 1988.
6. M H Alabadi and D P Rooke, *Numerical fracture mechanics*, Kluwer, Dordrecht, 1991.
7. R N Ibrahim and H L Stark, Crack propagation at room temperature in an extruded aluminium, *Engineering Fracture Mechanics,* Vol 30 , No 3, pp 409-414, 1988.
8. R N Ibrahim, The development of a small specimen for the evaluation of plane strain fracture toughness and the investigation of creep crack growth in aluminium pressure vessels. *PhD. Thesis in Mechanical Engineering,* University of NSW, 1989.
9. R N Ibrahim and H L Stark, Establishing KIc from eccentrically fatigue cracked small circumferentially grooved cylindrical specimens, *Int J of Fracture*, **44**, 1990, p179 -188.
10. Ibrahim, R N "CNT Small Specimen Testing Procedure to Evaluate Fracture Toughness" pp 735-743, ICPVT-9 Sydney, 9-14 April,2000

VERIFICATION OF AN EXPERIMENTAL METHOD TO MEASURE THE STRESS-ELONGATION LAW FOR AN ADHESIVE LAYER USING A DCB-SPECIMEN

Tobias Andersson and Ulf Stigh

Department of Engineering Science, University of Skövde
P.O. Box 408, SE-541 28 Skövde, SWEDEN

ABSTRACT

A method to measure the stress-elongation law for a thin adhesive layer is presented. It is noted that the experimental results give a law that resemble the cohesive law that has been used *ad hoc* in general investigations of fracture and specifically in numerical simulations of adhesive bonds.

The method is based on the balance of energetic forces and a direct measurement of the elongation of the adhesive at the start of the layer. In the experiments, only the surfaces of the adherends are accessible for measurement. However, due to anticlastic deformation, the elongation at the interior is larger than at the surface. The method is also based on the assumption of linear elastic adherends. Influences of these prerequisites are studied using the finite element method.

Experimental and simulated results compare well up to the initiation of crack propagation. After this point, the simulations give, as expected, a constant J, while the experiments show a rapidly decreasing J. Similarly, the force-displacement records agree well up to the start of crack propagation. However, the experiments show a more rapidly decreasing force after this point than the simulations.

KEYWORDS

Thin layer, adhesive, test method, stress-elongation law

INTRODUCTION

Although of significant engineering importance, the design of adhesive joints is largely based on engineering practice and experimental verification. To this end, we suggest a design method based on finite element simulations using a constitutive law for the adhesive, c.f. [1,2,3,4].

In [5] Olsson and Stigh suggests a method to measure the stress-elongation relation for an adhesive layer. The method is based on the possibility to solve an inverse problem, namely to determine the stress-elongation relation for an adhesive layer in a DCB-specimen from measurable properties, see Figure 1.
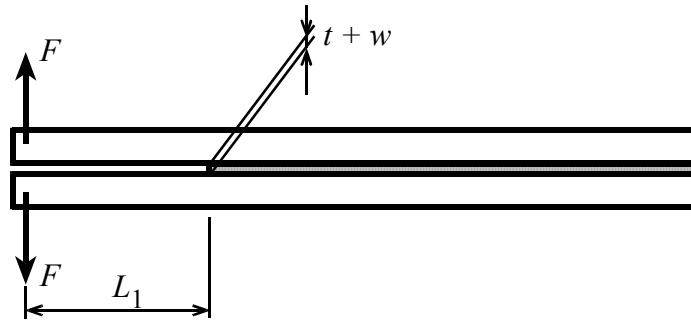
Figure 1: DCB-specimen

By continuously measure the applied force, F, the rotation of the points of load application, θ, and the elongation of the adhesive layer at its start, w, the stress-elongation relation is derived from

$$\sigma(w) = \frac{2}{b} \frac{\mathrm{d}(F\theta)}{\mathrm{d}w} \tag{1}$$

where b is the width of the specimen. In [5] Eqn. 1 is derived based on the assumption that the adherents behave as linear elastic Euler-Bernoulli beams. However, the relation is more general and in [4] the equation is derived based on the principle of balance of energetic forces. An energetic force is the energy-conjugated quantity corresponding to a change in position of an object[1]. Thus, the energetic force for a crack tip is known as the J-integral of the crack.

In [4] it is shown that the energetic force corresponding to an applied force, F, is the product of the force and the rotation, θ, of the loading point. Thus, $2F\theta$ is the applied energetic force, J_{applied}, of the specimen while $J_{\text{adhesive}} = \int_0^w \sigma(\tilde{w})\,\mathrm{d}\tilde{w}$ is the energetic force per unit width corresponding to the start of the adhesive layer, see [3,7]. If the specimen is long enough so that it can viewed as semi-infinite these two energetic forces must be in balance, see [4].

The experimental method is described in [4] and in more detail in [8]. Eqn. 1 incorporates a differentiation of the measured data. Different methods have been tested to evaluate the data. Originally, in [8], a simple numerical differentiation is used. A typical result is shown in Figure 2a. These curves end after about 30 to 40 μm. After this, the laser interferometric method used to measure w fail to operate. This is due to aliasing, see [4].
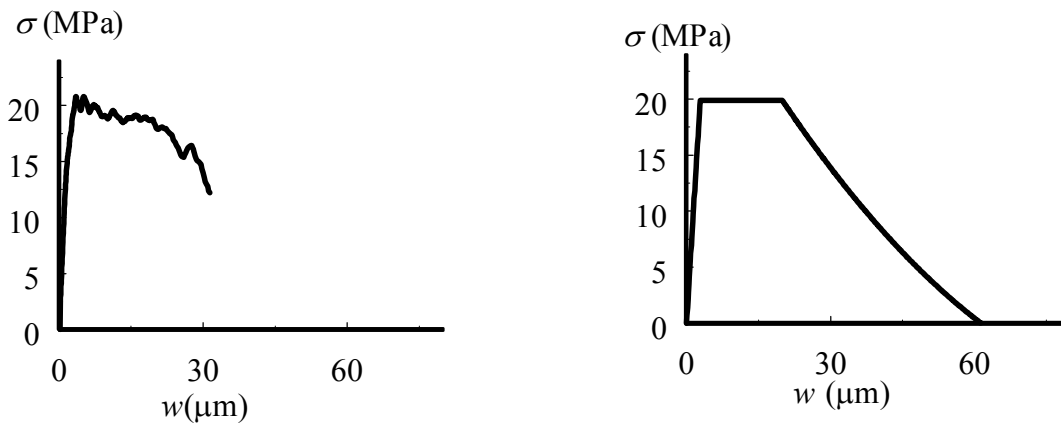

Figure 2: a) Typical result after numerical differentiation, b) The same data using the five-parameter curve

---

[1] The concept of an energetic force is introduced in solid mechanics by Eshelby [6] and can be viewed as the basis for Rice's J-integral [7].

Based on Fig. 4a and the corresponding curves of several experiments, a five-parameter curve is introduced in [4], see Figure 2b. The adjustment of this curve is done before the differentiation and under the condition that the area under the stress-elongation curve should equal the maximum J_{applied} of the experiment. Thus, only four parameters are adjusted.

It is interesting to note the similarity with the stress-elongation law used by Tvergaard and Hutchinson in several numerical investigations of fracture, *e.g.* [9], and by Yang *et al*. [10] in simulations of fracture of adhesive joints. The difference between their *ad hoc* law and the present experimentally measured one is the form of the descending part. They use a linear relation while a parabolic relation adjusts better to the experimental data presented in [4]. As explained above, the form of the descending part is not fully captured in our experiments. However, the experimental data do not fit well to a linearly descending curve.

A prerequisite for the presented method is that no unloading takes place in the adhesive from a non-elastically deformed state. Another prerequisite is that no plastic deformation is allowed in the adherends throughout the experiment. These two requirements are examined here.

A shortcoming of the specimen is that only the surface is available for measurement of the elongation of the adhesive. Due to anticlastic deformation of the beams, the adhesive elongates more at the centre than at the surface of the specimen. Effects of this shortcoming are also examined.

CRITICAL EXAMINATION OF THE METHOD

The finite element method is used to simulate the experiments. In these simulations, the commercial program ABAQUS ver. 5.8 is used. The symmetry of the geometry and loading are utilised. Thus, only the upper adherend and the upper half of the adhesive layer are modelled. Beam elements (type B23) are used for the adherend and spring elements (type SPRING1) are used for the adhesive.

The total length of the adherend is 115 mm and the unbounded length is $L_1 = 50$ mm. The width is $b = 4.4$ mm and the height is $h = 5.5$ mm, for one adherend. The total thickness of the adhesive layer is nominally $t = 0.2$ mm.

The element size is determined in order to capture the gradients in the displacement field. This is done using an analytical solution [2] for the specimen with the stress-elongation curve as a saw-tooth, see Figure 3a. The stress-elongation curve is, in this case, described by three parameters; w_0, w_L and σ_0. To approximate the stress-elongation curve of Figure 2b we put w_0 equal to the elongation at the end of the linear elastic part of the curve, w_L equal to the maximum elongation and σ_0 equal to the maximum stress. From the analytical solution, we obtain the elastic part of the separation w along the adhesive, see Figure 3b. The strained region is about 20 mm long and 100 elements seem appropriate for this length. This gives 575 beam elements for the whole model. However, since the beam model is rather simple we finally chose 1000 beam elements, *i.e.* there are 1001 nodes in the model. This gives an element length of 0.115 mm which results in 566 spring elements.

The beams are made of steel with the yield strength larger than 450 MPa. In the finite element method, we use 206 GPa as the Young's modulus and 0.3 for the Poisson's ratio. The adhesive is modelled with springs. Except for the first spring, each spring element has a force-elongation relation according to $F = \sigma(w) l_e b$, where $l_e = 0.115$ mm is the beam element length along the adhesive layer and $b = 4.4$ mm is the width of the adherents. For the first element, only half of l_e is used.

As in the experiments, a simulation is done with a monotonically increasing displacement of the loading point.

To examine the difference between the simulations and the experiments the force vs. loading point displacement curves are first compared. Figure 4a shows the results from an experiment and a simulation of

the same experiment. From this curve, we can observe that the simulation corresponds well to the experimental result up to the maximum of the curve. The maximum force is in this case 84.1 N and from the simulation the maximum force is 86,8 N thus, an error of only 3 %. However, the maximum force is very sensitive to the length L_1 and some small differences exist between the test specimens. By varying L_1 a few tenths of a mm from the nominal value, a satisfying agreement can be achieved between the experiments and simulations for all experiments and for all curves, see Figures 4 and 5.
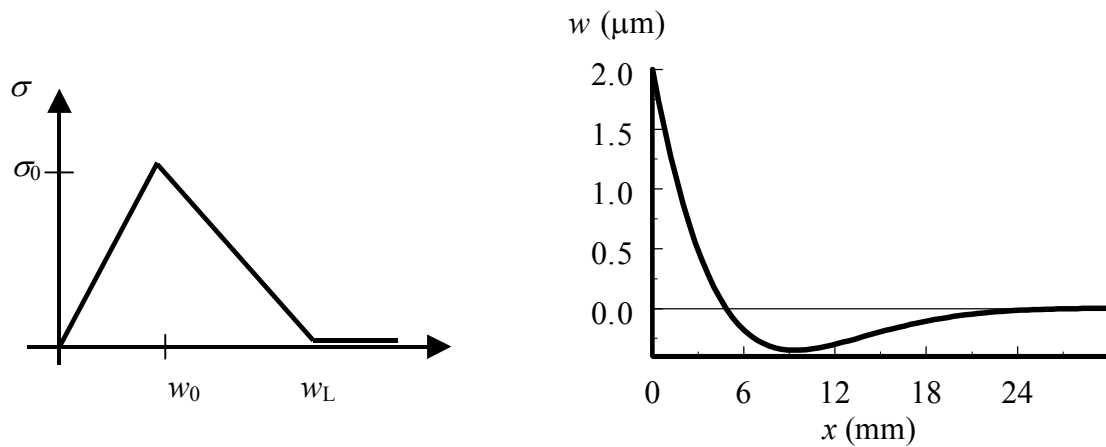
Figure 3: a) stress-elongation law used in analytical solution, b) elongation of adhesive along the specimen.

From Figure 4a, it is observed that the curves diverge soon after the maximum point is passed. The inserted line "critical displacement" indicates the value of the separations of the loading points corresponding to the maximum value of w; in this experiment 60 μm, see Figure 2b. As seen in Figure 4b, J still increases after this point. That is, the maximum elongation of the adhesive appears to be larger than the value derived from the adjusted curve. However, as soon as the maximum value of J is reached, J starts to decrease. This is not the case in the simulation. This can be attributed to the formation of a sharp crack within the adhesive layer when the crack starts to propagate. However, no recording of the start of crack propagation is done in these experiments.
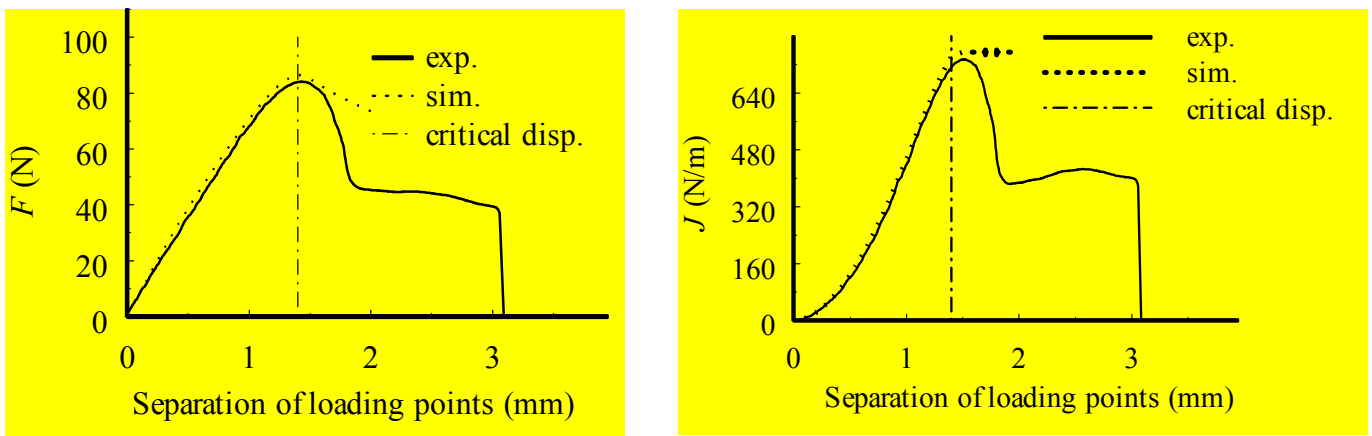

Figure 4: a) force vs. separation of loading points as recorded from a typical experiment and simulation; b) $J_{applied}$ vs. separation of loading points

Figures 5 show force vs. elongation and rotation vs. elongation respectively. Both curves agree well with the simulations, though one curve is consistently below and the other consistently above the experimental result.

The use of the present method is critically dependent on the assumption of a unique stress-elongation relation for the adhesive. This is not a realistic assumption for an adhesive; unloading from a severely deformed state is likely to take place along another path than the curve shown in Figure 2b. However, if the

adhesive experiences monotonically increasing or decreasing elongation during an experiment then the difference between a unique stress-elongation curve and the true one is without significance.
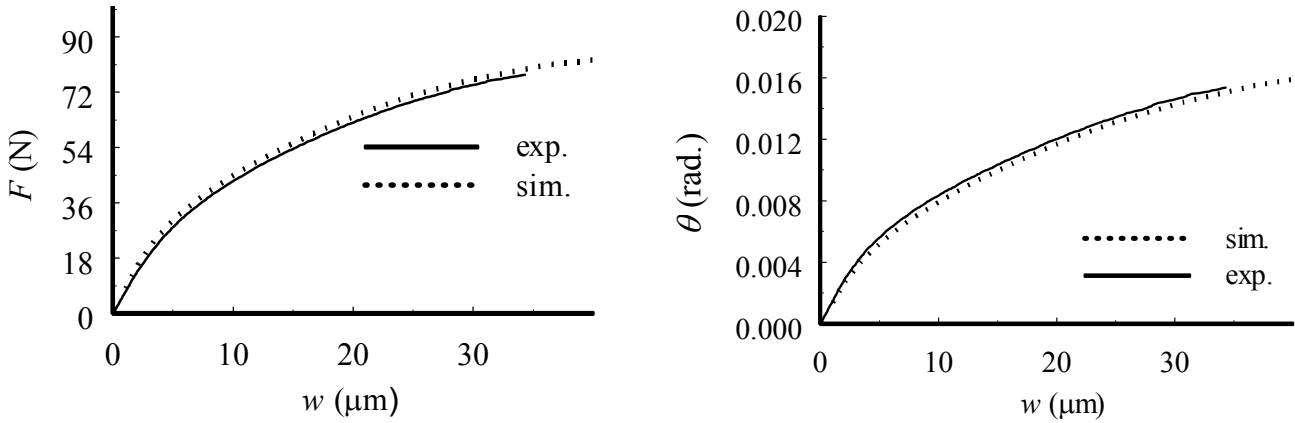

Figure 5: a) force vs. elongation; b) loading point rotation vs. elongation.

Figure 6 shows the elongation of the adhesive at consecutive points along the adhesive layer, the distance between the points is 2.3 mm. The first curve shows the elongation at the start of the layer. This part of the adhesive experiences a monotonically increasing elongation, as should be expected. Elements of the adhesive further inside the layer first experiences a compression, which is later followed by an elongation. The initial compression is understood from the well-known solution for a beam on an elastic foundation.
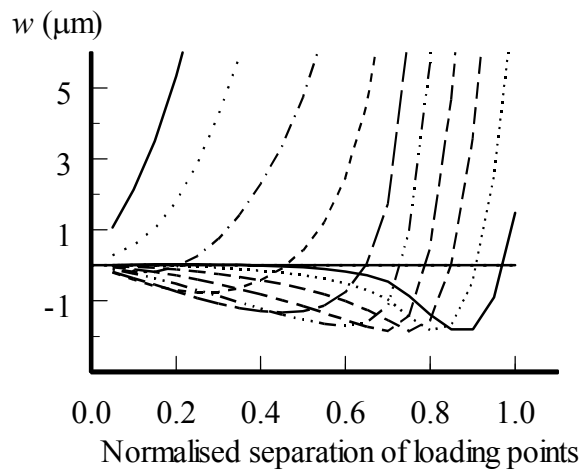

Figure 6: Elongation vs. normalised separation of loading points of different point of the adhesive according to simulation. Normalisation relative to the value corresponding to splitting of specimen.

The maximum compression of any element of the layer does not exceed 2 μm which corresponds to $\sigma_0 = 19.6$ MPa. Thus, no inelastic deformation is expected at any part of the layer before it starts to elongate. Moreover, no element of the adhesive experiences unloading from an elongated state before a crack starts to elongate. Thus, the use of a unique stress-elongation relation in the theoretical basis for the method is consistent with the results of the simulations.

The maximum beam bending stress from the simulations does not exceed 270 MPa. Considering the low peel stress (about 20 MPa) by which the adhesive affects the adherends it can be conclude that no plastic deformation takes place in the beam elements.

The influence of anticlastic bending is studied using the elementary beam bending theory, see [11]. Since the peel stress from the adhesive is small, its influence is neglected. The cross section of the lower beam is shown in Figure 7. The displacement u is given by

$$u(x,y) = -v\frac{x^2 - y^2}{2R} \tag{2}$$

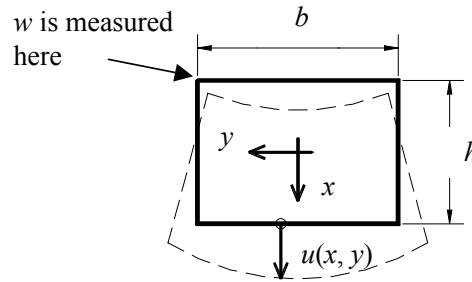where R is the radius of curvature of the beam given by $R = EI/M = EI/FL_1$.

Figure 7: Cross section of lower beam

The difference between u at the surface and at the interior is then given by

$$\delta = u\left(-\frac{h}{2}, \frac{b}{2}\right) - u\left(-\frac{h}{2}, 0\right) = \frac{vb^2}{8R} = \frac{4vbFL_1}{3Eh^3} \tag{3}$$

The total contribution to the separation w is 2δ. With the maximum force $F = 100$ N the maximum displacement $2\delta_{max} = 0.68$ μm is obtained. Comparing with the corresponding value of $w = 60$ μm the error is less than 1 %. Thus, it is possible to neglect the influence of anticlastic bending.

REFERENCES

1. Stigh, U. (1987). In: *Mechanical behaviour of adhesive joints*, pp 237-248, Verchery, G. and Cardon, A.H. (Eds.). Editions Pluralis, Paris, France.
2. Stigh, U. (1988). *International Journal of Fracture*, **37**, R13.
3. Alfredsson, K. A. and Stigh, U. (1997). In: *Advances in Fracture Research – Proceedings of ICF9*, pp. 2667-2674, Karihaloo, B. L., Mai, Y.-W., Ripley, M. I. and Ritchie, R. O. (Eds.). Pergamon, Amsterdam.
4. Stigh, U. and Andersson, T. (2000). In: *Fracture of polymers, composites and adhesives, ESIS Publication 27. Proceedings of the 2ndESIS Conference*, Williams, J. G. and Pavan, A. (Eds.), Elsevier, Amsterdam.
5. Olsson, P. and Stigh, U. (1989). *International Journal of Fracture*, **41**, R71.
6. Eshelby, J. D. (1951). *Phil. Trans. R. Soc. London* **A244**, 87.
7. Rice, J. (1968). *Journal of Applied Mechanics* **35**, 379.
8. Andersson, T. (1998). MSc thesis, University of Skövde.
9. Tvergaard, V. and Hutchinson J.W. (1992). *Journal of the Mechanics and Physics of Solids*, **40**, 1377.
10. Yang *et al.* (1999). *Journal of the Mechanics and Physics of Solids*, **47**, 1337.
11. Goodier, J.N. and Timoshenko, S.P. (1970). *Theory of Elasticity*, McGraw-Hill, Singapore.

VIBRATIONS OF A CROSS-PLY CERAMIC MATRIX COMPOSITE BEAM WITH MATRIX CRACKS IN LONGITUDINAL AND TRANSVERSE LAYERS

V. Birman[1] and L.W. Byrd[2]

[1]University of Missouri-Rolla, Engineering Education Center
8001 Natural Bridge Road, St. Louis, MO 63121, USA
[2]Air Force Research Laboratory, AFRL/VASM, Bldg. 65, 2790 D Street
Wright-Patterson Air Force Base, OH 45433-7531, USA

ABSTRACT

The paper illustrates the effect of matrix cracks in longitudinal and transverse layers of a cross-ply ceramic matrix beam (CMC) on its stiffness and vibration frequencies. Even if vibration amplitudes are small, the physical nonlinearity is introduced by the interfacial fiber-matrix friction in the vicinity of matrix cracks in the longitudinal layers. A closed-form solution for mechanical properties of a cross-ply beam with matrix cracks is developed in the paper. The frequency of free vibrations of a simply supported beam is derived as a function of the amplitude, accounting for the effect of matrix cracks. The conclusions that follow from the numerical analysis enable us to suggest a simple and accurate design formula for the fundamental frequency.

KEYWORDS

Ceramic matrix composites, matrix cracks, vibrations, physical nonlinearity, bimodular material.

INTRODUCTION

As follows from observations of a matrix crack development in cross-ply beams, cracks appear in transverse layers at a relatively low load [1]. These cracks, called tunneling cracks, are perpendicular to the load direction and parallel to the fibers of the corresponding layer. As the load increases, the crack density increases as well, until the tunneling cracks reach saturation. After saturation, the density of tunneling cracks remains constant under increasing load.

As the load continues to increase, cracks begin to develop in longitudinal layers where they are perpendicular to the fibers. The cracks approaching the fiber-matrix interface can break the fiber or pass it and continue their propagation in the matrix. The cracks propagating in the matrix of a longitudinal layer, without breaking the fibers, are called bridging cracks. Such cracks represent a typical mode of damage in CMC.

The density of cracks in transverse layers is often different than that in longitudinal layers. For example, Erdman and Weitsman [2] reported measurements of the matrix crack density in cross-ply SiC/CAS composites. Dependent on the lay-up, the saturation density in transverse layers varied between 20 and 40 cracks/inch. However, the saturation density in longitudinal layers was between 122 and 238 cracks/inch.

This illustrates that the analysis should not be conducted by assumption that the densities of cracks in transverse and longitudinal layers are identical.

ANALYSIS

The analysis utilizes the following assumptions.
1. During the first phase of the initial quasi-static loading cracks in transverse layers have reached saturation.
2. Continued loading of the beam resulted in cracking of longitudinal layers that occurred without further changes in the stiffness of transverse layers.
3. Cracks in longitudinal and transverse layers remain open during the tensile part of the cycle of motion. Under compression, the cracks in all layers are closed.
4. The mode shape of vibration of the beam is not affected by damage.
5. Energy dissipation due to damping, interfacial friction, thermoelastic effect, and closing and opening of the cracks is disregarded.

The solution for the stiffness of a cross-ply CMC beam with matrix cracks in longitudinal and transverse layers is based on the theories of Han and Hahn for a cross-ply material with cracks limited to transverse layers [3] and Pryce and Smith for a unidirectional material with bridging matrix cracks [4]. In particular, the stiffness of a cross-ply material where tunneling cracks in transverse layers reached saturation, while longitudinal layers are still intact is [3]:

$$E' = E_i[1 + (h_l/\xi s_T)(E_T/E_L)\tanh(\xi s_T/h_l)]^{-1} \tag{1}$$

where s_T is a crack spacing (saturation spacing, in this case), h_l is a layer thickness, E_L and E_T are the longitudinal and transverse moduli of elasticity of a layer, $E_i = (E_L + E_T)/2$ is the composite modulus of the intact material, and ξ is a shear lag parameter. Note that the modulus given by (1) is used for the analysis of vibration cycling, when the cracks already exist. Accordingly, residual thermal stresses do not affect this modulus.

Once the value of E' has been determined, the modulus of the transverse layers can be obtained as $E_T' = 2E' - E_L$. The modulus of transverse layers remains unaffected by the stress during cycling, as long as the cracks remain open, i.e. the material is subject to tension. Under compression, the cracks are closed and $E_T' = E_T$ corresponds to the modulus of the intact material.

The average modulus corresponding to reverse fatigue loading of a unidirectional CMC lamina with bridging matrix cracks and the stress varying from zero to a maximum value was given in [5], based on the model of Pryce and Smith [4]:

$$E_L' = \tau[\tau/E_L + (r/4s_L)(\Delta\sigma_L/E_f)(V_mE_m/V_fE_L)^2]^{-1} \tag{2}$$

In (2), τ is an interfacial shear stress, r is the fiber radius, s_L is the matrix crack spacing in longitudinal layers, $\Delta\sigma_L$ is the range of stresses applied to the longitudinal layer, E_f and E_m are the moduli of fibers and matrix, respectively, and V_f and V_m are the volume fractions of the fibers and matrix, respectively.

Residual thermal stresses do not affect the average modulus E_L', as can easily be shown using the solution [4]. The interfacial shear stress decreases with cycling due to wear, as was shown by Holmes and Cho [6]. Other factors, such as lubrication, strain rate, and temperature have also been shown to affect this stress. However, during small-amplitude steady state vibrations, the changes of the factors affecting the interfacial stress are slow. Accordingly, the value of the interfacial stress during one cycle may be assumed constant. Equation (2) was obtained by assumption of a partial slip along the fiber-matrix interface during cycling, as can be expected in the case of small-amplitude vibrations. The limits of applicability of this equation are specified in [4].

The range of stresses acting in the longitudinal layer can be determined keeping in mind that the average stiffness of transverse layers remains constant during the tensile part of the vibration cycle. Accordingly, the ratio between the stress ranges in adjacent longitudinal and transverse layers is

$$\Delta\sigma_L/\Delta\sigma_T = E_L'(\Delta\sigma_L)/E_T' \tag{3}$$

where E_T' is constant. At the same time, the range of the applied composite stress is

$$\Delta\sigma = (\Delta\sigma_L + \Delta\sigma_T)/2 \tag{4}$$

Solving (3) and (4) together with (2), it is possible to obtain the stress range $\Delta\sigma_L$ and the average modulus for the longitudinal layers E_L' as functions of the range of the applied composite stress $\Delta\sigma$. Then the average composite modulus of the material with matrix cracks in both longitudinal and transverse layers, $E = E(\Delta\sigma)$, is available as $E = (E_L' + E_T')/2$. This modulus remains constant during the tensile part of the cycle when the stress varies from zero to a maximum value. During the compressive part of the cycle the modulus $E_L' = E_L$, according to (2). Physically this is justified since the crack closing strain could be estimated as a ratio of the crack opening displacement to the crack spacing. This ratio is small and it may be assumed equal to zero.

Consider now a nonlinear relationship between the range of the applied stresses and the range of strains for the section of a cross-ply CMC beam with matrix cracks that is subject to tension during reversed bending. The permanent offset strain that remains in the material after removal of the load that caused cracking does not explicitly affect the average modulus of elasticity during the motion. However, the effect of preloading is incorporated in the solution via the matrix cracks spacing. As shown above, we can determine the modulus E as a nonlinear function of the applied stress range $\Delta\sigma$. Subsequently, it is possible to find the corresponding strain range $\Delta\varepsilon = \Delta\sigma/E(\Delta\sigma)$.

It is necessary to characterize the curve $E = E(\Delta\varepsilon)$ by an analytical expression that can be used in the frequency analysis. For example, as shown below, the following function was in an excellent agreement with numerical results:

$$E_a = E_c + a\Delta\varepsilon + b\Delta\varepsilon^n \tag{5}$$

where E_c is the modulus of the damaged material subjected to a negligible tensile strain that does not affect the modulus of longitudinal layers, a and b are constants that have to be determined and n is an integer. Note that E_c in (5) is independent of the crack density in longitudinal layers. This is because the modulus of elasticity of longitudinal layers with bridging cracks based on the model of Pryce and Smith [4] is affected by the crack density only in the presence of applied stress. Physically, this model is justified since opening a crack in a longitudinal layer requires a tensile force to overcome friction along the damaged section of the fiber-matrix interface.

The solution for small-amplitude vibrations of a simply supported cross-ply CMC beam with matrix cracks in longitudinal and transverse layers is obtained by the energy method, based on the assumption that the energy dissipation is negligible. Accordingly, in the case of harmonic vibrations, the squared frequency is obtained from

$$\omega^2 = U_{max}/T_{max} \tag{6}$$

where U and ω^2T are the strain and kinetic energies, respectively.

The evaluation of the maximum value of the strain energy is complicated due to the fact that the modulus of elasticity varies throughout the depth and the length of the beam. As explained above, if the dynamic strains are compressive, the modulus of the material remains constant and equal to E_i. Therefore, the cross-ply beam material behaves in a manner that resembles a nonlinear material of "bimodular" type, though in the

present problem the response is more complicated since the material exhibits physical nonlinearity during the tensile part of the cycle but retains constant stiffness under compression.

The location of the neutral curve of the beam can be determined from $z_n = B/A$ where A and B are extensional and coupling stiffnesses, respectively. For example, if the section, $z_n < z < h/2$, of a unit-width beam of thickness h is subject to tension and the crack densities in both the longitudinal and transverse layers are independent of the thickness z-coordinate, these stiffnesses become

$$\{A,B\} = \int_{z_n}^{h/2} [E_c + a\Delta\varepsilon(z) + b\Delta\varepsilon(z)^n]\{1,z\}dz + \int_{-h/2}^{z_n} E_i\{1,z\}dz \qquad (7)$$

Note that $\Delta\varepsilon$ at each location is equal to the maximum dynamic strain achieved during the cycle. Given the value of $\Delta\varepsilon_{max} = \Delta\varepsilon(z=h/2)$, it is possible to obtain the local dynamic strain range as

$$\Delta\varepsilon(z) = [(z-z_n)/(h/2 - z_n)]\Delta\varepsilon_{max} \qquad (8)$$

Therefore, it is possible to determine z_n, as long as $\Delta\varepsilon_{max}$ is prescribed.

Now the maximum strain energy can be evaluated as $U_{max} = U_t + U_c$ where two components in the right side correspond to the contribution of the parts of the beam cross section subject to tension and compression, respectively. In the following analysis, the cracks are assumed uniformly distributed along the beam. Then the neutral curve becomes the neutral axis, i.e. z_n is independent of the axial coordinate. The maximum kinetic energy of the beam is readily available since it is not affected by cracks.

The analysis is carried out assuming that the mode shape of vibrations is unaffected by damage (assumption 4). Then the squared nondimensional frequency is the following nonlinear function of the amplitude of free vibrations (W):

$$F^2 = f_0 + f_1 W + f_n W^n \qquad (9)$$

where f_0, f_1 and f_n are constants dependent on geometry, material, and damage and F is the ratio of the natural frequency of the damaged structure to that of the intact beam.

The position of the neutral axis can be found evaluating the extensional and coupling stiffnesses in terms of z_n. A quadratic equation for $Z_n = z_n/h$ is

$$n_2 Z_n^2 + n_1 Z_n + n_0 = 0 \qquad (10)$$

where n_i (i = 0, 1, 2) are functions of a, b, E_c, E_i and the strain range $\Delta\varepsilon_{max}$ (these functions are omitted here for brevity).

NUMERICAL EXAMPLES AND DISCUSSION

The material considered in the following examples is SiC/CAS with the following properties [7]: $E_f = 200$ GPa, $E_m = 97$ GPa, r = 8 μm, τ = 5 MPa, $V_f = 0.35$. The layer thickness adopted in these examples is 125 μm. The longitudinal and transverse moduli of this material are $E_L = 133$ GPa and $E_T = 118$ GPa, respectively. The transverse shear modulus that is needed to calculate the shear lag parameter was taken equal to 45 GPa. It should be noted that a relatively low value of the interfacial shear stress is adopted here to reflect the experimentally observed fact that these stresses decrease during vibrations due to a gradual smoothening of the fiber-matrix interface [6].

The ranges of stresses in longitudinal and transverse layers differ significantly, as the range of the applied composite stress increases, as follows from Figure 1. A difference between these ranges increases if the matrix crack spacing in longitudinal layers becomes larger. This is predictable since if damage in the longitudinal layers is relatively small, they absorb a larger fraction of the applied load.

Relationships between the composite modulus and the modulus of longitudinal layers and the range of the composite strain are shown in Figure 2. As follows from these results and other cases not presented here due to the space limitation, a very accurate approximation of the relationship $E = E(\Delta\varepsilon)$ can be obtained from equation (5) using $n = 2$. The coefficients a and b in equation (5) are listed in Table 1 for various matrix crack spacings in the longitudinal layers. These coefficients appeared insensitive to the matrix crack spacing s_T. However, the modulus E_c varied dependent on this spacing. The nonlinear quadratic representation of the composite modulus-applied strain relationship is very accurate. Maximum deviations of equation (5) with $n = 2$ and the coefficients listed in Table 1 from the actual curves were under 1%. It is also evident from Table 1 that the quadratic term in (5) is negligible when the strain range is small. This is reflected in Figure 2 where the composite modulus is almost a linear function of the range of the applied strain.

The changes in the position of the neutral axis due to a large strain were very small, not exceeding 5%, even as the tensile strain on the beam surface $z = h/2$ reaches 1%. This results in an important conclusion that it is possible to assume that the position of the neutral axis is unaffected by the strain. Accordingly, this position can be calculated from a simplified version of (10) that is simplified even more due to the observation that the quadratic term has little effect on the value of Z_n. Therefore, given the values of E_c and E_i, one can determine the position of the neutral axis from

$$Z_n = -(1/4)(1 - E_n)/(1 + E_n) \tag{11}$$

The analysis of (9) with $n = 2$ illustrates that the effect of the amplitude of motion on the frequency is negligible. Then the nondimensional fundamental frequency is available form the simplified version of (9):

$$F^2 = [(1 + 2Z_n)^3 + E_n(1 - 2Z_n)^3]/2 \tag{12}$$

The master curves are shown in Fig. 3. These curves can be convenient for the analysis of small-amplitude vibrations of cross-ply CMC beams with matrix cracks in longitudinal and transverse layers.

ACKNOWLEDGEMENT

REFERENCES

1. Beyerle, D.S., Spearing, S.M. and Evans, A.G. (1992). *J. Amer. Ceramic Society*, 75, 3321.

2. Erdman, D.L. and Weitsman, Y. (1998). *International Journal of Solids and Structures*, 35, 5051.

3. Han, Y.M. and Hahn, H.T. (1989). *Composites Science and Technology*, 35, 377.

4. Pryce, A.W. and Smith, P.A. (1993). *Acta Metallurgica et Materialia*, 41, 1269.

5. Sorensen, B.F. and Holmes, J.W. (1996). In: *Fatigue under Thermal and Mechanical Loading*, pp. 487-499, Bressers, J. and Remy, L. (Eds). Kluwer Academic Publishers, Dordrecht, Netherlands.

6. Holmes, J.W. and Cho, C. (1992). *J. Amer. Ceramic Society*, 75, 929.

7. Birman, V. and Byrd, L.W. (2001). *Composite Structures*. In press.

Table 1: Coefficients (a, b) in equation (5) obtained using n = 2

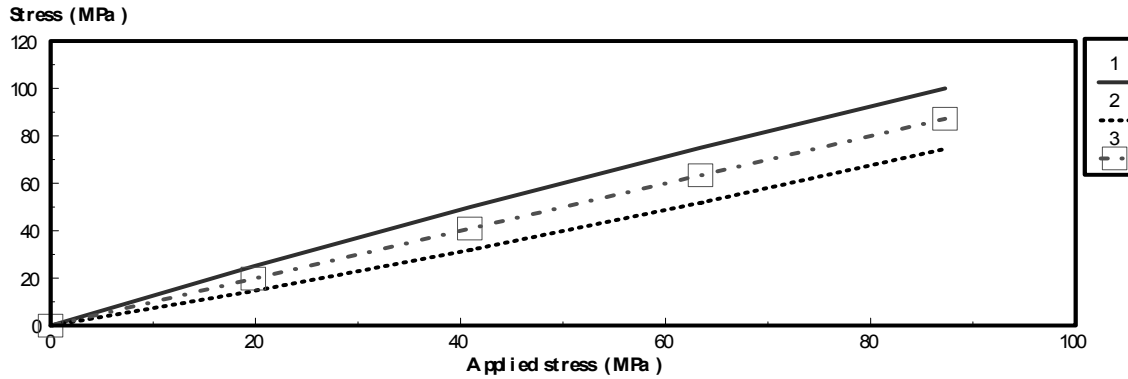| s_L (μm)	125	250	500
a, b (GPa)	-268.83, 940.07	-153.0, 428.45	-81.46, 151.67

Figure 1: Relationships between the range of the applied composite stress (3) and the range of stress in longitudinal (1) and transverse layers (2) for the case where $s_L = 0.125$ mm and $s_T = 0.250$ mm.
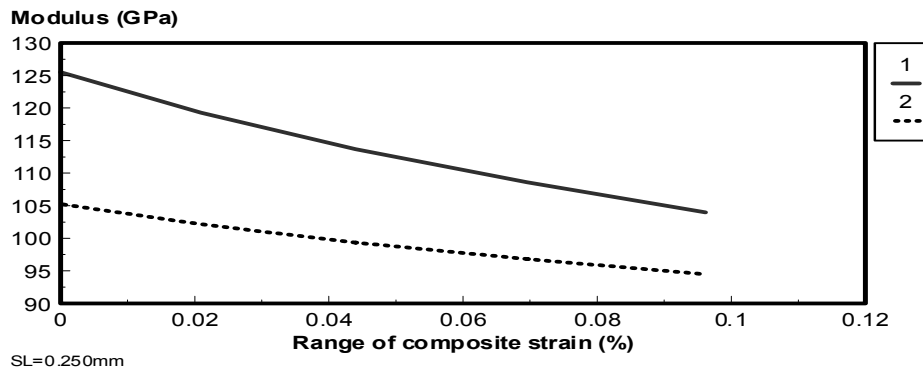

Figure 2: Relationships between the modulus of longitudinal layers (1) and the composite modulus (2) and the range of composite strain ($s_L = 0.250$ mm, $s_T = 0.500$ mm).
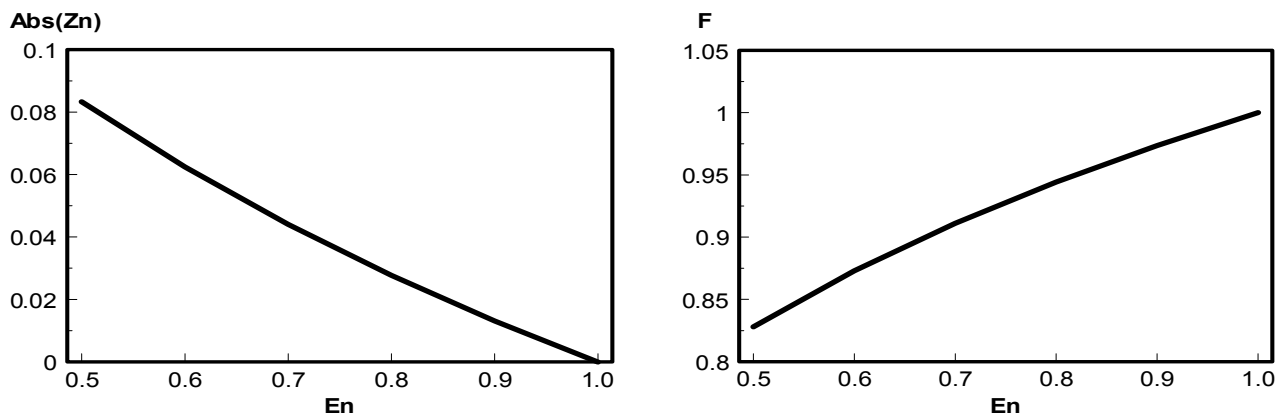

Figure 3: "Master curves" representing the nondimensional location of the neutral axis (left figure) and the nondimensional fundamental frequency, i.e. a ratio of the frequency of the beam with cracks to that of the intact beam, (right figure) as functions of the nondimensional stiffness of the beam ($E_n = E_c/E_i$).

VIBRODIAGNOSTICS OF FATIGUE CRACKS
IN CYLINDER SHELLS

A. B. Roytman and O. A. Titova

Department of Applied Mathematics, Zaporozhye State University, Ukraine

ABSTRACT

The experimental-theoretical method of vibrodiagnostics of "breathing" cracks in cylinder shells is offered. By "breathing" crack, we understand the following. In the first of the semicycles of oscillations fibers with the crack are compressed, the crack is closed and the crack's influence is neglected. In the second semicycle of oscillations the fibers with the crack are stretched the crack is open and the shell's thickness being under stretching is decreased by crack's depth. The offered method is based on registration of a modification of frequency of a signal. The method is convenient for units of constructions, in which it is possible to rather easily excite oscillations bringing the material of shell in a state of tension - squeezing. The analytic model of oscillations of a cylinder shell with a "breathing" crack is constructed. The shape of oscillations is picked depending on an aspect of a crack, its orientation and location on the shell. The diagnostic function permitting approximately to define depth of a crack depending on its location and parameters a shell is constructed.

KEYWORDS

Vibrodiagnostics, Fatigue Crack, Cylinder Shell, Oscillations, Diagnostic Function.

INTRODUCTION

The units of modern constructions, for example aerospace constructions, work in rather heavy duties. As a result, during the oscillations there may be observed fractures that are preceded by formation of cracks caused by vibrations of details.

The restricted number of researches is devoted to problems of calculation of a stressedly-deformed state and diagnostics of cracks in elements construction[1 - 3]. In this connection the problems of diagnostics of cracks in shells remain actual.

The researches are developed in directions of practical application (aerospace engineering, atomic engineering, construction of pipelines, sea drilling platforms, shipbuilding, etc). The problem of finding the reliable criteria of damage estimation is of particular interest.

The paper [4] represents the set of indicators of damages (diagnostic functions), which can be used for diagnostics of cracks in units of machine-building constructions, with the definition of their advantages and disadvantages. In the paper more than one hundred papers devoted to this subject are surveyed. The following basic types of indicators are considered : 1. Natural frequencies, 2. The modal forms, 3. Damping, 4. Resonant frequencies, 5. Amplitudes of oscillations, 6.

Transitional or superharmonic indicators, 7. Forced oscillations, 8. Phase curves. The method of natural frequencies is regarded the most acceptable for measuring with a rather high level of accuracy.

The damages of such a type were presumably the cause of catastrophes of the first jet passenger planes and atomic submarines. The cracks were a corollary of low-cycle fatigue. During each take-off (immersion) at considerable height (depth) a fuselage of the plane or hull of a submarine were essentially deformed in comparison with a state on ground (sea level). The complexity of diagnostics of such cracks is caused by that in a unloaded state the cracks it are not discovered, and "are uncovered" only at take-off (immersion) on considerable height (depth).

In the present paper the experimental-theoretical method of vibration diagnostics of "breathing" cracks of cylinder shells is offered.

BODY OF PAPER

The solution of the problem of free oscillations of the circular cylinder shells without the crack is the function [5]:

$$w = C_{m,n} \sin \frac{x m \pi}{l} \cos n \varphi \cos \omega t. \tag{1}$$

Here m - number of half-waves in the longitudinal direction, n - number of waves in the transverse direction, the axis x is directed along the symmetry axis of the median surface of shell, l - length of the shell, t - time of the oscillations. The model of shell is presented on Figure 1.

The parameters of oscillations of such shell can be found with the help of the energy method. It is supposed, that the system is conservative and that is $K + \Pi = const$, where K and Π - kinetic and potential energy of oscillations of shell respectively. In the process of oscillations the shell transits some positions, at one of which $K = K_{max}$, $\Pi = 0$, and at the second - $K = 0$, $\Pi = \Pi_{max}$. Then $K_{max} = \Pi_{max}$. Using last equality we shall find the frequency of oscillations of the cylinder shell without the crack.

By reviewing oscillations of shell we count, that $m = 1$, $n = 0$ in a case, when it has a circular transversal crack at $l/2$, whose depth is much less than half of width of shell (Figure 2), and $m = 1$, $n = 2$, when it has a longitudinal crack (Figure 3).

By reviewing oscillations of a cylinder shell with other configuration of the crack it is necessary to select other form of oscillations, more convenient, for example tortional form of oscillations for the crack, which is located at angle on the surface of shell.
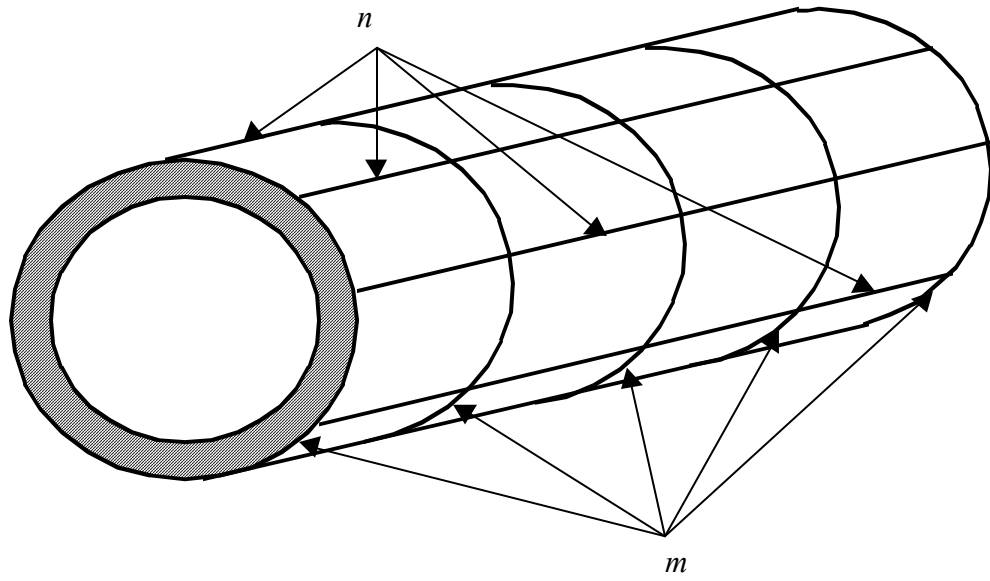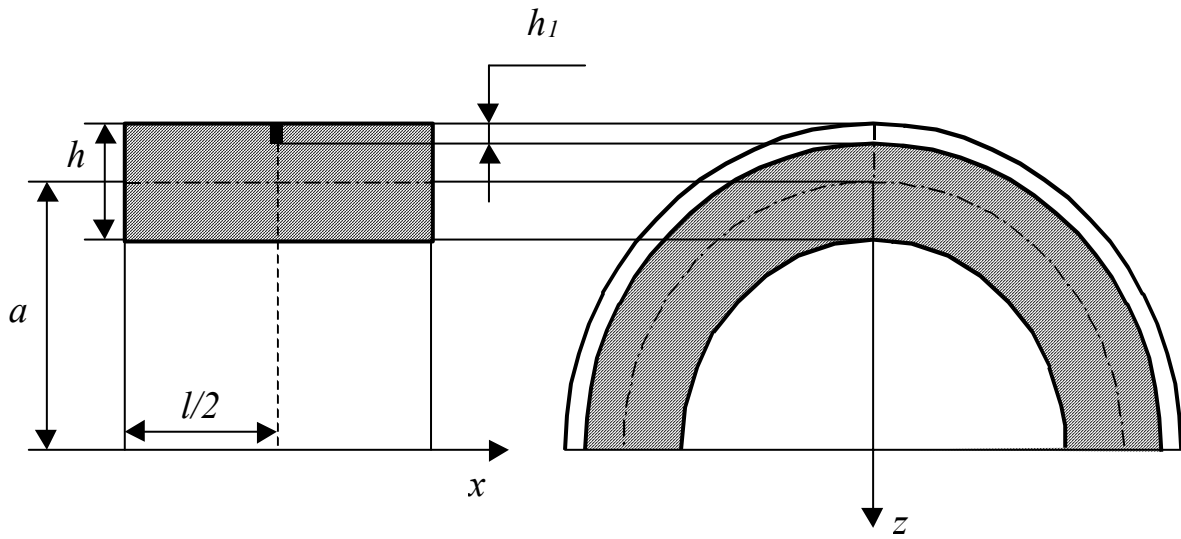
Figure 1: The modes of vibration of shell
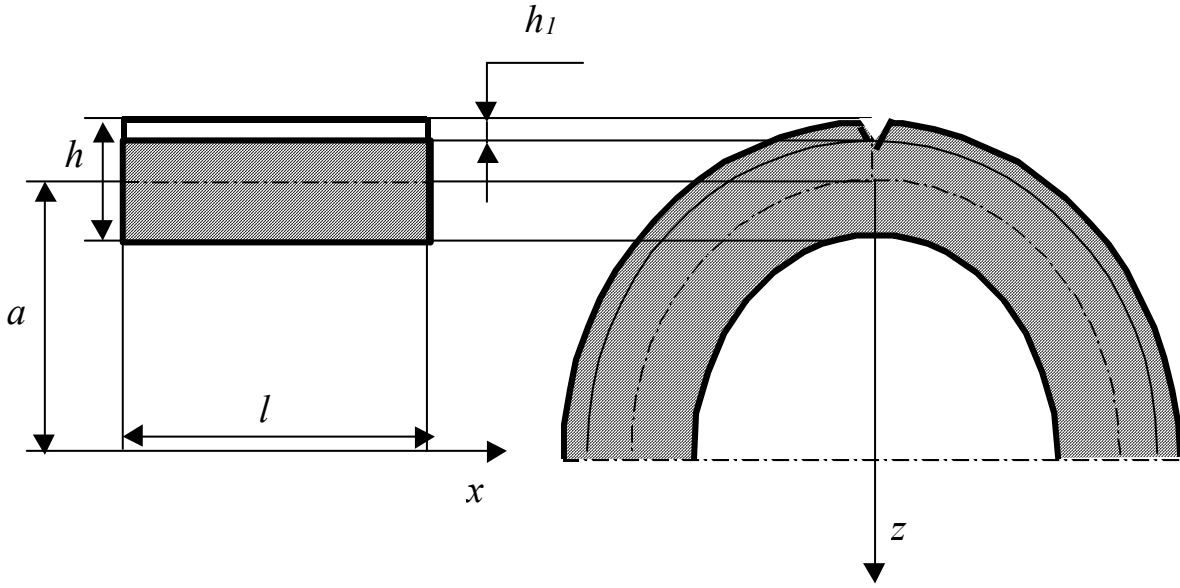

Figure 2: The shell with transversal crack

Figure 2: The shell with longitudinal crack

The oscillations of the shell start at the moment when the load acting on the shell is removed. The crack is closed and does not influence the process of oscillation. Further shell reaches a neutral position, the crack opens up to the maximum value, starts to close and the shell transits neutral and achieves an initial position.

It is supposed, that two frequencies will appear in period of oscillations cycle T: ω_0, corresponding to the closed crack, and ω_1, corresponding to the open crack. The period of oscillations is written as follows [2, 5]:

$$T = \frac{\pi}{\omega_0} + \frac{\pi}{\omega_1} = \frac{\pi(\omega_1 + \omega_0)}{\omega_1 \omega_0}. \tag{2}$$

The oscillations will transit with the averaged frequency $\overline{\omega} = \dfrac{2\pi}{T} = \dfrac{2\omega_1\omega_0}{\omega_1 + \omega_0}$. In this case w is possible to be written as follows:

$$w = \begin{cases} A_0 \sin\dfrac{\pi x}{l} \cos\omega_0 t, & 0 \le t \le \dfrac{\pi}{2\omega_0}, \text{the crack is closed,} \\[2ex] A_1 \sin\dfrac{\pi x}{l} \cos\omega_1\left(t + \dfrac{\pi}{2\omega_1} - \dfrac{\pi}{2\omega_0}\right), & \dfrac{\pi}{2\omega_0} < t \le \dfrac{\pi}{2\omega_0} + \dfrac{\pi}{\omega_1}, \text{the crack is opened,} \\[2ex] A_0 \sin\dfrac{\pi x}{l} \cos\left(t + \dfrac{\pi}{\omega_0} - \dfrac{\pi}{\omega_1}\right), & \dfrac{\pi}{2\omega_0} + \dfrac{\pi}{\omega_1} < t \le T, \text{the crack is closed,} \end{cases} \tag{3}$$

where A_0 - amplitude of oscillations of shell on the semicycle with the closed crack, A_1 - on the semicycle with the closed crack.

With the help of the energy method we can find the frequency ω_1. For this purpose it is necessary to remove the material of shell, in which the elastic energy of deformation is absent. Using the energy method we can find amplitude A_1 and A_0.

As analytical indicators of cracks it is possible to consider the following diagnostic functions: ω_0/ω_1 and A_1/A_0.

The graphs of the ratios of frequencies and amplitudes of oscillations depending on relative depth of the crack are showed on Figure 4.
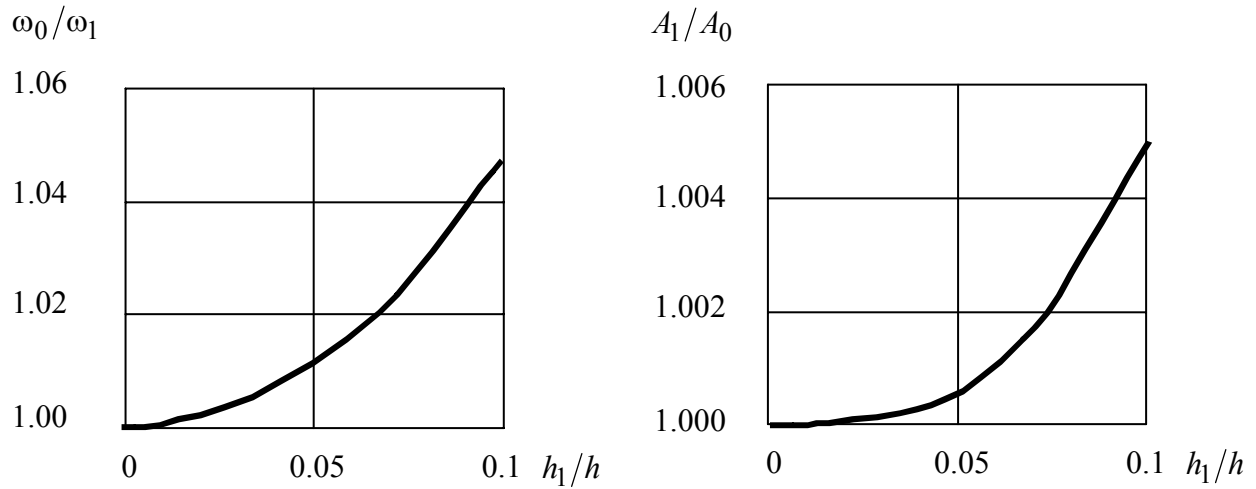

Figure 4: The graphs of the ratios of frequencies and amplitudes of oscillations depending on relative depth of the transversal crack

The function (3) in a Fourier series is decomposed:

$$w(x,t) = \frac{a_0}{2} + \sum_{k=1}^{n}(a_k \cos k\overline{\omega}t + b_k \sin k\overline{\omega}t),$$ (4)

In this case indicator of the crack can be diagnostic function, which characterizes the ratio of amplitude k-harmonic, which is exhibited at presence of the crack, to amplitude of the first harmonic:

$$d_k = \frac{\sqrt{a_k^2 + b_k^2}}{\sqrt{a_1^2 + b_1^2}} = \left|\frac{a_k}{a_1}\right|$$ (5)

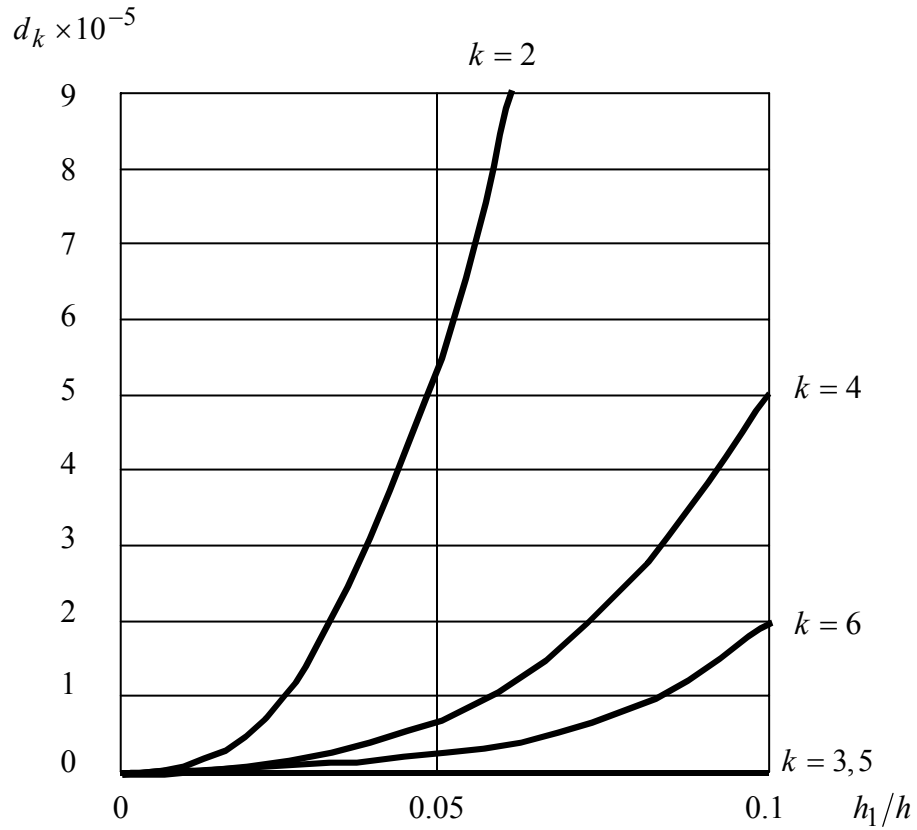The graphs of functions (5) for transversal cracks are shown in the Figure 5.

Figure 5: The graphs of functions (5) for transversal crack

REFERENCES

1. Bovsunovsky, A.P. and Matveev, V.V. (2000) *Journal of Sound and Vibration* 235(3), pp. 415-434.
2. Roytman, A.B., Pylov, A.A. and Aleksandrova, N.B. (1999) *Strength of Materials* 31, pp. 23-34.
3. Boltezar, M. , Strangar, B. and Kunelj, A. (1998) *Journal of Sound and Vibration* 211(5), pp. 729-734.
4. Krawczuk, M. and Ostachowicz, W. (1996) *Journal of Theoretical and Applied Mechanics* 34, pp. 307-326.
5. Roytman, A.B., Shamrovsky, A.D. and Titova, O.A. (2000) *Proceedings of the International Conference "Mechanika-2000"*, Kaunas, Litvenia.